Derivation of Forest Productivity and Structure Attributes from Remote Sensing Imaging Technology

by

Geoffrey S. Quinn
B.A., Brock University, 2004
MSc., The University of Victoria, 2010

A Dissertation Submitted in Partial Fulfillment
of the Requirements for the Degree of

DOCTOR OF PHILOSOPHY

in the Department of Geography

© Geoffrey Stewart Quinn, 2018
University of Victoria

All rights reserved. This dissertation may not be reproduced in whole or in part, by photocopy or other means, without the permission of the author.

Derivation of Forest Productivity and Structure Attributes from
Remote Sensing Imaging Technology

by

Geoffrey S. Quinn
B.A., Brock University, 2004
MSc., The University of Victoria, 2010

Supervisory Committee

Dr. K. Olaf Niemann, Supervisor
Department of Geography

Dr. Cosmin N. Filipescu, Departmental Member
Department of Geography

Dr. Fred Wrona, Department Member
Department of Geography

Dr. Barbara Hawkins, Outside Member
Department of Biology

Abstract

There are considerable expenditures by government and private forest industry to enhance the growth of forests and reduce time required for crop rotation. The effectiveness of some of these treatments is dependent on site productivity. In addition, as responsible stewards of the forest resource and habitat, it is important that the state of forests are actively monitored, especially in the face of a changing climate and increased rates of disturbance. This dissertation reports on the development of a method for estimating and mapping forest productivity.

The Shawnigan Lake thinning and fertilization forest installation, established in 1971 by CFS, was selected as the study site largely for its rich mensuration history. Square treatment plots were 0.04ha in area and included two thinning levels (1/3 & 2/3 of the basal area), two fertilization treatments (224kg & 448kg N/ha) with repeated fertilizations and macronutrient experiments (S, P) and control plots. A sample of plots was selected for high precision ground based lidar reference surveys. In September of 2012 a multi-sensor airborne survey of SLP was conducted that collected high-density lidar (up to ~70pnts/m^2) and VNIR imaging spectroscopy. A thorough empirical radiometric calibration was conducted in addition to a spatial calibration at the Victoria International Airport.

A combination of area based height percentile, point density ratios and statistical moments with individual lidar tree metrics including height distribution and proximity metrics were generated. Topographic metrics were also generated from the lidar ground classified point cloud. A library of spectral indices was computed from the imaging spectrometer data, with an emphasis on those indices known to be associated with vegetation health. These metrics were summarized to the plot level for a coarse scale regression analysis. A control survey and ground based lidar was used to facilitate an individual tree based fine scale of analysis, where reference data could unambiguously be matched to airborne collected data through the projected positions.

Regression analysis was conducted applying the best subset regression with exhaustive feature selection search criteria and included a critical evaluation of the resulting selected features. Models were investigated considering the data source and in combination, that is, lidar metrics were considered independent of spectroscopy as well as the converse, and lidar metrics in combination with spectral metrics.

The contribution of this study is the revelation that existing area based point cloud metrics are highly correlated, potentially noisy and sensitive to variations in point density, resulting in unstable feature selection and coefficients in model building. The approach offered as an alternative is the gridded lidar treetops method, which is evidently lacking within the literature and which this study overwhelmingly advocates. Additionally, the breadth and diversity of metrics assessed, the size and quality of the reference data applied, and the fine spatial scale of analysis are unique within the research area. This study also contributes to the knowledge base, in that, productivity can be estimated by remote sensing technologies. The use of gridded generalizations of the individual tree approach reduced estimation errors for both structural and productivity attributes. At the plot-level, crown structure and crown health features best estimated productivity. This study emphasizes the dangers of empirical modeling; at the even-aged SLP installation, growth is strongly tied to structure and the extrapolation to other sites is expected to provide biased values. It is my perspective that physical lidar structural models of the dominant and co-dominant crown classes be used to augment spatially explicit tree and stand growth models. In addition, direct measures should be obtained by multi-temporal lidar surveys or as an alternative photogrammetric point clouds after an initial lidar survey to quantify growth and aid in calibrating growth models.

Table of Contents

Supervisory Committee ii
Abstract iii
List of Tables vi
List of Figures vii
List of Acronyms xxiv
Dedication xxvi
Acknowledgements xxvii

CHAPTER 1: INTRODUCTION 1
1.1 Forest Ecophysiology 2
1.2 Imaging Technology 9
1.3 Remote Sensing of Forest Structure and Productivity 10

CHAPTER 2: RESEARCH QUESTIONS 21

CHAPTER 3: METHODS 24
3.1 Shawnigan Lake Study Site 24
3.2 Ground Reference Data Collection 27
3.2.1 Selection of Treatment Plots for Model Building 28
3.3 Airborne Data Acquisition 35
3.4 Survey and Terrestrial Lidar Acquisition 40
3.4.1 Global Navigation Satellite System Control Survey 41
3.4.2 Total Station Control Survey 46
3.4.3 Terrestrial Laser Scanner Data Acquisition and Pre-Processing 51
3.4.4 Ground Survey and TLS Discussion 62
3.5 Data Calibration and Processing 63
3.5.1 Deriving Geometry from INS Measurements 69
3.5.2 Characterization of Target BRF 77
3.5.3 Evaluation of Spectral Mixing in Airborne Spectra 81
3.5.4 Radiometric Correction of Imaging Spectrometer 86
3.5.5 Imaging Spectrometer Geometric Calibration 89
3.5.6 Validating Geometry of Imaging Spectrometer 98
3.6 Reference Productivity Derived from the CFS Database 107

CHAPTER 4: MODELLING AREA BASED RS ENHANCED FOREST INVENTORY 179
4.1 Deriving Structural Metrics from Airborne Laser Scanner 180
4.2 Airborne Imaging Spectroscopy Metrics for Productivity Attribution 192
4.3 Area Based Forest Plot Structure Regression 198
4.4 Area Based Forest Plot Productivity Regression 250

CHAPTER 5: DERIVATION OF INDIVIDUAL TREE MORPHOMETRICS 339
5.1 Extracting Stem Position and DBH from TLS 340
5.2 Extracting Height to Live Crown and Bole Parameters from TLS 367
5.3 Extracting Individual Tree Height and Crown Length 381
5.4 Individual Tree Detection by ALS 387
5.5 Extracting Crown Dimensions 420

CHAPTER 6: MODELLING INDIVIDUAL TREE PRODUCTIVITY 424

CHAPTER 7: CHANGING GAP STRUCTURE, A CASE STUDY FOR GVWSA 452
7.1 Multi-Temporal ALS and AIS Methods 454
7.2 Multi-Temporal ALS and AIS Gap Results 459
7.3 Multi-Temporal ALS and AIS Discussion and Conclusions 462

CHAPTER 8: CONCLUSIONS AND DISCUSSION 467
REFERENCES.....492
APPENDICES 507
APPENDIX 1: Previous studies conducted at the Shawnigan Lake Project site.....507
APPENDIX 2: Radiometric Calibration of Airborne Data.....510
1.1.1 Laboratory Radiometric Data Acquisition 511
1.1.2 Laboratory Radiometric Data Analysis.....517
1.1.3 Initial Evaluation of Materials 521
1.2 Target Deployment and Field Spectroscopy.....538
1.3 AISA Eagle Radiometric Processing 551
1.4 Radiometric Correction Discussion 570
1.5 Radiometric Correction Conclusions 571
APPENDIX 3: Modelling Tree Height from DBH.....578
1.1 Height-DBH Regression Fitting for Sampling Year 2002.....578
1.2 Height-DBH Regression Fitting for Sampling Year 2012.....611
1.3 Plot Based Volume Increment Boxplots 644

List of Tables

TABLE 1.1 POTENTIAL CONTRIBUTIONS OF LIDAR REMOTE SENSING FOR FORESTRY APPLICATIONS 17
TABLE 3.1: VARIABLES TO CONSIDER WHILE PLANNING AN AIRBORNE DATA COLLECTION 36
TABLE 3.2: FLIGHT PARAMETERS FOR SHAWNIGAN LAKE PROJECT 38
TABLE 3.3 CONTROL POSITIONS SURVEYED BY POST-PROCESSED L1/L2, C/A AND CARRIER GPS 45
TABLE 3.4. UNCORRECTED SLP CLOSED TRAVERSE AND CLOSED LOOP SURVEY ACCURACY 49
TABLE 3.5. WEIGHTED TENSION INDEX INDICATES THE FIT OF SCAN INTEGRATION PER PLOT 53
TABLE 3.6 BRDF GEOMETRY PARAMETERS FOR EAGLE MEASUREMENTS OF BRIGHT CALIBRATION TARGET 75
TABLE 3.7 BRDF GEOMETRY PARAMETERS FOR EAGLE MEASUREMENTS OF DARK CALIBRATION TARGET 76
TABLE 3.8 ASSESSMENT OF GROWTH DIFFERENCES BETWEEN TREATMENTS 138
TABLE 3.9 ASSESSMENT OF GROWTH DIFFERENCES BETWEEN PLOTS 160
TABLE 3.10 PERIODIC VOLUME INCREMENT AS A LINEAR MIXED MODEL 173
TABLE 3.11 PERIODIC VOLUME INCREMENT AS A LINEAR MODEL WITHOUT A RANDOM EFFECT FOR PLOT 174
TABLE 3.12 VOLUME INCREMENT AS A LINEAR MIXED MODEL OF STRUCTURAL ATTRIBUTES IN CFS DATABASE 176
TABLE 3.13 PLOT PRODUCTIVITY FORM CFS DATABASE SORTED BY PAI OF PLOT VOLUME 177
TABLE 4.1 BOOTSTRAP OF TOTAL PLOT VOLUME SIMPLE LINEAR MODEL (N:1000) 201
TABLE 4.2 BOOTSTRAP OF TOTAL PLOT MERCHANTABLE VOLUME SIMPLE LINEAR MODEL (N:1000) 203
TABLE 4.3 BOOTSTRAP OF PLOT BASAL AREA SIMPLE LINEAR MODEL (N:1000) 207
TABLE 4.4 BOOTSTRAP OF AVERAGE MEASURED TREE HEIGHT SIMPLE LINEAR MODEL 211
TABLE 4.5 BOOTSTRAP OF AVERAGE MEASURED AND ESTIMATED TREE HEIGHT WITHIN THE DOMINANT AND CO-DOMINANT CROWN CLASS SIMPLE LINEAR MODEL 213
TABLE 4.6 BOOTSTRAP OF AVERAGE MEASURED AND ESTIMATED TREE HEIGHT WITHIN THE DOMINANT AND CODOMINANT CROWN CLASS WITHOUT THE INFLUENTIAL PLOT 41 SIMPLE LINEAR MODEL 216
TABLE 4.7 BOOTSTRAP OF PLOT TOP HEIGHT FROM AVERAGE CHM TREETOP HEIGHT 219
TABLE 4.8 BOOTSTRAP OF PLOT TOP FROM AVERAGE HEIGHT ABOVE 85TH PERCENTILE 221
TABLE 4.9 BOOTSTRAP OF PLOT AVERAGE HTLC ESTIMATED FROM LHQ 10 223
TABLE 4.10 BOOTSTRAP OF PLOT AVERAGE HTLC FROM PRI COEFFICIENT OF VARIATION 226
TABLE 4.11 EFFECT OF CROWN CLASS ON FIT AND FEATURE SELECTION 266
TABLE 4.12 EFFECT OF CROWN CLASS ON FIT AND FEATURE SELECTION FOR ESTIMATING MEAN PAI VOLUME 276
TABLE 4.13 BOOTSTRAP OF MLR MODEL PREDICTING PLOT MEAN PAI IN VOLUME FROM THE MEDIAN LIDAR TREETOP HEIGHT AND THE STANDARD DEVIATION OF THE CHM 288
TABLE 4.14 BOOTSTRAP OF MLR MODEL PREDICTING PLOT MEAN PAI IN VOLUME FROM THE AVERAGE FOUR TALLEST LIDAR TREETOP HEIGHTS AND THE COEFFICIENT OF VARIATION OF THE CHM 292
TABLE 4.15 EFFECT OF CROWN CLASS ON FIT AND FEATURE SELECTION FOR ESTIMATING PAI TOTAL VOLUME 295
TABLE 4.16 BOOTSTRAP OF MULTIPLE LINEAR REGRESSION PARAMETERS 305
TABLE 4.17 BOOTSTRAP OF MULTIPLE LINEAR REGRESSION PREDICTING PAI PLOT VOLUME ALL CROWN CLASSES 319
TABLE 4.18 BOOTSTRAP OF MULTIPLE LINEAR REGRESSION PREDICTING PAI PLOT VOLUME ALL CROWN CLASSES 320
TABLE 4.19 MULTIPLE REGRESSION PARAMETERS FOR PAI TOTAL VOLUME IN ALL CROWN CLASSES 321
TABLE 4.20 BOOTSTRAP OF MULTIPLE LINEAR REGRESSION PREDICTING PAI PLOT VOLUME ALL CROWN CLASSES 324
TABLE 5.1 LIDAR TREETOP EXTRACTION PARAMETERS AND THE EFFECT OF TREETOP RETRIEVAL ACCURACY 389
TABLE 6.1 BOOTSTRAP OF SLR PREDICTING TREE PAI IN VOLUME FROM THE LIDAR TREETOP HEIGHT 434
TABLE 6.2 BOOTSTRAP OF SLR WITH NON-LINEAR PARAMETER ESTIMATION FOR PREDICTING TREE PAI IN VOLUME FROM THE LIDAR TREETOP HEIGHT 437
TABLE 6.3 BOOTSTRAP OF MLR WITH NON-LINEAR PARAMETER ESTIMATION FOR PREDICTING TREE PAI IN VOLUME FROM THE LIDAR TREETOP HEIGHT AND PLOT AVERAGE LIDAR TREETOP HEIGHT 441
TABLE 6.4 BOOTSTRAP OF MLR WITH NON-LINEAR PARAMETER ESTIMATION FOR PREDICTING TREE PAI IN VOLUME FROM THE LIDAR TREETOP HEIGHT AND PLOT AVERAGE LIDAR TREETOP HEIGHT AND THE INTERACTION 442
TABLE 6.5 BOOTSTRAP OF MLR WITH NON-LINEAR PARAMETER ESTIMATION FOR PREDICTING TREE PAI IN VOLUME FROM THE LIDAR TREE CROWN 50TH PERCENTILE AND TREETOP HEIGHT TO PLOT HEIGHT RATIO 445
TABLE 6.6 BOOTSTRAP OF MLR WITH NON-LINEAR PARAMETER ESTIMATION FOR PREDICTING TREE PAI IN VOLUME FROM THE LIDAR TREETOP HEIGHT AND PLOT AVERAGE LIDAR TREETOP HEIGHT AND A CROWN SHAPE ATTRIBUTE 448

List of Figures

FIGURE 3.1. FLNRO SITE INDEX CURVES FOR COASTAL DOUGLAS-FIR [97] 25
FIGURE 3.2. THE SHAWNIGAN LAKE PROJECT AND LEVELS OF GROWING STOCK SITE AND PLOT LOCATIONS MAP PROVIDED BY C. FILIPESCUE (NRCAN, CANADIAN WOOD FIBRE CENTRE) 27
FIGURE 3.3. PLOT SELECTION APPROACH BASED ON LATENT STRUCTURE OF FIELD MEASUREMENTS. SCATTERPLOT MATRIX OF THE SLP FIELD DATA DEMONSTRATES INTER-CORRELATION AND REDUNDANT INFORMATION. COLOURS REPRESENT THOSE PLOTS ESTABLISHED IN DIFFERENT YEARS. 30
FIGURE 3.4. PLOT SELECTION APPROACH BASED ON LATENT STRUCTURE OF FIELD MEASUREMENTS - SLP PLOT FIELD DATA PROJECTED BY A PRINCIPAL COMPONENT TRANSFORMATION. THE FIRST TWO COMPONENTS REPRESENT 92% OF THE TOTAL VARIANCE IN THE FIELD BASED MEASUREMENT DATA 31
FIGURE 3.5. SCATTERPLOT OF PRINCIPAL COMPONENTS ONE AND TWO WITH THE INFLUENCE OF THE ORIGINAL DIMENSIONS ILLUSTRATED BY RED VECTORS 32
FIGURE 3.6. PLOT SELECTION FOR SAMPLING BASED ON STRUCTURAL DATA. PRINCIPAL COMPONENT ONE AND TWO FROM THE SLP PLOT FIELD DATA. CONSTANT PERCENTILE INTERVAL SELECTION OF PLOTS TO CAPTURE WITHIN SITE VARIABILITY. SELECTED PLOTS INDICATED BY GREEN POINT SYMBOLS. 33
FIGURE 3.7. PLOT SELECTION APPROACH BASED ON LATENT STRUCTURE OF FIELD MEASUREMENTS. PC PERCENTILE RANK SELECTION OMITTED SOME TREATMENTS. THE PRINCIPAL COMPONENT SCORES WERE TRANSFORMED TO PERCENTILE RANKS AND AT EQUAL PERCENTILE INTERVALS THE CLOSEST DATA POINT WAS SELECTED FOR COMPONENT ONE AND TWO (BASED ON THE PROPORTION OF TOTAL VARIANCE EXPLAINED), SHOWN IN RED. THIS APPROACH DID NOT SELECT ALL FERTILIZER AND THINNING TREATMENTS, WHICH ARE INDICATED AS GREEN SYMBOLS. THIS APPROACH ENSURES SAMPLING OF PLOTS WILL PROVIDE REPRESENTATIVE VARIABILITY AND MODELS WILL INTERPOLATE RATHER THAN EXTRAPOLATE TO UNTRAINED PLOT DATA. 34
FIGURE 3.8. FLIGHT PATH OF THE AIRBORNE ACQUISITION OVERLAID ON THE CRD ORTHOPHOTOS. SEPT. 13TH FLIGHT ILLUSTRATED AS A RED POLYLINE COVERAGE INCLUDING RADIOMETRIC CALIBRATION FLIGHTS AT THE DRY SORTING LOT AND THE SLP COLLECTION. SEPT 19TH FLIGHT ILLUSTRATED AS A BLUE POLYLINE COVERAGE INCLUDED THE GVWSA AND SLP, RADIOMETRIC CALIBRATION SITE AT THE SADDLE DAM QUARRY AS WELL AS THE GEOMETRY CALIBRATION SITE AT THE VICTORIA INTERNATIONAL AIRPORT. 39
FIGURE 3.9 SLP GROUND CONTROL SURVEY MAP INDICATING THE POSITIONS OF GPS SURVEY MONUMENTS; TURNING POINT MONUMENTS AND TLS REFERENCE MONUMENTS. COLORS REPRESENT SEPARATE CONNECTING TRAVERSES AND GREY SQUARES ARE THE CORE TREATMENT PLOTS EXTRACTED FROM THE GEOREFERENCED TLS PLOT SCANS. SURVEY DATA ARE OVERLAID ON AN ALS BARE EARTH MODEL DISPLAYED IN PSEUDO COLOR. 50
FIGURE 3.10 VERTICAL CROSS SECTION OF THE ALS POINT CLOUD AT LOGS PLOT 8, DEFAULT POINTS ARE ILLUSTRATED IN GREEN WHILE GROUND POINTS ARE COLOURED MAGENTA. THE THREE CYAN POINTS ARE THREE STEM POSITIONS FROM THE CONTROL SURVEY, WHICH WERE COLLECTED AS A VALIDATION OF THE GROUND SURVEY. THE VERTICAL DISCREPANCY IS A KNOWN MIS-CALIBRATION IN THE 2012 ALS DATASET. 54
FIGURE 3.11 THE CONTROL SURVEY REFERENCE POSITIONS OF ISOLATED TREES IN LOGS PLOT 8. THE SURVEY DATA SUPERIMPOSED ONTO THE ALS CHM DEMONSTRATES A SUFFICIENT ACCURACY HAS BEEN ACHIEVED TO IDENTIFY INDIVIDUAL TREE STEMS. NOTE THE TWO REFERENCE POSITIONS EAST OF THE TRAVERSE LINE ARE PLOT REFERENCE POSITIONS AND NOT TREE VALIDATION POSITIONS. 55
FIGURE 3.12 A VERTICAL CROSS SECTION OF THE TLS AND ALS INTEGRATED POINT CLOUD AT PLOT 67. THIS FIGURE DEMONSTRATES THAT THE POSITIONING OF THE TLS DATA RELATIVE TO THE ALS IS SUFFICIENT TO ASSOCIATE TREES WITHIN THE TLS TO THOSE IN THE ALS DATASET 55
FIGURE 3.13 TLS POINT CLOUD CLASSIFICATION AT PLOT 2 (T0F0) INCLUDED AN AUTOMATED GROUND DEFINITION (RED) THAT WAS MANUALLY REFINED AND THE MANUAL CLASSIFICATION OF OVERSTORY (LIGHT GREEN), UNDERSTORY (MAGENTA), GROUND COVER VEGETATION (YELLOW) AND COARSE WOODY DEBRIS (CYAN). THE TLS DATA ARE INTEGRATED WITH THE ALS POINT CLOUD. THE ALS DEFAULT (VEGETATION) CLASS IS DISPLAYED AS GREEN. 57
FIGURE 3.14 TOP: RAIN AND FOG BACKSCATTER IS SUFFICIENT TO REGISTER LIDAR POINTS. RAIN AND FOG POINTS OBSERVED AT SPECIFIC DISTANCES FROM THE SCANNER AND WITH SPECIFIC RETURN INTENSITIES. BOTTOM: THE LOW-DENSITY REGION WITHIN THE RETURN INTENSITY-DISTANCE DATA SPACE DELINEATED THESE GROUPS. 58
FIGURE 3.15 PLOT 2 CANOPY HEIGHT MODEL OF THE UNDERSTORY VEGETATION CLASS, REPRESENTED BY A 10CM RASTER GRID SIZE. THE NORMALIZATION PROCESS PRODUCES A DATASET WHERE HEIGHT VALUES ARE REFERENCED TO THE GROUND SURFACE AND THUS DATA VALUES REPRESENT TREE/FOLIAGE HEIGHT FROM GROUND. SOME OCCLUSION IS VISIBLE IN THE UPPER LEFT OF THE IMAGE WHERE OVERSTORY STEMS BLOCK POINTS FROM BEING REGISTERED FROM SOME UNDERSTORY CANOPIES. 60

FIGURE 3.16 A 5MM GRID RASTER OF A HORIZONTAL CROSS SECTION (50CM DEEP) AT PLOT 67 IS OVERLAID ONTO THE ALS CHM. THE CROSS SECTION RASTER IS SATURATED TO PRODUCE A BINARY IMAGE OF THE STEM LOCATIONS AND BACKGROUND IS TRANSPARENT, THUS ONLY STEMS ARE DISPLAYED IN BLACK. THERE APPEARS TO BE GOOD CORRESPONDENCE BETWEEN HIGH POINTS (TREETOPS) IN THE ALS CHM AND THE TLS BOLE LOCATIONS. 61
FIGURE 3.17 CALIBRATION TARGETS DEPLOYED AT THE DRY SORTING LOT FOR THE SEPT 13 DATA COLLECTION, WHEN ATMOSPHERIC CONDITIONS APPEARED FAVOURABLE 64
FIGURE 3.18 CALIBRATION TARGETS DEPLOYED AT THE DRY SORTING LOT FOR THE SLP PROJECT ON SEPTEMBER 13. THE TWO 5X4M TARGETS WERE POSITIONED ON A FLAT ASPHALT AREA 64
FIGURE 3.19 CALIBRATION TARGETS DEPLOYED IN THE FIELD FOR THE AIRBORNE CAMPAIGN ON SEPTEMBER 19TH 2012 64
FIGURE 3.20 CALIBRATION TARGETS DEPLOYED AT THE SADDLE DAM QUARRY WITHIN THE GVWD FOR THE AIRBORNE CAMPAIGN ON SEPTEMBER 19TH 65
FIGURE 3.21 AISA EAGLE RADIANCE SPECTRA OF THE DEPLOYED CALIBRATION TARGETS 68
FIGURE 3.22 AISA EAGLE TIME SYNCHRONIZATION. AN EXAMPLE OF THE LED PPS TIMING SIGNAL. EACH TRANSITION FROM ON TO OFF AND OFF TO ON MARK THE FRAME LOCATION OF THE INTEGER SECOND, THE FRAME RATE IS 43F/S. NOTE THE UNDERLYING GREY SCALE IMAGE OF BAND 583NM WITH FODIS PPS TIMING AT TOP. 70
FIGURE 3.23 BRF SURFACES FOR BRIGHT AND DARK SAMPLE TARGETS MEASURED IN THE LAB SETTING AND COMPUTED WITH LOESS (LOCALLY WEIGHTED POLYNOMIAL REGRESSION FITTING). BRF, REPRESENTED BY SPECTRAL MEDIANS (400-1000NM) ARE PLOTTED TO CARTESIAN COORDINATES FROM THE SURFACE POLAR COORDINATES (SURFACE ROTATION AND INCLINATION). THE BRIGHT TARGET RESPONSE CLEARLY HAS A MORE DOMINANT HEMISPHERICAL SCATTERING, WHILE THE DARK SAMPLE PRODUCES A PRONOUNCED AND MORE CONCENTRATED CONICAL SCATTERING RESPONSE. SURFACES CAN BE READ AS THE X,Y ORIGIN REPRESENTS THE NADIR OBSERVATION, HORIZONTAL ANGLES FROM THE ORIGIN REPRESENT CHANGES IN OBSERVATION AZIMUTH, AND DISTANCE FROM THE ORIGIN (*I.E.* RADIUS ISO-LINES) REPRESENT CHANGES IN OBSERVATION ZENITH ANGLE. 78
FIGURE 3.24 OFF-NADIR SPECTRA DIVIDED BY THE NADIR MEASUREMENTS OF THE SAME TARGET DEMONSTRATE THE SPECTRAL INVARIANCE OF BIDIRECTIONAL REFLECTANCE FACTORS FOR THE TARGET SAMPLES 79
FIGURE 3.25 DARK TARGET SAMPLE SPECTRA PRODUCED WITH SIMULATED GEOMETRIES FROM AIRBORNE COLLECTION. VALUES ARE RELATIVE REFLECTANCE FROM NORMALIZATION TO A NADIR OBSERVED WHITE REFERENCE (SPECTRALON). GIVEN SOLAR ZENITH ANGLES ARE INVARIANT. MAGNITUDE DIFFERENCES ARE LARGELY ATTRIBUTED TO CHANGES IN RELATIVE AZIMUTH. 80
FIGURE 3.26 BRIGHT TARGET SAMPLE SPECTRA PRODUCED WITH SIMULATED GEOMETRIES FROM AIRBORNE COLLECTION. VALUES ARE RELATIVE REFLECTANCE FROM NORMALIZATION TO A NADIR OBSERVED WHITE REFERENCE (SPECTRALON), TITANIUM OXIDE ABSORPTION IS APPARENT IN WAVELENGTHS LESS THAN ~425NM. GIVEN SOLAR ZENITH ANGLES ARE INVARIANT. MAGNITUDE DIFFERENCES ARE LARGELY ATTRIBUTED TO CHANGES IN RELATIVE AZIMUTH. 81
FIGURE 3.27 FOR CLARITY, THE DARK RATIO FOR THE 2004 AND 1957 IS ACTUALLY 1957/2004, ALL OTHER SPECTRA ARE AS THE LABEL SUGGESTS. RATIO COMBINATIONS NOT DISPLAYED ARE OMITTED TO VISUALIZE RATIO SCALE FOCUSED ON HIGHER QUALITY TARGET RESPONSES. 84
FIGURE 3.28 RADIOMETRICALLY CORRECTED AISA EAGLE DATA FROM THE SEPT.19 COLLECTION WITH *INSITU* REFLECTANCE SPECTRA FROM THE GROUND REFERENCE TARGETS. 88
FIGURE 3.29 GPS TRIGGERED LED PULSE PER SECOND ON THE INTEGER SECOND SIGNAL RECORDED INTO THE FODIS REGION ON THE DETECTOR. A) TRUE COLOR COMPOSITE OF ONE OF THE YYJ CALIBRATION FLIGHTS B) ENHANCED GREY SCALE IMAGE ILLUSTRATES THE PPS SIGNAL WITHIN THE FODIS REGION 91
FIGURE 3.30 AISA EAGLE TIME SYNCHRONIZATION. TO PROVIDE THE GREATEST POSSIBLE SIGNAL FOR THE TIMING SYNCHRONIZATION THE SPECTRAL EMISSION OF THE LED WAS INVESTIGATED. THE MAXIMUM SPECTRAL EMISSION OCCURS AT 583.5NM 92
FIGURE 3.31 AISA EAGLE TIME SYNCHRONIZATION. TO PROVIDE THE GREATEST POSSIBLE SIGNAL FOR THE TIMING SYNCHRONIZATION THE SPATIAL EMISSION OF THE LED WAS INVESTIGATED. THE MAXIMUM SPECTRAL EMISSION OCCURS AT THE SIXTH SPATIAL PIXEL. THEREFORE, THE OPTIMAL TIMING SIGNAL WAS EXTRACTED FROM THE SIXTH SAMPLE OF THE 583.5NM CHANNEL 93
FIGURE 3.32 AISA EAGLE TIME SYNCHRONIZATION. AN EXAMPLE OF THE LED PPS TIMING SIGNAL FROM ONE OF THE CALIBRATION LINES. EACH TRANSITION FROM ON TO OFF AND OFF TO ON MARKS THE FRAME LOCATION OF THE INTEGER SECOND, THE FRAME RATE IS 43F/S. 94
FIGURE 3.33 AISA EAGLE TIME SYNCHRONIZATION. THE FLOATING-POINT TIMING OFFSET FOR INS AND SPECTROMETER SYNCHRONIZATION IS DETERMINED BY THE CONSTANT FRAME RATE OF 43F/S AND THE NUMBER

of frames before the first PPS signal. In this example the first frame occurs >36 and <37 frames before the first PPS signal. Since the duration of each frame is 23.25ms (1sec /43frames) the time adjustment is 0.837seconds (23.25ms*36). The timing adjustment is either -0.837s or +0.163 (1sec-0.837) depending on which PPS is referenced in the header/options file. There is one frame of uncertainty in this process and therefore the time synchronization is <23.25ms. 95
Figure 3.34 AISA Eagle time synchronization. a) Calibration flight of YYJ without floating point second timing synchronization. Incorrect platform behaviour and positions are associated with imaging frames producing a distorted image. b) Calibration flight of YYJ with floating point second timing synchronization. With proper time sync the correct platform behaviour and positions are associated with imaging frames producing an image that preserves the geometry of the imaged scene. Although relative positions are accurate, absolute accuracy requires bore sight calibration and projection to a DSM. 96
Figure 3.35 AISA Eagle bore sight calibration. Calibration flights of YYJ with opposing flight headings. Figures a) and c) depict unresolved pitch and roll bore sight misalignment respectively, while b) illustrates the corrected pitch but unresolved roll bore sights. Figure d represents the corrected pitch and roll bore sight misalignment. 97
Figure 3.36 AISA Eagle bore sight calibration. Two perpendicular calibration flights with calibrated timing and bore sights at YYJ (red and green). A lidar intensity raster (blue) is displayed to qualitatively demonstrate the spatial correspondence between the lidar and the spectrometer flight lines. 98
Figure 3.37 Discriminating vegetation and non-vegetation from radiance data, scatterplot of radiance values from 551nm (green) and 750nm (NIR) produces dissimilar clusters for vegetated and non-vegetated surfaces 101
Figure 3.38 Discriminating vegetation and non-vegetation from radiance data for the isolation of the runway so that lidar points from the runway paint lines can be stratified by intensity and evaluated against the positions of the spectrometer data. 102
Figure 3.39 Extracting paint line extents from spectrometer data. Delineation is based on runway paint line transect values of a visible albedo channel. The true extents are underestimated to avoid mixed pixels. For scale the runways are 60m across and the lines are 2.5 x 30m. 103
Figure 3.40 Extracting paint line extents from lidar point cloud. Delineation is based on an intensity value of 5400; this threshold was identified by the intensity distribution. Intensity classes were produced by natural breaks. 104
Figure 3.41 Lidar intensity values of point cloud subset within 4 meters of runway paint lines; a value of 5400 was selected to discriminate paint lines from background asphalt. 105
Figure 3.42 Convex hull delineated paint line lidar points, convex points indicated in green, lidar points illustrated in red. Overlaid on digital orthophotos ~30cm resolution 106
Figure 3.43 For every point on each convex hull of the lidar delineated paint line a distance is computed to the closest point on the raster (spectrometer) delineated paint lines. The histogram of these measured errors suggests that 75% of the spectrometer data are within ~1m of its true location (as represented by the lidar point cloud). 107
Figure 3.44 Quartile curves for selected treatments at SLP illustrating the initial increase in growth rate and the slow decline in the effect, but the change in productivity has produced significant differences in diameter. 111
Figure 3.45 Quartile curves PAI in diameter (cm/yr.) for selected treatments at SLP illustrating the initial increase in growth rate after treatment and the slow decay of that effect. 112
Figure 3.46 26 Plot basal area through time coloured by treatment (selected for clarity), illustrating that basal area is highest in the control plots but basal area increments maybe higher in plots with both thinning and fertilization treatments 113
Figure 3.47 PAI of plot basal area through time illustrate the convergence of growth at 10-15 years after the treatments were applied. Anomalous abrupt decrease in BA in the 2003 sampling is unaccounted for perhaps buffer tree destructive sampling. Thinning treatment application is evident as the initial low extremes, the PAI of which are not shown. 114
Figure 3.48 Histograms of tree volume in 2002 and 2012 at plot 10 where three distinct groups are observed and their respective volume increments over ten years. 117

FIGURE 3.49 HISTOGRAMS OF TREE VOLUME IN 2002 AND 2012 AT PLOT 24 WHERE THERE HAS BEEN THE LEAST AMOUNT OF GROWTH OVER THE TEN-YEAR PERIOD, ACCORDING TO THE OBSERVATIONS WITH MEASURED HEIGHTS. 118
FIGURE 3.50 HISTOGRAMS OF TREE VOLUME IN 2002 AND 2012 AT PLOT 41, WHICH HAS EXPERIENCED THE GREATEST GROWTH OVER THE TEN-YEAR PERIOD. 119
FIGURE 3.51 ILLUSTRATING THE DEPENDENCE OF INITIAL VOLUME ON THE VOLUME INCREMENT OF TEN YEARS. IDEALLY THIS TREND WILL BE REMOVED AND THE RESIDUALS WILL BE THE TARGET ATTRIBUTE FOR MODELING PRODUCTIVITY. BECAUSE THIS MODEL IS BUILT FROM THE CONTROL GROUP THE PRODUCTIVITY INDEX WOULD BE RELATIVE TO THE GROWTH OF THE CONTROL GROUP. 120
FIGURE 3.52 SHAPIRO-WILK TEST FOR NORMALITY IN TREATMENT AND PLOT DATA SUGGEST THAT THERE IS LITTLE CONSISTENCY THROUGH TIME WITH RESPECT TO THE NORMALITY OF DBH MEASUREMENTS 122
FIGURE 3.53 TESTING FOR TREATMENT AND PLOT DIFFERENCES IN DBH THROUGH ALL SAMPLING YEARS. SHAPIRO-WILK, BARTLETT AND BROWN-FORSYTH SUGGEST THE USE OF KRUSKAL WALLIS TEST OVER F-STATISTIC. NEARLY EACH TEST (YEAR) PRODUCES SIGNIFICANT RESULTS SUGGESTING AT LEAST ONE GROUP IS DIFFERENT. 123
FIGURE 3.54 BOXPLOTS OF TREATMENT MAI OF DBH DISTRIBUTIONS ILLUSTRATING DIFFERENCES IN CENTRAL TENDENCY AND SPREAD. THE DATA ARE GRAPHED BY QUARTILES, THE LARGEST AND SMALLEST POINT NO GREATER THAN 1.5*(IQR) FROM THE QUARTILES (0.25 AND 0.75)AND ALL POINTS GREATER THAN THOSE LIMITS. NOTE THAT TREATMENTS WITH THE "GT73"SUFFIX ARE TREATMENTS ESTABLISHED AFTER THE YEAR 1973. . 127
FIGURE 3.55 BOXPLOTS OF TREATMENT PAI OF DBH DISTRIBUTIONS ILLUSTRATING DIFFERENCES IN CENTRAL TENDENCY AND SPREAD. THE DATA ARE GRAPHED BY QUARTILES, THE LARGEST AND SMALLEST POINT NO GREATER THAN 1.5*(IQR) FROM THE QUARTILES (0.25, 0.75) AND ALL POINTS GREATER THAN THOSE LIMITS. NOTE THAT TREATMENTS WITH THE "GT73"SUFFIX ARE TREATMENTS ESTABLISHED AFTER THE YEAR 1973. . 128
FIGURE 3.56. BOXPLOTS OF TREATMENT PAI/MAI OF DBH DISTRIBUTIONS ILLUSTRATING DIFFERENCES IN CENTRAL TENDENCY AND SPREAD. THE DATA ARE GRAPHED BY QUARTILES, THE LARGEST AND SMALLEST POINT NO GREATER THAN 1.5*(IQR) FROM THE QUARTILES(0.25, 0.75) AND ALL POINTS GREATER THAN THOSE LIMITS. NOTE THAT TREATMENTS WITH THE "GT73"SUFFIX ARE TREATMENTS ESTABLISHED AFTER THE YEAR 1973. . 129
FIGURE 3.57 BOXPLOTS OF TREATMENT MAI OF HEIGHT DISTRIBUTIONS ILLUSTRATING DIFFERENCES IN CENTRAL TENDENCY AND SPREAD. THE DATA ARE GRAPHED BY QUARTILES, THE LARGEST AND SMALLEST POINT NO GREATER THAN 1.5*(IQR) FROM THE QUARTILES (0.25, 0.75) AND ALL POINTS GREATER THAN THOSE LIMITS. NOTE THAT TREATMENTS WITH THE "GT73"SUFFIX ARE TREATMENTS ESTABLISHED AFTER THE YEAR 1973. . 131
FIGURE 3.58 BOXPLOTS OF TREATMENT PAI OF HEIGHT DISTRIBUTIONS ILLUSTRATING DIFFERENCES IN CENTRAL TENDENCY AND SPREAD. THE DATA ARE GRAPHED BY QUARTILES, THE LARGEST AND SMALLEST POINT NO GREATER THAN 1.5*(IQR) FROM THE QUARTILES (0.25, 0.75) AND ALL POINTS GREATER THAN THOSE LIMITS. NOTE THAT TREATMENTS WITH THE "GT73"SUFFIX ARE TREATMENTS ESTABLISHED AFTER THE YEAR 1973. . 132
FIGURE 3.59 BOXPLOTS OF TREATMENT PAI/MAI OF HEIGHT DISTRIBUTIONS ILLUSTRATING DIFFERENCES IN CENTRAL TENDENCY AND SPREAD. THE DATA ARE GRAPHED BY QUARTILES, THE LARGEST AND SMALLEST POINT NO GREATER THAN 1.5*(IQR) FROM THE QUARTILES (0.25, 0.75) AND ALL POINTS GREATER THAN THOSE LIMITS. NOTE THAT TREATMENTS WITH THE "GT73"SUFFIX ARE TREATMENTS ESTABLISHED AFTER THE YEAR 1973. . 133
FIGURE 3.60 BOXPLOTS OF TREATMENT MAI (1948-2012) OF VOLUME DISTRIBUTIONS ILLUSTRATING DIFFERENCES IN CENTRAL TENDENCY AND SPREAD. THE DATA ARE GRAPHED BY QUARTILES, THE LARGEST AND SMALLEST POINT NO GREATER THAN 1.5*(IQR) FROM THE QUARTILES (0.25, 0.75) AND ALL POINTS GREATER THAN THOSE LIMITS. NOTE THAT TREATMENTS WITH THE "GT73"SUFFIX ARE TREATMENTS ESTABLISHED AFTER THE YEAR 1973. . 135
FIGURE 3.61 BOXPLOTS OF TREATMENT PAI OF VOLUME DISTRIBUTIONS ILLUSTRATING DIFFERENCES IN CENTRAL TENDENCY AND SPREAD. THE DATA ARE GRAPHED BY QUARTILES, THE LARGEST AND SMALLEST POINT NO GREATER THAN 1.5*(IQR) FROM THE QUARTILES 90.25, 0.75) AND ALL POINTS GREATER THAN THOSE LIMITS. NOTE THAT TREATMENTS WITH THE "GT73"SUFFIX ARE TREATMENTS ESTABLISHED AFTER THE YEAR 1973. . 136
FIGURE 3.62 BOXPLOTS OF TREATMENT PAI/MAI OF VOLUME DISTRIBUTIONS ILLUSTRATING DIFFERENCES IN CENTRAL TENDENCY AND SPREAD. THE DATA ARE GRAPHED BY QUARTILES, THE LARGEST AND SMALLEST POINT NO GREATER THAN 1.5*(IQR) FROM THE QUARTILES(0.25, 0.75) AND ALL POINTS GREATER THAN THOSE LIMITS. NOTE THAT TREATMENTS WITH THE "GT73"SUFFIX ARE TREATMENTS ESTABLISHED AFTER THE YEAR 1973. . 137
FIGURE 3.63 HASSE DIAGRAM REPRESENTATION OF POST-HOC TESTS (WILCOXON RANK SUM) FOR TREATMENT DIFFERENCES IN MAI OF DBH. THE POSITION OF GROUP VERTICES IN THE CHART IS REPRESENTATIVE OF THE MAGNITUDE OF THE VARIABLE. THE BOX SIZES ARE PROPORTIONAL TO TREATMENT GROUP SAMPLE SIZES. WHERE SIGNIFICANCE IS LESS THAN 0.05 LINE WEIGHT IS INVERSELY PROPORTIONAL TO SIGNIFICANCE OF THE

test and where lines do not connect treatments the two treatments are not significantly different. To simplify the chart connections are compressed using a point symbol. 140
Figure 3.64 Hasse diagram representation of post-hoc tests for treatment differences in PAI (ΔDBH/ΔTime). The position of group vertices in the chart is representative of the magnitude of the variable. The box sizes are proportional to treatment group sample sizes. Where significance is less than 0.05 line weight is inversely proportional to significance of the test and where lines do not connect treatments the two treatments are not significantly different. To simplify the chart connections are compressed using a point symbol 141
Figure 3.65 Hasse diagram representation of post-hoc tests for treatment differences in PAIDBH (2002-2012)/MAIDBH (1948-2002). The position of group vertices in the chart is representative of the magnitude of the variable. The box sizes are proportional to treatment group sample sizes. Where significance is less than 0.05 line weight is inversely proportional to significance of the test and where lines do not connect treatments the two treatments are not significantly different. To simplify the chart connections are compressed using a point symbol 142
Figure 3.66 Hasse diagram representation of post-hoc tests for treatment differences in MAI in measured height (1948-2002). The position of group vertices in the chart is representative of the magnitude of the variable. The box sizes are proportional to treatment group sample sizes. Where significance is less than 0.05 line weight is inversely proportional to significance of the test and where lines do not connect treatments the two treatments are not significantly different. To simplify the chart connections are compressed using a point symbol 144
Figure 3.67 Hasse diagram representation of post-hoc tests for treatment differences in PAI in measured height (2002-2012). The position of group vertices in the chart is representative of the magnitude of the variable. The box sizes are proportional to treatment group sample sizes. Where significance is less than 0.05 line weight is inversely proportional to significance of the test and where lines do not connect treatments the two treatments are not significantly different. To simplify the chart connections are compressed using a point symbol 145
Figure 3.68 Hasse diagram representation of post-hoc tests for treatment differences in PAI(2002-2012)/MAI (1948-2002) in measured height. The position of group vertices in the chart is representative of the magnitude of the variable. The box sizes are proportional to treatment group sample sizes. Where significance is less than 0.05 line weight is inversely proportional to significance of the test and where lines do not connect treatments the two treatments are not significantly different. To simplify the chart connections are compressed using a point symbol 146
Figure 3.69 Hasse diagram representation of post-hoc tests for treatment differences in MAI(1948-2012) in volume with measured height . The position of group vertices in the chart is representative of the magnitude of the variable. The box sizes are proportional to treatment group sample sizes. Where significance is less than 0.05 line weight is inversely proportional to significance of the test and where lines do not connect treatments the two treatments are not significantly different. To simplify the chart connections are compressed using a point symbol 147
Figure 3.70 Hasse diagram representation of post-hoc tests for treatment differences in PAI(2002-2012) in volume. With measured height The position of group vertices in the chart is representative of the magnitude of the variable. The box sizes are proportional to treatment group sample sizes. Where significance is less than 0.05 line weight is inversely proportional to significance of the test and where lines do not connect treatments the two treatments are not significantly different. To simplify the chart connections are compressed using a point symbol 148
Figure 3.71 Hasse diagram representation of post-hoc tests for treatment differences in PAI(2002-2012)/MAI(1948-2002) in volume. With measured height The position of group vertices in the chart is representative of the magnitude of the variable. The box sizes are proportional to treatment group sample sizes. Where significance is less than 0.05 line weight is inversely proportional to significance of the test and where lines do not connect treatments the two treatments are not significantly different. To simplify the chart connections are compressed using a point symbol 149
Figure 3.72 Comparison of measured and modeled tree height from the plot specific Weibull function(left) and a modified log function (right). Using the 2002 field data, the Weibull form

BETTER CAPTURES THE LOWER DBH TREND WITH HEIGHT, A LOW-DENSITY DATA SPACE THAT IS UNLIKELY TO BE REPRESENTED BY STATISTICAL APPROACHES ALONE. 152
FIGURE 3.73 COMPARISON OF MEASURED AND MODELED TREE HEIGHTS, MODELS BUILD AT THE PLOT LEVEL ARE ILLUSTRATED IN THE UPPER ROW WHILE MODELS FIT WITH TREATMENT STRATIFICATION ARE ILLUSTRATED IN THE SECOND ROW. THE 2002 DATA ARE DEPICTED IN FIRST COLUMN WHILE THE 2012 DATA ARE SHOWN IN THE SECOND COLUMN. SMALLER RESIDUALS WERE PRODUCED IN THE PLOT FIT MODELS THAN THE TREATMENT SPECIFIC MODELS AND THE EXTRAPOLATION OF THE PLOT MODELS APPEARED TO FIT LOW RANGE OBSERVATIONS BETTER. 154
FIGURE 3.74 PERIODIC ANNUAL INCREMENT (2002-2012) IN VOLUME STRATIFIED BY TREATMENT ILLUSTRATES AN APPARENT ASSOCIATION WITH TREATMENT LEVELS. THIS METRIC IS APPROPRIATE FOR THE INDIVIDUAL STEMS BUT OMITS INFORMATION ON PLOT OCCUPANCY AND IS THEREFORE NOT APPROPRIATE FOR PLOT LEVEL ANALYSIS. 157
FIGURE 3.75 HASSE DIAGRAM REPRESENTATION OF POST-HOC TESTS FOR TREATMENT DIFFERENCES IN PAI(2002-2012) IN VOLUME. WITH MEASURED AND ESTIMATED HEIGHT THE POSITION OF GROUP VERTICES IN THE CHART IS REPRESENTATIVE OF THE MAGNITUDE OF THE VARIABLE. THE BOX SIZES ARE PROPORTIONAL TO TREATMENT GROUP SAMPLE SIZES. WHERE SIGNIFICANCE IS LESS THAN 0.05 LINE WEIGHT IS INVERSELY PROPORTIONAL TO SIGNIFICANCE OF THE TEST AND WHERE LINES DO NOT CONNECT TREATMENTS THE TWO TREATMENTS ARE NOT SIGNIFICANTLY DIFFERENT. TO SIMPLIFY THE CHART CONNECTIONS ARE COMPRESSED USING A POINT SYMBOL 158
FIGURE 3.76 BOXPLOTS OF MAI OF VOLUME WITH MEASURED AND MODELED HEIGHT ILLUSTRATING DIFFERENCES IN CENTRAL TENDENCY AND SPREAD. THE DATA ARE GRAPHED BY QUARTILES, THE LARGEST AND SMALLEST POINT NO GREATER THAN 1.5*(IQR) FROM THE QUANTILES (0.25, 0.75) AND ALL POINTS GREATER THAN THOSE LIMITS. ALTHOUGH THE TREATMENTS ARE INDICATED IN THE DATA LABELS THEY ARE ALSO COLOR CODED TO EASE THE USE OF SUCH A LARGE NUMBER OF DISTRIBUTIONS. 161
FIGURE 3.77 BOXPLOTS OF PLOT PAI OF VOLUME WITH MEASURED AND MODELED HEIGHT DISTRIBUTIONS ILLUSTRATING DIFFERENCES IN CENTRAL TENDENCY AND SPREAD. THE DATA ARE GRAPHED BY QUARTILES, THE LARGEST AND SMALLEST POINT NO GREATER THAN 1.5*(IQR) FROM THE MEDIAN AND ALL POINTS GREATER THAN THOSE LIMITS. ALTHOUGH THE TREATMENTS ARE INDICATED IN THE DATA LABELS THEY ARE ALSO COLOR CODED TO EASE THE USE OF SUCH A LARGE NUMBER OF DISTRIBUTIONS. 162
FIGURE 3.78 HASSE DIAGRAM REPRESENTATION OF POST-HOC TESTS FOR PLOT DIFFERENCES IN PAI(2002-2012) IN DBH THE POSITION OF GROUP VERTICES IN THE CHART IS REPRESENTATIVE OF THE MAGNITUDE OF THE VARIABLE. THE BOX SIZES ARE PROPORTIONAL TO SAMPLE SIZES. WHERE SIGNIFICANCE IS LESS THAN 0.05 LINE WEIGHT IS INVERSELY PROPORTIONAL TO SIGNIFICANCE OF THE TEST AND WHERE LINES DO NOT CONNECT GROUPS THE TWO GROUPS ARE NOT SIGNIFICANTLY DIFFERENT. TO SIMPLIFY THE CHART CONNECTIONS ARE COMPRESSED USING A POINT SYMBOL 163
FIGURE 3.79 HASSE DIAGRAM REPRESENTATION OF POST-HOC TESTS FOR PLOT DIFFERENCES IN PAI(2002-2012) IN MEASURED AND MODELED HEIGHT THE POSITION OF GROUP VERTICES IN THE CHART IS REPRESENTATIVE OF THE MAGNITUDE OF THE VARIABLE. THE BOX SIZES ARE PROPORTIONAL TO SAMPLE SIZES. WHERE SIGNIFICANCE IS LESS THAN 0.05 LINE WEIGHT IS INVERSELY PROPORTIONAL TO SIGNIFICANCE OF THE TEST AND WHERE LINES DO NOT CONNECT GROUPS THE TWO GROUPS ARE NOT SIGNIFICANTLY DIFFERENT. TO SIMPLIFY THE CHART CONNECTIONS ARE COMPRESSED USING A POINT SYMBOL 164
FIGURE 3.80 HASSE DIAGRAM REPRESENTATION OF POST-HOC TESTS FOR PLOT DIFFERENCES IN PAI(2002-2012) IN VOLUME FROM MEASURED AND MODELED HEIGHT THE POSITION OF GROUP VERTICES IN THE CHART IS REPRESENTATIVE OF THE MAGNITUDE OF THE VARIABLE. THE BOX SIZES ARE PROPORTIONAL TO SAMPLE SIZES. WHERE SIGNIFICANCE IS LESS THAN 0.05 LINE WEIGHT IS INVERSELY PROPORTIONAL TO SIGNIFICANCE OF THE TEST AND WHERE LINES DO NOT CONNECT GROUPS THE TWO GROUPS ARE NOT SIGNIFICANTLY DIFFERENT. TO SIMPLIFY THE CHART CONNECTIONS ARE COMPRESSED USING A POINT SYMBOL 165
FIGURE 3.81 THE DISTRIBUTION OF THE PAI OF VOLUME WAS POSITIVELY SKEWED, WITH A SQUAREROOT TRANSFORMATION THE PAI DISTRIBUTION BECAME MORE APPROXIMATELY NORMAL. 167
FIGURE 3.82 THE SHAPES OF THE PAI IN VOLUME DISTRIBUTIONS WERE DIFFERENT ACCORDING TO THE THINNING TREATMENTS. THE CONTROL GROUP WAS CLEARLY MORE POSITIVELY SKEWED THAN EITHER OF THE T1 OR T2 TREATMENTS. ROWS ONE THROUGH FOUR DEPICT DISTRIBUTIONS FOR ALL PLOTS, T0, T1 AND T2 THINNING TREATMENT PLOTS RESPECTIVLEY. 168
FIGURE 3.83 DISTRIBUTIONS OF PAI IN VOLUME STRATIFIED BY CROWN CLASS MIGHT SUGGEST THAT THE SOURCE OF THE DEPARTURE FROM NORMAL SHAPES COULD BE ATTRIBUTED TO THE DIFFERENT CROWN CLASSES 169

FIGURE 3.84 THE PAI AND MAI DATA SPACE COLOURED BY CROWN CLASS ILLUSTRATED THAT CROWN CLASS, FOR OBVIOUS REASONS, CONTAINS IMPORTANT INFORMATION RELATED TO PRODUCTIVITY. IT WOULD BE VALUABLE TO ESTIMATE CROWN CLASS FROM RS DATA IN ORDER TO DERIVE INFORMATION ABOUT TREE LEVEL PRODUCTIVITY. 169
FIGURE 4.1. 50CM RESOLUTION CANOPY HEIGHT MODEL OF THE SLP STUDY AREA, THE RELATIVELY LARGER TREE HEIGHTS ALONG THE KOKSILAH RIVER SKEW THE ENHANCEMENT SO THAT HEIGHT DIFFERENCES ARE NOT AS APPARENT WITHIN THE SLP AREA 185
FIGURE 4.2. TREETOP AND CANOPY EXTENT VECTOR FILES (ILLUSTRATED AS BLACK STARS AND POLYGONS RESPECTIVELY) WERE GENERATED FROM THE 50CM RESOLUTION RASTER CANOPY HEIGHT MODEL (DISPLAYED IN PSEUDO COLOUR). THE EXAMPLE ABOVE IS TAKEN FROM A HEAVILY THINNED PLOT WITHIN THE LOGS TREATMENT AREA. 186
FIGURE 4.3. GROUND NORMALIZED CANOPY POINT CLOUD AT PLOT 10 (ESTABLISHED 1971 T1F0). LIDAR METRICS ARE DERIVED FROM THESE DATA TO REPRESENT VERTICAL AND HORIZONTAL CANOPY STRUCTURE. SECONDARY X-AXIS ON HISTOGRAM IS GENERATED BY A KERNEL DENSITY ESTIMATION AND REPRESENTS PROBABILITY DISTRIBUTION. 189
FIGURE 4.4. LIDAR DERIVED 1M BARE EARTH MODEL DISPLAYED WITH A COLOR RAMP AND SUPERIMPOSED ON A HILL SHADE (SOLAR AZIMUTH 60°, ZENITH 40°). FROM THE BEM, DERIVATIVES ARE GENERATED THAT DESCRIBE THE GROUND SURFACE. 190
FIGURE 4.5. THROUGH THE USE OF SLOPE AND ASPECT DATA DERIVED FROM THE LIDAR BEM A FLOW MODEL IS BUILT TO INDICATE THE RELATIVE QUANTITY/MAGNITUDE, AND FLOW DIRECTION OF SURFACE WATER. 191
FIGURE 4.6. THE TOPOGRAPHIC MOISTURE INDEX IS GENERATED AS THE FLOW MODEL NORMALIZED BY THE SLOPE DATA. THE TWI IS USED AS A PROXY FOR SITE PRODUCTIVITY AS THERE IS AN ASSOCIATION BETWEEN MOISTURE AND NUTRIENT AVAILABILITY. 192
FIGURE 4.7 FLIGHTLINE NORMALIZATION PROCEDURE TO RESOLVE RADIOMETRIC DIFFERENCES BETWEEN FLIGHTLINES. THE OVERLAPPING AREA WAS SPATIALLY REDUCED TO ELIMINATE EXTREME OBSERVATION ZENITH ANGLES. 194
FIGURE 4.8. SPECTRA EXTRACTED FROM PLOT 10 WITHIN THE AISA EAGLE DATA, WHICH WAS CORRECTED TO SURFACE RELATIVE REFLECTANCE. THE TOTAL 316 EXTRACTED SPECTRA ARE ILLUSTRATED AND THE ASSOCIATED QUARTILE CURVES WERE COMPUTED AND ARE SHOWN IN RED. 196
FIGURE 4.9. DERIVATIVE SPECTRA EXTRACTED FROM PLOT 10 WITHIN THE AISA EAGLE DATA, WHICH WAS CORRECTED TO SURFACE RELATIVE REFLECTANCE. THE TOTAL 316 EXTRACTED SPECTRA ARE ILLUSTRATED AND THE ASSOCIATED QUARTILE CURVES WERE COMPUTED AND ARE SHOWN IN RED. 197
FIGURE 4.10. CONTINUUM REMOVED AND DEPTH NORMALIZED SPECTRA EXTRACTED FROM PLOT 10 WITHIN THE AISA EAGLE DATA, WHICH WAS CORRECTED TO SURFACE RELATIVE REFLECTANCE. THE TOTAL 316 EXTRACTED SPECTRA ARE ILLUSTRATED AND THE ASSOCIATED QUARTILE CURVES WERE COMPUTED AND ARE SHOWN IN RED. 198
FIGURE 4.11. LINEAR MODEL FOR THE PREDICTION OF TOTAL PLOT VOLUME. PLOT 5 IS AN OUTLIER WITH RESPECT TO THE REST OF THE DATA AND PLOT 67 IS AN INFLUENTIAL POINT. CCF_{70} WAS SELECTED THROUGH THE COMPARISON OF SPEARMAN'S CORRELATION COEFFICIENTS AS THE BEST PREDICTOR OF TOTAL PLOT VOLUME 201
FIGURE 4.12. LINEAR MODEL FOR THE PREDICTION OF TOTAL PLOT VOLUME OMITTING PLOT 5. CCF_{70} WAS SELECTED THROUGH THE COMPARISON OF SPEARMAN'S CORRELATION COEFFICIENTS AS THE BEST PREDICTOR OF TOTAL PLOT VOLUME 202
FIGURE 4.13 LINEAR MODEL FOR THE PREDICTION OF MERCHANTABLE PLOT VOLUME. CCF_{70} WAS SELECTED THROUGH THE COMPARISON OF SPEARMAN'S CORRELATION COEFFICIENTS AS THE BEST PREDICTOR OF TOTAL PLOT VOLUME 204
FIGURE 4.14. LINEAR MODEL FOR THE PREDICTION OF MERCHANTABLE PLOT VOLUME WITHOUT PLOTS 5 AND 21. CCF_{70} WAS SELECTED THROUGH THE COMPARISON OF SPEARMAN'S CORRELATION COEFFICIENTS AS THE BEST PREDICTOR OF TOTAL PLOT VOLUME 205
FIGURE 4.15. LINEAR MODEL FOR THE PREDICTION OF PLOT BASAL AREA. CCF_{65} WAS SELECTED THROUGH THE COMPARISON OF SPEARMAN'S CORRELATION COEFFICIENTS AS THE BEST PREDICTOR. THE STANDARD ERROR OF THE ESTIMATE IS $0.20M^2$. THE CONSTANT IN THIS CASE IS NOT SIGNIFICANT (P: 0.42) A RESULT THAT IS PHYSICALLY MEANINGFUL; A PLOT WITH NO BASAL AREA WILL HAVE ZERO CANOPY CLOSURE. 207
FIGURE 4.16 THE AVERAGE OF MEASURED TREE HEIGHTS PREDICTED FROM THE LHQ_{85} (HEIGHT OF THE 85TH PERCENTILE OF THE CHM POINTS). THE RESIDUAL STANDARD ERROR IS 1.05M. 210

FIGURE 4.17 THE AVERAGE OF MEASURED TREE HEIGHTS PREDICTED FROM THE MEDIAN CHM TREETOP. THE INTERCEPT COEFFICIENT MAY NOT BE DIFFERENT FROM ZERO (T-TEST: -0.54. P:0.60) AND THE SLOPE COEFFICIENT IS VERY CLOSE TO ONE, IT IS BELOW ONE BY 2X10-5. THE STANDARD ERROR OF THE ESTIMATE IS 0.99M. 211
FIGURE 4.18 THE AVERAGE OF MEASURED AND MODELED TREE HEIGHTS WITHIN THE DOMINANT AND CO-DOMINANT CROWN CLASSES PREDICTED FROM THE MEDIAN CHM TREETOP. THE INTERCEPT COEFFICIENT MAY NOT BE DIFFERENT FROM ZERO (T-TEST: -1.407. P:0.17), THE SLOPE IS CLOSE TO ONE AND THE RESIDUAL STANDARD ERROR IS 0.55M. THE RESIDUAL ERROR IS GREATLY REDUCED BY OMITTING INTERMEDIATE AND SUPPRESSED CROWN CLASSES. 213
FIGURE 4.19 DIAGNOSTIC PLOTS IDENTIFIED PLOT 41 AS AN INFLUENTIAL OBSERVATION WHICH PRODUCED A COOKS DISTANCE GREATER THAN 1, SUGGESTING ITS OMISSION WOULD SIGNIFICANTLY AFFECT THE MODEL PARAMETERS. 214
FIGURE 4.20 THE AVERAGE OF MEASURED AND MODELED TREE HEIGHTS WITHIN THE DOMINANT AND CO-DOMINANT CROWN CLASSES PREDICTED FROM THE MEDIAN CHM TREETOP AND OMITTING PLOT 41. THE INTERCEPT COEFFICIENT IS NOW DIFFERENT FROM ZERO (T-TEST: -2.758. P:0.01) AND THE SLOPE HAS INCREASED. THE RESIDUAL STANDARD ERROR IS SLIGHTLY LOWER (0.48M) THAN WITH THE INCLUSION OF PLOT 41. 216
FIGURE 4.21 PLOT TOP HEIGHT MEASURED IN THE FIELD PREDICTED FROM THE AVERAGE OF THE TREETOPS EXTRACTED FROM A 50CM RASTER REPRESENTING THE MAXIMUM HEIGHT OF THE CHM LIDAR POINTS. THE RESIDUAL STANDARD ERROR WAS 0.59M. THE INTERCEPT MAY NOT BE DIFFERENT FROM ZERO (T-TEST:1.91, P:0.07)..... 219
FIGURE 4.22 PLOT TOP HEIGHT MEASURED IN THE FIELD PREDICTED FROM THE AVERAGE HEIGHT OF LIDAR RETURNS GREATER THAN THE 85TH PERCENTILE OF LIDAR RETURNS. THE RESIDUAL STANDARD ERROR WAS 0.57M. THE INTERCEPT MAY NOT BE DIFFERENT FROM ZERO (T-TEST:1.39, P:0.18) 220
FIGURE 4.23 AVERAGE PLOT HEIGHT TO LIVE CROWN MEASURED IN THE FIELD PREDICTED FROM THE HEIGHT AT THE TENTH PERCENTILE OF LIDAR CHM POINT HEIGHTS. THE RESIDUAL STANDARD ERROR IS 0.58M. INTERESTINGLY CONTROL PLOTS AND LOW STEM DENSITY (VIA ROOT DISEASE) PLOTS PRODUCE A DATA CLUSTER WITH LOW HTLC AND LHQ_{10}. 222
FIGURE 4.24. RESIDUAL PLOTS FOR SIMPLE LINEAR REGRESSION OF HTLC FROM LHQ10 DOES NOT STRONGLY SUPPORT DURBAN-WATSON TEST OF VARIANCE HOMOGENEITY (DW: 1.79, P: 0.54). WHILE THE SPREAD IN THE RESIDUAL PLOT MIGHT SUGGEST A POSITIVE ERROR VARIANCE TO FITTED VALUE ASSOCIATION, THE SCALE PLOT DOES NOT STRONGLY SUGGEST THAT THE ABSOLUTE ERRORS INCREASE WITH THE FITTED VALUES. 223
FIGURE 4.25. AVERAGE PLOT CROWN LENGTH MEASURED IN THE FIELD PREDICTED FROM THE COEFFICIENT OF VARIATION OF THE PHOTOCHEMICAL REFLECTANCE INDEX. THE RESIDUAL STANDARD ERROR WAS 0.92M. THERE IS STRUCTURE IN THE RESIDUALS WHERE THE MODEL OVER ESTIMATES CROWN LENGTH AT LESS NEGATIVE PRI CV FOLLOWED BY A REGION OF UNDER ESTIMATION NEAR -0.6 PRI CV. 225
FIGURE 4.26. RESIDUAL PLOTS FOR SIMPLE LINEAR REGRESSION OF CL FROM PRI CV. THERE IS AN APPARENT NON-CONSTANT ERROR TREND IN THE RESIDUAL PLOT SUGGESTING THAT THE MODEL FORM IS INCORRECT. 226
FIGURE 4.27. AVERAGE PLOT CROWN LENGTH MEASURED IN THE FIELD PREDICTED FROM THE TRANSFORMED COEFFICIENT OF VARIATION OF THE PHOTOCHEMICAL REFLECTANCE INDEX. THE RESIDUAL STANDARD ERROR WAS 0.90M. THE STRUCTURE IN THE RESIDUALS WAS NOT ELIMINATED BY THE TRANSFORMATION. 228
FIGURE 4.28. RESIDUAL PLOTS FOR SIMPLE LINEAR REGRESSION OF CL FROM PRI CV. THERE IS AN APPARENT NON-CONSTANT ERROR TREND IN THE RESIDUAL PLOT SUGGESTING THAT THE MODEL FORM IS INCORRECT. 229
FIGURE 4.29. AVERAGE PLOT CROWN LENGTH MEASURED IN THE FIELD PREDICTED FROM THE MEDIAN CHM TREETOP HEIGHT AND THE LHQ_{10}. THE RESIDUAL STANDARD ERROR WAS 0.87M. 231
FIGURE 4.30. RESIDUAL PLOTS FOR SIMPLE LINEAR REGRESSION OF CL FROM MEDIAN CHM TREETOP HEIGHT AND LHQ_{10}. PLOT 41 HAS A HIGH LEVERAGE VALUE. 232
FIGURE 4.31. AVERAGE PLOT CROWN WIDTH MEASURED IN THE FIELD PLOTTED WITH THE STANDARD DEVIATION OF THE CHM. PLOTS 65 AND 67 ARE OUTLIERS IN TERMS OF THEIR CHM STANDARD DEVIATIONS. THEIR EXTREME VALUES ARE ATTRIBUTED TO CANOPY GAPS. 233
FIGURE 4.32. AVERAGE PLOT CROWN WIDTH MEASURED IN THE FIELD PLOTTED WITH THE STANDARD DEVIATION OF THE CHM IDENTIFIED A NUMBER OF OUTLIERS WHOSE DEPARTURE WERE ATTRIBUTED TO THE OCCURRENCE OF CANOPY GAPS, SEE PLOTS 67, 65, 11 AND 48. 234
FIGURE 4.33. CANOPY GAPS CONFOUNDED THE RELATIONSHIP BETWEEN CROWN WIDTH AND CHM STANDARD DEVIATION. CCF IS A LIDAR REPRESENTATION OF GAP THAT WAS EXPECTED TO IMPROVE THE CROWN WIDTH MODEL. CCF IS COMPUTED AT LIDAR HEIGHT QUANTILE INTERVALS OF 5%. THE R^2 WAS PLOTTED FOR EACH QUANTILE, WHICH REPRESENTS THE FIT WHEN THE CHM STANDARD DEVIATION MODEL INCLUDES THE CCF AT

THE CORRESPONDING HEIGHT PERCENTILE. THE FIT OF CROWN WIDTH AND ESTIMATES ARE MAXIMIZED AT CCF_{60}. 235
FIGURE 4.34. AVERAGE CROWN WIDTH ESTIMATED FROM THE STANDARD DEVIATION OF THE CHM AND THE CANOPY CLOSURE AT THE 60TH HEIGHT PERCENTILE. THE RESIDUAL STANDARD ERROR IS 0.17. 236
FIGURE 4.35. RESIDUAL PLOTS FOR MULTIPLE LINEAR REGRESSION OF CROWN WIDTH FROM CHM STANDARD DEVIATION AND CCF_{60}. THE RESIDUALS ARE GENERALLY WELL BEHAVED, BUT THERE MAY BE EVIDENCE IN THE SCALE-LOCATION PLOT FOR POSITIVELY CORRELATED VARIANCES. 237
FIGURE 4.36. AVERAGE CROWN WIDTH ESTIMATED FROM PLOT MEAN 680NM FEATURE SYMMETRY AND STANDARD DEVIATION OF THE CHM. THE RESIDUAL STANDARD ERROR IS 0.15M. 241
FIGURE 4.37. RESIDUAL PLOTS FOR MULTIPLE LINEAR REGRESSION OF CROWN WIDTH FROM 680NM FEATURE SYMMETRY AND CHM STANDARD DEVIATION. THE RESIDUAL PLOT DOES NOT STRONGLY SUGGEST THAT ASSUMPTIONS HAVE BEEN VIOLATED. 242
FIGURE 4.38. AVERAGE CROWN WIDTH ESTIMATED FROM MEDIAN CHM EXTRACTED TREETOP AND THE COEFFICIENT OF VARIATION IN CHM. THE RESIDUAL STANDARD ERROR IS 0.15M ON 24 DEGREES OF FREEDOM. 244
FIGURE 4.39. RESIDUAL PLOTS FOR MULTIPLE LINEAR REGRESSION OF CROWN WIDTH FROM MEDIAN CHM EXTRACTED TREETOPS AND THE COEFFICIENT OF VARIATION IN THE CHM. THE RESIDUAL PLOTS DO NOT STRONGLY SUGGEST THAT ASSUMPTIONS HAVE BEEN VIOLATED. 245
FIGURE 4.40. THE STANDARD DEVIATION OF PIXEL HEIGHTS IN THE CHM WAS SELECTED AS THE MOST CORRELATED REMOTE SENSING METRIC WITH STEMS PER PLOT BY THE SPEARMAN'S AND PEARSON'S CORRELATION COEFFICIENTS. LARGELY ATTRIBUTED TO PLOTS 2, 21, 65 AND 67 THE RELATIONSHIP HAD A NON-LINEAR TREND. 247
FIGURE 4.41. THE STANDARD DEVIATION OF PIXEL HEIGHTS IN THE CHM WAS SELECTED AS THE MOST CORRELATED REMOTE SENSING METRIC WITH STEMS PER PLOT BY THE SPEARMAN AND PEARSON COEFFICIENT. THE VARIABLES WERE TRANSFORMED TO REMOVE THE NON-LINEAR TREND. 248
FIGURE 4.42. RESIDUAL PLOTS FOR SIMPLE LINEAR REGRESSION OF STEM PER PLOT FROM STANDARD DEVIATION OF CHM HEIGHTS. THE RESIDUAL PLOTS DO NOT SUGGEST THAT ASSUMPTIONS OF NORMALITY AND HETEROSCEDASTICITY HAVE BEEN VIOLATED, NOR ARE THERE INFLUENTIAL OBSERVATIONS. 249
FIGURE 4.43 EXPONENTIAL TRANSFORMS OF THE STANDARD DEVIATION OF THE CHM WERE ASSESSED BUT A NATURAL LOGARITHM WAS USED TO LINEARIZE THE STANDARD DEVIATION OF THE CHM DATA. THE SOURCE OF THE NON-LINEARITY MAY BE ATTRIBUTED TO PLOTS WITH CANOPY GAP COMPONENTS. 252
FIGURE 4.44. LINEAR MODEL PREDICTING PLOT MEAN PERIODIC ANNUAL INCREMENT IN DIAMETER FROM THE NATURAL LOG TRANSFORMED STANDARD DEVIATION OF THE PLOT HEIGHTS IN THE CHM. THE RESIDUAL STANDARD ERROR OF THE ESTIMATES IS 0.036CM/YR. (DF: 25). THE RELATIONSHIP APPEARS TO BE SENSITIVE TO PLOT DENSITY, AS PLOTS 65 AND 67 BOTH HAVE CANOPY GAPS, WHILE CONTROL PLOTS 2 AND 21 ARE CLOSEST TO THE ORIGIN. 253
FIGURE 4.45. RESIDUAL PLOTS FOR SIMPLE LINEAR REGRESSION OF MEAN PAI DBH FROM THE NATURAL LOG TRANSFORMED STANDARD DEVIATION OF CHM HEIGHTS. THE RESIDUAL PLOTS SUGGEST THAT PLOT 67 IS A HIGHLY INFLUENTIAL OBSERVATION. 254
FIGURE 4.46 CONTINUUM NORMALIZED REFLECTANCE OF THE 680NM ABSORPTION FEATURE OF THE MOST AND LEAST PRODUCTIVE PLOTS AND THE RATIO OF THE TWO MEDIAN CR ABSORPTION SPECTRA (1-CR). THE RATIO SUGGESTS, WITH THE EXCEPTION OF ~725NM (WHICH MIGHT BE ATTRIBUTED TO CHLOROPHYLL FLORESCENCE OR ATMOSPHERIC H_2O), THERE IS VERY LITTLE STRUCTURE WITHIN THE RATIO CURVE BEYOND THE CHLOROPHYLL TREND. THE MAXIMUM DEPTH OF THE FEATURE (~680NM) IS RELATED TO THE PIGMENT CONTENTS WITHIN THE IFOV. THIS OBSERVATION IS INTERPRETED AS A REDUCED CHLOROPHYLL LEVEL IN PLOT 67 RELATIVE TO PLOT 41. 257
FIGURE 4.47. MULTIPLE LINEAR MODEL PREDICTING PLOT MEAN PERIODIC ANNUAL INCREMENT IN DIAMETER FROM THE STANDARD DEVIATION OF THE PLOT HEIGHTS IN THE CHM AND THE MEAN CONTINUUM REMOVED MAXIMUM DEPTH. THE RESIDUAL STANDARD ERROR OF THE ESTIMATES IS 0.030CM/YR. (DF: 24). 258
FIGURE 4.48. RESIDUAL PLOTS FOR MULTIPLE LINEAR REGRESSION OF PLOT MEAN PAI OF DBH FROM STANDARD DEVIATION OF CHM HEIGHTS AND MEAN CONTINUUM REMOVED MAX DEPTH. THE RESIDUAL PLOTS SUGGEST THAT PLOT 67 IS A HIGHLY INFLUENTIAL OBSERVATION. 259
FIGURE 4.49 MULTIPLE LINEAR MODEL PREDICTING PLOT MEAN PERIODIC ANNUAL INCREMENT IN DIAMETER OF DOMINANT TO INTERMEDIATE CROWN CLASS FROM THE STANDARD DEVIATION OF THE PLOT HEIGHTS IN THE CHM AND THE MEDIAN CONTINUUM REMOVED MAXIMUM DEPTH. THE RESIDUAL STANDARD ERROR OF THE ESTIMATES IS 0.022CM/YR (DF:24). 262

FIGURE 4.50. RESIDUAL PLOTS FOR MULTIPLE LINEAR REGRESSION OF PLOT MEAN PAI OF DBH FROM DOMINANT TO INTERMEDIATE CROWN CLASSES PREDICTED FROM STANDARD DEVIATION OF CHM HEIGHTS AND MEDIAN CONTINUUM REMOVED MAX DEPTH. THE RESIDUAL PLOTS SUGGEST THAT PLOT 67 IS A HIGHLY INFLUENTIAL OBSERVATION AND THE NORMAL PLOT SUGGESTS THE TAILS OF THE RESIDUAL DISTRIBUTION MAYBE SLIGHTLY DIFFERENT FROM NORMAL. BOTH OF THESE CONDITIONS ARE LESSENED BY TAKING THE NATURAL LOG OF BOTH THE INDEPENDENT VARIABLES. 263
FIGURE 4.51. PLOTTING THE COEFFICIENT OF VARIATION OF REFLECTANCE WITH WAVELENGTH ILLUSTRATES THE NOISE COMPONENT AS A FUNCTION OF WAVELENGTH. SPECTRAL INDICES THAT USE BANDS WITH HIGH NOISE CONTENTS SHOULD BE CONSIDERED UNRELIABLE AND MORE A FUNCTION OF NOISE THAN OF THE TARGET OF INTEREST. 265
FIGURE 4.52 MULTIPLE LINEAR REGRESSION MODEL PREDICTING PERIODIC ANNUAL INCREMENT IN LIVE BASAL AREA FROM THE STANDARD DEVIATION OF THE PLOT HEIGHTS IN THE CHM AND THE MEDIAN RED EDGE POSITION. THE RESIDUAL STANDARD ERROR OF THE ESTIMATES IS $0.006 M^2/YR$ (DF:24). 267
FIGURE 4.53. RESIDUAL PLOTS FOR MULTIPLE LINEAR REGRESSION OF PLOT PAI OF BA PREDICTED FROM STANDARD DEVIATION OF CHM HEIGHTS AND MEDIAN REP. PLOT 67 IS A HIGHLY INFLUENTIAL OBSERVATION BECAUSE OMITTING IT PRODUCES ZERO VARIANCE IN REP_{MED}. 268
FIGURE 4.54. MULTIPLE LINEAR REGRESSION MODEL PREDICTING PERIODIC ANNUAL INCREMENT IN LIVE BASAL AREA FROM THE RATIO OF THE NUMBER OF LIDAR RETURNS ABOVE THE 45TH LIDAR HEIGHT PERCENTILE TO THE TOTAL NUMBER OF POINTS (CCF_{45}) AND THE PLOT MEDIAN OF THE PRI INDEX. THE RESIDUAL STANDARD ERROR OF THE ESTIMATES IS $0.005 M^2/YR$. (DF: 23). 270
FIGURE 4.55. RESIDUAL PLOTS FOR MULTIPLE LINEAR REGRESSION OF PLOT PAI OF BA PREDICTED FROM CCF45 AND MEDIAN PRI WITHOUT PLOT 67. 271
FIGURE 4.56. MULTIPLE LINEAR REGRESSION MODEL PREDICTING PERIODIC ANNUAL INCREMENT IN LIVE BASAL AREA FROM THE RATIO OF THE CCF_{45}, PLOT MEDIAN PRI AND PLOT MEDIAN REP. THE RESIDUAL STANDARD ERROR OF THE ESTIMATES IS $0.005 M^2/YR$. (DF: 23). 273
FIGURE 4.57. RESIDUAL PLOTS FOR FINAL MULTIPLE LINEAR REGRESSION OF PLOT PAI OF BA PREDICTED FROM CCF45, MEDIAN PRI AND MEDIAN REP. 274
FIGURE 4.58 CHARACTERIZATION OF THE NONLINEAR RELATIONSHIP BETWEEN MEAN VOLUME INCREMENT AND CHM MAXIMUM HEIGHT THROUGH NONLINEAR LEAST SQUARES. THE INITIAL SIMPLE LINEAR REGRESSION IDENTIFIED PLOT 65 AND 41. OMITTING PLOT 65 (BLUE) FROM SHAPE ESTIMATION PRODUCED A SUPERIOR FIT ACCORDING TO THE SUBSEQUENT LINEAR REGRESSION 278
FIGURE 4.59. RANKED CORRELATION ANALYSIS SELECTED MAXIMUM CHM AS MOST ASSOCIATED. THE NON-LINEAR TREND WAS ESTIMATED WITHOUT THE INFLUENCE OF PLOT 65. THE MAXIMUM CHM DATA WERE TRANSFORMED AND THE SIMPLE LINEAR REGRESSION WAS ESTIMATED. THE ESTIMATED PARAMETERS INCLUDED THE SHAPE PARAMETER OF 3.799 (STD. ERROR: 0.44), A SCALE COEFFICIENT OF 3.282×10^{-8} (STD ERROR: 4.428×10^{-9}) AND A NON-SIGNIFICANT (T: 1.06, P:0.3) CONSTANT OF 2.309×10^{-3} (STD. ERROR: 2.188×10^{-3}). THE R^2 WAS FOUND AS 0.687 WITH A RESIDUAL STANDARD ERROR OF 0.0034 (DF: 25). THE REGRESSION PRODUCED AN F-STATISTIC OF 54.93 ($P<0.0001$). 279
FIGURE 4.60. RESIDUALS FROM THE SIMPLE LINEAR REGRESSION CLEARLY ILLUSTRATE HETEROSCEDASTICITY IN THE SCALE-LOCATION PLOT AND THE PRESENCE OF INFLUENTIAL OBSERVATIONS IN THE LEVERAGE PLOT. 280
FIGURE 4.61 ROOT DISEASE SITE ADJACENT TO PLOT 57 USED TO ILLUSTRATE THAT THE PSRI INDEX IS SENSITIVE TO BOTH SHADOW AND DEAD TOPS AND IN THIS CASE NOT AT ALL SENSITIVE TO CHLOROTIC CROWNS. THE PSRI DISPLAY RANGE HAS BEEN RESTRICTED TO THE DATA RANGE OF -0.11(MINIMUM) TO -0.04 TO OMIT SHADOWED REGIONS. THE DISPLAY IS CLIPPED TO THE SPECIFIED DATA RANGE; IT IS TRANSPARENT OUTSIDE THAT RANGE. THE PSRI IS OVERLAYED ON TOP OF THE SPECTROMETER DATA. THE ORTHOPHOTO ILLUSTRATES THE ROOT DISEASE SITE WITH SNAGS AND A GAP WITH CHLOROTIC CROWNS AT ITS EDGE. THE CHLOROTIC CROWNS ARE NOT APPARENT IN THE PSRI. 284
FIGURE 4.62 THE BEST TWO VARIABLE SUBSET MODEL FOR ESTIMATING MEAN VOLUME INCREMENT WAS PRODUCED FROM THE MEDIAN HEIGHT OF THE LIDAR TREETOPS AND THE MEDIAN ABSOLUTE DEVIATION OF THE OPTICAL PIGMENT INDEX PSRI. 284
FIGURE 4.63. RESIDUALS FROM THE MULTIPLE LINEAR REGRESSION OF MEDIAN LIDAR TREETOP HEIGHT AND THE MEDIAN ABSOLUTE DEVIATION OF THE PSRI INDEX DO NOT STRONGLY SUGGEST THAT STATISTICAL ASSUMPTIONS HAVE VIOLATED 285
FIGURE 4.64 BOOTSTRAPPED CORRELATION ANALYSIS INDICATED THE MOST ASSOCIATED (MEAN R AND MEAN RHO) REMOTE SENSING METRIC WITH MEAN VOLUME INCREMENT WAS THE MAXIMUM IN THE CHM AND THE RELATIONSHIP WAS NON-LINEAR. THE MAXIMUM CHM DATA WERE TRANSFORMED BY A FIT EXPONENT.

REITERATED ANLYSIS INDICATED THAT THE TRANSFORMED VARIABLE WAS THE MOST ASSOCIATED FEATURE, IT WAS APPLIED IN A SIMPLE LINEAR REGRESSION. THE RESIDUALS OF THE SIMPLE LINEAR MODEL WERE SUMBITTED TO THE BOOTSTRAPPIING SCRIPT WHICH IDENTIFIED THE MEDIAN ABSOLUTE DEVIATION OF THE PSRI INDEX AS MOST CONTRIBUTING. THIS MODEL MIGHT BE CONSIDERED INFERIOR TO THE BEST TWO VARIABLE SUBSET MODEL AS IT REQUIRES THE ESTIMATION OF FOUR PARAMETERS AS APPOSED TO THREE. IN ADDITION, DEGREES OF FREEDOM DO NOT REFLECT THE ADDITIONAL SHAPE PARAMETER ESTIMATION.....286

FIGURE 4.65. RESIDUALS FROM THE MULTIPLE LINEAR REGRESSION OF TRANSFORMED MAXIMUM CHM HEIGHT AND THE MEDIAN ABSOLUTE DEVIATION OF THE PSRI INDEX DO NOT STRONGLY SUGGEST THAT STATISTICAL ASSUMPTIONS HAVE BEEN VIOLATED 287

FIGURE 4.66 PLOT MEAN PAI IN VOLUME (CROWN CLASSES DOMINANT TO SUPPRESSED) ESTIMATED FROM MEDIAN LIDAR TREETOP HEIGHT AND THE STANDARD DEVIATION OF THE CHM. THE RESIDUAL STANDARD ERROR PRODUCED FOR THIS REGRESSION MODEL IS 0.0028 289

FIGURE 4.67. RESIDUALS FROM THE MULTIPLE LINEAR REGRESSION OF MEDIAN LIDAR TREETOP HEIGHT AND THE STANDARD DEVIATION OF THE CHM DO NOT STRONGLY SUGGEST THAT STATISTICAL ASSUMPTIONS HAVE BEEN VIOLATED, ALTHOUGH THE LARGE GAP OF PLOT 67 PRODUCES A LARGE STANDARD DEVIATION IN THE CHM, FOR THIS REASON PLOT 67 IS IDENTIFIED AS AN INFLUENTIAL OBSERVATION. WITHOUT PLOT 67 THE REGRESSION PARAMETERS ARE: $Y=0.0012*TT_{MEDIAN}+0.0027*CHM_{SD}-0.0288$, ADJ. R^2: 0.74, RESIDUAL STANDARD ERROR: 0.0027, F-STAT: 35.92 (DF: 23).....290

FIGURE 4.68 PLOT MEAN PAI IN VOLUME (CROWN CLASSES DOMINANT TO SUPPRESSED) ESTIMATED FROM THE MEAN HEIGHT OF THE FOUR TALLEST LIDAR TREETOP HEIGHTS AND THE COEFFICIENT OF VARIATION OF THE CHM. THE RESIDUAL STANDARD ERROR PRODUCED FOR THIS REGRESSION MODEL WAS 0.0026 293

FIGURE 4.69. RESIDUALS FROM THE MULTIPLE LINEAR REGRESSION OF MEAN HEIGHT OF THE FOUR TALLEST LIDAR TREETOPS AND THE COEFFICIENT OF VARIATION OF THE CHM DO NOT SUGGEST THAT STATISTICAL ASSUMPTIONS HAVE BEEN VIOLATED. IN CONTRAST TO THE PREVIOUS MODEL PLOT 67 IS NOT IDENTIFIED AS AN INFLUENTIAL OBSERVATION. THE DIFFERENCE WITH REFERENCE TO PLOT 67 IS THAT ALTHOUGH THE STANDARD DEVIATION IN THE CHM IS HIGH THE MEAN IS RELATIVELY LOW.....294

FIGURE 4.70 PEARSON'S CORRELATION MATRIX ILLUSTRATING THAT VERY LITTLE INFORMATION DIVERSITY EXISTS WITHIN THE LIDAR HEIGHT QUANTILE DATA, ONLY THE FOUR EXTREME BINS CONTAIN VARIATION THAT IS NOT HIGHLY CORRELATED WITH THE OTHER BINS. ONLY $LHQ_{0, 5,95,\&100}$ HAVE CORRELATION COEFFICIENTS LESS THAN 0.90. 297

FIGURE 4.71. CHANGES IN LIDAR HEIGHT DISTRIBUTION ARE APPARENT WITH CHANGES IN POINT DENSITY. EACH PROFILE WAS DETERMINED BY ADDING CONSECUTIVE FLIGHT LINES. THE EFFECT OF INCREASING POINT DENSITY WAS THE GREATER PROPORTION OF RETURNS FROM LOWER CANOPY POSITIONS (*I.E.* ~12-18M). ALL PROFILES WERE BUILT FROM A 20X20M AREA (ALIGNED NORTH AND SOUTH) CENTERED AT 44730E, 5387363N, APPROXIMATELY TREATMENT PLOT 29.....299

FIGURE 4.72. LIDAR HEIGHT PERCENTILES BELOW THE 60TH HEIGHT PERCENTILE ARE INCREASINGLY AFFECTED BY POINT DENSITY WITH DECREASING HEIGHT PERCENTILE. THIS SUGGESTS A GREATER PENETRATION TO LOWER CANOPY POSITIONS WITH HIGHER POINT DENSITIES. INCREASING POINT DENSITY INCREASES THE MAXIMUM HEIGHT, IN LINE WITH THE INCREASED PROBABILITY OF INTERSECTING THE HIGHEST OBSTRUCTION. THE LOWEST DENSITY PROFILE DID NOT RETURN A POSITION AT THE HEIGHT THRESHOLD VALUE OF 4.01M, WHICH IS IN LINE WITH THE REDUCED PENETRATION ASSUMPTION. THE HEIGHTS ACROSS THE FIRST TWO QUARTILES WERE LOWERED WITH INCREASING POINT DENSITY.....300

FIGURE 4.73. INCLUDING PLOT 67, THE BEST TWO-VARIABLE SUBSET MODEL WAS PRODUCED BY THE MEAN CONTINUUM REMOVED DEPTH NORMALIZED RIGHT AREA AND THE MEDIAN GREENNESS INDEX (R_{554}/R_{677}). WITHOUT PLOT 67 THE BEST TWO-VARIABLE MODEL WAS PRODUCED BY TWO METRICS SUSPECTED OF HAVING A CONSIDERABLE NOISE CONTENT, ONE OF WHICH, $TCARI_{SKEWNESS}$ WAS NOT SIGNIFICANTLY ASSOCIATED WITH THE VOLUME INCREMENT ALONE. OMITTING PLOT 67 AND $TCARI_{SKEWNESS}$ THE BEST TWO-VARIABLE MODEL WAS ALSO THAT PRODUCED WITH RIGHT AREA MEAN AND THE GI MEDIAN. THE STANDARD ERRORS OF THE MODEL PARAMETERS WERE: CONSTANT WAS 0.483 (T: -8.2, P<0.0001), RA_{MEAN} WAS 0.0083 (T: 9.12, P<0.0001), AND GI_{MEDIAN} WAS 0.069 (T: 5.33, P<0.0001). THE ADJUSTED R^2 WAS 0.767, THE RESIDUAL STANDARD ERROR WAS 0.0434 (DF: 24), AND THE F-STATISTIC WAS 43.75 (P<0.0001).....302

FIGURE 4.74. INCLUDING PLOT 67, THE BEST TWO-VARIABLE SUBSET MODEL WAS PRODUCED BY THE MEAN CONTINUUM REMOVED DEPTH NORMALIZED RIGHT AREA AND THE MEDIAN GREENNESS INDEX (R_{554}/R_{677}). THE RESIDUAL PLOTS DID NOT OVERWHELMINGLY SUGGEST VIOLATIONS OF THE STATISTICAL ASSUMPTIONS AND THAT THE OUTLIER (PLOT 67) WAS NOT AN INFLUENTIAL OBSERVATION. 303

FIGURE 4.75. THE SINGLE MOST PAI TOTAL VOLUME ASSOCIATED FEATURE (MEAN CR DEPTH) WAS HIGHLY SUSCEPTIBLE TO THE PLOT 67 OUTLIER. WITHOUT THE EFFECT OF PLOT 67, LOWER LIDAR HEIGHT QUANTILES WERE MOST ASSOCIATED WITH PAI IN TOTAL VOLUME. WITHOUT HIGHER ORDER STATISTICAL MOMENTS OF THE TCARI INDEX, THE BEST TWO-VARIABLE MODEL INCLUDED THE MEAN CRDNRA AND THE MEDIAN GI, WHICH WERE THE SAME FEATURES SELECTED FOR THE BEST TWO-VARIABLE SUBSET MODEL WHEN PLOT 67 WAS INCLUDED. 304
FIGURE 4.76. THE STANDARD ERROR OF THE MODEL PARAMETERS WERE 1.91 FOR THE CONSTANT (T:-4.71, P<0.0001), 0.0040 FOR THE MEDTTHT COEFFICIENT (T:3.31, P: 0.003), AND 2.07 FOR THE CRDEPTH MEAN COEFFICIENT (T:4.68, P<0.0001). THE ADJUSTED R^2 WAS 0.709, THE RESIDUAL STANDARD ERROR WAS 0.0484 (DF:24) AND THE F-STATISTIC WAS 32.68 (P<0.0001). 306
FIGURE 4.77. RESIDUALS OF THE MULTIPLE LINEAR MODEL PRODUCED BY THE MEDIAN LIDAR TREETOP HEIGHT AND MEAN CONTINUUM REMOVED DEPTH. THE RESIDUAL PLOTS DID NOT OVERWHELMINGLY SUGGEST VIOLATIONS OF THE STATISTICAL ASSUMPTIONS AND THAT THE OUTLIER (PLOT 67) WAS NOT AN INFLUENTIAL OBSERVATION. 307
FIGURE 4.78 THE STANDARD ERROR OF THE MODEL PARAMETERS WERE 0.23 FOR THE CONSTANT (T:-4.01, P:0.0005), 0.060 FOR THE NATURAL LOG TRANSFORMED STANDARD DEVIATION OF THE CHM COEFFICIENT (T:4.68, P: 0.0001), AND 0.202 FOR THE CCF_{60} COEFFICIENT (T:6.67, P<0.0001). THE ADJUSTED R^2 WAS 0.624, THE RESIDUAL STANDARD ERROR WAS 0.0550 (DF:24) AND THE F-STATISTIC WAS 22.61 (P<0.0001). 309
FIGURE 4.79. RESIDUAL PLOTS FOR THE MULTIPLE LINEAR REGRESSION PRODUCED BY THE LN TRANSFORMED CHM STANDARD DEVIATION AND LIDAR CANOPY CLOSURE AT THE 60TH HEIGHT PERCENTILE. THE RESIDUAL PLOTS DID NOT OVERWHELMINGLY SUGGEST HETEROSCEDASTICITY AND ALTHOUGH VERY CLOSE TO THE COOK'S DISTANCE THRESHOLD PLOTS 2 AND 67 ARE NOT CLASSIFIED AS INFLUENTIAL. 310
FIGURE 4.80. THE STANDARD ERROR OF THE MODEL PARAMETERS WERE 0.103 FOR THE CONSTANT (T:-0.14, P:0.89), 0.004 FOR THE MEDIAN LIDAR TREETOP HEIGHT COEFFICIENT (T:5.74, P< 0.0001), AND 0.0004 FOR THE STANDARD DEVIATION OF THE LIDAR TOPOGRAPHIC CATCHMENT AREA COEFFICIENT (T:-3.16, P:0.004). THE ADJUSTED R^2 WAS 0.569, THE RESIDUAL STANDARD ERROR WAS 0.049 (DF:23) AND THE F-STATISTIC WAS 17.52 (P<0.0001).NOTE THAT ALTHOUGH PLOT 67 IS ILLUSTRATED ABOVE IT DID NOT CONTRIBUTE TO THE MULTIPLE LINEAR REGRESSION. 311
FIGURE 4.81. RESIDUAL PLOTS FOR THE MULTIPLE LINEAR REGRESSION PRODUCED BY THE MEDINA LIDAR TREETOP HEIGHT AND THE STANDARD DEVIATION OF THE LIDAR TOPOGRAPHIC CATCHMENT AREA. THE RESIDUAL PLOTS MIGHT SUGGEST A SUBTLE NONLINEAR TREND. 312
FIGURE 4.82. THE STANDARD ERROR OF THE MODEL PARAMETERS WERE 0.202 FOR THE CONSTANT (T:-4.99, P<0.0001), 0.052 FOR THE LN TRANSFORMED STANDARD DEVIATION OF THE CHM COEFFICIENT (T:5.56, P< 0.0001), AND 0.178 FOR THE CCF_{60} COEFFICIENT (T:8.24, P<0.0001) AND 0.00038 FOR THE MEAN OF THE LIDAR TOPOGRAPHIC CATCHMENT AREA COEFFICIENT (T:-3.09, P:0.005). THE ADJUSTED R^2 WAS 0.723, THE RESIDUAL STANDARD ERROR WAS 0.047 (DF:23) AND THE F-STATISTIC WAS 23.62 (P<0.0001). 313
FIGURE 4.83. RESIDUAL PLOTS FOR THE MULTIPLE LINEAR REGRESSION PRODUCED BY THE NATURAL LOG TRANSFORMED CHM STANDARD DEVIATION, THE LIDAR CANOPY CLOSURE AT THE 60TH HEIGHT PERCENTILE AND THE MEAN UPSLOPE CATCHMENT AREA. THE RESIDUAL PLOTS DO NOT SUGGEST THAT VIOLATIONS OF THE STATISTICAL ASSUMPTIONS HAVE OCCURRED. 314
FIGURE 4.84. THE CANOPY CLOSURE PROFILES FOR THE SELECTED SLP TREATMENT PLOTS ILLUSTRATED THAT THERE WAS LITTLE VARIATION BELOW THE 60TH HEIGHT PERCENTILE. AFTER THE 60TH PERCENTILE THERE IS A DOWNWARD TRAJECTORY THAT WOULD BE CONSISTENT WITH THE LOCATION WHERE INDIVIDUAL CROWNS ARE EMERGENT AND ABOVE WHICH THE APICAL SHAPE OF THE INDIVIDUAL CROWNS COULD EXPLAIN THE CCF PROFILE SHAPE. 316
FIGURE 4.85. PEARSON'S CORRELATION COEFFICIENT MATRIX AMONG THE CANOPY CLOSURE FEATURES AT LIDAR HEIGHT PERCENTILE (5 PERCENTILE INTERVALS), ILLUSTRATING THE HIGH DEGREE OF ASSOCIATION BETWEEN THE CCF METRICS LESS THAN THE 60TH HEIGHT PERCENTILE (0.6). 317
FIGURE 4.86. THE STANDARD ERROR OF THE MODEL PARAMETERS WERE 16.3 FOR THE CONSTANT (T:-7.02, P<0.0001), 1.99 FOR THE MEDIAN PRI COEFFICIENT (T:5.94, P< 0.0001), AND 0.453 FOR THE CCF_{30} COEFFICIENT (T:-5.02, P<0.0001) AND 0.023 FOR THE MEDIAN RED EDGE POSITION COEFFICIENT (T:7.08, P<0.0001). THE ADJUSTED R^2 WAS 0.777, THE RESIDUAL STANDARD ERROR WAS 0.068 (DF:23) AND THE F-STATISTIC WAS 31.2 (P<0.0001). 318
FIGURE 4.87. RESIDUAL PLOTS FOR THE MULTIPLE LINEAR REGRESSION PRODUCED BY THE MEDIAN PRI INDEX, THE LIDAR CANOPY CLOSURE AT THE 30TH HEIGHT PERCENTILE AND THE MEDIAN RED EDGE POSITION. THE RESIDUAL PLOTS DO NOT STRONGLY SUGGEST THAT VIOLATIONS OF THE STATISTICAL ASSUMPTIONS HAVE OCCURRED.

NOTE HOWEVER THAT PLOT 67 IS MISSING AS ITS LEVERAGE IS 1 AND IS THE REASON FOR THE MEDIAN REP WHICH IS FUNCTIONALLY A DUMMY VARIABLE TO ACCOUNT FOR THAT PLOTS DISSIMILAR PRODUCTIVITY. 319
FIGURE 4.88 MULTIPLE LINEAR REGRESSION PREDICTING PAI IN TOTAL PLOT VOLUME WITH ALL CROWN CLASSES FROM PLOT MEAN PRI, LIDAR CANOPY CLOSURE AT THE 45TH LIDAR HEIGHT PERCENTILE AND THE PLOT MEAN CONTINUUM REMOVED DEPTH. THIS MODEL IS THE LIMIT OF REASONABLE NUMBER OF INDEPENDENT VARIABLES. THE FEATURE SELECTION CAN BE RATIONALIZED BY PHYSICAL RELATIONSHIPS BETWEEN PRODUCTIVITY AND THE SELECTED METRICS. THE PRI IS INDICATIVE OF LIGHT USE EFFICIENCY, CONTINUUM REMOVED DEPTH IN THE 680NM FEATURE IS REPRESENTATIVE OF CHLOROPHYLL CONTENT AND THE LIDAR CCF ATTRIBUTE REPRESENTS THE CROWN HORIZONTAL EXTENT, WHICH IS ALSO RELATED TO BASAL AREA. TO ENCORPORATE PLOT 67 THE REP ATTRIBUTE WAS INCLUDED AND THE REGRESSION RESULTS ARE PRESENTED IN FIG. 4.90 AND TABLE 4.20 322
FIGURE 4.89. RESIDUAL PLOTS FOR THE MULTIPLE LINEAR REGRESSION PRODUCED BY THE MEAN PRI INDEX, THE LIDAR CANOPY CLOSURE AT THE 45TH HEIGHT PERCENTILE AND THE MEAN CONTINUUM REMOVED DEPTH. THE RESIDUAL PLOTS DO NOT SUGGEST THAT VIOLATIONS OF THE STATISTICAL ASSUMPTIONS HAVE OCCURRED.... 323
FIGURE 4.90.THE MULTIPLE LINEAR REGRESSION MODEL WAS AUGMENTED WITH THE REP MEDIAN ATTRIBUTE TO ACCOUNT FOR THE REDUCED PRODUCTIVITY AND MORTALITY IN PLOT 67. THE PRESENCE OF WOODY DEBRIS, THIN AND OR CHLOROTIC CROWNS WOULD CONTRIBUTE TO THE SEPARATION OF PLOT 67 FROM THE OTHER PLOTS BY THE SHORTWAVE MIGRATION OF THE RED EDGE SLOPE INFLEXION. HOWEVER, GIVEN ONLY ONE OBSERVATION EXHIBITED THESE CHARACTERISTICS THE MEDIAN REP COEFFICIENT SHOULD NOT BE CONSIDERED STABLE OR VALID, BUT WOULD SUGGEST THE METRIC OR THE SIMILAR WOULD BE USEFUL FOR CHARACTERIZING CANOPY HEALTH. 324
FIGURE 4.91. THE CANOPY CLOSURE AT THE 45TH LIDAR HEIGHT PERCENTILE THAT SIGNIFICANTLY CONTRIBUTED TO EXPLAINING VARIATION IN THE PLOT VOLUME INCREMENT WAS ALSO ASSOCIATED WITH THINNING LEVEL, WHERE PLOTS THAT WERE THINNED TO A THIRD OF BASAL AREA HAD A REDUCED CANOPY CLOSURE RELATIVE TO A THINNING TO 2/3 BA AND THE CONTROL TREATMENTS. 326
FIGURE 4.92 THE POINT CLOUDS OF PLOTS 31 AND 67, EXAMPLES OF HIGH AND LOW VOLUME RESPECTIVELY. THE CCF AT THE 70TH PERCENTILE PROVIDES AN ACCURATE PREDICTION OF PLOT VOLUME. THE 70TH PERCENTILE FOR PLOT 31 OCCURS AT A HEIGHT OF 27.25M WHILE THAT FOR PLOT 67 OCCURS AT 19.57M. THE CCF_{70} OF PLOT 31 IS 0.82 AND IN PLOT 67 IT IS 0.24. 330
FIGURE 4.93. THE POINT CLOUDS OF PLOTS 41 AND 67, EXAMPLES OF HIGH AND LOW HTLC RESPECTIVELY. THE 10TH PERCENTILE OF THE LIDAR CHM POINT CLOUD PROVIDES AN ACCURATE PREDICTION OF PLOT HTLC. THE LHQ_{10} FOR PLOT 41 OCCURS AT A HEIGHT OF 23.9M WHILE THAT FOR PLOT 67 OCCURS AT 14.58M. 333
FIGURE 5.1 DATA PROCESSING SEQUENCE FOR STEM MAPPING AND DBH MODELING THROUGH TLS WITH AN INDEPENDENTLY COLLECTED VALIDATION DATASET. 344
FIGURE 5.2 DERIVING DBH FROM TLS PSEUDO HORIZONTAL POINT CLOUD SECTIONS. THE CLUSTER RANGE CENTER IS REPRESENTED IN RED, POINTS ARE STRATIFIED INTO AZIMUTH BINS (GREY DASHED), BIN MINIMUM DISTANCE POINTS ARE DETERMINED (CYAN), CENTER (GREEN 1 & 2), IS ADJUSTED BASED ON TRANSECTS (BLUE DASHED). 345
FIGURE 5.3 THE UNCALIBRATED ERROR OF THE GEOMETRIC SOLUTION FOR ESTIMATING DBH PRODUCED A MEDIAN ERROR OF -1.73CM BUT PRODUCED RARE ERRORS AS HIGH AS -12CM FOR INDIVIDUAL OBSERVATIONS. THE ERROR DISTRIBUTION WAS NEGATIVELY SKEWED WHERE UNDERESTIMATION WAS FAR MORE LIKELY THAN OVERESTIMATION. 346
FIGURE 5.4 SCATTERPLOT AND LINEAR REGRESSION RESULTS OF PLOT MEAN DBH, DEMONSTRATED A HIGH DEGREE OF ASSOCIATION. 348
FIGURE 5.5 SCATTERPLOT AND LINEAR REGRESSION RESULTS OF AVERAGE PLOT DBH RESIDUALS AND SCAN INTEGRATION FIT INDEX (TENSION). DBH ERROR INCREASES WITH POOR SCAN INTEGRATION FIT. 350
FIGURE 5.6 SCATTERPLOT AND LINEAR REGRESSION OF ALL CORE STEMS, EXTREME VALUES ARE IDENTIFIED AS THE LARGEST ONE PERCENT OF THE ABSOLUTE RESIDUAL AND ARE LABELED BY PLOT ID (ABOVE) AND TREE ID (BELOW). RESIDUAL PLOTS FOR INITIAL DBH REGRESSION OF FIELD MEASURED AND TLS MODELED DBH VALUES. OUTLIERS AND INFLUENTIAL DATA POINTS ARE CLEARLY EVIDENT IN THE RESIDUAL AND LEVERAGE PLOT RESPECTIVELY 352
FIGURE 5.7 SCATTERPLOT AND LINEAR REGRESSION OF CORE STEMS WITHOUT INFLUENTIAL POINTS. THE INTERCEPT WAS SIGNIFICANTLY DIFFERENT FROM ZERO AND THE RESIDUAL STANDARD ERROR DECREASED BY 0.01CM. .. 353
FIGURE 5.8 DBH ESTIMATION ERROR FROM THE GEOMETRIC APPROACH PRODUCED A MEDIAN ERROR THAT WAS 1.7CM SMALLER THAN THE FIELD MEASURED DIAMETERS. 354

FIGURE 5.9 SCATTERPLOT AND LINEAR REGRESSION OF ALL CORE STEMS, WITH A MEDIAN BIAS OF -1.7 REMOVED. EXTREME VALUES ARE IDENTIFIED AS THE LARGEST ONE PERCENT OF THE ABSOLUTE RESIDUAL AND ARE LABELED BY PLOT ID (ABOVE) AND TREE ID (BELOW). RESIDUAL PLOTS FOR THE ADJUSTED DBH ESTIMATES REGRESSED WITH FIELD MEASURED DBH VALUES SUGGEST NO SCALE DEPENDENCY WITHIN THE ESTIMATED DATA. RESIDUALS PLOTS SUGGEST CONSTANT AND UNIFORM VARIANCE WITHOUT THE PRESENCE OF OUTLIERS AND INFLUENTIAL DATA POINTS 355
FIGURE 5.10 SCATTERPLOT AND LINEAR REGRESSION RESULTS OF DBH RESIDUALS AND RADIAL STEM COVERAGE. REGRESSION ANALYSIS SUGGESTED SMALLER DBH ERRORS FOR STEMS WITH A GREATER PROPORTION OF THEIR STEM MEASURED BY TLS. THE RESIDUAL PLOTS ILLUSTRATE THAT THE TRANSFORMATION HAS RESOLVED THE RESIDUAL AUTOCORRELATION AND NON-PARAMETRIC DISTRIBUTION IN THE UNTRANSFORMED MODEL. THE LOWESS CURVE OF THE SCALE-LOCATION PLOT MAY INDICATE VARIANCE INEQUALITY, BUT MAY ALSO BE AN ARTEFACT OF LOW DATA DENSITY AT HIGHER FITTED RESIDUAL ERRORS (FITTED VALUES), ACTUALLY THE PRODUCT OF LOW DENSITY IN LOW TLS STEM COVERAGE. 357
FIGURE 5.11 THE MARGINAL IMPROVEMENT IN THE RESIDUAL ERROR OF MLR OVER SLR RAISED CONCERNS ABOUT THE VALIDITY OF THE MORE COMPLEX MULTIVARIATE MODEL. THE RESIDUAL PLOTS FOR THE MLR DBH MODEL ILLUSTRATES THAT THE ASSUMPTIONS OF THE STATISTICAL APPROACH WERE WITHIN REASON. THE TAILS OF THE RESIDUAL DISTRIBUTION MAY BE SLIGHTLY HEAVY RELATIVE TO A NORMAL DISTRIBUTION AND THERE MAY BE A DATA POINT THAT IS INFLUENTIAL BUT IS NOT AN OUTLIER IN TERMS OF THE MODEL; MULTICOLLINEARITY WAS NOT ASSESSED BUT IS EXPECTED AT LEAST BETWEEN TLS DBH MEASUREMENTS AND STEM DENSITY. 358
FIGURE 5.12 A: POOR DBH ESTIMATES TENDED TO OCCUR IN PLOTS WITH POOR SCAN INTEGRATION AND HIGH STEM DENSITIES. PLOT 2 HAD THE WEAKEST SCAN INTEGRATION AND THE GREATEST STEM DENSITY WITH DEVELOPING UNDERSTORY AND PRODUCED THE WEAKEST FIT OF ALL PLOT BASED REGRESSION MODELS. B: THE STRONGEST PLOT BASED MODEL WAS PRODUCED FOR PLOT 36, WHICH HAD A STEM DENSITY OF 1400 STEMS/HA. IT IS SUGGESTED THAT THE RANGE OF DBH VALUES, WHICH IS THE LARGEST OF ALL PLOTS AND PARTICULARLY THE THREE LARGE STEMS ~45CM, CONTRIBUTES TO ITS STRONG MODEL. 364
FIGURE 5.13 TLS POINT CLOUDS OF STEMS USED FOR DBH MEASUREMENT. STEM ATTRIBUTE WERE DERIVED FROM INFORMATION ON STEM COVERAGE DISTRIBUTIONS (GREEN) AND MINIMUM RADIUS DISTANCE DISTRIBUTIONS (RED). CLUSTERING APPROACHES (RED POINT AND CIRCLE) DID NOT PRODUCE SUFFICIENTLY ACCURATE RESULTS. A STRATEGY CONSIDERING ORTHOGONAL TRANSECTS AND MINIMUM DISTANCES FROM PSEUDO CENTER POSITION TO STEM CIRCUMFERENCE IMPROVED DBH MODELING. THIS STRATEGY PERFORMS WELL UNDER CONDITIONS OF FULL STEM COVERAGE AND HIGH POINT DENSITIES A), OR PARTIAL COVERAGE HIGH POINT DENSITIES B), OR PARTIAL STEM COVERAGE AND LOW POINT DENSITIES C). 365
FIGURE 5.14 ESTIMATING HTLC FROM AREAL GAP FRACTION PROFILES. HTLC WAS ESTIMATED AS THE HEIGHT DIFFERENCE BETWEEN THE MINIMUM HEIGHT BIN AND THE HEIGHT OF THE BIN WITH THE MAXIMUM DECREASE IN AREAL GAP FRACTION. THIS FIRST MODELING ITERATION SEVERELY UNDER ESTIMATED HTLC IN THE LOWER RANGE OF THE DATA. 370
FIGURE 5.15 THE MAXIMUM NEGATIVE SLOPE IN THE DELTA GAP PROFILE UNDER ESTIMATED THE HTLC AS IT WAS SENSITIVE TO REMNANT LIMBS STILL ATTACHED TO THE BOLE BUT NO LONGER PHOTOSYNTHETICALLY ACTIVE. THE VOXEL FILE WAS USED TO QUERY VERTICAL SLICES TO DETERMINE AN APPROPRIATE STRATEGY FOR HTLC DETECTION. GAP AND DELTA GAP PROFILES ARE ILLUSTRATED FOR TREE 16 IN PLOT 55 WITH A FIELD MEASURED HTLC OF 24.3M (~374.3M ELEVATION). A VOXEL COMPOSITE IMAGE IS DISPLAYED IN THE RIGHT PANEL AS RGB: HEIGHT BIN 7 (354M), 28 (375M), 12 (359M). THE SELECTED HEIGHT BINS CORRESPOND WITH THE MAXIMUM GAP FRACTION, MINIMUM GAP FRACTION AND THE MAXIMUM DECREASE IN GAP FRACTION RESPECTIVELY. THESE HEIGHT LEVELS APPEAR TO CORRESPOND WELL WITH HEIGHTS REPRESENTING THE STEM (WHITE), CROWN (GREEN) AND REMNANT LIMBS (CYAN) RESPECTIVELY. 371
FIGURE 5.16 HTLC MEASUREMENTS BY TLS AREAL GAP FRACTION PROFILE AND BEM GROUND HEIGHT PRODUCED A MEDIAN ERROR OF 0.68M 373
FIGURE 5.17 ESTIMATING HTLC FROM AREAL GAP FRACTION PROFILES. HTLC WAS ESTIMATED AS THE HEIGHT DIFFERENCE BETWEEN THE LOCAL MINIMUM GAP FRACTION DERIVATIVE AND THE BEM HEIGHT. THE METRIC WAS BUILT TO PHYSICALLY CAPTURE HTLC MEASUREMENTS AND WAS ONLY EXPECTED TO CONTAIN AN ERROR CONSTANT, WHICH WAS ESTIMATED AS THE MEDIAN ERROR 0.68M. THE ERROR CONSTANT WAS REMOVED AND A LINEAR REGRESSION WITHOUT AN INTERCEPT WAS USED TO DETERMINE IF THE SCALE OF THE HTLC ERROR WAS VASTLY DIFFERENT FROM ONE. ALTHOUGH THE LINEAR REGRESSION SUGGESTED A BEST FIT OF ONE, THERE REMAINED A TREND IN THE RESIDUALS THAT TENDED TO DECREASE THE RESIDUAL WITH INCREASING HTLC. 374
FIGURE 5.18 ESTIMATING HTLC FROM AREAL GAP FRACTION PROFILES. HTLC WAS ESTIMATED AS THE HEIGHT DIFFERENCE BETWEEN THE LOCAL MINIMUM GAP FRACTION DERIVATIVE AND THE BEM HEIGHT. THE METRIC

was built to physically capture HTLC measurements and was only expected to contain an error constant, which was estimated as the median error 0.68m. The error constant was removed and a linear regression without an intercept was estimated. The residuals were negatively associated with measured HTLC, including a constant term resolved the residual trend. However, this result was interpreted as spurious and dependent on a cluster of large residual errors with low TLS estimated HTLC. 375
Figure 5.19 Stepwise linear regression with a maximum of five features was used to estimate HTLC and produced marginal improvements over the simple regression model. The highly complex model did not seem warranted although the residuals were much better behaved and the coefficients and features selected were reasonable. 378
Figure 5.20 HTLC estimates from the MLR produced a median error of 0.10m 379
Figure 5.21 HTLC errors from local minimum areal gap fraction derivative grouped by plot and treatment. It was expected that errors might be specific to treatment types, where greater thinning and fertilizer would promote early growth and perhaps less remnant non-photosynthetic limbs, in which case the minimum gap fraction derivative without reference to the maximum canopy closure would be the better parameter used. The plot does not suggest a strong treatment effect is present. 381
Figure 5.22 50cm CHM at TLS stem position, tree ht= 0.657*CHM+8.363 384
Figure 5.23 50cm CHM at TLS stem position, tree ht= 0.888*CHM+1.568, Note this evaluation was not done for prediction but rather to investigate the influence of DBH on the CHM height versus field measured height relationship. The inverted form of this model would be 2012 height=CHM*1.1261-1.7658. Open circles are omitted observations and closed circles are observations used in model building. 385
Figure 5.24 50cm CHM at TLS stem position with a plot based DBH percentile threshold filter. The plot-based percentile was used to test if the relative DBH size was a better attribute to use in explaining the occurrence of large residuals in height modeling. Even with an aggressive 55percentile filter the residual standard error was very similar to that produced with the global or whole sample percentile threshold. Open circles are omitted observations and closed circles are observations used in model building. 387
Figure 5.25 Investigating the relationship between omission errors and commission errors the appropriate parameter combination was sought. 391
Figure 5.26 Plotting omission, commission and height errors stratified by lidar treetop extraction parameters helped to visualize trends in the treetop extraction results and provided an objective means for evaluating appropriate algorithm parameters. The 20cm CHM produced far too many commission errors to be considered. The detection accuracy increase by applying noise reduction filters. The remaining parameter combinations (50cm CHM with filtering) were very similar and the selection of one over the other was a compromise between commission and omission errors. In this case a low omission error was considered a priority over commission error since tree locations were known. 393
Figure 5.27 Tree height regression with accurately detected treetops found through the local binary maximum filter, produced encouraging results but identified several large outliers that were attributed to incorrectly associated ground data to RS data and one instance of point cloud noise. 395
Figure 5.28 Tree height regression residuals from lidar treetops, produced encouraging results but identified several large outliers that were attributed to incorrectly associated ground data to RS data and one instance of point cloud noise. Aside from the few large errors the residuals suggested a constant average near zero through the height range with an approximately normal distribution and constant variance without evidence of influential points. 396
Figure 5.29 Tree height regression residuals from lidar treetops, several large outliers were attributed to incorrectly associated ground data to RS data and one instance of point cloud noise. 397
Figure 5.30 One of the large tree height residuals was attributed to point cloud noise at tree ID 77 at plot 65, possibly the effect of light rain. It was resolved by terrestrial lidar stem tracing by high-density voxels. 398
Figure 5.31 The large magnitude height estimate errors were attributed to a small group of observations incorrectly matched with field reference data and one instance of point cloud

noise. When these known error observations were removed the residuals more closely approximated a normal distribution. 399
Figure 5.32 The omission of the large residuals with known error sources produced a fit that was very near the 1:1 line. This analysis demonstrates if the treetop parameters can converge on a solution that minimizes commission and omission then the lidar treetop product may be applicable for height estimation without costly field campaigns. Open circles are omitted observations and closed circles are observations used in model building. 401
Figure 5.33 The omission of the large residuals with known error sources produced a fit that was very near the 1:1 line. The error evaluation in the regression diagnostic plots did not suggest a violation of assumptions or the presence of influential observations. 402
Figure 5.34 At a fine spatial scale of analysis, the omissions errors tended to have lower heights, note that these heights do not indicate that the heights are accurate, only that they have been detected, or at least a local maximum near the horizontal position of the stem was detected. Relative to the coarse scale treetop extractions the heights of the fine scale results appear to produce slightly shorter heights for the correctly detected trees (~25m). 404
Figure 5.35 At a coarse spatial scale of analysis, the omissions errors behaved as expected by missing a larger proportion of taller trees. 405
Figure 5.36 Post-hoc comparison tests illustrate the effect of spatial scale, as provided by extraction parameters, on the number of omission errors and the height of the omission errors. Where, coarse neighbourhoods produce more omissions and the height of those omissions tend to be taller. 406
Figure 5.37 Semivariogram range was qualitatively used to support decisions on neighbourhood scale for treetop extractions. The semivariogram range is the x-location were the slope of semivariance levels off indicating that dissimilarity does not further increase with increasing distance. Conversely below the range, values are increasingly similar with decreasing distance. 408
Figure 5.38 Predicting lidar treetop omission errors from plot stem count. A simple linear regression demonstrates that the density of a forest stand is strongly related to success of a lidar individual tree survey. The treetop omission errors increase with increasing stem density. According to these data and processing stream, lidar will capture all individual treetops (omission error=0) below a plot density of approximately 20.3 411
Figure 5.39 Neighbour metrics generated to predict lidar treetop omission errors, trees with more distant (row one), shorter (row two) neighbours are better detected. Row three illustrates the interaction of distance and height differential further separates correct and omitted. 413
Figure 5.40 Conditional density plots illustrate the effect of neighbour proximity and height differential on the likelihood of lidar CHM treetop detection. The change in direction of the nearest neighbour plot identifies the smallest resolvable treetop distance permitted by the lidar processing (1.5m distance). The steep transition in the height differential plot suggested it would be helpful in discriminating the groupings and the interaction term separates the group probabilities further. 419
Figure 5.41 The fitted probabilities of omission by binary logistic regression further separated the distributions of omission errors and correctly detected trees. However, there still remained some overlap in omission probability between the omitted and correct trees 419
Figure 6.1 Modeling periodic annual increment in tree volume from the individual tree remote sensing metrics. Some trees were incorrectly matched to the ground reference data, in many of these instances the lidar treetop was displaced from the ground reference location. Using the distance between the reference and target, the data were iteratively filtered and the impact on the model fit was plotted. 428
Figure 6.2 The ground reference database is translated to the remote sensing database by the nearest horizontal distance to a TLS surveyed stem, which is then translated to the nearest neighbour (3D) lidar treetop. Only those trees with an associated delineated crown are retained. Limitations with individual crown segmentation cause multiple trees to be located within one crown; this tends to change the shape of the crown segments, which may be detected in shape/compactness indices. Note that all but two core trees in plot 54 are co-dominant, tree 83 and 54 are dominant. 430

FIGURE 6.3 INVESTIGATING THE CHANGE IN PAI VOLUME PREDICTION FROM INDIVIDUAL TREE METRICS STRATIFYING BY CROWN SHAPE/COMPACTNESS. QUALITATIVELY, CROWNS BELOW A METRIC VALUE OF ROUGHLY $3M^2$ APPEARED PROPERLY DELINEATED. THIS INQUIRY SUGGESTS THE USE OF A SHAPE METRIC OF APPROXIMATELY $2.1M^2$. HOWEVER, THE DISTRIBUTION OF THE SHAPE METRIC IS POSITIVELY SKEWED AND SAMPLE SIZES CHANGE DRAMATICALLY AT THE LOWER INTERVALS FROM 10 TO 134 IN THE FIRST THREE INTERVALS. THUS THE VARIABLE SAMPLE SIZE IS LIKELY TO CONFOUND FIT INDEX VALUE TRENDS AT THESE LOWER INTERVALS. 431
FIGURE 6.4 THE RESIDUAL DISTRIBUTION OF THE SLR FOR ESTIMATING PAI VOLUME FROM LIDAR TREETOP HEIGHT SUGGESTS AN IMPROVEMENT COULD BE ACHIEVED BY ESTIMATING A CURVATURE PARAMETER. 433
FIGURE 6.5 SLR RESIDUAL DISTRIBUTION HISTOGRAM DENSITY AND NORMAL DISTRIBUTION SUGGEST MINOR SKEWNESS AND KURTOSIS DEPARTURES FROM NORMALITY 434
FIGURE 6.6 CURVE ESTIMATION FOR PAI IN VOLUME AND LIDAR TREETOP HEIGHT.. 435
FIGURE 6.7 THE EXPONENT TRANSFORMED LIDAR TREETOPS HAD RESOLVED THE PREVIOUSLY OBSERVED TREND IN THE RESIDUALS OF THE SLR. NOTE THE FIT INDEX DOES NOT ADEQUATELY REPRESENT THE TRUE DEGREES OF FREEDOM AS THE CURVATURE PARAMETER WAS ESTIMATED PRIOR TO THE SLR ILLUSTRATED HERE. 436
FIGURE 6.8 THE RESIDUAL DISTRIBUTION OF PAI VOLUME ESTIMATES FROM THE EXPONENT TRANSFORMED LIDAR TREETOPS IS MARGINALLY LESS SKEWED WITH A LOWER KURTOSIS RELATIVE TO THE RESIDUAL DISTRIBUTION PRODUCED FROM THE ORIGINAL SLR 437
FIGURE 6.9 THE BEST TWO-FEATURE MODEL WAS SELECTED BY THE EXHAUSTIVE SEARCH REGRESSION SUBSET, WHICH IDENTIFIED THE LINEARIZED LIDAR TREETOP HEIGHT AND THE AVERAGE PLOT LIDAR TREETOP HEIGHT. AN EXPONENT TRANSFORMATION RESOLVED OBSERVED TRENDS IN THE INITIAL RESIDUAL PLOTS. THESE TWO ATTRIBUTES EXPLAIN NEARLY 67% OF THE VARIATION IN INDIVIDUAL TREE PRODUCTIVITY. THE RESULTING MODEL PREDICTS PAI VOLUME WITH A PRECISION OF 0.005 (RSE). 439
FIGURE 6.10 THE RESIDUAL DISTRIBUTION FROM THE TWO-FEATURE REGRESSION MODEL PREDICTING PAI VOLUME IS APPROXIMATELY NORMAL. THE RESIDUALS ARE SLIGHTLY SKEWED 0.67 AND SLIGHTLY LEPTOKURTIC (5.91) RELATIVE TO THE NORMAL DISTRIBUTION (SKEWNESS: 0.0, KURTOSIS: 3.0). THE KURTOSIS OF THE RESIDUALS SUGGESTS THAT THERE IS A HIGH DENSITY OF LOW MAGNITUDE ERRORS. 440
FIGURE 6.11 APPLYING THE LIDAR TREETOP HEIGHT, PLOT AVERAGE LIDAR TREETOP HEIGHT AND THE INTERACTION EXPLAINED 2% MORE VARIATION IN PRODUCTIVITY OVER THE PREVIOUS TWO-FEATURE MODEL WITHOUT THE INTERACTION. 441
FIGURE 6.12 RESIDUAL DISTRIBUTION PRODUCED BY ESTIMATING PAI VOLUME FROM LINEARIZED LIDAR TREETOP HEIGHT, PLOT AVERAGE LIDAR TREETOP HEIGHT AND THEIR INTERACTION. 442
FIGURE 6.13 APPLYING THE RELATIVE LIDAR TREETOP HEIGHT VARIABLE WITH THE WITHIN CROWN MEDIAN LIDAR POINT HEIGHT EXPLAINED 3% MORE VARIATION IN PRODUCTIVITY OVER THE PREVIOUS TWO-FEATURE MODEL BUILT FROM LIDAR TREETOP HEIGHT AND PLOT AVERAGE LIDAR TREETOP HEIGHT. 444
FIGURE 6.14 RESIDUAL DISTRIBUTION PRODUCED BY PAI VOLUME ESTIMATION FROM LIDAR TREE CROWN 50TH PERCENTILE HEIGHT AND TREETOP HEIGHT TO PLOT HEIGHT RATIO. THE RESIDUAL DISTRIBUTION IS SLIGHTLY LEPTOKURTIC AND POSITIVELY SKEWED RELATIVE TO NORMAL. 445
FIGURE 6.15 CROWN SHAPE ATTRIBUTES WERE ASSESSED FOR THEIR ABILITY TO INDICATE TREE CLUSTERS RATHER THAN INDIVIDUAL CROWNS AND EXPLAINED 2% MORE VARIATION IN THE VOLUME INCREMENTS. 447
FIGURE 6.16 RESIDUAL DISTRIBUTION PRODUCED BY PAI VOLUME ESTIMATION FROM LIDAR TREETOP, TREETOP HEIGHT TO PLOT HEIGHT RATIO AND A CROWN SHAPE ATTRIBUTE. THE RESIDUAL DISTRIBUTION IS SLIGHTLY LEPTOKURTIC AND POSITIVELY SKEWED RELATIVE TO NORMAL. 448
FIGURE 7.1 THE TRESTLE FOREST MANAGEMENT UNIT WITHIN THE GVWSA, VANCOUVER ISLAND, BRITISH COLUMBIA, CANADA. THE SITE HAS 419M OF RELIEF (183-602M MSL), SLOPES UP TO 73° WITH A MEDIAN OF 15°, AZIMUTHS LARGELY IN THE 240° DIRECTION. ELEVATION AND SHADED RELIEF OVERLAID ON ORTHOMOSAIC 30CM. 455
FIGURE 7.2 CRTA DISTRIBUTIONS OF THE MANAGEMENT UNIT BETWEEN THE TWO SAMPLING DATES. SCALED KERNEL DENSITY ESTIMATES OVERLAY HISTOGRAMS. 460
FIGURE 7.3 THE IDENTIFICATION OF SPATIALLY AUTO-CORRELATED LOW CHLOROPHYLL, AS REPRESENTED BY THE AREA OF THE NORMALIZED CHLOROPHYLL ABSORPTION FEATURE. VALUES LESS THAN -1.96 REPRESENT STATISTICALLY SIGNIFICANT SPATIAL CLUSTERS OF LOW PRODUCTIVITY. 463
FIGURE 7.4 THE UNION OF SPATIALLY AUTO-CORRELATED 2006 POOR HEALTH AND SPATIALLY AUTO-CORRELATED WINDTHROW IS USED TO IDENTIFY LIKELY REGIONS OF ACTIVE ROOT DISEASE 464

List of Acronyms

AIS: airborne imaging spectrometer
ALS: airborne laser scanner
APAR: absorbed photosynthetically active radiation
ARP: antenna reference point
ATP: adenosine triphosphate

BCACS: British Columbia Active Control System
BEM: bare earth model
BRDF: bidirectional reflectance distribution function
BRF: bidirectional reflectance factor

CACS: Canadian Active Control System
CAI: current annual increment
CFS: Canadian Forest Service, Government of Canada
CHM: canopy height model

DBH: diameter at breast height
DGPS: differential corrected global positioning system
DSM: digital surface model

ELC: empirical line calibration

FLAASH: fast line-of-sight atmospheric analysis of spectral hypercubes

GPP: gross primary production
GPS: Global positioning system
GVWSA: Greater Victoria Water Supply Area

HTLC: height to live crown

IFOV: instantaneous field of view
IMU: inertial measurement unit
INS: inertial navigation system

LAI: leaf area index
LOESS: locally weighted least squares regression

MAI: mean annual increment
MASCOT: Management of Survey Control Operations & Tasks
MODTRAN: moderate resolution atmospheric transmission

NADH: nicotinamide adenine dinucleotide
NDVI: normalized difference vegetation index
NIR: near infrared
NPP: net primary production

PAI: periodic annual increment
PAR: photosynthetically active radiation
PDOP: percent dilution of precision
PRF: pulse repetition frequency

Ra: autotrophic respiration
REP: red edge position
RGB: red green blue
RS: remote sensing

SAM: spectral angle mapper
SLP: Shawnigan Lake Project
SR: simple ratio
SV: space vehicle
SWIR: shortwave infrared
S/N: signal to noise ratio

VIS: visible
VNIR: visible and near infrared

Dedication

I lovingly dedicate this work to my family. In loving memory of my Dad, whose commitment to his family and his own discipline has provided me with so much, including the behavioural traits that have enabled me to persist and complete my education.

To my children Jonah and Ellie, who may one day, recognize this document as a tangible symbol that they need not place limitations on their ambitions; irrespective of our personal limitations, sufficient will is all that is required. I wish for them, the bravery to honestly weigh their options without regard to others expectations.

Most of all to my wife Ashley, who has sacrificed much to facilitate my education. I have been so dependent on her, especially in the last five years of parenthood; she has gracefully accepted the challenge and thrived. She is simply the best, most patient, loving and selfless mother on the planet. I am excited for the next chapters in our lives together, where I can focus all my energy on being the best parent and partner that I can be.

Acknowledgements

I want to give gracious thanks to The Canadian Wood Fibre Centre, Natural Resources Canada for their financial support of this study. I acknowledge Dr. Xiaoping Yuan and The Ministry of Forest, Lands and Natural Resource Operations and Rural Development for being so accommodating with my time in the last few months to finalize the project.

Thank you to the members of my committee, including Dr. Fred Wrona (Environmental Monitoring and Science, Alberta Government), for their time and involvement in my program. I want to specifically thank Dr. Barbara Hawkins of the University of Victoria's Centre for Forest Biology, for the inspiring workshop on Forest Ecophysiology, which became the catalyst for this study. I want to also recognize Dr. Cosmin Filipescu of the Canadian Wood Fibre Centre for the helpful conversations we shared and for providing the CFS reference data for the Shawnigan Lake Project area.

I would like to acknowledge my supervisor and friend Dr. Olaf Niemann, not only for the years of support, but also for always providing an exciting environment to work and learn. I am grateful for his support, encouragement and the many inspiring conversations we have shared, which I hope will continue long after his impending retirement.

I would like to acknowledge my undergraduate remote sensing professor Dr. Marilyne Jollineau at Brock University; it was her enthusiasm for the topic that changed my perception of higher education and my own potential.

All my friends at the Hyperspectral and lidar Research Group should be acknowledged as all of them have contributed to the mutual progress that has occurred within our lab. I want to recognize Roger Stephen for the many discussions around the technical aspects of sensor integration and spatial calibration, Fabio Visintini for his discussions related to spectroscopy and radiometric calibration as well as his participation in the ground campaign. I want to recognize Rob Skelly for his guidance in scripting, Diana Parton and Astrid Niemann for their participation in the ground control survey, and Georgia Clyde for her positivity and encouragement.

I extend my gratitude to Terra Remote Sensing Inc. for the opportunity to partner with them once again on this project. Terra Remote generously provided ground survey equipment and processing support, which was invaluable for this study. In addition, Terra Remote conducted the airborne survey, flown on two occasions for this project.

Lastly, I must acknowledge the many scientists who contribute to, and those that have historically contributed to the rich legacy of the Shawnigan Lake thinning and fertilization project.

CHAPTER 1:INTRODUCTION

This project addressed the potential for emergent remote sensing technologies to inform on forest attributes pertinent to growth productivity, which can relate to the quality and quantity of wood fibre in standing forests [1]–[3]. The ultimate goal of this project is to demonstrate information extraction techniques from remote sensing technologies that may support an enhanced forest inventory system. Such forest information systems will provide a means to inform decision support for stand management and may help to reduce the uncertainty in commercial wood fibre products. In addition, the successful derivation of productivity proxy metrics will enable an opportunity to calibrate and/or validate existing forest growth model projections, which is becoming more important in the face of climate change [4]–[6]. As such, there is economic, ecological and moral merit in this research.

The remote sensing community has long been focused on the analysis of vegetation and has been building a capacity for information extraction since its first application to forested environments nearly a century ago. Recent research efforts have addressed remote sensing questions related to forest structure [7], [8], species composition [9], [10], health [11]–[13] and productivity [13]. Previous research also assessed how a discrete lidar dataset could be applied to describe the vertical and horizontal distribution of the forest canopy [14]. Canopy structural characteristics are largely attributed to stand evolution through growth productivity and disturbance. Forest productivity reaches a maximum during the stand development stage where there is a re-initiation of understory vegetation [15]. Thus, there is a benefit to forest management for information on stand health and development status. Health can be inferred by foliar

nutrient contents [16]–[19] which have specific electromagnetic absorption traits [20], while developmental status can be determined from the three dimensional structure of the canopy (top height, canopy closure and the vertical distribution of canopy), which can be determined with a sufficiently dense height point sampling [14]. Recent advances in the analysis of airborne lidar data, which provide precise height and point location measurements, have enabled a more complete measurement and understanding of three-dimensional forest canopy structure. These data constitute a technology innovation that provides an opportunity to develop innovative inventory products that will improve efficiencies within the forest sector and help to capture the maximum value for the Canadian fibre resource.

This project provides an empirical demonstration of the capacity to estimate growth and site productivity from lidar integrated with imaging spectroscopy, but more operationally it derives a series of metrics that can be used with multi-temporal data to describe forest productivity. The objectives of the proposed study are firstly, to empirically demonstrate the site and stand attributes that determine growth productivity and secondly, determine the feasibility of modelling the growth significant site and stand attributes from remotely sensed datasets. Lastly, the project will investigate the relationships between remotely derived structural metrics and reflectance. This project will employ training and validation sites from the Shawnigan Lake Project (SLP) and the Greater Victoria Water Supply Area (GVWSA).

1.1 Forest Ecophysiology

Forest productivity is a term, with many variants, found in the discourse of forestry and forest ecology, where in this discipline it refers to the rate of dry matter accumulation.

Forest productivity is assessed through, geocentric (related to site), phytocentric (related to vegetation) and dendrocentric (related to volume and site index) indicators [21].

The term site productivity refers to the potential productivity that a geographic location can support through its climatic, topographic and edaphic properties, which are assumed internally homogenous, both spatially and temporally. Site productivity may also refer to the realized portion of this site potential, that is wood production [21]. The realized portion of site potential is temporally dependent.

There has been much research in the characterization of species composition stratified by site productivity, where, for example, a particular ground cover vegetation may be indicative of rich soil nutrition or moisture availability [22]. Additionally, the tree community through resource competition, or autecology, imparts limitations on productivity. Thus, stand productivity is partially determined by stand structural developmental stage as resource availability is strongly tied to stem densities and competition [23]. It should be noted that in addition to the autecology perspective there is also a definitive inter-species competition factor that is pronounced at specific structural stages, salal versus Douglas-fir at initiation, for example [24], [25].

Applied forestry has derived a standardized tool called site index to infer productivity from the height of site trees, within the dominant canopy class, and age at breast height (1.3m). The site index concept was developed from the observation that mean stand height is associated with stand volume and that dominant trees are less influenced by competition and are thus more indicative of site productivity. Skovansky and Vanclay [21] present the three fundamental principals of forest growth from this perspective, and the evolution of this concept through time. The first principal of forest

growth is that stand height is indicative of forest productivity class. The site index curve characterizes the change in height with increments of age, where sites of higher potential will achieve a taller stand height at a younger breast height age. Site index is typically standardized to the height at a reference age (*e.g.* 50 yrs.). Holding age constant, height is related to productivity class. The second fundamental principal of forest growth is Eichhorn's rule, which specifies that stand volume production is a function of stand height and species, irrespective of age or productivity (site class). The thinning response hypothesis is identified as the third fundamental concept, which states, stand volume does not change with stocking or thinning levels, until ~50% basal area, after which there is a progressive reduction in volume. However, Assman's yield level theory stipulates that there are site-specific variations of the volume increment per height increment relationship and these findings contradict the first two principals of forest growth. Furthermore, Assman's natural, optimal and critical basal area theory demonstrates a greater sensitivity in volume production to thinning treatments than was implied in the third principal of forest growth. This theory illustrated that volume production is greater at the optimal basal area than at the unthinned control (natural basal area) or thinning more than the critical basal area (5% less volume increment than optimal basal area). The thinning response pattern is age, species and site specific [21]. Thus, with ancillary data it may be possible to indicate productivity through structural information on stand height, species, and stem density for even-aged forest stands.

In most instances the empirical association between geocentric, phytocentric and dendrocentric indicators of productivity is preferred to process based approaches, as there are an insurmountable number of conditions and interactions that ultimately produce the

realized proportion of site potential. However, the preference for simplicity does not supersede the requirement to understand the growth process at its most fundamental level.

Forest productivity, referring specifically to dry matter accumulation is represented by the concept of net primary productivity (NPP). NPP, in contrast to gross primary productivity (GPP), accounts for dry matter consumed through autotrophic respiration (Ra), (NPP=GPP-Ra) [26], [27]. Since GPP is the total amount of carbohydrate generated through photosynthesis and that respiration in the above equation refers to maintenance respiration, productivity is related to the proportion of photosynthesizing tissue relative to respiring tissues [28]. These two attributes are conceptually achievable from the representation of fine scale canopy structure. In very simple terms, regardless of the scale of analysis, any factor that influences photosynthetic and respiration processes will impart an effect on net primary productivity and if sustained will impart an effect on growth and structure.

Photosynthesis is an intricate, and exceptionally complex, pathway from CO_2, water and light to the production of carbohydrates by the facilities within plants. However, accounting for the factors that influence the efficiency of photosynthesis is essential for understanding growth. In very simple terms and in non-limiting resource availability, growth and maintenance are dependent on a constant supply of stored chemical energy in the form of ATP (adenosine triphosphate). The ATP is generated in the cellular organelles called mitochondria. Mitochondrial respiration is dependent on the supply of carbohydrates and oxygen. The carbohydrate (*i.e.* sucrose) supply is provided by the process of photosynthesis occurring in the chloroplast of foliar tissues. Finally,

photosynthesis is dependent on the supply of PAR (photosynthetically active radiation), carbon dioxide, and water. Although these mentioned reactants are necessary for growth they would be useless without the proteins, organelles and structures (and in turn the nutrients required for their construction) that support the processes of photosynthesis and respiration [29].

Forest canopy architecture as the three-dimensional distribution of foliage is the result of site productivity, species composition, phenotype dependent growth rates, age and disturbance. There are well established models of forest structural development for the Coastal Western Hemlock biogeoclimatic zone, which lay out a generalized chronology for even-aged forested stands. The most simple structural development model is that presented by Oliver and Larson [30], and includes, in sequence: stand initiation, stem exclusion, understory initiation, and old growth. This traditional model is overly reductionist and pertains to even-aged unidirectional development, when natural stands are neither unidirectional nor exclusive to any one stage. As such, that proposed by Franklin Spies and Pelt et al. [31] is a more realistic model that includes: disturbance/legacy creation, cohort establishment, canopy closure, biomass accumulation/competitive exclusion, maturation, vertical diversification, horizontal diversification, and pioneer cohort loss. Increased productivity accelerates the structural development process. In order to understand the structure of forest canopies we must be aware of the influences that determine its morphology at finer levels. Productivity is partially determined by available PAR. Light provides the excitation energy that produces the proton gradient for ATP synthesis and the activation of enzymes that produce NADH. These light reaction products are then used in the carbon reactions to fix CO_2 into sucrose

that is ultimately used in respiration for maintenance and growth in meristematic tissues [29]. Light availability is modified by latitude, climate, topography and overstory vegetation. Forest structure is modified by the availability of light - as canopy closure increases, lower foliage senesces and abscises to become litter. Similarly, inter-canopy competition for light resources ultimately causes an increase in mortality and stand self-thinning. At the ground surface, PAR intensities are below the light compensation of the overstory species and they do not thrive. Shade tolerant species colonize and grow in the understory contributing another level to stand structure. Productivity is also a function of temperature. Temperature affects photosynthesis and the respiration rate by altering the performance of enzymes and chemical reactions. Temperature has an effect on humidity and subsequently affects transpiration rates and, in turn, stomatal conductance through vapour pressure deficit, thus temperature alters internal CO_2 concentration and its availability to photosynthesis. Temperatures vary according to incident solar radiation, which once incident with matter, is converted to heat. Solar irradiance is a function of solar zenith angle, which varies with time of day, season (also alters photoperiod) and latitude. Energy is spread over larger surface areas and experiences longer optical path lengths through the attenuating atmosphere with increased zenith angles. Irradiance is also reduced by local weather and climate where clouds inhibit energy from warming the earth surface. Topography, slope and aspect also affect irradiance by both intercepting light and casting shade and though diluting finite energy over larger surfaces. Temperature varies with elevation as the lapse rate reduces temperature by roughly 10**°C** with every 1km increase in elevation. Growth is largely affected by the availability of

water, which provides the medium for nutrient transport, tissue hydration and the initial electron for the light reactions of photosynthesis.

The availability of moisture is dependent on precipitation, topography and soil structure (field capacity). Canopy structure is modified by variations in moisture availability. During drought events, carbohydrates can be allocated to belowground growth while above ground growth may slow or cease. High stand densities are a strain on moisture resources and constitute a source of competition, where deep-rooted species have a competitive advantage over those with shallow roots under water deficit conditions. Conversely, other species may be better adapted to moist soils. As a result, site moisture status may affect forest canopy and species structure.

Growth is also partially limited by CO_2, which once fixed, becomes the source of all heterotrophic energy. The availability of CO_2 is tied to the availability of moisture by stomatal conductance as well as social interactions.

Lastly, soil nutrition is critical for forest productivity and is dependent on parent material, climate, time, soil cation exchange capacity, and symbiotic diazotrophs. Structural effects of variations in nutrient availability may be the foliar abscission of the upper and peripheral leaves within the canopy or the lower and internal foliage, depending on the mobility of the deficient nutrient [26], [29]. In addition, nutrient demands are moderated by structural development stage, especially for mobile nutrients. The demand for soil nitrogen is high at stand initiation when the pool of nitrogen available for translocation is small, needle retention is low and herbaceous competition for water and nutrients is high. At later structural stages much of the nitrogen demands

are met by translocation from older foliage and the dependence on soil nitrogen is lessened [32].

All these factors occur within the process of forest development and species succession to ultimately arrive at a given state of forest stand structure. Forest structure is primarily the product of growth, competition, regeneration and replacement. It is suggested that by quantifying the developmental stage of a forest by measuring the structural complexity of the canopy, the productivity of the stand may be inferred.

1.2 Imaging Technology

Remote sensing is a very broad discipline that is characterized by the observation and analysis of objects and phenomena without being in direct contact with the target subject [33]. Remote sensing technologies applied to forestry can include passive optical sensors including: aerial photography [34]–[36], multispectral imaging [37], [38] and imaging spectroscopy [39]–[42], active optical sensors through fluorescence imaging[43]–[45] and laser scanners [46], [47] and to a lesser extent active microwave sensors like synthetic aperture radar [33]. The many processing methodologies are diverse, emergent techniques typically remain within the discourse of the sensor type for which they were developed but occasionally crosses between sensor types and, frequently, processing streams benefit from multisensory integration [48], [49].

Remote sensing technologies have long been integrated into the periphery of commercial forestry practices. Remote sensing is increasingly being applied in forest inventory, monitoring and evaluation. Forest applications from remotely sensed data that are currently being realized include: habitat monitoring [50], mapping forest disturbance [51], soil characteristics [52], vegetation mapping [53] and harvest/operation support

[54]. Within the application of vegetation mapping, remote sensing has a capacity to inform on: height [55], density, gap structure [7], stem and canopy surveys [46], [56], biomass [51], growth [13], forest types and species [48], [57], leaf area index [58], health [59], net primary production [60] and timber supply [61]. The capacity for forest information products from remote sensing is the result of the progression in tools and techniques developed throughout the relatively short history of the discipline.

Remote sensing technologies fall very coarsely into two categories of sensors, either passive or active instruments. A passive sensor, like the human eye, is one that does not provide the initial signal but can observe the interaction of a signal originating elsewhere, from the sun for example. Multispectral and hyperspectral (spectroscopic) instruments are examples of passive sensors. Active sensors act as both the source and detector of a signal. Radar (radio detection and ranging) and lidar (light detection and ranging) are two examples of active systems that emit an electromagnetic signal that is reflected off a target and returned to the sensor where it is recorded. Many forward-looking forest resource entities have embraced active lidar systems for their efficiency in data collection and the ease of interpretation.

1.3 Remote Sensing of Forest Structure and Productivity

From the passive optical approach, omitting spatial analysis techniques, two general spectral traits enable the investigation of growth and health, the influence of pigments on visible wavelengths and the LAI (the one sided projected leaf area as a proportion of the ground surface area) dependent, multiple scattering of near-infrared energy. Since LAI and pigments have a vital role in the carbon assimilation capacity of trees they are clearly involved with growth and health. The leaf surface provides the area required to capture

light that drives the photosynthetic process, it is also the surface from which gas exchange occurs, which is also a necessity for photosynthesis.

Foliar pigments are the required proteins for the absorption of light energy. Their abundance determines the maximum potential for the light reactions in photosynthesis, and foliar pigments can be measured with optical remote sensing. Leckie [62] assessed tree damage represented by a measure of needle loss through the use of high-resolution airborne multispectral data. The study leveraged a 60cm spatial resolution to identify individual tree canopies to omit confounding mixed pixel responses. Through the process of selecting the mean sunlit canopy response, the authors effectively minimized the anisotropic reflectance effects that are present at canopy levels. Through single band reflectance and vegetation indices (*i.e.* simple ratio (SR): NIR/Red, normalized difference vegetation index (NDVI): (NIR-Red)/(NIR+Red)) with bandwidths of 25nm, the study was able to discriminate healthy from severely damaged trees. The authors describe that 83% of the variation in needle loss was explained by reflectance at 656nm. Because this band is within 25nm of the absorption maximum of chlorophyll, the effective loss of chlorophyll occurring in concert with the reduced LAI makes this channel sensible to variations in LAI. The relationship with needle loss was marginally improved (from R^2: 0.83) through the use of vegetation indices (R^2: 0.89). Vegetation indices are a large topic within the discipline of remote sensing and their early application to multispectral channels contributed greatly to remote sensing application development.

The general consensus is that the coarse spatial and spectral resolutions and non-contiguous spectral sampling inherent in spaceborne multispectral sensors are insufficient to provide information required for forest inventory including species and canopy closure

[63]. Many species occur in mixed stands and therefore the scale of analysis should be the individual, otherwise surrounding features will contaminate observations. Although sensor technologies have changed drastically since, Rock [64] stated that coarse resolutions is one of the chief limitations of multispectral data for vegetation analysis. Despite sufficient spectral resolutions, forest applications using coarse spatial resolution data will suffer from contaminated spectral responses especially where canopy closure is low. Wulder [65] and Strahler [66] refer to two types of spatial resolutions, L-resolutions and H-resolutions. The L-resolution refers to the situation where the objects or elements under investigation are smaller than the raster cell sizes and the inverse is the case for the H-resolution. Although the idea seems intuitive, the remote sensing community has taken considerable time to adapt to the H-resolution approach, a reality imposed by the limitations of sensor characteristics at the time.

Despite a large body of literature that details the potential of airborne imaging spectroscopy, it has received little attention from commercial forestry operations. High spatial resolution imaging spectroscopy has potential applications to commercial forestry in two major areas. The first is the discrimination of species, while the other is the measurement of biophysical/biochemical properties: pigment and moisture contents and LAI. On the basis that species-specific taper equations have been developed for volume estimates [34], [67], there is an interest in providing inventory data on forest species [48].

An alternative to broad area-based forest classifications and inventory, such as those typically employing satellite-based earth observation data products, is one that defines and assesses forests on an individual tree basis. The popularity of forest species classification research based on individual trees basis has increased with the advent of

higher spatial resolution datasets. In many instances such fine scale analysis requires the integration of auxiliary data (*e.g.* lidar), while others extract information from spatial attributes. As an example, Gougeon [68] conducted an individual tree species classification applying 60cm multispectral imagery, which produced an accuracy of 88%. A similar approach was adopted in other research, where an airborne laser scanning dataset was exploited to identify individual tree canopies [46], [48]. Representative tree reflectance spectra were classified with the spectral angle mapper (SAM). These authors reported accuracies of 76% across five coniferous species, a broad hardwood class and a severely damaged (red attack) class.

The SAM classifier is an example of an analysis technique that deviates from the standard statistically based parametric classifiers that have been so broadly applied to multispectral datasets. It is also one of the later emerging techniques that take advantage of the contiguous, near complete spectrum for each pixel. Other exclusively spectroscopic methods include derivative analysis [69], binary encoding [70], continuum removal [71] and spectral feature fitting [72]. These methods rely on contiguous spectral sampling that can characterize spectral shape. The continuum removal and spectral feature fitting methods are designed to emphasize spectral absorption features. Such methods also provide a capacity for more than the detection of these absorbing materials, they have demonstrated the potential for inferring concentrations.

Much like the case for classification approaches, many different procedures have been developed to estimate biochemical contents of foliar vegetation. Beginning with observations made by Rock *et al* [64] variations in spectral shape were related to vegetation vigour. The authors characterized changes in the slope of leaf spectra within

the transitional wavelengths between chlorophyll absorption and NIR scattering. They describe a shortwave spectral shift of the red-NIR slope inflection point. The well-recognized blue shift of the red edge was associated with variations in chlorophyll contents that were attributed to damage caused by air pollution. Since then, the red edge position (REP) has been applied in many stress detection studies [73]–[75] and in non-destructive chlorophyll measurements [76], [77]. The estimation of foliar chemistry from laboratory spectroscopy was summarized in Curran [20], where he dealt with the wide range of compounds that, in the absence of water, are detectable as discrete absorption positions. Since this article, much research has focused on scaling *in vivo* biochemistry estimates to the canopy level. Pigments, nitrogen and to a lesser extent, lignin have received attention in the remote sensing community for their roles in health, growth and decomposition, respectively. Serrano [78] investigated landscape level canopy nitrogen and lignin through stepwise multiple regression (criticized elsewhere for a high likelihood of over fitting when applied to leaf spectroscopy [79]). This work, in agreement with others [8], concludes that canopy closure has a strong influence on the biochemical estimates. This result again outlines the need to account for canopy structure in optical modeling. A broad range of multivariate modeling approaches to biochemical estimates include the use partial least squares regression [80], [81], while other researchers take a more conceptually tractable approach through absorption feature analysis of lignin [82], [83], water [84], [85], nitrogen [19].

As an extension of the work conducted on broadband vegetation indices, there has been much research in the development of narrowband pigment estimation indices. These techniques for airborne remotely sensed pigment estimations have delivered ambiguous

results across different vegetation types and environments. These methods are relatively recent and remain an intensively studied area in imaging spectroscopy [39].

Regardless, of the underlying properties, imaging spectroscopy has demonstrated a capacity for measuring growth. Other researchers [13] have taken a more direct approach to investigating spectral responses and forest growth. The authors demonstrate a consistent decrease in canopy shortwave infrared reflectance with an increase in growth (represented by mean site annual growth increment from tree cores with a second order trend removed and normalized to the mean annual increment of all sites). A coefficient of determination spectrum (R^2 values between reflectance and growth index from 450-2500nm) illustrated spectrally fine peaks of high association. The observed growth signal was attributed to the increased amount of moisture in productive forest sites and the subsequent increased absorption of these wavelengths by foliar moisture. The authors suggest the growth rate of the trees within their study site is associated with moisture availability and that these parameters are measurable through airborne imaging spectroscopy.

Coarse scale analysis of forest biochemistry is confounded by the L-resolution condition, whether by the mixing of understory vegetation/ground or by the bidirectional reflectance effects on the signal to noise ratio. Several studies have reported that accuracies are significantly impacted by canopy closure and the consequent understory signal or the decrease in overstory signal. Eriksson [86] determined that canopy reflectance varied by 18% and 10% in the red and NIR regions, respectively with differing understory densities and that the effect is more severe in coniferous forests where understory densities are high, relative to deciduous forests. Other authors have

demonstrated that pigment and moisture content estimates from hyperspectral remote sensing data deteriorate as canopy closure fraction decreases [12].

High spatial resolution imaging spectroscopy presents an opportunity for more critical sampling, especially if augmented with concurrently collected lidar data [8]. Lidar data is becoming more integrated with optical datasets as it offers the potential to omit canopy gaps, which are highly problematic for environments with vegetated understories. The use of lidar to facilitate pixel sampling in optical datasets extends valid chemistry estimates to forests within the lower ranges of canopy closures.

High spectral resolution optical datasets provide information on canopy chlorophyll, which may directly relate to health and growth through an indication of the potential of the light dependent reactions of photosynthesis. Chlorophyll estimates may also provide a proxy measure for foliar nitrogen, which may be used in physically based models for net primary production [60]. Relationships have been developed from optical data for the estimation of LAI, which may reflect the degree of carbohydrate synthesis and allocation to canopies. Lidar data however, provides a much more direct association with above ground biomass, and for this reason, in addition to its relative simplicity (relative to radar and spectroscopy), the forest industry has been quick to embrace the technology.

Lidar (light detection and ranging) is an active remote sensing tool that was made possible by advancements in other fields, namely GPS, gyroscopes and accelerometer sensors. Lidar systems emit pulses of highly collimated monochromatic light usually within the NIR range, and after the pulse has been reflected off a surface and returned to the detector, the time and intensity of the pulse is recorded. The time of flight of the pulse

is translated into a range distance based on the speed of light (~30cm/ns or 300,000km/s). When these sensors are integrated with DGPS (Differential Global Positioning System) and IMU (Inertial Measurement Unit) technology the scan angle and range data provided by the lidar can be augmented with precise position and directional information.

The IMU sensor translates the responses of three orthogonal accelerometers and gyroscopes into three-dimensional velocities and variations in orientation, respectively. The IMU communicates theses values to the Inertial Navigation System (INS) software in an integrated computer system as the digital representation of platform behaviour (heading, pitch and roll) at a registered DGPS position. Thus, airborne lidar or airborne laser scanner (ALS) systems measure the vertical and horizontal distribution of forest and ground surfaces with accuracies as high as 5cm [87], while also retaining monochromatic reflectance data. Although lidar data are being used in operational support, such as the planning and design of forest roadwork [54], the majority of lidar forest applications are focused on the measurement and extraction of structural parameters and volume estimates (Table 1.1).

Table 1.1 Potential contributions of lidar remote sensing for forestry applications

Forest characteristic	Lidar derivation
Canopy height	Direct retrieval
Sub canopy topography	Direct retrieval
Vertical distribution of intercepted surfaces	Direct retrieval
Above-ground biomass	Modeled
Basal area	Modeled
Mean stem diameter	Modeled
Vertical foliar profiles	Modeled
Canopy volume	Modeled
Large tree density	Inferred
Canopy cover, leaf area index	Fusion with other sensors Inferred
Life form diversity	Fusion with other sensors

(Adapted from [88]*)*

The body of literature for lidar forest applications is focused primarily on describing canopy structure and modeling biomass and volume. Prior to any vegetation analysis, however, the lidar point cloud must be converted so that the z values are relative to the ground surface, and therefore represent the height of the vegetation. With multi-echo technology the extraction of vegetation height by topographic normalization is simplified. First returns will be reflected from the opaque surface nearest to the instrument, as the signal penetrates deeper into the canopy it may encounter other surfaces and will return as many as five responses, the last of which is, ideally reflected from the ground surface. There are currently two distinct forms of lidar systems in operation, the discrete lidar system that registers points if the returned signal exceeds a threshold power level, and the waveform lidar system, which records the continuous return profile for each outgoing pulse. Waveform lidar datasets are complicated by the fact that the typically larger footprint may have more significant topographic variations. The ground surface must be approximated from the height distribution, therefore the accuracy of vegetation height estimates in large footprint waveform lidar are poor in areas with high relief, (slopes > ~10°) [89]. Applying morphological algorithms or a variety of other point filtering approaches, ground hits can be discriminated from other forest structures [90]. Once this point classification is completed, the vegetation hits can be isolated, analyzed, transformed and applied in modeling for a particular application - forest inventory modeling for example.

There are two approaches to lidar enhanced forest inventory that are found within the literature, the first of which applies to stand or plot level analysis of the vertical distribution of forest canopies represented by the lidar point cloud. The height percentiles

of the distribution of canopy heights have been a source of information in extracting mean tree height, basal area and volume [91], and one of the first uses of this approach was conducted on a dataset collected at the SLP [92]. For example, Packalen [34] used stepwise regression for lidar feature extraction that ultimately selected three variables: the proportion of first return vegetation hits, the proportion of last return hits above the 30th height percentile, and the height percentile corresponding to the 60th height percentile of first return lidar points. Their model applied across pine, spruce and a deciduous class produced an RMSE of 18.88%. The models that included red and NIR optical data were slightly improved when tree classes were modeled separately. Lidar modeling, when height percentile profiles are considered for predictor variables, is similar to the high dimensional condition of imaging spectroscopy. Musk [93] applied a different approach called the Brieman's Random Forest algorithm that is apparently robust to over fitting. Musk also applied a wide variety of height percentile data, density estimates and statistical moments to estimate basal area, mean dominant height, stocking and merchantable stand volume of eucalyptus stands. Statistical modeling produced encouraging results with R^2 values of 0.75, 0.96, 0.64 and 0.84 for basal area, mean dominant height, stocking and merchantable stand volume, respectively.

The second popular approach to lidar enhanced forest inventory modeling found in the literature uses discrete return lidar datasets to build digital surface representations of the forest canopy. The high-resolution canopy height model (CHM) permits the extraction of individual tree heights and crown diameters. Lidar CHM treetops spatially matched well with individual treetops determined through photogrammetry (horizontally within 2m, vertically within 1m) [94]. The tree heights can be related to estimates of

timber volume, when DBH is known [34]. Multi-temporal, high-resolution and discrete return lidar data also has obvious potential for measuring tree growth. Andersen [95] demonstrated growth estimates through discrete return small footprint lidar. Individual trees were delineated and the changes in height between the acquisition dates (five growing seasons) were characterized between free to grow and heavily thinned stands. The authors describe how height growth was less pronounced in the heavily thinned stands (0-2m) because growth was allocated to crown expansion rather than to primary leader growth. In the control stands, height growth was in the range of 1 to 3m. The authors were also able to decipher the age dependency of growth where the height growth of younger 35 year old stands (3-5m) was greater than that of more mature stands. Although multi-temporal data sets require additional flight campaigns and are therefore quite expensive, being able to discern height growth increments with an accuracy of 5cm, and spatially mapping regions of observed high and low productivity would undoubtedly be an asset for forest management.

CHAPTER 2: RESEARCH QUESTIONS

1 ***What is the potential for mapping variations in forest productivity through the use of remotely operated sensors?***

Hypothesis:

Certain topographic and canopy structures are associated with specific levels of productivity and certain reflectance properties are also associated with differing productivity

2 ***How can a lidar point cloud be organized to represent forest structure related to productivity?***

Hypothesis:

Organization or generalization strategies that capture social position and growing space encroachment as well as general developmental stage will correlate well with productivity (phytocentric perspective). Topographic characterization that captures fine scale watershed features may indicate potential moisture availability and may correlate with productivity (incomplete geocentric perspective)

3 ***How can a spectrometer dataset be organized to represent forest growth productivity?***

Hypothesis:

By leveraging the reflective properties of tree canopies attributed to moisture and pigment contents and leaf area index, it may be possible to infer productivity. Chemistry is apparent in spectral shape but intensity differences caused by differing geometry may induce changes in shape not associated with chemistry.

The overarching research objective for this study is to determine the potential for mapping variations in forest productivity through the use of remotely operated sensors. With the scarcity of multi-temporal datasets to truly evaluate productivity outside the SLP training area, much of the effort will be allocated to producing and assessing metrics derived from airborne remote sensing data that can be applied in monitoring forest productivity. It is anticipated that certain topographic and canopy structures are

associated with specific levels of productivity and certain reflectance properties are also associated with productivity.

Intrinsic to the major research question are the issues or options on how to pre-process and organize a lidar point cloud and a spectrometer dataset to represent forest structure and forest growth related to productivity. It is hypothesized that organization or generalization strategies that capture social position and growing space encroachment as well as general development stage will correlate well with productivity (phytocentric). In addition, topographic characterization that captures fine scale watershed or watercourse features may indicate potential moisture availability and may correlate with productivity (incomplete geocentric). By leveraging the reflective properties of tree canopies attributed to moisture and pigment contents and leaf area index, it may be possible to infer productivity. Chemistry is apparent in spectral shape but intensity differences caused by different geometries may induce changes in shape not associated with chemistry.

Lastly, how can a similar historical dataset be incorporated with the current data to map productivity over a more structurally diverse forest? It is theorized that once a thorough data quality assessment is completed, the four datasets can be analyzed together. Based largely on yield level height increments, dominant crown heights can be individually mapped with lidar and normalized by the initial height to indicate incremental positive growth. Alternatively, mapping windthrow through multi-temporal lidar CHM data and newly formed dead tops through reflectance data will provide an indication of negative growth or reductions in productivity. Mapping changes in relative canopy chlorophyll may also provide an indication of the health trajectory of forest

stands. Acquisition and sensor parameters including flight heights, velocity and lidar PRF may limit the extent to which the datasets can be integrated and may prohibit or confound comparisons.

CHAPTER 3: METHODS

The methods section that follows will deal exclusively with the pre-campaign considerations and data pre-processing. The establishment and measurement history of the study site will be presented, followed by the strategy that was used in selecting the specific forest plots for further measurement, as an exhaustive collection campaign was not an option given time and financial constraints. Details on the flight campaign, instrumentation and calibration procedures will be provided followed by the validation testing of the spatial, spectral and radiometric calibrations. The full details of the radiometric calibration/validation are included in the appendices.

3.1 Shawnigan Lake Study Site

In the autumn of 1970, a forest research site ~5km west of Shawnigan Lake was established as an extension of the USDA Forest Service's Levels-Of-Growing-Stock (LOGS) study [96]. This research program was a joint, cooperative program between US state and federal agencies, industry and academia and Canadian provincial and federal organizations. The location of the research forest is characterized as being a nutrient poor site within the very dry maritime Coastal Western Hemlock biogeoclimatic subzone (CWHxm1) [96]. The species structure in the dominant tree layer is Douglas-fir (*Pseudotsuga menziesii* [Mirb.] Franco) with scattered western white pine (*Pinus monticola* Dougl.). There is a developing intermediate canopy consisting of western red cedar (*Tuja plicata* Donn) and western hemlock (*Tsuga heterophylla* [Raf.] Sarg.). The shrub layer is largely salal (*Gaultheria shallon*, Pursh) with common incidences of Oregon-grape (*Mahonia nervosa* [Pursh.] Nutt.), sword fern (*Polystichum munitum* [Kaulf.] Presl), and bracken fern (*Pteridium aqualinum* [L.] Kuhn). Where canopy

densities are sufficiently high to limit understory growth, step (*Hylocomium splendens* [Hedw.] B.S.G.) and Oregon beaked mosses (*Kindbergia oregano* [Sull.] Ochyra) are typically present. The stand was established in 1948 with planted, two year old Douglas-fir seedlings, and at an age of 24yrs (when the treatment plots were established), the stem density was ~3950 stems/ha and the site index was 25m at 50 years [96] (Fig. 3.1).

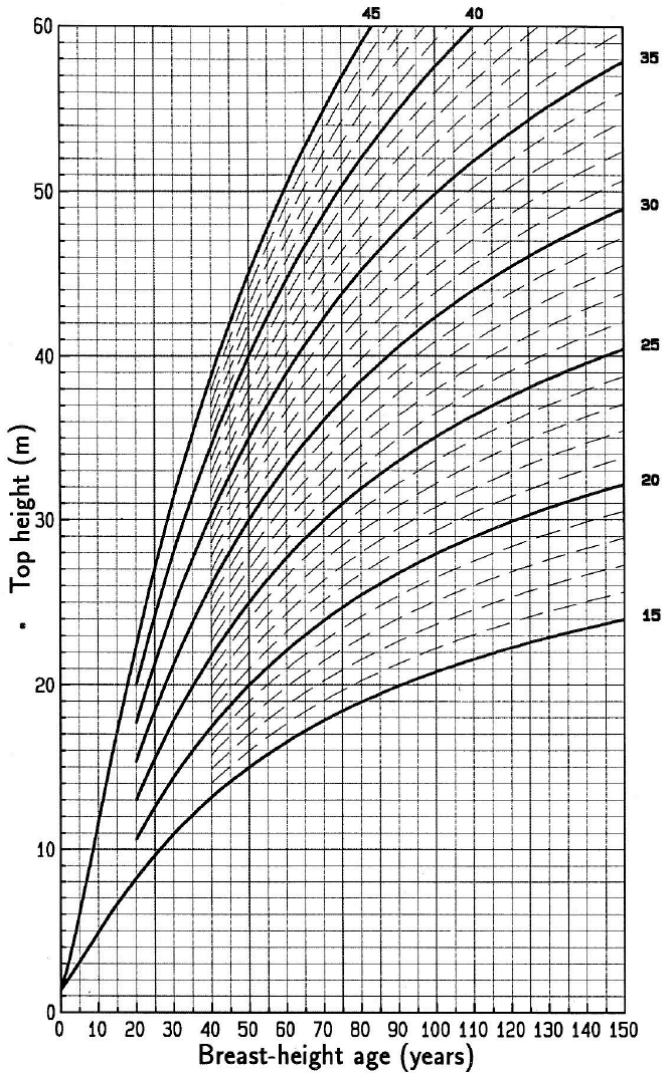


Figure 3.1. FLNRO site index curves for Coastal Douglas-fir [97]

The objective of the LOGS program was to investigate the effects on productivity of nine different levels of growing stock retention maintained through repeated thinning. The LOGS experiment was established as 27 treatment plots with dimensions of 28.46 x 28.46m (810m^2) and 10.1m buffers, with an additional ten plots equally sized with two different initial calibration thinning treatments [98]. The following year (1971), the Canadian Forest Service established another experimental forest, the Shawnigan Lake Project (SLP), slightly northwest of the LOGS plots, which would investigate the physiological response to silvicultural treatments (Fig. 3.2). Three thinning treatments and five fertilization conditions were spread across 36 forest plots 405m^2 in area (~20x20m). Peripheral studies also included an investigation of fertilization sources (ammonium nitrate, urea, nitrogen with both phosphorus and sulphur) and the effects of thinning on the water balance, which contributed an additional 24 treatment plots [99]. The Shawnigan Lake experimental forest has been the subject of 40 years of forest research and has been re-measured as recently as the winter of 2012. The SLP offers a data source with a well-documented history of available nutrient and moisture fluxes and the associated growth responses. The site is therefore an invaluable asset as a source of data to develop remotely sensed productivity models. The spatial regularity also offers an opportunity to characterise the spatial limitations of the airborne raster dataset. The study site can also be used to investigate questions regarding the lidar point density required to adequately characterize canopy structure, which is achievable through multiple lidar passes to increase density. See appendix 1 for a non-exhaustive list of studies conducted at the Shawnigan Lake Project site.

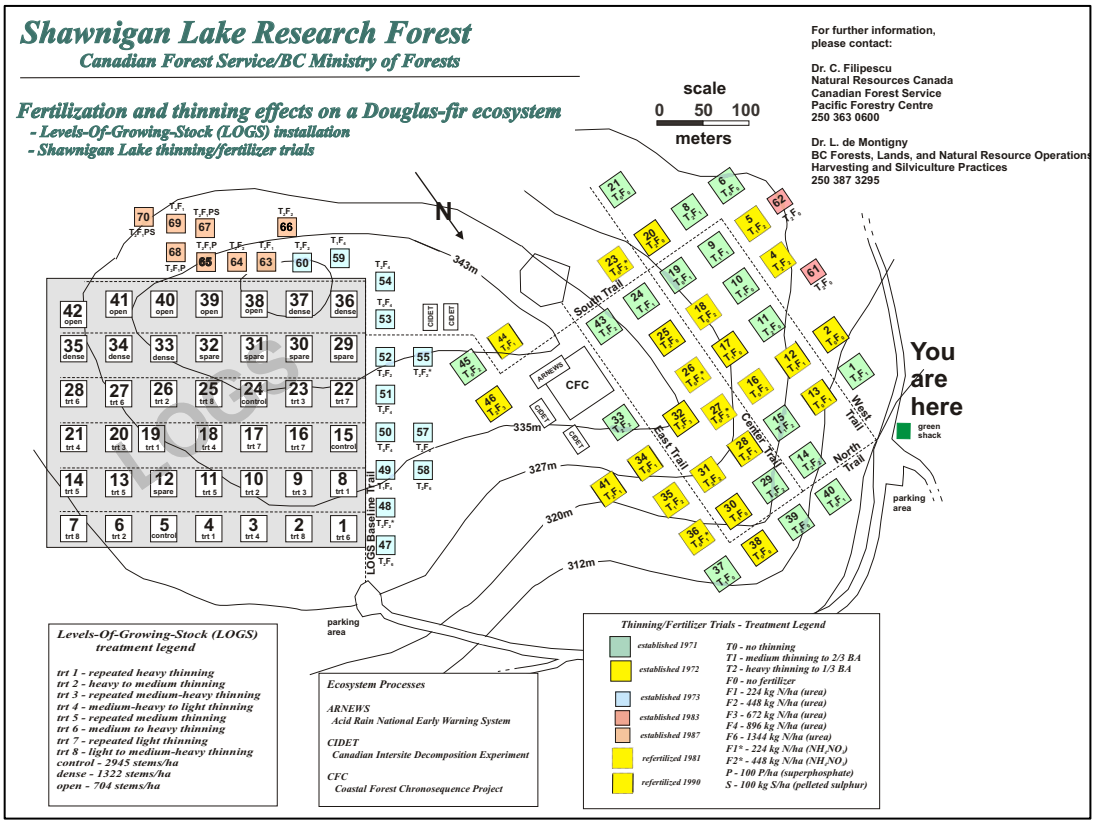


Figure 3.2. The Shawnigan Lake Project and Levels of Growing Stock site and plot locations map provided by C. Filipescue (NRCan, Canadian Wood Fibre Centre)

3.2 Ground Reference Data Collection

Reference data collected by Natural Resources Canada, Canadian Forest Service, from the Shawnigan Lake forest site included measurements from consecutive years beginning in 1970-1989. Measurement campaigns also occurred in 1995, 2002, 2003 and 2012. The measurements and observations conducted during these campaigns included: the positions of stems, species, thinning treatment, fertilization treatment, mortality, competitive stress index (the area of open grown tree living space occupied by neighbouring tree canopies [100], height, height to live crown, DBH, tree class (live, thinned, dead, live/damaged), crown class (dominant, co-dominant, intermediate,

suppressed, dead), the occurrence of damage, crown width northerly and crown width westerly. Several attributes were also calculated at the individual and plot levels including: estimated volume, estimated volume inside bark, estimated merchantable volume, estimated height, stem density, basal area, quadratic mean diameter, mean annual increment, periodic mean annual increment and crown length. Located south of the SLP installation is a weather station that was in operation between the years 1993 and 2005. Daily measurements were made for total precipitation, average air temperature, maximum and minimum air temperature, average relative humidity, minimum and maximum humidity and total solar radiation. These data provide an opportunity to quantify plot level growth rates as they relate to thinning and fertilization treatments and site level growth rates related to temperature, precipitation, humidity and irradiance.

3.2.1 *Selection of Treatment Plots for Model Building*

Based on field measured structural diversity (stem density, basal area, quadratic mean diameter, volume, height, crown length, height to live crown, and crown width) plots were selected (1, 2, 5, 10-12, 16, 21, 23, 25, 27, 31, 32, 36, 40, 41, 43, 46, 48, 49). These plots were selected by a principal component re-projection of the plot level field attributes and a subsequent percentile interval selection of components one and two (accounting for 92% of the total variance). This approach to plot selection was chosen to ensure model training would be inclusive of all potential variation within the study area. Because many of the ground based measurements are inter-correlated (Fig. 3.3), the projection into latent variables would decorrelate the data and reduce the dimensionality, simplifying the plot selection based on inherent plot variability. The dataset was reduced to five uncorrelated principal components (Fig. 3.4-3.6). The first two components were

then used to select plots at an equal interval of the ranked data, which selected 19 plots as unique. However, the treatments 11, 12, 13 and 15 corresponding to T0F2 ammonium nitrate, T2F2 ammonium nitrate, T2F3 urea and T1F4 urea, respectively, were not represented in the structure-selected plots (Fig 3.7). Eight more plots were selected based on the plot treatments that were not selected through the initial approach, these included plots: 23, 27, 32, 46, 48, 49, 55 and 59. This selection strategy ensured that statistical models built from these sampling plots would not extrapolate to structures that were not well represented in model building.

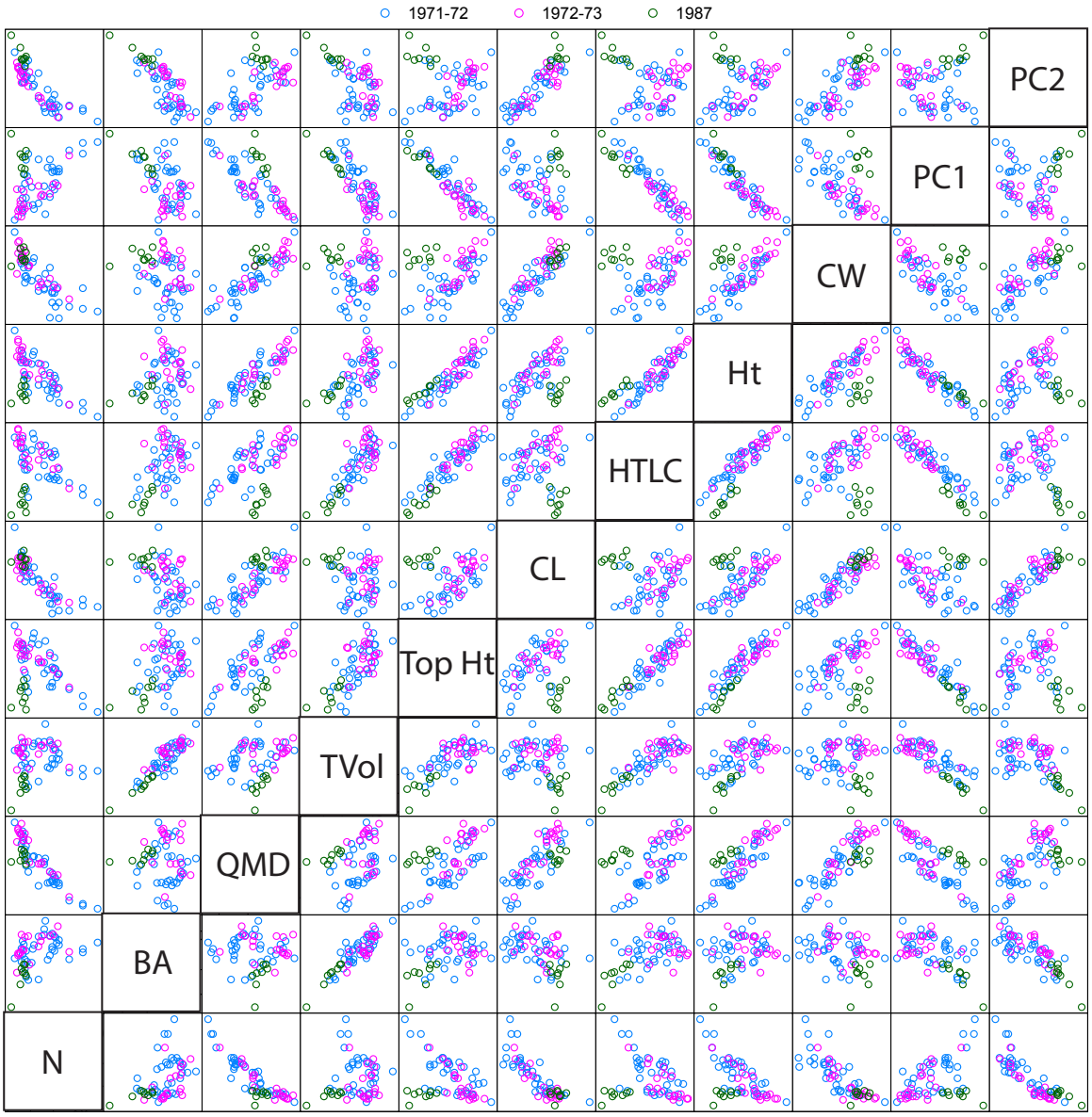


Figure 3.3. Plot selection approach based on latent structure of field measurements. Scatterplot matrix of the SLP field data demonstrates inter-correlation and redundant information. Colours represent those plots established in different years.

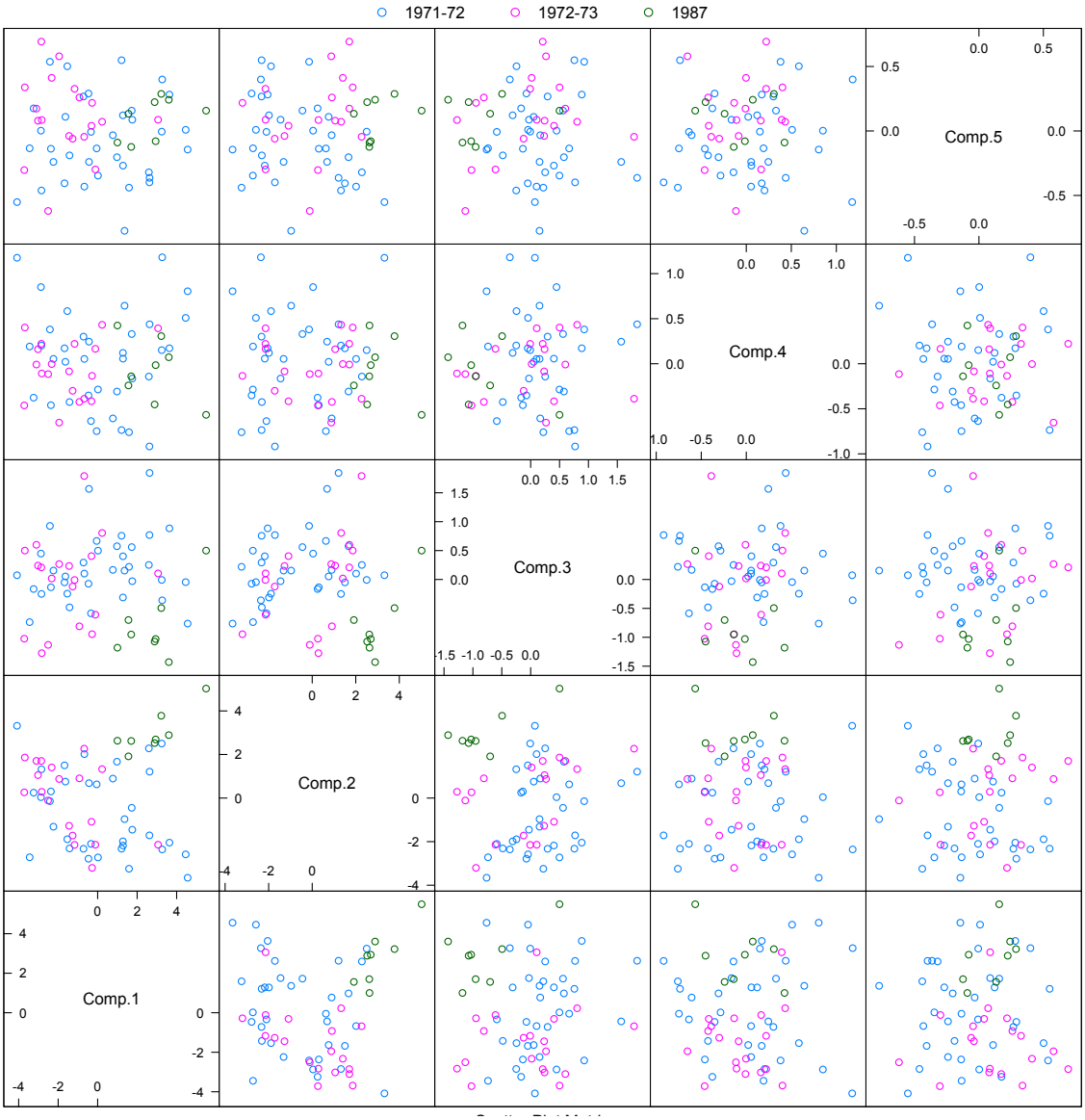


Figure 3.4. Plot selection approach based on latent structure of field measurements - SLP plot field data projected by a principal component transformation. The first two components represent 92% of the total variance in the field based measurement data

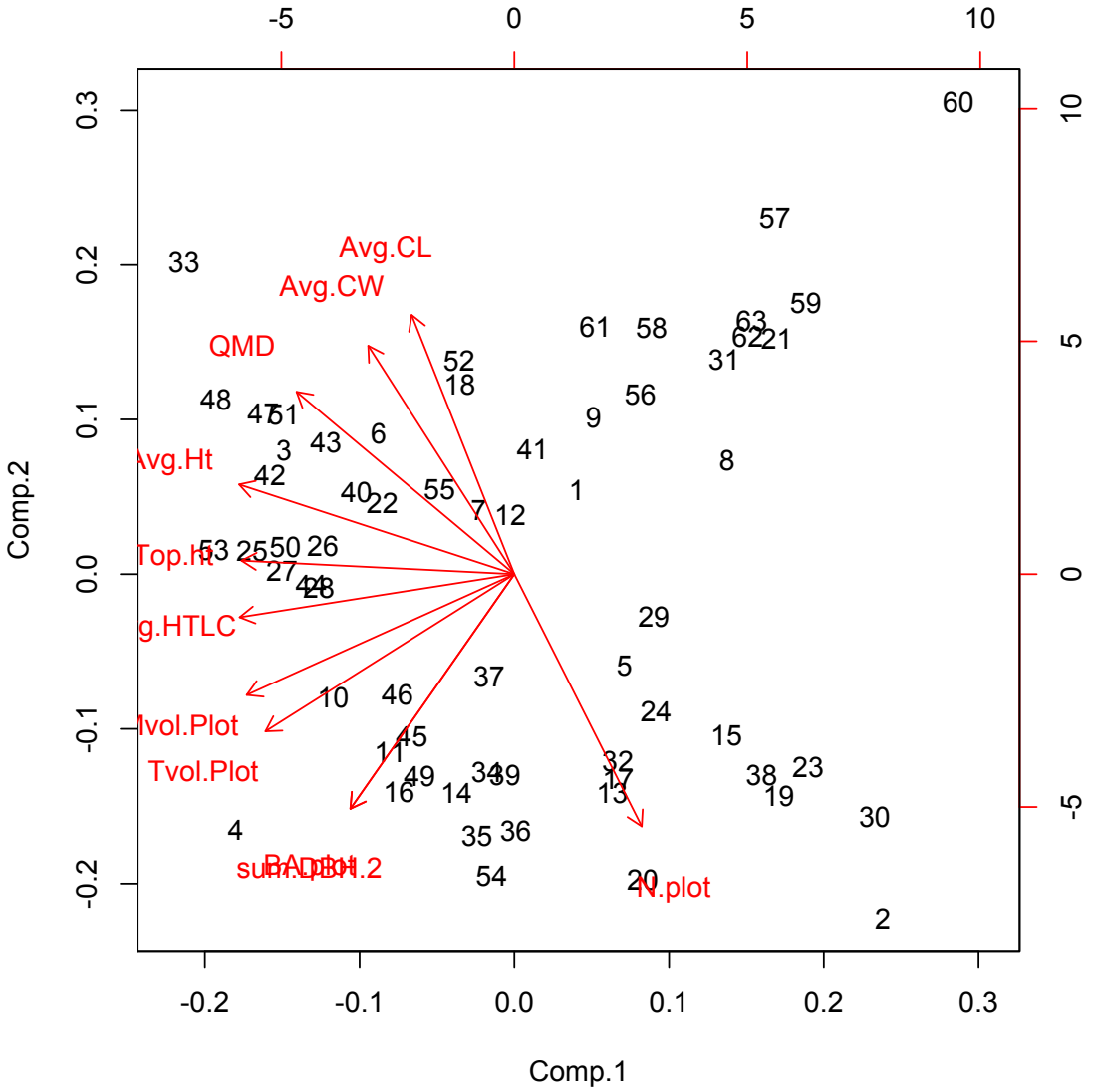


Figure 3.5. Scatterplot of principal components one and two with the influence of the original dimensions illustrated by red vectors

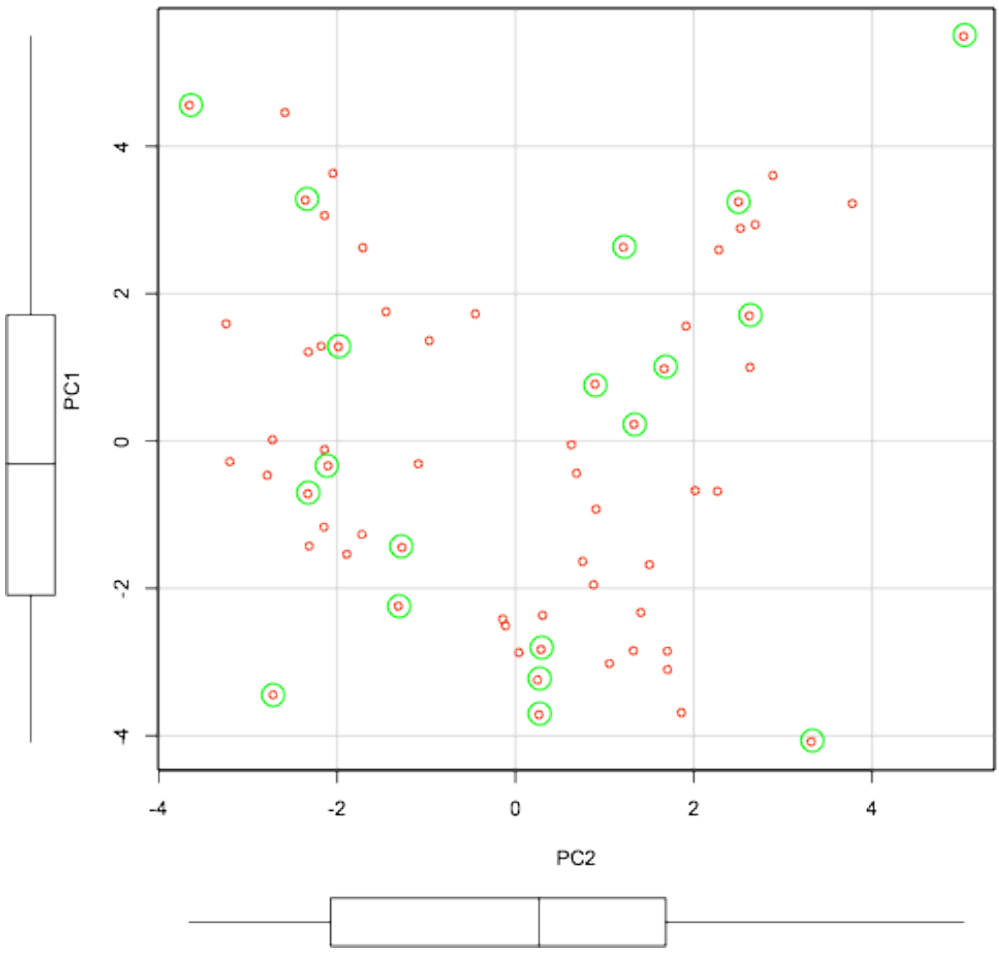


Figure 3.6. Plot selection for sampling based on structural data. Principal component one and two from the SLP plot field data. Constant percentile interval selection of plots to capture within site variability. Selected plots indicated by green point symbols.

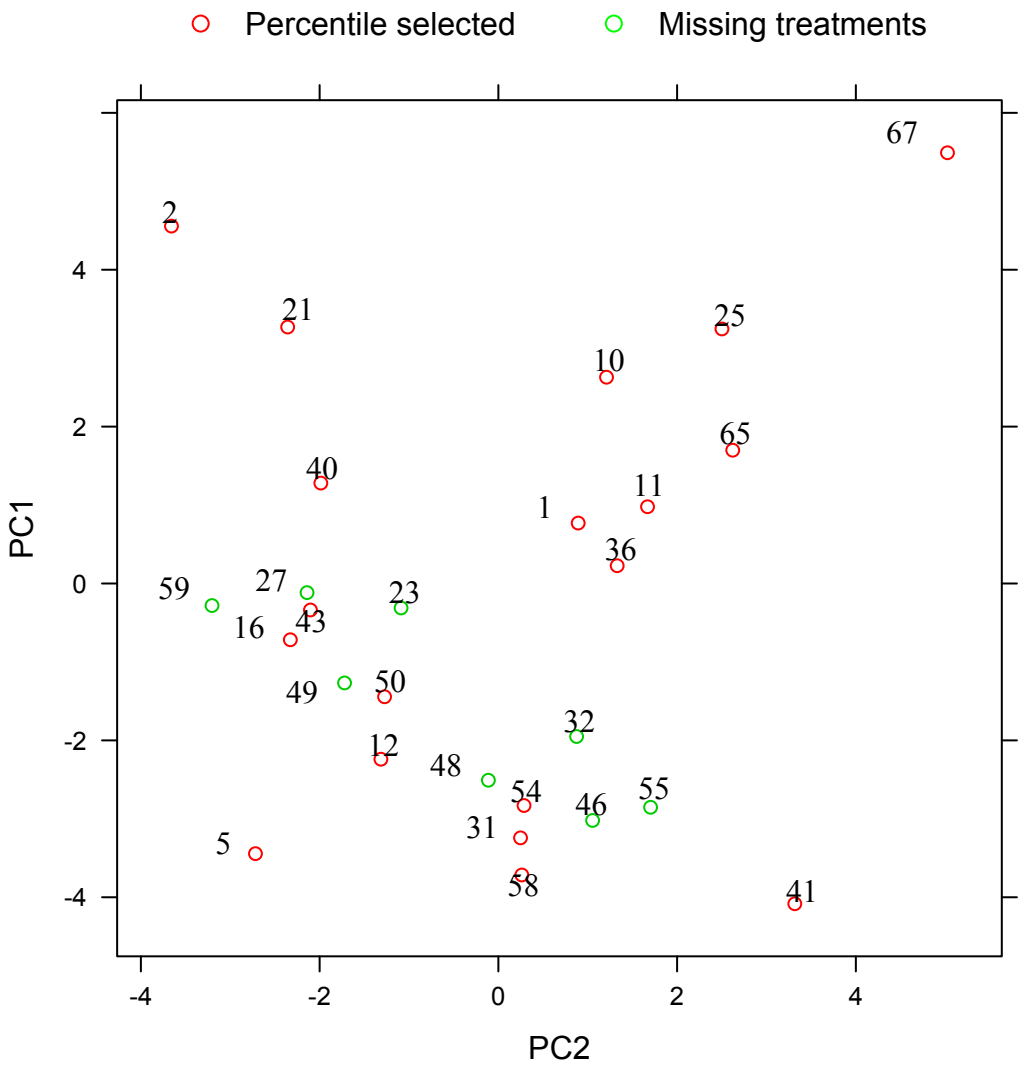


Figure 3.7. Plot selection approach based on latent structure of field measurements. PC percentile rank selection omitted some treatments. The principal component scores were transformed to percentile ranks and at equal percentile intervals the closest data point was selected for component one and two (based on the proportion of total variance explained), shown in red. This approach did not select all fertilizer and thinning treatments, which are indicated as green symbols. This approach ensures sampling of plots will provide representative variability and models will interpolate rather than extrapolate to untrained plot data.

3.3 Airborne Data Acquisition

Terra Remote Sensing Inc. deployed their Piper Navajo fixed wing platform and flew an airborne campaign designed to acquire data for this project. The instrumentation mounted in the aircraft included a full range imaging spectrometer (AISA dual), a high pulse repetition frequency (250 kHz) laser scanner, RGB camera, inertial measurement unit and survey grade global positioning system. The spectrometer acquisition was optimized for the collection of forested targets by binning the spectral domain of the CCD array. This reduced the spectral detail while maintaining the highest nominal spatial resolution.

The planning of an airborne collection campaign is a complex process, as there are several flight and sensor parameters that must be considered to ultimately provide a dataset that is appropriate for the intended application (Table 3.1). Many of the flight and sensor parameters are interrelated and must be balanced for an optimal collection.

Through a previous survey with the same instrumentation flown within the nearby Greater Victoria Water Supply Area, it was determined that the spatial resolution for this acquisition should be finer than 2m [101]. A finer resolution dataset would better capture the extent of large-scale objects (spatial representation is reduced less relative to the real world) - individual tree canopies in this instance. Tree canopies are variable in horizontal extent and therefore a finer resolution would provide for a greater likelihood of discrimination between individual canopies. A conscious decision was made to limit the spectral measurements to the VNIR range because there is relatively little information that can be derived for vegetation from the SWIR range as moisture masks all other energy interactions. The SWIR range is largely determined by the presence of water, however there are two prominent features that occur within the NIR that are directly

caused by the presence of water. From this standpoint, there is little information lost by omitting the SWIR range.

Table 3.1: Variables to consider while planning an airborne data collection

Collection conditions/instrumentation		Data consideration
Weather conditions	Wind velocity	Platform stability, spatial resolution
	Wind direction	Platform stability, spatial resolution
	Aerosols	Radiometric correction
	Humidity	Radiometric correction
Platform attributes	Altitude	Spatial resolution
	Forward velocity	Spatial resolution
	Angular stability	Spatial resolution
	Service ceiling	Spatial resolution
Sensor attributes	IFOV/footprint	Spatial resolution, S/N
	FOV/scan angle	Spatial resolution and extent, BRDF,
	Integration time	Spatial resolution, S/N
	Frame rate	Spatial resolution, ground sampling
	Pulse repetition frequency	Point density
	Scan rate	Point density
	Scan pattern	Point density
	Flight line length / duration	Spatial extent, Radiometric resolution
	Radiometric stability	Radiometric resolution
	Time since dark current	Radiometric resolution
	Spectral sampling	Spectral resolution
	Spectral FWHM	Spectral resolution, S/N
Solar conditions	Time of year	BRDF
	Time of day	BRDF
	Irradiance stability	Radiometric calibration
Acquisition costs	Fuel expenses	Feasibility
	Duration of acquisition	Feasibility
	Mobilization	Feasibility
	Extent & scale of collection	Feasibility
Target attributes	Topographic relief	BRDF, Spatial resolution, point density
	Object scale	Spatial resolution, point density
	Object spectral response	Spectral resolution
	Object structure	BRDF
Calibration & validation	Radiometric	Uncertainty
	Spectral	Uncertainty
	Geometric	Uncertainty

A constant challenge for passive airborne remote sensing projects is the effect of bidirectional reflectance (or bidirectional reflectance distribution function). The effects of BRDF are most apparent at the edges of the swath where viewing angles are up to 11° off nadir from a level platform. The BRDF effect becomes more pronounced with variations in platform behaviour causing variations in observation azimuth and zenith angles. Due to the aircraft's constant positive pitch angle during flight (*e.g.* flight 1923: ~5.7°, flight 1927: ~5.5°) the heading will partially determine the viewing azimuth direction, which again samples a slightly different position of the total geometry space. In effect, opposing flight headings will be 180° different in viewing azimuth. In an effort to minimize variations in viewing geometry, a flight plan was proposed that would ensure two complete site coverage collections with opposing flight headings. With this flight plan, one data mosaic could be constructed for all easterly flights and an additional mosaic could be generated from the westerly flights, thus minimizing the effect of variations in viewing azimuth. In addition, flight line overlap was increased to 50%, which would provide greater coverage of the site with near nadir observations and limiting larger observation zenith angles (extremes of the flight swath can be removed without sacrificing coverage).

On board a fixed wing aircraft the AISA Dual (Eagle VNIR active, Hawk SWIR disabled) and Terra Remote Sensing's proprietary lidar system was flown and collected data over the study site. The onboard INS (inertial navigation system) was used to measure platform attitude, which was applied in pre-processing to geometrically correct the push broom spectrometer data. Flight parameters are indicated in table 3.2. The flight acquisition covered a total area of 91.5km^2 including a ~89km^2 area that extended into

the Greater Victoria Water Supply Area, south of the Shawnigan lake site. In addition to flying the calibration site, the Shawnigan lake site and the Greater Victoria Water Supply Area, timing and IMU calibration flights were conducted at the Victoria International Airport. Terra Remote Sensing reported a lidar point absolute accuracy of 30cm. The data collections were completed on September 19, 2012 and included high-resolution orthophotography, discrete lidar and imaging spectrometer datasets. See Figure 3.8 for flight paths extracted from navigation files.

Table 3.2: Flight parameters for Shawnigan Lake Project 2287, September 13th (day 257) and 19th (day 263), 2012

Flight Date (Julian Date)		**257**	**263**
Mission Start Time (GPS time)		18 : 44	18 : 07
Mission End Time (GPS time)		20: 30	21 : 16
Weather Conditions		Foggy and Lots of smoke in the atmosphere	Sunny
Flying Height (meter)		1250	1150
Flying Air Speed (km/hr)		208	234
PDOP during each mission		< 2	< 2
Lidar System Operation Parameters	Laser pulse rate (kHz)	125	100
	Maximum scan angle	+/- 26°	+/- 26°
	Scanning Speed (Hz/Sec)	34	34
Hyper-spectral System	Sensor Spec	Eagle	Eagle
	Spatial Resolution (meter)	1.5*	1.5
	Frame Rate (FPS)	45*	43
	Binning	4, 2*	4, 2
	Samples	512*	512
	Spectral Resolution (Bands)	132*	132

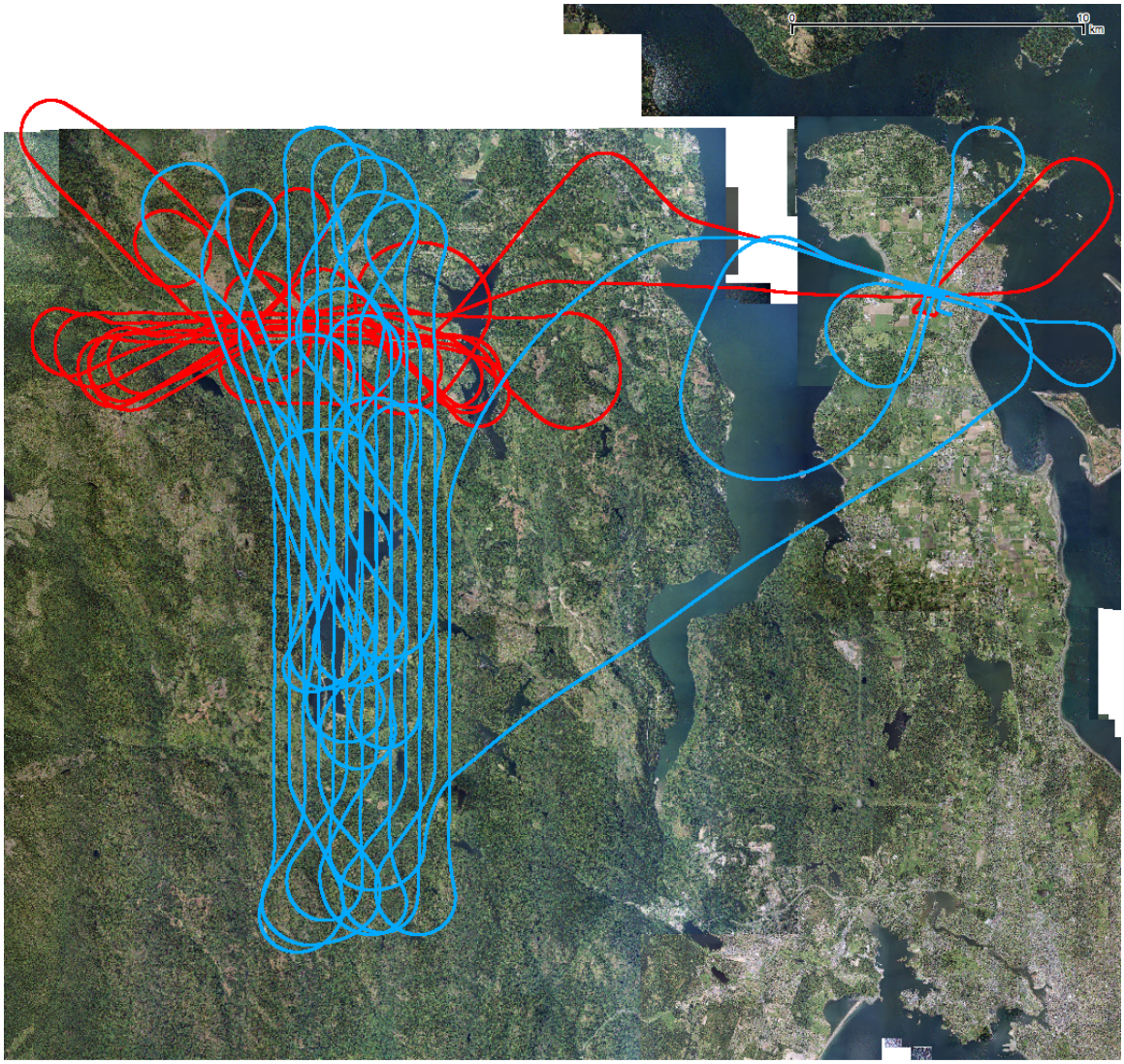


Figure 3.8. Flight path of the airborne acquisition overlaid on the CRD orthophotos. Sept. 13th flight illustrated as a red polyline coverage including radiometric calibration flights at the dry sorting lot and the SLP collection. Sept 19th flight illustrated as a blue polyline coverage included the GVWSA and SLP, radiometric calibration site at the saddle dam quarry as well as the geometry calibration site at the Victoria International Airport.

3.4 Survey and Terrestrial Lidar Acquisition

In order to relate airborne collected datasets to *in-situ* measurements, plot positions were required, since tree positions provided by NRCan were relative and not geographically located, thus a plot survey was conducted. The spatial study of individual crowns is complicated by the variable size of the target tree crowns and the potential low contrast between canopy and understory vegetation. Younger trees with smaller canopies require a finer raster cell size to be distinguished from their surroundings. At coarse spatial resolutions relative to the crown diameters, individual pixels may be the product of the responses from multiple small crowns, impeding the ability to locate the crowns and extract appropriate spectra. Crowns may be distinguished in the optical raster dataset where the nominal pixel size is at least a third of the canopy diameter, thus providing at least one response exclusively from the canopy. This is valid provided there are radiometric differences between canopies and canopy fringe or gaps, in high-density and low-density forests, respectively (enabling the discrimination between individual crowns and the surroundings). Additionally, to quantify within canopy spectral variations the spatial resolution must be finer still. Where crowns are larger than the nominal pixel dimension and radiometric differences are apparent, then the association between a relative survey and the airborne dataset is simplified. In this situation, the transformation of the ground survey to the airborne survey is achieved by the estimation of two horizontal offsets and a rotational parameter with reference to the minimization of RMSE between survey positions and crown positions from the raster. The reality of airborne collected spectrometer datasets is that the spatial resolution (<=1m) is similar to young tree diameters, which limits the contrast between canopies. For this reason, it cannot be

assured that all crowns are distinguishable in the raster dataset. This emphasizes the importance of precise stem positioning if analysis is to be conducted at the crown level. To ensure an efficient integration of field and airborne collected data, the positional errors in the survey should be contained within the targeted smallest canopy x and y spatial dimensions, which is >0.5m with the exception of one canopy (as assessed in the 2012 measurement campaign).

Traditional survey methods were used to provide a dataset that could produce unambiguous stem positions in the selected treatment plots. A survey grade GPS and a total station were used to establish a local control network and to complete closed precision traverses, respectively. Using this approach, the survey errors could be corrected and monuments could be established at control and turning point positions to facilitate future measurement and additional surveys of treatment plots. The typical survey provides positions that generalize the forest plots to individual points for the individual trees, however very little information concerning forest form and function can be extracted from this simplified model. Much more detail is required to characterize and differentiate forests in terms of the three dimensional distribution of canopy components and understory materials. A terrestrial laser scanner was employed to quantify forest structural detail at the treatment plots.

3.4.1 *Global Navigation Satellite System Control Survey*

Using an Ashtech Z-Xtreme GPS receiver and the Ashtech Geodetic IV antenna, a post-process static collection campaign was conducted. Under typical multipath conditions, with at least 5 satellite signals and a percent dilution of precision less than 4, the expected horizontal accuracy is 5mm (+1ppm). The Ashtech receiver records the coarse acquisition

(C/A) code and the carrier phase measurements on the L1 frequency (1575 MHz) as well as the precise (P) code phase and carrier phase measurements on the L1 and the L2 (1227 MHz) satellite signals. The receiver records these measurements on up to 12 parallel channels and provides for more productive and precise measurements with a capacity for ionosphere perturbation corrections [102]. The accuracy of the positioning is a function of occupation time, baseline distance, obstruction/multipath conditions and satellite geometry. In an attempt to compensate for the high multipath condition of the forested site, the positions were occupied for a minimum of two hours. The positions to be registered by survey grade GPS were selected where sky obstructions were less abundant and for locations that could accommodate connecting precision traverses during total station surveying. The selected sites were: the logging road intersection at the east & north trail head (C100), the weather station clear cut (C400), the LOGS parking lot (C500) and the shore of the water body where the pumping station was located (C600). Two other positions were located adjacent to the road intersection point, one to facilitate the initial forward azimuth (C300) and a second backup/testing point (C200). Two reference positions were also located at the dry sorting area at the SW corner of the dark reference target (R200) and the NE corner of the bright reference target (R100). At each of these locations, with the exception of the reference points (R100&200) and C500, 30cm sections of rebar were driven into the ground flush with the surface and marked with flagging tape. The LOGS parking lot is largely exposed bedrock and the references are located on paved asphalt, which made rebar installation impossible for the establishment of semi-permanent monuments. As an alternative, small holes were drilled into these surfaces using a ½" bit. With semi-permanent monuments established at each

of the control positions, the control network could be surveyed. At each position the antenna was place on a tripod and precisely positioned over the rebar (or hole) through the use of an optical plummet integrated within a tribrach adapter. The height of the antenna reference point (ARP) above the ground was measured and recorded. The collection parameters included a 1-second position sampling interval, 10˚ elevation mask and a static sampling mode. No data collection limitations were placed on the minimum number of space vehicles (SV) or a maximum percent dilution of precision (PDOP). This would provide for more control over data cleaning and post-processing in the NovAtel GrafNet post processing software (www.novatel.com). GrafNet is a static baseline processor and network adjustment software package. Reference data were imported into the software from the Canadian Active Control System (CACS) as well as the British Columbia Active Control network (BCACS). These are monuments whose positions are continuously collected, transmitted and published for users to download and integrate into survey corrections. The quality of data from several control positions was assessed for the duration of the SLP survey. Discrepancies in control positions were identified in the GrafNet computed tie lines. Only the references that had strong agreement were retained. Ultimately, the two BCACS references (BCNS and BCES) produced the most consistent tie lines. BCNS is located in North Saanich ~800m west of the Victoria International Airport. The monument BCES is located at the Canadian Forces Base Esquimalt. The network adjustment corrected the GPS survey with baseline distances averaging 25.82km. In addition to the SLP survey, two positions were collected at the University of Victoria. These two positions were the locations of a MASCOT (80H3844) monument and a municipal survey marker (Campus center) and were used as a quality

assurance check. Within GrafNet, the survey is processed through a network adjustment whereby the error is spread out within the whole network by a weighted least-squares approach. An L1/L2 fixed solution (resolved integer ambiguities, determined number of signal cycles) was found with ionosphere corrections for all surveyed points with the exception of C500 and C200. The control positions were: BCNS 466782.897, 5388479.682, 22.501 and BCES 468287.710, 5364101.081, 39.679, while the BCACS published positions for these monuments are: BCNS: 466782.902, 5388479.682, 22.499 and BCES: 468287.705, 5364101.079, 39.678 (UTM NAD83 HTV2.0). The measured control positions differed from the published positions by a northing of 6mm (both positions) and an easting of 2mm for BCES and <1mm for BCNS. BCNS was 2mm and BCES was 1mm off of their BCACS published orthometric heights. The GrafNet software applied an average semi-major-axis baseline error of 3.3mm and an average height error of 4.6mm, this from stations with an average RMSE of 22.4mm. The independently observed error in the position of the MASCOT monument at the University provided further confidence in the survey positioning. The campus monument had an error of 6mm northing, 1mm easting and 5mm in height. The published horizontal uncertainty of the monument is 4mm in each direction [103]; therefore the observed position is off by 2mm. Two additional reference positions were surveyed at the corners of deployed reflectance targets each with dimensions of 4.9x3.7m.

The aerial survey conducted in 2012, collected RGB photography that was orthorectified in Terrasolid's TerraPhoto in the Microstation software environment. The resulting 20cm orthophotography illustrated that the two reference positions were at least as accurate as the orthophoto mosaic resolution. The caveat in equating the accuracy of

the reference and validation positions to the control network positions is that the multipath environment is much more severe at the study site where the sky view is, at least partially obstructed by tree canopies. Multipath situations are known to produce perturbations in measured timing and thus variation in position measurements [104], [105]. An obstructed sky view blocks SV signals that could otherwise provide additional positions or may block SV passes, entirely. To augment the validation of the control survey, positions of large isolated trees were collected during total station precision traverses and were contrasted with the airborne lidar and orthophoto survey. The two positions that did not produce fixed solutions were re-surveyed. These two positions were occupied for three additional hours, which was sufficient for their correction in GrafNet. A list of positions surveyed for the SLP control network is presented in Table 3.3. Having established the local control network for the SLP study site, connecting traverses were conducted.

Table 3.3 Control positions surveyed by post-processed L1/L2, C/A and carrier GPS

ID	Northing	Easting	Ortho height	Baseline distance	
				BCES	BCNS
80H3844	5367734.938	476845.464	57.519	9.297	23.056
BCES	5364101.081	468287.710	39.679	0	24.425
BCNS	5388479.682	466782.897	22.501	24.425	0
C100	5387381.725	446908.446	312.248	31.609	19.907
C201	5387424.867	446950.226	308.852	31.613	19.863
C300	5387359.985	446871.168	312.551	31.618	19.945
C400	5387071.629	447127.608	345.940	31.233	19.708
C501	5387204.943	447490.193	333.440	31.087	19.337
C600	5386875.511	447023.692	322.240	31.159	19.826
CNTR	5367818.841	476924.018	57.986	9.402	23.016
R100	5388202.052	446319.437	137.123	32.611	20.480
R200	5388189.357	446305.744	137.391	32.611	20.480
C501 and C201 are distinguished from C500 and C200 as the second fixed solution of those positions					

3.4.2 *Total Station Control Survey*

A Nikon Total station was levelled at C100 and the horizontal origin and reference grid was initialized by the positions of C100 and C300. The initial forward azimuth was calculated as 239.75˚. Six connecting traverses were conducted to provide reference positions for geo-referencing the TLS (terrestrial laser scanner) data collects. Traverses were conducted from C100 to C400 (west to south trail), M6 (center and south trail intersection corrected from the previous traverse) to C600, C400 to C100 (east to north trail), M6 to F25 (FARO reference monument corrected in previous traverse), C400 to C501 (south trail to LOGS baseline), M24 (south trail and LOGS baseline intersection, corrected in previous traverse) to C600 (LOGS baseline trail). A final open traverse was conducted from M24 to F51 (FARO reference monument). Several positions were collected at the end of the open traverse to provide for an assessment of the open traverse survey accuracy and potentially provide an avenue for correction. Two positions were surveyed at each of the treatment plots selected for sampling. Monuments were established at each of these plot positions. Vertical discrepancies between the surveyed closing position and the corresponding control position were corrected by the proportion to length of leg approach:

$$h_i = h_{i-1} + \Delta h + (HD/\sum HD * (\sum \Delta h - \Delta h_{control}),$$

where: h_i is the height of a given surveyed position, h_{i-1} is the height of the surveyed position prior to position *i,* and $\Delta h_{control}$ is the height difference between the control positions (known start and end heights). Using the compass rule, the error of closure was corrected from the connecting traverses.

$$LAT_{new} = LAT + ((HD/\sum HD) * (-1 * (N_{survey} - N_{control}))).$$

Each traverse position was converted to latitude (LAT=ΔN) and departures (DEP=ΔE) for the horizontal corrections. The closure error (difference between surveyed end point northing and or easting and the control northing or easting) was distributed along the traverse as a proportion of the length of the legs relative to the total length of the traverse (Table 3.4). The final control survey was converted to a vector shape file, which included all control positions turning points and scanner reference positions for the selected plots (Fig. 3.9).

The results of the connecting traverse survey are presented in Table 3.4. According to maximum closure errors, the survey is horizontally accurate to better than 70cm. However, it was determined that this error was largely a function of the control network and thus represented the compounded error of both the GPS and total station survey. This conclusion was made after repeated traverses were unable to meet the 1:5000 accuracy standard [106]. A closed loop traverse was completed to eliminate the influence of a possible inaccurate traverse closing position. The closed loop survey easily exceeded the accuracy standard, therefore the estimated positional error attributed to solely the precision traverse was <10.7cm horizontally or 6.3mm per turning point. The error in the precision traverse is distributed in, proportion to the total length. As a result, there was a distribution of correction distances. Correction distances range from 1-85cm, with a median distance of 55cm. The reference tree positions collected during traverse surveys were evaluated against the ALS data. The reference positions used to evaluate the TLS positioning included several stem locations in LOGS plot 8 and SLP plot 67. These validation positions were strategically selected at the further extents of the survey, as any compounding bias would be most apparent there. Plotting the control survey data with

airborne data (section 3.4.3), demonstrated that the effective accuracy of the control survey was sufficient to position individual trees and thus for building a precise ground reference database from the union of TLS data with the CFS database of traditional ground measurements. The correspondences between the surveyed positions, ALS and TLS features were observed through point cloud profiles and raster products.

A vertical discrepancy was observed between the control survey and the ALS data, not attributed to differing vertical reference as both were processed to HTV2.0 (based on the Canadian Geodetic Vertical Datum of 1928). The vertical displacement was investigated by sampling non-vegetated positions within the GPS control survey. Although the sample size was small and there was some variation, the median difference was 1.767m. This observation is in agreement with a comparison made of an overlapping 2006 ALS dataset, which produced a median difference of 1.770m. A 1m bare earth difference surface model was generated from the two datasets. The difference histogram was computed from exposed ground surfaces, which provided the difference value of 1.77m. From these observations it was concluded that the 2012 ALS data had a mis-calibrated vertical reference of +1.77m.

Table 3.4. Uncorrected SLP closed traverse and closed loop survey accuracy

Traverse No. (monuments, trails)	Turning points and side shots (n)	Distance (m)	Vertical closure error (m)	Horizontal closure error (m)	Distance/ Horizontal error*
1) C100-C400, west & south	tp: 8 ss: 16	556.942	0.015 (2mm/tp)	0.090 (11mm/tp)	6172
2) M6-C600, center trail	tp: 5 ss: 2	226.700	0.083 (17mm/tp)	0.290 (58mm/tp)	782
3) C400-C100, east & north	tp: 9 ss: 10	501.547	0.064 (7mm/tp)	0.155 (17mm/tp)	3238
4) M6-F25, center trail	tp: 5 ss: 6	310.808	1.000 (20cm/tp)	0.222 (44mm/tp)	1401
5) C400-C501, south & LOGS baseline	tp: 8 ss: 18	537.055	0.102 (13mm/tp)	0.431 (54mm/tp)	1146
6) M24-C600, LOGS baseline	tp: 5 ss: 6	282.371	0.035 (7mm/tp)	0.70 (14mm/tp)	406
7) M24-F51, LOGS line 6	tp: 2 ss: 7	111.010	N/A	N/A	N/A
C100-west-south-east-north-C100 closed loop	tp: 17 ss: 27	949.006	0.064 (4mm/tp)	0.107 (6mm/tp)	8837

* Acceptable accuracy ratio expressed as 1:(total distance/closure error) is 1:5000. Following the traditional survey convention, the east-south-west-north trail surveys were repeated. When the 1:5000 was unachievable after three repeated surveys, it was concluded that the error is likely in start and end control positions. This suspicion was confirmed by the closed loop traverse achieving an accuracy of 1:8836 (closure error: 0.107m, loop distance: 949.006m)

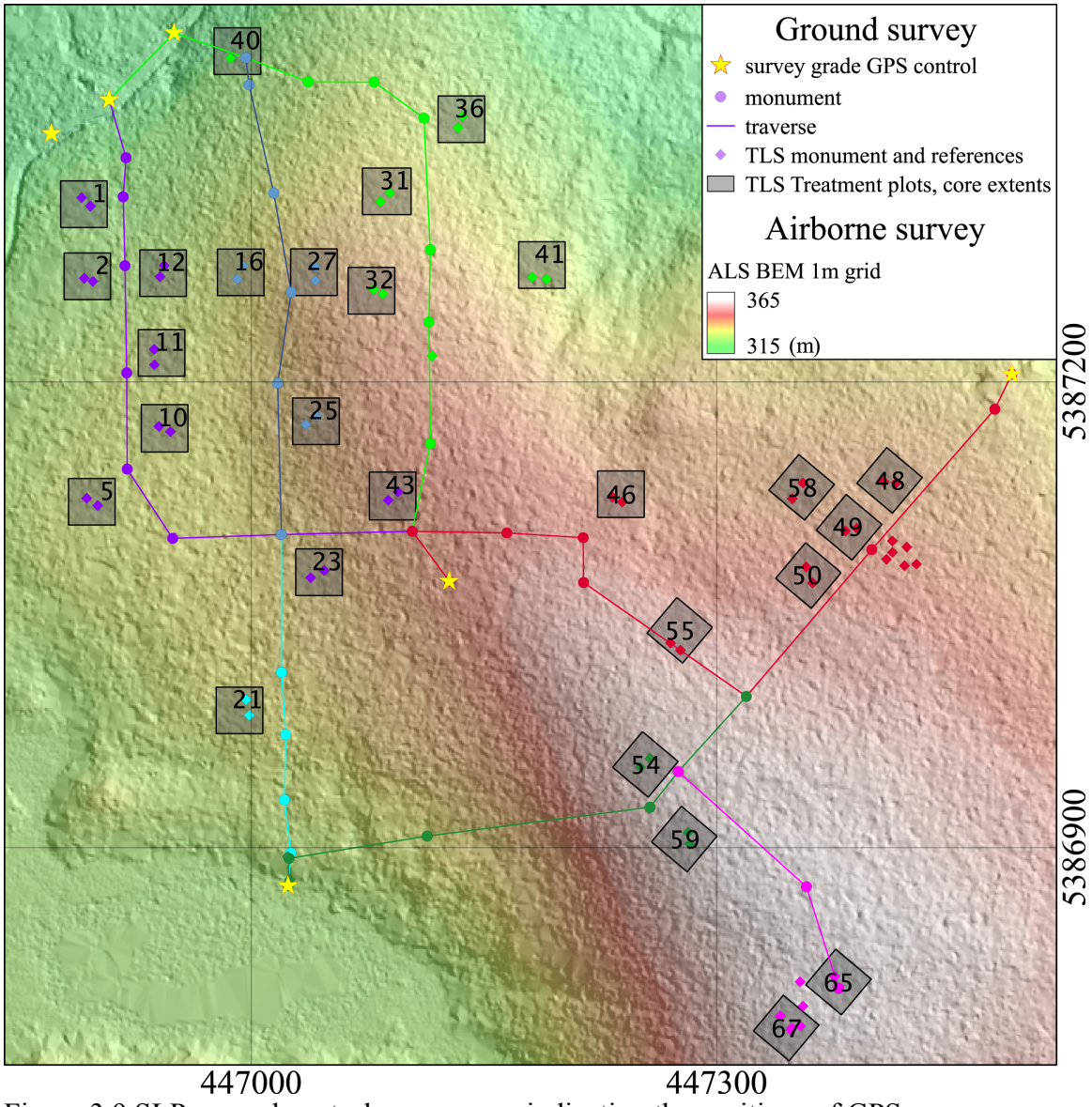


Figure 3.9 SLP ground control survey map indicating the positions of GPS survey monuments; turning point monuments and TLS reference monuments. Colors represent separate connecting traverses and grey squares are the core treatment plots extracted from the georeferenced TLS plot scans. Survey data are overlaid on an ALS bare earth model displayed in pseudo color.

3.4.3 *Terrestrial Laser Scanner Data Acquisition and Pre-Processing*

Once the reference positions within the selected treatment plots were surveyed to a known position, the terrestrial laser scanner could be deployed to survey the structure of the treatment plot. It was necessary to collect multiple scans from the treatment plots to be able to capture different geometries of the trees within the plot. Additionally, the multiple scans would help minimize the impact of occlusion (unsampled areas due to obstructions). The scanning protocol included establishing a set of reference targets within the treatments plots. To provide for a three dimensional solution, three targets are required to fix the reference plane. One will provide an absolute position, a second will provide a horizontal and a vertical rotation angle and the third provides a rotation angle relative to the axis of positions one and two. Because the FARO Focus 3D scanner has an integrated inclinometer, the vertical axis is predetermined and a third point represents a redundancy rather than a necessity. Two of these reference spheres were precisely positioned above the surveyed plot positions with tripods and optical plummets. The third reference sphere was positioned such that the targets were roughly the same distance from each other and that they were collectively centered in the core treatment area. With the reference targets in place the foundation for the scanning was complete and collection could begin. Three, roughly equidistant, scan positions were determined that had clear line of sight to the reference targets. At each of these positions scans were collected. Scanner parameters used during these collections included: imaging resolution of 20480x8534 (0.0175˚ interval) with even weighted metering (hemispherical normalization), 174.8M outgoing points, vertical scan range -60-90˚, horizontal scan range 0-360˚, active sensors: inclinometer, compass and altimeter, eye safe distance of

20.3m and a scan duration of 30.34 minutes. These parameters produce a point cloud with a point spacing of 6.1mm and a footprint diameter of 6.9mm at 20m from the instrument.

Once the TLS collection phase was complete, the scans were imported into the FARO Scene software environment. The software has a capacity for simple filtering and co-registration of multiple scans. This software was used for removing isolated and duplicate points as well as scan integration. The scan integration proceeds by generating and collocating simple geometric models within the individual scans. The procedure begins by the user selecting the target area on a raster representation of the scan. In this case, the spheres were selected. The software selects the points that occur within the user defined selection and fits a sphere model. The model is saved as a new object with a position at the center of the sphere. The model fitting can be constrained by a given sphere radius, which was used in this case (20cm). Constraining the fit is important because at lower point densities, the characterization of the sphere curvature may not be well defined. With one fixed master scan the other two scans were translated to the coordinate reference of the master scan. The software computes a scan-to-scan fit index to suggest the accuracy of the integration (Table 3.5). Positions within the integrated scan (plot scan) are relative positions where the scanner position of the master scan is the origin. In order to georeference the plot scans, the control survey plot positions needed to be related to the corresponding relative positions in the plot scans. To facilitate matching scan sphere objects and control positions, one of the reference spheres was painted and its location noted. The referencing of the plot scan was done through an initial origin shift to the position of the first reference sphere. The azimuth to the second reference sphere was

calculated in both the survey and the shifted plot scans. The plot scan was then rotated accordingly. Then the UTM position of the first reference point could be used as the plot scan offset shift, providing the georeferenced plot scan.

Table 3.5. Weighted tension index indicates the fit of scan integration per plot

Plot	Scan integration fit index (weighted tension)		
	Mean	Deviation	Max
2*	0	0	0
1	0.0046	0.0043	0.0111
31	0.0053	0.0038	0.0119
32	0.0055	0.0036	0.0104
11	0.0057	0.0069	0.0216
36	0.0066	0.0040	0.0119
59	0.0068	0.0042	0.0117
65	0.0068	0.0050	0.0138
10	0.0073	0.0073	0.0187
67	0.0073	0.0048	0.0145
12	0.0074	0.0071	0.0198
43	0.0076	0.0049	0.0134
50	0.0076	0.0059	0.0168
5	0.0078	0.0053	0.0170
40	0.0079	0.0057	0.0178
48	0.0081	0.0061	0.0170
49	0.0081	0.0069	0.0198
46	0.0083	0.0051	0.0139
58	0.0084	0.0054	0.0149
21	0.0085	0.0064	0.0187
23	0.0091	0.0066	0.0202
54	0.0093	0.0060	0.0174
16	0.0101	0.0061	0.0160
41	0.0101	0.0082	0.0246
27	0.0111	0.0080	0.0225
55	0.0113	0.0082	0.0245
25	0.0119	0.0079	0.0222

Scan integration fit index is calculated from the positions of reference targets between the different scans, the details of the calculation are not provided. The scans are ranked in order of increasing tension (decreasing quality of fit). * Required manual placement in correspondence view, after which, tensions are not computed

During the control survey, several positions were collected for features that would be apparent in both AIS and TLS. These positions were not used to translate plot scans to georeferenced positions. The independent positions used to evaluate the TLS positioning included several stem locations in LOGS plot 8 and SLP plot 67. In addition, a smaller tree stem was registered adjacent to control monument C600 at the pumping station. The correspondence between the surveyed positions, ALS and TLS features were qualitatively observed through point cloud profiles and raster products (Fig. 3.10-3.12).

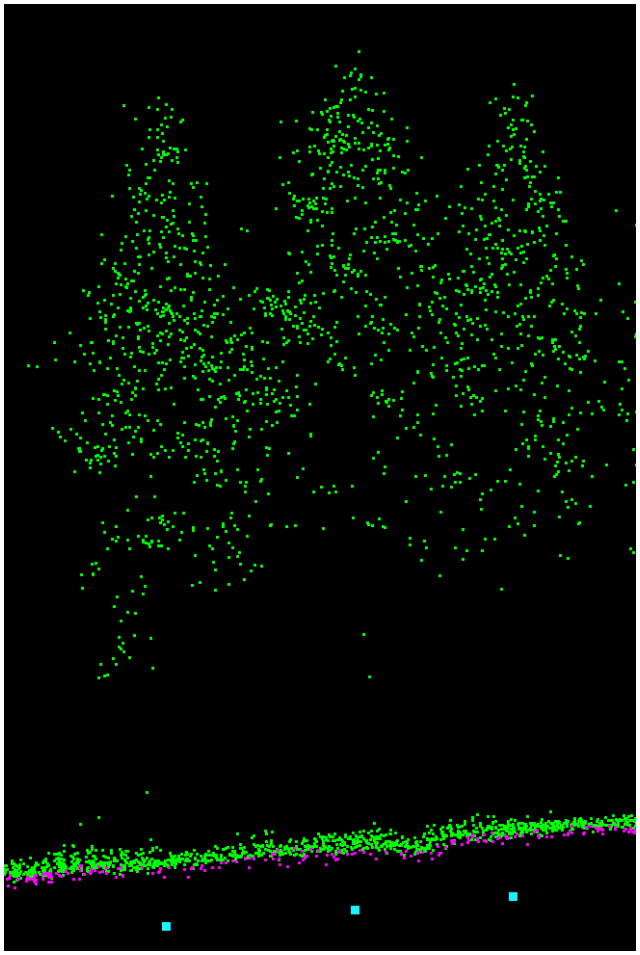


Figure 3.10 Vertical cross section of the ALS point cloud at LOGS plot 8, default points are illustrated in green while ground points are coloured magenta. The three cyan points are three stem positions from the control survey, which were collected as a validation of the ground survey. The vertical discrepancy is a known mis-calibration in the 2012 ALS dataset.

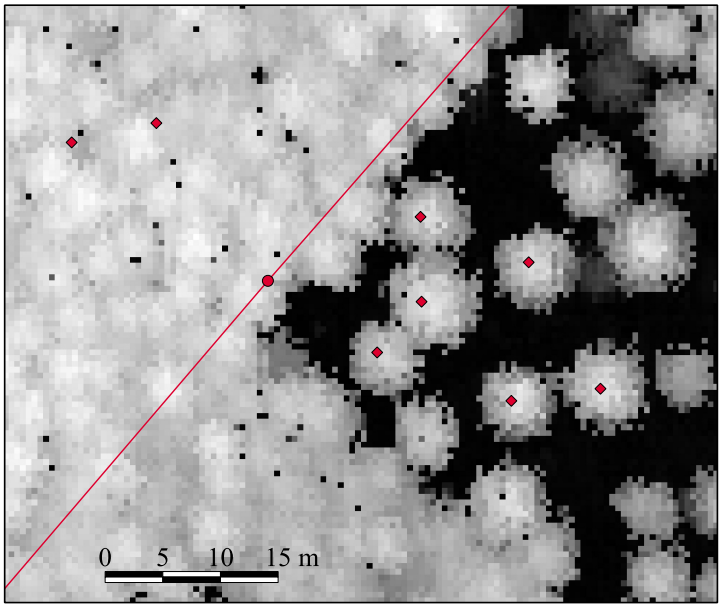


Figure 3.11 The control survey reference positions of isolated trees in LOGS plot 8. The survey data superimposed onto the ALS CHM demonstrates a sufficient accuracy has been achieved to identify individual tree stems. Note the two reference positions east of the traverse line are plot reference positions and not tree validation positions.

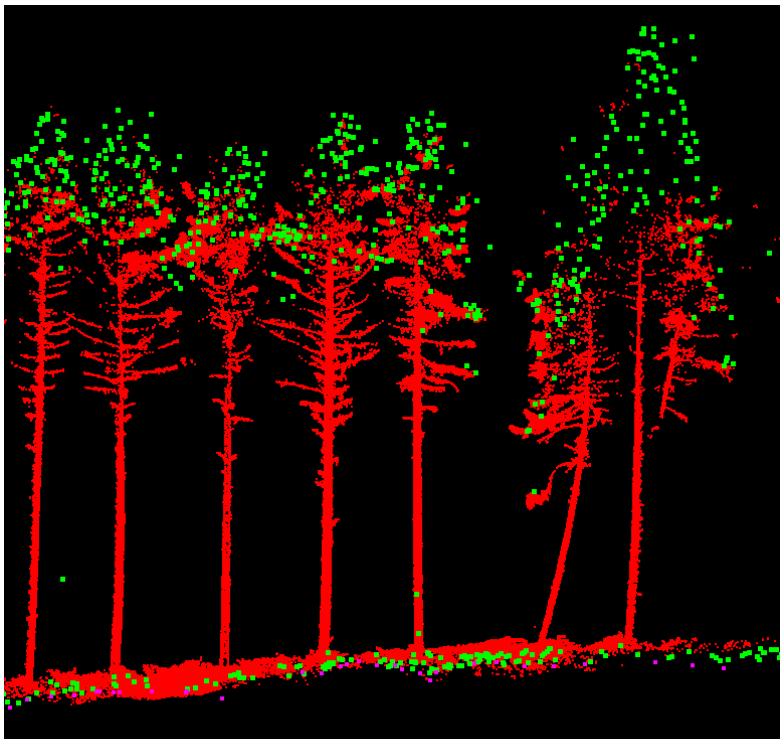


Figure 3.12 A vertical cross section of the TLS and ALS integrated point cloud at plot 67. This figure demonstrates that the positioning of the TLS data relative to the ALS is sufficient to associate trees within the TLS to those in the ALS dataset

The TLS point cloud was classified within the Microstation TerraScan software environment. The software has a limitation on the number of points that can be loaded. The plot scans were subsampled by 10% producing a point cloud of roughly 30M points per plot. A macro was constructed to classify ground points. The ground classification performed an iterative TIN (triangular irregular network) surface construction. The TIN surface was initiated by a sparse, low point selection that assumed the lowest point within a given square dimension was a ground point. The initial sparse ground surface was built from the lowest point in every 5x5m area. Lidar points were then classified as ground with reference to the initial TIN surface of the sparse low points. A point was classified as ground only if it was less than 1.0m orthogonally from the TIN facet and if the angle formed between the point under consideration, the closest sparse ground point and the TIN facet surface below the point in question was less than 10°. A maximum terrain angle was also a parameter for the ground classification macro; the terrain angle could not exceed 40°. The parameters used for the ground classification were modified from those used in the airborne lidar ground classification as point densities were much greater and penetration through ground cover vegetation was expected to be greater. It should be noted that the detail of ground characterization diminishes with distance from the ground-based scanner. This is attributed to both decreased point density and ground cover vegetation density within the signal path. The default classification described above was refined manually. The manual classification was iteratively performed on 1m vertical cross sections, which were confirmed and or refined in another iteration of the cross sections in an orthogonal direction. The manual classification refined the automated

ground classification and also classed overstory, understory and ground cover vegetation as well as coarse woody debris (Fig. 3.13). Because the manual classification was so detailed it also functioned as a quality assurance step.

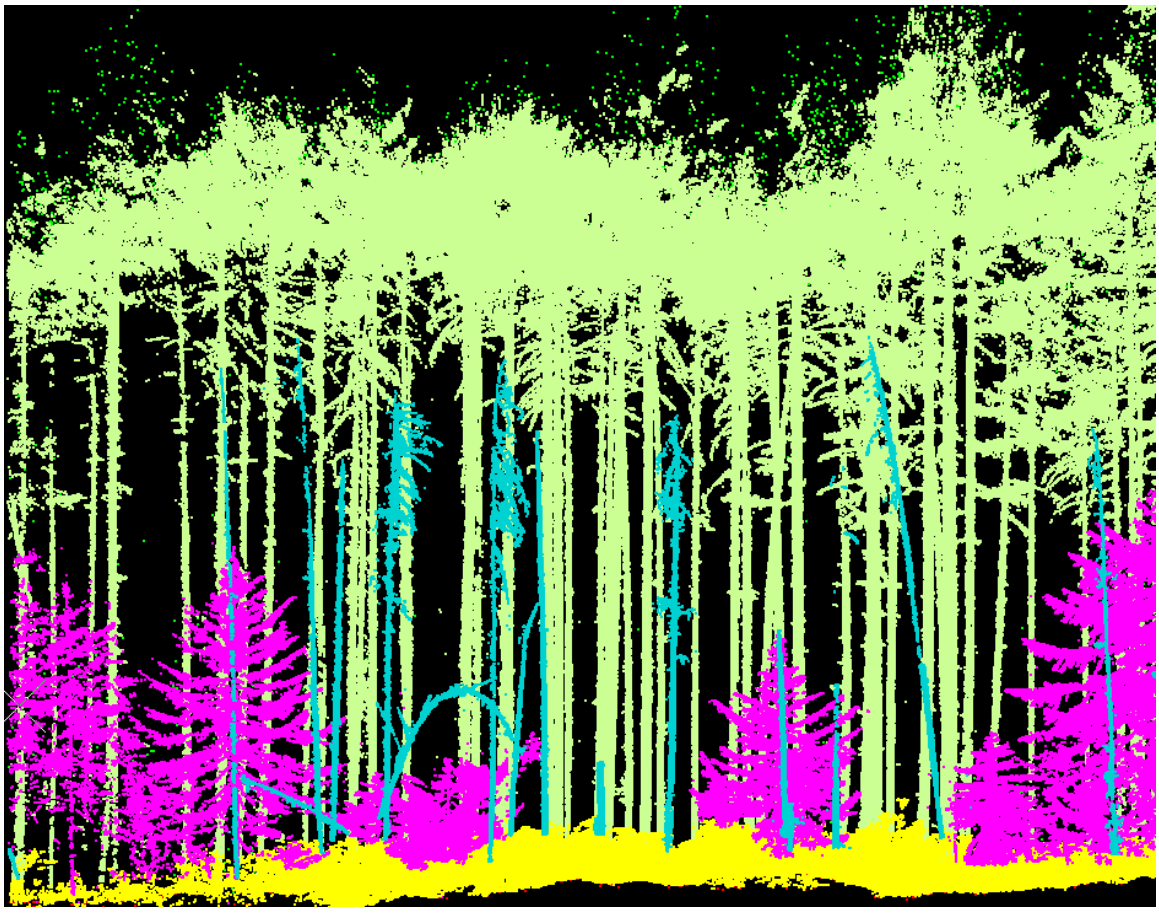


Figure 3.13 TLS point cloud classification at plot 2 (T0F0) included an automated ground definition (red) that was manually refined and the manual classification of overstory (light green), understory (magenta), ground cover vegetation (yellow) and coarse woody debris (cyan). The TLS data are integrated with the ALS point cloud. The ALS default (vegetation) class is displayed as green.

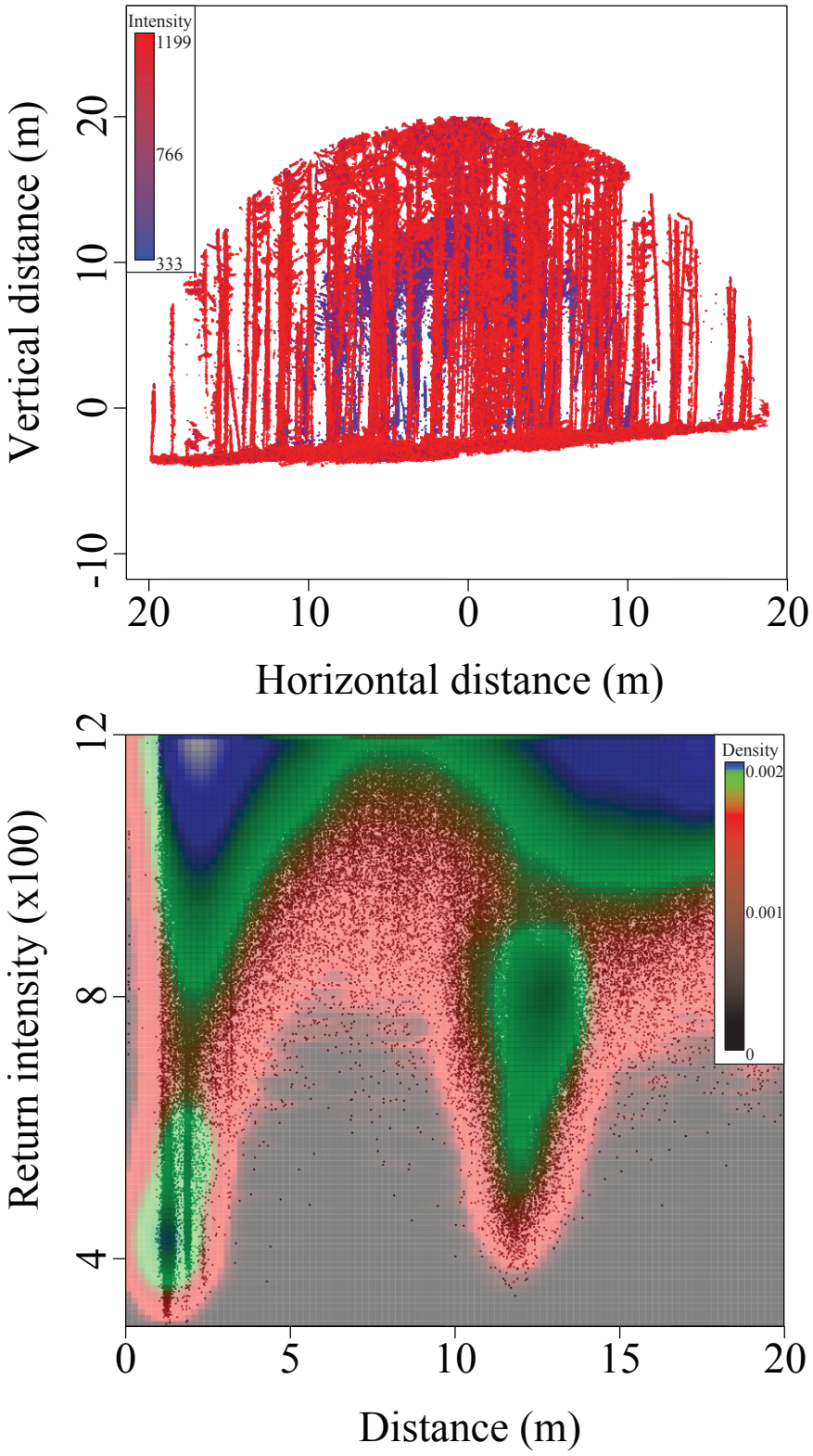


Figure 3.14 Top: Rain and fog backscatter is sufficient to register lidar points. Rain and fog points observed at specific distances from the scanner and with specific return intensities. Bottom: The low-density region within the return intensity-distance data space delineated these groups.

In one instance the impact of rain was apparent in the TLS data. At plot 5, heavy fog and some rain occurred during two of the three scans. The effect of the moisture was observed as two hemispherical high densities and low intensity returns at distances of approximately 2 and 12 meters. The occurrence at particular distances was presumably because of the relationship between pulse footprint size, droplet size and moisture density. The rain within the point cloud was discriminated by delineating local minima vectors in the intensity scan distance data space (Fig. 3.14). Once the classification and pre-processing was completed, the lidar data were then in a state where a terrain normalization could be conducted.

Several raster products were generated from the TLS point cloud; these included a bare earth model, a digital surface model and a canopy height model (BEM, DSM, CHM). Additionally, density based rasters were generated for each of the point cloud classes. Density information was considered important because, in contrast to ALS, the TLS point density is extremely variable and is partially a function of distance to the scanner. The bare earth and digital surface model were output as a summary of lidar points that fall within a given raster grid cell. The bare earth model was generated as a summary of only the ground points that occur within each grid cell, where the DSM is generated as a summary of all points (max height within a cell). The generation of the CHM requires that the lidar point cloud be transformed or normalized to the underlying terrain. The inverted TLS ground points facilitated the terrain normalization. Multiplying the height components of each ground point by -1 generates the new ground transformation point set. The ‘adjust to geoid’ operation within Terra Scan effectively subtracts, from each lidar data point, the value of the transformation TIN facet directly

below. The computed point cloud then has z values that represent the height from the modeled ground surface. The resulting CHM (canopy height model) point cloud was used to produce a series of raster products from each of the TLS classes (Fig. 3.15). The terrain normalized point cloud is also the data source from which canopy structural and physical metrics are generated. A full resolution (all points) 50cm (vertical thickness) horizontal cross section was taken per plot above the ground cover vegetation. The stem cross sections were used to generate 5mm rasters and would also be used for stem mapping and DBH modeling (Fig. 3.16).

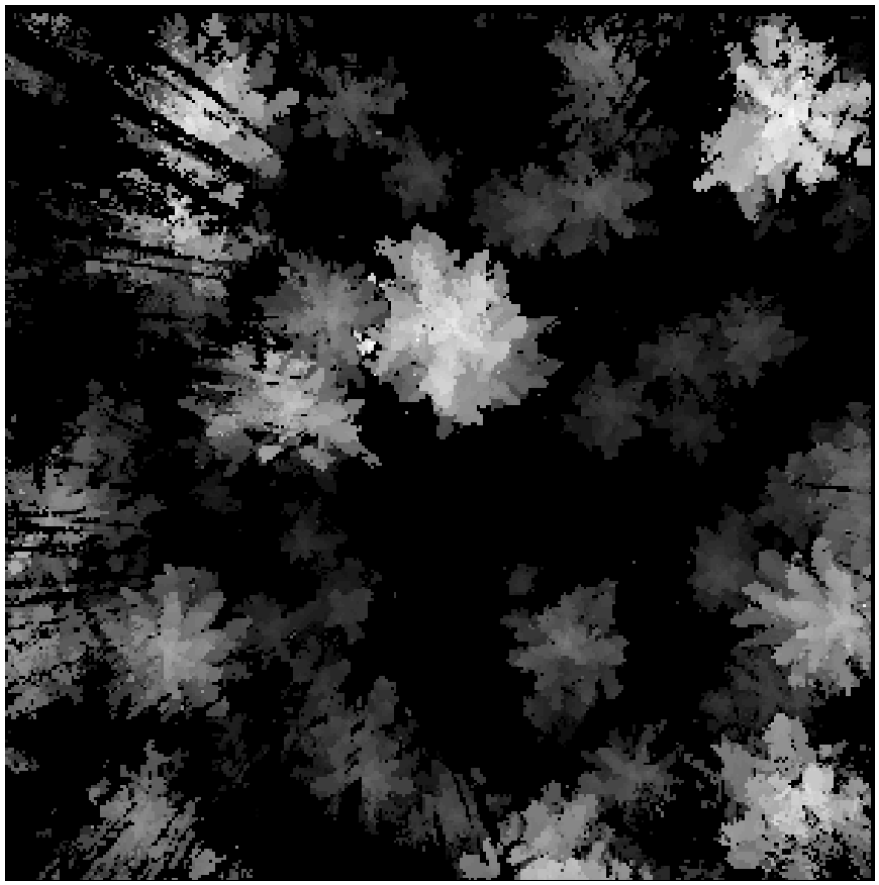


Figure 3.15 Plot 2 canopy height model of the understory vegetation class, represented by a 10cm raster grid size. The normalization process produces a dataset where height values are referenced to the ground surface and thus data values represent tree/foliage height from ground. Some occlusion is visible in the upper left of the image where overstory stems block points from being registered from some understory canopies.

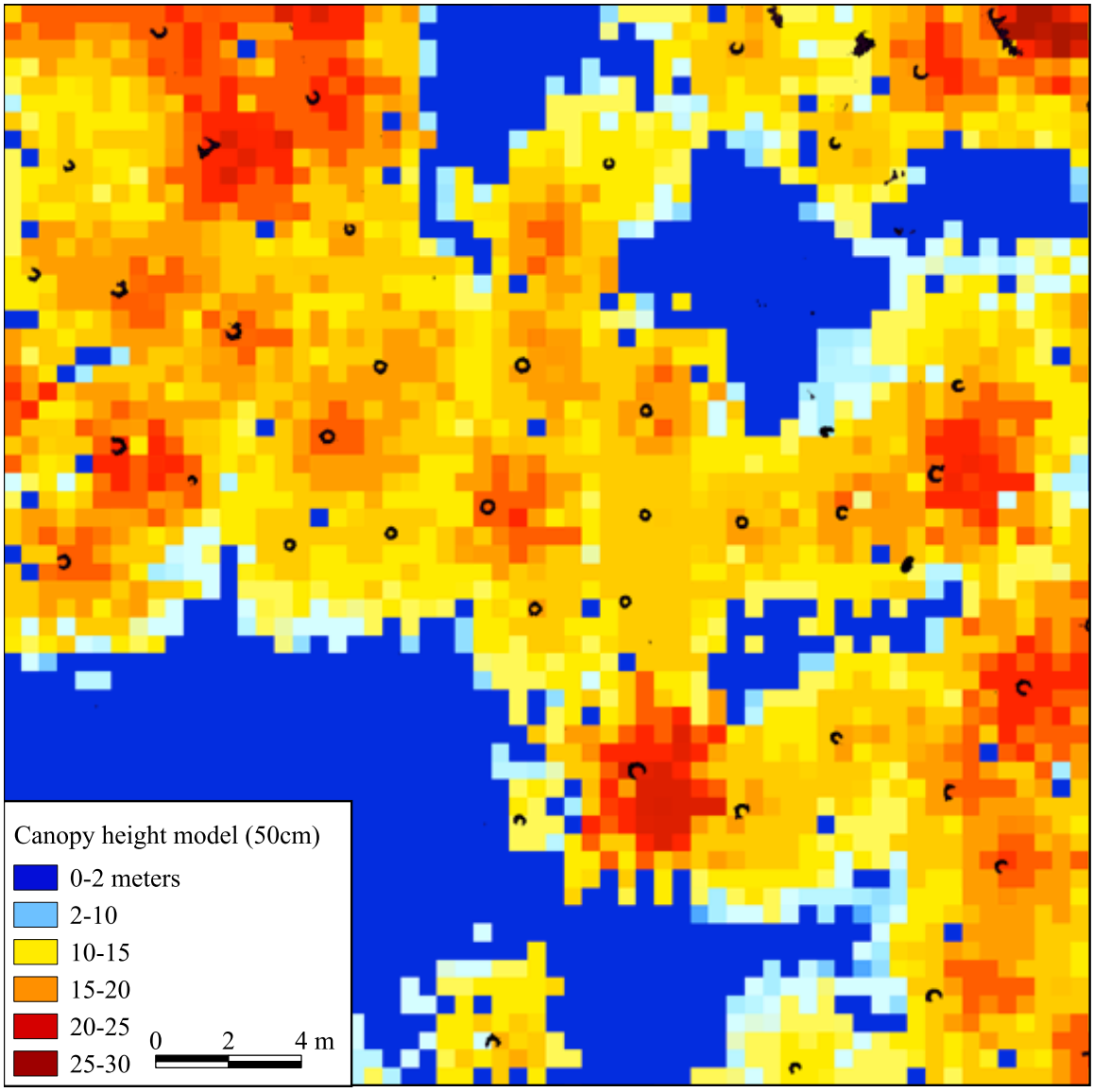


Figure 3.16 A 5mm grid raster of a horizontal cross section (50cm deep) at plot 67 is overlaid onto the ALS CHM. The cross section raster is saturated to produce a binary image of the stem locations and background is transparent, thus only stems are displayed in black. There appears to be good correspondence between high points (treetops) in the ALS CHM and the TLS bole locations.

3.4.4 *Ground Survey and TLS Discussion*

The necessary foundation for conducting terrestrial laser scanning surveys with absolute positioning is a precise and accurate ground control network survey. Where established control is not available, one must be established with survey grade GPS receivers with post processing software or with receivers capable of real time radio transmitted corrections from active control stations. This is assuming that required accuracies are finer than one meter; such is the case for individual stem and crown positioning. Irrespective of the stated quality of the GNSS network adjustment accuracies, the control survey should have redundancies built into the strategy. In the case of the SLP TLS acquisition these redundancies occurred in the form of the closed loop survey and independent qualitative evaluations of positioning.

Reference targets are a necessity if scan integrations or absolute positioning is required. In the SLP case, spherical reference targets were deployed, which can be modelled with a given radius and their center positions inferred. From these reference positions, translation and rotation factors can be computed to unify multiple scans and to position scans with reference to an established control network. The weighted tension index output from the scan integration process may be a valuable piece of information in TLS analysis where it will be possible to observe the effect of the accuracy of the integration on TLS products and empirical modeling.

Through the identification of individual core treatment stems within the concurrently collected color images, the extent of the core treatment area was determined. The TLS data were filtered to include only this area and to eliminate areas with very low point densities and areas outside the treatment area.

The TLS data were classified into distinct classes and raster products were generated. Once a ground class was defined, the data were normalized to the ground surface so that the point heights represented the height of vegetation, and again, several raster products were produced from this point cloud. The ground normalization process used might be excessive as there is very little vertical relief within individual core treatment plots. It may be sufficient to define a minimum plane surface to represent the ground for the ground normalization process. In the case for a plane ground, the effect of spatially variable ground characterization (where ground in distal areas is less well defined or where ground points tend to track ground cover vegetation rather than true ground) may be mitigated.

3.5 Data Calibration and Processing

Significant effort was given to the process of the radiometric calibration especially in the evaluation of calibration target materials. Details of the procedures for material evaluation are contained within Appendix 2. Ideally, targets will be featureless and well separated spectrally [107]. Results suggested that plant-based textiles were not spectrally invariant. Of the materials assessed and in general agreement with Knighton [108], optically thick surfaces of latex paints produced the best results. These samples were spectrally invariant in the specified range. However, some samples were more isotropic in terms of reflectance and more spectrally uniform depending on the brand and brightness. Targets were constructed and deployed in the summer of 2012 (Fig. 3.17-3.21).



Figure 3.17 Calibration targets deployed at the dry sorting lot for the Sept 13 data collection, when atmospheric conditions appeared favourable

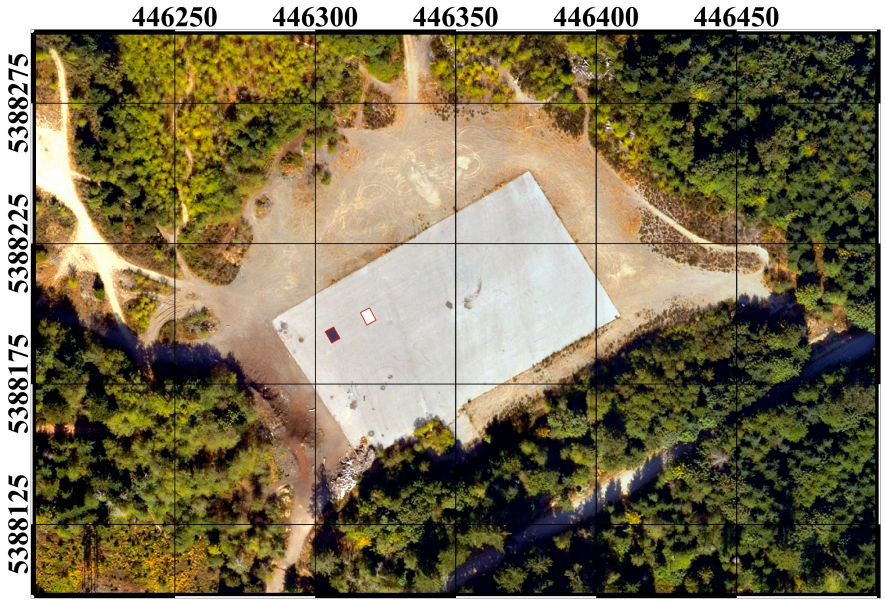


Figure 3.18 Calibration targets deployed at the dry sorting lot for the SLP project on September 13. The two 5x4m targets were positioned on a flat asphalt area



Figure 3.19 Calibration targets deployed in the field for the airborne campaign on September 19th 2012

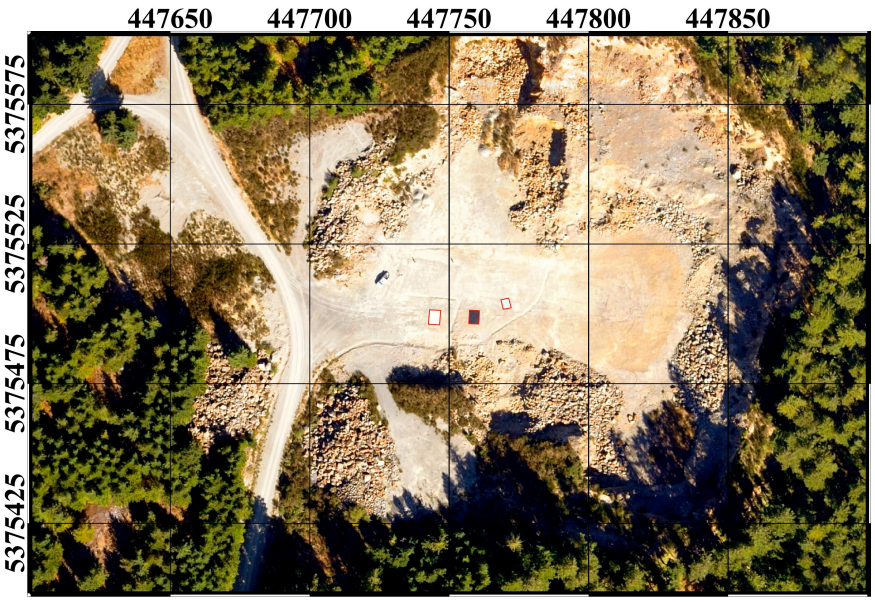


Figure 3.20 Calibration targets deployed at the saddle dam quarry within the GVWD for the airborne campaign on September 19th.

The September 13th dataset was omitted from the main study as a result of the sensor operator's observations of atmospheric aerosols originating from active forest fires in Washington State. This claim was unsubstantiated through a data comparison. The September 13 acquisition offered an opportunity to evaluate the repeatability of the spectrometer observations, as the flight plan was designed to make several varied geometry acquisitions of the deployed targets. The September 13th dataset was used to investigate the association between target response and acquisition geometry.

The AISA Eagle spectrometer data were received as raw unrectified digital number (DN). For the intended application these data need to be rectified or geometrically corrected and geo-located. Additionally, the data need to be spectrally transformed to represent energy interactions at the earth surface rather than solar irradiance, detector sensitivity and atmospheric energy interactions. Specifically for this

study, the radiometric correction is vital to make any comparison with auxiliary radiometric data. Beginning with the radiance transformation, the multiplicative calibration coefficients were applied to the data. In the calibration files there is a coefficient for each sensor element in the detector array that converts the voltage DN representation of photon counts to the physical units of radiance ($W/m^2/Sr/nm$). These gain factors are provided by the manufacturer's sensor calibration. In this case, the radiometric calibration was provided for the unbinned configuration of the sensor, 1024 bands. The four times spectral binning option was applied for this collection, CaliGeo is Specim's proprietary rectification software [109], which was applied to convolve the calibration file to be compatible with the binned dataset (132 bands). Because the detector array is larger than the usable area of projected spectral light (assumed to be confounded by higher order spectral diffraction), not all the binned bands are retained, only the center 132 channels are used. In this case the binning configuration used was a 4X hardware binning, where the detector electronics sum adjacent band DNs to effectively broaden the wavelength ranges, facilitating a fast integration time without a decreasing signal (whereas, maintaining the FWHM of the unbinned configuration would require 4x the integration time to achieve a similar signal level). Within the radiometric calibration process there is also a subtractive coefficient that is extracted from the dark current images collected before each flight line. These measurements characterize the baseline noise level (largely dependent on temperature) on a detector element basis. The subtractive term is determined as a frame average (n=30) of the dark current values for each sensor element (spatial and spectral dimensions) while a shutter is closed and no light is projected onto the detector. These processes were performed through Specim's

CaliGeo software version 4.9.7. Because the AISA Eagle is a frame transfer CCD sensor, the CaliGeo software is required to apply a frame transfer smear correction. The frame transfer smear correction removes the radiometric noise caused by the transfer of the area array detector to the masked readout portion of the sensor. The detector is still active for the duration of the frame transfer and therefore there is an effective smearing of detector frames that have a greater number of transfers. This effect is most apparent in columns that transfer bright DN values [110]. The radiance data are then calculated within CaliGeo as:

$$L_{k,i} = \frac{a_{k,i} * \left(\left(DN_{k,i} - b_{k,i} \right) - FTS_{k,i} \right)}{T} \qquad \text{[Equation 1]}$$

Where: $L_{k,i}$ is radiance in (μ m/cm^2*Sr*nm) in band k and spatial pixel *i*, a is the calibration gain factor (units: μ W/((Sr*cm^2*nm)(DN*ms)), DN is the image raw digital number, b is the average dark image digital number, FTS is the frame transfer digital number (see following equation) and T is the integration time in milliseconds.

$$FTS_{k,i} = (dt/T) * \sum_{j=0}^{k-1} s_{j,i} \qquad \text{[Equation 2]}$$

where: $FTS_{k,j}$ is the frame transfer smear at band k and spatial pixel *i*, dt is the time duration for the frame transfer in ms, T is the integration time in ms, $s_{j,i}$ is the dark subtracted DN at band j and spatial pixel *i*.

It should be noted that the smear retrieval method is slightly different when spectral hardware binning is applied. One option is to scale the above equation by the binning factor [111]. From the FTS equation it is seen that the smear for a given band and pixel is dependent on the measurements made at that spatial pixel in the bands before band k in the direction of the readout portion of the detector. Given the duration of frame transfer and the measurements made during the image capture period as an estimate of what would be captured during frame transfer, the DN contribution of each frame transfer

can be accounted for and removed before calibration factors are applied. The dependence of smear on the measured signal explains why this noise is not accounted for in dark current measurements. After the radiometric conversion to radiance was performed, target spectra were extracted from the unrectified flight lines (Fig 3.21). The unrectified images were selected because through the orthorectification process, pixels can be omitted based on the projected pixel position and frame sequence. In the case of one flight line the purest bright target pixel was omitted from the rectified imagery, validating the approach to using the unrectified flight lines for target spectra extraction. It was hypothesized that the observed variation in the target responses was largely determined by acquisition geometry.

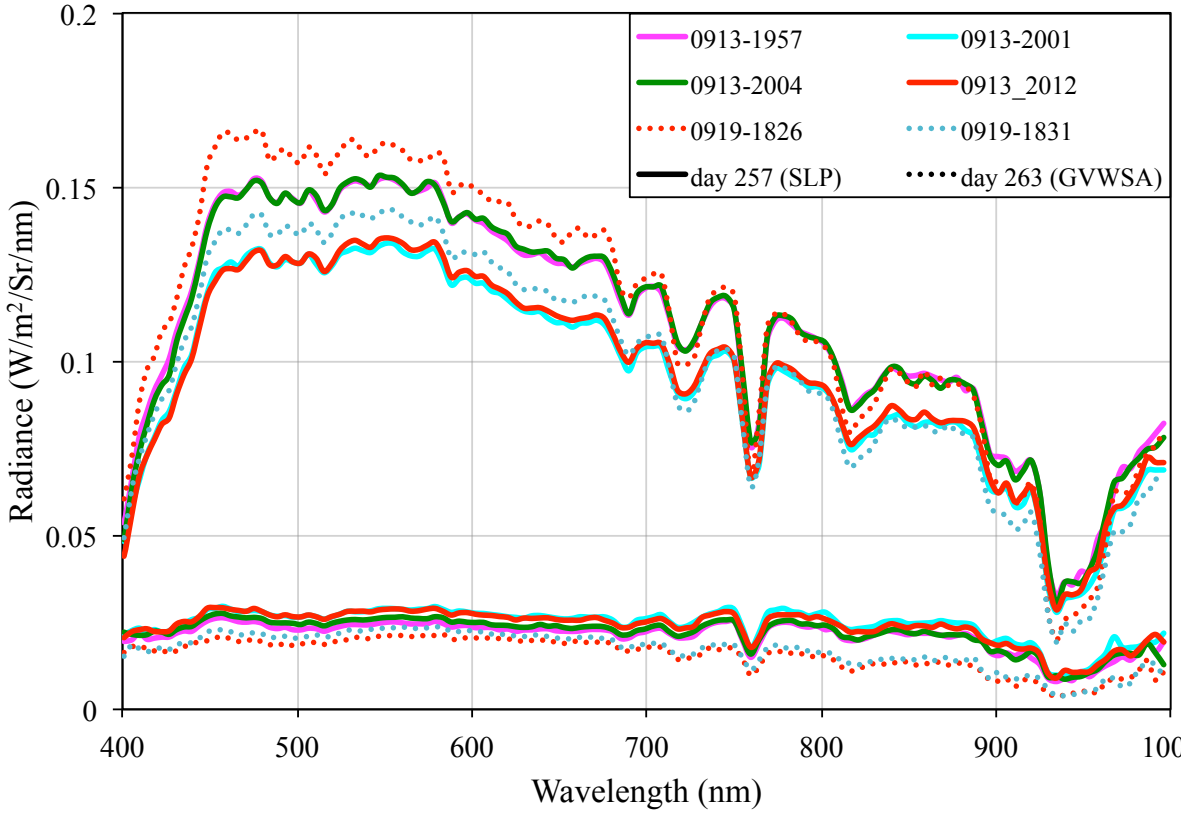


Figure 3.21 AISA Eagle radiance spectra of the deployed calibration targets

3.5.1 *Deriving Geometry from INS Measurements*

The underlying assumption of direct georeferencing is that there is precise data synchronization between the imaging system and the INS. The navigation data measured by the INS includes platform position, and instantaneous roll, pitch and heading values (Fig. 3.8). Although the orthorectified data was not necessary for this portion of the study, the INS data provided information on the geometry of the sensing platform and therefore offered the opportunity to investigate the observed variation in target responses attributed to changing observation geometries. In order to extract the appropriate platform position and attitude data from the navigation data, the time synchronization discrepancy had to be resolved. In order to resolve timing synchronization issues, the integer second signal that is generated by the Applanix POS/AV INS system is used to drive a timing signal that is directly read into the image. The AISA imaging system is designed such that the first 28 spatial pixels are reserved for metadata acquisition and FODIS (fibre optic down welling irradiance sensor). Within this region of the detector array, an LED (light emitting diode) is projected and operated by the integer second signal from the GPS. The systems integrated hardware assigns a GPS time string with the integer second signal. The time of the first integer second of each flight line is read into the header file of each collected flight line. More precise timing synchronization is achieved by way of the apparent constant frame rate. By counting the number of frames collected before the first pulse per second (PPS) signal transition and multiplying by the time duration for each frame, the timing synchronization is improved to less than 23.25ms. Occasionally the GPS integer time written into the header file actually references the integer second occurring before, not after, the first recorded data frame. In such cases, the timing offset

is adjusted to represent the time between the integer second and the time the first frame was collected (i.e. 1sec – (#frames*0.02325sec). See Figure 3.22 for a graphical representation of the timing synchronization.

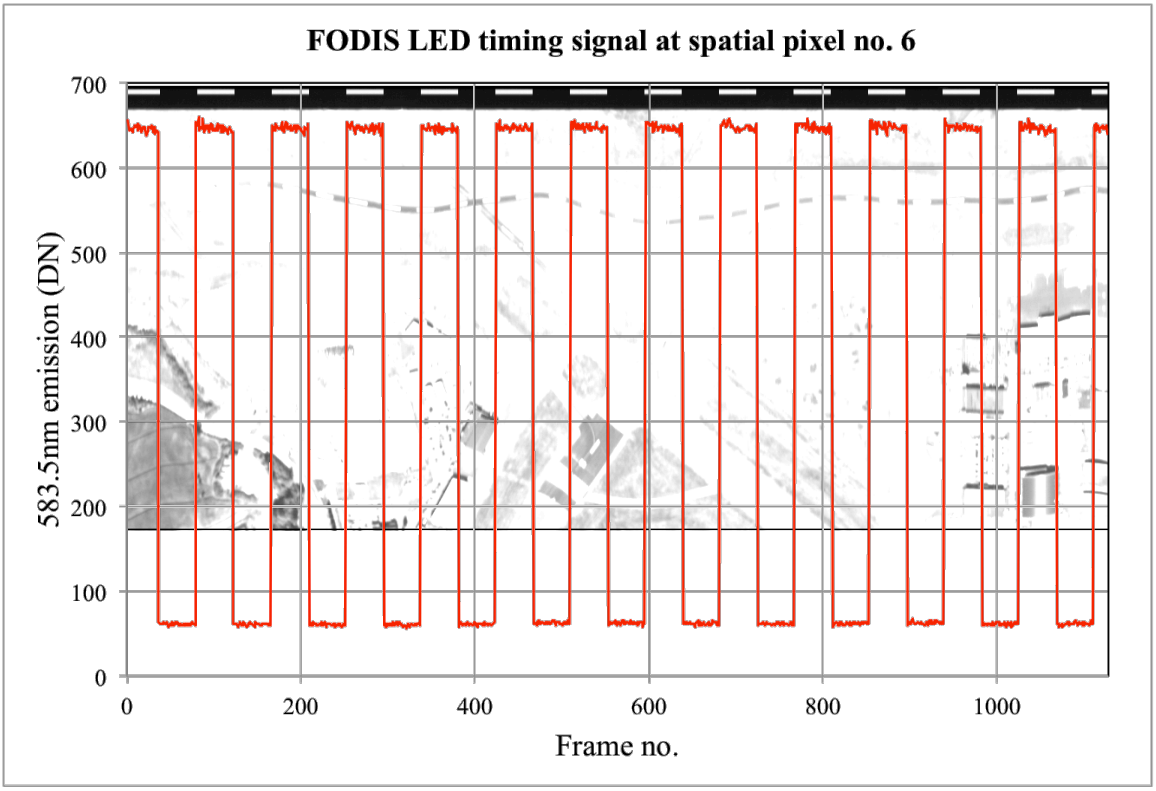


Figure 3.22 AISA Eagle time synchronization. An example of the LED PPS timing signal. Each transition from on to off and off to on mark the frame location of the integer second, the frame rate is 43f/s. Note the underlying grey scale image of band 583nm with FODIS PPS timing at top.

With the timing synchronization resolved, the precise time of collection for a particular frame could be determined. With the start of line time, the frame rate and the frame number that measured a deployed target, the time the measurements took place was determined. Platform latitude, longitude, altitude, roll, pitch and heading data that temporally corresponded with the frames that captured the calibration targets were extracted from the navigation data. Through the use of a lidar derived 50cm digital

surface model (ground and default) the platform altitude was translated to height above the surface (altitude-DSM). The platform attitude data was corrected for bore sight misalignment, caused by slight angular differences in the INS and spectrometer coordinate reference frames. The boresight calibration was performed using oppositely flown data over long linear ground features, the Victoria International Airport, in this case. Observation geometry (referenced to vertical) was then calculated using platform height, bore sight corrected roll and pitch, and the across-track pixel number (Eq. 3-6). Computing the observation zenith and azimuth angles from roll and pitch would be valid for only the principal pixel, therefore to correctly determine the observation geometry the roll used in the calculation must incorporate the angle between the spatial pixel that captured the target and the principal pixel. The AISA Eagle has an asymmetric field of view caused by the FODIS region, which occupies the first 28 detector elements. The optical axis is incident on the detector at element number 256.5. With a known focal length and the detector element dimensions, the across track angle from the principal pixel can be calculated and incorporated into the roll parameter (Eq. 4).

$$y = (alt - dsm) * \tan(\varphi_p) \quad \text{[Equation 3]}$$

where: y is the along track horizontal distance from the aircraft to the observed pixel position, alt is the altitude of the platform at the time the frame was captured, DSM is the ground elevation at the target pixel, $\varphi_p$is the pitch angle of the platform at the time the frame was captured.

$$x = (alt - dsm) * \tan\left[\varphi_r \pm \left[(p - s) * \tan^{-1}\left(\frac{d * bin}{f}\right)\right]\right] \quad \text{[Equation 4]}$$

where: x is the across track horizontal distance from the aircraft to the observed pixel position, φ_r is the roll angle of the platform at the time the frame was captured, p is the principal pixel detector element number, s is the sample number that captured the target, d is the detector element size, bin is the spatial binning factor and *f* is the focal length. Note; where s>p roll was adjusted by summation, while s<p roll was adjusted by subtraction.

$$\theta_{obs} = \left(\theta_h + \tan^{-1}\left(\frac{x}{y}\right)\right) \pm 180° \quad \text{[Equation 5]}$$

$$\varphi_{obs} = 90° - \tan^{-1}\left[\frac{alt - dsm}{\sqrt{y^2 + x^2}}\right] \quad \text{[Equation 6]}$$

Where: θ_{obs} is the observation azimuth from the ground surface perspective and relative to north, ϕ_{obs} is the observation zenith from the ground surface perspective and relative to vertical and θ_h is the platform heading at the time the frame was captured,

The referencing of geometry to vertical is arbitrary and does not have a meaningful relation to the incident and reflected light. For this reason, the geometry should be related to the surface normal vector (Eq. 7-10). In addition, the azimuth angle, relative to north is also an arbitrary convention. To investigate the impacts of varying geometries, these angles should be reduced to relative azimuths, that is the angle between the observation and illumination azimuths (Eq. 11).

$$Sen_x = \sqrt{x^2 + y^2} * \sin(\theta_{obs} - 180°) \quad \text{[Equation 7]}$$

$$Sen_y = \sqrt{x^2 + y^2} * \cos(\theta_{obs} - 180°) \quad \text{[Equation 8]}$$

$$Sen_z = alt - dsm \quad \text{[Equation 9]}$$

where: $Sen_{x,y,z}$ is the three dimensional point representation of the observation vector with an origin located at the target pixel, these parameters were determined for the platform, the source and the ground surface normal vectors. Note that the azimuth constant term is based on the third quadrant (platform is south west of target pixel), but is different for each.

$$\varphi_{Obs_Tnorm} = \left[\cos^{-1}\left(\frac{\sum(Sen_i * Tar_i)}{\sqrt{\sum(Sen_i^2)} * \sqrt{\sum(Tar_i^2)}}\right)\right] * \frac{180}{\pi} \quad \text{[Equation 10]}$$

$$\theta_{rel} = \sqrt{(\theta_{obs} - \theta_{sol})^2} \quad \text{[Equation 11]}$$

Where: ϕ_{Obs_Tnorm} is the observation zenith angle from the ground surface perspective and relative to the ground surface normal, Sen_i is the x,y and z parameters for the point representation of the observation or sensor vector, Tar_i is the x,y and z parameters for the point representation of the surface or target normal vector. The solar zenith was computed in the same manner by substituting Sen_i with Sol_i, θ_{rel} is the relative azimuth representing the angle between the solar azimuth and the observation azimuth.

While the observation geometry was captured in the INS data, the surface geometry was derived from a topographic analysis of the 50cm lidar digital surface model. Slope and aspect were computed by ITT's ENVI topographic modeling, where the estimates are determined by the partial first order differential equations of the general quadratic equation (*i.e.* $z=ax^2+by^2+cxy+dx+ey+f$) fitted to a 3x3 kernel. The partial derivatives are combined and the origin shifted to the kernel center to produce the slope equation: $slope\ (°) = \tan^{-1}\left(\sqrt{d^2 + e^2}\right)$, the aspect equation is also derived from the partial derivatives: $aspect\ (°) = \tan^{-1}(e/d)$ [112]. Lastly, the solar position was found through the NOAA Earth System Research Laboratory, Global Monitoring Division's Solar Calculator (URL: http://www.esrl.noaa.gov/gmd/grad/solcalc/). See Tables 3.6 and 3.7 for radiometric flight line ancillary data. The geometry data suggested that the footprints projected to the ground surface were slightly different between the two data collections (day 257 and 263), where the SLP data (day 257) had footprints that were roughly 10cm larger than those produced in the GVWSA collection (across track

dimension). The geometry data also illustrated that there was little variation (<7°) in the solar zenith angles between flight lines in the SLP collection but the GVWSA solar zenith angles were approximately 6° smaller than those from the SLP collection. In terms of the observation zenith geometry flight line 0919-1826, was a significant departure from the other samples, with an angle roughly three times that observed for the other flight lines. The large observation zenith value for flight 1826 was produced by the collection geometry where the targets were captured at the edge of the swath width. The relative azimuth of flight line 1826 places the geometry closer to the principal plane and closer to the effect of the specular hotspot. Given the laboratory evaluation of the target BRF the dark target has a more pronounced affect when geometries approach the forward scattering hotspot.

Table 3.6 BRDF geometry parameters for Eagle measurements of bright calibration target						
Flight ID	0913-1957	0913-2001	0913-2004	0913-2012	0919-1826	0919-1831
Easting	446255.3	446396.9	446301.9	446289.1	448116.5	447632.3
Northing	5388151.5	5388154.9	5388323.4	5388284.0	5375384.3	5375642.7
Height a.g.l.	1236.3	1238.9	1232.7	1246.3	1161.4	1175.2
Roll	-0.110	1.053	3.921	-1.893	17.341	5.972
Pitch	3.599	3.876	4.082	3.337	4.6705	3.377
Heading	50.422	330.686	259.968	103.221	73.851	241.436
Across track IFOV	1.608	1.612	1.609	1.620	1.513	1.528
Along track IFOV	0.806	0.808	0.804	0.812	0.759	0.765
Along track sampling	1.231	1.282	1.252	1.234	1.187	1.222
Azi_{obs}	230.422	150.686	79.968	283.221	253.851	61.436
Zen_{obs}	3.601	4.016	5.651	3.834	17.888	6.849
Azi_{sol}	175.59	176.96	177.86	180.87	137.80	140.15
Zen_{sol}	45.31	45.27	45.25	45.24	39.39	38.65
Azi_{tar}	184.49	184.49	184.49	184.49	184.98	184.98
Zen_{tar}	3.19	3.19	3.19	3.19	5.27	5.27
$Sol\text{-}tar_{norm}$	44.98	44.94	44.92	44.91	38.92	38.18
$Obs\text{-}tar_{norm}$	3.38	3.72	5.58	3.75	17.68	6.55
Azi_{rel}	54.83	26.27	97.89	102.35	116.05	78.71
*target perspective, Tar superscript indicates the directionality of the target normal, Roll in 1826 is large because the sampling spatial pixel number is 482 far from the principal pixel. Attitude values are corrected for bore sight misalignment and spatial pixel number. All values pertain to only the specific sample and frame that collected the deployed target. With the exception of easting, northing, height, and IFOV values, which are in meters, all values are degrees.						

Table 3.7 BRDF geometry parameters for Eagle measurements of dark calibration target						
Flight ID	0913-1957	0913-2001	0913-2004	0913-2012	0919-1826	0919-1831
Easting	446245.1	446393.5	446294.1	446285.8	448116.5	447632.3
Northing	5388141.7	5388158.1	5388314.2	5388287.3	5375384.3	5375642.7
Height a.g.l.	1236.3	1238.9	1232.6	1246.2	1161.3	1175.2
Roll	0.081	1.657	3.724	-2.480	16.672	6.567
Pitch	3.592	3.876	4.080	3.338	4.671	3.377
Heading	54.046	338.692	258.704	96.009	73.254	243.723
Across track IFOV	1.608	1.612	1.609	1.620	1.512	1.528
Along track IFOV	0.806	0.808	0.804	0.812	0.759	0.765
Along track sampling	1.231	1.282	1.252	1.234	1.187	1.222
Azi_{obs}	234.046	158.692	78.704	276.009	253.254	63.723
Zen_{obs}	3.593	4.213	5.515	4.155	17.246	7.371
Azi_{sol}	175.59	176.96	177.86	180.87	137.80	140.15
Zen_{sol}	45.31	45.27	45.25	45.24	39.39	38.65
Azi_{tar}	172.24	172.24	172.24	172.24	188.93	188.93
Zen_{tar}	6.58	6.58	6.58	6.58	11.75	11.75
$Sol\text{-}tar_{norm}$	44.63	44.59	44.56	44.57	38.29	37.54
$Obs\text{-}tar_{norm}$	3.16	3.55	5.33	4.05	16.71	6.71
Azi_{rel}	58.46	18.27	99.16	95.14	115.45	76.43
*target perspective, With the exception of easting , northing, height, and IFOV values, which are in meters, all values are degrees.						

3.5.2 *Characterization of Target BRF*

It was important that ground based and airborne radiometric measurements of the calibration targets were predictable. From this perspective the variation in observed responses attributed to changing geometry had to be quantified. With the geometry of the airborne target responses determined, an effort was made to precisely reproduce the airborne geometry in the lab to empirically determine the variation in target response attributed to these geometries. From these measurements, reflectance was empirically modeled from the sampled geometry. An initial approach applied a multiple linear approximation to fit geometry and reflectance values. The multiple linear regression approach was recognized as a coarse approximation to the true response, which is known to be a cyclical response varying observation azimuth with constant observation and illumination zeniths. The true response is known to be cyclical as the observation angle passes through the two theoretical hotspots, backscattered and specular bright response positions. The MLR approach failed to capture the important hot spot effects; as a result, surface fitting approaches were considered a better alternative as the interpolation across the bivariate data space could be more or less generalized. The airborne geometries were simulated in the lab setting applying a desktop goniometer (Appendix 2). From the sampled geometry space the cyclical pattern for reflectance followed that of a non-lambertian reflector with a more dominant specular hotspot and very little indication of a backscatter hot spot, in the form:

$$R = f(\phi) \cdot 0.5 \cdot \sin\left(\frac{\pi}{180}(\theta - 90)\right) + f(\phi) \cdot 0.5 \qquad \text{[Equation 12]}$$

Where: R is the reflectance of the sample target, φ is the observation zenith angle that shortens the amplitude and migrates the baseline and θ is the relative azimuth angle from observation to illumination.

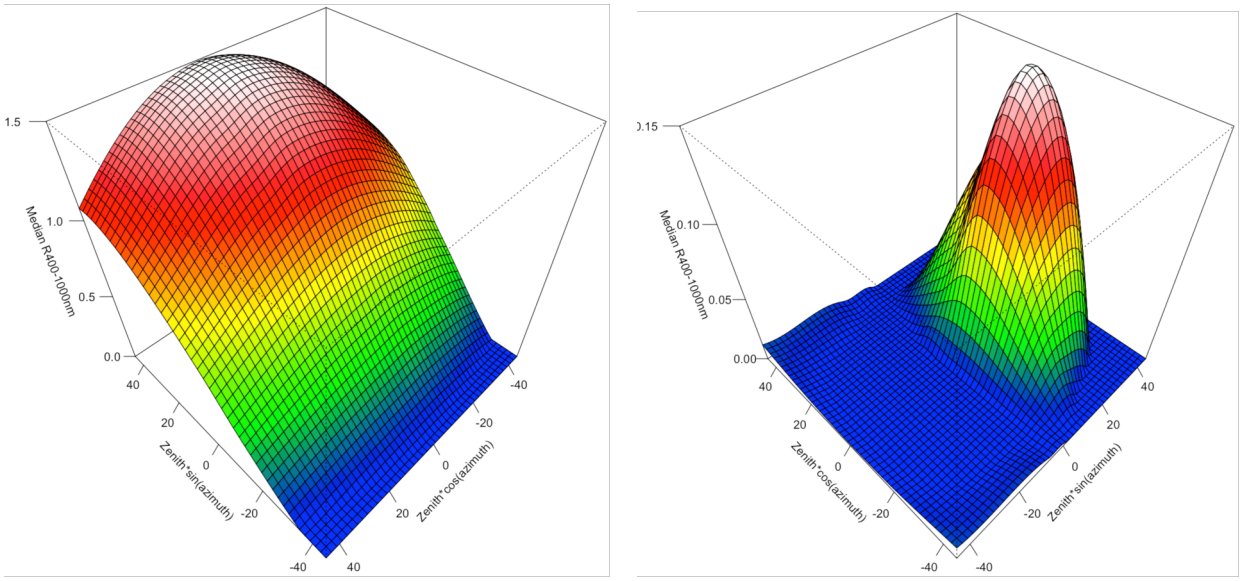


Figure 3.23 BRF surfaces for bright and dark sample targets measured in the lab setting and computed with LOESS (locally weighted polynomial regression fitting). BRF, represented by spectral medians (400-1000nm) are plotted to Cartesian coordinates from the surface polar coordinates (surface rotation and inclination). The bright target response clearly has a more dominant hemispherical scattering, while the dark sample produces a pronounced and more concentrated conical scattering response. Surfaces can be read as the x,y origin represents the nadir observation, horizontal angles from the origin represent changes in observation azimuth, and distance from the origin (*i.e.* radius iso-lines) represent changes in observation zenith angle.

The lab based measurements demonstrated a lowered amplitude associated with smaller zenith angles and a less defined sinusoidal pattern for the dark target, illustrated in locally weighted polynomial regression fitted (LOESS) surfaces of BRF (Fig. 3.23).

Each airborne target spectrum from day 0913 was considered and their geometries were reproduced in the lab with the desktop goniometer. The illumination geometry was considered constant at a 45° zenith while the relative azimuth and observation zenith angles were rounded to the nearest degree (Tables 3.6 and 3.7). Reflectance spectra were computed from nadir white references. Geometry correction factors were computed by normalizing the off-nadir measurements by the nadir equivalent. The lab measurements

illustrated that off nadir measurements did not induce any spectral non-uniformity, that is, all off nadir measurements could reproduce nadir values with a simple scale factor and the factor was not wavelength dependent (Fig. 3.24). This simplified the objective because a spectral summary statistic could then be used to model the effect of geometry. This result suggested that the LOESS median BRF surfaces could be normalized to the nadir geometry and applied as an interpolation lookup table to account for target specific acquisition geometry.

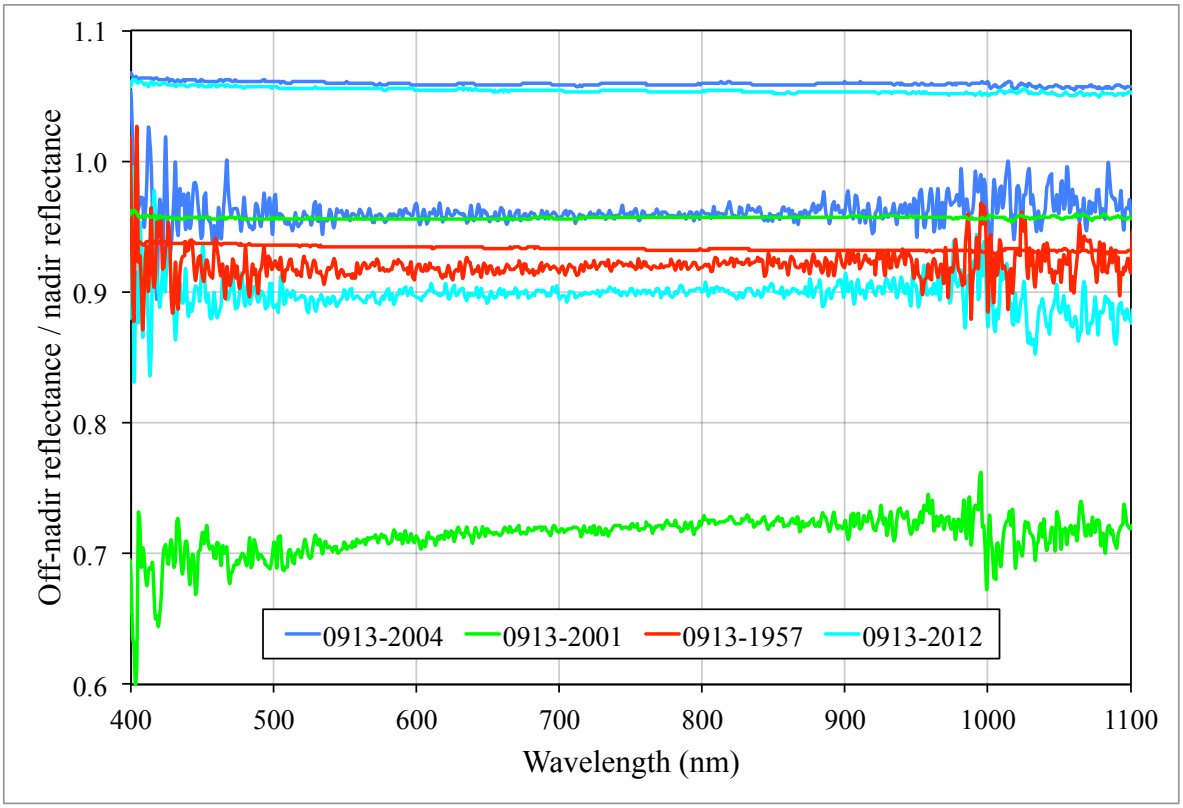


Figure 3.24 off-nadir spectra divided by the nadir measurements of the same target demonstrate the spectral invariance of bidirectional reflectance factors for the target samples

Airborne collected responses (Fig. 3.21) were compared against lab based target spectra collected with similar geometries to that produced in the airborne campaign (Fig. 3.25 & 3.26). Little can be objectively concluded from a dataset of four paired

observations however the rank correspondence of lab based and airborne responses agreed in two of the target cases, *i.e.* the extremes where flight line 2004 was the brightest and 2001 was the darkest. However, in the airborne dataset the four flights fell into two distinct groups, where flight line 1957 was a near replicate of 2004 and 2001 was very similar to 2012. Although a trend for two flight lines was apparent and agreed with the expected result, the remaining two observations did not conform. Therefore, the variation in target responses was not solely caused by variations in collection geometry. It was inconclusive whether the variation in observed airborne target data was partially the effect of geometry.

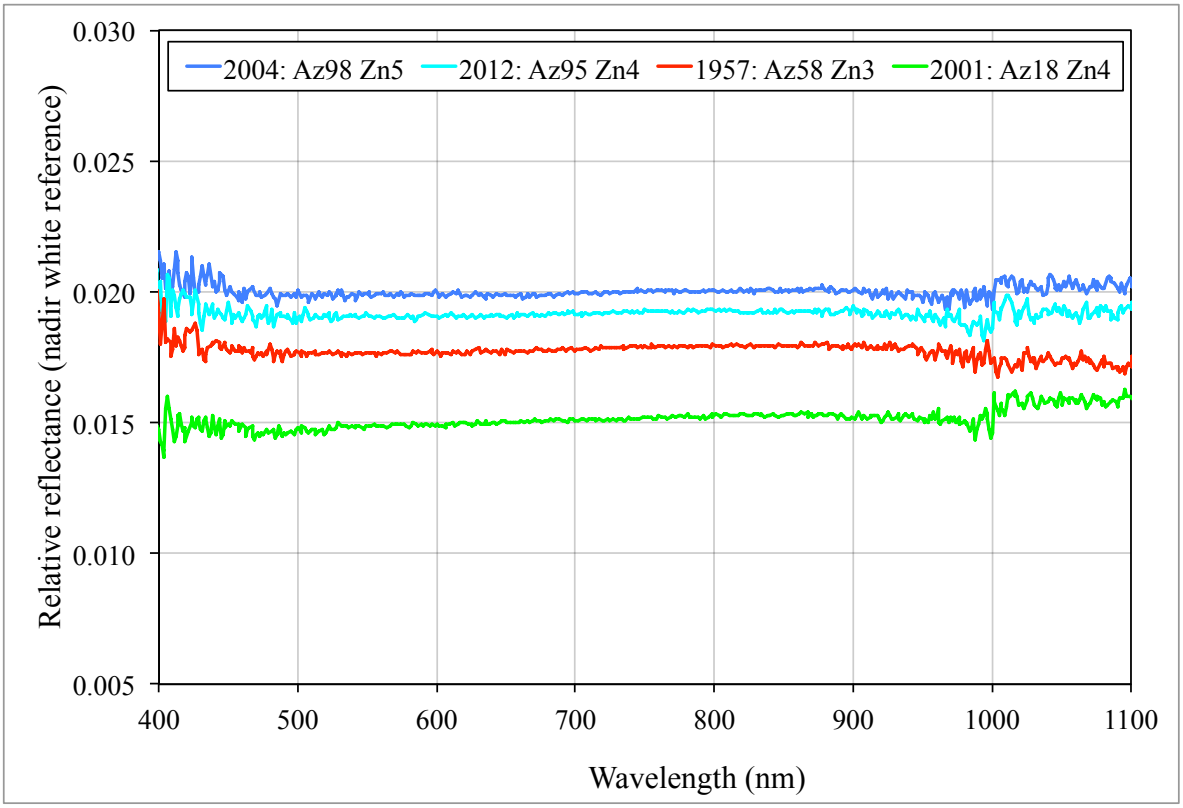


Figure 3.25 Dark target sample spectra produced with simulated geometries from airborne collection. Values are relative reflectance from normalization to a nadir observed white reference (Spectralon). Given solar zenith angles are invariant. Magnitude differences are largely attributed to changes in relative azimuth.

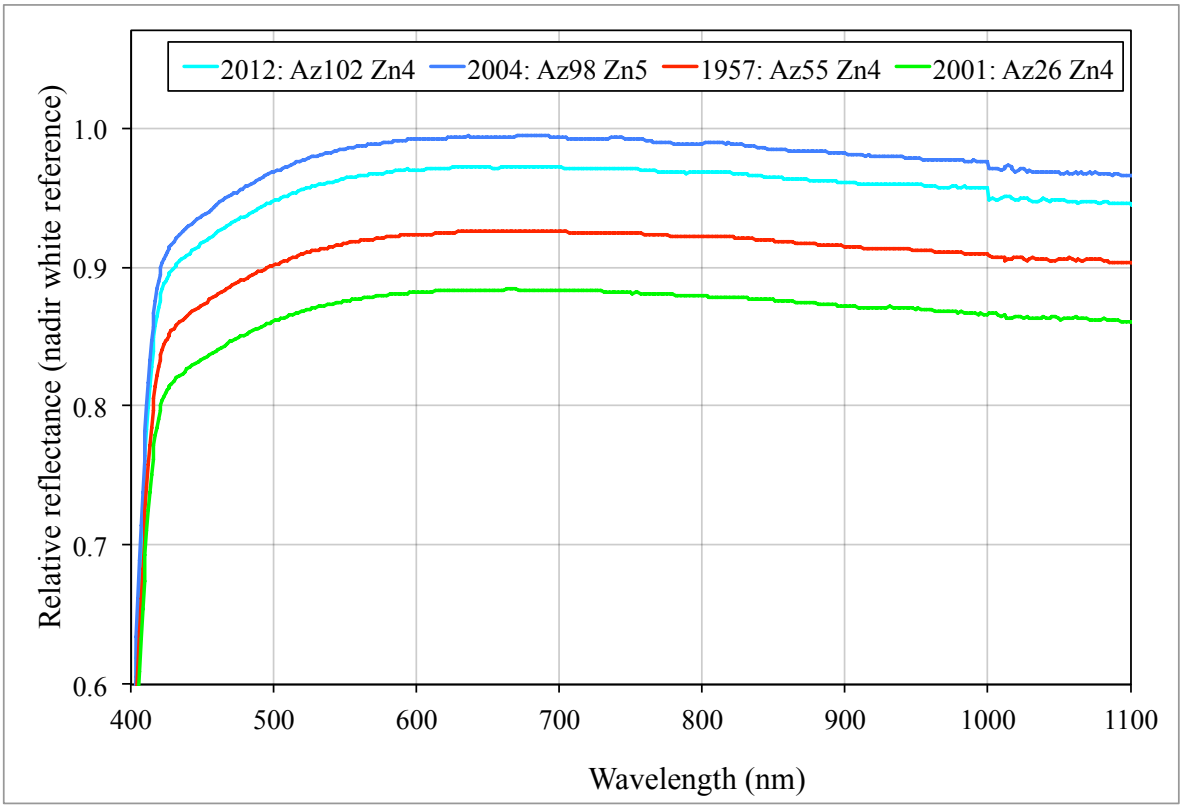


Figure 3.26 Bright target sample spectra produced with simulated geometries from airborne collection. Values are relative reflectance from normalization to a nadir observed white reference (Spectralon), titanium oxide absorption is apparent in wavelengths less than ~425nm. Given solar zenith angles are invariant. Magnitude differences are largely attributed to changes in relative azimuth.

3.5.3 *Evaluation of Spectral Mixing in Airborne Spectra*

Since there was a poor rank correspondence between the airborne data relative to the lab BRF data, efforts to explain the variation in the target response was refocused on the likelihood of spectral mixtures. Forward velocities are not constant and have the potential to depart from the nominal spatial resolution. In the case of the flight lines that collected the target responses, forward velocities ranged from 59.04 to 68.78 m/s, as determined from successive navigation data at 5ms intervals. This range of speed equates to an along

track ground sampling difference of ~6.8cm (x'=t*v+h*x/l where: *x'* is the along track ground sampling distance in meters, *t* is the integration time in seconds, *v* is the instantaneous forward velocity in meters per second, *h* is the vertical distance in meters from target to sensor, *x* is the detector element dimension in millimeters and *l* is the focal length of the sensor optics in millimeters). In addition, the ground-sampling interval is determined by the frame period and forward velocity, and it is not equal to the ground sampling distance. The sampling void between successive frames is determined as x"=v(f-t)-(h*x/l), where: *x"* is the along track unsampled distance in meters, *f* is the frame period in seconds and the remaining terms are as previously introduced. The along track sampling pattern produced from the actual flight parameters, as opposed to the nominal reported parameters, suggests that there is a high likelihood that the deployed targets may not be large enough for capturing a single unmixed response. For example, the lower velocity of 59.04m/s and the lower flight height of 1232.7m produces a footprint of 1.60m (across track) x 1.21m (along track) with an along track void dimension of 15.9cm. Even at this lower end of footprint dimensions, the risk of not achieving a pure pixel is high. To ensure a pure response the targets are required to be at least three times the spatial sampling dimension, in which case, and with the above example, the targets would need to be at least 4.12m (along track) and 4.80m across track. The targets being 3.66x4.88m would suggest that the occurrence of pure pixels might be more dependent on the near randomness of the temporal sampling initiation. Motivated by this inquiry, the target responses were assessed for the presences of contaminated background spectral responses.

A strategy to identify a mixed target was built based on the expectation that the ratio of two spectra from a common target collected from two flight lines will be constant. For each unrectified flight line, an average spectrum was computed for the dry sorting lot asphalt surface omitting the targets (n=160-165). For each combination of flight lines, a ratio spectrum of the average asphalt spectra was computed. These curves represented the general radiometric scale differences between the two flight lines largely determined by the acquisition geometry. The asphalt ratio is interpreted as the ratio spectrum of no change between the two flight lines, in other words the very same materials. Because a larger area was used to compute the spectra, there was less potential for inaccurate spatial positions to impact the analysis. For each of the deployed targets and each of the flight lines, the ratio spectra were computed. This spectrum with reference to the asphalt ratio would suggest significant departures from unmixed responses. If one of the two spectra used in the target ratio was mixed (or the proportions of the mixture were vastly different) then this ratio spectra would deviate significantly from the location of the asphalt ratio (Fig. 3.27). For example, the average asphalt spectrum produced from flight line 2004 was divided by that of 1957 (where it could be confidently stated that the outliers, that were not representative of the asphalt, were few, and the spectra on average represented the same material). This curve was straight throughout the spectral range and any departure from a value of one represented the differences attributed to the acquisition geometry. The ratio of the bright target spectrum from flight line 2004 to that of 1957 was computed and compared to the ratio spectrum produced from the asphalt spectra; the same was done for the dark target. The closer the target ratio spectrum was to the asphalt ratio spectrum, the less likely the two target

spectra were mixed with background material (or perhaps the more equal the mixing proportions). In practice, however, the target ratio spectrum would rarely (should not) be the same as the asphalt ratio, because unlike the asphalt ratio, which is collected over a longer duration, the target spectra are single pixels and therefore have a greater likelihood of more significant geometry variations between the two individual pixels (platform attitude variations are not averaged out). One caveat in this analysis was that it was assumed that there were flight lines with mixed target responses and flight lines with unmixed target responses, which might not be the case given the footprint dimension calculations.

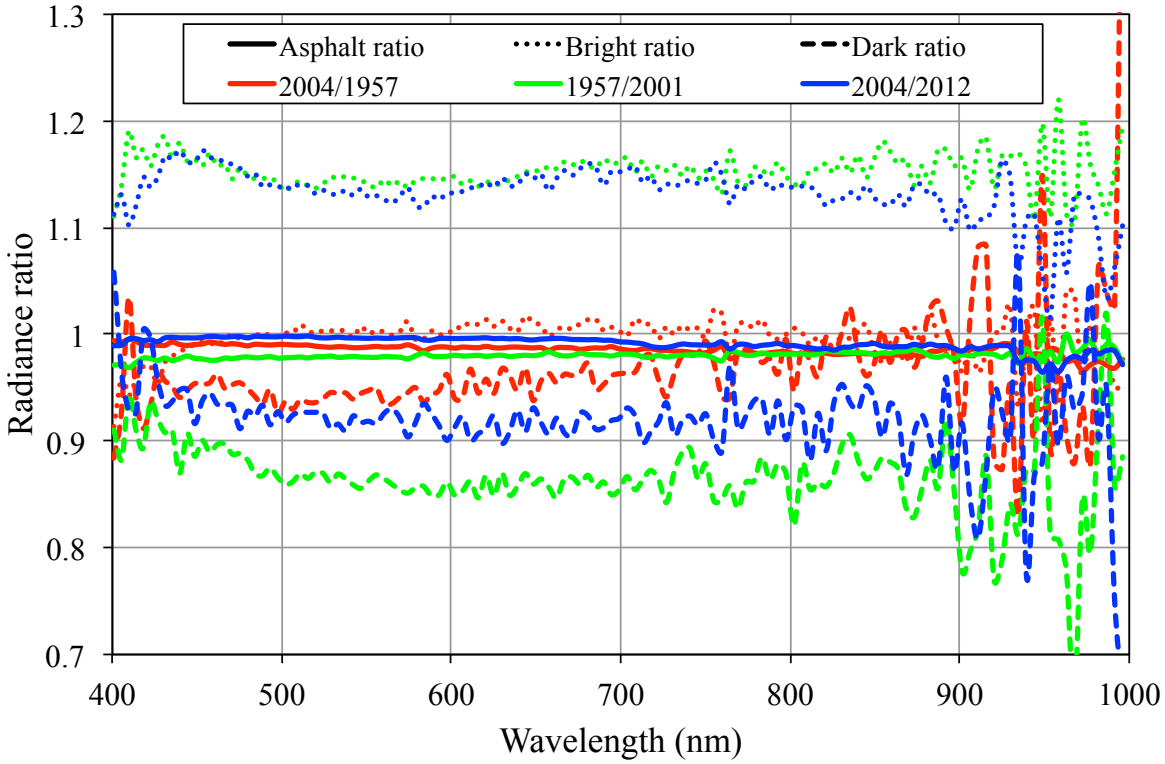


Figure 3.27 For clarity, the dark ratio for the 2004 and 1957 is actually 1957/2004, all other spectra are as the label suggests. Ratio combinations not displayed are omitted to visualize ratio scale focused on higher quality target responses.

This approach suggested that flight lines 2004 and 1957 had the least amount of mixing in the target responses. The bright target ratio was clearly more similar to the

asphalt ratio than any other comparison. This conclusion is supported by the fact that the radiance values of the bright targets within these flight lines were brighter than the others and the dark targets were darker than those from the other flight lines. If these responses were mixed with the intermediate reflecting asphalt, the bright target would appear darker and the dark target would appear brighter. The bright target ratio for flight line 1826 and 1831 also seemed to have little mixing relative to the other ratio comparisons. The dark target ratio for the 1826 and 1831 comparison was quite far from the asphalt ratio (in this case gravel ratio), suggesting that the two dark target spectra were not similar. From this investigation it was determined that for the SLP acquisition the most appropriate target responses for the deployed targets were those collected in flight lines 2004 and 1957. These two flight lines were flown in a configuration that produced a slightly smaller across track footprint relative to the others, which may have provided for a greater likelihood of capturing an unmixed target response (Table 3.6 & 3.7). Also supporting this perspective is the fact that the 1957 and 2004 flight lines were collected such that the larger dimension of the targets were aligned in the across track direction. Given the actual footprint dimensions are slightly wider than they are long by ~40cm, this also provides a greater likelihood of capturing an unmixed target compared to flight lines 2001 and 2012, which were flown perpendicular to 1957 and 2004.

This analysis demonstrated a procedure for evaluating mixing with respect to radiometric targets and also demonstrated the dangers of parameterizing flight acquisitions with the minimum requirement for spatial resolutions. The implied mixing information is in agreement with footprint and ground sampling calculations. The target ratio of 2004 and 1957 has a smaller departure from the asphalt ratio, while any

combination of either line 2001 or 2012 produce relatively larger departures from the asphalt ratio. The 2001 flight line parameters produced the largest ground sampling distance and the 2012 parameters produced the largest IFOV. Given the orientation of the target's larger dimension was not in line with the across track dimension, it was conceivable that these measurements were contaminated by background responses. It is concluded that the variation in target response is likely caused by variations in flight parameters that alter the ground-sampling footprint. Therefore, either the 2004 or the 1957 flight line collections would be best for correction for the September 13th dataset. In addition, the calculation of ground projected spectrometer footprints suggested that the lower altitudes of the September 19th collection would provide for a smaller footprint and thus a more reliable radiometric correction.

3.5.4 *Radiometric Correction of Imaging Spectrometer*

Focusing on the collection of September 19th the data were radiometrically transformed to represent at surface reflectance using the FLAASH implementation of MODTRAN (a radiative transfer model) to derive atmospheric characteristics and an empirical line calibration to correct for local conditions. Details of the radiometric procedures used are contained within Appendix 2.

The field targets were deployed in an open unobstructed area, in this case a rock quarry on saddle dam road. Two flight lines captured the targets and both were used to derive empirical correction coefficients. Options for the empirical calibration that were assessed were the number of targets for correction and the potential for applying data collected over the reservoir for estimating Rayleigh scatter.

Despite all efforts to produce a very dark reference target, it proved to be insufficient as the use of the dark target produced reflectance values less than zero and greater than one, which is a physical impossibility. Conceptually however, it is logical to expect this type of effect as shadowed areas within the imagery violate the expectation that each pixel receives the same amount of irradiance, as these areas receive a reduced amount of light caused by obstructive features. These radiometric anomalies were most apparent in vegetation spectra, where the high absorption in the visible range was consistently below zero and the highly scattered near infrared was frequently greater than one. Given that this research is focused on vegetation applications it was vital that these samples be properly corrected.

Using only the bright target considerably improved the correction but the effect of atmospheric wavelength dependent scattering was apparent in the adjusted data. This Rayleigh scattering produced high reflectance values throughout the shortwave visible region. As an alternative, areas of dark open water were expected to avoid the adjacency issues, or perhaps the along track spectral mixing, seen with the dark reference target. A simple threshold of a radiance ratio (red/near-infrared) isolated water regions. Dark non-specular reflections were isolated through a VNIR albedo channel, which produced a bimodal distribution for the water class. The average spectrum of the dark water class approximated the effect of Rayleigh scatter with a wavelength dependent decrease in radiance that was nearly zero beyond the visible range. The water spectrum was used as the subtractive component in the empirical correction to surface reflectance. For each wavelength a multiplicative and additive coefficient was computed from two data points, namely the bright reference target and the open dark water. The ground collected bright

reference target and a zero spectrum (producing offset values that were the inverse of the water spectrum) provided response values (y-axis) and the airborne radiance values occurring on the x-axis. With the computed coefficients the airborne data were corrected to at surface relative reflectance. This approach produces the most reasonable transformation with very few negative values or values greater than one. Vegetation spectra were reasonable, yet still the dark target appeared to be brighter than that observed at the ground surface, suggesting either, or both, adjacency scattering and mixing was occurring (Fig. 3.28).

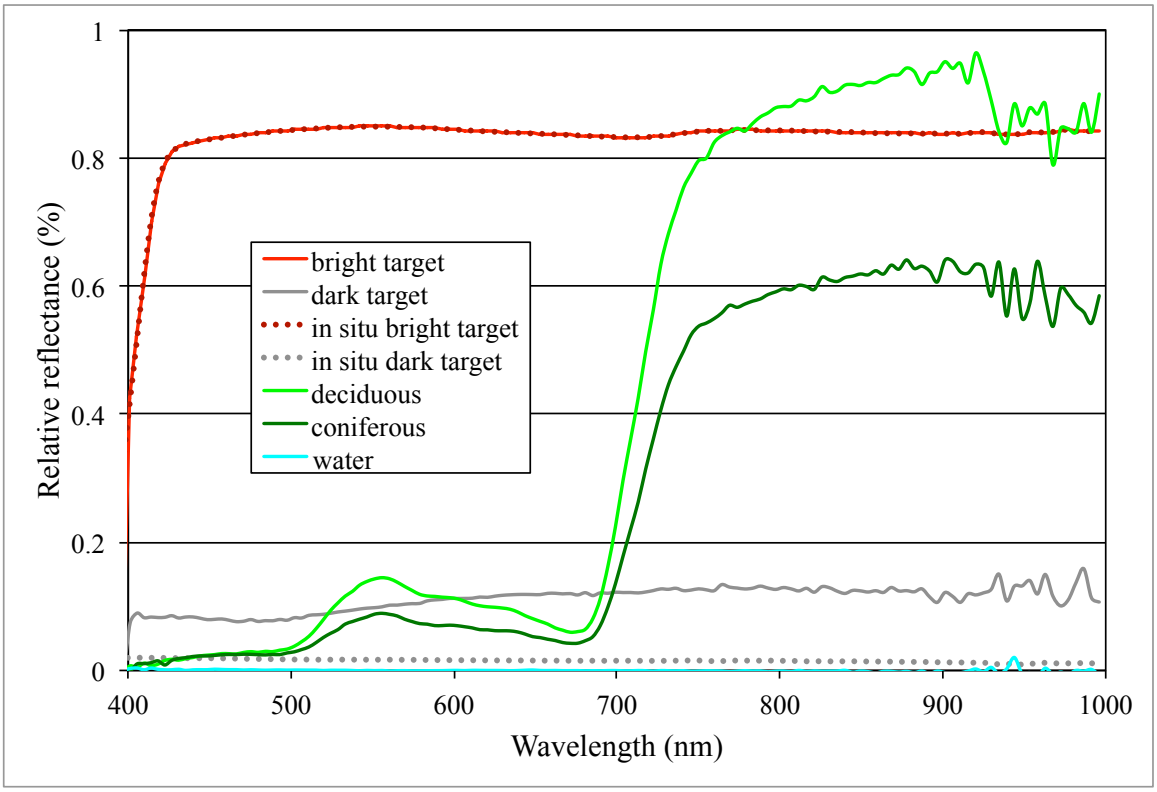


Figure 3.28 Radiometrically corrected AISA Eagle data from the Sept.19 collection with *insitu* reflectance spectra from the ground reference targets.

3.5.5 *Imaging Spectrometer Geometric Calibration*

The geometric correction of the AISA Eagle data was performed by leveraging a multi-sensor platform. The direct georeferencing approach for correcting push broom scanner data was used. Direct georeferencing relies on a tight integration between the INS and the spectrometer. With a camera model that describes interior orientation (focal length, principal point and lens distortion) and an INS that describes platform position and behaviour for exterior orientation, and finally with a detailed, lidar derived DSM surface on which to project the exterior orientation, these imaging data can be translated into georeferenced/ orthorectified data. In very simple terms knowing the angular field of view (FOV) of the instrument and the precise time a given frame was collected, the platform position (with altitude) and orientation at that same moment can be associated with that frame and photogrammetrically projected onto a digital surface model. With this, instrument precise time synchronization and bore sight misalignment has been a challenge. Bore sight misalignment refers to the slight angular misalignment between the INS and the imaging coordinate system. These errors result in spatially displaced imagery, while an incorrect timing synchronization produces a very distorted image with obvious platform behaviour artefacts. A requirement of the direct georeferencing approach to rectification is precise timing synchronization. To put this into context, the frame rate of the spectrometer is 43 frames per second, that is a frame every 23.25 milliseconds and within that time duration the platform, traveling at 234km/hr (65m/s), has traveled 1.51m. If the synchronization between the INS and the spectrometer acquisition computer is out by half a second, then even without accounting for the severe displacement caused by platform attitude, the image will be misregistered by 32.5m.

In order to resolve timing synchronization issues, the integer second signal that is generated by the Applanix POS/AV INS system is used to drive a timing signal that is directly read into the image. The AISA imaging system is designed such that the first approximately 30 spatial pixels are reserved for metadata acquisition and FODIS (fibre optic down welling irradiance sensor), within this region of the detector array a light emitting diode is projected and operated by the integer second signal from the INS. Terra Remote Sensing has integrated hardware that is capable of assigning a GPS time with the integer second signal, the time of the first integer second of each flight line is read into the header file of each collected flight line. More precise timing synchronization is achieved by way of the assumed constant frame rate. By counting the number of frames collected before the first pulse per second (PPS) signal transition and multiplying by the time duration for each frame, the timing synchronization is improved to less than 23.25ms (one frame). Occasionally the GPS integer time written into the header file actually references the integer second occurring before, not after, the first recorded data frame. In such cases the timing offset is adjusted to represent the time between the integer second and the time the first frame was collected (*i.e.* 1sec – (#frames*0.02325sec). See Figures 3.29 through 3.34 for graphical representation of timing adjustments. With the timing resolved, a proprietary software package maintained by Terra Remote Sensing Inc. was used to project the rectified data. At this point the timing is corrected but the bore sight misalignment is not. Because the misalignment angles are static, the displacement of ground features can be mapped by collections that have opposite flight headings. For example, if we consider a roll bore sight misalignment, two opposing flight headings will image the same features but will be separated in the across track direction.

By adjusting the roll bore sight alignment angle, these two flight lines and the features imaged within them can be properly aligned. Along track linear features are ideal for evaluating and adjusting roll misalignment while across track linear features are ideal for pitch and, to a lesser extent, yaw misalignments. Because elevation has a dramatic effect on image scale, the orthorectification software permits the projection onto a lidar derived DSM and at the same time the user can evaluate the bore sight calibration against a raster representation of the lidar intensity data. See Figures 3.35 and 3.36 for a graphical representation of the bore sight calibration. However, this process of evaluation is very qualitative. To provide a more quantitative check of the positioning of the spectrometer data, a procedure was developed.

a)



b)

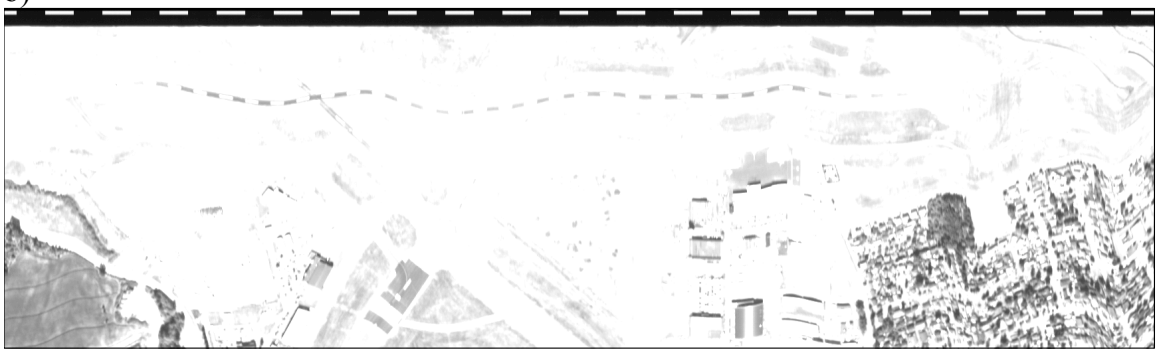


Figure 3.29 GPS triggered LED pulse per second on the integer second signal recorded into the FODIS region on the detector. a) True color composite of one of the YYJ calibration flights b) Enhanced grey scale image illustrates the PPS signal within the FODIS region

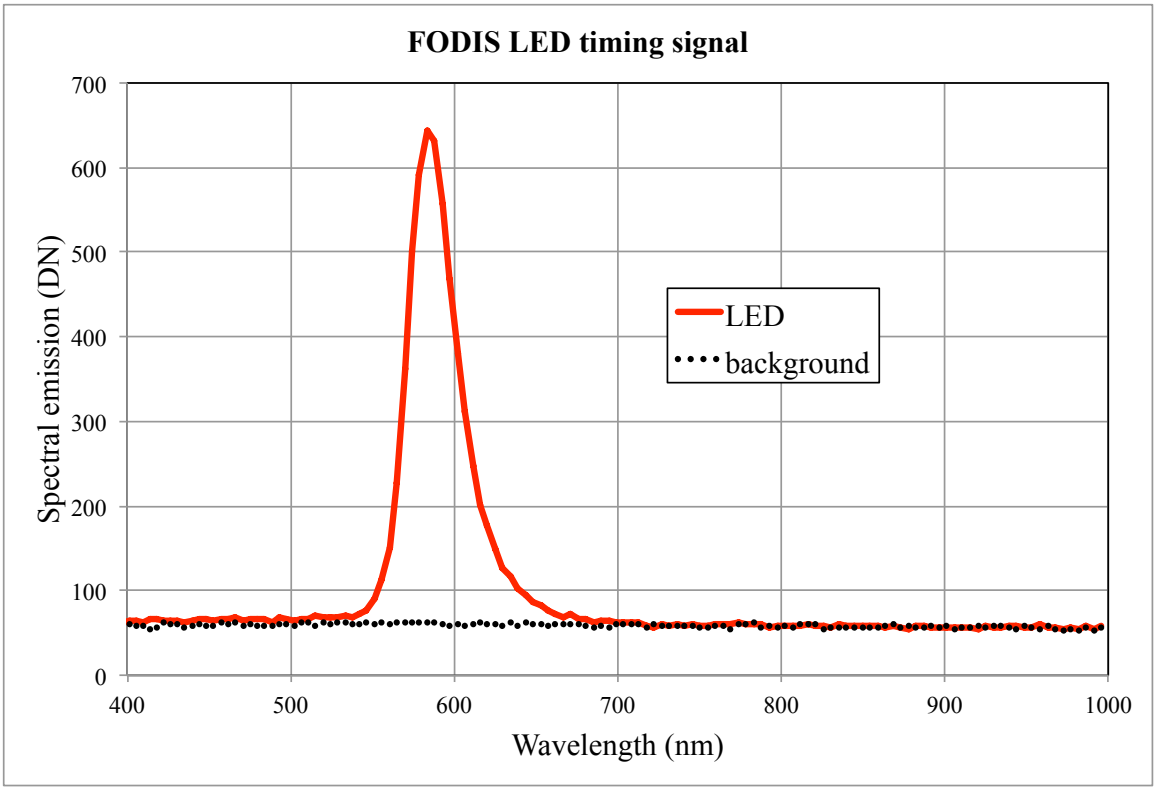


Figure 3.30 AISA Eagle time synchronization. To provide the greatest possible signal for the timing synchronization the spectral emission of the LED was investigated. The maximum spectral emission occurs at 583.5nm

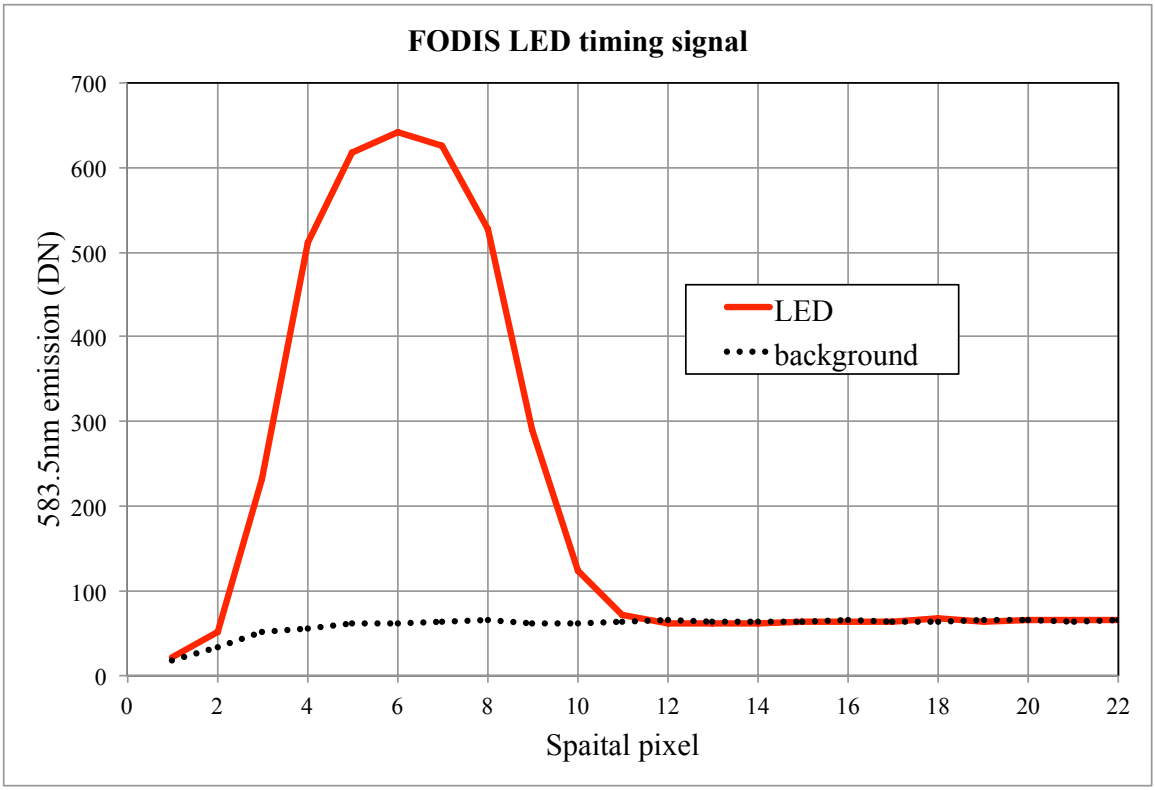


Figure 3.31 AISA Eagle time synchronization. To provide the greatest possible signal for the timing synchronization the spatial emission of the LED was investigated. The maximum spectral emission occurs at the sixth spatial pixel. Therefore, the optimal timing signal was extracted from the sixth sample of the 583.5nm channel

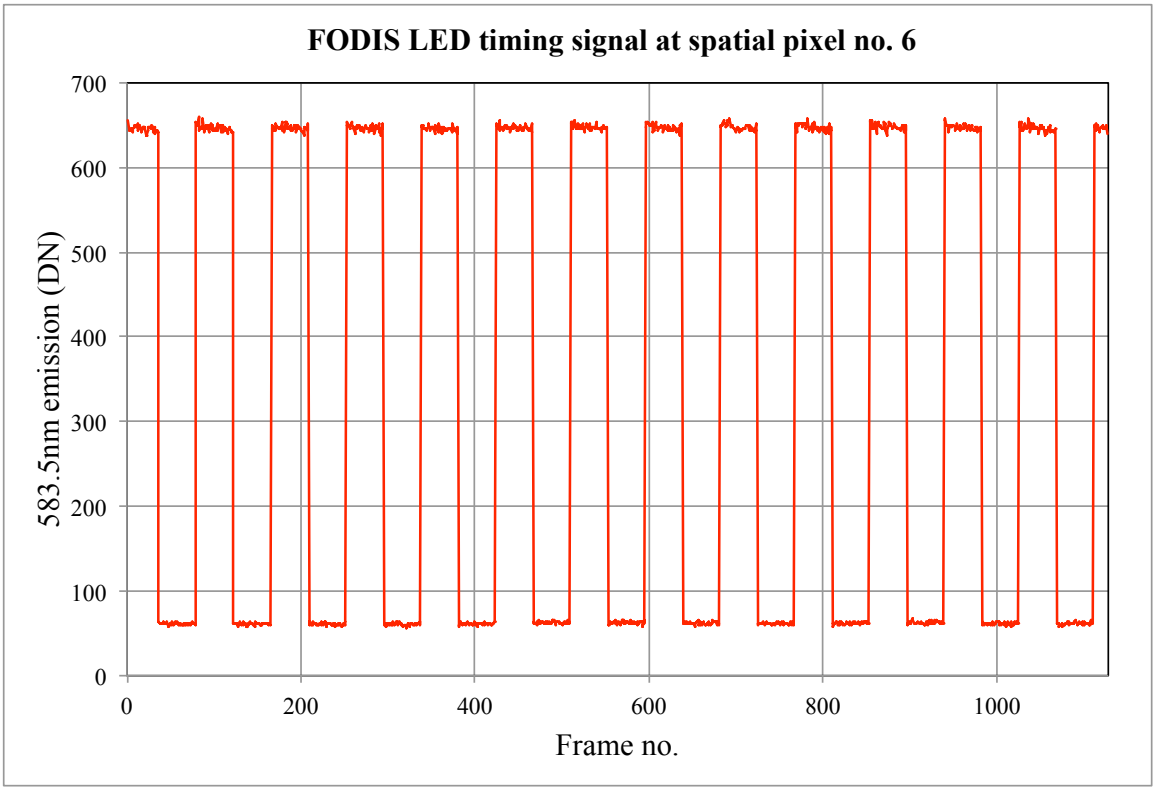


Figure 3.32 AISA Eagle time synchronization. An example of the LED PPS timing signal from one of the calibration lines. Each transition from on to off and off to on marks the frame location of the integer second, the frame rate is 43f/s.

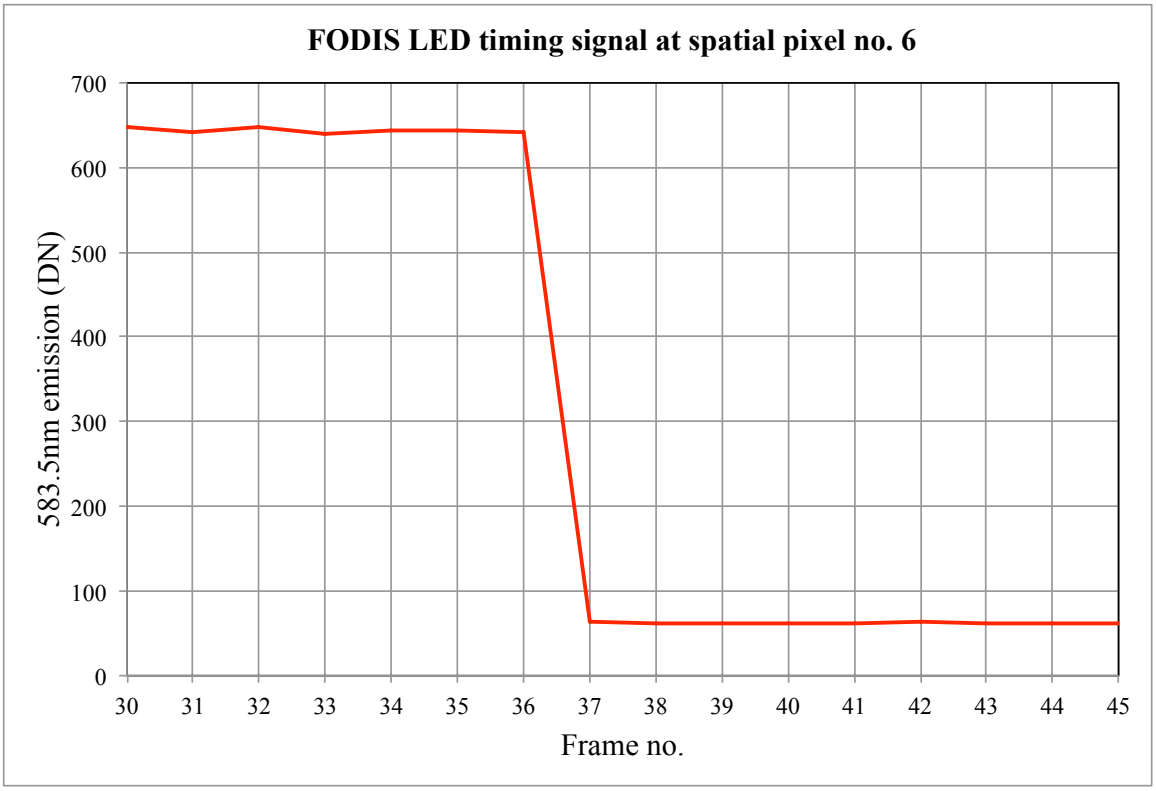


Figure 3.33 AISA Eagle time synchronization. The floating-point timing offset for INS and spectrometer synchronization is determined by the constant frame rate of 43f/s and the number of frames before the first PPS signal. In this example the first frame occurs >36 and <37 frames before the first PPS signal. Since the duration of each frame is 23.25ms (1sec /43frames) the time adjustment is 0.837seconds (23.25ms*36). The timing adjustment is either -0.837s or +0.163 (1sec-0.837) depending on which PPS is referenced in the header/options file. There is one frame of uncertainty in this process and therefore the time synchronization is <23.25ms.

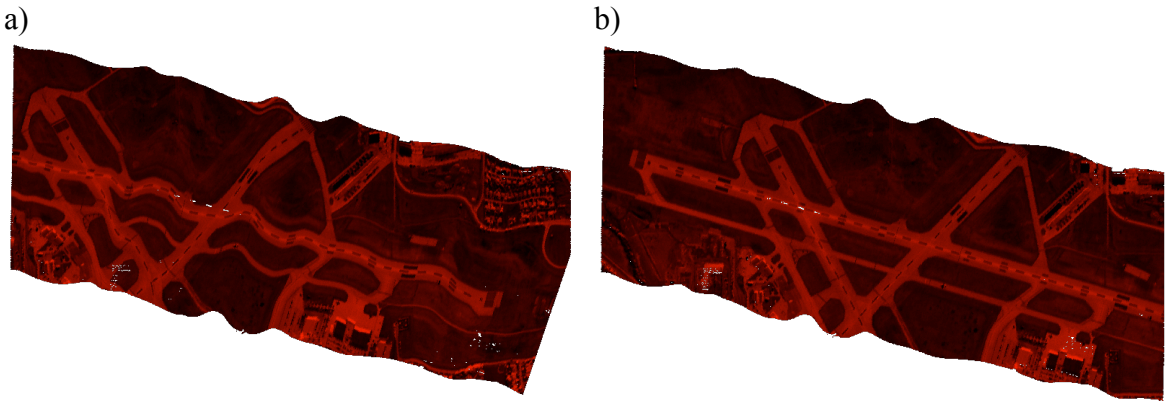


Figure 3.34 AISA Eagle time synchronization. a) Calibration flight of YYJ without floating point second timing synchronization. Incorrect platform behaviour and positions are associated with imaging frames producing a distorted image. b) Calibration flight of YYJ with floating point second timing synchronization. With proper time sync the correct platform behaviour and positions are associated with imaging frames producing an image that preserves the geometry of the imaged scene. Although relative positions are accurate, absolute accuracy requires bore sight calibration and projection to a DSM.

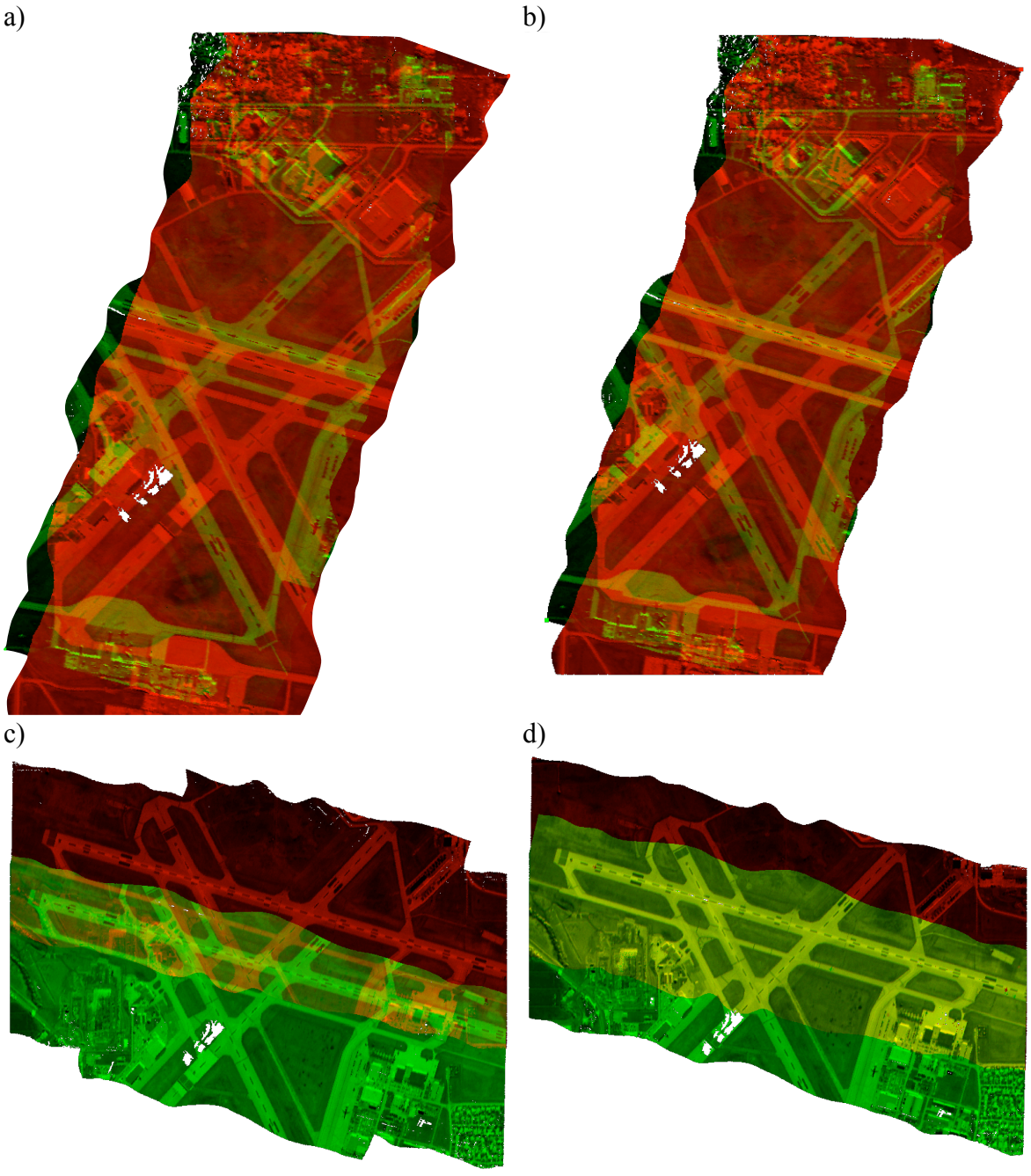


Figure 3.35 AISA Eagle bore sight calibration. Calibration flights of YYJ with opposing flight headings. Figures a) and c) depict unresolved pitch and roll bore sight misalignment respectively, while b) illustrates the corrected pitch but unresolved roll bore sights. Figure d represents the corrected pitch and roll bore sight misalignment.

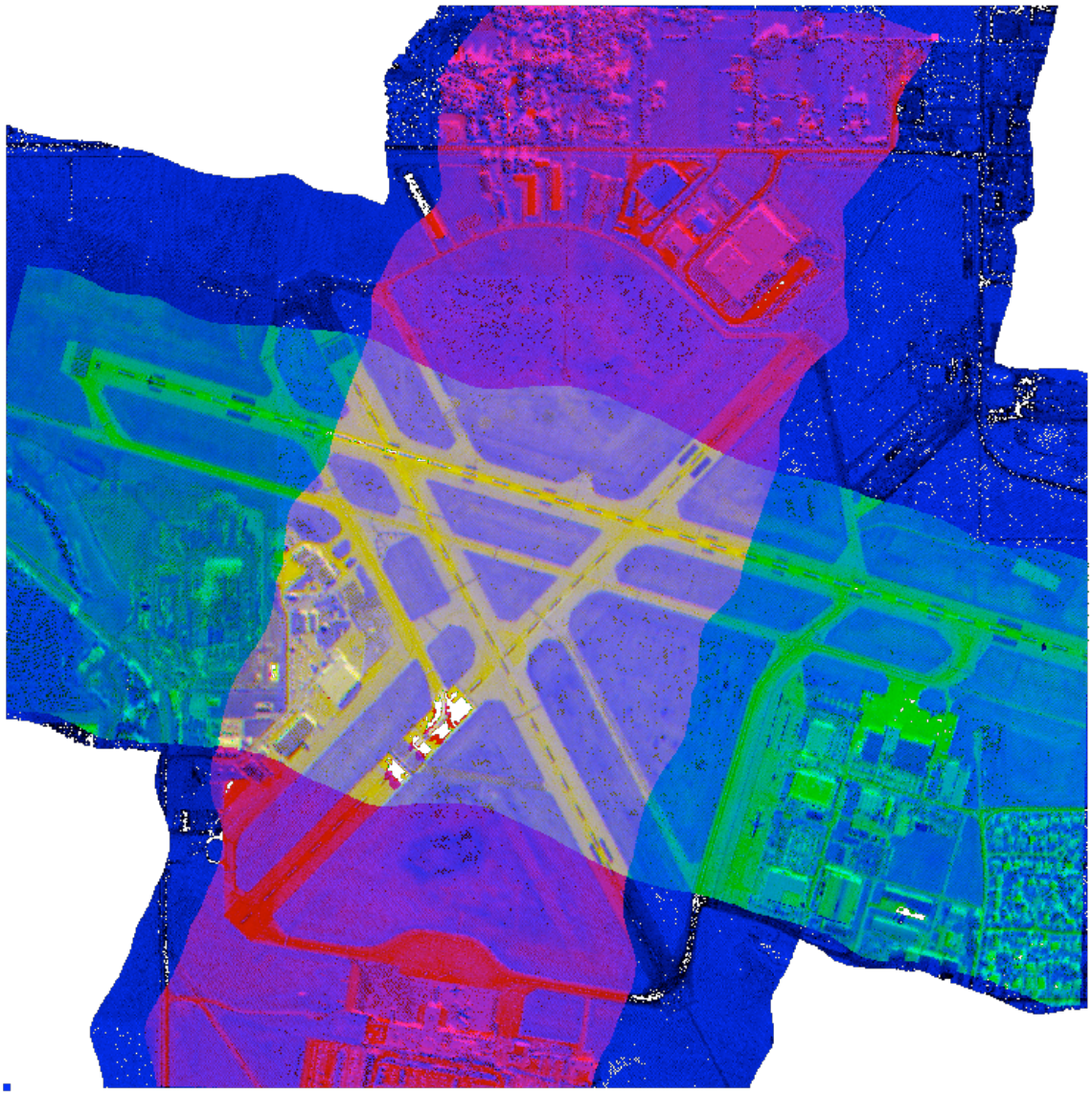


Figure 3.36 AISA Eagle bore sight calibration. Two perpendicular calibration flights with calibrated timing and bore sights at YYJ (red and green). A lidar intensity raster (blue) is displayed to qualitatively demonstrate the spatial correspondence between the lidar and the spectrometer flight lines.

3.5.6 *Validating Geometry of Imaging Spectrometer*

The intention of the quantitative assessment of the spectrometer positioning was to avoid the use of overly generalized representation of the lidar point cloud. This was a challenge because the accuracy of the positioning in some cases approached the precision of the raster resolutions. The lidar needed to be isolated based on intensity. Using lidar points

reflected from the bright runway lines, the positions of the runway lines in the spectrometer data could be evaluated. The lidar points from the runway could not be isolated solely based on intensity because vegetation greatly scatters energy at 1064nm (the wavelength where the lidar operates). The spectrometer data provides a good source to discriminate non-vegetated regions as illustrated in the scatterplot of near infrared and green radiance values (Fig. 3.37). Considering the green and near-infrared regions, these cover types are very different and the spectral curves demonstrate a positive slope for vegetation while non-vegetated regions have a negative slope (Fig. 3.38). A ratio of radiance 551/750nm would produce values greater than one for non-vegetation surfaces and values less than one for vegetation spectra. The distribution of the green to NIR ratio was dominantly bimodal and confirmed that the two distributions could be separated with a threshold of one. To isolate the runway lines in the spectrometer dataset, an albedo channel was generated as the sum of radiance values from 461-671nm and the vegetation mask (derived from the green/NIR index) was also applied. Ideally, the isolation of the paint lines would capture all unmixed pure pixels of exclusively runway paint. A global (flight line) albedo threshold however, failed to delineate the paint lines in the desired fashion, in some cases mixed pixels were included and in one instance an entire line was omitted. Plotting the profiles on the runway paint lines demonstrated the variability in brightness within and between the flight lines. The albedo profiles suggested that no single threshold value would adequately delineate the runway paint lines, as a result the minimum albedo value along the paint line transect was selected as the threshold for that runway and that flight line without including boundary pixels. The selected pixels would be used to represent the unmixed extent of runway paint lines in the spectrometer data set

and would be evaluated against an equivalent delineation based on the lidar point cloud (Fig. 3.39).

The lidar points reflected from the runway paint lines were extracted based on intensity. The raster delineated paint lines were used to build a buffer of 4 meters and this layer was used to extract all lidar points (Fig. 3.40). The distribution of lidar intensity values of the extracted points clearly demonstrated the separation between the bright paint lines and the darker background asphalt. Using the lidar intensity value of 5400, all lidar points not incident to paint lines were omitted (Fig. 3.41). From the isolated lidar points of runway paint lines, a convex hull operation was performed. This process delineates the extent of the lidar points such that no point falls outside the polygon line segments. The convex hull representation of runway paint lines was used to evaluate against the positions of the spectrometer extracted runway paint lines (Fig. 3.42). A minimum distance was computed for every position of the convex hull to the nearest raster delineated paint line polygon. The computed distances were output to a histogram and distribution metrics were computed (Fig. 3.43). Evaluated by the above method the mean positional error of the spectrometer data is 0.78 meters.

The spatial evaluation of the spectrometer provided further confidence in the positional accuracy of the data, over the correspondence with lidar, orthophotography and the ground reference survey. With the airborne data radiometrically and geometrically rectified, the focus of the project could be redirected to ground reference data and the extraction of metrics that would be applied in the empirical modeling of forest structure and productivity.

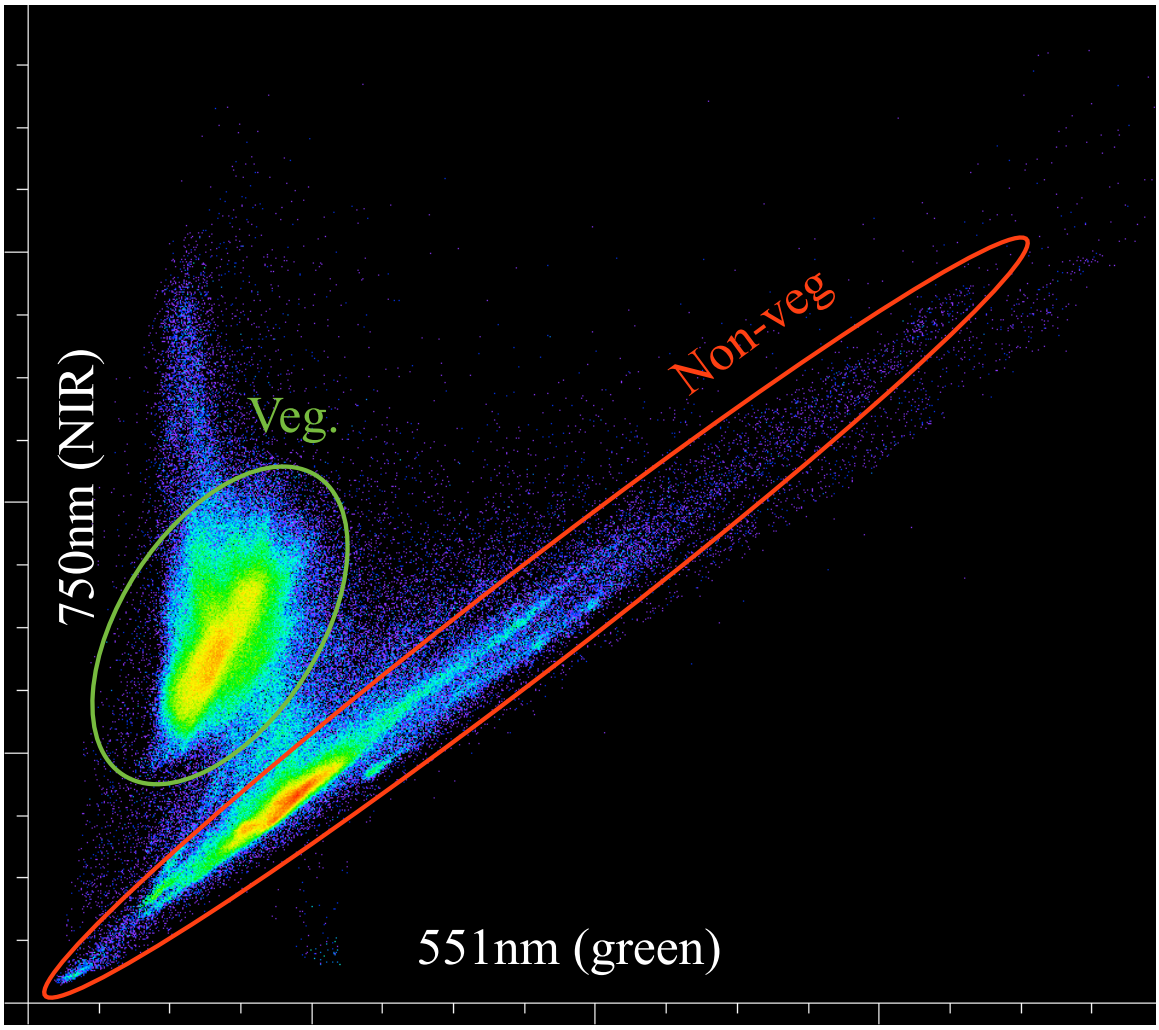


Figure 3.37 Discriminating vegetation and non-vegetation from radiance data, scatterplot of radiance values from 551nm (green) and 750nm (NIR) produces dissimilar clusters for vegetated and non-vegetated surfaces

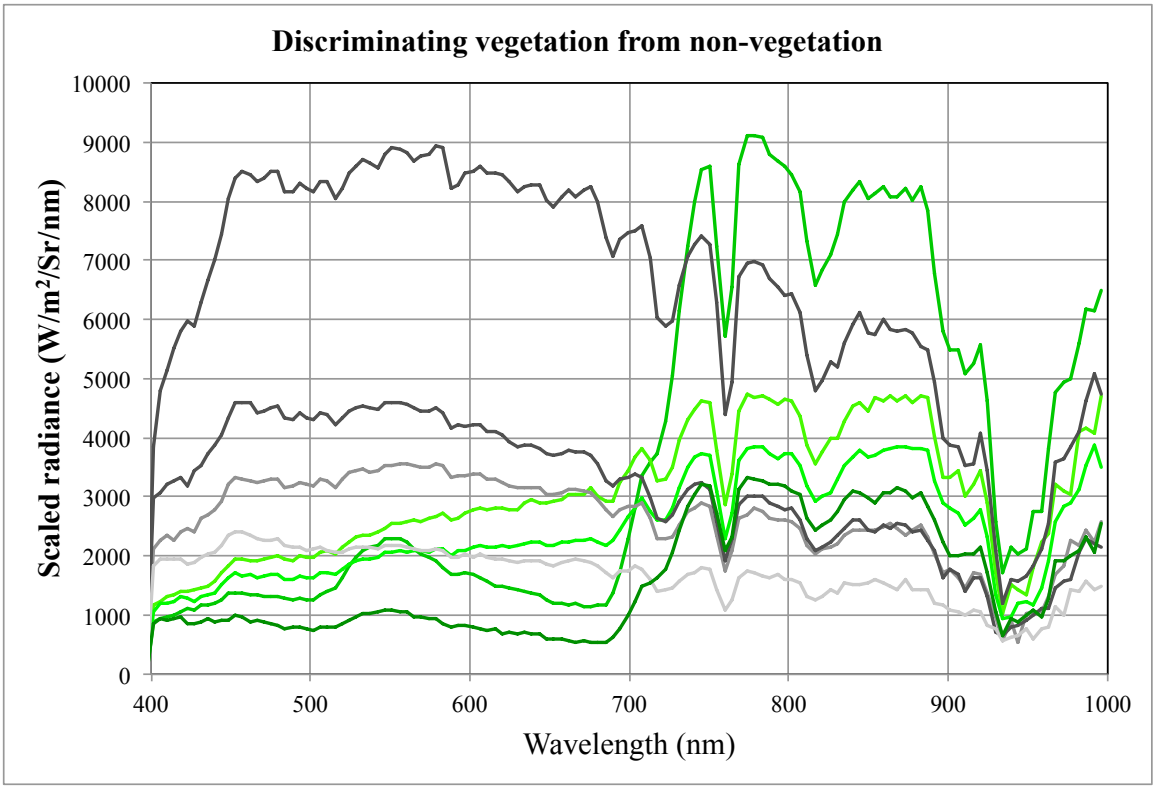


Figure 3.38 Discriminating vegetation and non-vegetation from radiance data for the isolation of the runway so that lidar points from the runway paint lines can be stratified by intensity and evaluated against the positions of the spectrometer data.

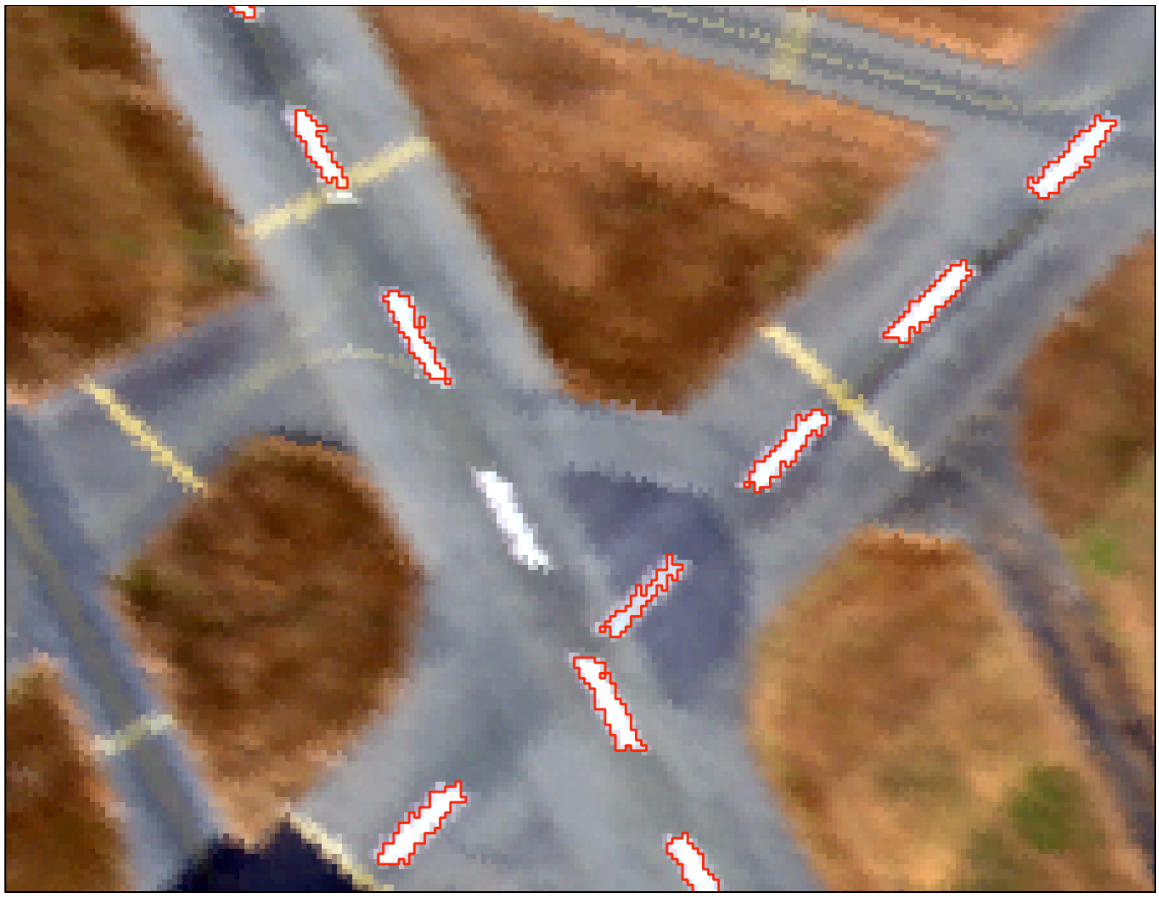


Figure 3.39 Extracting paint line extents from spectrometer data. Delineation is based on runway paint line transect values of a visible albedo channel. The true extents are underestimated to avoid mixed pixels. For scale the runways are 60m across and the lines are 2.5 x 30m.

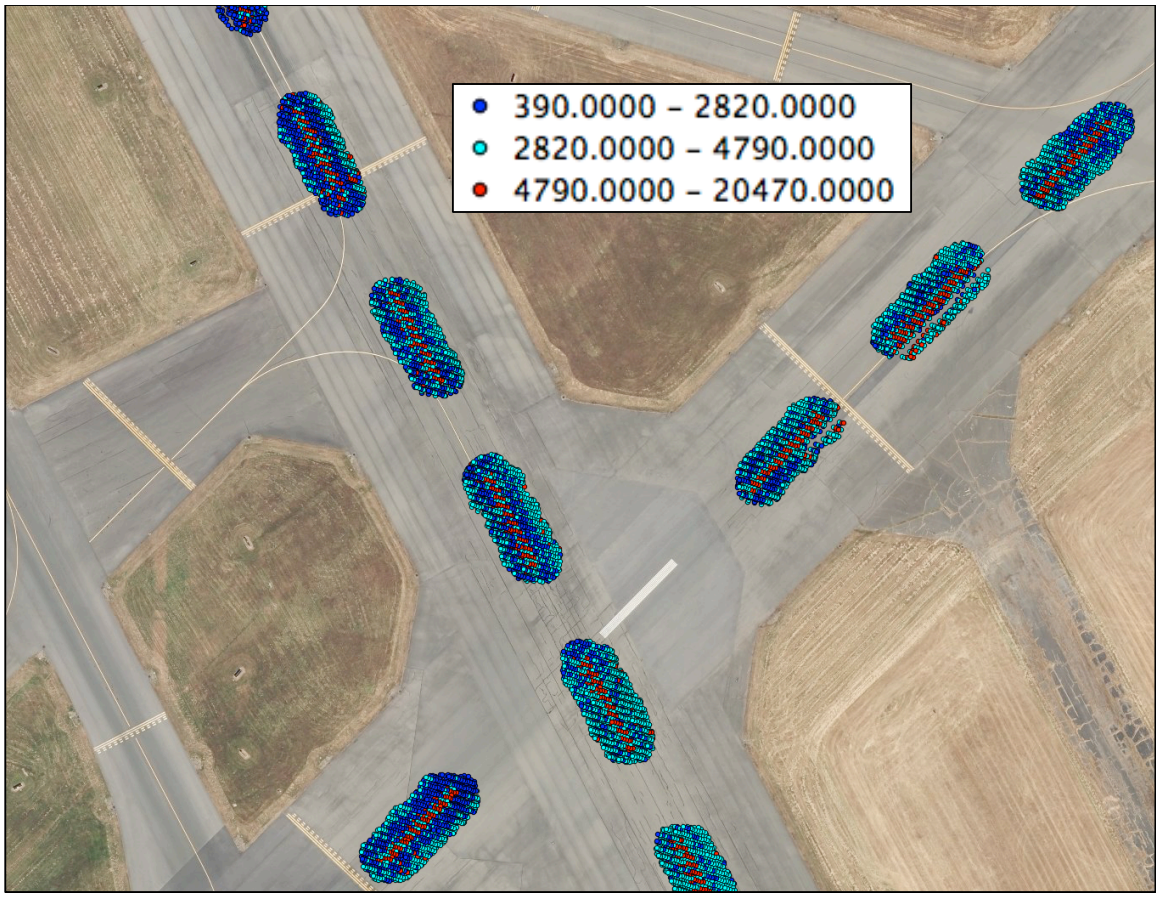


Figure 3.40 Extracting paint line extents from lidar point cloud. Delineation is based on an intensity value of 5400; this threshold was identified by the intensity distribution. Intensity classes were produced by natural breaks.

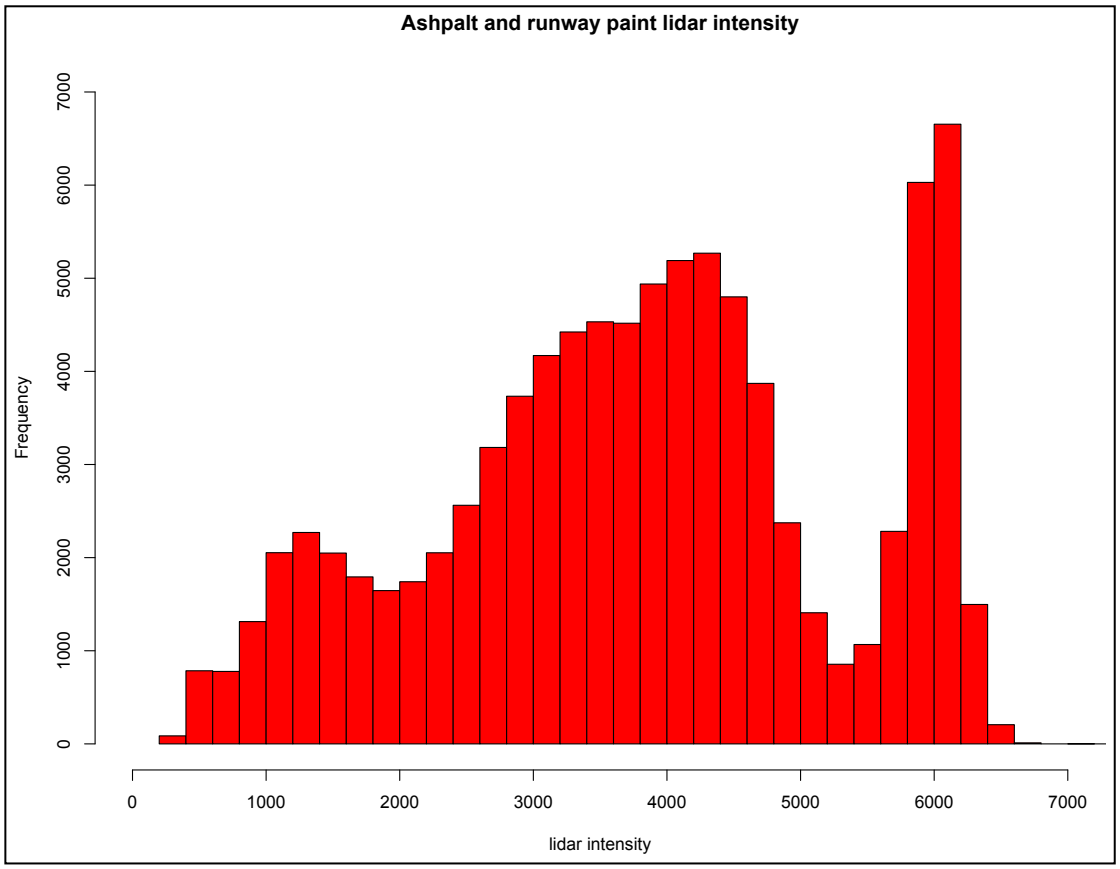


Figure 3.41 Lidar intensity values of point cloud subset within 4 meters of runway paint lines; a value of 5400 was selected to discriminate paint lines from background asphalt.

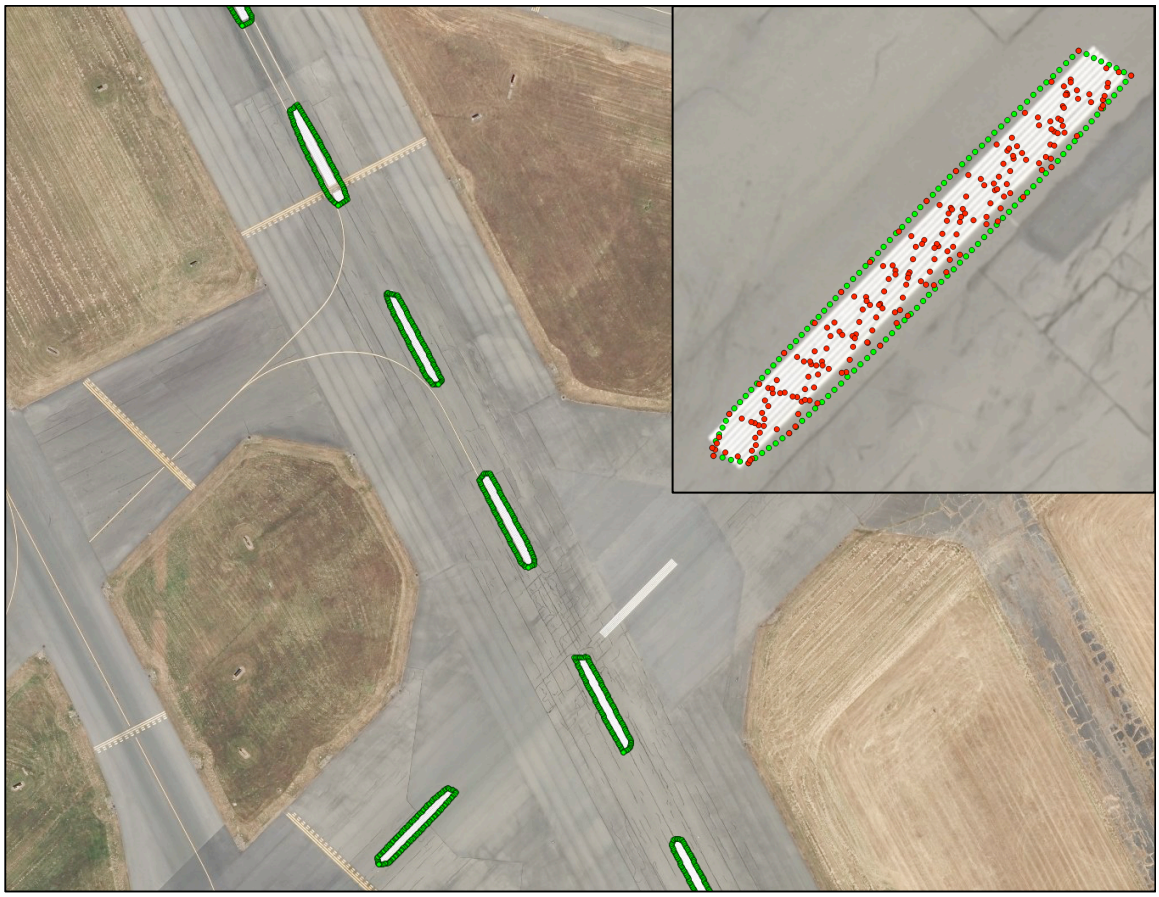


Figure 3.42 Convex hull delineated paint line lidar points, convex points indicated in green, lidar points illustrated in red. Overlaid on digital orthophotos ~30cm resolution

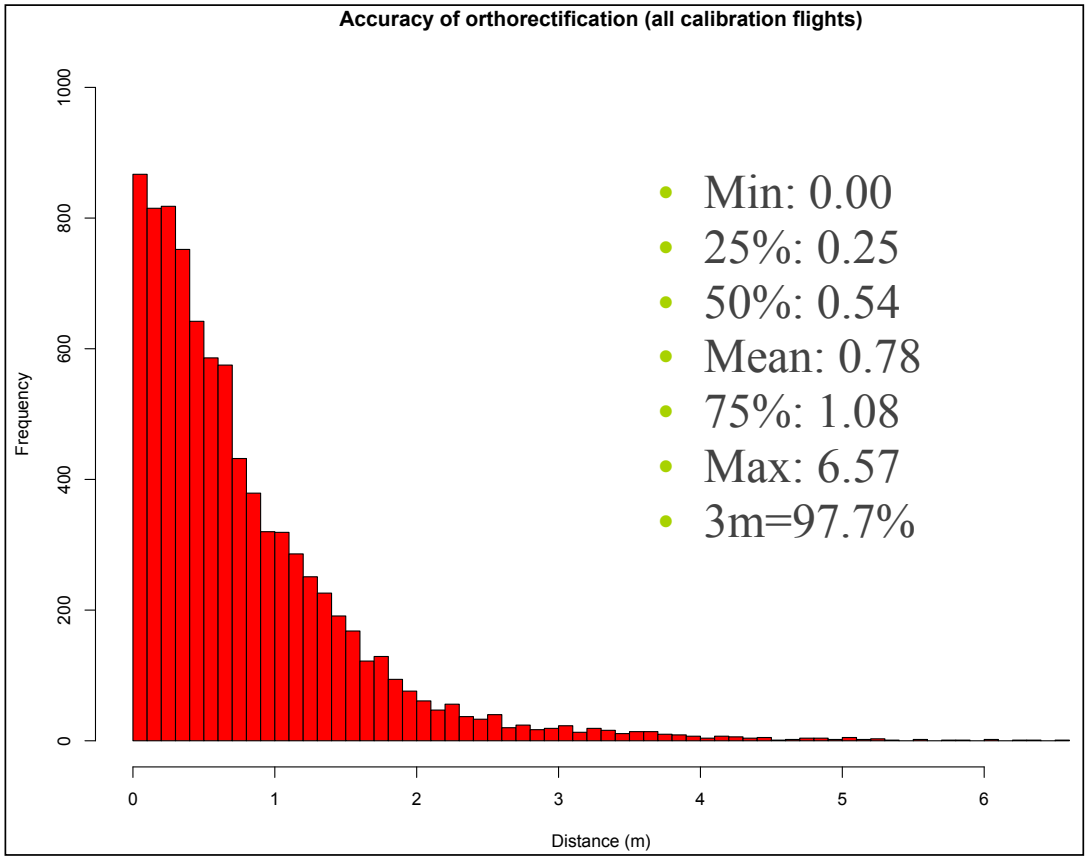


Figure 3.43 For every point on each convex hull of the lidar delineated paint line a distance is computed to the closest point on the raster (spectrometer) delineated paint lines. The histogram of these measured errors suggests that 75% of the spectrometer data are within ~1m of its true location (as represented by the lidar point cloud).

3.6 *Reference Productivity Derived from the CFS Database*

Complicated by the fact that the SLP assessment of remote sensing indicators of productivity was reliant on a single survey, a metric representing growth productivity needed to be derived from the CFS field measurements. Otherwise a multi-temporal survey, like that of the GVWSA, would offer the possibility of directly measuring change between the two dates. With a single survey and a productivity metric based on historical growth, the association between remote sensing metrics and the productivity metric could be evaluated.

The approach to generating a productivity index was initially an exploratory exercise that investigated the change in DBH and basal area and volume through time. DBH, if variations in growth form were ignored, was expected to be a suitable proxy for productivity because the treatment plots were established in an even-aged stand (established in 1948) and therefore DBH represented the integration of all factors affecting growth and not confounded by age. This is not the case in unmanaged stands, which may be composed of many different age cohorts, progenies and species. However, data exploration suggested that variations in DBH to height ratios existed and were associated with particular treatments. This supported the decision to use volume increments as opposed to DBH alone.

The periodic annual increment and mean annual increments in DBH, height and volume were determined and used to explore variations in growth. Determining tree volume was problematic as only a sample of only about 20 trees per plot was measured for height. It is standard practice to measure a subset of trees to build height to diameter relationships and to estimate heights from the derived models. Frequently, unmeasured trees had diameters outside the ranges used to build height to diameter models and residual errors were quite large. Different functional forms were investigated with different stratification approaches. The model residuals were compared and the most suitable models were selected based on RSE and whether the prediction for unmeasured heights would produce a large portion of unreasonable extrapolations. The derived variables were initially summed up to the plot level, to describe variations in expressed productivity and as dependent response variables to be estimated from remote sensing based independent explanatory variables.

The modeling of structure and productivity was conducted initially at the plot level and serves as a methodological validation; however the research intentions are to scale this analysis to the individual tree level, while at the same time investigate new derived RS metrics. The derivation of individual tree positions would be required for the individual analysis, which would take much greater data processing and an additional field campaign. These empirical models should incorporate the rate of change in not only DBH but also height, crown width and crown length (top height – HTLC). Where modeling is applied at the plot level rate of change in stem density and/or mortality must also be accounted for. By accounting for the morphology of secondary growth as well as the top height and canopy expansion, a more detailed presentation of dry matter accumulation can be made. In this initial phase of empirical modeling, treatment plot structure attributes defined from the SLP field data included: top height, average height, stem density, and canopy characteristics such as HTLC and crown width.

Investigating the change in diameter through time, and stratified by treatment, helped to provide an understanding of the effect of the applied treatments on growth and to demonstrate the effect of variations in productivity on tree morphology. The most conspicuous effect was a dramatic increase in diameter soon after the treatment applications. This lasted several years and, gradually decreased to the point that the changes in growth between many of the main treatments appeared to converge to roughly the same levels, approximately ten years after the treatments were applied (Fig. 3.44 & 3.45). However, due to the initial increase in growth, the diameters at the last field sampling were considerably larger in some of the treatments. Changes in diameter were more sensitive to thinning treatments than to fertilization (in the ordinal treatment

intervals established) and the productivity effects appeared to have a longer duration than those in the T0 treatments. This observation would suggest that the decay in productivity with time, which is moderated by thinning, might be the result of canopy closure and inter-crown competition and the onset of the stem-exclusion structural stage. It is recognized that individual tree diameter growth may adequately represent productivity, however, productivity at the plot level is confounded by differences in stem density. That is, a plot with fewer but larger trees may not have the same periodic increment as a plot with many but smaller trees. At a point in stand development, stem exclusion will result in a loss of volume thus a reduction in productivity, where an optimal thinning treatment would concentrate the production into fewer individuals and capture the production that would otherwise be lost to self-thinning. Thus, at the individual level, productivity should theoretically be associated with the magnitude of thinning and fertilization levels. Where greater thinning provides for greater APAR, greater fertilization would have initially increased photosynthetic efficiency, then secondly increased needle retention and crown volume yielding a more sustained production benefit.

The investigation of basal area provided a means to explore the difference in productivity at the plot level that would incorporate differences in stem density (Fig. 3.46). As expected those treatments that produced the largest diameters also exhibited lower plot basal areas. While thinning without fertilization appeared to follow a more linear trajectory of basal area increment, thinning treatments that also had fertilization more quickly approached the level of basal area typical for the control (Fig 3.47).

The overlap of treatment growth increment distributions made the separation of more or less productive groupings challenging and prompted the statistically analysis of treatment and plot differences in growth.

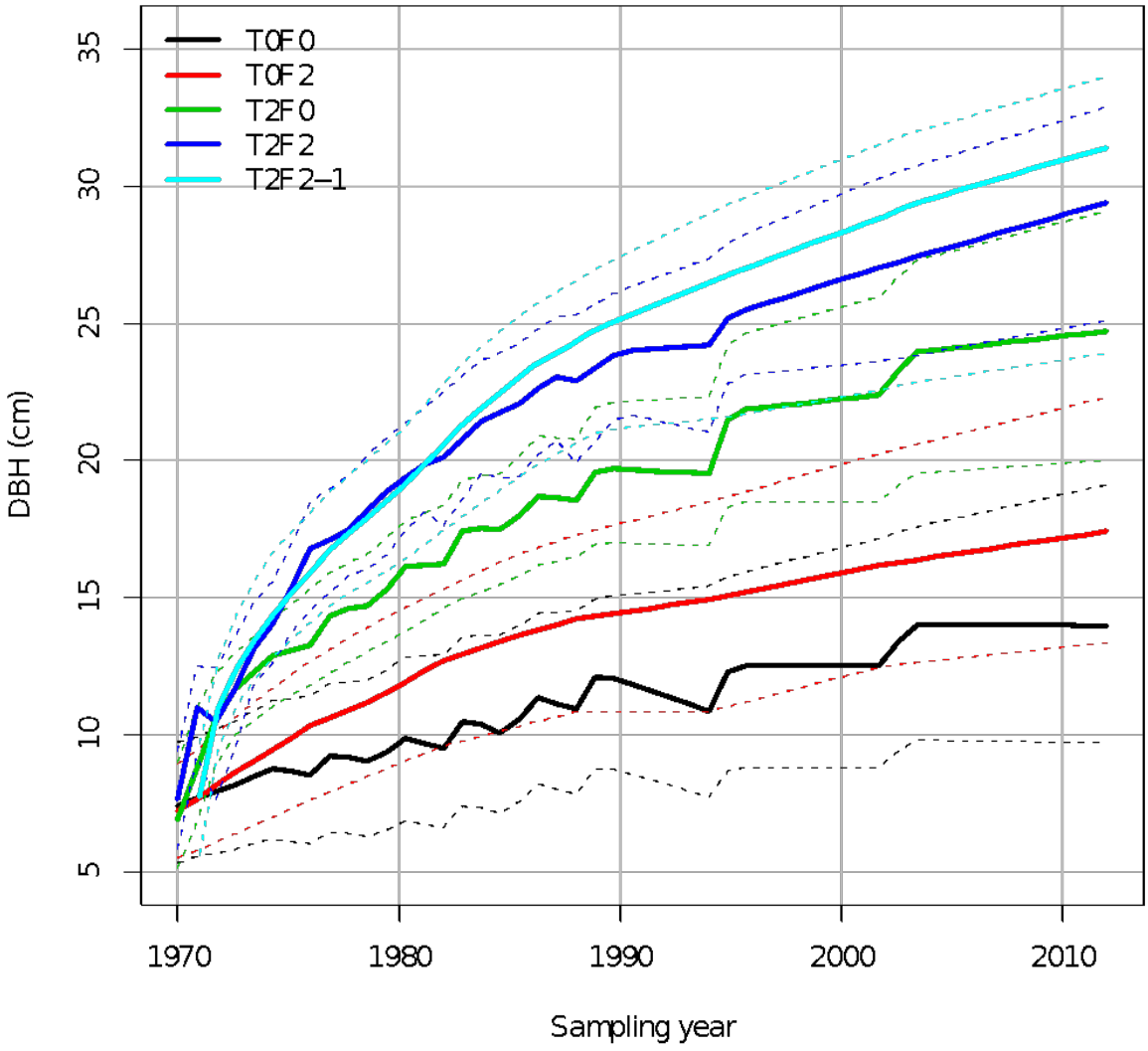


Figure 3.44 Quartile curves for selected treatments at SLP illustrating the initial increase in growth rate and the slow decline in the effect, but the change in productivity has produced significant differences in diameter.

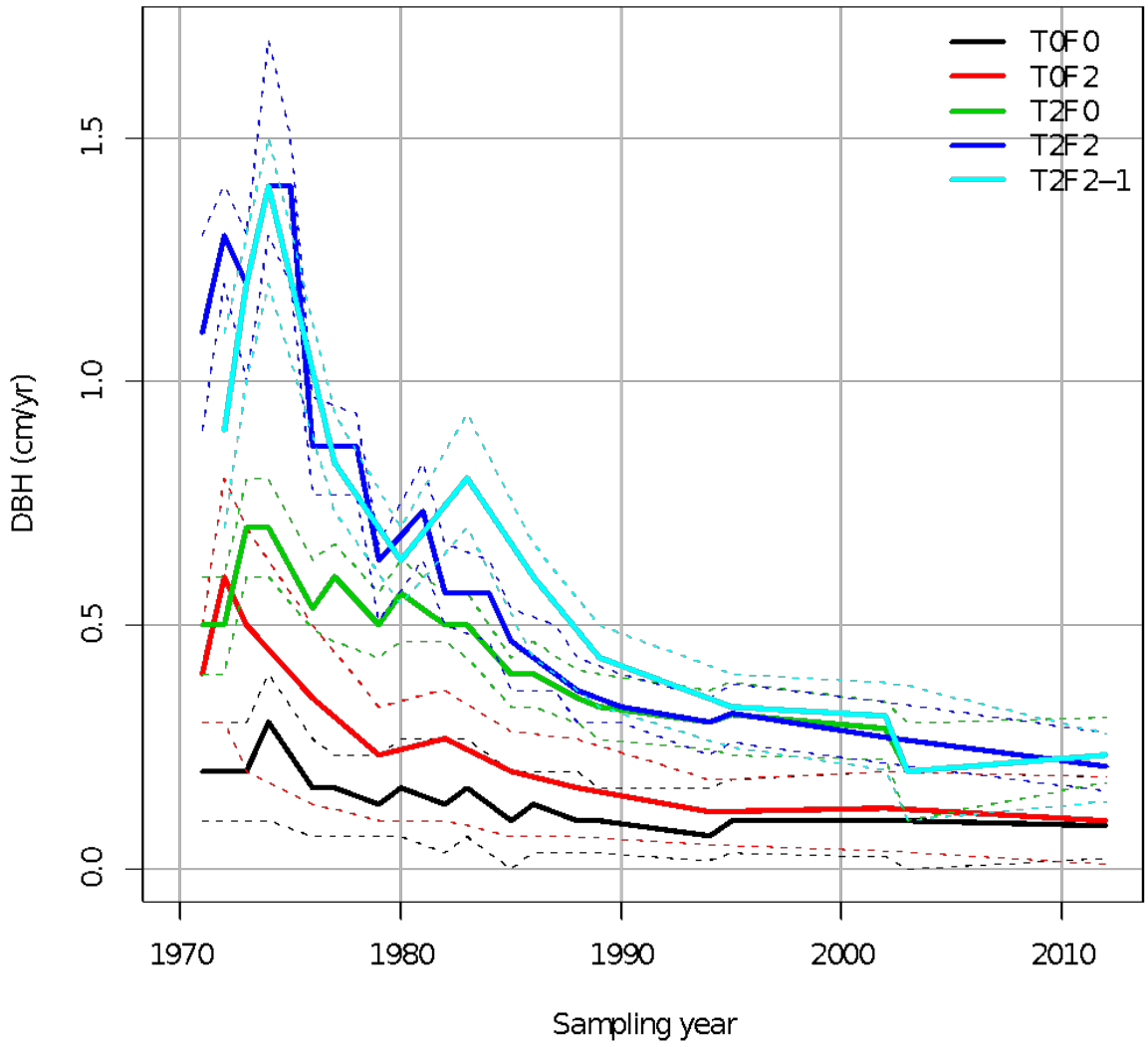


Figure 3.45 Quartile curves PAI in diameter (cm/yr.) for selected treatments at SLP illustrating the initial increase in growth rate after treatment and the slow decay of that effect.

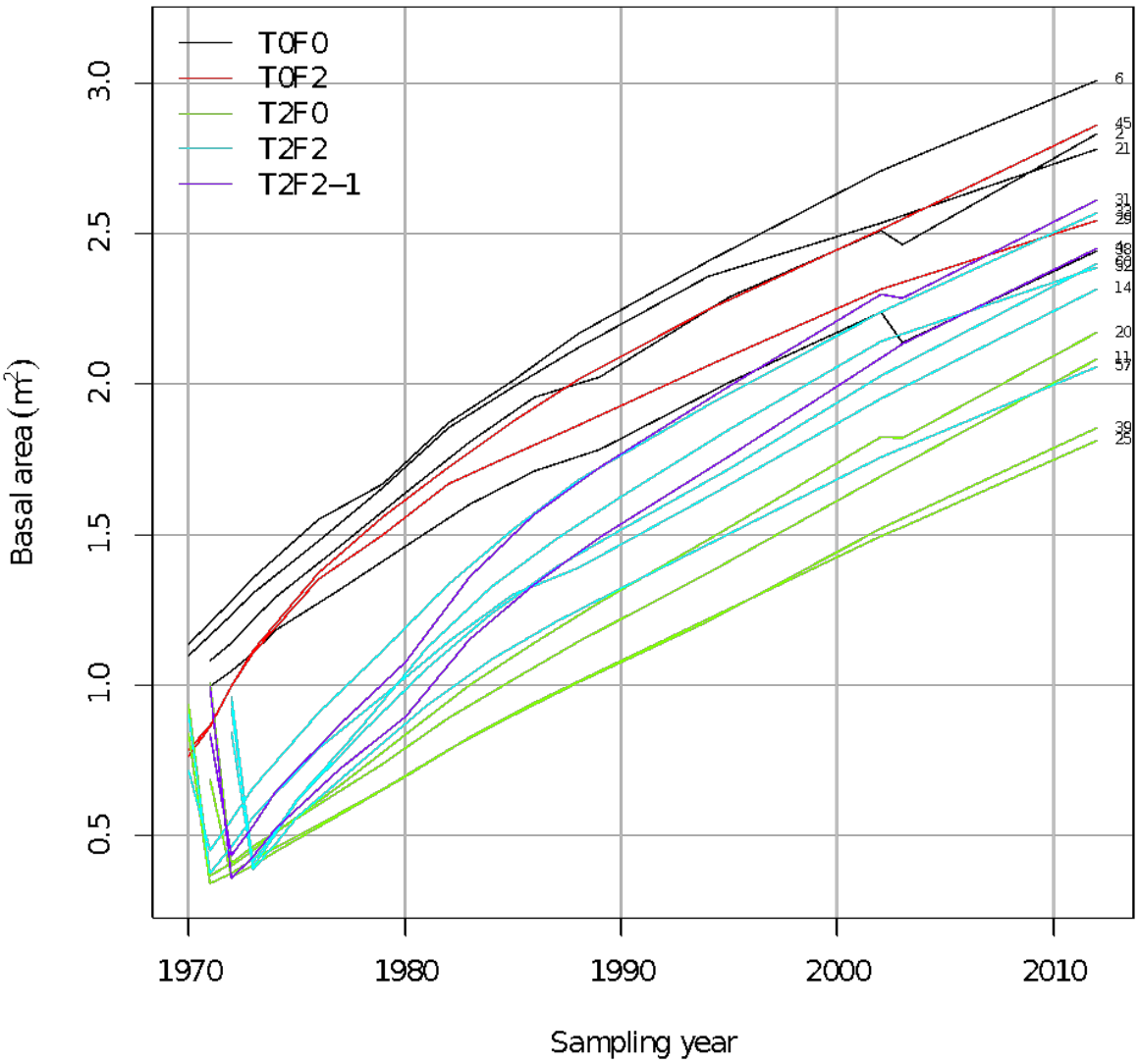


Figure 3.46 26 Plot basal area through time coloured by treatment (selected for clarity), illustrating that basal area is highest in the control plots but basal area increments maybe higher in plots with both thinning and fertilization treatments

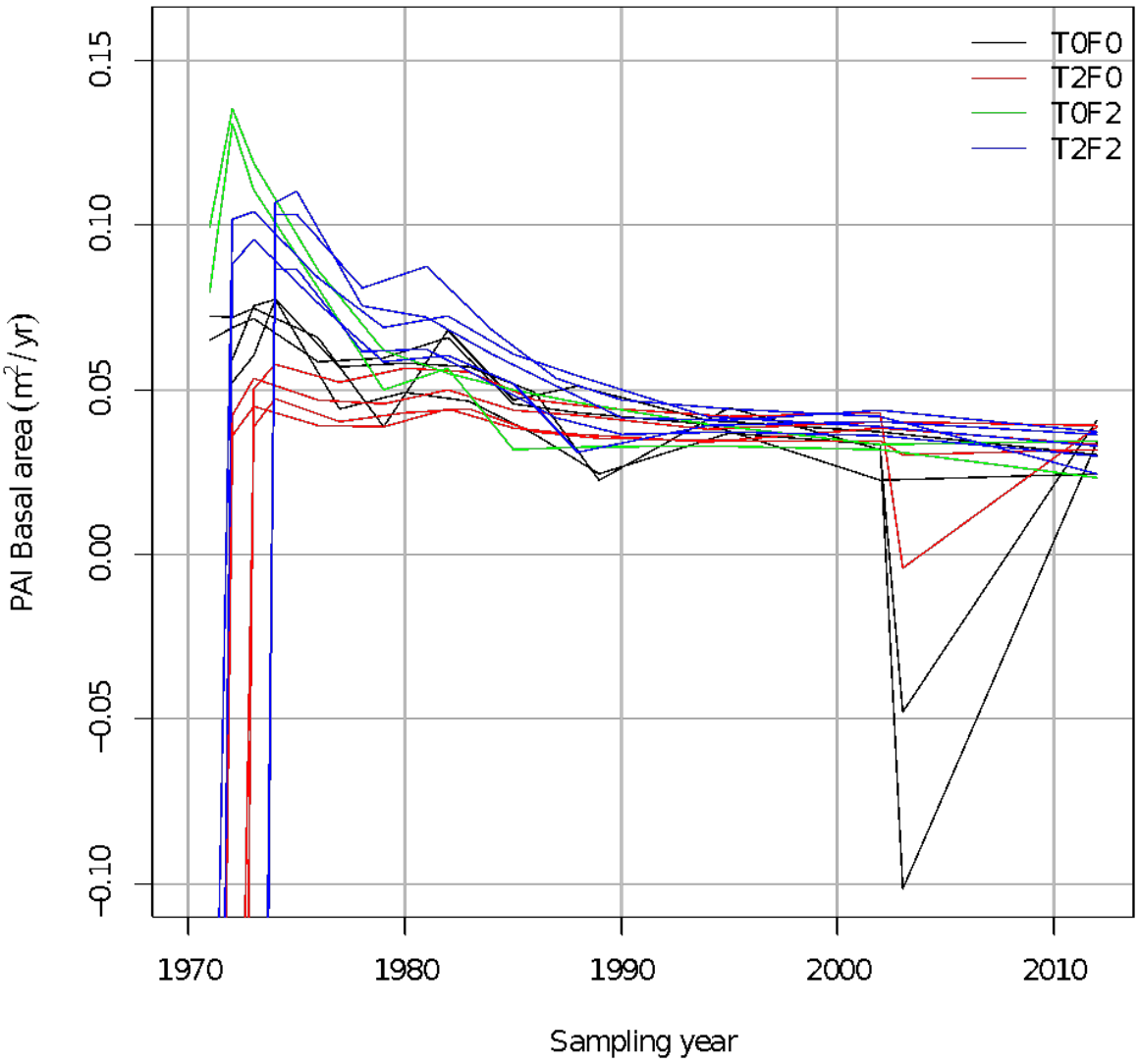


Figure 3.47 PAI of plot basal area through time illustrate the convergence of growth at 10-15 years after the treatments were applied. Anomalous abrupt decrease in BA in the 2003 sampling is unaccounted for perhaps buffer tree destructive sampling. Thinning treatment application is evident as the initial low extremes, the PAI of which are not shown.

Growth related attributes were submitted to a series of hypothesis testing criteria to illustrate the presence, if any, of the ordinal structure of the treatments and the plots. It was expected that differences would exist in a predictable way and would be associated with the degree of thinning and fertilization. If these approaches confirmed the presence of differences between treatments then it may be reasonable to assume that the derived

metric reliably represents productivity and could then be applied in regression modeling with remote sensing attributes. Productivity metrics applied included 2002-2012 PAI and MAI of DBH, height and volume expressed both as an individual tree increment, a plot level increment as well as the scaled increment per hectare. A temporal lag of ten years was selected to determine productivity increments for two reasons; firstly, the 2012 and the 2002 campaign had complete data coverage of all selected plots and secondly the end of the measurement interval corresponds with the RS acquisition. It was determined that the 2002 data collection only sampled those stems occurring within the treatment core area. To generate central tendency increment, a pre-screening of observations omitted measurements collected from buffer trees, tree classes 1-3 (dead and damaged) in either 2002 or 2012, and those observations that did not have valid data for both sampling years of DBH and height. Volume was computed for both sampling years through the following equation:

V=e^(-9.896325907+1.83478844*ln(DBH)+1.00511916*ln(height))

where, V is the estimated tree volume in m^3, DBH is the diameter in centimeters at breast height (~1.3m), and height is the tree height in meters [113]. The volume accumulation was then computed as the difference between the two sampling periods normalized by the 10 years between sampling. Because the filtering of data points only used those individuals with height measurements, each plot had approximately 20 observations and due to these low sample sizes, normality was not assumed. Using only observations with measured heights would avoid errors in estimating height from diameters, but in effect omits information on site occupation; in addition, it assumes there is no sampling bias. Plot periodic volume increment was represented as the difference in median volume of

live and measured trees between 2002 and 2012. An initial approach considered computing plot volumes though plot median DBH and median height multiplied by the stems per plot, but was abandoned due to the potential of introducing significant error through the misrepresentation of diameter and height distributions. The median PAI in volume of the individuals with measured heights would fail to capture the influences of stem density and mortality either by suppression or by root disease and is thus less favourable for a plot based productivity metric.

Figures 3.48 through 3.50 illustrate some differences in volume distributions of measured trees between 2002 and 2012. The volume distributions helped to visualize the growth of different volume cohorts within the plots. In plot ten for example, there are three apparent volume groups and the growth between these groups is not an additive constant. This demonstrates the compounding return on the investment in growth, that is the larger the volume at time one, the larger the growth increment will be at time two. Alternatively, but in parallel, this disproportionate growth may be the result of the different crown classes, where growth is greater in the dominant and co-dominant classes, which would tend to be the larger cohort, relative to the intermediate and suppressed classes, which would tend to be smaller. This is also seen in the distributions of the plots with the greatest and least PAI, namely plot 41 and plot 24 respectively. In plot 41 the median volume of trees with measured heights is $0.887m^3$ in 2002 and in 2012 it has grown to $1.179m^3$ whereas, the 2002 median volume of measured trees in plot 24 is $0.223m^3$, which only grows to $0.248m^3$ by 2012. The relationship between PAI and 2002 volume was further investigated with a simple linear regression.

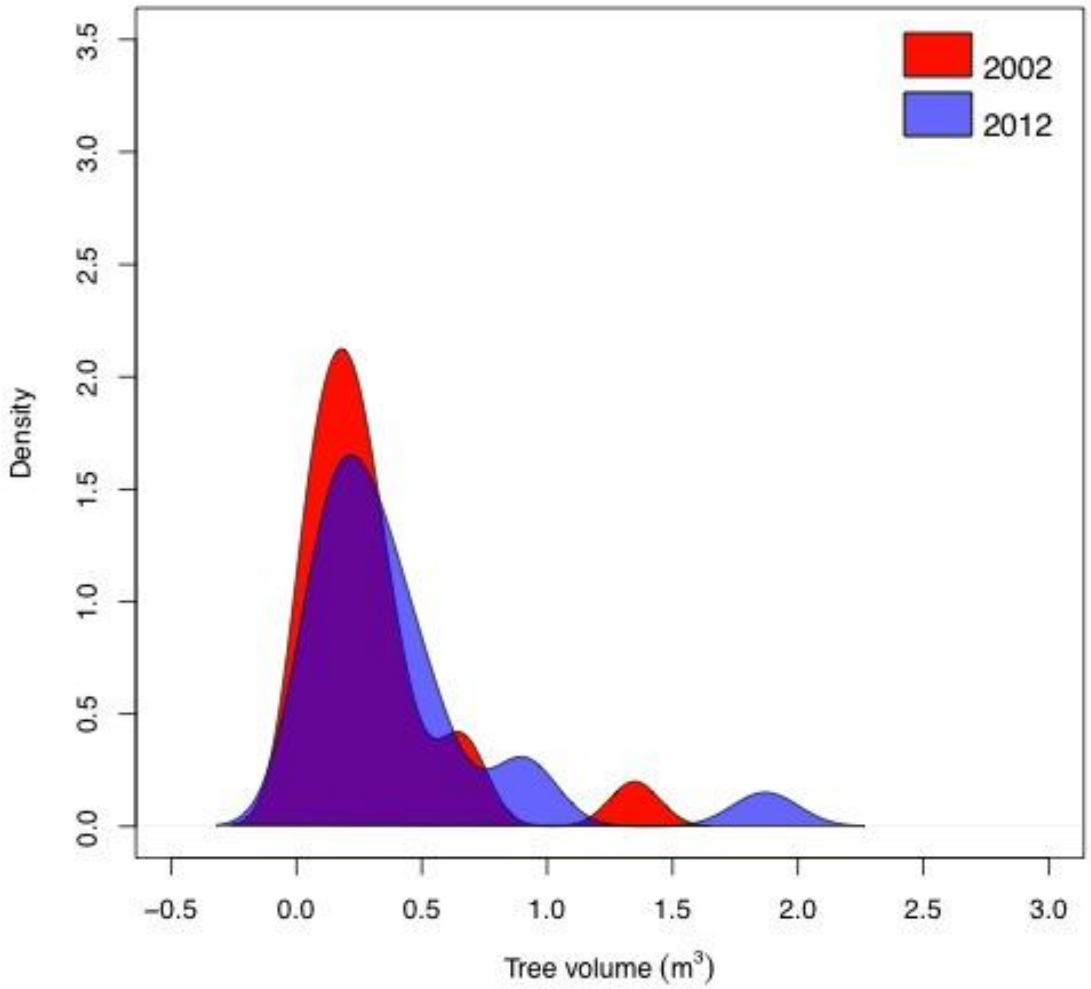


Figure 3.48 Histograms of tree volume in 2002 and 2012 at plot 10 where three distinct groups are observed and their respective volume increments over ten years.

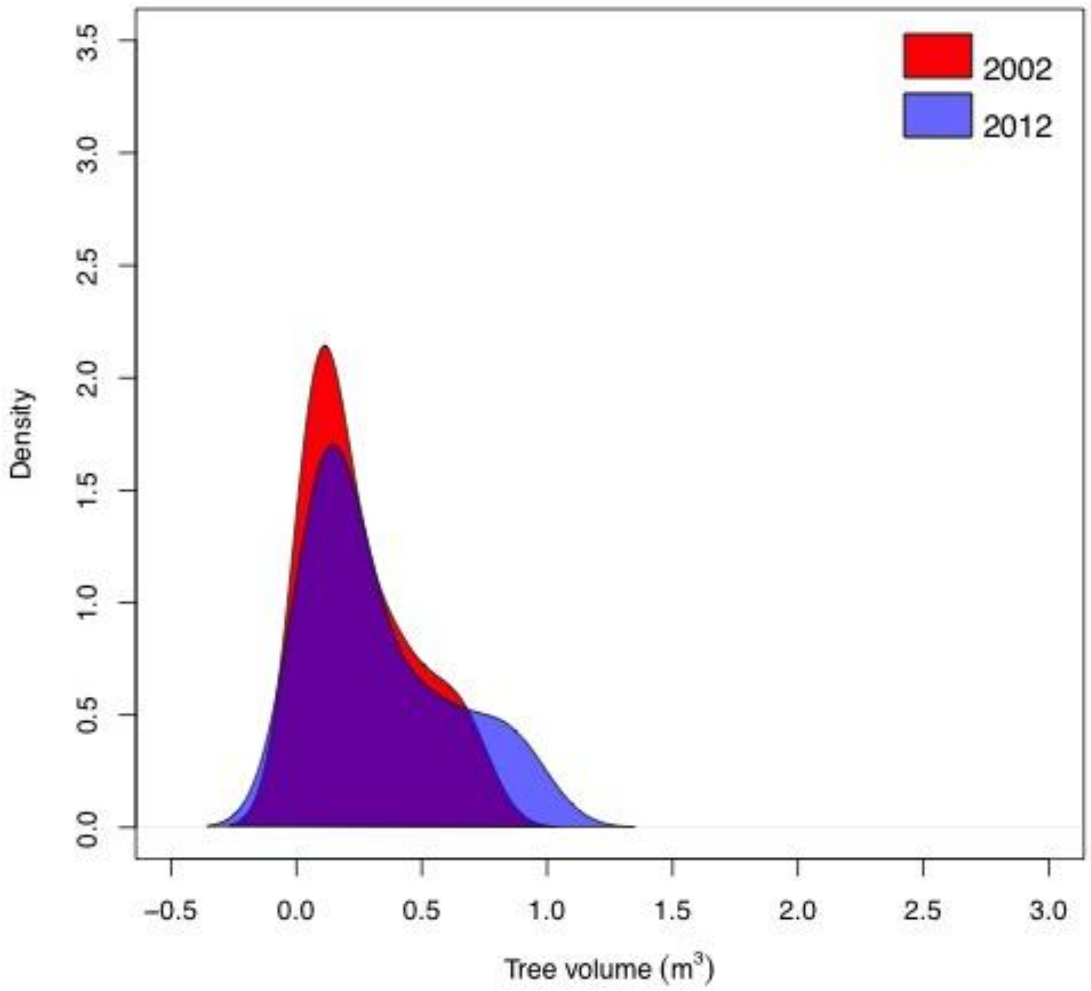


Figure 3.49 Histograms of tree volume in 2002 and 2012 at plot 24 where there has been the least amount of growth over the ten-year period, according to the observations with measured heights.

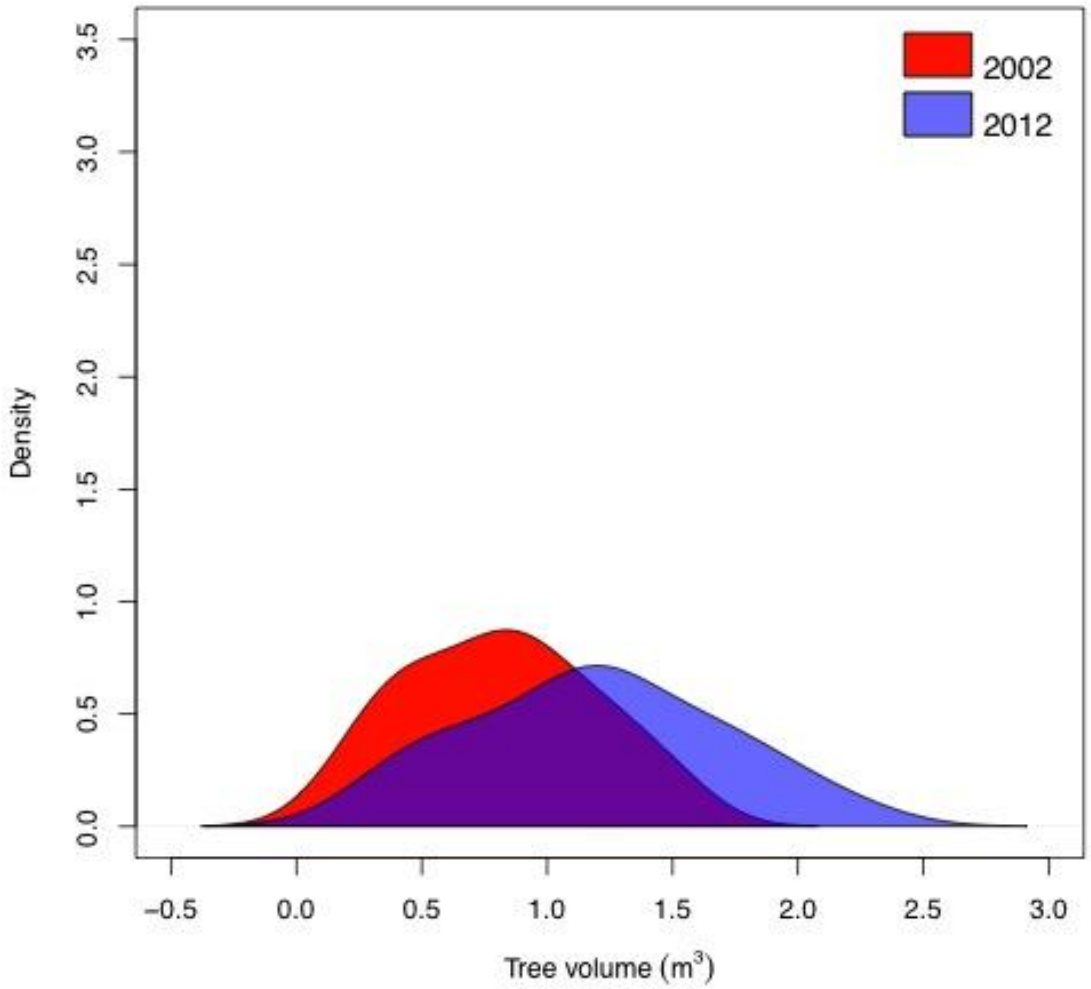


Figure 3.50 Histograms of tree volume in 2002 and 2012 at plot 41, which has experienced the greatest growth over the ten-year period.

An initial linear regression suggests that the relationship between PAI and 2002 volume is linear in the form of $\Delta Vol_{2012\text{-}2002} = 0.473(Vol_{2002}) - 0.03$ with a coefficient of determination of 0.93. The regression model was significant ($p<0.000$) with model coefficients between (95% confidence interval) -.042 to -.017 and .439 to .508 for the intercept and slope coefficients, respectively. There is evidence to suggest heteroscedasticity (Fig. 3.51); nevertheless it is clear that there is a certain degree of serial autocorrelation that exists. This does not impose a problem for the intended analysis as paired data were not queried but it does suggest that structure at a given time,

in this case 2002 volume is related to productivity as represented by the volume increment from 2002 to 2012.

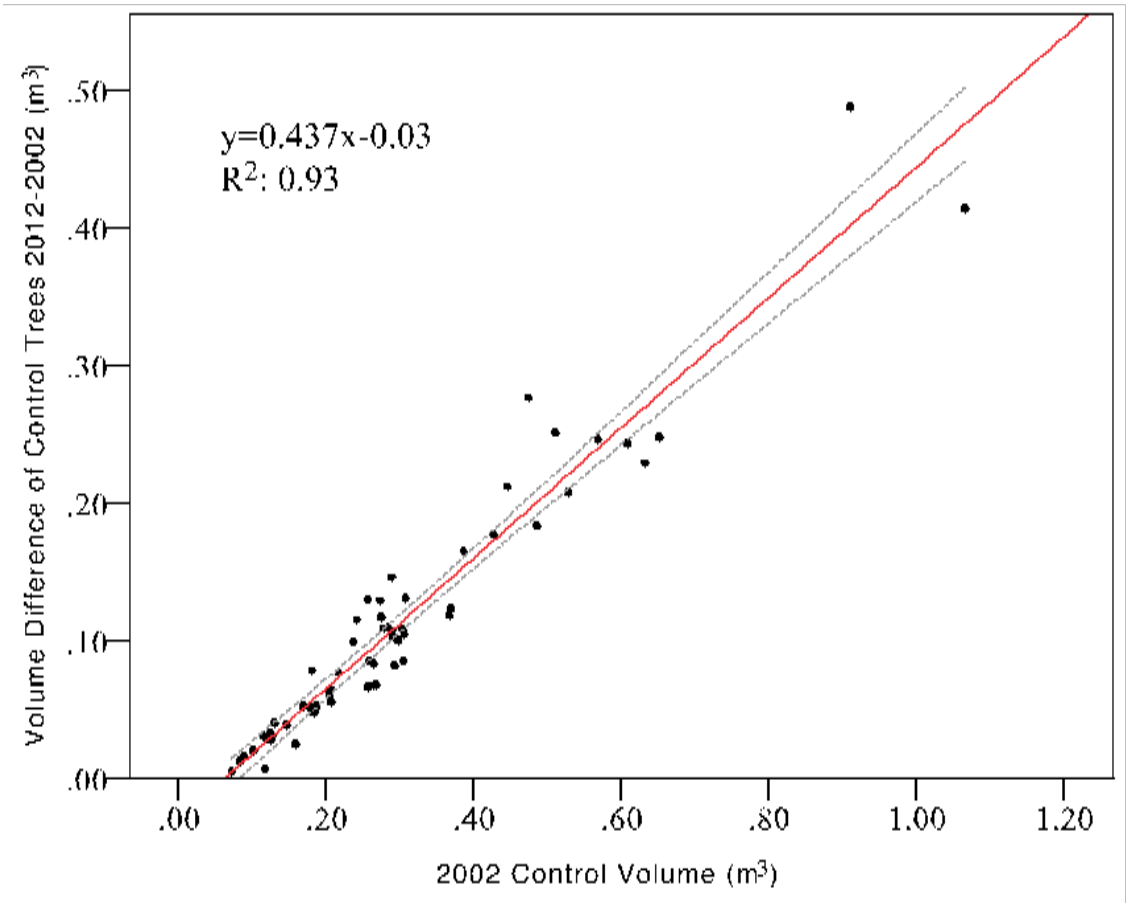


Figure 3.51 Illustrating the dependence of initial volume on the volume increment of ten years. Ideally this trend will be removed and the residuals will be the target attribute for modeling productivity. Because this model is built from the control group the productivity index would be relative to the growth of the control group.

In order to establish the productivity rank of the treatment and sampling plots, the field data were graphically and statistically analyzed. The data were submitted to a one-way analysis of variance. In order to appropriately apply this method, the data needed to be evaluated for violations of ANOVA assumptions. The normality and variance homogeneity of the plot and treatment data were statistically and graphically assessed for each year of sampling. The Shapiro-Wilk test for normality was computed for each year for each plot and each treatment. The test statistic was plotted through time for each plot and treatment to easily visualize the result. The normality tests suggested that there was no consistency with respect to the normality of the dataset. The significance of the Shapiro-Wilk test occasionally exceeded the 0.05 alpha level. This suggested in many cases the samples were significantly different from normal, while in others there was little evidence to conclude that the samples were taken from a non-normally distributed population (H_0: sample distribution is not different from normal). There was also little consistency in the case of normality for the plot data (Fig. 3.52). When addressing the normality of DBH distribution of treatments, only 94 of all 300 tests produced significance values greater than 0.05 and when assessed as a population for each year the Shapiro-Wilk test was never significant. Similarly, 366/740 normality tests of plot DBH suggested normal distributions and the plot pooled DBH distributions per year suggested that each year was significantly different from normal. This analysis suggested, overwhelmingly, that the DBH data would need to be transformed or a non-parametric equivalent test should be applied. In the same type of approach, the variance equality was assessed between plots and between treatments for each year of sampling. Through the

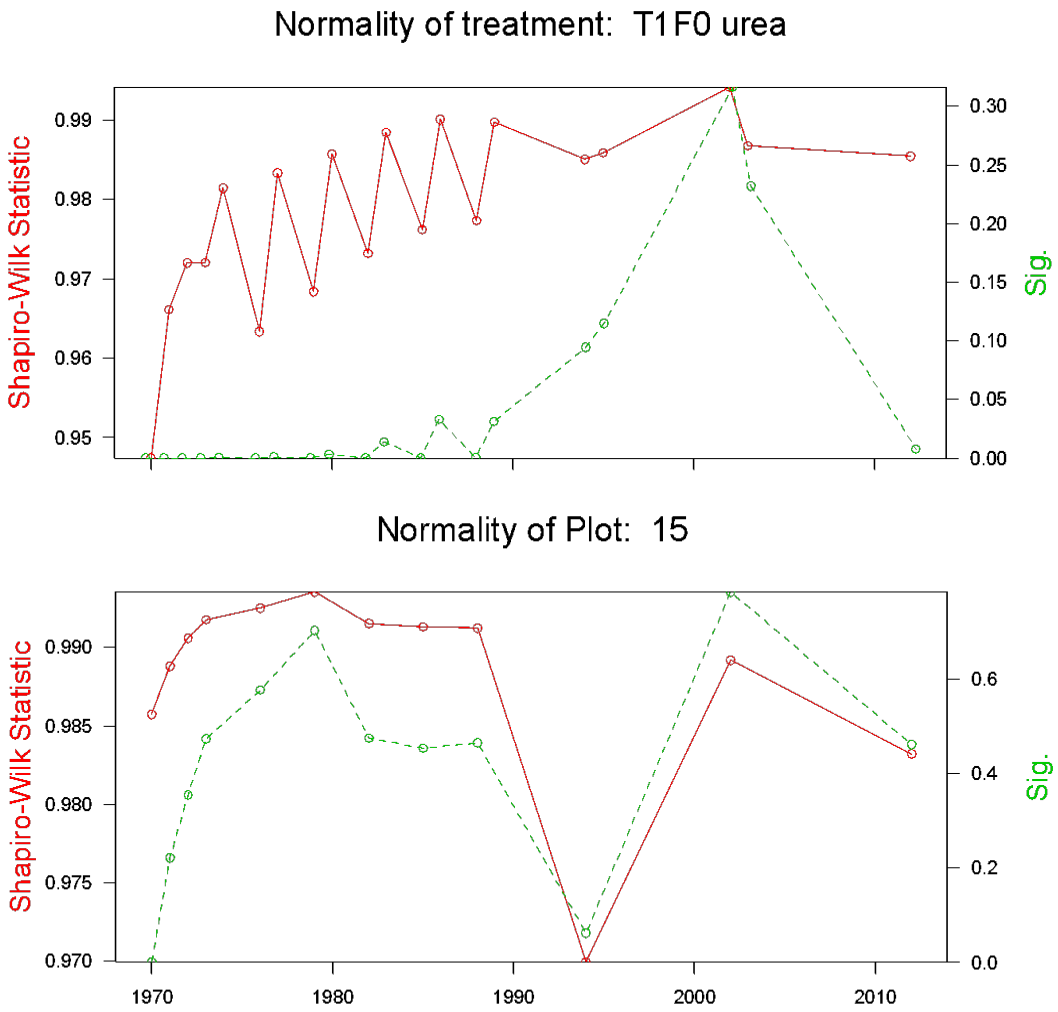


Figure 3.52 Shapiro-Wilk test for normality in treatment and plot data suggest that there is little consistency through time with respect to the normality of DBH measurements

Brown-Forsyth (non-parametric variance equality test) and Bartlett (parametric) tests, only the years 1990 and 2003 for variance equality between treatments produced non-significant test results (1990 Bartlett p: 0.25 and 2003 Brown-Forsyth p: 0.27) suggesting that variance equality could not be assumed for all years, except perhaps 1990 and 2003. Note that the parametric Bartlett test was considered appropriate for the 1990 comparison as five of the six treatments measured in that year's campaign produced non-significant ($p>0.05$) normality tests. The same analysis produced significant tests for each year when

assessing variance equality between plots. Testing the assumptions of the ANOVA clearly suggested that a non-parametric equivalent test that was robust to violations of variance equality and unbalanced sample sizes was warranted. As an alternative to the traditional ANOVA F-statistic, the Kruskal-Wallis rank sum test was applied.

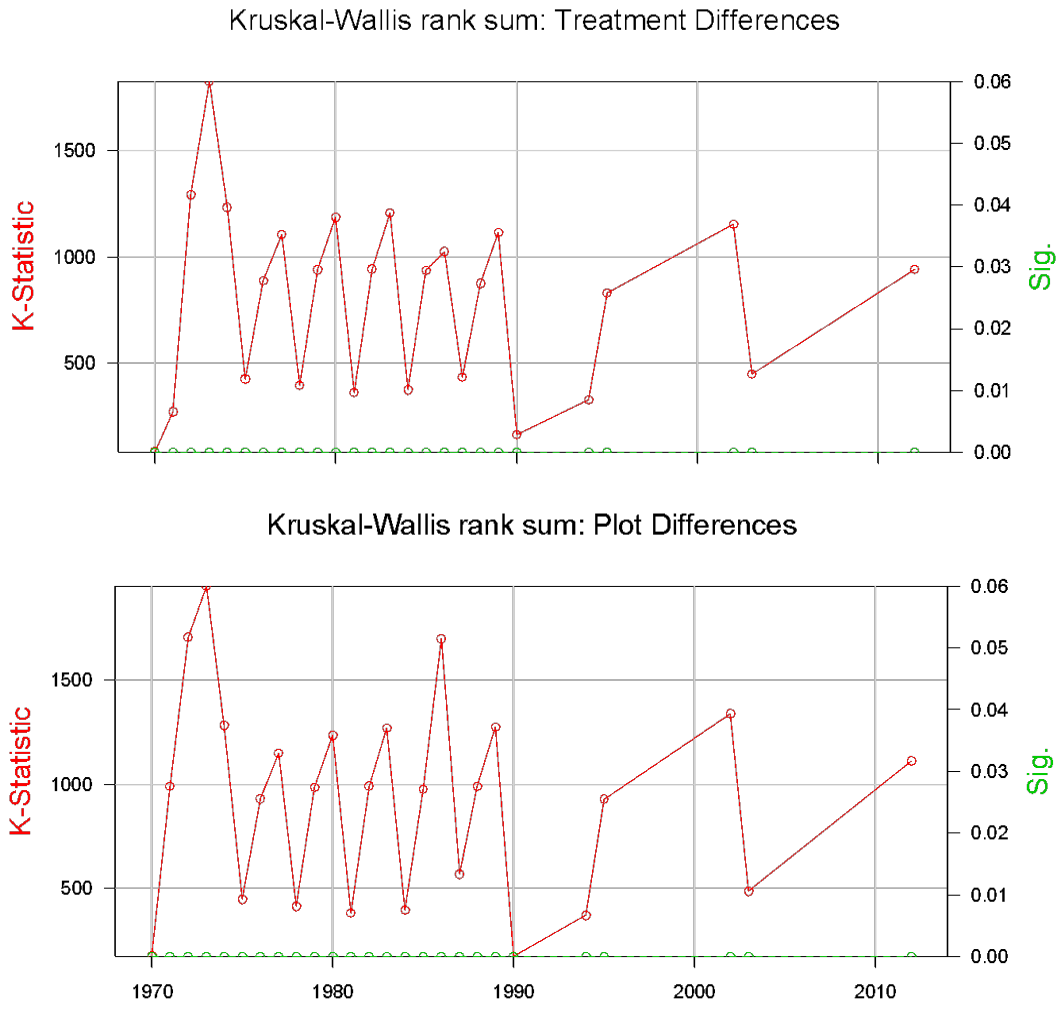


Figure 3.53 Testing for treatment and plot differences in DBH through all sampling years. Shapiro-Wilk, Bartlett and Brown-Forsyth suggest the use of Kruskal Wallis test over F-statistic. Nearly each test (year) produces significant results suggesting at least one group is different.

The ANONA and the NP-ANOVA (Kruskal-Wallis statistic) was computed to test for statistically significant differences between treatments and between plots. Regardless of the statistic applied (F or Kruskal-Wallis) and the stratification of the DBH data (by treatment or plot) each year produced significant tests suggesting that in every year of sampling at least one treatment, or at least one plot, was significantly different from the others in terms of DBH (Fig. 3.53). The data were also submitted to post-hoc analyses to identify those groups that were significantly different and contributed to the ANOVA significant result. These post-hoc tests could then be used to describe the ordinal nature of the treatments and plots with respect to the attribute assessed. The post-hoc tests applied included Wilcoxon, TukeyHSD and the Games-Howell tests. These tests were included in the statistical script written for this analysis based on the spread of possible data characteristics that could be encountered. The TukeyHSD is the most limited with assumptions of normality, homogeneity of variance and balanced groups, the Wilcoxon is a nonparametric alternative and the Games-Howell is robust to violations of homogeneity of variance and unbalanced samples. Although the post-hoc tests were run on each sampling date, particular attention was given to the 2002-2012 interval. Boxplots were generated to visualize the growth metric distributions stratified by treatment and by plots. The use of Hasse diagrams to visualize post-hoc analysis with many groups helped to discriminate the natural groupings within the dataset, which becomes challenging with large numbers of groupings (the interested reader is directed to the *paircompviz* package in R).

Focusing on the most recent and complete sampling interval (2002 and 2012), periodic annual increments were computed for DBH, height and volume. The mean

annual increment (MAI) was also computed for the expected case that current growth rates would be uniform across the study area, as research has shown that the efficacy of fertilization treatments do not persist beyond 7-12 years after treatment [114]–[116]. The distributions of MAI in DBH suggested there were differences in diameter growth among the treatments, and at least from the perspective of the extremes, the control (T0F0) exhibited the least diameter growth and treatments with heavy thinning and greater than 448kg N/ha (F2) produced largest diameters (Figure 3.54). The treatment distributions of PAI in DBH demonstrated the apparent convergence of DBH increment for many of the treatments. The obvious exceptions are the larger diameter increment T2 treatments and especially those treatments installed after 1973 (label suffix GT73), which exhibited even larger diameter increments than all other treatments (Fig. 3.55). Evident in the boxplots is the reduction in PAI variance with thinning treatments, although it is recognized that this variability may be at least partially caused by between plot (plot replicates) and within treatment variation (no replicate for treatment T1F1-2, although this treatment does not support this presumption), it is most likely caused by the reduction of supressed and intermediate cohorts within the 2/3 thinned treatments. Normalizing the PAI in DBH by the MAI in DBH enhanced the difference between those plots established in 1970-1973 from those established in 1987 (Fig. 3.56). The boxplot of the PAI/MAI ratio mirrors the pattern of the PAI boxplots and suggests that there is little difference in diameter growth, relative to the mean historical increment, between all the T0 and T1 treatments. Further, it might be concluded that within the T0 and T1 treatments there is little diameter growth differences that is not explained by their respective diameter sizes. This interpretation is derived from the fact that all trees are the same age so MAI in this case is simply the

DBH in 2002 scaled by 1/55, thus the ratio represents diameter growth normalized by the diameter prior to the increment (2002). The rationale for investigating the PAI/MAI ratio stems from its ability to indicate growth trajectories and thus its relevance to productivity. The volume increment ratio has a utility in commercial forestry for indicating optimal harvesting times or the biological rotation age, which for unthinned Douglas-fir is quite short relative to its lifespan [117]. The underlying premise relies on the variation in PAI and MAI with age, where PAI peaks at a young age and declines and MAI increases to a maximum, which corresponds to the intersection of the PAI and MAI curves, after which both have decreasing trajectories.

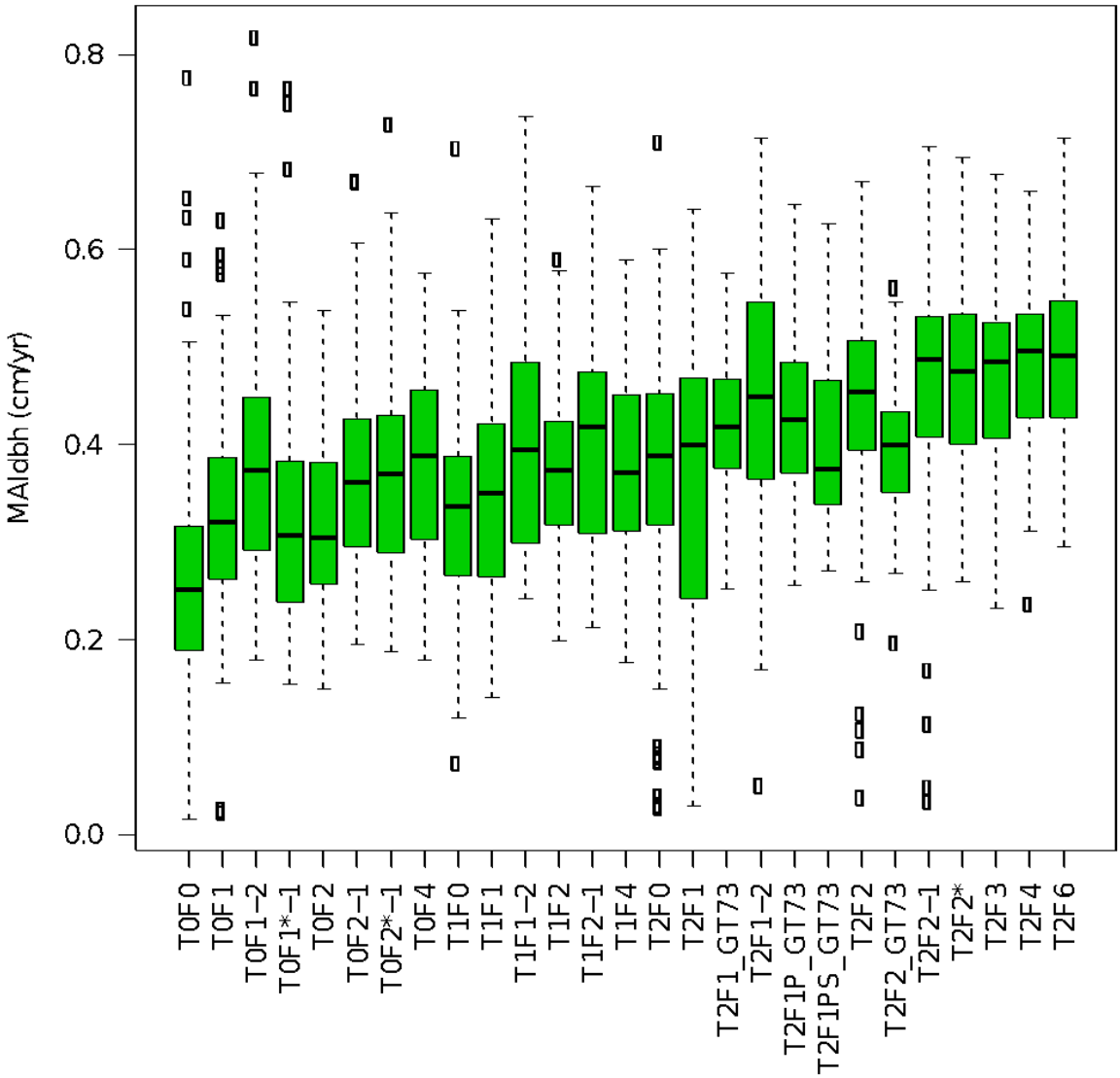


Figure 3.54 Boxplots of treatment MAI of DBH distributions illustrating differences in central tendency and spread. The data are graphed by quartiles, the largest and smallest point no greater than 1.5*(IQR) from the quartiles (0.25 and 0.75)and all points greater than those limits. Note that treatments with the "GT73"suffix are treatments established after the year 1973.

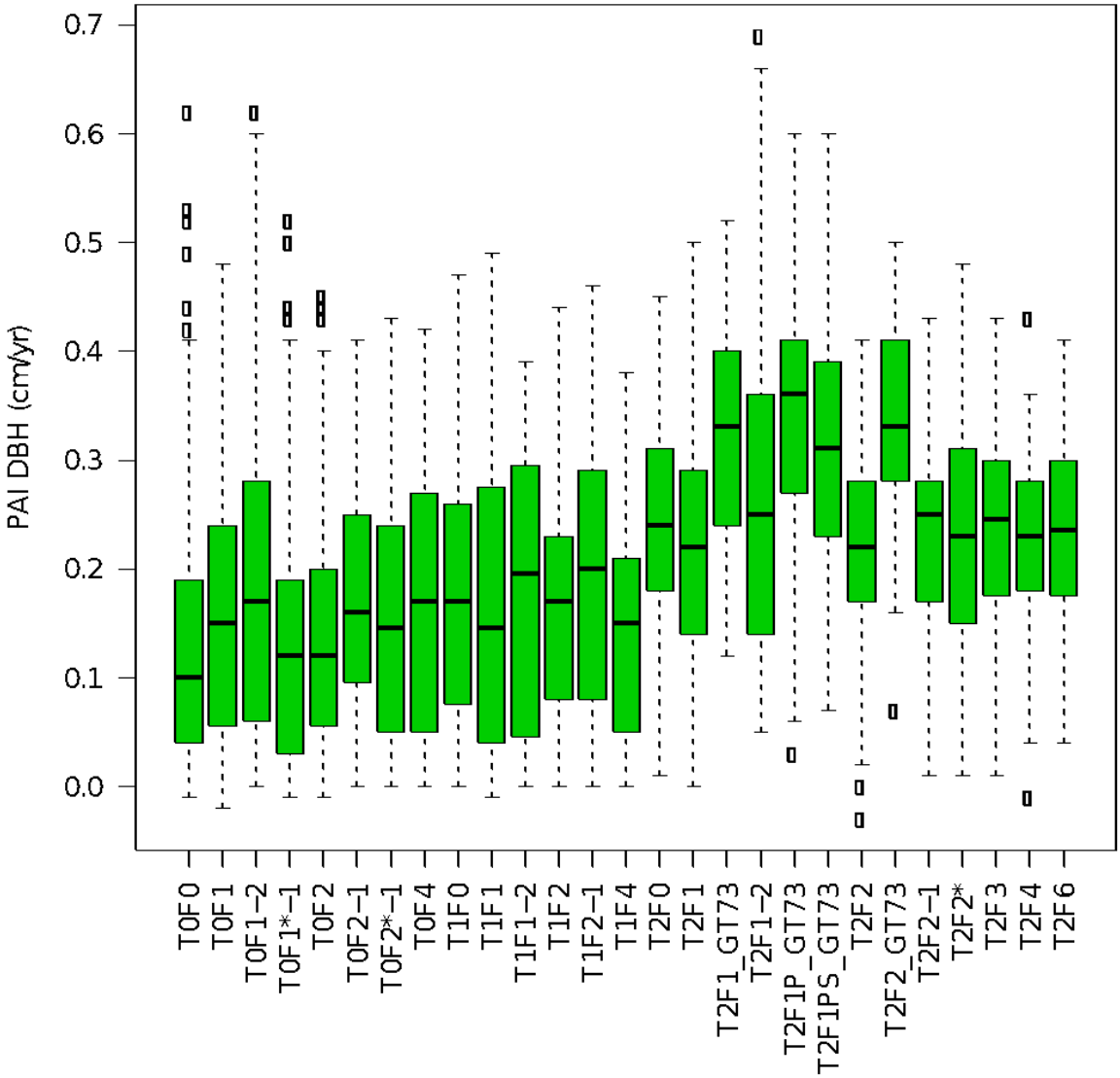


Figure 3.55 Boxplots of treatment PAI of DBH distributions illustrating differences in central tendency and spread. The data are graphed by quartiles, the largest and smallest point no greater than 1.5*(IQR) from the quartiles (0.25, 0.75) and all points greater than those limits. Note that treatments with the "GT73"suffix are treatments established after the year 1973.

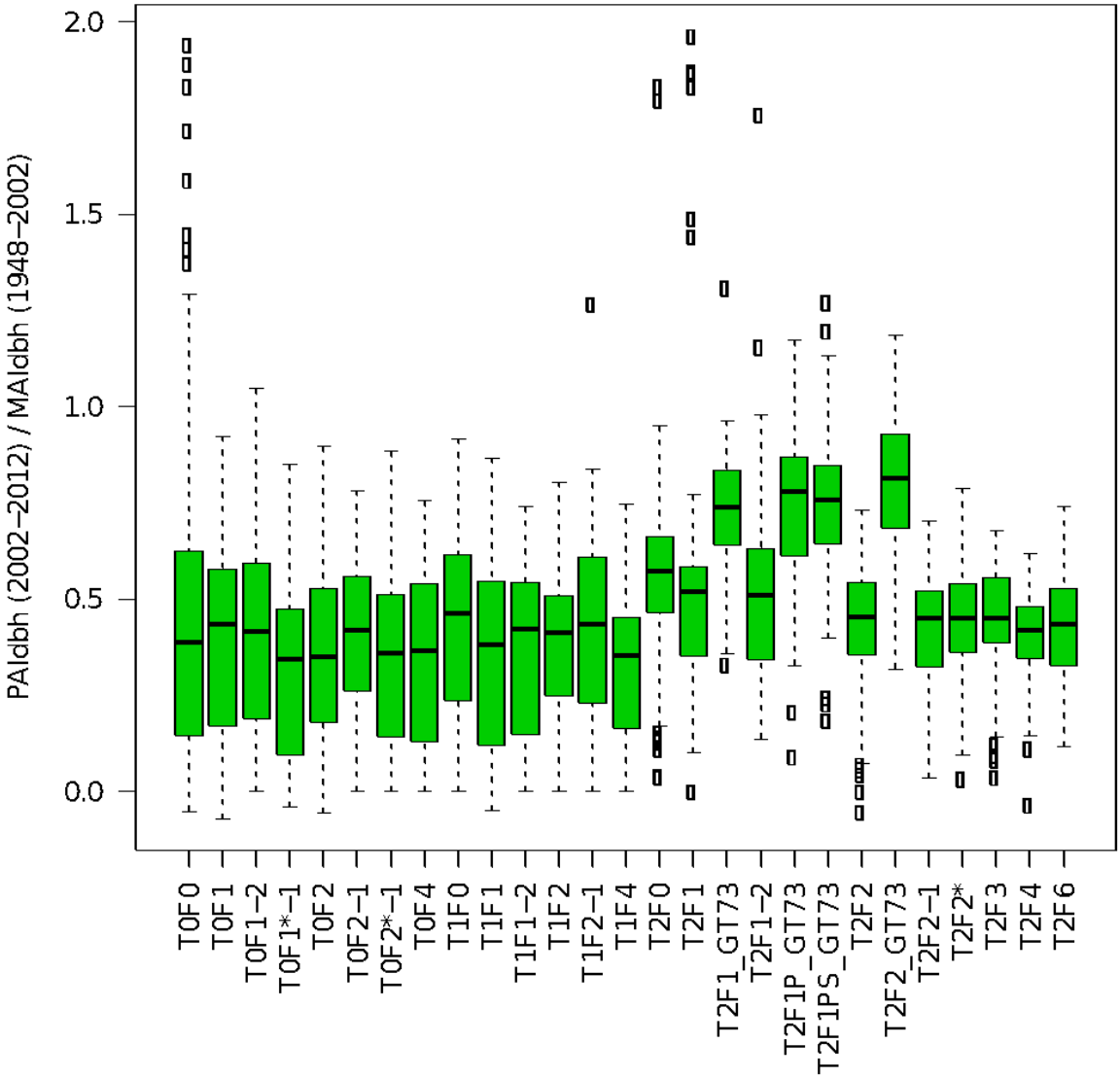


Figure 3.56. Boxplots of treatment PAI/MAI of DBH distributions illustrating differences in central tendency and spread. The data are graphed by quartiles, the largest and smallest point no greater than 1.5*(IQR) from the quartiles(0.25, 0.75) and all points greater than those limits. Note that treatments with the "GT73"suffix are treatments established after the year 1973.

Height growth, although showing evidence of treatment differences did not follow a coherent pattern associated with the treatments (Fig. 3.57). The plots that were installed in 1987, which tended to have lower height increments, confounded the expected pattern of MAI of height stratified by thinning and fertilization treatments. It might be reasonable to expect that the effect of treatments on the 1987 plots would be

lessened for MAI, as they would have experienced growth typical of the control plots for an additional 14-16 years thus lowering the MAI in growth rates. The treatments established in 1987 represent a different growth form than the other treatments and are in opposition of the initial presumption that DBH alone could represent productivity. Under these treatments diameters are at the higher range for the site while the heights occur at the lower limit for the site. Excluding the 1987 plots, the treatment effect is apparent. Although overlap is present in the treatment MAI of height distributions, there seems to be a trend for increased height growth with combinations of thinning and fertilization. The PAI and the PAI/MAI ratio for height stratified by treatment displayed little obvious coherent association with the treatments as depicted in boxplots (Fig 3.58 & 3.59). However, while controlling for thinning treatment, the PAI/MAI distributions appeared to have a potentially inverse association with fertilization, especially for the T0 thinning treatment. This observation might suggest that the increased fertilization supported crown growth at an increased rate and advancing crown closure and between crown competition, effectively reducing PAI. The reduced PAI (relative to the plots past) and a higher MAI caused by the more aggressive treatment (supported by Fig 3.57) would result in a reduced PAI/MAI ratio.

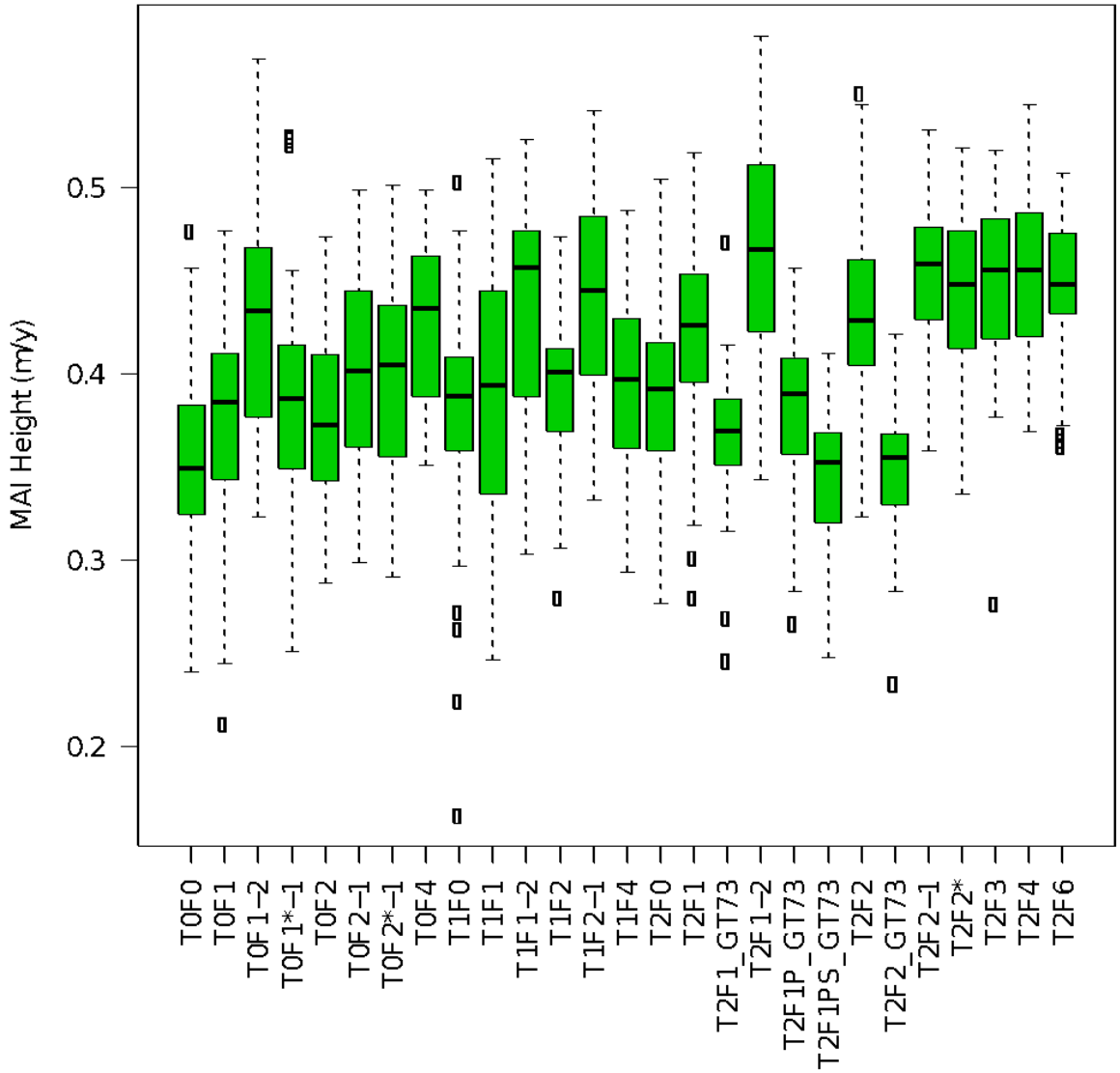


Figure 3.57 Boxplots of treatment MAI of height distributions illustrating differences in central tendency and spread. The data are graphed by quartiles, the largest and smallest point no greater than 1.5*(IQR) from the quartiles (0.25, 0.75) and all points greater than those limits. Note that treatments with the "GT73"suffix are treatments established after the year 1973.

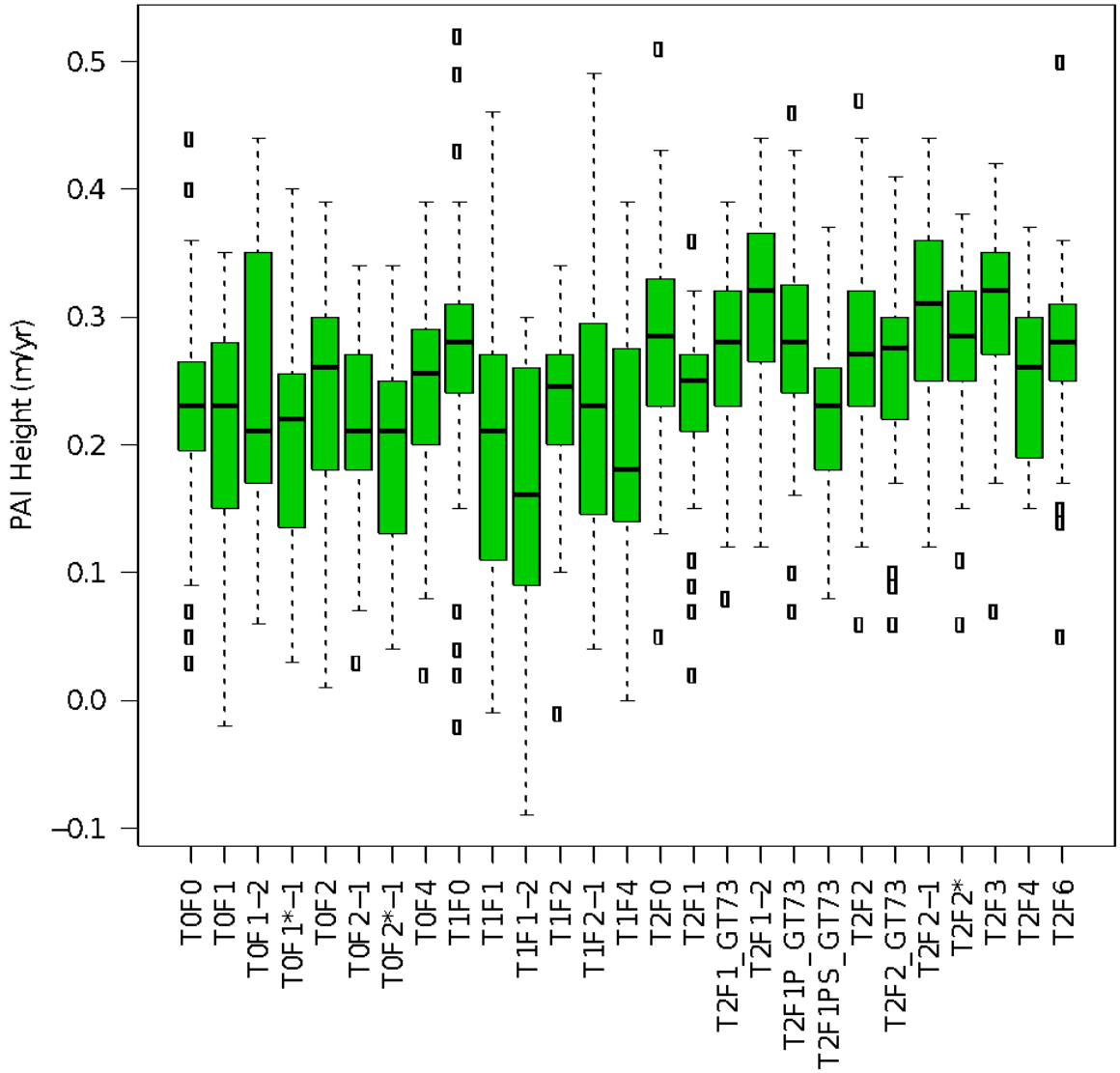


Figure 3.58 Boxplots of treatment PAI of height distributions illustrating differences in central tendency and spread. The data are graphed by quartiles, the largest and smallest point no greater than 1.5*(IQR) from the quartiles (0.25, 0.75) and all points greater than those limits. Note that treatments with the "GT73"suffix are treatments established after the year 1973.

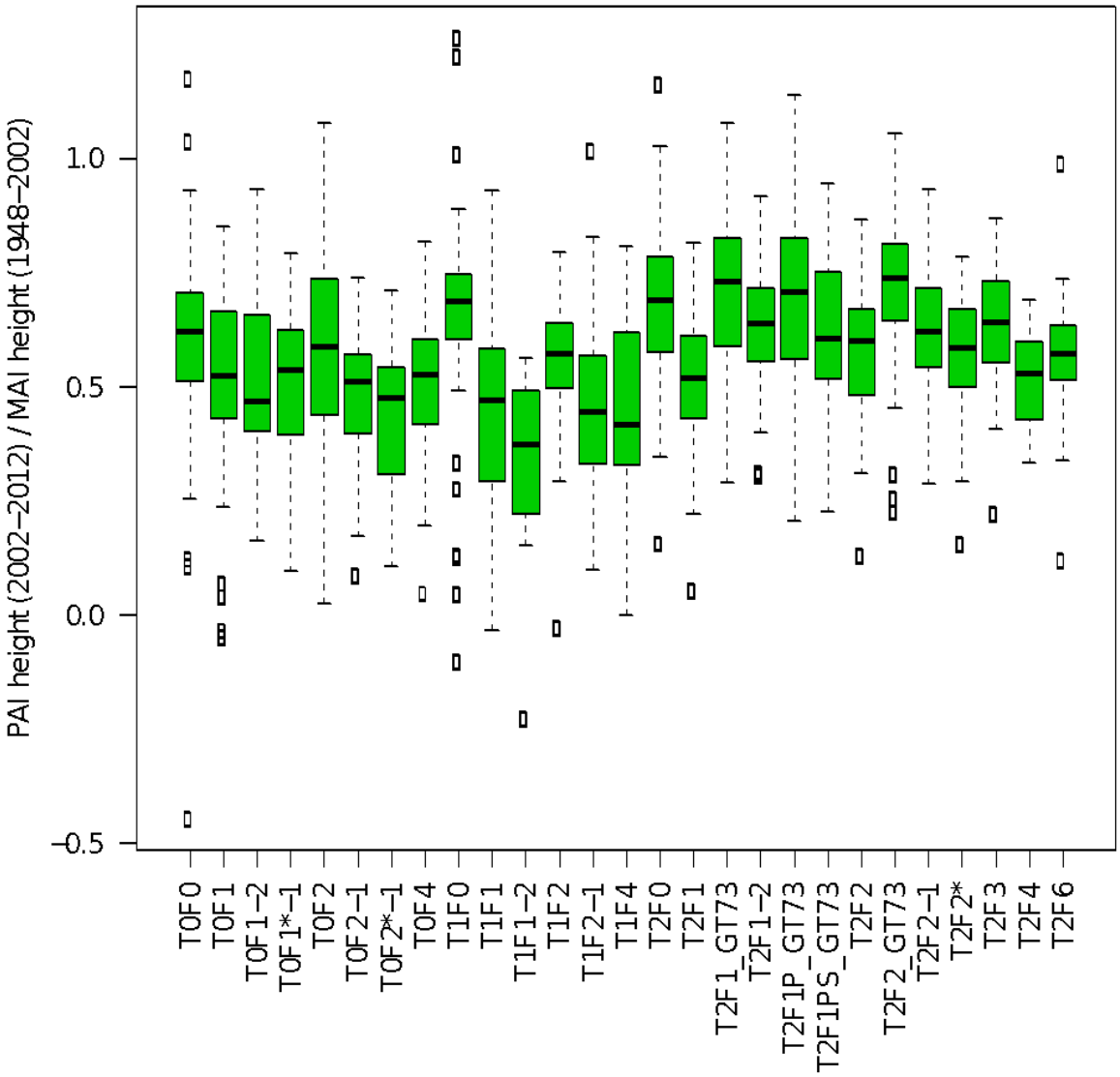


Figure 3.59 Boxplots of treatment PAI/MAI of height distributions illustrating differences in central tendency and spread. The data are graphed by quartiles, the largest and smallest point no greater than 1.5*(IQR) from the quartiles (0.25, 0.75) and all points greater than those limits. Note that treatments with the "GT73"suffix are treatments established after the year 1973.

Boxplots of volume MAI did not produce obviously separated distributions for the treatment groupings (Fig. 3.60). However, and in line with DBH observations, the T2 treatments appear to exhibit greater periodic volume increments than the T0 and T1 treatments (Fig. 3.61). The other notable observation made of the volume metrics was that treatment T2F1-2 appeared to have much greater volume increments for both MAI

and PAI. The growth as a proportion of MAI again separated the post 1973 installations from the others, suggesting that these treatments are experiencing more growth relative to their past growth rates (Fig.3.62). It is suspected that this observation is the product of reduced competition and the time lag since the treatment was applied. While the whole site is likely experiencing a downward trend in MAI, as the MAI of Coastal Douglas-fir is expected to peak at about 20years [115], the 1987 plots may be slightly behind the other treatments.

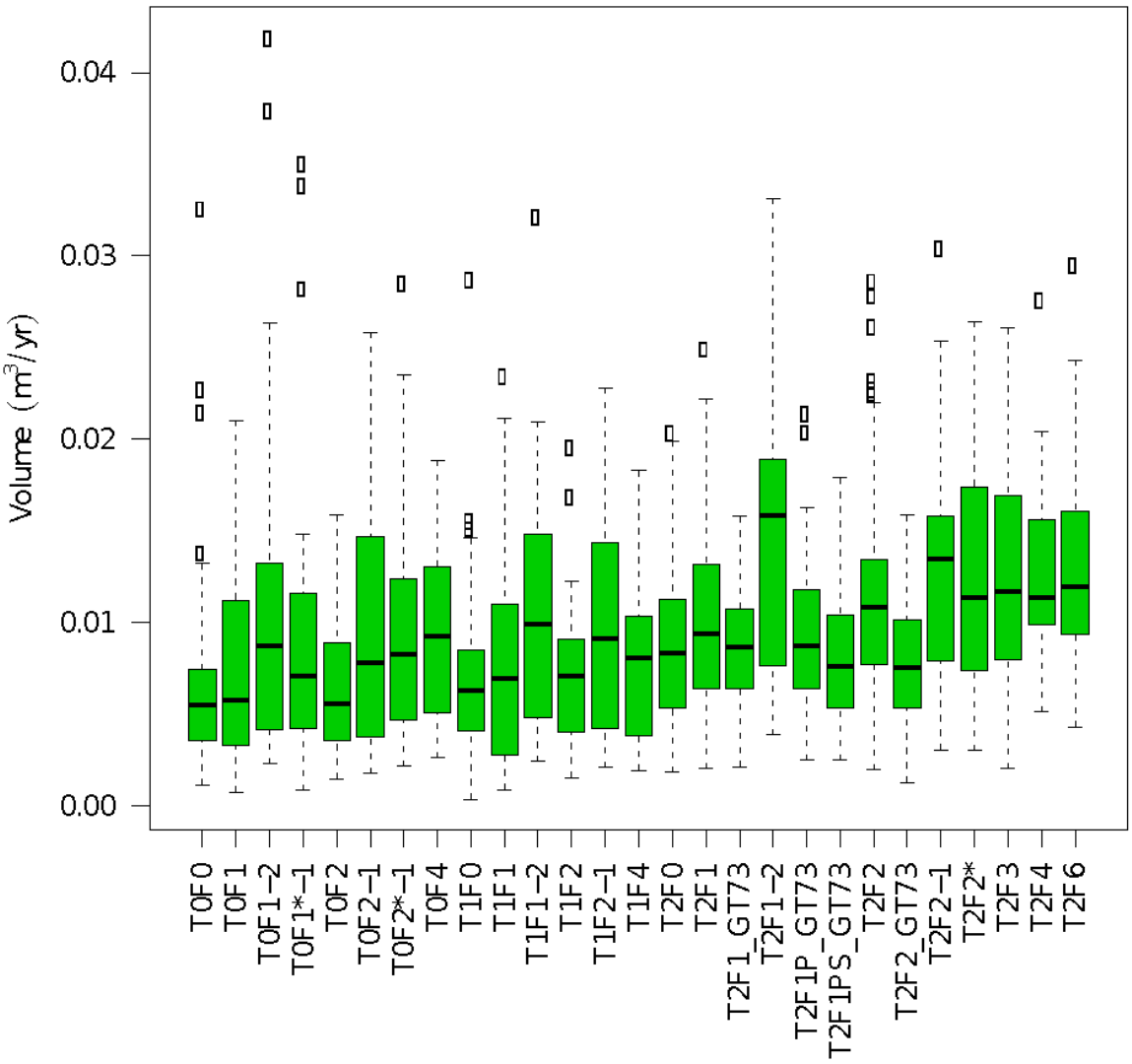


Figure 3.60 Boxplots of treatment MAI (1948-2012) of volume distributions illustrating differences in central tendency and spread. The data are graphed by quartiles, the largest and smallest point no greater than 1.5*(IQR) from the quartiles (0.25, 0.75) and all points greater than those limits. Note that treatments with the "GT73"suffix are treatments established after the year 1973.

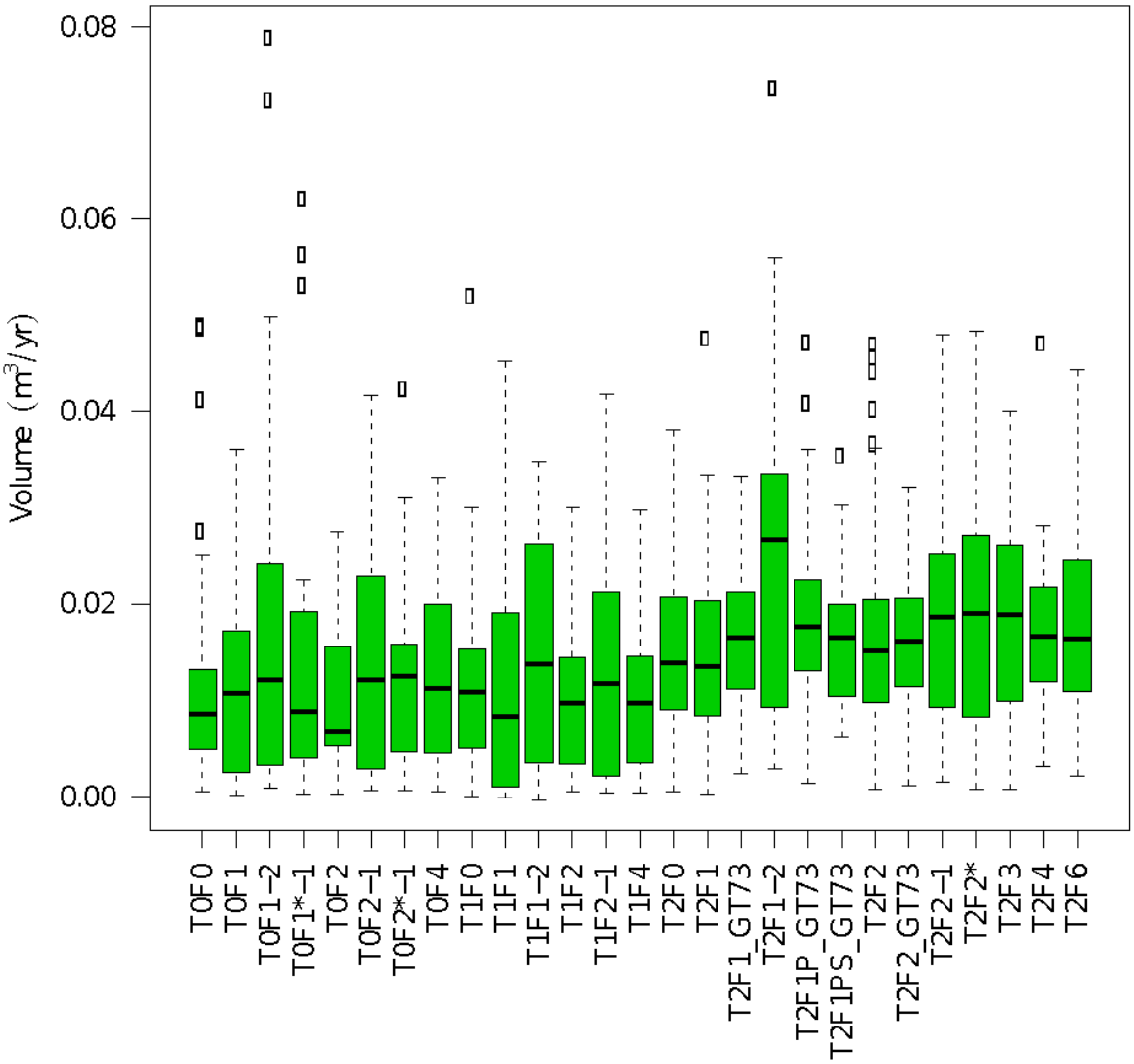


Figure 3.61 Boxplots of treatment PAI of volume distributions illustrating differences in central tendency and spread. The data are graphed by quartiles, the largest and smallest point no greater than 1.5*(IQR) from the quartiles 90.25, 0.75) and all points greater than those limits. Note that treatments with the "GT73"suffix are treatments established after the year 1973.

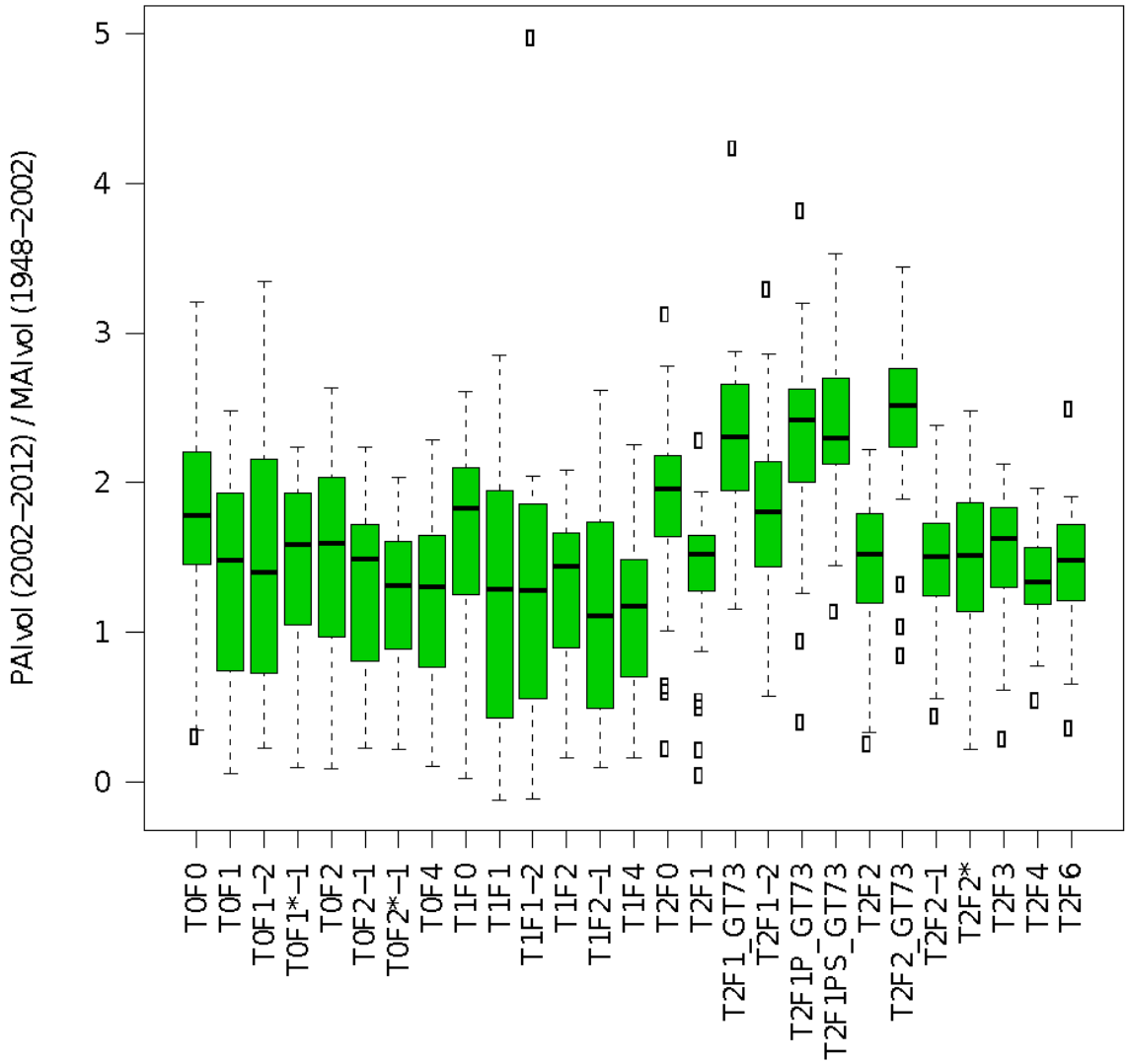


Figure 3.62 Boxplots of treatment PAI/MAI of volume distributions illustrating differences in central tendency and spread. The data are graphed by quartiles, the largest and smallest point no greater than 1.5*(IQR) from the quartiles(0.25, 0.75) and all points greater than those limits. Note that treatments with the "GT73"suffix are treatments established after the year 1973.

Table 3.8 Assessment of growth differences between treatments						
Metric	Shapiro	Norm (n)	Bartlett	B-Forsyth	ANOVA-F	K-Wallis
MAI-DBH	0.994**	15/27	188.4**	4.75**	39.24**	802.42**
PAI-DBH	0.963**	11/27	126.3**	3.87**	25.56**	551.10**
PAI/MAI-DBH	0.281**	5/27	5184.0**	5.89**	6.34**	521.04**
MAI-HT†	0.998(0.09)	22/27	68.6**	2.66**	20.23**	383.63**
PAI-HT†	0.986**	18/27	62.1**	2.11*	6.44**	156.74**
PAI/MAI-HT†	0.987**	19/27	89.7**	1.95*	9.17**	218.91**
MAI-VOL†	0.923**	12/27	131.9**	3.10**	6.53**	167.91**
PAI-VOL†	0.922**	9/27	127.9**	3.29**	4.07**	109.09**
PAI/MAI-VOL†	0.993**	17/27	95.9**	4.34**	17.31**	324.75**
MAI-HT††	0.998*	15/27	121.2**	4.70**	89.48**	1283.99**
PAI-HT††	0.961**	5/27	184.6**	4.45**	24.02**	615.13**
PAI/MAI-HT††	0.935**	6/27	344.5**	5.71**	20.74**	579.28**
MAI-VOL††	0.916**	6/27	252.7**	7.04**	40.23**	873.70**
PAI-VOL††	0.914**	7/27	225.3**	6.53**	25.54**	644.83**
PAI/MAI-VOL††	0.991**	13/27	242.8**	9.40**	31.58**	602.69**

ANOVA assumption test for normality by Shapiro-Wilk test without plot grouping (Shapiro) and stratified by groups (Norm: number of non-significant tests ($p>0.05$)/number of treatment tests) demonstrate a non-normal tendency. ANOVA assumption tests for variance homogeneity by the parametric Bartlett test and the non-parametric Brown-Forsyth test demonstrate that equal variance cannot be assumed. The non-parametric ANOVA by the Kruskal-Wallis test is appropriate in each of the metrics. At least one grouping (treatment) is different from the others in each tested metric. Significance >0.05 are in parentheses, *:$p<0.05$, **$p<0.001$, † attribute derived from measured heights only, †† attribute derived from measured and modeled heights

Analysis of variance suggests statistically significant differences exist among the treatments for all metrics evaluated (Table 3.8). Post-hoc tests of DBH MAI indicate that there is a direct association between treatments and the mean annual increment. All T2 treatments with greater than F2 fertilization (T2F2_GT73 being the exception) exhibit the highest MAI in DBH ($p< 0.05$), and there is no evidence to suggest there are differences between the T2 with >F2 treatments. At the opposite end of MAI of DBH, the T0F0 treatment is statistically less than all other treatments. While the remainder of the treatment groups exhibit statistically significant differences the sequence of thinning and fertilizations are not discrete, for example at the level of comparison above T0F0, all but the F3-F6 fertilization treatments are represented but only T0 and T1 occur (Fig. 3.63).

The post-hoc tests for PAI of DBH between treatment differences illustrate a clear thinning treatment dependence (Fig. 3.64). There is no evidence to suggest the control is different from five of the seven other T0 treatments. The T0F1-2 and T0F2-1 are significantly greater than the control grouping and the T1F1 and T1F4 may not be different from the control grouping. The remaining four T1 treatments are spread between a T2 grouping (T1F2-1, T1F1-2) and a small group consisting of only T1F0 and T1F2 that is statistically greater than the control and significantly less than the T2 grouping. Finally, all the treatments installed after 1973 are significantly greater than the T2 grouping (with the exception of T2F2* and T2F1-2). This test demonstrated, as expected, that thinning intensity as applied at SLP increases diameter growth [96].

The significant treatment differences produced by the post-hoc tests of the diameter PAI/MAI ratio demonstrated that the 1987 treatments had the greatest magnitude ratios (Fig.3.65). The large ratio for the 1987 plots is conceptually caused by either a larger PAI or smaller MAI, although it might be reasonable to expect a lower MAI caused by the later treatment establishment, the post-hoc test of PAI indicates that the larger ratio values are likely caused by the large PAI rather than a low MAI. The treatment stratification that is illustrated by the Hasse diagram of the Wilcoxon post-hoc tests demonstrates that treatments with less thinning but greater fertilization express a lower PAI/MAI ratio, treatments T2F1 and especially T2F0 are significantly greater than the other treatments (omitting 1987 plots).

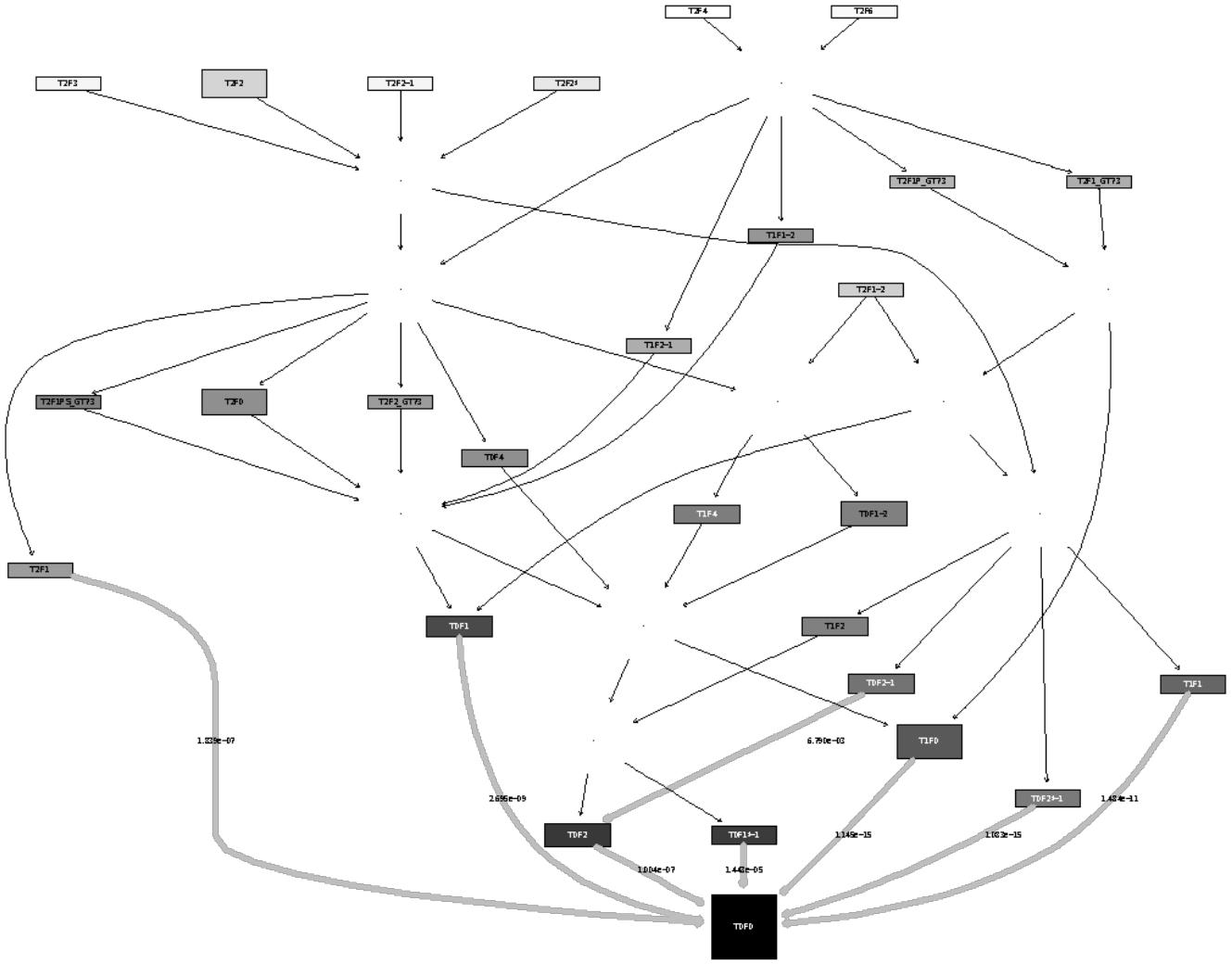


Figure 3.63 Hasse diagram representation of post-hoc tests (Wilcoxon rank sum) for treatment differences in MAI of DBH. The position of group vertices in the chart is representative of the magnitude of the variable. The box sizes are proportional to treatment group sample sizes. Where significance is less than 0.05 line weight is inversely proportional to significance of the test and where lines do not connect treatments the two treatments are not significantly different. To simplify the chart connections are compressed using a point symbol.

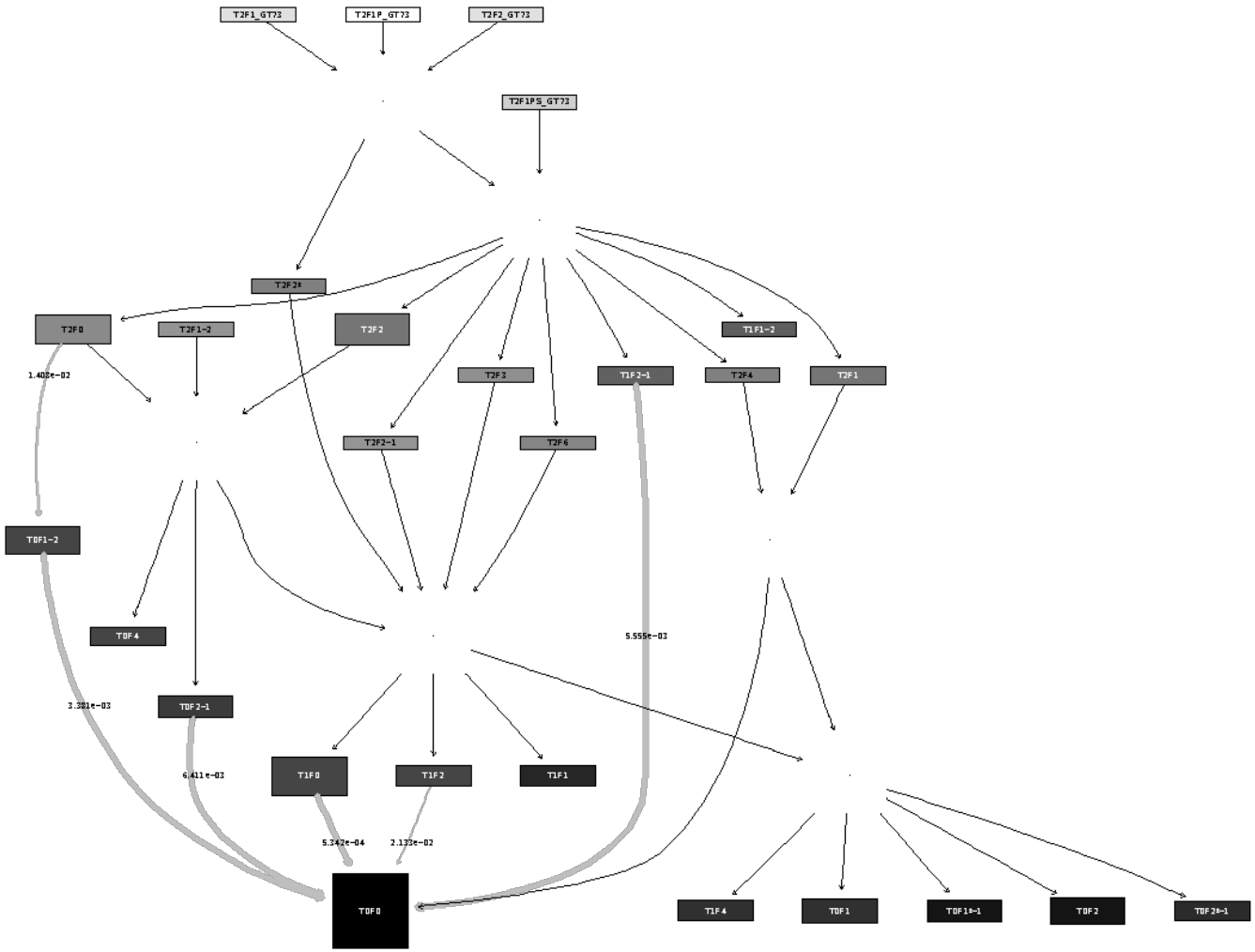


Figure 3.64 Hasse diagram representation of post-hoc tests for treatment differences in PAI (ΔDBH/Δtime). The position of group vertices in the chart is representative of the magnitude of the variable. The box sizes are proportional to treatment group sample sizes. Where significance is less than 0.05 line weight is inversely proportional to significance of the test and where lines do not connect treatments the two treatments are not significantly different. To simplify the chart connections are compressed using a point symbol

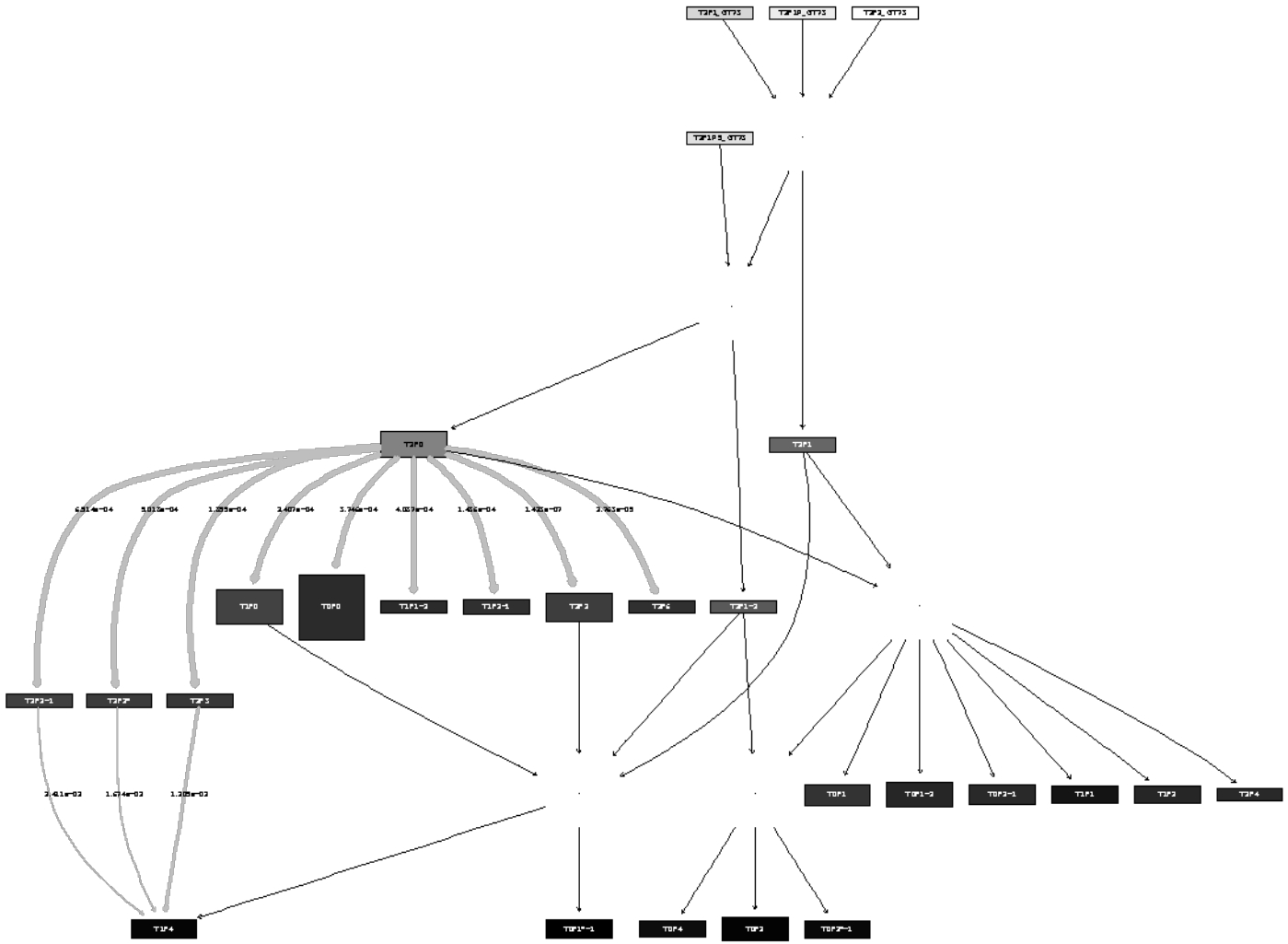


Figure 3.65 Hasse diagram representation of post-hoc tests for treatment differences in PAIdbh (2002-2012)/MAIdbh (1948-2002). The position of group vertices in the chart is representative of the magnitude of the variable. The box sizes are proportional to treatment group sample sizes. Where significance is less than 0.05 line weight is inversely proportional to significance of the test and where lines do not connect treatments the two treatments are not significantly different. To simplify the chart connections are compressed using a point symbol

Post hoc test of MAI of height produced a pattern that paralleled the MAI of DBH, one that followed the treatment effects (Fig. 3.66-3.68). The investigation of the volume of the measured trees was not encouraging for investigating differences in productivity, as the tests suggested that there was very little difference in PAI of volume (Fig. 3.69-3.71). The Games-Howell post hoc tests produced slightly more tests that were significant relative to the Wilcoxon test (7 significant tests), but there were still only 18 treatment comparison tests that were significant. The Games-Howell post-hoc analysis suggested that treatment T2F1-2 (plots 41 and 28) were statically greater than treatments T0 with F0, F1, F2 and F4 and T1 with F0, F2, and F4 ($p<0.049$) and that treatment T2F1P_GT73 had a greater increment than T0F2, T1F2 and T1F4 ($p<0.049$), T2F3 was greater than T0F2, T1F2, T1F4 ($p<0.032$) and T2F6 was greater than T0F2, T1F2 ($p<0.046$) and T2F2-1 was greater than T0F2, T1F2 ($p<0.044$) and finally T2F2 was greater than T1F2 ($p=0.042$). While median volume increment might have some potential to describe production at the plot level it does not account for site occupation as a result it was considered important to invest the time into modeling height from DBH to estimate total plot volume.

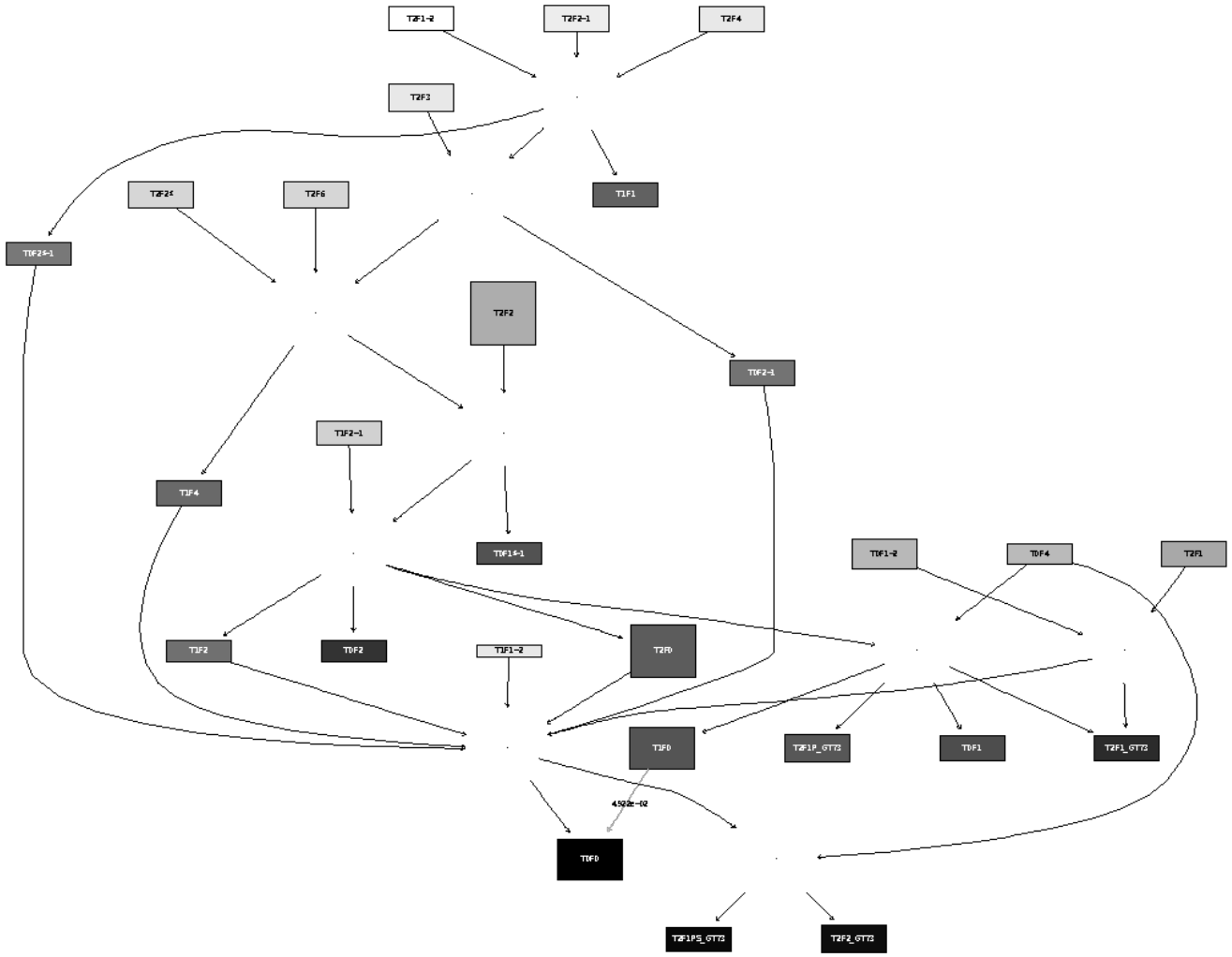


Figure 3.66 Hasse diagram representation of post-hoc tests for treatment differences in MAI in measured height (1948-2002). The position of group vertices in the chart is representative of the magnitude of the variable. The box sizes are proportional to treatment group sample sizes. Where significance is less than 0.05 line weight is inversely proportional to significance of the test and where lines do not connect treatments the two treatments are not significantly different. To simplify the chart connections are compressed using a point symbol

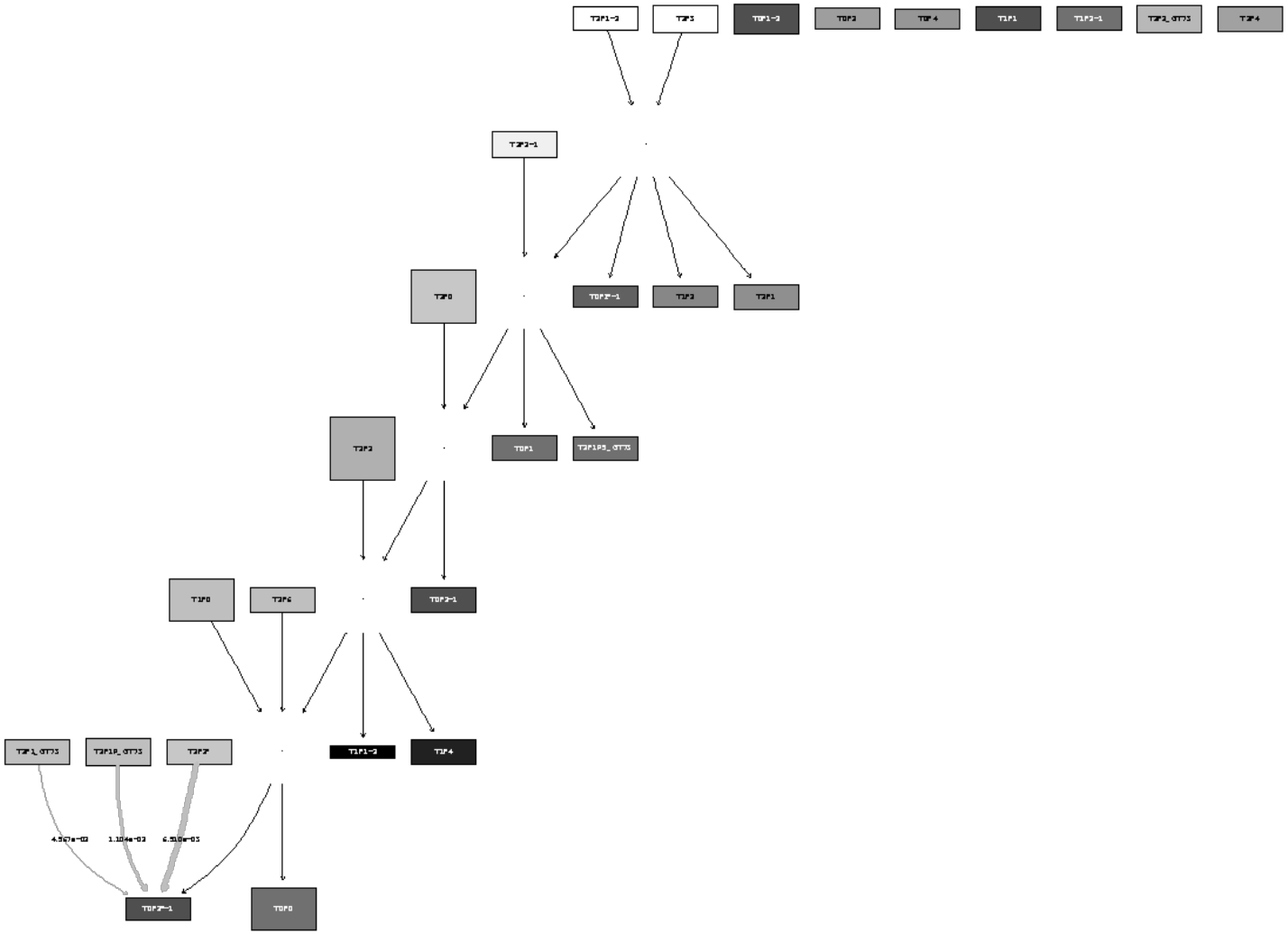


Figure 3.67 Hasse diagram representation of post-hoc tests for treatment differences in PAI in measured height (2002-2012). The position of group vertices in the chart is representative of the magnitude of the variable. The box sizes are proportional to treatment group sample sizes. Where significance is less than 0.05 line weight is inversely proportional to significance of the test and where lines do not connect treatments the two treatments are not significantly different. To simplify the chart connections are compressed using a point symbol

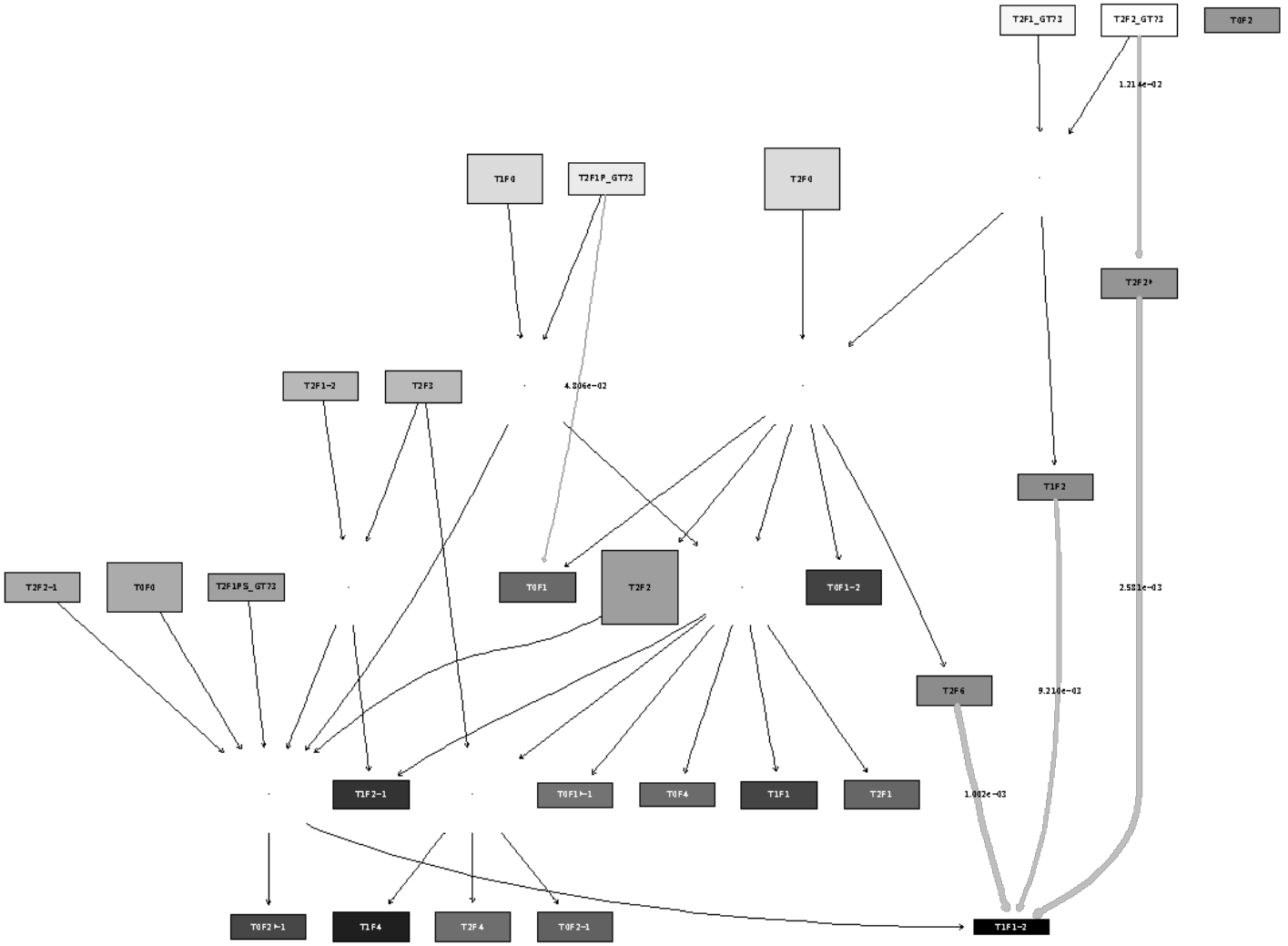


Figure 3.68 Hasse diagram representation of post-hoc tests for treatment differences in PAI(2002-2012)/MAI (1948-2002) in measured height. The position of group vertices in the chart is representative of the magnitude of the variable. The box sizes are proportional to treatment group sample sizes. Where significance is less than 0.05 line weight is inversely proportional to significance of the test and where lines do not connect treatments the two treatments are not significantly different. To simplify the chart connections are compressed using a point symbol

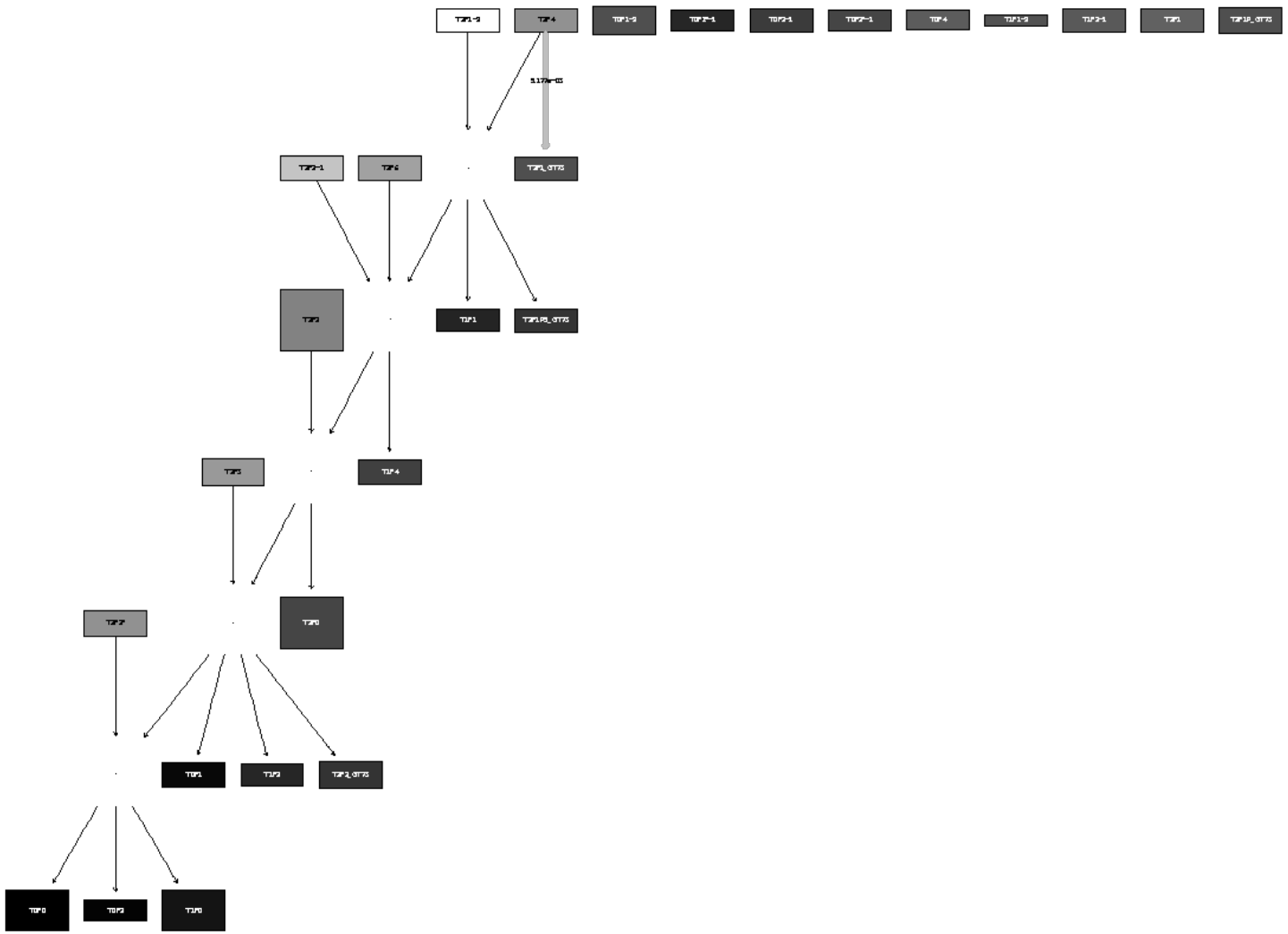


Figure 3.69 Hasse diagram representation of post-hoc tests for treatment differences in MAI(1948-2012) in volume with measured height . The position of group vertices in the chart is representative of the magnitude of the variable. The box sizes are proportional to treatment group sample sizes. Where significance is less than 0.05 line weight is inversely proportional to significance of the test and where lines do not connect treatments the two treatments are not significantly different. To simplify the chart connections are compressed using a point symbol



Figure 3.70 Hasse diagram representation of post-hoc tests for treatment differences in PAI(2002-2012) in volume. With measured height The position of group vertices in the chart is representative of the magnitude of the variable. The box sizes are proportional to treatment group sample sizes. Where significance is less than 0.05 line weight is inversely proportional to significance of the test and where lines do not connect treatments the two treatments are not significantly different. To simplify the chart connections are compressed using a point symbol

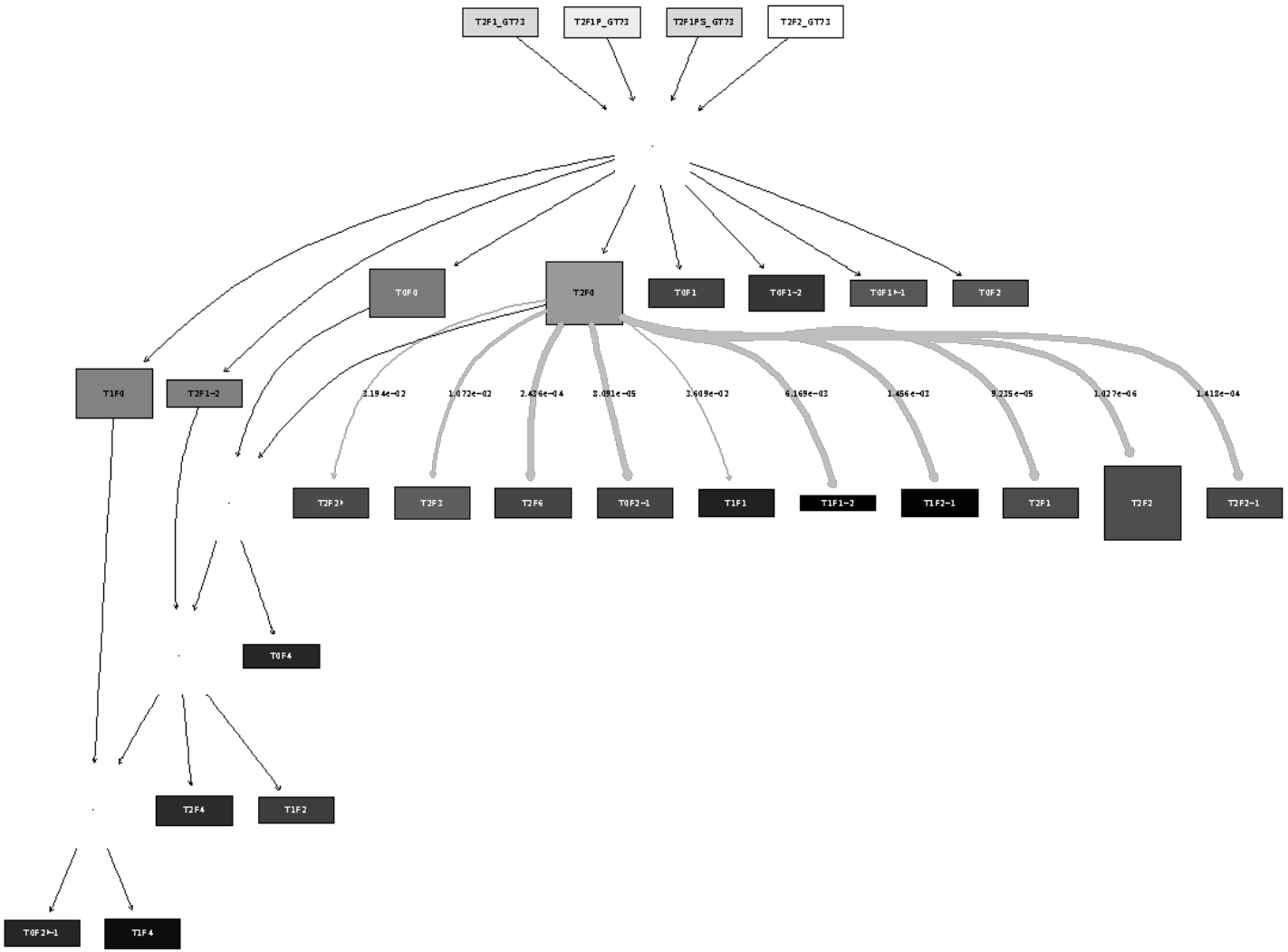


Figure 3.71 Hasse diagram representation of post-hoc tests for treatment differences in PAI(2002-2012)/MAI(1948-2002) in volume. With measured height The position of group vertices in the chart is representative of the magnitude of the variable. The box sizes are proportional to treatment group sample sizes. Where significance is less than 0.05 line weight is inversely proportional to significance of the test and where lines do not connect treatments the two treatments are not significantly different. To simplify the chart connections are compressed using a point symbol

Tree heights were estimated from DBH stratified by plots and by treatments and by year (2002 and 2012). Linear regression models were built with quadratic and natural log forms and, as CFS has done in the past, a Weibull form, which was fit with non-linear least squares regression [118]–[121]. Functional forms were summarized by their respective average residual standard errors, which suggested that for the 2002 plot data, the Weibull form contained marginally less error than the other forms (quad, log, Weibull: 1.010, 1.009, 1.008) and that stratification by plots produced less error than stratification by treatments (average Weibull plot model RSE: 1.008, average Weibull treatment model RSE: 1.300). The intention was to apply the plot specific model that produced the minimum RSE. However, since the prediction of unmeasured heights would potentially exceed the data range for which the models were built, the extrapolation could produce biases based on model form. The intercept was computed for all plot based log models and ranged from roughly -15 to 5m with a median of -3.9m. Therefore, in instances of low DBH, log models would, on average, produce a negative bias on heights. In light of this observation, both the log and quadratic models were recomputed to force a 1.3m intercept (Eq. 14-15), which the Weibull form had already accounted for (Eq. 13).

$$Ht = 1.3 + b1(1 - e^{b2 \cdot DBH^{b3}}) \quad \text{[Equation 13]}$$

$$Ht = 1.3 + e^{(b1 \cdot ln\,(DBH) + b2)} \quad \text{[Equation 14]}$$

$$Ht = 1.3 + b1 \cdot DBH + b2 \cdot DBH^2 \quad \text{[Equation 15]}$$

The rationale behind this static intercept is the fact that diameters are measured at 1.3m above ground, thus the DBH of any tree less than 1.3m is zero. The differences in the models were investigated further for the likelihood of unfit extrapolations. The quadratic form tended to have quite large second order coefficients, which produced unrealistic fits,

while the log and the Weibull forms appeared to preserve reasonable upward and downward extrapolations. According to the average RSE, the transformation to include a static intercept increased the residual error in both the log and quadratic forms. The RSE of the transformed log model increased to 1.030m thus the Weibull model was still slightly better than the transformed log model. However, 38 of the 59 plot model comparisons (four plots had un-converged Weibull models, thus 59/63 possible comparisons) had lower standard errors in the transformed log models over the Weibull function. On a plot model basis the transformed log models were the best-fit option in 38 plots, (Weibull: 17, quadratic: 8). There was very little difference visible between the Weibull and transformed log plot based models. However, once the unmeasured heights were estimated with both the Weibull and the transformed log equations, it became clear that the Weibull produced a greater curvature at the lower end of the DBH range, which appeared to agree better with the measured observations (Fig. 3.72). The log form produced a very steep slope from the intercept to the first integer cm in DBH. For the first integer increment in DBH, the log models produced height increments that ranged from 3.1 to 10.4m (median: 6.0m), relative to the Weibull increments from 1.5 to 9.2m (median: 4.6m). This observation suggested that the approach to preserving the static intercept for the log equation was insufficient to capture the physical relationship at low DBH. Given that the training data did not sufficiently sample the low DBH range, numeric least squares approaches without practical growth considerations would fail to capture the true functional form. The Weibull function was selected as the most appropriate function for describing the diameter-height relationship, as further modification of the log form would only narrow the functional differences between the

two equations. From the perspective of both the minimal RSE and extrapolation for model selection, the Weibull function was selected as superior in both the plot and treatment specific diameter-height models for 2002. In the four instances where the non-linear least squares Weibull fitting did not converge (plots: 14, 52, 58, 60), the transformed log form was used in extrapolation.

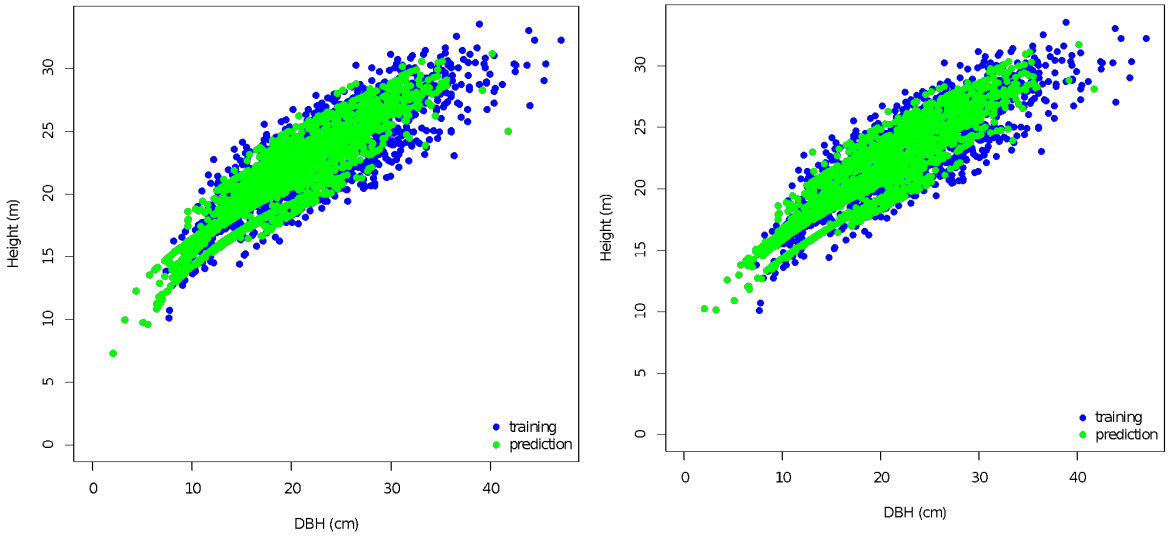


Figure 3.72 Comparison of measured and modeled tree height from the plot specific Weibull function(left) and a modified log function (right). Using the 2002 field data, the Weibull form better captures the lower DBH trend with height, a low-density data space that is unlikely to be represented by statistical approaches alone.

Modeling tree heights in the 2012 dataset mirrored that of the 2002 data, where the Weibull form produced slightly better average residual standard errors relative to the log and quadratic forms (with 1.3m intercepts). The average residual standard error for the plot specific models was 1.20, 1.25 and 1.39m for the Weibull, log, and quadratic respectively. The treatment specific models followed the same trend as the plot models with respect to average RSE but contained slightly larger errors, 1.49, 1.52, 1.69 for the Weibull, log and quadratic respectively. Again, the Weibull function was selected over the other forms for its more gradual curvatures at both high and low DBH levels as well as its low RSE. In two instances, namely plots 14 and 31, the Weibull function did not

converge on a parameter solution. In plot 14, the DBH range was small and heights were quite variable, the log form produced a low curvature coefficient and biased the predictions to larger heights than the data spread supported, the quadratic form was selected in this case. For plot 31 the log form was selected for its fit and low RSE. Figure 3.73 illustrates the measured and modeled tree heights produced from plot specific and treatment specific analysis (See Appendix 3 for individual plot models).

The advantage of the treatment plots over the plot specific models is the assumption of normality can be relaxed in the treatment specific models because of the larger number of observations (n>30), while the plot specific models were built with as few as 18 observations. The Shapiro-Wilk test was run on the plot specific model residuals and identified violations of normality. Non-normal residuals were found for the 2002 pooled plot model and plots: 39, 43, 13, and 25, with significance values of 0.00002, 0.0001, 0.036, 0.045, 0.046 respectively. Non-normal residuals were found for the 2012 pooled plot model and plots: 39, 65, 45 and 4, with significance values of 0.0001, 0.003, 0.007, 0.011 and 0.032 respectively. The source of the departure from normality was largely (6/10 departures) attributed to one or few residual outliers, while the remainder, including the plot pooled models, appeared to be caused by slightly negative skewed residual distributions, where there were a greater number of small magnitude underestimates and fewer but larger magnitude overestimates. Further, the lower sample size reduces the statistical power of the linear regression and increases β, the probability of a type II error, incorrectly retaining the null. The extrapolation of lower height and DBH was better fit by plot specific models than the treatment specific models. This is likely the effect of data space density as the concentration of data increases, the

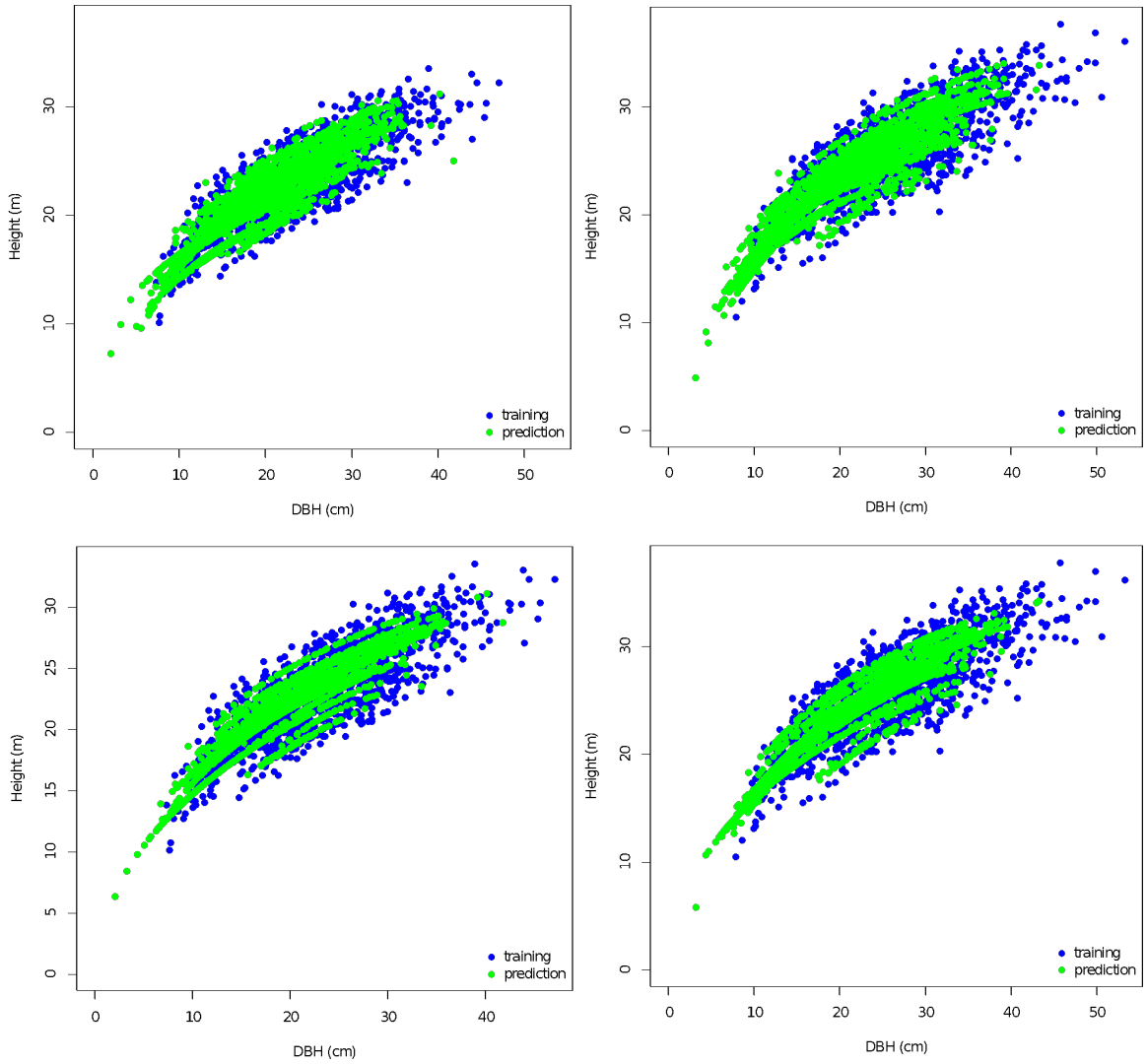


Figure 3.73 Comparison of measured and modeled tree heights, models build at the plot level are illustrated in the upper row while models fit with treatment stratification are illustrated in the second row. The 2002 data are depicted in first column while the 2012 data are shown in the second column. Smaller residuals were produced in the plot fit models than the treatment specific models and the extrapolation of the plot models appeared to fit low range observations better.

lower probability range (low DBH) produces less influence on the ultimate model and thus the estimates can deviate from the few observations that occur at the low DBH/height space. Unmeasured heights were estimated by plot specific Weibull models, barring the exceptions for unconverged fits. With these computed heights, volume increments were reassessed.

With the newly computed height and volume attributes, the ANOVA script was executed but did not alter conclusions of the statistical tests suggesting no considerable sampling bias was present in the trees selected for height measurements (Table 3.8 & 3.9). The post-hoc tests, however, revealed much more structure than those produced from data with only measured heights, perhaps the effect of increased sample size on statistical power. The PAI in volume in particular produced many more significant treatment comparison tests relative to the same results produced from only observations with measured heights. The PAI in volume was again clearly tied to differences in treatment levels (Fig. 3.74). There was clear separation of the T2 thinning treatments, which in most cases had exhibited statistically significant greater volume growth than the T1 and T0 treatments. The exceptions were treatments T1F2-1, T1F1-2 and T0F4, which were not significantly different from all the T2 treatments (Fig. 3.74 & 3.75). These analyses demonstrated that there was an ordinal structure in productivity that was associated with the thinning and fertilization treatments. The PAI of volume between the 2002 and the 2012 CFS field sampling campaigns was considered a viable metric for investigating productivity from remote sensing metrics. For plot based productivity attributes, PAI and MAI of plot basal area were computed along with PAI and MAI of plot total volume. In contrast to median volume increments where observations were required to be living in both 2002 and 2012, plot based productivity metrics were generated from all living observations. For example, stems living in 2002 but dead in 2012 contributed to the 2002 metric but not that in 2012 thus accounting for reductions in productivity. However, it is noted that this estimate of growth is an underestimate when plots experience mortality in large stems. When considering a periodic interval during

which a mortality event for a large tree has occurred, the whole volume of the dead tree would be incorporated into the volume increment. This mortality event produces an underestimated growth increment because, as explained in Oliver & Larson [30], it incorporates volume that was produced outside the periodic interval being considered. This effect is particularly evident in plot basal area and volume where plots had experienced root disease mortality. While root disease mortality was present (n<=2) in plots 57, 63, 64, 68, 69, and 70, plot 67 had seven such events, which had reduced 2012 volume by 3.16m^3; a value that represents 30% of the living plot volume in 2012 (plot 67 PAI of total living volume: -0.006 m^3/yr., dead or alive: 0.310 m^3/yr.).

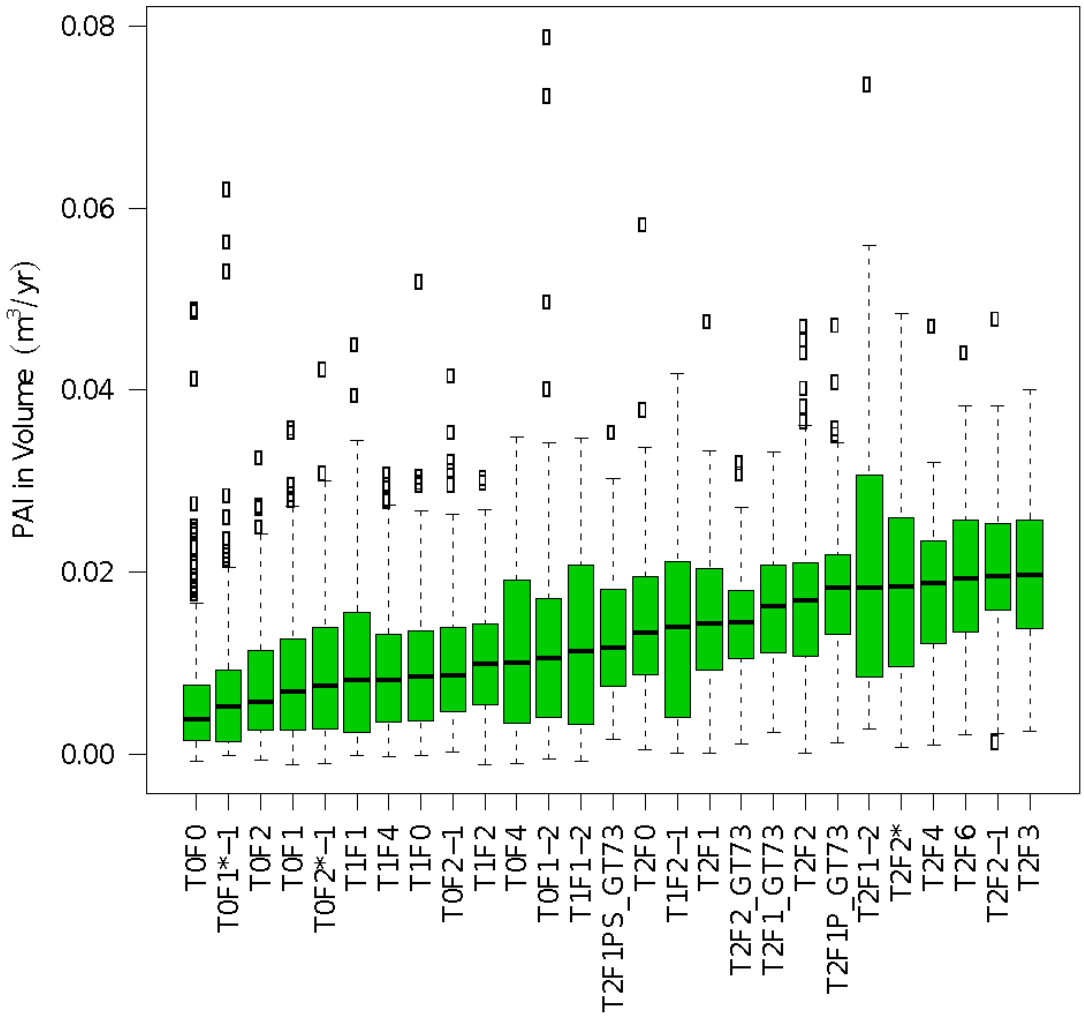


Figure 3.74 Periodic annual increment (2002-2012) in volume stratified by treatment illustrates an apparent association with treatment levels. This metric is appropriate for the individual stems but omits information on plot occupancy and is therefore not appropriate for plot level analysis.

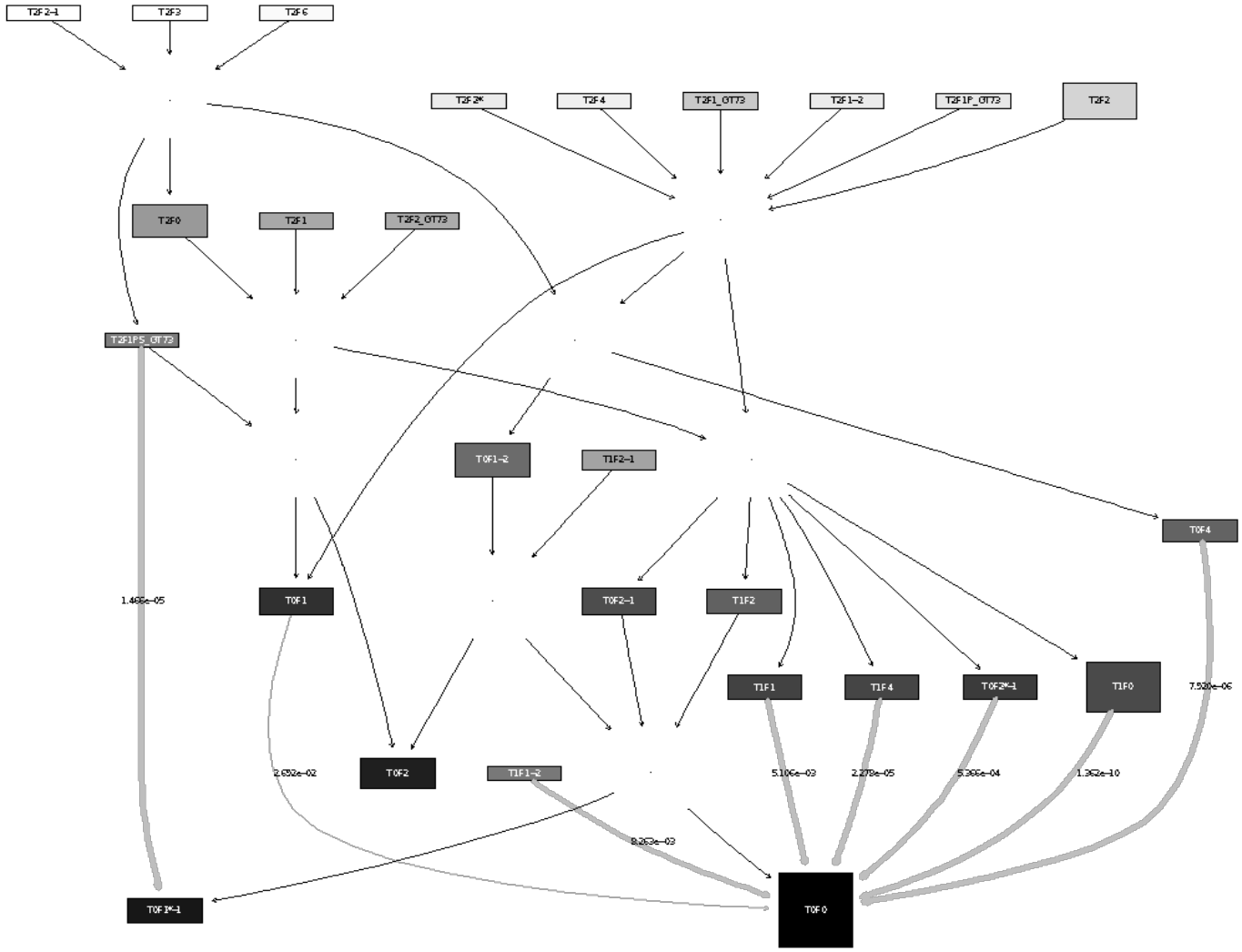


Figure 3.75 Hasse diagram representation of post-hoc tests for treatment differences in PAI(2002-2012) in volume. with measured and estimated height The position of group vertices in the chart is representative of the magnitude of the variable. The box sizes are proportional to treatment group sample sizes. Where significance is less than 0.05 line weight is inversely proportional to significance of the test and where lines do not connect treatments the two treatments are not significantly different. To simplify the chart connections are compressed using a point symbol

Stratifying the CFS database by plots; forest productivity was investigated with the same approach applied to the treatments. Boxplots suggested, in agreement with the treatment analysis, that there was an apparent treatment influence on the diameter and measured height increments (Fig. 3.76 and 3.77 and Table 3.9 see Appendix 3.1.3 for plot based boxplots). As expected, the plot differences were greater in the MAI than the PAI metrics. There was considerable overlap in the plot volume increments when only the observations from measured trees were applied. There was greater separation between plot volumes when measured and modeled heights were applied. However, plot 41 (T2F1-2) drastically stood out as the most productive plot in terms of volume production on an individual basis (median PAI in volume). The boxplot comparison of MAI in measured height growth isolates plot 41 as having exceptionally high height growth. Given the position of this plot and its proximity to topographic contours indicating potential moisture flow accumulation, it was hypothesized that plot 41 may be benefitting from greater shoot extension and growth duration as a result of reduced water stress in dry summer months [122], [123]. Further evidence for this suspicion was provided when investigating the distribution of plot maximum PAI in volume, where plots 41 and the adjacent plot 34 were identified as outliers with maximum PAI in volume greater than 1.5 times the IQR from the third quartile. Although not an outlier by the above definition, plot 36 was the next largest maximum PAI volume and is located south of plot 34 and parallel with the suspected drainage feature. In addition, plots 41, 34, 35 and 36 corresponded to the 100, 98.4, 92.1 and the 88.9^{TH} percentiles of the plot maximum height in 2012 (n=63). As a result of these observations it was considered important to investigate lidar terrain metrics and especially the topographic wetness index, with

reference to productivity. As with previous analysis stream, the post-hoc tests were run and plot differences were determined and are illustrated in figures 3.78 to 3.80. Particular attention was given to plot differences in periodic volume increments. Larger mean PAI in volume was associated with more aggressive treatment levels.

Table 3.9 Assessment of growth differences between plots

Metric	Shapiro	Plot Norm	Bartlett	B-Forsyth	ANOVA-F	K-Wallis
MAI-DBH	0.994**	45/63	327.7**	3.86**	19.89**	897.90**
PAI-DBH	0.963**	35/63	197.8**	2.61**	12.25**	607.78**
PAI/MAI-DBH	0.281**	27/63	6094.8**	4.04**	4.36**	593.56**
MAI-HT†	0.998 (0.09)	56/63	106.6**	1.44*	14.52**	527.47**
PAI-HT†	0.986**	50/63	147.3**	1.75**	5.56**	284.79**
PAI/MAI-HT†	0.987**	50/63	161.3**	1.42*	7.26**	353.81**
MAI-VOL†	0.923**	45/63	222.0**	2.13**	4.36**	232.46**
PAI/MAI-VOL†	0.993**	53/63	137.2**	2.30**	8.85**	378.23**
MAI-HT††	0.998*	41/63	207.4**	2.96**	57.79**	1578.34**
PAI-HT††	0.961**	22/63	406.0**	3.91**	18.11**	953.57**
PAI/MAI-HT††	0.935**	17/63	503.7**	3.38**	18.71**	1040.30**
MAI-VOL††	0.916**	34/63	551.4**	4.78**	21.18**	987.31**
PAI -VOL††	0.914**	29/63	512.8**	4.80**	13.75**	726.79**
PAI/MAI-VOL	0.991**	44/63	308.4**	5.04**	15.67**	693.17**

ANOVA assumption test for normality by Shapiro-Wilk test without plot grouping (Shapiro) and stratified by groups (Plot Norm: number of non-significant tests/number of plot tests) demonstrate a non-normal tendency. ANOVA assumption tests for variance homogeneity by the parametric Bartlett test and the non-parametric Brown-Forsyth test demonstrate that equal variance cannot be assumed. The non-parametric ANOVA by the Kruskal-Wallis test is appropriate in each of the three metrics. At least one grouping (plot) is different from the others in each tested metric. Significance >0.05 are in parentheses, *:$p<0.05$, **$p<0.001$, † attribute derived from measured heights only, †† attribute derived from measured and modeled heights

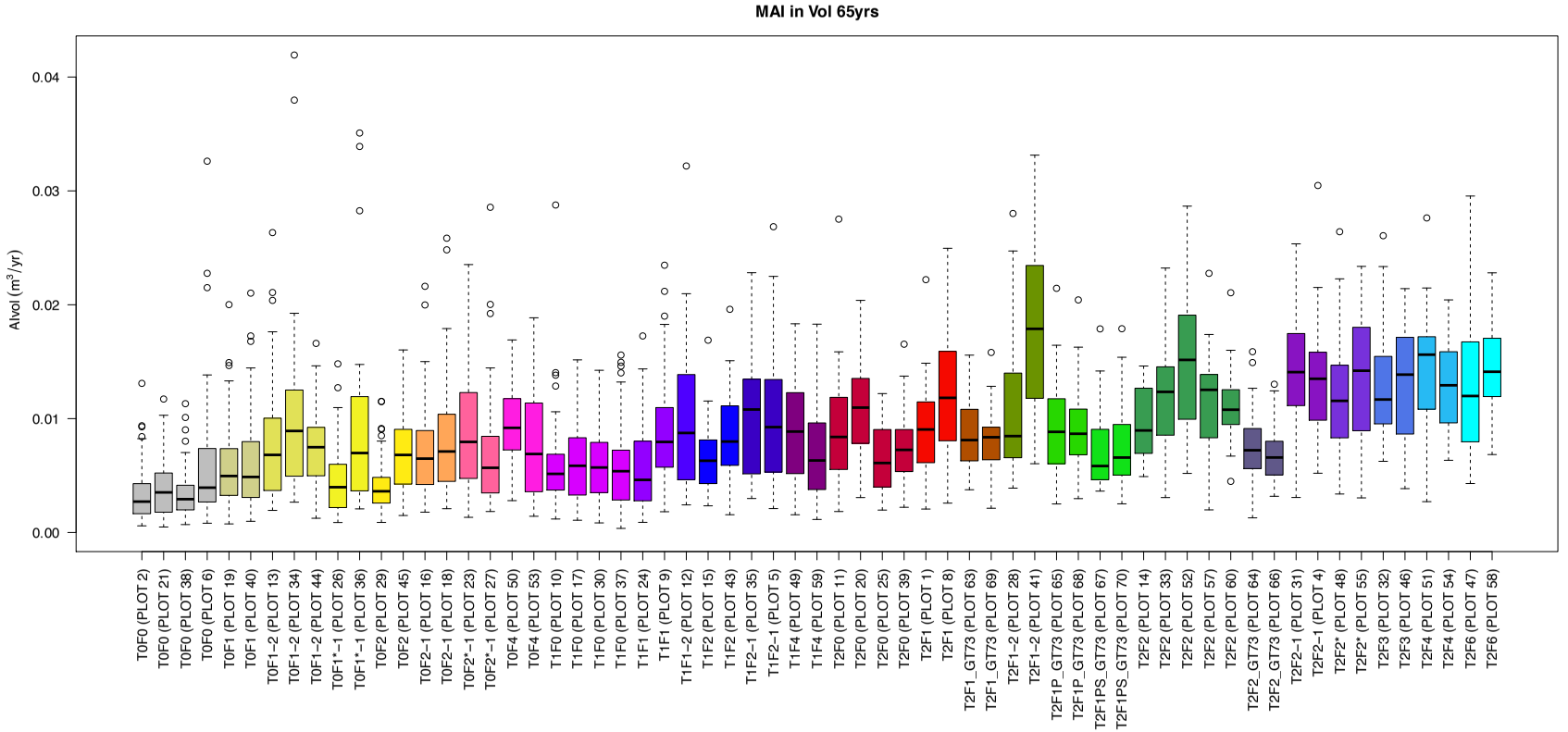


Figure 3.76 Boxplots of MAI of volume with measured and modeled height illustrating differences in central tendency and spread. The data are graphed by quartiles, the largest and smallest point no greater than 1.5*(IQR) from the quantiles (0.25, 0.75) and all points greater than those limits. Although the treatments are indicated in the data labels they are also color coded to ease the use of such a large number of distributions.

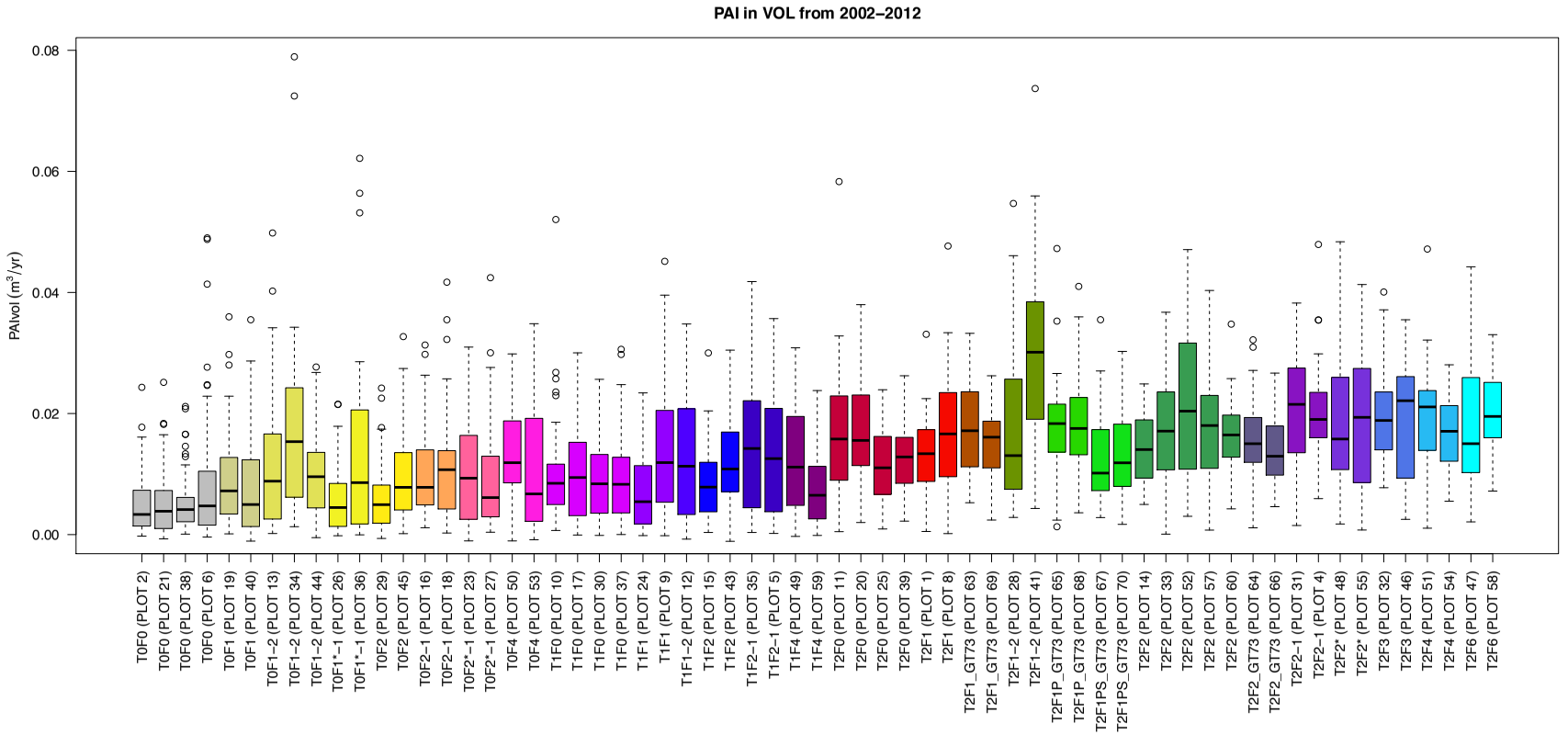


Figure 3.77 Boxplots of plot PAI of volume with measured and modeled height distributions illustrating differences in central tendency and spread. The data are graphed by quartiles, the largest and smallest point no greater than 1.5*(IQR) from the median and all points greater than those limits. Although the treatments are indicated in the data labels they are also color coded to ease the use of such a large number of distributions.

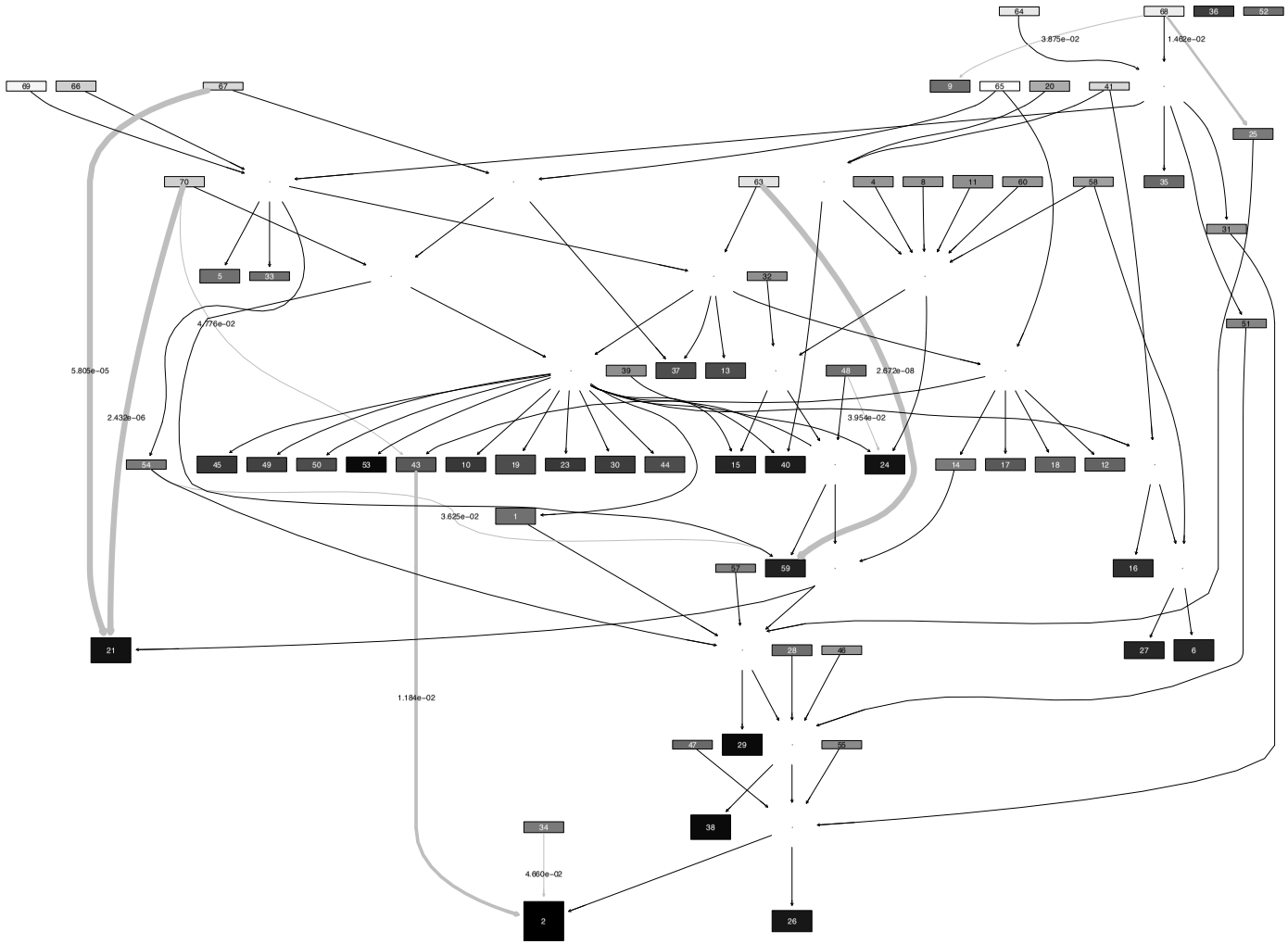


Figure 3.78 Hasse diagram representation of post-hoc tests for plot differences in PAI(2002-2012) in DBH The position of group vertices in the chart is representative of the magnitude of the variable. The box sizes are proportional to sample sizes. Where significance is less than 0.05 line weight is inversely proportional to significance of the test and where lines do not connect groups the two groups are not significantly different. To simplify the chart connections are compressed using a point symbol

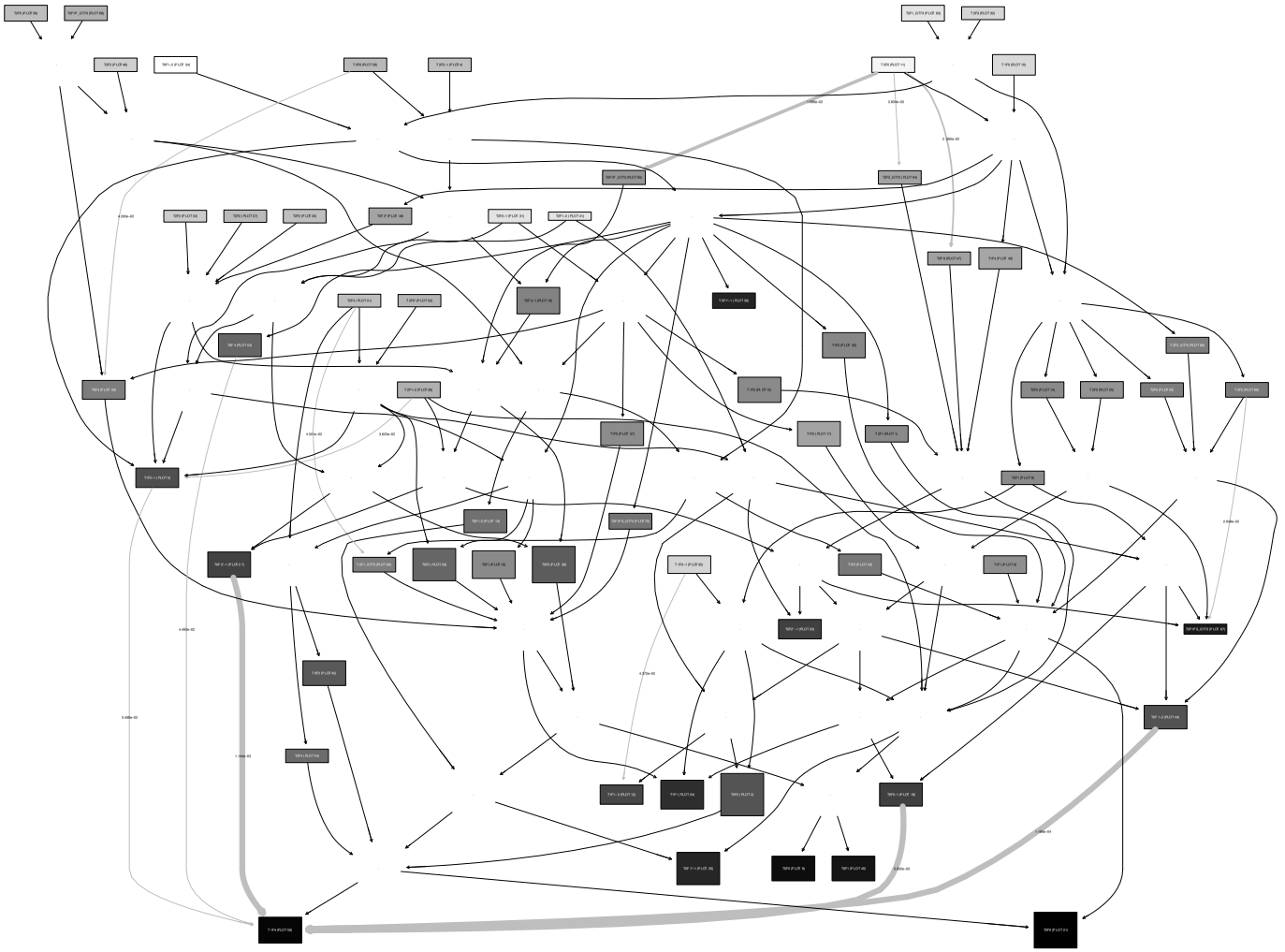


Figure 3.79 Hasse diagram representation of post-hoc tests for plot differences in PAI(2002-2012) in measured and modeled height The position of group vertices in the chart is representative of the magnitude of the variable. The box sizes are proportional to sample sizes. Where significance is less than 0.05 line weight is inversely proportional to significance of the test and where lines do not connect groups the two groups are not significantly different. To simplify the chart connections are compressed using a point symbol

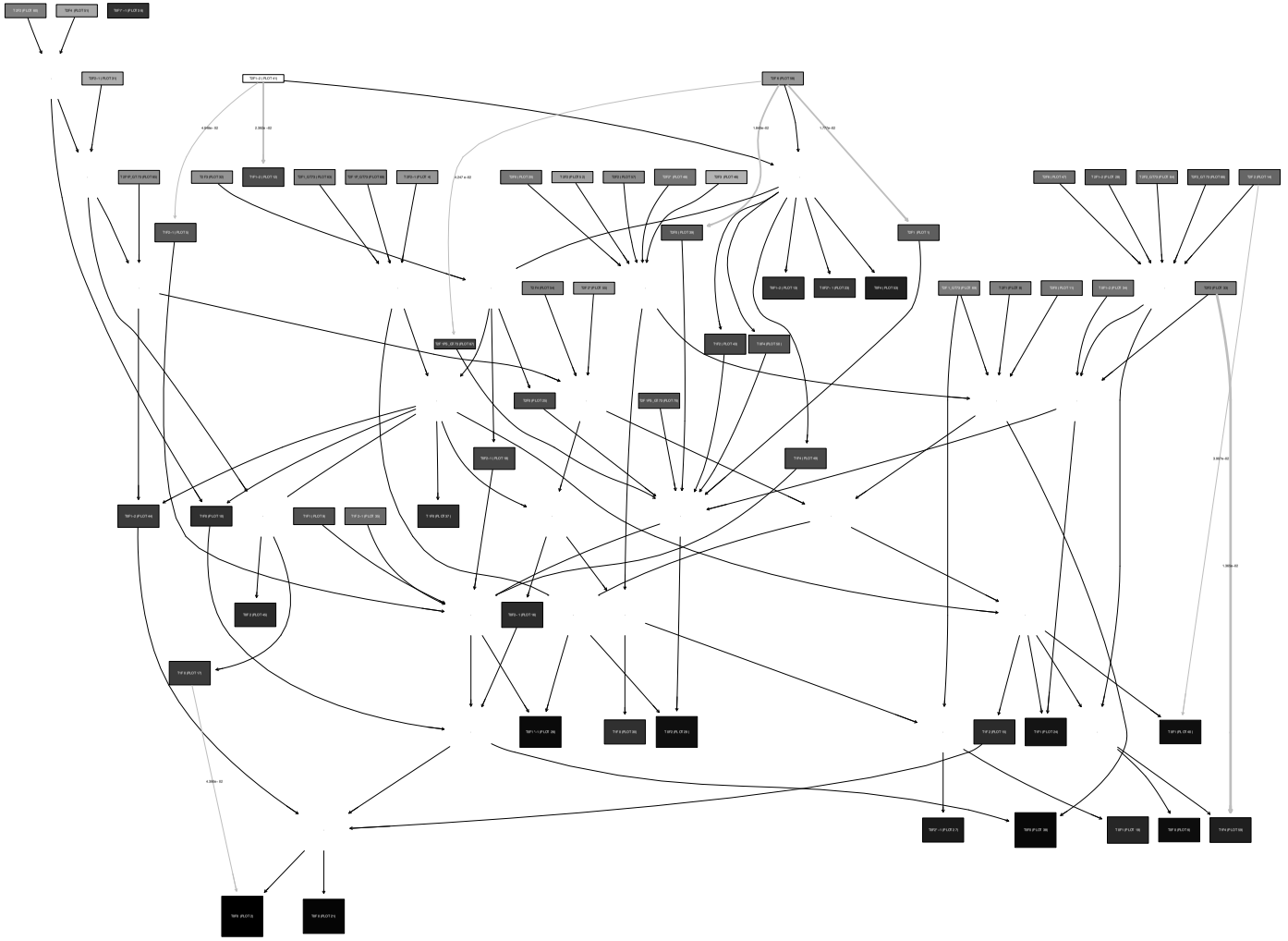


Figure 3.80 Hasse diagram representation of post-hoc tests for plot differences in PAI(2002-2012) in volume from measured and modeled height The position of group vertices in the chart is representative of the magnitude of the variable. The box sizes are proportional to sample sizes. Where significance is less than 0.05 line weight is inversely proportional to significance of the test and where lines do not connect groups the two groups are not significantly different. To simplify the chart connections are compressed using a point symbol

Interestingly, in many cases there seemed to be little treatment level coherence in periodic volume increments, like that of T2F1-2, yet others, like the control and T1F0, seemed to converge on roughly the same ranges. This observation, in addition to the assumed spatial autocorrelation that is to some degree expected, marks a violation of the statistical assumption of observation independence. The fact that there is some degree of variance explained by the treatment levels suggests that a linear mixed model or the similar should be applied. Initially, a random block ANOVA was considered as the appropriate test to continue with the processing stream established but was of limited use given the unbalanced nature of the plot factor. A linear mixed model was used to explore volume increment as a function of the fixed effects of treatment and the random effect of the plots.

The PAI in volume was strongly skewed (1.31) to larger increments and as an alternative to the non-parametric approach taken, the data were easily transformed to near normal with a square root and refined further with a 0.52 power by evaluating changes in histogram distribution (Fig 3.81). Investigating the transformation revealed that there was an apparent difference in the volume increment distributions between thinning treatments. The control, with respect to the T1 and T2 treatments was considerably more positively skewed (Fig. 3.82). This could have been expected for the T0 treatment, as the individuals would diverge into their respective crown classes earlier in time. It would be expected that the few individuals within the dominant crown class would be experiencing greater volume increments than the many suppressed to co-dominant individuals. Plotting histograms provided evidence that the different crown classes had caused the non-normality in the volume increment distribution of the T0 treatment (Fig. 3.83).

Homogeneity of variances in the transformed volume increments across plots could not be assumed, as per the significant Bartlett and Brown-Forsythe tests (K^2:298.48 p: $<2.2e^{-16}$ & F=4.99 p: $<2.2e^{-16}$) Additionally, the crown class pattern was apparent in the PAI/MAI plots (Fig. 3.84) providing further evidence that the crown class variable contained information on productivity, or more importantly for this analysis that the PAI of volume captured information on productivity.

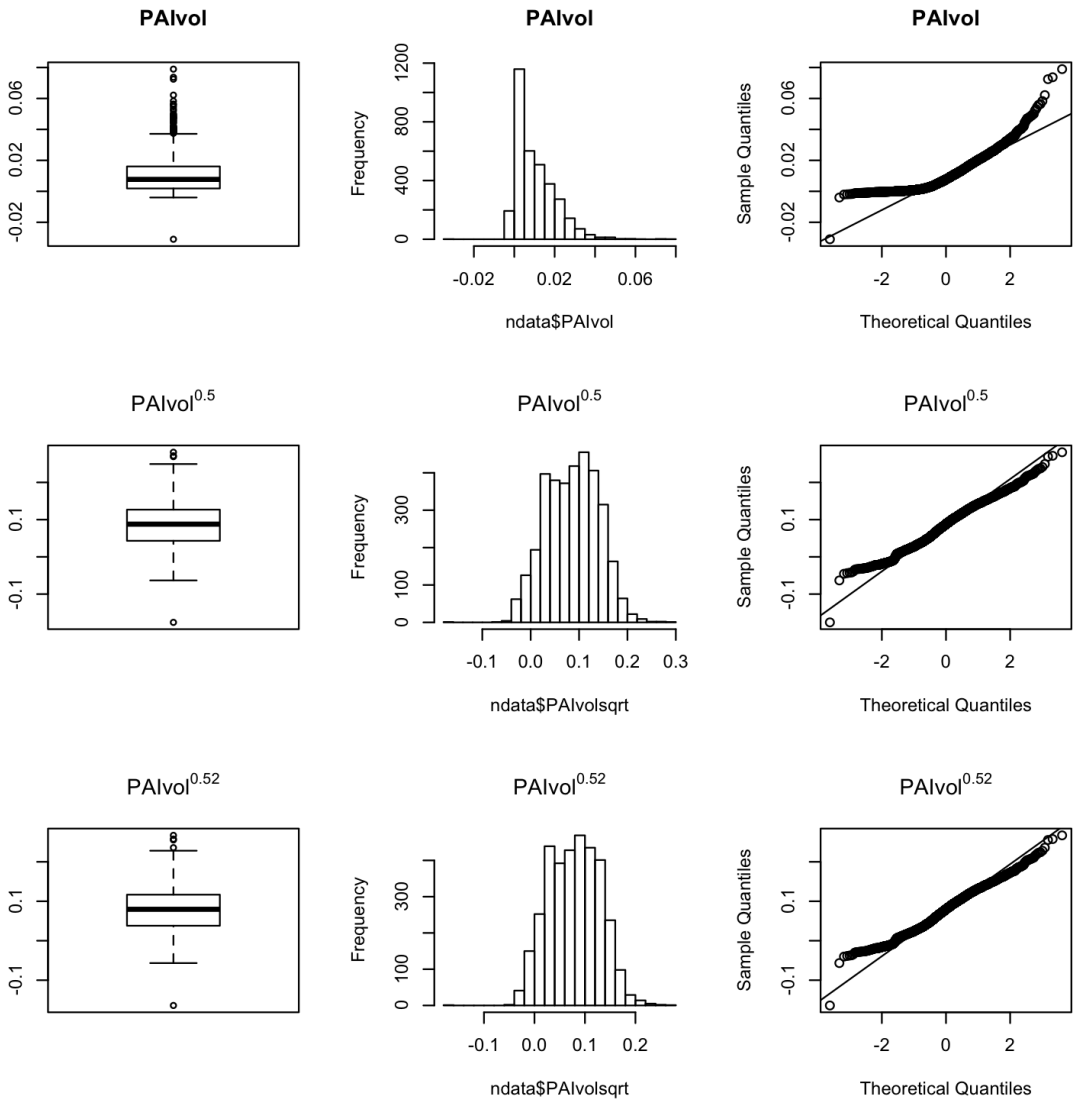


Figure 3.81 The distribution of the PAI of volume was positively skewed, with a squareroot transformation the PAI distribution became more approximately normal.

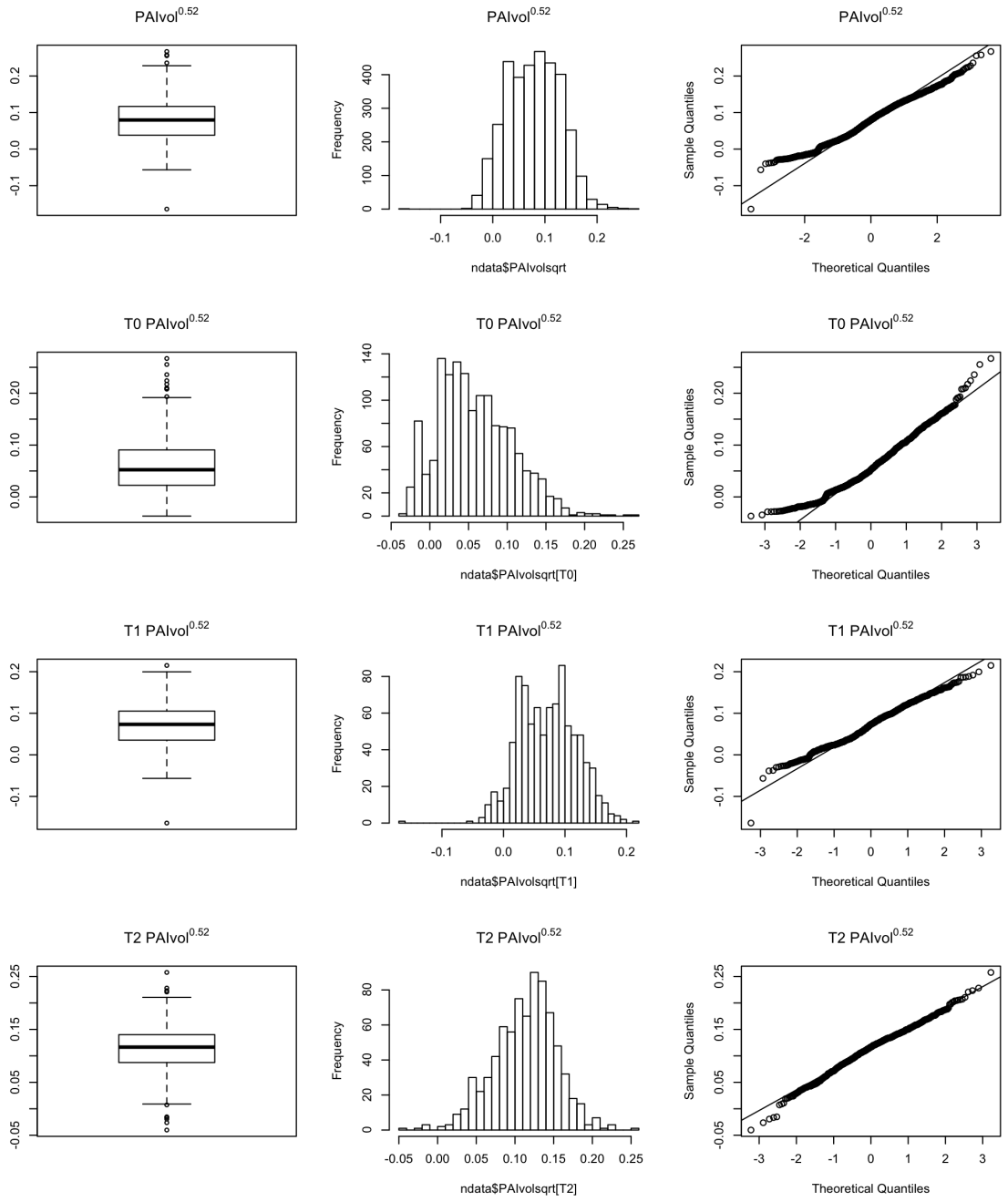


Figure 3.82 The shapes of the PAI in volume distributions were different according to the thinning treatments. The control group was clearly more positively skewed than either of the T1 or T2 treatments. Rows one through four depict distributions for all plots, T0, T1 and T2 thinning treatment plots respectivley.

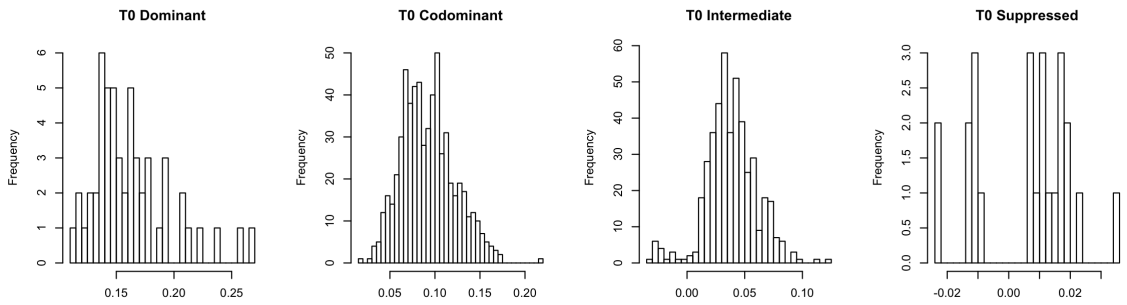


Figure 3.83 Distributions of PAI in volume stratified by crown class might suggest that the source of the departure from normal shapes could be attributed to the different crown classes

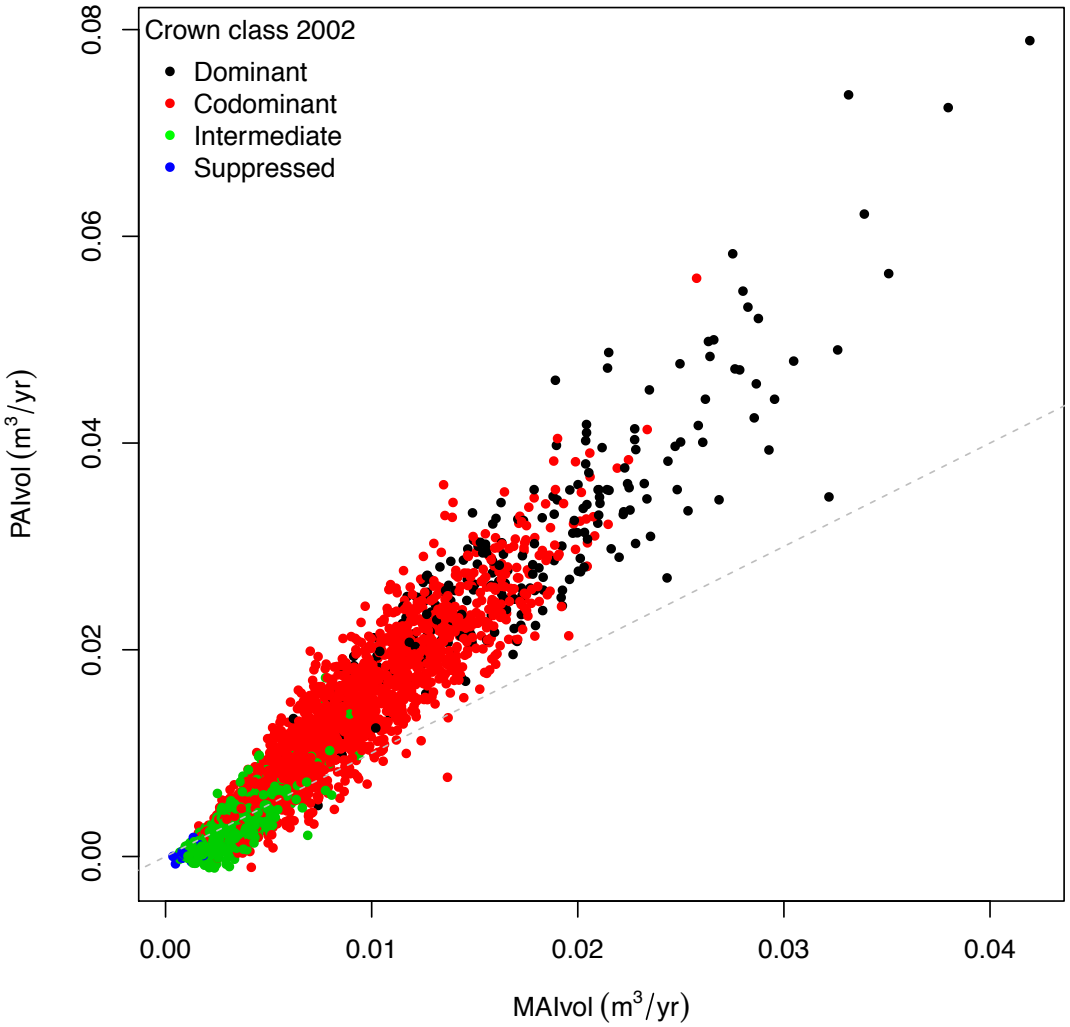


Figure 3.84 The PAI and MAI data space coloured by crown class illustrated that crown class, for obvious reasons, contains important information related to productivity. It would be valuable to estimate crown class from RS data in order to derive information about tree level productivity.

The treatment factor was transformed into ordinal thinning and fertilization variables and a repeated fertilization variable was dummy coded to 0, 1 and 2 for no repeat, 1981 and the 1990 re-fertilizations respectively. In addition the plot establishment year and the crown class attributes were considered. The plot attribute was coded as the random effect variable and a stepwise mixed-effect model with interactions was run. The possibility of an interaction effect between fertilization and thinning was expected and as such all interactions were evaluated. Ultimately, feature selection based on backward selection and an alpha level of 5% retained the thinning, fertilization, re-fertilization, crown class in 2012 and two unexpected interaction terms thinning with crown class and re-fertilization with crown class (Table 3.10). The correlation matrix suggests there is little multicollinearity as only the interaction variables with one of its corresponding individual variables produce coefficients as high as -0.569. Surprisingly, the treatment interaction, which was the justification for including interactions at all, was eliminated from the final model on the fourth iteration, out of a total of ten iterations. The included interaction terms imply that volume increments are dependent on thinning (or re-fertilization) and the slopes of those effects change with crown class. The crown class attribute further characterizes the local condition for the individual observations (trees) as the factor thinning clearly only accounts for plot based density. All fixed effects had coefficient signs that were in line with expected responses - note that crown class is coded from 0-3 for dominant, co-dominant, intermediate and suppressed respectively and is therefore inverted with respect to volume increment. In addition to the intercept random effect presented here, a slope term was also evaluated for both thinning and fertilizer with respect to the plot factor. Models including the slope coefficients for the

random effect of plot did not reduce residual variance sufficiently to warrant the more complex approach. The unaccounted for residual variance was unchanged between the two models and the likelihood ratio test for two slopes were both not significant (p:>0.9). This was also true for a random effect slope for the individual treatment case (T or F) with respect to plot, that is, only one random effect slope coefficient for either thinning or fertilization. Although the likelihood ratio test on the random effect intercept was significant (L.Ratio: 121.79, p: 0.0001), the random effect of plot accounted for very little variation in the periodic volume increment (st.dev: 0.0091), which called into question the merit of the more complex mixed effect model. The equivalent model was built without the random plot effect (Table 3.11) and the two output models were compared with the lmeTest::anova test, which is another implementation of the likelihood ratio test, which produced corroborating results. Although the between predictor correlations slightly increased for the GLM, the absolute correlations of non-interaction variables were less than 0.5. Additionally, the Akaike Information Criterion (AIC) index was -11908.19 for the GLM while the equivalent for the mixed effect model was -12027.98, therefore the generalized linear model was considered preferable over the mixed effect model. These models were built with a re-fertilization dummy variable that coded 0-3 as factors. The re-fertilization variable was changed to ordinal data as, the number of fertilization campaigns applied more fertilizer and thus has an ordinal structure and the greater fertilization was expected to produce an associated increase in productivity. The change in data type had no effect on feature selection for the mixed model and the resulting AIC was slightly increased from -12027.98 to -12048.06, suggesting that the multi-model output of the factor variable is less complex than the single model output

with the ordinal re-fertilization variable. In both cases the likelihood ratio test was significant indicating that the random effect of plot contributed to explaining variation in periodic volume increment. However, in each case that the linear mixed model was evaluated against the equivalent generalized linear model, the AIC was smaller for the GLM. However, the intent of applying the linear mixed effect model approach was to overcome the assumption of observation independence, by accounting for the plot factor as a random effect the dependence of spatial autocorrelation was mitigated. Removing any variables from the modeling process based on the significance of the F-statistic only increased the AIC index. However, for exploratory purposes all interactions were removed from the mixed model, the AIC decreased considerably from -12027.98 to -11994.57. The reduced complexity, however, came at the expense of residual error, where the median residual increased from 0.00030 to 0.00097 $((m^3/yr.)^{0.52})$. Irrespective of model performance, which is not the objective in this case, these analyses demonstrate that the productivity signal inherent in the treatment applications and the crown classes are captured in the derived periodic volume increments. Moving forward it could be reasonably assumed that periodic volume increment represents growth productivity.

Table 3.10 Periodic volume increment as a linear mixed model of treatment conditions and crown class while accounting for the random effect of plot, the model is fit by the restricted maximum likelihood (REML) approach

*REML crit.	BIC	loglik	AIC
-12050	-11961.57	6024.99	-12027.98

Plot random effect:		
Groups	Variance	Std Dev.
Plot (intercept)	0.00008	0.0091
Residuals	0.00114	0.0337

Treatment fixed effects:					
	Value	Std.error	DF	t-value	p-value
Intercept	0.0778	0.003	3045	25.60	0.0000
Thinning	0.0226	0.0018	50	12.2	0.0000
Fertilization	0.0029	0.001	50	2.83	0.0066
Refert 1981	0.0111	0.004	50	2.74	0.0085
Refert 1990	0.0204	0.005	50	4.11	0.0001
Crown class	-0.0088	0.0003	3045	-28.31	0.0000
Thinning : Crown class	-0.0026	0.0004	3045	-7.06	0.0000
Refert 1981 : Crown class	-0.0011	0.0006	3045	-1.84	0.0656
Refert 1990 : Crown class	-0.0045	0.0009	3045	-4.81	0.0000

Correlation:								
	(Intr)	THIN	FERT	Fert. 81	Fert. 90	C.class	Th:CC	Fert81:CC
Thinning	-0.557							
Fertilization	-0.447	-0.193						
Refert 1981	-0.406	0.271	-0.061					
Refert 1990	-0.316	0.039	0.140	0.164				
Crown class	-0.302	0.275	0.015	0.173	0.097			
Thin:CC	0.133	-0.343	0.007	-0.057	0.016	-0.569		
Refert81:CC	0.120	-0.073	-0.013	-0.341	-0.049	-0.439	0.177	
Refert90:CC	0.056	0.017	-0.010	-0.038	-0.364	-0.174	-0.087	0.097

Standardized within group residuals:				
Min	Q1	Median	Q3	Max
-6.85	-0.676	0.009	0.616	4.307
Number of observations: 3104				
Number of groups: 55				

t-tests use Satterthwaite approximations to degrees of freedom, * REML criterion were generated with the lme4::lmer function while log likelihood, Akaike information criterion and Bayesian information criterion where produced by lme::nlme function while random effects. The lme model was retained to enable the model comparison test lmerTest::anova, which produced a significant likelihood ratio test: 121.79, p: 0.0001.

Table 3.11 Periodic volume increment as a linear model of treatment conditions and crown class without a random effect for plot, the model is fit by the restricted maximum likelihood approach

AIC	BIC	loglik
-11908.19	-11847.82	5964.097

Treatment fixed effects:				
	Value	Std.error	t-value	p-value
Intercept	0.0766	0.0015	50.65	0.0000
Thinning	0.0224	0.0011	20.97	0.0000
Fertilization	0.0030	0.0005	6.31	0.0000
Refert 1981	0.0114	0.0022	5.06	0.0000
Refert 1990	0.0202	0.0029	6.95	0.0000
Crown class	-0.0087	0.0003	-28.00	0.0000
Thinning : Crown class	-0.0026	0.0004	-7.24	0.0000
Refert 1981 : Crown class	-0.0011	0.0006	-1.80	0.0724
Refert 1990 : Crown class	-0.0047	0.0010	-4.90	0.0000

Correlation:								
	(Intr)	THIN	FERT	Fert. 81	Fert. 90	C.class	Th:CC	Fert81:CC
Thinning	-0.558							
Fertilization	-0.393	-0.176						
Refert 1981	-0.408	0.236	-0.067					
Refert 1990	-0.279	0.003	0.100	0.148				
Crown class	-0.655	0.500	0.048	0.336	0.182			
Thin:CC	0.307	-0.632	0.001	-0.117	0.023	-0.562		
Refert81:CC	0.265	-0.135	-0.035	-0.656	-0.092	-0.426	0.168	
Refert90:CC	0.118	0.029	-0.022	-0.073	-0.656	-0.170	-0.089	0.093

Standardized residuals:				
min	Q1	median	Q3	Max
-6.99	-0.676	-0.005	0.635	4.801
Residual standard error: 0.0348				
Number of observations: 3104				

Model is fit by nlme::gls linear model using generalized least squares with the restricted maximum likelihood approach by maximizing the restricted log likelihood. The generalized linear model is very similar to the linear mixed effect model and has a lower Akaike Information Criterion index..

Having established that the periodic annual volume increment captured a productivity signal, efforts were then refocused to investigate whether the structural data within the CFS database could also inform on productivity. DBH attributes were omitted, as this type of information was deemed inaccessible from remote sensing data. Attributes included in the test included height in 2012, crown class, stem density as represented by the number of core stems per plot, and a series of proximity metrics derived from the relative survey coordinates. The proximity metrics were included as they were expected

to capture between crown competition for resources. The distance to the nearest neighbour and the mean distance to the nearest three neighbours were included as a more local representation of stand density, the K nearest neighbour was intentionally kept small as to avoid edge effects. The height differences between the adjacent trees were determined as this could inform on crown dominance. It was calculated for the closest neighbour (K-1) and as a mean difference of the three nearest neighbours (K-3), although the K-1 neighbour metrics (distance and height differential) was abandoned as it would contribute to multicollinearity. Interaction variables were included as the height differential was expected to be less important as distances increased. The backward feature selection by F-stat significance eliminated all but 5 interaction variables, which again were difficult to conceptually justify. Interaction terms were produced for crown class with height, crown class with height differential, height with neighbour distance, height with height differential and neighbour distance with height differential. It was suspected that many of the interactions accounted for distance mediated competition and potentially could contribute to multicollinearity. The correlation of the fixed effects suggested that co-linearity did exist between height and neighbour distance (R:0.753). With the neighbour distance removed, significant terms were found for crown class, height, height differential, and interaction variables crown class with height, crown class with height differential and height with height differential (Table 3.12). The random effect term was significant, evaluated by the likelihood ratio and the normality of model residuals appeared approximately normal but was leptokurtic in shape (kurtosis: 20.0). See Table 3.13 for final plot level productivity data.

Table 3.12 Periodic volume increment as a linear mixed model of structural attributes in CFS database while accounting for the random effect of plot, the model is fit by the restricted maximum likelihood approach

*REML crit.	BIC	loglik	AIC
-19085.8	-19012.7	9542.90	-19067.8

Plot random effect:		
Groups	Variance	Std Dev.
Plot (intercept)	0.00056	0.0237
Residuals	0.00018	0.0135

Treatment fixed effects:					
	Value	Std.error	DF	t-value	p-value
Intercept	-0.204	0.0056	3308	-35.86	0.000
Crown class	0.007	0.0006	3308	10.7	0.000
Height	0.012	0.0001	3308	61.64	0.000
Height difference K-3	-0.005	0.0005	3308	-8.92	0.000
Crown class : Height	-0.0004	0.00003	3308	-14.67	0.000
Crown class : dHeight K-3	-0.0002	0.00003	3308	-6.49	0.000
Height : dHeight K-3	0.0003	0.00002	3308	14.03	0.000

Correlation:								
	(Intr)	THIN	FERT	Fert. 81	Fert. 90	C.class	Th:CC	Fert81:CC
Crown class	-0.334							
Height	-0.848	0.425						
dHeight K-3	0.192	0.283	-0.185					
CC:Height	0.258	-0.971	-0.350	-0.367				
CC:dHeight	-0.189	0.323	0.204	-0.577	-0.185			
Height:dHeight	0.019	-0.407	-0.069	-0.950	0.476	0.460		

Standardized within group residuals:				
Min	Q1	Median	Q3	Max
-14.91	-0.54	0.03	0.59	7.16
Number of observations: 3377				
Number of groups: 63				

t-tests use Satterthwaite approximations to degrees of freedom, * REML criterion were generated with the lme4::lmer function while log likelihood, Akaike information criterion and Bayesian information criterion where produced by lme::nlme function while random effects. The lme model was retained to enable the model comparison test lmerTest::anova.

Table 3.13 Plot productivity form CFS database sorted by PAI of plot volume				
Plot ID	Treatment	Median PAI volume	PAI total plot volume	PAI basal area
34	T0F1-2	0.015	0.6899	0.0382
48	T2F2*	0.016	0.6772	0.0442
58	T2F6	0.020	0.6538	0.0396
28	T2F1-2	0.013	0.6117	0.0392
46	T2F3	0.022	0.6080	0.0342
4	T2F2-1	0.019	0.6035	0.0351
31	T2F2-1	0.022	0.6033	0.0321
41	T2F1-2	0.030	0.6018	0.0332
63	T2F1_GT73	0.017	0.5975	0.0447
52	T2F2	0.020	0.5910	0.0321
11	T2F0	0.016	0.5849	0.0371
8	T2F1	0.017	0.5712	0.0377
68	T2F1P_GT73	0.018	0.5682	0.0421
5	T1F2-1	0.013	0.5657	0.0333
32	T2F3	0.019	0.5632	0.0321
65	T2F1P_GT73	0.018	0.5627	0.0457
55	T2F2*	0.019	0.5620	0.0323
20	T2F0	0.016	0.5564	0.0386
13	T0F1-2	0.009	0.5481	0.0315
54	T2F4	0.017	0.5434	0.0354
60	T2F2	0.016	0.5396	0.0371
51	T2F4	0.021	0.5324	0.0276
35	T1F2-1	0.014	0.5316	0.0256
33	T2F2	0.017	0.5245	0.0268
49	T1F4	0.011	0.5173	0.0253
14	T2F2	0.014	0.5151	0.0358
47	T2F6	0.015	0.4952	0.0266
66	T2F2_GT73	0.013	0.4936	0.0451
18	T0F2-1	0.011	0.4857	0.0297
53	T0F4	0.007	0.4807	0.0237
45	T0F2	0.008	0.4782	0.0265
1	T2F1	0.013	0.4693	0.0312
39	T2F0	0.013	0.4652	0.0330
30	T1F0	0.008	0.4649	0.0277
69	T2F1_GT73	0.016	0.4547	0.0377
44	T0F1-2	0.010	0.4510	0.0269
17	T1F0	0.009	0.4501	0.0272
64	T2F2_GT73	0.015	0.4495	0.0377
70	T2F1PS_GT73	0.012	0.4452	0.0373

Table 3.13 cont'd				
19	T0F1	0.007	0.4438	0.0230
9	T1F1	0.012	0.4416	0.0217
59	T1F4	0.006	0.4414	0.0324
12	T1F1-2	0.011	0.4360	0.0241
15	T1F2	0.008	0.4311	0.0216
43	T1F2	0.011	0.4291	0.0194
27	T0F2*-1	0.006	0.4136	0.0215
25	T2F0	0.011	0.4058	0.0296
38	T0F0	0.004	0.4044	0.0255
37	T1F0	0.008	0.4020	0.0204
10	T1F0	0.008	0.3957	0.0186
24	T1F1	0.005	0.3954	0.0239
36	T0F1*-1	0.009	0.3884	0.0217
57	T2F2	0.018	0.3785	0.0179
16	T0F2-1	0.008	0.3706	0.0106
2	T0F0	0.003	0.3673	0.0189
50	T0F4	0.012	0.3600	0.0139
26	T0F1*-1	0.004	0.3272	0.0183
6	T0F0	0.005	0.3159	0.0133
21	T0F0	0.004	0.3124	0.0192
40	T0F1	0.005	0.3109	0.0144
23	T0F2*-1	0.009	0.3074	0.0118
29	T0F2	0.005	0.2835	0.0081
67	T2F1PS_GT73	0.010	-0.0065	-0.0070

The SLP ground reference database was investigated once it had passed through a quality control process, which omitted dead trees and obvious errors. The database, being temporal measurements of tree characteristics, needed to be transformed in order to represent rates of growth or productivity. This process would also provide an opportunity to become familiar with the characteristics of each of the plots and perhaps identify those that could be considered unique. The data were initially investigated in terms of DBH with respect to year. Given the establishment of the stand occurred at the same time, the general trend of revealed through this process should reflect growth productivity at the individual scale. The DBH increments were summarized at both the plot and treatment levels. The ground reference data were recomputed as rates of change in DBH, for every instance of a measurement that had been preceded in previous years a difference was computed and normalized by the duration of years between the two values. The newly computed database represents estimates of diameter increments per year sampled from 1971 to 2012. This growth rate data was also investigated with respect to year, treatment as well as by plot.

A hypothesis testing statistical approach was selected for discriminating plots or treatments with significantly different growth rates and/or DBH distributions. The typical one-way analysis of variance (ANOVA) test was used; however the limitations of this approach are restrictive to the assumptions, which if violated increase the likelihood of falsely rejecting the null hypothesis when it may be true (type 1 error). Therefore, the ground reference data were assessed for the assumptions of the ANOVA test. Normality was evaluated graphically through boxplots and statistically through the Shapiro-Wilk

test. Variance equality was assessed through the use of the Bartlett and the Brown-Forsyth tests. In addition to one-way ANOVA a non-parametric equivalent was also performed, the Kruskal-Wallis rank sum test. Post-hoc tests included the Games-Howell, Wilcoxon and the Tukey-HSD. Visualizations of the ANOVA-post hoc tests were generated as Hasse diagrams, where box height represents sample sizes, line widths represent the inverse significance values, and chart position represents the magnitude of the variable. Ultimately, periodic annual increments of volume at the individual and plot level were produced that were significantly related to plot treatment criteria and crown class. The productivity attributes would be applied in analysis investigating the potential for associations with RS metrics.

4.1 Deriving Structural Metrics from Airborne Laser Scanner

Lidar data pre-processing occurred exclusively within the Microstation Terrascan/Terra modeller software environment. Within this software the point cloud was visualized, classified, transformed and exported to various data products. The data arrived from the Terra Remote Sensing Inc. with a default classification applied. This classification was omitted so that a more thorough classification could be performed. The one class that was retained from the default classification was the extreme scan angle class. This class is omitted from all analysis, as these points tend to have greater error rates. Measurements from the extreme scan angles tend to underestimate range distances as a result of scanner acceleration and deceleration, additionally these regions have different point densities/sampling due to the scanning pattern of the oscillating mirror. The lidar point cloud classification is focused on the discrimination between ground surfaces and vegetation cover. The Terra Scan software permits the user to define iterative conditions

in macro processes to classify individual lidar returns. A macro was constructed to classify ground points. The ground classification performed an iterative TIN surface construction, which is initiated by a sparse, low point selection that assumes that the lowest point within a given square dimension is a ground point. The initial sparse ground surface was built from the lowest point in every 60x60m area. Lidar points are then classified as ground with reference to the TIN surface of the sparse low points. A point is classified as ground only if it is less than 1.3m orthogonally from the TIN facet and if the angle formed between the point under consideration, the closest sparse ground point on the TIN and the TIN facet surface below the point in question is less than 6°. A maximum terrain angle is also a parameter for the ground classification macro; the terrain angle should not exceed 88°. A below ground classification was also performed, which considered the ground class. The below ground classification was performed by computing a plane, fit to the nearest 25 points, the considered point is classified as a low point if it is either greater than five standard deviations or 10cm below the plane. Occasionally, lidar signals are generated with small range distances, whether generated as a source of noise or by echoes from airborne targets like birds, aircraft or aerosols. Since, the analysis is largely dependent on height distributions and some products generated from the highest lidar point, it is important that these “air hits” be classified out of the point cloud. The air hit routine works in a similar fashion to that for classifying below ground, where a local statistic is used to flag large deviations in height. A neighbourhood is defined as five meters and points within this area are used to compute a median and a standard deviation. A given lidar point is classified as an air hit if there is at least 30 points within the neighbourhood and the point exceeds 10 standard deviations from the

neighbourhood median. Following the execution of the above macro processes, a manual classification is performed as the parameters used in the macros do not operate well under all circumstances, high relief areas are particularly troublesome for these algorithms. Built structures, weather stations, homes, buildings, hydro lines and towers are also classified to a building class so that they may be omitted from future analysis. Once the classification was completed, the lidar data were then in a state where raster and point cloud products could be generated.

Several relatively simple raster products can be generated from the lidar point cloud, these include a bare earth model, a digital surface model and a canopy height model (BEM, DSM, CHM). The bare earth and digital surface model are output as a summary of lidar points that fall within a given raster grid cell. The bare earth model is generated as a summary of only the ground points that occur within each grid cell, where the DSM is generated as a summary of the ground and vegetation (default class) points. The generation of the CHM requires that the lidar point cloud be transformed. In order to represent the heights of vegetation points relative to the ground surface the vegetation points must be normalized by the underlying ground representation. This process is initiated by generating an inverted representation of the ground points. Multiplying the height components of each ground point by -1 generates the new ground transformation point set. The 'adjust to geoid' operation within Terra Scan effectively subtracts, from each lidar data point, the value of the transformation TIN facet directly below. The computed point cloud then has z values that represent the height of the points from the modeled ground surface. The vegetation points within this computed point cloud is used to populate raster grid cells within the CHM. The topography normalized point cloud is

also the data source from which canopy structural metrics are generated. Because there are a finite number of points that can be used to populate the raster grid cells there is a limit to the raster resolution (limit in cell size) that can be made without inducing empty cells. With regard to output cell size, there is a compromise that must be struck between horizontal precision and the spatial contiguity of the data. Because there are considerably fewer ground points than vegetation points, there is a larger cell size limit for generating the BEM than the DSM. In an effort to maximize spatial resolution and contiguity in the raster products, multiple resolutions were generated for each of the three models. Raster images were generated with 25, 50, 100 and 150cm cell sizes with a variety of point summary approaches and pixel filling/interpolation (average, minimum, maximum, standard deviation, TIN, point count). Ancillary data were also generated from lidar intensity values, which were required for the spatial bore sight calibration but also constitute a source of additional information.

The lidar data were processed to ultimately extract metrics that would aid in the modelling of canopy structure and productivity. A number of different approaches were taken for the extraction of pertinent variables. Data were extracted from model trees derived from the raster based CHM, from the point cloud representation of the CHM and site metrics were extracted from the raster representation of the ground surface. The most basic data extracted from the raster was a representation of the canopy height model (Fig. 4.1). Each pixel falling within a distance of 15 meters of a GPS surveyed plot center was assigned to represent a sample of the tree canopy for that plot. Distribution metrics of maximum heights within each plot were extracted including: average, standard deviation, extremum, coefficient of variation and the median. An in-house software package

developed by The HLRG [46] was used to perform an initial extraction of tree crowns and positions from the raster based CHM at a 50cm resolution. One module of the software locates local maxima pixels to identify tree top locations. In this instance a moving 3x3 kernel was applied to find local maxima within the 50cm CHM, hereafter referred to as lidar treetops. These treetops are then the seed locations for delineating the extent of crowns, hereafter referred to as lidar crowns. The crowns are conceptually built by expanding out from the seed pixel until there is an increase in CHM height or until either a percent of treetop height threshold is exceeded or a maximum crown radius is reached. The tree crown delineation parameters used for the plot level SLP run included a tree height range of 3-100m, a maximum crown radius of 7 meters and a height threshold of no less than 75% of the treetop height (Fig. 4.2). These parameters were extracted by optimizing for the LOGS plots where individual crowns could be easily distinguished from each other. As a result these parameters may not be ideal for more closed canopy areas like that of the SLP.

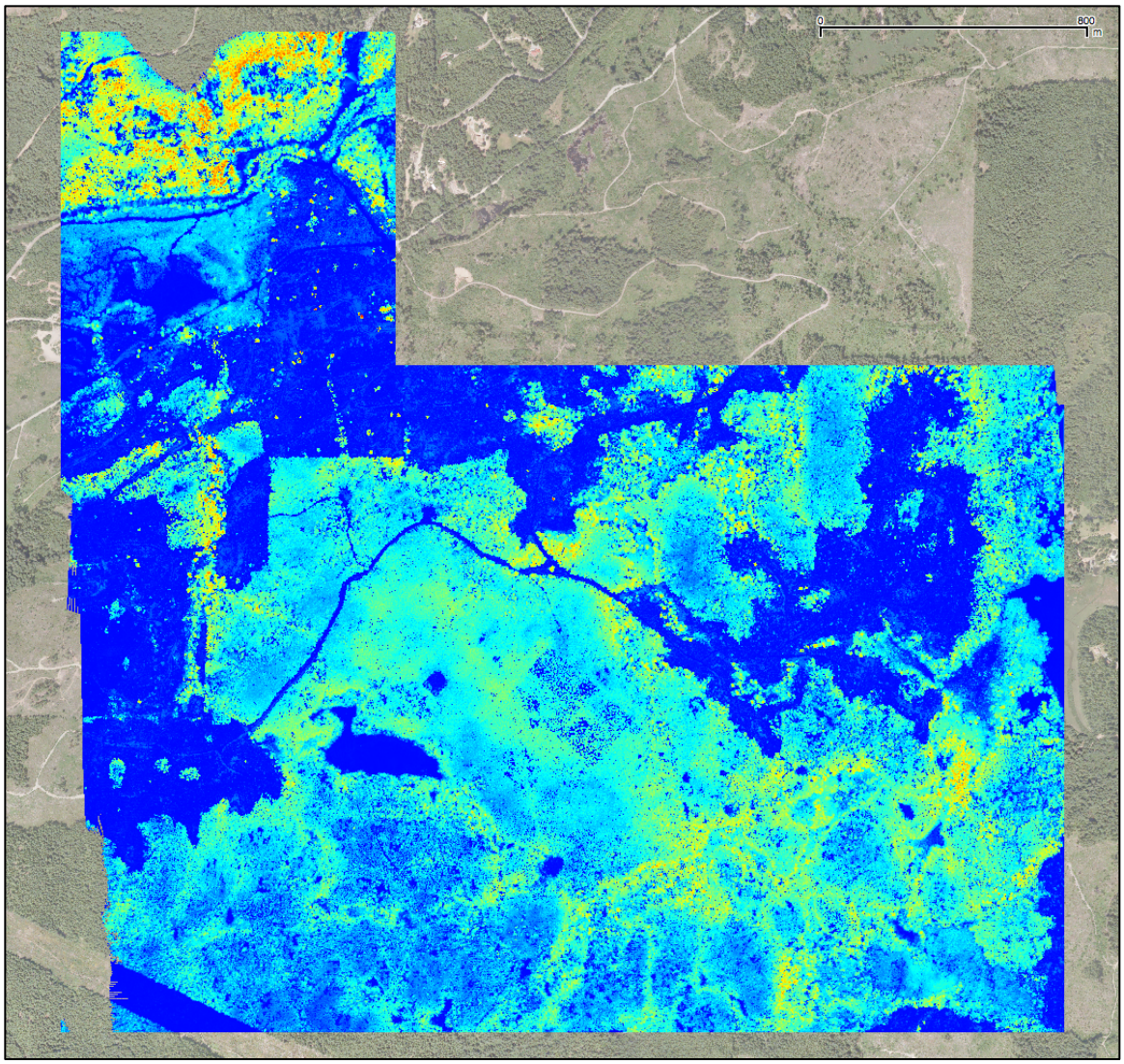


Figure 4.1. 50cm resolution canopy height model of the SLP study area, the relatively larger tree heights along the Koksilah river skew the enhancement so that height differences are not as apparent within the SLP area

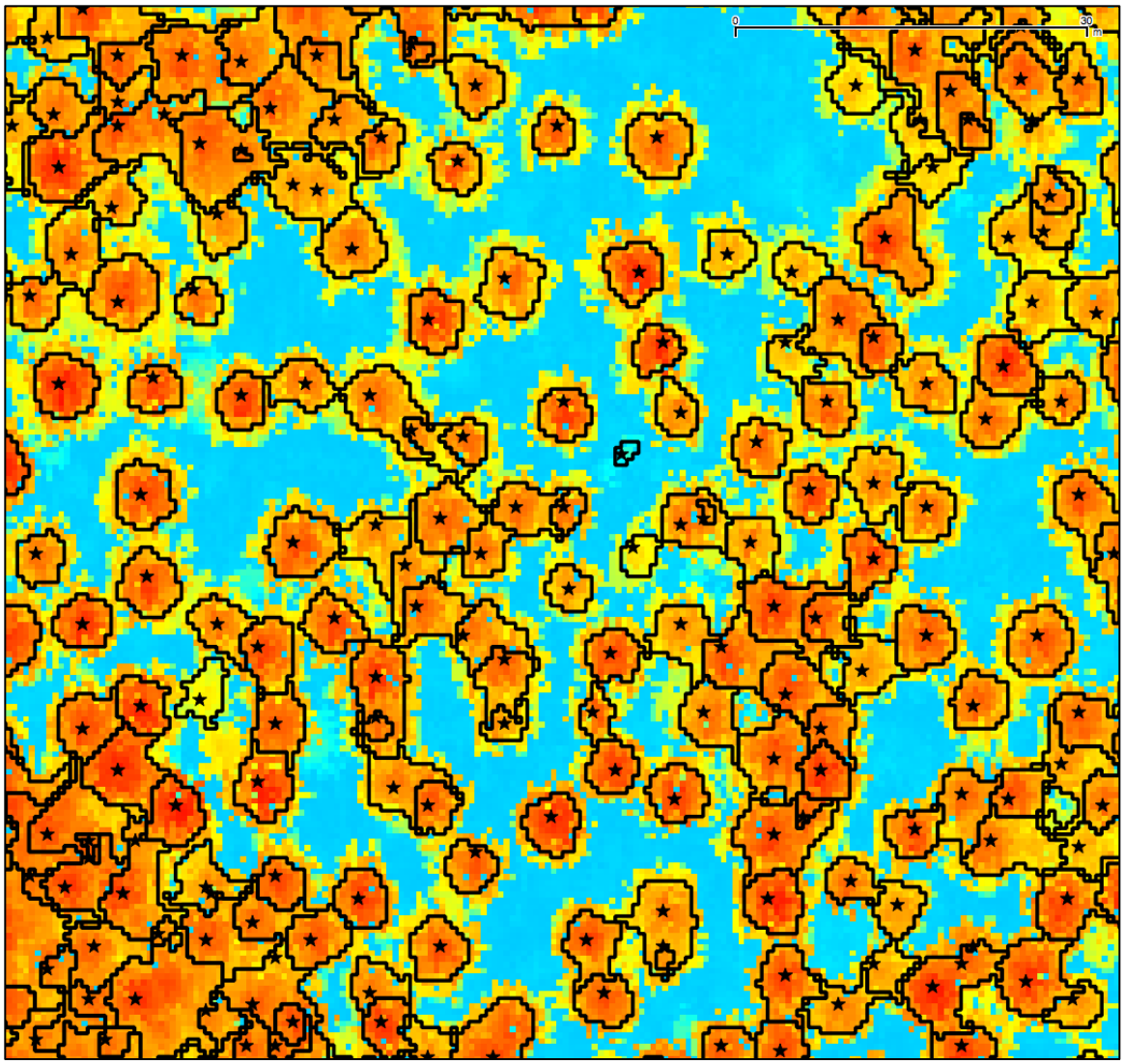


Figure 4.2. Treetop and canopy extent vector files (illustrated as black stars and polygons respectively) were generated from the 50cm resolution raster canopy height model (displayed in pseudo colour). The example above is taken from a heavily thinned plot within the LOGS treatment area.

The 50cm CHM vector products were then filtered by location relative to treatment plot centers and given an appropriate identifier code linking the field collected data with the remote sensing information. The treetop vector file variables that were generated included dominant tree stem density and distribution metrics of the treetop heights per plot. From the tree crown vector layer, attributes were extracted for each crown polygon, areas were computed and average crown width was computed (assuming

circular crowns and applying the derived area values). Plots were summarized by distribution metrics of both tree crown area and tree crown width. Because these attributes are clearly representative of canopy structure they warranted being included in this analysis, the question is, to what extent does the approach need to be refined in terms of the raster generation and the parameters for tree top and tree crown extraction.

The next set of lidar-derived metrics that were resolved were those derived directly from the point cloud (Fig. 4.3). The reader should note that these are much more computationally intensive which is a motivation for using a raster to generate metrics, however it may be the case that the raster based approach provides too much generalization which may introduce error into the metrics. From this perspective there may be an interest in deriving the treetop and crown vectors directly from the point cloud. The normalized canopy point cloud for each plot was generalized to a variety of vertical and horizontal structural metrics. The metrics derived from the point cloud can be grouped into five different classes [8].

- The traditional statistical moments and distribution descriptors: sample size, minimum, maximum, range, mean, 0.1 trimmed mean, median, standard deviation, variance, median absolute deviation from the median, standard error, coefficient of variation, skewness and kurtosis
- L-moments: L-mean, L-coefficient of variation, L-skewness, L-kurtosis
- Quantile metrics: height at given height percentile (5 percentile intervals from 0-100%)

- Cumulative probability metrics: probability above / probability below percentile height threshold (5 percent intervals from 0-100%), maximum 2nd derivative of the CDF
- Horizontal structure: rugosity (cv equivalent of the canopy surface) and gap fraction (CDF equivalent to cumulative probability metrics but inclusive of ground points with a 2m height threshold)

The lidar derived metrics; both from the raster and the point cloud provide generalizations of horizontal and vertical canopy structure as sampled by the airborne instrument. Many of these variables will have obvious direct associations with ground based measurements; top heights for example may be associated with the heights of the extracted treetop vector. Some of the lidar metrics may be less intuitive but have merit none the less, for example the cumulative probability ratios represent the canopy closure at specific height cross sections from the ground to the top of the canopy and the change in the slope of the CDF represents the height to live crown.

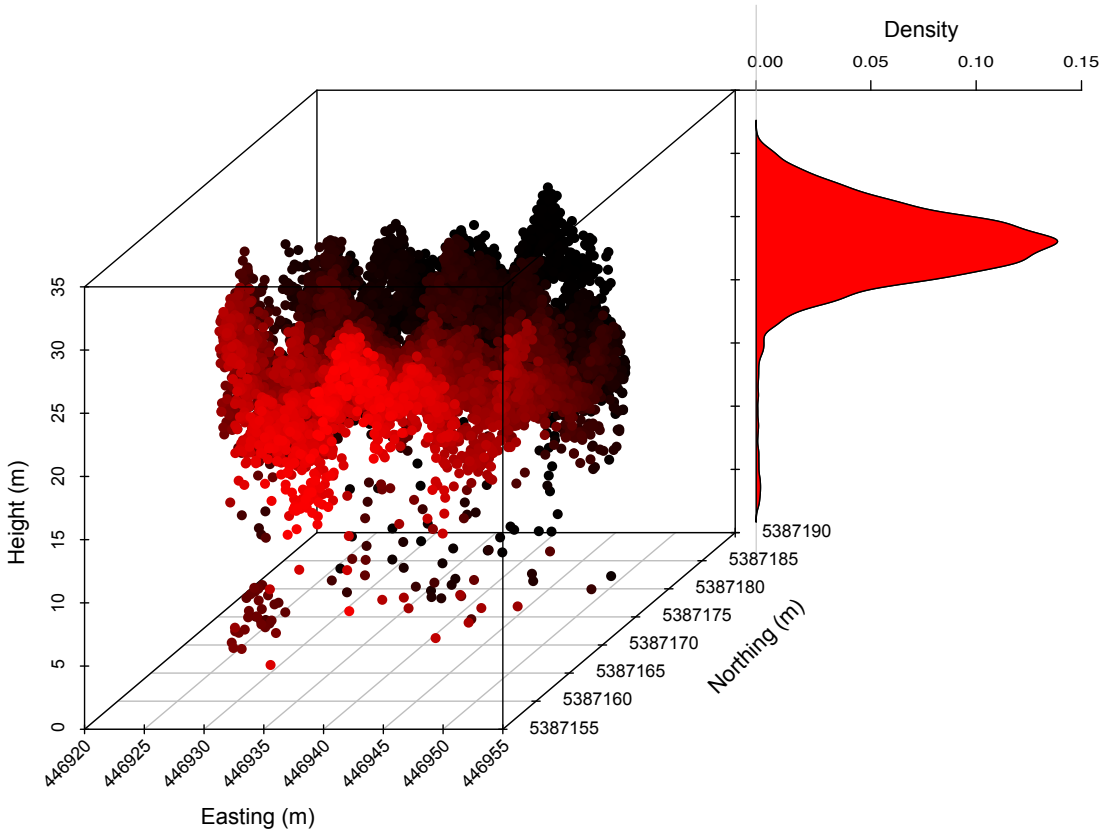


Figure 4.3. Ground normalized canopy point cloud at plot 10 (established 1971 T1F0). Lidar metrics are derived from these data to represent vertical and horizontal canopy structure. Secondary x-axis on histogram is generated by a kernel density estimation and represents probability distribution.

Site metrics were also defined from a raster representation of the lidar ground points (Fig. 4.4). The BEM was ultimately constructed as a 1meter raster, which maximized data contiguity and spatial precision (minimizing cell size). Raster cells were populated with values of the average height of ground points that occur within the raster cell. From these data, derivative products were generated including slope, aspect, curvatures and a topographic wetness index. Fitting a quadratic surface to elevation values within a 3x3 kernel window and computing the rate of change in elevation for the center pixel and the direction of the surface normal vector, slope and aspect respectively, were determined. Convexity and curvature indices were determined as the second

derivative of the quadratic surface. The topographic wetness index was computed by determining the upslope drainage area from the aspect data and normalizing this area to the slope at the given pixel location. The TWI is therefore a relative indicator of surface water availability and residency. Given the association between nutrient and moisture availability, the TWI may prove to be an informative proxy for site productivity (Fig. 4.5 & 4.6)

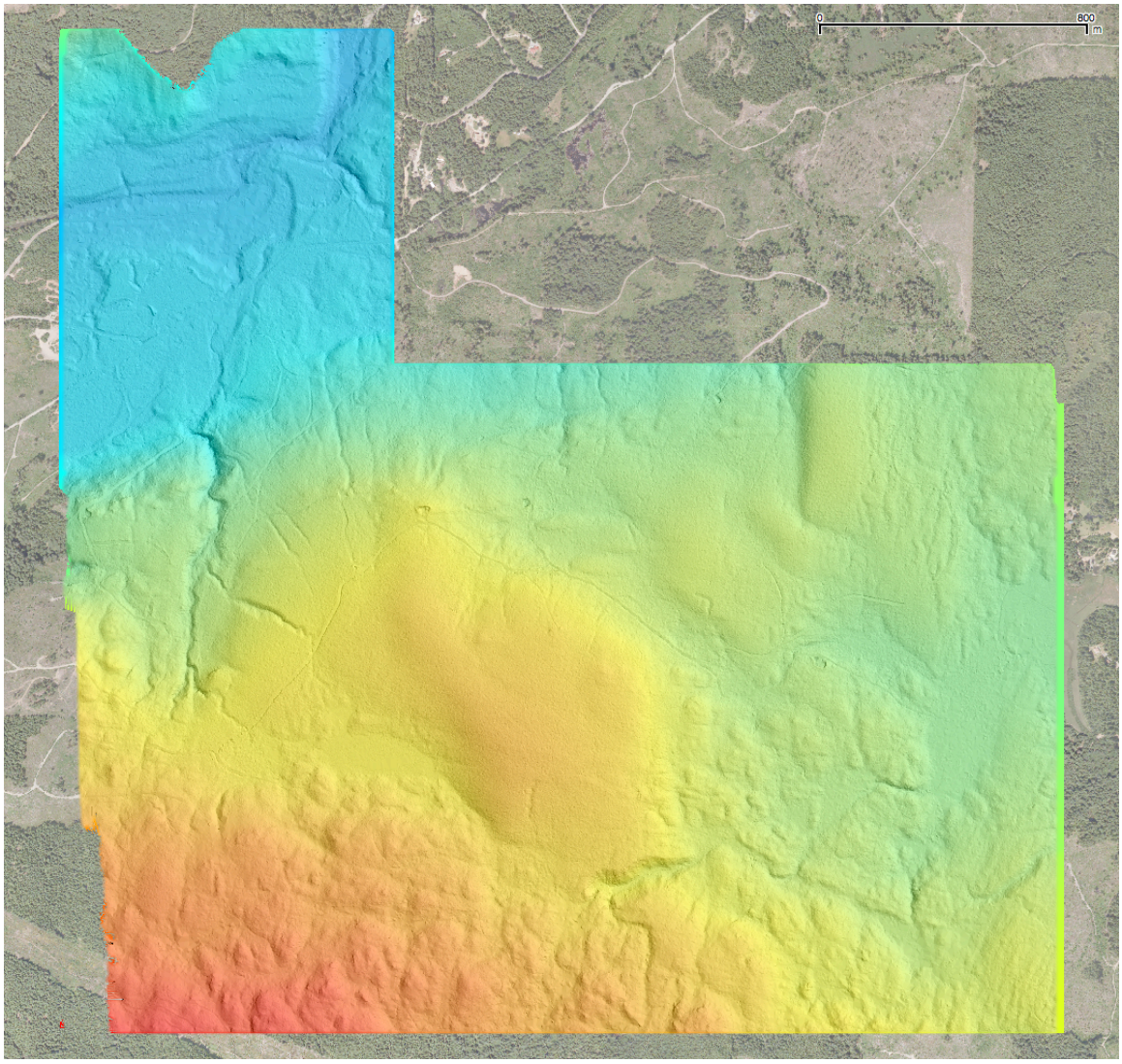


Figure 4.4. Lidar derived 1m bare earth model displayed with a color ramp and superimposed on a hill shade (solar azimuth 60°, zenith 40°). From the BEM, derivatives are generated that describe the ground surface.

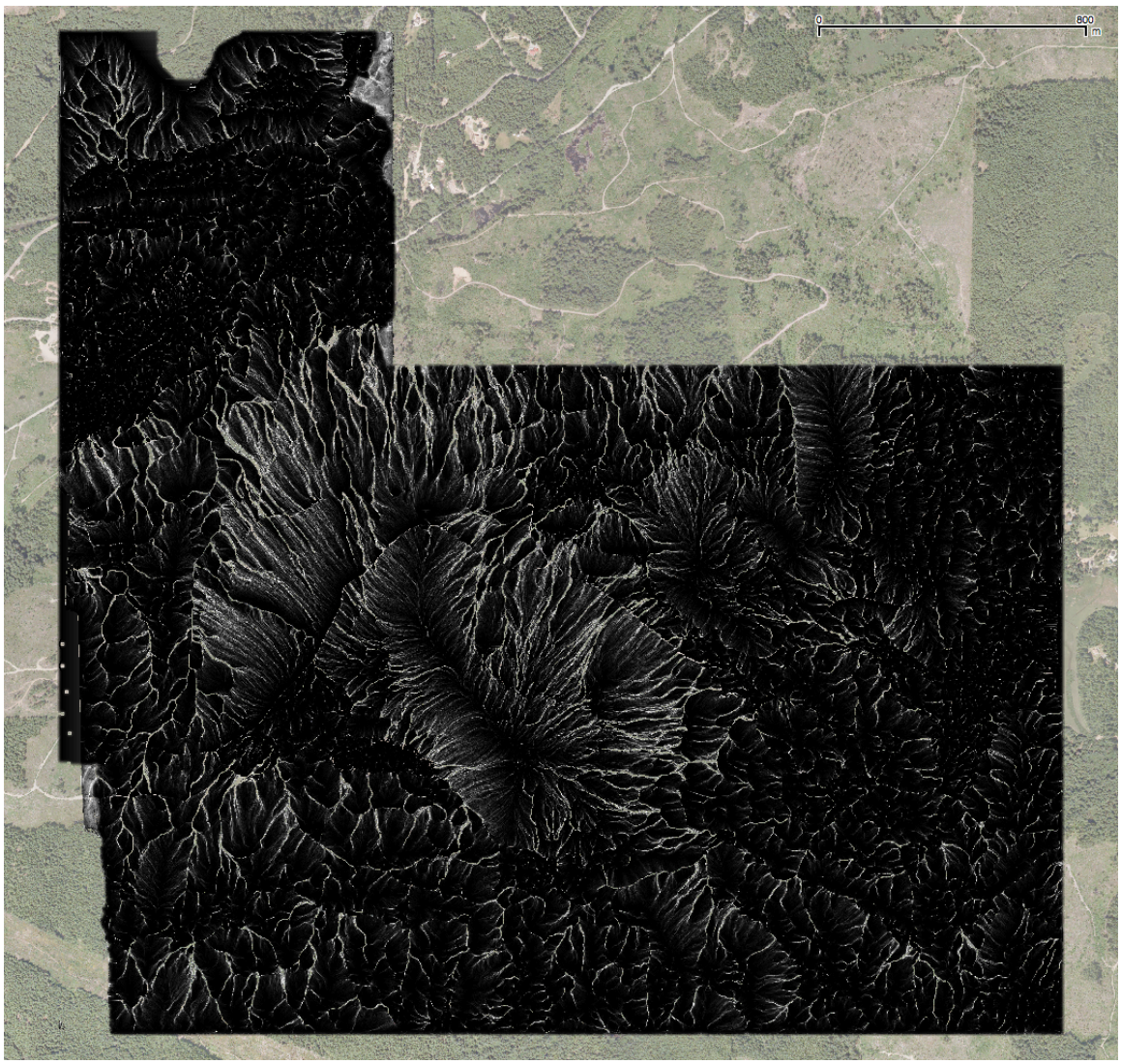


Figure 4.5. Through the use of slope and aspect data derived from the lidar BEM a flow model is built to indicate the relative quantity/magnitude, and flow direction of surface water.

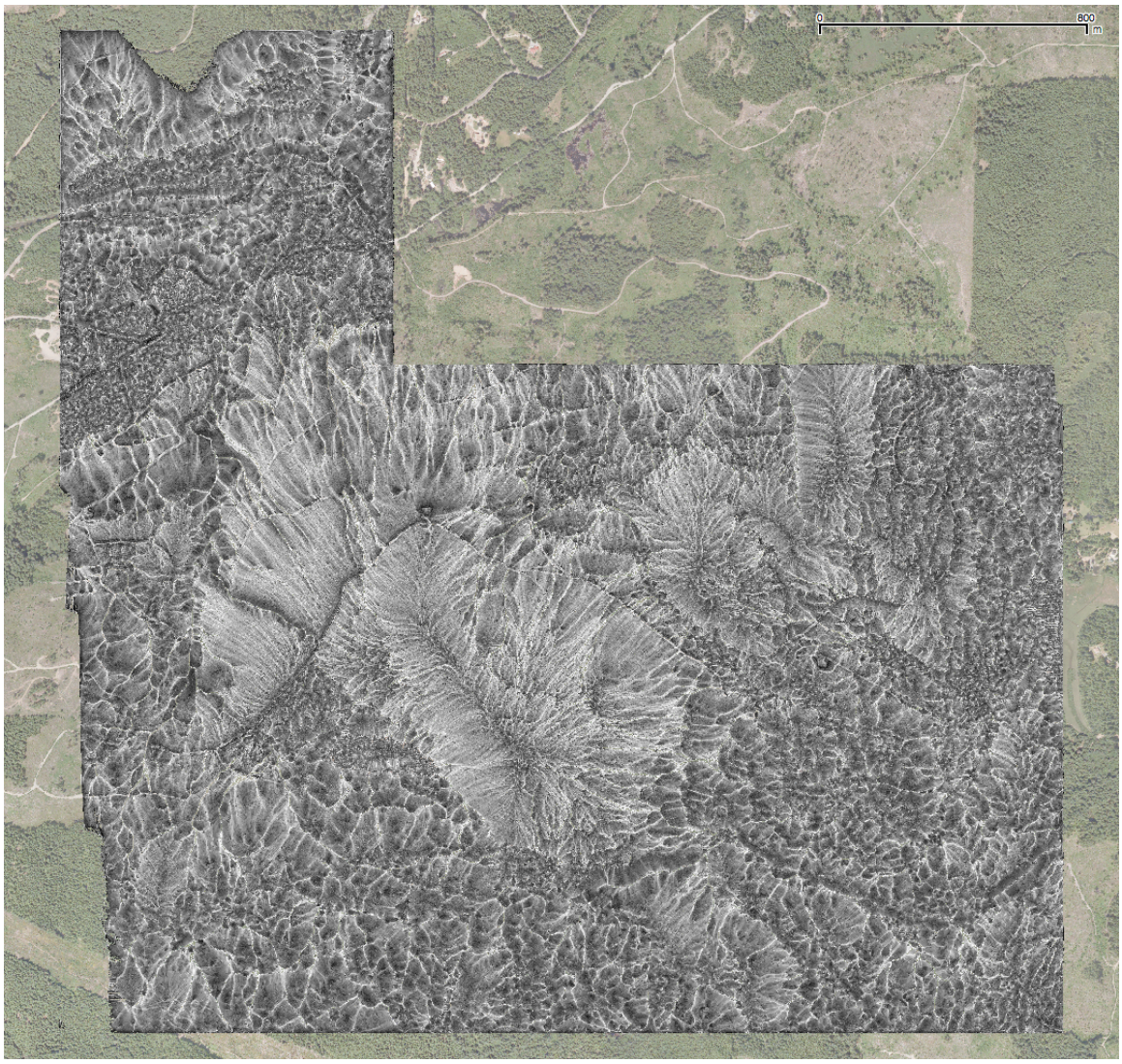


Figure 4.6. The topographic moisture index is generated as the flow model normalized by the slope data. The TWI is used as a proxy for site productivity as there is an association between moisture and nutrient availability.

4.2 Airborne Imaging Spectroscopy Metrics for Productivity Attribution

A considerable amount of processing is required before the spectrometer data is in a useable form to extract measurements; this is especially the case when the region of interest crosses multiple flight lines. Prior to the use of the data, a mosaic of the study site was built. Because the extent of the SLP site is relatively small, the entire treatment area including the LOGS plots was contained within only two flights. This reduced the effort

required to correct for illumination differences between multiple flight lines. As detailed in the processing section, the data were corrected to relative reflectance values. Because the two flight lines were flown in opposing directions and slightly displaced temporally, the illumination between the flights was slightly different. Further processing was required to reduce the effect of differing illumination between flights. The two flight lines were spatially subset to contain only the study site. The data were also spatially restricted to omit data collected at the extremes of the senor swath. If the data were not limited in such a way, the seam of the two flight lines would be apparent in the mosaic where data were collected from larger observation zenith angles. Overlap between flight lines is variable as a result of variations in platform attitude. The minimum overlap between the two flights was observed and the two lines were subset to reduce this overlap to ~30pixels. This approach reduced the amount of extreme viewing zenith angles but also helped to ensure that the data of the overlapping area were not confounded by different viewing geometries, this is important for the normalization between flight lines, otherwise only the topmost flight would need to be subset away from the seam of the mosaic. By subsetting both flights away from the seam line, the overlapping areas have more similar geometries when sampled and thus more similar bidirectional effects. The overlapping area could be used to scale one flight line to the other and ensure similar values. This process drastically reduced the radiometric differences between flight lines (Fig. 4.7).

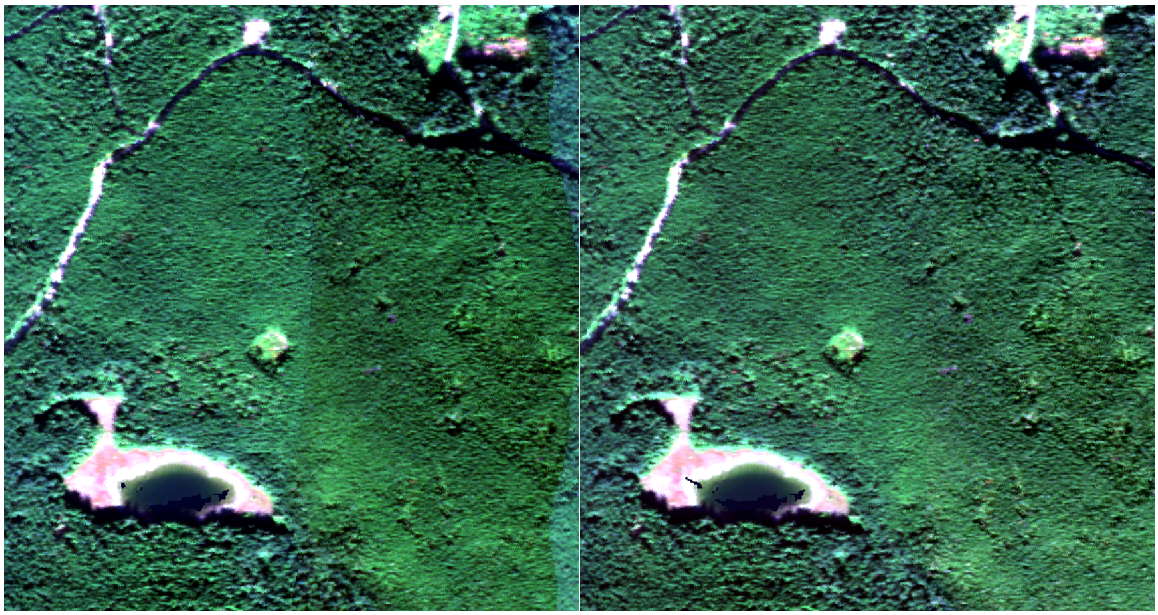


Figure 4.7 Flightline normalization procedure to resolve radiometric differences between flightlines. The overlapping area was spatially reduced to eliminate extreme observation zenith angles.

The lidar data were used to refine the spectrometer data to ensure that appropriate samples were collected for the analysis. A 1.5m CHM was generated from the lidar point cloud so that the data would have corresponding cell sizes and origins. From the CHM, a binary image was generated to omit pixels that were collected from surfaces less than 4m from the ground surface. This binary mask was applied to the AISA Eagle reflectance mosaic. Spectra were then extracted from the imagery; pixels that occurred within a 15m buffer of the GPS plot centers were targeted for spectral extraction (Fig. 4.8). The spectra were submitted to a library of spectral indices that were selected because of their association with biophysical parameters [124]. The indices selected are typically sensitive to the effects of foliar pigmentation on reflected electromagnetic energy, greenness and to some extent a combination of the influence of pigments and NIR scattering. In addition to the traditional indices, spectral derivatives were computed and derivative attributes were

determined (Fig. 4.9). The red edge position is of particular interest as it has a demonstrated capacity for chlorophyll estimation. The red edge is located by the maximum first derivative and is located at approximately 720nm, the longwave region of chlorophyll absorption. The magnitude and the wavelength position of the red edge were extracted from derivative curves. Full range albedo was calculated as the sum of all reflectance channels. Finally, a continuum removal was applied to the reflectance data [125]. Continuum removal is the spectroscopic analogue of ratio indices, where the spectral curves of absorption features are normalized to the background reflectance. The background reflectance is the reflectance that would occur without the absorption of the targeted material. This background is approximated from a linear line segment defined by the absorption feature extents. In this application of continuum removal the interval selected was 551-750nm. This range was selected to enhance the variability in absorption caused by variable amount of photosynthetic pigments. Because there remained a slight possibility that residual illumination differences between flight lines existed, a second normalization was applied to further reduce the impact of varied collection geometry. Each spectral position in the continuum-removed curves was expressed as a proportion of the maximum depth (Fig. 4.10). Several attributes of the continuum removal process were extracted, these included: the slope and intercept of the background continuum line, the position and magnitude of the maximum depth, the total area of the depth normalized continuum removed curves, the left and right portions of the total area (defined by the feature limits to the maximum depth) and the symmetry of the feature (left area/right area). Previous work has demonstrated that the left area of the continuum removed

spectra is a robust proxy for the prediction of foliar biochemistry [10]. These data were applied to a predictive model to indicate pigment concentrations represented as a proportion of pigment to sample fresh weight (chla=0.014e$^{(0.053*\text{left area})}$). In following with the plot representation by the lidar metrics, spectral attributes were summarized by statistical moments and distribution metrics.

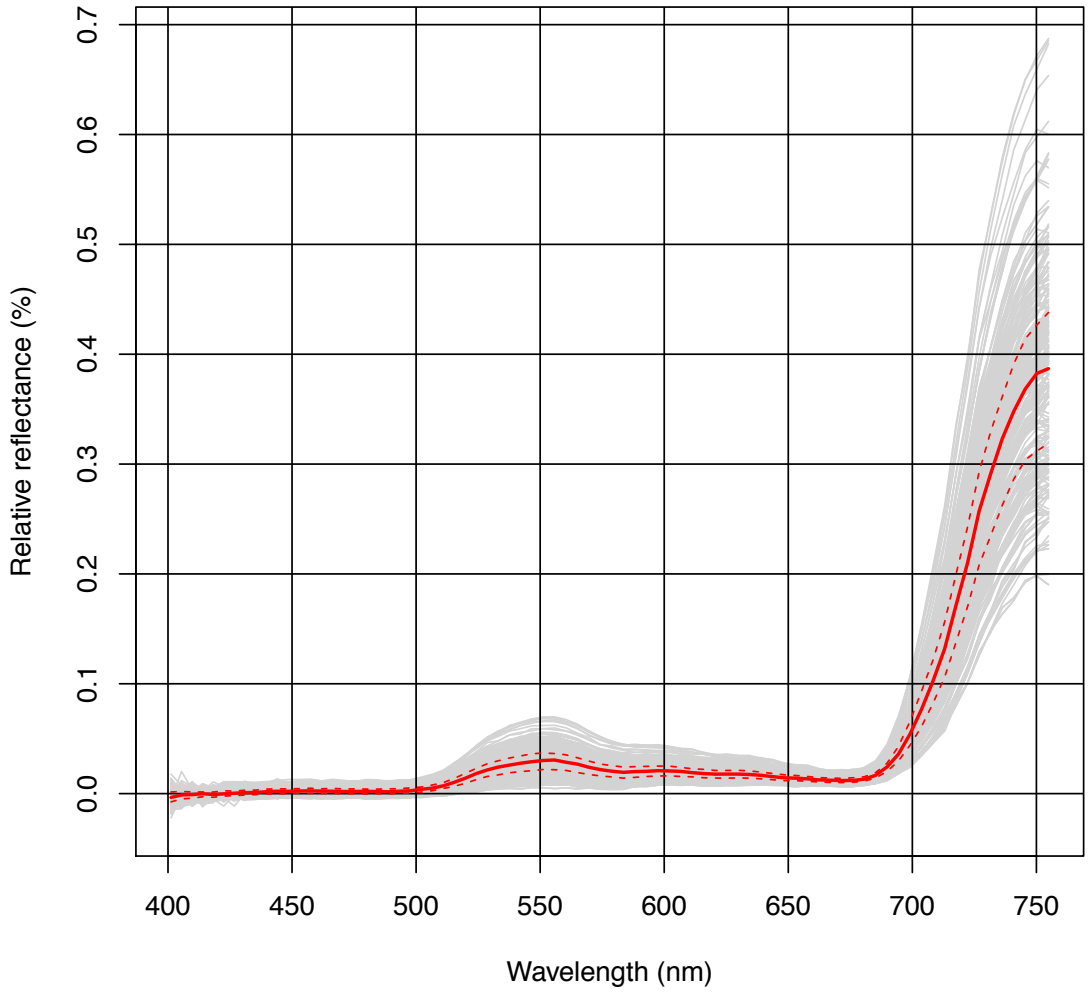


Figure 4.8. Spectra extracted from plot 10 within the AISA Eagle data, which was corrected to surface relative reflectance. The total 316 extracted spectra are illustrated and the associated quartile curves were computed and are shown in red.

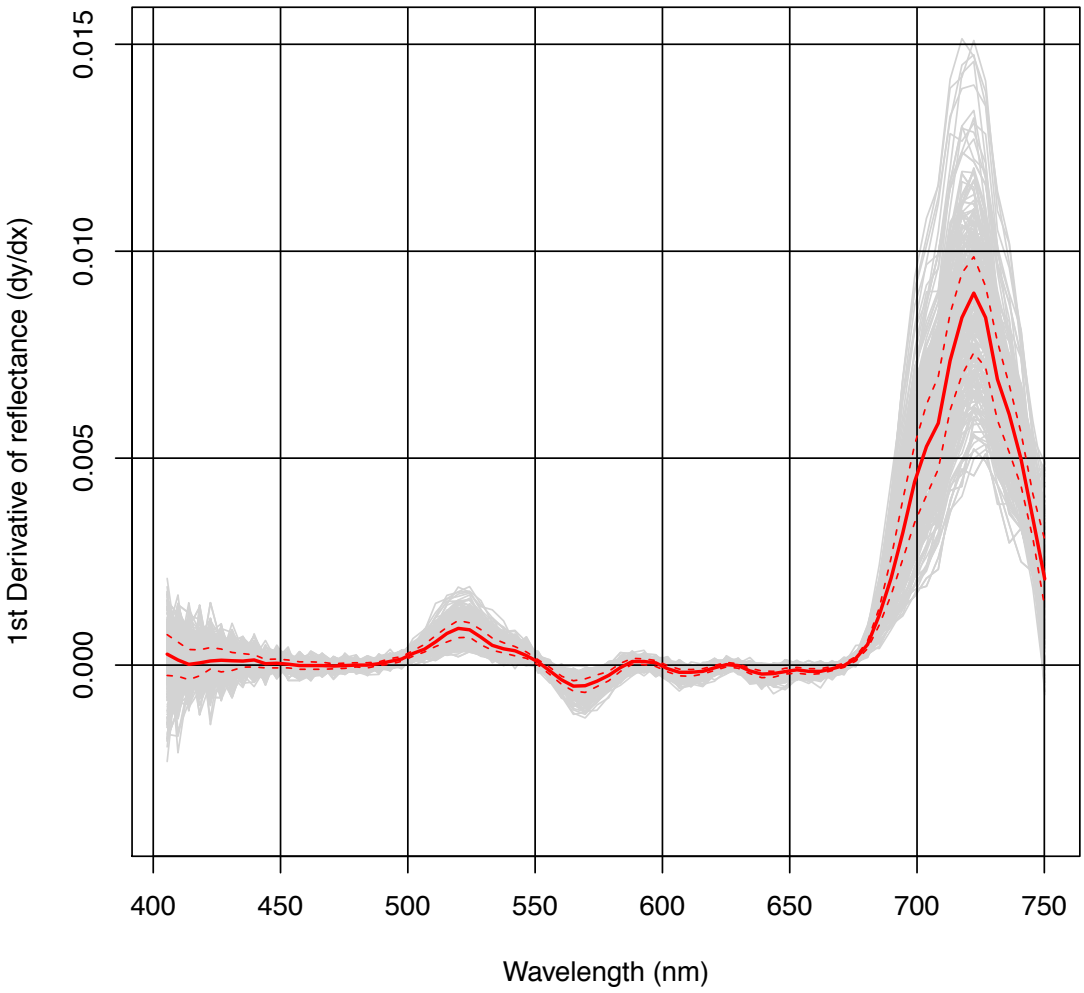


Figure 4.9. Derivative spectra extracted from plot 10 within the AISA Eagle data, which was corrected to surface relative reflectance. The total 316 extracted spectra are illustrated and the associated quartile curves were computed and are shown in red.

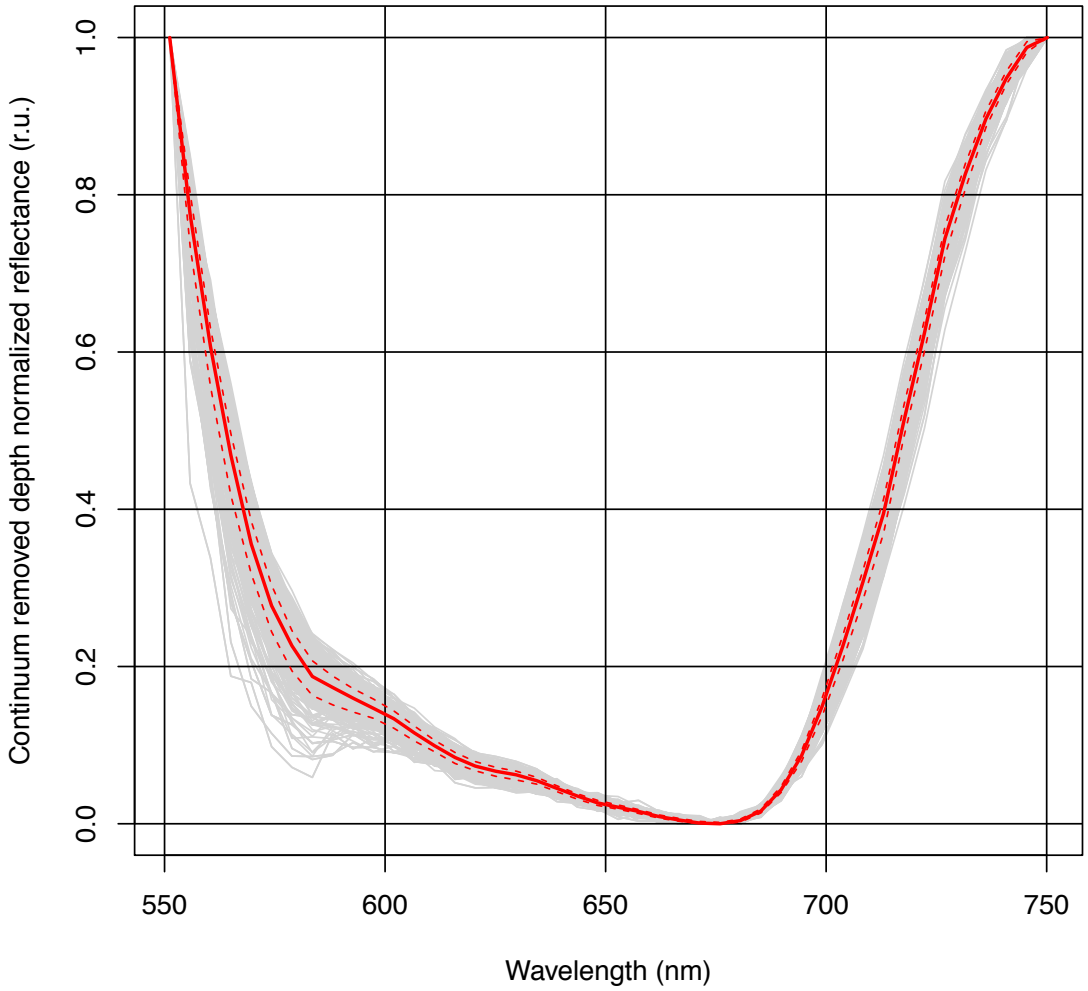


Figure 4.10. Continuum removed and depth normalized spectra extracted from plot 10 within the AISA Eagle data, which was corrected to surface relative reflectance. The total 316 extracted spectra are illustrated and the associated quartile curves were computed and are shown in red.

4.3 Area Based Forest Plot Structure Regression

A correlation analysis was conducted as a first step towards uncovering the relationships between the dependent variables measured in the field and the independent variables derived from the remotely sensed datasets. To ensure that nonlinear relationships were not missed and to not be restricted to normal data, the nonparametric Spearman's correlation coefficient was applied, which is simply the Pearson correlation coefficient

applied to the ranked dataset. Pearson's correlation coefficient was also considered. Where strong non-linear associations were found, appropriate transformations were considered. The greatest correlation for each of the dependent variables was investigated further through simple linear regression. Only the strong relationships with a coefficient of determination greater than 0.6 will be presented, they are stratified into three groups; those related to volume (total plot volume, plot merchantable volume and basal area), those related to forest structure (top height, average height, height of sampled trees, height to live crown and stem density) and a final group related to forest productivity (PAI of basal area, PAI of total volume and median PAI of volume).

The largest magnitude of Spearman's rho for total plot volume was produced by the canopy closure fraction at the 70th percentile (CCF_{70}). This CDF metric considers the ratio of the number of lidar points above the 70th height percentile, to the total number of lidar points. Thus, the metric conceptually samples the degree to which the canopy at a given height limits the penetration of lidar points. The Spearman's correlation coefficient between total plot volume and CCF_{70} was 0.812 with a significance $p < 0.000$. The scatterplot of the two variables demonstrated that plot 5 was clearly an outlier with respect to the linear model and plot 67 was a suspected influential point (Fig. 4.11). The large total volume of plot 5 was attributed to relatively high individual stem volumes (62 percentile of median plot volume, n=63), in addition to a relatively high stem density (59 percentile of plot stem count, n=63). To address the effect of the outlier, plot 5 was removed and the linear model was computed. The omission of plot 5 slightly increased the slope and intercept coefficients, the coefficient of determination increased from 0.78 to 0.84 and the F statistic increased by 50% from 88.3 to 126.5. It was recognized that

plot 67 had a low stem density and a high occurrence of root disease that reinforced the low plot volume that would be expected from such a plot. This assumption was evaluated to investigate the impact of plot 67 on the predictive model. With the removal of plot 67, the explained variance was reduced to 69% and the F-stat decreased to 52.5. Slope and intercept coefficients remained relatively stable with the omission of plot 5 (intercept increased by ~0.2, slope decreased by~0.8). However, with the removal of plot 67 the intercept increased by 1.8 and the slope decreased by 2.6. As depicted in figure 4.12, with an increase in canopy closure at nearly three quarters up the lidar distribution there is an associated increase in plot volume. The standard error of the estimates is $1.93m^3$; the Durban-Watson statistic for correlated residuals is 1.95 suggesting, because it is close to a value of 2, that the model errors are uncorrelated. However, the calculated significance of the statistic is 0.81; there is insufficient data to suggest that the residuals are uncorrelated. Bootstrapping the linear regression by 1000 times with replacement produced a mean coefficient of determination of 0.76 and a mean standard error of $2.28m^3$ (Table 4.1).

It was suspected that the relationship between remotely detected data and plot-measured attributes would be more specific to the dominant and co-dominant tree layers. Therefore, the plot-based attributes were computed accordingly, and the relationships were assessed with reference to those data not stratified by crown class. In the case of plot total volume, crown class stratification did not produce a predictive benefit.

Table 4.1 Bootstrap of total plot volume simple linear model (n:1000)						
	Intercept	CCF_{70}	R^2	RSE	F-stat	P-value
Minimum	-1.24	18.12	0.30	1.24	10.66	<0.000
Q1	2.89	27.90	0.70	2.01	58.63	<0.000
Mean	4.08	29.77	0.76	2.28	96.13	<0.000
Median	3.96	29.73	0.77	2.26	85.14	<0.000
Q3	5.22	31.63	0.83	2.56	118.98	<0.000
Maximum	11.82	39.30	0.95	3.68	439.16	0.0032
1000 Bootstrap iterations each built from randomly sampling the plot data with replacement 27 times to equal the number of selected plots.						

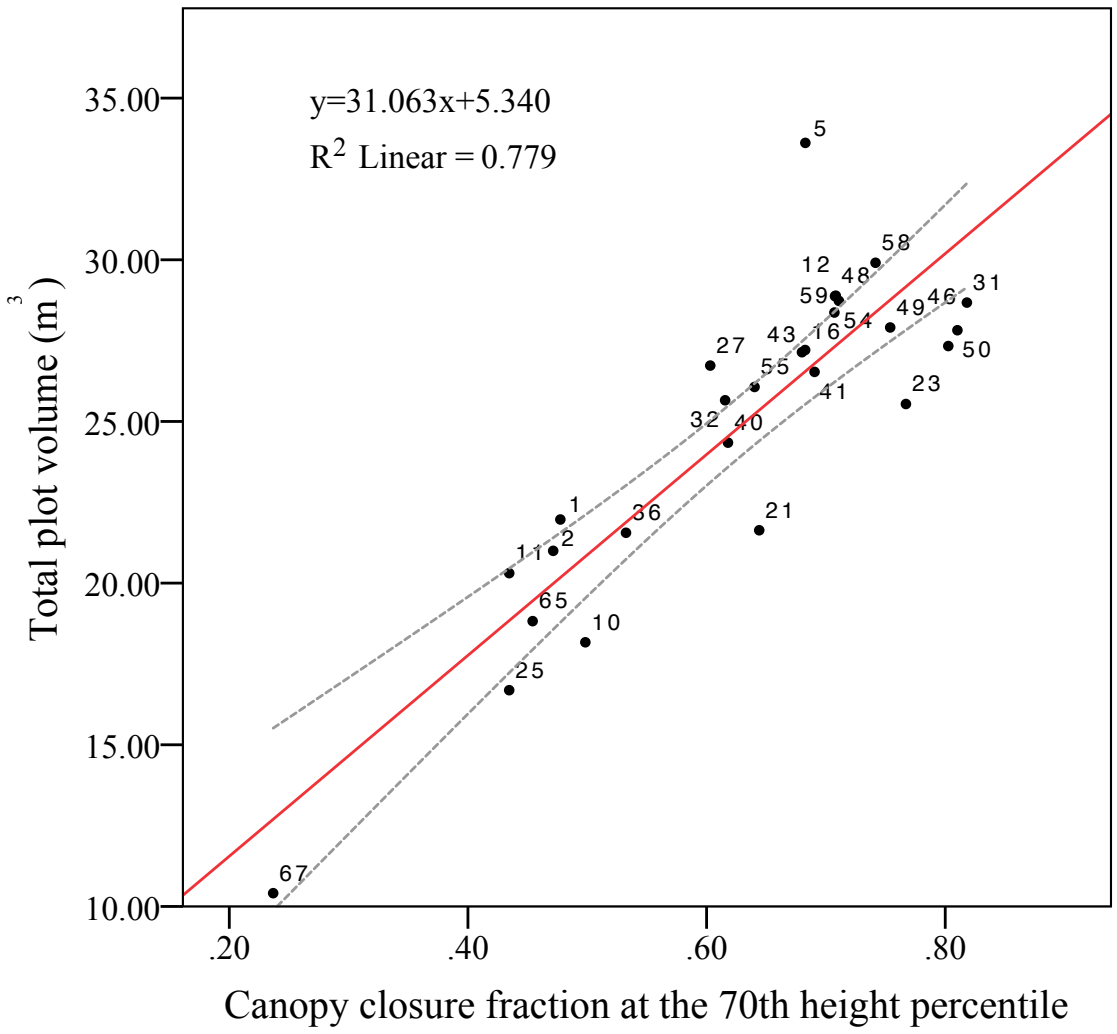


Figure 4.11. Linear model for the prediction of total plot volume. Plot 5 is an outlier with respect to the rest of the data and plot 67 is an influential point. CCF_{70} was selected through the comparison of Spearman's correlation coefficients as the best predictor of total plot volume

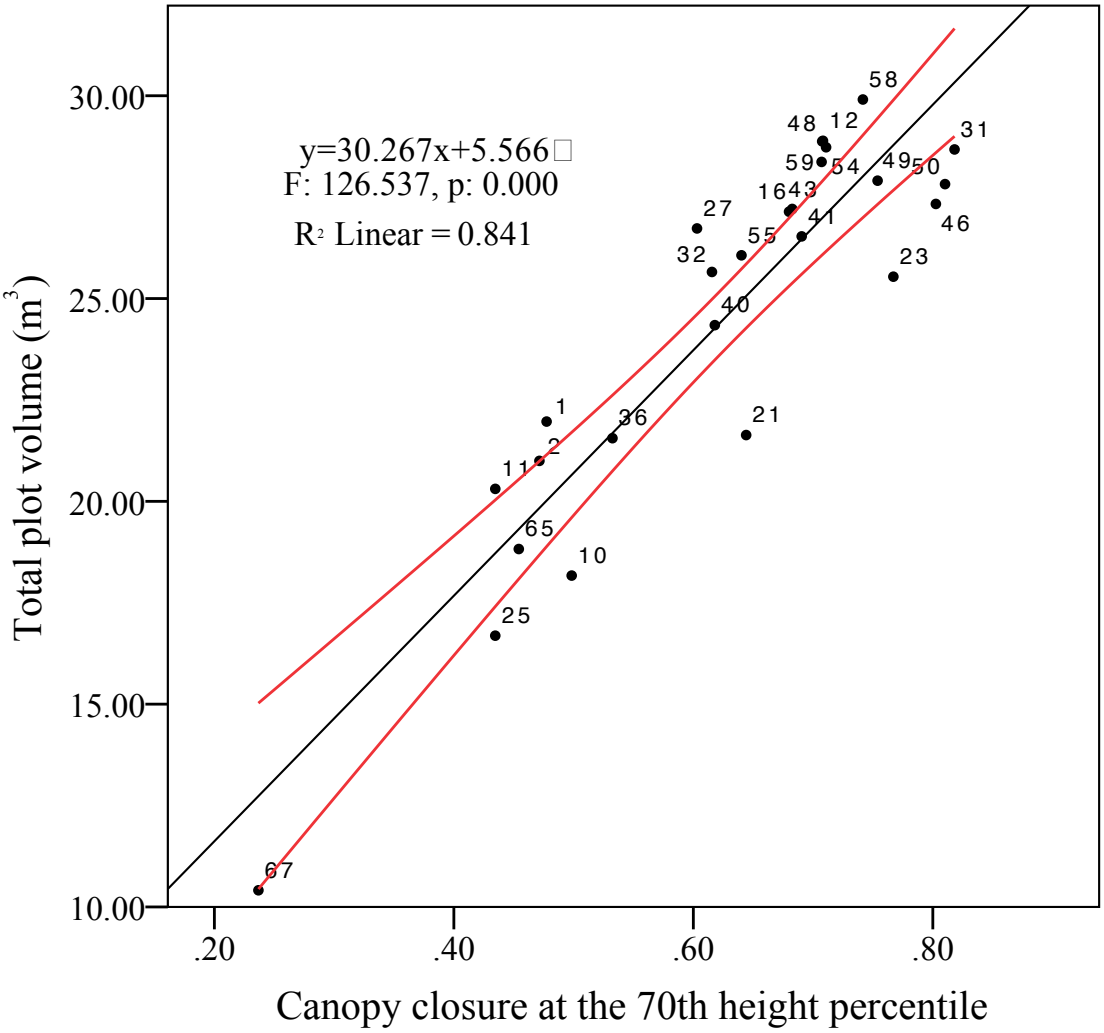


Figure 4.12. Linear model for the prediction of total plot volume omitting plot 5. CCF_{70} was selected through the comparison of Spearman's correlation coefficients as the best predictor of total plot volume

Not surprisingly, plot merchantable volume also produced a significant relationship with CCF_{70}. It was determined that there was significant correlation between total plot volume and merchantable volume (R; 0.99, $p<0.000$). The Spearman's rho for plot merchantable volume and CCF_{70} was 0.821 with a significance of $p <0.000$. In parallel with the regression for total plot volume, plot 5 was again an evident outlier; as

well plot 21 appeared to deviate more than had been seen with total plot volume. The predictive power of the model is very much in line with what was found for total plot volume, the increase in both the F-statistic and the fit index are expected to be the result of omitting plot 21 which was not assessed in the total volume model (Fig 4.13 and 4.14), variations in model parameters were nearly identical with that produced with the total volume model (Table 4.2). The linear model for merchantable volume produced a standard error of the estimate of 2.41m^3 and produced a non-significant intercept term (t-test: 1.841, p: 0.078). There was little evidence of heteroscedasticity in the model residuals.

Table 4.2 Bootstrap of total plot merchantable volume simple linear model (n:1000)

	Intercept	CCF_{70}	R^2	RSE	F-stat	P-value
Minimum	-3.36	18.12	0.30	1.14	10.66	<0.000
Q1	2.87	27.93	0.70	2.01	58.58	<0.000
Mean	4.07	29.77	0.76	2.28	96.01	<0.000
Median	3.91	29.84	0.77	2.26	85.37	<0.000
Q3	5.15	31.66	0.83	2.55	120.68	<0.000
Maximum	11.88	42.48	0.95	3.68	439.16	0.0032

1000 Bootstrap iterations each built from randomly sampling the plot data with replacement 27 times to equal the number of selected plots.

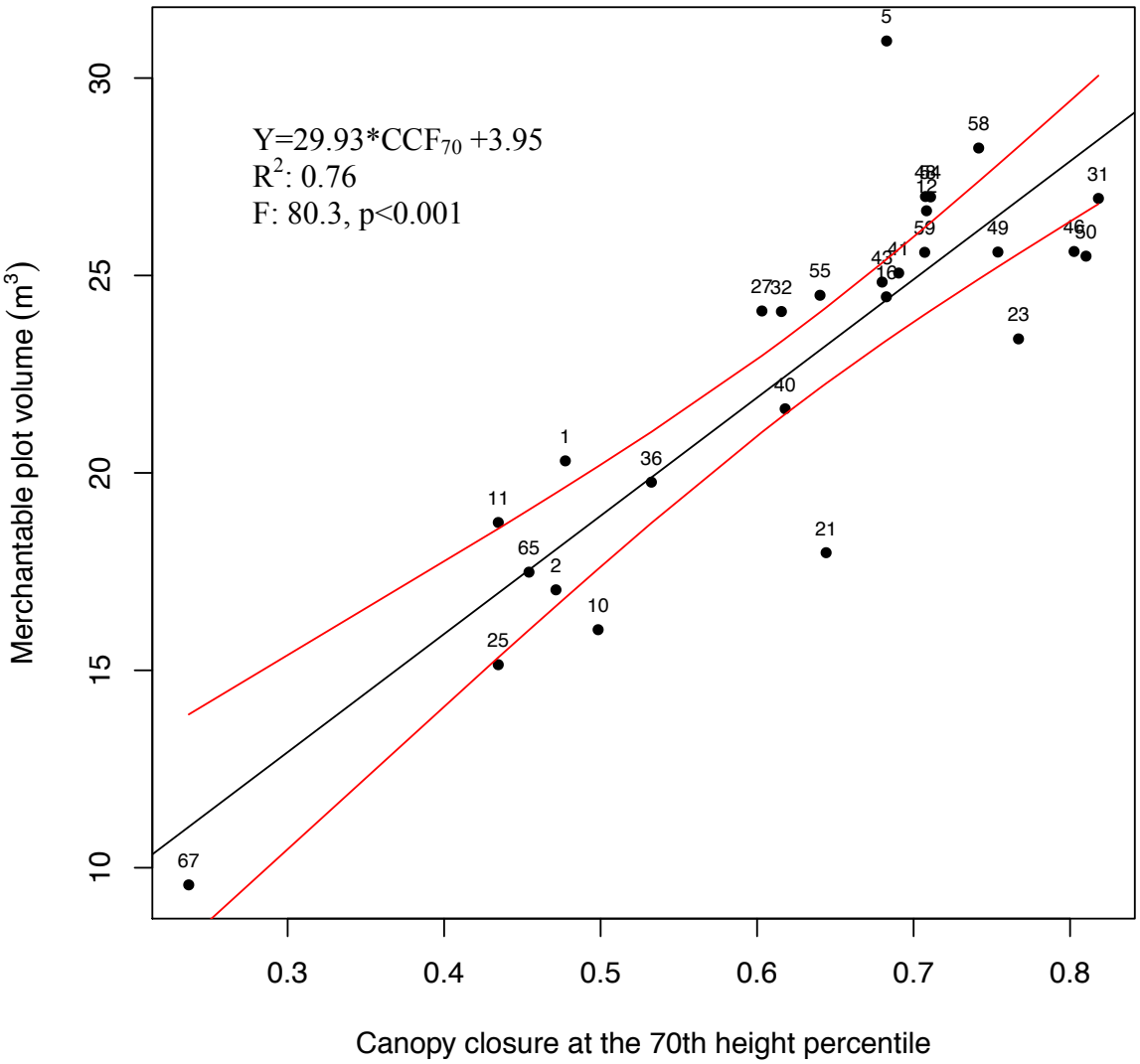


Figure 4.13 Linear model for the prediction of merchantable plot volume. CCF_{70} was selected through the comparison of Spearman's correlation coefficients as the best predictor of total plot volume

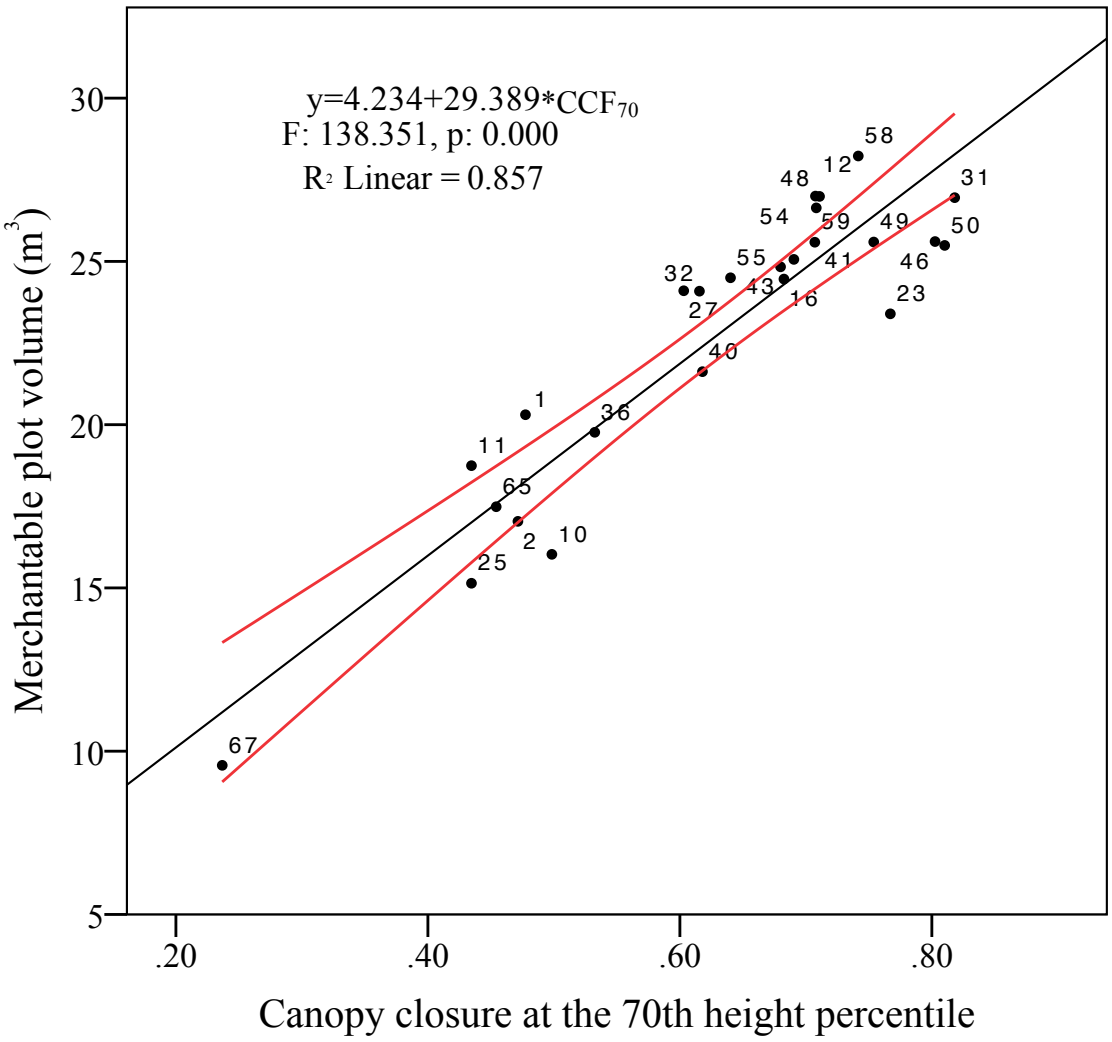


Figure 4.14. Linear model for the prediction of merchantable plot volume without plots 5 and 21. CCF_{70} was selected through the comparison of Spearman's correlation coefficients as the best predictor of total plot volume

The simple linear regression analysis applied to the prediction of basal area was conducted. Interestingly, the greatest correlation coefficient for plot basal area was also produced from its association with a CDF metric (CCF_{65}). It is recognized that the selection of this variable may in fact be the same signal identified in volume modeling with perhaps, in this case, a noise or error component providing a slightly elevated correlation coefficient. The correlation coefficient for basal area and CCF_{65} was 0.85 ($p<$

0.000). There was greater spread within the scatterplot than was produced in the volume models. Plot 67 was again dissimilar from the other plots but was not identified as an influential observation in leverage plots and the Cook's distance index. Plot 5, although an extreme value in basal area was not an outlier as it was in the volume analysis. The relationship between canopy closure and basal area seems more intuitive than the relationship with volume. Trees grown in high densities have greater competition for light resources and could allocate greater amounts of photosynthate to primary leader growth. Alternatively, the relationship may be the effect of volume losses due to disease. Plots 65, 67 and 36 each was documented as having clear evidence of root disease. These three points along with four others make up a sparse cluster within the data space that largely determines the linear trend (Fig 4.15). Whether the variations in basal area are the result of treatments and photosynthate allocation or disease, these data suggest that the CCF_{65} is affected, and its influence is measureable. Bootstrapping the linear regression by 1000 times with replacement produced a mean coefficient of determination of 0.70 and a mean standard error of $0.20m^2$ (Table 4.3).

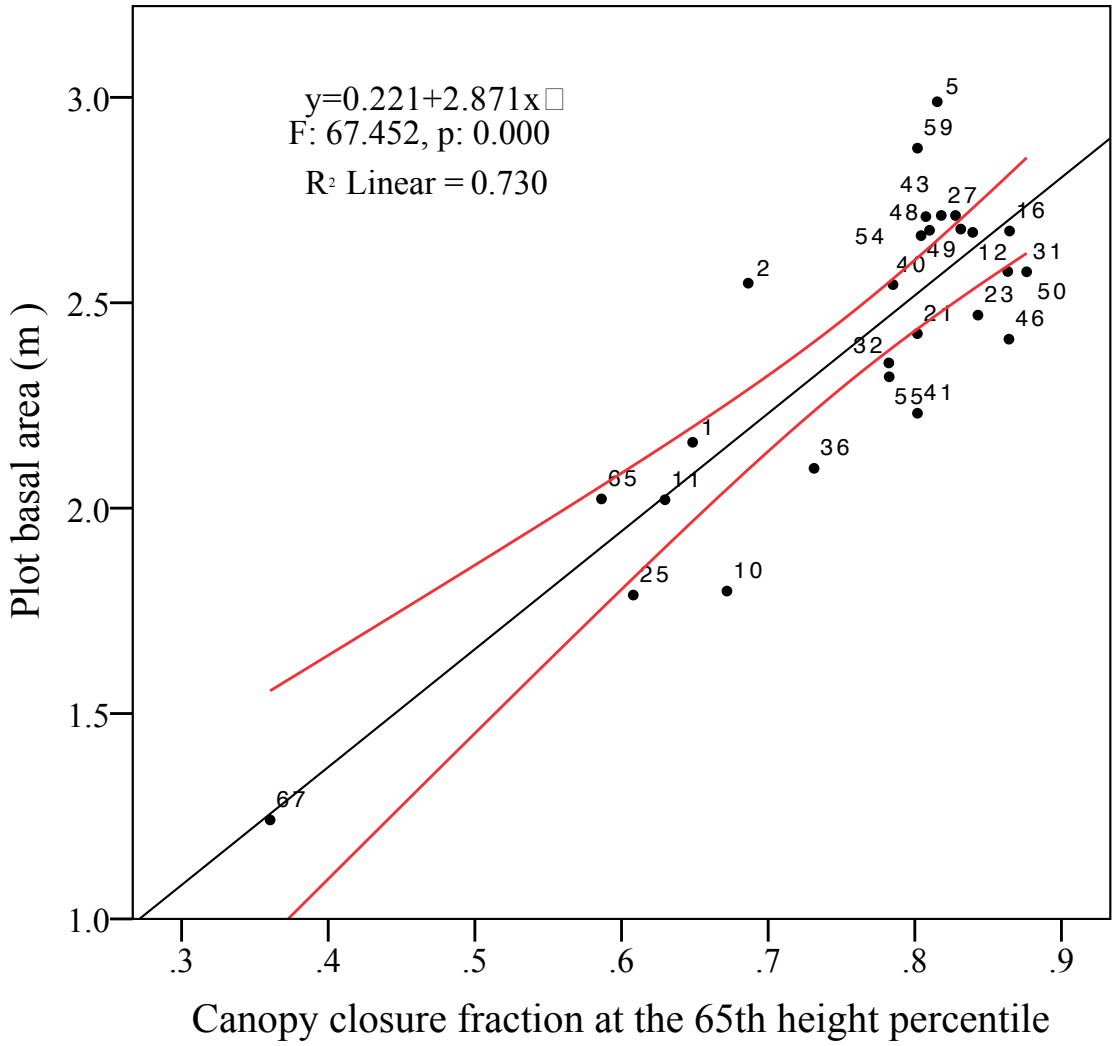


Figure 4.15. Linear model for the prediction of plot basal area. CCF_{65} was selected through the comparison of Spearman's correlation coefficients as the best predictor. The standard error of the estimate is 0.20m^2. The constant in this case is not significant (p: 0.42) a result that is physically meaningful; a plot with no basal area will have zero canopy closure.

Table 4.3 Bootstrap of plot basal area simple linear model (n:1000)						
	Intercept	CCF_{65}	R^2	RSE	F-stat	P-value
Minimum	-1.15	1.27	0.11	0.13	2.97	<0.000
Q1	0.10	2.70	0.62	0.18	41.49	<0.000
Mean	0.23	2.86	0.70	0.20	75.08	0.0003
Median	0.22	2.87	0.73	0.20	68.59	<0.000
Q3	0.34	3.03	0.80	0.22	97.85	<0.000
Maximum	1.58	4.68	0.93	0.27	313.91	0.097
1000 Bootstrap iterations each built from randomly sampling the plot data with replacement 27 times to equal the number of selected plots.						

As might be expected, the field attributes that represent the three-dimensional organization of tree canopy components were the best estimated by lidar metrics, as lidar directly measures the physical position of objects. Three representations of canopy top height were derived from the field data. One method used only those heights that were actually measured in the field ($n \approx 20$) and plots were represented as the mean of these measurements, hereafter referred to as plot height. A second method applied the tree height and DBH measurements to derive an allometric equation for each plot, which was then used to predict the height of unmeasured trees within each plot. The average plot heights were then represented as the average of all measured and modeled tree heights ($28<n<133$), hereafter referred to as average height. The third plot height variable was defined as the average of the four trees within the plot with the largest DBH measurements (in relation to the 100 largest per hectare, *i.e.* $100/(10{,}000m^2/400m^z)=4$), hereafter referred to as top height. A final consideration was given to tree heights stratified by crown class. It was expected that height, above all other attributes derived from a top down remote sensing geometry, would be sensitive to the vertical obstruction/occlusion captured in crown classes.

The correlation analysis with plot height (measured), reinforced observations found elsewhere in the literature [14], where the 85th height percentile was most associated with plot height, producing a Spearman's rho (ρ) of 0.906 ($p:<0.000$). However, scatterplots and transformations did not warrant a nonlinear form (Fig. 4.16). In the comparison of Pearson's correlation coefficients, the 85th percentile was the fifth largest absolute value, being preceded by the 70, 75 and 80th percentiles and the largest occurring from the median treetop height (which was third most correlated in

Spearman's). Note however, that the 35 most associated features were all generalizations of the lidar vertical height distribution or CHM treetop statistics (producing R^2 values greater than 0.7). It is clear that the height signal is being resolved within these inter-correlated metrics and that slight variations in how this attribute is represented both within the field data and within the lidar height data are producing slight variations in the simple linear models.

Relative to the tree height model produced from the measured heights and the $LHQ_{85,}$ (Fig 4.17) there was a marginally larger coefficient of determination and a slightly smaller standard error of the estimates from the model produced with the median treetop heights (Fig 4.18, Table 4.4). The intercept coefficients in both cases were not significantly different from zero (LHQ 85: t-test: 0.044, p: 0.965, median TT: t-test:-0.54, p: 0.60). A zero intercept is physically meaningful; in a plot with no trees there would be no canopy points and all the lidar height quantiles would be equal to zero and the physically modeled treetops should directly parallel the heights of individual trees (although a bias could be expected). The difference between the two quantities being regressed is that from the field data, all trees are accessible for measurements regardless of their position within the canopy and the spatial extent of their crowns. The lidar data however, is conceptually limited in terms of its penetration into the canopy and its ability to resolve intermediate or suppressed trees. At the same time the lidar point density and footprint places a limit on the minimum size of a resolvable tree crown.

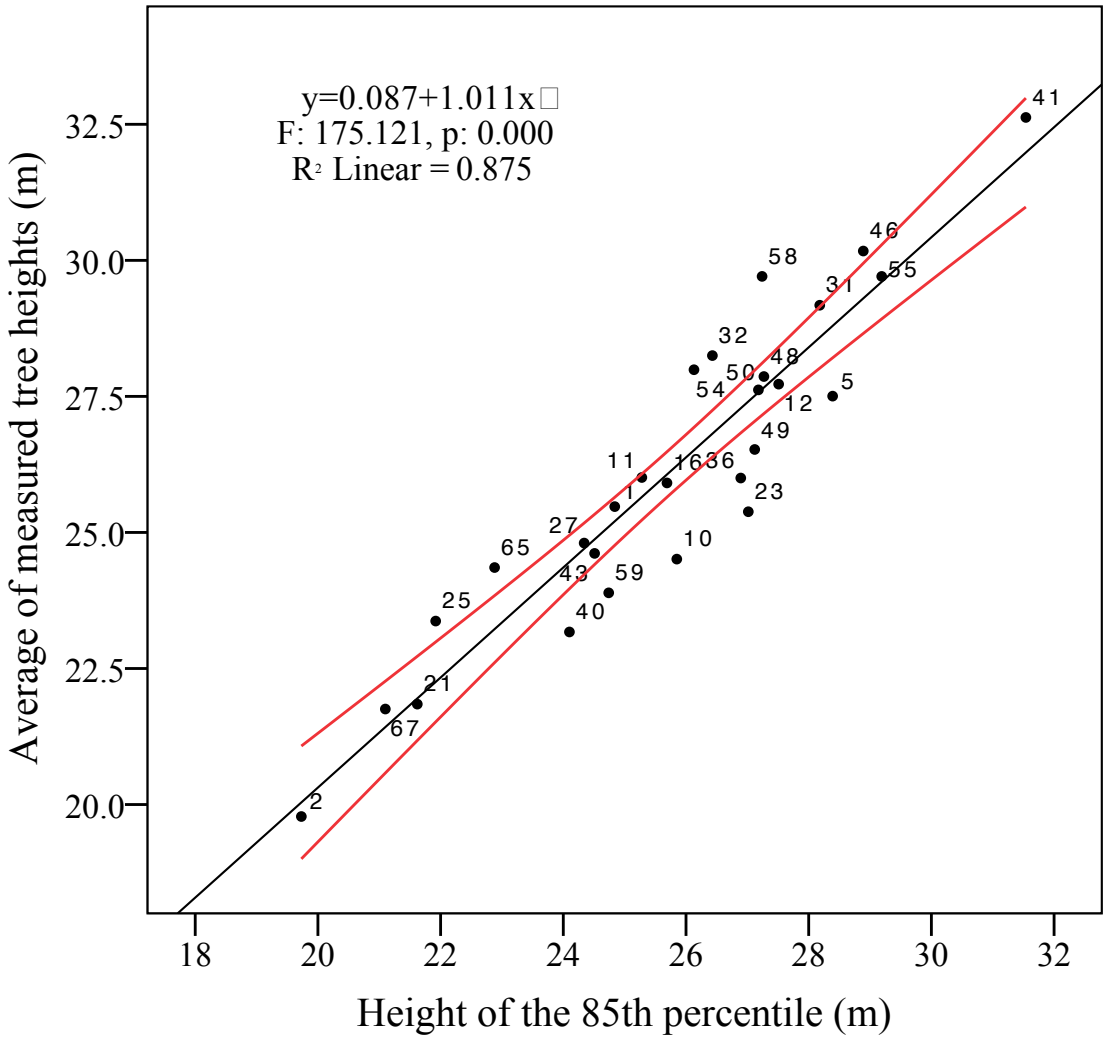


Figure 4.16 The average of measured tree heights predicted from the LHQ_{85} (height of the 85th percentile of the CHM points). The residual standard error is 1.05m.

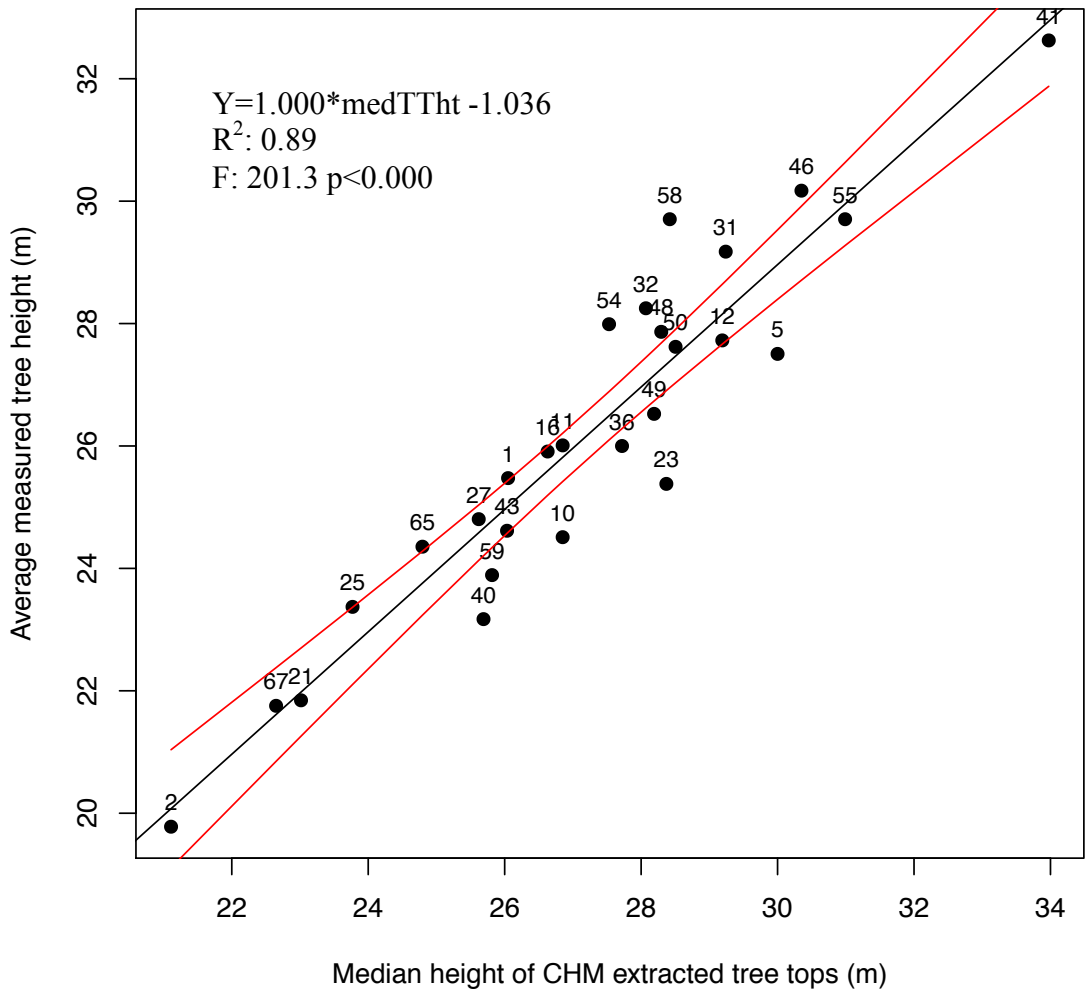


Figure 4.17 The average of measured tree heights predicted from the median CHM treetop. The intercept coefficient may not be different from zero (t-test: -0.54. p:0.60) and the slope coefficient is very close to one, it is below one by 2x10-5. The standard error of the estimate is 0.99m

Table 4.4 Bootstrap of average measured tree height simple linear model						
	Intercept	medTTht	R^2	RSE	F-stat	P-value
Minimum	-8.39	0.82	0.57	0.54	33.30	<0.000
Q1	-1.86	0.97	0.86	0.85	150.42	<0.000
Mean	-1.17	1.00	0.88	0.95	230.79	<0.000
Median	-1.08	1.00	0.89	0.95	204.95	<0.000
Q3	-0.34	1.03	0.92	1.04	286.02	<0.000
Maximum	3.54	1.27	0.97	1.36	913.44	<0.000
1000 Bootstrap iterations each built from randomly sampling the plot data with replacement 27 times to equal the number of selected plots.						

It was suspected that the field based estimate for average tree height contained variation that was attributed to stems outside the dominant and co-dominant crown classes. It was anticipated that a more appropriate attribute could be directly built from those crown classes. Again the median treetop height attribute produced the greatest association with average dominant and co-dominant plot height, irrespective of correlation method (Pearson's or Spearman's). The standard error of the estimates was greatly reduced to 0.55m, the coefficient of determination was increased to 0.97 and the F-statistic was increased to 762.1 ($p<0.000$). This linear model was clearly superior to those previously assessed and suggests that the signal captured by the lidar CHM treetop data are the heights of those trees within the dominant and co-dominant crown layers (Fig. 4.18, Table 4.5). Other stratifications were assessed cumulatively from the dominant to the suppressed class, which produced a progressive decrease in fit indexes with the inclusion of lower crown position (after an initial increase from only the dominant class to the members of the dominant and co-dominant layer). *i.e.* average dominant height (R^2:0.94), average dominant and co-dominant height (R^2:0.97), average dominant co-dominant and intermediate (R^2:0.89), average dominant co-dominant intermediate and suppressed (R^2:0.87), all crown classes including dead (R^2:0.81).

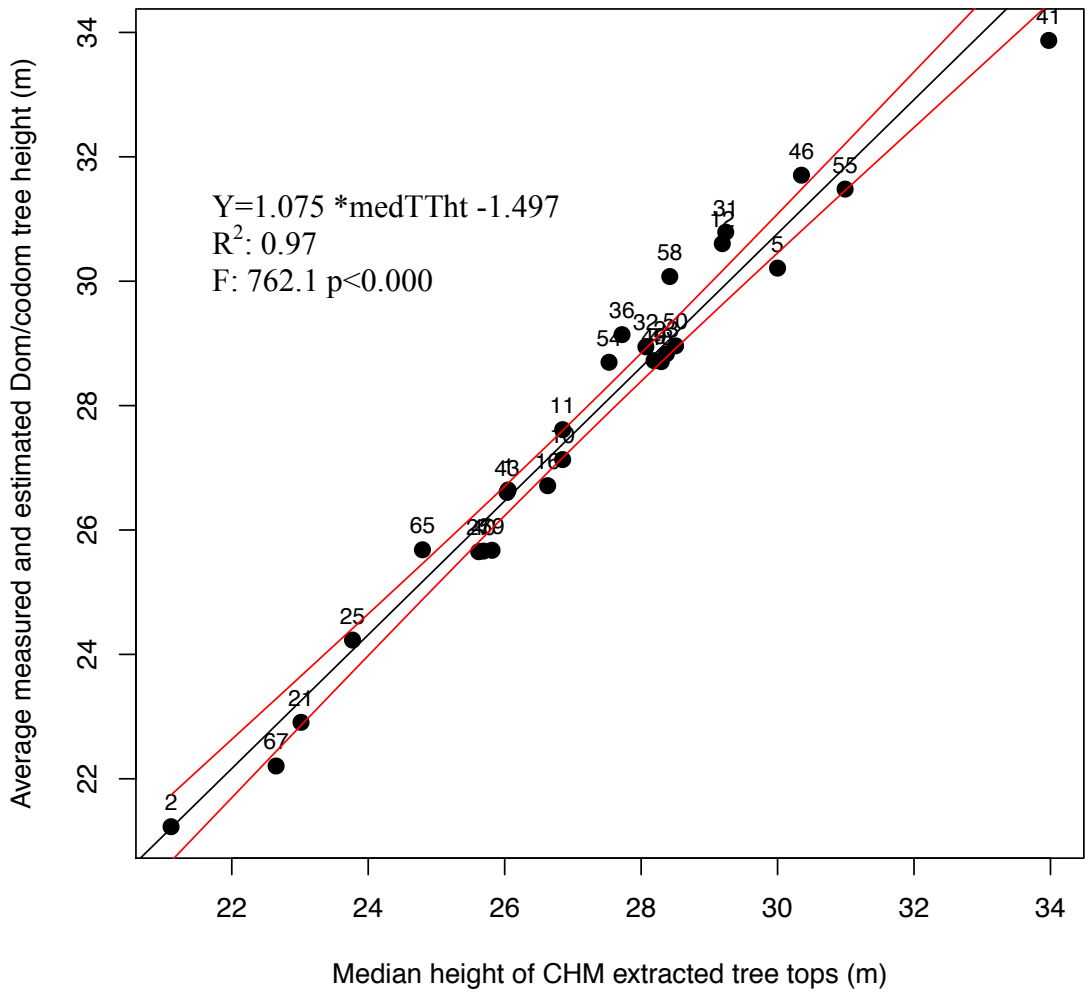


Figure 4.18 The average of measured and modeled tree heights within the dominant and co-dominant crown classes predicted from the median CHM treetop. The intercept coefficient may not be different from zero (t-test: -1.407. p:0.17), the slope is close to one and the residual standard error is 0.55m. The residual error is greatly reduced by omitting intermediate and suppressed crown classes.

Table 4.5 Bootstrap of average measured and estimated tree height within the dominant and co-dominant crown class simple linear model

	Intercept	medTTht	R^2	RSE	F-stat	P-value
Minimum	-7.55	0.96	0.91	0.36	249.50	<0.000
Q1	-2.65	1.05	0.96	0.47	670.21	<0.000
Mean	-1.75	1.09	0.97	0.52	857.43	<0.000
Median	-1.63	1.08	0.97	0.51	819.62	<0.000
Q3	-0.76	1.12	0.98	0.56	995.44	<0.000
Maximum	1.75	1.30	0.99	0.68	2235.26	<0.000
1000 Bootstrap iterations each built from randomly sampling the plot data with replacement 27 times to equal the number of selected plots.						

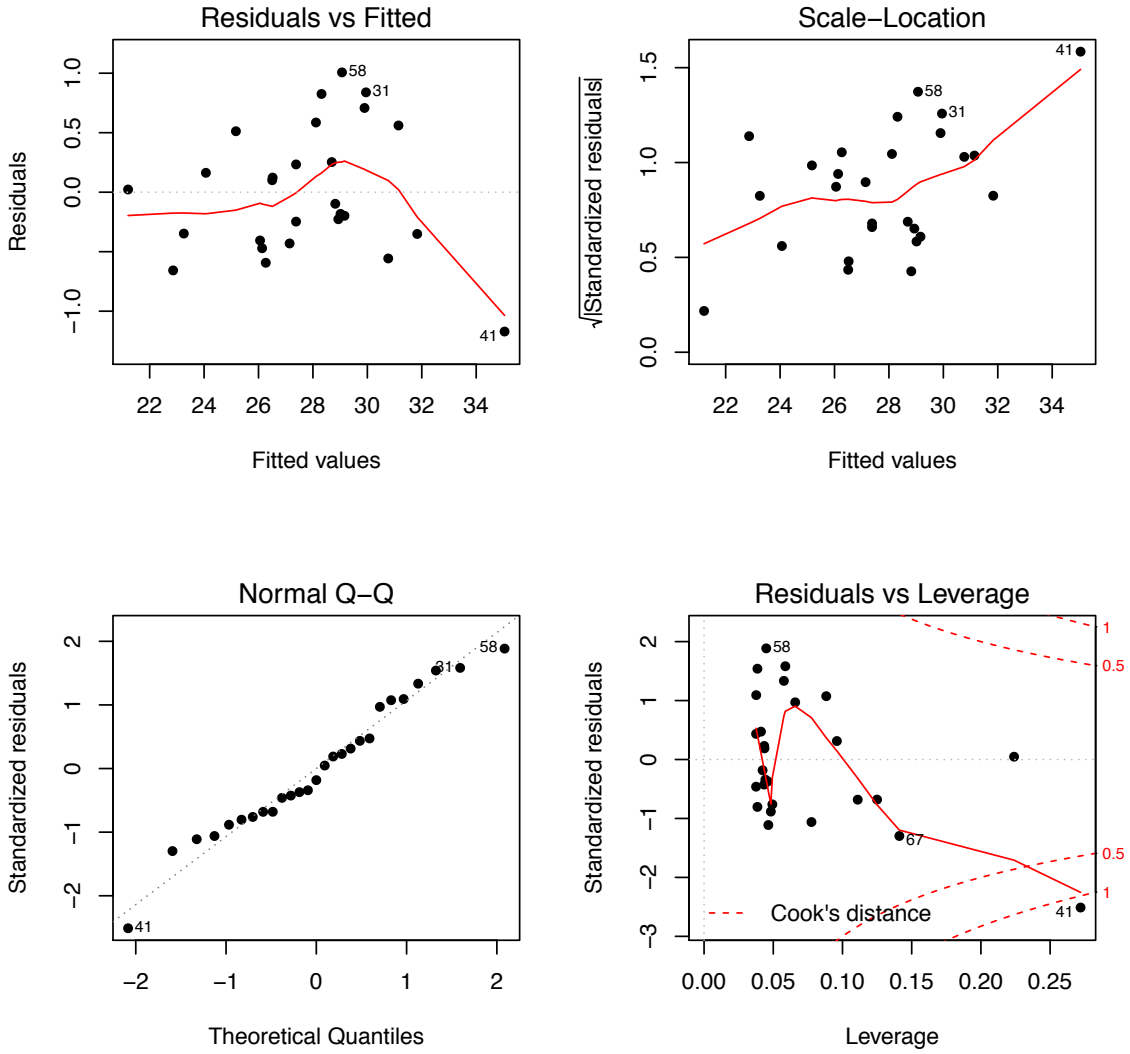


Figure 4.19 Diagnostic plots identified plot 41 as an influential observation which produced a Cooks distance greater than 1, suggesting its omission would significantly affect the model parameters.

A residual analysis suggested that plot 41 contributed to a violation of variance homogeneity and was also considered an influential observation with a Cook's distance greater than 1 (Fig. 4.19). There was no obvious justification for removing this point, height estimations did not produce spurious height extrapolations (Appendix 3) and DBH values, although relatively large, were within reason. The linear model was recomputed omitting plot 41 (Fig. 4.20). The effect of removing the influential plot 41 was an

increase in the slope coefficient to 1.13 and a decrease in intercept to -2.95. The residual standard error was reduced to 0.48m and the f-statistic was increased to 818.1 ($p<0.000$). The coefficient of determination was unchanged with the removal of plot 41. A bootstrapping of the linear model without plot 41 demonstrated a general decrease in parameter variation. The intercepts were ~30% lower and the slopes were ~1.5% higher, the explained variation was marginally increased and the residual error was reduced (Table 4.6). Although the statistical diagnostics imply that the model is marginally better without the impact of plot 41, from a practical point of view it would seem that the model produced including plot 41 is more intuitively accurate as the model parameters are less biased, that is, that the intercept is potentially zero and the slope is close to one.

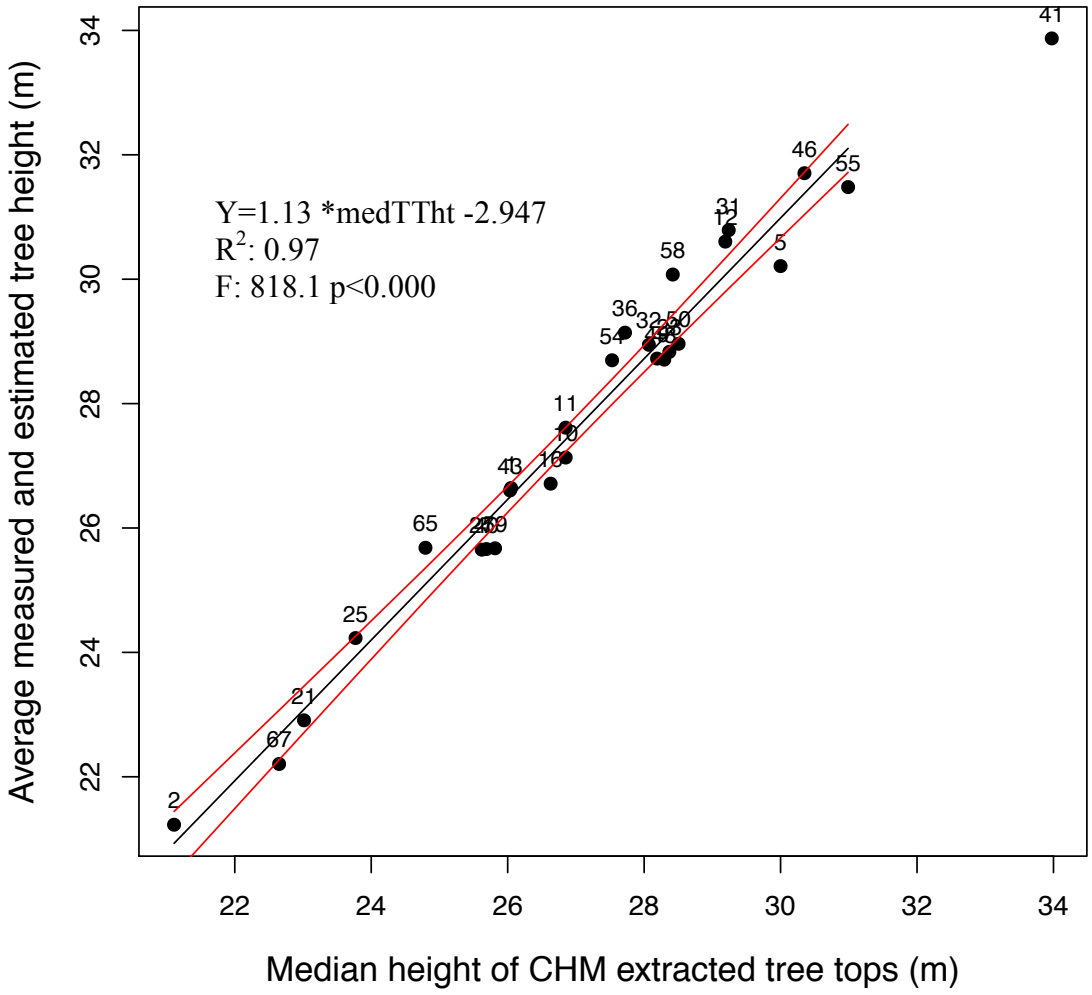


Figure 4.20 The average of measured and modeled tree heights within the dominant and co-dominant crown classes predicted from the median CHM treetop and omitting plot 41. The intercept coefficient is now different from zero (t-test: -2.758. p:0.01) and the slope has increased. The residual standard error is slightly lower (0.48m) than with the inclusion of plot 41.

Table 4.6 Bootstrap of average measured and estimated tree height within the dominant and codominant crown class without the influential plot 41 simple linear model						
	Intercept	medTTht	R^2	RSE	F-stat	P-value
Minimum	-7.54	1.01	0.92	0.31	241.88	<0.000
Q1	-3.72	1.11	0.97	0.43	683.60	<0.000
Mean	-3.06	1.14	0.97	0.46	900.65	<0.000
Median	-2.99	1.13	0.97	0.46	873.51	<0.000
Q3	-2.38	1.16	0.98	0.49	1063.88	<0.000
Maximum	0.37	1.30	0.99	0.60	2341.06	<0.000
1000 Bootstrap iterations each built from randomly sampling the plot data with replacement 26 times to equal the number of selected plots.						

When it is considered that the lidar data provides its best structural description of the uppermost tree crowns it would be logical to expect that the larger trees within a plot would be those best characterized by the lidar data. The Spearman's rho provided evidence that this was the case with a correlation coefficient of 0.96 ($p = 0.000$) produced from top height and average CHM treetop height. The top height attribute is populated from heights from the four trees with the largest DBH. Since the trees with the largest DBH are also likely to be the four tallest trees they are most likely to be well characterized within the CHM raster and to be captured within the local maximum filter used to generate the CHM treetop database. The most correlated remotely sensed metric with top height, according to Spearman's rho, was the average height of the CHM treetops. An attempt was made to approximate the top height attribute from the CHM treetops by averaging the four tallest extracted treetops. Height in this case was taken as a surrogate for diameter because at this plot level analysis no link is made between the individual in the ground database and the airborne survey data, (in contrast to the individual scale of analysis to be under taken in chapters 5 and 6). The treetop equivalent of top height was identified as the second most correlated metric according to Spearman's rho and the 18th most correlated according to Pearson's rho (R: 0.97, rho: 0.97) The linear regression applying the average treetop height produced a fit that was comparable to that produced for the dominant and co-dominant height model. This result was expected, as the stratification by more dominant crown classes would cause a convergence towards the top height values, which should theoretically be built from the most dominant individuals (largest DBH). The R^2 produced from the regression of top height and average CHM treetop height was 0.96 with a standard error of the estimate of

0.59 (Fig. 4.21). As with many of the previous height models the constant term was not significantly different from zero (t-test: 1.909, p: 0.068). Residual analysis again suggested that plot 41 caused a violation of homoscedasticity and was again identified as an influential point. The removal of plot 41 marginally increased the slope coefficient to 1.07 and the R^2 to 0.97 and reduced the RSE to 0.52m. Since the average treetop height was selected through the Spearman's Rho and because it was not the highest correlated feature when assessed by Pearson's R, the data were transformed to determine if a better fit was possible. It was determined that transformations that reduced larger values yielded increases in the R^2 (*i.e.* a square root transform increased the R^2 from 0.96 to 0.97). The 1% benefit of this transformation was considered insufficient given a lack of rationalization for the transformation and the difficulty in interpreting the physical meaning of the transform. It was concluded that the combination of noise inherent within the data and the low observation density at the higher top heights produced a spurious increase in fit with the square root transform. In the previous feature selections for height attribute estimation, features were correlated irrespective of correlation index. For top height, however, the average height above the 85th percentile was ranked 3 and 1 for Spearman's, and Pearson's, respectively, in contrast to the average treetop's rank of 1 and 3, thus the average height above the 85th percentile was also investigated.

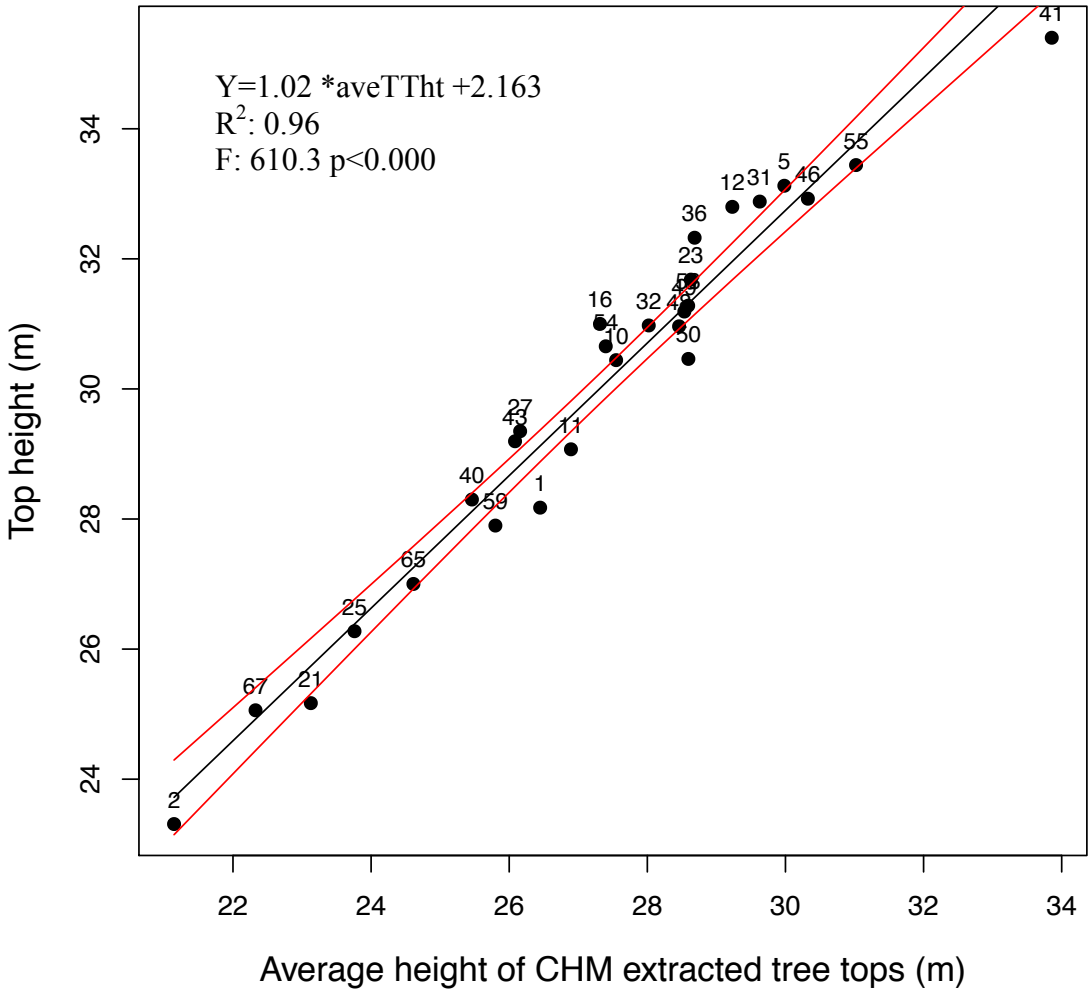


Figure 4.21 Plot top height measured in the field predicted from the average of the treetops extracted from a 50cm raster representing the maximum height of the CHM lidar points. The residual standard error was 0.59m. The intercept may not be different from zero (t-test:1.91, p:0.07)

Table 4.7 Bootstrap of plot top height from average CHM treetop height						
	Intercept	aveTTht	R^2	RSE	F-stat	P-value
Minimum	-1.88	0.88	0.88	0.34	195.72	<0.000
Q1	1.08	0.99	0.95	0.50	508.70	<0.000
Mean	2.01	1.03	0.96	0.55	709.41	<0.000
Median	2.05	1.02	0.96	0.56	652.93	<0.000
Q3	2.91	1.06	0.97	0.61	836.26	<0.000
Maximum	6.32	1.18	0.99	0.74	2269.90	<0.000
1000 Bootstrap iterations each built from randomly sampling the plot data with replacement 27 times to equal the number of selected plots.						

The resulting simple linear regression applying the height above the 85th percentile produced a nearly equivalent fit compared with the average CHM treetop height model (Fig. 4.22, table 4.8). The difference in the RSE between these two models was 2cm, and according to the bootstrapping results, the average residual standard error was 1cm smaller for that produced by the heights above the 85th percentile. In addition, the residuals from the heights above the 85th percentile model were slightly better behaved in the sense that plot 41 was less influential and thus variance homogeneity was less of a concern.

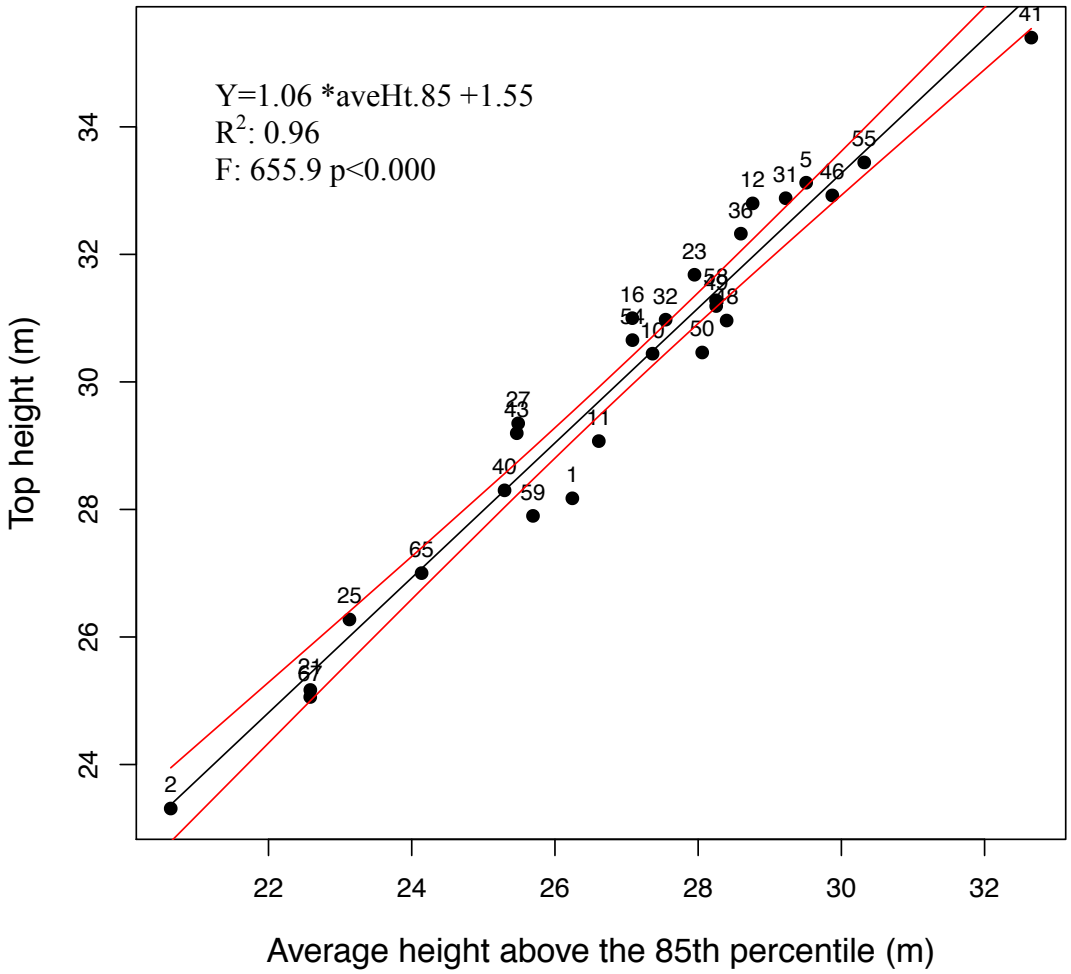


Figure 4.22 Plot top height measured in the field predicted from the average height of lidar returns greater than the 85th percentile of lidar returns. The residual standard error was 0.57m. The intercept may not be different from zero (t-test:1.39, p:0.18)

Table 4.8 Bootstrap of plot top from average height above 85th percentile						
	Intercept	aveHt85	R^2	RSE	F-stat	P-value
Minimum	-1.58	0.94	0.86	0.30	149.45	<0.000
Q1	0.96	1.04	0.95	0.51	517.30	<0.000
Mean	1.49	1.06	0.96	0.54	728.19	<0.000
Median	1.51	1.06	0.96	0.55	676.44	<0.000
Q3	2.02	1.08	0.97	0.58	878.42	<0.000
Maximum	4.82	1.18	0.99	0.69	3266.10	<0.000
1000 Bootstrap iterations each built from randomly sampling the plot data with replacement 27 times to equal the number of selected plots.						

The largest magnitude correlation coefficient produced for height to live crown was with the LHQ_{10} quantile metric, irrespective of correlation index. It is physically logical that a low height percentile would be correlated with the height to live crown, as the lower portion of the lidar height distribution would correspond to lidar positions returned from tree stems or potentially some regenerating individuals. In the Spearman's correlation analysis the eight most correlated metrics were all lidar height quantiles from the 5th to the 40th percentile, the strength of the association decreasing as they became further from the 10th percentile. A similar pattern was found in the Pearson correlation results, the exception being that the 5th percentile was ranked 22nd. The Spearman's rho for HTLC and LHQ_{10} was 0.95 ($p < 0.000$) and decreased by approximately 0.002 with every 5 percentile from the 10th percentile, to 0.936 at the 40th height percentile. In the simple linear regression of HTLC and LHQ_{10}, the fit was positive and again very strong, with a coefficient of determination of 0.94 and a standard error of the estimate of 0.58 (Fig 4.23, 4.24 and Table 4.9). The Durbin-Watson statistic of 1.79 suggested there was a slight positive autocorrelation in the residuals, although the variance of errors in diagnostic plots appeared to be uniform.

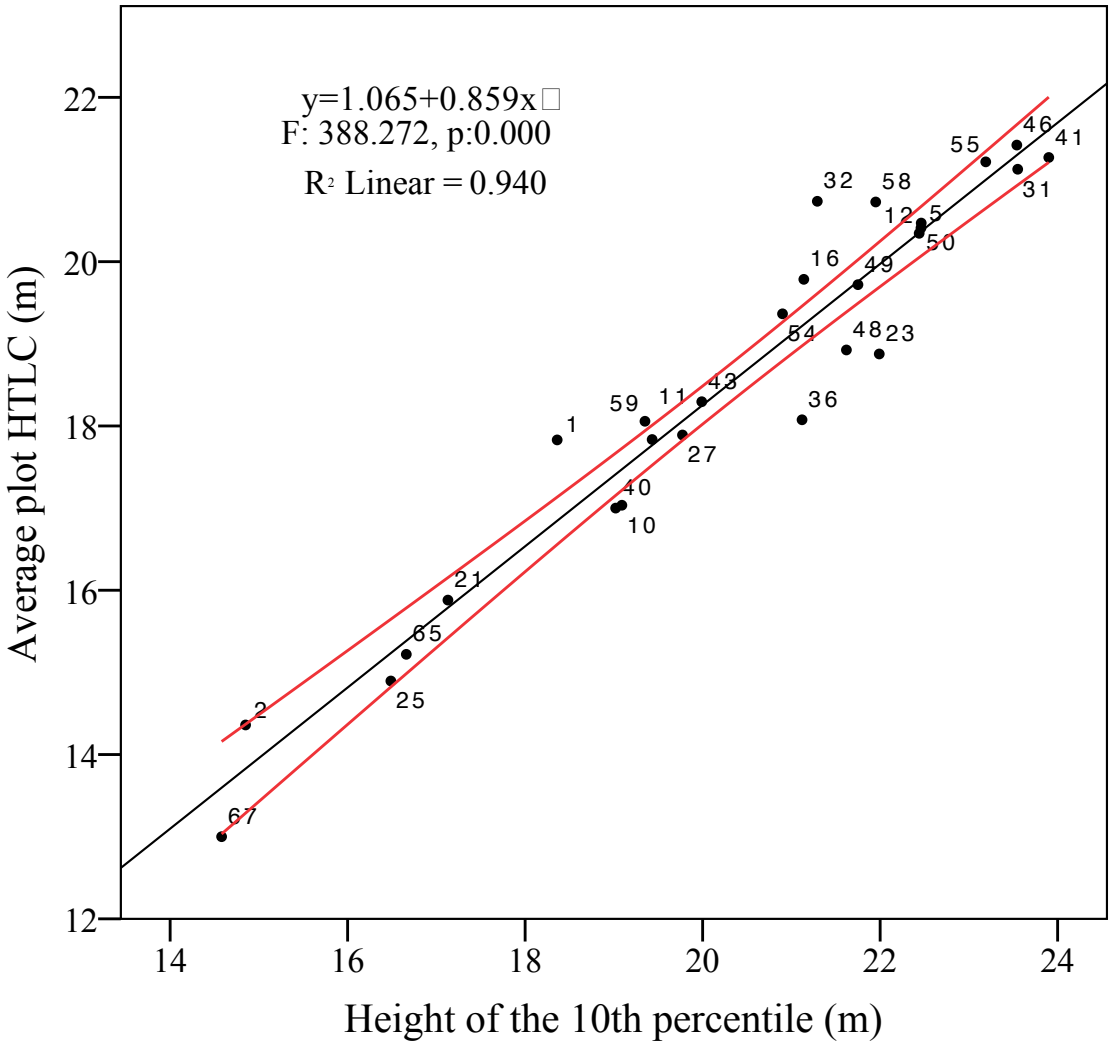


Figure 4.23 Average plot height to live crown measured in the field predicted from the height at the tenth percentile of lidar CHM point heights. The residual standard error is 0.58m. Interestingly control plots and low stem density (via root disease) plots produce a data cluster with low HTLC and LHQ_{10}.

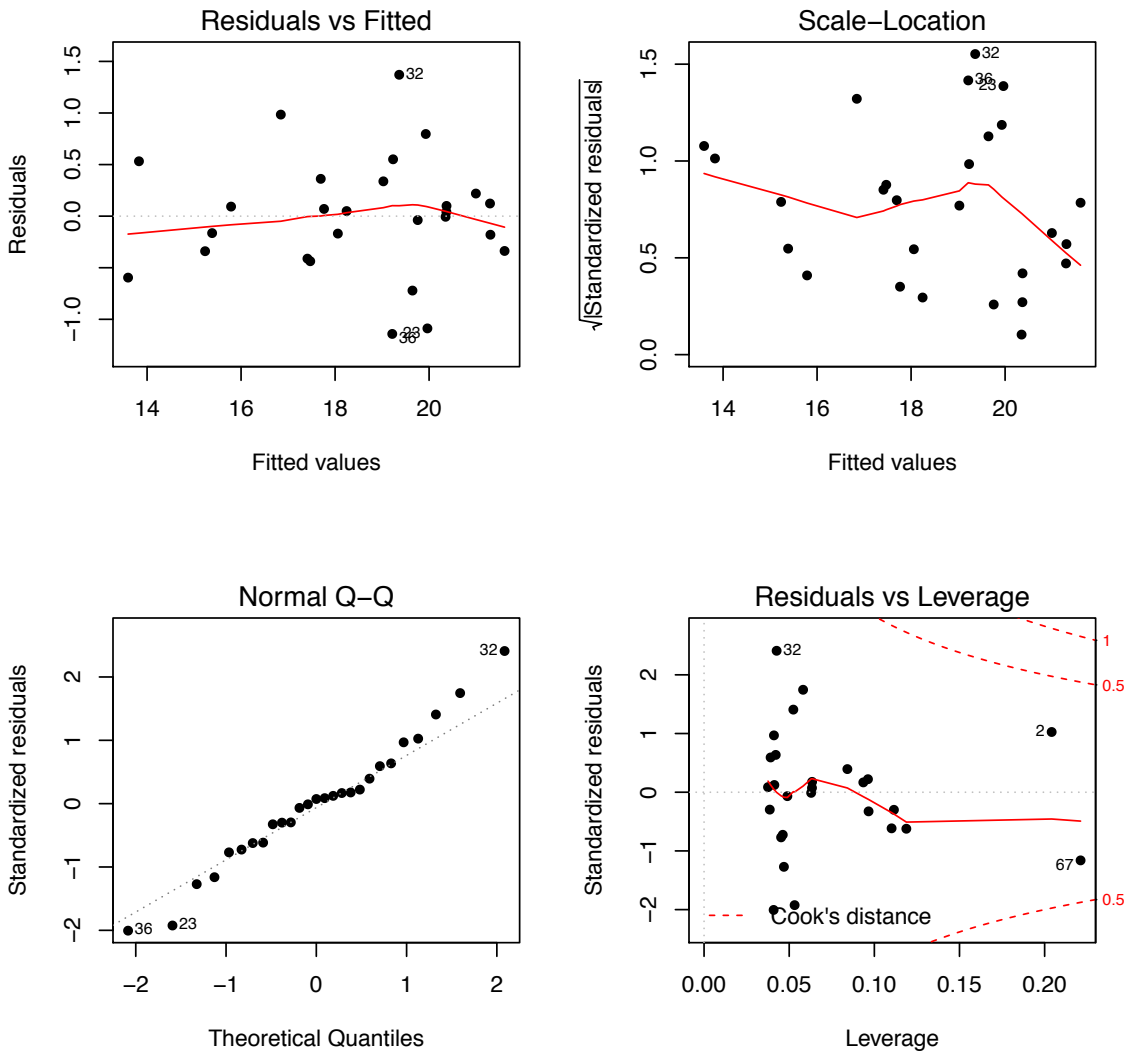


Figure 4.24. Residual plots for simple linear regression of HTLC from LHQ10 does not strongly support Durban-Watson test of variance homogeneity (DW: 1.79, p: 0.54). While the spread in the residual plot might suggest a positive error variance to fitted value association, the scale plot does not strongly suggest that the absolute errors increase with the fitted values.

Table 4.9 Bootstrap of plot average HTLC estimated from LHQ 10						
	Intercept	LHQ_{10}	R^2	RSE	F-stat	P-value
Minimum	-1.06	0.74	0.80	0.23	98.28	<0.000
Q1	0.54	0.84	0.92	0.49	301.36	<0.000
Mean	1.06	0.86	0.94	0.55	468.61	<0.000
Median	1.07	0.86	0.94	0.55	412.44	<0.000
Q3	1.56	0.88	0.96	0.61	584.86	<0.000
Maximum	3.47	0.98	0.99	0.80	2793.04	<0.000
1000 Bootstrap iterations each built from randomly sampling the plot data with replacement 27 times to equal the number of selected plots.						

Average crown length was processed through a correlation analysis for feature selection, which selected two features representing the variation within the CHM raster (standard deviation and coefficient of variation) as the most associated with Spearman's Rho values of 0.85 and 0.67 respectively. These features were not identified as the most correlated when Pearson's correlation was queried. Therefore, the nonlinear association was investigated for an appropriate transformation. The scatterplot of these data suggested a logarithmic or an exponential transformation. Two model forms were estimated with nonlinear least squares in the form $CL=a*\ln(sdCHM)+b$ and $CL=a*sdCHM^b$. The fitted exponent model produced a scale value of 4.58 and an exponent of 0.39, the resulting transformation yielded an R^2 of 0.50 and a RSE of 0.95. The fitted logarithm model produced a constant term of 3.329 and a coefficient of 3.327, the resulting transformation produced an R^2 of 0.53 and an RSE of 0.92. Both of these linear transformations were inferior to the best linear predictor identified by the Pearson's correlation. According to the Pearson's R, the six most associated features with crown length were variation metrics of the photochemical reflectance index (PRI).

The PRI index is sensitive to de-epoxidation states of the xanthophyll cycle pigments [126], [127]. The xanthophyll cycle provides a means of photo protection through heat dissipation. Under excessive light conditions violaxanthin, containing two oxygen bound ring structures is converted to zeaxanthin (without either of the two oxygen containing rings) through the intermediate antheraxanthin. In the process, excitation energy is converted to heat. At the same time, these transformations from violaxanthin have concurrent reflectance changes where an absorption feature is produced at ~531nm. Due to the role these pigments play in non-photochemical

quenching of excitation energy, the relative xanthophyll contents are indicative of light use efficiency [39], [128]–[130]. It is speculated that the increased variation in PRI with larger crown lengths is produced by the structural effect of a more varied canopy surface and thus more variation in irradiance. The varied irradiance would in turn produce variations in the demands of non-photochemical quenching and variations in zeaxanthin and antheraxanthin content.

Relative to other structural attributes previously assessed, the explained variance in crown length by PRI_{cv} was considerably lower, at roughly 50 percent (Fig.4.25 & 4.26). The PRI coefficient of variation was the feature most associated with crown length producing a Pearson's R of 0.73.

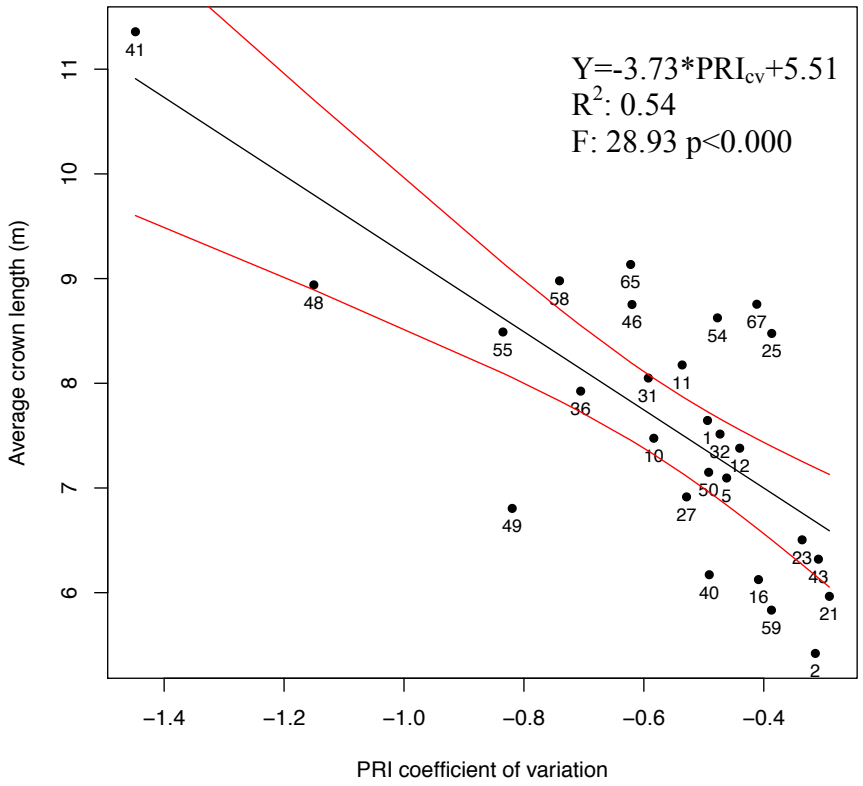


Figure 4.25. Average plot crown length measured in the field predicted from the coefficient of variation of the photochemical reflectance index. The residual standard error was 0.92m. There is structure in the residuals where the model over estimates crown length at less negative PRI CV followed by a region of under estimation near -0.6 PRI CV.

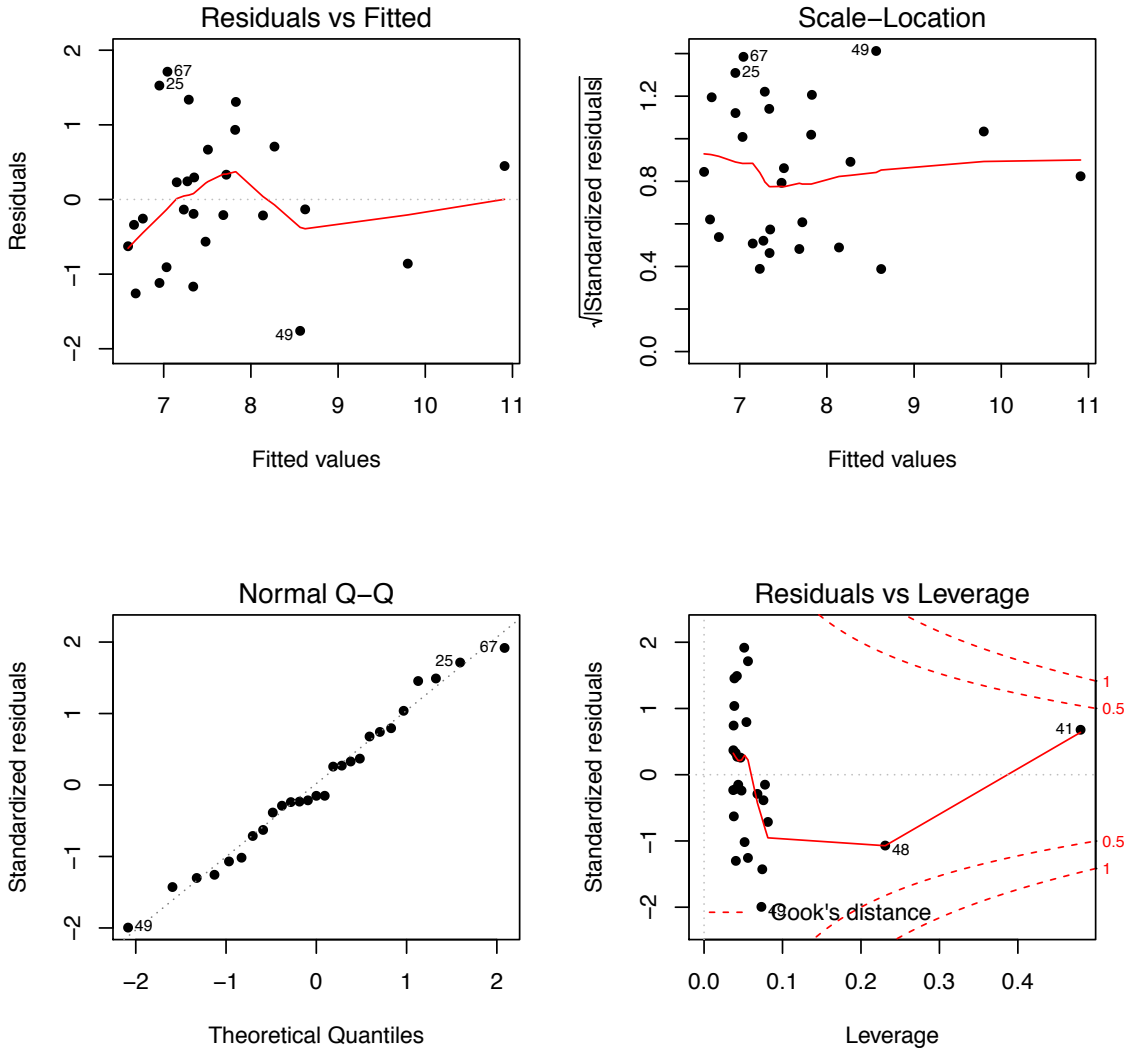


Figure 4.26. Residual plots for simple linear regression of CL from PRI CV. There is an apparent non-constant error trend in the residual plot suggesting that the model form is incorrect.

Table 4.10 Bootstrap of plot average HTLC from PRI coefficient of variation						
	Intercept	PRI_{cv}	R^2	RSE	F-stat	P-value
Minimum	2.88	-8.73	0.00	0.48	0.06	<0.000
Q1	5.20	-4.17	0.40	0.81	16.39	<0.000
Mean	5.50	-3.76	0.51	0.88	33.87	0.006
Median	5.47	-3.78	0.54	0.89	29.00	<0.000
Q3	5.81	-3.31	0.64	0.95	44.36	<0.000
Maximum	7.35	-0.39	0.87	1.19	172.40	0.803
1000 Bootstrap iterations each built from randomly sampling the plot data with replacement 27 times to equal the number of selected plots.						

The linear regression and residual analysis suggested that there might be some structure in the model residuals. The linear model tended to overestimate at less negative PRI_{cv} followed by a region of underestimation at slightly more negative PRI_{cv}, Additionally, the bootstrap result demonstrated much variation in the coefficient of determination, calling into question the consistency of this attribute for estimating crown length. Perhaps these results are spuriously caused by the sampling. In an effort to resolve the non-constant residuals, an exponent of absolute PRI_{cv} transformation was considered. The parameters of the non-linear fit were found as 9.288 for the scale and 0.318 for the exponent term. The linear regression applying the transformed PRI_{cv} marginally decreased the residual standard error to 0.90 and slightly increased the R^2 to 0.54 (Fig. 4.27). However, the residuals analysis illustrated that the trend observed in the untransformed data, although reduced, was not entirely removed and according to the scale-location plot, the transformation had induced heteroscedasticity, where the variance of the errors increased with crown length (Fig. 4.28). The residual autocorrelation was interpreted as being largely dependent on the low data density at high crown length and high transformed PRI_{cv} levels, a perspective that would be supported by the bootstrap results.

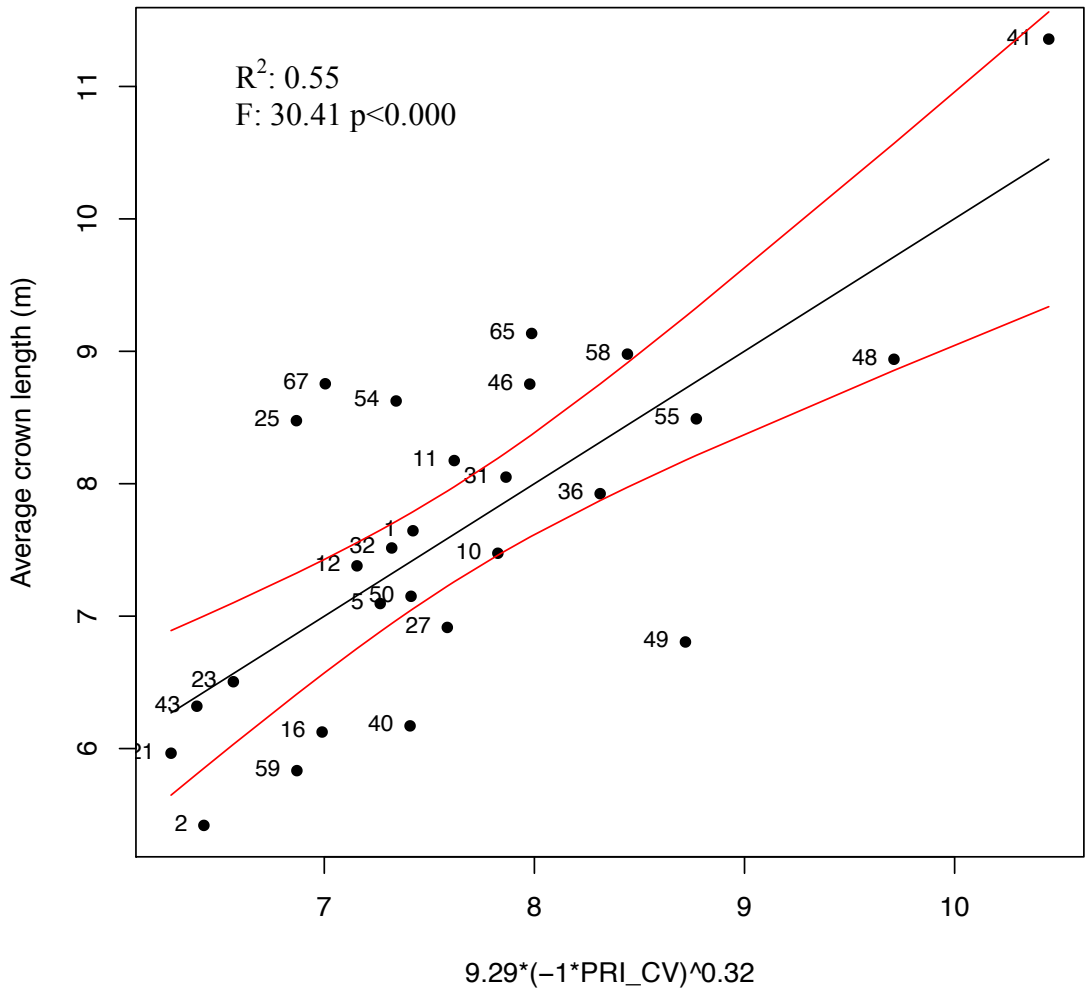


Figure 4.27. Average plot crown length measured in the field predicted from the transformed coefficient of variation of the photochemical reflectance index. The residual standard error was 0.90m. The structure in the residuals was not eliminated by the transformation.

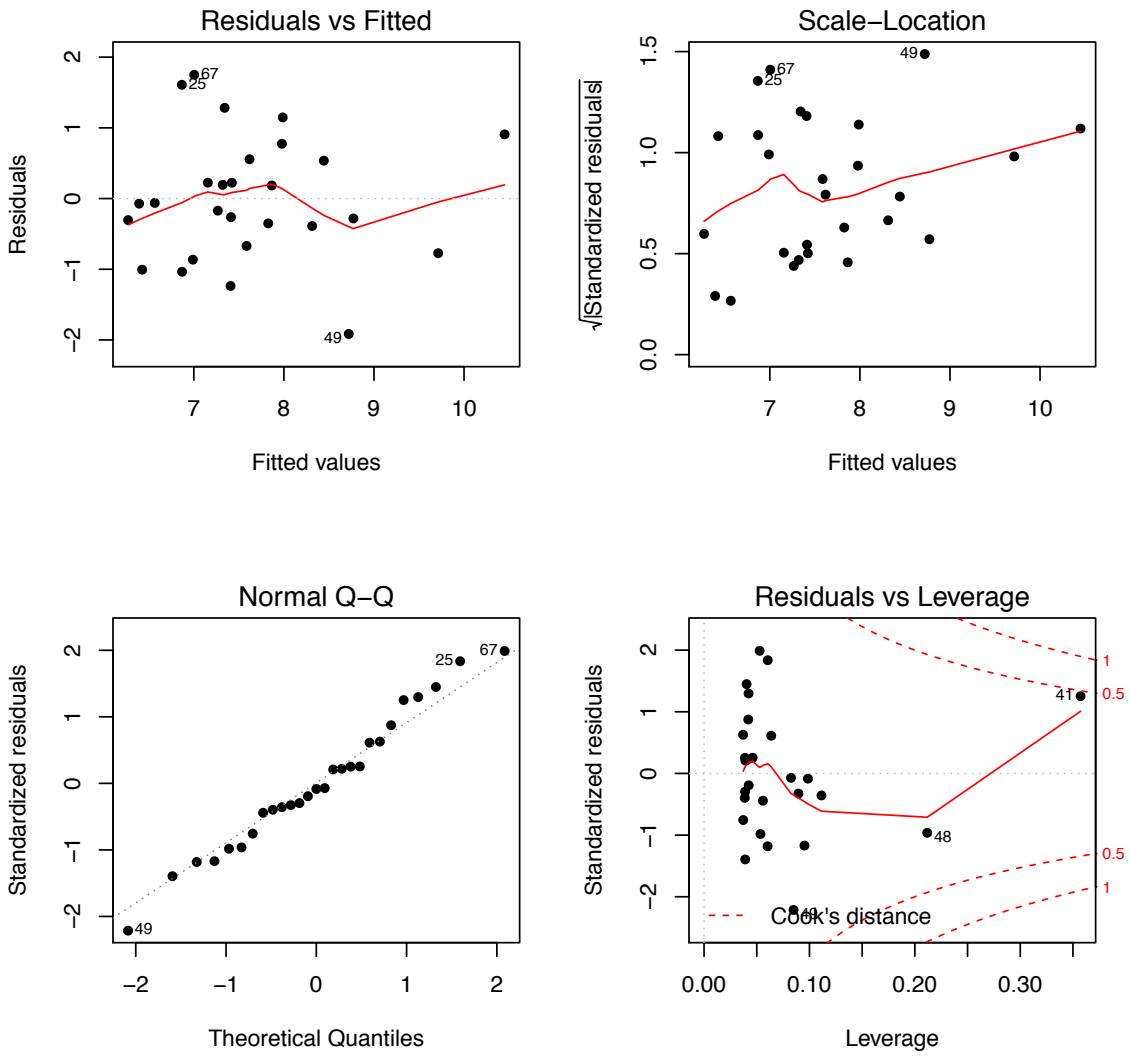


Figure 4.28. Residual plots for simple linear regression of CL from PRI CV. There is an apparent non-constant error trend in the residual plot suggesting that the model form is incorrect.

Given the successes in estimating height and height to live crown through lidar metrics, crown length was estimated using the previously identified metrics of median treetop height and the LHQ_{10}. The linear model produced a residual standard error of 0.87m and coefficients of 0.98 (se: 0.18, p:<0.000) for the median TT height variable and a -0.83 (se: 0.18, p:<0.000) for the LHQ_{10} variable and a constant of -2.25 (se: 1.84, p: 0.23). Given the coefficients and their standard errors (containing the value of one for the treetops and -1 for the LHQ_{10}), the crown length model could potentially be applied as

the difference between the two variables, perhaps after a constant bias is determined (although the above model with coefficients not equal to 1 suggested that the constant may not be different from zero). The adjusted R^2 for the multiple linear regression was 0.56; the multiple linear model explains only one percent more of the variation in crown length than the PRI_{cv} equivalent model. However, the multiple linear model is a much more attractive option from the sense that the relationship between these variables and crown lengths are more directly and physically related (Fig. 4.29). Plot 41 was clearly an outlier with reference to the other observations but aligned well with the model, the residual-leverage plot illustrated that plot 41 exhibited a large leverage statistic signifying that it had much influence on the resulting model. The analysis was recomputed without the inclusion of plot 41. The result produced slightly different and more variable parameters, with an intercept of -2.15 (se: 2.56, p = 0.41), a treetop coefficient of 0.97 (se: 0.25, p:<0.000) and a LHQ_{10} coefficient of -0.82 (se: 0.24, p = 0.002). While the residual standard error was 0.89m, only 2cm larger than the model that included the high leverage plot 41, the adjusted coefficient of determination plummeted to 0.36. To reiterate, there was no obvious reason to explain why plot 41 would be different from the other plots evaluated, aside from its low stem density, and greater growth and consequently its taller plot height.

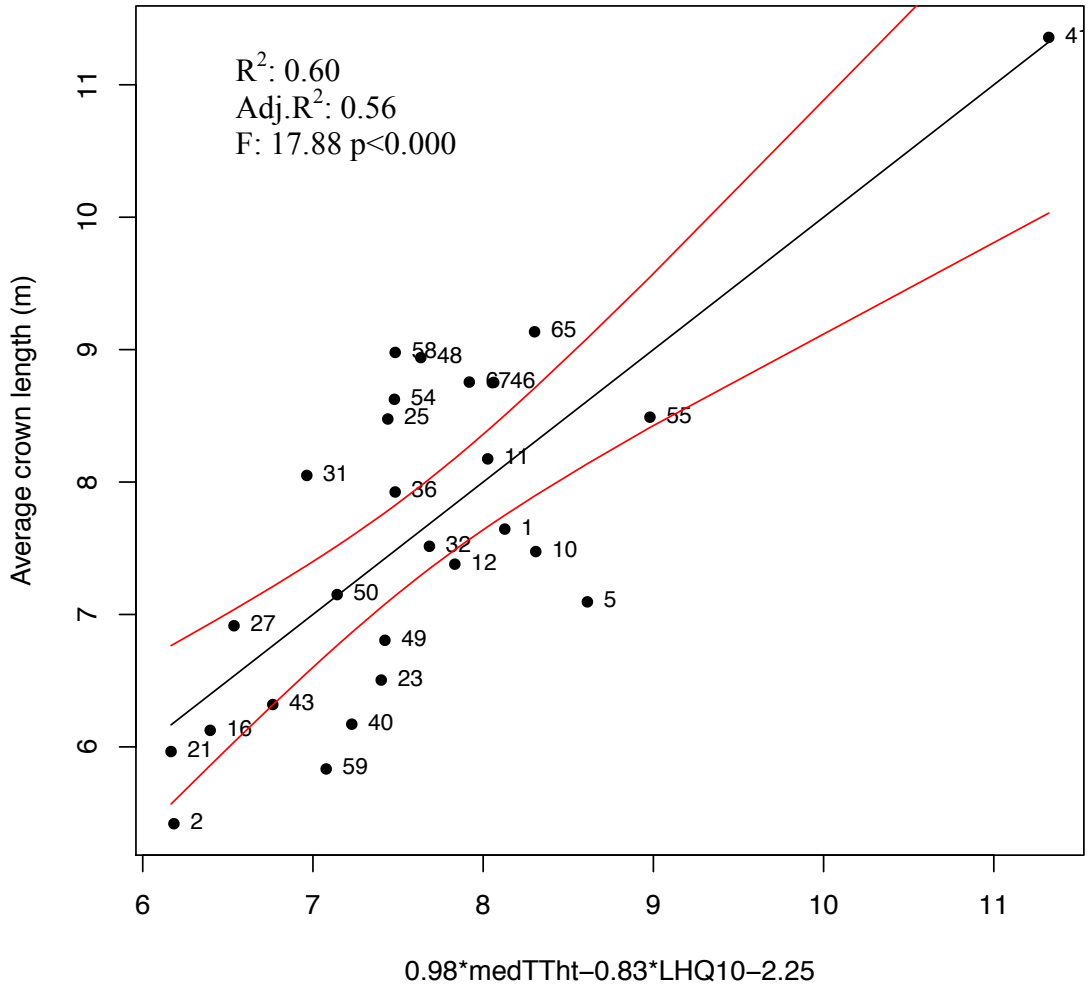


Figure 4.29. Average plot crown length measured in the field predicted from the median CHM treetop height and the LHQ_{10}. The residual standard error was 0.87m.

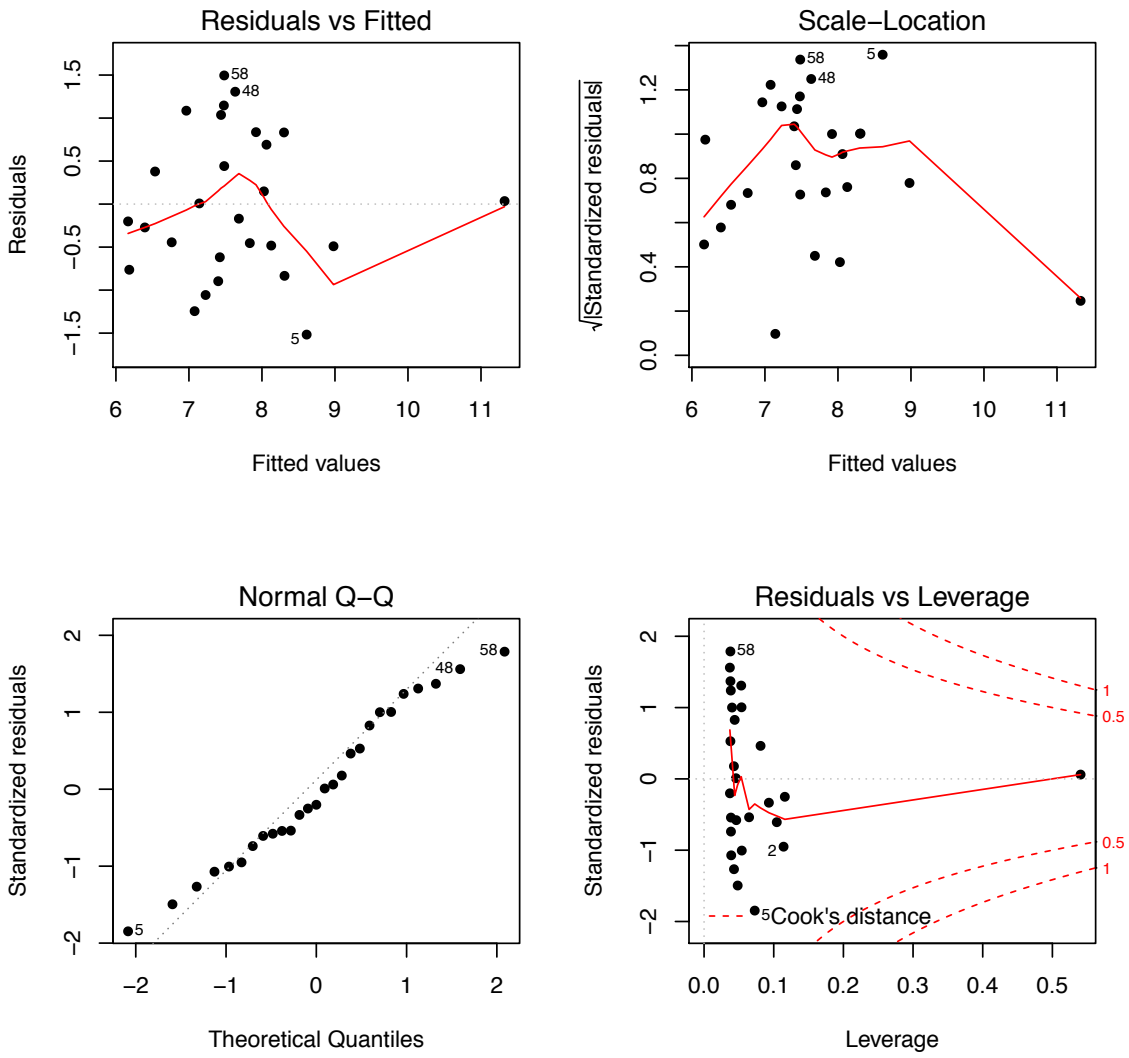


Figure 4.30. Residual plots for simple linear regression of CL from median CHM treetop height and LHQ_{10}. Plot 41 has a high leverage value.

The correlation analysis of plot average crown width suggested that the standard deviation of the CHM was most associated (Spearman's). However, correlation coefficients were smaller in magnitude than even the crown length correlation results (Rho: 0.68). The association between CHM standard deviation and crown width was considered reasonable, as wider crowns were expected to result in a greater number of CHM cells that capture the apical shape of individual crowns. In addition, wider crowns were expected to have larger vertical relief from crown boundaries to treetops, thus

explaining why it would be reasonable to expect greater CHM variation in plots that exhibit larger crown radii. The scatterplot of CHM standard deviation with crown width identified that plot 67 and plot 65 were outliers relative to the rest of the data and a transformation would be required (Fig. 4.31). A reciprocal transformation was required to linearize the CHM standard deviation data. The source of the outlier pattern was apparent when mapping the GPS plot extents against the 50cm CHM data. As illustrated in figure 4.32 the plots with large CHM standard deviations are those that have a canopy gap component, namely plots 67, 65, 11, 48 and to a lesser extent 25 and 1.

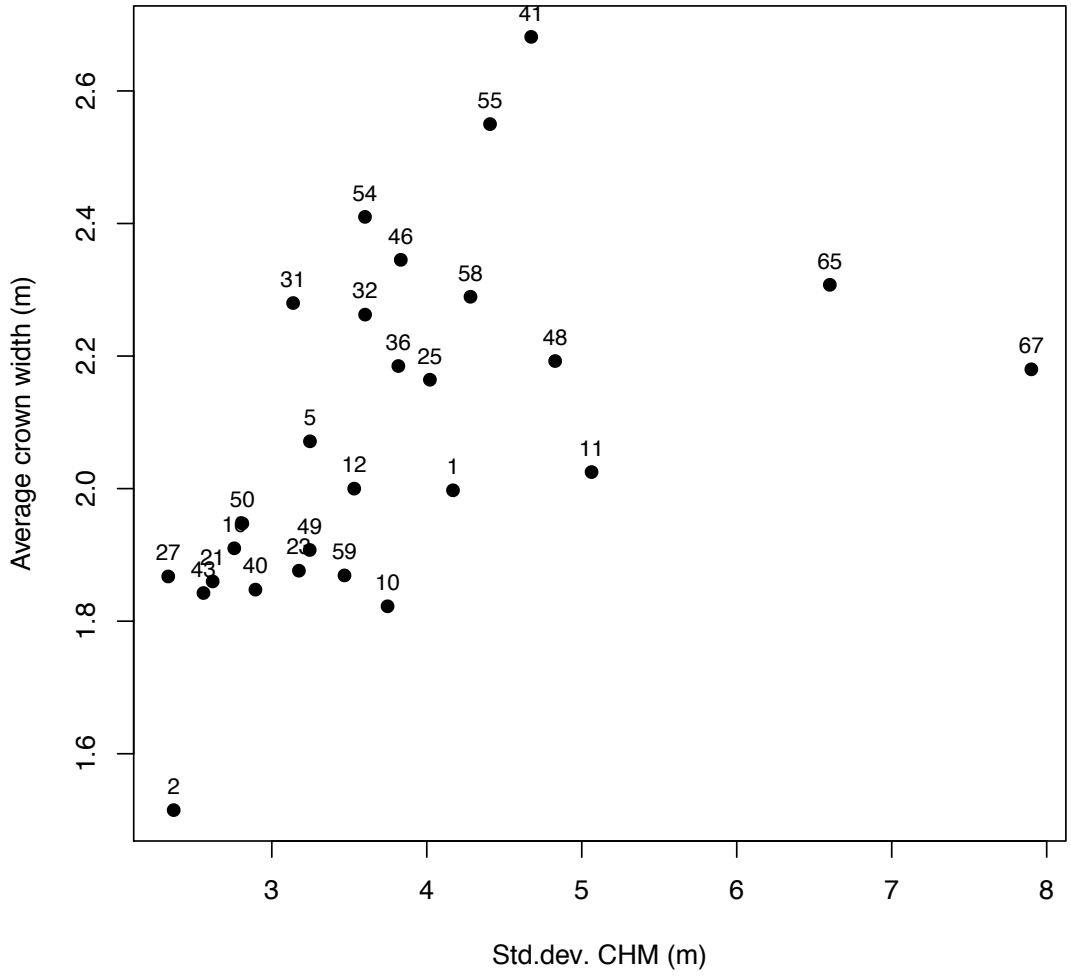


Figure 4.31. Average plot crown width measured in the field plotted with the standard deviation of the CHM. Plots 65 and 67 are outliers in terms of their CHM standard deviations. Their extreme values are attributed to canopy gaps.

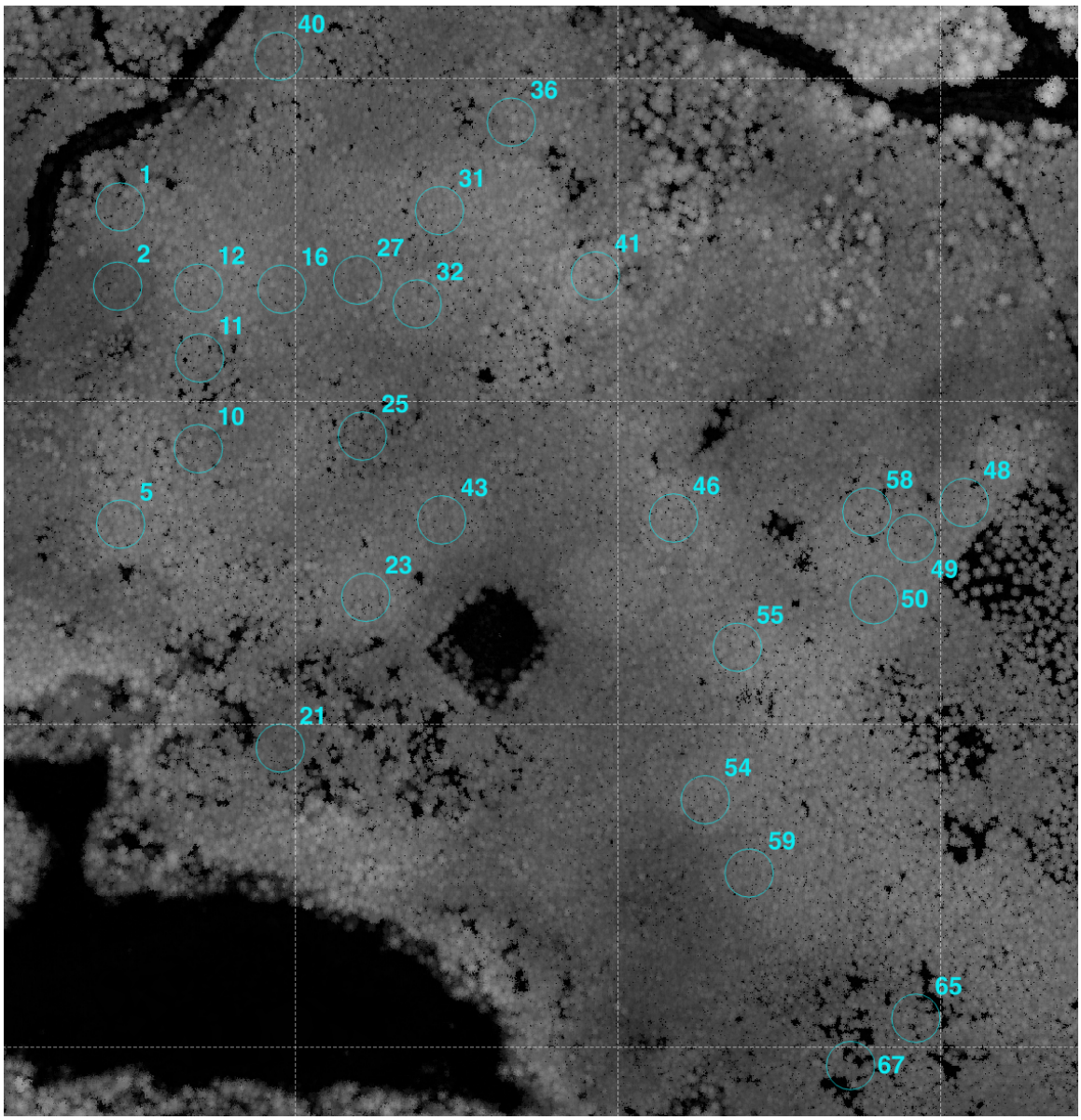


Figure 4.32. Average plot crown width measured in the field plotted with the standard deviation of the CHM identified a number of outliers whose departure were attributed to the occurrence of canopy gaps, see plots 67, 65, 11 and 48.

Given the confounding effect that gap structure had on the relationship between crown width and CHM standard deviation, a lidar representation of canopy closure was assessed for improving the estimation of crown width. Linear regression models were built that included the transformed CHM standard deviation and one canopy closure fraction at

each of the 5th lidar height percentiles. The coefficient of determination for each model was plotted to visualize the amount of explained variation with each of the CCF quantiles (Fig 4.33). The explained variation in crown width was quite small (Fig. 4.34 & 4.35). Efforts were redirected to the most linearly associated remote sensing metric. Given the potential for plot 2 to exhibit a strong model influence, a bootstrap was included in the feature sorting based on R^2 values.

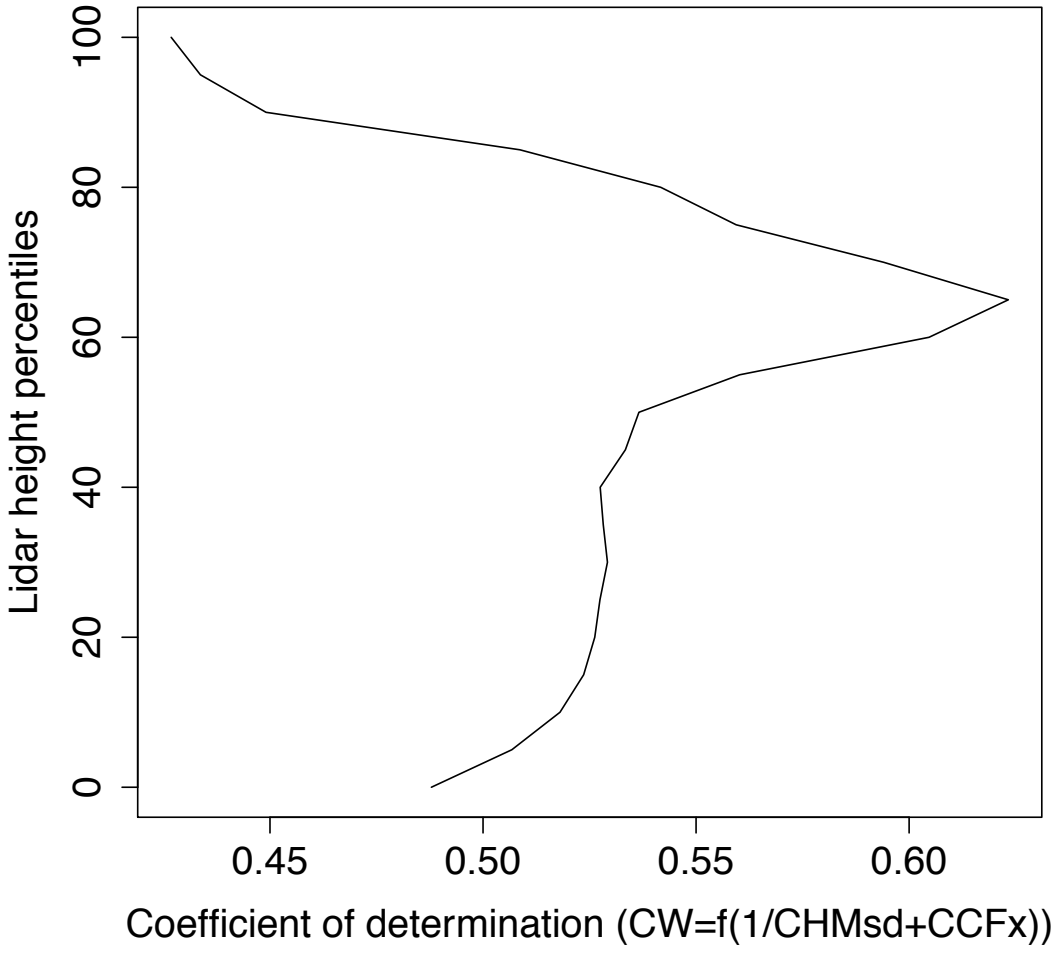


Figure 4.33. Canopy gaps confounded the relationship between crown width and CHM standard deviation. CCF is a lidar representation of gap that was expected to improve the crown width model. CCF is computed at lidar height quantile intervals of 5%. The R^2 was plotted for each quantile, which represents the fit when the CHM standard deviation model includes the CCF at the corresponding height percentile. The fit of crown width and estimates are maximized at CCF_{60}.

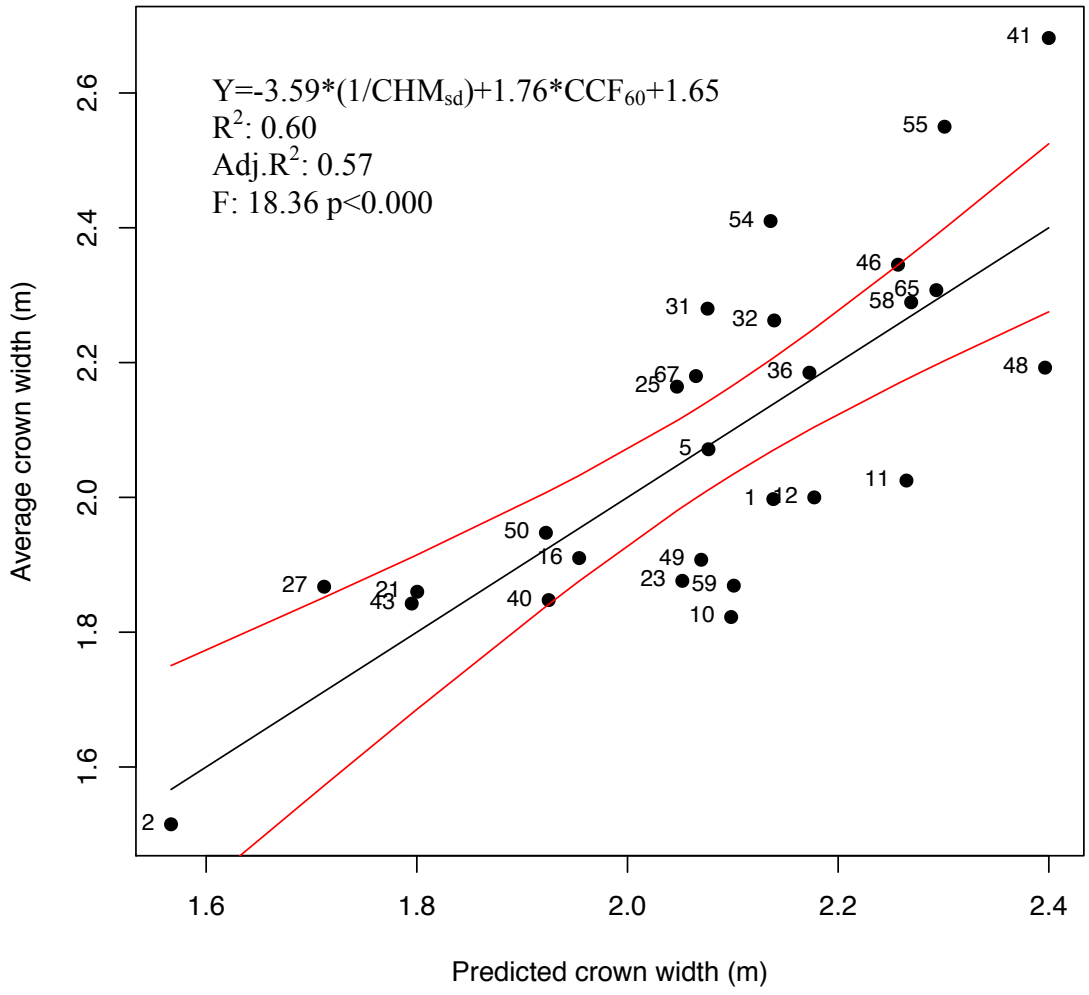


Figure 4.34. Average crown width estimated from the standard deviation of the CHM and the canopy closure at the 60th height percentile. The residual standard error is 0.17.

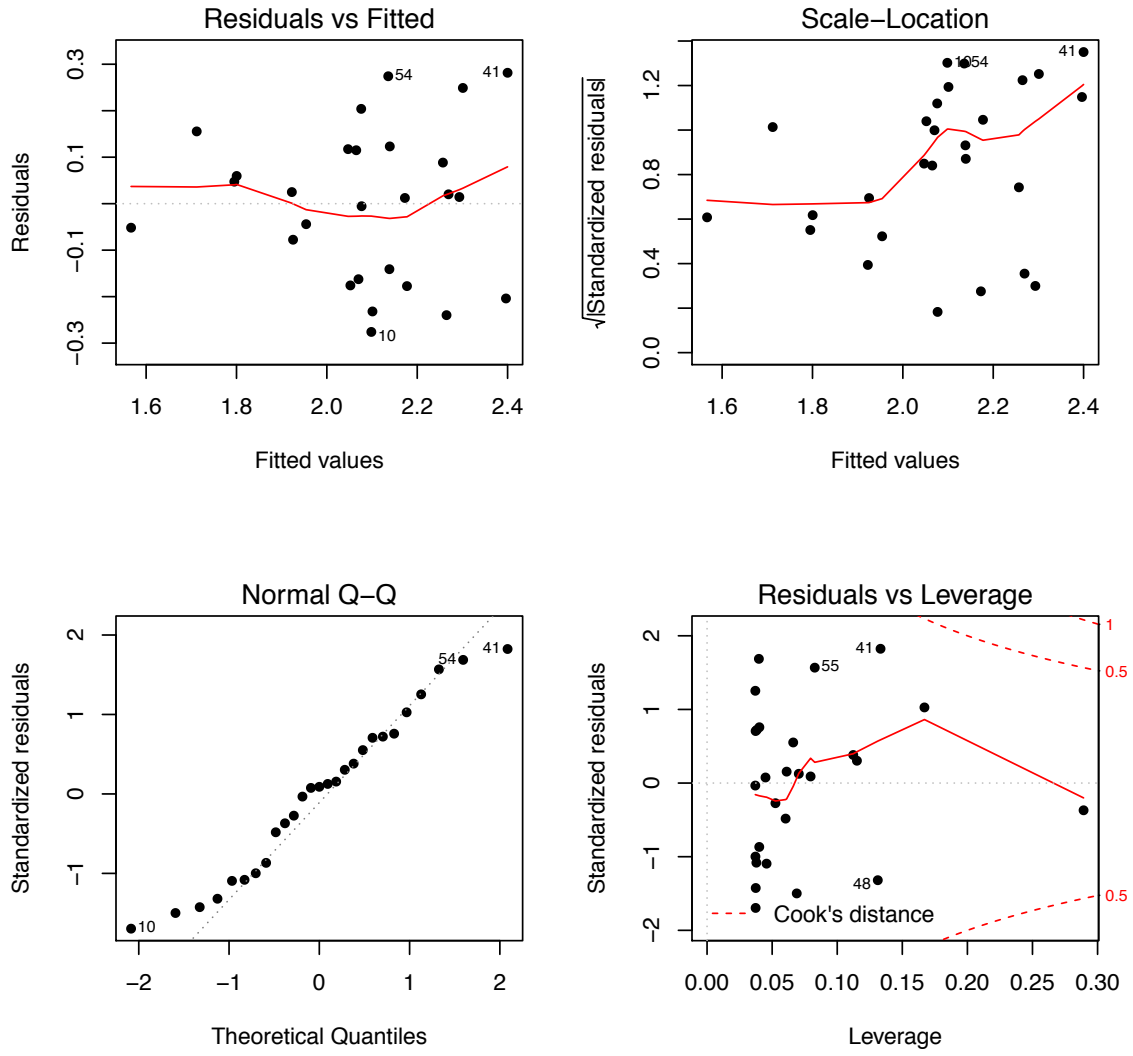


Figure 4.35. Residual plots for multiple linear regression of crown width from CHM standard deviation and CCF_{60}. The residuals are generally well behaved, but there may be evidence in the scale-location plot for positively correlated variances.

According to the mean R^2 value, the most linearly associated metric with average plot crown width was, surprisingly, not a lidar horizontal structure metric but the symmetry metric of the chlorophyll absorption feature (plot average left area/right area) derived from the spectrometer data. Interestingly, the bootstrap had no effect on the metric sequence of the three most associated features. The justification of the symmetry

metric for estimating crown width is not overwhelmingly strong, but if there is an argument to be made in support of its use, it might be related to crown density and the correlation of crown width and crown length. The Pearson coefficient produced from average plot crown width and average plot crown length was 0.88 suggesting that nearly 77% of the variation in crown width can be explained by crown length. Previous laboratory spectroscopy work suggested there was little health-related utility for the feature symmetry metric [10], [101], however these studies, while investigating pigment estimation, controlled leaf area, which is certainly not the case in this project. The right area metric is known to be affected by variations in foliar cell structure. At the canopy scale, this should translate to a sensitivity to variations in LAI, perhaps confounded by crown structure [8]. These data suggest that 22% of the variation in the right area metric is explained by crown length and an additional 41% is explained by HTLC (perhaps capturing variations in crown closure). However, when all structural attributes were considered for explaining right area variations, top height was the only attribute that contributed significantly (R^2: 0.70, F: 56.99, p:<0.0001). The plot right area extremes provide the metric with some merit. Plot 41, which has stood out as having tall and wide crowns, also exhibits the maximum mean right area, while plots 2 (T0F0), 21 (T0F0) and 67 (active root disease with large gaps) all have the lowest three right areas. Of these three plots, plot 2 has the smallest measured crown widths, plot 21 is approximately the 18th percentile of the plot average measured crown widths and plot 67 occurs at roughly the 63rd percentile. Plot 67 is different in this case as it has the lowest right area but slightly larger than average (2.1m) crown widths. Additionally, plot 67 has an 85th percentile crown length. This suggests that the right area response becomes more

sensitive under open canopy conditions. The response of plot 67 is interpreted as, either the crowns are experiencing shorter needle retention and are more optically transmissive, and/or the low stem density and high gap is producing a condition where the reflected response of crown boundary pixels, which may have one or few lidar returns above the 2m threshold, are largely produced from the desiccated and necrotic ground cover vegetation. Equally as likely is the case for the effect of reduced canopy chlorophyll on the left area metric, as this attribute is strongly affected by pigment contents. Investigating the left area metric revealed that plot 67 and plot 10 were the extremes, which also corresponded to the extreme residuals of a CW=m*CRDNRA+b model. Explaining the variation in left area through the field data attributes placed an emphasis on the separation of plot 67, that is, the three factors representing the year of plot establishment, sulphur treatment and re-fertilization were most associated with the left area metric ($P<0.008$). These analyses suggested that the symmetry metric is a hybrid index that contains information about foliar pigment contents and crown volume (or more specifically top height). Although residuals and diagnostic plots for the crown width and symmetry model suggested the assumptions were reasonably met, the symmetry metric still was only able to explain 49.0% of the variation in average plot crown width. The intercept was significantly different from zero (t: 6.09 $p<0.000$) and the slope coefficient was found as -3.97 (standard error: 0.81, t: -4.90, p: <0.000). The f-statistic was 24.02 ($p<0.000$). The resulting residuals were submitted to the feature selection process to investigate if there could be more information extracted from the remote sensing metrics. The standard deviation of the CHM was again selected as significantly contributing to the variation in crown width. The reciprocal of the CHM metric was again applied and

increased the explanatory power of the model (Fig. 4.36). The model residuals were considered normal with a median residual of 0.01 and a residual standard error of 0.15 (df: 24, n: 27) and an adjusted coefficient of determination of 0.66 (R^2: 0.68) (Fig. 4.37). The resulting f-statistic was 25.74 (p: 0.0001). While, this model was an improvement over the previous crown width model, the lack of an association with the lidar derived tree crowns was unexpected. Average plot tree crown width was derived from the lidar extracted tree crowns and an assumption of circular crown extents. The lidar derived tree crown widths only explained 2% of the variation in measured crown width. The linear association was not significant (p:0.51). This observation clearly demonstrated that the crown extraction parameters would need to be refined with ground based positional information.

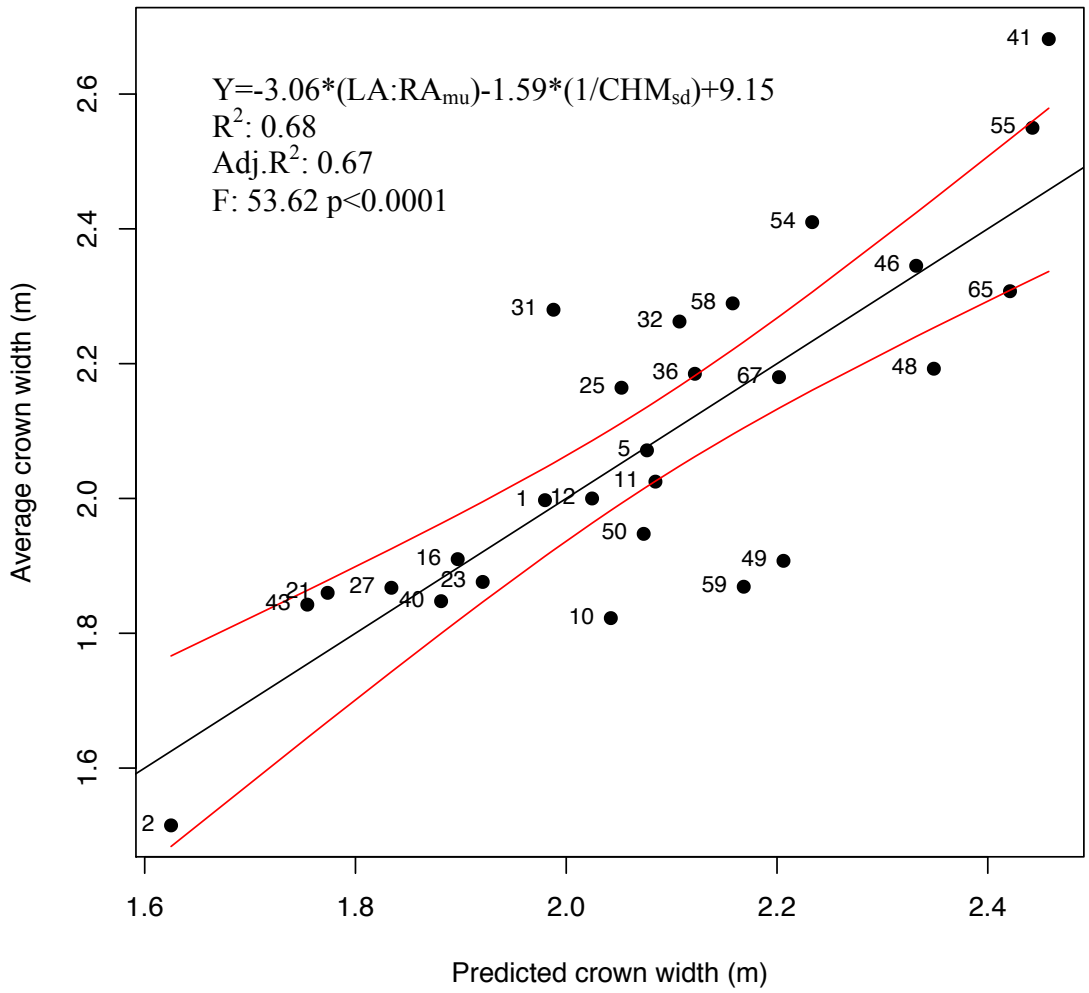


Figure 4.36. Average crown width estimated from plot mean 680nm feature symmetry and standard deviation of the CHM. The residual standard error is 0.15m.

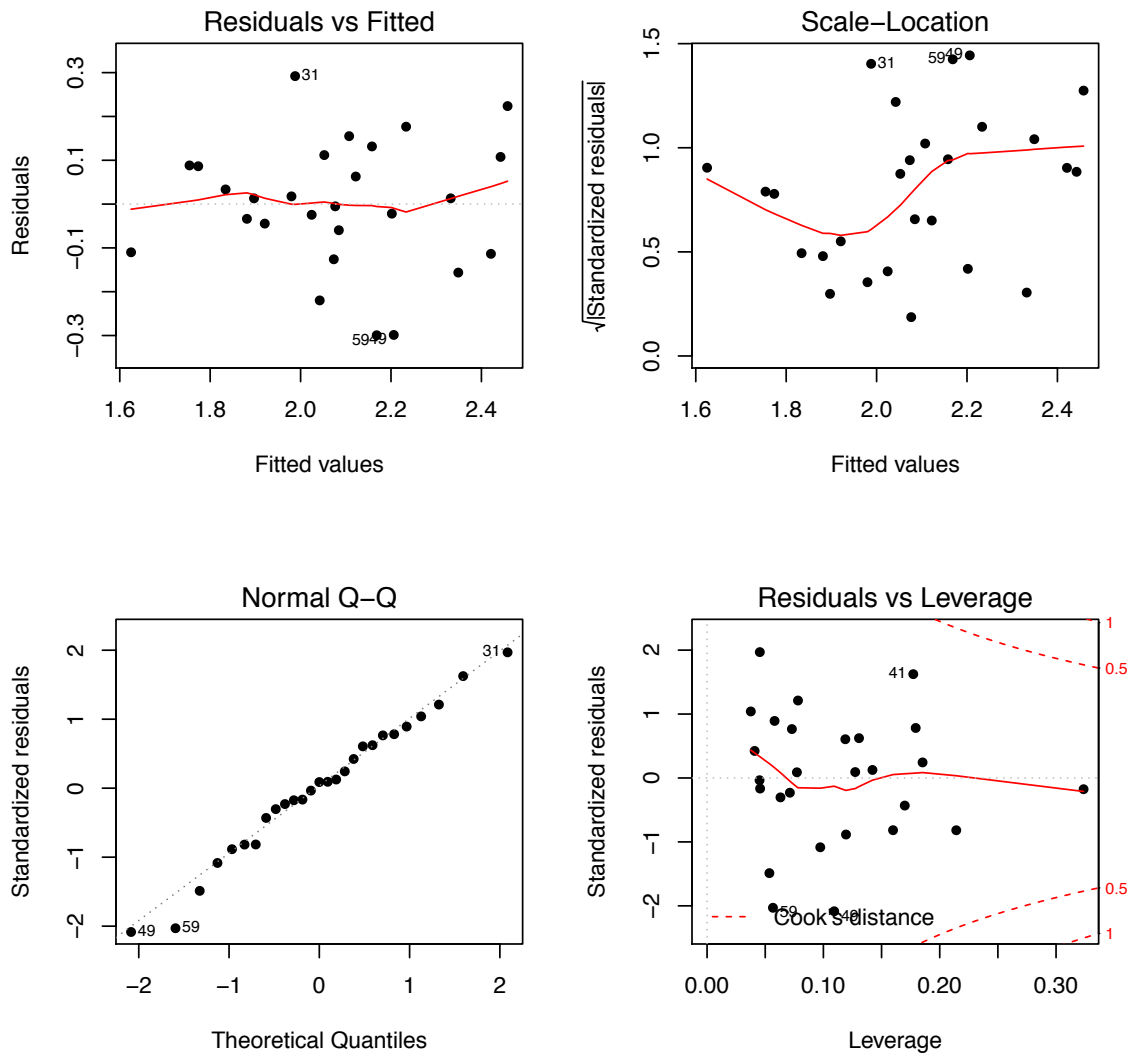


Figure 4.37. Residual plots for multiple linear regression of crown width from 680nm feature symmetry and CHM standard deviation. The residual plot does not strongly suggest that assumptions have been violated.

Because a significant lidar model was expected given the characterization of the upper crown surface by lidar surveys, spectrometer metrics were omitted and a best-fit model was sought with only lidar derived metrics. The most associated lidar attribute with average crown width was the median treetop height metric. The model was improved by including the coefficient of variation of the CHM heights. The last significantly contributing lidar metric to improve the model was the coefficient of variation of tree crown area. The association of the CV tree crown area was suspected to

be spurious. As detailed prior, there is very little information in the lidar tree crown diameters (as parameterized in this analysis) that is associated with average measured crown diameters. Both models with and without cvTCarea will be reported but it is suspected that the contribution of the tree crown attribute is not sensible. With the inclusion of the lidar tree crown area dispersion metric, the explained variation in average measured crown width was 72% (adjusted R^2:0.72, R^2: 0.75) with a residual standard error of 0.14m (df: 23). The model produced an intercept of -0.09 that may not be different from zero (p: 0.84). The fit coefficients for median treetop height, coefficient of variation of CHM heights and coefficient of variation of tree crown areas were 0.07, -0.08 and 0.44 respectively. The f-statistic was 23.38 ($p < 0.0001$). Without the tree crown area metric, the explained variance in crown width was 5% less (adjusted R^2: 0.67, R^2:0.70) with a residual standard error of 0.15m (df: 24). The model parameters were 0.71 for the constant (p:0.02), 0.07 for the median treetop height coefficient and -0.08 for the coefficient of variation of the CHM heights (Fig. 4.38 and 4.39). The F-statistic was 27.57 (p: <0.0001).

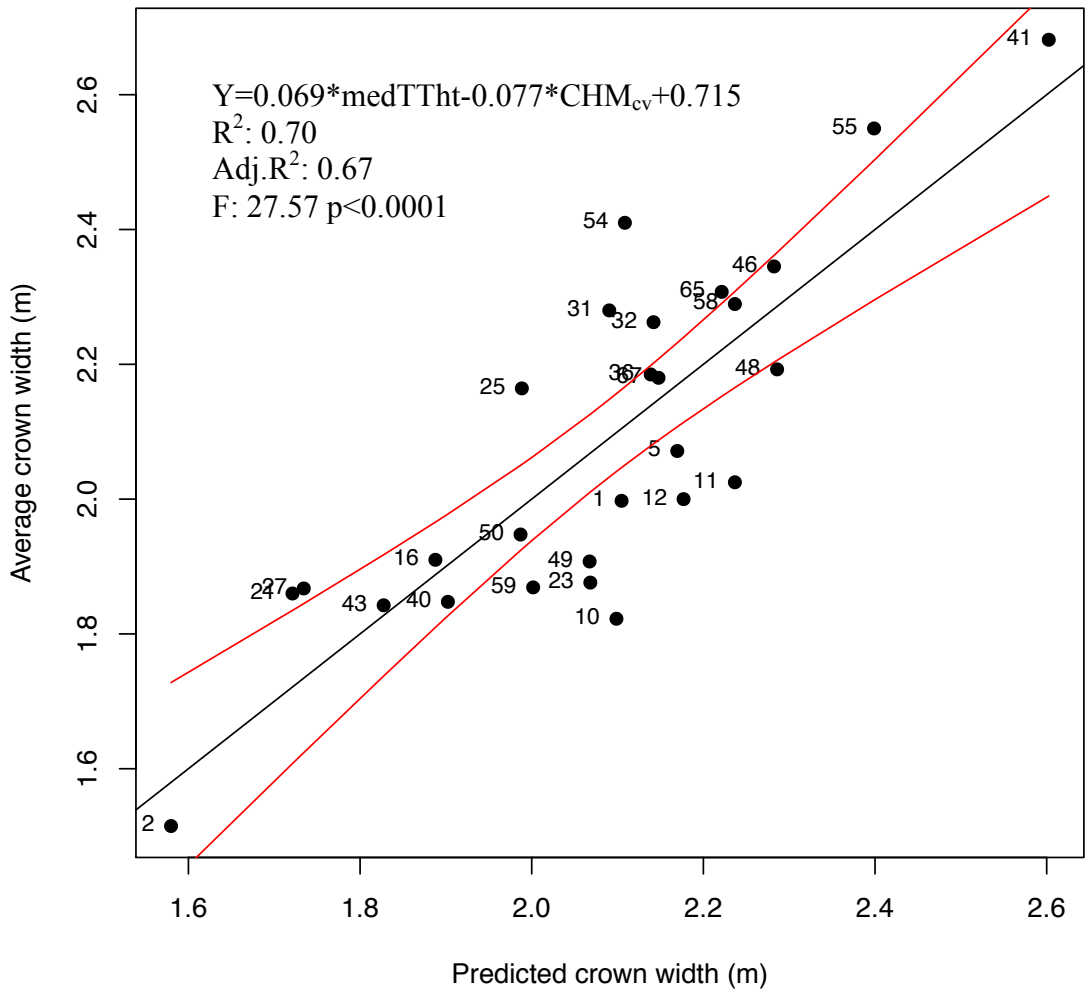


Figure 4.38. Average crown width estimated from median CHM extracted treetop and the coefficient of variation in CHM. The residual standard error is 0.15m on 24 degrees of freedom.

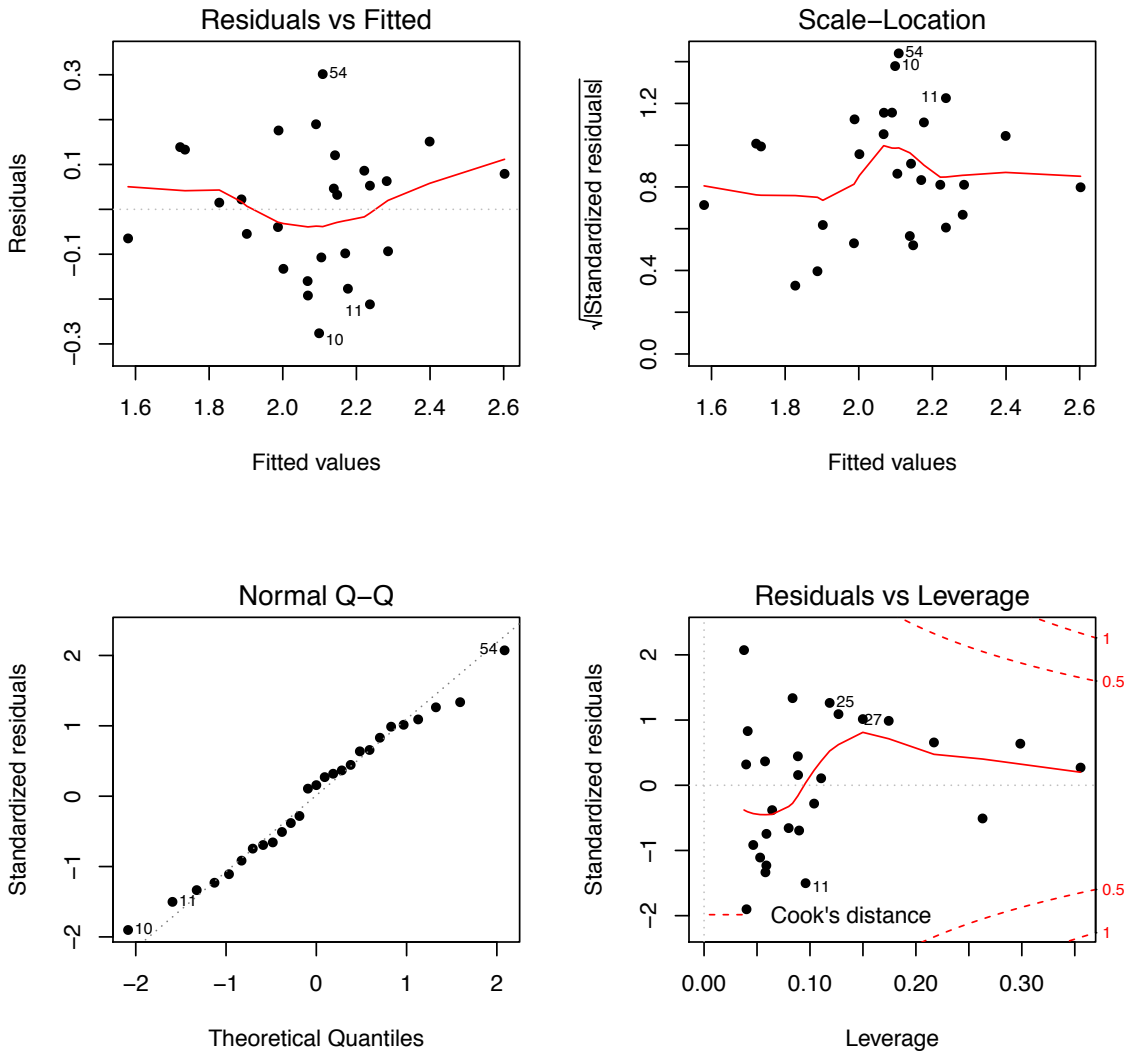


Figure 4.39. Residual plots for multiple linear regression of crown width from median CHM extracted treetops and the coefficient of variation in the CHM. The residual plots do not strongly suggest that assumptions have been violated.

The strongest correlation found for an attribute representing stem density was that found for the relationship between the number of stems per plot and the standard deviation of plot heights in the CHM. The Spearman's rho for the standard deviation of the CHM and the stems per plot was -0.803 (p: 0.000). The strong inverse association suggests that, as the number of stems increase, the standard deviation of the heights in the CHM decreases. The direction of the relationship is logical because with more stems, the

canopy space would be more uniformly occupied, that is, more stems translate to shorter vertical distances from crown boundaries to treetops. Alternatively, in lower stem density plots, lidar positions will be returned from lower (relative to the treetop) crown peripheries and in the case for very low density stands with gaps, lidar returns will be produced from less dominant tree crowns or ground cover; both of these conditions contribute to an increased variation in the CHM surface. In the case of stems per plot only three metrics exceeded a Spearman's rho of 0.6, all three of which were measures of spread (standard deviation CHM, standard error of the point cloud and the coefficient of variation of the CHM heights). The comparison between the field measured stems per plot and the standard deviation of the CHM appeared to have a strong non-linear form (Fig. 4.40). The relationship was fit by nonlinear least squares with a constant, and both scale and shape coefficients. The scale coefficient however, was not significantly different from zero with an estimated value of 477.98 and a standard error of 412.51 (t: 1.16, p:0.26). When the scale parameter was omitted from the fit, neither the shape nor the constant was significant, the constant was omitted which produced significant terms for the scale and shape parameters, 210.24 and -1.22 respectively. Both of the nonlinear models produced non-constant variance within the residuals. The error was positively associated with stem density with R-values of 0.62 ($p<0.001$) and 0.53 ($p<0.01$) for the nonlinear fit with and without the constant term, respectively. As an alternative to nonlinear fitting, the data were transformed by the reciprocal, which both linearized the data and provided the best fit relative to exponential and natural log transforms (Fig. 4.41). The fit of the stems per plot model is moderate-strong with an R^2 value of 0.68 and a standard error of the estimate of 0.005 (df: 25, *N.B.* 1/y). The departure of the Durbin-

Watson statistic from a value of 2 (test statistic is symmetric around two when autocorrelation is zero), in this case 1.2 (p:0.01), suggests that there is some significant positive correlation within the model residuals, however the residual plots suggest that the auto correlation is minor (Fig. 4.42). A linear best-fit line to the residuals produced an R^2 value of 0.32, which may call into question the significance of the linear model.

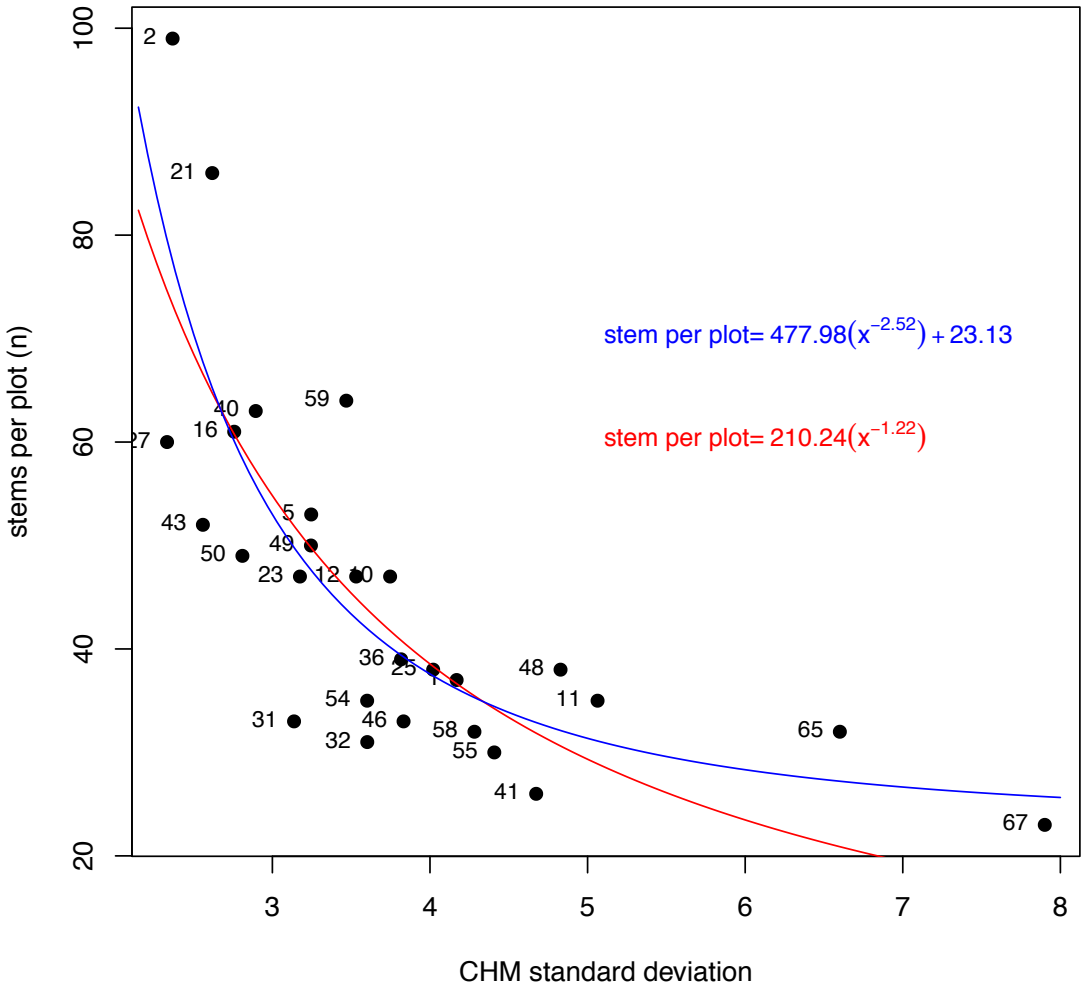


Figure 4.40. The standard deviation of pixel heights in the CHM was selected as the most correlated remote sensing metric with stems per plot by the Spearman's and Pearson's correlation coefficients. Largely attributed to plots 2, 21, 65 and 67 the relationship had a non-linear trend.

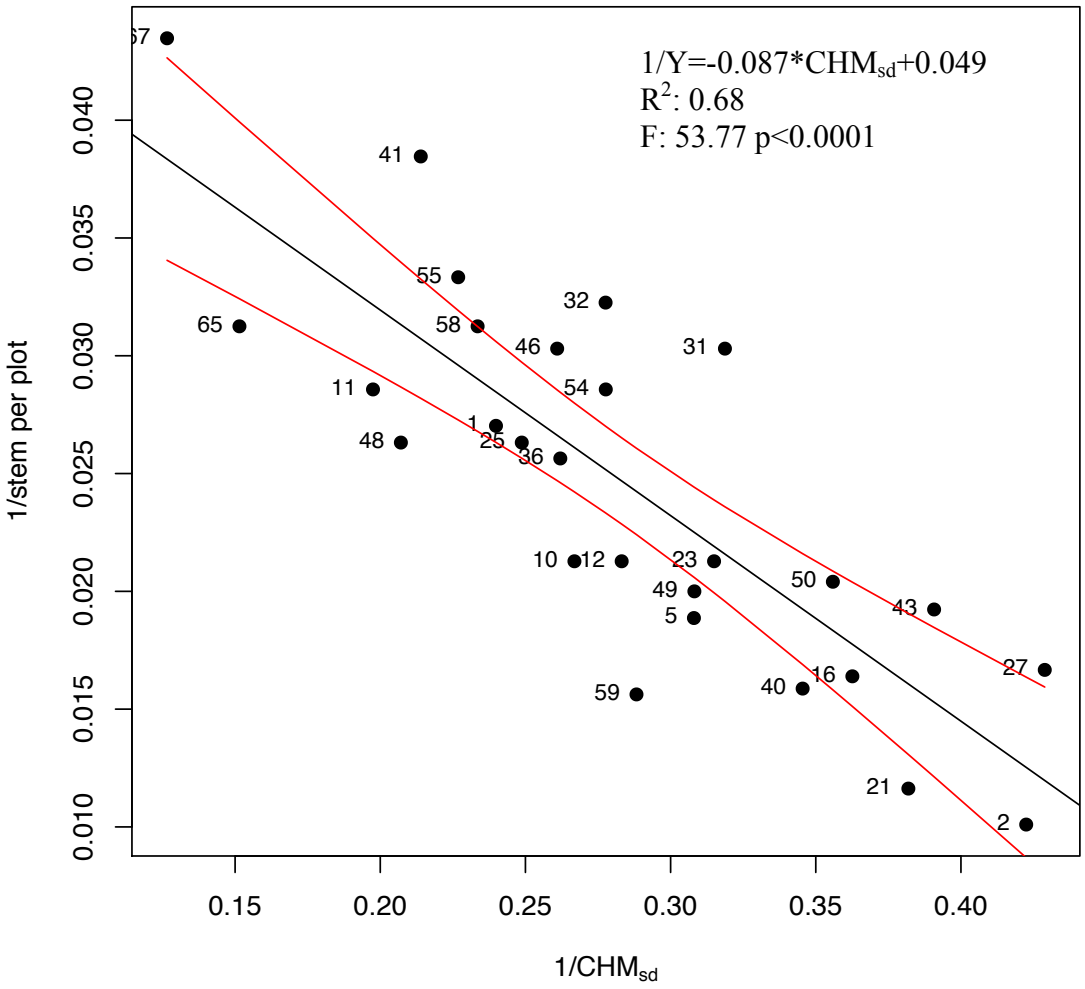


Figure 4.41. The standard deviation of pixel heights in the CHM was selected as the most correlated remote sensing metric with stems per plot by the Spearman and Pearson coefficient. The variables were transformed to remove the non-linear trend.

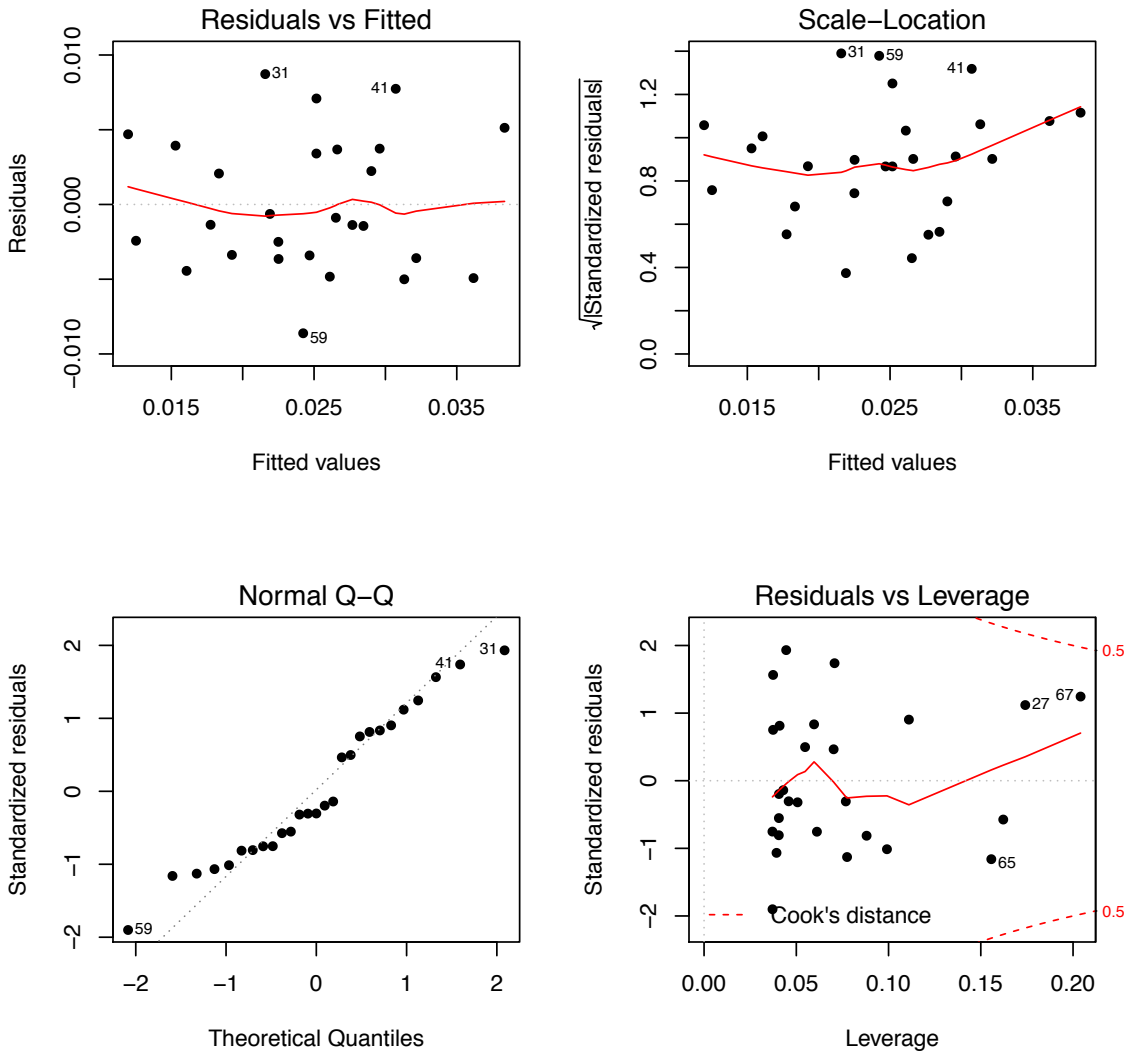


Figure 4.42. Residual plots for simple linear regression of stem per plot from standard deviation of CHM heights. The residual plots do not suggest that assumptions of normality and heteroscedasticity have been violated, nor are there influential observations.

4.4 Area Based Forest Plot Productivity Regression

The remaining regression models that will be presented for the area based plot analysis are those involved with the estimation of productivity indices derived from the field data, namely periodic annual increments of both basal area and total plot volume. The individual tree representation of these metrics will also be evaluated, that is, the PAI of DBH generalized to the plot scale as the plot median PAI of DBH and the plot median PAI of tree volume. The first productivity index was derived from the diameter at breast height increment ending in 2012. The DBH increments were expressed as the diameter difference normalized by the time lapse in years. Plots were represented as the mean diameter growth rate (cm/yr.). The Spearman's correlation coefficient reached a maximum with the standard deviation of the heights in the CHM at 0.82. The strength of the association dropped off quickly after the standard deviation of the CHM to -0.64 and 0.63 for the coefficient of variation of the CHM heights and the standard error of the point cloud, respectively. The scatterplot of the mean PAI of DBH and CHM standard deviation produced a slightly non-linear trend (Fig. 4.43). An exponential fit in the form $PAI_{DBH}=CHM_SD^{a}+b$ produced significant coefficients, however a natural log transformation was found to be equivalent in terms of fit quality (exponent model R^2: 0.69, Ln model R^2: 0. 70) but perhaps superior for simplicity and portability. The linear association of the transformed data was assessed (Fig. 4.44). The model fit was strong and positive with a coefficient of determination of 0.70 and a standard error of the estimate of 0.034. The Durbin-Watson test suggested that the residuals were correlated (DW: 2.04, p:0.52). In agreement, the residual plots demonstrated that the variance of the residuals was approximately uniform with fitted values until the departure at high

standard deviation CHM levels (*i.e.* plots 65 and 67) (Fig. 4.45). With the omission of the influential plot 67 according to the Cook's distance index, the model parameters change considerably from an intercept of -0.061 (std. error: 0.032) and coefficient of 0.184 (std. error: 0.024) to an intercept of -0.097 (std. error: 0.035) and a coefficient of 0.214 (std. error: 0.027). With the omission of plot 67, the coefficient of determination increases from 0.70 to 0.72 and the residual standard error decreased from 0.0358 to 0.0338cm/yr. The F-statistic increased from 57.44 (df denominator: 25, $p<0.0001$) to 62.56 (df denominator: 24 $p<0.0001$). In addition, the omission of plot 67 removed the apparent heteroscedasticity in the residual plots. The removal of the influential plot 67 also confirmed suspicions that it was responsible for the non-linear trend. The regression with the untransformed standard deviation of the CHM heights omitting plot 67 produced an R^2 value of 0.74, a residual standard error or 0.033 (df: 24), an F-statistic of 67.08 ($p<0.0001$), a constant term of -0.031 (t: -1.212, p:0.237) and a coefficient of 0.056 (t: 8.19, p: <0.0001). The residual plots of the regression with the untransformed data gave no indication that assumptions had been violated.

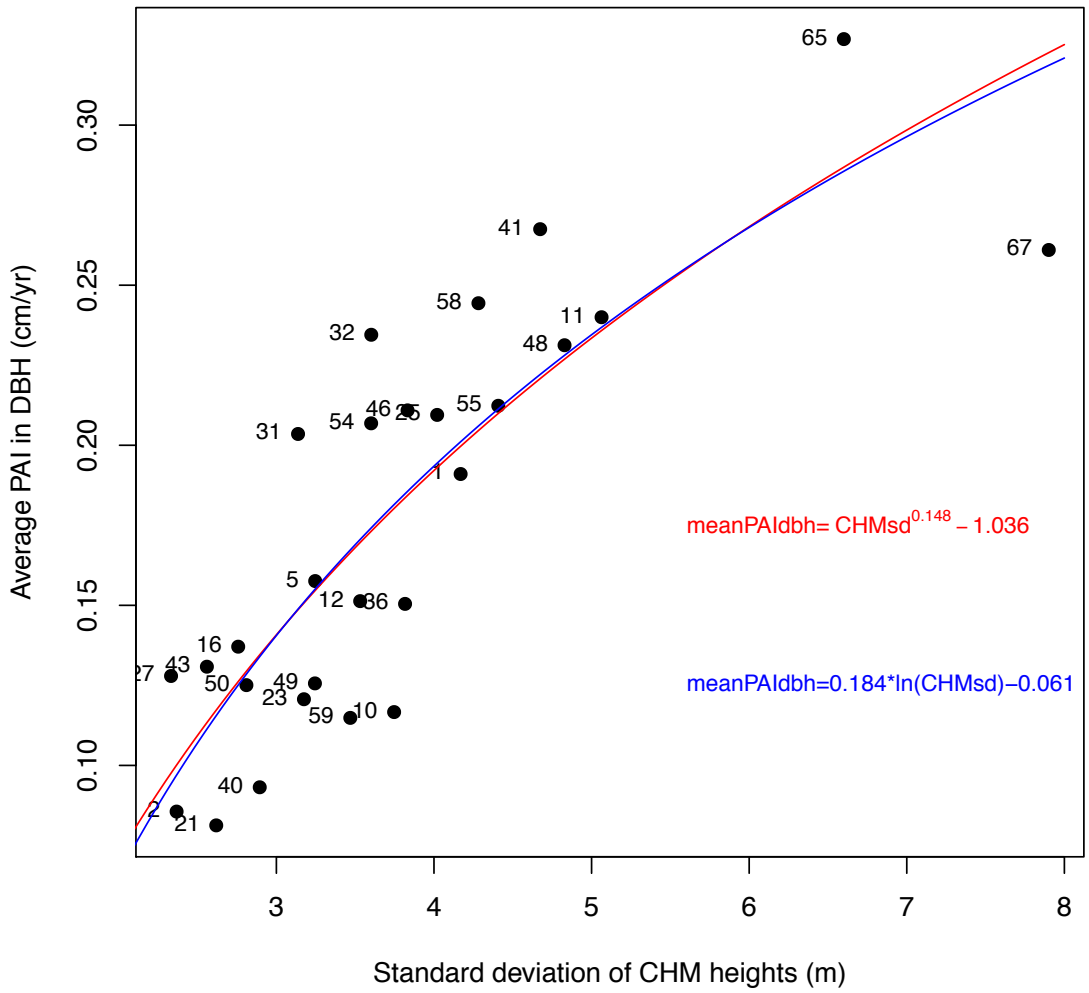


Figure 4.43 Exponential transforms of the standard deviation of the CHM were assessed but a natural logarithm was used to linearize the standard deviation of the CHM data. The source of the non-linearity may be attributed to plots with canopy gap components.

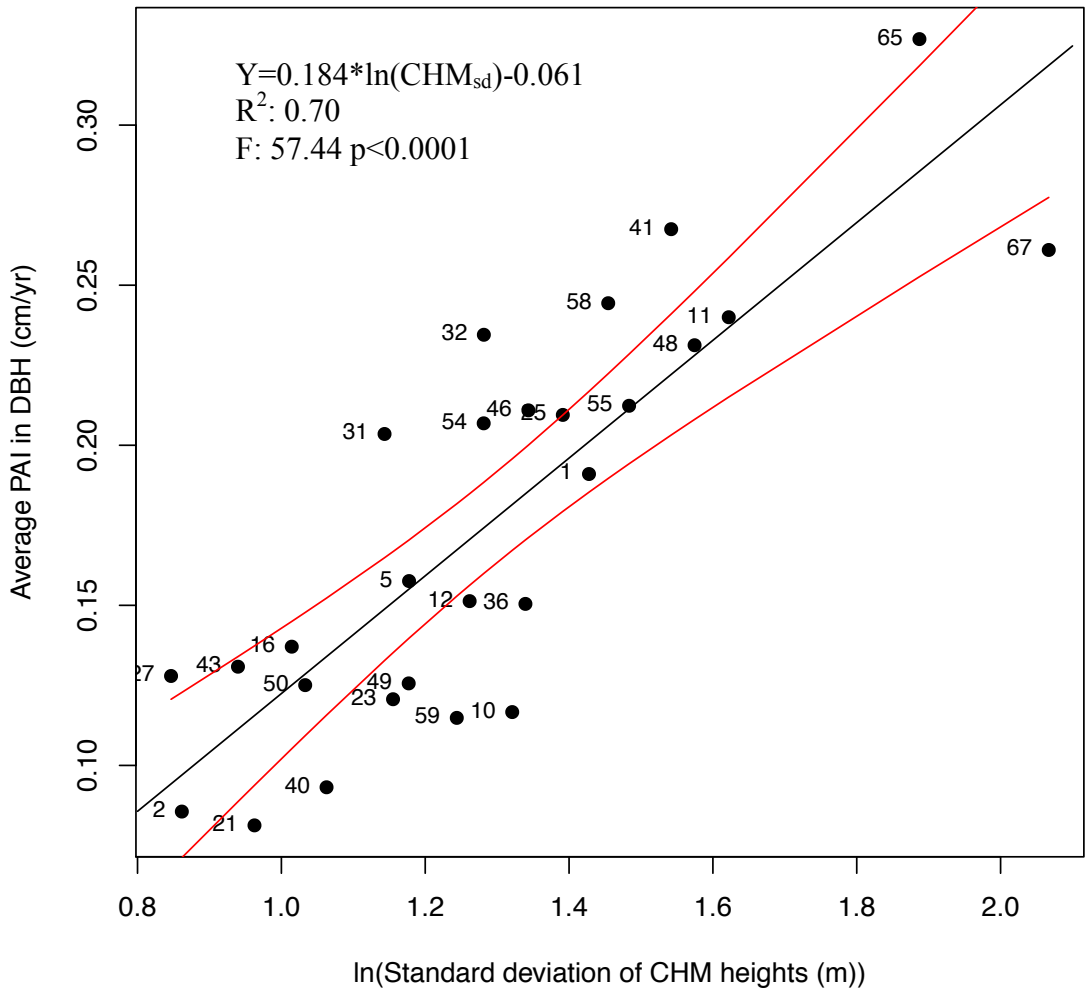


Figure 4.44. Linear model predicting plot mean periodic annual increment in diameter from the natural log transformed standard deviation of the plot heights in the CHM. The residual standard error of the estimates is 0.036cm/yr. (df: 25). The relationship appears to be sensitive to plot density, as plots 65 and 67 both have canopy gaps, while control plots 2 and 21 are closest to the origin.

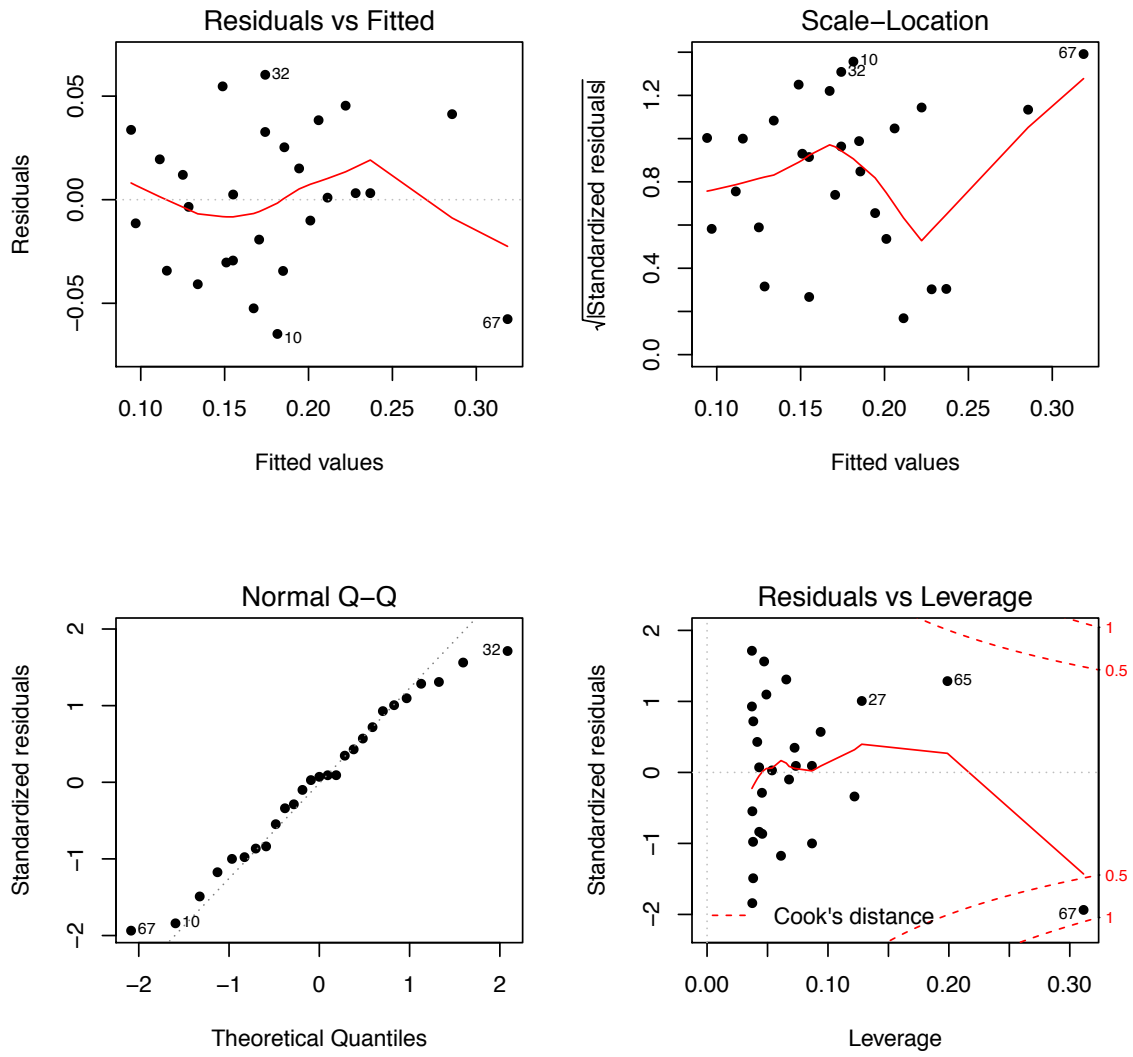


Figure 4.45. Residual plots for simple linear regression of mean PAI DBH from the natural log transformed standard deviation of CHM heights. The residual plots suggest that plot 67 is a highly influential observation.

To determine if there was additional information inherent in the remote sensing database, a multi linear regression was conducted. To avoid over fitting, conservative feature selection restricted the final model to as few metrics as possible without exceeding three. Of all 525 metrics assessed, 21 out of the 23 most associated features were derived from the spectrometer data. The two metrics producing the largest mean R^2 values, when bootstrapped and regressed against the residuals of the simple linear model,

were extremes of optical indices, namely plot maximum TCARI=3[(R_{700}-R_{670})-0.2(R_{700}-R_{550})(R_{700}/R_{670})] and plot min ARI=$(R_{550})^{-1}$-$(R_{700})^{-1}$.

The TCARI is the transformed chlorophyll absorption reflectance index; it is an adaptation of the CARI index, which was designed to measure absorption at 670nm relative to a continuum defined by reflectance at 550 and 700nm [131]. The adaptation was intended to compensate for background reflectance from exposed soil and non-photosynthetic vegetation, however the TCARI index is still sensitive to soil effects under low LAI [132]. By incorporating the plot maximum TCARI the regression explained 83% (adj. R^2: 0.83, R^2: 0.84) of the variation in mean PAI of DBH, with a residual standard error of 0.026 (df: 24) and an F-statistic of 63.68 ($p<0.0001$). The residual plots identified plot 67 as an influential observation. The legitimacy of the model was questioned, as the added attribute of the maximum TCARI value occurring within the plot area, would be very sensitive to data noise.

The second most residual associated metric was also an extreme; the plot minimum of the anthocyanin reflectance index (ARI), which was developed to estimate the foliar content of the anthocyanin pigment from laboratory diffuse reflectance data [133]. The accumulation of anthocyanin is often associated with vegetation stress of varied sources (e.g. strong light, UV-B, macronutrient deficiencies, low temperatures, drought, fungal infections) [134], [135]. The resulting multiple regression produced an adjusted R^2 of 0.76 (R^2:0.78) with a residual standard error of 0.031 (df: 24). However, residual plots suggested the presences of heteroscedasticity, which was attributed to large over estimates of plots 65 and 67. Primarily, for the same reason stated from the TCARI

index model, the inclusion of the ARI was suspected overfit as the generalization to the plot level was through the minimum value and thus also susceptible to data noise.

The third most information-contributing metric was the plot mean of the continuum removed (CR) maximum depth (Fig. 4.46). The benefit of the CR depth metric was recognized while investigating the residuals of the simple linear model (CHM_{sd}) where, plot 67, with a depth of 0.928 was a clear outlier, in this case 5.27 times the interquartile range (0.004) from the mean (0.950). The multiple linear regression produced an adjusted R^2 of 0.79 (R^2: 0.80), a residual standard error of 0.030 (df: 24), an F-statistic of 48.8 ($p < 0.0001$), a constant of -5.62 (t: -4.46, p: 0.0002), standard deviation of the CHM coefficient of 0.055 (t: 9.80, $p<0.0001$) and a mean depth max coefficient of 5.88 (t: 4.47, p:0.0002) (Fig. 4.47 & 4.48).

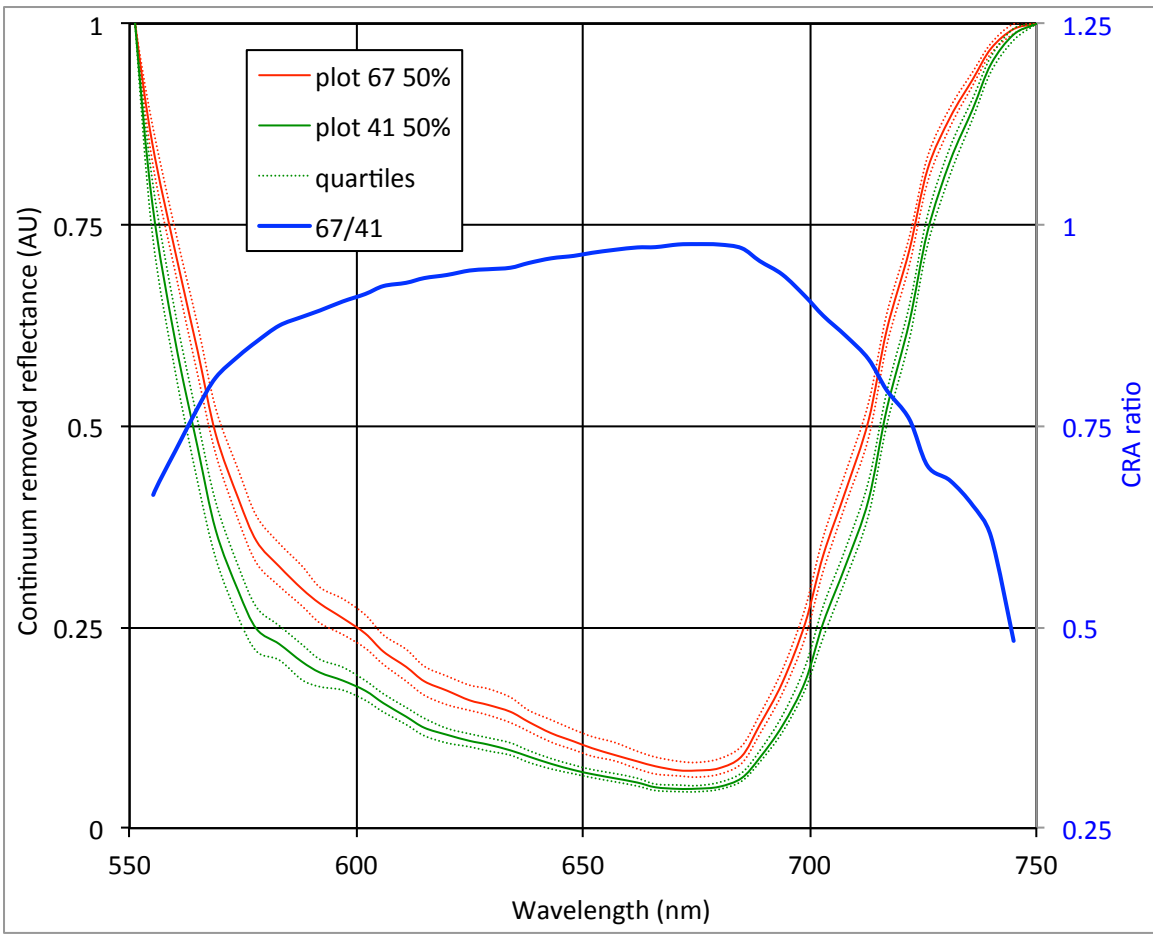


Figure 4.46 Continuum normalized reflectance of the 680nm absorption feature of the most and least productive plots and the ratio of the two median CR absorption spectra (1-CR). The ratio suggests, with the exception of ~725nm (which might be attributed to chlorophyll florescence or atmospheric H_2O), there is very little structure within the ratio curve beyond the chlorophyll trend. The maximum depth of the feature (~680nm) is related to the pigment contents within the IFOV. This observation is interpreted as a reduced chlorophyll level in plot 67 relative to plot 41.

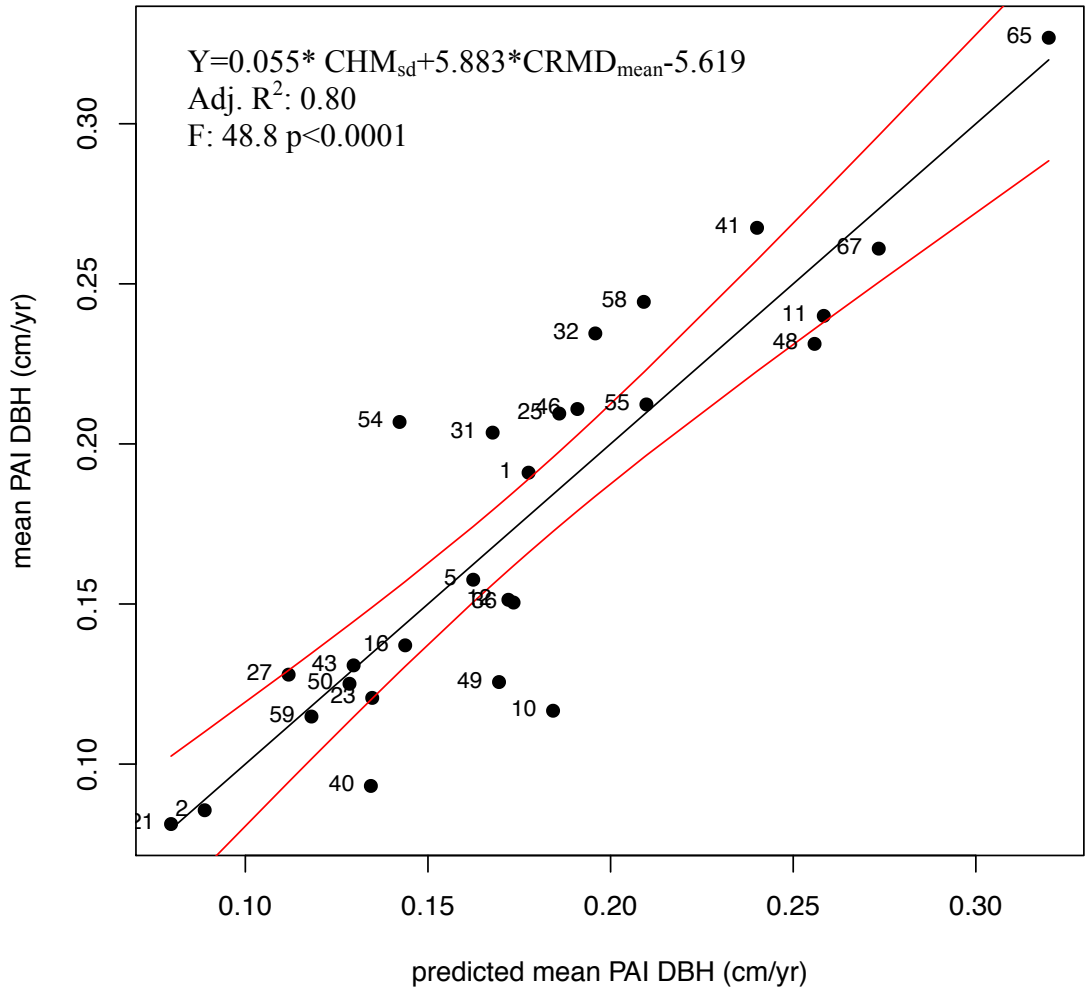


Figure 4.47. Multiple linear model predicting plot mean periodic annual increment in diameter from the standard deviation of the plot heights in the CHM and the mean continuum removed maximum depth. The residual standard error of the estimates is 0.030cm/yr. (df: 24).

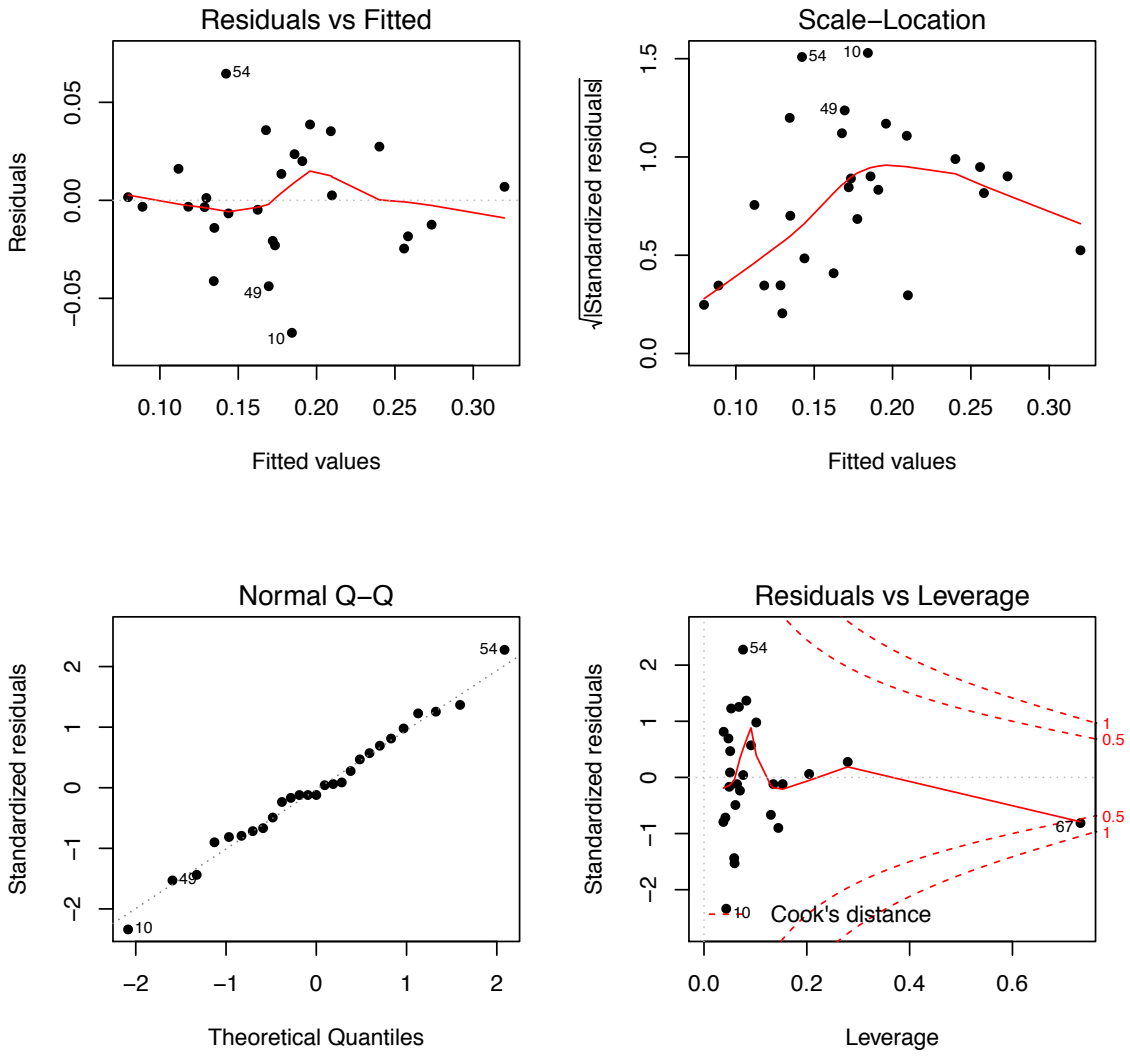


Figure 4.48. Residual plots for multiple linear regression of plot mean PAI of DBH from standard deviation of CHM heights and mean continuum removed max depth. The residual plots suggest that plot 67 is a highly influential observation.

The effect of omitting the influential plot 67 was to decrease the adjusted R^2 to 0.78, explaining 1% less of the variation in PAI of DBH, reducing the F-statistic to 44.2 ($p<0.0001$). The residual standard error was unchanged to a precision of 0.001. The changes to the model parameters were as follows: constant +1.035, CHM_{sd} coefficient +0.002, mean CR depth max -1.097, producing the model:

$$Y=0.057*CHMsd+4.786*CRDM_{mean}-4.584$$

Differences were apparent in the significance of the intercept and the depth max coefficient, both of which were reduced to 0.02. However, the recognition that the selection of this feature was directly tied to the conditions of plot 67, which would otherwise produce a large residual in the simple linear model, warranted its inclusion. In addition, having established the source of the variation in plot 67 as having a large gap component, which was different from the majority of the treatment plots, it could be confidently assumed that its variation was not attributed to noise.

As a consequence of the survey geometry and the density of the canopy, it was expected that crown class would affect the relationship between the remote sensing metrics and the productivity attributes. By running the bootstrap feature selection script iteratively, removing the least dominant crown class the change in model fit and feature selection was observed. Interestingly, the lowest R^2 was produced using all the crown classes, as was the case for the above analysis. The fit between the most associated remote sensing metric and mean PAI in DBH increased with the removal of less dominant classes to an R^2 of 0.76 with inclusion of the dominant, co-dominant and intermediate crown classes, after which there was a decrease in fit down to 0.64 and a change in the most associated remote sensing metric. This observation prompted the regression of mean plot PAI in DBH of only the dominant to intermediate classes with the remote sensing metrics.

The change in the dependent variable had little impact on feature selection. The standard deviation of the CHM was most associated with mean PAI of DBH in the dominant to intermediate crown classes, however the curvilinear trend observed previously was not as apparent. As with the previous analysis, the plot maximum of the

TCARI index was the next most associated remote sensing metric. The resulting regression model including the plot maximum TCARI within the dominant to intermediate crown classes was: $PAI_{DBH}=0.047*CHM_{sd}-1.39*TCARI_{max}+0.207$. The adjusted R^2 was 0.849 (R^2: 0.86) with a residual standard error of 0.021 (df: 24) and an F-statistic of 74.32 ($p<0.0001$). Although there were no influential observations in the residual vs. leverage plot, there was some subtle evidence for heteroscedasticity. The generalization of the index to the plot level by representation of the maximum index value was suspected to be spuriously overfit to these data, a perspective that was not supported by the bootstrapping approach. If the model was overfit, the bootstrap was expected to produce a lower mean R^2 and/or an inflated R^2 standard deviation, neither of which were the case. The difference with the regression stratifying by crown class was that the second most associated remote sensing attribute was not the ARI index but the median of the continuum removed depth maximum (and in contrast to the previous model that identified the mean CR depth) (Fig. 4.49). Again, the residual plot suggested that plot 67 was an influential point, however this was anticipated given that the inclusion of the chlorophyll sensitive metric reduced the large residual error of plot 67 in the simple linear model (Fig. 4.50).

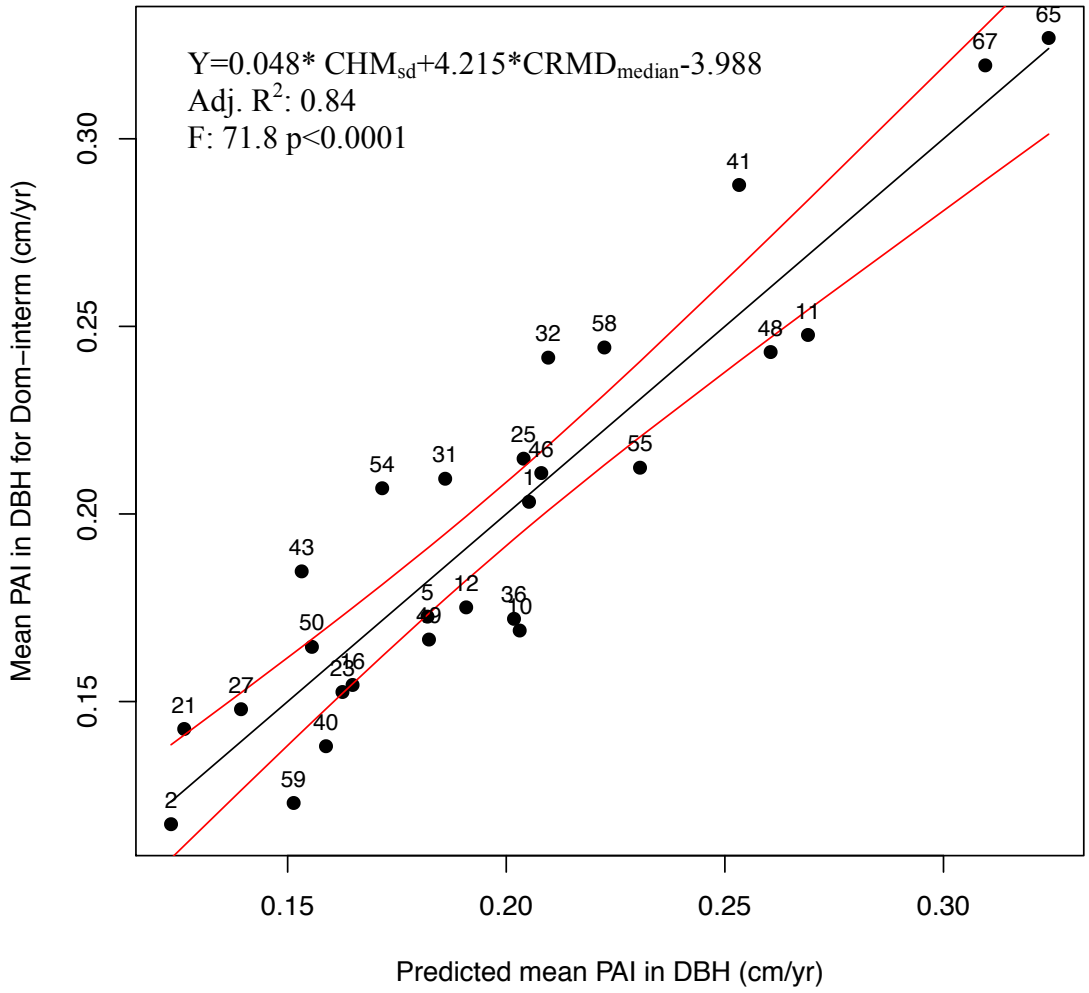


Figure 4.49 Multiple linear model predicting plot mean periodic annual increment in diameter of dominant to intermediate crown class from the standard deviation of the plot heights in the CHM and the median continuum removed maximum depth. The residual standard error of the estimates is 0.022cm/yr (df:24).

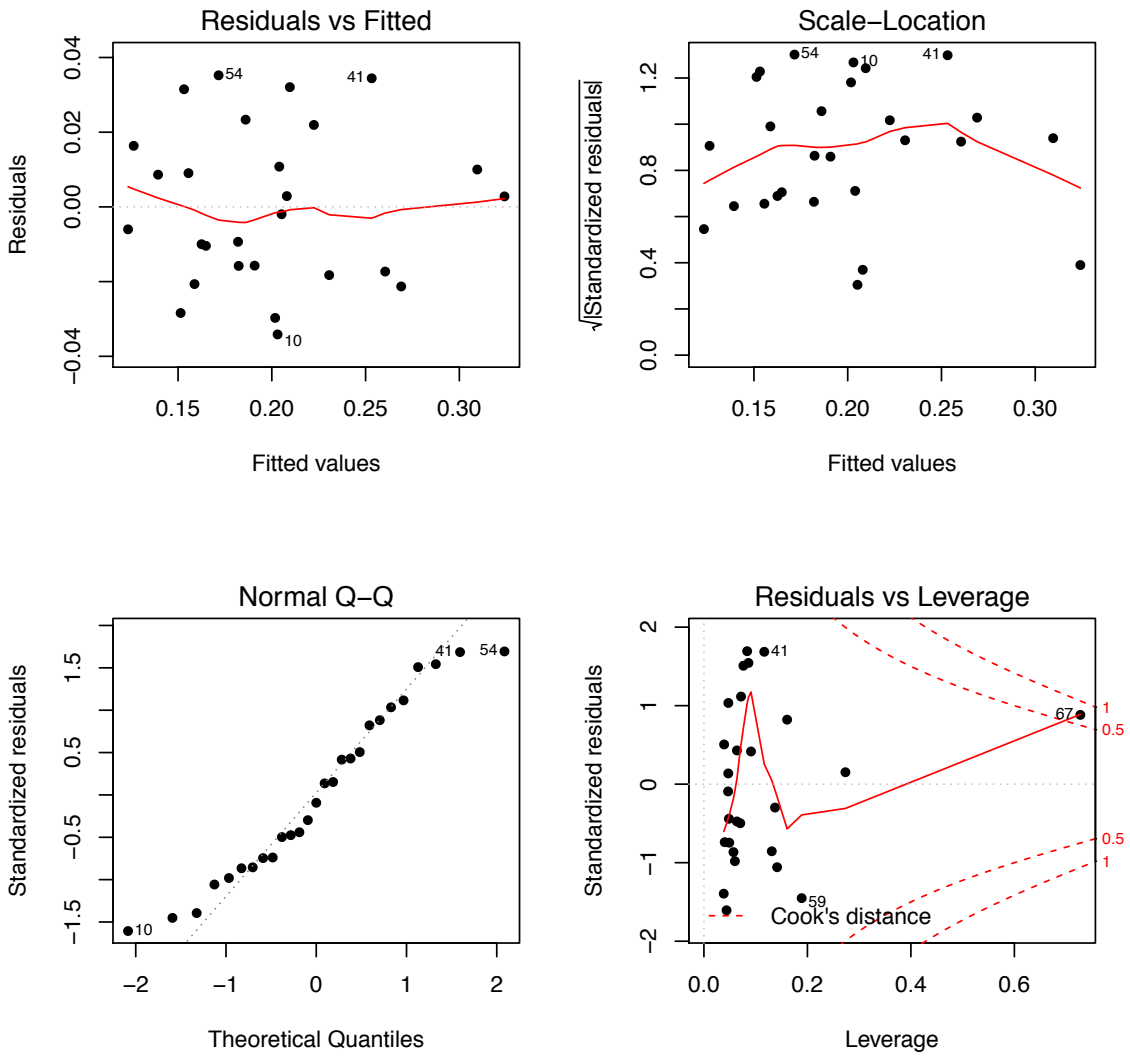


Figure 4.50. Residual plots for multiple linear regression of plot mean PAI of DBH from dominant to intermediate crown classes predicted from standard deviation of CHM heights and median continuum removed max depth. The residual plots suggest that plot 67 is a highly influential observation and the normal plot suggests the tails of the residual distribution maybe slightly different from normal. Both of these conditions are lessened by taking the natural log of both the independent variables.

This analysis presented remote sensing metrics that were significantly associated with plot mean PAI in diameter. It is suspected that these relationships are not interpretable as a productivity index as it is confounded by site occupation and growth form (variation in the DBH to height allometry). Plots 65 and 67 had large secondary growth indices (mean PAI in DBH) and were observed to be very sparse relative to the

other plots. The individuals remaining in plots 65 and 67 have greater access to resources through reduced inter crown competition (although pathogen presence is a negative growth factor). The lower density plots tend to have greater access to irradiance and thus the amount of self-thinning of lower branches is reduced, which can have an associated change in the diameter to height ratios. In addition, root disease is known to induce allometric variations [136], [137]. Where stem densities are greater, the secondary growth rates may be lower. However, the rate of dry matter accumulation may be greater as a result of the allocation of photosynthate to primary growth, a greater occupation of living space and the consequent greater absorption of PAR by the tree layer. Therefore, it was considered important that this productivity attribute be summarized to the plot level not by a mean but rather by the sum of the linear diameter increments or equivalently, the plot basal area increment.

Estimation of the basal area increments by simple linear regression was poor, with the seven most associated features being spread metrics of the normalized difference pigment chlorophyll index (NPCI= R_{680}-R_{430}/R_{680}+R_{430}). It was suspected that the association with this spectral index was confounded by sensor noise, as the sensitivity of photo detectors decreases as you approach the limits of its spectral range. In addition, as a result of Rayleigh scatter, the reflected electromagnetic signal also becomes less reliable with the inverse of wavelength, at least within the visible range. To provide evidence of the impact that the data noise level may have on the 430nm range, the coefficient of variation in the reflectance data was plotted as a representation of the signal to noise ratio (Fig. 4.51). Although the noise component was on a downward trajectory with wavelength at 430nm, the noise level was still very high at the 91 percentile of the

coefficient of variation. The selection of the minimum NPCI index is entirely dependent on two dark, likely shaded, outlier spectra occurring in plots 48 and 65. These two outlier spectra contain negative reflectance values at the 430nm band, which in turn reverses the index operators producing large negative index values (~-1000). Plots 65 and 48 happen to have the two largest basal area increments (~0.045m^2/yr.). The remaining remote sensing metrics failed to explain more than 30% of the variation in PAI of basal area in the dominant to intermediate classes, according to the mean coefficient of determination.

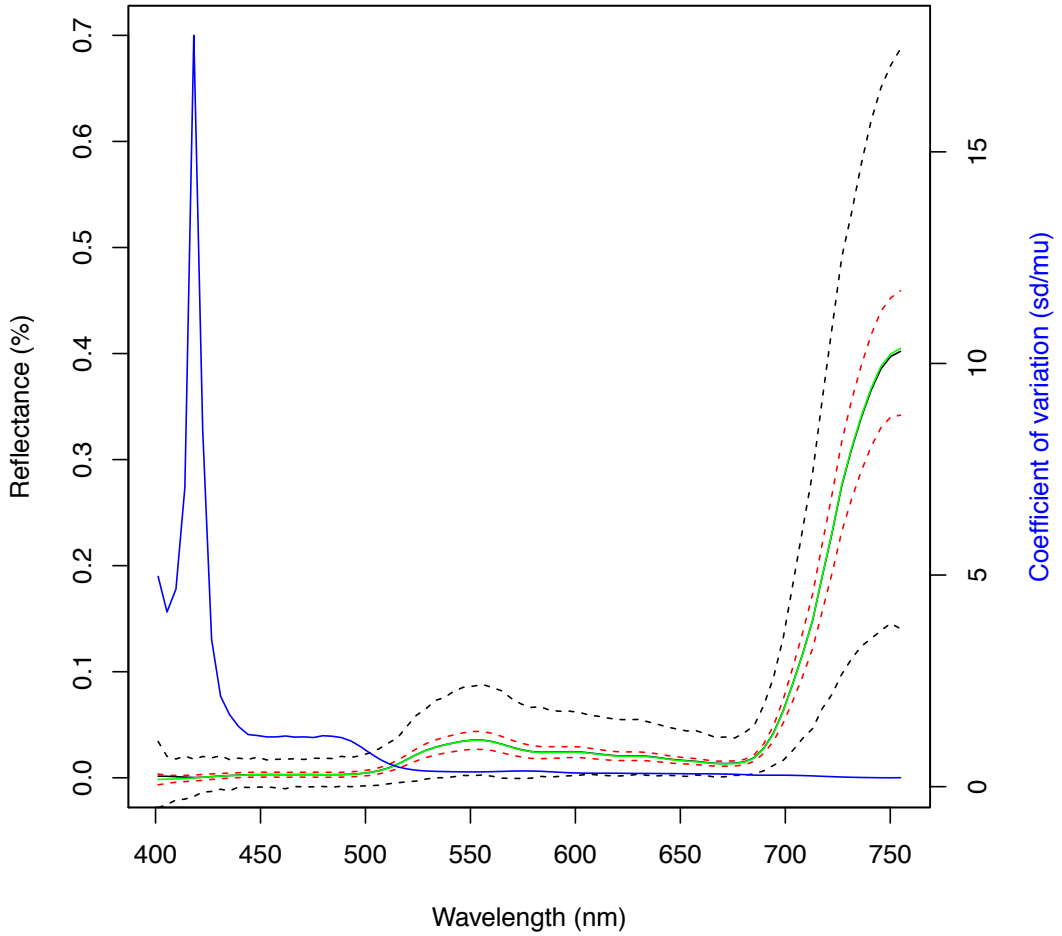


Figure 4.51. Plotting the coefficient of variation of reflectance with wavelength illustrates the noise component as a function of wavelength. Spectral indices that use bands with high noise contents should be considered unreliable and more a function of noise than of the target of interest.

Table 4.11 Effect of crown class on fit and feature selection				
Crown classes in PAI BA	SLR	R^2	MLR	Adj.R^2
Dominant	$TCARI_{mad}$	0.21	$BDmax_{kurtosis}$ + $TCARI_{kurtosis}$	0.12
Dom – co-dominant	$NPCI_{sd}$	0.34	GVI_{cv} + $RGI_{std.\ error}$	0.54
Dom - intermediate	$NPCI_{min}$	0.39	$MNDVI2_{CV}$ + $TCARI_{mad}$	0.54
Dom - suppressed	$NPCI_{min}$	0.39	$MNDVI2_{CV}$, $TCARI_{mad}$	0.54
Dom - dead	REP_{med}	0.32	$Ln(CHM_{sd})$ + REP_{med}	0.71

Using the regsubsets::leaps function in R, the exhaustive search for the best two-variable model was built for each of the five crown class stratifications, that is, the PAI of BA was determined iteratively, removing the least dominant class (Table 4.11). The best fit was produced when all crown classes contributed to the PAI in basal area. The two attributes selected for the best-fit two-variable model were the natural log transformed standard deviation of the CHM heights and the median of the red edge position. However, the transformation of the CHM data had no effect on the model fit indices but improved the residual distributions. As with the analysis of mean PAI in DBH, one of the selected attributes (REP) resolved the dissimilarity of plot 67 with regards to the relationship between the productivity attribute and the variation in the surface of the canopy (CHM standard deviation). The rationale for the inclusion of the REP metric is related to either reduced canopy chlorophyll content or an increase in pixel mixing with necrotic ground cover vegetation. The wavelength position of the inflection of the first derivative of reflectance spectra in the range of 680-750nm is related to chlorophyll content. As chlorosis progresses there is a concurrent blue shift of the inflection position [10], [76], [101], [138]. In the case of the SLP plots, plot 67 has a large gap component, which contributes to a large standard deviation of the canopy height model. In addition, plot 67 has an active root disease component that has induced many mortality events. In

the time lag considered for the PAI interval, seven such mortality events had occurred. Because only live individuals contributed to the basal area of the respective years, the mortality at plot 67 produced a negative basal area increment. The REP has a precision of ~4.5nm and is a limitation of the spectral sampling of the spectrometer, the only variation in the plot median REP is plot 67 which is one channel lower than all the other plots.

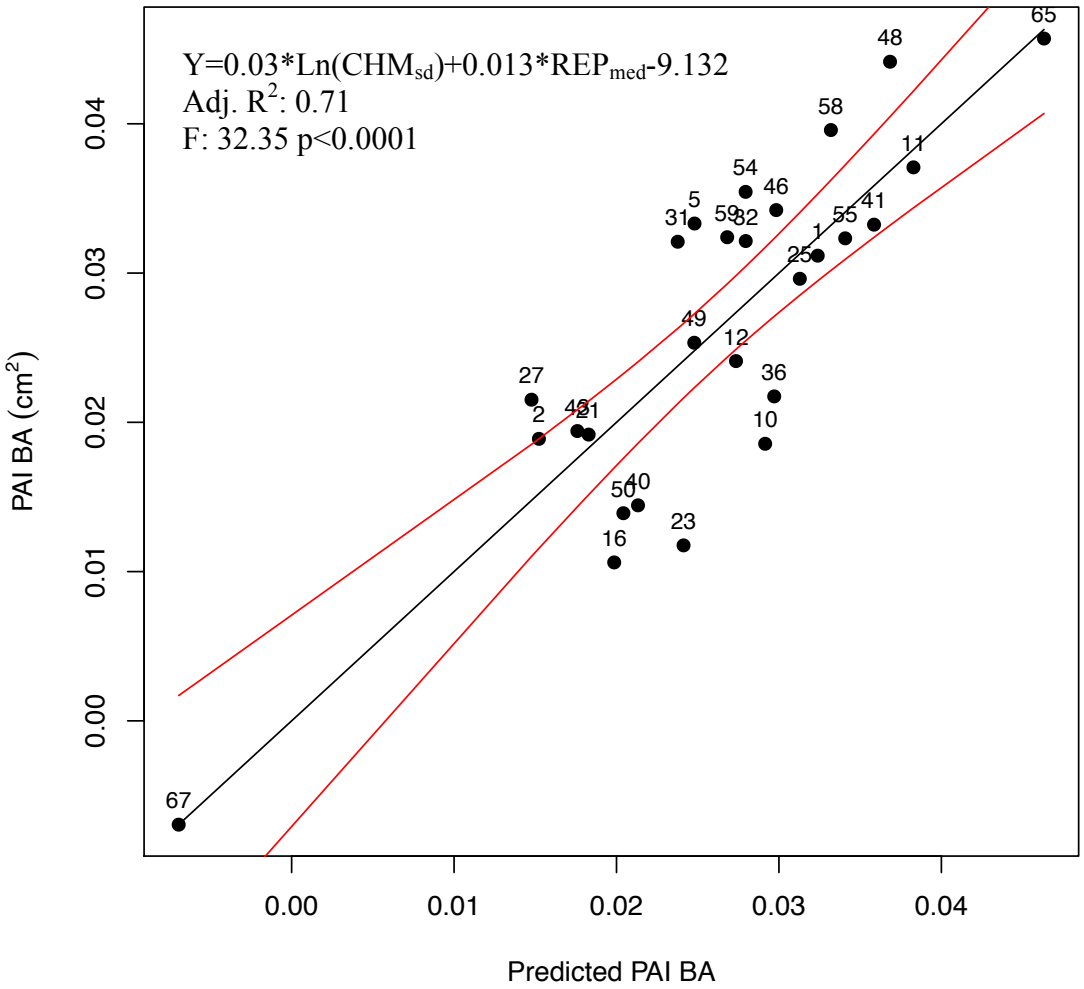


Figure 4.52 Multiple linear regression model predicting periodic annual increment in live basal area from the standard deviation of the plot heights in the CHM and the median red edge position. The residual standard error of the estimates is 0.006m^2/yr (df:24).

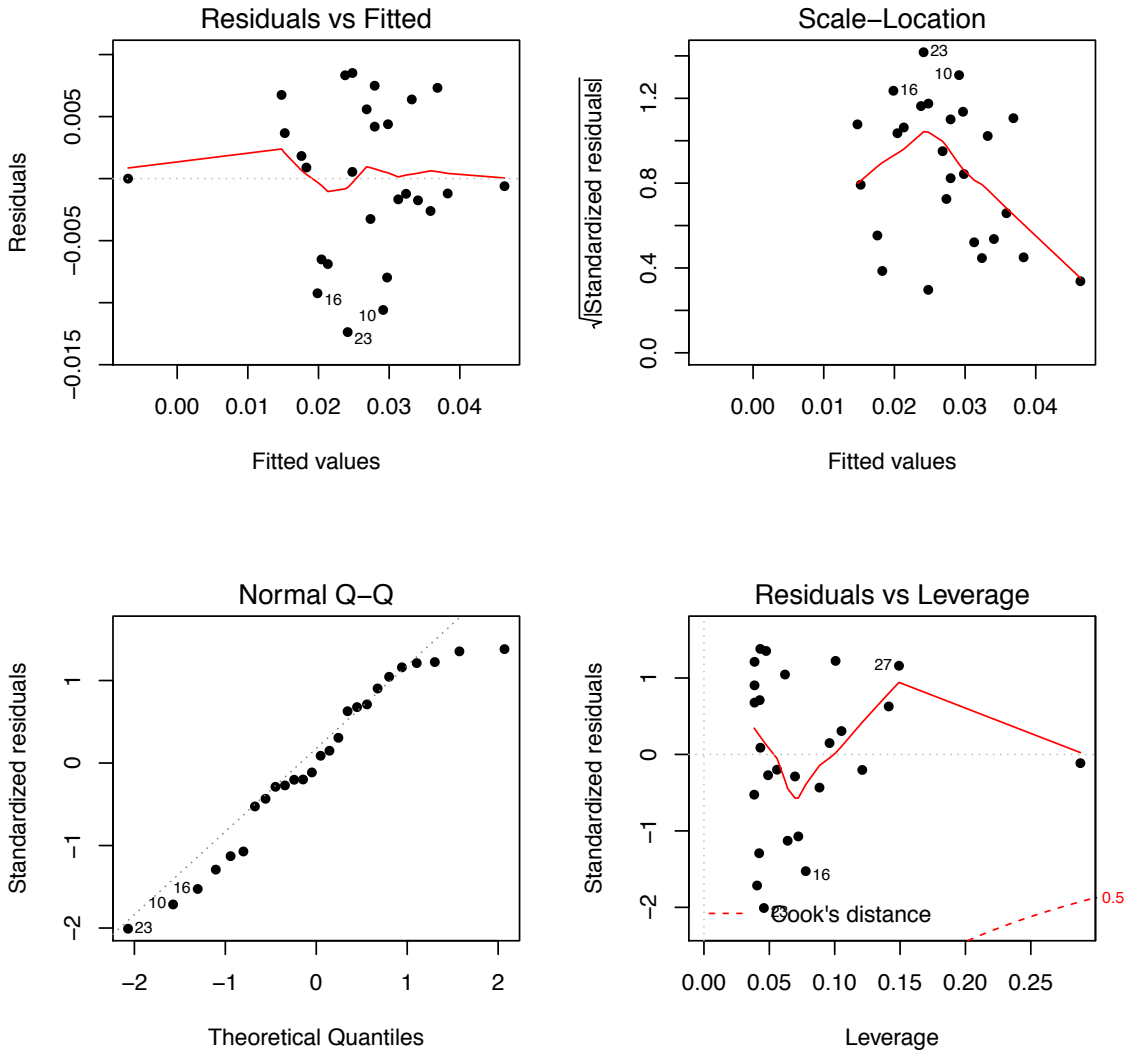


Figure 4.53. Residual plots for multiple linear regression of plot PAI of BA predicted from standard deviation of CHM heights and median REP. Plot 67 is a highly influential observation because omitting it produces zero variance in REP_{med}.

When plot 67 was omitted from the analysis, the quality of the PAI BA model fit and the features selected were altered. The crown class stratification did not change with the omission of plot 67, where the best fit was produced when all crown classes contributed to the PAI in BA. The most explanatory, two-variable subset model was that produced by the lidar canopy closure fraction at the 45th height percentile and the plot median PRI (photochemical reflectance index). The adjusted R^2 value was 0.71 with a residual standard error of 0.005 (df: 23), the F-statistic was computed as 31.89

($p<0.0001$) and the fit model was determined as $PAI\text{-}BA=0.742(PRI_{med})-0.254(CCF_{45})+0.291$ (Fig. 4.54 & 4.55). Thus, in conditions of high canopy closure and without the influence of disease (both conditions of plot 67), the periodic annual increment in basal area is related to the canopy closure at the height of the central tendency of the lidar point cloud and the light use efficiency of the canopy foliage. These two remote sensing metrics were normalized to infer their importance in PAI BA prediction. The coefficients for the normalized variables were -0.008 and 0.005 for CCF_{45} and median PRI respectively, which suggested that the canopy closure contributed slightly more to the prediction than PRI. Regressed independently, CCF_{45} explained 44% of the variation in PAI BA, while plot median PRI explained only 2% (adj. R^2). Additionally, the median PRI does not significantly explain PAI in BA without the contribution from CCF_{45}, (t: 1.21, p: 0.24, F: 1.46, p: 0.24). Conceptually, the combination of these two attributes is meaningful because the CCF attribute quantifies crown area structure and the PRI quantifies crown photosynthetic functioning, both of which should theoretically contribute to the productivity of the stand. This model is also more attractive than others previously produced as the generalizations to the plot level are expected to be more stable (canopy closure at the median lidar height and the plot median PRI). Note, that the best-fit model was produced by the inclusion of the CCF_{45}, as opposed to the CCF_{50}. The difference in explained PAI BA by changing the CCF by one increment (CCF_{40} and CCF_{50}) was ~1%, which could possibly be attributed to noise.

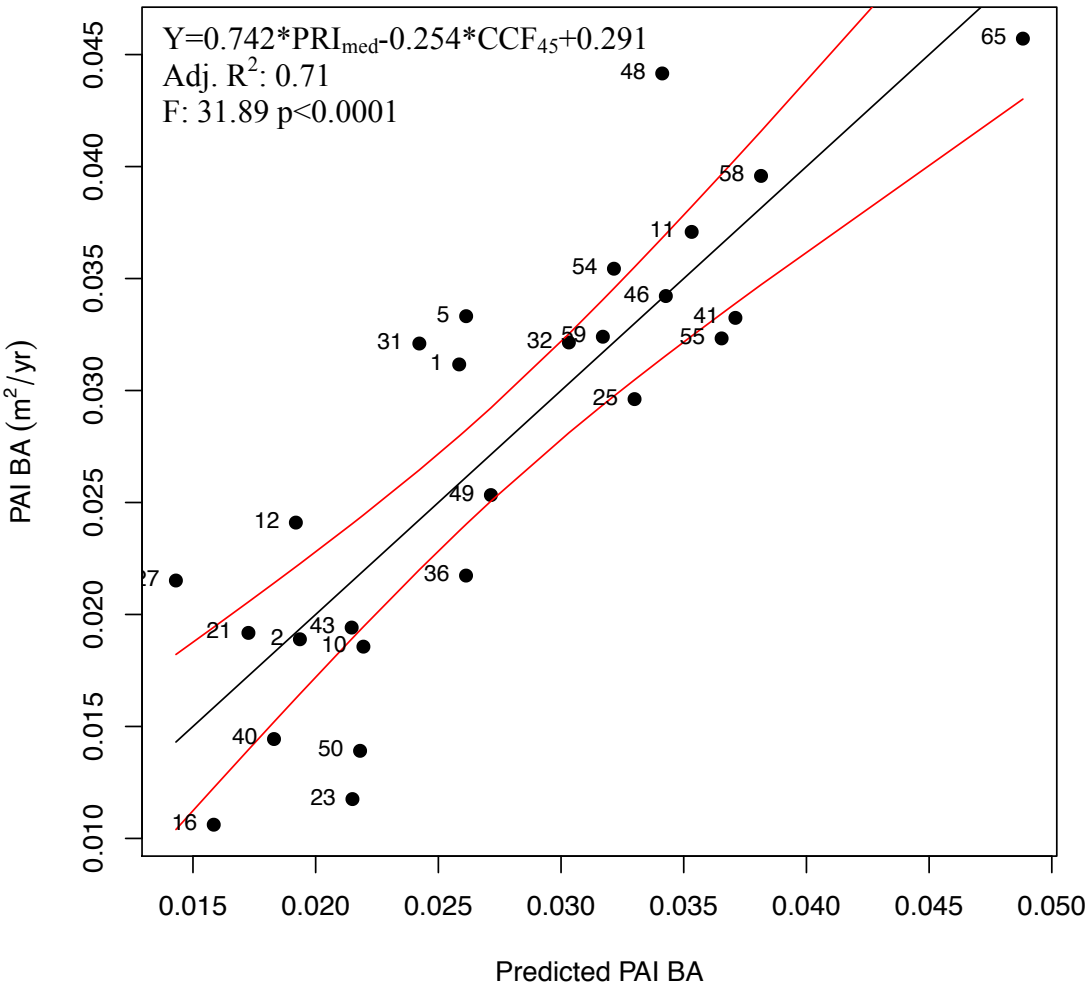


Figure 4.54. Multiple linear regression model predicting periodic annual increment in live basal area from the ratio of the number of lidar returns above the 45th lidar height percentile to the total number of points (CCF_{45}) and the plot median of the PRI index. The residual standard error of the estimates is 0.005m^2/yr. (df: 23).

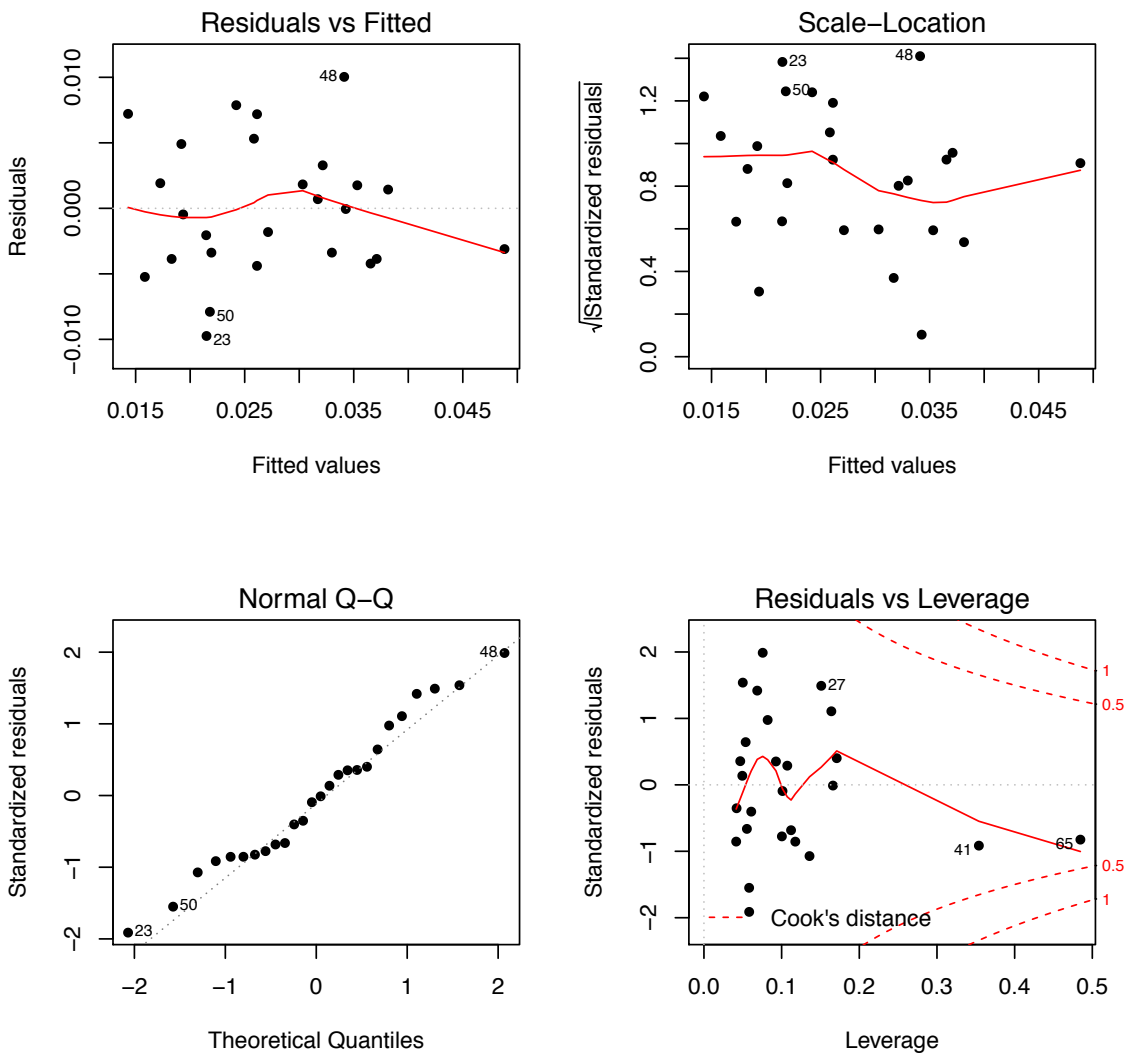


Figure 4.55. Residual plots for multiple linear regression of plot PAI of BA predicted from CCF45 and median PRI without plot 67.

The final model produced for estimating PAI in BA was constructed from the best-fit model without the influence of plot 67. It was established that the inclusion of the median REP variable served only to distinguish plot 67 from the other plots as it had a drastically different PAI in BA attributed to mortality. As well, the spectral responses of plot 67 were also very different, the interpretation of which were in line with what would be expected from stressed canopies (Fig. 4.46). Therefore, the median REP was included

in a three-feature model, which also included CCF_{45} and median PRI. The final model form was:

$$\text{PAI BA}=0.016(REP_{med})+0.742(PRI_{med})-0.254(CCF_{45})-11.587$$

The standard errors of the model parameters were 1.273 for the constant, 0.033 for the CCF_{45} coefficient, 0.002 for the median REP coefficient and 0.153 for the median PRI coefficient. All the estimated parameters were significantly different from zero ($p<0.0001$). The adjusted coefficient of determination was 0.796 (R^2: 0.82) and the F-statistic was 34.99 ($p<0.0001$) (Fig. 4.56). The most explanatory three-variable subset model was determined and was nearly the same as that produced above, the only difference being that the PRI mean was selected over the median. However the difference in the explained variation in PAI BA was 0.04%, the difference in the residual standard error was $5.3x10^{-5}$ and the models were considered equivalent.

The estimation of plot basal area increment by remote sensing metrics demonstrated that secondary growth productivity is the consequence of crown structure and function. Plot 67 deviated significantly from the plot dataset. This plot had experienced much mortality, which was reflected in the basal area increment. The optical data were stratified by lidar height. No pixel with a maximum lidar return below two meters would contribute to the plot representation. However, standing dead, necrotic and chlorotic crowns would contribute to the plot level reflectance data. Additionally, in low-density stands the periphery of canopy gaps would have lidar returns greater than the two-meter height threshold, and the spatially corresponding optical data would, therefore, contribute to the plot level reflectance data. However, these gap periphery pixels would be largely produced from the reflected energy of the non-target ground cover vegetation.

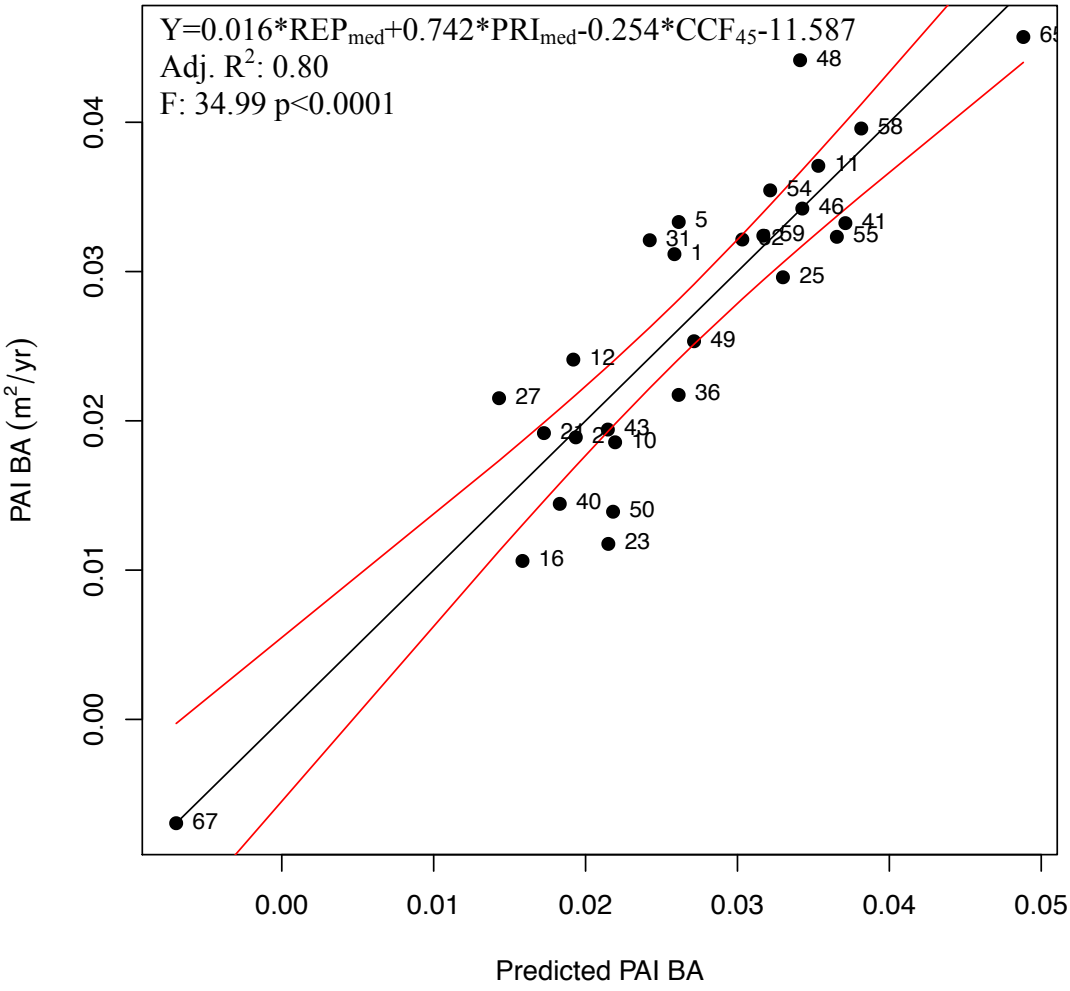


Figure 4.56. Multiple linear regression model predicting periodic annual increment in live basal area from the ratio of the CCF_{45}, plot median PRI and plot median REP. The residual standard error of the estimates is 0.005m^2/yr. (df: 23).

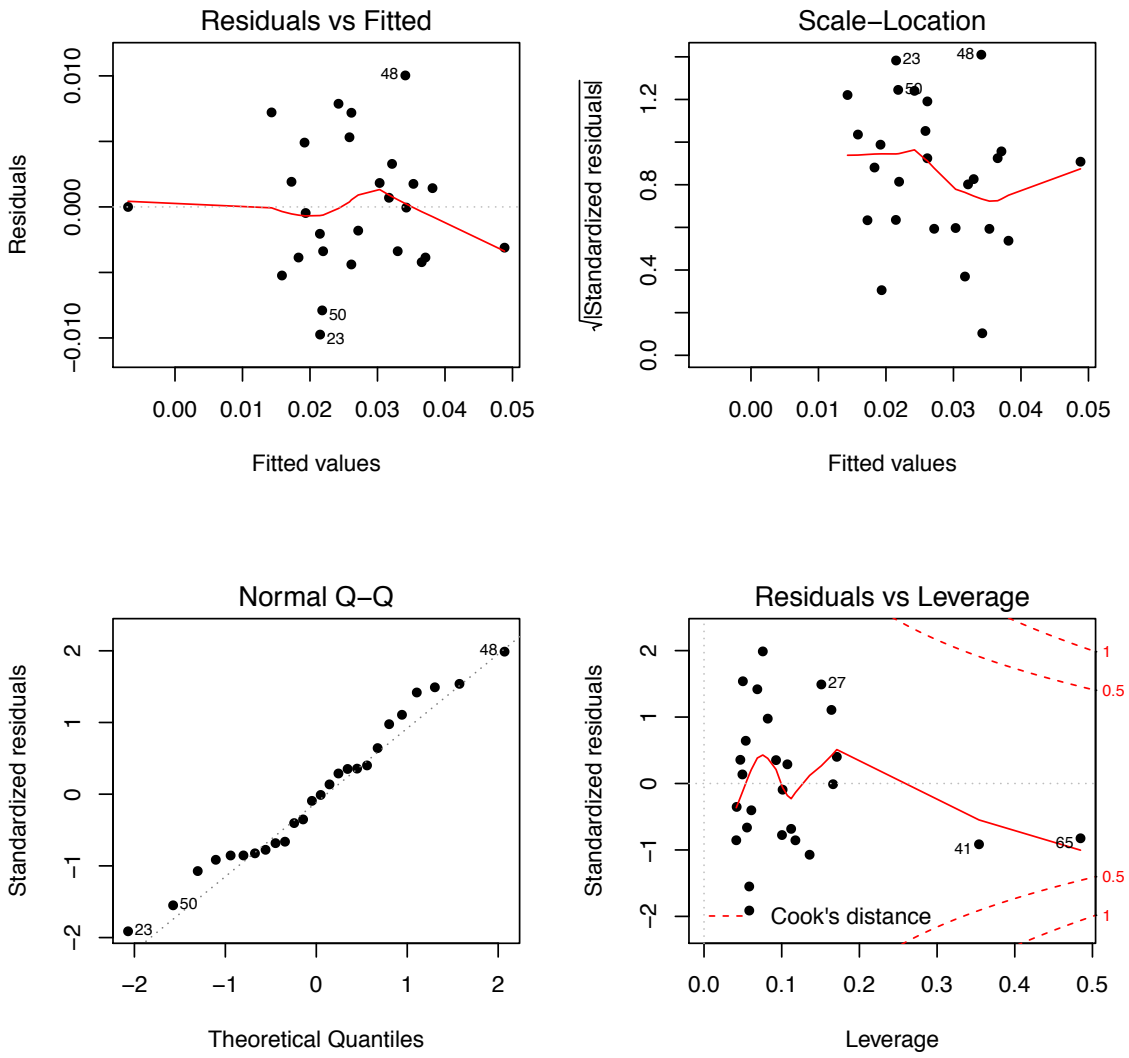


Figure 4.57. Residual plots for final multiple linear regression of plot PAI of BA predicted from CCF45, median PRI and median REP.

Whether by the effect of canopy health or spectral mixing at gaps, the canopy at plot 67 produced a signal that indicated lower chlorophyll levels. The median red edge position at plot 67 was one spectral channel shorter than all the other plots, Throughout the modeling of PAI BA, the median REP factor significantly contributed to explaining the large variation in the basal area increment of plot 67. The initial model selected the standard deviation of the canopy surface. As the variation of the canopy surface increased, so did the basal area increment; plot 67 being the large departure from this

trend by having the greatest standard deviation of the CHM but the lowest PAI BA. Therefore, the median REP factor accounted for the contribution of mortality to the PAI in BA. Omitting plot 67 from the regression analysis produced a linear model that was easily justified by considering a conceptual, process-based productivity model. Feature selection identified the CCF_{45} and median PRI, which represent the horizontal canopy area fraction and the foliar light use efficiency, respectively. The final model was augmented with the median REP to account for the variation in plot 67.

It was recognized that the diameter growth increment ignored variations in primary height growth, which is known to vary between some of the treatment plots as evidenced by the variations within the CHM and the field data analysis. Volume increments were considered the best attribute to model growth productivity as they would incorporate both height and diameter growth. The data applied here included observations from trees whose heights were measured or modeled. The difference in volume for each tree was computed and divided by the time lag in years (10 years). Mean plot PAI in volume was computed and applied in analysis. The effect of crown class and feature selection was investigated with simple linear regression and the best (exhaustive) two-variable subset multiple linear regression. In terms of the crown class stratification, the fit was best when only the dominant and co-dominant crown classes contributed to the plot level mean PAI in tree volume (Table 4.12).

Table 4.12 Effect of crown class on fit and feature selection for estimating mean PAI volume				
Crown classes	SLR	R^2	MLR	Adj.R^2
Dominant	GI_{cv}	0.62	$lidar_{range}$ + $MCARI_{cv}$	0.75
Dom – co-dominant	CHM_{max}	0.63	TT_{med} + $PSRI_{mad}$	0.85
Dom - intermediate	PRI_{cv}	0.51	CHM_{cv} + TT_{topht}	0.73
Dom - suppressed	PRI_{cv}	0.51	CHM_{cv} + TT_{topht}	0.73
Dom - dead	PRI_{cv}	0.45	$TCARI_{max}$ + $Ln(CHM_{sd})$	0.71
Note that dominant crown class membership per plot was low ranging from 1 to 5 individuals, the majority being split between 1, 2 and 3. Including the co-dominant class increased the average plot membership to 54 individuals and ranging from 28 to 133.				

The bootstrapped simple linear regression that applied mean PAI of volume from the dominant to co-dominant crown classes identified a coherent pattern where the ten most associated features (average R^2) were dominated by metrics that were sensitive to the top of the lidar point cloud (CHM_{max}, maximum point cloud height, LHQ_{100}, median lidar treetop, maximum lidar treetop, LHQ_{95}, height range of the lidar point cloud, average lidar treetop, average height greater than the lidar 85th percentile, LHQ_{90}). The three most associated features (LHQ_{100}, point cloud maximum and CHM maximum) represent the same data, they only differ in the manner in which they were extracted. The max height features were also the most associated features with volume increment when assessed by the mean Spearman's correlation. Plotting the CHM maximum with mean volume increment demonstrated that there was some evidence for a curvilinear relationship. The observed nonlinearity was rationalized by the fact that shorter plots experiencing higher densities and greater competition would experience smaller growth increments relative to more productive (at the individual level) less dense plots. As the trees grow taller more resources are captured and concentrated into fewer individuals and not lost to self-thinning. A quadratic fit produced significant scale and shape coefficients

($p<0.02$), however using non-linear least squares, the data were best fit with an exponential form ($PAIvol=1.4x10^{-7}*CHM_{max}^{3.418}$) (Fig. 4.58). The CHM maximum was transformed and submitted to a simple linear regression. The coefficient of determination for this initial model was 0.68 with a residual standard error of 0.003 (df: 25) and an F-statistic of 53.54 ($p<0.0001$). Residual analysis indicated the presence of both heteroscedasticity as well as influential points (plot 65 and plot 41). Plot 65 was clearly a departure from the general trend so the shape coefficient was re-estimated without its influence. Without plot 65 contributing to the exponent parameter, the linear model of mean PAI from the CHM maximum height was estimated as

$$meanPAI_{volume}=3.728x10^{-8}*CHM_{max}^{3.798707}$$

The shape parameter was estimated through nonlinear least squares and the scale parameter was estimated by the linear regression fit. When applying the transformed CHM maximum data to linear regression the intercept of $2.3x10^{-3}$ (standard error: $2.2x10^{-3}$) was not significant (t: 1.06, p:0.3), while the scale coefficient was estimated as $3.7x10^{-8}$ with a standard error of $4.4x10^{-9}$ (t:7.411, $p<0.0001$). This regression produced an F-statistic of 54.93 (df: 25, $p<0.0001$).

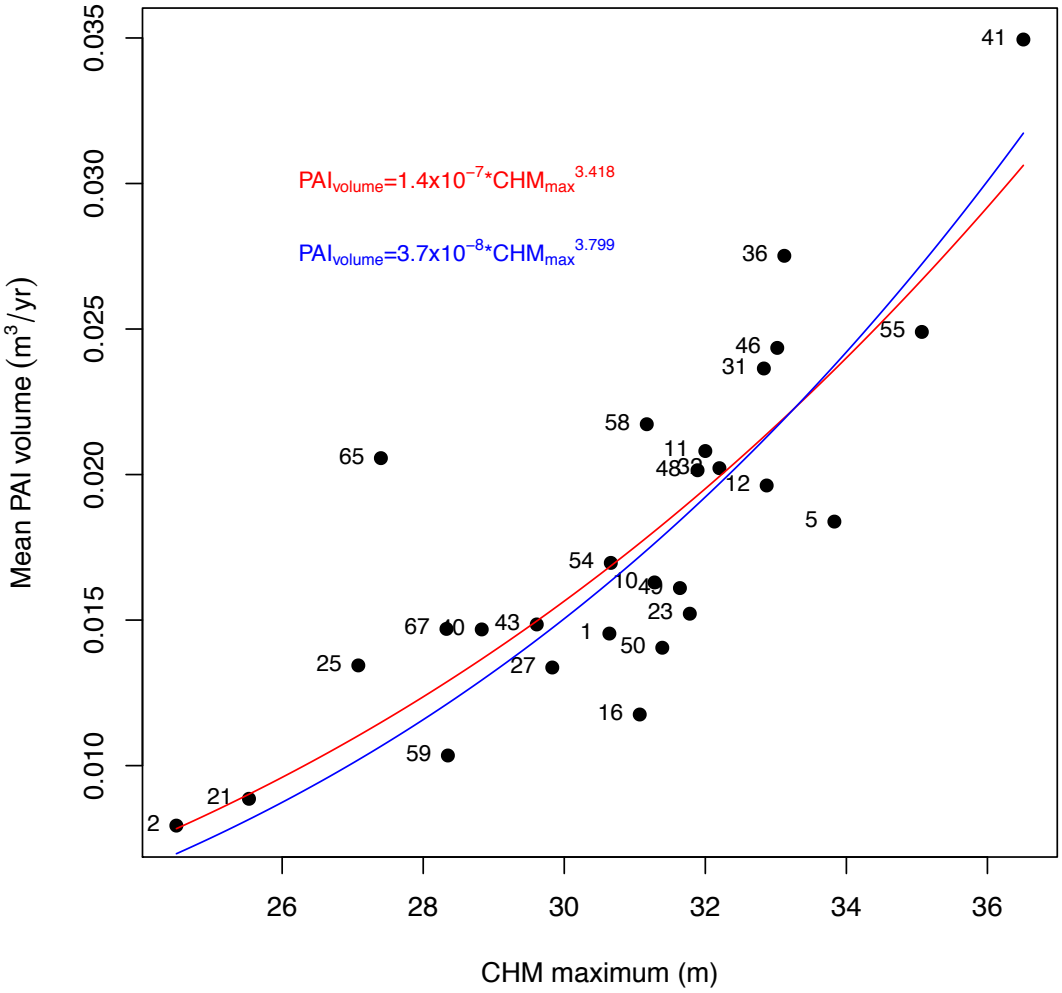


Figure 4.58 Characterization of the nonlinear relationship between mean volume increment and CHM maximum height through nonlinear least squares. The initial simple linear regression identified plot 65 and 41. Omitting plot 65 (blue) from shape estimation produced a superior fit according to the subsequent linear regression

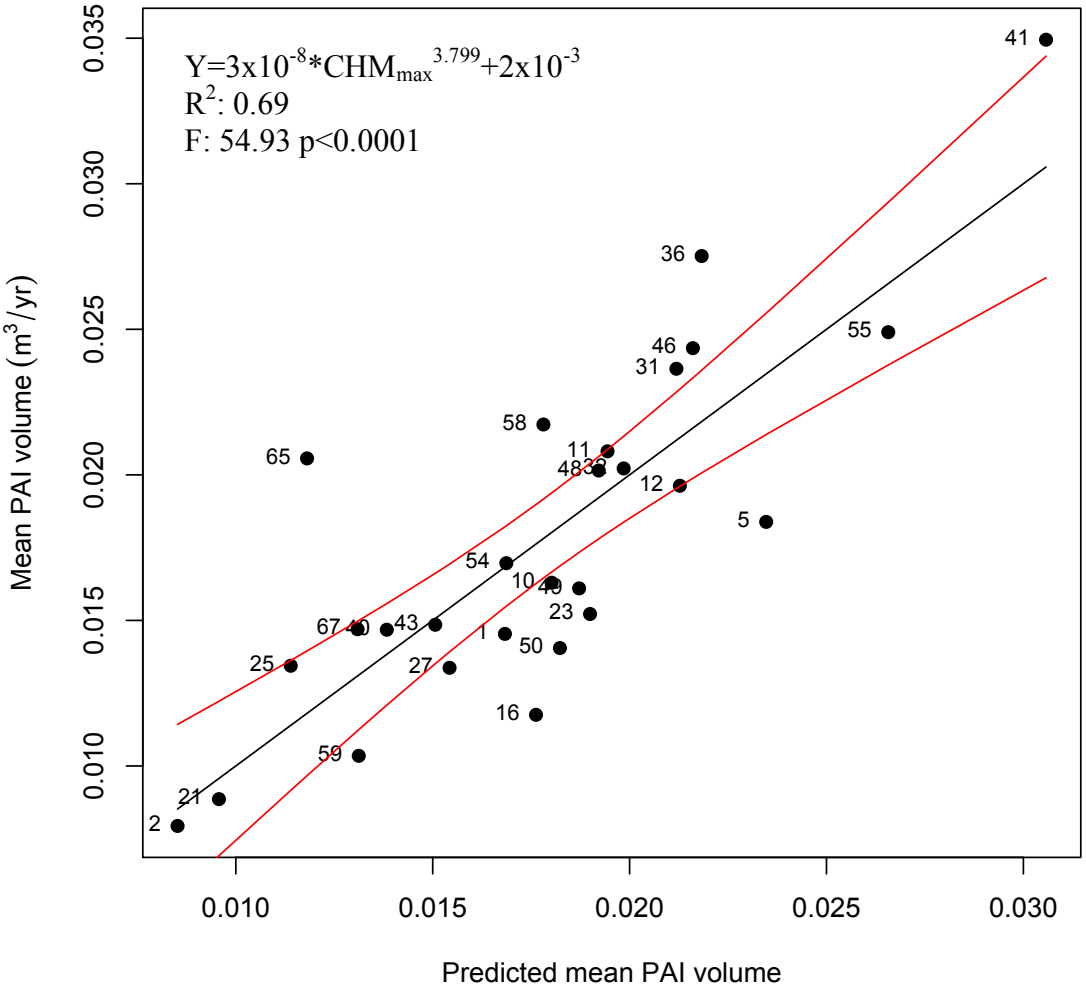


Figure 4.59. Ranked correlation analysis selected maximum CHM as most associated. The non-linear trend was estimated without the influence of plot 65. The maximum CHM data were transformed and the simple linear regression was estimated. The estimated parameters included the shape parameter of 3.799 (std. error: 0.44), a scale coefficient of 3.282×10^{-8} (std error: 4.428×10^{-9}) and a non-significant (t: 1.06, p:0.3) constant of 2.309×10^{-3} (std. error: 2.188×10^{-3}). The R^2 was found as 0.687 with a residual standard error of 0.0034 (df: 25). The regression produced an f-statistic of 54.93 ($p<0.0001$).

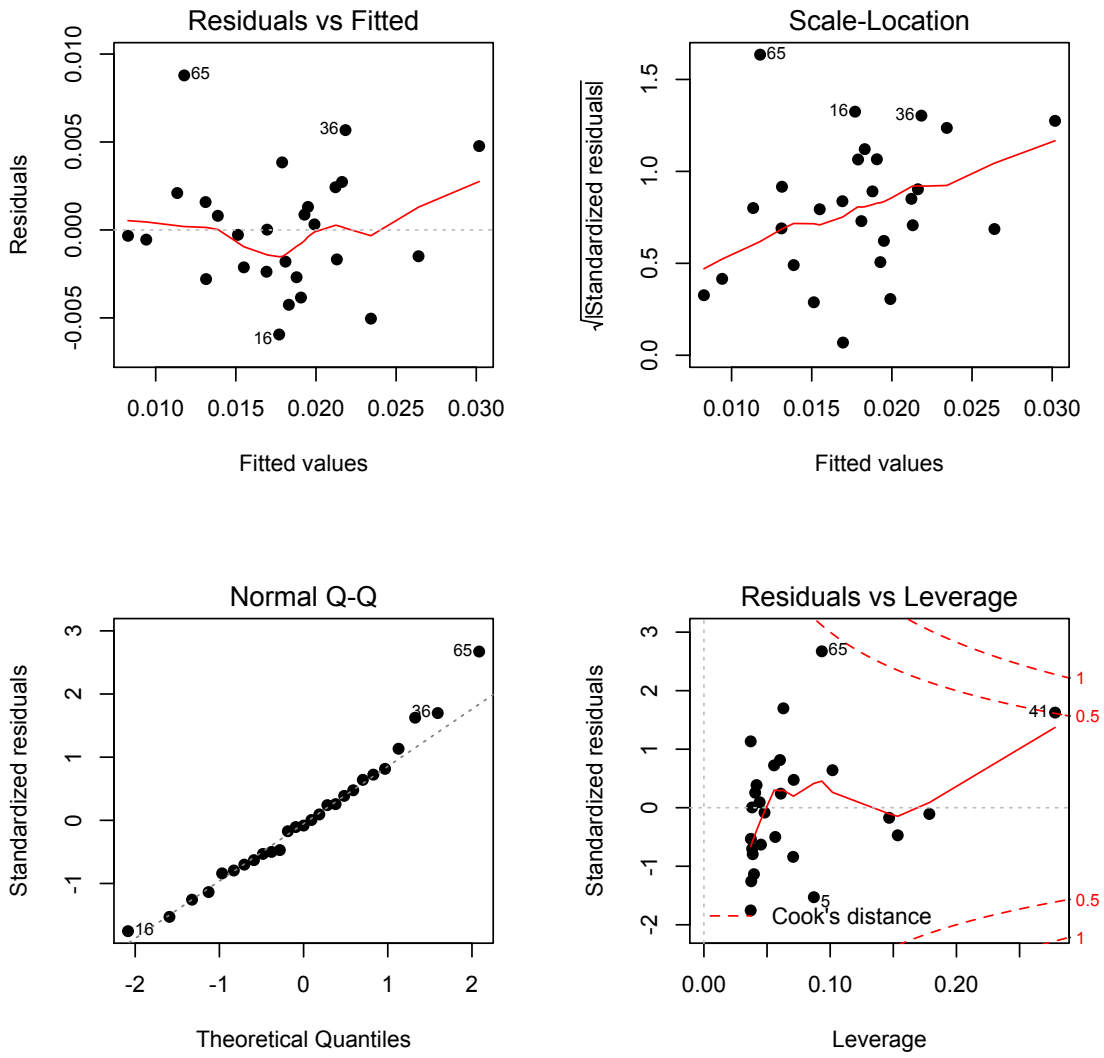


Figure 4.60. Residuals from the simple linear regression clearly illustrate heteroscedasticity in the scale-location plot and the presence of influential observations in the leverage plot.

Removing plot 65 from the non-linear fit estimation process increased the R^2 to 0.69 and marginally reduced the residual standard error (Fig. 4.59). The heteroscedasticity illustrated in the scale-location plot remained and was not entirely resolved even with the omission of the other influential plot 41 (Fig. 4.60). Other independent explanatory variables were explored for their ability to capture the residual sum of squared error.

Two approaches were taken to improve the mean PAI in volume estimation, a forward selection of the feature that most significantly contributed to the explanation of the variation in the mean volume increment and secondly the best two-variable subset model selected by exhaustive feature selection. In both cases of feature selection, the median absolute deviation from the median in the plant senescence reflectance index ($PSRI=(R_{678}-R_{500})/R_{750}$) was selected. However, the best two-variable subset model selected the median lidar treetop height as the other most explanatory independent feature. The forward selection of the most significantly associated feature with the residuals from the simple model selected the median absolute deviation of the PSRI index (Fig. 4.64 & 4.65), which was also the most associated feature selected through the bootstrap regression (mean R^2 and mean Rho). The bootstrapping result that listed in decreasing order the most contributing attributes, illustrated a coherent pattern of metrics that were sensitive to the variation in pigment absorption. Ordered by decreasing mean R^2, the first feature that was not a variation attribute (*i.e.* MAD, range, SD, SE, Var, CV) of a pigment sensitive spectroscopy metric (*e.g.* PSRI, CRTA (depth normalized Continuum Removed Total Area), TCARI, REP) was the coefficient of variation of the CHM, and was the 30th most contributing feature. Again, this result was interpreted as an indication that productivity is best estimated when the canopy structure (in this case height attributes) is augmented with a canopy function attribute (variation in pigmentation). The feature selection applied in these data was greatly affected by the inter-correlation of the remote sensing metrics, as the transformed maximum CHM was strongly associated with the median lidar treetop height (R:0.95, $p<0.0001$). The benefits of one model over the other are not obvious. The multiple linear model produced from

regressing the mean volume increment of the dominant to co-dominant crown classes with the median lidar treetop height and the median absolute deviation of the PSRI took the form

$$\text{meanPAIvolume}=0.0015*TT_{med}+1.74*PSRI_{mad}-0.034$$

The standard error for the model parameters were: 0.005, 0.0002, 0.27 for the constant, median lidar treetop and the $PSRI_{mad}$ parameters, respectively ($p < 0.0001$). This best two-variable subset model explained 85% of the variation in the mean volume increment (R^2:0.860, adj R^2: 0.849) with a residual standard error of 0.002m^3/yr. (df:24). The multiple linear regression produced an F-statistic of 74.23 ($p<0.0001$) (Fig. 4.62 & 4.63).

As is the case with many of the published optical reflectance indices and in contrast to its designated name, the PSRI is a hybrid index that is physically tied to both chlorophyll content and leaf area. The underlying rationale offered by some research is that the scattering environment or scattering response in the NIR can be leveraged to represent the optical path length and therefore represent the relative length over which a photon or ray is able to interact with matter [139]. Thus in a low LAI crown, the scattering will be reduced as is the opportunity for a visible photon to be absorbed. However, it is the case that these two attributes of forest crowns may vary independently and will theoretically have an impact on the optical index. Furthermore, the PSRI, like many optical data products, is severely confounded by forest structure, as it is very sensitive to shadow. In the cases of inter crown shadow pixels, the magnitude of the responses are so diminished that the green peak signal is below the noise level, while the red well feature is more dominated by scattering and therefore produces a positive index value. The orientation of the flight acquisition would have helped minimize the effect of

shadow, as any flight with a south facing heading would capture the majority of the dark spot caused by the geometry of bidirectional reflectance, the vertical relief of tree crowns and the positive pitch of the airframe during acquisition. The east-west and west-east orientations served to minimize the variation in bidirectional reflectance, however a shadow component is always present. The only case where shadow is minimized is for flights flown in a northerly direction (and with a view zenith greater than the illumination zenith) or over flat terrain. An investigation into the structural attributes that are associated with the $PSRI_{mad}$ determined that the single most associated attribute was the mean PAI in DBH of the dominant and co-dominant tree layer (R^2: 0.67, F: 49.92, $p<0.0001$. Given previous analysis that suggested that the DBH increments were related to stem densities and the observed sensitivity of the PSRI to shade (Fig. 4.61), the underlying signal detected by the PSRI was questioned. A two variable subset model selected average crown length and the skewness of DBH as most predictive of $PSRI_{mad}$ (adj. R^2: 0.60, F: 20.57, $p<0.0001$). The selection of these two independent variables supports the presumption that the $PSRI_{med}$ is providing not a health related signal but one tied to the canopy surface geometry. Longer crowns and a more positively skewed DBH distribution are attributes that are consistent with post stem exclusion structural stages, or in this case, increased thinning and high productivity or disease related gap formation.

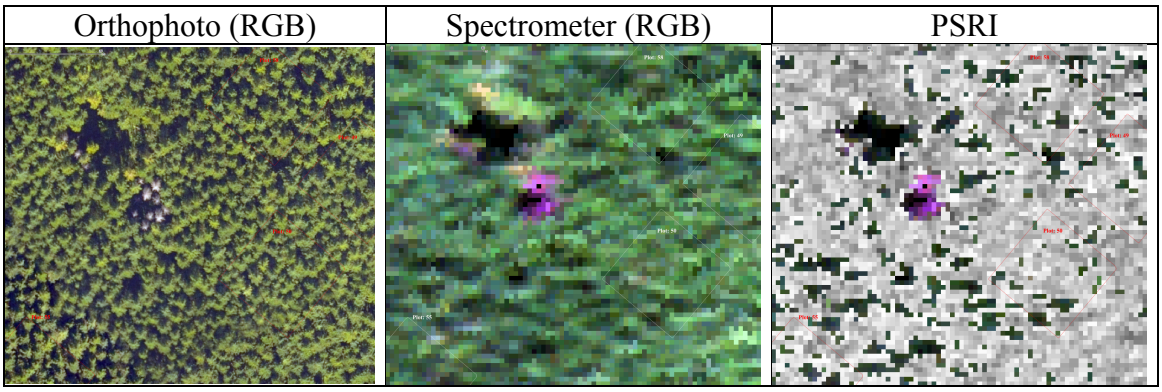


Figure 4.61 Root disease site adjacent to plot 57 used to illustrate that the PSRI index is sensitive to both shadow and dead tops and in this case not at all sensitive to chlorotic crowns. The PSRI display range has been restricted to the data range of -0.11(minimum) to -0.04 to omit shadowed regions. The display is clipped to the specified data range; it is transparent outside that range. The PSRI is overlayed on top of the spectrometer data. The orthophoto illustrates the root disease site with snags and a gap with chlorotic crowns at its edge. The chlorotic crowns are not apparent in the PSRI.

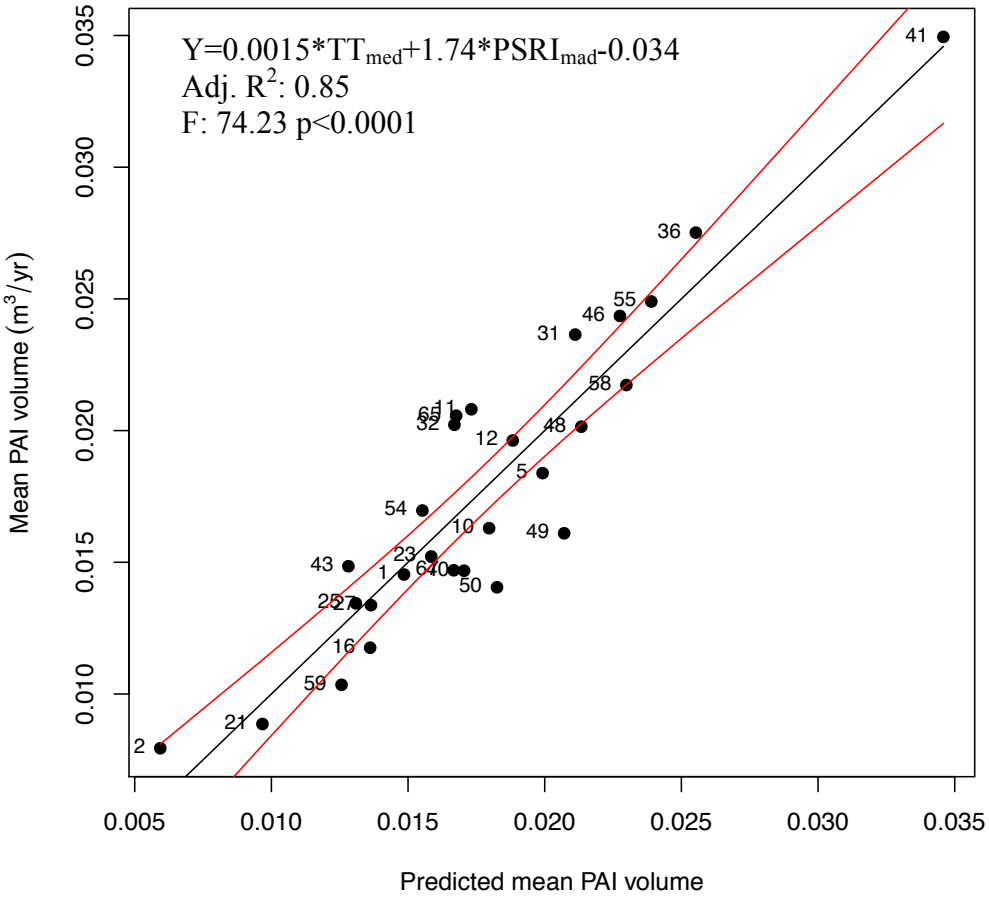


Figure 4.62 The best two variable subset model for estimating mean volume increment was produced from the median height of the lidar treetops and the median absolute deviation of the optical pigment index PSRI.

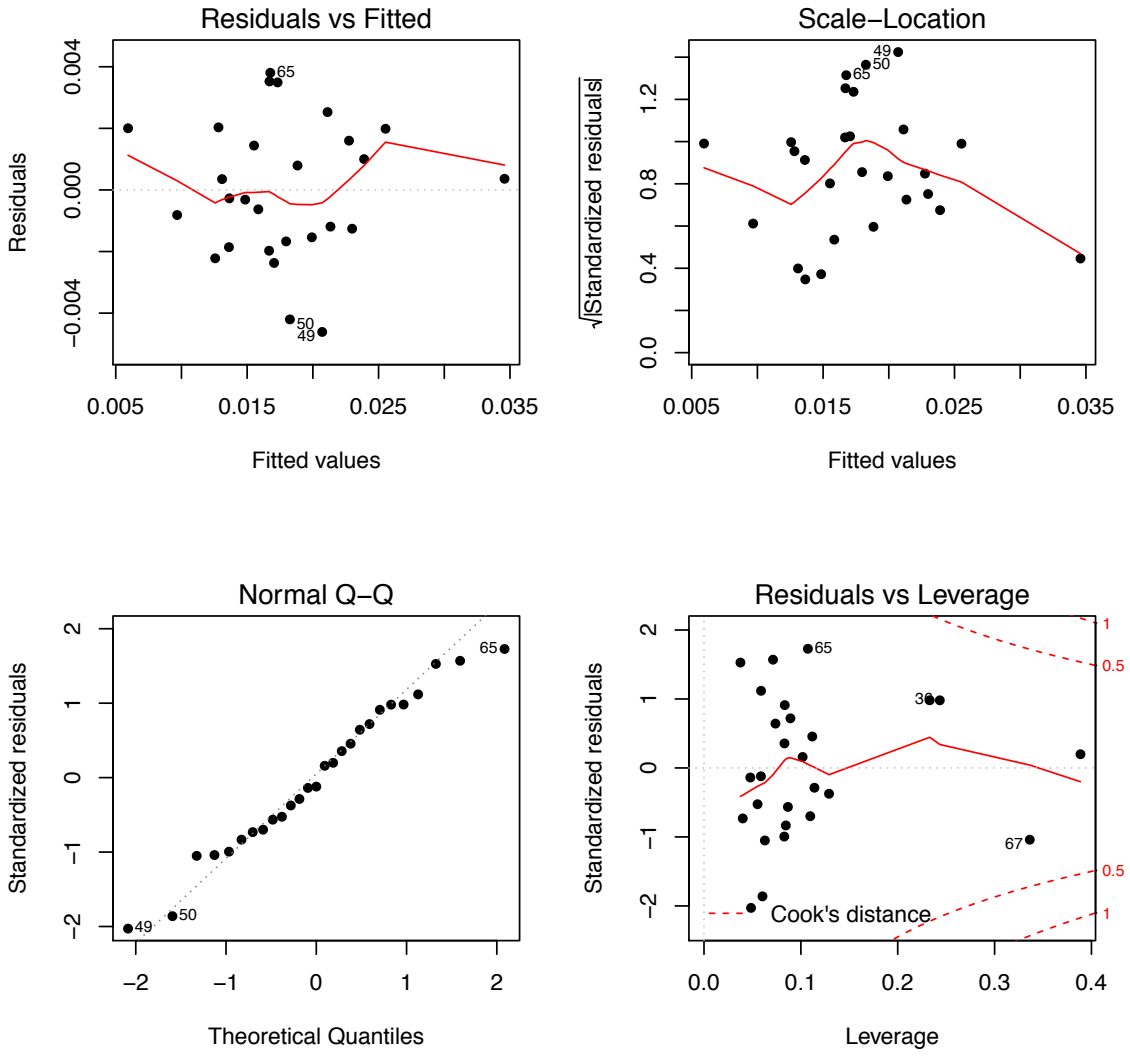


Figure 4.63. Residuals from the multiple linear regression of median lidar treetop height and the median absolute deviation of the PSRI index do not strongly suggest that statistical assumptions have violated

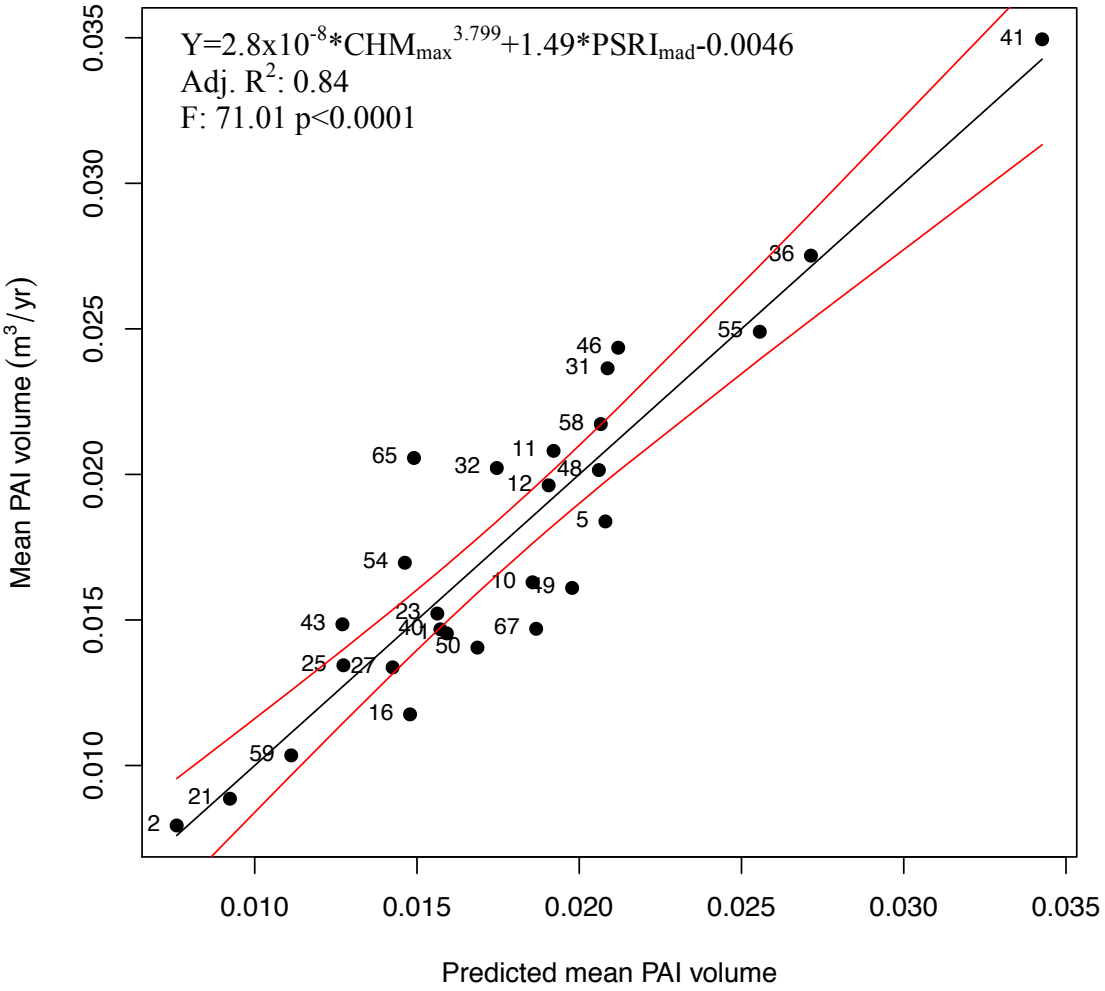


Figure 4.64 Bootstrapped correlation analysis indicated the most associated (mean R and mean Rho) remote sensing metric with mean volume increment was the maximum in the CHM and the relationship was non-linear. The maximum CHM data were transformed by a fit exponent. Reiterated anlysis indicated that the transformed variable was the most associated feature, it was applied in a simple linear regression. The residuals of the simple linear model were sumbitted to the bootstrappiing script which identified the median absolute deviation of the PSRI index as most contributing. This model might be considered inferior to the best two variable subset model as it requires the estimation of four parameters as apposed to three. In addition, degrees of freedom do not reflect the additional shape parameter estimation.

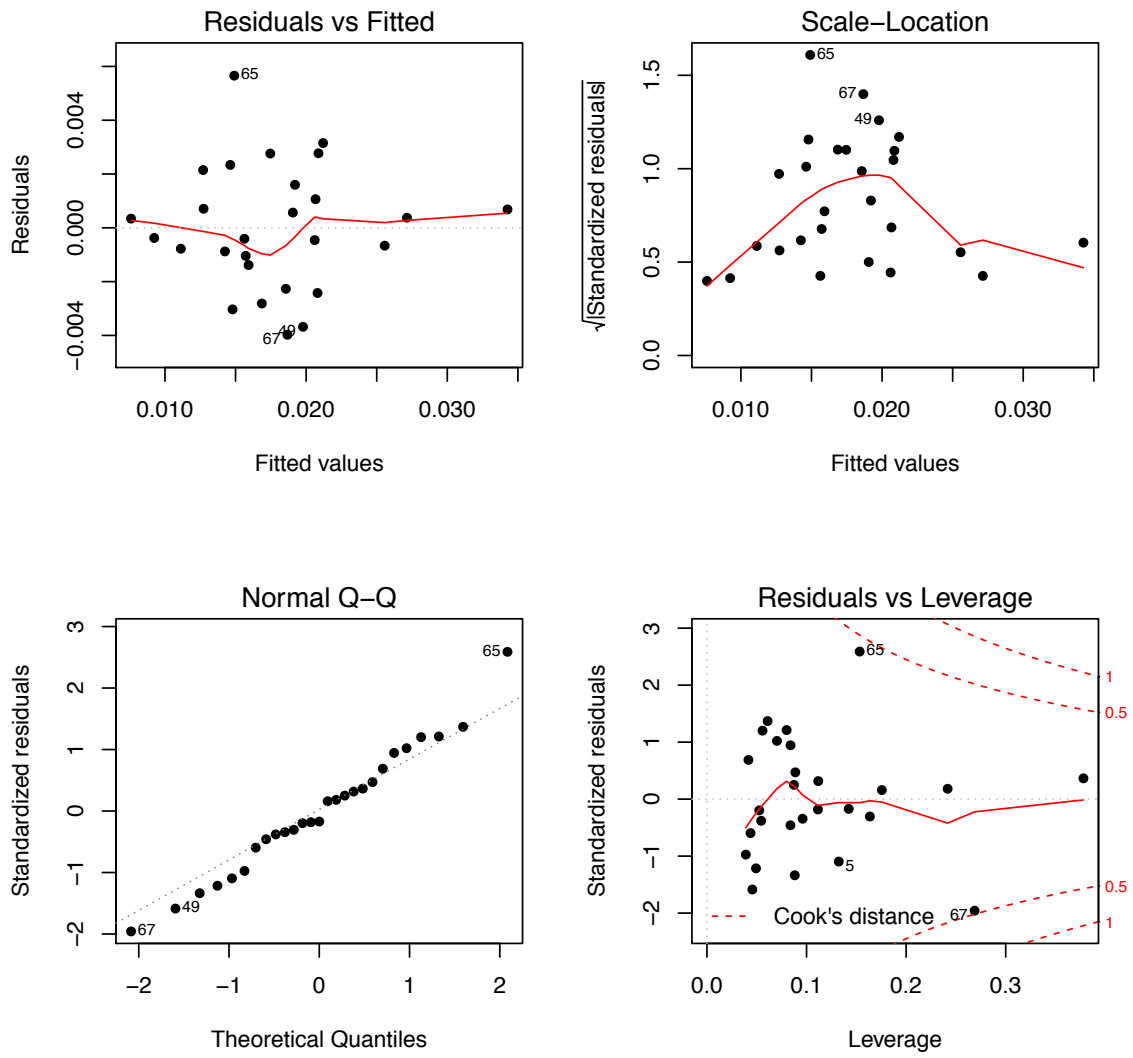


Figure 4.65. Residuals from the multiple linear regression of transformed maximum CHM height and the median absolute deviation of the PSRI index do not strongly suggest that statistical assumptions have been violated

Considering that omitting the intermediate crown class ignores as much as 31.9 percent of the total plot volume (plot 36), all but the dead crown class was included to determine the effect on estimating the mean volume increment. For reference, the ranges of total plot volume stratified by crown class were 0-26% in the dominant class, 43-92% in the co-dominant class, 2-32% in the intermediate class, 0-2% in the suppressed class and 0-14% in the dead class for all the CFS treatment plots. The bootstrap approach to feature selection identified the coefficient of variation of the PRI and the zero lidar height

quantile (adj R^2: 0.58, F: 18.65, $p<0.0001$). The LHQ_0 was not the most contributing metric without the bootstrap, suggesting that the model might be unstable. This assumption was supported by the result of the first iteration of the feature selection. When the remote sensing metrics were ordered by decreasing mean R^2 for the association of mean volume increment in the dominant to suppressed crown classes, there was a coherent pattern with the exception of the PRI_{cv}, which happened to be at the top of the list. The majority of the most associated metrics (*i.e.* 24/30) were height related metrics, the median lidar treetop height being the most associated metric behind the PRI_{cv}. In addition, the LHQ_0 contained a considerable amount of noise and its selection raised concern. The LHQ_0 represents the height of the lowest lidar return within the plot area after the heights have been adjusted to heights from the defined ground surface and a height threshold is used to omit ground noise (*i.e.* 2m). As the selected features did not inspire confidence, the initial feature was changed to the median lidar treetop height and the second feature selection was run, which selected the standard deviation of the CHM (Table 4.12). This combination explained 12% more of the variation in mean volume increment than the forward selected model (Fig. 4.66 & 4.67).

Table 4.13 Bootstrap of MLR model predicting plot mean PAI in volume from the median lidar treetop height and the standard deviation of the CHM

	Intercept	TT_{median}	CHM_{sd}	R^2	F-stat	P-value
Minimum	-0.048	0.0006	0.0011	0.32	5.63	<0.000
Q1	-0.033	0.0012	0.0018	0.68	25.23	<0.000
Mean	-0.030	0.0013	0.0022	0.73	37.85	<0.000
Median	-0.030	0.0013	0.0021	0.74	34.38	<0.000
Q3	-0.027	0.0014	0.0025	0.79	45.88	<0.000
Maximum	-0.014	0.0020	0.0049	0.92	135.40	0.010

1000 Bootstrap iterations each built from randomly sampling the plot data with replacement 27 times to equal the number of selected plots.

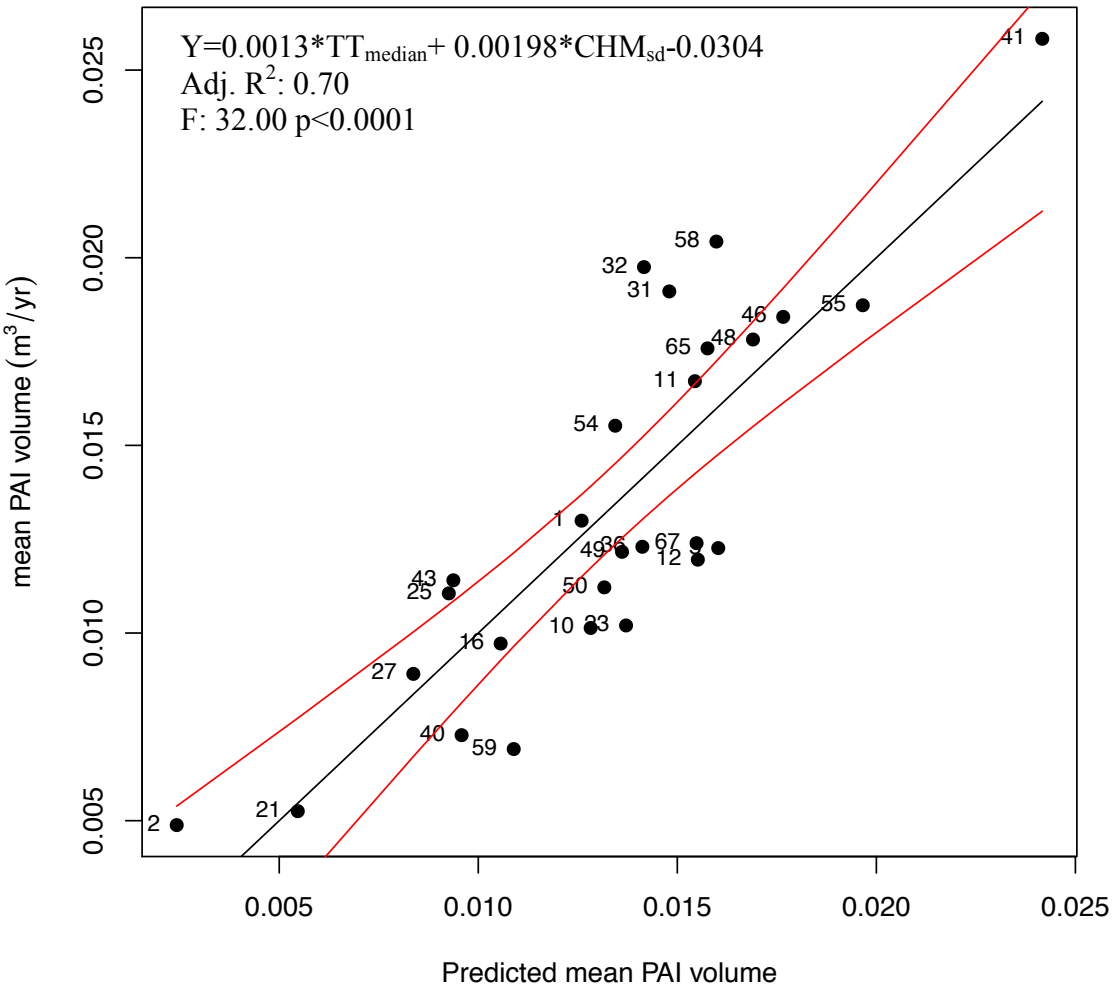


Figure 4.66 Plot mean PAI in volume (crown classes dominant to suppressed) estimated from median lidar treetop height and the standard deviation of the CHM. The residual standard error produced for this regression model is 0.0028

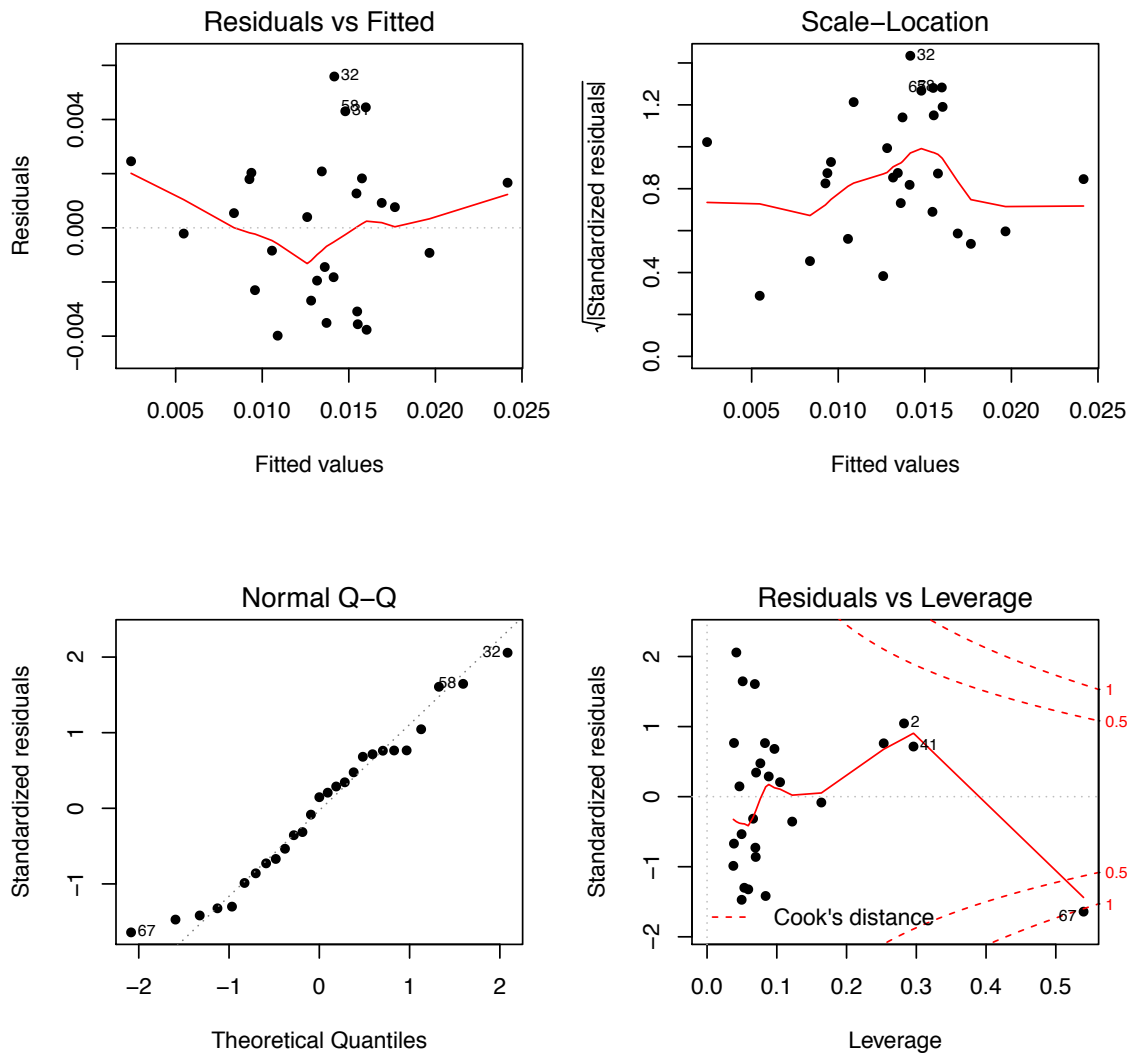


Figure 4.67. Residuals from the multiple linear regression of median lidar treetop height and the standard deviation of the CHM do not strongly suggest that statistical assumptions have been violated, although the large gap of plot 67 produces a large standard deviation in the CHM, for this reason plot 67 is identified as an influential observation. Without plot 67 the regression parameters are: $Y=0.0012*TT_{median}+0.0027*CHM_{sd}-0.0288$, adj. R^2: 0.74, residual standard error: 0.0027, F-stat: 35.92 (df: 23).

The model estimating live mean PAI in volume was further improved with the best two-variable subset model, which was very similar to the previous model, but applied the scale normalized variation within the CHM (CV) and an attribute that was initially created to estimate the measured plot top heights (the average height of the four

tallest lidar treetops) (Fig. 4.68 & 4.69, Table 4.14). Aside from being slightly more informative on volume increments the residual plots indicated that plot 67 in this model was not an influential observation, a result that was supported by the smaller spread in the distribution of the bootstrapped coefficient (CHM_{sd}: ~0.004 vs., CHM_{cv}: ~0.001). The link between the tree height attribute and volume increment is intuitive. SLP plots with taller trees are growing at a faster rate. However, approximately 55 percent of the error in this simple relationship is accounted for by the spread in the CHM (SLR adj. R^2: 0.40, MLR adj. R^2: 0.73). Using plots 67, 65 and 25 as an example, these plots have greater volume increments than can be explained by their tree heights alone. They are short (Top height percentiles for plot 67: P_7, plot 65: P_{19}, plot 25: P_{15}) for their volume increments. However, the canopy structures of these plots are a clear departure from the general attributes of the others, as these plots have much longer crowns (crown length percentiles of plot 67: P_{85}, plot 65: P_{96}, plot 25: P_{70}) than others with comparable top heights. The longer crown lengths might suggest a higher photosynthetic yield and explain the abnormally (departure from other SLP plots) high volume increments for plots with lower top heights. For reference, only the control plots had similarly short top heights to plots 67, 65 and 25. To sustain longer crown lengths, the canopy must allow for light penetration deeper into the crowns, a condition that would be perceivable as a more varied top-of-canopy surface. As previously noted, Plots 67 and 65 have canopy gaps which is reflected in the standard deviation of the CHM with percentiles of 96 and 100, respectively. The low top heights of these plots are also reflected in the mean CHM values, which places these plots at the lowest end of the coefficient of variation in the CHM data, hence the inverse coefficient for CHM_{cv} relative to that produced for the

CHM_{sd}. Although the ground reference data suggest that the mean live PAI in volume is best estimated from quadratic mean diameter and average crown length (Y=0.0009*QMD+0.0014*CL-0.020, adj. R^2: 0.92, residual std. error: 0.001 (df: 24), F: 150.2, p: <0.0001), it also provides the RS model with merit by producing a significant relationship with top height and crown length (Y=0.0005*Topht+0.0028*CL-0.025, adj. R^2: 0.82, residual std. error: 0.002 (df: 24), F: 58.62, p: <0.0001).

Table 4.14 Bootstrap of MLR model predicting plot mean PAI in volume from the average four tallest lidar treetop heights and the coefficient of variation of the CHM

	Intercept	TT_{top}	CHM_{cv}	R^2	F-stat	P-value
Minimum	-0.028	0.0009	-0.0025	0.32	5.71	<0.000
Q1	-0.017	0.0014	-0.0018	0.70	27.94	<0.000
Mean	-0.014	0.0015	-0.0017	0.75	41.59	<0.000
Median	-0.014	0.0015	-0.0016	0.76	38.21	<0.000
Q3	-0.012	0.0016	-0.0015	0.81	49.78	<0.000
Maximum	0.001	0.0020	-0.0007	0.92	134.06	0.009

1000 Bootstrap iterations each built from randomly sampling the plot data with replacement 27 times to equal the number of selected plots.

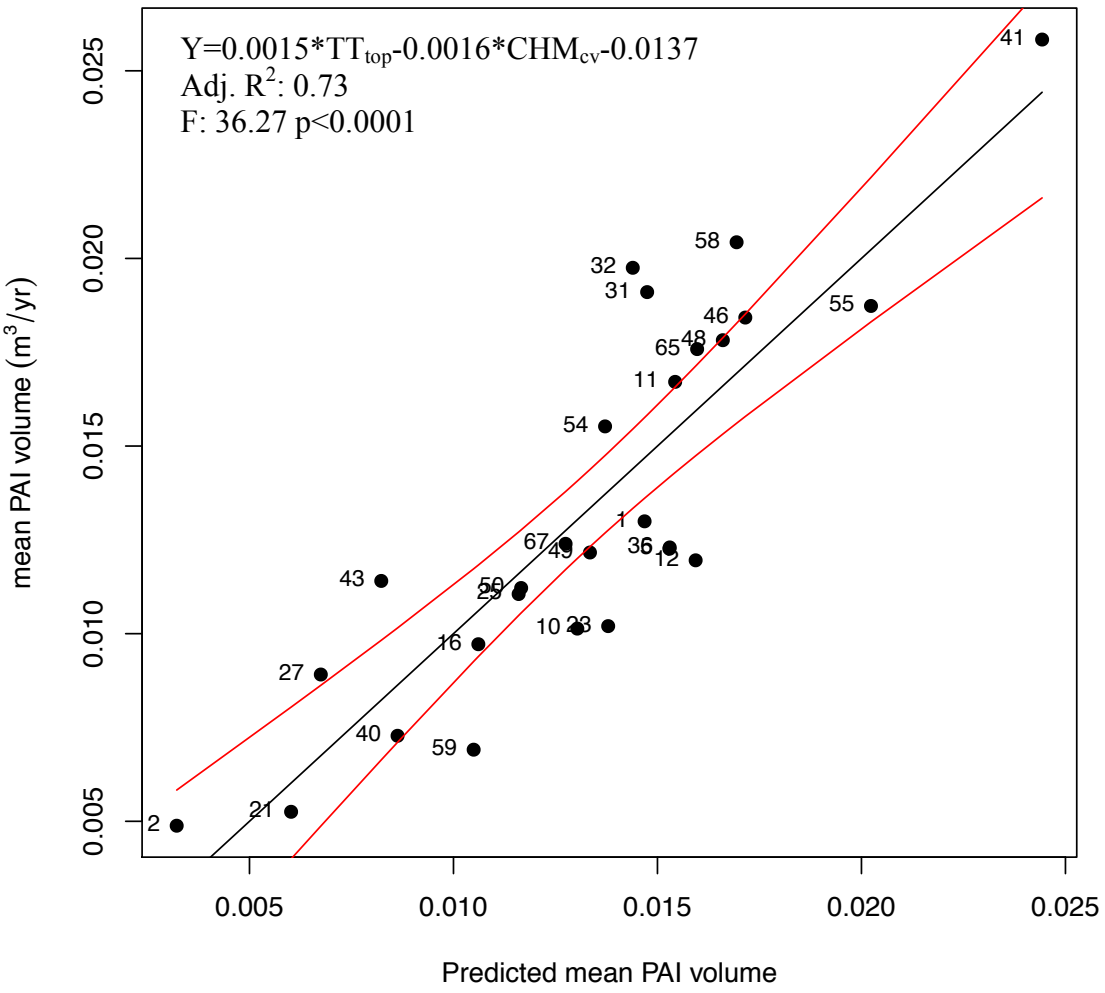


Figure 4.68 Plot mean PAI in volume (crown classes dominant to suppressed) estimated from the mean height of the four tallest lidar treetop heights and the coefficient of variation of the CHM. The residual standard error produced for this regression model was 0.0026

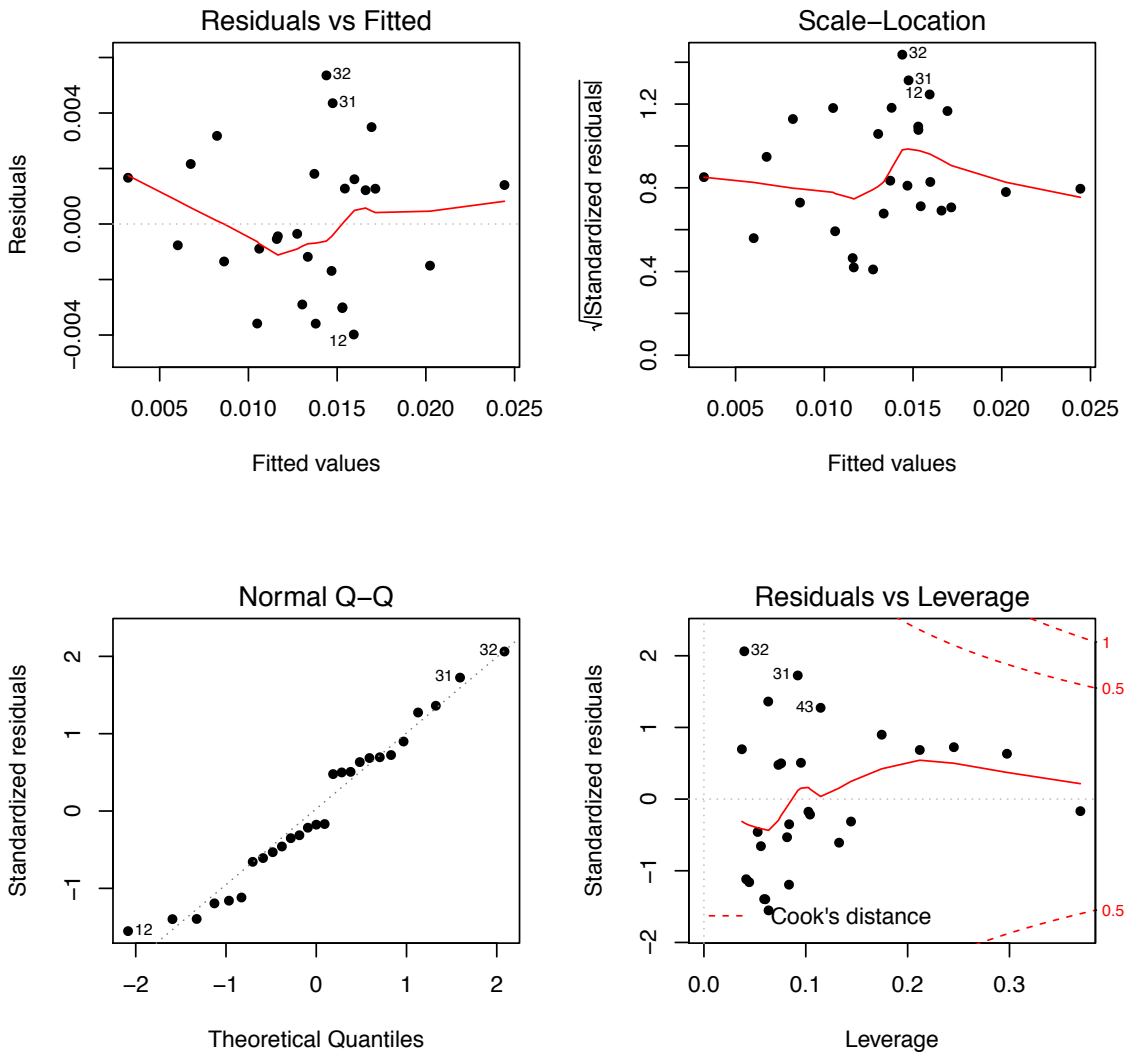


Figure 4.69. Residuals from the multiple linear regression of mean height of the four tallest lidar treetops and the coefficient of variation of the CHM do not suggest that statistical assumptions have been violated. In contrast to the previous model plot 67 is not identified as an influential observation. The difference with reference to plot 67 is that although the standard deviation in the CHM is high the mean is relatively low

The final productivity attribute to be evaluated was the periodic annual increment in total plot volume, which was suspected to be the most valuable for plot based estimates of productivity. The assumption that total volume increment would be the best metric for remote estimation was based on the agreement between scale of representation and analysis, that is plot based remote sensing metrics and a productivity attribute that take

into consideration not only volume increment but also site occupation. As before, crown classes were investigated with reference to linear fit and feature selection (Table 4.15). In contrast to much of the previous productivity modeling the features selected for total plot volume increment were dominated by spectroscopic metrics. The only instance of a selected lidar metric was the simple linear regression of total plot volume increment in the dominant to co-dominant crown classes, where the 20th lidar height percentile was selected. The predictive power reached a maximum when the intermediate class was included and not surprisingly, including the low volume increment within the suppressed class did not have a sensible effect on model performance.

Table 4.15 Effect of crown class on fit and feature selection for estimating PAI total volume

Crown classes	SLR	R^2	MLR	Adj.R^2
Dominant	VOG_{mad}	0.17	$CRI_{mad} + ARI_{mad}$	0.47
Dom – co-dominant	LHQ_{20}	0.49	$LA/RA_{range} + TCARI_{max}$	0.66
Dom - intermediate	$CRDepth_{mean}$	0.61	$CRDNRA_{mean} + GI_{median}$	0.77
Dom - suppressed	$CRDepth_{mean}$	0.61	$CRDNRA_{mean} + GI_{median}$	0.77
Dom - dead	$CRDNRA_{mean}$	0.49	$PRI_{sd} + PSRI_{var}$	0.65

Note that dominant crown class membership per plot was low ranging from 1 to 5 individuals, the majority being split between 1, 2 and 3. Including the co-dominant class increased the average plot membership to 54 individuals and ranging from 28 to 133. Crown classes were defined by 2012 campaign.

Plotting the relationship between the single most associated feature, the mean continuum removed depth, and the total plot volume increment, within the dominant to suppressed crown classes illustrated a large dependency on plot 67, which was also confirmed in a residual leverage plot. The mean continuum removed depth of plot 67 (P_0), being more than five interquartile ranges beneath the median, was an outlier. Plot 67 was also an outlier within the total plot volume increment (P_0), being more than twice the interquartile range below the median PAI in total volume. Plot 67 was unique in both the

data and the trend with total plot volume increment (Fig. 4.75). The simple linear model produced a significant constant of -11.9 (std. error: 2.00) and coefficient of 13.1 (std. error: 2.11), an R^2 of 0.609 with a residual standard error of 0.0572 (df: 25), and finally an F-statistic of 38.96 (P<0.0001). Although a non-linear exponential pattern may exist for the relationship between total volume increment and mean CR depth, there is no sense in characterizing the non-linearity based on one observation alone. Nonetheless, abiding by the linear assumption, the depth data was raised to the 80th power, which forced the appearance of a linear pattern for all the data. The transformation marginally increased the quality of the fit and did not flag plot 67 as an outlier in the residual analysis ($PAI_{total\ volume}$=13.8*$CRDepth_{mean}$^80+0.31, R^2: 0.614, residual std. error: 0.0569 (df: 25), F-statistic: 39.69 p<0.0001). To reduce the effect of the subjective nature of defining the transformation, nonlinear least squares was used to derive the exponential transformation. The non-linear fit produced a shape coefficient of 39.56 (a standard error of 33.72 reflects the fact the nonlinearity is dependent on one observation). The new transformation again marginally increased the R^2 to 0.63 and increased the F-statistic to 42.57. Given the untransformed residual analysis and previous investigations, which also demonstrated that plot 67 exhibited divergent attributes, model building considered the implications of including or omitting plot 67. The feature selection was run without the inclusion of plot 67 and this omission had a drastic effect on the selection of the single most associated feature. Without the inclusion of plot 67, 17 of the 30 most associated metrics were the lidar height quantiles ranging from P_{10} to P_{90} and centered on $P_{35.}$ The remaining 30 most associated features were point cloud height location statistics (median, mean, and 2% trimmed mean), lidar treetop height location (median and mean), average four tallest lidar

treetop heights, mean continuum removed depth and lastly three PRI index features (mean, median and mean PRI_2). There was little difference in predictive power between these thirty best features, which produced mean R^2 values from 0.41 to 0.45. The LHQ_{35} explained 45% of the variations in total volume increments with plot 67 omitted. Irrespective, it was clear that a height related signal had been identified and the feature ranks may be of little consequence. The Pearson correlation coefficient between LHQ_{35} and the remaining 15 most associated LHQ features were all greater than 0.98 (Fig. 4.70).

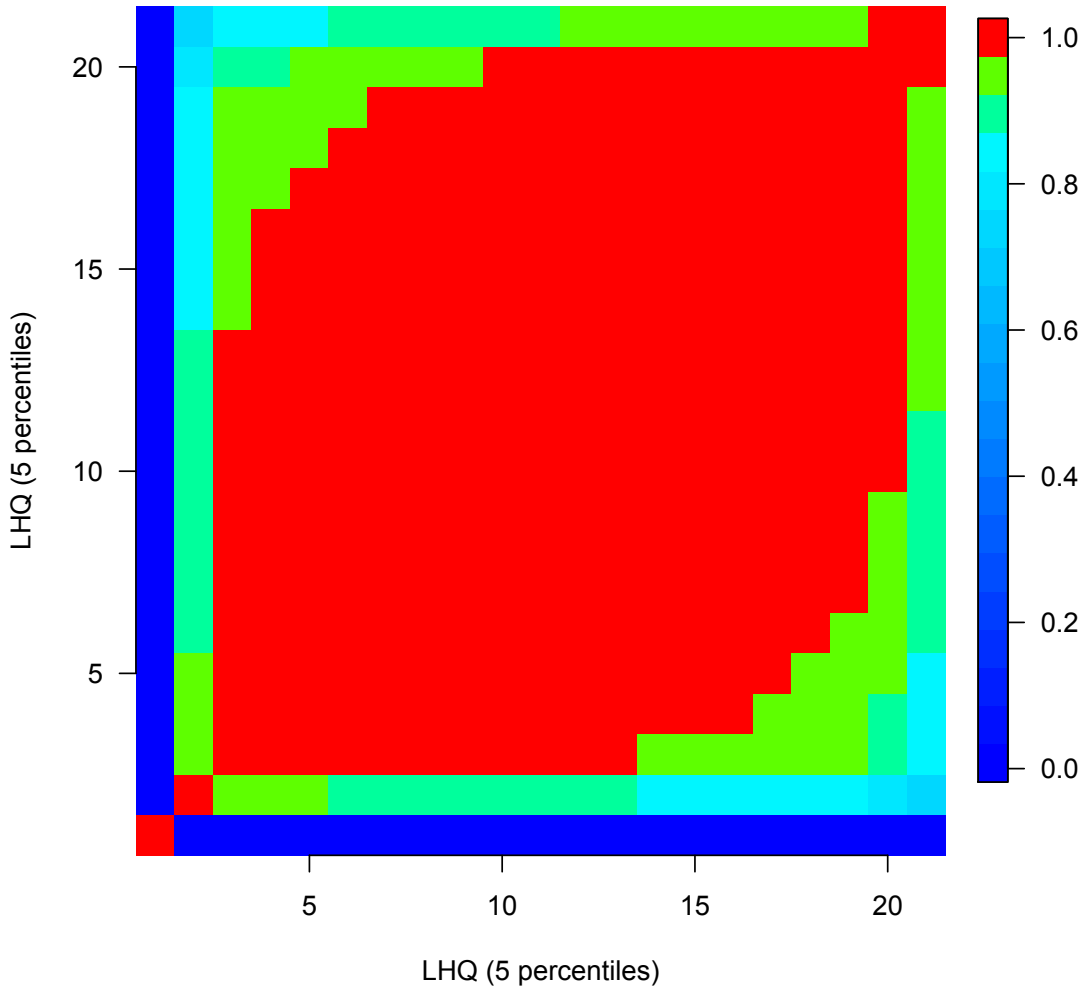


Figure 4.70 Pearson's correlation matrix illustrating that very little information diversity exists within the lidar height quantile data, only the four extreme bins contain variation that is not highly correlated with the other bins. Only $LHQ_{0,\ 5,95,\&100}$ have correlation coefficients less than 0.90.

In favor of robustness and model transferability, the most associated height related metric not susceptible to variations in point density or footprint size was selected for model inclusion. The SLP project offered an opportunity to investigate the impact of changes in point density on lidar metrics. Because ten separate flight lines were flown to cover the project area, individual flight lines could be iteratively added and the effect on lidar height distributions could be observed. A sample 20x20m location that did not occur on flight edges and that was entirely covered by a maximum number of flight lines was selected (UTM center: 447030, 5387363 approximately plot 29, eight total flight lines). The closed canopy sample location demonstrated that increasing point density increases the number of lidar returns from the lower portion of the canopy (Fig. 4.71 & 4.72). It also illustrated that lidar height percentiles become increasingly more susceptible to variations in point density with decreasing height percentile below approximately the 60th percentile. Additionally, the maximum height was also different according to point density. The impact of point density appeared to saturate at roughly 30 returns per square meter, up to ~65 points/m^2. These statements on point density must be qualified by stating that the vertical distribution of returns is largely dependent on footprint size (flight height and beam divergence) as well as the density of the forest canopy, which in combination quantify beam penetration into and through the canopy to define the lower range of the height distribution. Conversely, the stem density and the height of a forest stand will largely determine the upper portion of the lidar height distribution.

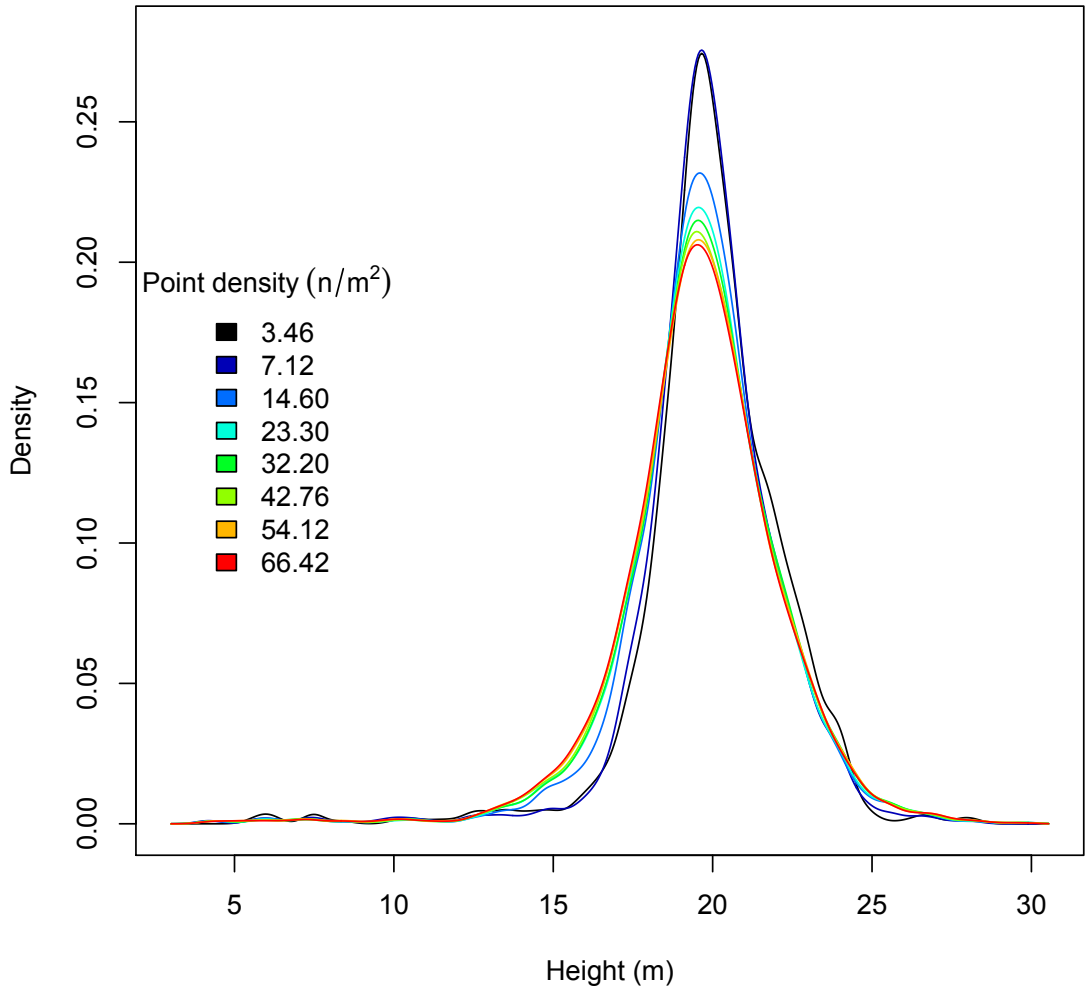


Figure 4.71. Changes in lidar height distribution are apparent with changes in point density. Each profile was determined by adding consecutive flight lines. The effect of increasing point density was the greater proportion of returns from lower canopy positions (*i.e.* ~12-18m). All profiles were built from a 20x20m area (aligned north and south) centered at 44730E, 5387363N, approximately treatment plot 29.

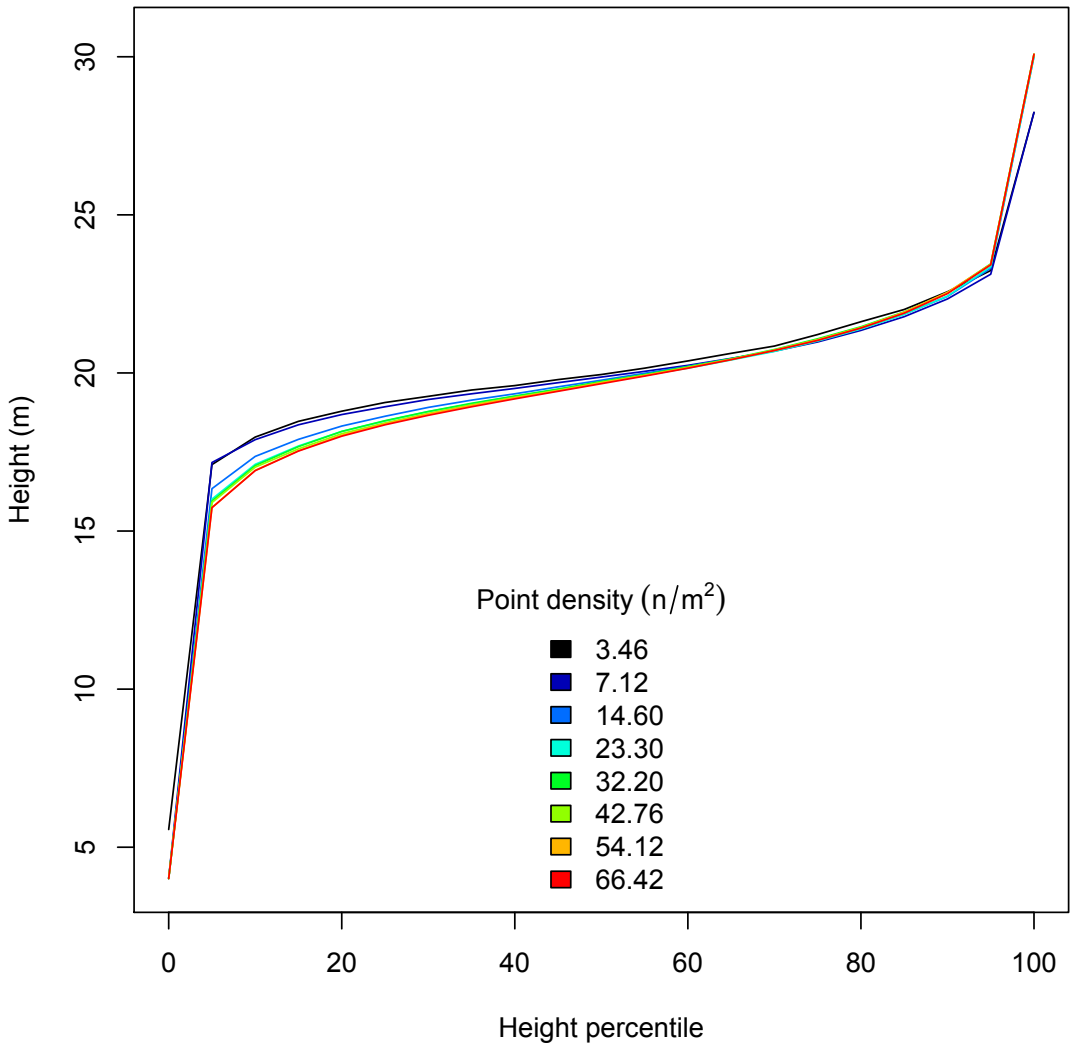


Figure 4.72. Lidar height percentiles below the 60th height percentile are increasingly affected by point density with decreasing height percentile. This suggests a greater penetration to lower canopy positions with higher point densities. Increasing point density increases the maximum height, in line with the increased probability of intersecting the highest obstruction. The lowest density profile did not return a position at the height threshold value of 4.01m, which is in line with the reduced penetration assumption. The heights across the first two quartiles were lowered with increasing point density.

The first point density resistant height related attribute selected as most associated with volume increment was the median lidar treetop height (20th largest mean R^2). The median lidar treetop height explained 43% of the variation in total plot volume increment, and also identified plot 67 as influential and potentially suggested the presence of

heteroscedasticity. Given that, only about 50% of the variation in total plot volume increment was accounted for by any one feature. A multiple linear regression analysis was conducted to improve productivity estimates.

The five best two-variable subset models all contained the higher order statistical moment, skewness of the TCARI index. The best two-variable subset model was produced from the LHQ_{100} (maximum lidar point height) and the TCARI skewness. The residual plots did not indicate violations of residual normality but potentially implied heteroscedasticity ($PAI_{total\ volume}$=0.022*LHQ_{100}-0.17*$TCARI_{skew}$-0.12, adj. R^2: 0.68, residual std. error: 0.042 (df: 23), F-statistic: 27.76, p<0.0001). The best two-variable subset model was not considered ideal as both the selected attributes have a high likelihood of being confounded by noise and when plot 67 was included, the model performed poorly, although terms were still significant (adj R^2: 0.52). Additionally, the TCARI skewness variable, on its own, is not significantly associated with total plot volume increment (F-statistic: 0.25, p:0.62). Omitting the higher order statistical moments of the TCARI, the best two-variable subset model selected the same features identified with the omission of plot 67, (*i.e.* $CRDNRA_{mean}$, GI_{median}) (Fig. 4.73). The right area and greenness model was best fit as Y=0.76(RA_{mean})+0.37(GI_{median})-3.94 with standard errors of: 0.483 (t: -8.2, p<0.0001), 0.0083 (t: 9.12, p<0.0001), 0.069 (t: 5.33, p<0.0001) for the constant, RA_{mean} and GI_{median} terms respectively. The adjusted R^2 was 0.767, the residual standard error was0.0434 (df: 24), and the F-statistic was 43.75 (p<0.0001), making it the most accurate of the models assessed.

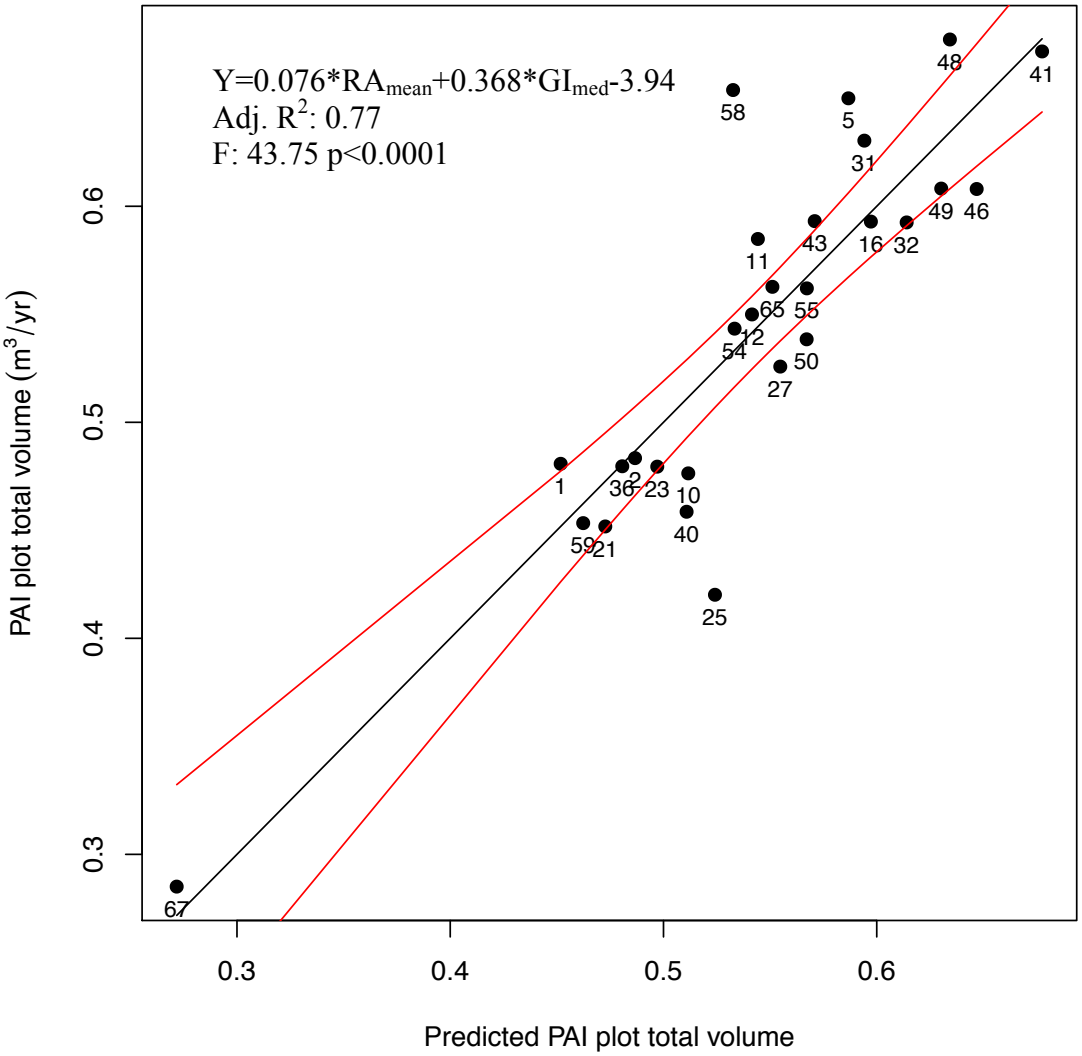


Figure 4.73. Including plot 67, the best two-variable subset model was produced by the mean continuum removed depth normalized right area and the median greenness index (R_{554}/R_{677}). Without plot 67 the best two-variable model was produced by two metrics suspected of having a considerable noise content, one of which, $TCARI_{skewness}$ was not significantly associated with the volume increment alone. Omitting plot 67 and $TCARI_{skewness}$ the best two-variable model was also that produced with right area mean and the GI median. The standard errors of the model parameters were: constant was 0.483 (t: -8.2, $p<0.0001$), RA_{mean} was 0.0083 (t: 9.12, $p<0.0001$), and GI_{median} was 0.069 (t: 5.33, $p<0.0001$). The adjusted R^2 was 0.767, the residual standard error was 0.0434 (df: 24), and the F-statistic was 43.75 ($p<0.0001$).

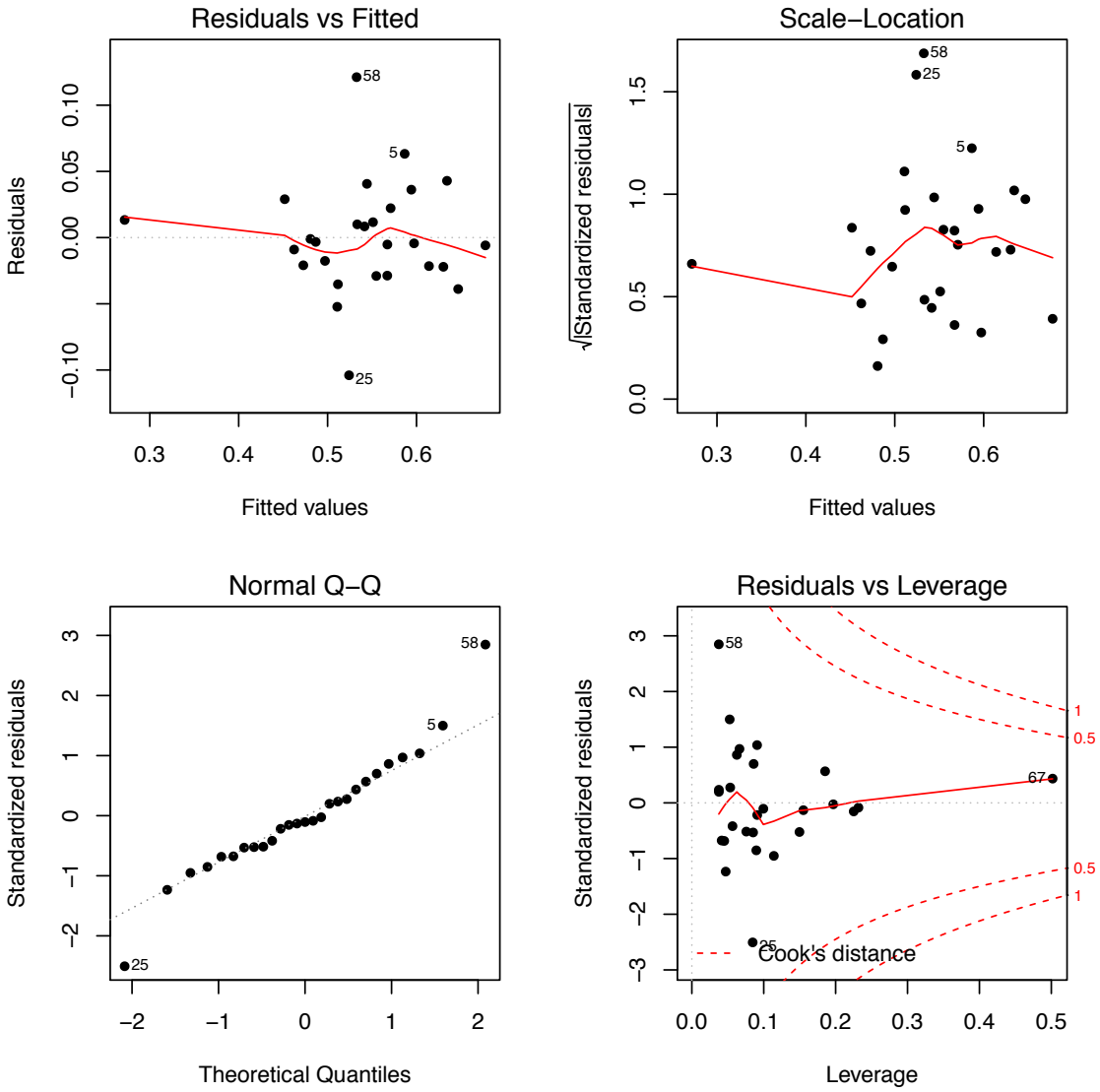


Figure 4.74. Including plot 67, the best two-variable subset model was produced by the mean continuum removed depth normalized right area and the median greenness index (R_{554}/R_{677}). The residual plots did not overwhelmingly suggest violations of the statistical assumptions and that the outlier (plot 67) was not an influential observation.

Justifying the physical relationship of the GI to the model was problematic. Perhaps the GI index is selected for an ability to resolve the hybrid nature of the right area metric, being sensitive to both chlorophyll and to a lesser extent LAI dependent scattering, where the GI index would be largely dependent on pigment contents. However, many of the other spectral metrics are designed to measure greenness in the

form of chlorophyll and feature selection was inconsistent in selecting other similar spectral metrics when maintaining the mean right area metric. In addition, the median greenness index alone was not significantly associated with the plot volume increments, and therefore is clearly a conditional association with volume increment. Also curious was the fact that structural attributes were conspicuously missing from the best two-variable subset models.

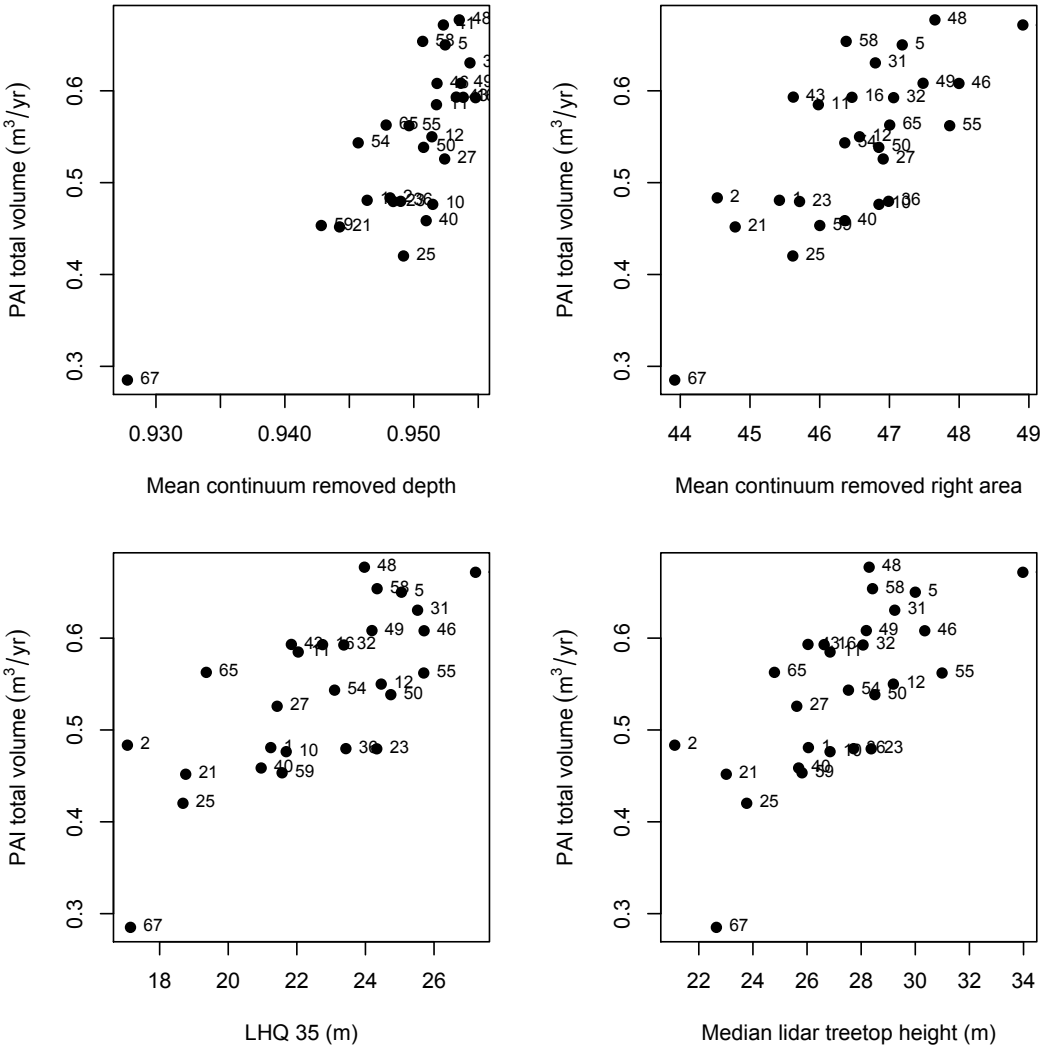


Figure 4.75. The single most PAI total volume associated feature (mean CR depth) was highly susceptible to the plot 67 outlier. Without the effect of plot 67, lower lidar height quantiles were most associated with PAI in total volume. Without higher order statistical moments of the TCARI index, the best two-variable model included the mean CRDNRA and the median GI, which were the same features selected for the best two-variable subset model when plot 67 was included.

The median lidar treetop model was assessed for potential improvements through missing independent variables. Omitting plot 67 and the TCARI skewness, the best two–variable subset models forcing the inclusion of the median lidar treetop height, included variations of GI, CRdepth and the standard deviation of the catchment area (lidar derived upslope drainage area). When plot 67 was included the selected features included variations of the CR depth, GI, NDVI and SR indices. Of the model assessed the most confidence inspiring result was that produced from the median treetop height and the mean CR depth (Fig. 4.76). This model was selected for its high signal attributes, its physical interpretability through tree height and crown chlorophyll/vigor, and statistically through its relatively high adjusted R^2 value and low Bayesian information criterion (BIC: -24.89 next smallest: -23.67). The model was slightly improved if the depth attribute was scaled by the 35th power (fit by nonlinear least squares) and produced an adjusted R^2 value of 0.718. There was a significant correlation between the median lidar treetop height and the mean continuum removed depth (R: 0.52, p: 0.005), which could have implications for coefficient stability. The feature selection script was augmented to accept multiple linear models and to output the mean and standard deviation of coefficient significance, the result again, selected the mean CR depth as having the lowest mean significance and the largest mean adjusted R^2, this feature also had the sixth lowest standard deviation of the coefficient p-value. The bootstrap result for the multiple linear model is shown in table 4.16.

Table 4.16 Bootstrap of multiple linear regression parameters

	F-stat	p-value	Adj R^2	medTTht	sig. medTTht	mean CRD	sig. mean CRD
Value	32.68	$1.4x10^{-7}$	0.709	0.018	0.035	13.559	0.0042
Mean	37.55	$5.5x10^{-5}$	0.693	0.013	$1.7x10^{-2}$	10.094	0.0077
stdev	21.27	$4.1x10^{-4}$	0.117	0.004	0.0498	2.041	0.0409

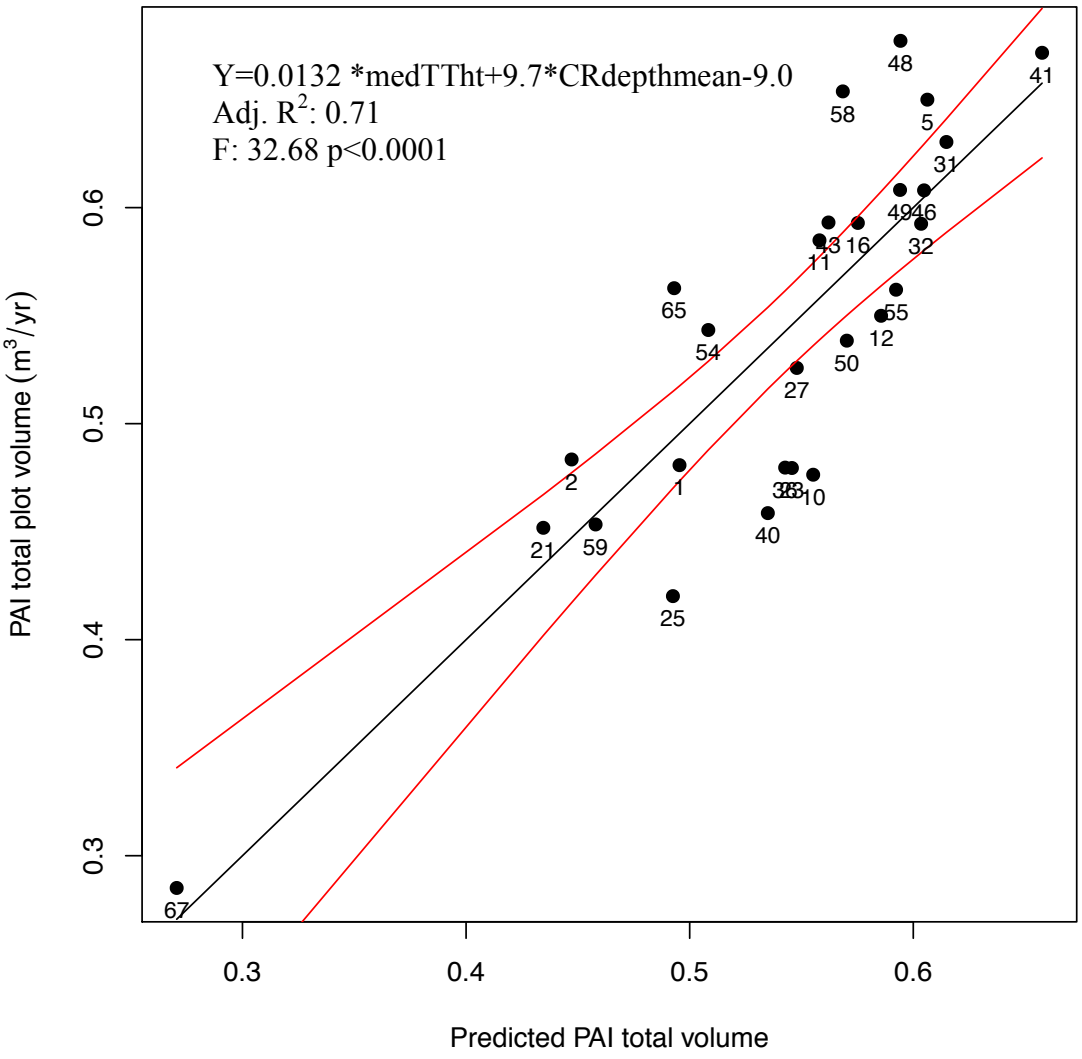


Figure 4.76. The standard error of the model parameters were 1.91 for the constant (t:-4.71, p<0.0001), 0.0040 for the medTTht coefficient (t:3.31, p: 0.003), and 2.07 for the CRdepth mean coefficient (t:4.68, p<0.0001). The adjusted R^2 was 0.709, the residual standard error was 0.0484 (df:24) and the f-statistic was 32.68 (p<0.0001).

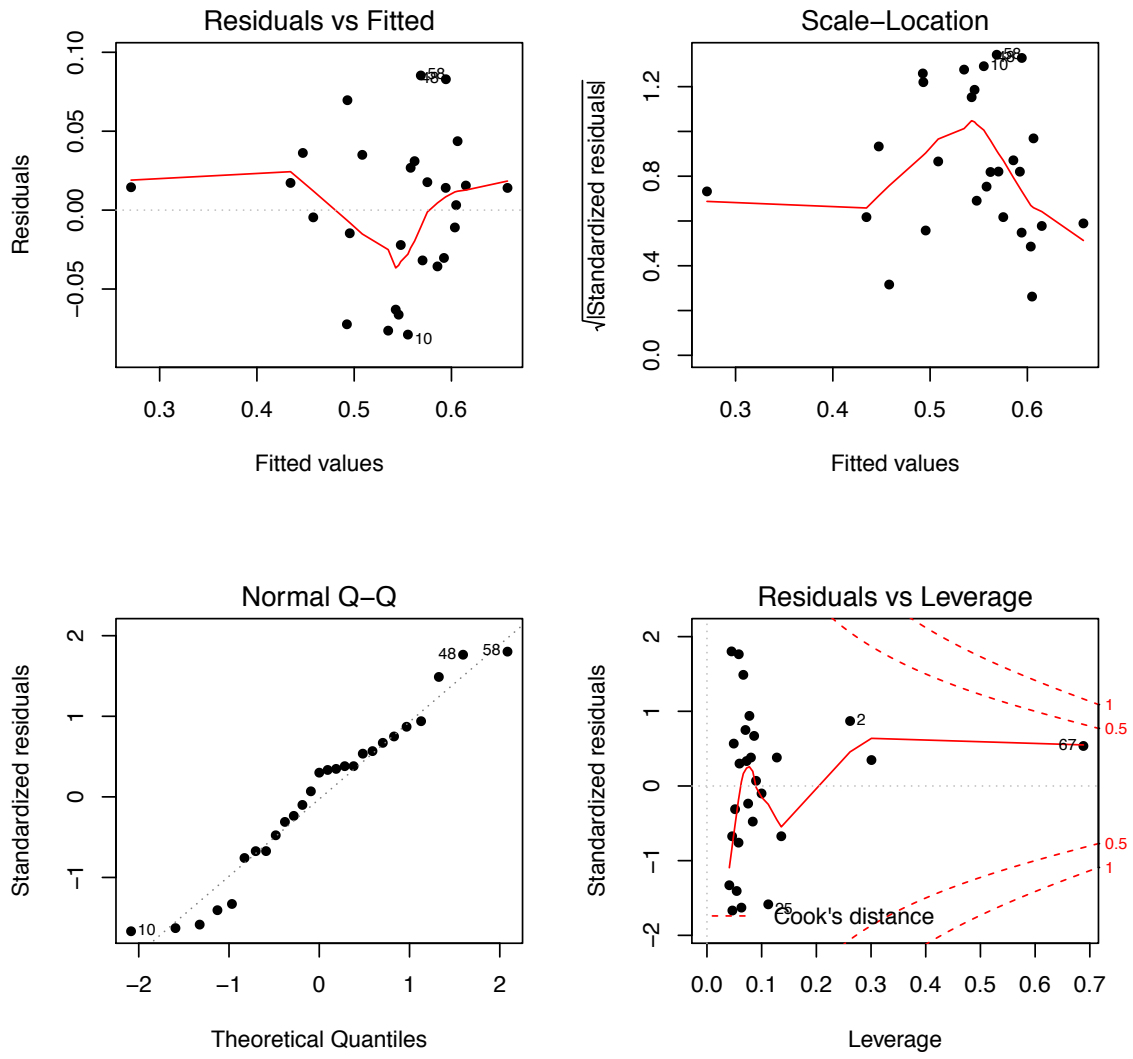


Figure 4.77. Residuals of the multiple linear model produced by the median lidar treetop height and mean continuum removed depth. The residual plots did not overwhelmingly suggest violations of the statistical assumptions and that the outlier (plot 67) was not an influential observation.

In order to understand how much the spectroscopy was aiding in the productivity estimation, a productivity model was produced from exclusively lidar metrics. The best two-variable model was produced from the CHM standard deviation and the canopy closer at the 60th height percentile. The trend for feature selection in the three best two-variable models was that information on height and canopy closure was selected. This was interpreted as a height attribute that physically relates to productivity and a canopy

closure feature that would capture predominantly the low productivity of plot 67, but may also inform on horizontal canopy extent and or vertical crown density by photon occlusion. The remaining 27 best two-variable models all selected height related features and topographic attributes, specifically those related to location and spread of the upslope drainage areas. The presumption that crown closure was selected because of canopy gaps at plot 67 was supported by feature selection with the omission of plot 67, which selected height related features and topographic drainage but no canopy closure metrics for the thirty best two-variable models. Residual plots of the total volume increment model from CHM standard deviation and the canopy closure at the 60th height percentile demonstrated both a heteroscedastic trend and that plot 67 was an influential observation. Omitting plot 67 from the regression did not eliminate the heteroscedastic nature of the model. However, as with previous models, taking the natural logarithm of the CHM standard deviation resolved the issues of the influential point and in this case also produced a more homoscedastic regression model (Fig. 4.78 &4.79). With the omission of plot 67 the best-fit model was produced from the lidar treetop heights and the standard deviation of the catchment area or upslope drainage area (Fig. 4.80 & 4.81)

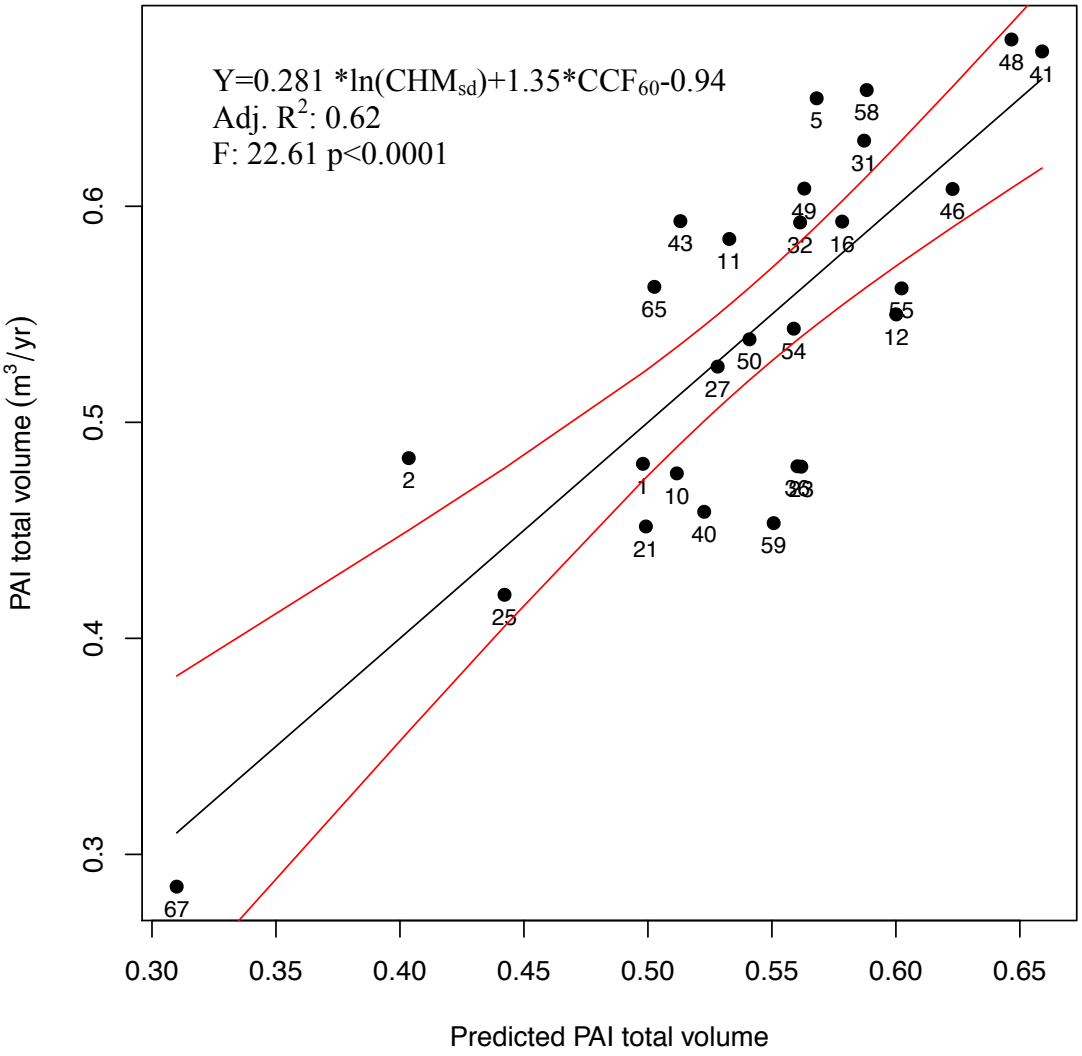


Figure 4.78 The standard error of the model parameters were 0.23 for the constant (t:-4.01, p:0.0005), 0.060 for the natural log transformed standard deviation of the CHM coefficient (t:4.68, p: 0.0001), and 0.202 for the CCF_{60} coefficient (t:6.67, p<0.0001). The adjusted R^2 was 0.624, the residual standard error was 0.0550 (df:24) and the F-statistic was 22.61 (p<0.0001).

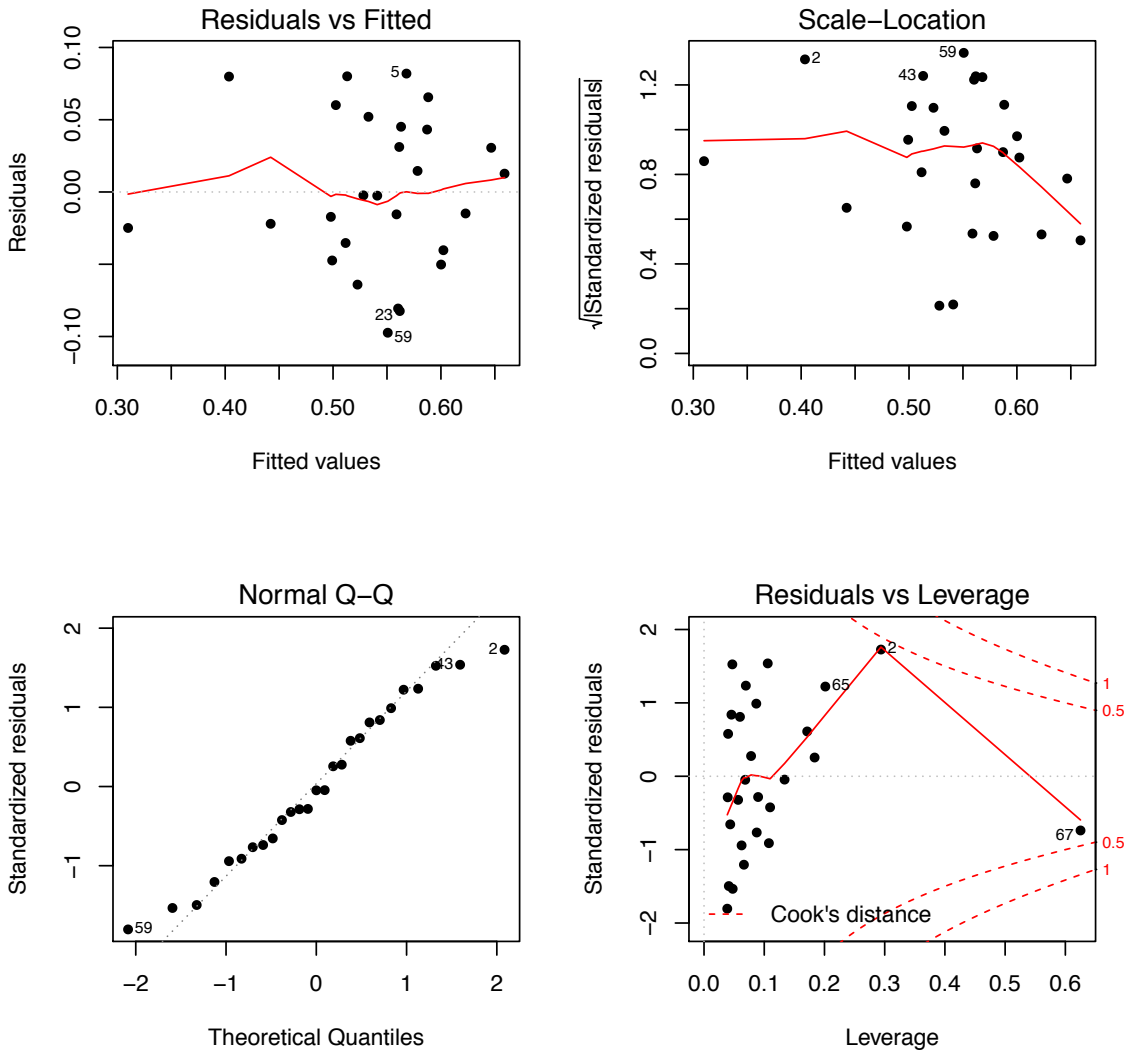


Figure 4.79. Residual plots for the multiple linear regression produced by the ln transformed CHM standard deviation and lidar canopy closure at the 60th height percentile. The residual plots did not overwhelmingly suggest heteroscedasticity and although very close to the Cook's distance threshold plots 2 and 67 are not classified as influential.

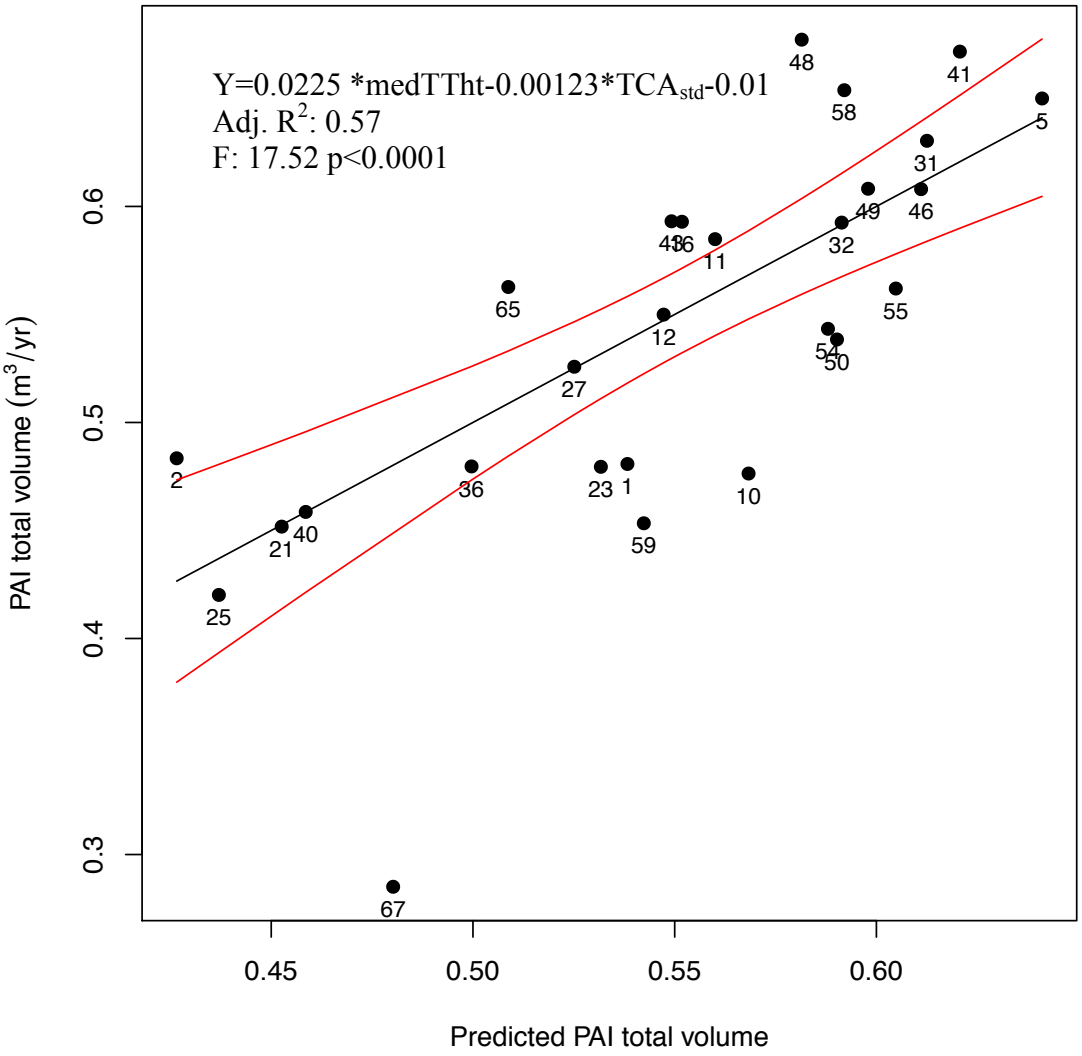


Figure 4.80. The standard error of the model parameters were 0.103 for the constant (t:-0.14, p:0.89), 0.004 for the median lidar treetop height coefficient (t:5.74, p< 0.0001), and 0.0004 for the standard deviation of the lidar topographic catchment area coefficient (t:-3.16, p:0.004). The adjusted R^2 was 0.569, the residual standard error was 0.049 (df:23) and the F-statistic was 17.52 (p<0.0001).Note that although plot 67 is illustrated above it did not contribute to the multiple linear regression.

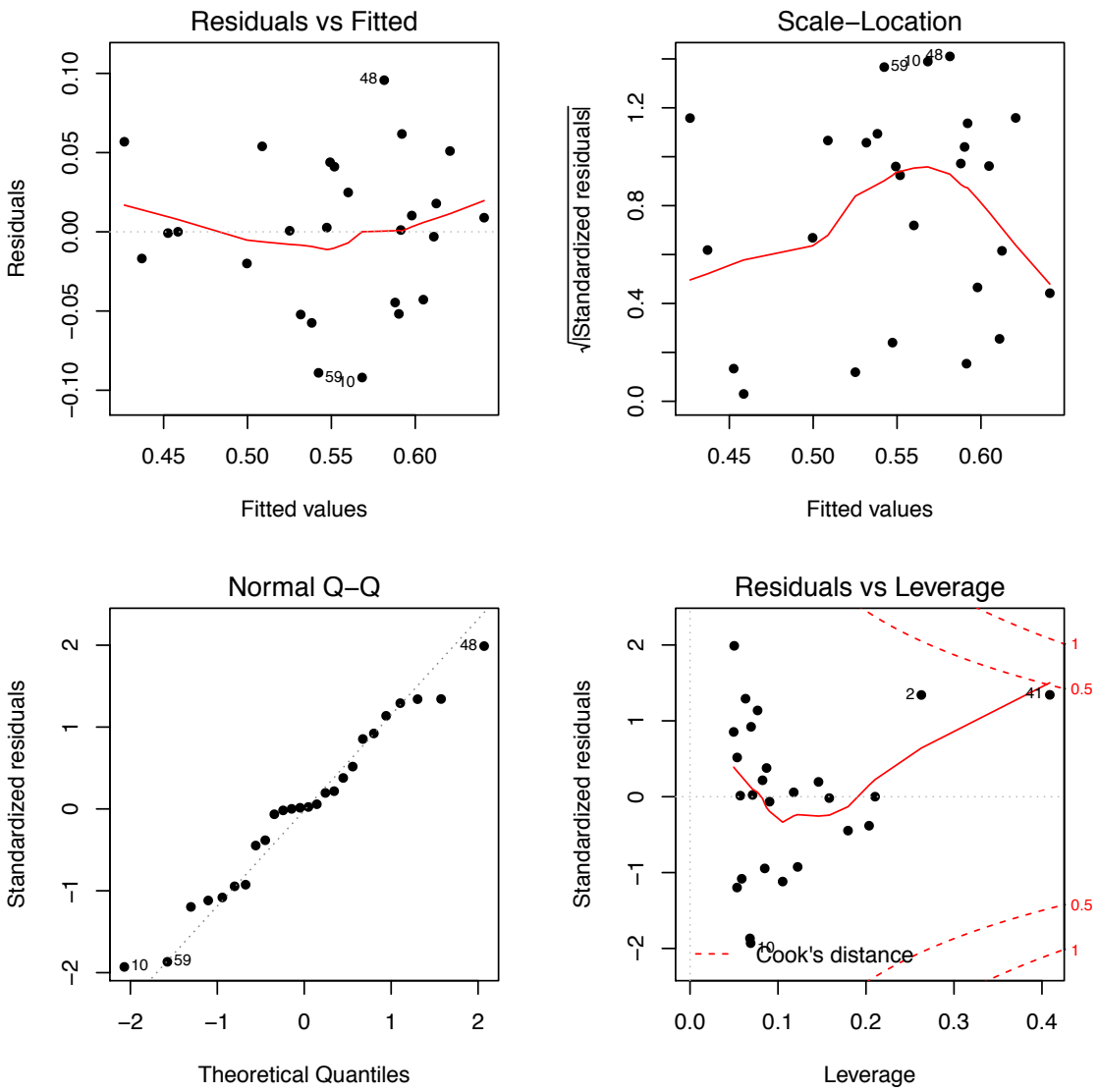


Figure 4.81. Residual plots for the multiple linear regression produced by the medina lidar treetop height and the standard deviation of the lidar topographic catchment area. The residual plots might suggest a subtle nonlinear trend.

The initial model predicting PAI total plot volume from CHM standard deviation and canopy closure at the 60th lidar height percentile was augmented with the catchment area information, which produced a superior fit (Fig. 4.82 & 4.83).

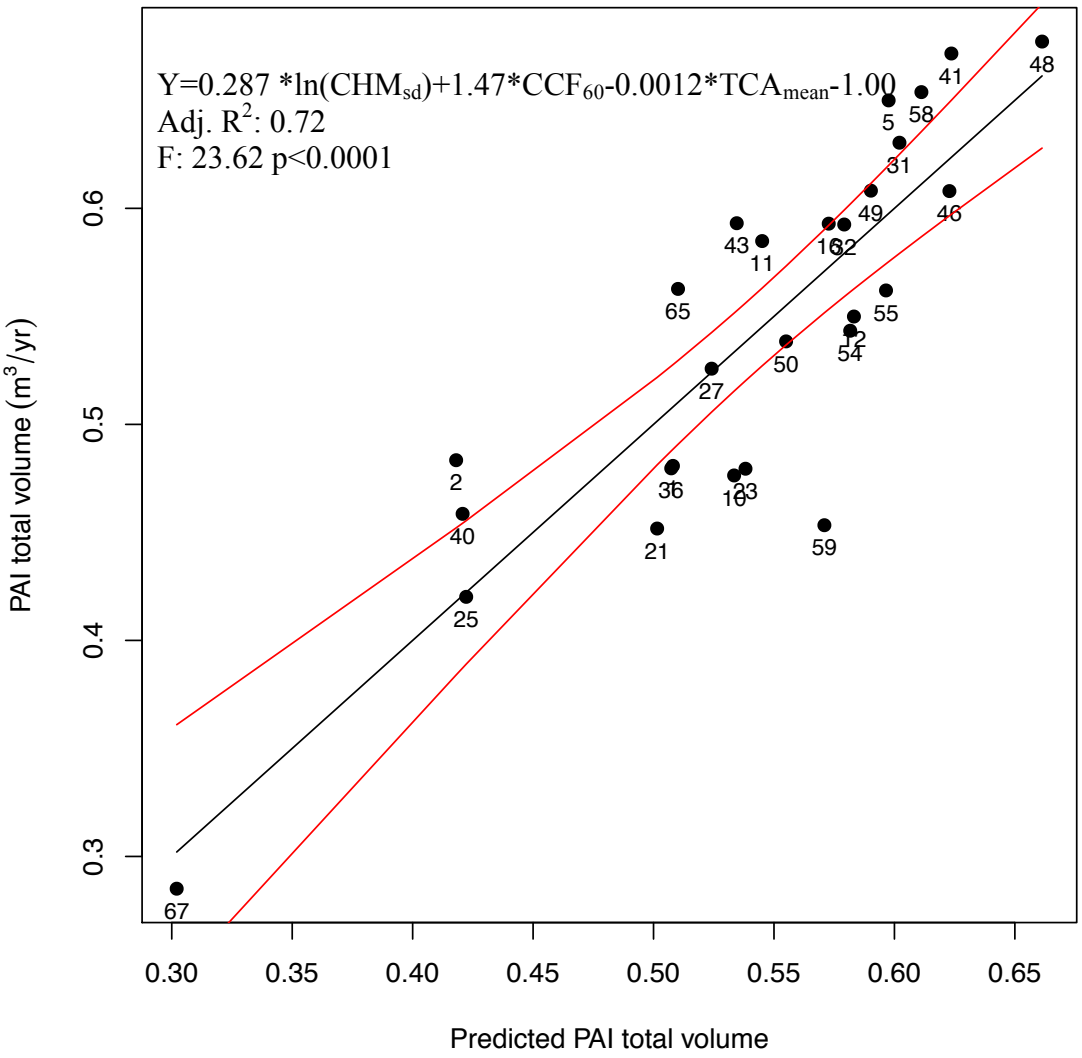


Figure 4.82. The standard error of the model parameters were 0.202 for the constant (t:-4.99, p<0.0001), 0.052 for the ln transformed standard deviation of the CHM coefficient (t:5.56, p< 0.0001), and 0.178 for the CCF_{60} coefficient (t:8.24, p<0.0001) and 0.00038 for the mean of the lidar topographic catchment area coefficient (t:-3.09, p:0.005). The adjusted R^2 was 0.723, the residual standard error was 0.047 (df:23) and the F-statistic was 23.62 (p<0.0001).

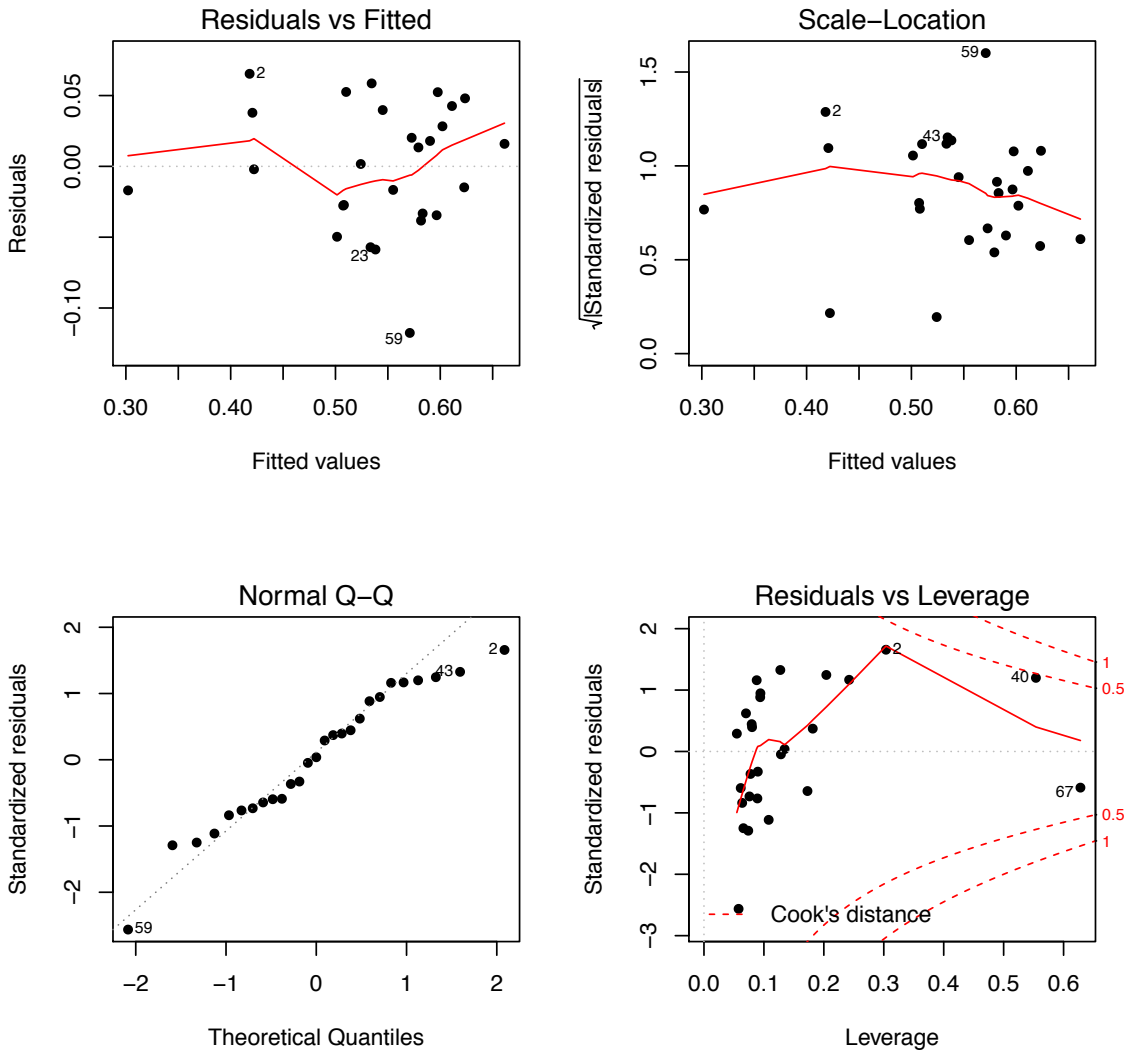


Figure 4.83. Residual plots for the multiple linear regression produced by the natural log transformed CHM standard deviation, the lidar canopy closure at the 60th height percentile and the mean upslope catchment area. The residual plots do not suggest that violations of the statistical assumptions have occurred.

It is worth noting that when all crown classes were included in the plot total volume increment and plot 67 was omitted there was a coherent pattern in the 30 best two-variable models regarding feature selection. The analysis consistently identified a central tendency of the PRI index and a canopy closure fraction attribute and explained a maximum of 63% of the variation in total plot volume increment including reductions attributed to mortality (crown class 9: dead). Given the influence plot 67 exhibited, the

REP metric was leveraged as a dummy variable as only plot 67 had a median REP that was different from all others. Forcing the REP_{med} dummy variable and including plot 67, the feature selection was recomputed, and reinforced the observation that canopy closure and the PRI index were directly related to the plot volume increment. Only three of the best 30 models had variables other than PRI location (mean, trimmed mean, or median) and canopy closure fraction (5-55 height percentiles). The departures from the feature selection trend were instances where the coefficient of variation of the PRI was paired with catchment area, another where the same was paired with a modified version of the catchment area and lastly mean PRI with the CHM standard deviation. Selecting an appropriate model in this manner was not a trivial task as 281 models of a possible 42,778 models with the restrictions that the REP_{med} feature be applied to account for the outlier plot 67 and high order statistical moments were ignored. The approach adopted first considered the consistency in the selection of similar features, followed by model significance, residual behavior and finally sampling sensitivity through a bootstrap analysis. This approach was intended to combat the high potential for over fitting when analysis is only motivated by reductions in explained variance or complexity penalized fit indices like the AIC or BIC and when the volume of independent data is so large. Nowhere else in this plot level productivity analysis was the consistency in feature selection so apparent, however, as detailed previously with LHQ, there is much co-linearity in the canopy closure fraction profile data. For the plot level SLP data there is very little information diversity ($R>0.9$) in the CCF profile below the 60th height percentile (Fig. 4.84 & 4.85).

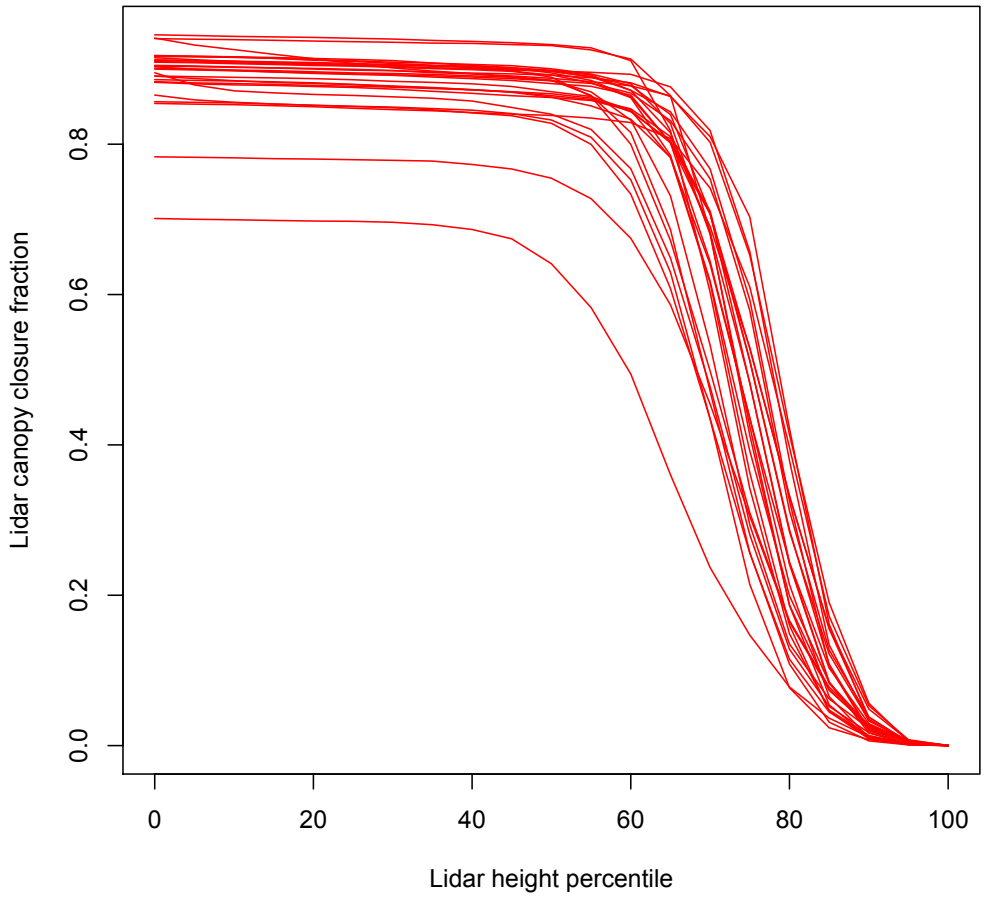


Figure 4.84. The canopy closure profiles for the selected SLP treatment plots illustrated that there was little variation below the 60th height percentile. After the 60th percentile there is a downward trajectory that would be consistent with the location where individual crowns are emergent and above which the apical shape of the individual crowns could explain the CCF profile shape.

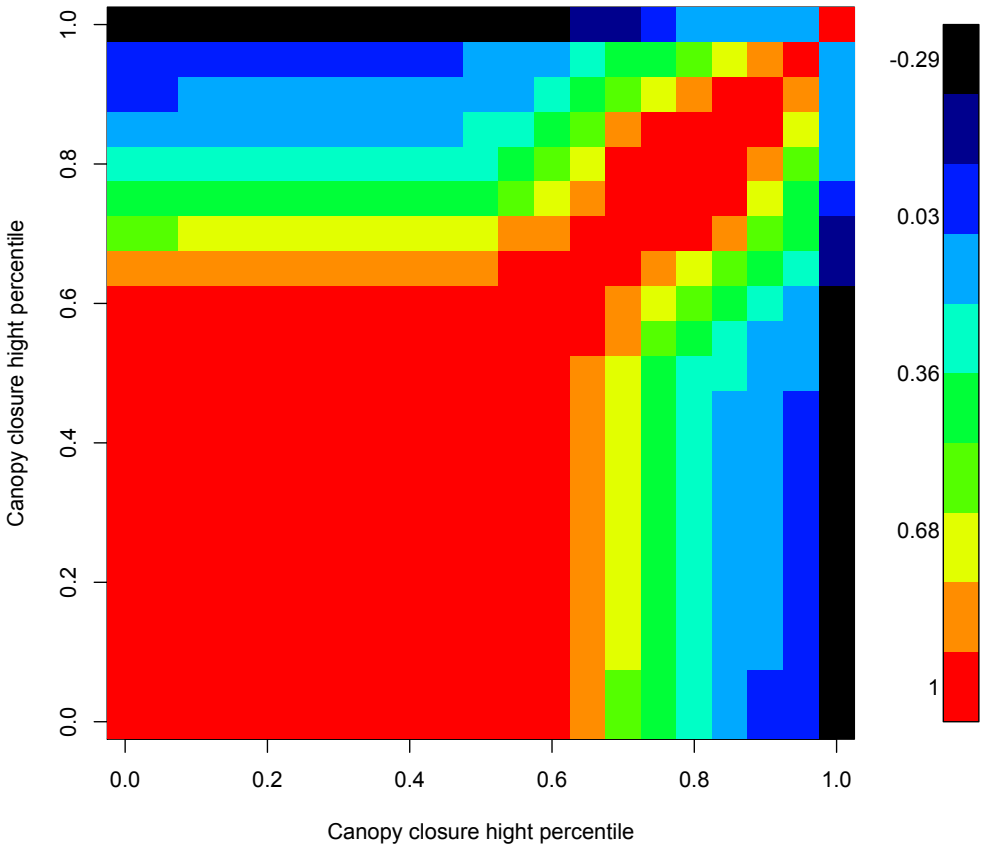


Figure 4.85. Pearson's correlation coefficient matrix among the canopy closure features at lidar height percentile (5 percentile intervals), illustrating the high degree of association between the CCF metrics less than the 60th height percentile (0.6).

If the CCF_{30} were replaced by the CCF_{50}, which might be a more stable metric, the predictive power of the regression would not be adversely affected. It had a subtle reduction in the adjusted R^2 from 0.777 to 0.765 and an increase in the residual standard error from 0.068 to 0.070. The standard errors of the model parameters were such that the coefficients of the two models overlapped (Tables 4.17 & 4.18). The two multiple linear regression models took the following form:

$$PAItotvol=11.81*PRI_{med}-2.27*CCF_{30}+0.162*REP_{med}-114.3,$$

$$PAItotvol=11.78*PRI_{med}-1.99*CCF_{50}+0.170*REP_{med}-119.7$$

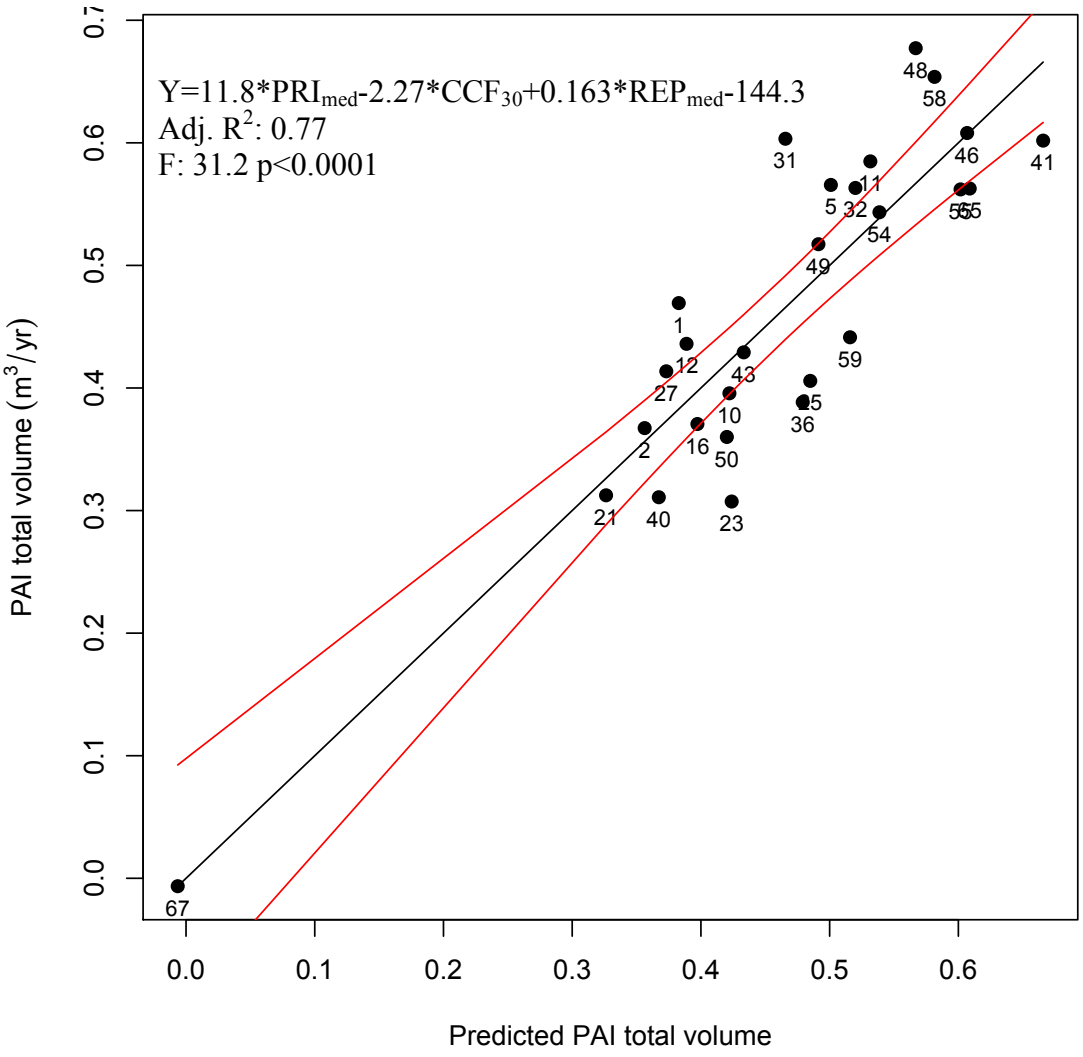


Figure 4.86. The standard error of the model parameters were 16.3 for the constant (t:-7.02, p<0.0001), 1.99 for the median PRI coefficient (t:5.94, p< 0.0001), and 0.453 for the CCF_{30} coefficient (t:-5.02, p<0.0001) and 0.023 for the median red edge position coefficient (t:7.08, p<0.0001). The adjusted R^2 was 0.777, the residual standard error was 0.068 (df:23) and the F-statistic was 31.2 (p<0.0001).

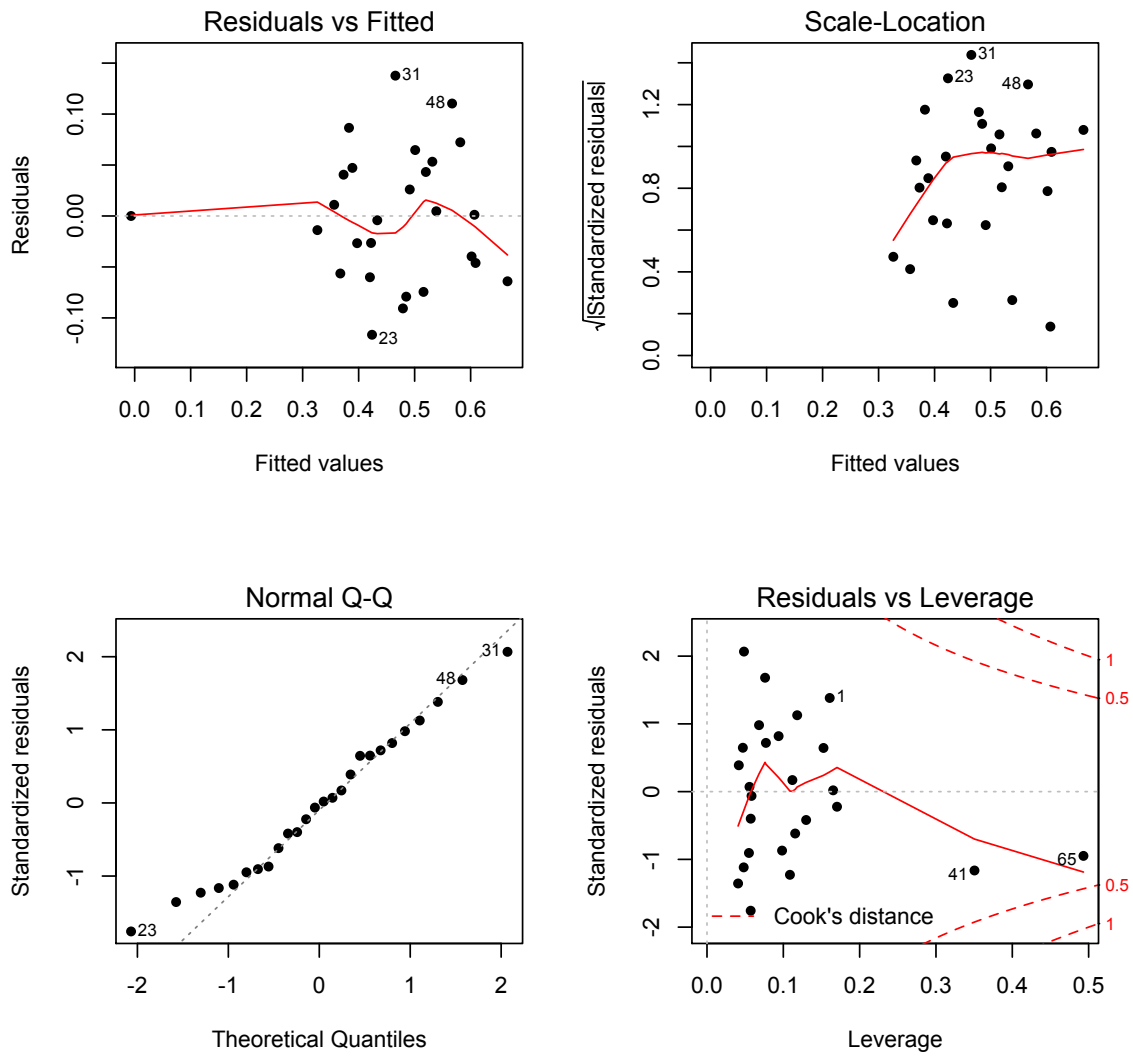


Figure 4.87. Residual plots for the multiple linear regression produced by the median PRI index, the lidar canopy closure at the 30th height percentile and the median red edge position. The residual plots do not strongly suggest that violations of the statistical assumptions have occurred. Note however that plot 67 is missing as its leverage is 1 and is the reason for the median REP which is functionally a dummy variable to account for that plots dissimilar productivity.

Table 4.17 Bootstrap of multiple linear regression predicting PAI plot volume all crown classes							
	F-stat	p-value	Adj R^2	PRI $_{mean}$	sig. PRI_{mean}	CCF_{30}	sig. CCF_{30}
Q1	17.03	<0.0001	0.562	0.490	<0.0001	-0.126	<0.0001
Q2	24.48	<0.0001	0.653	0.553	<0.0001	-0.116	<0.0001
Q3	34.75	<0.0001	0.730	0.604	0.0001	-0.105	0.0006
Note without plot 67 REP_{med} is invariant and is therefore omitted along with plot 67							

Table 4.18 Bootstrap of multiple linear regression predicting PAI plot volume all crown classes							
	F-stat	p-value	Adj R^2	PRI_{mean}	sig. PRI_{mean}	CCF_{50}	sig. CCF_{50}
Q1	17.27	<0.0001	0.565	0.505	<0.0001	-0.114	<0.0001
Q2	24.32	<0.0001	0.651	0.560	<0.0001	-0.105	<0.0001
Q3	34.94	<0.0001	0.731	0.610	0.0001	-0.095	0.0006
Note without plot 67 REP_{med} is invariant and is therefore omitted along with plot 67							

The potential for over fitting in this analysis was high due to the relatively low sample size, the large number of independent variables, many of which were inter-correlated, and the exhaustive best subset model search approach applied. Therefore, it was important to be critical of the best-fit models and to ensure that a reasonable limitation was placed on the number of independent variables used [140]. Without the influence of plot 67, the feature selection was run and the three-variable subset models were considered. In support of the two-variable model analysis, the 30 best three-variable models all selected variants of the PRI index and canopy closure metrics. The third feature to be selected was a variant of the continuum-removed depth in 13 of the 30 best models; in another 10 of the 30 best models, the depth feature was replaced with either the mean or standard deviation of the upslope catchment area. In six of the 30 best models, the feature selection produced models with location variants of the PRI, CHM_{sd} and catchment area. The adjusted R^2 values for these 30 best subset models were all greater than 0.719. The consistency in feature selection inspired confidence that the models were not gravely influenced by noise and the most robust of each metric could be manually selected. The best three-variable subset model without plot 67 was produced from the mean of both PRI and CRdepth and the CCF45, and produced an adjusted R^2 of

0.74, an F-statistic of 24.88 (df:3/25, $p<0.0001$), and a residual standard error of 0.057 (Table 4.19 & Fig. 4.88 & 4.89). In an effort to reduce potential idiosyncratic associations, the CCF_{45} was substituted for the CCF_{50}, which did not significantly change the coefficients or model performance ($Y=9.61*PRI_{mean}-2.37*CCF_{50}+13.07CRD_{mean}-9.33$, adj. R^2: 0.72, F-statistic: 22.75, (df:3/22), $p<0.0001$, residual std. error: 0.059).

Table 4.19 Multiple regression parameters for PAI total volume in all crown classes

	estimate	Std error	t-value	p-value
Intercept	-9.67	3.87	-2.50	0.02
CCF45	-2.56	0.38	-6.74	<0.0001
meanCRdepth	13.62	4.13	3.30	0.003
Mean PRI	9.53	1.63	5.85	<0.0001

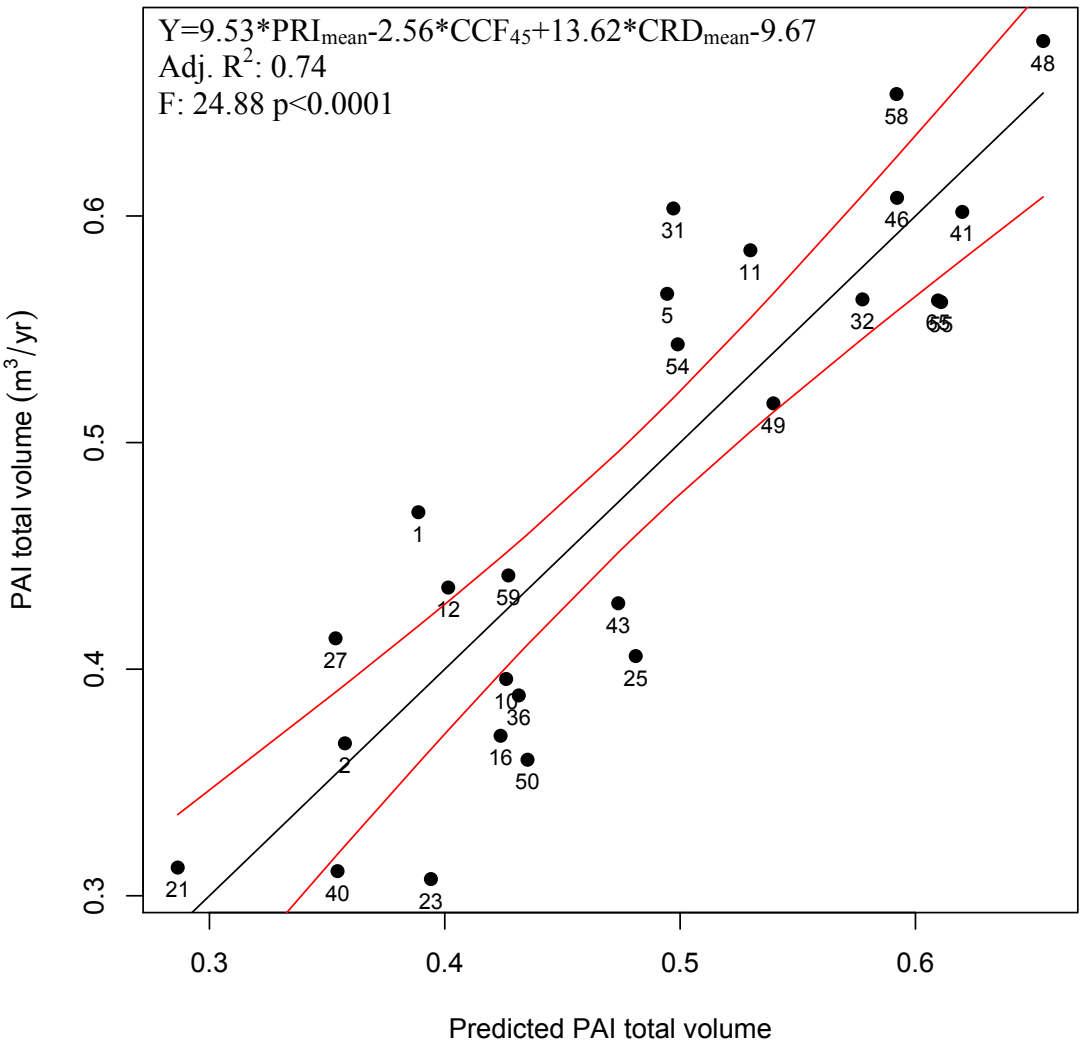


Figure 4.88 Multiple linear regression predicting PAI in total plot volume with all crown classes from plot mean PRI, lidar canopy closure at the 45th lidar height percentile and the plot mean continuum removed depth. This model is the limit of reasonable number of independent variables. The feature selection can be rationalized by physical relationships between productivity and the selected metrics. The PRI is indicative of light use efficiency, continuum removed depth in the 680nm feature is representative of chlorophyll content and the lidar CCF attribute represents the crown horizontal extent, which is also related to basal area. To encorporate plot 67 the REP attribute was included and the regression results are presented in Fig. 4.90 and Table 4.20

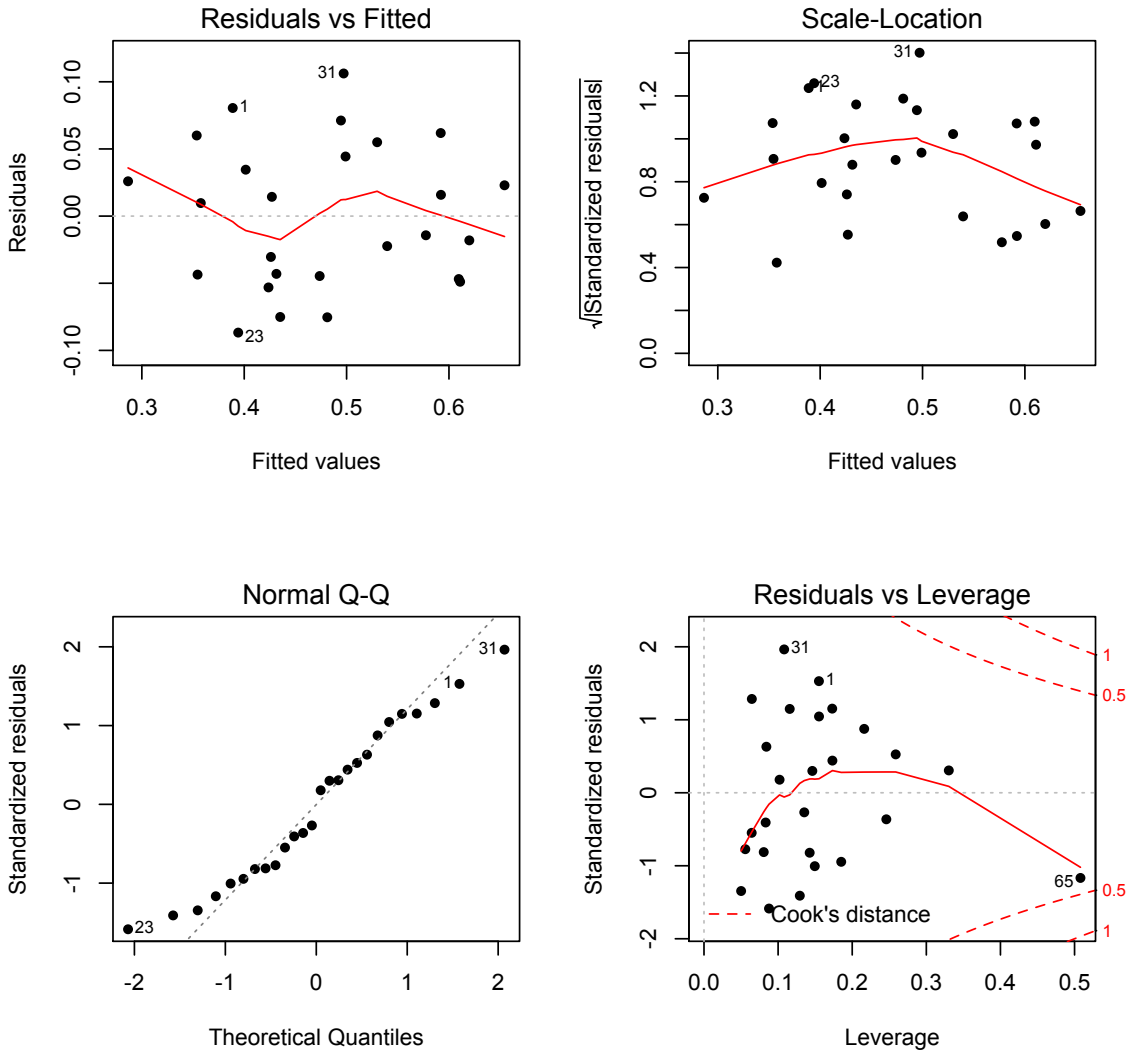


Figure 4.89. Residual plots for the multiple linear regression produced by the mean PRI index, the lidar canopy closure at the 45th height percentile and the mean continuum removed depth. The residual plots do not suggest that violations of the statistical assumptions have occurred.

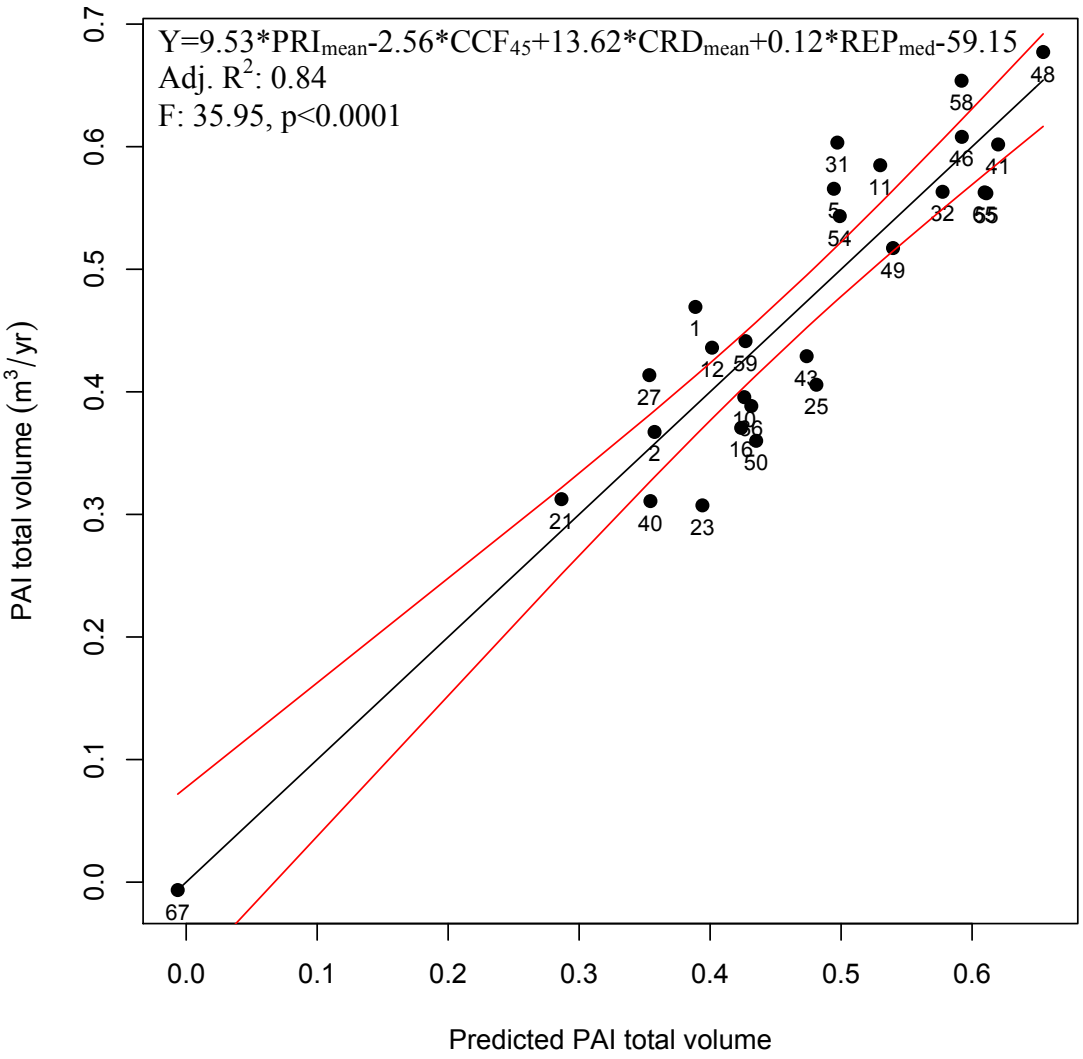


Figure 4.90.The multiple linear regression model was augmented with the REP median attribute to account for the reduced productivity and mortality in plot 67. The presence of woody debris, thin and or chlorotic crowns would contribute to the separation of plot 67 from the other plots by the shortwave migration of the red edge slope inflexion. However, given only one observation exhibited these characteristics the median REP coefficient should not be considered stable or valid, but would suggest the metric or the similar would be useful for characterizing canopy health.

Table 4.20 Bootstrap of multiple linear regression predicting PAI plot volume all crown classes

	f-stat	p-value	Adj R^2	PRI_{mean}	sig.PRI_{mean}	CCF_{45}	sig.CCF_{45}	CRD_{mean}	sig.CRD_{mean}
Q1	21.4	<0.0001	0.710	0.420	<0.0001	-0.139	<0.0001	0.508	0.0002
Q2	27.6	<0.0001	0.762	0.481	<0.0001	-0.128	<0.0001	0.672	0.004
Q3	37.9	<0.0001	0.816	0.543	0.0001	-0.119	<0.0001	0.032	0.03
Note without plot 67 REP_{med} is invariant and is therefore omitted along with plot 67									

The direction of the coefficients make logical sense, in that the PRI is directly associated with light use efficiency [126], and the depth of the absorption feature is directly associated with chlorophyll content [10] both of which have positive coefficients, while the CCF attribute produced a negative coefficient suggesting that canopy closure, at this height percentile is inversely associated with productivity. Initially, it was expected that the CCF was selected for its association with plot basal area, and although CCF_{45} explained 91% of the variation in CCF_{60} (most associated with basal area) the earlier analysis determined that the relationship was a positive association. The negative canopy closure coefficient is interpreted as describing the structural development stage that is occurring at the SLP, where a greater canopy closure also indicates greater inter-crown competition and less crown class separation. It was considered likely that the crown closure attribute was sensitive to the crown structure induced by thinning treatments. This assumption was confirmed through boxplots (Fig. 4.91). However, the potential for this relationship to be confounded by root disease-induced windthrow was observed with plot 67, which exhibited the lowest canopy closure and the lowest plot volume increment. If a training dataset had a subpopulation of stands with such structure altering disease that reduced growth and induced canopy gaps, this data could produce positive coefficients between CCF and volume increments.

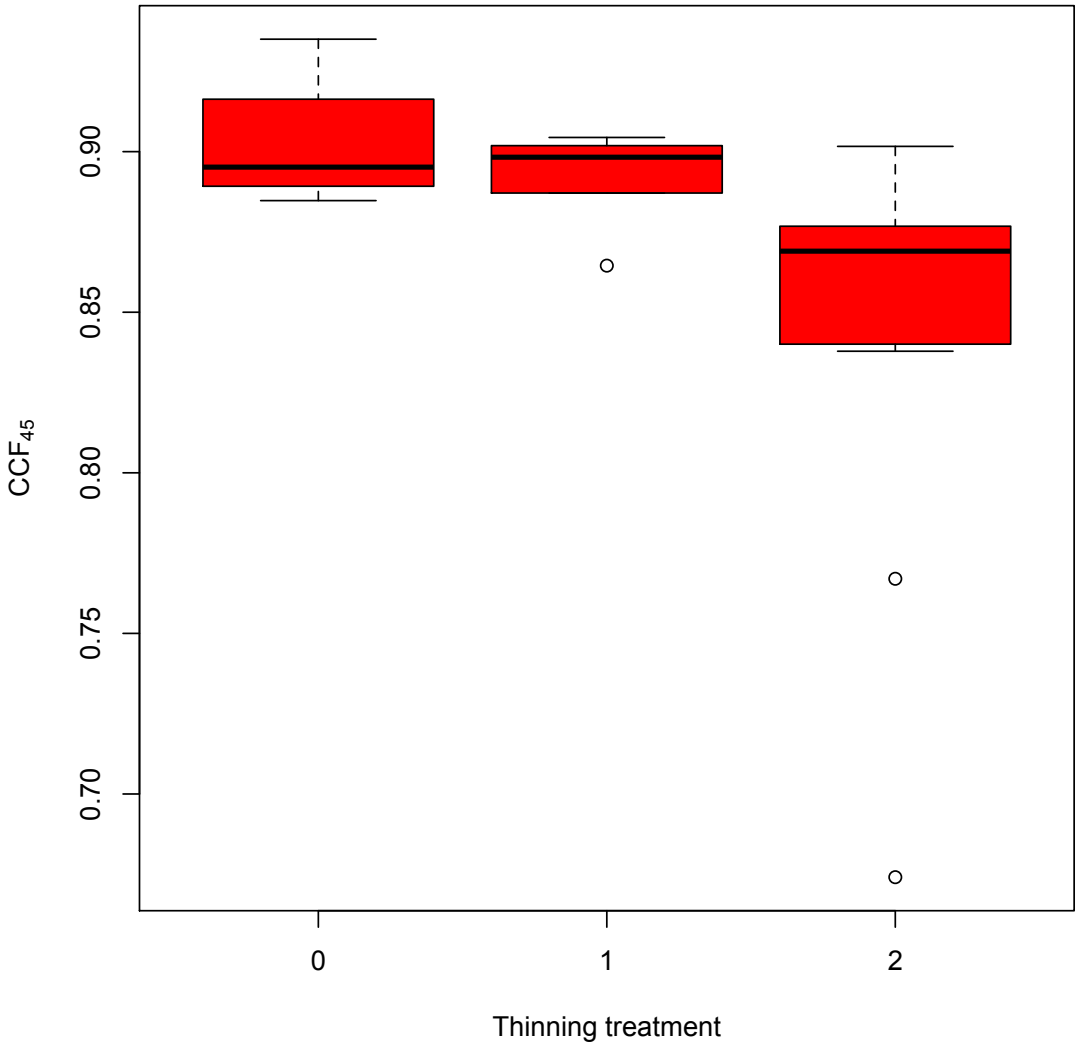


Figure 4.91. The canopy closure at the 45th lidar height percentile that significantly contributed to explaining variation in the plot volume increment was also associated with thinning level, where plots that were thinned to a third of basal area had a reduced canopy closure relative to a thinning to 2/3 BA and the control treatments.

In summary, the analysis of this portion of the study has taken the form of four dominant categories: pre-processing of airborne remote sensing datasets, analysis of field collected biophysical data, the extraction of pertinent attributes from both data sources and finally the modeling of canopy structure and forest productivity.

The plot-level modeling component of this research produced some promising results for the ultimate goal of mapping forest structure and productivity from airborne

lidar integrated with imaging spectroscopy. The structural metrics that were related to variations in height were successfully modeled from simple relationships with lidar local maximum treetop heights. A stratification by crown class demonstrated that lidar was more sensitive to individuals within the dominant and co-dominant crown classes, where only 3% of the variation in measured and modeled tree height remained unaccounted for. Ground reference data related to volume within the treatment plots was best estimated by lidar metrics that were generated from the reciprocal cumulative distribution of lidar heights (canopy closure metrics). Structure-related attributes were estimated with varying degrees of success. The height to live crown was closely related to the tenth lidar height percentile. Using strictly statistical approaches to estimate average crown length failed to produce meaningful predictive models. However, applying a more intuitive approach using metrics previously identified as sensitive to tree height and height of the live crown improved estimations and confidence in the applied features. The regression of crown widths with lidar-delineated crowns demonstrated that the algorithm was poorly parameterized for the SLP plots, but had moderate to strong results applying the lidar treetop heights and the variation in the canopy height model. The last structurally related attribute to be assessed was the stem density, which was best estimated by the inverse of the variation in the canopy height model. Forest productivity was evaluated by several approaches with differing quantifications of reference productivity, as individual attributes: mean diameter increment and mean volume increment and at the plot level as basal area increment and total plot volume increment. Predominantly, six features were selected as significantly informative of productivity, based on which reference productivity was applied, crown class stratification and whether the diseased plot 67 was

included. The estimation of the individual productivity attributes (*i.e.* mean PAI DBH & mean PAI volume) both selected variation in the canopy height model as contributing to explaining productivity. Structural models identified that the variation in the CHM was related to stem density and crown widths and in turn thinning treatments all of which are pertinent to growth. The second selected feature in a two-variable model for mean diameter increment was a mean spectroscopic chlorophyll metric (continuum removed depth), while the mean volume increment model selected the median lidar treetop height feature. The mean diameter increment model was sensitive to crown class stratification and produced its best results when the supressed and dead classes were omitted. These results suggested that mean diameter increment was best estimated from data related to stem density and crown foliar health, while mean volume increment was best estimated by stem density and crown height possibly leveraging on the serial auto-correlated nature of productivity with volume.

There was little variation in the selection of the best predictor for volume related field measurements. The canopy closure at the 70th height percentile was selected as the best predictor. In both cases of total volume and merchantable volume, plot 5 was identified as an outlier caused by its much higher volume without a proportional increase in its CCF_{70}. Plot 5 belongs to the T1F2-2 treatment group. This treatment had one third of its basal area thinned and it had been fertilized with 448kg N/ha on two separate occasions, on initiation of the treatment (1972) and again in 1981. Plot 67 was determined to be an influential point as the model changed significantly with its removal, the CCF_{70} explained nearly 10% less of the variation in total volume when plot 67 was removed (R^2 0.69). However, even without this data point the linear model remained

strong. Plot 67 occurred as an extreme point in many of the models not just those in volume modeling. It belongs to the treatment group T2F1-PS that is, the plot had 2/3 its basal area thinned and had 224kg N/ha applied with 100kg/ha each of superphosphate and pelleted sulphur. Additionally, the treatment for plot 67 was not established until 1987, 14-16 years after the plots of the main experiment were installed. Field observations made during the GPS survey of the plot centers noted that there was considerable evidence of root disease, including numerous wind thrown trees with small root balls and laminated annual rings. The plot had extensive salal growth, which was interesting in contrast to plots 1 and 41 with similar treatments (T2F1-1, T2F1-2, respectively) that did not appear to have nearly as much salal growth. It is anticipated that the basal area lost to root disease has provided the salal with increased access to resources. The large canopy gaps and unhealthy crowns exhibited by plot 67 produced obvious data departures in many of the remote sensing metrics. In some cases, the different conditions of plot 67 foiled an otherwise apparent pattern in productivity and remote sensing metrics (*i.e.* standard deviation in the CHM). These observations present the major limitation of this study and many empirically derived remote sensing models. The very limited structural diversity of the project area does not account for natural variation and should not be extrapolated beyond the conditions under which it was built.

With respect to merchantable volume, the CCF_{70} was also selected as the most powerful predictor. This is not surprising given that merchantable volume is derived from a DBH dependent fraction of the total volume [113]. The CCF variables quantify the density of the tree layer; the CCF_{70} considers the proportion of points that are above the 70th percentile of lidar CHM points. Essentially, this metric quantifies how much of the

sampled area at a given normalized height (percentiles) is tree canopy. If we consider the point clouds of plots 31 and 67, which are extreme plots in Figure 4.11 (total plot volume vs. CCF_{70}), it can be seen that the sparse trees of plot 67 have wider canopies that extend further towards the ground whereas, in plot 31 the canopy is quite dense at a relatively higher position in the canopy (Fig 4.92). In plot 31, the 70th height percentile (27.25m) occurs at a position very near the maximum density of its histogram, while in plot 67, the 70th percentile (19.57m) occurs at a position that is above its maximum density. In other words there is more canopy above the 70th height percentile at plot 31 than there is at plot 67. Therefore, from these data it can be said that high volume plots have more dense canopies potentially made up of tall individuals with short, small diameter crowns.

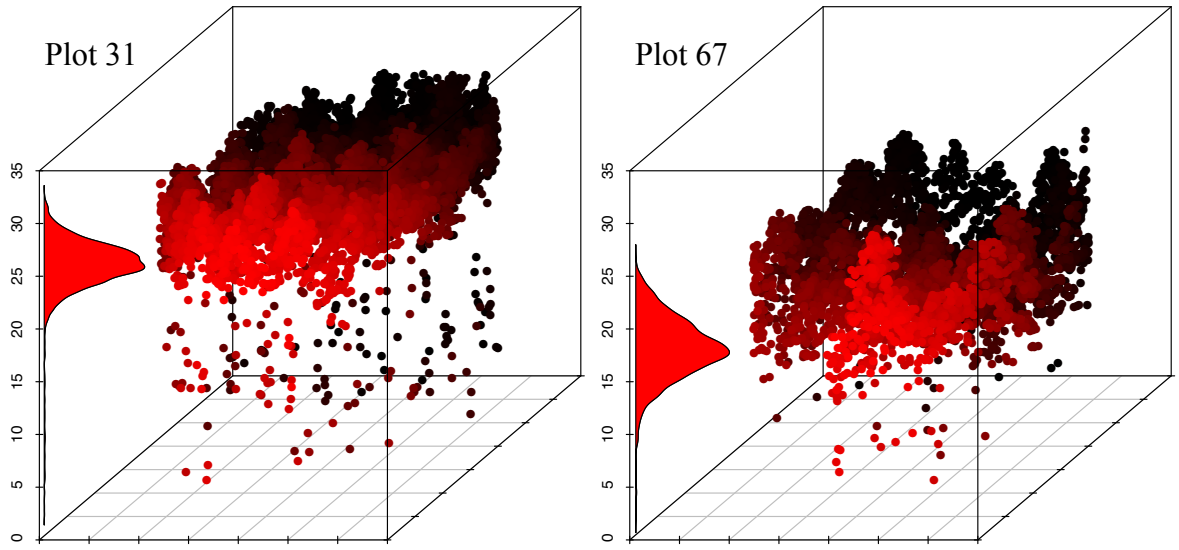


Figure 4.92 The point clouds of plots 31 and 67, examples of high and low volume respectively. The CCF at the 70th percentile provides an accurate prediction of plot volume. The 70th percentile for plot 31 occurs at a height of 27.25m while that for plot 67 occurs at 19.57m. The CCF_{70} of plot 31 is 0.82 and in plot 67 it is 0.24.

With the exception of crown length and width, the structure attributes produced more accurate models. The most accurate model was that produced through the dependent height variable within the dominant to co-dominant crown classes and the median CHM treetop height predictor variable. The median height of the CHM treetops explained 97% of the variation in average measured and modelled tree height within the dominant and co-dominant crown classes. The success of this linear model is attributed to the fact that the more dominant crown classes were used to characterize average tree height. These trees are the tallest of the plot and this is an important aspect to whether the lidar data will capture these individuals. The lidar points cannot penetrate through objects; therefore a crown further down within a canopy is sampled less than the dominant individuals at the top of the canopy. The simple treetop finding algorithm does not consider the point cloud but a raster representation of the point with the maximum height within a given cell size. As a result there are limitations to this approach for resolving the heights of all trees within a plot. The crown size and vertical position within the canopy, the point density and raster resolution all play a role in limiting the algorithm in locating individual treetops. However, with the exception of lidar point density, locating the tallest few trees may be less affected by the other confounding conditions. Two of the three canopy height attributes were best predicted by the location moments (mean, median) of the CHM treetops, while the other was best predicted by the average lidar height above the LHQ_{85}. The height of only the measured trees was best predicted by lidar median treetop height, as was the case for the average height of measured and modelled tree height. The relationship was improved by omitting crown classes from intermediate to dead. Although, the average height above the LHQ_{85} best estimated top

height, the difference between that model and the equivalent applying the mean lidar treetop height was slight (RSE: 0.57, 0.59, R^2:0.963, 0.961). With respect to the LHQ_{85}, it is logical to expect a convex curve for the profile of the coefficient of determination and height quantile. That is because points that occur near the ground or within the lower canopy have very little relation to those points that occur at the top of the canopy surface. Conversely, the 100th height percentile will represent the single tallest crown within the plot, which is not representative of the average tree height within a plot. Therefore, some height quantile, which turns out to be the 85th, is the maximum predictive fit between tree height and the range of lidar height quantiles. However, the selection of height quantiles and/or reciprocal empirical cumulative distribution values at height quantiles offers an opportunity for idiosyncratic associations and over fitting, and it is more justified to instead apply the lidar treetop heights that have an unambiguous physical relation with height.

The height to live crown is another canopy structural attribute. It is measured from the ground surface to the live crown and is important as it relates to the age-productivity related structural changes in forest growth. The HTLC is also the length of the clear bole, which for timber production is a valuable attribute. Much like the analysis conducted for predicting tree height the HTLC was theorized to be related to lidar height quantiles. It is suspected that the slope change in height distributions would resolve the height position of the HTLC, as it is expected that there would be an abrupt increase in the probability of lidar hits above this height. In the data assessed, it appears that the first 10% of lidar CHM points are returned from stems and in some plots (1,2,5,10,11,21,41,48) from understory growth. The predictions of HTLC were on par

with that for plot heights. The 10th percentile of the lidar heights explained 94% of the variation in HTLC measurements conducted in the field. This model, like those of the canopy heights, produced a sound distribution of data points without evidence of outliers, influential points or heteroscedasticity in the model residuals. From Figure 4.93 it is evident that the 10th percentile occurs at a position in the lidar point probability distribution where there are sudden increases in lidar points. In this example, plot 41 (2/3 basal area thinned and 244kg N/ha applied at establishment and in 1990) represents a high HTLC while plot 67 (T2F1-PS) represents a very low HTLC. Even with the very skewed distribution of plot 41, the representation by quantiles captures the lower reaches of the canopy.

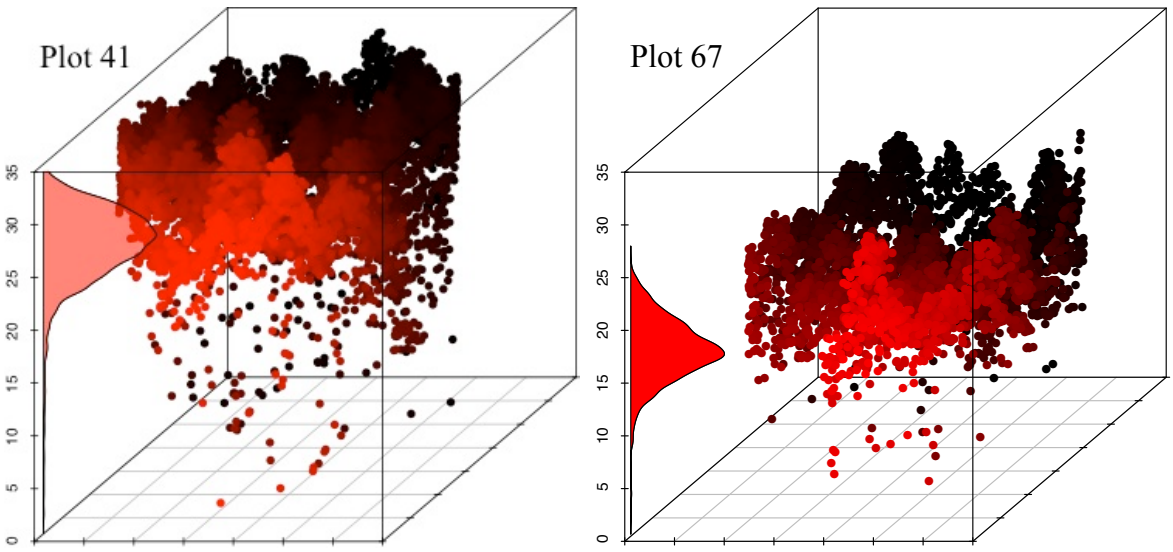


Figure 4.93. The point clouds of plots 41 and 67, examples of high and low HTLC respectively. The 10th percentile of the lidar CHM point cloud provides an accurate prediction of plot HTLC. The LHQ_{10} for plot 41 occurs at a height of 23.9m while that for plot 67 occurs at 14.58m.

The productivity modeling was a greater challenge than volume and structure modeling and required more complex models to explain greater than 60% of the variation. Ideally, two airborne datasets separated temporally by several years would provide a more direct measurement of growth productivity. With data assessed in this project, however, the real question that is being assessed is what structural and reflective characteristics of the forest at a given time are correlated with the growth that has occurred in its recent past. Changes in diameter and volumes between the last two CFS sampling years were computed. This change was used to represent a productivity index. Throughout the productivity modelling analysis the diseased plot 67 was identified as a consistent outlier and biased feature selection. Root disease induced wind throw at the plot produced a less closed canopy than the other treatment plots and this attribute was reflected in remote sensing metrics that characterised gap fraction and canopy closure. Additionally, plot 67 was dissimilar from the other plots in metrics that describe the photosynthetic pigment contents of the crown where plot 67 was lower in these metrics. Therefore, plot 67 was often removed from the dataset to evaluate the impact the dissimilar plot would have on feature selection and model performance. Regression analysis demonstrated overwhelmingly that spectroscopy had a role in productivity estimation, more specifically the spectral metrics sensitive to foliar xanthophyll and chlorophyll contents. The exception was the case for mean volume increment, which produced estimates from median lidar treetop height and the variation in the canopy height model. The only case where crown class stratification produced a predictive benefit was from the mean diameter increments, where the attribute was best estimated when only the dominant to intermediate classes were considered. This finding was not

surprising as the other attributes were related to volume increments where the majority of the volume occurs within the more dominant crown classes. Regression models produced with either of the plot level productivity attributes (basal area increment and ultimately total plot volume increment), selected the median of the PRI index. This index is linked with the epoxidation state of xanthophyll pigments. This group of pigments function to dissipate excess absorbed PAR as heat in a photoprotective function to limit the oxidation of the photosystems. The function of the xanthophyll is reversible which permits the photosystem to respond to the light environment [141]. This becomes a fundamental necessity during high VPD and drought conditions where photosynthesis slows or ceases entirely. Under these conditions nearly 100% of the absorbed photosynthetically active radiation must be safely dissipated as heat otherwise the photosystems will be damaged and reduce the photosynthetic capacity. The positive coefficients produced for the median PRI term suggest that highly productive plots have high PRI values and according to a substantial amount of literature, PRI is associated with radiation use efficiency (CO_2 assimilated/APAR) [142]. The coherent pattern of feature selection throughout the model building analysis demonstrated three predominant trends. Features describing the structure of the plots, namely height (median lidar treetop) and density (standard deviation of the CHM and CCF) were sensitive to the productivity attributes. The rationalization of these selected features were intuitive and would be linked to the premise of serial auto-correlated productivity, high volume plots have had high historical growth rates and are likely to have future high growth rates. Secondly, attributes relating to the photosynthetic capacity of the crown were frequently selected. The PRI as previously noted and also the continuum-removed depth, which was selected in three of a

total of six productivity models (4 productivity attributes, two of which had crown class stratifications). Lastly, in cases where plot 67 was not omitted from model building, features were selected that would isolate the unique response of the diseased site, namely the median red edge position. Thus, in order to predict productivity, information on height and density, photosynthetic capacity and disease were required. The final model produced in the productivity estimation section estimated total plot volume increments from median PRI, mean CRMD and $CCF_{45,}$ the selection of these features fit very well with findings detailed in Garbulsky et al. [142]. The authors detail the confounding conditions of pigment pool sizes and vegetation structure on the PRI-LUE relationship. In this situation, pigment pools are sampled by the chlorophyll sensitive CRMD metric and crown structure is directly captured by the lidar survey and represented in the crown closure metric.

It is expected that there are meaningful links between topography, three-dimensional canopy structure, tree species composition and growth productivity. This work has demonstrated that fine scale topographic variation and the characterization of canopy structure are achievable through airborne discrete lidar data. Vegetation health has been a long-standing topic within the discourse of vegetation imaging spectroscopy. Since these site attributes are measurable through these imaging technologies, it stands to reason that it may be possible to infer growth from these conditions. This project has suggested that there is promise for inferring growth from imaging spectroscopy, however refinements are required. Species composition and structural complexity change throughout the development of a forested stand with a concurrent change in growth productivity. This project cannot address the impacts of age, complex structures and

species on productivity. Future work should expand from this foundation and consider more structural and demographic diversity. Irrespective, this project demonstrates a capacity for productivity estimation through remote sensing technologies, which would be beneficial for forest silviculture strategies. A detailed forest inventory that provides key information related to growth, wood quantity and quality would be an invaluable tool to improve efficiency and competitiveness for the Canadian forest industry.

This project developed and evaluated forest information extraction techniques from modern airborne imaging technologies. The result of this project was the development of an enhanced forest inventory in the form of a variety of volume, structural and productivity related attributes derived from these imaging technologies. These remotely collected attributes will contribute to the competitiveness of the Canadian forest sector by reducing the resources required by private forest companies and forest tenure holders to survey their areas, and at the same time reduce the need for spatial extrapolation. The project has determined there is a certain capacity for the determination of volume and canopy architecture attributes through high resolution imaging technologies. Largely attributed to the lidar dataset, three-dimensional structure is measured and generalized to adequately represent traditional ground based measures of structure and volume. Spectroscopic methods for measuring differences in foliar chemistry, namely, xanthophyll and chlorophyll pigments appear to be associated with growth productivity. The metrics that made these relationships apparent relied on the development of digital surfaces representing the bare earth, the reflective surface and a terrain-normalized canopy height surface. As part of the digital surface processing, site fertility was quantified by a relative surface moisture model that was output to a digital

database. Additionally, using established chemometric relationships a foliar biochemistry database was generated from spectroscopic attributes, as these appear to relate to forest productivity. Although this work is ongoing, there is promise that these developed forest information products and those yet to come from extensions of this work will constitute an innovation in forest resource information extraction that will benefit decision making and in turn improve the effectiveness and efficiency of the Canadian forest sector.

CHAPTER 5:DERIVATION OF INDIVIDUAL TREE MORPHOMETRICS

Traditional surveying techniques can be applied to map individual tree stems of interest for ground referencing remote sensing studies. However, these data are limited in their ability to describe forest structure aside from tree spatial distribution. Terrestrial laser scanner (TLS) data are increasingly being incorporated into operational surveying practices [143], [144], where their accuracy and ability to describe detailed individual tree and stand characteristics have been recognized. Several morphological attributes, conventionally sought for their utility in inferring additional physiological parameters were investigated with reference to the measured point cloud, these included: diameter at breast height (DBH), top height, and height to live crown (HTLC). Additional morphological attributes were derived as intermediates during processing and also have merit in providing forest information, these included: crown width and density, stem position sweep and lean, and clear bole length.

TLS is a ranging instrument, scanner and angle encoder integrated system that is typically deployed in a static position. The laser ranging system measures distances to surfaces either by time of flight or by phase shift methods [145]. The scanner and angle encoder, typically a rotating mirror, distributes the outgoing light within the measurement area while assigning the outgoing pulse geometry with the intensity and range information of the returned signal. As the scanner rotates at a given rate (*e.g.* horizontal: 0.5mHz, vertical: 97Hz), laser pulses are emitted at a specified rate (*e.g.* ~976kHz). A point cloud is constructed from the returned TLS measurements characterizing the scanned area, the data density being dependent on scanner and laser attributes. TLS has been increasingly applied in forest research for its ability to directly and precisely

measure physical dimensions like those related to the 3D arrangement of forest components, also termed forest structure [146], [147]. Some work has focused on tree crowns [148] and their impact on light transmission [149], [150]. The technology has also been investigated for its capacity to provide valuable inventory information for forest management through measuring biomass [151]–[153], volume [154], [155], wood fibre quality [156] and by providing operational infrastructure support [157]. There is also evidence that these type of data capture information pertinent to habitat mapping [158].

The FARO scanner has the added benefit of collecting full hemispherical photography during TLS collection. Within the Scene software, the images were positioned to the relative coordinate reference using the recorded image geometries. As part of the CFS field measurement campaign, each individual stem within the core treatment area was painted with its appropriate identification number. The positions of these ID numbers were registered in Scene, thus an object for each visible specimen was created with a relative scan position and a specimen ID number. This incomplete object data could then be used to define the rotation and translation values required to transform the entire CFS relative survey positions to UTM. The product of the absolute positioning process is a spatially consistent reference and remote/proximal-sensing dataset, which enables the comparison of metrics with ground measured attributes.

5.1 Extracting Stem Position and DBH from TLS

Two of the more common attributes derived in forest mensuration are DBH and tree height, which are sought for their long-known proxy value for other structural attributes [159]. Traditional means of measuring top heights in the field are complicated by the necessity for an unobstructed line of sight to the treetop from the ground, which is

problematic in high-density stands. In many cases a subsample of stems are measured and allometric relationships of DBH to top height are derived [118]. From these morphologic relationships the unmeasured top heights are inferred [121]. Airborne lidar scanner (ALS) surveys may offer an alternative to these top height estimates, especially in cases of high stem densities. ALS directly measures heights and through processing, treetop heights can be derived for the dominant and co-dominant canopy [160]. Extracting inventory parameters, particularly diameter at breast height (DBH), from TLS point clouds is an emergent research area. Common approaches to estimating DBH can generally be divided into two classes: least squares fitting of shape primitives [154] and pragmatic geometric approaches [155]. Considerable research effort has gone into the extraction of stem shape parameters through the use of TLS; however the integration of ALS and TLS data for the automated extraction of tree morphometrics has not been explored as fully. This chapter documents the processing stream required to produce and refine a highly detailed, absolute referenced, multi-mode lidar dataset. The investigation and derivation of a simple but robust approach for DBH measurements from TLS is presented. This study extends the work performed by others by investigating potential confounding factors within the environment and in the collection design.

Stem positions were derived from the TLS data through a simple 2-D clustering strategy. An iterative migrating k-means algorithm was implemented in the R language and included splitting and merging parameters. The merge and split thresholds were interpreted as the minimum distance between stems and the maximum stem radius respectively. For this study the join maximum distance was set to 0.3 meters and the minimum split distance was specified as 0.5 meters. Resulting cluster centers with

Euclidian distances less than the join distance were merged, while clusters with an RMSE value greater than the split distance were re-iterated through the clustering.

Each cluster was filtered for duplicate 2D positions, and by a user specified percentile distance from cluster centers. This study applied a percentile filter of 99%. The point filtering was necessary because point density varied significantly with directionality towards the scanner positions, as a result cluster centers tended to occur on stems where the greatest concentration of the points occurred. Cluster positions needed to fall within the inner convex area of the stem; this condition was not met in cases where broken branches, captured within the stem sections, biased the horizontal position of stem centers. To improve the cluster positions they were modified from being x, y median positions to range centers, justifying the importance of the filtering procedure. The stem centers were then used to seed the DBH extraction algorithm.

A geometric approach was designed assuming a circular model. Points were stratified for each stem by a 12˚ azimuth-binning interval, where the origin was the location of the range center. For every bin, a point was generated with the azimuth bin midpoint and the bin minimum distance to the range center. Additional attributes were derived for the bin intervals including point count. From these data, stem point coverage information was calculated as the proportion of bins with membership. The approach to DBH modeling was premised on two opposing transects that cross a migrating center position. The transects were defined by the maximum distance between two bins minimum distance points, this condition bisects a theoretical circle, as the maximum distance from any two points on a circle circumference is that which occurs directly opposite the circle centroid. For stems with complete coverage, the first transect was

defined as the azimuth bin with the greatest minimum distance to the center. The center was adjusted along that azimuth by a distance equal to the difference between the two distances from the center on that transect. The second, orthogonal transect was defined and the center position was adjusted in the same manner.

Where the stems had incomplete coverage, the initial transect starting point was defined as the first or last bin with membership. The end point of the first transect was that corresponding to the bin azimuth closest to the opposing direction of the start point from the range center. The center position was adjusted accordingly given the two distances to the range center and the transect azimuth. The second transect remained orthogonal to the first. Where the second transect had both start and end points the process was the same as if it had complete coverage. However, when a transect segment had no point membership the center was adjusted along the transect segment with membership to a distance that was half the difference of that transect segment minus the average of the first two transect segments (Fig. 5.1 & 5.2). The data and point attributes were recalculated using the new stem positions. For each stem a bole radius was calculated as the median minimum distance within the binned database.

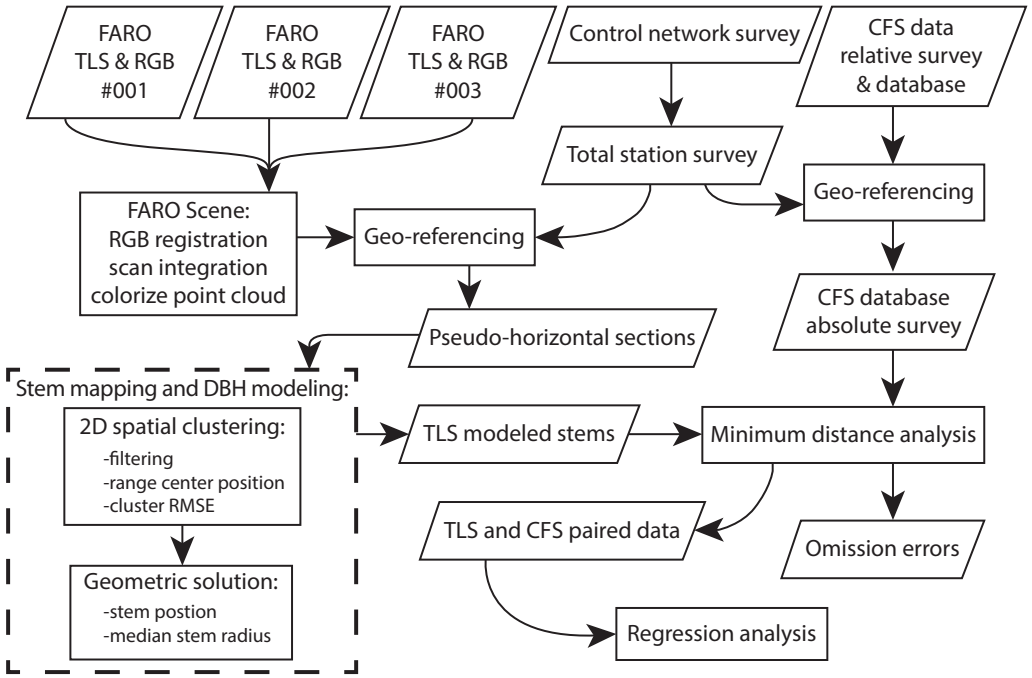


Figure 5.1 Data processing sequence for stem mapping and DBH modeling through TLS with an independently collected validation dataset.

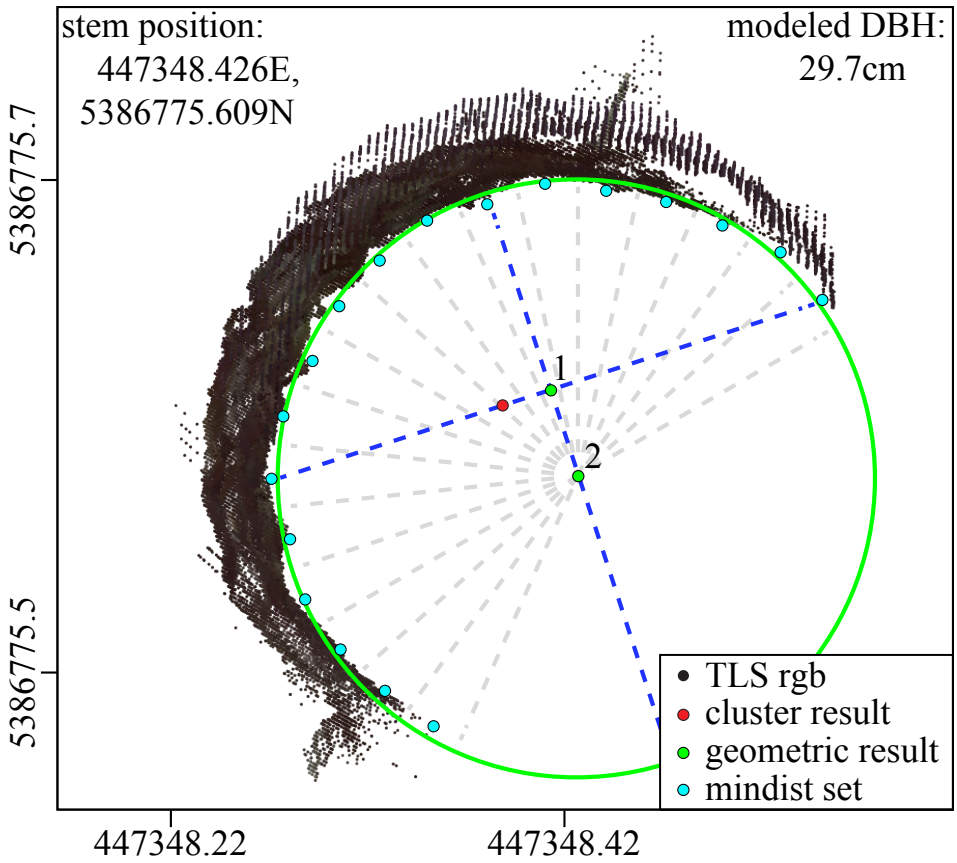


Figure 5.2 Deriving DBH from TLS pseudo horizontal point cloud sections. The cluster range center is represented in red, points are stratified into azimuth bins (grey dashed), bin minimum distance points are determined (cyan), center (green 1 & 2), is adjusted based on transects (blue dashed).

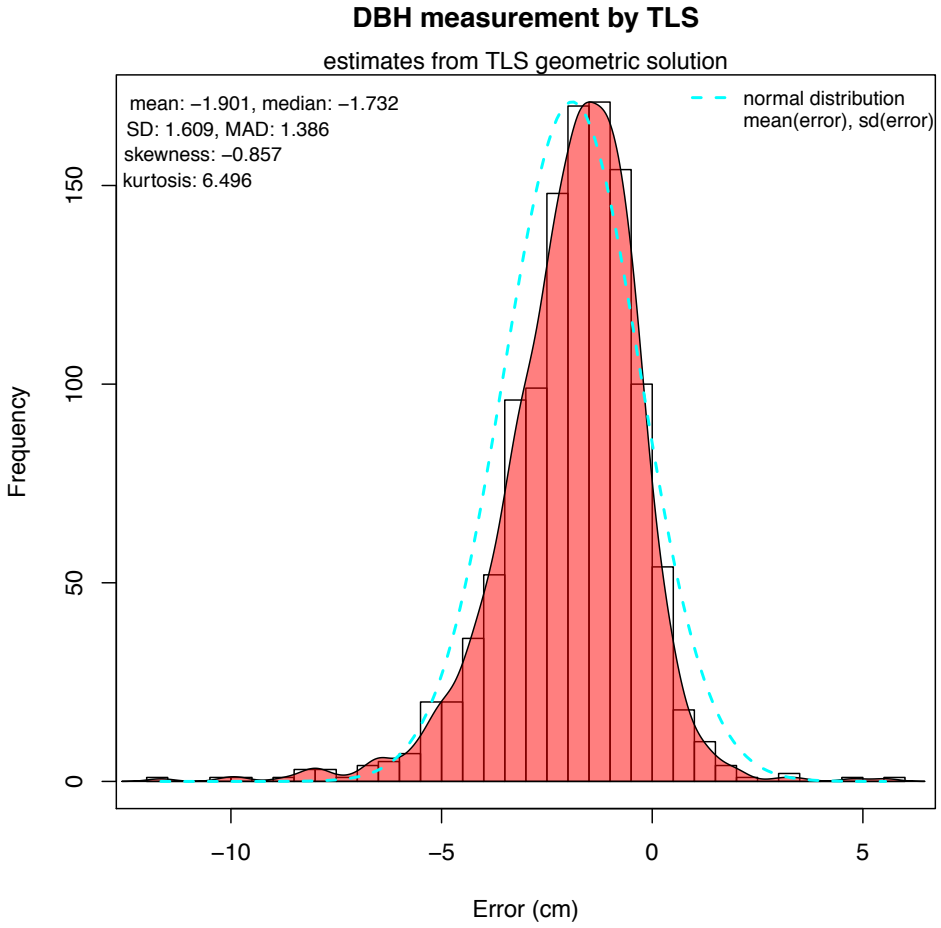


Figure 5.3 The uncalibrated error of the geometric solution for estimating DBH produced a median error of -1.73cm but produced rare errors as high as -12cm for individual observations. The error distribution was negatively skewed where underestimation was far more likely than overestimation.

The TLS derived stem map was evaluated for errors against the CFS relative survey. There was a 5% omission error in the TLS stem map (49/1189). However, these stems were also missing from the cross-sections used as inputs to the mapping/DBH script. The largest contributing factor to the omission errors was the result of a hard definition of the core plot extents. During the point cloud processing, a clipping boundary was defined as a 20x20m extent encompassing all core trees (omitting trees within the treated buffer area) identified in the photography. Of the core specimens, 1.85%

(22/1189) occurred outside a core extent of 20x20m; therefore these trees were not captured in the stem sections. The second largest contributor to the stem omission errors, which constituted a quarter of the omissions and one percent of the core trees, occurred during point cloud clipping. In plots with abundant understory, manual clipping of vegetation mistakenly removed 12 stems of core trees. Because these stems were omitted from the stem section the stem mapping procedure was unable to identify them. Six omission errors were attributed to stem occlusion and four errors were found to be incorrect relative survey positions. One omission error was attributed to a failed cluster seed, where a small stem with very little point coverage was omitted. There was no evidence for the existence of the remaining four omission errors in either the TLS or the ALS data. The DBH of these missing data ranged from 9.3 to 46.2cm (mean 23.3cm, median 22.2cm, standard deviation 7.24cm, n=45). The distribution of the missing values was consistent with that of the non-missing data, thus, it was concluded that the omission of the 49 samples would not compromise, or bias, the statistical analysis sufficiently to warrant the re-exporting of the stem sections.

A statistical analysis script was written in R to evaluate the agreement between TLS and traditional field measurements of DBH. The script produced scatterplots and tabular outputs for Spearman's correlation, linear regression and the analysis of model residuals. Assumptions of statistical analyses were investigated through hypothesis testing and in model residuals. Additionally, model residuals were investigated for associations with data quality and stem representation indices. Linear associations were queried at multiple scales; average plot DBH was regressed, as well as all the trees in each individual plot and, finally, all trees within the selected plots of the study area.

Three conditions were anticipated for the analyses. Firstly, as a result of the scanner and static nature of TLS collection the effective point density is non-uniform. This is expected to have significant implications for the results. Secondly, the geometry of TLS collection presents a challenge for spatial coverage when target objects are both distal and proximal to the scanner. In these situations, boles near the scanner will occlude or obscure those behind it. Errors in TLS products were expected to increase in concert with factors that increase the degree of occlusion. Thirdly, scan integration accuracy was expected to be a significant source of error in modeling DBH.

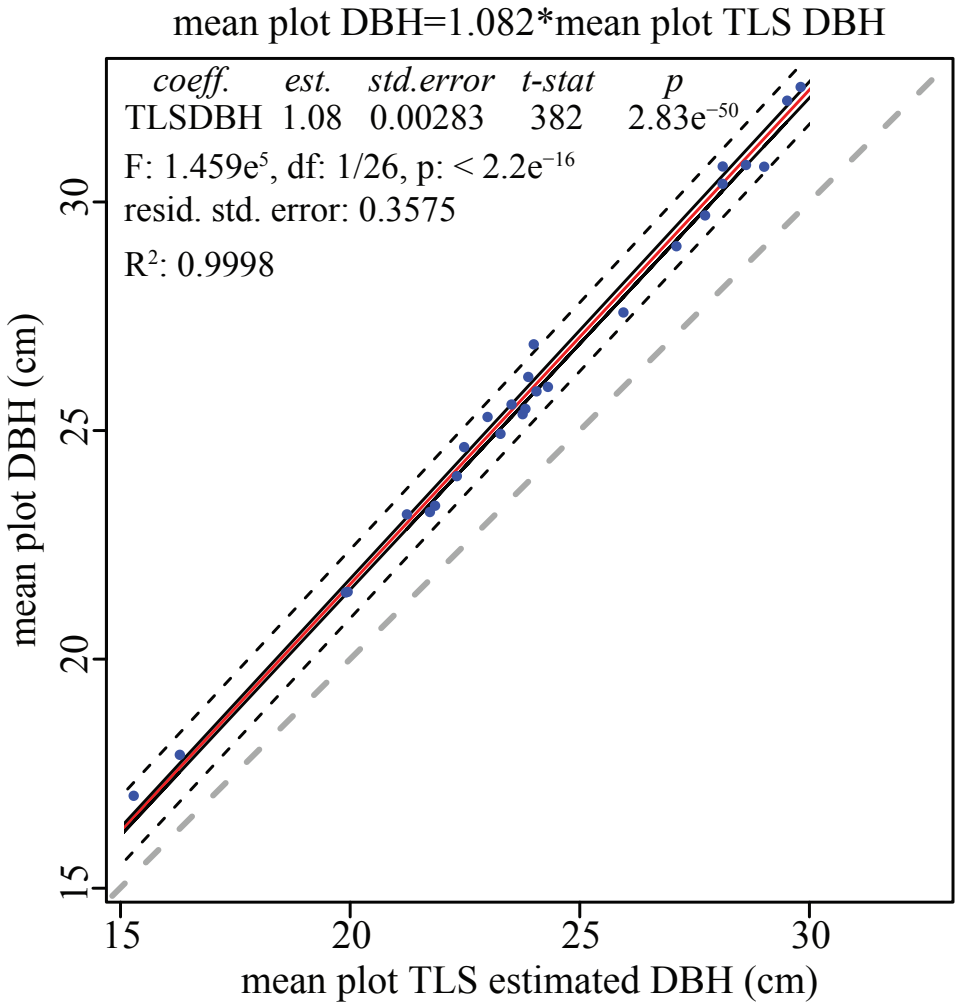


Figure 5.4 Scatterplot and linear regression results of plot mean DBH, demonstrated a high degree of association.

The TLS DBH estimates were submitted to a regression analysis to determine the operational accuracy, via the defined approach. The data were scaled up to the plot level by computing the plot means for both field and TLS DBH values. Figure 5.4 illustrates the scatterplot with the simple linear regression results. A Spearman's correlation coefficient suggested a strong positive association (rho=0.99, p<0.000) and the scatterplot clearly demonstrates a linear form. The intercept parameter failed to produce a significant difference from zero (t-stat=1.12, p=0.27) and therefore was removed from the model. The resulting linear regression demonstrated a significant (F-statistic = 145,90, p<0.000) and very strong (R^2=0.9998) linear relationship. The analysis produced a significant slope coefficient of 1.08 and a standard residual error of 0.36 cm. Residual plots did not provide overwhelming evidence for assumption violations or influential data points.

The plot average analysis offered an opportunity to investigate whether the errors in modeling DBH were related to plot-based parameters. The DBH residuals were regressed with plot stem density and the plot TLS scan integration index. Although a positive trend appeared to exist for the 27 data points, analysis of DBH residuals and plot stem density did not suggest there was a significant relationship (Spearman's ρ =0.21 p=0.3 & F-statistic=2.69 p=0.11). This result suggested that for this site and given the methods and geometry for TLS acquisition, occlusion did not appear to be a significant contributing factor to the errors in DBH estimation. Statistical analysis did suggest that scan integration significantly explained the variation in the errors of DBH estimates (Fig. 5.5). Correlation between absolute DBH errors and the maximum scan tension (scan integration index) demonstrated a weak to moderate, but significant, positive association (ρ =0.46, p=0.02). The linear regression of the same data was significant (F-

statistic=6.29, p=0.020, coefficient t-test p<0.02). The linear regression determined that nearly 22% of the error in the residual plot average DBH estimate could be explained by the worst scan fit (maximum scan tension) within the plot TLS point cloud (R^2=0.215). Since the true benefit for TLS applied to plot characterization lies in the description of the individual rather than a plot, regression analysis was conducted at the individual tree level.

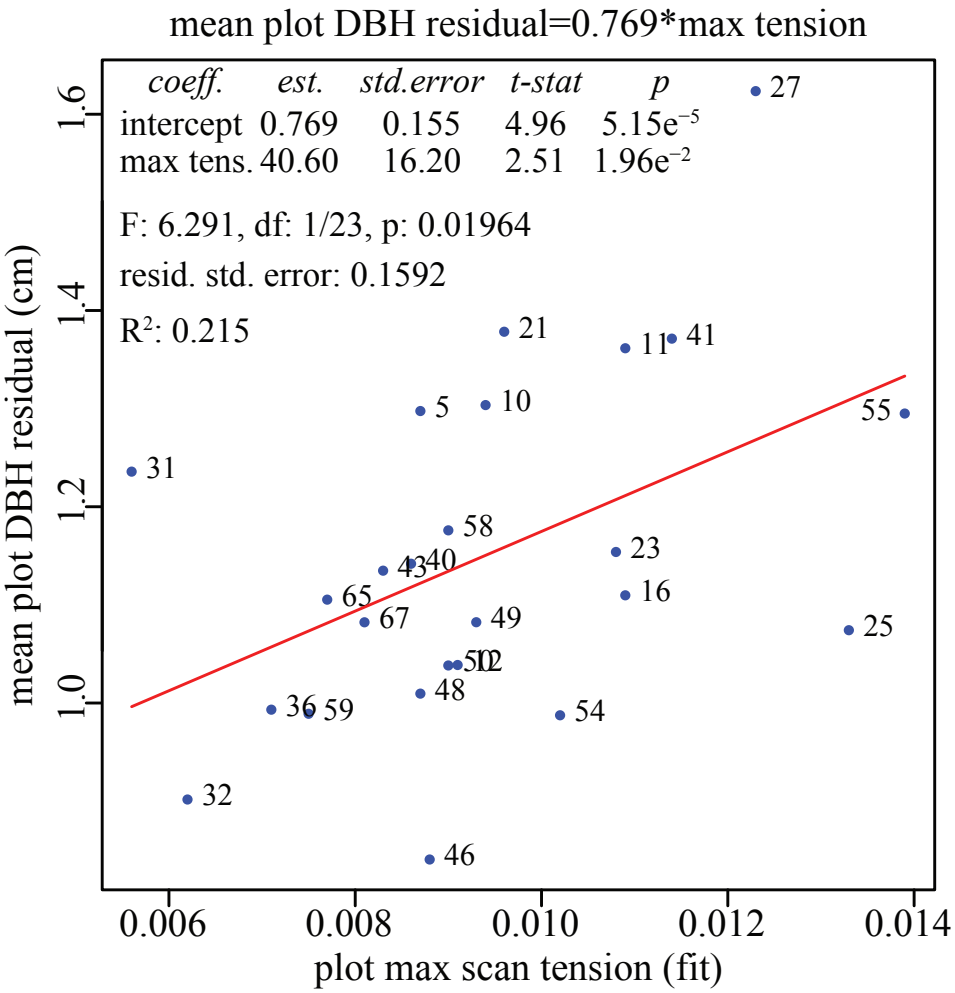


Figure 5.5 Scatterplot and linear regression results of average plot DBH residuals and scan integration fit index (tension). DBH error increases with poor scan integration fit.

Stem-level regression analysis illustrated under which circumstances the DBH modeling was poorly suited. The initial result produced a small number of influential points with large errors. The causes of these outliers were attributed to severe lean and clustering failures, where small, suppressed stems were closer to core trees than the split rule. The influential data were omitted from the analysis. Point omission was conservative at 0.336% (4/1189 stems). The linear regression without the effect of influential points appeared to converge with the plot level model when an intercept was not applied. Although the coefficient of determination and the F-statistic for the model without an intercept was larger than the model that included the intercept estimation, the standard residual was 0.1 mm larger. In addition, the residual analysis of the scale-only model suggested auto-correlated errors with under estimation at lower DBH values. This observation indicated a poorly defined relation at small diameters; a condition remedied by incorporating an intercept into the model. In light of the residual observations, and a significant intercept estimate ($p<0.000$), the slope and intercept model was selected as superior (Fig. 5.6). The individual DBH estimates relative to field measurements produced a very strong and significant correlation (ρ : 0.977, $p<0.000$). Linear regression related the field measurements to the estimates in the form:

$$DBH_{field}=1.027(\pm0.007)*DBH_{TLS}+1.288(\pm0.159)$$

The regression produced significant coefficients ($p<0.000$), an F-statistic of 23900 ($p<0.000$) and a coefficient of determination of 0.95. The standard error of the DBH estimates was found to be 1.626 cm. The residual plots for the DBH estimates illustrate uncorrelated, unbiased and uniform variance in the model errors without the presence of influential points. The normal-quantile plots suggest slightly heavier tails in the residual

distribution, which indicates a minor departure from normality in the errors. Efforts to resolve heavy tails by transformations produced variance inequality and auto-correlated errors.

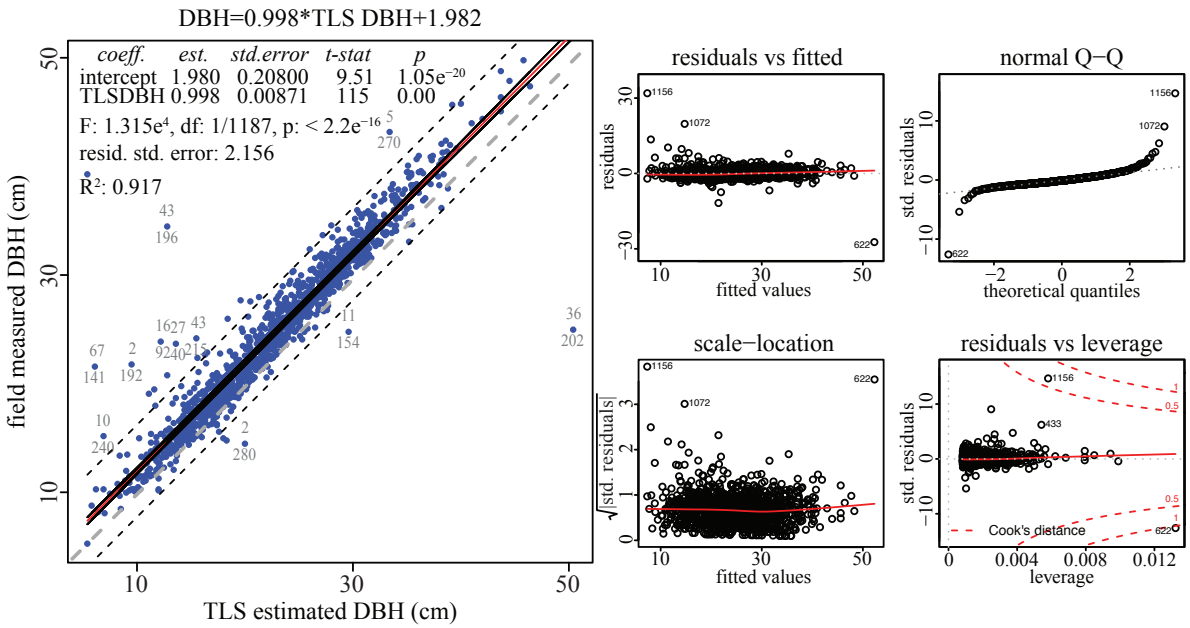


Figure 5.6 Scatterplot and linear regression of all core stems, extreme values are identified as the largest one percent of the absolute residual and are labeled by plot ID (above) and tree ID (below). Residual plots for initial DBH regression of field measured and TLS modeled DBH values. Outliers and influential data points are clearly evident in the residual and leverage plot respectively

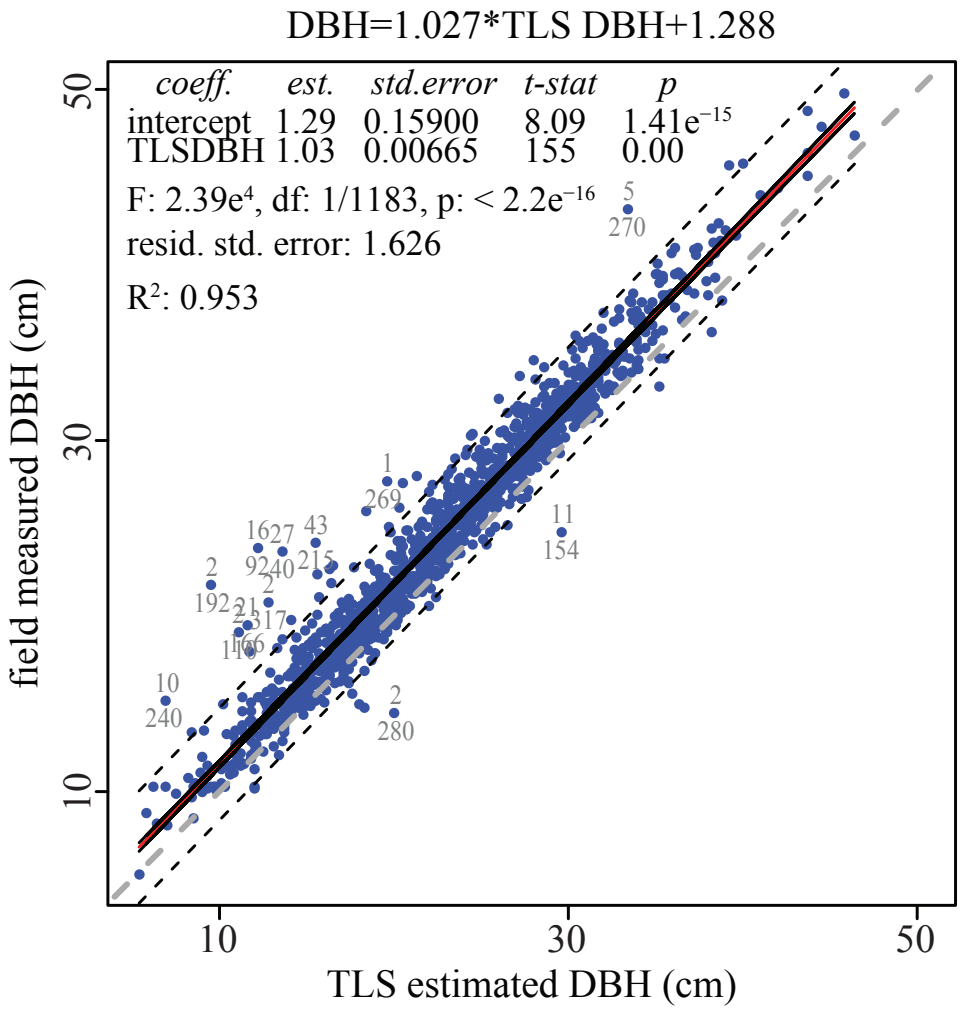


Figure 5.7 Scatterplot and linear regression of core stems without influential points. The intercept was significantly different from zero and the residual standard error decreased by 0.01cm.

Given the direct nature of the diameter measurements, it was expected that the relationship could be more directly related than implied by a slope and offset model, in other words, the significant slope coefficient was produced only because of idiosyncrasies of the data and the existence of an offset. The errors of the estimates were determined and an offset estimated as the median residual (Fig. 5.8). With an error bias determined as -1.7 the TLS estimates were adjusted accordingly and a slope-only fit was investigated. The resulting model produced a slope coefficient of 1, with a standard error

of the estimate of 0.0018, a value that exceeds the precision of the ground based measurements (Fig. 5.9). The coefficient estimate of the error adjusted TLS measurements supported the hypothesis that the estimated diameters had a bias error but no scale dependent error.

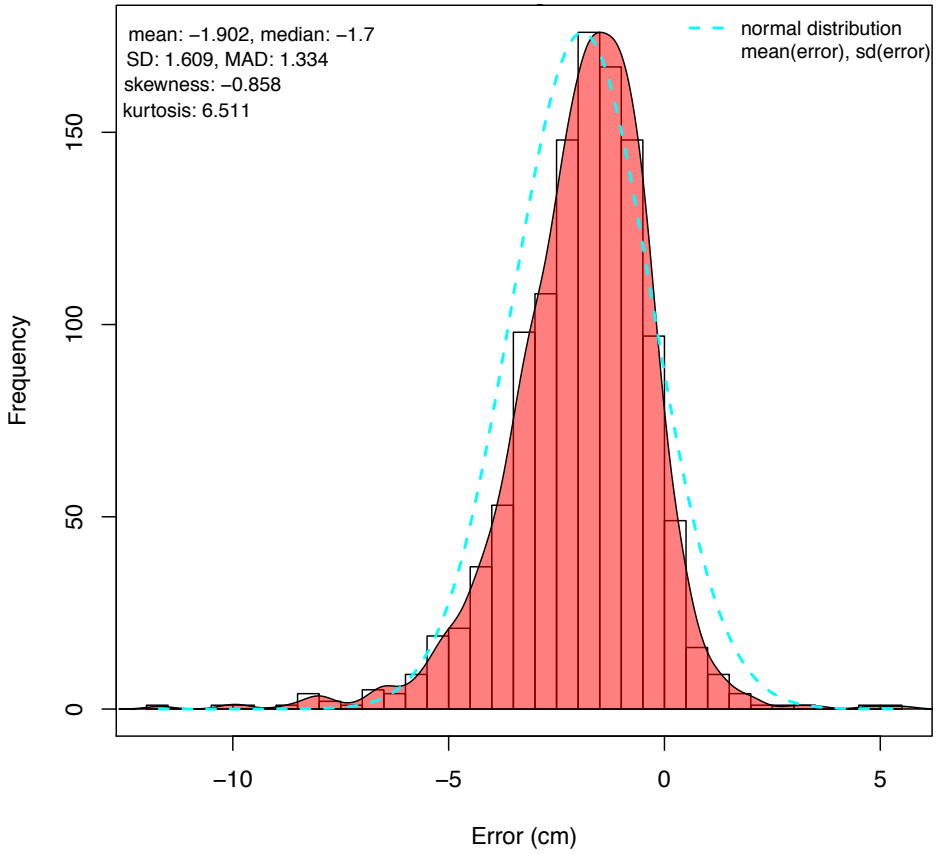


Figure 5.8 DBH estimation error from the geometric approach produced a median error that was 1.7cm smaller than the field measured diameters.

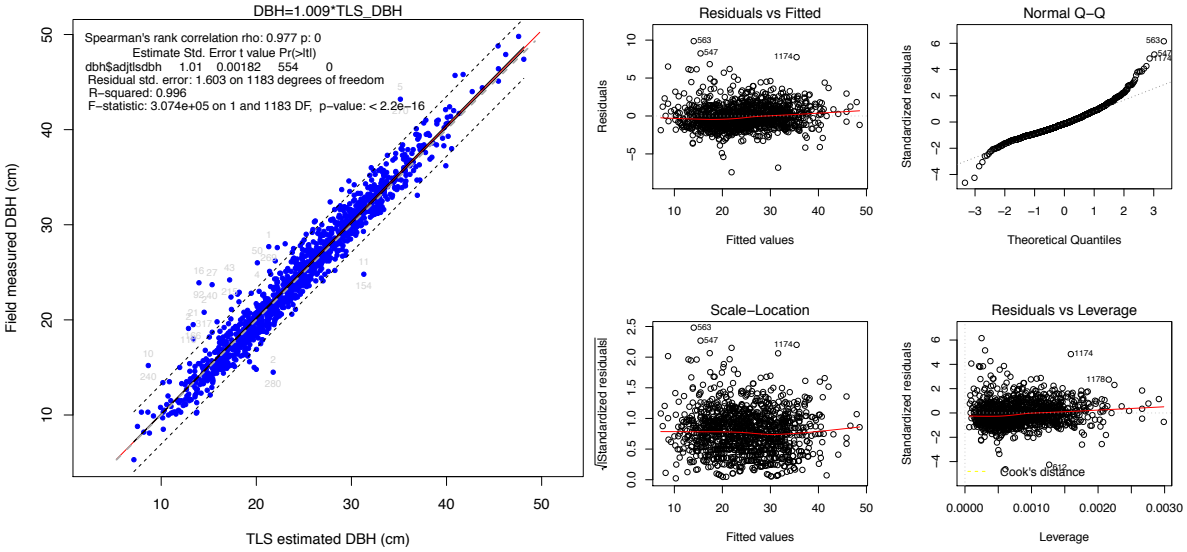


Figure 5.9 Scatterplot and linear regression of all core stems, with a median bias of -1.7 removed. Extreme values are identified as the largest one percent of the absolute residual and are labeled by plot ID (above) and tree ID (below). Residual plots for the adjusted DBH estimates regressed with field measured DBH values suggest no scale dependency within the estimated data. Residuals plots suggest constant and uniform variance without the presence of outliers and influential data points

Errors in the DBH estimates were investigated with reference to the number of TLS points that represented each stem, the proportion of stem sampled, point density and the distance to scanner positions. Point count was expected to be the most significant attribute affecting DBH estimate accuracies. Initial observations noted the large variation in TLS point density (range: 257-4M points.); the distribution was severely skewed with a median of ~62K points. Although no significant relationship was found between point count and DBH residual, evidence for violations of normality were clearly apparent in the residual normal-quantile plot. The data were transformed by the fourth root, which resolved both the severe skewness of the point count distribution and the heavy tails in the residual distribution. The resulting regression marginally met the alpha level of significance (p: 0.046). In addition, the transformed point count per stem explained less than half a percent of the variation in DBH estimate errors (R^2: 0.003).

The analysis investigating DBH residuals associated with point density and the minimum distance to a scanner position did not produce significant relationships. These attributes describe the potential causes of variations in point count and thus it is not surprising that these results would mirror those found in the stem point count regression. The minimum distance to scanner relationship is over simplified, as it omits the influence of occlusion. Two other attributes were evaluated against DBH residuals, sampled circumference and proportion of stem coverage. These attributes are not independent because sampled circumference was derived through the use of stem coverage. Stem coverage is defined as the proportion of azimuth bins with point membership relative to all bins. Sampled circumference was derived by scaling stem circumference (π DBH_{field}) by stem coverage. A significant association between DBH residuals and sampled circumference was found. However, the relationship was quite weak, where sampled circumference explained only 1.8% of the variation in DBH estimate errors. Data transformations that were used to meet the assumption of normality had no effect on the conclusion of this comparison. Similar results were found when the DBH residuals were regressed with the proportion of stem coverage data. The relationship was statistically significant; in this case the coefficient of determination was slightly elevated relative to sampled circumference. Stem coverage explained at most 6% of the variation in the errors of DBH estimates. Again, the data exhibited heavy tailed distributions relative to normal. The conclusions remained the same when the data were transformed to appear more approximately normal. However, there was an associated decrease in the coefficient of determination to 0.36 with the transformation (Fig. 5.10).

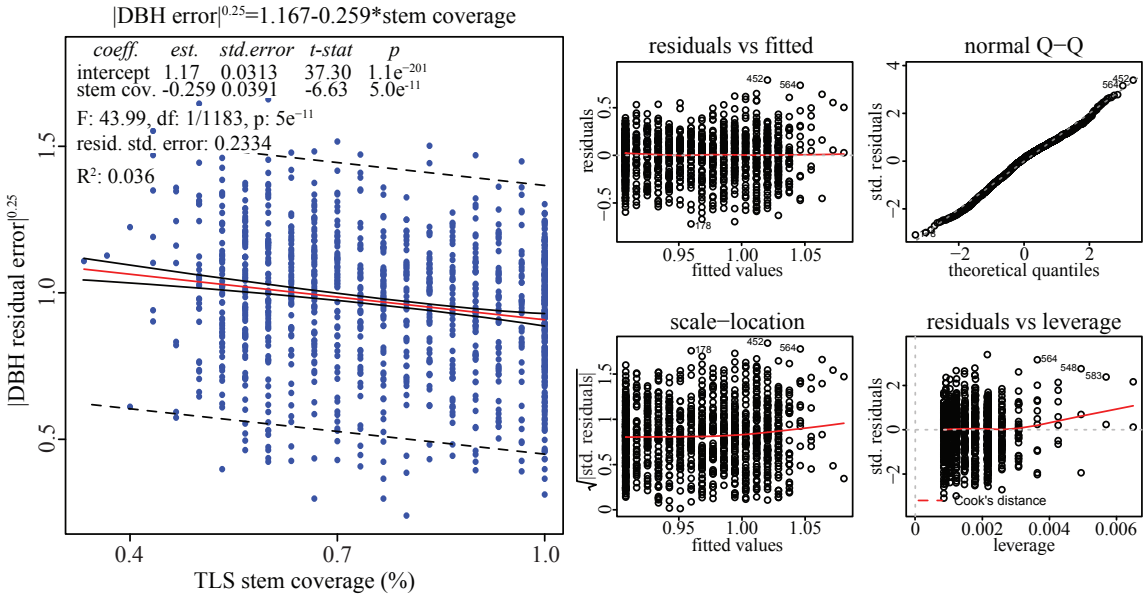


Figure 5.10 Scatterplot and linear regression results of DBH residuals and radial stem coverage. Regression analysis suggested smaller DBH errors for stems with a greater proportion of their stem measured by TLS. The residual plots illustrate that the transformation has resolved the residual autocorrelation and non-parametric distribution in the untransformed model. The LOWESS curve of the scale-location plot may indicate variance inequality, but may also be an artefact of low data density at higher fitted residual errors (fitted values), actually the product of low density in low TLS stem coverage.

A multiple linear regression (MLR) analysis was conducted with the attributes previously assessed as well as interaction terms (*i.e.* point count and stem coverage, distance to scanner and sampled circumference) and plot effects. The MLR confirmed the results produced in simple regression, but also produced significant coefficients for point count and plot stem density. There was a marginal benefit for the more complicated multivariate model, which equated to a reduction in the residual standard error of half a millimeter (Fig. 5.11). To evaluate the relative contribution of the independent variables in explaining the variation in DBH, they were normalized and the model was recomputed. The importance ranks, as represented by the magnitude of the coefficients was, as expected led by the TLS estimates and followed by attributes related to the

probability of errors; in sequence: stem coverage, point count, stem density and maximum scan tension within the plot point cloud. It should be recognized that, in this case, stem density might have produced a significant coefficient because of the negative association between DBH and stem density rather than explaining occlusion/DBH residuals.

The application of TLS to stem modeling is a relatively new technology that appeared in the literature in 2003 [161], but has quickly gained much attention. The approaches to apply these data for this application have generally been focused on least squares fitting of shape primitives, although much work has also investigated alternatives for operationally improving extraction accuracies.

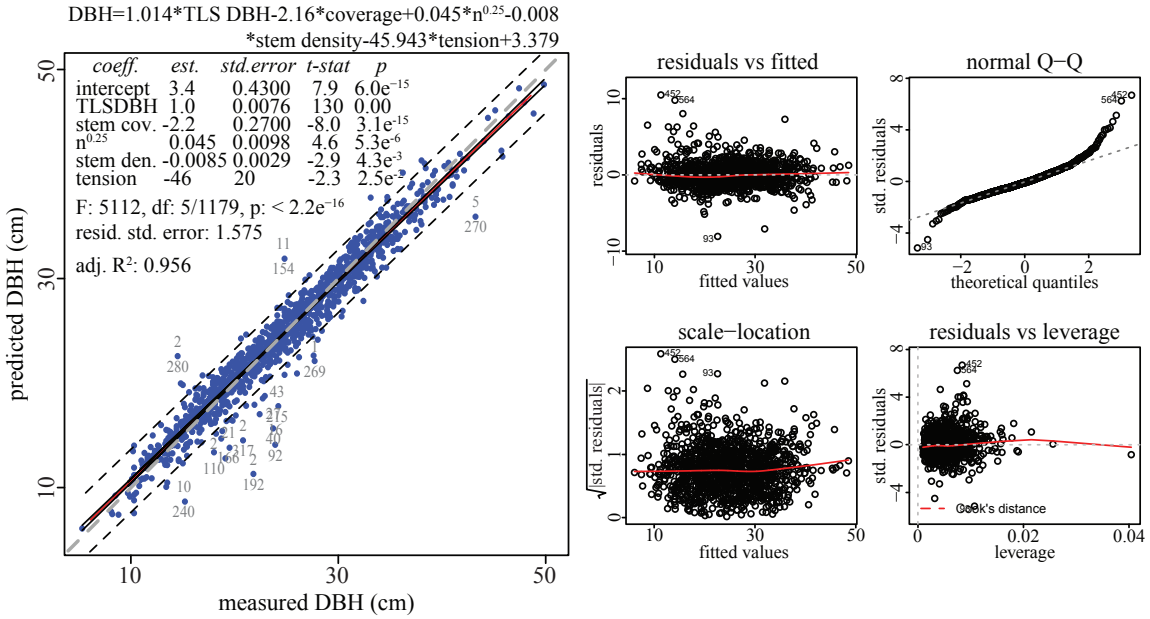


Figure 5.11 The marginal improvement in the residual error of MLR over SLR raised concerns about the validity of the more complex multivariate model. The residual plots for the MLR DBH model illustrates that the assumptions of the statistical approach were within reason. The tails of the residual distribution may be slightly heavy relative to a normal distribution and there may be a data point that is influential but is not an outlier in terms of the model; multicollinearity was not assessed but is expected at least between TLS DBH measurements and stem density.

The available research on the topic has addressed DBH estimation from single scans [154], [162]–[164] and integrated scans [154], [165], [166], applying circle fitting [154], [162], [165], [167], [168], multiple circle fitting at height intervals [162], cylinder fitting [162], [169], [170], and other geometric approaches [155], [163], [167], [171]. As always, there appear to be benefits and limitations for scanning mode and for each of the algorithms. As an example, primitive shape fitting is limited to a horizontally circular model and thus tends to fail with noisy data typical of TLS scans or when stems deviate from circular, whether by growth form or by poor scan integration [167]. Conversely, geometric solutions, similar to that applied in this study, may fail in instances with significant sweep or lean, and may be sensitive to data noise.

Several authors have alluded to possible sources of errors within their respective projects, including: scan integration or buttressing [167], bark fissure depth [162], departures from circularity [154], leaning and sweep [162], scanner collection parameters [172], scan distance [157], ground surface slope [157], point density [165], [166], occlusion [165], [166] and uncertainty in ground level [154]. This current study supported many of these authors' conclusions. Evidence for effects of scan integration quality on DBH estimates was observed in residual regression as well as through qualitative evaluation of bole point clouds. While few instances were observed, sweep and lean produced very large errors in DBH estimation. Although theory would suggest scanner distances and point densities are important for stem characterization, this study did not support this, presumably because these data were collected at relatively close proximity to the sampled stems (4-6m, max: 14.5m) with very high point densities (~750K/m^2). Under these circumstances, stems are captured with high detail from a large

number of closely spaced points. In lidar data, feature measurements (*i.e.* DBH) are only as precise as the lidar point spacing, thus low-density data are less able to capture accurate distance measurement. Point sampling in this case is nearly spatially contiguous with a computed point spacing of 6.1mm and a footprint diameter of 6.9mm assuming an equidistant surface at 20m from the scanner.

The effect of ground surface generalization may have impacted these results. What is rarely considered within the literature, Chasmer et al. [173] being the exception, is the appropriateness of the lidar modeled ground surface used to determine the absolute breast height. The attention given to the integration of the ALS and TLS data provided insight on this potential source of error. Discrepancies were observed between the ground heights measured by TLS and ALS. The ground height discrepancy could be attributed to either, or both, the propagation of surveyed height errors, which tend to be greater than horizontal errors, and poor penetration of optical signals through dense overstory and ground cover vegetation. Irrespective of these points, stem taper is expected to be very slight for the trees and heights sampled here, as taper is known to be prominent at the base as flare and within the top zone of actively growing foliage [174]. In addition, this approach defines the stem surface as the smallest perimeter the point cloud supports and is thus theoretically biased to larger heights from ground.

Much of the literature applies to smaller data sets from few forest plots or very few sample trees, thus many represent proof of concept studies rather than robust statistical evaluations. The results of DBH modeling within the literature are therefore varied, with errors ranging from 8mm [165] to 7.0cm [162]. Pueschel et al. [154] summarized the varied algorithms, scene/scanning parameters, instruments and the

consequent inconsistencies in DBH estimate residuals within the literature. They evaluated the benefit of integrated scans with a large robust dataset; finding elevated accuracies where multiple scans captured more of the stem circumference, to the point where specifics of the algorithm became less influential. The article also demonstrated that point cloud noise increased DBH errors; which was mitigated by a linear fit of diameter profiles. This SLP study supported the authors' sentiments as a significant negative association was found between the magnitude of DBH error and stem coverage. With reference to the studies cited in Pueschel et al. [154], as a selection of those with robust sample sizes, the RMSE produced in this study was consistent with the better performing approaches, being marginally surpassed by Mass et al. [175] (1.5cm) and Pueschel [154] (<1.2cm).

Of the previously published algorithms within the sampled literature, the one applied here appears to be most similar to that of Adams [167], which also applied minimum distances with azimuth bins to model tree stems and overcome limitations of least squares circle fitting in instances where scan integration is not optimal. However, in the case of Adams [167], the resulting points were used to build a smoothed non-circular, dynamic diameter stem model. In such a case however, deviations from circularity may be more representative of misaligned lidar scans rather than growth form.

The relationship between the TLS DBH estimates and traditionally measured diameters clearly took a linear form. The linear fit model suggested that the TLS DBH was biased by 3%. The scale dependency of the bias is explained through the modeling approach and bark fissure depth. Because the approach uses minimum distances to a stem center, the circumference points tend to occur at the deepest points of bark fissures.

Therefore, with fissure development there is a divergence between tape-measured and TLS measured DBH. The additive bias in the individual model was not easily explained and it is unlikely that bark structure could explain the significant intercept, given the smooth surfaces of very young trees. It is suggested that either, or a combination of the following is responsible for the offset bias: point cloud noise, the particular sampling bias and annual incremental growth. Given there are few young small diameter stems, perhaps the true scale of fissure depth change with diameter increment is not captured well for these small diameters. Another viable explanation for the significant intercept is the annual growth increment that had occurred between the field measurements and the TLS survey. It is therefore, recommended that this application of TLS span a variety of age classes without a measurement lag between traditional and TLS DBH measurements; this may provide a more complete understanding of the sources of TLS DBH biases.

Within the scope of deriving forest productivity from remotely sensed datasets, the process detailed has been sufficient to derive stem diameters. The ALS/TLS provides an opportunity to physically model individual tree volumes and repeated surveys will indicate the repeatability of the application, but more significantly will provide a means for quantifying forest structural dynamics including variations in growth increments and thus productivity. Supplementing this forest structural survey with AIS will indicate whether crown chemistry, accessible through spectroscopy, truly reflects the physiological state of the forest.

The intensive field campaign in support of an ALS/AIS acquisition incorporated a ground control survey and terrestrial lidar. The TLS offered the opportunity to derive stem maps and tree morphological attribution. The accuracy of DBH retrieval was

assessed against traditional diameter tape measurements. Statistical analysis applied to a large dataset of 1,189 stems, with a diameter range from 5.3-49.8cm and stem densities from 550-3,125 stem/ha, suggested accuracies that are comparable to the better results found in the literature [148], [154]. Simple linear regression produced an RMSE of 1.6cm and R^2 of 0.95 for an individual stem model and an RMSE 0.4cm and R^2 of 0.99 for a plot average model. Significant residual covariates were identified as scan integration fit metrics and stem point coverage, although these attributes explained very little of the overall variation in residual errors (<10% individual model and ~20% plot model).

It is hypothesized that the success of this study is attributed to the relative simplicity of the scene. Understory regeneration was infrequent but produced greater residual variation and omission errors. In addition, relief within the study area is small, reducing the likelihood of errors attributed to poor ground representation. Distortions in stem morphology associated with slope gradient are minimal in this study (*i.e.* sweep, lean departures from circularity). The modeling approach performed best in circumstances with high point density and complete stem coverage, but was not adversely affected by low ranges of either attribute. The approach tended to perform poorly in conditions where stems deviated from vertical, instances of poor scan integration, or high noise levels or in initial spatial cluster omissions/stem commission errors (Fig. 5.12 & 5.13). In light of these observations, the slightly more complicated approach of least squares cylinder fitting taken by other researchers appears to have little benefit over the geometric approach used here. The obvious exception is, as noted by Brolly and Kiraly [162], that stems with considerable lean and or sweep would be better characterized in a shape primitive fitting approach.

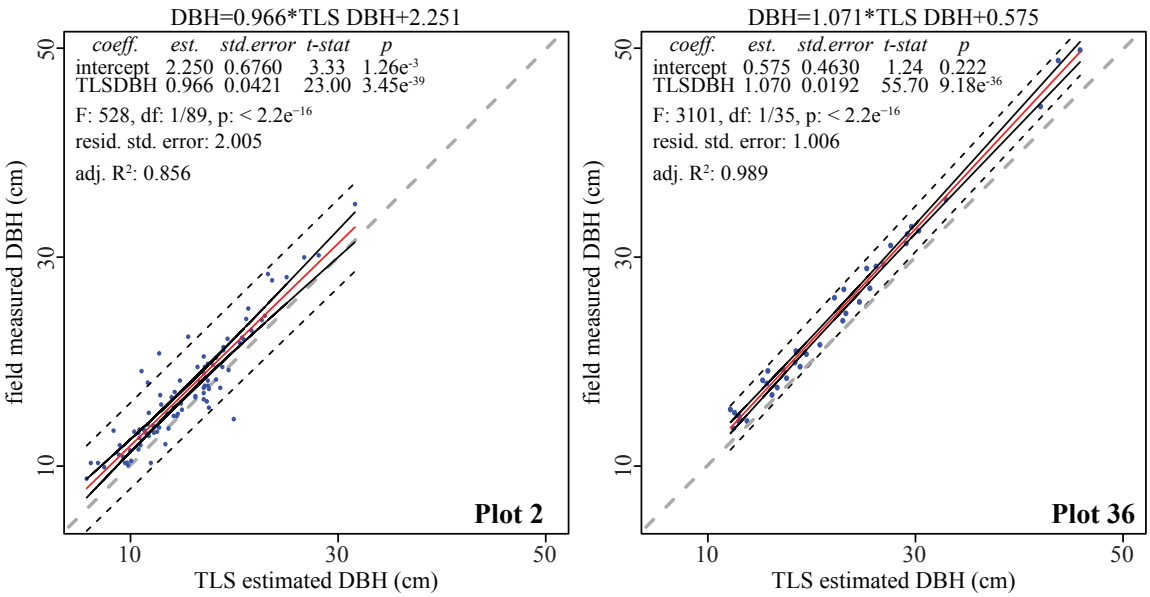


Figure 5.12 a: Poor DBH estimates tended to occur in plots with poor scan integration and high stem densities. Plot 2 had the weakest scan integration and the greatest stem density with developing understory and produced the weakest fit of all plot based regression models. b: The strongest plot based model was produced for plot 36, which had a stem density of 1400 stems/ha. It is suggested that the range of DBH values, which is the largest of all plots and particularly the three large stems ~45cm, contributes to its strong model.

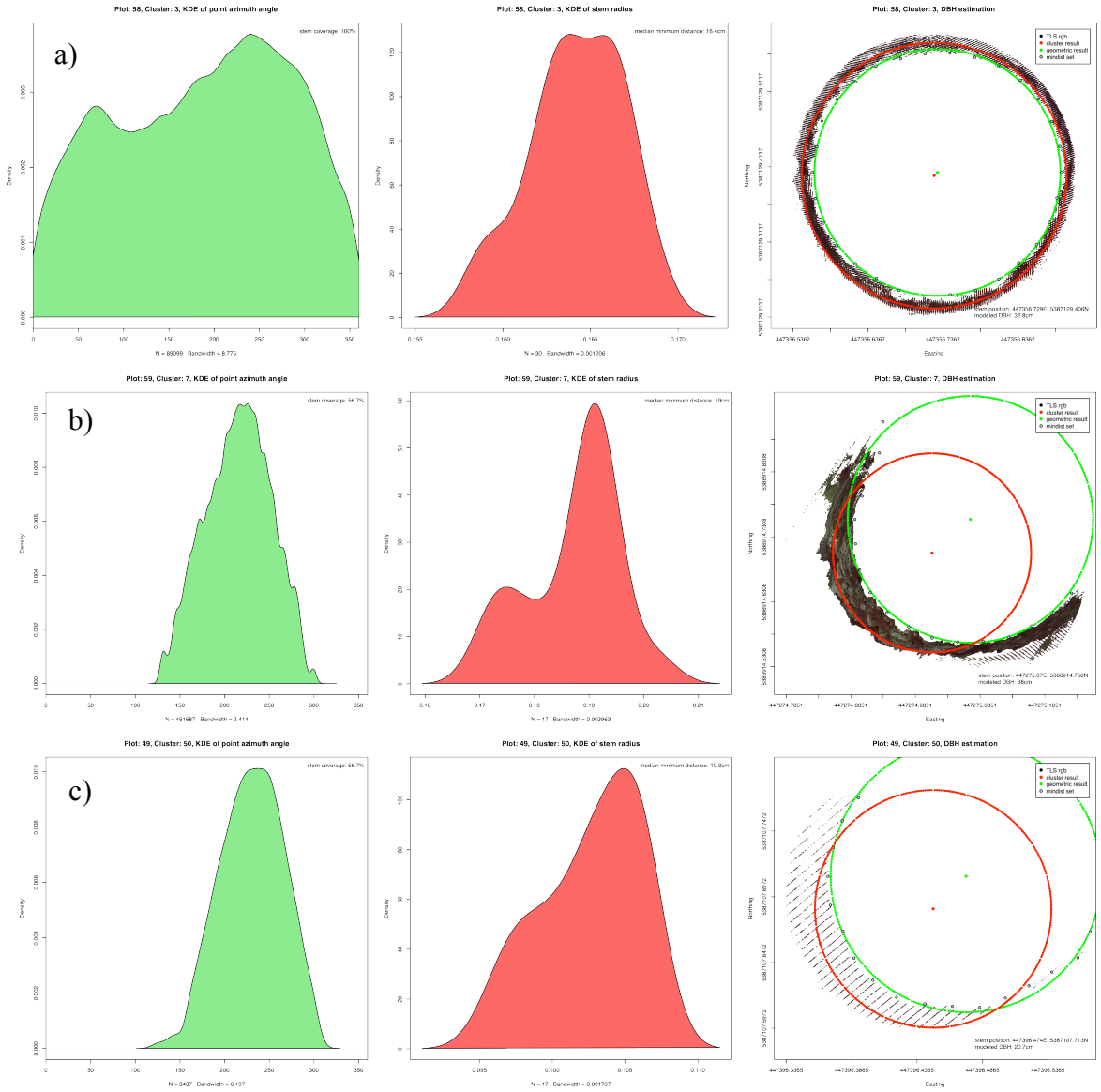


Figure 5.13 TLS point clouds of stems used for DBH measurement. Stem attribute were derived from information on stem coverage distributions (green) and minimum radius distance distributions (red). Clustering approaches (red point and circle) did not produce sufficiently accurate results. A strategy considering orthogonal transects and minimum distances from pseudo center position to stem circumference improved DBH modeling. This strategy performs well under conditions of full stem coverage and high point densities a), or partial coverage high point densities b), or partial stem coverage and low point densities c).

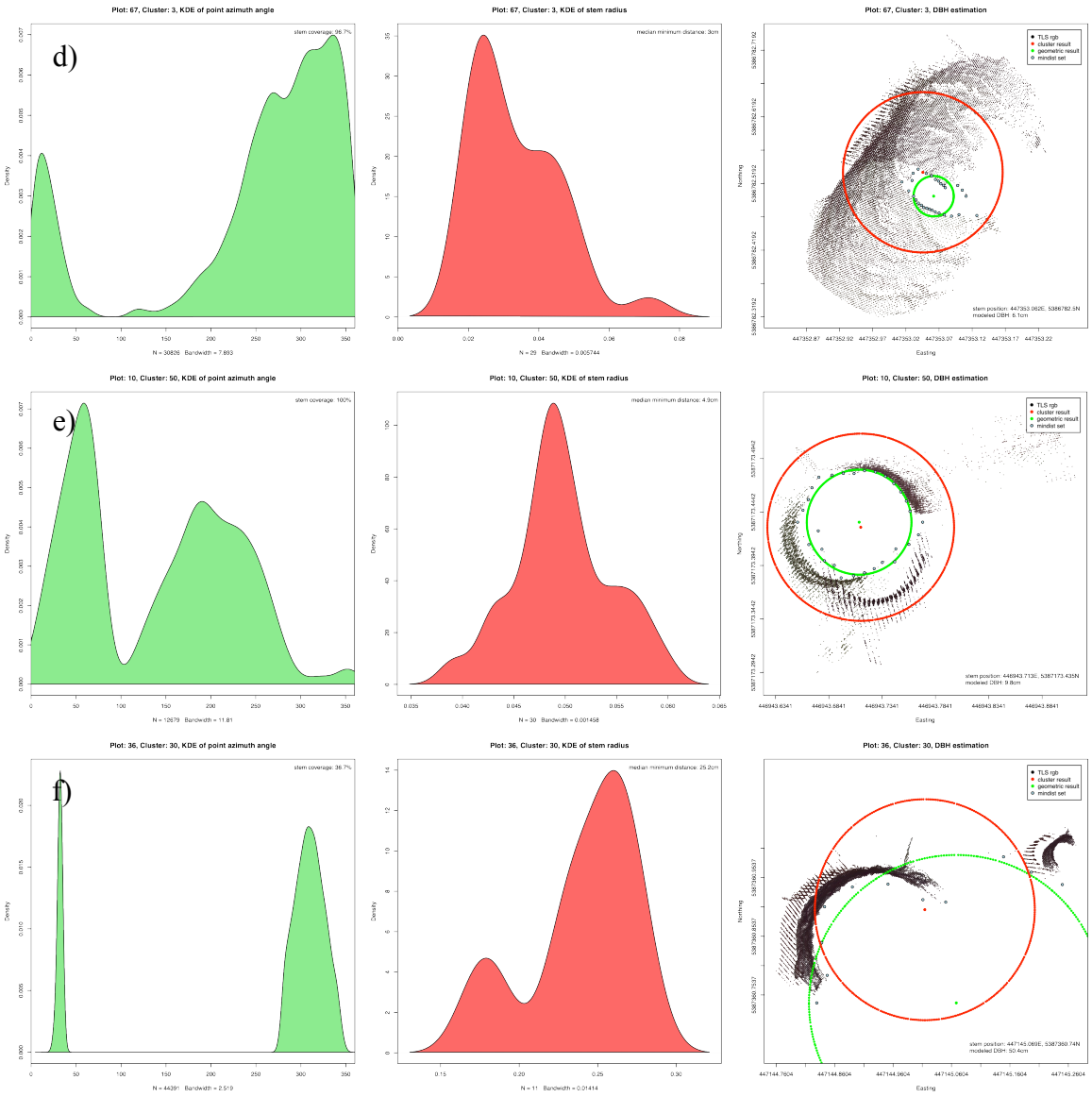


Figure 5.13 cont'd: The developed strategy estimates DBH poorly under conditions where stems have significant lean or sweep d), obvious scan misalignment e), incidences where clustering failed to isolate individual stems f).

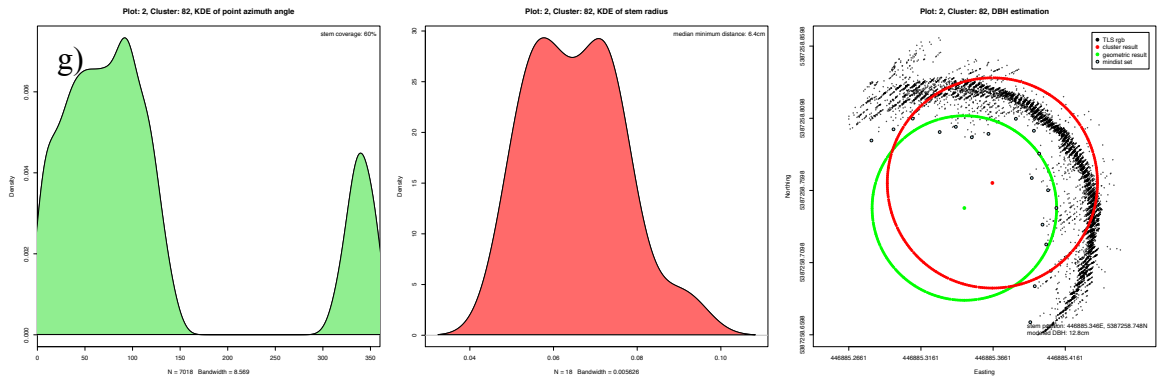


Figure 5.13 cont'd: The developed strategy estimates DBH poorly where random point noise is abundant g).

5.2 Extracting Height to Live Crown and Bole Parameters from TLS

The full resolution TLS point cloud was binned into 0.25x0.25x1m (x,y,z) volumetric pixels (voxels). A voxel tiff file was populated with the calculated point density values. The voxel file was then used to trace the horizontal trajectories of each stem with changing height. Concurrent with stem tracing was the derivation of HTLC. Beginning with the 3-dimensional TLS stem positions and a 0.75m neighbourhood definition, the voxel files were queried. For each height slice greater than the DBH elevation, the stem position was adjusted. With each height increment (slice) in the voxel file, the stem position was migrated from its position in the previous slice to the voxel with the highest point density in the current slice, given the search radius neighbourhood. With the adjusted position and neighbourhood, the areal gap fraction was computed (1-(occupied voxel count/neighbourhood voxel count)). The areal gap fraction profiles were plotted along with their first derivatives. The elevation of the live crown per tree was determined from the gap profiles, where the highest local minimum (maximum negative) in the gap fraction derivative profile was interpreted as the transition from high gap stem or stem and non-productive woody twigs to low gap productive crown. The ground elevation was

extracted from a 1m gridded representation of the TLS ground points. The HTLC estimates were then calculated as the difference in the elevation of the local minimum gap fraction derivative at the horizontal position of the projected stem and the 1m TLS BEM at the horizontal position of the DBH seed. In order to determine the crown density profile, the stem needed to be resolved. The voxel raster stack was used for this purpose.

The individual tree stems were resolved, and vertically traced within the TLS voxel data by flagging the higher density voxels per height bin. The logic behind the definition of the stem was that stems should have high gap fractions that are consistent with height increments. From the gap derivative profiles (dGapF), data were selected that had less than 20% change (dGapF: -0.2 to 0.2) between height iterations. This would identify vertical bins that were adjacent and consistent in terms of their occupied areas. Vertically contiguous selections (without missing bins in the above selection) were grouped together and the lowest grouping was selected as representative of the stem. In order for the stem to be characterized as captured, the following criteria needed to be met: at least two consistently low gap fraction slices at low elevations were selected in the above, the minimum height in the stem trace needed to be lower than the minimum gap fraction above DBH (lower height than the maximum canopy closure). From the stem data two linear best-fit models were used to generalize the stem trace into a linear three-dimensional trajectory, in other words easting and northing were both linearly described as a function of z. The stem lean was then computed as the angle in degrees from vertical to the generalized stem trace. Finally, individuals with leans greater than 10˚ were flagged. A total of 22 individual stems were measured as having significant lean (>10˚), 13 of which were not identified as core sample trees and are therefore likely to represent

reinitiated trees since the treatments were applied. The identified leaning stems tended to occur in the two highest stem density plots, where 41% (9/22) occurred in either plots 2 or 21. These two plots contain 125 (3125 st/ha) and 118 (2950 st/ha) stems respectively. The next highest density plot (16) had only 87 stems (2175 st/ha). When the identified leaning stems were ranked by mean gap fraction, the correctly identified leaning stems were concentrated at the upper range. Where gap fraction was low, stems were more occluded by understory regeneration, which appeared to inflate lean estimates. There were four stems that were confidently (mean gapF >0.65) identified as leaning (plot:tree:lean, 67:141:23.0, 59:167:10.0, 21:195:12.1, 21:234:11.4) and five other identified that are likely affected by occluding understory vegetation (5:268:10.3, 2:305:15.6, 2:98:18.5, 21:26:20.6, 54:32:10.0). Conceptually, high occlusion of low gap stems would increase the likelihood that the high point density stem trace would alternate between stem aspects (based on multiple scanner position) and shortening the vertical section used to estimate the lean angle. In the stem trace generalization, the effect could erroneously imply a lean within the stem. However, depending on the resolved stem length, the magnitude of this error could be below the selection criteria of 10°. In the best case scenario, a vertical stem with a 50cm DBH in an unobstructed scan might capture a tall HTLC of 25m, the resulting incorrect lean would only be ~1°. Conversely, in a highly occluded condition and applying the minimum criteria for stem identification, whereby two vertical bins are required, a 50cm DBH across a 2m height interval would produce an incorrect lean angle of ~14°. When individual stems of trees with mean gap fractions less than 0.65 were omitted, the remaining individuals seemed reasonable when qualitatively evaluated against the voxel animations. However, only 3 of the detected 9 core stems had

associated field remarks in 2012 that suggested the stem had any degree of lean or sweep. Of the plots sampled, the 2012 qualitative field data suggested there were 61 stems with deviations from vertical and whose terminology ranged from minor sweep to severe lean. With the locations of stems and their approximate trajectories into the canopy determined, efforts were refocused on structural attribute estimation.

The first iteration of modeling HTLC applied the minimum slope in the gap fraction profile, or the steepest decrease in gap within the binned height profile. Although there seemed to be some observations where the TLS HTLC agreed with the field measurements, especially in the higher HTLC values, most of the data was severely underestimated by the minimum slope in the gap profile (Fig. 5.14 & 5.15). Analyzing the voxel data and the gap profiles, suggested that frequently, the minimum delta gap occurred at the height where dead limbs remained, left by the upward movement of live crown with crown development.

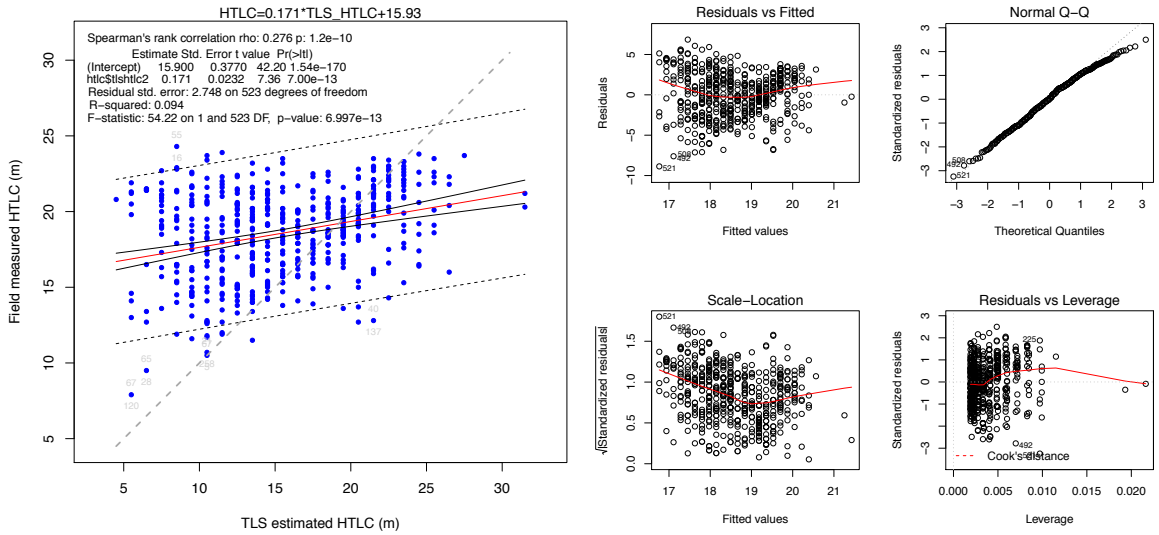


Figure 5.14 Estimating HTLC from areal gap fraction profiles. HTLC was estimated as the height difference between the minimum height bin and the height of the bin with the maximum decrease in areal gap fraction. This first modeling iteration severely under estimated HTLC in the lower range of the data.

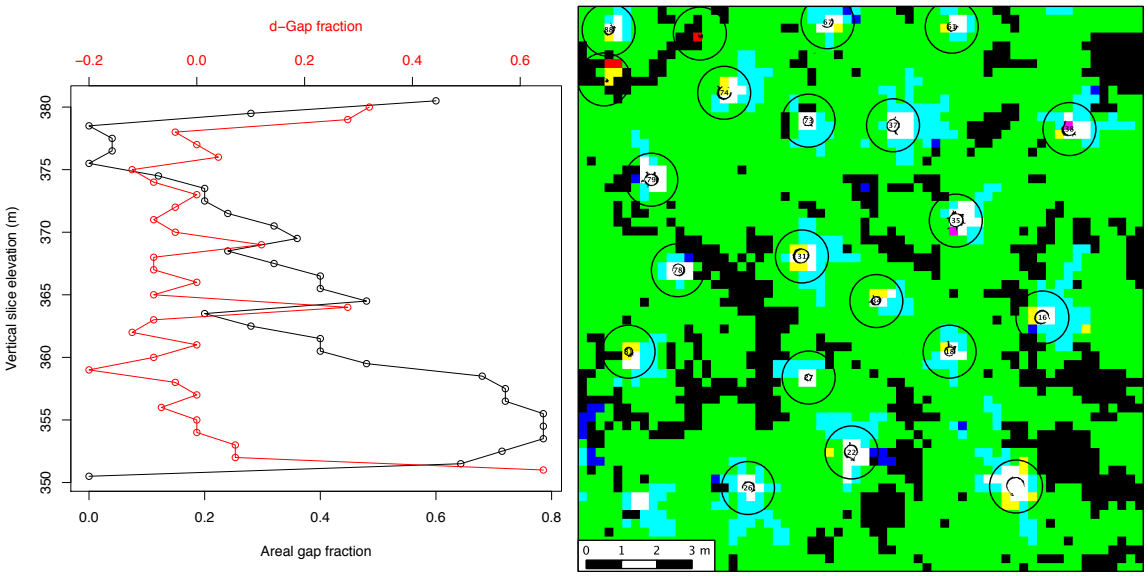


Figure 5.15 The maximum negative slope in the delta gap profile under estimated the HTLC as it was sensitive to remnant limbs still attached to the bole but no longer photosynthetically active. The voxel file was used to query vertical slices to determine an appropriate strategy for HTLC detection. Gap and delta gap profiles are illustrated for tree 16 in plot 55 with a field measured HTLC of 24.3m (~374.3m elevation). A voxel composite image is displayed in the right panel as RGB: height bin 7 (354m), 28 (375m), 12 (359m). The selected height bins correspond with the maximum gap fraction, minimum gap fraction and the maximum decrease in gap fraction respectively. These height levels appear to correspond well with heights representing the stem (white), crown (green) and remnant limbs (cyan) respectively.

Therefore, the maximum negative slope was not considered an appropriate metric to use in HTLC estimation. Based on observations of gap profiles and the voxel height data, a local maximum negative gap fraction derivative metric was considered. The altered estimation approach was rationalized by the realization that in relatively closed canopy stands, the HTLC would occur just below the height of maximum areal occupation (minimum gap fraction), that is the lowest whorl of photosynthetically active limbs would tend to be the longest, although depending on needle retention, they might not be the fullest, the augmented strategy became to find the minimum gap fraction derivative just below the minimum gap fraction. In addition, the HTLC precision was

increased by extracting the 1m TLS BEM TIN floating-point values rather than the voxel 1m bin interval.

From these data, three lower crown definition values and three ground representation values were produced for a total of 9 combinations to explain HTLC. The three crown metrics were the minimum gap derivative (representing large decreases in gap with vertical increments), minimum gap fraction above breast height (representing the height of maximum crown closure) and the local minimum gap derivative (representing a transition from high to low gap that occurred below the height of maximum crown closure. Ground definitions included the TLS BEM TIN values, the minimum height bin slice with point occupation given the tree location and the neighbourhood definition, and the slice height of the minimum gap fraction below breast height.

Of the nine combinations, the most accurate HTLC estimate was produced by the difference of the height of the local minimum gap derivative and the height of the minimum gap below breast height. These estimates had a median error of +0.45m, the magnitude of which was finer than the height resolution of the TLS HTLC metric given a voxelization height bin of 1m (HTLC+/- 2m). Although this approach may produce the smallest error bias without calibration (linear regression), the errors were not the least variable, it was possible that after a linear fit, the metric would not be the most accurate of the evaluated metrics, especially since a constant error only model was sought. The approach that produced the least amount of spread in the errors was that produced by the HTLC estimates from the local minimum delta gap and the TLS BEM surface (Fig. 5.16). This result was expected given the finer precision of that metric, which was offered by

the ground definition over the coarse height binned voxel ground definition. Relative to the first HTLC model iteration, the local delta gap approach produced encouraging results (Fig. 5.17), however considerable error within the estimates remained. The approach taken that assumed only a constant error resulted in a non-constant residual, such that the error was negatively associated with measured HTLC. The inclusion of both the scale and constant terms entirely resolved the residual trend. However, the resulting linear model appeared to deviate from the bulk of the observations especially in the upper range of HTLC (Fig. 5.18). The constant only term was considered superior for transferability purposes. The source of the remaining HTLC error was not resolvable using any combination of the physically modelled metrics derived.

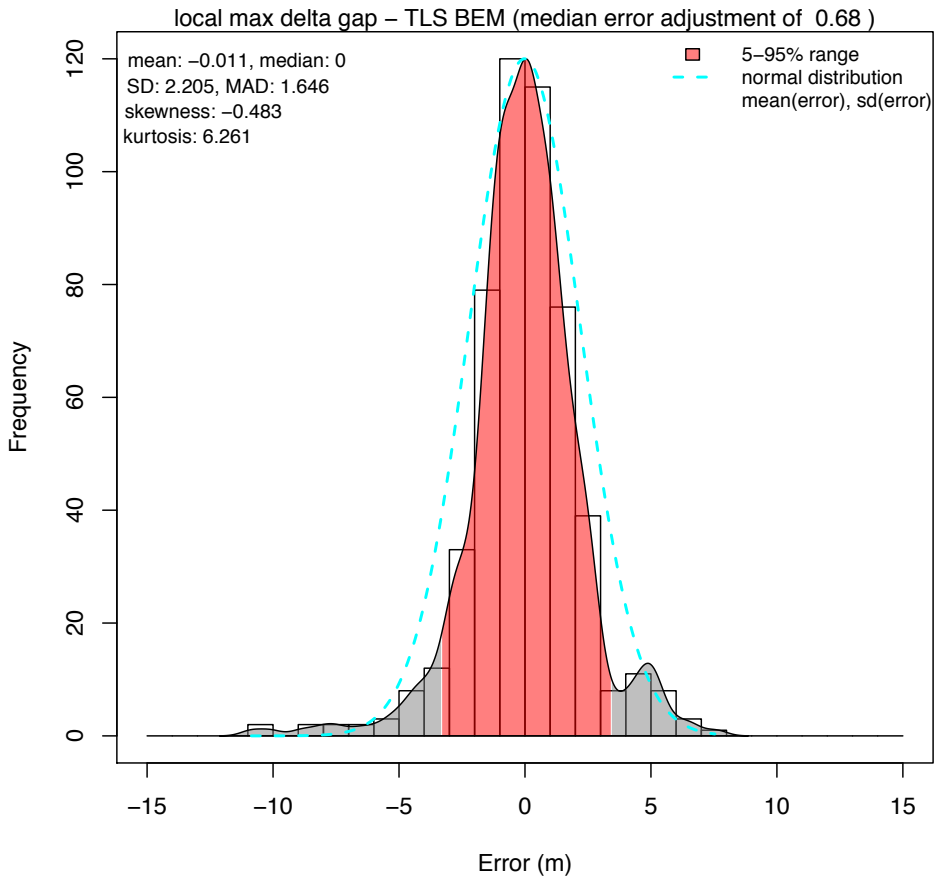


Figure 5.16 HTLC measurements by TLS areal gap fraction profile and BEM ground height produced a median error of 0.68m

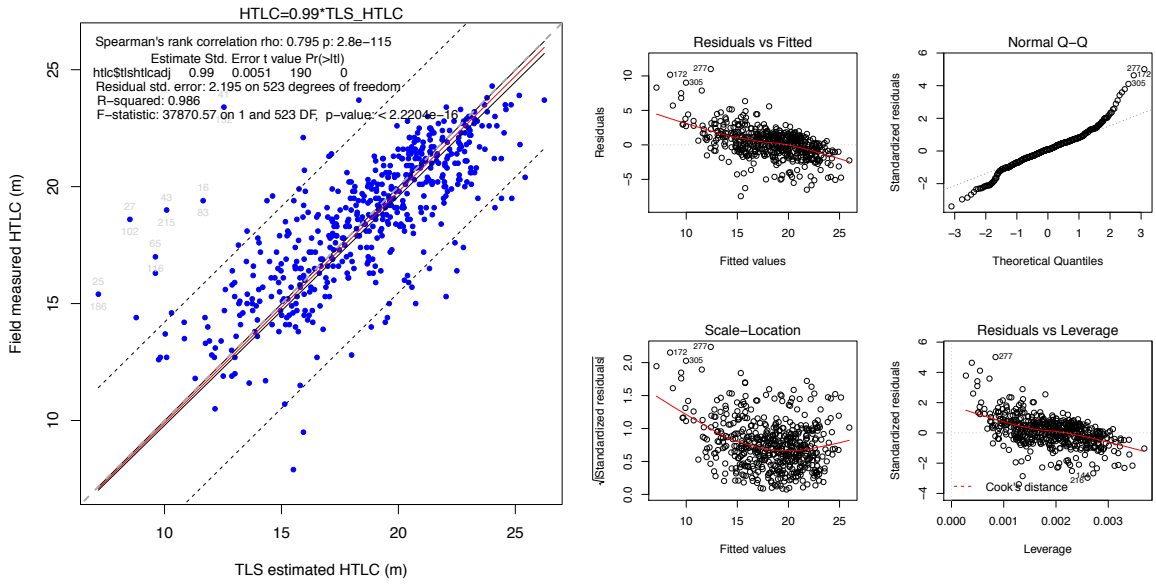


Figure 5.17 Estimating HTLC from areal gap fraction profiles. HTLC was estimated as the height difference between the local minimum gap fraction derivative and the BEM height. The metric was built to physically capture HTLC measurements and was only expected to contain an error constant, which was estimated as the median error 0.68m. The error constant was removed and a linear regression without an intercept was used to determine if the scale of the HTLC error was vastly different from one. Although the linear regression suggested a best fit of one, there remained a trend in the residuals that tended to decrease the residual with increasing HTLC.

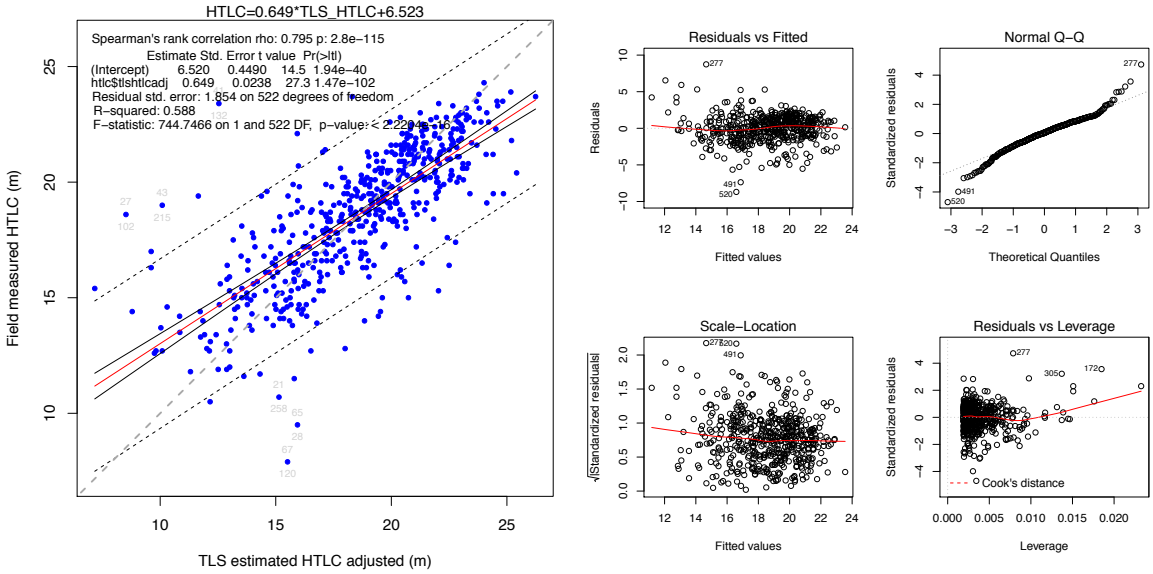


Figure 5.18 Estimating HTLC from areal gap fraction profiles. HTLC was estimated as the height difference between the local minimum gap fraction derivative and the BEM height. The metric was built to physically capture HTLC measurements and was only expected to contain an error constant, which was estimated as the median error 0.68m. The error constant was removed and a linear regression without an intercept was estimated. The residuals were negatively associated with measured HTLC, including a constant term resolved the residual trend. However, this result was interpreted as spurious and dependent on a cluster of large residual errors with low TLS estimated HTLC.

In an effort to reduce the error in HTLC estimation, additional attributes were produced that were expected to influence HTLC. Given the influence imposed by neighbouring crowns on resource availability it was expected that metrics capable of capturing the competition status for each tree might explain some of the variation in crown structure. Whether by the effects of competition, or simply a characterization of stand development status, social position metrics were expected to be associated with HTLC measurements. Therefore, a number of neighbourhood attributes were extracted from the point cloud data. Social position attributes included the distance to the nearest neighbour stem and the mean distance to the nearest eight stems (two sampled per cardinal quadrant up to a maximum of 6.5m) were determined. The maximum distance

threshold was defined to allow the most solitary tree in the dataset (tree: 5, plot: 67) to have at least one neighbour. Since the relative size of the neighbours was expected to also inform on either the relative age or suppression status of the target tree, the TLS-DBH of the nearest neighbour and the mean TLS-DBH of the K-NN trees were taken as attributes that could be associated with measured HTLC. The number of identified neighbours given the selection conditions (2/cardinal quadrant and <6.5m) was also retained as an intermediate predictor. Boundary trees presented a restriction for the spatial attributes used in the prediction of HTLC. The trees that had adjacent stems that were not captured in the data and for which neighbourhood attributes were impossible to determine, were classed as boundary trees. Therefore, when building the empirical models, the boundary trees were omitted from the analysis. Boundary trees within each plot were identified as those that were missing stem membership in any one cardinal direction irrespective of distance. Conceptually this approach would leverage the relationship between the proximity and relative size of the neighbours, where small DBH surrounded by large DBH trees would likely have low HTLC (if shade tolerant regenerating individuals), and trees with close proximities tend to be earlier structural development stages and thus lower HTLC. The multiple regression used all the derived attributes in a stepwise linear regression with AIC model selection. The stepwise regression selected the following features as significantly explaining variation in the HTLC at the individual level: four gap fraction profile metrics (height of the local minimum gap fraction derivative, the height of the minimum gap fraction above breast height, the height and magnitude of the minimum gap fraction below breast height), installation year, fertilization treatment, the TLS DBH and two neighbour metrics (the DBH of the nearest neighbour and the mean

DBH of all stems within the neighbourhood). This overly complex model explained 74% of the variation in HTLC with a residual standard error of 1.47m. Although, there are justifications for the underlying relationships with each of these selected attributes, the volume of data may not support the number of selected features. In backwards selection mode via significance value, and with a limitation of a maximum five-feature model, the resulting model included three gap fraction profile metrics (height of the local minimum gap fraction derivative, height of the minimum gap fraction above breast height, height of the minimum gap fraction below breast height), the plot establishment year and the TLS-DBH. The directions of the coefficients were logical; where the metrics represented the height of the base of the crown, the coefficients were positive. Conversely, the height of the minimum gap below breast height was negative and roughly twice the magnitude of the coefficients of the two metrics representing the height of the crown base, the product being approximately the HTLC. The installation year coefficient was negative implying that the later the treatment was applied the lower the canopy base would be (likely capturing the low crown heights of the open plots 65 and 67 installed in 1987). These plots would have had proportionally less time to produce more advanced structural development traits, but more likely depict crown architectures that are typical of open grown stands. Lastly, the TLS-DBH was a positive coefficient, which is logical in that the larger stems are more likely to exhibit more advanced structural stages in closed canopy stands, the exception being in more open grown plots. The MLR model produced a median bias of 0.97m and a standard residual error of 1.51 on 516 degrees of freedom. The MLR model explained 72% of the variation in HTLC (adjusted R^2), and produced an

F-statistic of 275.5 ($p<0.000$). All the coefficient estimates in the MLR were significant ($p<0.000$).

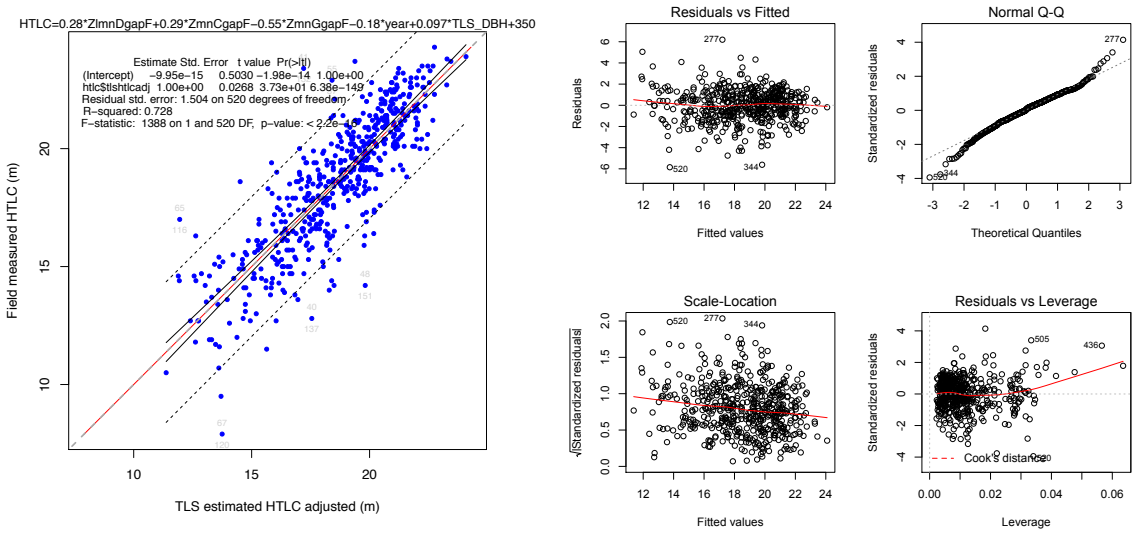


Figure 5.19 Stepwise linear regression with a maximum of five features was used to estimate HTLC and produced marginal improvements over the simple regression model. The highly complex model did not seem warranted although the residuals were much better behaved and the coefficients and features selected were reasonable.

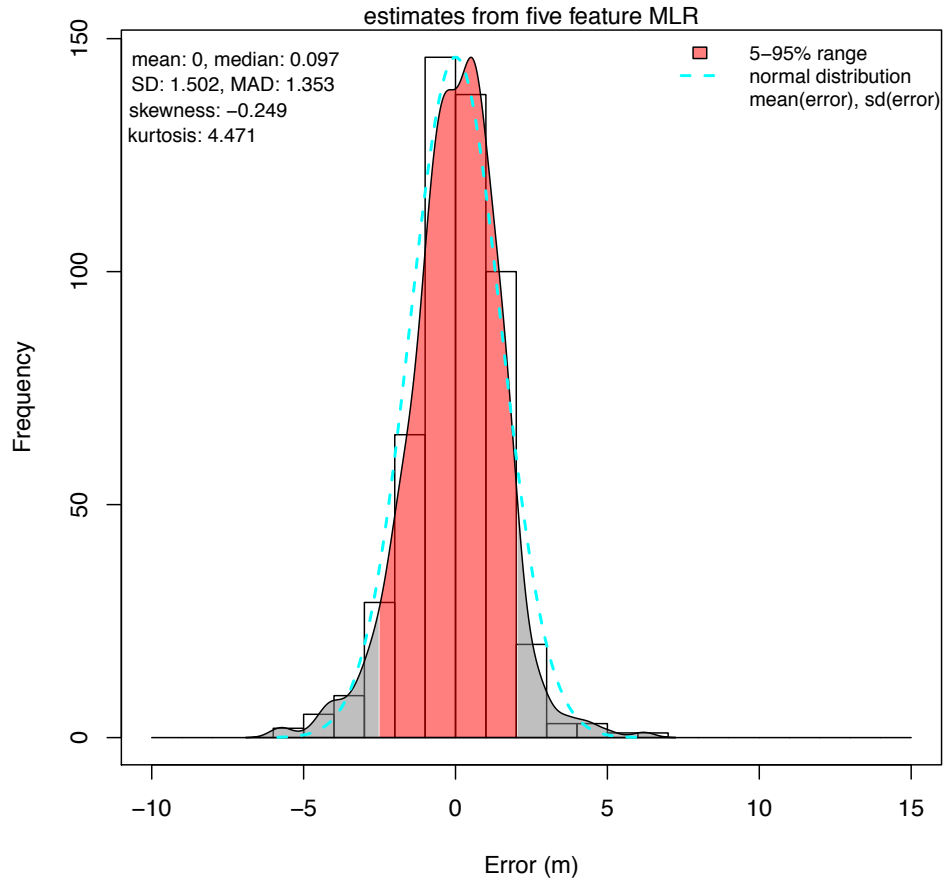


Figure 5.20 HTLC estimates from the MLR produced a median error of 0.10m

Ultimately, the empirical model produced from the MLR of both social and crown attributes produced the most accurate estimates with a residual standard error of 1.515m. However, the considerably more complex model yielded only marginal improvements over the others, even the simplest models (i.e. standard error of 2.195m from the difference of the height of the local minimum areal gap fraction derivative and the TLS BEM). The simple linear model produced from regressing the difference of the local minimum areal gap fraction derivative profile and the TLS interpolated ground with the field measured HTLC was selected as the superior HTLC estimator. The form of the HTLC model was HTLC= 0.99*(height of the local minimum areal gap fraction derivative below the maximum canopy closure-the interpolated ground classified lidar

points-0.680m). However, it is quite likely that the 0.99 coefficient produced is an artefact of the measurement and sampling bias, which if assumed the model might equivalently be HTLC=(TLS-HTLC)-0.68m. The offset term is interpreted as the result of the integrated effects of point cloud generalizations and field measurement bias/protocol. It was expected that most of the bias contributing to the offset term might be caused by the specificity of field HTLC measurements with the presence of incompletely vegetated whorls of limbs below the crowns and the overly simplistic voxel gap fraction approach. This perspective was reached through investigating the initial HTLC errors with reference to plot and treatment conditions (Fig. 5.21). Visualizing HTLC errors demonstrated that 57% of the observations had errors greater than one meter, thus it could not be concluded that the sole confounding condition in HTLC extraction was the precision of the vertical height binning in the point cloud voxelization process.

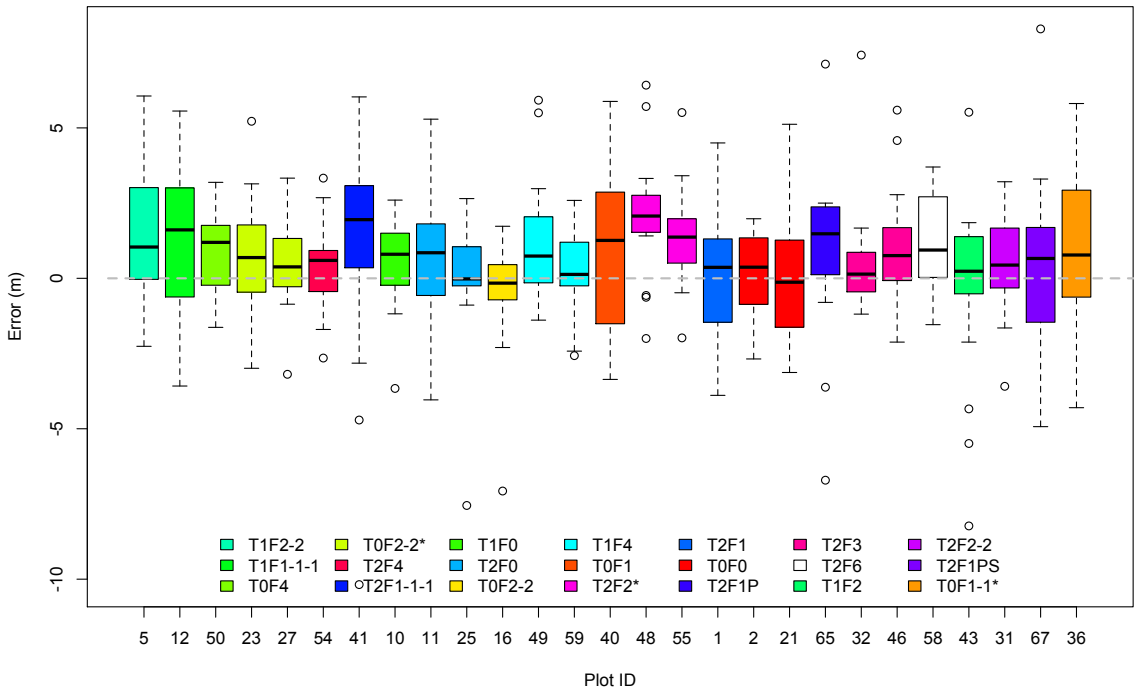


Figure 5.21 HTLC errors from local minimum areal gap fraction derivative grouped by plot and treatment. It was expected that errors might be specific to treatment types, where greater thinning and fertilizer would promote early growth and perhaps less remnant non-photosynthetic limbs, in which case the minimum gap fraction derivative without reference to the maximum canopy closure would be the better parameter used. The plot does not suggest a strong treatment effect is present.

5.3 Extracting Individual Tree Height and Crown Length

Two strategies were used to retrieve individual tree height measurements. One typical approach relies on the apical dominance of crowns and an airborne lidar sampling. In this case, the point cloud is generalized to a 2D raster that is populated with the maximum lidar point height after an initial topographic normalization process. Therefore, for crowns that are three times the spatial resolution of the CHM grid, a local maximum kernel will identify the treetops. This approach typically performs well for emergent and dominant crowns where parameters are appropriate (local neighbourhood), but has the tendency to produce severe commission errors when parameters are too fine scale. The second approach leveraged the previously resolved stem maps to extract heights at the

TLS-stem positions from the CHM. The limitation of this approach is that it does not consider the relative size of the stem and therefore small reinitiated or suppressed stems that comprise the suppressed and intermediate tree layer are greatly over estimated, this condition was evident in height residuals that were correlated with DBH. A DBH mediated modification of this approach yielded better results, where treetop searches were stratified by DBH.

The local maximum filter has been widely applied in mapping treetops. However, quantitative validation data are consistently lacking. Parameters for the treetop detection include the matching of a kernel size or neighbourhood for the maximum height search and the height of the kernel center. This approach is intended to combat the trade-off of commission errors for large crowns when applying a finer scale neighbourhood definition. The approach is qualitatively successful in multi-age cohort stands that have a variety of crown sizes. This was evaluated against CHM grid representations rather than true stem surveys. The SLP project offered a very unique opportunity to evaluate the treetop detection approach with an accurate stem survey, however the site relative to naturally grown stands is very homogeneous in terms of structural development. Thus, it was anticipated that the height proportional neighbourhood definition would have little benefit for the SLP. The treetop extraction was performed varying the input parameters, including: CHM grid resolution, CHM smoothing and the size of the static maximum height neighbourhood or kernel. In this evaluation the ALS and TLS datasets were combined, although the majority of the CHM signal originates from the ALS as the TLS is vertically occluded in most situations (evidenced by TLS point density inversely associated with height). Two spatial representations of the CHM were submitted to the

process, a 20 and a 50cm grid, the CHM filtering included: none, mean and Gaussian with square 3 and 5 pixel kernels and finally the maximum search kernel was 3x3, 5x5 and 7x7 for a total of 24 results for the treetop detection by a top down ALS approach. All 24 outputs were evaluated for detection accuracy and quantified in terms of the omission and commission errors. A given treetop detection was considered accurate if a TLS stem was horizontally located within 1m

Irrespective of the top down treetop extraction procedure, the tree heights were evaluated based on the known position of tree stems. The CHM was sampled from the stem location and regressed with the field-measured values. The objective in this case was to derive an approximate lower limit of DBH that may still produce valid lidar height measurement. However, it must be recognized that this analyses does not apply to other more complex structures where more divergent age cohorts will have a larger impact on occlusion and omission errors.

In this analysis, DBH was considered a limiting factor for estimating tree heights. Given that the approach for treetop mapping applied a top down, 2.5 dimension data source, that is the CHM, it is conceivable and likely that vertically occluded stems that maybe regenerating or suppressed would not be accurately represented by the CHM values. DBH is associated with height, thus it was theorized that if smaller DBH stems were omitted from the analysis there would be a high likelihood that the suppressed stems would also be excluded and the linear model relating CHM height and field height would improve (Fig. 5.22). Iterating through DBH quantiles the linear regression models were built. The largest improvement occurred when observations below the 25th percentile of DBH were omitted, which corresponded with an absolute DBH of 21.4cm (Fig. 5.23).

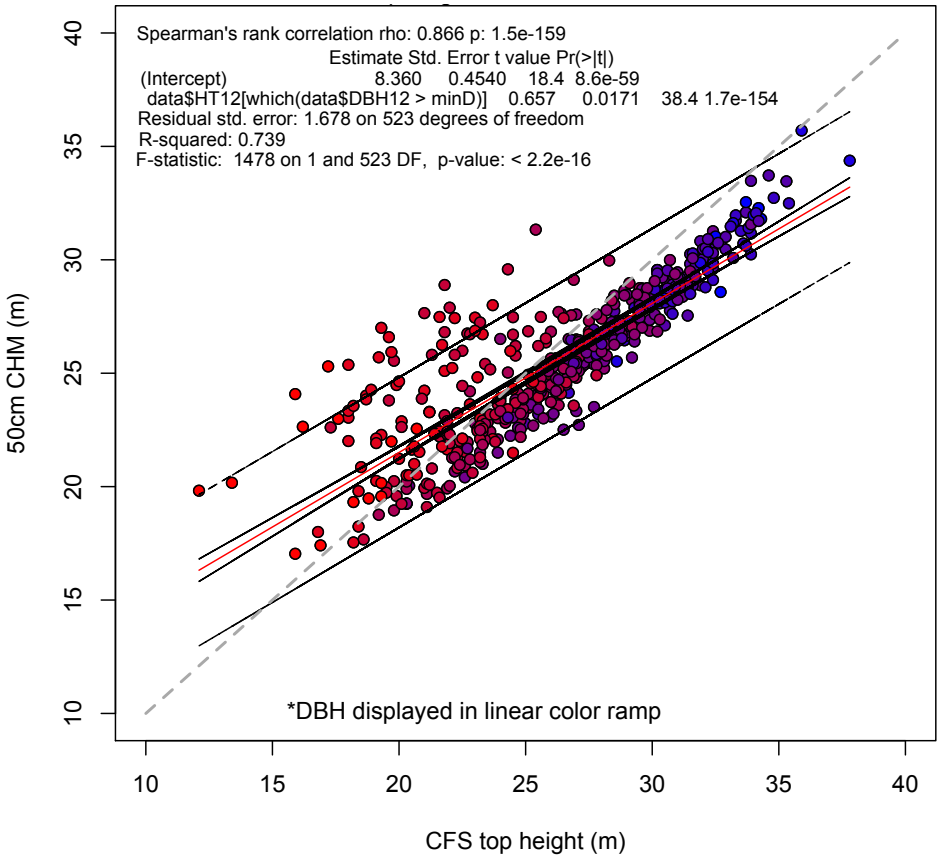


Figure 5.22 50cm CHM at TLS stem position, tree ht= 0.657*CHM+8.363

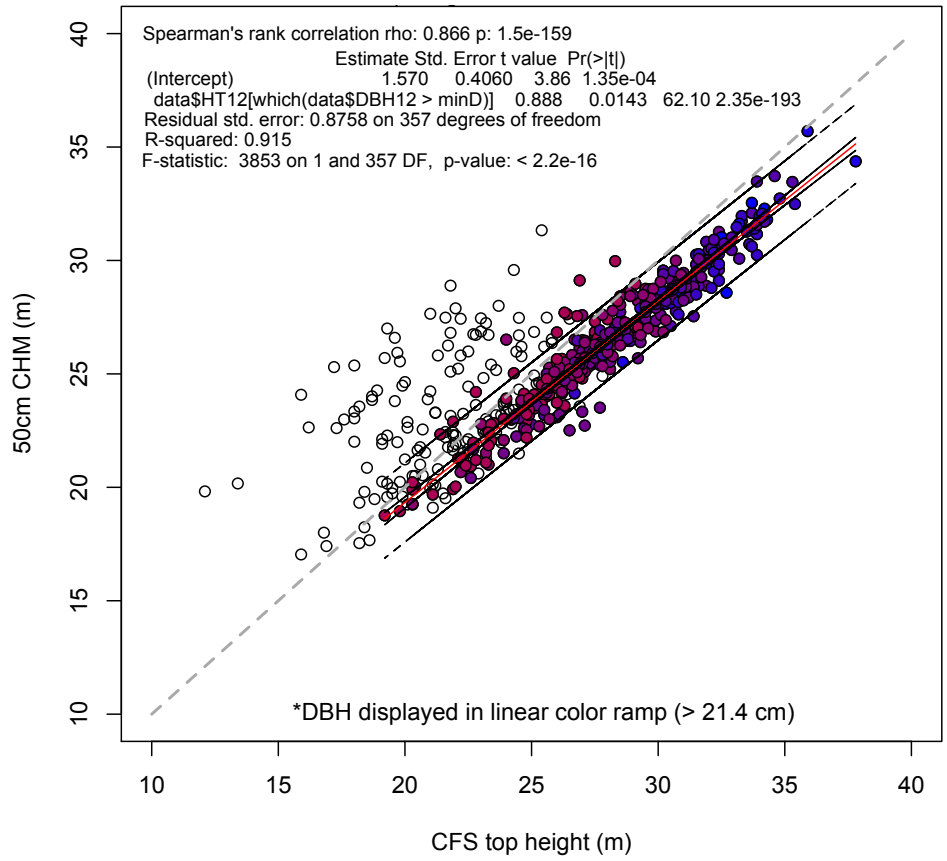


Figure 5.23 50cm CHM at TLS stem position, tree ht= 0.888*CHM+1.568, Note this evaluation was not done for prediction but rather to investigate the influence of DBH on the CHM height versus field measured height relationship. The inverted form of this model would be 2012 height=CHM*1.1261-1.7658. Open circles are omitted observations and closed circles are observations used in model building.

These results demonstrate one of two possibilities, that the smaller DBH trees have smaller and less vertically differentiated crowns that are less readily resolved in the gridded product, and/or the co-dominant tree layer to some extent, obscures the smaller trees. The reality of the objective is one of relative size structure rather than absolute. The likelihood of occlusion and subsequent omission of any given stem is related to the proximity of more prominent crowns. Thus, it is conceivable that a plot level DBH percentile threshold would be more successful than a whole sample percentile threshold.

Regression with a plot level DBH percentile threshold considered the distribution of DBH at the plots as a factor that would limit the accuracy of the height extraction. For example, the stem with the smallest DBH at each plot would not be identified in the CHM; a relative condition that is more likely true than the absolute DBH. The benefit for modeling by applying a DBH threshold would be particularly evident in natural regenerating stands and perhaps not at all evident in aggressively thinned plots. Although there was a clear trend towards an increased positive skewness in residuals with a concurrent increased in the DBH percentile threshold, there was not an apparent benefit for the plot-based percentiles over the whole sample percentile threshold (Fig. 5.24), perhaps a reflection of the low structural diversity of the treatment plots. This analysis demonstrated that after a global percentile threshold there was not an increase in accuracy with more aggressive filtering nor was there a plot level percentile that yielded superior estimation over the global threshold. In turn, these observations supported the idea that the majority of errors in the height modeling were occlusion-based rather than scale-based. These observations were interpreted as the effect of suppressed and overtopped individuals that remained in higher density treatment plots. However there remained an unevaluated positional error associated with treetop positions. It could not be reasonably assumed that the sample trees had no lean, or that residual airborne to terrestrial scanner data integration was seamless. Therefore, the treetop height modeling was evaluated through a top down analysis rather than the bottom up approach.

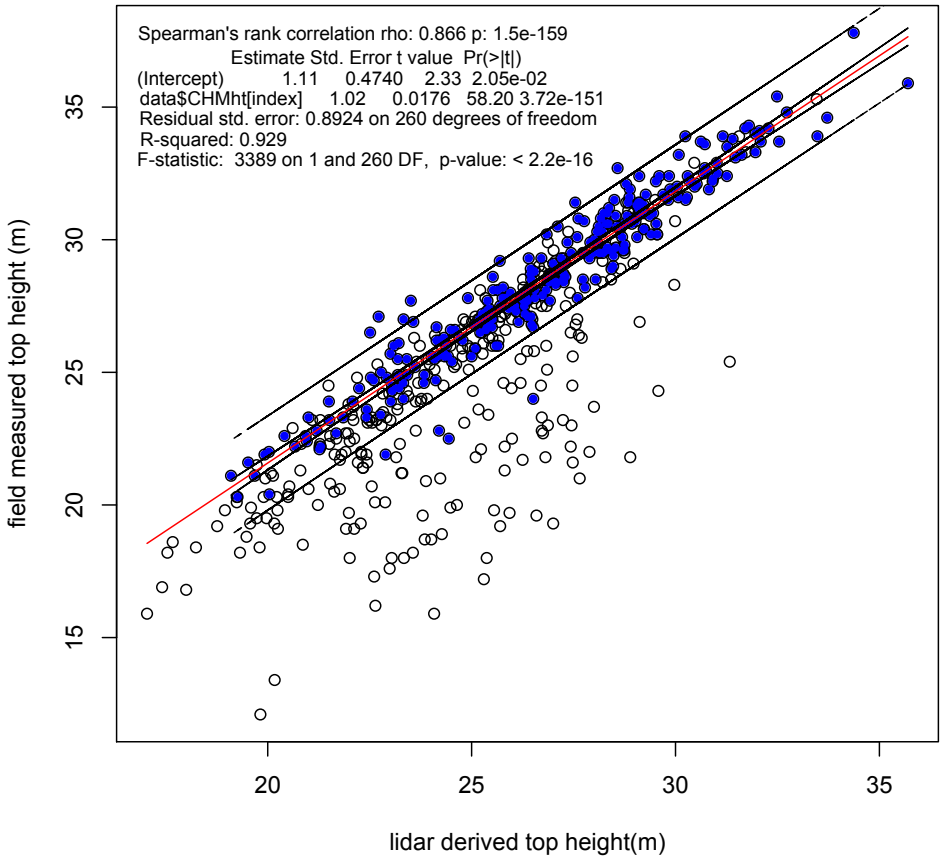


Figure 5.24 50cm CHM at TLS stem position with a plot based DBH percentile threshold filter. The plot-based percentile was used to test if the relative DBH size was a better attribute to use in explaining the occurrence of large residuals in height modeling. Even with an aggressive 55percentile filter the residual standard error was very similar to that produced with the global or whole sample percentile threshold. Open circles are omitted observations and closed circles are observations used in model building.

5.4 Individual Tree Detection by ALS

To map the individual treetops, a canopy height model was submitted to a focal maximum function filter or moving binary maximum kernel. The process considered each pixel value in relation to a user defined neighbourhood and generated a treetop position where the center pixel qualified as a local maximum. The algorithm, initially developed for application to unmanaged mature forests, includes additional parameters that help to avoid commission errors. These errors tend to occur for large tree crowns,

where deviations from conical shapes can produce multiple local maxima within a single crown. This is especially the case for old growth coastal forest stands. This option evokes separate treetop finding parameters for discrete height intervals, such that taller crowns can be evaluated with a larger kernel (neighbourhood). With high point density lidar becoming more readily available, the individual tree approaches have gained considerable attention in the research and operational forestry communities [94], [153], [169]–[178]. The treetop height regression that applied the CHM height at the TLS stem location with DBH percentile filtering supported the hypothesis that smaller DBH trees are not captured by the CHM, being a 2.5 dimension dataset (only a portion of the z dimension is captured) these smaller diameter crowns are obscured by more dominant adjacent trees. The largest reduction in height estimation performance with percentile DBH filtering occurred between the absolute DBH of 17.57 and 21.4cm, where the residual standard error was increased from 0.88cm to 1.26m. The lowest residual standard error was 0.74m which was observed with a DBH filter of >32.68cm. For reference the residual standard error estimated for the height from the DBH model was 2.31m. In contrast, the lidar treetop height from the local maximum (50cm 3x3 kernel with a 3x3 mean filter) produced a residual standard error of 1.09m, when correctly identified samples were regressed (see below).

$$Ht=1.3+64.961*(1-\exp(-0.075*DBH^{0.575}) \quad \text{RSE: 2.31} \qquad \text{[Equation 16]}$$

$$HT=1.006*TT_{50cm_3x3_mean}+0.48, \quad \text{RSE:1.09, n:252} \qquad \text{[Equation 17]}$$

$$HT_{DBH>24cm}=0.907*CHM_{at_TLS_position}+0.935, \quad \text{RSE:0.79, n:306} \qquad \text{[Equation 18]}$$

Table 5.1 Lidar treetop extraction parameters and the effect of treetop retrieval accuracy							
CHM res (cm)	Kernel size	Smoothing	Commission* (n, %)	Omission (n, %)	Detection accuracy (%)	Height error (RSE)	Calibrated Height error (RSE, R^2)
50	7	Gaus 5	66, 16.0	1170, 77.1	84.0	1.30	1.10, 0.89
50	7	Gaus 3	80, 17.2	1131, 74.6	82.8	1.33	1.16, 0.88
50	7	Mean	76, 16.7	1139, 75.1	83.3	1.33	1.17, 0.87
50	7	None	131, 25.7	1138, 75.0	74.3	1.33	1.21, 0.88
50	5	Gaus 5	79, 16.7	1122, 74.0	83.3	1.27	1.05, 0.90
50	5	Gaus 3	109, 18.8	1045, 68.9	81.2	1.29	1.12, 0.90
50	5	Mean	97, 17.8	1068, 70.4	82.2	1.30	1.12, 0.89
50	5	None	243, 31.6	992, 65.4	68.4	1.33	1.21, 0.88
50	3	Gaus 5	84, 16.4	1088, 71.7	83.6	1.25	1.02, 0.90
50	3	Gaus 3	150, 22.0	986, 65.0	78.0	1.27	1.10, 0.90
50	3	Mean	151, 22.1	985, 64.9	77.9	1.27	1.09, 0.90
50	3	None	1688, 62.8	518, 34.1	37.2	2.03	2.03, 0.75
20	7	Gaus 5	622, 46.5	800, 52.7	53.5	1.80	1.63, 0.81
20	7	Gaus 3	1166, 57.5	654, 43.1	42.5	2.01	1.95, 0.74
20	7	Mean	1122, 56.6	655, 43.2	43.4	1.92	1.84, 0.77
20	7	None	2065, 66.3	467, 30.8	33.7	1.91	1.89, 0.77
20	5	Gaus 5	1032, 54.7	662, 43.6	45.3	1.90	1.78, 0.78
20	5	Gaus 3	2851, 71.4	374, 24.7	28.6	2.13	2.10, 0.72
20	5	Mean	2251, 67.9	452, 29.8	32.1	2.11	2.07, 0.73
20	5	None	6853, 82.6	76, 5.0	17.4	2.26	2.24, 0.72
20	3	Gaus 5	1687, 63.2	535, 35.3	36.8	2.04	1.96, 0.75
20	3	Gaus 3	6085, 81.5	135, 8.9	18.5	2.28	2.27, 0.70
20	3	Mean	7542, 84.5	131, 8.6	15.5	2.33	2.32, 0.69
20	3	None	24935, 94.3	0, 0.0	5.7	2.29	2.26, 0.72
*Omission denominator is 1517 all stems within core area of selected sampling plots							

Given the large amount of processing options that were available to produce a final lidar treetop result, the parameters were varied and the results with respect to detection and height estimation was investigated (Table 5.1). The commission error rate was clearly inversely proportional to the omission error rate and the scale of analysis modified this relationship. This was particularly obvious in scatterplots of commission and omission errors, while stratifying the data space into the common algorithm parameters. This pattern was first identified while plotting errors for treetop extraction results grouped by algorithm parameters. The plotting of these error rates also helped to

identify where spurious increases in accuracies were produced not as a function of increased treetop detection accuracy but rather as a confounding condition of increased commission errors. In other words, with parameters that increased the number of detected potential treetops, the likelihood of those being associated with actual trees increased and spuriously resulted in a decreased omission error. The appropriate parameter set was sought by investigating the correlation of commission and omission errors. High commission errors were associated with low omission errors, the relationship had a linear form and displayed an obvious departure at the low commission and high omission data space region. The general trend best-fit line was determined (commission=-0.866*omission+92.0) and by stratifying the observations into suspected different clusters; the residual standard error was reduced from 4.75 to 2.39. In Figure 5.25 it can be seen that the lower red grouping produced lower commission errors than the blue observations with the same level of omission error. These findings were interpreted as the red observations capturing an appropriate omission error for obstructed or occluded and less dominant crowns (which is not resolvable by changes in CHM scale), while also applying parameters that did not inflate the commission errors. These red observations were the results achieved from the 50cm CHM raster.

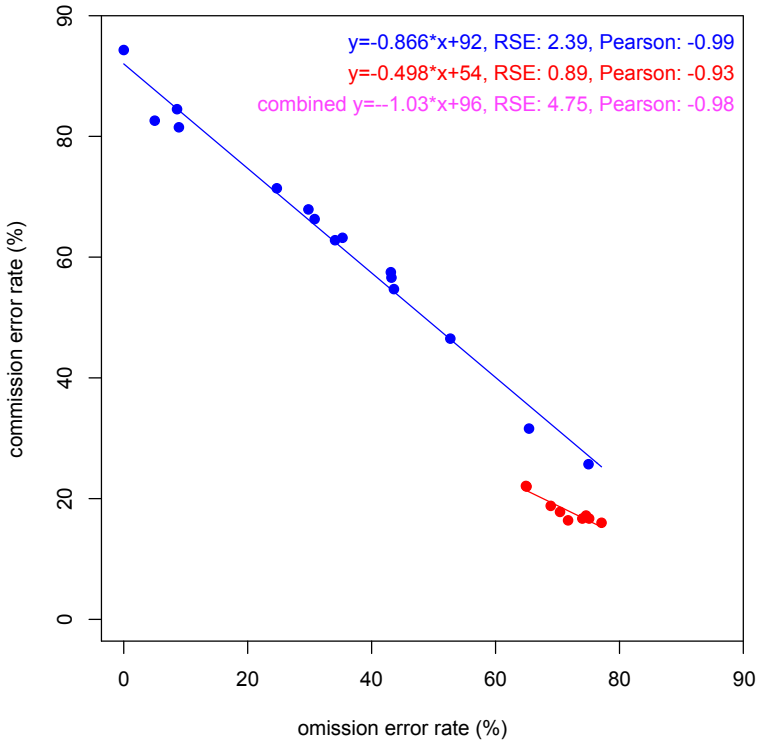


Figure 5.25 Investigating the relationship between omission errors and commission errors the appropriate parameter combination was sought.

Accuracy variations occurred in concert with changes in both kernel size and noise reduction filtering. Commission errors were inversely associated with kernel size. With attention to the 50cm CHM results, the effect of the kernel size was dependent on the smoothing approach. Kernel size had the greatest impact on commission errors where no smoothing was applied. In addition, when no smoothing was applied there was no deviation from the linear relationship established between commission and omission errors (the two blue observations with >60% omission error and commission error ~30% in Figure 5.25). Irrespective of the smoothing type, commission errors were reduced when smoothing was applied. The results produced by the smoothed 50cm CHM represented a departure from the error covariance and were considered a better solution over the other parameter combinations.

Based on the commission error and the previous scatterplot observations, the lidar treetop results produced from a smoothed (mean, Gaussian 3, Gaussian 5) 50cm CHM with any of the three kernel sizes were further evaluated. The larger spatial smoothing of the Gaussian 5x5 CHM produced the lowest commission errors and higher omission errors, while there seemed to be very little difference between the Gaussian 3x3 and the mean filter results. When these results were plotted sorted by extraction parameters, the kernel effect had a cyclical character for the omission error but a progressive one in the commission errors, where the general trend appeared to be a cyclical pattern (e.g. sinusoidal) superimposed onto a background progressive trend (Fig. 5.26). It was determined that user detection accuracy in concert with tree height extraction accuracy should govern the selection strategy, where the parameter combination that produced a result that is in line with the group of the highest detection accuracies, has the lowest omission errors of the same group and retains low

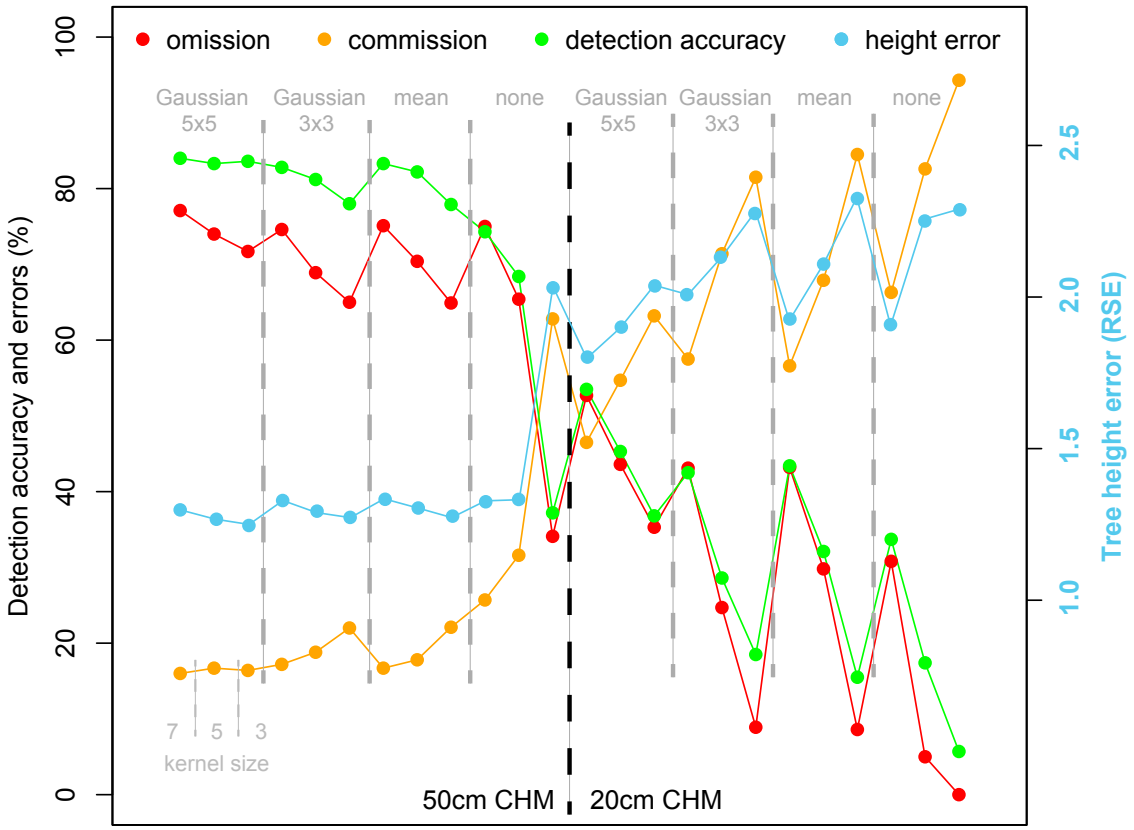


Figure 5.26 Plotting omission, commission and height errors stratified by lidar treetop extraction parameters helped to visualize trends in the treetop extraction results and provided an objective means for evaluating appropriate algorithm parameters. The 20cm CHM produced far too many commission errors to be considered. The detection accuracy increase by applying noise reduction filters. The remaining parameter combinations (50cm CHM with filtering) were very similar and the selection of one over the other was a compromise between commission and omission errors. In this case a low omission error was considered a priority over commission error since tree locations were known.

residual height errors. There were only subtle differences among those treetop extraction results produced from the 50cm CHM with a noise reduction filter. Calculated height residual standard errors for treetops extracted from smoothed 50cm canopy height models occurred between 1.25 and 1.34m; while results from the 20cm CHM differed. The 20cm CHM results were different in that the results were worse than those produced by the 50cm CHM but also that the Gaussian 5x5 result was better (1.8-2.0m) than the others, which appeared to be roughly equivalent in performance (1.9-2.3m). It was also

interesting to note that the direction of association with kernel size and extracted height error was inverted between the 50cm and 20cm results. The RSE for the 50cm CHM was positively associated with kernel size, suggesting that the larger kernel was confounding the height values, although only slightly (ΔRSE ~5cm). This observation was inverted for the results found using the 20cm CHM. In these cases, the height residual standard errors increased (ΔRSE ~28cm) with decreasing kernel size and to a greater degree than the 50cm CHM results. This observation suggests that the higher resolution CHM captures finer crown detail that can have the effect of producing multiple local maxima that do not correspond to individual tree crown maxima. This interpretation supports the rational for applying smoothing algorithms to facilitate better tree height extractions. These analyses suggested that the optimal result was produced by a smoothed 50cm CHM and treetops identified with a 3x3 kernel binary maximum. These results produced the smallest RSE (1.25m) and the largest coefficients of determination (R^2: 0.90). However, there is only a marginal difference in performance among the different smoothing approaches, holding constant the 50cm resolution of the CHM and the 3x3 binary kernel. It is important to recognize that raster smoothing was only applied for treetop detection. The extracted heights were sampled from the unsmoothed CHM but at the location of the smoothed raster local maximum. A large portion of the CHM extracted height error is expected to be the effect of footprint fill factor and apical dominance along with primary leader growth that has occurred between CFS sampling and the lidar acquisition. The lidar treetop extraction result produced from the 50cm CHM with a 3x3 kernel and a mean filter was further investigated with its correspondence with *in-situ* measured and modeled tree height.

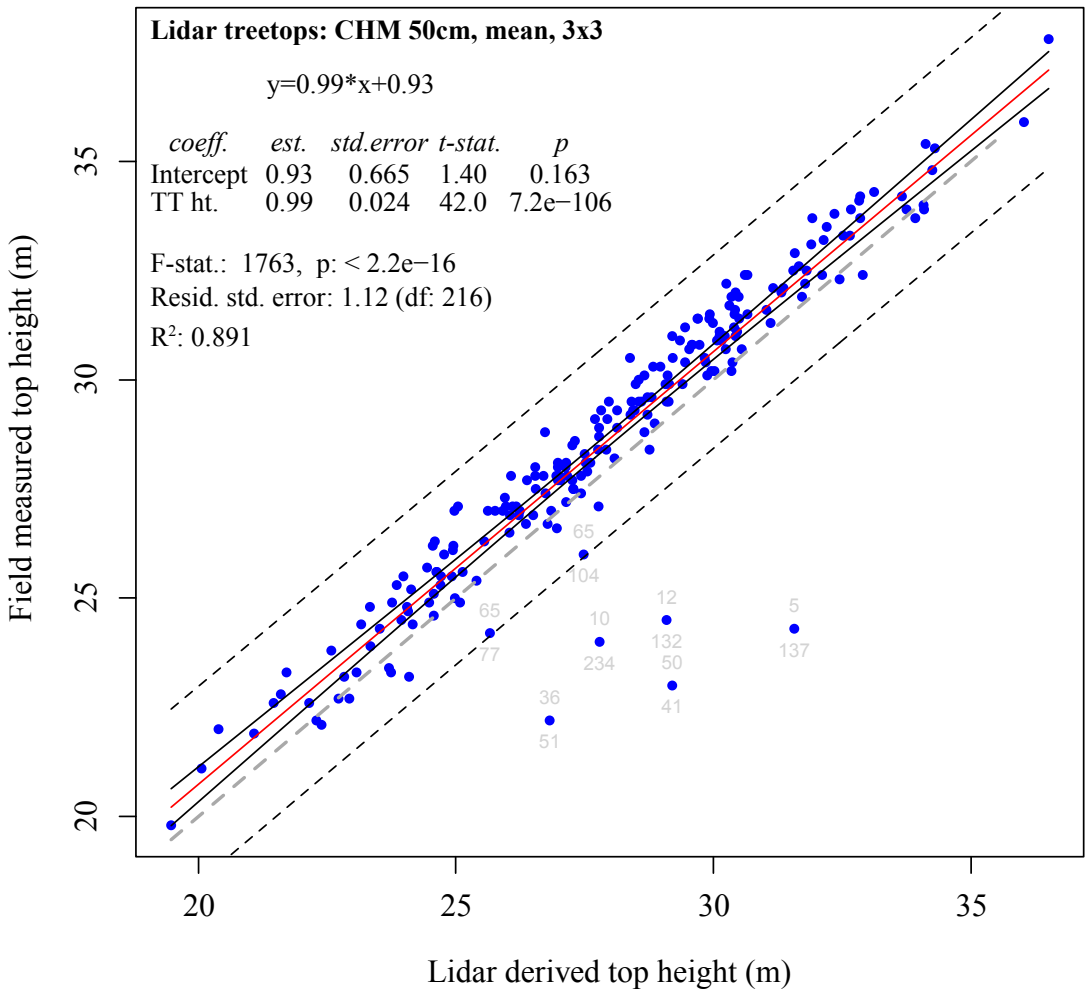


Figure 5.27 Tree height regression with accurately detected treetops found through the local binary maximum filter, produced encouraging results but identified several large outliers that were attributed to incorrectly associated ground data to RS data and one instance of point cloud noise.

There was an apparent grouping of large negative residuals in each height regression investigated (Fig. 5.27, 5.28 & 5.29). It was assumed that these large errors represented cases where smaller diameter and thus shorter trees were obscured by adjacent and more prominent tree crowns. A DBH stratification process illustrated an increase in performance by eliminating smaller diameter stems, which supported the idea that smaller partially or entirely obstructed crowns were at least partially responsible for

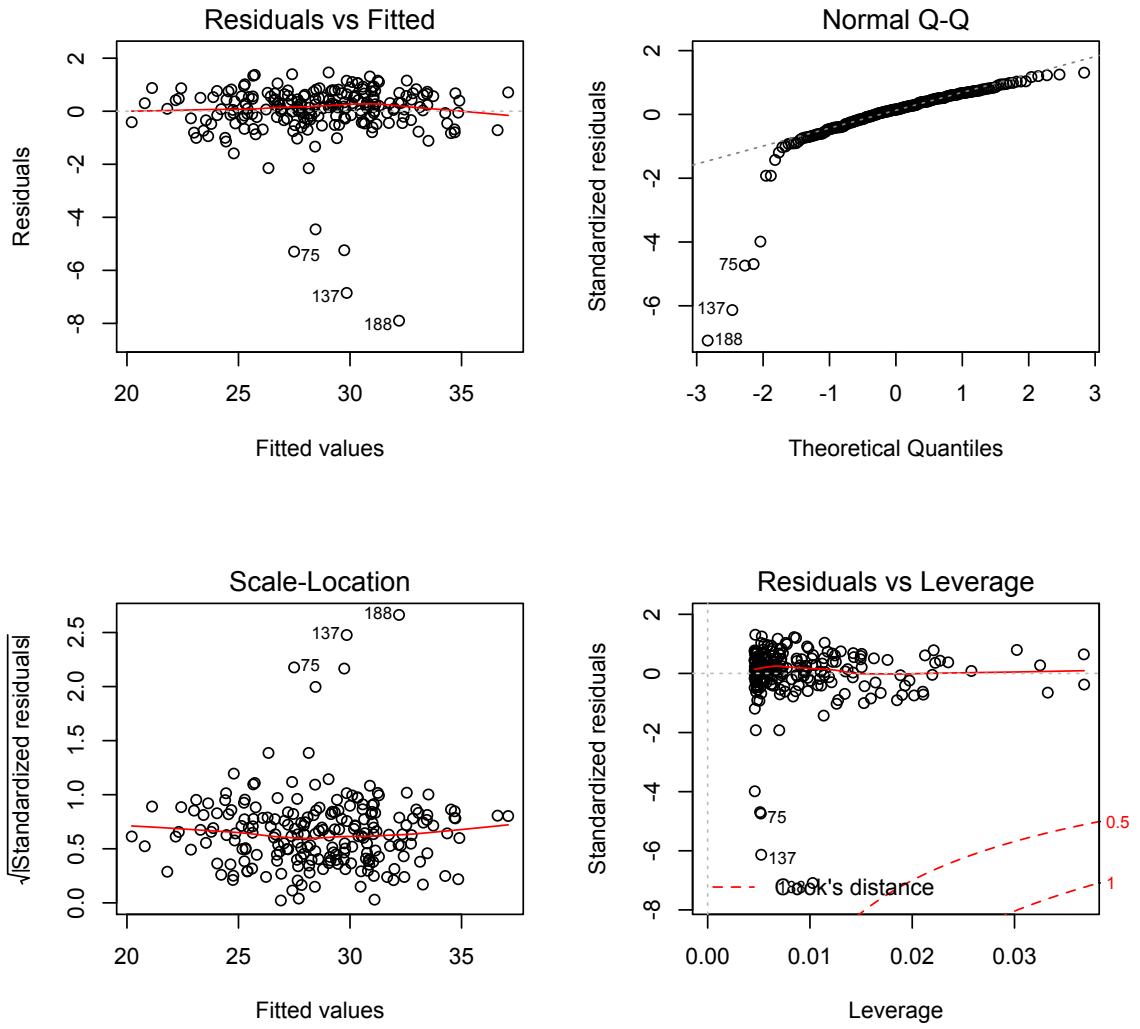


Figure 5.28 Tree height regression residuals from lidar treetops, produced encouraging results but identified several large outliers that were attributed to incorrectly associated ground data to RS data and one instance of point cloud noise. Aside from the few large errors the residuals suggested a constant average near zero through the height range with an approximately normal distribution and constant variance without evidence of influential points.

the large negative residuals. While evaluating the regression of lidar treetops with field-measured heights, the large residuals were identified and were considered with reference to the terrestrial lidar stem cross-sections, voxel files and the CHM raster. It was determined that the majority of these observations (plot:tree, 5:137, 50:41, 36:51, 12:132) were the result of mis-associated field measurements. The field to lidar tree association

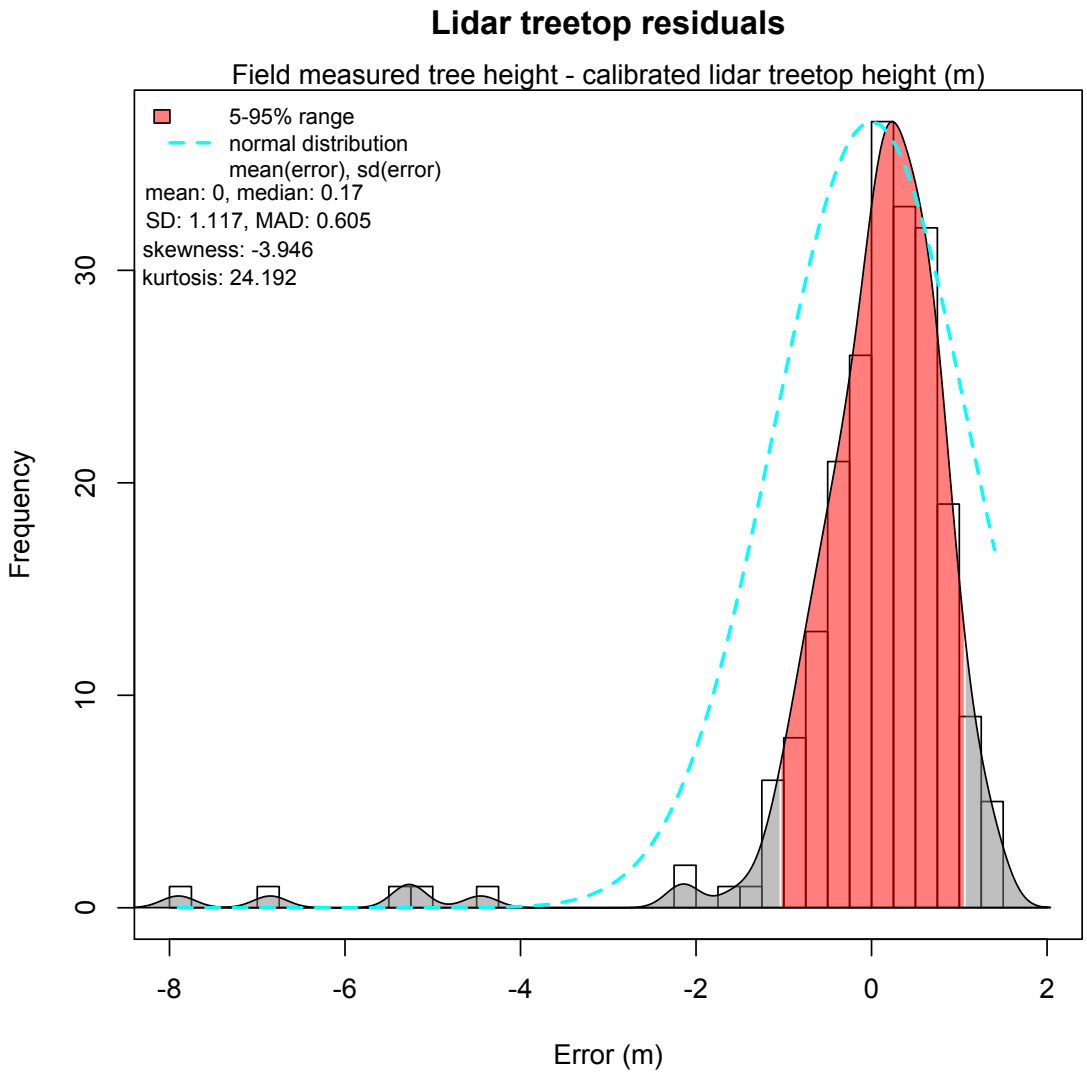


Figure 5.29 Tree height regression residuals from lidar treetops, several large outliers were attributed to incorrectly associated ground data to RS data and one instance of point cloud noise.

was based on a minimum distance from the TLS stem map. In these cases a smaller diameter stem was found to be horizontally closer to the identified treetop than the stem position of the correct larger diameter stem. Therefore, these instances represent not a failure of extraction but rather of the field data to remote sensing data association. One of the seven large residuals was attributed to point cloud noise where tree ID 77 in plot 65 was assigned to a CHM location that was taller than the field measured value and

appeared to be located within a canopy gap according to the CHM (Fig. 5.30). By following the occupied cells of the TLS voxel file the correct location of the treetop was determined which, if considered would have reduced its residual from -2.15 to +0.46m. The sources of the remaining two large residuals (10:234, 65:104) were undetermined; spatially, they agreed with the voxel stem tracing and heights were not divergent globally or locally. These extreme outliers represented a total of 3.21% of the total observations with both field measurements and lidar derived treetop positions.

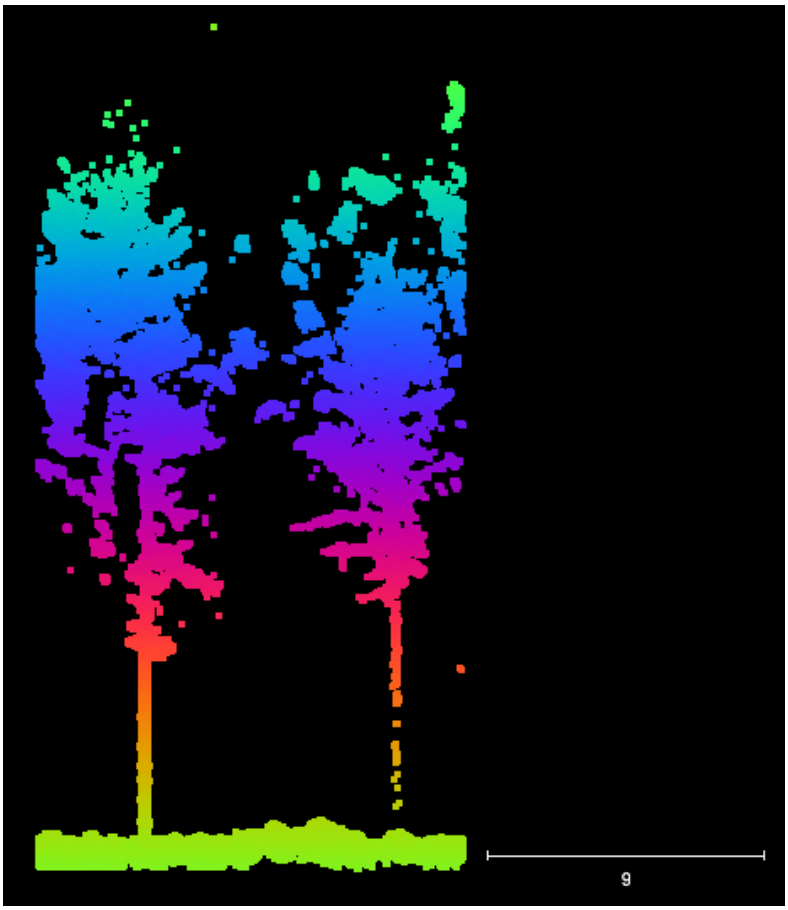


Figure 5.30 One of the large tree height residuals was attributed to point cloud noise at tree ID 77 at plot 65, possibly the effect of light rain. It was resolved by terrestrial lidar stem tracing by high-density voxels.

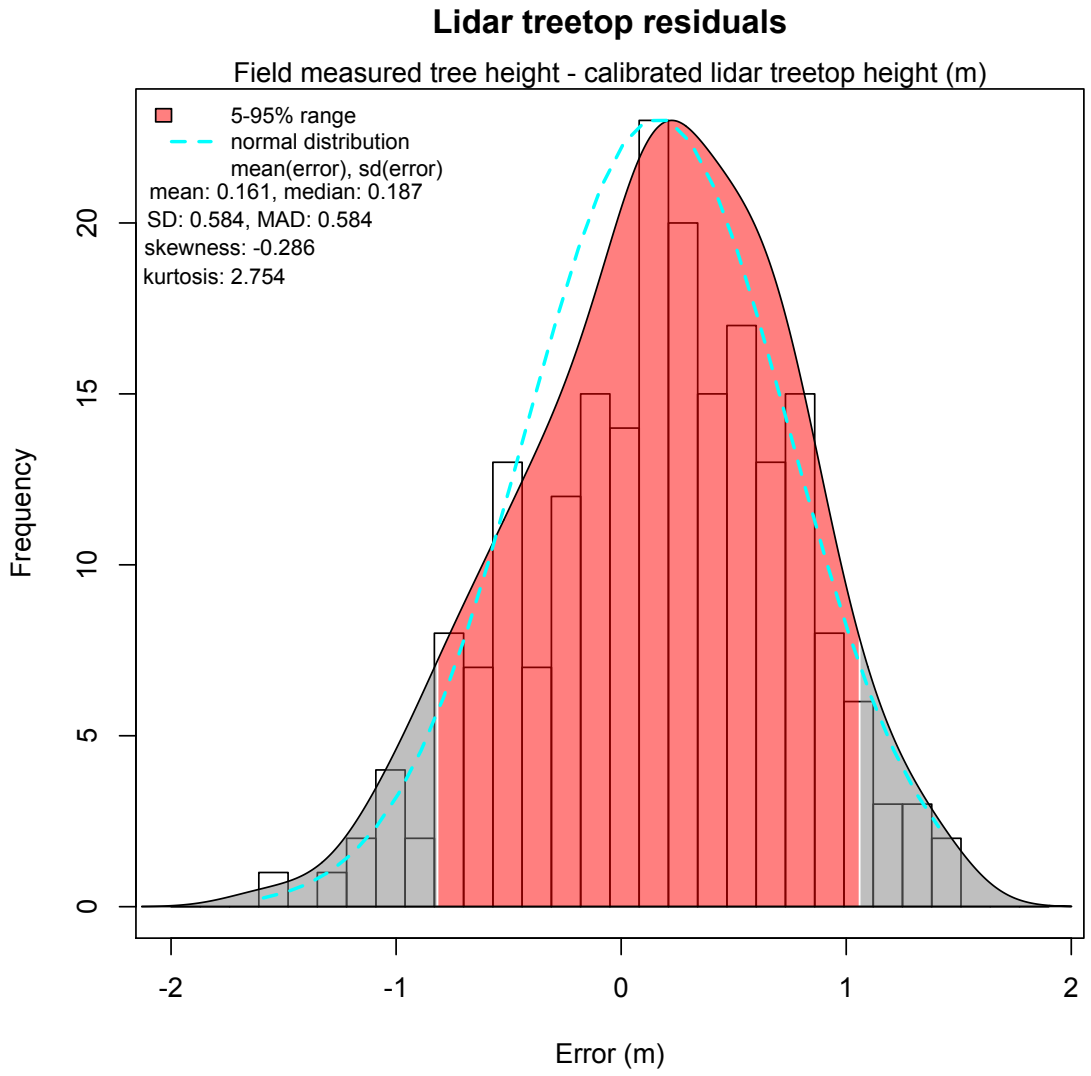


Figure 5.31 The large magnitude height estimate errors were attributed to a small group of observations incorrectly matched with field reference data and one instance of point cloud noise. When these known error observations were removed the residuals more closely approximated a normal distribution.

When the extreme residuals with known error sources were removed the residual distribution more closely approximated a normal distribution with an equivalent mean and standard deviation (Fig. 5.31).

The considerable effort placed on explaining the source of error in the height estimates was largely based on the perspective that many forest attributes may not

require calibration models. The major operational hurdle for lidar based forest inventory is that the community has adopted the empirical area based approach, which requires calibration models that may be based on lidar metrics that are only loosely tied to the attributes they intend to describe, and in other cases are entirely unrelated. This treetop approach is intended to demonstrate the physical relationship between measured field heights and measured lidar treetop height, which do not require calibration. When the known erroneous observations were omitted, the linear model describing the relationship between field measured tree heights and lidar derived treetop heights was very near the line of equality (Fig. 5.32). The best-fit is parallel to the line of equality with a coefficient of 1.004±0.012, while the bias is 0.723±0.384 and is likely the result of the lidar footprint fill factor in combination with growth occurring between the measurement and survey campaigns. In this particular case, sampling bias is not considered a significant source of error given the high point density and footprint size producing a near continuous measured surface approaching an oversampled condition. The challenge for the successful application of lidar treetops for forest information is the algorithm parameterization with the intent to increase detection rates and reduce omission and commission error rates.

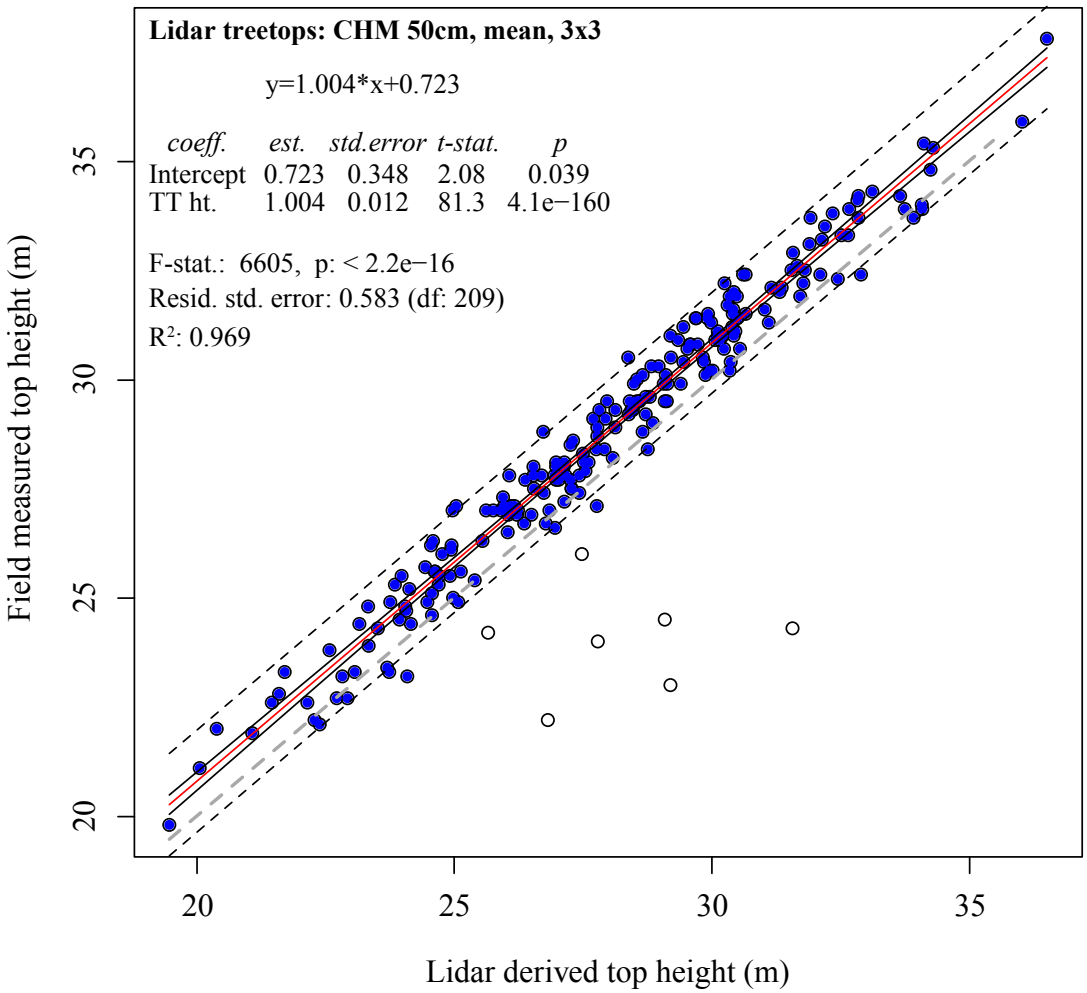


Figure 5.32 The omission of the large residuals with known error sources produced a fit that was very near the 1:1 line. This analysis demonstrates if the treetop parameters can converge on a solution that minimizes commission and omission then the lidar treetop product may be applicable for height estimation without costly field campaigns. Open circles are omitted observations and closed circles are observations used in model building.

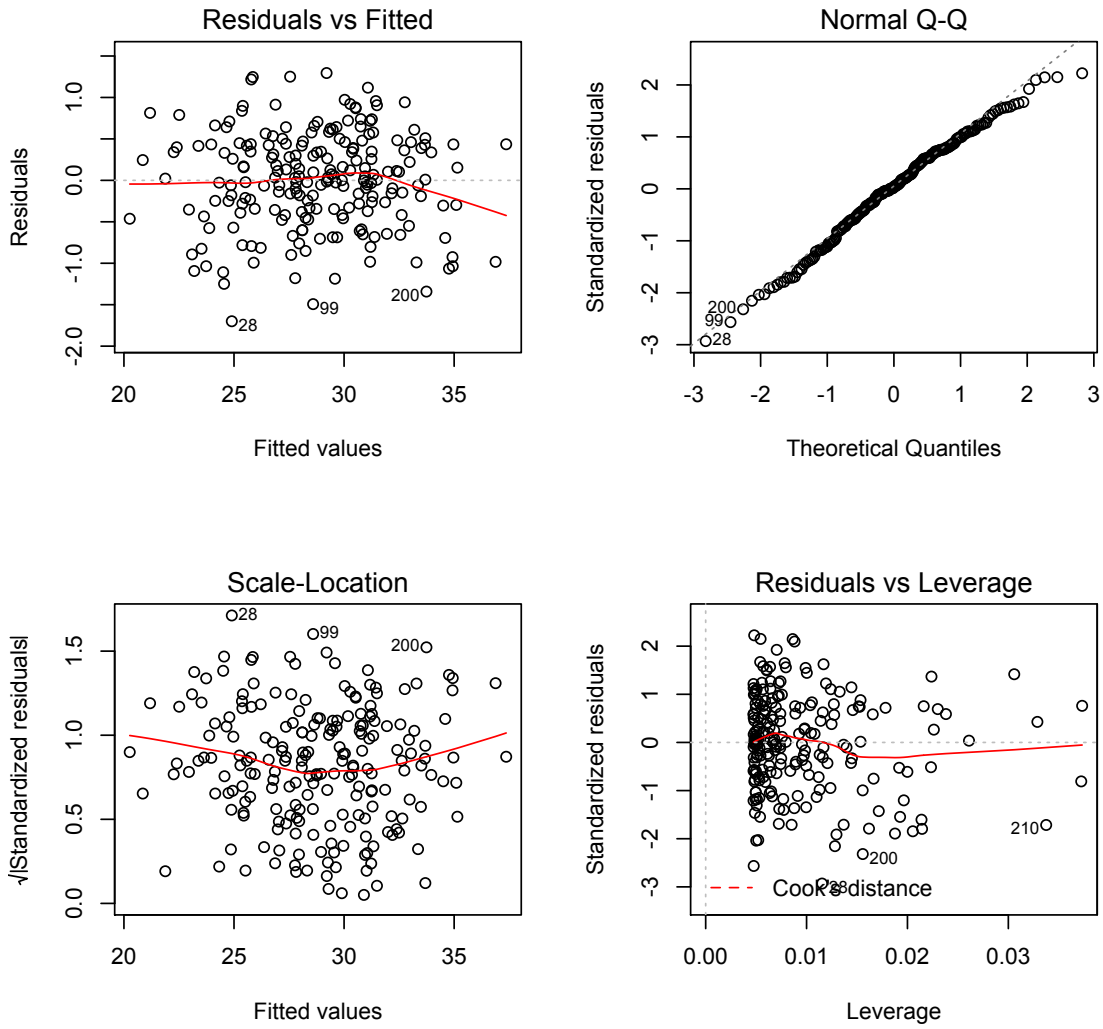


Figure 5.33 The omission of the large residuals with known error sources produced a fit that was very near the 1:1 line. The error evaluation in the regression diagnostic plots did not suggest a violation of assumptions or the presence of influential observations.

In an attempt to increase treetop detection accuracy the variable kernel size option was considered. The heights of the omission errors were evaluated with the Kruskal-Wallis test for each possible treetop extraction parameter combination. The purpose of this investigation was to determine if there was a scale dependency on extraction accuracy. The premise was that taller trees may produce wider crowns and that these larger crowns may produce multiple local maxima. In order to reduce the commission errors the extraction kernel size can be adaptive based on the height of the considered

cell. If this is the case for the SLP site there should be an apparent height difference in omission errors and correctly identified treetops in the coarser scale extractions. Plotting the kernel density estimates of the field measured heights from correctly identified treetops and the field heights from the omission errors, it would be expected that there would be a shorter central tendency for the omission error distribution than that of correctly identified treetops in the coarse scale extraction. These distributions produced very little coherent patterns with the exception of that produced by the extreme scale ranges. When evaluating the heights of the omission errors versus the correctly identified treetops for the fine scale extractions the distributions appeared to be quite different (Fig. 5.34). When parameters changed to more coarse spatial scales the effect was to increase the heights of the omission errors (Fig. 5.35). There were no clear changes in the commission errors that would suggest a greater proportion of taller extractions were occurring in finer spatial scale extractions. There was little evidence to suggest that a height dependent kernel size would improve the extraction accuracy for the SLP site.

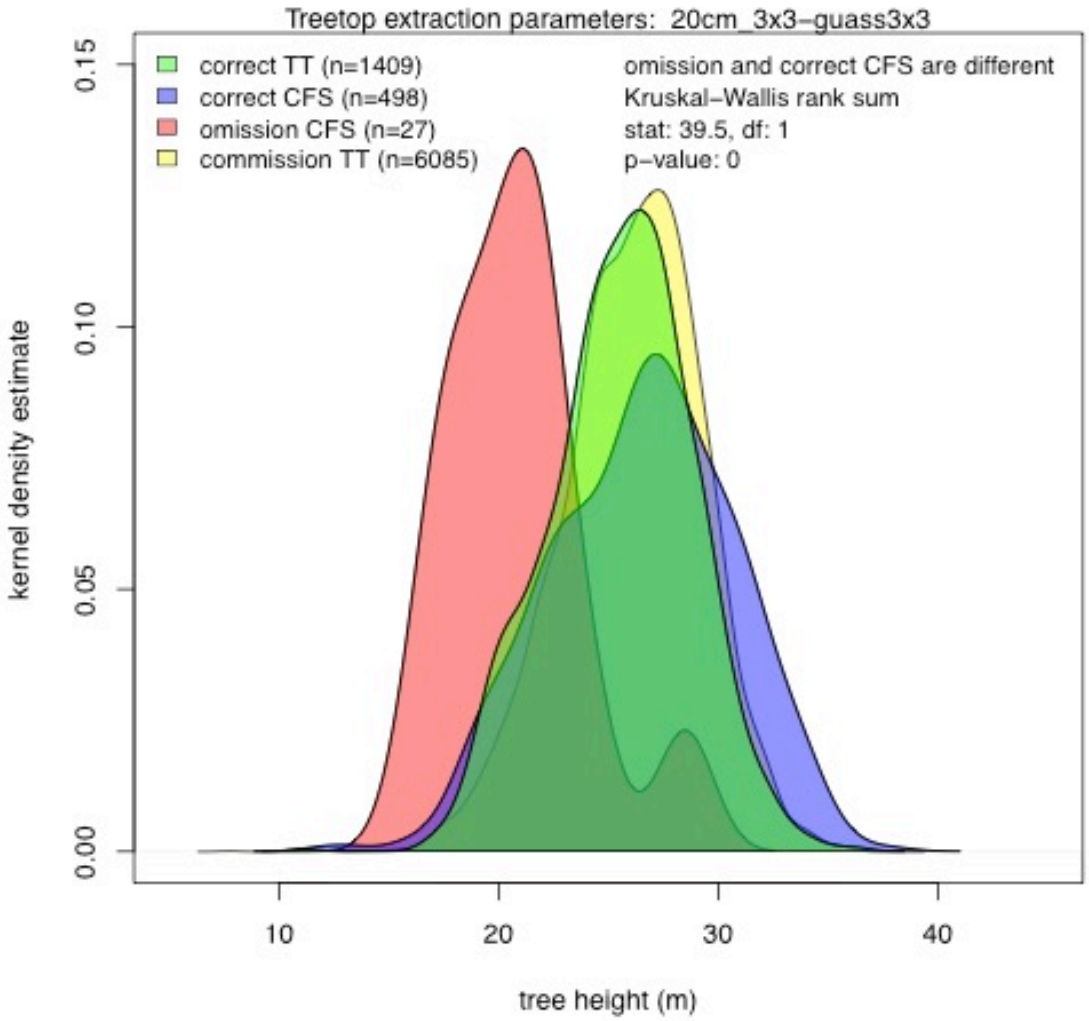


Figure 5.34 At a fine spatial scale of analysis, the omissions errors tended to have lower heights, note that these heights do not indicate that the heights are accurate, only that they have been detected, or at least a local maximum near the horizontal position of the stem was detected. Relative to the coarse scale treetop extractions the heights of the fine scale results appear to produce slightly shorter heights for the correctly detected trees (~25m).

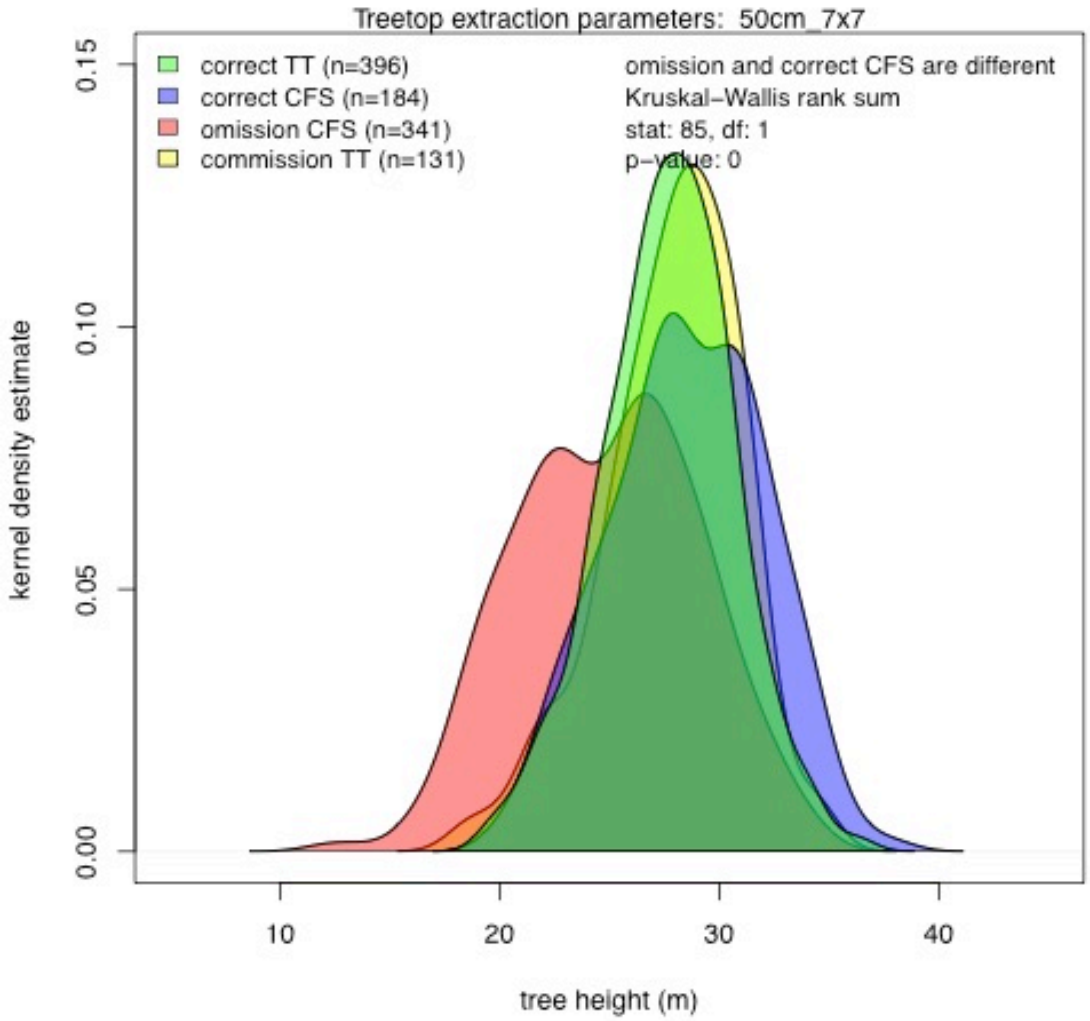


Figure 5.35 At a coarse spatial scale of analysis, the omissions errors behaved as expected by missing a larger proportion of taller trees.

The evaluation of the detection errors related to the neighbourhood size and extracted top height provided evidence of a height dependency for the omission errors, where the omitted stems tended to be fewer and shorter for smaller neighbourhoods. This result is in line with the hypothesis that more dominant adjacent stems would occlude suppressed or less productive individuals. The post-hoc, pairwise comparison testing of treetop omission height errors also supported the observations made from height distribution plots. The hypothesis test results were summarized in Hasse diagrams, which

suggested that both the omission error rate, and the height of the omission errors were a function of the effective scale produced by parameter combinations.

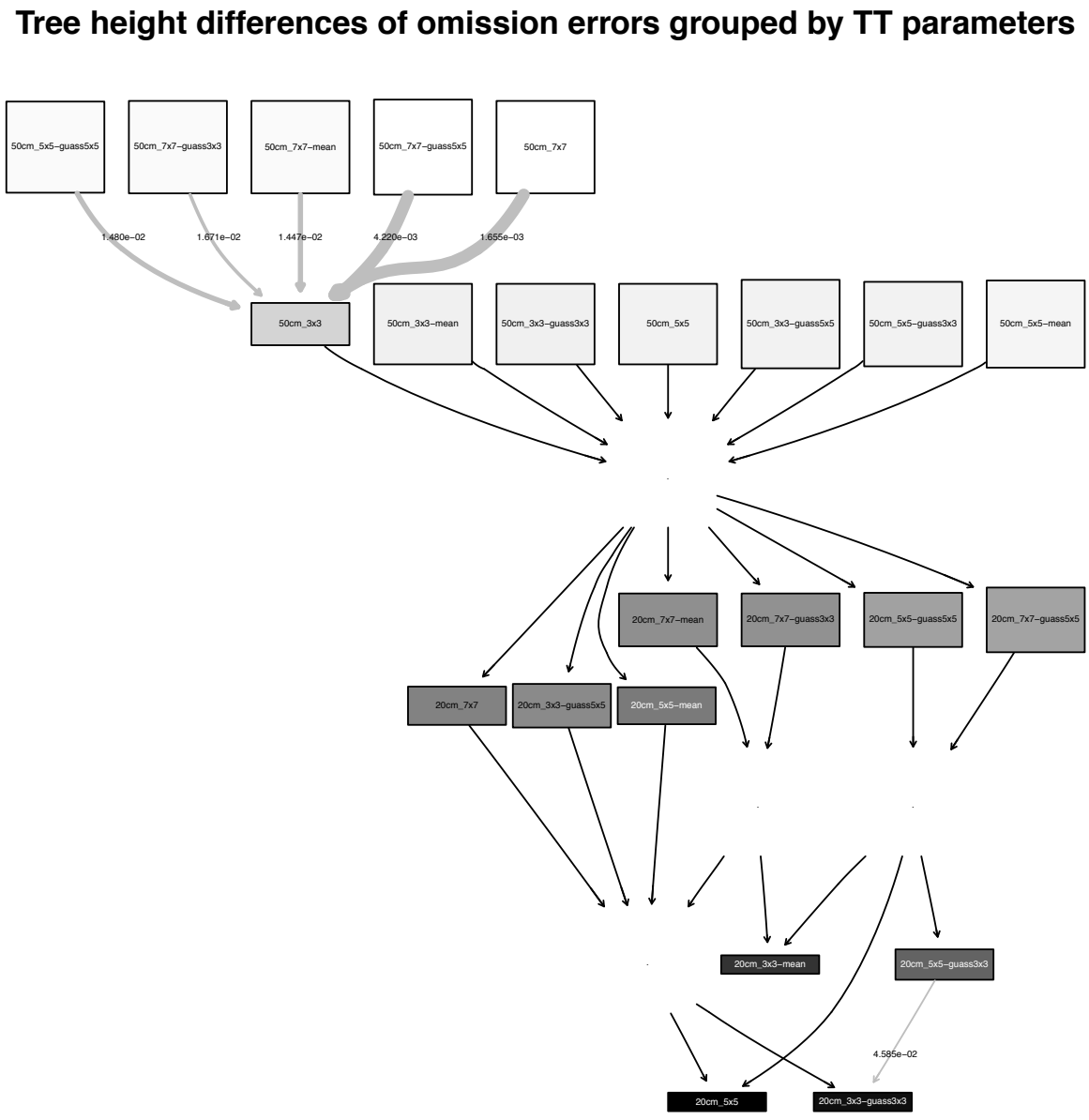


Figure 5.36 Post-hoc comparison tests illustrate the effect of spatial scale, as provided by extraction parameters, on the number of omission errors and the height of the omission errors. Where, coarse neighbourhoods produce more omissions and the height of those omissions tend to be taller.

As an alternative investigation into spatial scale and treetop extraction, semivariograms were built for each plot and treatment with 50cm (one pixel) lag intervals on the CHM, up to a distance of 20m. The approach was used to indicate an appropriate scale of analysis for treetop extraction, in this case to identify the scale of the objects of interest, the tree, as represented by the CHM. The treatment plot CHM semivariograms had indicated a range (distances of spatial autocorrelation) at approximately the third to fourth lag distance, which at a 50cm lag corresponds to 1.5-2.0m (Fig. 5.37). The semivariogram range may have adequately captured the scale of the tree objects, as the measured crown widths according to the CFS 2012 field campaign ranged from 0 to 4.1m with a median (& mean) of 2.1 and standard deviation of 0.61m. Of those trees correctly identified by the treetop algorithm, the measured widths ranged from 0.75 to 4.1m with a median (and mean) of 2.4m and a standard deviation of 0.49. The semivariogram range approach to scale determination was not considered overly informative for the neighbourhood determination, beyond which had been suggested by the previous analysis. Others have found semivariograms helpful for spatial analysis and particularly for forest applications [56].

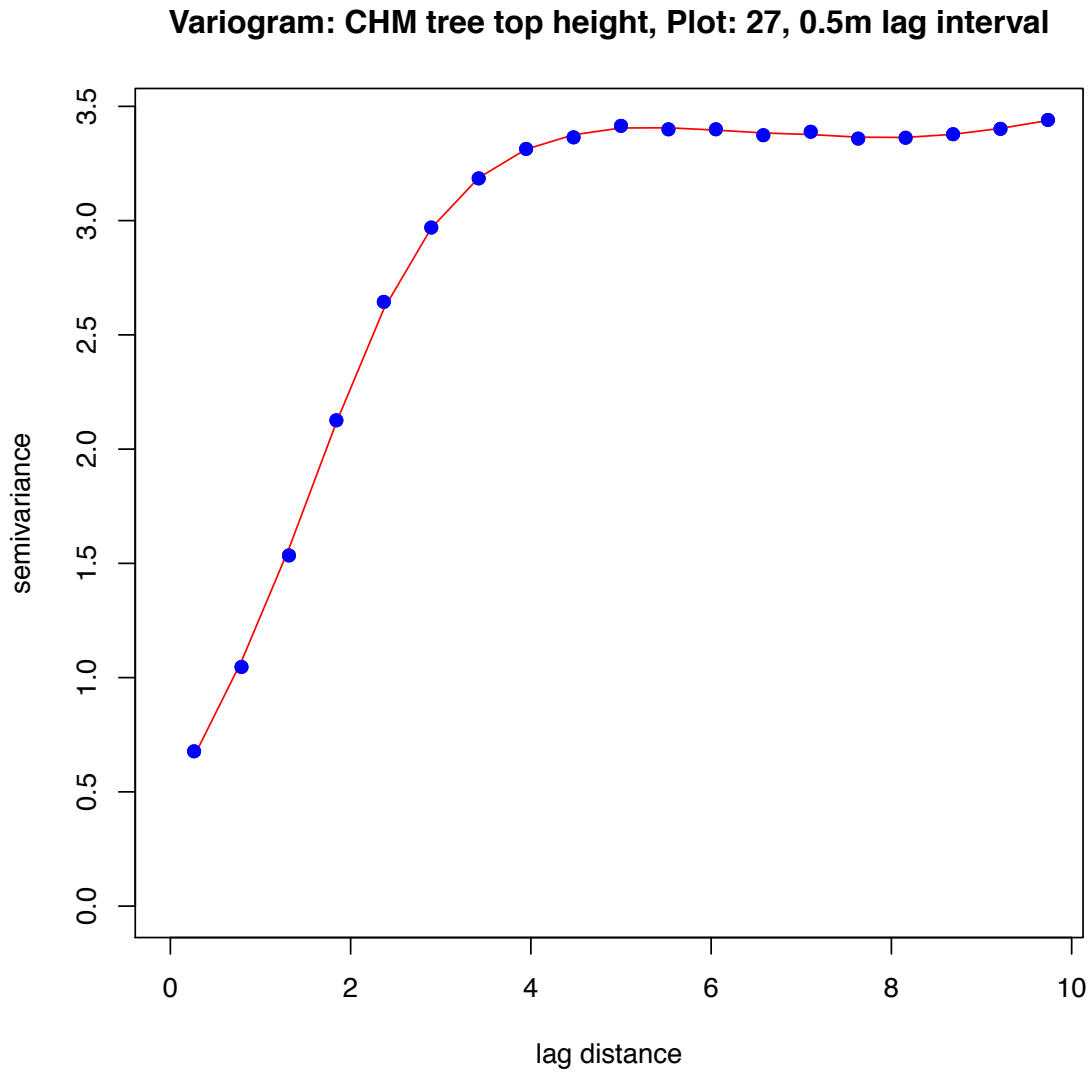


Figure 5.37 Semivariogram range was qualitatively used to support decisions on neighbourhood scale for treetop extractions. The semivariogram range is the x-location were the slope of semivariance levels off indicating that dissimilarity does not further increase with increasing distance. Conversely below the range, values are increasingly similar with decreasing distance.

A manual investigation was conducted into the lidar treetop omission errors, where using the CHM and local data enhancements, individual treetops were identified. It was determined that 793 of the total 1517 TLS stem surveyed individuals were not apparent in the ALS CHM. Of the omitted observations, 293 were not identified in the CFS database and are therefore assumed to be reinitiated trees, a suspicion that was

supported by the DBH data. The omission errors, which were thought to be caused by their membership within the suppressed/understory class had a mean diameter that was 10.9cm smaller than the mean of all other core stems (assumed suppressed: μ:11.9, σ :6.5, n:327, med:11.2, Core trees: μ:22.8, σ:7.2, n:1190, med:22.6). When these errors were stratified into their respective plots it became obvious that there was a strong treatment group influence. With the exception of plot 41 (T2F1-1-1), the number of omissions assumed to be within the suppression class were less than 4 for all T2 treatment plots. These assumed suppressed observations increased in number from a plot mean (±sd) of 2±2 (n=13) in the T2 treatments to 12±6 (n=6) in the T1 treatments and finally 24±6 (n=8) in the thinning control group. There did not seem to be a coherent pattern in the occurrence of treetop omission errors that could be tied to the fertilization treatments. The number of omission errors attributed to the suppression class explains 91% of the variation in the total plot omission errors, suggesting that the underlying process causing suppression is also related to the omission errors that were occurring in the co-dominant tree class. The omissions within the dominant and co-dominant class followed a very similar pattern where the T2 treatments had fewer omission errors and the thinning control had a greater number of omission errors. Within the T2 and T1 treatments there was not an obvious association with error and fertilization treatment. However, within the thinning control group there was a clear decrease in omission error with increasing fertilization treatment. The eight plots that comprised the thinning control group were spread across six treatment groups, listed by increasing omission errors these treatments were: T0F4, T0F1-1*, T0F2-2*, T0F2-2, T0F2-2*, T0F1, T0F0, T0F0. If the fertilization sources (urea or ammonium nitrate) are considered equivalent and the T0F1-

1* plot is omitted as it is confounded by the effects of root disease, then there is a clear inverse relationship with fertilization and lidar treetop omission errors. A structural development model for stands transitioning into the stem exclusion stage might aid the interpretation of these findings. This would suggest that the increased productivity in the form of available nitrogen increased growth rates and in turn advanced structural development, producing slightly fewer stems with slightly taller heights with increased fertilization. However, in reviewing initial stem densities for the T0 treatments reported in the appendices of Crown [186] it can be seen that the densities are inversely associated with fertilization application rates, (presumably this was done to ensure that productivity gains from fertilization were not lost to stem exclusion). Irrespective of the cause of the variation in stem density of these plots it has produced a conspicuous result in the error analysis of lidar derived treetop detection. This investigation lead to the conclusion that with these data, although specific to this site and processing stream, error rate predictions might be possible given stem density. Regression analysis suggests that the omission error is zero below a stem plot count of 20.3±3.7, which translates to a stem density of 507.5±92.5 (Fig. 5.38). While, this result is meaningful for plot level attribution and the use of lidar derived treetops, the solutions is an over simplification of the true nature of lidar treetop omission.

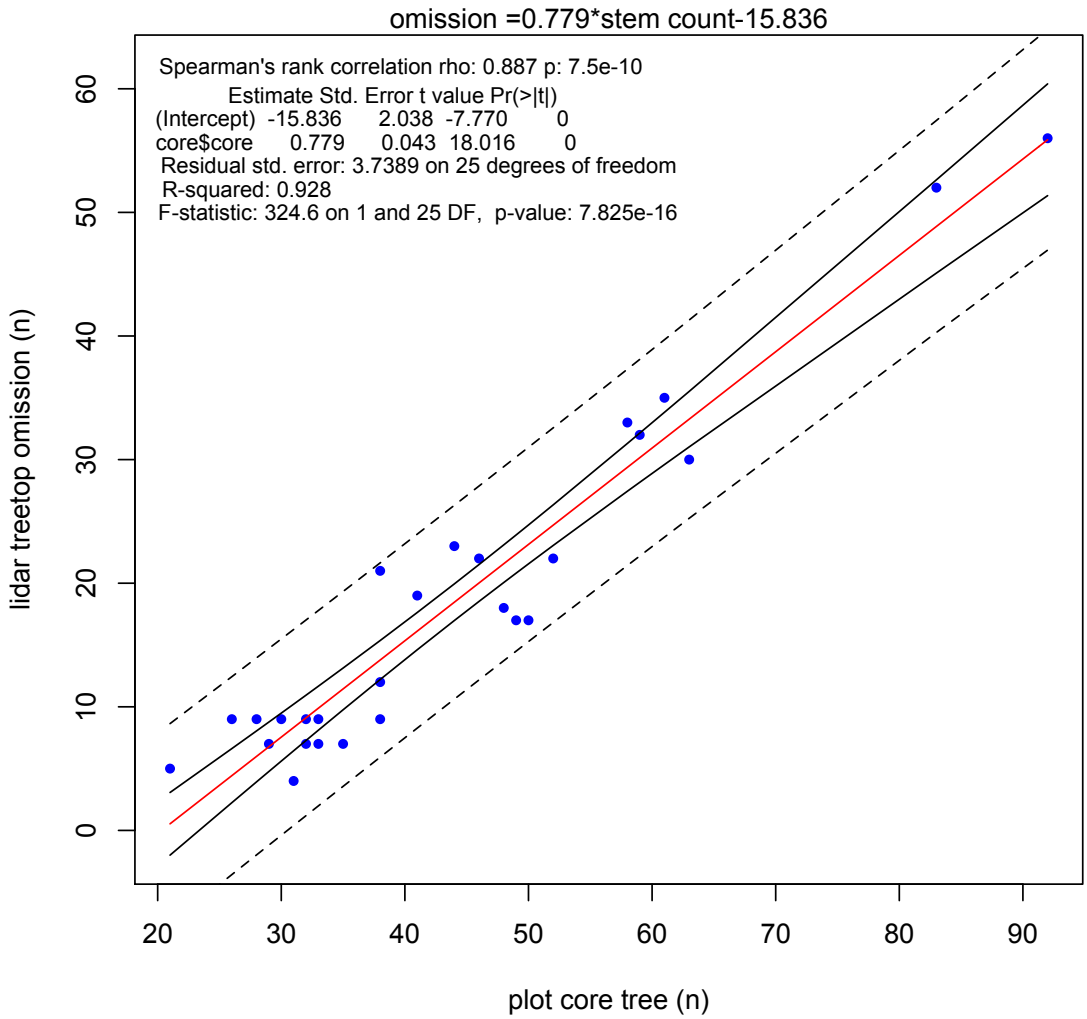


Figure 5.38 Predicting lidar treetop omission errors from plot stem count. A simple linear regression demonstrates that the density of a forest stand is strongly related to success of a lidar individual tree survey. The treetop omission errors increase with increasing stem density. According to these data and processing stream, lidar will capture all individual treetops (omission error=0) below a plot density of approximately 20.3

The true cause for lidar treetop omission errors is related to the three-dimensional spatial arrangement of the individual treetops. Therefore, it is hypothesized that individual omission error observations could be predicted as a function of neighbourhood metrics that capture the proximity to neighbours and the height differential to these neighbours. Clearly the underlying scale of the CHM is also a significant factor, but for these investigations is held constant. The neighbourhood metrics were based on the single

nearest neighbour, multiple (k) nearest neighbours and by quadrant-stratified neighbours. Given each plot had a finite spatial extent; neighbour metrics would be biased for boundary trees. Edge tree detection was defined as those trees without neighbours within a 120º range in any direction and within ten meters. Neighbour metrics were computed and edge trees were omitted from further investigation. The differences in neighbour distances and neighbour heights were evaluated between correctly detected trees and lidar treetop omitted trees (Fig. 5.39).

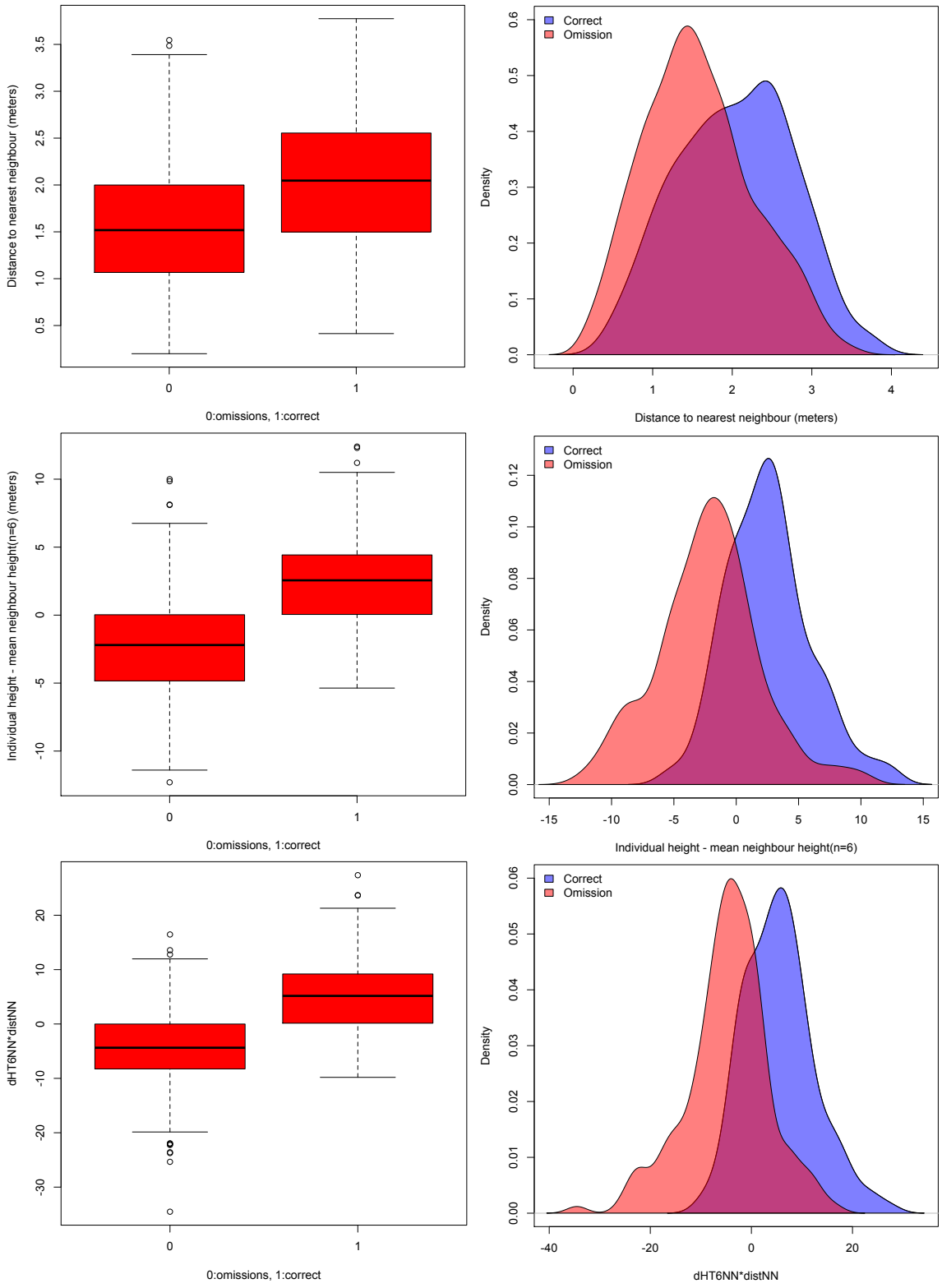


Figure 5.39 Neighbour metrics generated to predict lidar treetop omission errors, trees with more distant (row one), shorter (row two) neighbours are better detected. Row three illustrates the interaction of distance and height differential further separates correct and omitted.

According to the distributions of the nearest neighbour distance (distNN), 95% of the omission errors occurred when a nearest neighbour was within 2.81m from the omitted individual. This is a result that is not supported by the processing details, where a finer resolution grid was applied to treetop detection, which assumed that the nearest resolvable tree distance was 1meter (50cm grid, 3x3 filter). This observation suggested that the omitted trees were not captured due to occlusion and not because of the spatial scale. The overlap of the neighbour distance distributions of correctly identified and omitted trees suggested that distance alone is not particularly useful for separating the two groups. The height differences were clearly better at resolving the two groups. According to the distribution of local tree height difference (ΔHT6NN: height-mean six neighbour height) 74.8% of the omitted trees were shorter than the mean of their closest six neighbours. There was considerably less overlap in the height difference distributions for correctly identified trees and the omission errors. The interquartile range of the local tree height difference (ΔHT6NN) in the omission group did not overlap with that of the correctly detected group, for reference, 54% of the interquartile range of the distance metric for the omission group overlapped with that of the correctly detected group. Conceptually, there should be a distance limitation to the height difference separation of the two groups; at some distance the height difference should not have any bearing on treetop detection.

The neighbourhood metric distributions were evaluated for normality. The distribution of the nearest neighbour distance for the omission group was not normal (Shapiro-Wilk: 0.985, p:<0.000, n:681), nor was the distribution of the correct group

(Shapiro-Wilk: 0.989, p:0.019, n:310). Neither outlier removal nor transformations produced non-significant Shapiro-Wilk tests. Variance equality could not be assumed (Fligner-Killeen test: 2.95, p:0.086). As a result, the non-parametric Kruskal-Wallis rank sum test was used to evaluate statistical differences between the groups, which suggested that in general, omitted individuals had significantly shorter distances to their nearest neighbour (KW: 80.89, $p<0.000$). The neighbourhood equivalent of distances (mudist6NN) produced a similar result with a KW test (KW: 87.39, $p< 0.000$). It was concluded that the mean distance to the 6 nearest neighbours was on average closer for omission errors than it was for correctly identified trees. According to the overlap of the interquartile ranges of distance metrics for omission and correctly detected trees, the neighbourhood distance metric did not have a benefit over the nearest neighbour distance metric (IQR overlap 53.6%, 54.0% for the nearest neighbour and k=6 nearest neighbour distance metrics respectively.)

The nearest neighbour height difference (ΔHTNN) for the omission group distribution produced a non-significant Shapiro-Wilk test (p:0.283) while the correct group did and thus could not be assumed normal (SW:0.95, p: 0.01). Variance homogeneity could be assumed according to the Fligner-Killeen test (FK: 2.96, p: 0.086). One-way analysis of variance, as well as the Kruskall-Wallis test, suggested that the nearest neighbour height difference was significantly lower than correctly identified trees. Specifically, omitted observations had nearest neighbour trees that were larger than themselves, and the correctly identified trees had a tendency to have shorter nearest neighbours. Distributions for the height difference, relative to the six nearest neighbours (ΔHT6NN), were all considered normal, where Shapiro-Wilk tests were not significant at

the 95% confidence level (aggregated groups: SW:0.995, p:0.433, omissions: SW: 0.985, p:0.0765, correct: SW: 0.9816, p:0.0575). There was insufficient evidence to suggest that group variances were different (FK: 2.77, p:0.0957), as a result the one-way analysis of variance was considered a viable unbiased test for this variable. The ANOVA produced a significant ($p<0.000$) F-test of 123.6, which agreed with the previous nearest neighbour test, where omitted lidar treetops are generally shorter than their neighbours. The greater significance and F-statistic for the neighbourhood comparison is attributed to the 50% larger variance of the nearest neighbour height difference in the omission group (six neighbours: 16.55, nearest neighbour: 24.67). According to the overlap of the interquartile ranges of height difference metrics for omission and correctly detected trees, the neighbourhood distance metric may provide a benefit over the nearest neighbour height differential. The neighbourhood metric IQR of omitted and correctly detected trees did not overlap, while those of the equivalent nearest neighbour metric overlapped by 1.7% (as a proportion of the omission IQR). From these analyses it is concluded that in general, lidar treetop identification will fail when trees are shorter than the mean height of their six nearest neighbours and for treetops less than a meter and a half apart. This conclusion however, cannot be extrapolated to open or partially open canopies or for non-even aged and multi-tiered stands. To account for the effect of more open canopies where there is an anticipated reduction of influence of the height differential with increasing distance, a regression-based model was investigated.

A binomial logistic regression was run with the response variable representing treetop detection or omission and explanatory variables for the two neighbour distance metrics and the two height differential metrics along with their interactions. Interactions

were expected to be significant because at some horizontal distance the height differential must theoretically have a negligible effect. The binomial logistic regression approach was selected over other methods due to the binary response variable and the non-linear restrictions imposed by linear discriminant analysis and ordinary least squares regression. Although, several interactions were selected as significantly contributing to explaining the log probabilities of treetop detection (ΔHT6NN, ΔHT6NN:ΔHTNN, distNN:ΔHTNN, mudist6NN:ΔHTNN), this result was thought to be over fit due to the high degree of multicollinearity inherent in the data (Pearson R: 0.86 and 0.88 for height differential and distance metrics respectively). The final model produced by backward selection with interaction terms was found as:

Log(probability(TTclass))=0.009-0.531*ΔHT6NN+0.040*ΔHT6NN:ΔHTNN.

However, this model was rejected on the basis that it did not capture the distance dependency of omission. In the forward selection approach, the distance dependence was captured at the first enter iteration, where the distNN:ΔHT6NN interaction was selected as the single most sensitive variable to omission. The logistic model was improved with the addition of the distNN attribute. A third iteration produced no additional significant associations. The final, and accepted model with forward selection was found to be:

p(omission)=exp(2.58426-0.94998*distNN-0.20624*distNN:ΔHT6NN).

Figure 5.40 illustrates the probability of a correct lidar treetop detection, or omission, as a function of neighbour distance and neighbour height difference and their interaction. These plots demonstrate that the interaction term would considerably help to distinguish omission from correctly detected trees by its steep transition from predominantly omission at low values to largely correct detections at higher interaction values (Fig.

5.41). It is expected that this relationship will scale better to more structurally diverse forest stands. A condition that is obviously not represented in the SLP dataset, and one that is expected to depart from the described relationship is the case for more structurally complex forest stands. Specifically, cases of advancing vertical and horizontal complexity with increased understory growth and crown expansion of more mature individuals; under these conditions the effect of nearest neighbour distance and height differences on probability of omission is likely changed. Additionally, since the densities of SLP are not representative of low canopy closure, it is expected that the interaction term will converge to a more accurate value with the inclusion of such data. Further, changes in forest type and species are expected to alter the observed relationship; where narrow crown species will provide for better detection at nearer neighbour distances, mature coastal forests represent the extreme case for omission probability. As such, these findings should be augmented with research targeting more structurally diverse forests.

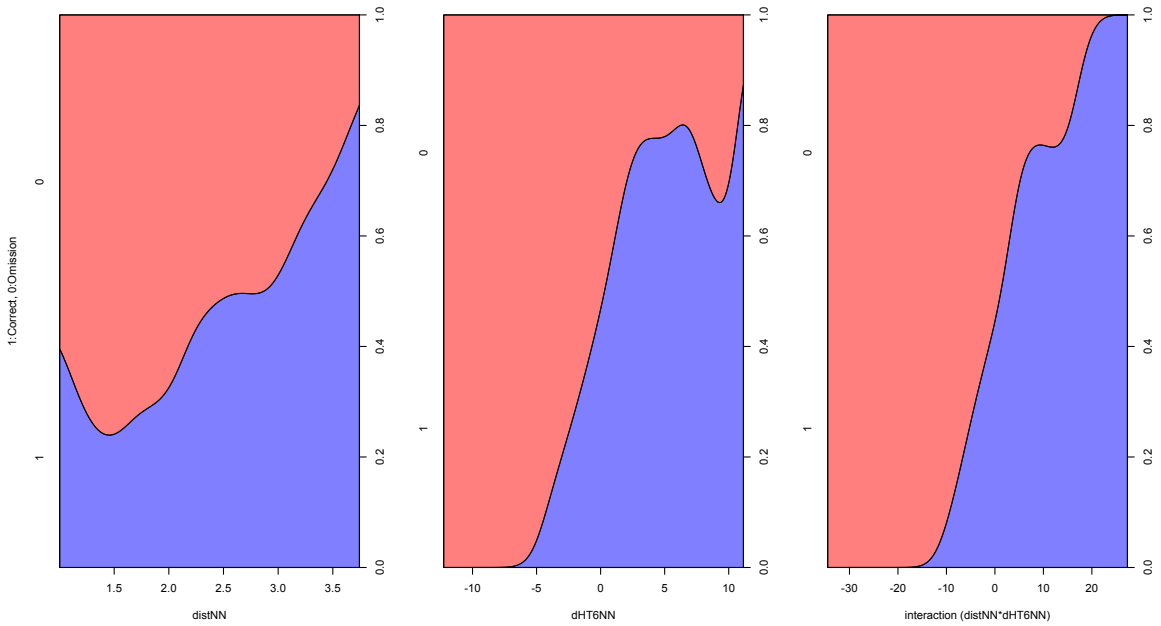


Figure 5.40 Conditional density plots illustrate the effect of neighbour proximity and height differential on the likelihood of lidar CHM treetop detection. The change in direction of the nearest neighbour plot identifies the smallest resolvable treetop distance permitted by the lidar processing (1.5m distance). The steep transition in the height differential plot suggested it would be helpful in discriminating the groupings and the interaction term separates the group probabilities further.

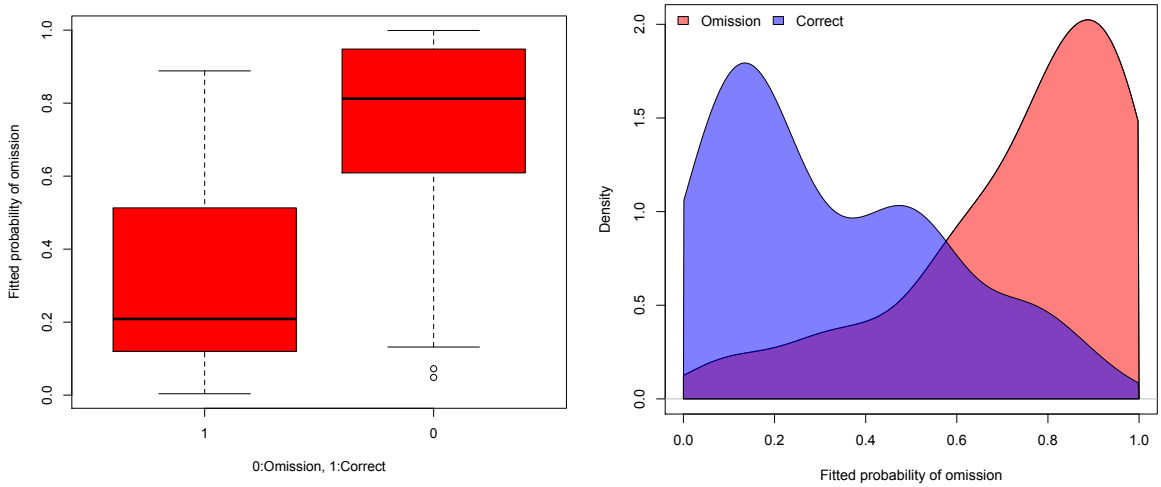


Figure 5.41 The fitted probabilities of omission by binary logistic regression further separated the distributions of omission errors and correctly detected trees. However, there still remained some overlap in omission probability between the omitted and correct trees

5.5 Extracting Crown Dimensions

Working towards a biologically significant model for productivity, it was expected that quantifying the volume of photosynthetic crown would contribute to explaining individual tree-level potential productivity. To this end, individual tree crowns were delineated from the 50cm CHM [46], [181]. The CHM raster data at 50cm has a contribution of noise that has the potential to cause problems in crown delineation. Efforts were taken to resolve the apparent CHM noise. The problematic CHM pixels were queried with reference to a lidar point density raster. The majority of the CHM noise was attributed to unsampled canopy surfaces, which also had lower crown or ground returns present. The unsampled crown pixels are likely the result of tree crown occlusion and high-density crown layers. The empty cells were filled applying a local median filter; all other cells that did not meet the criteria of zero point occupation were preserved. The second type of error affecting the CHM quality are situations where the upper crown layer is void of sample points while the ground surface has both ground and default classified points. These observations are presumably caused by acquisition and tree crown geometries (high scan angle or low altitude and crown occlusion). The result of these conditions produces obvious depressions in an otherwise full tree canopy. These CHM depressions were resolved through a two-step process of smoothing the whole dataset with a median kernel followed by computing the raster difference (filtered-unfiltered). Pits were identified through the global difference distribution, where the upper 99th percentile was selected (10m difference: 99.05 percentile). These observations were replaced by the local median filter. The ultimate CHM data retained all valid crown

height measurements and interpolated unsampled crown locations to produce a cleaned but valid data source for crown delineation.

For comparative purposes the cleaned CHM was used to extract individual treetops. The results did not suggest that the CHM refinement process had a significant beneficial impact on treetop extraction. Relative to the extraction of the 50cm CHM raster with a mean filter, the cleaned equivalent extraction found 526 trees, six less than the unrefined CHM. In addition, commission and omission errors were marginally increased to 21 and six respectively for the refined CHM. Commission errors for the refined CHM totalled 172, while omission errors summed to 991.

The automated crown extraction has been an ongoing effort within the research community and is still in need of much attention before it can be deemed a fruitful endeavour. The initial attempt at crown delineation produced a large number of incidences where multiple crowns were associated with a single treetop location. This lead to the realization that when the crown delineation is dominated by the height percentile stopping rule, crowns were no longer mutually exclusive. That is, the boundary for one tree of a given height has no bearing on the boundary of its neighbours. Therefore, the boundary of a taller tree could incorporate neighbouring crowns if these height values are within the height range defined by the tall tree and percent height selection. The algorithm was modified to handle any one of the crown-growing stopping rules (inflection, maximum radius or percentile of tree height) as well as an unbiased one-pixel growth per tree per iteration [187].

The apparent linkage between stem density and crown diameter was apparent in the CHM at the SLP, this was especially the case for the LOGs installation where there is

considerable variation in density. An effort was made to predict crown widths from a nearest neighbour analysis. For each lidar-identified treetop, the mean distance of the six closest neighbours was computed and was related to crown width. Through manual data extractions, a small dataset was built that considered the crown boundaries of several individual crowns that spanned a range of stem densities. Focussing particularly on the levels of growing stock treatments, crown measurements in the CHM were made in the cardinal directions these data were then used to empirically model the average crown diameters from densities as represented by the local neighbour metric. An exponential term was incorporated to capture the saturation point were above a certain neighbour distance there should theoretically be no effect on crown width. Fit to the small dataset, the model took the approximate form $CW=16(1-e^{-0.14x})-6$. This form was fit qualitatively as the training set was small and did not capture the expected asymptote. Further investigation of this relationship revealed a discrepancy with larger isolated individuals that occurred downslope from the installation. Retention tree canopies deviated from the observed trend in that they were much wider with shorter mean distances (n=6); these observations supported a linear model form. This suggested that the saturation point initially selected was too small. The LOGS installations, thinning treatments and variable retention are all conditions that impact densities and further, crown width should theoretically be influenced by the temporal departure from the treatment application. When this foundation was evaluated against the crown width data within the SLP field data it was poorly fit and did not support the hypothesis that crown width can be determined by stem densities. There are however, many challenges in comparing the observed crown width-density relationship to the SLP reference dataset. Firstly the

magnitude and range of crown widths within the reference data are quite small, to the extent that there is little evidence of non-linearity between crown width and height. As mentioned, the CHM model was queried with very few samples and results would erroneously suggest a higher degree of fit while the SLP data are larger with an adequate amount of variation and although significant (F: 42.21, p:<0.000), produce poor fit metrics with a residual standard error of estimated average crown width of 0.62m and a weak (0.11) coefficient of determination. These observations provided evidence of the suspected disparity between lidar tree crown dimensions and those based on ground measurements. The difference in these two variables originates from the fact that the CHM approach observes the top down view and maps boundaries where tree crowns intersect, where on the ground there can be a certain degree of inter-tree crown growth. From the lidar perspective, it is not the crown dimensions that are being mapped but rather the dimensions of the portions of crowns that are exposed.

Without the ability to map individual crown sizes, the physical quantification of photosynthetic volume was considered not plausible. As an alternative, the data were queried to uncover any empirical relationships that may exist between any derived remote sensing metrics and the dependent productivity attribute. In order to evaluate the capacity for estimating individual tree-level productivity, an object was required to represent the individual. A database was built that spanned both the individual and plot level scales and included attributes generated for lidar treetops, lidar crowns, lidar plots, lidar topography and crown and plot spectroscopy.

Lidar treetop attributes were generated from the CHM local maxima tree list; statistical moments and percentiles were generated for the 2D and 3D treetop distance distributions as well as for the treetop heights. The lidar treetop attributes were populated for the treatment plot extents including the 5m buffer area (~30x30m). As an extension of previously developed methods that have been applied to more coarse scale forest inventory attribution, the traditional lidar moments, percentiles and canopy closure metrics were determined for the delineated crowns. In addition, several shape descriptors were generated for the delineated crowns. The crown shape metrics were expected to be helpful in discriminating correctly delineated and problematic crowns. It was suspected, and suggested by the crown width inquiry, that many of the crowns were not individual crowns but potentially an assemblage of more than one crown. In such problematic crowns, the shapes tended to deviate from circular or elliptical extents. A metric was devised and computed as the area difference of the geometry of the crown and the geometry of a circle defined by the crown polygon area and centroid; the larger the

remaining area (metric) the more the lidar crown would deviate from the circular model and the more likely it represents a crown assemblage. Such shape metrics are expected to provide an avenue for iteratively refining the tree crown delineation. Finally, the imaging spectrometer data, in reflectance, were extracted for each delineated crown. The established suite of vegetation indices (see section 4.2 and [124]) were computed, along with albedo, derivatives, continuum removal and signal to noise ($\mu_\lambda/\sigma_\lambda$ after z-score transform) metrics. The computed metrics were then summarized to the object level by summary statistics. The initial database was excessively large with nearly 6,000 explanatory variables. The database variables were filtered, omitting attributes that were not expected to be useful in productivity modelling or were expected to be noise prone. Omitted attributes included higher order object summary statistics and extremes (min and max).

For the regression-based productivity analysis, the individual objects were required to be associated with an individual in the ground reference dependent variable database. A three-dimensional nearest neighbour criteria was applied to associate the remote sensing data with the ground reference data. Each tree within the TLS survey was associated with its nearest lidar treetop. In some instances the tree survey position was not clearly located at the identified lidar treetop location for example in tree assemblages (one lidar crown with multiple surveyed trees). In an effort to account for these types of errors, the distance between the lidar treetop and the selected ground reference position was retained as a potential stratification attribute. It was anticipated that the use of this distance metric could be used to filter observations that had incorrectly matched ground reference data.

The reduced database was processed through an exhaustive model selection of the regression subset script with a maximum model length of three features. The models were selected with the periodic annual increment of volume as the dependent variable. Without consideration of crown class, 3D distance to the ground reference position or the lidar crown shape, prediction accuracies were low ~0.007m^3/yr. (RSE), which is roughly 50 percent of the interquartile range of the PAI of tree volume. The fit of the best model was weak (adjusted R^2: 0.54), which lead to the inquiry of the strata information. The prediction performance was evaluated by eliminating observations that had a crown class of intermediate or suppressed. When only dominant and co-dominant crowns were considered, the best model explained ~15 percent more of the variation in PAI in tree volume. There was no benefit to productivity prediction by only considering the dominant tree class. The rational for omitting these observations is intuitive, intermediate crowns are obstructed by more dominant adjacent or overtopping trees, therefore attributes defined from the top down perspective of the remote sensing data would be misleading. The crown class strata are indicative of the physical limitation of the approach to tree attribution from airborne remote sensing. Another limitation to model building for tree attribution from remote sensing data was the confusion of the individual tree in the airborne data and that in the ground reference data. The individual tree confusion was expected to be a significant confounding condition, despite the efforts taken to unambiguously associate ground reference and airborne data.

Two conditions existed in the individual tree survey that had the potential to confuse the matching of the remote sensing and ground reference database. In instances where the crown surface relief is less variable and where that relief variation occurs in

close horizontal proximities, the lidar treetop detection will fail. In other words, where treetops are close together and crowns are co-dominant and spatially contiguous, lidar tree detection may fail, as shown in section 5.4 on predicting lidar tree detection errors. Secondly, as this approach requires the definition of a tree object for data metric determination, lidar crowns were delineated. In the process of generating crown objects, reference trees are omitted when they are horizontally located within a larger crown, in crown assemblages for example. This tended to be common for trees on the periphery of the core treatment plot, where larger more dominant crowns existed within the buffer area and grew (algorithmically) to incorporate the location of the reference tree. In this situation the remote sensing metrics potentially represent a larger buffer tree while the associated ground reference data may represent a less dominant tree crown. In many of these core border trees, the location of the lidar treetop was horizontally, and in some cases also vertically, displaced from the TLS survey reference location. The three-dimensional distance from the reference tree (2012 tree height and TLS horizontal position) and the lidar detected treetop was computed and the regression exercise repeating while increasing the upper limit of the reference to target distance. Eighteen equal intervals (0.25m) were defined for the upper limit of the distance variable, observations with greater distances were omitted, and the model fit was determined for each (Fig. 6.1). There was a strong inverse relationship between the fit index and the reference to target distance. Although there was a large increase in the fit index below a distance of 3.5 meters, the fit steadily improved with decreasing distance down to 0.5m (note that at the most aggressive filtering <0.25m the number of observations was 85 down from 692 matches). The trend between the fit index and distance was expected, as

the dependent variable is not independent of the distance being used for the filtering. The intention was to use the distance attribute to identify incorrectly matched observations but because it is a 3-dimensional distance it also contains variation that is associated with height, and height is selected as an attribute related to volume increments. Therefore, it was recognized that this approach had the potential to bias model building so a conservative (large distance) selection threshold should be applied.

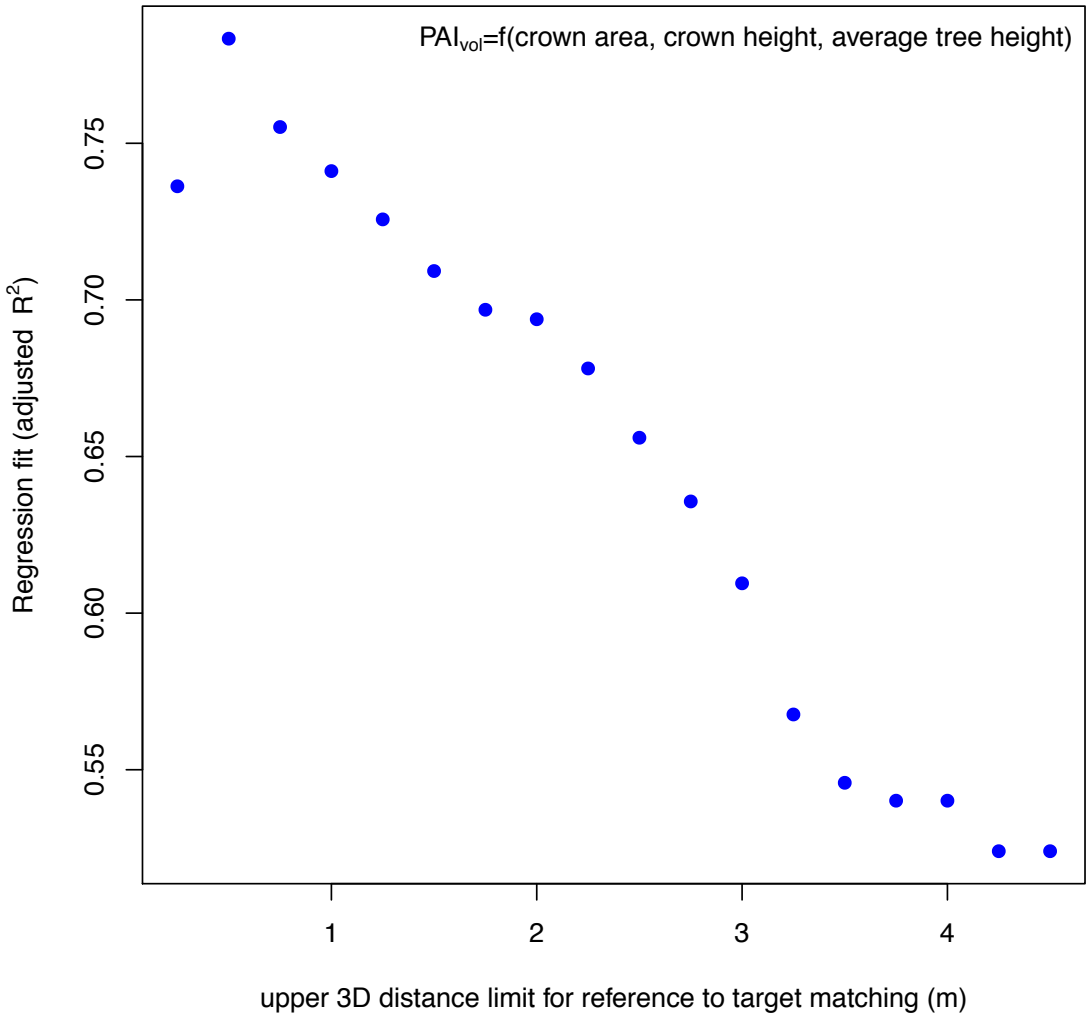


Figure 6.1 Modeling periodic annual increment in tree volume from the individual tree remote sensing metrics. Some trees were incorrectly matched to the ground reference data, in many of these instances the lidar treetop was displaced from the ground reference location. Using the distance between the reference and target, the data were iteratively filtered and the impact on the model fit was plotted.

Another observation made in assessing the lidar crown delineation result, was that in some cases crowns deviated from circular or roughly elliptical crowns. These divergent crown shapes tended to occur in high stem density plots where crown clusters appeared to confuse the algorithm, and as a result presented a problem for the one-to-one lidar tree crown to ground reference tree matching. In an effort to capture these problematic delineated crowns, shape metrics were generated. A shape metric seemed to capture these seemingly erroneous lidar crowns, by summing the area of the crown that falls outside the extent of a circle located at the centroid of the crown and with an area equivalent to that of the crown (Fig 6.2). In a manner similar to that applied to the reference distance, intervals of the crown shape metric were used to filter matched trees in order to remove potentially error prone crowns. The trend between model fit and the crown shape metric intervals in this comparison was not unidirectional or monotonic. The first interval did not fit any local trend because the filtering only selected ten samples (shape metric: $<1.02m^2$, R^2: 0.75). Beyond the first interval, sample sizes increased and two fit index maxima occurred at outside circle areas of $2.1m^2$ and $5.7m^2$ with adjusted coefficients of determination of 0.66 and 0.55 respectively. The qualitative evaluation of the shape metric with reference to the location of dominant and co-dominant reference trees suggested that a shape metric of less than approximately $3m^2$ identified the crowns that were roughly circular. This value corresponded with the end of a downward trend in the fit index with an increasing shape metric value (Fig. 6.3).

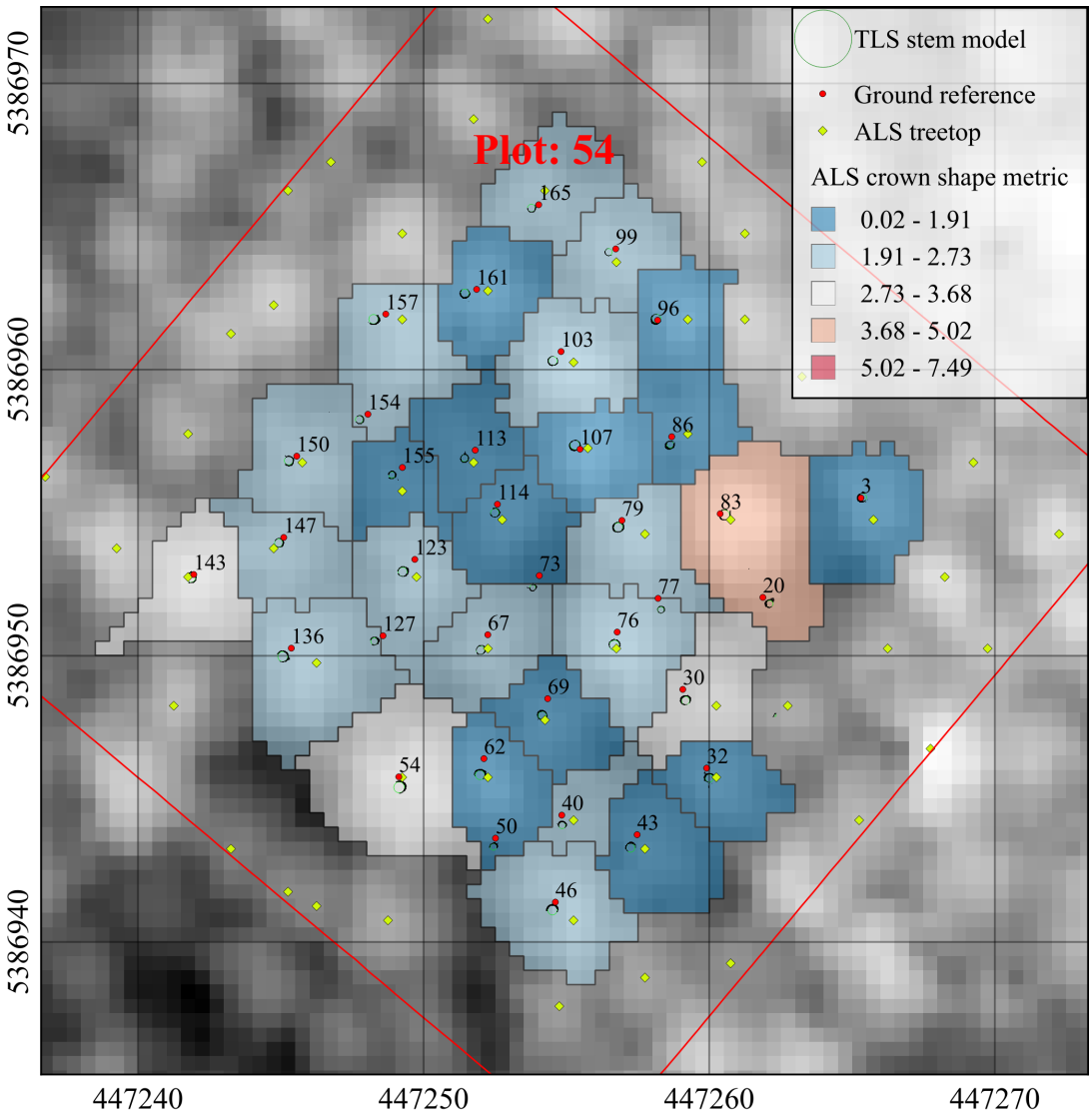


Figure 6.2 The ground reference database is translated to the remote sensing database by the nearest horizontal distance to a TLS surveyed stem, which is then translated to the nearest neighbour (3D) lidar treetop. Only those trees with an associated delineated crown are retained. Limitations with individual crown segmentation cause multiple trees to be located within one crown; this tends to change the shape of the crown segments, which may be detected in shape/compactness indices. Note that all but two core trees in plot 54 are co-dominant, tree 83 and 54 are dominant.

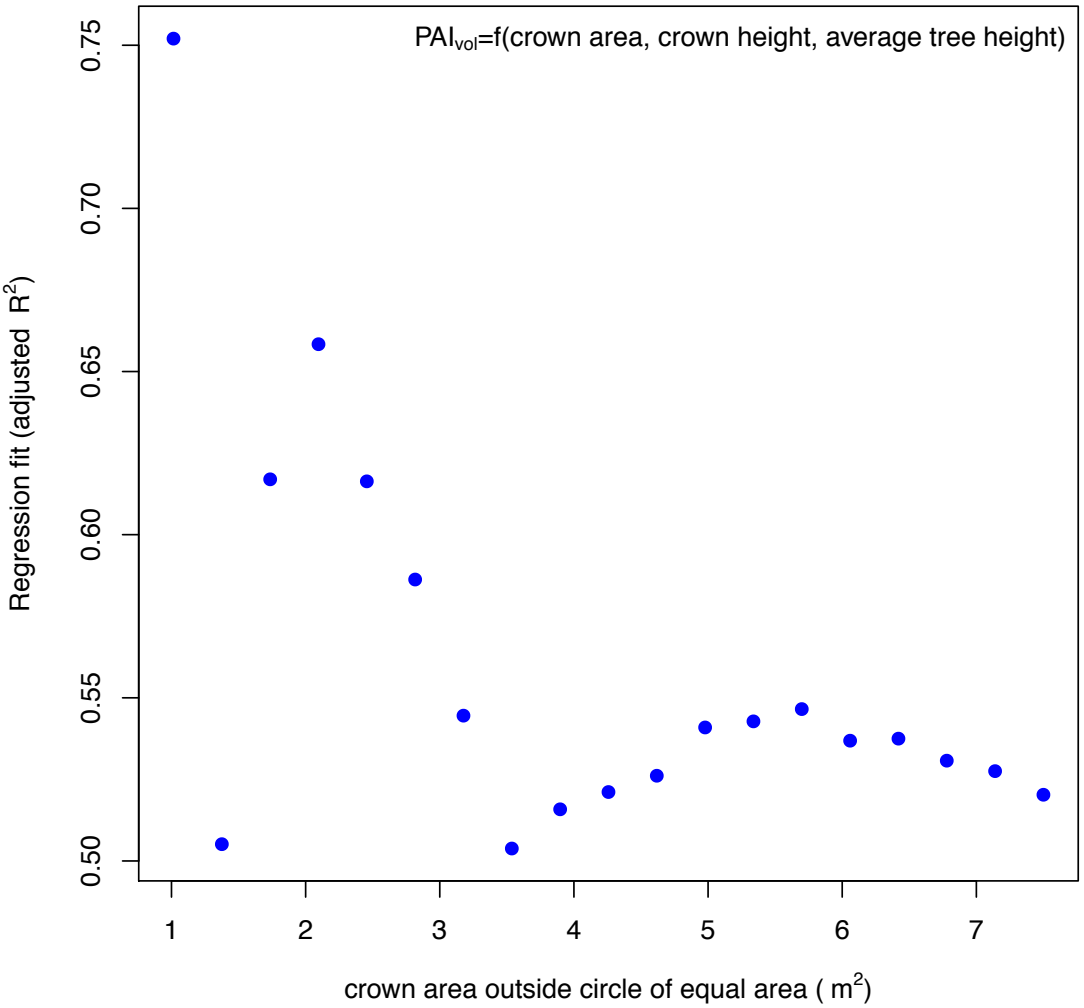


Figure 6.3 Investigating the change in PAI volume prediction from individual tree metrics stratifying by crown shape/compactness. Qualitatively, crowns below a metric value of roughly $3m^2$ appeared properly delineated. This inquiry suggests the use of a shape metric of approximately $2.1m^2$. However, the distribution of the shape metric is positively skewed and sample sizes change dramatically at the lower intervals from 10 to 134 in the first three intervals. Thus the variable sample size is likely to confound fit index value trends at these lower intervals.

In the modelling efforts investigating the three strata of crown class, reference distance and crown shape compactness it was determined that the benefit offered by the shape attribute (<1% explained variance) in concert with the reduction to the sample (n=478) was insufficient to warrant its use. The sample was filtered by only crown class and reference distance. Observations were retained if they met both the crown class

criteria as dominant and co-dominant, and the reference 3-D distance criteria, where lidar treetops were located within three meters of a reference tree. The filtered database contained 600 observations with 659 features. The candidate features included a binary attribute for crowns that had multiple references within, the reference distance, seven crown shape attributes, 53 lidar crown features, two lidar treetop heights, 87 plot level lidar treetop features, 365 spectral indices, 117 continuum removal metrics and 26 spectral signal to noise attributes.

The single most associated feature with periodic annual volume increment was the lidar treetop height. The consistency of feature selection provided some assurance that the single feature selection was not by chance. Of the 40 best single feature models, 27 of them selected features that were related to individual tree heights. There was some evidence of a non-linear trend in the relationship between the PAI volume and the individual lidar treetop height. The apparent non-linearity was largely dependent on extreme values, the model performance was not improved with standard logarithm, power or exponential transforms. The performance of the post-transformed models was evaluated by the fit indices, the residual standard errors and by the normality of the residuals. Although the SLR results suggested a sound statistical relationship (F-stat: 573.5, $p<0.00$), with only minor trends within the residuals (underestimates for shorter trees ~<22m), minor departures from residual normality and the absence of influential points, the predictive power of the SLR was low (RSE:0.0066, adjusted R^2: 0.4487). The lidar treetop height explained only 48.87% of the variation in the tree volume production rate. Clearly, the growth of individual trees is not exclusively a function of tree height. However, for the age and structural conditions at the SLP it is the case that taller trees are

more productive and that the measurement of individual tree height from lidar is able to capture this trend (Fig. 6.4, 6.5 & Table 6.1).

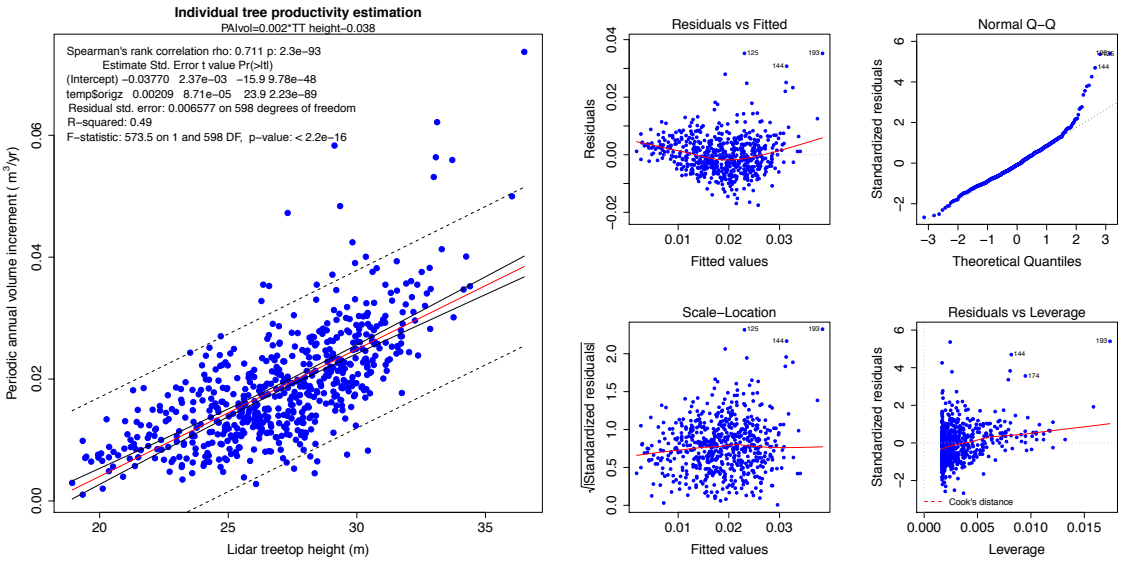


Figure 6.4 The residual distribution of the SLR for estimating PAI volume from lidar treetop height suggests an improvement could be achieved by estimating a curvature parameter.

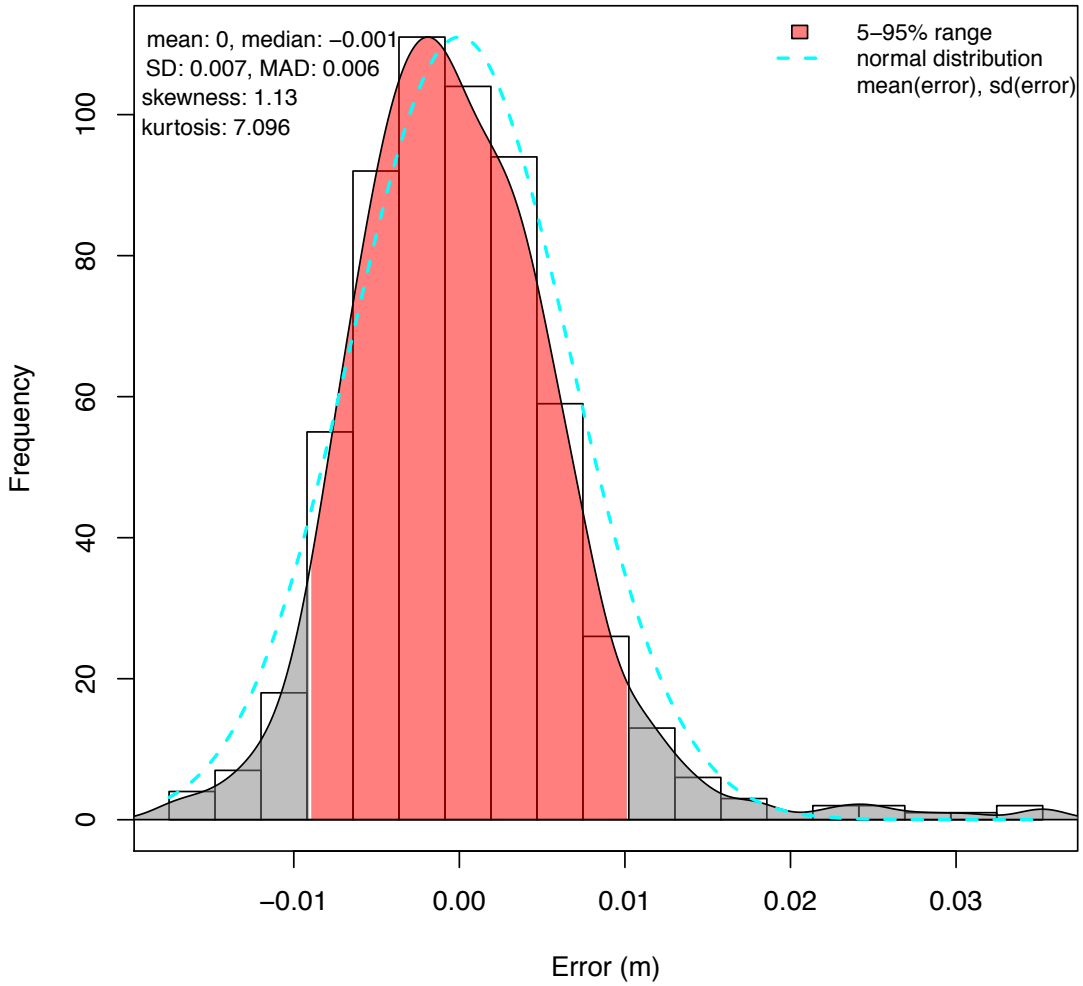


Figure 6.5 SLR residual distribution histogram density and normal distribution suggest minor skewness and kurtosis departures from normality

Table 6.1 Bootstrap of SLR predicting tree PAI in volume from the lidar treetop height						
	Intercept	TT_{height}	R^2	RSE	F-stat	P-value
Minimum	-0.048	0.0018	0.37	0.0055	376.21	<0.000
Q1	-0.040	0.0020	0.47	0.0064	533.90	<0.000
Mean	-0.038	0.0021	0.49	0.0066	576.63	<0.000
Median	-0.038	0.0021	0.49	0.0066	571.53	<0.000
Q3	-0.036	0.0022	0.51	0.0068	617.92	<0.000
Maximum	-0.029	0.0025	0.57	0.0077	787.68	<0.000
1000 Bootstrap iterations each built from randomly sampling the individual tree data with replacement 600 times to equal the number of individual tree observations.						

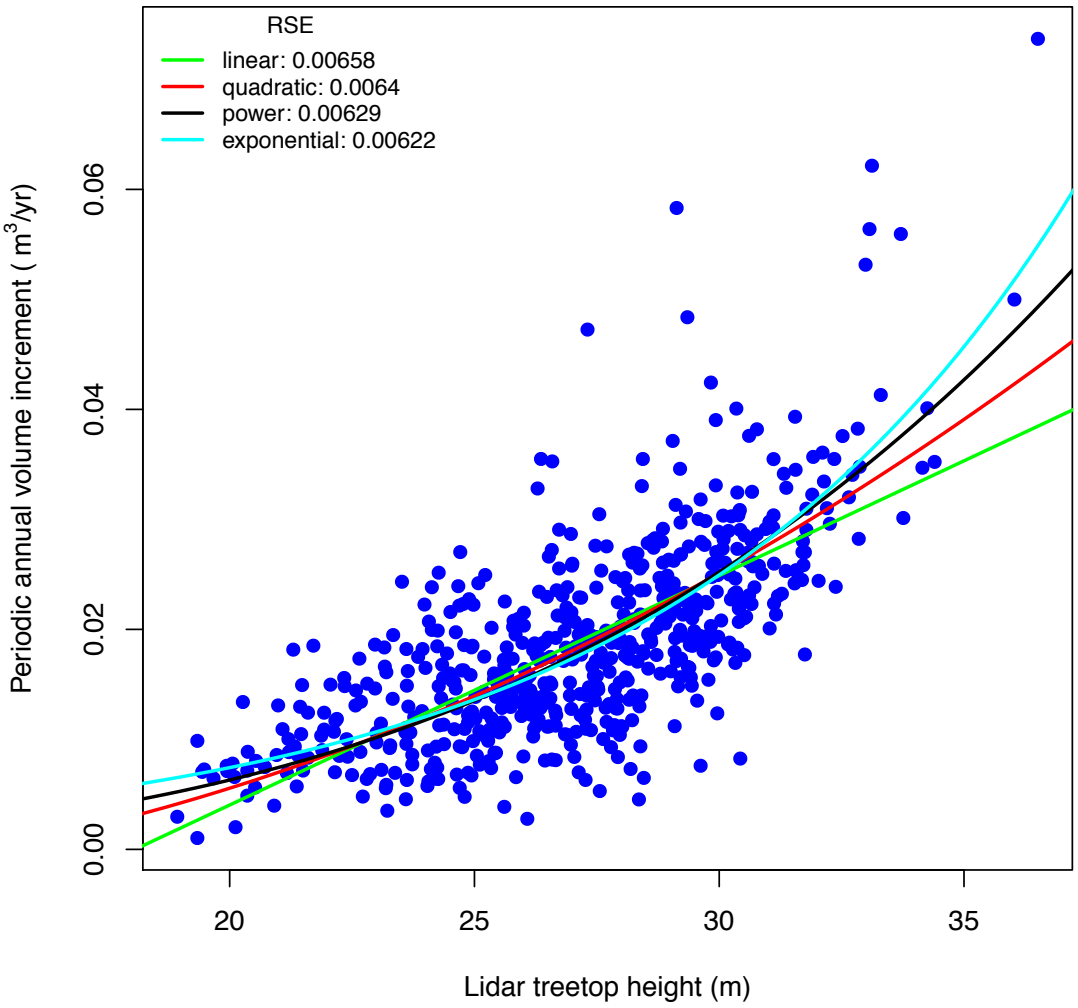


Figure 6.6 Curve estimation for PAI in volume and lidar treetop height. A linear and quadratic model with intercepts, and power and exponential forms without intercepts were fit. The residual standard errors were 6.40×10^{-3}, 6.29×10^{-3} and 6.22×10^{-3} for the quadratic, power and exponential models respectively. The exponential fit was considered best and took the form PAIvol=6.593×10^{-4}*1.129^TT height. The isolated observations with high PAI were all dominant crown classed trees. Stratification by crown class did not improve modeling or change non-linear trends.

The non-linearity in productivity and lidar treetop height was estimated with a quadratic, power and an exponential fit (Fig. 6.6). The approach that produced the smallest residual standard error was the non-linear fit of the exponential model. The residual standard errors were 6.397×10^{-3}, 6.295×10^{-3} and 6.216×10^{-3} for the quadratic, power and exponential models respectively. The exponential base shape parameter

estimate converged to a value of 1.128746, and the transformed lidar treetop heights were then submitted to a simple linear regression without the intercept estimate (Fig. 6.7, Table 6.2). The transformed data resolved the trends observed previously in the residual plots, however the heavy tailed shape in the residuals persisted (Fig. 6.8). Although the data transformation resolved statistical concerns, the transformation should be logical and physically meaningful. The transformation suggested that taller trees produce proportionally greater volume, which is conceivable for the SLP where inter-crown competition might limit growth.

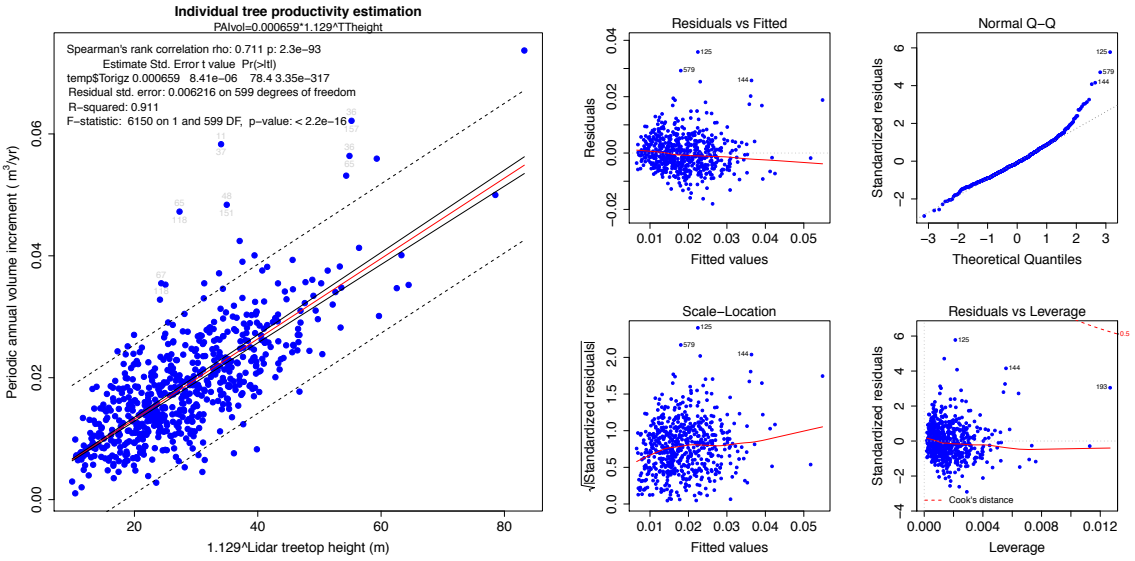


Figure 6.7 The exponent transformed lidar treetops had resolved the previously observed trend in the residuals of the SLR. Note the fit index does not adequately represent the true degrees of freedom as the curvature parameter was estimated prior to the SLR illustrated here.

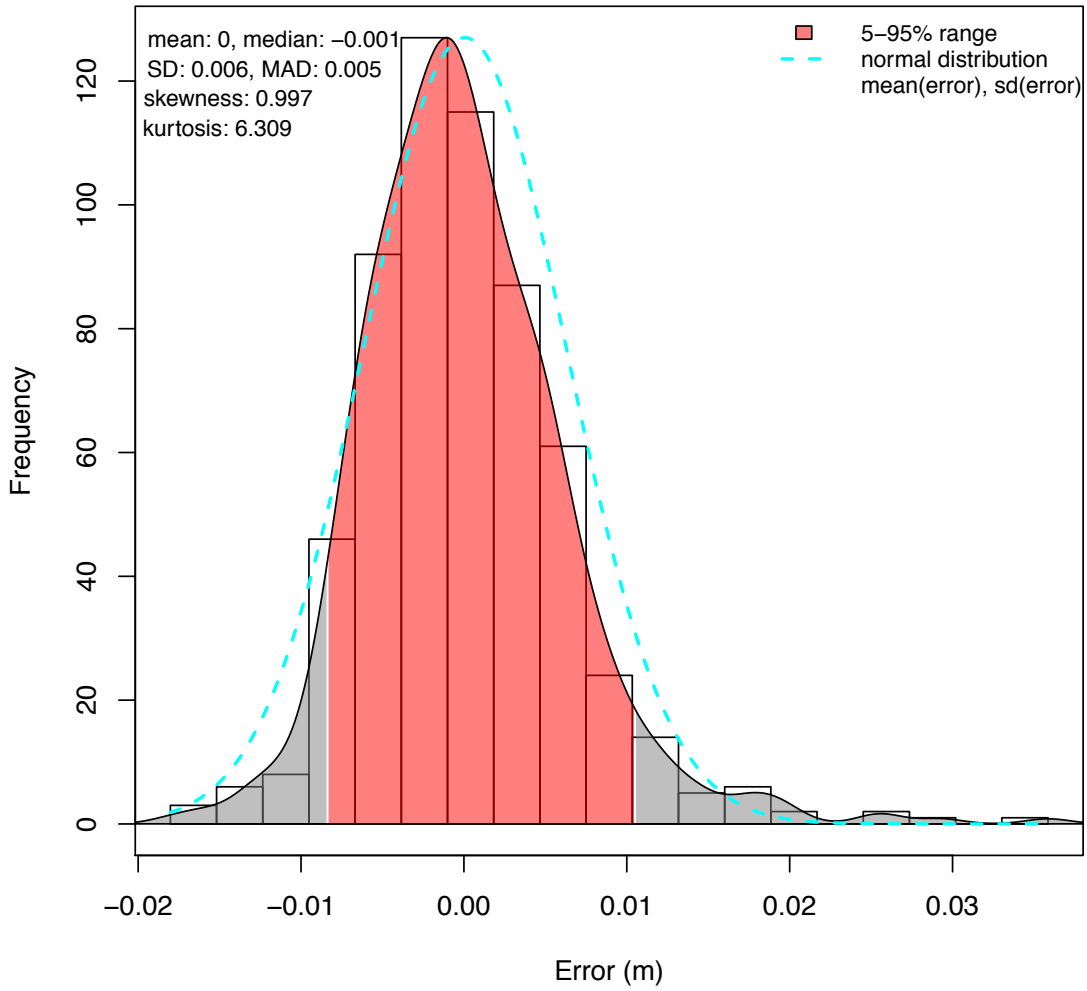


Figure 6.8 The residual distribution of PAI volume estimates from the exponent transformed lidar treetops is marginally less skewed with a lower kurtosis relative to the residual distribution produced from the original SLR

Table 6.2 Bootstrap of SLR with non-linear parameter estimation for predicting tree PAI in volume from the lidar treetop height

	Base (b)	b^TTht	R^2	RSE	F-stat	P-value
Minimum	1.108	3.25×10^{-4}	0.89	0.0052	4688.74	<0.000
Q1	1.124	5.88×10^{-4}	0.91	0.0060	5812.83	<0.000
Mean	1.129	6.67×10^{-4}	0.91	0.0062	6212.84	<0.000
Median	1.129	6.62×10^{-4}	0.91	0.0062	6217.65	<0.000
Q3	1.133	7.41×10^{-4}	0.92	0.0064	6579.79	<0.000
Maximum	1.156	1.13×10^{-3}	0.93	0.0072	8293.25	<0.000

1000 Bootstrap iterations each built from randomly sampling the individual tree data with replacement 600 times to equal the number of individual tree observations. Note that values for the exponential base are the base values, while the values for the "b^TTht" are the coefficients that apply to the transformed lidar treetop heights. R^2 and P-values do not reflect the -1 degrees of freedom from the non-linear parameter estimation.

The regression analysis that considered a model with a feature length of two supported the initial SLR model, where individual lidar treetop height significantly contributed to explaining the variation in PAI volume. In 32 of the 40 best two-feature linear models the individual tree height (or a similar metric e.g. ICT_LHQ100) was paired with a plot level height attribute, mostly lidar treetop plot level height descriptors. The feature selection for the two-variable model is biologically meaningful as the selection of the individual height and the heights of its neighbours would imply that the model is selecting attributes that capture the crown class of the individual. These two attributes identify how tall the tree is relative to the surrounding trees; if the tree is taller than its neighbours it likely has a larger crown, and has had a history of greater productivity relative to its neighbours and is experiencing less competition for resources. The model selected as best fit with productivity selected the lidar treetop height, and the average plot level lidar treetop height. Given that the average of the lidar treetop heights is less influenced by noise than other summary statistics (*i.e.* percentile intervals, which made up a large portion of the next best two-feature models), this best model was retained and analysed further.

The initial two-feature model produced a residual standard error of $0.00529 m^3/yr$. however there was an apparent tend towards over prediction at the lower PAI range (Fig. 6.9 & Table 6.3). This non-linearity, which was previously observed and attributed to the PAI to lidar treetop relation, was removed by the exponent transformation. The transformation came at the expense of the prediction error, where the RSE was slightly increased by $2x10^{-5}$ to $0.00531 m^3/yr$. The residual distribution more closely approximated a normal distribution when the transformation was applied. The

transformation reduced the skewness of the residual distribution from 0.75 to 0.67, and also reduced the kurtosis from 6.59 to 5.92 (Fig. 6.10). These distribution attributes are outside the range for a normal distribution of size 600 drawn 100,000 times, which was -0.41 to 0.48 for skewness and 2.35 to 4.37 for kurtosis.

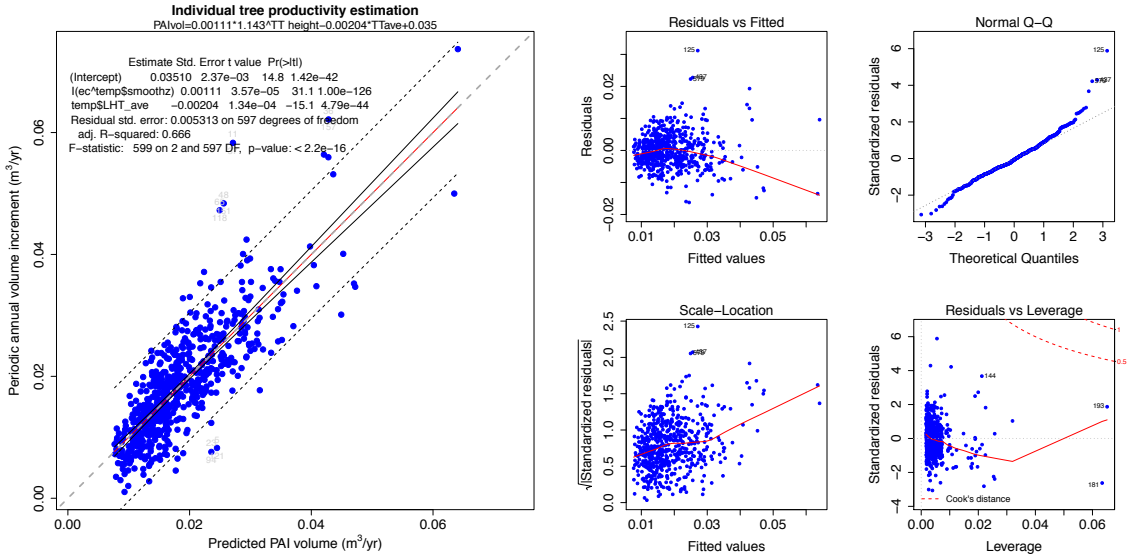


Figure 6.9 The best two-feature model was selected by the exhaustive search regression subset, which identified the linearized lidar treetop height and the average plot lidar treetop height. An exponent transformation resolved observed trends in the initial residual plots. These two attributes explain nearly 67% of the variation in individual tree productivity. The resulting model predicts PAI volume with a precision of 0.005 (RSE).

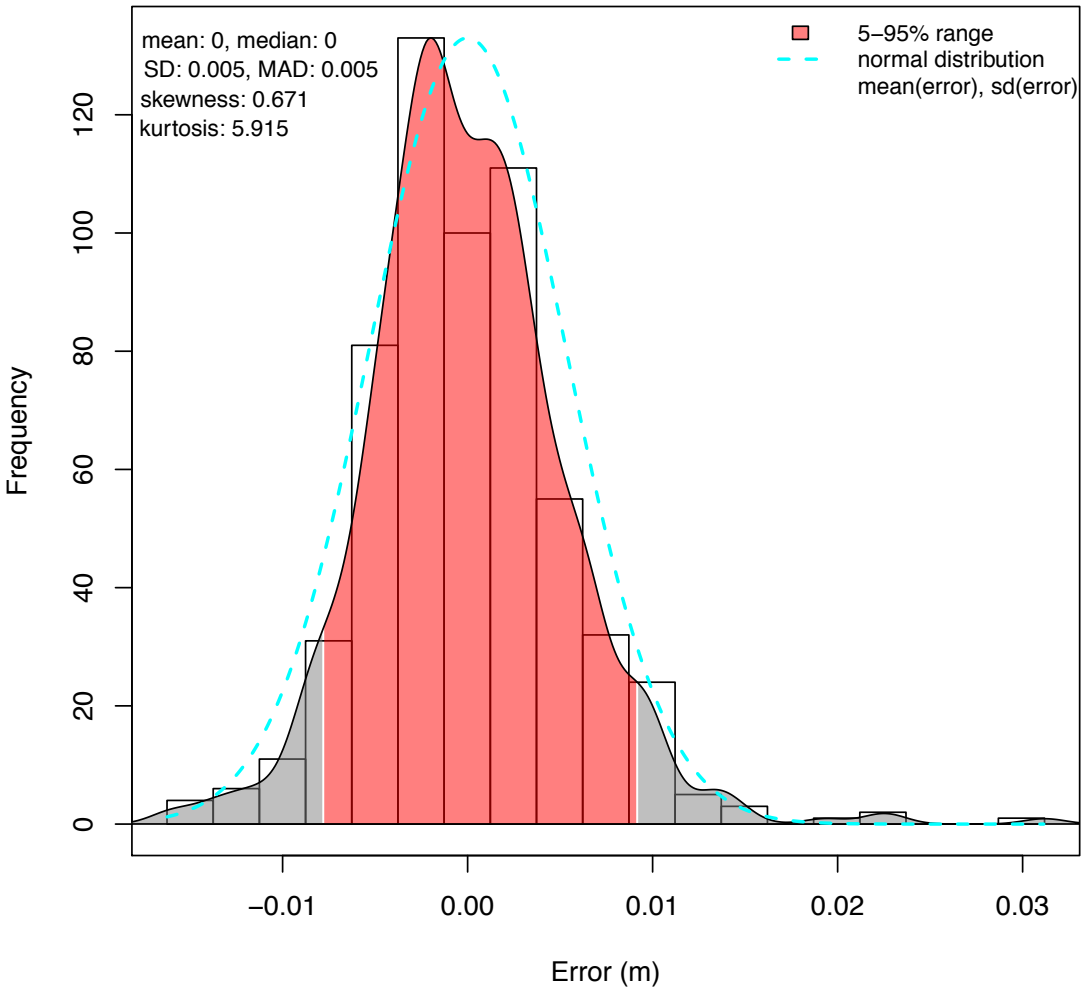


Figure 6.10 The residual distribution from the two-feature regression model predicting PAI volume is approximately normal. The residuals are slightly skewed 0.67 and slightly leptokurtic (5.91) relative to the normal distribution (skewness: 0.0, kurtosis: 3.0). The kurtosis of the residuals suggests that there is a high density of low magnitude errors.

Table 6.3 Bootstrap of MLR with non-linear parameter estimation for predicting tree PAI in volume from the lidar treetop height and plot average lidar treetop height							
	Base (b)	Intercept	b^TTht	TTave	R^2	RSE	F-stat
Minimum	1.118	0.02568	0.00045	-0.00258	0.58	0.0046	414.47
Q1	1.137	0.03351	0.00096	-0.00215	0.65	0.0051	561.26
Mean	1.143	0.03531	0.00113	-0.00205	0.67	0.0053	611.43
Median	1.143	0.03507	0.00111	-0.00205	0.67	0.0053	603.67
Q3	1.148	0.03719	0.00129	-0.00195	0.69	0.0055	655.58
Maximum	1.177	0.04371	0.00212	-0.00155	0.76	0.0062	960.21
1000 Bootstrap iterations each built from randomly sampling the individual tree data with replacement 600 times to equal the number of individual tree observations. Note that values for the exponential base are the base values, while the values for the "b^TTht" are the coefficients that apply to the transformed lidar treetop heights. R^2 do not reflect the -1 degrees of freedom from the non-linear parameter estimation.							

The selection of the individual height and the plot level average height suggested that the relative dominance of the individual was a significant feature related to individual productivity. It was recognized that it was overly simplistic to assume that only unique effects existed for this particular model. Clearly the relationship between tree height and productivity would be modulated by the average plot heights. The interaction term was included and the model was improved (Fig. 6.11 & Table 6.4).

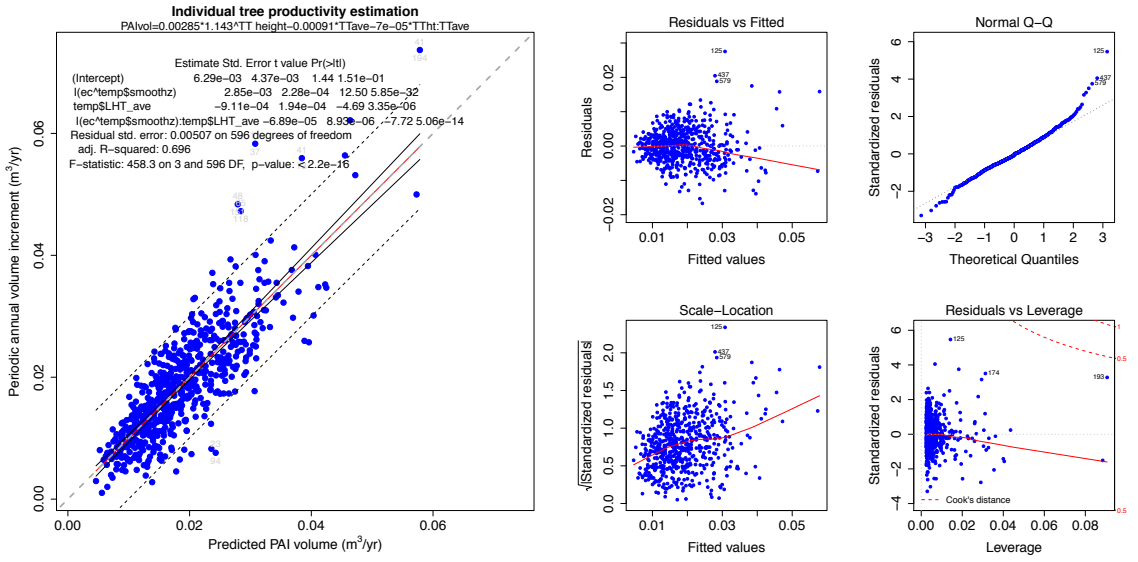


Figure 6.11 Applying the lidar treetop height, plot average lidar treetop height and the interaction explained 2% more variation in productivity over the previous two-feature model without the interaction.

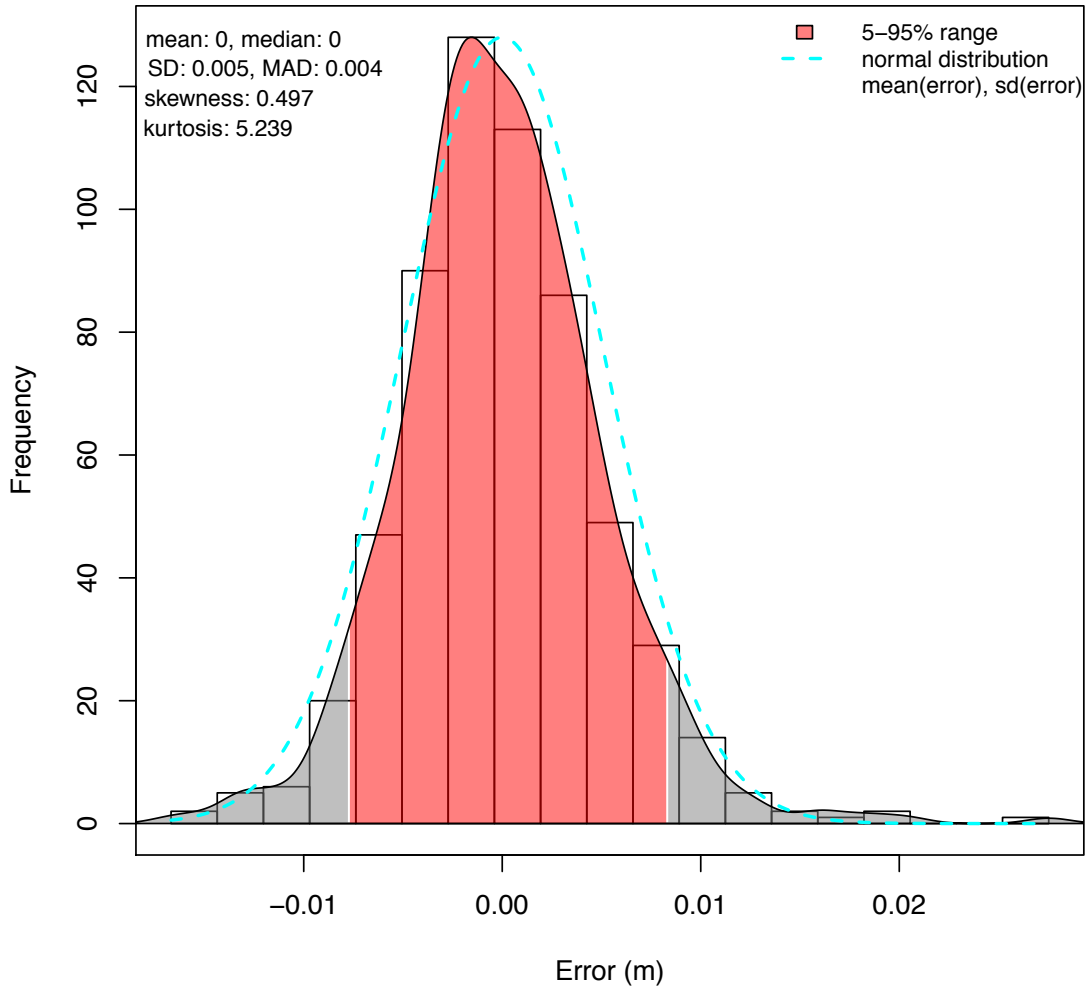


Figure 6.12 Residual distribution produced by estimating PAI volume from linearized lidar treetop height, plot average lidar treetop height and their interaction.

Table 6.4 Bootstrap of MLR with non-linear parameter estimation for predicting tree PAI in volume from the lidar treetop height and plot average lidar treetop height and the interaction

	Base	Int.	b^TTht	TTave	Interaction	R^2	RSE	F-stat
Min	1.118	-0.0165	0.00111	-0.00157	-0.00015	0.61	0.0045	319.07
Q1	1.137	0.0025	0.00239	-0.00106	-0.00008	0.68	0.0049	429.14
Mean	1.143	0.0066	0.00289	-0.00092	-0.00007	0.70	0.0050	468.25
Med	1.143	0.0067	0.00283	-0.00093	-0.00007	0.70	0.0050	465.38
Q3	1.148	0.0104	0.00332	-0.00078	-0.00006	0.72	0.0052	502.77
Max	1.177	0.0233	0.00576	-0.00005	-0.00002	0.79	0.0058	738.93

1000 Bootstrap iterations each built from randomly sampling the individual tree data with replacement 600 times to equal the number of individual tree observations.

A significant interaction term between the lidar treetop height and the plot average lidar treetop height, suggested that an arithmetic combination of the two would benefit the productivity model. This prompted the inclusion of an additional attribute into the pool of potential independent variables, the linearized individual lidar treetop height was normalized by the plot level average lidar treetop height and the feature selection was re-iterated. Conceptually, the ratio made logical sense because it would capture the relative crown dominance directly as opposed to the interaction, which would moderate the main effect of tree height on PAI according to the average plot tree height. While the interaction may compare well for growth prediction at the SLP site, extrapolation to more varied ages and structures is expected to change feature selection, not to mention the significant influence of site attributes that would also modify these results. The regression subset with the tree height ratio variable identified the lidar tree height to average plot lidar tree height ratio as the single best feature for estimating tree-level productivity. The ratio alone explained nearly 65% of the variation in tree-level productivity. Of the forty best two-feature models for predicting periodic annual volume increments, all included some variant of the relative lidar treetop height attribute (lidar treetop height/ plot average lidar treetop height). In 26 of the forty best two-feature models, an individual lidar point height attribute was selected as significantly contributing to explaining the variation in productivity. The ten best two-feature models selected a within crown lidar percentile height between the 15th and the 50th percentile, (the 85th and the 90th were also selected within the best ten). The explained variance within these ten best models varied little, the best two-feature model only explained two tenths of a percent more variation in PAI volume than the tenth best two-feature model. The attribute expected to be most

robust and less affected by noise was selected for further investigation. The selected two-feature model was that produced from the regression of the individual crown median lidar height and the relative lidar treetop height ratio. This second iteration of the two-feature model was a slight improvement in terms of the explained variance and the residual standard error, which increased to 70% and decreased to 0.00504m^3/yr. respectively. There appeared to by some minor structure in the residual plots with over predictions of PAI at the lower range of predicted PAI volume (Fig. 6.13 & Table 6.5).

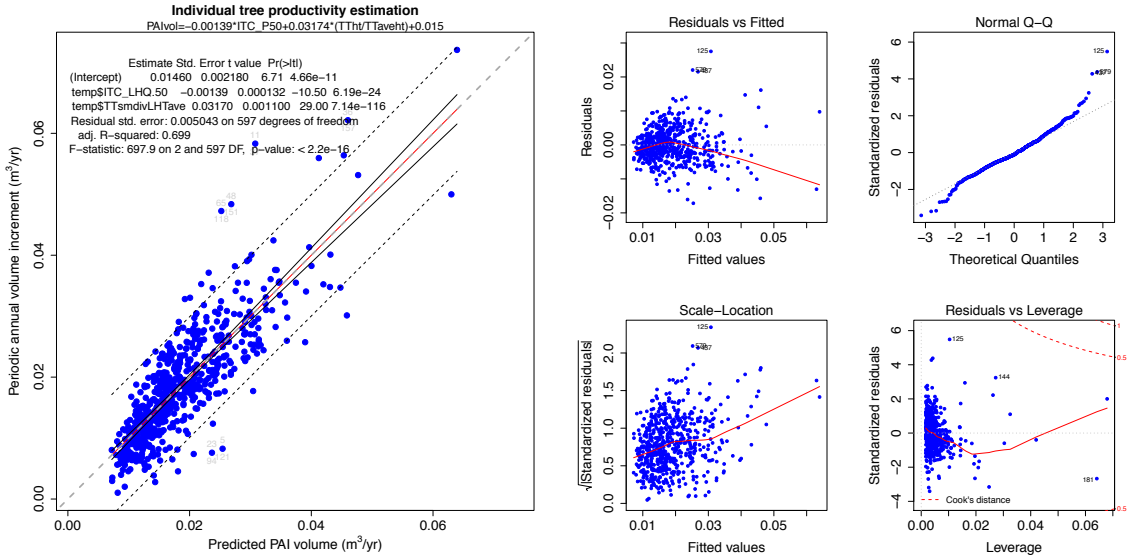


Figure 6.13 Applying the relative lidar treetop height variable with the within crown median lidar point height explained 3% more variation in productivity over the previous two-feature model built from lidar treetop height and plot average lidar treetop height.

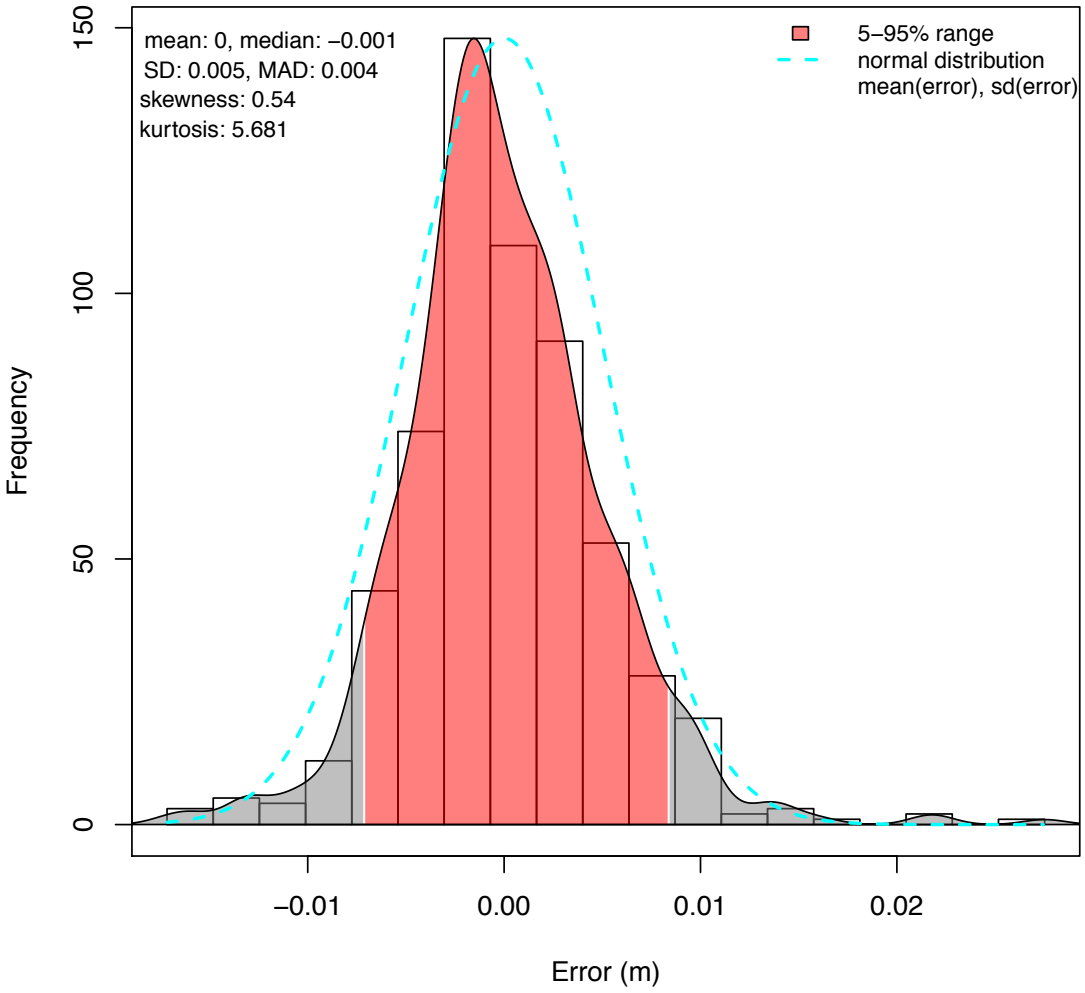


Figure 6.14 Residual distribution produced by PAI volume estimation from lidar tree crown 50th percentile height and treetop height to plot height ratio. The residual distribution is slightly leptokurtic and positively skewed relative to normal.

Table 6.5 Bootstrap of MLR with non-linear parameter estimation for predicting tree PAI in volume from the lidar tree crown 50th percentile and treetop height to plot height ratio

	Intercept	ITC P50	TTht/TTave	R^2	RSE	F-stat	p-value
Minimum	0.008	-0.0019	0.0264	0.62	0.0044	482.56	<0.000
Q1	0.013	-0.0015	0.0308	0.68	0.0049	644.71	<0.000
Mean	0.015	-0.0014	0.0319	0.70	0.0050	712.30	<0.000
Median	0.015	-0.0014	0.0319	0.70	0.0050	704.88	<0.000
Q3	0.016	-0.0013	0.0330	0.72	0.0052	772.65	<0.000
Maximum	0.023	-0.0009	0.0366	0.79	0.0057	1151.77	<0.000
1000 Bootstrap iterations each built from randomly sampling the individual tree data with replacement 600 times to equal the number of individual tree observations.							

As a last effort to improve the productivity modelling an additional term was included. The exhaustive model search overwhelmingly selected a crown shape attribute. The area to perimeter ratio was selected in 29 of the 40 best three-feature models. The selection of the crown shape parameter is interpreted as not being sensitive to productivity but rather indicative of problems in the delineation of the individual. The area to perimeter is commonly used in the GIS community as a compactness index. Area to perimeter ratio is maximized for a circle, so in circumstances of tree clusters in one lidar crown, the shapes will deviate from circular and reduce the area/perimeter index. However, the benefit of including the crown shape index, which happens to be quite small, comes at the expense of increased model complexity. The benefit of the shape index over the best two-feature model is 2% more explained variation and $1.66 \times 10^{-4} m^3/yr$ less residual standard error. The residual distribution produced by the three-feature model did not exhibit the same over prediction structure observed in the two-feature model. The previous two-feature model was built replacing the lidar median point height with the lidar treetop height and the residuals were not over predicted at the lower range of PAI in volume (Fig. 6.15 & 6.16, Table 6.6). Therefore, it was determined that the non-linearity from the previous model was attributed to the same signal initially observed in the lidar treetop height, which was removed by the exponential transform. The non-linear trend suggests that the lidar treetop height models for productivity are not as sensible to variation in productivity at low levels.

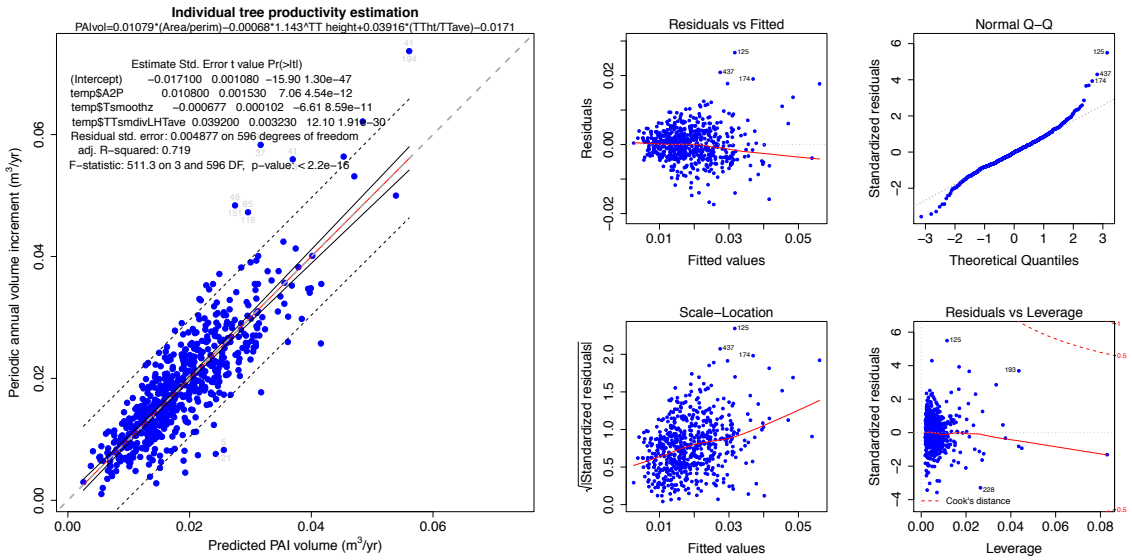


Figure 6.15 Crown shape attributes were assessed for their ability to indicate tree clusters rather than individual crowns and explained 2% more variation in the volume increments.

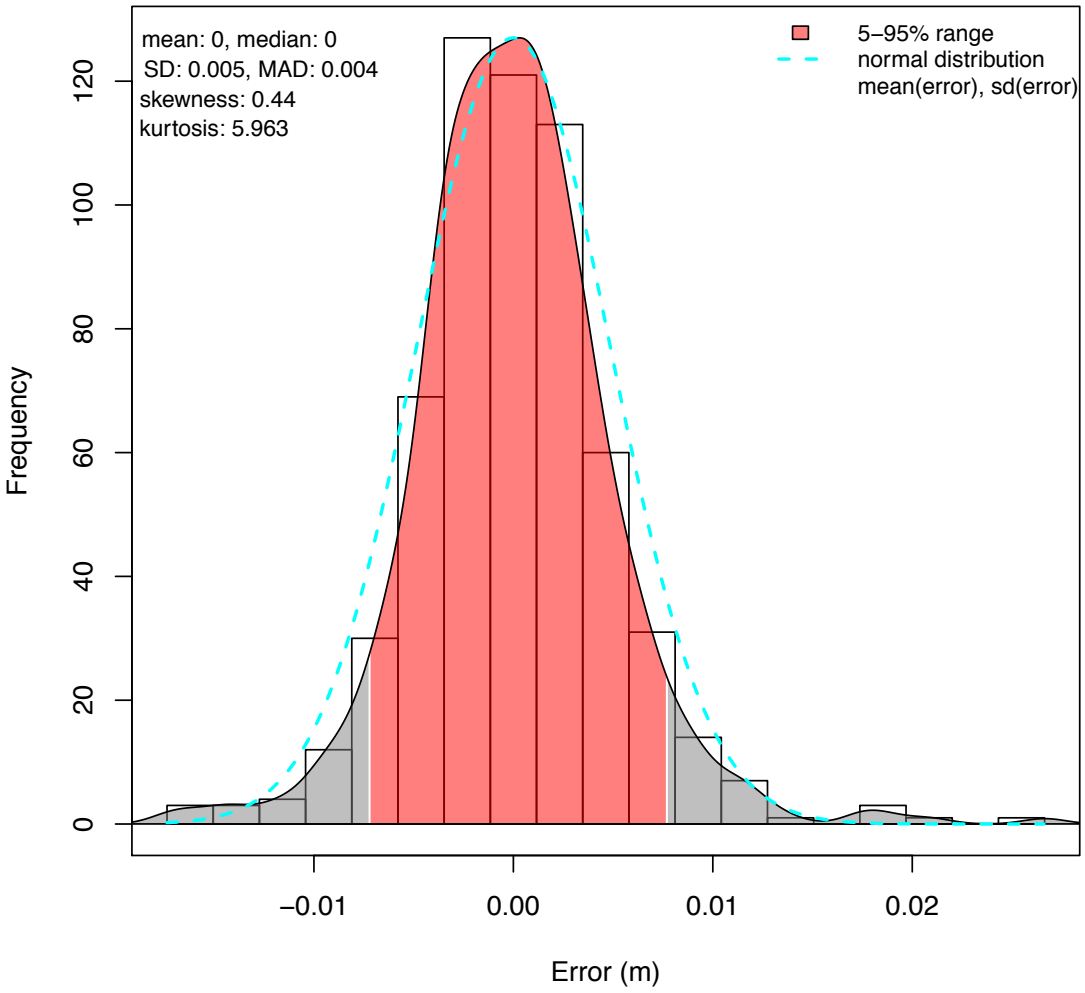


Figure 6.16 Residual distribution produced by PAI volume estimation from lidar treetop, treetop height to plot height ratio and a crown shape attribute. The residual distribution is slightly leptokurtic and positively skewed relative to normal.

Table 6.6 Bootstrap of MLR with non-linear parameter estimation for predicting tree PAI in volume from the lidar treetop height and plot average lidar treetop height and a crown shape attribute

	Intercept	Area/perim.	TTht	TTht/TTave	R^2	RSE	F-stat
Min	-0.0214	0.0062	-0.00111	0.0290	0.64	0.0042	359.64
Q1	-0.0182	0.0098	-0.00077	0.0367	0.71	0.0047	478.49
Mean	-0.0172	0.0108	-0.00068	0.0394	0.72	0.0049	521.30
Med	-0.0172	0.0109	-0.00068	0.0394	0.72	0.0048	519.57
Q3	-0.0162	0.0118	-0.00060	0.0421	0.74	0.0050	559.39
Max	-0.0120	0.0156	-0.00035	0.0527	0.80	0.0056	786.23

1000 Bootstrap iterations each built from randomly sampling the individual tree data with replacement 600 times to equal the number of individual tree observations. The lidar treetop heights were linearized by an exponent transform with the base 1.142768.

The efforts to build a processing stream for the morphometric attribution of individual trees from an integrated remote sensing database were rewarded by physically relevant empirical regression models. A considerable amount of time and effort was required to establish a dataset that was capable of calibrating an individual tree model. The time, work and instrumentation required to build the training dataset calls into question the practicality of such a study for operational forest inventory. Considering the investment required, the utility of a physically based model that is less likely to change when extrapolated to other sites is obvious. The confluence of remote sensing and forest growth modelling is a research area that should see increased activity in the future.

This portion of the study presented the details of establishing a control network to support a lidar ground survey. The lidar ground survey was a necessity for stem mapping and providing confidence in the proper association between the airborne remote sensing database and the CFS ground reference survey. The TLS data, although an intensive strain on processing and time resources proved to be rich in information, the extent of which exceeds what has been applied here. The TLS survey analysis demonstrated that a ground reference survey is possible to map the absolute locations of standing trees. In addition, individual tree attributes were measured from the ground reference point cloud including diameter, height to live crown and bole lean. The detail within these TLS datasets, and modern ALS introduces a new paradigm in remote sensing research, where the limiting factor for information extraction is not a data quality issue, as has been the case in the past, but rather the lack of algorithms designed for such highly detailed point clouds.

The evaluation of mapping individual trees through airborne lidar demonstrated a limited capacity under the stand conditions present at the SLP site. The analysis concluded with some results that could have been expected. Tree crowns that do not occur within the dominant and co-dominant classes were largely omitted from the top down local maxima approach. However, it should be noted that this study did provide some evidence that understory development could be discerned within plot level lidar height distributions. The coarse spatial scale required for such information limits the ability to map individual trees in the intermediate or suppressed crown classes. The amount of detail in the reference database for this study offered an opportunity to investigate the conditions under which the individual survey approach would break down. Through a logistic regression it was shown that the lidar tree survey would fail at increased densities and with crown dominance (height differential). A significant interaction term implied that the distance of the neighbouring tree crowns moderates the effect of the height differential on tree detection. The implication of this conclusion is the success of a lidar individual tree survey is largely dependent on the structural development stage of the targeted forest stand.

Finally, this chapter presented the empirical modeling of productivity at the individual scale. Productivity in this case was represented as the periodic annual increment in bole volume. The annual increment was derived from the CFS database occurring between 2002 and 2012. Volumes were determined by DBH and heights. Tree heights were not all measured in the field and therefore DBH to height models were required. Initial efforts without observation filtering were unsuccessful (less than 60% explained variation). Given the lessons of the lidar tree mapping exercise, it was expected

that crown class filtering would improve the results. The remote sensing database was also plagued by crown segmentation. As evidenced by the TLS ground survey, the individual crown segment objects tended to group multiple tree crowns; this was especially the case for many of the control treatment plots. In these cases, the object descriptive metrics represented a crown amalgamation but were associated with the ground reference attributes of the individual. The data available for describing the forest cover in this project was considerably large. Nearly 6,000 attributes were built from the lidar and spectrometer datasets to describe 693 individual trees. Ultimately, the productivity model was built from the individual lidar treetop height and the height proportional to the plot average height. Model performance marginally improved with additional terms but the validity of those attributes was questioned. The precision of the estimates did not reduce much beyond 0.005m^3/yr. and the models explained 70% of the variation in productivity. The individual productivity model agreed well with the analysis of chapter three section six, where it was demonstrated that the periodic annual increment in volume was related to height, height relative to the height of neighbours and crown class. In contrast to the area-based approach, the inclusion of spectroscopy did not significantly contribute to productivity modelling. The omission of AIS metrics in the PAI modelling is expected to be the result of a low spatial resolution relative to the scale of crowns at the SLP site. Alternatively, crown health at SLP may be invariant in which case the observed variation in productivity is the result of structural conditions and its impact on resource competition.

CHAPTER 7: CHANGING GAP STRUCTURE, A CASE STUDY FOR GVWSA

To support forest management operations for residential drinking water quality and quantity, a study was conducted to identify likely areas affected by root disease. A multi-temporal lidar surface model identified locations of toppled trees. The lidar product was used to sample regions in an airborne imaging spectrometer (AIS) dataset collected at the initial sampling date. The AIS data were used to produce relative estimates of canopy chlorophyll through the continuum removal approach. The union of spatially auto-correlated windthrow and spatially auto-correlated poor health identified likely root disease infection areas. The analysis suggested that between sampling dates greater than 3,200 trees were toppled, 10% of which occurred in spatial concentrations above ambient. In 2006 there was 73ha of forest classified as spatially correlated poor health, which decreased to 65ha in 2012. Ultimately, 10.3ha were identified as potential root disease sites experiencing spatially auto-correlated windthrow and poor health in 2006.

The quality and quantity of the water resource is intimately associated with the condition of the forest vegetation in a given drainage basin. The services provided by forested areas include, among others, increased infiltration rates and soil moisture capacity thereby slowing overland runoff and the consequent soil erosion. In turn, healthy forests maintain the quality of the water resource by decreasing sediment load and turbidity, the largest single water pollutant in the United States. Forests also maintain lower dissolved elements, cooler temperatures, and higher dissolved oxygen all of which contribute to higher quality water, irrespective of resource use [188]

Forests of the Pacific Northwest are affected by root disease, a natural disturbance agent that has the potential to increase stream sediment load and decrease slope stability

by increasing the occurrence of windthrow. Root disease constitutes a considerable risk to water quality.

Root disease is an economically important disease, causing significantly reduced wood production and quality in the primary host, Douglas-fir (*Pseudotsuga menziesii*). Lost revenue for the North American economy is estimated at between $314-330M USD annually (4.4M m^3 lost volume [189], $70-75 USD/$m^3$ average grade, west cascades, Douglas-fir [190]). The persistence and spread of the disease is facilitated by forest timber production management practices. Instead of immune early seral species occupying the post-harvest stand, and through time reducing active inoculum, the economically viable species and primary host is reinitiated and residual inoculum is activated, further extending the infection site.

The two prominent root disease agents are the fungi *Phellinus sulphurascens* and *Armillaria ostoyae*, which travel, as mycelium (vegetative phase), between roots of adjacent trees. Structural stability of the root systems and nutrient transport from roots to crowns are compromised as lignin and cellulose are metabolized. Therefore, symptomatic infected forest stands are expressed as increased windthrow events, which manifest changes in canopy gap structure and reduced foliar chlorophyll at a greater rate relative to unaffected stands. Given the pathology of the disease, the symptoms of root disease have a tendency to be co-located and spatially auto-correlated. Previous research investigating root disease and the foliage of infected trees through laboratory pigment assays and spectroscopy [11], [101] is extended here by incorporating a multi temporal sampling of airborne lidar and imaging spectroscopy.

7.1 Multi-Temporal ALS and AIS Methods

A high priority forest management unit within the Greater Victoria Water Supply Area (GVWSA) on Vancouver Island, British Columbia, Canada, was selected as the study area. The GVWSA occurs largely within the dry subzones of the Coastal Western Hemlock Biogeoclimatic zone. The species composition within the GVWSA is predominantly Douglas-fir with minor incidences of western red cedar (*Thuja plicata*), western hemlock (*Tsuga heterophylla*), grand fir (*Abies grandis*), western white pine (*Pinus monticola*), red alder (*Aluns rubra*) big leaf maple (*Acer macrophyllum*) and pacific madrone (*Arbutus menziesii*). The shrub layer is largely salal (*Gaultheria shallon*) with common incidences of Oregon-grape (*Mahonia aquifolium*), sword fern (*Polystichum munitum*), and bracken fern (*Pteridium aquilinum*). Structurally the forest area is composed of a mosaic of stand ages resulting from limited forestry activity that ceased after 1993 and regeneration following historical wildfire. The topography of the 498ha study site can be described as gentle to steep slopes facing WSW towards the major Sooke reservoir, steeper slopes occur north of a valley bisecting the width of the management unit (Fig. 7.1).

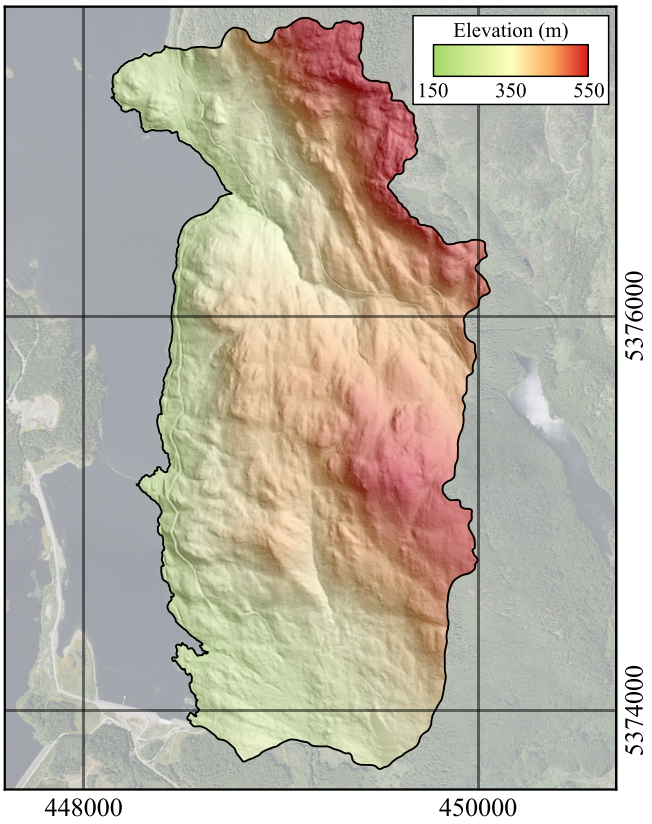


Figure 7.1 The Trestle forest management unit within the GVWSA, Vancouver Island, British Columbia, Canada. The site has 419m of relief (183-602m msl), slopes up to 73° with a median of 15°, azimuths largely in the 240° direction. Elevation and shaded relief overlaid on orthomosaic 30cm.

In late July of 2006 an airborne remote sensing campaign was initiated by the regional government (Watershed Protection Division of the Capital Regional District), which collected discrete return lidar at 3.5pnts/m^2 and nominally 2m spatial resolution full range (400-2500nm, ~3nm FWHM) AIS. Six years later a similar dataset was collected in late September 2012. Lidar point density was equivalent, but only the VNIR instrument was used (Specim Eagle) with 4x spectral binning (FWHM: ~5nm). A ground campaign was conducted in concert with the airborne acquisition that applied ground calibration targets (4.9x3.7m). The selection of ground targets was supported by a lab based BRDF study [191].

In support of both processing and analysis of the AIS, the lidar data sets were processed through a ground classification, ground normalization and raster product generation. A DSM (digital surface model) was generated at 1 and 2m resolutions from the 2006 lidar and at 1 and 1.5m from the 2012 lidar. Rasters were created for temporal comparison (1m) and for AIS processing (2 and 1.5m). In addition, CHMs (canopy height model) were generated at the nominal resolution of the respective year's spectrometer data. To facilitate sample collection in AIS processing a delta-DSM (dDSM: DSM_{2012}-DSM_{2006}) was used to identify individual wind thrown trees. Individual windthrow events were identified by a segmentation of the dDSM, where differences less than -4m and populations greater than 9 (queens contiguity) were retained.

AIS data were processed to orthorectified surface reflectance. The geometry of the data was calibrated through time synchronized INS (inertial navigation system) and lidar intensity rasters at an equivalent spatial resolution. Bore sight misalignment angles were derived from opposite and intersecting flights over the Victoria International Airport. In contrast to usual convention, unsampled grid locations were left empty during orthorectification. Platform altitude and velocity, along with instrument spatial binning, integration time and frame rate determined the appropriate orthorectified cell resolution. The 2012 data were intentionally collected at a lower altitude to provide for a finer resolution; 2012 AIS were processed to a 1.5m resolution while the 2006 were processed to a 2m resolution. All geometric processing was performed with proprietary software provided by Terra Remote Sensing Inc.

The AIS were transformed to radiance by dark current correction and applying the calibration gain coefficients in the Specim Caligeo software [109]. Radiance data were

converted to reflectance through the FLAASH implementation of MODTRAN with a maritime mid-latitude summer atmospheric model. MODTRAN (moderate resolution atmospheric transmission) is a physical radiative transmission model that is used to determine the amount of radiation that is able to pass through the atmosphere; it does so at spectral increments taking into account wavelength specific absorption by the molecular composition of the atmosphere. Other software, including FLAASH, use MODTRAN inversions to remove the effects of the atmosphere of measured radiance [192], [193]. Deployed calibration target spectra were extracted from the unrectified 2012 reflectance data and were used with the ASD collected field spectra to derive an empirical radiometric correction (ELC). The dark calibration target was severely affected by adjacency scattering, in its place a mean dark open water spectrum from the reservoir was used as the subtractive correction in ELC. A temporally invariant feature common to both AIS datasets was used to force-fit the 2006 physically modelled reflectance to the 2012 ELC corrected data. Finally, the flight lines that surveyed the management unit were mosaicked together while computing adjustment factors but holding fixed the flight for which the corrections were derived.

In order to reduce confounding effects of shadow and non-treed regions, the data were masked with their respective CHM data, where only cells with a maximum vegetation height greater than 4m were retained. In addition, shadow cells were eliminated using a visible albedo (sum of reflectance intensities between 450-700nm) of the FLAASH output, where any pixel with a negative VIS-albedo was omitted. The data were submitted to a continuum removal (CR) normalization, the absorption feature of interest was defined by the green peak and the NIR plateau (550-750nm). The CR data

were inverted, summed and multiplied by their respective mean FWHM. The result of the CR processing is a unitless metric representing the area of the absorption feature under investigation (CRTA). Although the CRTA can empirically be translated to absolute chlorophyll [10], the extraordinarily high costs of foliar sampling and the complications of sampling to adequately represent a canopy may yield unreliable values. This study opted for working with the area metric as a surrogate for a relative measure of canopy chlorophyll.

The identified windthrow events or objects as represented as newly formed contiguous gaps were populated with the mean 2006 CRTA values and were compared against the global mean CRTA. This initial approach provided an indication whether the chlorophyll absorption feature as measured by the instrument, is sensitive to the physiological changes that may be occurring within the canopy.

The CRTA data were then submitted to a spatial analysis to indicate the degree of spatial autocorrelation. The Getis-Ord Gi statistic (Eq. 19) was selected as a local indicator of spatial autocorrelation (LISA) [194]. The Getis statistic was selected over others, as it is capable of identifying both hot and cold spots within spatial data, that is, spatially auto-correlated high values and spatially auto-correlated low values. An additional advantage of this statistic is that it is a z-score so values can be interpreted in terms of their significance and probability of occurrence. The statistic was computed at multiple lag distances, given the symptoms of the disease operate at scales from the individual crown to the stand level. Since there can be no assurances on the size of infection sites, lag distances up to ~25m were used to evaluate plot sizes up to ~50m in diameter and included all intermediate lags. Areas that were identified as having spatially

auto-correlated low chlorophyll and windthrow are characterized as having a higher likelihood of root disease.

$$G_i^* = \frac{\sum w_{i,j}x_j - \bar{X}\sum w_{i,j}}{S\sqrt{\left[n\sum w_{i,j}^2 - \left(\sum w_{i,j}\right)^2\right]/n-1}} \quad \text{[Equation 19]}$$

where: $x_{i,j}$ is either the CRTA or dDSM of the center pixel in neighbourhood j and $w_{i,j}$ is the spatial weight from i to j, $\bar{X}$ and S are the global mean and standard deviation respectively

7.2 Multi-Temporal ALS and AIS Gap Results

The dDSM data analysis proved to be an extremely valuable source of information that is capable of mapping potential root disease sites. There was considerable high spatial frequency noise in the dDSM, which appeared less coherent than the more aggregated negative dDSM values. Top height gains were relatively small in magnitude, yet values as high as 43m were found. These large increases are attributed to crown expansion, a condition that is supported by the data where these large magnitude positive changes occur on the periphery of crowns. The dDSM of the management unit suggested that within the six years between the airborne surveys 3,205 new contiguous canopy gaps were formed that were at least 9m^2 in area each. The height of the wind thrown trees ranged up to 63m tall. The summed new gap area was 7.98ha, which represents 1.6% of the management unit area. The LISA analysis suggested that 11% of the wind thrown segments occur within areas prone to windthrow, that is, statistically significant spatially auto-correlated decreases in the dDSM. According to the dDSM with a 40m neighbourhood the affected area was 41ha. The dDSM successfully mapped regions of age dependent productivity, where younger stands had a pronounced and contiguous

positive top height growth between the two sampling dates, presumably due to both high crown closure and high growth rates of younger stands. The dDSM also identified regions of concentrated windthrow events these were confirmed through spatial analysis. The most obvious windthrow region was located near the reservoir in the southwest of the study site, while all others appeared to be much smaller scale disturbances.

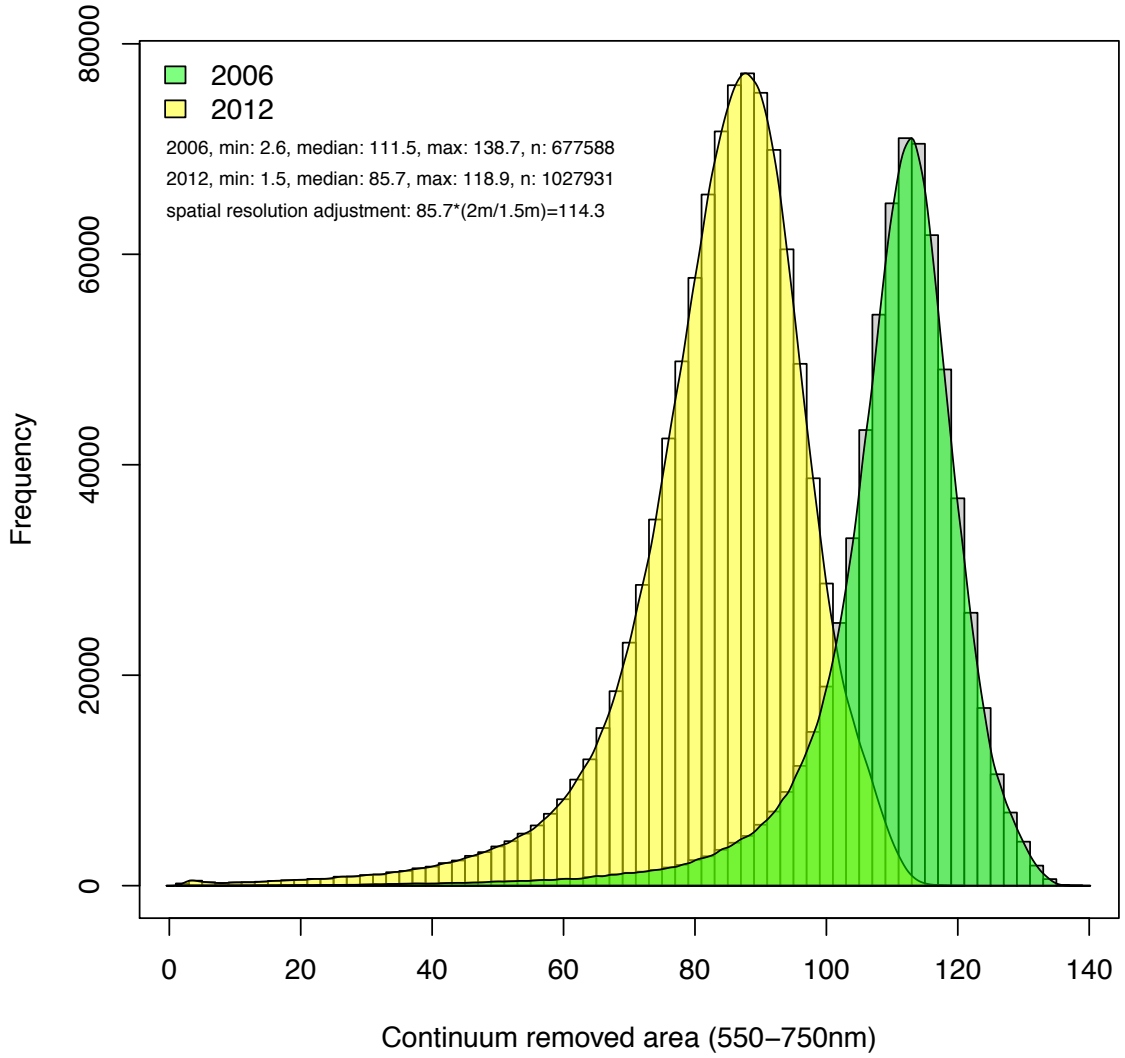


Figure 7.2 CRTA distributions of the management unit between the two sampling dates. Scaled kernel density estimates overlay histograms.

The absorption feature analysis demonstrated greater relative chlorophyll levels with less variability in the 2006 data than the 2012 (Fig. 7.2); these differences are addressed in the discussion. There were strikingly consistent spatial patterns in health across the management unit area between the two dates (Fig. 7.3). The age dependent expression of productivity was again evident in the three young stands, which exhibited spatially auto-correlated high relative chlorophyll. The younger stands, which are clearly evident in the orthophotography, are located in the northwest, south and to the east. In reference to the consistent lower health regions, there were spatial concentrations of low chlorophyll in the northeast of the study area and a region that extended along the north slope of the bisecting valley. Qualitatively, the low health regions occurred in the same areas between the two dates, the exception being a region in the southwest quadrant. An apparent difference in the chlorophyll levels suggests that in 2006 a region was experiencing a stress that was not detected in the 2012 data. There appeared to be very little expansion of poor health areas from 2006 to 2012, a condition that would not be expected from root disease infected areas. In fact, the opposite was observed, where in some areas the statistically significant spatial clusters of low relative chlorophyll were larger in 2006 than in 2012. The total area of significant spatially auto-correlated poor health was 73.4ha in 2006 and 65.2ha in 2012. The significant spatially auto-correlated windthrow and poor health in 2006 suggested a diseased area of 10.3ha (Fig. 7.4).

Wind thrown objects were evaluated for their relative chlorophyll levels in 2006. The distribution of the segment objects' mean chlorophyll area metric produced a central tendency that was low relative to that of the global study area. 2,145 of the total 3,205

segments (67%) had lower than average chlorophyll levels. Despite this finding there was not always good correspondence between smaller windthrow event and low chlorophyll.

7.3 Multi-Temporal ALS and AIS Discussion and Conclusions

Forest health was mapped across a small forest management unit within the Greater Victoria Water Supply Area. The processing stream developed here leveraged on a multi-temporal airborne lidar dataset to provide definitive reference data for diseased and otherwise healthy or asymptomatic forest. This study demonstrated that almost 70% of tree crowns that would ultimately be wind thrown by 2012 were physiologically stressed in 2006. These findings are promising and reinforce the varied utility offered by multi sensor integration, however more research is required to evaluate confounding issues uncovered in the process.

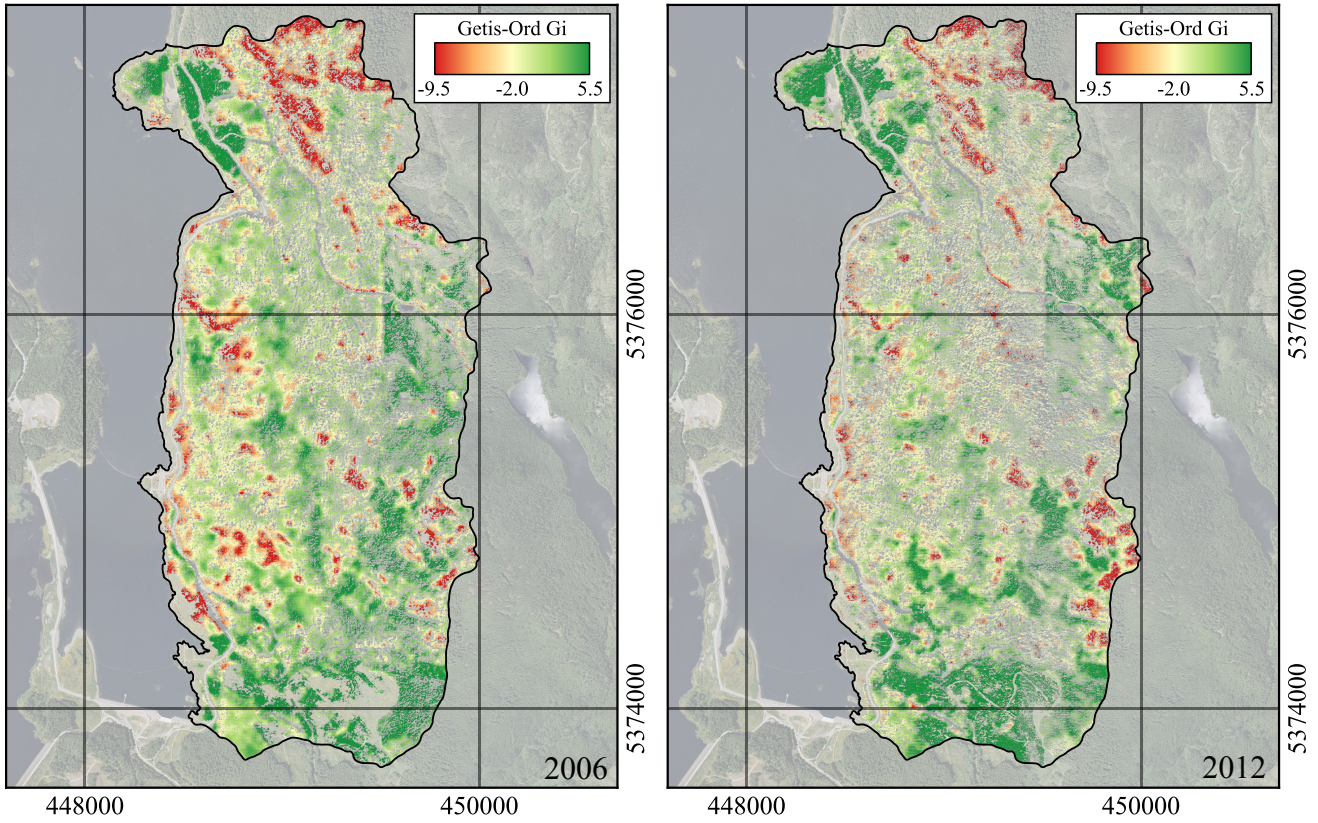


Figure 7.3 The identification of spatially auto-correlated low chlorophyll, as represented by the area of the normalized chlorophyll absorption feature. Values less than -1.96 represent statistically significant spatial clusters of low productivity.

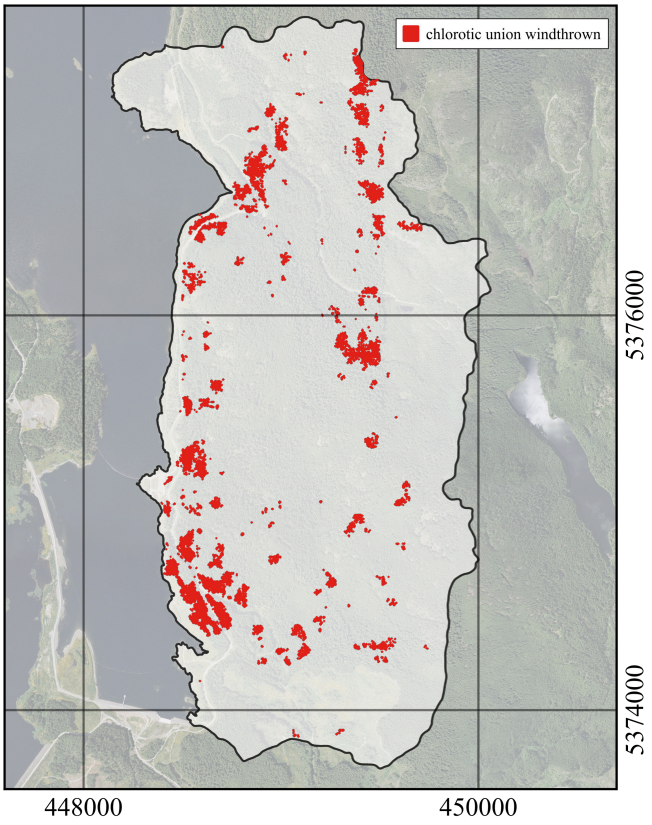


Figure 7.4 The union of spatially auto-correlated 2006 poor health and spatially auto-correlated windthrow is used to identify likely regions of active root disease

Considerable effort was directed towards maintaining the integrity of the da used in this study. Exclusion of areas with low signal to noise yielded sparse AIS da The 2012 data experienced shadows and unsampled regions attributed to variations attitude and platform velocity. Younger stands that in the 2006 data did not meet heig requirements for lidar forest thresholding, by 2012 had grown to heights above th threshold; all these attributes contribute to the differing spatial sampling distributio between the two years. As these data were referenced to the global distribution it wou be expected that differences between the two dates could be the product of differences the post-filtered dataset ground sampling.

From a theoretical perspective the CRTA is not exclusively a function of chlorophyll, therefore it is conceivable that the signal reported here is inflated for regions of higher LAI [10]. Conversely, low LAI or low stem densities in some regions of the study area may also have reduced measured relative chlorophyll through spectral mixing of less drought tolerant understory vegetation, which was desiccated, chlorotic or necrotic at the time the survey was conducted. The differences in the CRTA distributions suggest that the forest cover of the management unit in 2012 was experiencing higher levels of stress than the 2006 year. This observation would be supported by the fact that the late summer of 2012 was experiencing a significant drought event relative to that of 2006, as evidenced by observations of reservoir levels and exposed ground cover vegetation in the accompanying orthophotography. It is recognized however, that the differences in location and dispersion of these distributions may be influenced by the slightly different spatial resolutions. The smaller footprint of the 2012 data is expected to increase variability and reduce absolute chlorophyll intercepted by the footprint and thus reduce the location of the distribution, traits which are apparent in the produced distributions. It is suspected that the observed differences in the health between the two dates is also affected by the larger resolution of the 2006 data where the larger footprint may be contaminated by mixing of chlorotic shrub layer vegetation. As a result, it cannot be definitively stated whether the observed differences are derived from physiological differences of the target or by the physics of the sampled ground area and chlorophyll absorption.

Future efforts should include an infield validation campaign to derive an estimate for the accuracy of the derived process and for the parameterization of the approach for

appropriate scales of analysis and dDSM magnitude. Field campaigns should visit identified potential root disease affected areas to observe the presence of residual inoculum in wind thrown root mats, in addition to fine scale photography from UAV platforms.

CHAPTER 8:CONCLUSIONS AND DISCUSSION

The three research questions presented in chapter 2 ask how spectrometer and lidar datasets can be organized or manipulated to represent characteristics related to forest productivity (Questions 3 and 2, respectively) and how well these metrics in combination are able to estimate productivity (Question 1). To reiterate, the questions in sequence are: what is the potential for mapping variations in forest productivity through the use of remotely operated sensors?, how can a lidar point cloud be organized to represent forest structure related to productivity?, how can a spectrometer dataset be organized to represent forest growth productivity?

In order to answer question 1, questions 2 and 3 were required to be assessed first. A foundational knowledge was required to answer the question of how to organize spectrometer data to represent forest growth related metrics. With an abundance of literature that identifies particular wavelengths and wavelength combinations that are associated with biophysical parameters of vegetation, these spectral metrics could be reproduced for this study. Particular attention was given to the radiometric calibration of the spectrometer data to ensure results found elsewhere would not be obscured by the state of the data applied here.

Similarly, previous research on lidar enhanced forest inventories has produced a suite of lidar point cloud attributes that have been statistically linked to structural attributes. In addition to these traditional metrics, an effort was made to characterize the individual within the point cloud, an objective that is only recently possible with the advent of higher point density lidar. Intermediate data products of the individual tree

approach were generalized to the plot level and included into the pool of potential attributes related to forest productivity.

In order to address question 1 a regression-based design was adopted. The process of feature selection would identify which of the data organization strategies have produced metrics that were related to forest productivity, thus providing answers to questions 2 and 3. The results of the regression analysis in the form of explained and unexplained variation, would indicate the potential for estimating productivity. By querying potential confounding conditions a more thorough prescription for operational use of these results could be provided.

This research has investigated the potential for estimating forest attributes pertinent to growth productivity, at both the plot and the individual scales. A framework was developed and implemented for information extraction from remote sensing technologies to provide an enhanced forest inventory system. The successful application of both ALS and AIS in productivity mapping has the potential to increase the efficiency of the forest industry at the planning and harvest levels. Operations can be improved by reducing uncertainties in standing timber attributes, and by better allocation of resources in pre-harvest (*i.e.* spatially targeted fertilization). The derived forest information systems can provide a means to informed decision support for stand management and operations. This research area should be expanded to more varied forests where ultimately these types of remote sensing data will be capable of matching site, canopy architecture, and chemistry characteristics with silvicultural prescriptions and ultimately wood products.

The study of forest productivity has wide reaching applications, especially in the presence of a changing climate. Although climate change is a natural cyclical global

pattern on geologic timescales, anthropogenic factors have contributed to an increased rate of global climate change [195]. There is uncertainty in the projected response of forests to anthropogenic accelerated climate alterations [196]. However, if unchecked, changes in climatic conditions may put the viability of forest ecosystems at risk by exceeding the acclimation (physiological adjustment) capacity [197] and in turn the adaptation capacity (genotypic adjustment and may include habitat migration) of forests. There is a consensus that it is more important than ever to establish a baseline and to monitor ecosystem change [195]. Remote sensing technologies have the capacity to inform users and consumers on a diversified range of ecosystem attributes. Recently, active remote sensing has been adopted within the forest industry to enhance resource management efficiencies. A forest productivity monitoring program could help identify regions of forest decline. Forest productivity by definition is directly tied to carbon fixation rates, which has a role in the carbon cycle and climate and atmospheric sciences. Thus strategies that increase forest productivity may help to mitigate the effects of greenhouse gas emissions.

An active area of research and controversy within the climate and forest research domain is the concept of assisted migration. Assisted migration is the deliberate movement of genotypes within or outside a species' natural geographic distribution to facilitate or mimic natural range expansion in response to climate change. A major concern for assisted migration is the potential for adverse impacts on the indigenous ecosystem and the requirement to monitor for maladaptation, where the local conditions, including pathology, exceed the adaptive capacity of the genotype [195], [198], [199]. Remote sensing of forest structure and productivity would offer the opportunity to

measure and spatially map the status of migration trials and the status of natural genotypic range distributions.

Second growth forest management practices have placed an emphasis on increasing wood production; these practices can be costly and could benefit from a monitoring program. In managed timber production forests, treatments including thinning and fertilization are applied to increase growth rates and shorten crop rotation period. The benefits of fertilization treatments tend to be inversely associated with site productivity, where responses to treatments are more pronounced for low productivity sites [200]. Therefore, an efficient fertilization campaign would identify low productivity sites that are likely to respond favourably to the treatment. Typical urea application rates are 200-225kg/ha. With an approximate cost of urea at $512/ton the fertilization costs are estimated at $260-275/ha, inclusive of delivery and application [201]. The Forest Practices Branch of the B.C. Ministry of Forests Lands and Natural Resource Operations and Rural Development has published data suggesting that the average area of forested crown land fertilized is 13,144.6 hectares per year [202]. This estimate puts the yearly fertilization expenditures between $3.4M and $3.6M. A forest productivity-mapping product would greatly benefit planning efficiency of intensively managed forests. Urea application rates could be appropriately matched to specific locations, and would constitute a simultaneous economic benefit to operational costs with the treatment benefitting production.

Productivity is inversely related to wood quality [1] and thus there is economic value in developing a method for mapping forest productivity. More productive tree growth is associated with wider annual growth increments and lower wood density. The

initial saplings of managed stands overwhelmingly originate from tree improvement programs designed to maximize wood production [115]. In addition, the climate of the Pacific Northwest is expected to increased spring temperatures and lower summer precipitation, which would increase early wood and decrease latewood production [203]. The early to late wood ratio is known to be associated with variation in wood fibre properties that translate to wood quality, specifically the modulus of elasticity (stiffness) and the modulus of rupture (strength) [204]. A forest information product that could indicate productivity and in turn, a coarse indication of wood quality, would provide a means to matching a standing forest inventory with appropriate wood products. Forest managers would be better able to supply the market with precisely the wood product in demand.

Foliar pigments are the required proteins for the absorption of light energy; their abundance determines the maximum potential for the light reactions in photosynthesis. There is a huge body of work within the remote sensing literature that presents evidence for the remote measurement of foliar pigments [10], [19], [39], [40], [83], [85], [101], [142], [205]–[215]. Remote sensing of foliar pigments was largely induced by forest pathology and ecophysiology work that demonstrated a pigment response to physiological stressors [64], [75], [216]–[221]. Whether caused by nitrogen deficient sites or by defoliating disease, foliar pigmentation is expected to reflect, at least partially, a tree's ability to assimilate CO_2 and to grow.

This work provided evidence that forest structural attributes and productivity can be estimated from airborne laser scanner data and airborne imaging spectroscopy at both the plot and individual tree levels. The height-related attributes were the best-estimated

metrics at both the plot and individual scales. However, crown class confounded many of the attribute predictions at the individual scale. The success in productivity modeling was due largely to the inter-correlation of periodic annual volume increment with structural attributes. Occasionally, the influence of competition on productivity was also identified by significant neighbour proximity metric coefficients in productivity models. At the plot level, there was an identified influence of crown function represented by AIS metrics related to pigmentation. At the individual level, however, there was no additional benefit of information on crown function as represented by AIS metrics. Although there seemed to be a trend for more productive plots to be located adjacent to micro drainage features (e.g. plot 41), topographic metrics did not significantly contribute to productivity models in all cases. The individual scale of analysis was exceptionally difficult to investigate, as the absolute positioning of individual trees was required to match target and reference tree data. Training data for individual model development required a control network, plot total station surveys and TLS to unambiguously match the RS metric database with that of the CFS ground sampling survey. The individual scale of analysis modelling results did not overwhelmingly warrant its use, at least with the crown definition of the individual and the spatial resolution of the passive data. However, the lidar treetop metrics were consistently selected as significantly contributing to explaining the variation in response attributes. This finding supports the development of a physically based tree list approach to inventory attribute modeling. This project also explicitly identified the dangers of empirical modeling where productivity estimates were produced from structural attributes. For the SLP site, productivity is related to structural attributes, however the site represents a homogeneous age, species, and site index structure and

therefore a more widely applicable model would require *a priori* structural based strata or an entirely different feature selection.

The use of light detection and ranging (lidar) has, over the last 10 years been increasingly adopted by the forest industry, largely for its ability to facilitate timber harvest planning and on the periphery, for estimating forest inventory attributes. Lidar forest studies have increased in complexity in concert with the development of sensor and platform technologies. Recently, there has been a concentrated effort on forest inventory attribute prediction, which has largely been the result of increased availability of airborne lidar data. The application of ALS to forest inventory modelling has been thoroughly vetted within the scientific and academic domain and is now considered a matured, operational technique [222], [223]. These forest information products are largely determined by the area based analysis (ABA) point metric method, whereby; multivariate linear calibrations relate field measured forest attributes at the plot scale to lidar point metrics. This concept has a history stemming back to 1960 when canopy cross sectional profiles were related to timber volumes [224]. Typically, metrics that describe the vertical distribution of lidar returns are used as explanatory variables to estimate forest inventory attribute response variables. For instance, much research has demonstrated that a high height percentile metric, in combination with a point density ratio, explains most of the variation in measured plot level timber volume [91]. Given the mechanics of lidar measurements there is a physical relationship between the lidar survey and forest canopy height. Thus, inventory attributes relating to height (dominant height, mean height) tend to be more accurately modeled by lidar metrics, usually a high point height percentile [14]. Many of the other forest attributes estimated from lidar data benefit from

morphological interrelationships. For example, quadratic mean diameter is often estimated by a lidar percentile height metric [14], which relies on the intrinsic relationship between tree height and DBH [118]. Further, inventory attributes that integrate individuals, plot volume and basal area for example, require a surrogate or proxy for stem density; a condition that is met by lidar density proportion ratios [34], which are conceptually related to crown closure or density. Accuracies, as evaluated by residual RMSE, of lidar derived forest inventory attributes tend to be quite good, ~3m for height attributes, ~3cm for quadratic mean diameter, ~8m^2/ha for basal area, ~65m^3/ha for volume and ~46m^3/ha for total above ground biomass [14]. However, because of the empirical modelling nature of the area based approach and the long list of unstandardized and collinear independent variables (point cloud distribution metrics), successes in model transferability may be compromised. In addition, the impact of acquisition and sensor parameters on potential ABA metrics have not been fully quantified or understood, again adding to the challenges of model transferability. In its current framework, the application of ABA for forest inventory modeling will always require costly ground sampling for each inventory project in order to develop attribute models. Therefore, the success of an ABA lidar inventory will always be dependent on the quality of the ground sampling design, and whether the calibration data capture the full gradient of the dependent response variables (inventory attributes), and whether it applies appropriate strata. An example of when strata might be appropriate would be when acquisitions cross large areas with varied biogeoclimatic ecosystem classification zones. The relationship between plot volume and lidar height distribution metrics is expected to be vastly different between BEC zones (i.e. volume ranges and crown architecture between CWH,

IDF and ESSF) as a consequence of both stem density and species-specific crown architecture.

The ABA framework was developed at a time when lidar datasets had point densities of lower than three points per square meter, current lidar surveys are producing densities that are roughly ten times that value. The details apparent in the point cloud of modern acquisitions are sufficient to characterize even branching structure and crown foliar density. With high-density lidar, the challenge to attribute modelling is related less to data quality, than it is to the development of algorithms that are able to mimic what the human mind is able to decipher while visualizing these point clouds. As a result of the availability of these highly detailed lidar surveys, the individual tree approach has been a popular theme in both remote sensing research and in commercial pursuits [225]. However, in many cases the methodology has not changed from the ABA approach, with the exception of the areal unit (20m cell versus individual delineated crowns). The individual approach is conceptually plagued by underrepresentation, where training data do not capture the diversity of crown architectures associated with variation in species, age, density, and site index. It is expected that the development of physical modelling approaches could be an alternative to ABA where lidar derived tree lists are married with process based growth models like TASS [6] in order to describe forest traits at the plot level. Theoretically, the benefit of a physically founded, biologically meaningful approach would relax the dependence on extensive and costly ($1000CAD/11.28m radius ground samples) calibration and validation ground samples and increase the potential for model transferability. This suggestion is similar to that proposed in [226], with the exception that the lidar would be applied to derive a tree list, which in turn, is used to

parameterize a tree list growth model, rather than using lidar area metrics to impute tree-lists for the growth model.

This study was structured based on the hypothesis that information on canopy structure, canopy pigmentation and surface drainage would be associated with growth productivity. Canopy and ground structures are directly measured by the airborne lidar survey, while canopy chemistry is sampled by the imaging spectrometer. These data were then translated into metrics that would distil the signals that are biologically meaningful to forest productivity, namely: tree height, crown length, tree spatial distribution, pigment concentrations, ground slope aspect and upslope drainage area.

Firstly, the ground reference data were interrogated to reveal whether plot structure at the SLP site was related to a ten-year lag productivity index. Theses analysis suggested that 82% of the variability in individual productivity, as represented by the periodic annual volume increment could be estimated with structural data that was accessible to lidar. Individual productivity was estimated from tree height, crown class, the height differential (k3 nearest neighbours), height and crown class interaction, height class and height differential interaction, lastly height and height differential interaction. The ultimate model form was interpreted as one that captured the degree of competition whether induced by growth or the thinning treatment. This interpretation is in line with other research that investigated the spatial pattern of trees and species in mixed stands [227]. However the discipline of forest growth modelling is deep with varied and complex approaches that may be either empirical, mechanistic or process, hybrid, gap or ecological in nature [4]. The investigation of the CFS database supported a structurally

based productivity model that could theoretically be achieved through processing and metric extraction of the lidar data.

The plot level structural attribute modeling for the SLP project initially produced results that were in line with those produced elsewhere [14], [91], [156], [228], [229]. The feature selection process identified the 85th lidar height percentile as most associated with plot average height and explaining 88% of the variation in plot mean height with a residual standard error of 1.05m, where Naesset [228] reported on mean plot height estimates from 5-12% for Scandinavian forests. Niemann *et al.* [14] reported on the prediction error (RMSE) of the basal area weighted Lorey's height, where the authors produced an estimated error of 2.19m for TFL 18 in Clearwater BC. Lorey's height will more closely reflect the height of larger individuals, which in theory and in practice is better predicted by lidar metrics, especially in cases of uneven aged stands. The improved performance in height estimation for the case of SLP cannot be separated from the flight and data parameters, in particular, the increased point sampling produced from multiple acquisitions at SLP relative to the above older examples, which ranged from 0.1 to 10/m^2. The effect of point density is known to be positively associated with the accuracy of stand height estimation [230], [231]. In addition, the low diversity in age and stand structure and site variations that would otherwise be related to geographic spread provide for conditions that would produce better fit empirical models.

Total plot volume was best estimated by the canopy closure at the 70th lidar height percentile, explaining 76% of the variation in total plot volume with a residual standard error of 2.28m^3. It is common in the literature that volume is estimated by the combination of a crown closure metric and a lidar height percentile metric [14]. In

addition, the volume error produced for SLP was comparable with that produced by [14] (64.8m^3/ha) when the total plot volume standard error was scaled to the hectare level (2.28m^3*1/(400m^2/10,000m^2)=57m^3/ha). The success of modeling plot volume with the simple linear regression in these analyses was also attributed to the narrow variation in structure and age at the SLP site. However, the diversity of modeling approaches, model complexity and forest types can contribute to a wide range of empirical modelling results. Bouvier [232] applied a conservative feature selection approach with non-traditional ALS metrics to attribute modelling and produced volume estimates with errors of 12.4% and 14.6% (stem and wood volume, respectively) for coniferous stands. A study by Naesset [233] produced RMSE of volume from 32.9-67.8m^3/ha, which was reduced to 15.1-35.1m3/ha when reference plots were stratified by age and site quality; reducing the 57 total plots to only 19 plots per strata (young, mature poor site quality , mature good site quality).

Plot basal area was best predicted by the canopy closure at the 65th lidar height percentile, which was one height bin from that selected in the volume model. Feature selection for BA modelling suggested that the explained volume signal was attributed to plot occupation by proxy of crown closure. The physical link between lidar attributes and basal area is clearly not direct and it is unreasonable to expect that the sum of stem diameters is sampled by airborne lidar. It is for this reason that the ability to predict BA from lidar is driven by the underlying association of tree heights and density, and provides a justification for the relatively lower prediction accuracy. Elsewhere in the recent literature basal area estimates were 13.9-18.2% which were produced from a two term model applying the interaction of a lidar percentile height (p80) and the number of

vegetation first returns and a lidar height standard deviation [234]. It should be noted, however, that the authors of that study were attempting to estimate basal area for the whole of Sweden and were thus expected to capture a wide array of structural diversity, justifying the increased model complexity. Others in comparable plantations types as the SLP site, but dissimilar geography and forest type (Brazil, pine), produced a BA RMSE of 1.96-3.04m^2 (7.54-11.71%) with a range of model complexity [235]. Similar to the prediction error produced for this SLP study, [14] achieved a basal area estimated error of 7.79m^2/ha for the Clearwater TFL 18 study area. The plot level basal area error produced by the ABA approach for this study was 0.20m^2, which is equivalent to 5m^2/ha. In contrast, the final BA model produced here was fit by simple linear regression and did not require complex models to describe the variation in measured basal area.

When the individual lidar treetops were generalized to the plot level, the feature selection was altered, where the percentile height metric was replaced by a central tendency of the lidar treetop height as most informative of plot tree height (although a marginal improvement over 85th percentile). However, the slope coefficient for the lidar treetop model was 1.00 (IQR: +/- 0.03) when only the field-measured trees were applied, providing confidence for the treetop heights. When dead, suppressed and intermediate crown classes were omitted from the computation of the average plot height, the lidar treetop model was drastically improved explaining 97% of the variation in average plot height, the error was also reduced by nearly half (0.55m from 1.05m).

Top height is a parameter that is computed based on the height of the 100 largest DBH trees per hectare and is important in determining site quality due to the reduced influence of stand structure. In addition, operational forest inventory have developed

growth and yield models (*i.e.* Variable Density Yield Projection), which apply top height as a major component for producing forest attribute projection estimates [236]. Given the allometric relationship between diameter and height these large DBH trees tend to also be the tallest and therefore most accessible to airborne remote sensing. It is not surprising that the top height attribute was strongly associated with the lidar height metrics. The top height model demonstrated a similar response as the dominant/co-dominant plot average height regression. The estimation of plot top height from average lidar treetop height produced a residual standard error of 0.59m and the estimates explained 96% of the variation in plot top height. Interestingly, a model produced from the more traditional ABA metrics (average above the 85th percentile) produced a very similar model differing only in a 0.5m smaller intercept, (however in bootstrapping results the IQR of the intercepts overlap greatly). The result found for top height was similar to the conclusions of others [237], [238] where a comparison between ABA and ITA approaches suggested little advantage (represented by RMSE) of one over the other. However, the advantage offered by the ITA over ABA should be obvious, as the ITA, being more physically associated, would effectively relax the dependence on ground reference.

Individual tree height estimation, although an exceptionally onerous process to calibrate, was an obvious success, achieving prediction errors of 0.58m. The lidar treetop heights explained 97 percent of the variation in measured (and predicted) tree height, or 89 percent without observation filtering. The model parameters instilled confidence that the lidar treetop heights could be used operationally as the slope coefficient was very near one (1.00±0.012) and the offset was near zero (0.72±0.348). The dominant challenge for extracting individual tree heights was not the estimation of heights but was related to the

detection accuracies. From the top down approach, suppressed and potentially intermediate crowns are obstructed and constitute omission errors. Extraction parameters were modified to increase the detection rates, however in many cases there was a corresponding increase in commission errors. Observing the pattern of omission, commission and height errors in concert, the extraction parameters were fixed. Ultimately, the probability of a stem being omitted from the lidar treetop extraction was determined as a function of local height differences, local density and their interaction. It should be recognized, however, that the results presented here relied on a known stem map to stratify the lidar treetops as correctly detected or commission errors, which would defeat the purpose of deriving a method that requires little calibration. The problem for the treetop approach is the absence of *a priori* knowledge of the stem map and thus the ability to recognize commission and omission errors. There may be two avenues for dealing with the undetermined extraction parameters. One approach might involve a stand structural classification that would infer which structure classes are likely to produce severe commission errors, in which case specific structural classes could be matched with appropriate search windows and noise reduction pre-processing. Another approach would be to err on the side of low commission, high omission errors and apply the extraction as a sample of the dominant and co-dominant stems in a larger, perhaps gridded, population.

The height to live crown was also investigated for its ability to inform on crown dimensions and thus photosynthetic potential. At the plot level the 10th percentile lidar height metric explained 94% of the variation in average plot height to live crown with an error of 0.55m. This result was encouraging, however, while investigating the impacts of

varied point density on traditional lidar ABA metrics it was shown that the extremes of the lidar height quantiles were especially sensitive to variation in point density. Therefore, a height to live crown model based on the 10th percentile lidar height would be sensitive to variations in point density, which can be induced by variable flight line overlap (within an acquisition) and/or variations in flight height and/or sensor configurations (between acquisitions). Chasmer *et al.* [173] estimated the height to live crown with an integrated airborne and terrestrial lidar dataset and found an error of 1.4m (sd: 2.4m); they also concluded with similar findings found in this study, where TLS estimates of HTLC were sensitive to on-stem dead branches. Other sources of literature that estimated HTLC, of which there are few, produced RMSE greater than 1m [156].

The analysis of average plot crown width demonstrated that 70% of the variation in average plot crown width was explained by median lidar treetop height and the 1m CHM coefficient of variation. The two feature linear model produced a residual standard error of 0.14m. The selection of these features is logically defensible in that taller trees are expected to have larger and more exposed crowns, which would produce taller lidar treetop heights and a more varied canopy surface. The coefficient of variation selected as significantly explaining variation in crown width, in this case is taking into account that the variation in the CHM will be positively correlated with the average canopy height. Interestingly, the direction of the CHM_{cv} coefficient was reversed from the expected trend. Investigating the prediction of crown width through various metrics revealed that two feature models tended to account for the structural differences of plots with root disease. The opposite direction of the CHM_{cv} coefficient is attributed to the divergence between the root disease plots (plots 65 and 67) and the others. The two root disease plots

had conspicuously shorter residual trees that were also wide relative to those of the other plots. Additionally, the other plots were largely closed canopies, while the root disease plots had large gaps, thus contributing to an increased variation in the canopy surface. The analysis of predicting crown width through the ABA approach again demonstrates the potential for producing poorly founded models as a result of sampling bias that does not capture important structural diversity. Although, efforts were made to investigate an individual tree model for crown width through a crown delineation method, relationships were not resolved by the data as applied in this study. An observation was made in the process of parameterizing the crown delineation algorithm, where there was an apparent relationship between local tree density and crown width as seen through the CHM. Efforts to distil the stem density to crown size relationship were impeded by neighbouring stands (harvested with residual) which did not follow the trend observed within the SLP plots. Other more elaborate algorithms, spatial wavelet analysis for example, have been developed for crown delineations and have resolved multi-scale issues that hinder other extraction algorithms. The literature has shown that there is an association between the accuracy of crown diameter estimates and canopy closure, depending on the approach taken, but accuracies for a mixed-conifer temperate forest in north-central Idaho ranged from 1.29-2.02m (RMSE) [178]. Although VanLeeuwen *et al.* [156] report on lidar crown diameter prediction errors as low as 0.47m, the spread of the relationship for the referenced study is considerable, the fit is weak (adj. R^2: 0.2) and the slope is only 0.2, these are conditions that are not encouraging for a more physically based model [239]. It is suspected that the problem for characterising the individual tree crown dimensions through lidar is related to tree proximity as open grown trees are more

easily captured, for example Kato, Moskal *et al.* [240] captured crown widths with a low RMSE of 0.93m for non-forest trees.

Stem density was best estimated through the variation of the canopy surface. A non-linear trend was observed between plot stem density and CHM standard deviation. While the power relationship may be reasonable, the trend as described by these data was not linear largely attributed to only four observations, the low density and high CHM standard deviation of the two root disease sites and the high density low CHM relief of the treatment control plots 2 and 21. More plots that characterize these extreme data space regions should be included to determine if this non-linear trend is the product of sampling bias. The lidar treetop product did not significantly contribute to the estimation of stem density. The 2.5-D nature of the CHM raster, the 3-D organization of individual trees and the resulting detection accuracies of the lidar treetops extraction were the major limitation to producing accurate stem density estimates; this condition is cited within the literature [184], [241]. In a comparison of lidar tree detection algorithms by the individual tree approach, stem density errors ranged from 162 to 685 with detection accuracies as low as 45.2%. These results varied based on five dissimilar sites and six separate algorithms [176].

Four productivity indices were applied in the ABA modeling approach, including periodic annual increment of basal area, PAI of total plot volume, plot mean PAI of volume and plot mean PAI of diameter. For the plot mean PAI of diameter estimation, the best solution was found when suppressed and intermediate stems were omitted from the derivation of mean PAI of diameter. The selected features for the estimation of mean diameter increment were the standard deviation of the CHM and the median depth of the

chlorophyll absorption feature. The two-feature model explained 84 percent of the variation in diameter increment with a computed residual standard error of 0.02cm/year. Although the productivity index may not be optimal as it omits variation in site occupation and height growth, the resultant model is easily interpretable. The feature selection for the mean diameter increment model captures structural information in the form of density and crown functional information in the form of photosynthetic potential. The basal area increment produced a similar result to that of the mean diameter increment. Again, the root disease plots presented an additional complexity that needed to be addressed; when mortality occurred between the sampling interval the reduction of the dead basal area at the later date produced a large negative increment. With the inclusion of this plot (plot 67) the second feature selected was again a chlorophyll content metric (REP). However, when plot 67 was omitted, the basal area increment was determined by canopy closure at the central tendency of the lidar point cloud ($CCF_{\sim 50}$) and the light use efficiency of the crown (PRI_{median}). The linear model estimated basal area increment with a standard error of $0.005 m^2$/yr. and explained 71 percent of the variation in basal area increment. To ensure that the productivity index accounted for primary height growth as well as secondary diameter growth, volume increments were considered. Average PAI in volume of the dominant and co-dominant tree layer was best estimated with the median lidar treetop height and a spread statistic of a hybrid optical index ($PSRI_{MAD}$). This two-feature model explained 85 percent of the variation in mean volume increment with a residual standard error of $0.002 m^3$/yr. When all live stems contributed to the plot mean volume increment, feature selection was changed to the mean height of the four tallest lidar treetops and the CHM coefficient of variation. This regression model explained 73

percent of the variation in plot mean live volume increment with an error of 0.003m^3/yr. Finally, the total plot volume increment of the dominant and co-dominant tree layer was best estimated by median lidar treetop height and the mean chlorophyll absorption feature depth, explaining 71 percent of the variation in total plot volume increment with an error of 0.048m^3/yr. More complex models were built for the prediction of total plot volume increment, which marginally increased the amount of explained variation, however there was no parallel decrease in the residual standard error. It is worth noting that feature selection suggested that upslope drainage area contained variation that was related to plot total volume increment in the dominant and co-dominant tree layer (when CHM spread and canopy closure were accounted for). This was an interesting result as it suggests that these data were able to capture some degree of the influence of site quality on productivity. Feature selection appeared to converge on a more coherent pattern when all tree crown layers were included. In this case, where all tree crown layers were included the clear result was that PRI, chlorophyll depth and canopy closure were strongly related to the plot level total volume increment. There was little model performance benefit for different variants of these three metrics, for the sake of parsimony means of the two optical indices were selected and the canopy closure at the 50th lidar height percentile were used. This model was preferred for its biological interpretability in that it captured crown structure, light use efficiency and photosynthetic potential.

In contrast to the structural attribute modeling results produced within this study, only the plot-based prediction of productivity selected remote sensing metrics derived from the spectrometer. With the exception of live plot mean volume increment, all plot level productivity models included a spectral metric that related to photosynthetic

potential/efficiency. The one exception to this observation selected the mean height of the four tallest lidar treetops, which is assumed to capture the variation in site quality, as with traditional top height. In all cases where spectral features were selected as significantly contributing to productivity estimation, at least one other lidar derived feature accounted for plot based structural differences. Within the literature there has been relatively little lidar remote sensing work pertaining to growth or productivity; where these studies do exist they tend to involve multi-temporal lidar [242] or by augmenting pre-existing growth models [243]–[245], rather than applying the area based approach.

The analysis of individual tree productivity and remote sensing metrics demonstrated that although the scale of analysis was changed, the ability to estimate productivity remained constant. At best the individual productivity model explained 72 percent of the variation in dominant and co-dominant tree volume increment. The residual errors for the individual models were an order of magnitude smaller than plot-based estimates, a reflection of the volume magnitude differences. Ultimately, the regression analysis demonstrated that the metric database applied was capable of producing many models that were near equally capable of estimating productivity at the SLP site. However, challenges with defining the individual object limited the application of individual level attributes. The confusion of the individual was supported by a significant crown compactness metric. Although, the two best models were produced with individual crown metrics (compactness and the 50th lidar height percentile) alternatives to feature selection without individual crown attributes demonstrated near equivalent success. The initial best three-feature model for example, estimated dominant/co-dominant tree volume increment from lidar treetop height, plot average lidar

treetop height and their interaction. This treetop model would be preferred over others for its high signal metrics and its ease of interpretability. Further, this treetop model missed only two percent of the variation that was explained by more questionable models and exhibited only 0.0002 more standard error.

It was interesting that spectroscopic metrics were dominantly selected as contributing to explaining plot volume increments, even to the point that the best performing plot based model did not include a lidar structural metric ($PAI_{vol}=f(CRRA_{mean},GI_{median})$, adj R^2: 0.77, RSE: 0.043m^3/yr.), while at the individual level there was a conspicuous absence of the contribution of spectral metrics. In the plot level analysis, health related attributes were selected as significantly explaining forest productivity. The diseased plot 67 had a strong influence on feature selection; the red edge position was invariant across all plots but plot 67. When plot 67 was omitted from the analysis, health related spectral attributes were still selected for a capacity to inform on productivity. At the individual level and even with complex models the spectral data struggled to explain 60% of individual volume increments. The difference in the results between the two scales of analysis, although difficult to discern, is interpreted as an effect of measurement scale. The nominal spatial resolution reported by the data vendor was 1.3m. However, during the process of the radiometric calibration of the spectrometer data, it was determined that the effective scale might represent a larger area, recognizing that sampled area is continuously variable depending on flight parameters. According to the CFS database, crown widths did not exceed 4.1m, the mean crown width was 2.1m. The size of the crows relative to the nominal spatial resolution of the spectral data approaches a L-resolution condition and calls into question the suitability of the data for

an individual scale of analysis. Additionally, the method of defining the individual was problematic, the crown delineation by the CHM was not sufficient in all cases and thus the accuracy of the spatial representation of the individual was dependent on crown class. It is expected that the non-discrete tree crown sampling of the spectrometer and the issues with the individual segmentation contributed to the absence of an association between individual volume increment and the spectral database. Sampling bias cannot be omitted from the potential sources of differences between the two scales. Unlike the plot level analysis, the individual approach relied on an individual treetop detection approach. The treetop detection had observed omission errors and therefore represented a slightly different sample than that applied at the plot level.

Until recently most provincial and federal forest inventory programs around the world have been based on technologies and techniques that were derived in 1982 [246]. The typical process for conducting a forest inventory is largely based on the acquisition of high-resolution four-channel optical frame based airborne imagery. Digital air photos are viewed in a software environment that loads the images in stereo pairs and interacts with viewing hardware, called soft-copy stereo viewing. Stereoscopic vision, being the perception of three dimensions, may be obtained in a number of ways, for example using an active shutter system. In the active shutter system, viewing hardware, synchronized with the display frame rate, blocks each eye iteratively while the display swaps each stereo pair. Effectively, each eye only sees its intended image, and the refresh rate is so rapid that no image interruption can be perceived; the result is digitally induced perception of depth. In the soft-copy stereo viewing environment, expertly trained photo interpreters digitize spatially homogeneous forest stands and provide estimates of stand

height, basal area, density, species and other forest inventory attributes. The methods derived as part of the work reported on in this dissertation have the potential to aid traditional air photo interpretation in the form of auxiliary data or potentially to derive an entirely new, more accurate and objective system of forest inventory. The Ministry of Forests, Lands and Natural Resource Operations and Rural Development has a history of supporting the development of remote sensing derived forest inventories and is currently applying ALS for a TSA wide fully attributed inventory.

In conclusion, this study demonstrates that ALS and AIS have potential for forest attribution at both the plot and individual scales. More diverse forests must be incorporated that include natural stand structures. The relatively simple models produced here do not capture conditions that are expected to confound the relationship between volume increment and the remote sensing metrics investigated. Productivity of dominant trees that is more tied to site quality than competition, and the age related decline in productivity are two examples of conditions not reflected in the simple associations found in this study.

The complexities of the conditions that contribute to forest productivity make the estimation of the attribute by remote sensing an optimistic over simplification that may limit its spatial extrapolation. The alternative to the estimation of productivity by ALS and AIS features, and one that is advocated, is the direct measurement of growth by ALS. The multi-temporal ALS analysis for the GVWSA demonstrated a capacity to map crown expansion, height growth, mortality and windthrow. The added expense of an additional lidar acquisition campaign may deter prospective land base managers. However,

alternatives exist in the form of photogrammetric point clouds, which could be applied once an initial lidar collect resolves the ground surface.

REFERENCES

[1] C. N. Filipescu, M. U. Stoehr, and D. R. Pigott, "Variation of lumber properties in genetically improved full-sib families of Douglas-fir in British Columbia, Canada," *Forestry*, vol. 91, no. 3, pp. 320–326, 2018.

[2] H. D. Erickson and T. Arima, "Douglas-Fir Wood Quality Studies Part II: Effects of Age and Stimulated Growth on Fibril Angle and Chemical Constituents," *Wood Sci. Technol.*, vol. 8, no. 4, pp. 255–265, 1974.

[3] E. Swift and I. Duchesne, "Canadian Wood Fibre Centre, Fibre Facts, Improving Fibre Quality Through Silviculture," Fredrickton, New Brunswick, 2008.

[4] C. Peng, "Growth and yield models for uneven-aged stands: past, present and future," *For. Ecol. Manage.*, vol. 132, no. 2–3, pp. 259–279, Jul. 2000.

[5] M. Battaglia and P. Sands, "Process-based forest productivity models and their application in forest management," *For. Ecol. Manage.*, vol. 102, no. 1, pp. 13–32, 1998.

[6] A. Brunner, "A light model for spatially explicit forest stand models," *For. Ecol. Manage.*, vol. 107, no. 1–3, pp. 19–46, Aug. 1998.

[7] G. W. Frazer and D. K. O. Niemann, "Fine-scale, Multidimensional Spatial Patterns of Forest Canopy Structure Derived from Remotely Sensed and Simulated Datasets," *Department of Geography*, vol. Doctor of. University of Victoria, Victoria, p. 251, 2007.

[8] K. Niemann, G. Quinn, D. G. Goodenough, F. Visintini, and R. Loos, "Addressing the Effects of Canopy Structure on the Remote Sensing of Foliar Chemistry of a 3-Dimensional, Radiometrically Porous Surface," *IEEE J. Sel. Top. Appl. Earth Obs. Remote Sens.*, vol. PP, no. 99, pp. 1–10, 2011.

[9] D. G. Goodenough, K. O. Niemann, G. S. Quinn, and H. Chen, "AISA AND MULTI-ANGLE CHRIS FOR COASTAL FOREST CLASSIFICATION," in *Hyperspectral Workshop 2010, ESRIN*, 2010, pp. 5–9.

[10] G. S. Quinn, F. Visintini, and K. O. Niemann, "Considering the implications of species on pigment estimation from leaf spectroscopy," in *Workshop Hyperspectral Image and Signal Processing: Evolution in Remote Sensing*, 2012.

[11] G. S. Quinn, K. O. Niemann, and D. G. Goodenough, "Lidar integrated airborne imaging spectroscopy for root disease detection and measurement of foliar chemistry," in *IEEE 30th International Geoscience and Remote Sensing Symosium*, 2010.

[12] K. Niemann and D. G. Goodenough, "Estimation of foliar chemistry of western hemlock using hyperspectral data," *Remote Sens. For. Environ. Concepts Case Stud.*, 2003.

[13] K. O. Niemann, D. G. Goodenough, and A. S. Bhogal, "Remote sensing of relative moisture status in old growth Douglas fir," *Int. J. Remote Sens.*, vol. 23, no. 2, pp. 395–400, 2002.

[14] K. O. Niemann, "Evaluation of Emerging Remote Sensing Technologies for the Assessment of Forest Resources," Victoria, BC, Canada, 2007.

[15] S. A. Acker, C. B. Halpern, M. E. Harmon, and C. T. Dyrness, "Trends in bole biomass accumulation, net primary production and tree mortality in Pseudotsuga menziesii forests of contrasting age," *Tree Physiol.*, vol. 22, pp. 213–217, 2002.

[16] S. Solberg, E. Naesset, H. Lange, and O. M. Bollandsas, "Remote Sensing of Forest Health," *Int. Arch. Photogramm. Remote Sens. Spat. Inf. Sci.*, vol. 36, no. 8, pp. 161–166, 2004.

[17] S. Solberg, T. K. Rindal, and G. Ogner, "Pigment composition in Norway spruce needles suffering from different types of nutrient deficiency," *Trees*, vol. 12, pp. 289–292, 1998.

[18] G. A. Blackburn, "Hyperspectral remote sensing of plant pigments," *J. Exp. Bot.*, vol. 58, no. 4, pp. 855–867, 2007.

[19] Z. Huang, brian J. Turner, S. J. Dury, I. R. Wallis, and W. J. Foley, "Estimating foliage nitrogen concentration from HYMAP data using continuum removal analysis," *Remote Sens. Environ.*, vol. 93, pp. 18–29, 2004.

[20] P. J. Curran, "Review: Remote Sensing of Foliar Chemistry," *Remote Sens. Environ.*, vol. 30, pp. 271–278, 1989.

[21] J. P. Skovsgaard and J. K. Vanclay, "Forest site productivity: a review of the evolution of dendrometric concepts for even-aged stands," *Forestry*, vol. 81, no. 1, pp. 13–31, Feb. 2008.

[22] K. Klinka, V. . Krajina, A. Ceska, A. . Scagel, G. of Canada, and P. of B. Columbia, *Indicator Plants of Coastal British Columbia*. Vancouver, British Columbia, Canada: UBC Press, 1995.

[23] D. Binkley, J. L. Stape, M. G. Ryan, H. R. Barnard, and J. Fownes, "Age-related Decline in Forest Ecosystem Growth: An Individual-Tree, Stand-Structure Hypothesis," *Ecosystems*, vol. 5, no. 1, pp. 58–67, Jan. 2002.

[24] B. E. Roth and M. Newton, "Survival and growth of Douglas-fir relating to weeding, fertilization, and seed source," *West. J. Appl. For.*, vol. 11, no. 2, pp. 62–69, 1996.

[25] D. T. Price, T. A. Black, and F. M. Kelliher, "Effects of salal understory removal on photosynthetic rate and stomatal conductance of young Douglas-fir trees," *Can. J. For. Res.*, vol. 16, pp. 90–97, 1986.

[26] J. P. Kimmins, *Forest Ecology, A foundation for sustainable management*, 2nd ed. New Jersey: Prentice-Hall, Inc., 1996.

[27] C. C. Grier, K. M. Lee, N. M. Nadkarni, G. O. Klock, and P. J. Edgerton, "Productivity of forests of the United States and its relation to soil and site factors and management practices: a review," US Department of Agriculture, Forest Service, Pacific Northwest Research Station, Portland, Oregon, 1989.

[28] P. J. Kramer and T. T. Kozlowski, *Physiology of woody plants*. New York: Academic Press, Inc., 1979.

[29] L. Taiz and E. Zeiger, *Plant Physiology*, Fifth. Sunderland, Massachusetts, USA: Sinauer Associates Inc., Publishers, 2010.

[30] C. D. Oliver and B. C. Larson, *Forest stand dynamics*. New York: Wiley & Sons, Inc., 1996.

[31] J. F. Franklin, T. a Spies, R. Van Pelt, A. B. Carey, D. a Thornburgh, D. R. Berg, D. B. Lindenmayer, M. E. Harmon, W. S. Keeton, D. C. Shaw, K. Bible, and J. Chen, "Disturbances and structural development of natural forest ecosystems with silvicultural implications, using Douglas-fir forests as an example," *For. Ecol. Manage.*, vol. 155, no. 1–3, pp. 399–423, Jan. 2002.

[32] H. G. Miller, "The influence of stand development on nutrient demand, growth and allocation," *Plant Soil*, vol. 168–169, no. 1, pp. 225–232, 1995.

[33] T. M. M. Lillesand, R. W. Kiefer, and J. W. Chipman, *Remote sensing and image interpretation.*, 5th ed. New York: John Wiley & Sons, Inc., 2004.

[34] P. Packalen and M. Maltamo, "Predicting the plot volume by tree species using airborne laser scanning and aerial photographs," *For. Sci.*, vol. 52, no. 6, pp. 611–622, 2006.

[35] G. Frazer, R. Fournier, and J. Trofymow, "A comparison of digital and film fisheye photography for analysis of forest canopy structure and gap light transmission," *Agric. For.*, vol. 109, pp. 249–263, 2001.

[36] M. Standish, "The use of aerial photographs in forestry," *J. For.*, vol. 43, no. 4, pp. 252–257, 1945.

[37] K. Soudani, C. Francois, G. le Maire, V. V. Le Dantec, E. Dufrênea, and E. Dufrene, "Comparative analysis of IKONOS, SPOT, and ETM+ data for leaf area index estimation in temperate coniferous and deciduous forest stands," *Remote Sens. Environ.*, vol. 102, no. 102, p. 15, 2006.

[38] D. E. Ahl, S. T. Gower, S. N. Burrows, N. V Shabanov, R. B. Myneni, and Y. Knyazikhin,

"Monitoring spring canopy phenology of a deciduous broadleaf forest using MODIS," *Remote Sens. Environ.*, no. 104, p. 8, 2006.

[39] S. L. Ustin, a. a. A. Gitelson, S. S. Jacquemoud, M. E. Schaepman, G. P. Asner, J. a. Gamon, and P. J. Zarco-Tejada, "Retrieval of foliar information about plant pigment systems from high resolution spectroscopy," *Remote Sens. Environ.*, vol. 113, pp. S67–S77, Sep. 2009.

[40] P. H. P. Sampson, P. J. P. Zarco-Tejada, G. H. Mohammed, J. R. Miller, and T. L. Noland, "Hyperspectral Remote Sensing of Forest Condition: Estimating Chlorophyll Content in Tolerant Hardwoods," *For. Sci.*, vol. 49, no. 3, p. 10, 2003.

[41] A. Mathur, L. M. Bruce, J. Byrd, and A. D. Collection, "Discrimination of Subtly Different Vegetative Species via Hyperspectral Data," vol. 00, no. C, pp. 805–808, 2002.

[42] D. G. Goodenough, K. O. Niemann, A. Dyk, G. Hobart, and M. Loisel, "A Comparison of Forest Products from AISA and AVIRIS," in *ASTRO*, 2008.

[43] P. J. Zarco-Tejada, J. R. Miller, D. Haboudane, N. Tremblay, and S. Apostol, "Detection of Chlorophyll Fluorescence in Vegetation from Airborne Hyperspectral CASI Imagery in the Red Edge Spectral Region," *Geosci. Remote Sens. Symp. 2003. IGARSS '03. Proc. 2003 IEEE Int.*, vol. 1, pp. 598–600, 2003.

[44] L. Liu, Y. Zhang, J. Wang, and C. Zhao, "Detecting Solar-Induced Chlorophyll Fluorescence From Field Radiance Spectra Based on the Fraunhofer Line Principle," *IEEE Trans. Geosci. Remote Sens.*, vol. 43, no. 4, p. 6, 2005.

[45] I. Moya, L. Camenen, S. Evain, Y. Goulas, Z. G. Cerovic, G. Latouche, J. Flexas, and A. Ounis, "A new instrument for passive remote sensing 1. Measurements of sunlight-induced chlorophyll fluorescence ," *Remote Sens. Environ.*, no. 91, p. 12, 2004.

[46] R. Loos and K. O. Niemann, "Identification of individual trees and canopy shapes using lidar data for fire management," in *Proc. IEEE International Conference on Geoscience and Remote Sensing Symposium*, 2006, pp. 3755–3757.

[47] N. C. Coops, T. Hilker, M. a. Wulder, B. St-Onge, G. Newnham, A. Siggins, and J. a. (Tony) Trofymow, "Estimating canopy structure of Douglas-fir forest stands from discrete-return LiDAR," *Trees*, vol. 21, no. 3, pp. 295–310, Jan. 2007.

[48] K. O. Niemann, G. W. Frazer, R. Loos, and F. Visintini, "Lidar-guided analysis of airborne hyperspectral data," in *First Hyperspectral Image and Signal Processing: Evolution in Remote Sensing*, 2009.

[49] G. A. Blackburn, "Remote sensing of forest pigment using airborne imaging spectrometer and LIDAR imagery," *Remote Sens. Environ.*, vol. 82, pp. 311–321, 2002.

[50] G. J. McDermid, R. J. Hall, G. A. Sanchez-Azofeifa, S. E. Franklin, G. B. Stenhouse, T. Kobliuk, and E. F. LeDrew, "Remote sensing and forest inventory for wildlife habitat assessment," *For. Ecol. Manage.*, vol. 257, pp. 2262–2269, 2009.

[51] S. Frolking, M. W. Palace, D. B. Clark, J. Q. Chambers, H. H. Shugart, and G. C. Hurtt, "Forest disturbance and recovery: A general review in the context of spaceborne remote sensing of impacts on aboveground biomass and canopy structure," *J. Geophys. Res.*, vol. 114, Jul. 2009.

[52] C.-W. Cheng, D. A. Laird, M. J. Mausbach, and C. R. J. Hurburgh, "Near-Inrared Reflectance Spectroscopy-Principal Components Regression Analysis of Soil Properties," *Soil Sci. Soc. Am. J.*, vol. 65, pp. 480–490, 2001.

[53] M. a. Lefsky, W. B. Cohen, and T. a. Spies, "An evaluation of alternate remote sensing products for forest inventory, monitoring, and mapping of Douglas-fir forests in western Oregon," *Can. J. For. Res.*, vol. 31, no. 1, pp. 78–87, 2001.

[54] E. COULTER, W. CHUNG, and A. AKAY, "Forest road earthwork calculations for linear road segments using a high resolution digital terrain model generated from LIDAR data," in *the First International Precision Forestry Cooperative Symposium*, 2001.

[55] K. Lim, P. Treitz, M. Wulder, B. St-Onge, and M. Flood, “LiDAR remote sensing of forest structure,” *Prog. Phys. Geogr.*, vol. 27, no. 1, pp. 88–106, Mar. 2003.

[56] M. Wulder, K. O. Niemann, and D. G. Goodenough, “Local Maximum Filtering for the Extraction of Tree Locations and Basal Area from High Spatial Resolution Imagery,” *Remote Sens. Environ.*, vol. 73, pp. 103–114, 2000.

[57] C. Vaiphasa, S. Ongsomwang, T. Vaiphasa, and A. K. Skidmore, “Tropical mangrove species discrimination using hyperspectral data: A laboratory study,” *Estuar. Coast. Shelf Sci.*, vol. 65, pp. 371–379, 2005.

[58] G. Zheng and L. M. Moskal, “Retrieving Leaf Area Index (LAI) Using Remote Sensing: Theories, Methods and Sensors,” *Sensors*, vol. 9, no. 4, pp. 2719–2745, Apr. 2009.

[59] R. D. Jackson, “Remote Sensing of Biotic and Abiotic Plant Stress,” *Annu. Rev. Phytopathol.*, vol. 24, pp. 265–287, 1986.

[60] J. Liu, J. M. Chen, J. Cihlar, and W. M. Park, “A process-based Boreal ecosystem productivity simulator using remote sensing inputs,” *Remote Sens. Environ.*, vol. 62, no. 2, pp. 158–175, 1997.

[61] R. Nelson, K. J. Ranson, G. Sun, D. S. Kimes, V. Kharuk, and P. Montesano, “Estimating Siberian timber volume using MODIS and ICESat/GLAS,” *Remote Sens. Environ.*, vol. 113, no. 3, pp. 691–701, Mar. 2009.

[62] D. G. Leckie, C. Jay, F. A. Gougeon, R. N. Sturrock, and D. Paradine, “Detection and assessment of trees with Phellinus weirii (laminated root rot) using high resolution multi-spectral imagery,” *Int. J. Remote Sens.*, vol. 25, no. 4, pp. 793–818, 2004.

[63] P. Holmgren and T. Thuresson, “Satellite remote sensing for forestry planning — A review,” *Scand. J. For.*, vol. 13, pp. 90–110, 1998.

[64] B. N. Rock, T. Hoshizaki, and J. R. Miller, “Comparison of In Situ and Airborne Spectral Measurements of the Blue Shift Associated with Forest Decline,” *Remote Sens. Environ.*, vol. 24, pp. 109–127, 1988.

[65] M. Wulder, “Optical remote-sensing techniques for the assessment of forest inventory and biophysical parameters,” *Prog. Phys. Geogr.*, vol. 22, no. 4, pp. 449–476, Oct. 1998.

[66] A. H. Strahler, C. E. Woodcock, and J. a. Smith, “On the nature of models in remote sensing,” *Remote Sens. Environ.*, vol. 20, no. 2, pp. 121–139, Oct. 1986.

[67] R. M. Newnham, “Variable-form taper functions for four Alberta tree species,” *Can. J. For. Res.*, vol. 22, pp. 210–223, 1992.

[68] F. A. Gougeon and D. G. Leckie, “Individual tree crown image analysis - A step towards precision forestry,” in *the First International Precision Forestry Cooperative Symposium*, 2001.

[69] T. H. Demetriades-Shah, M. D. Steven, and J. A. Clark, “High Resolution Derivative Spectra in Remote Sensing,” *Remote Sens. Environ.*, vol. 33, pp. 55–64, 1990.

[70] A. S. Mazer, M. Martin, M. Lee, and J. E. Solomon, “Image processing software for imaging spectrometry data analysis,” *Remote Sens. Environ.*, vol. 24, no. 1, pp. 201–210, Feb. 1988.

[71] R. N. Clark and T. L. Roush, “Reflectance Spectroscopy: Quantitative Analysis Techniques for Remote Sensing Applications,” *J. Geophys. Res.*, vol. 89, no. B7, pp. 6329–6340, 1984.

[72] R. N. Clark, A. J. Gallagher, and G. A. Swayze, “Material absorption band depth mapping of imaging spectrometer data using the complete band shape least-squares algorithm simultaneously fit to multiple spectral features from multiple materials.,” in *Proceedings of the 3rd Airborne Visible/Infrared Imaging Spectrometer (AVIRIS) Workshop*, 1990, pp. 176–186.

[73] L. Li, S. L. Ustin, and M. Lay, “Application of AVRIS data in detection of oil-induced vegetation stress and cover change at Jornada, New Mexico,” *Remote Sens. Environ.*, vol. 94, pp. 1–16, 2005.

[74] K. L. L. Smith, M. D. D. Steven, and J. J. J. Colls, “Use of hyperspectral derivative ratios in the

red-edge region to identify plant stress responses to gas leaks," *Remote Sens. Environ.*, vol. 92, no. 2, pp. 207–217, Aug. 2004.

[75] P. K. E. Campbell, B. N. Rock, M. E. Martin, C. D. Neefus, J. R. Irons, E. M. Middleton, and J. Albrechtova, "Detection of initial damage in Norway spruce canopies using hyperspectral airborne data," *Int. J. Remote Sens.*, vol. 25, no. 24, pp. 5557–5583, 2004.

[76] I. Filella and J. Penuelas, "The red edge position and shape as indicators of plant chlorophyll content, biomass and hydric status," *Int. J. Remote Sens.*, vol. 15, no. 7, pp. 1459–1470, 1994.

[77] P. J. Curran, J. L. Dungan, and S. E. Plummer, "The effect of a red leaf pigment on the relationship between red edge and chlorophyll concentration," *Remote Sens. Environ.*, vol. 35, pp. 69–76, 1991.

[78] L. Serrano, J. Penuelas, and S. L. Ustin, "Remote sensing of nitrogen and lignin in Mediterranean vegetation from AVIRIS data: Decomposing biochemical from structural signals," *Remote Sens. Environ.*, vol. 81, pp. 355–364, 2002.

[79] Y. Grossman, S. Ustin, and S. Jacquemoud, "Critique of stepwise multiple linear regression for the extraction of leaf biochemistry information from leaf reflectance data," *Remote Sens. Environ.*, vol. 56, pp. 182–193, 1996.

[80] M.-L. Smith, M. E. Martin, L. Plourde, and S. V Ollinger, "Analysis of Hyperspectral Data for Estimation of Temperate Forest Canopy Nitrogen Concentration: Comparison Between an Airborne (AVIRIS) and a Spaceborne (Hyperion) Sensor," *IEEE Trans. Geosci. Remote Sens.*, vol. 41, no. 6, pp. 1332–1337, 2003.

[81] D. G. Goodenough, J. Y. Li, G. P. Asner, M. E. Schaepman, S. L. Ustin, and A. Dyk, "Combining Hyperspectral Remote Sensing and Physical Modeling for Applications in Land Ecosystems," in *IEEE International Geoscience and Remote Sensing Symposium*, 2006, no. Denver, CO, pp. 2000–2004.

[82] R. F. Kokaly, B. W. Rockwell, S. L. Haire, and T. V. V. King, "Characterization of post-fire surface cover, soils, and burn severity at the Cerro Grande Fire, New Mexico, using hyperspectral and multispectral remote sensing," *Remote Sens. Environ.*, vol. 106, no. 3, pp. 305–325, Feb. 2007.

[83] R. F. Kokaly, G. P. Asner, S. V Ollinger, M. E. Martin, and C. A. Wessman, "Characterizing canopy biochemistry from imaging spectroscopy and its application to ecosystem studies," *Remote Sens. Environ.*, vol. 113, pp. S78–S91, 2009.

[84] H. C. Stimson, D. D. Breshears, S. L. Ustin, and S. C. Kefauver, "Spectral sensing of foliar water conditions in two co-occurring conifer species: Pinus edulis and Juniperus monosperma," *Remote Sens. Environ.*, vol. 96, pp. 108–118, 2005.

[85] J. Penuelas, J. Pinol, R. Ogaya, and I. Filella, "Estimation of plant water concentration by the reflectance Water Index WI (R900/970)," *Int. J. Remote Sens.*, vol. 18, no. 13, pp. 2869–2875, 1997.

[86] H. M. Eriksson, L. Eklundh, A. Kuusk, and T. Nilson, "Impact of understory vegetation on forest canopy reflectance and remotely sensed LAI estimates," *Remote Sens. Environ.*, vol. 103, no. 4, pp. 408–418, Aug. 2006.

[87] E. Næsset, J. G. Gjevestad, and E. Naesset, "Performance of GPS Precise Point Positioning Under Conifer Forest Canopies," *Photogramm. Eng. Remote Sensing*, vol. 74, no. 5, pp. 661–668, 2008.

[88] R. Dubayah and J. B. Drake, "Lidar remote sensing for forestry," *J. For.*, vol. 98, no. 6, pp. 44–46, 2000.

[89] M. a. Wulder, J. C. White, R. F. Nelson, E. Næsset, H. O. Ørka, N. C. Coops, T. Hilker, C. W. Bater, and T. Gobakken, "Lidar sampling for large-area forest characterization: A review," *Remote Sens. Environ.*, vol. 121, pp. 196–209, Jun. 2012.

[90] Z. Chen, B. Gao, and B. Devereux, "State-of-the-Art: DTM Generation Using Airborne LIDAR Data," *Sensors*, vol. 17, no. 150, 2017.

[91] J. Hyyppa, H. Hyyppa, D. Leckie, F. Gougeon, X. Yu, and M. Maltamo, "Review of methods of small‐footprint airborne laser scanning for extracting forest inventory data in boreal forests," *Int. J. Remote Sens.*, vol. 29, no. 5, pp. 1339–1366, 2008.

[92] S. Magnussen and P. Boudewyn, "Derivations of stand heights from airborne laser scanner data with canopy-based quantile estimators," *Can. J. For. Res.*, vol. 28, no. 7, pp. 1016–1031, 1998.

[93] R. Musk, "Stand level inventory of eucalypt plantations using small footprint LiDAR in Tasmania, Australia," in *SilviLaser 2011, 11th International Conference on LiDAR Applications for Assessing Forest Ecosystems*, 2011.

[94] H.-E. H. E. Andersen, S. E. Reutebuch, and G. F. G. F. Schreuder, "Automated individual tree measurement through morphological analysis of a LIDAR-based canopy surface model," in *Proc. of the 1st International Precision Forestry Symposium*, 2001, pp. 11–21.

[95] H. Andersen and R. McGaughey, "Forest measurement and monitoring using high-resolution airborne lidar," Portland, Oregon, 2005.

[96] A. Omule, A. K. Mitchell, W. L. Wagner, and Canadian Wood Fibre Centre, *Fertilization and thinning effects on a Douglas-fir ecosystem at Shawnigan Lake: 32-year growth response*. Canadian Wood Fibre Centre, 2011.

[97] J. Thrower, "Site index curves and tables for British Columbia: coastal species," *BC Min. For., Victoria, BC L. Manag. Handb. F.*, 1991.

[98] D. Beddows, *Levels-of-growing-stock Cooperative Study in Douglas-fir. Report No. 16, Sayward Forest and Shawnigan Lake*, no. 16. Canadian Forest Service, Pacific Forestry Centre, 2002.

[99] A. Omule, A. K. A. Mitchell, W. W. L. Wagner, and Canadian Wood Fibre Centre, *Fertilization and thinning effects on a Douglas-fir ecosystem at Shawnigan Lake: 32-year growth response*. Canadian Wood Fibre Centre, 2011.

[100] S. H. Smith and J. F. Bell, "Using competitive stress index to estimate diameter growth for thinned Douglas-fir stands," *For. Sci.*, vol. 29, no. 3, pp. 491–499, 1983.

[101] G. S. Quinn, "Towards an operational root disease mapping methodology through lidar integrated imaging spectroscopy," University of victoria, 2010.

[102] Magellan Corporation and Ashtech Precision Products, "Z-Xtreme GPS Reciever, Operation & Reference Manual." Santa Clara, CA, p. 66, 2001.

[103] A. Kharaghani, "GeoBC, Geospatial Reference, Reference Systems and Survey Monuments, MASCOT Home," 1996. [Online]. Available: http://a100.gov.bc.ca/pub/mascotw/public/index.html.

[104] Magellan Corporation and Ashtech Precision Products, "Z-Xtreme, Technical Reference Manual." Santa Clara, CA, p. 266, 2001.

[105] G. Enterprise Spatial Services Branch, "Province of British Columbia, Specifications and Guidelines For Control Surveys Using GPS Technology," 2010.

[106] "Natural Resources Canada, Land Survey Standards, Accuracy Standard for Legal Surveys," 2015. [Online]. Available: http://clss.nrcan.gc.ca/standards-normes/e4-v1-eng.php.

[107] E. Ben-Dor, B. C. Kindel, and A. F. H. Goetz, "Quality assessment of several methods to recover surface reflectance using synthetic imaging spectroscopy data ," *Remote Sens. Environ.*, vol. 90, pp. 389–404, 2004.

[108] N. Knighton and B. Bugbee, "A Mixture of Barium Sulfate and White Paint is a Low-Cost Substitute Reflectance Standard for Spectralon," 2004.

[109] Spectral Imaging Ltd., "SPECIM CaliGeo 4.9.7 AISA+ /AISA Eagle/AISA Hawk Data Processing Tool Operating Manual Ver. 1.30," Finland, 2009.

[110] W. Ruyten, "Smear correction for frame transfer charge-coupled-device cameras.," *Opt. Lett.*, vol.

24, no. 13, pp. 878–80, Jul. 1999.

[111] R. Bars, “Smear correction of AISA data, Algorithms and examples for different cases,” Oulu, Finland, 2011.

[112] J. D. Wood, “The geomorphological characterisation of digital elevation models,” University of Leicester, 1996.

[113] S. Omule, V. Fletcher, and K. Polsson, “Total and merchantable volume equations for small coastal Douglas-fir,” Victoria, BC, Canada, 1987.

[114] H. Brix, “Effects of thinning and nitrogen fertilization on growth of Douglas-fir: relative contribution of foliage quantity and efficiency,” *Can. J. For. Res.*, vol. 13, no. 1, pp. 167–175, 1983.

[115] E. D. Vance, D. A. Maguire, and R. S. Zalesny, “Research strategies for increasing productivity of intensively managed forest plantations,” *J. For.*, vol. 108, no. 4, pp. 183–192, 2010.

[116] K. A. Stegemoeller and H. N. Chappell, “Growth response of unthinned and thinned Douglas-fir stands to single and multiple applications of nitrogen,” *Can. J. For. ...*, vol. 20, pp. 343–349, 1990.

[117] A. W. D’Amato, B. J. Palik, and C. C. Kern, “Growth, yield, and structure of extended rotation Pinus resinosa stands in Minnesota, USA,” *Can. J. For. Res.*, vol. 40, no. 5, pp. 1000–1010, May 2010.

[118] C. N. Filipescu, A. Groot, D. A. MacIsaac, M. G. Cruickshank, and J. D. Stewart, “Prediction of diameter using height and crown attributes: A case study,” *West. J. Appl. For.*, vol. 27, pp. 30–35, 2012.

[119] R. Yang, A. Kozak, and J. Smith, “The potential of Weibull-type functions as flexible growth curves,” *Can. J. For. ...*, vol. 8, pp. 424–431, 1978.

[120] B. J. Hawkins and M. Stoehr, “Growth, phenology, and cold hardiness of 32 Douglas-fir full-sib families,” *Can. J. For. Res.*, vol. 39, no. 10, pp. 1821–1834, Oct. 2009.

[121] C. Staudhammer and V. LeMay, “Height prediction equations using diameter and stand density measures,” *For. Chron.*, vol. 76, no. 2, 2000.

[122] P. A. Beedlow, E. H. Lee, D. T. Tingey, R. S. Waschmann, and C. A. Burdick, “The importance of seasonal temperature and moisture patterns on growth of Douglas-fir in western Oregon, USA,” *Agric. For. Meteorol.*, vol. 169, pp. 174–185, 2013.

[123] W. H. Emmingham, “Comparison of selected Douglas-fir seed sources for cambial and leader growth patterns in four western Oregon environments,” *Can. J. For. Res.*, vol. 7, pp. 154–164, 1977.

[124] A. Agapiou, D. Hadjimitsis, and D. Alexakis, “Evaluation of broadband and narrowband vegetation indices for the identification of archaeological crop marks,” *Remote Sens.*, vol. 4, no. 12, pp. 3892–3919, Dec. 2012.

[125] R. F. Kokaly and R. N. Clark, “Spectroscopic Determination of Leaf Biochemistry Using Band-Depth Analysis of Absorption Features and Stepwise Multiple Linear Regression,” *Remote Sens. Environ.*, vol. 67, pp. 267–287, 1999.

[126] J. A. Gamon, J. Penuelas, and C. B. Field, “A Narrow-Waveband Spectral Index That Tracks Diurnal Changes in Photosynthetic Efficiency,” *Remote Sens. Environ.*, vol. 41, pp. 35–44, 1992.

[127] B. Demmig-Adams, W. W. Adams III, B. Demmig-Adams, and W. W. Adams, “Photoprotection in an ecological context: the remarkable complexity of thermal energy dissipation,” *New Phytol.*, vol. 172, no. 1, pp. 11–21, Jan. 2006.

[128] B. Demmig-Adams and W. W. Adams, “Photoprotection in an ecological context: the remarkable complexity of thermal energy dissipation.,” *New Phytol.*, vol. 172, no. 1, pp. 11–21, Jan. 2006.

[129] B. Demmig-Adams, A. M. Gilmore, and W. W. Adams III, “In vivo functions of carotenoids in

higher plants," *J. Fed. Am. Soc. Exp. Biol.*, vol. 10, pp. 403–412, 1996.

[130] T. Hilker, N. C. Coops, M. a Wulder, T. A. Black, and R. D. Guy, "The use of remote sensing in light use efficiency based models of gross primary production: a review of current status and future requirements.," *Sci. Total Environ.*, vol. 404, no. 2–3, pp. 411–23, Oct. 2008.

[131] M. S. Kim, C. S. T. Daughtry, E. W. Chappelle, J. E. McMurtrey, and C. L. Walthall, "The use of high spectral resolution bands for estimating absorbed photosynthetically active radiation (A par)," in *CNES, Proceedings of 6th International Symposium on Physical Measurements and Signatures in Remote Sensing*, 1994, pp. 299–306.

[132] D. Haboudane, J. R. Miller, N. Tremblay, P. J. Zarco-Tejada, and L. Dextraze, "Integrated narrow-band vegetation indices for prediction of crop chlorophyll content for application to precision agriculture," *Remote Sens. Environ.*, vol. 81, pp. 416–426, 2002.

[133] A. A. Gitelson, M. N. Merzlyak, and O. B. Chivkunova, "Optical Properties and Nondestructive Estimation of Anthocyanin Content in Plant Leaves¶," *Photochem. Photobiol.*, vol. 74, no. 1, pp. 38–45, 2007.

[134] J. L. Hatfield, a. a. Gitelson, J. S. Schepers, and C. L. Walthall, "Application of Spectral Remote Sensing for Agronomic Decisions," *Agron. J.*, vol. 100, no. Supplement_3, p. S-117, 2008.

[135] L. Chalker-Scott, "Environmental significance of anthocyanins in plant stress responses," *Photochemistry and Photobiology*, vol. 70, no. 1. pp. 1–9, 1999.

[136] A. R. Weiskittel, "Alterations in Douglas-fir Crown Structure, Morphology, and Dynamics Imposed by the Swiss Needle Cast Disease in the Oregon Coast Range," Oregon State University, 2003.

[137] M. G. Cruickshank and C. N. Filipescu, "Allometries of coarse tree, stem, and crown measures in Douglas-fir are altered by Armillaria root disease," *Botany*, vol. 90, no. 8, pp. 711–721, 2012.

[138] G. A. Blackburn, "Relationships between Spectral Reflectance and Pigment Concentrations in Stacks of Deciduous Broadleaves," *Remote Sens. Environ.*, vol. 70, pp. 224–237, 1999.

[139] T. C. Vogelmann, "Plant tissue optics," *Annu. Rev. Plant Physiol. Plant Mol. Biol.*, vol. 44, pp. 231–251, 1993.

[140] M. A. Babyak, "What you see may not be what you get: A brief, nontechnical introduction to overfitting in regression-type models," *Psychosom. Med.*, vol. 66, no. 3, pp. 411–421, 2004.

[141] B. Demmig-Adams, A. M. Gilmore, and W. W. Adams III, "In vivo functions of carotenoids in higher plants," *J. Fed. Am. Soc. Exp. Biol.*, vol. 10, pp. 403–412, 1996.

[142] M. F. Garbulsky, J. Peñuelas, J. Gamon, Y. Inoue, and I. Filella, "The photochemical reflectance index (PRI) and the remote sensing of leaf, canopy and ecosystem radiation use efficienciesA review and meta-analysis," *Remote Sens. Environ.*, vol. 115, no. 2, pp. 281–297, Feb. 2011.

[143] T. Schulz, "Calibration of a terrestrial laser scanner for engineering geodesy," Technical University of Berlin, 2007.

[144] "General Survey Guide," 2013. [Online]. Available: http://www.th.gov.bc.ca/publications/eng_publications/survey/general_survey_guide.pdf.

[145] M. Dassot, T. Constant, and M. Fournier, "The use of terrestrial LiDAR technology in forest science: application fields, benefits and challenges," *Ann. For. Sci.*, vol. 68, no. 5, pp. 959–974, Jul. 2011.

[146] J.-F. Côté, R. a. Fournier, G. W. Frazer, and K. Olaf Niemann, "A fine-scale architectural model of trees to enhance LiDAR-derived measurements of forest canopy structure," *Agric. For. Meteorol.*, vol. 166–167, pp. 72–85, Dec. 2012.

[147] T. Hilker, N. C. Coops, G. J. Newnham, M. van Leeuwen, M. A. Wulder, J. Stewart, and D. S. Culvenor, "Comparison of Terrestrial and Airborne LiDAR in Describing Stand Structure of a

Thinned Lodgepole Pine Forest," *J. For.*, vol. 110, no. 2, pp. 97–104, 2012.

[148] S. Srinivasan, S. C. Popescu, M. Eriksson, R. D. Sheridan, and N.-W. Ku, "Terrestrial Laser Scanning as an Effective Tool to Retrieve Tree Level height, Crown Width, and Stem Diameter," *Remote Sens.*, vol. 7, pp. 1877–1896, 2015.

[149] S. Hancock, R. Essery, T. Reid, J. Carle, R. Baxter, N. Rutter, and B. Huntley, "Characterising forest gap fraction with terrestrial lidar and photography: An examination of relative limitations," *Agric. For. Meteorol.*, vol. 189–190, pp. 105–114, Jun. 2014.

[150] M. Béland, D. D. Baldocchi, J.-L. Widlowski, R. a. Fournier, and M. M. Verstraete, "On seeing the wood from the leaves and the role of voxel size in determining leaf area distribution of forests with terrestrial LiDAR," *Agric. For. Meteorol.*, vol. 184, pp. 82–97, Jan. 2014.

[151] S. Srinivasan, S. C. Popescu, M. Eriksson, R. D. Sheridan, and N.-W. Ku, "Multi-temporal terrestrial laser scanning for modeling tree biomass change," *For. Ecol. Manage.*, vol. 318, pp. 304–317, Apr. 2014.

[152] X. Yu, X. Liang, J. Hyyppä, V. Kankare, M. Vastaranta, and M. Holopainen, "Stem biomass estimation based on stem reconstruction from terrestrial laser scanning point clouds," *Remote Sens. Lett.*, vol. 4, no. 4, pp. 344–353, Apr. 2013.

[153] V. Kankare, M. Holopainen, M. Vastaranta, E. Puttonen, X. Yu, J. Hyyppä, M. Vaaja, H. Hyyppä, and P. Alho, "Individual tree biomass estimation using terrestrial laser scanning," *ISPRS J. Photogramm. Remote Sens.*, vol. 75, pp. 64–75, Jan. 2013.

[154] P. Pueschel, G. Newnham, G. Rock, T. Udelhoven, W. Werner, and J. Hill, "The influence of scan mode and circle fitting on tree stem detection, stem diameter and volume extraction from terrestrial laser scans," *ISPRS J. Photogramm. Remote Sens.*, vol. 77, pp. 44–56, Mar. 2013.

[155] R. Hildebrandt and A. Iost, "From points to numbers: a database-driven approach to convert terrestrial LiDAR point clouds to tree volumes," *Eur. J. For. Res.*, vol. 131, no. 6, pp. 1857–1867, Jul. 2012.

[156] M. van Leeuwen, T. Hilker, N. C. Coops, G. Frazer, M. a. Wulder, G. J. Newnham, and D. S. Culvenor, "Assessment of standing wood and fiber quality using ground and airborne laser scanning: A review," *For. Ecol. Manage.*, vol. 261, no. 9, pp. 1467–1478, May 2011.

[157] T. Mengesha, M. Hawkins, and M. Nieuwenhuis, "Validation of terrestrial laser scanning data using conventional forest inventory methods," *Eur. J. For. Res.*, vol. 134, no. 2, pp. 211–222, 2014.

[158] P. Michel, J. Jenkins, N. Mason, K. J. M. Dickinson, and I. G. Jamieson, "Assessing the ecological application of lasergrammetric techniques to measure fine-scale vegetation structure," *Ecological Informatics*, vol. 3, no. 4–5. Elsevier B.V., pp. 309–320, 2008.

[159] T. J. Drew and J. W. Flewelling, "Stand Density Management : an Alternative Approach and Its Application to Douglas-fir Plantations," vol. 25, no. 3, pp. 518–532, 1979.

[160] H. Kaartinen, J. Hyyppä, X. Yu, M. Vastaranta, H. Hyyppä, A. Kukko, M. Holopainen, C. Heipke, M. Hirschmugl, F. Morsdorf, E. Næsset, J. Pitkänen, S. Popescu, S. Solberg, B. M. Wolf, and J. C. Wu, "An international comparison of individual tree detection and extraction using airborne laser scanning," *Remote Sens.*, vol. 4, pp. 950–974, 2012.

[161] M. Simonse, T. Aschoff, H. Spiecker, and M. Thies, "Automatic Determination of Forest Inventory Parameters," in *Proceedings of the ScandLaser Scientific Workshop on Airborne Laser Scanning of Forests*, 2003, pp. 251– 257.

[162] G. Brolly and G. Kiraly, "Algorithms for stem mapping by means of terrestrial laser scanning.," *Acta Silv. Lignaria Hungarica*, vol. 5, pp. 119–130, 2009.

[163] J. L. Lovell, D. L. B. Jupp, G. J. Newnham, and D. S. Culvenor, "Measuring tree stem diameters using intensity profiles from ground-based scanning lidar from a fixed viewpoint," *ISPRS J. Photogramm. Remote Sens.*, vol. 66, no. 1, pp. 46–55, Jan. 2011.

[164] X. Liang, P. Litkey, J. Hyyppä, H. Kaartinen, M. Vastaranta, and M. Holopainen, "Automatic stem mapping using single-scan terrestrial laser scanning," *IEEE Trans. Geosci. Remote Sens.*, vol. 50, no. 2, pp. 661–670, 2012.

[165] J. G. Henning and P. J. Radtke, "Detailed stem measurements of standing trees from ground-based scanning lidar," *For. Sci.*, vol. 52, no. 1, pp. 67–80, 2006.

[166] J.-F. Côté, R. a. Fournier, and R. Egli, "An architectural model of trees to estimate forest structural attributes using terrestrial LiDAR," *Environ. Model. Softw.*, vol. 26, no. 6, pp. 761–777, Jun. 2011.

[167] T. Adams, "Remotely Sensed Crown Structure as an Indicator of Wood Quality A comparison of metrics from Aerial and Terrestrial Laser Scanning," in *Silvilaser*, 2011.

[168] a Bienert, A. Bienert, S. Scheller, S. Scheller, E. Keane, E. Keane, F. Mohan, F. Mohan, C. Nugent, C. Nugent, R. Sensing, R. Sensing, T. R. Centre, T. R. Centre, C. Constraint, C. Constraint, C. Centre, and C. Centre, "Tree detection and diameter estimations by analysis of forest terrestrial laserscanner point clouds," *Isprs*, pp. 50–55, 2007.

[169] M. Thies, N. Pfeifer, D. Winterhalder, and B. G. H. Gorte, "Three-dimensional reconstruction of stems for assessment of taper, sweep and lean based on laser scanning of standing trees," *Scand. J. For. Res.*, vol. 19, no. 6, pp. 571–581, 2004.

[170] J. Hackenberg, C. Morhart, J. Sheppard, H. Spiecker, and M. Disney, "Highly accurate tree models derived from terrestrial laser scan data: A method description," *Forests*, vol. 5, no. 5, pp. 1069–1105, 2014.

[171] A. Brunner and B. Gizachew, "Rapid detection of stand density, tree positions, and tree diameter with a 2D terrestrial laser scanner," *Eur. J. For. Res.*, vol. 133, no. 5, pp. 819–831, 2014.

[172] P. Pueschel, "The influence of scanner parameters on the extraction of tree metrics from FARO Photon 120 terrestrial laser scans," *ISPRS J. Photogramm. Remote Sens.*, vol. 78, pp. 58–68, Apr. 2013.

[173] L. Chasmer, C. Hopkinson, and P. Treitz, "Investigating laser pulse penetration through a conifer canopy by integrating airborne and terrestrial lidar," *Can. J. Remote Sens.*, vol. 32, no. 2, pp. 116–125, 2006.

[174] R. Czaplewski, A. Brown, and D. Guenther, "Estimating merchantable tree volume in Oregon and Washington using stem profile models," Fort Collins, Colorado, 1989.

[175] H. -G. Maas, a. Bienert, S. Scheller, and E. Keane, "Automatic forest inventory parameter determination from terrestrial laser scanner data," *Int. J. Remote Sens.*, vol. 29, no. 5, pp. 1579–1593, 2008.

[176] J. Vauhkonen, L. Ene, S. Gupta, J. Heinzel, J. Holmgren, J. Pitkänen, S. Solberg, Y. Wang, H. Weinacker, K. M. Hauglin, V. Lien, P. Packalén, T. Gobakken, B. Koch, E. Næsset, T. Tokola, and M. Maltamo, "Comparative testing of single-tree detection algorithms under different types of forest," *Forestry*, vol. 85, no. 1, pp. 27–40, 2012.

[177] D. a Pouliot, D. J. King, and D. G. Pitt, "Development and evaluation of an automated tree detection-delineation algorithm for monitoring regenerating coniferous forests," *Can. J. For. Res.*, vol. 35, no. 10, pp. 2332–2345, 2005.

[178] M. J. Falkowski, A. M. S. Smith, P. E. Gessler, A. T. Hudak, L. a Vierling, and J. S. Evans, "The influence of conifer forest canopy cover on the accuracy of two individual tree measurement algorithms using lidar data," *Can. J. Remote Sens.*, vol. 34, no. S2, pp. S338–S350, 2008.

[179] D. Leckie, F. Gougeon, D. Hill, R. Quinn, L. Armstrong, and R. Shreenan, "Combined high-density lidar and multispectral imagery for individual tree crown analysis," *Can. J. Remote Sens.*, vol. 29, no. 5, pp. 633–649, 2003.

[180] M. Muller, A. Paula, B. Kersting, N. Y. Nakajima, R. T. Hosokawa, and N. C. Rosot, "INFLUENCE OF FLIGHT CONFIGURATION USED FOR LiDAR DATA COLLECTION ON

INDIVIDUAL TREES DATA EXTRACTION IN FOREST PLANTATIONS," *Floresta*, vol. 44, no. 2, pp. 279–290, 2014.

[181] R. Loos, K. O. Niemann, and F. Visintini, "Identification of partial canopies using first and last return lidar data," in *CRSS/ASPRS Our Common Borders- Safety, Sequrity, and the Environment Through Remote Sensing*, 2007, pp. 1–9.

[182] K. Olofsson, E. Lindberg, and J. Holmgren, "A method for linking field-surveyed and aerial-detected single trees using cross correlation of position images and the optimization of weighted tree list graphs," *SilviLaser 2008*, no. 2006, pp. 95–104, 2008.

[183] A. Khosravipour, A. K. Skidmore, T. Wang, M. Isenburg, and D. Khoshelham, "Effect of slope on treetop detection using a LiDAR canopy height model," *ISPRS J. Photogramm. Remote Sens.*, vol. 104, pp. 44–52, 2015.

[184] C. Vega, a. Hamrouni, S. El Mokhtari, J. Morel, J. Bock, J.-P. Renaud, M. Bouvier, and S. Durrieu, "PTrees: A point-based approach to forest tree extraction from lidar data," *Int. J. Appl. Earth Obs. Geoinf.*, vol. 33, pp. 98–108, 2014.

[185] J. Zhang, G. Sohn, and M. Brédif, "A hybrid framework for single tree detection from airborne laser scanning data : A case study in temperate mature coniferous forests in Ontario , Canada," *ISPRS J. Photogramm. Remote Sens.*, vol. 98, pp. 44–57, 2014.

[186] M. Crown and C. P. Brett, "Fertilization & Thinning Effects On a Douglas-Fir Ecosystem At Shawnigan Lake: An Establishment Report," Victoria, BC, Canada, 1975.

[187] R. Skelly, "ALS Individual Tree Algorithm (unpublished)." Victoria, B.C., 2017.

[188] M. Chang, *Forest hydrology: an introduction to water and forests*. Boca Raton, Florida: CRC Pres, 2003.

[189] W. G. Thies and R. N. Sturrock, "Laminated root rot in Western North America," vol. PNW-GTR-39. Forest Service, Portland, Oregon, 1995.

[190] A. Clyde, "Timber value, Alva Clyde, Scaling Supervisor at Garrett Log Services, recipient: Geoffrey S. Quinn, personal communication." 2016.

[191] G. S. Quinn, K. O. Niemann, F. Visintini, R. Stephen, and D. Parton, "Materials and geometey for the empirical radiometric calibration of an airborne imaging spectrometer," in *EARSeL*, 2015.

[192] T. Cooley, G. P. Anderson, G. W. Felde, M. L. Hoke, A. J. Ratkowski, J. H. Chetwynd, J. A. Gardner, S. M. Adler-Golden, M. W. Matthew, A. Berk, others, L. S. Bernstein, P. K. Acharya, D. Miller, P. Lewis, T. Cooleya, G. P. Andersona, A. J. Ratkowskia, D. Milled, and P. Lewise, "FLAASH, a MODTRAN4-based atmospheric correction algorithm, its application and validation," in *Geoscience and Remote Sensing Symposium, 2002. IGARSS'02. 2002 IEEE International*, 2002, vol. 3, no. C, pp. 1414–1418.

[193] B.-C. Gao, C. O. Davis, and A. F. H. Goetz, "A Review of Atmospheric Correction Techniques for Hyperspectral Remote Sensing of Land Surfaces and Ocean Color," *Geoscience and Remote Sensing Symposium, 2006. IGARSS 2006 IEEE International Conference on*. 2006.

[194] D. O'Sullivan and D. J. Unwin, *Geographic Information Analysis*. Hoboken, New Jersey: Wiley & Sons, Inc., 2003.

[195] R. K. Pachauri, L. A. Meyer, and IPCC, "IPCC Climate Change 2014: Synthesis Report. Contributions of Working Groups I,II and III to the Fifth Assessment Report of the Intergovernmental Panel on Climate Change," Geneva, Switzerland, 2014.

[196] G. Bonan, "Forests and climate change: forcings, feedbacks, and the climate benefits of forests," *Science (80-.).*, vol. 320, no. 5882, pp. 1444–9, Jun. 2008.

[197] L. K. Gray and A. Hamann, "Tracking suitable habitat for tree populations under climate change in western North America," *Clim. Change*, vol. 117, no. 1–2, pp. 289–303, 2013.

[198] R. K. Dumroese, M. I. Williams, J. A. Stanturf, and J. B. S. Clair, “Considerations for restoring temperate forests of tomorrow: forest restoration, assisted migration, and bioengineering,” *New For.*, vol. 46, no. 5–6, pp. 947–964, 2015.

[199] D. J. Chmura, P. D. Anderson, G. T. Howe, C. a. Harrington, J. E. Halofsky, D. L. Peterson, D. C. Shaw, and J. Brad St.Clair, “Forest responses to climate change in the northwestern United States: Ecophysiological foundations for adaptive management,” *For. Ecol. Manage.*, vol. 261, no. 7, pp. 1121–1142, Apr. 2011.

[200] H. Chappell, S. A. Y. Omule, and S. Gessel, “Fertilization in Coastal Northwest Forests: Using Response Information in Developing Stand-Level Tactics,” in *Forest Fertilization: Sustaining and Improving Nutrition and Growth of Western Forests*, H. N. Chappell, G. F. Weetman, and R. E. Miller, Eds. Seattle, Washington: College of Forest Resources, University of Washington, 1992, pp. 98–113.

[201] A. Hunter, “West Fraser 2005 Fertilizing Program: Some Operational Considerations, February 2, 2006, Prince George Civic Centre.,” 2006. [Online]. Available: https://www2.gov.bc.ca/assets/gov/environment/natural-resource-stewardship/land-based-investment/forests-for-tomorrow/west_fraser_2005_fertilization.pdf. [Accessed: 28-Oct-2018].

[202] F. Forest Practces Branch, “Summary of all silviculture activities and cumulative planting 1950-2016,” 2018.

[203] D. M. F. Gourley, “Impact of Climate and Disturbance on the Formation of Earlywood and Latewood in Douglas-fir at the Salal Fields Study Site,” Oregon State University, 2016.

[204] B. Lachenbruch, G. R. Johnson, G. M. Downes, and R. Evans, “Relationships of density, microfibril angle, and sound velocity with stiffness and strength in mature wood of Douglas-fir,” *Can. J. For. Res.*, vol. 40, no. 1, pp. 55–64, Jan. 2010.

[205] A. Bannari, K. S. Khurshid, K. Staenz, and J. W. Schwarz, “A Comparison of Hyperspectral Chlorophyll Indices for Wheat Crop Chlorophyll Content Estimation Using Laboratory Reflectance Measurements,” *IEEE Trans. Geosci. Remote Sens.*, vol. 45, no. 10, pp. 3063–3074, 2007.

[206] G. Blackburn and J. Ferwerda, “Retrieval of chlorophyll concentration from leaf reflectance spectra using wavelet analysis,” *Remote Sens. Environ.*, vol. 112, no. 4, pp. 1614–1632, Apr. 2008.

[207] D. B. I. V, “COMPARING HYPERSPECTRAL BASED PREDICTIVE MODELS FOR MAPPING SPATIAL VARIATION OF FOLIAR BIOCHEMISTRY IN NORWAY SPRUCE FOREST COMPARING HYPERSPECTRAL BASED PREDICTIVE MODELS FOR MAPPING SPATIAL VARIATION OF FOLIAR BIOCHEMISTRY IN,” *Geography*, 2011.

[208] T. P. Dawson, P. J. Curran, and S. E. Plummer, “LIBERTY-Modeling the Effects of Leaf Biochemical Concentration on Reflectance Spectra,” *Remote Sens. Environ.*, vol. 65, no. 98, pp. 50–60, 1998.

[209] G. le Maire, C. François, E. Dufrêne, G. Maire, C. Franc, E. Dufre, C. Francois, and E. Dufrene, “Towards universal broad leaf chlorophyll indices using PROSPECT simulated database and hyperspectral reflectance measurements,” *Remote Sens. Environ.*, vol. 89, no. 1, pp. 1–28, Jan. 2004.

[210] S. Jacquemoud and F. Baret, “PROSPECT: A Model of Leaf Optical Properties Spectra,” *Remote Sens. Environ.*, vol. 34, pp. 75–91, 1990.

[211] K. O. Niemann, G. Quinn, R. Stephen, F. Visintini, and D. Parton, “Hyperspectral Remote Sensing of Mountain Pine Beetle with an Emphasis on Previsual Assessment,” *Can. J. Remote Sens.*, vol. 41, no. 3, pp. 191–202, 2015.

[212] C. Wu, Z. Niu, Q. Tang, and W. Huang, “Estimating chlorophyll content from hyperspectral vegetation indices: Modeling and validation,” *Agric. For. Meteorol.*, vol. 148, no. 8–9, pp. 1230–1241, Jul. 2008.

[213] G. A. Blackburn, “Quantifying Chlorophylls and Carotenoids at Leaf and Canopy Scales: An

Evaluation of Some Hyperspectral Approaches," *Remote Sens. Environ.*, vol. 66, pp. 273–285, 1998.

[214] C. S. T. Daughtry, C. L. Walthall, M. S. Kim, E. B. de Colstoun, J. E. McMurtrey, and E. B. De Colstoun, "Estimating Corn Leaf Chlorophyll Concentration from Leaf and Canopy Reflectance," *Remote Sens. Environ.*, vol. 74, no. 00, pp. 229–239, 2000.

[215] F. Baret and T. Fourty, "Estimation of leaf water content and specific leaf weight from reflectance and transmittance measurements," *Agronomie*, vol. 17, pp. 455–464, 1997.

[216] G. P. Asner and A. Alencar, "Drought impacts on the Amazon forest: the remote sensing perspective.," *New Phytol.*, vol. 187, no. 3, pp. 569–78, Aug. 2010.

[217] M. F. Noomen, A. K. Skidmore, F. D. van der Meer, and H. H. T. Prins, "Continuum removed band depth analysis for detecting the effects of natural gas, methane and ethane on maize reflectance," *Remote Sens. Environ.*, vol. 105, pp. 262–270, 2006.

[218] K. L. Smith, M. D. Steven, and J. J. Colls, "Use of hyperspectral derivative ratios in the red-edge region to identify plant stress response to gas leaks," *Remote Sens. Environ.*, vol. 92, pp. 207–217, 2004.

[219] M. L. Adams, W. D. Philpot, and W. a. Norvell, "Yellowness index: An application of spectral second derivatives to estimate chlorosis of leaves in stressed vegetation," *Int. J. Remote Sens.*, vol. 20, no. 18, pp. 3663–3675, Jan. 1999.

[220] H. C. Claudio, Y. Cheng, D. A. Fuentes, J. A. Gamon, H. Luo, W. Oechel, H.-L. Qiu, A. F. Rahman, and D. A. Sims, "Monitoring drought effects on vegetation water content and fluxes in chaparral with the 970 nm water band index," *Remote Sens. Environ.*, vol. 103, no. 103, pp. 304–312, 2006.

[221] H. H. Muhammed, "Hyperspectral Crop Reflectance Data for characterising and estimating Fungal Disease Severity in Wheat," *Biosyst. Eng.*, vol. 91, no. 1, pp. 9–20, 2005.

[222] J. C. White, M. A. Wulder, A. Varhola, M. Vastaranta, N. C. Coops, B. D. Cook, D. Pitt, and M. Woods, "A best practices guide for generating forest inventory attributes from airborne laser scanning data using an area-based approach," Victoria, B.C., 2013.

[223] J. C. White, M. a Wulder, A. Varhola, M. Vastaranta, N. C. Coops, B. D. Cook, D. Pitt, and M. Woods, *A model development and application guide for generating an enhanced forest inventory using airborne laser scanning data and an area-based approach*, vol. 89. 2017.

[224] G. A. Maclean and W. B. Krabill, "Gross-merchantable timber volume estimation using an airborne lidar system," *Can. J. Remote Sens.*, vol. 12, no. 1, 1986.

[225] "Object Raku Technology," *2018*. [Online]. Available: www.objectraku.com. [Accessed: 28-Oct-2018].

[226] S. M. Lamb, D. A. MacLean, C. R. Hennigar, and D. G. Pitt, "Forecasting forest inventory using imputed tree lists for LiDAR grid cells and a tree-list growth model," *Forests*, vol. 9, no. 4, 2018.

[227] M. A. Ngo Bieng, T. Perot, F. de Coligny, and F. Goreaud, "Spatial pattern of trees influences species productivity in a mature oak-pine mixed forest," *Eur. J. For. Res.*, vol. 132, no. 5–6, pp. 841–850, 2013.

[228] E. Næsset, T. Gobakken, J. Holmgren, H. Hyyppä, J. Hyyppä, M. Maltamo, M. Nilsson, H. Olsson, Å. Persson, and U. Söderman, "Laser scanning of forest resources: The nordic experience," in *Scandinavian Journal of Forest Research*, 2004, vol. 19, no. 6, pp. 482–499.

[229] J. C. White, N. C. Coops, M. A. Wulder, M. Vastaranta, T. Hilker, and P. Tompalski, "Remote Sensing Technologies for Enhancing Forest Inventories: A Review," *Can. J. Remote Sens.*, vol. 42, no. 5, pp. 619–641, 2016.

[230] X. Yu, J. Hyyppä, H. Hyyppä, and M. Maltamo, "Effects of flight altitude on tree height estimation using airborne laser scanning," in *International conference NATSCAN*, 2004, vol. XXXVI-8, pp.

96–101.

[231] Y. Hirata, “The Effects of Footprint Size and Sampling Density in Airborne Laser Scanning to Extract Individual Trees in Mountainous Terrain,” *Int. Arch. Photogramm. Remote Sens. Spat. Inf. Sci.*, vol. XXXV1, no. 8, pp. 283–287, 2004.

[232] M. Bouvier, S. Durrieu, R. A. Fournier, and J. P. Renaud, “Generalizing predictive models of forest inventory attributes using an area-based approach with airborne LiDAR data,” *Remote Sensing of Environment*, vol. 156. pp. 322–334, 2015.

[233] E. Næsset, “Practical large-scale forest stand inventory using a small-footprint airborne scanning laser,” *Scand. J. For. Res.*, vol. 19, no. 2, pp. 164–179, 2004.

[234] M. Nilsson, K. Nordkvist, J. Jonzén, N. Lindgren, P. Axensten, J. Wallerman, M. Egberth, S. Larsson, L. Nilsson, J. Eriksson, and H. Olsson, “A nationwide forest attribute map of Sweden predicted using airborne laser scanning data and field data from the National Forest Inventory,” *Remote Sens. Environ.*, vol. 194, pp. 447–454, 2017.

[235] C. A. Silva, C. Klauberg, A. T. Hudak, L. A. Vierling, S. J. Fennema, and A. P. D. Corte, “Modeling and mapping basal area of Pinus taeda L. plantation using airborne lidar data,” *Ann. Brazilian Acad. Sci.*, vol. 89, no. 3, pp. 1895–1905, 2017.

[236] O. Garcia, “Growth & Yield in British Columbia Background and discussion,” pp. 1–10, 2001.

[237] E. Bergseng, H. O. Ørka, E. Næsset, and T. Gobakken, “Assessing forest inventory information obtained from different inventory approaches and remote sensing data sources,” *Ann. For. Sci.*, vol. 72, no. 1, pp. 33–45, 2015.

[238] J. Peuhkurinen, L. Mehtätalo, and M. Maltamo, “Comparing individual tree detection and the area-based statistical approach for the retrieval of forest stand characteristics using airborne laser scanning in Scots pine stands,” *Can. J. For. Res.*, vol. 41, no. 3, pp. 583–598, 2011.

[239] F. Morsdorf, E. Meier, B. Kötz, K. I. Itten, M. Dobbertin, and B. Allgöwer, “LIDAR-based geometric reconstruction of boreal type forest stands at single tree level for forest and wildland fire management,” in *Remote Sensing of Environment*, 2004, vol. 92, no. 3, pp. 353–362.

[240] A. Kato, L. M. Moskal, P. Schiess, M. E. Swanson, D. Calhoun, and W. Stuetzle, “Capturing tree crown formation through implicit surface reconstruction using airborne lidar data,” *Remote Sens. Environ.*, vol. 113, no. 6, pp. 1148–1162, Jun. 2009.

[241] M. Maltamo, K. Eerikäinen, J. Pitkänen, J. Hyyppä, and M. Vehmas, “Estimation of timber volume and stem density based on scanning laser altimetry and expected tree size distribution functions,” *Remote Sens. Environ.*, vol. 90, no. 3, pp. 319–330, 2004.

[242] X. Yu, J. Hyyppä, H. Kaartinen, M. Maltamo, and H. Hyyppä, “Obtaining plotwise mean height and volume growth in boreal forests using multi-temporal laser surveys and various change detection techniques,” in *International Journal of Remote Sensing*, 2008, vol. 29, no. 5, pp. 1367–1386.

[243] S. Harkonen, T. Tokola, P. Packalen, L. Korhonen, and A. Makela, “Predicting forest growth based on airborne light detection and ranging data , climate data , and a simplified process-based model,” *Can. J. For. Res.*, vol. 43, no. January, pp. 364–375, 2013.

[244] A. S. Antonarakis, J. W. Munger, and P. R. Moorcroft, “Imaging spectroscopy-and lidar-derived estimates of canopy composition and structure to improve predictions of forest carbon fluxes and ecosystem dynamics,” *Geophys. Res. Lett.*, vol. 41, pp. 1–8, 2014.

[245] R. H. Waring, N. C. Coops, and J. J. Landsberg, “Improving predictions of forest growth using the 3-PGS model with observations made by remote sensing,” *For. Ecol. Manage.*, vol. 259, no. 9, pp. 1722–1729, Apr. 2010.

[246] J. R. Jensen, “Issues involving the creation of digital elevation models and terrain corrected orthoimagery using soft-copy photogrammetry,” *Geocarto Int.*, vol. 10, no. 1, pp. 5–21, 1995.

[247] R. Richter, “Atmospheric / Topographic Correction for Airborne Imagery,” *ATCOR-4 User Guid. Version*, no. January, pp. 1–157, 2004.

[248] R. N. Clark, G. A. Swayze, K. E. Livo, R. F. Kokaly, T. V. V King, J. B. Dalton, J. S. Vance, B. W. Rockwell, T. Hoefen, and R. R. McDougal, “Surface Reflectance Calibration of Terrestrial Imaging Spectroscopy Data: a Tutorial Using AVIRIS,” in *Proceedings of the 10th JPL Airborne Earth Science Workshop*, 2002, vol. 02-1.

[249] G. M. Smith and E. J. Milton, “The use of the empirical line method to calibrate remotely sensed data to reflectance,” *Int. J. Remote Sens.*, vol. 20, no. 13, pp. 2653–2662, Jan. 1999.

[250] D. a Sims and J. A. Gamon, “Relationships between leaf pigment content and spectral reflectance across a wide range of species, leaf structures and developmental stages,” *Remote Sens. Environ.*, vol. 81, no. 2–3, pp. 337–354, Aug. 2002.

[251] L. Bousquet, S. Lacherade, S. Jacquemoud, and M. Ismael, “Leaf BRDF measurements and model for specular and diffuse components differentiation,” *Remote Sens. Environ.*, vol. 98, pp. 201–211, 2005.

[252] M. S. Moran, R. B. Bryant, T. R. Clarke, and J. Qi, “Deployment and calibration of Reference Reflectance Tarps for Use with Airborne Imaging Sensors,” *Photogramm. Eng. Remote Sensing*, vol. 67, no. 3, pp. 273–286, 2001.

[253] A. Kukko, “Sampling of bidirectional reflectance from multiangular high resolution airborne imagery,” in *International Society for Photogrammetry and Remote Sensing*, 2001, no. 1.

[254] U. Beisl and N. Woodhouse, “Correction of bidirectional effects in imaging spectrometer data,” in *International Society for Photogrametry and Remote Sensing*, 2004.

[255] S. S. Shapiro and M. B. Wilk, “An analysis of variance test for normality (complete samples),” *Biometrika*, vol. 52, no. 3, 4, pp. 591–611, 1965.

[256] W. J. Conover, M. Johnson, and M. Johnson, “A comparative study of tests for homogeneity of variances, with applications to the outer continental shelf bidding data,” *Technometrics*, vol. 23, no. 4, pp. 351–361, 1981.

[257] W. H. Kruskal and W. A. Wallis, “Use of Ranks in One-Criterion Variance Analysis,” *J. Am. Stat. Assoc.*, vol. 47, no. 260, pp. 583–621, 1952.

[258] F. Wilcoxon, “Individual Comparisons by Ranking Methods,” *Biometrics Bull.*, vol. 1, no. 6, pp. 80–83, 1945.

[259] E. Hecht, *Optics*, 4th ed. San Francisco, CA: Pearson Education, Inc., 2002.

[260] F. Tiarks, T. Frechen, S. Kirsch, J. Leuninger, M. Melan, a. Pfau, F. Richter, B. Schuler, and C.-L. Zhao, “Formulation effects on the distribution of pigment particles in paints,” *Prog. Org. Coatings*, vol. 48, no. 2–4, pp. 140–152, Dec. 2003.

[261] I. D. Sanches, M. P. Tuohy, M. J. Hedley, and M. R. Bretherton, “Large, durable and low-cost reflectance standard for field remote sensing applications,” *Int. J. Remote Sens.*, vol. 30, no. 9, pp. 2309–2319, May 2009.

APPENDICES

APPENDIX 1: Previous studies conducted at the Shawnigan Lake Project site

Pot, I. N. A., With, T., & Menziesii, P. (1976). BALANCE SHEET OF RECOVERED I5N-LABELLED UREA. *Canadian Journal of soil science*, *53*(3), 311–314.

Brix, H., & Mitchell, A. K. (1980). Effects of thinning and nitrogen fertilization on xylem development in Douglas-fir. *Canadian Journal of Forest Research*, *10*(2), 121–128. Retrieved from http://www.nrcresearchpress.com/doi/pdf/10.1139/x80-023

Pang, P., & McCULLOUGH, K. (1982). NUTRIENT DISTRIBUTION IN FOREST SOIL LEACHATES AFTER THINNING AND FERTILIZING DOUGLAS-FIR FOREST. *Canadian Journal of Soil Science*, *62*, 197–208. Retrieved from http://pubs.aic.ca/doi/abs/10.4141/cjss82-021

Brix, H., & Mitchell, A. K. (1983). Thinning and nitrogen fertilization effects on sapwood development and relationships of foliage quantity to sapwood area and basal area in Douglas-fir. *Canadian Journal of Forest Research*, *13*, 384–389. Retrieved from http://www.nrcresearchpress.com/doi/pdf/10.1139/x83-057

Thomson, A. J., & Barclay, H. J. (1984). Effects of thinning and urea fertilization on the distribution of area increment along the boles of Douglas-fir at Shawnigan Lake, British Columbia. *Canadian Journal of Forest Research*, Retrieved from http://www.nrcresearchpress.com/doi/pdf/10.1139/x84-157

Ballard, T. M. (1984). A simple model for predicting stand volume growth response to fertilizer application. *Canadian Journal of Forest Research*, *14*, 661–665. Retrieved from http://www.nrcresearchpress.com/doi/pdf/10.1139/x84-119

Barclay, H., & Brix, H. (1984). Effects of urea and ammonium nitrate fertilizer on growth of a young thinned and unthinned Douglas-fir stand. *Canadian Journal of Forest Research*, *14*, 952–955. Retrieved from http://www.nrcresearchpress.com/doi/abs/10.1139/x84-169

Barclay, H., & Brix, H. (1985). Effects of high levels of fertilization with urea on growth of thinned and unthinned Douglas-fir stands. *Canadian Journal of Forest Research*, *15*, 730–733. Retrieved from http://www.nrcresearchpress.com/doi/abs/10.1139/x85-120

Barclay, H. (1986). Aboveground biomass distribution within trees and stands in thinned and fertilized Douglas-fir. *Canadian Journal of Forest Research*, Retrieved from http://www.nrcresearchpress.com/doi/pdf/10.1139/x86-080

Barclay, Hugh J., & Hall, T. H. (1986). *SHAWN: a model of Douglas-fir ecosystem response to nitrogen fertilization and thinning: a preliminary approach* (p. 29). Victoria, BC, Canada. Retrieved from http://library.wur.nl/WebQuery/clc/324082

Brix, H., & Mitchell, A. K. (1986). Thinning and nitrogen fertilization effects on soil and tree water stress in a Douglas-fir stand. *Canadian Journal of Forest Research*, *16*. Retrieved from http://www.nrcresearchpress.com/doi/pdf/10.1139/x86-236

Pang, P. C. (1987). Aboveground nutrient distribution within trees and stands in thinned and fertilized Douglas-fir. *Canadian Journal of Forest Research*, Retrieved from http://www.nrcresearchpress.com/doi/abs/10.1139/x87-213

Duke, K. M., Townsend, G. M., & White, W. A. (1989). *An economic analysis of fertilization and thinning effects on Douglas-fir stands at Shawnigan Lake* (p. 19). Victoria, BC, Canada.

Jozsa, L. A., & Brix, H. (1989). The effects of fertilization and thinning on wood quality of a 24-year-old Douglas-fir stand. *Canadian Journal of Forest Research*, *19*, 1137–1145. Retrieved from http://www.nrcresearchpress.com/doi/abs/10.1139/x89-172

Strader, R. H., & Binkley, D. (1989). Mineralization and immobilization of soil nitrogen in two Douglas-fir stands 15 and 22 years after nitrogen fertilization. *Canadian Journal of Forest Research*. Retrieved from http://www.nrcresearchpress.com/doi/abs/10.1139/x89-121

Barclay, H., & Layton, C. (1990). Growth and mortality in managed Douglas fir: relation to a competition index. *Forest Ecology and Management*, *36*, 187–204. Retrieved from http://www.sciencedirect.com/science/article/pii/0378112790900257

Sachs, D., & Trofymow, J. A. (1991). *Testing the performance of FORCYTE-11 against results from the Shawnigan Lake thinning and fertilization trials on Douglas-fir* (p. 68). Victoria, BC, Canada.

Smith, N. J., & Borstad, G. A. (1991). Using high-resolution airborne spectral data to estimate forest leaf area and stand structure. *Canadian Journal of Forest Research*, *21*. Retrieved from http://www.nrcresearchpress.com/doi/abs/10.1139/x91-156

Trofymow, J. A., Barclay, H. J., & McCullough, K. M. (1991). Annual rates and elemental concentrations of litter fall in thinned and fertilized Douglas-fir. *Canadian journal of Forest Research*, *21*, 1601–1615. Retrieved from http://www.nrcresearchpress.com/doi/pdf/10.1139/x91-223

Mitchell, a. K. (1992). Research solutions to problems in the management of established stands. *Forest Ecology and Management*, *49*(1-2), 119–132. doi:10.1016/0378-1127(92)90165-6

Preston, C. M. (1992). The application of NMR to organic matter inputs and processes in forest ecosystems of the Pacific Northwest. *Science of The Total Environment*, *113*(1-2), 107–120. doi:10.1016/0048-9697(92)90019-O

Brix, H. (1993). *Fertilization and thinning effect on a douglas-fir ecosystem at shawnigan lake: a synthesis of project results* (pp. 1–64). Victoria, BC, Canada. Retrieved from http://library.wur.nl/WebQuery/clc/924950

Messier, C., & Mitchell, A. K. (1994). Effects of thinning in a 43-year-old Douglas-fir stand on above- and below-ground biomass allocation and leaf structure of understory Gaultheria shallon. *Forest Ecology and Management*, *68*(2-3), 263–271. doi:10.1016/0378-1127(94)90050-7

Preston, C. M., & Mead, D. J. (1995). Long-term recovery in the soil profile of 15N from Douglas-fir needles decomposing in the forest floor. *Canadian journal of forest research*. Retrieved from http://www.nrcresearchpress.com/doi/abs/10.1139/x95-090

Preston, C. M., & Newman, R. H. (1995). A long-term effect of N fertilization on the 13C CPMAS NMR of de-ashed soil humin in a second-growth Douglas-fir stand of coastal British Columbia. *Geoderma*, *68*(4), 229–241. doi:10.1016/0016-7061(95)00051-6

Mitchell, A. ., & Barclay, H. (1996). Biomass and nutrient element dynamics in Douglas-fir: effects of thinning and nitrogen fertilization over 18 years. *Canadian Journal of Forest Research*, *26*, 376–388. Retrieved from http://www.nrcresearchpress.com/doi/abs/10.1139/x26-042

Weetman, G., Prescott, C. E., Kohlberger, F. L., & Fournier, R. M. (1997). Ten-year growth response of coastal Douglas-fir on Vancouver Island to N and S fertilization in an optimum nutrition trial. *Canadian Journal of Forest Research*, *27*(9), 1478–1482. doi:10.1139/x97-105

Magnussen, S., & Boudewyn, P. (1998). Derivations of stand heights from airborne laser scanner data with canopy-based quantile estimators. *Canadian Journal of Forest Research*, *28*(7), 1016–1031. doi:10.1139/cjfr-28-7-1016

Barclay, H.J, & Trofymow, J. . (2000). Relationship of readings from the LI-COR canopy analyzer to total one-sided leaf area index and stand structure in immature Douglas-fir. *Forest Ecology and Management*, *132*(2-3), 121–126. doi:10.1016/S0378-1127(99)00222-4

He, F., & Barclay, H. J. (2000). Long-term response of understory plant species to thinning and fertilization in a Douglas-fir plantation on southern Vancouver Island, British Columbia. *Canadian Journal of Forest Research*, *30*(4), 566–572. doi:10.1139/cjfr-30-4-566

Brunner, A., & Nigh, G. (2000). Light absorption and bole volume growth of individual Douglas-fir trees. *Tree physiology*, *20*(5_6), 323–332. Retrieved from http://www.ncbi.nlm.nih.gov/pubmed/12651448

Beddows, D. (2002). *Levels-of-growing-stock Cooperative Study in Douglas-fir. Report No. 16, Sayward Forest and Shawnigan Lake*. Canadian Forest Service, Pacific Forestry Centre. Retrieved from http://dsp-psd.communication.gc.ca/Collection/Fo46-17-393E.pdf

Lim, K., & Treitz, P. (2004). Estimation of aboveground forest biomass using airborne scanning discrete return Lidar in Douglas-fir. *International Society for Photogrametry and Remote Sensing, Laser-Scanners for Forest and Landscape Assessment* (pp. 149–152). Freiburg, Germany. Retrieved from http://www.isprs.org/proceedings/XXXVI/8-W2/LIM.pdf

Preston, C., Trofymow, J., & Flanagan, L. (2006). Decomposition, δ13C, and the "lignin paradox". *Canadian Journal of Soil Science*, *86*, 235–245. Retrieved from http://pubs.aic.ca/doi/abs/10.4141/S05-090

Blanco, J. a., Seely, B., Welham, C., Kimmins, J. P. (Hamish), & Seebacher, T. M. (2007). Testing the performance of a forest ecosystem model (FORECAST) against 29 years of field data in a Pseudotsuga menziesii plantation. *Canadian Journal of Forest Research*, *37*(10), 1808–1820. doi:10.1139/X07-041

(Hamish) Kimmins, J. P., Blanco, J. a., Seely, B., Welham, C., & Scoullar, K. (2008). Complexity in modelling forest ecosystems: How much is enough? *Forest Ecology and Management*, *256*(10), 1646–1658. doi:10.1016/j.foreco.2008.03.011

Mead, D. J., Chang, S. X., & Preston, C. M. (2008). Recovery of 15N-urea 10 years after application to a Douglas-fir pole stand in coastal British Columbia. *Forest Ecology and Management*, *256*(4), 694–701. doi:10.1016/j.foreco.2008.05.022

Winder, R. (2010). qPCR to correlate the abundance of diazotrophic soil bacteria with the abundance of understory plants in a Douglas-fir (Pseudotsuga menziesii) forest on Vancouver. *eco.confex.com*. Pittsburgh. Retrieved from http://eco.confex.com/eco/2010/preliminaryprogram/abstract_26252.htm

Levy-Booth, D. J., & Winder, R. S. (2010). Quantification of nitrogen reductase and nitrite reductase genes in soil of thinned and clear-cut Douglas-fir stands by using real-time PCR. *Applied and environmental microbiology*, *76*(21), 7116–25. doi:10.1128/AEM.02188-09

Moore, T. R., Trofymow, J. a., Prescott, C. E., & Titus, B. D. (2010). Nature and nurture in the dynamics of C, N and P during litter decomposition in Canadian forests. *Plant and Soil*, *339*(1-2), 163–175. doi:10.1007/s11104-010-0563-3

Groot, A., & Schneider, R. (2011). Predicting maximum branch diameter from crown dimensions ,. *The Forestry Chronicle*, *87*(4), 542–551.

Brooks, J. R., & Mitchell, A. K. (2011). Interpreting tree responses to thinning and fertilization using tree-ring stable isotopes. *The New phytologist*, *190*(3), 770–82. doi:10.1111/j.1469-8137.2010.03627.x

Omule, A., Mitchell, A. K. A., Wagner, W. W. L., & Canadian Wood Fibre Centre. (2011). *Fertilization and thinning effects on a Douglas-fir ecosystem at Shawnigan Lake: 32-year growth response. Forestry*. Canadian Wood Fibre Centre. Retrieved from http://publications.gc.ca/collections/collection_2011/rncan-nrcan/Fo148-1-5-eng.pdf

Blanco, J. a. (2012). Forests may need centuries to recover their original productivity after continuous intensive management: an example from Douglas-fir stands. *The Science of the total environment*, *437*, 91–103. doi:10.1016/j.scitotenv.2012.07.082

Preston, C. (2012). Decomposition and change in N and organic composition of small-diameter Douglas-fir woody debris over 23 years. *Canadian Journal of Forest Research 42*, 1153–1167. doi:10.1139/X2012-076

APPENDIX 2: Radiometric Calibration of Airborne Data

High spectral resolution sensors capture depth and shape variations in atmospheric absorption features, enabling the retrieval of the contents of the attenuating compounds. Such constituents mask energy interactions with surface features. The inversion of radiative transmission models is a widely applied approach to account for the atmosphere [247]. The applications community has reported on residuals in physically modeled surface reflectance [107]. Consequently, empirical calibration and validation methods are still commonly employed [248]. The consistency of target responses translates to the stability of empirical correction coefficients [249]. Better-determined intercept and slope coefficients are achievable when the two targets are well-separated radiometrically and do not approach each other throughout the spectrum. Additionally, spatially invariant targets also reduce the likelihood of response mischaracterization in field measurements. Ideally, targets will be spectrally uniform, predominantly lambertian bright or dark reflectors, spatially homogeneous, temporally invariant and made of a material that is easily mobilized. Spectral responses of several artificial surfaces were assessed for deployable calibration targets for the AISA-Eagle spectrometer (350-1000nm) and evaluated on these ideal attributes.

1.1.1 *Laboratory Radiometric Data Acquisition*

The assessment of appropriate material for calibration targets must not only consider their spectral properties but also the logistical limitations. The mobility of calibration targets should be a high priority. Textile calibration materials are ideal because they can easily be rolled or folded and transported with the aircraft. Textile samples were acquired and reflectance measurements were made in a darkroom laboratory. Samples included 16 different textiles that ranged in shade from the darkest black available to the brightest white available, two additional samples were painted, one with black and the other with white paint. Based on the initial results of the painted textile samples and the results of Knighton & Bugbee's [108] study, two hardboard samples were painted black and white for each of three brands of paint, these were also assessed for calibration targets.

Motivated by the featureless VNIR responses of the painted textile samples, the spectral responses of several paint sources were assessed. Flat latex formulations were used to produce the darkest and brightest targets possible. Dark pigments were added to neutral basses to produce the dark black paints while the white untinted (exterior) flat formulas were used for the bright target paints. To ensure an optical thick opaque paint surface three coats were applied to ~13x13cm hardboard samples. The orientations of brush painted coats were altered between coats in an effort to reduce directional reflectance effects of these linear surface features. This strategy did not eliminate striations in the painted surface, for this reason rollers should be preferred over brushes to provide a more homogeneous painted surface in terms of surface roughness.

Each textile sample was clipped to a sample stage in order to reduce surface irregularities, which would increase variations in reflectance [250], [251]. The black

polystyrene sample stage produced a diffuse, spectrally flat and low reflectance response without apparent features. An ASD FieldSpec Pro Spectrometer (Analytical Spectral Devices, Inc.) was used to measure reflectance. The spectral range of the sensor is 350-2500nm sampled with variable bandwidths (VNIR: ~3nm, SWIR: ~11nm) and interpolated to produce 2151 bands. The initial collection saw the spectrometer and sources arranged in a constant geometry. The bare fibre optic and pistol grip of the ASD were oriented on a stationary tripod in a nadir looking position. The bare fibre optic ($\theta = 25^{\circ}$) was positioned ~4.5cm from the sample stage. The fibre optic produced a footprint diameter of ~1.9cm. Two Lowel Pro 50 watt quartz halogen cycle tungsten filament lamps, which approximate the solar profile, were adjusted to an elevation of ~40°, separated by ~90° and were ~ 0.5m from the sample stage. In order to capture the effects of micro surface variations the sample stage was rotated to three different orientations [57].

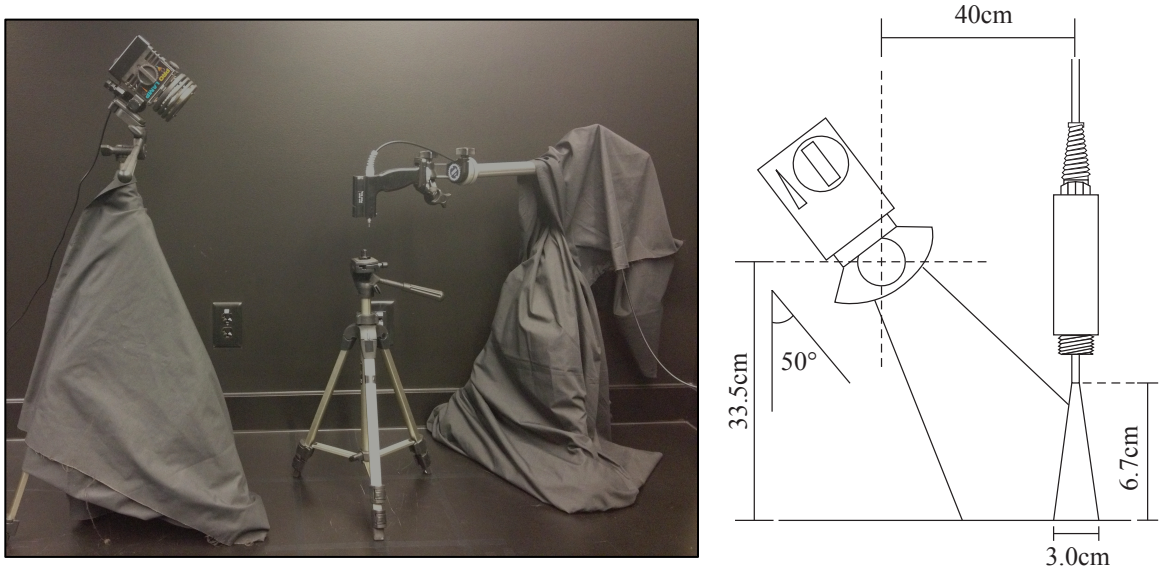


Figure 1 Dark room spectral apparatus for sampling BRDF of candidate radiometric calibration materials. The ASD FieldSpec Pro measured reflectance relative to level Spectralon reference

Samples were arranged level and oriented at angles of 0°, 120° and 240°. Reflectance at each orientation was recorded ten times followed by ten repeat measurements for a total of 100 measurements. In pre-processing, sample orientation spectra were generated as the average of 100 measurements, effectively reducing noise to one tenth of that present in a single ASD measurement ($1/n^{0.5}$). Sample spectra were computed by averaging sample orientation spectra; therefore, 300 measurements were used to generate sample spectra, reducing noise to 1/17 of that present in a single measurement. White reference (Spectralon) and dark current measurements were recorded after each sample was processed for reflectance.

The second collection strategy focused on describing the anisotropic reflectance traits of calibration samples. Again in the darkroom laboratory, where geometry could be controlled, the bare fibre optic was oriented in a nadir position (h=~6.77cm, footprint ~3cm) and under constant illumination conditions (zenith: ~50°). In contrast to the initial collection only one lamp was used in the second collection to enhance the BRDF signal (Fig. 1). References were all collected in a nadir orientation with a level Spectralon surface (±2°). At regular angular intervals**,** samples were rotated to twelve orientations (interval of 30°) for each of four inclinations (0-45° with and interval of 15°). This approach was used to demonstrate the diffuse and specular character of the materials [252]. This analysis would be valuable for indicating the potential for mischaracterizing reflectance responses in field spectroscopy with a given calibration material [253], [254].

In addition to the lab-based target evaluation, the airborne campaign collected imaging spectrometer data from a set of deployed radiometric calibration targets. The instrumentation mounted in the aircraft included a full range imaging spectrometer

(AISA dual), a high pulse repetition frequency (250 kHz) laser scanner, RGB photography, and inertial measurement unit and survey grade global positioning system. The spectrometer acquisition operated the AISA Eagle (VNIR) and was optimized for the collection of forested targets by a four time binning of the spectral domain of the CCD array, which produced a total of 132 spectral bands spanning a range of 392-996nm. A two-time spatial binning produced an image dimension of 512 pixels (484 without FODIS) with a FOV of 34.88° (element dimension 24μm, focal length 18.49mm) produces a swath width of 772.73m at 1230m above ground. The across track spatial resolution of this data is 1.60m at the SLP calibration site but is 1.33m at the forest treatments plots, which is an average of 213.3m higher in elevation. The along track IFOV at SLP was 0.80. At the GVWSA calibration site the average flight height was 1165.6m above ground which produced an across track spatial resolution of 1.51m and an along track IFOV of 0.76. The frame rate used in this collection was 45 and 43 frames per second for the SLP and the GVWSA sites respectively. The average flight speed during acquisition was approximately 64m/s for the SLP and 63m/s for the GVWSA collection. The integration times for both collection days were 7ms. These acquisition parameters produced along track footprint diameters of 1.25m and 1.20m for the SLP and GVWSA collections respectively. The different frame rates between the collections equated to slightly different ground sampling distances, where the SLP has 0.97m between the sampled pixels, while those in the GVWSA are 5cm further apart. All these will change greatly with variations in elevation and forward velocity, the above values are produced for specifically the data that sampled the deployed targets but assumes a nadir viewing geometry.

As the data were collected as part of a larger research program focused on forest structure and productivity the data were collected in the binning configuration to benefit that application. It was determined through previous collections that the spatial resolution for this acquisition should be finer than 2m [101]. A finer resolution dataset would better capture the extents of large-scale objects (spatial representation is reduced less, relative to the real world) that being individual tree canopies in this instance. Tree canopies are variable in horizontal extents and therefore a finer resolution would provide for a greater likelihood of being able to discriminate between individual canopies. A conscious decision was made to limit the spectral measurements to the VNIR range. The rational for which relies on the case that there is relatively little information that can be derived for vegetation from the SWIR range as a result of moisture masking all other energy interactions [20], [83]. The SWIR range is largely determined by the presence of water, however there are two prominent features that occur within the NIR that are directly caused by the presence of water, from this standpoint there is little information lost by omitting the SWIR range. It was for this reason that the SWIR region was omitted from the lab based analysis of radiometric calibration samples.

On board the fixed wing aircraft the Terra Remote Sensing Inc. proprietary lidar system was flown concurrent with the AISA Eagle collections. The lidar data was used to provide a highly detailed representation of the reflective surface that would ultimately be used to rectify the spectrometer data. The onboard INS (inertial navigation system) is used to measure platform positions, three-dimensional orientations and three-dimensional velocities, which are also applied in the process of orthorectification. Specifically related

to this study, precise timing, platform attitude, bore sight calibration and DSM (lidar) data provide the information necessary to compute observation angles.

The flight acquisition covered a total area of 91.5km^2 including a ~89km^2 area that extended into the Greater Victoria watershed, south of the Shawnigan lake site. In addition to flying the calibration site, the Shawnigan lake site and the Greater Victoria Water Supply Area, timing and IMU calibration flights were conducted at the Victoria International Airport. Terra Remote Sensing reported a lidar point absolute accuracy of 30cm. The data collections were completed on September 19th and included high-resolution orthophotography, discrete lidar and imaging spectrometer datasets. See section 3.3 for flight paths extracted from navigation files.

A constant struggle for passive airborne remote sensing projects is how to deal with the effect of bidirectional reflectance (or bidirectional reflectance distribution function). The effects of BRDF are most apparent at the edges of the swath where viewing angles are up to 11° off nadir from a level platform. The BRDF effect becomes more pronounced with variations in platform behaviour causing variations in observation azimuth and zenith angles. Due to the aircrafts constant positive pitch angle during flight (i.e. flight 1923: ~5.7°, flight 1927: ~5.5°) the heading will partially determine the viewing azimuth direction, which again samples a slightly different position of the total geometry space. This also demonstrates that the assumed nadir geometry may not be valid, especially if radiometric differences are found for the magnitude of geometries found in the airborne data.

The underlying rational for this analysis is that a nadir observation collection of field targets during airborne collection, as is customary to do, does not represent the

observation geometries sampled by the airborne sensor. It is assumed that while collection conditions will vary from the lab based analysis the target response to variations in geometry will not. Therefore, if the radiometry with given geometries are represented as a proportion of that observed from nadir geometries we can achieve multiplicative correction coefficients based on a laboratory derived BRDF that can be applied to correct field based nadir measurements given angular geometries of the platform, surface and solar position.

1.1.2 *Laboratory Radiometric Data Analysis*

An analytical strategy was devised to quantify the material samples in terms of 3 specific attributes: the spectral invariance (flatness); the reflectance magnitude (to indicate radiometric separation); and the lambertian component of reflectance (dependence on geometry). Given that the objective of the study was to determine an appropriate material for calibrating a visible/near-infrared spectrometer, the analysis was restricted to the spectral range between 400 and 1000nm. Spectra from the seven textiles and six painted samples, collected in a nadir geometry were submitted to a one-way ANOVA with post-hoc tests, ensuring statistical assumptions were not violated and adopting robust statistical tests where needed. The normality of data distributions were evaluated by the Shapiro-Wilk (S-W) test [255], variance homogeneity was evaluated through 2 separate tests, the Fligner-Killeen (F-K) and the nonparametric Brown-Forsythe (B-F) [256]. The Kruskal-Wallis (K-W) test was applied as a non-parametric ANOVA [257]. Finally, the Wilcoxon test was used as a non-parametric, pairwise, post-hoc comparison [258].

An assumption of the ANOVA analysis is the equality of variance across factors. Additionally, the same test, when applied to distributions of reflectance across a spectral

range, can indicate the spectral invariance of the samples. This assumes that each spectrum exhibits consistent signal to noise levels. The central tendency and dispersion of reflectance (400-1000nm) for the thirteen samples were also visualized through boxplots. This analysis described the brightest and darkest targets, as well as those targets that varied the least throughout the specified range. The sample material deemed sufficient in this analysis would be forwarded to an investigation on the angular dependence (BRDF) of their responses.

To assess the isotropic nature of each sample reflectance, 48 spectra were collected from each sample accounting for four slopes (0°, 15°, 30°, 45°) and twelve orientations (30° intervals 0-330°). Each measurement was reduced to a central tendency and a dispersion statistic from reflectance within the 400-1000nm spectral range. Thus, for each sample a distribution of the statistic was generated based on the 48 different geometry conditions. The sample distributions of central tendency and dispersion were each submitted to an ANOVA with post-hoc tests. The statistical tests of the first and second statistical moments indicate the geometry dependence of reflectance magnitude and spectral invariance respectively. The effect of varying geometry on reflectance was visualized through the use of boxplots and by local polynomial regression (LOESS) fitted surfaces. For each comparison the analysis followed a general procedure beginning with evaluating statistical assumptions followed by mean difference tests, pairwise comparisons and ultimately the two visualization tools in the form of box plots and geometry surface fitting.

With *a posteriori* knowledge of airborne collection geometry, lab-based measurements were conducted to investigate the relative difference in spectra given

similar geometries. To extract specific platform geometries for the observed target pixels, the precise timing of frame capture is required along with a sensor model of interior orientation and coordinate misalignment angles between the sensor and INS coordinate frames. The frame number (lines) identified as unmixed target pixels in the unrectified radiance data were recorded for both the bright and dark targets. With the frame rate of the Eagle acquisition and the INS time synchronization offset the floating-point week seconds of the target frames were calculated. The platform attitude was then extracted from the INS navigation files given the time interval for the selected flight line and target frames. Altitude, latitude, longitude, roll, pitch and heading were determined for each measured target. From a lidar derived 50cm digital surface model the elevation, slope and aspect of the targets were determined. The platform attitude data were adjusted for the sensor to INS boresight misalignments for roll pitch and heading. The observation angles were calculated by adjusting the heading angle to accommodate the spatial pixel that acquired the target response. Given the asymmetrical FOV of the Eagle sensor attributed to the FODIS region the angle from the principal pixel was determined through the focal length of the fore optics and the detector element size. The observation elevation angle was determined through simple trigonometric formulae by first calculating the horizontal distance (given roll and pitch angles) then applying horizontal distance and the sensor height (altitude – target height) to derive the elevation angle. The observation elevation angles were translated to zenith angles (compliment of elevation angle) from the target perspective. Finally, the National Oceanic and Atmospheric Administration's (NOAA) web based solar calculator (http://www.esrl.noaa.gov/gmd/grad/solcalc/) was used to provide solar positions for the radiometric calibration site locations and date/times of

collection. At this point these angles were relative to vertical but needed to be referenced to the surface normal vector. The observation, illumination and surface normal vectors were represented as projected x,y,z, vectors and the angles were determined by the vector dot products and the equation that relates the angle between the vectors to their magnitudes and their dot product ($\vec{a} \cdot \vec{b} = |\vec{a}|\,|\vec{b}|\cos\theta$).

It was recognized that variations in footprint size could confound the geometry to radiometry relation, thus as a part of this pre-processing step the along and across track footprint dimensions were calculated. The across track IFOV was determined by calculating the range distance from the sensor to the surface given attitude (principal pixel), the detector element size and the distance of the spatial pixel from the principal pixel. The along track IFOV was calculated in a similar way that considered the horizontal distance from the platform location (incorporating roll angles) to the position on the ground surface applying the pitch angle. This distance was computed for +/- the along-track angular IFOV (focal length, detector element size), the difference between these two quantities represented the along track ground projection of the IFOV. The effective along track footprint however is also a function of the integration time and forward velocity, therefore the along track footprint was computed as the ground projected along track IFOV (m) + velocity (m/s)*integration time (s).

The lab-based measurements were, for ease of design, collected from a static illumination and observation while altering surface normal zenith and azimuth angles. However for these data to be comparable to the airborne collected data they needed to be transformed into the traditional measures of geometry, that is: illumination and observation zenith angles and relative azimuths. BRDF were generated from these data

through regression analysis. These angles demonstrated that the relative azimuths sampled in the lab were limited to only 90° therefore further measurements were required to sample geometries captured in the airborne campaign. From these data the relative differences in radiometric responses between given geometries were determined and evaluated against the relative differences between the same geometries but from the Eagle data. The relative differences were evaluated in terms of their rank order to investigate the agreement between the two datasets with reference to geometry. This analysis would suggest whether a coherent pattern exists between the lab based values and the airborne values and if the fractions derived from the lab based measures could be used to correct field based nadir measurements. The observed lab based fractions were then applied to the field measurements of the calibration targets. The airborne data were corrected by different combinations of targets (dark, bright and natural targets) and different geometries. Each correction was evaluated against field collected validation spectra and the logical numerical limits of reflectance data (0-100%).

1.1.3 *Initial Evaluation of Materials*

For each sample spectrum reflectance values between 400 and 1000nm were collated and summarized. Through the S-K test for normality, it was determined that the distributions produced for each spectrum (400-1000nm) were not normally distributed (p:>2.27e-42, <1.87e-6) and were therefore represented by nonparametric summary statistics including: median, median absolute deviation from the median (MAD), and a non-parametric scale independent measure of variance (MAD/median). See figure 2 for several of the targets assessed.

The F-K and Brown-Forsythe (B-F) non-parametric equality of variance tests indicated that the variances were not equal producing significance levels of *p*: <2.2e-16 in both cases. Therefore, the K-W test was selected over the standard ANOVA test because it is known to be robust to violations of normality and equality of variance. Additionally, the equality of variance test quantitatively demonstrates that some of these spectra are more uniform than others. The non-parametric ANOVA K-W rank sum test suggested that at least one sample target was significantly different from the rest (p: <2.2e-16). Post-hoc tests were computed based on pairwise Mann-Whitney (M-W) tests with a significance adjustment by the Holms, and the more conservative Bonferroni method. The post-hoc tests did not indicate that there were differences between several of the target samples, suggesting that these spectra have similar magnitudes within the specified spectral range. Of these combinations specific samples were omitted based

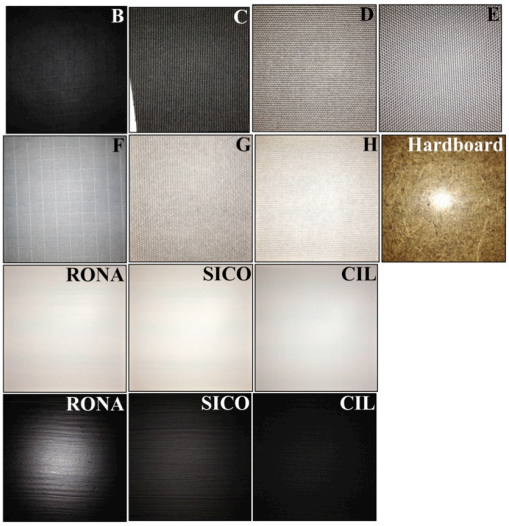


Figure 2 Sample images of targets assessed, indicating magnitude (brightness) visible uniformity (grey-scale vs. color), and lambertian nature (hotspot presence, *i.e.* Rona black) see appendix 1 for spectra.

on the spectral variation within the specified range. As such six samples exhibiting excessive variation were omitted from further analysis (omitted sample id: b, black1, grey1, grey3, e, hardboard). These samples were omitted because post-hoc test suggested that other samples had similar magnitudes and they exhibited greater spectral variability. The spectral curves that best fit the selection criteria were retained, which were largely the samples with painted surfaces.

In most cases, visible ranges, especially the blue, are not determined by electron transitions in pigment molecules (absorption), but by frequency specific scattering. In such cases the scattering is dependent on particle size, where there is an inverse relationship ($1/\lambda^4$) between scattering and wavelength. This condition becomes important when considering reflectivity and shortwave color in paints (blue). The distribution of particle sizes produces wavelength specific scattering when particles are smaller than the incident frequency ($\sim\lambda/15$). When the particles sizes approach the wavelength of the incident light the scattering becomes less wavelength dependent, this condition produces white light reflections and is known as Mie scatter. Titanium oxide is used as the scattering pigment in white paints; the particle has a diameter of approximately 200nm and as a result scatters bluish-white light [259]. Paints also contain other compounds such as calcium carbonate ($CaCO_3$) that are responsible for the finish of the painted surface. Water based paints also include compounds for binding the pigments, pigment dispersing agents and thickeners all of which will contribute to the full range spectral properties of a painted surface. These compounds effect the homogeneity of the painted surfaces, as demonstrated by [260], the types of binders and dispersing agents affect the distribution of TiO_2 particles and thus the homogeneity of color/brightness. The components in paint

formulations translate to the reflectance character of the final cured medium. The scattering particle size distribution determines spectral uniformity, while the calcium carbonate content determines the lambertian nature of the cured painted surface.

The painted hardboard surfaces provided for a more consistent, typically less variable or flat response. Differences between the three paint variants were slight (2% between CIL black > Rona black and 3% between CIL white < Rona white). It was expected that very slight differences in surface orientation could account for these slight differences. This provided one of

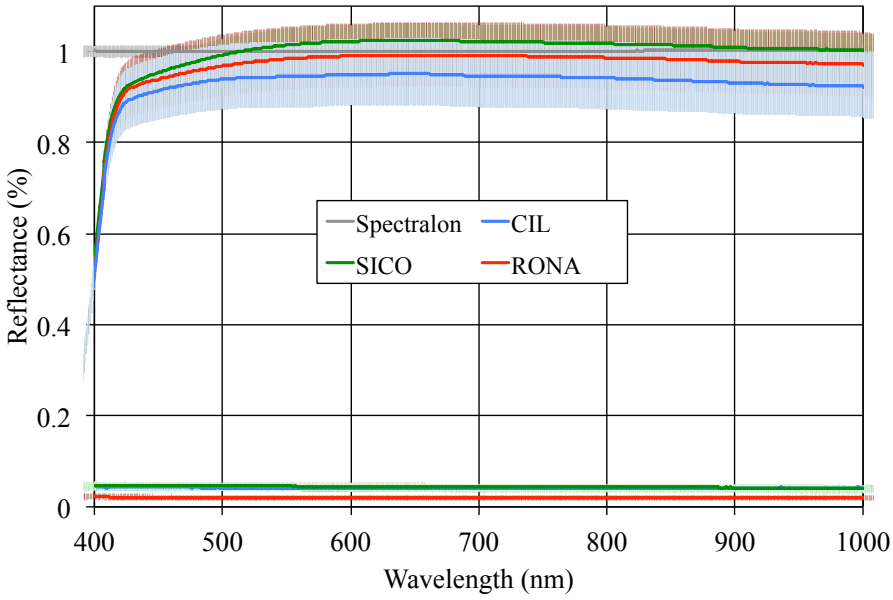


Figure 3 Six candidate painted surfaces for radiometric calibration targets and a Spectralon white reference. The 5-95th percentile is illustrated

two major motivations for assessing the specular and lambertian nature of the painted samples. Namely that the paint ultimately selected for building a calibration target is selected because it is actually the darkest or brightest response and not because the slight differences in orientation during collection produced reflectance differences. The other motivation being that an optimal target would be a predominantly lambertian reflector,

thus it would be less likely that in-field spectral collection would be confounded by geometry.

1.1.3.1 *Characterization of Target Isotropy*

For each of the six painted hardboard samples 48 spectra were produced from different target orientations. Using these measurements it was possible to qualitatively visualize and quantitatively test for differences in sample responses attributed to variations in geometry. By representing the spectra as the first and second statistical moments (central tendency and spread respectively) the effect of geometry on the magnitude and shape of the responses could be assessed respectively. The spectral invariance of the nadir measurements demonstrated that the bright and dark targets all produced very similar responses. The spread of the spectra represented by the 5-95 percentile range demonstrates the scale dependence of variation, which suggests that the analysis of variation attributed to geometry must consider the coefficient of variation if it is to be considered independent of reflectance magnitude (Fig. 3). These qualitative observations were addressed quantitatively through analysis of variance tests (ANOVA) of first and second statistical moments, representing location and scale, which are surrogates for reflectance magnitude and shape respectively. This approach is different from the initial analysis in that, the sample populations are generated from different geometries rather than reflectance values at different wavelengths. In this case each spectrum is generalized to a statistic and represents an observation specific to a given target. Because this analysis was conducted on a new set of data the assumptions of the statistical approach needed to be re-considered. Similar to the previous analysis, normality of reflectance values for each spectrum from 400 to 1000nm was

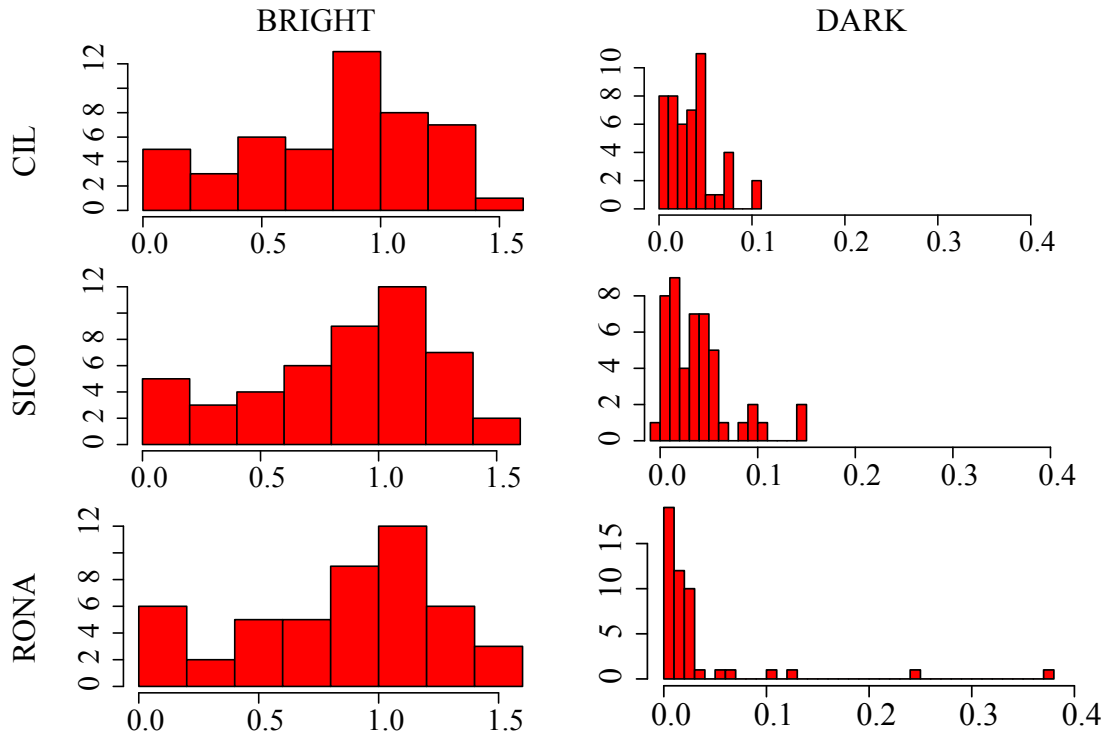


Figure 4 Histograms of samples with reference to level Spectralon (y=frequency, x=relative reflectance). Geometry sampling measured diffuse light without direct illumination, the specular hotspot and over represents nadir geometries which produced skewed distributions

tested by the S-W test. All reflectance distributions (spectra 400-1000nm) produced significant tests for normality ($p<0.0132$), therefore the null hypothesis was rejected in favour of the alternative, that the distributions were different from normal. This conclusion suggests that it would be inappropriate to represent the central tendency of the spectra with an average; the median of each spectrum was thus used to build the distributions of central tendency according to different geometries. Because these sample populations (n=48) would be used in the ANOVA, they needed to be considered for normality and equality of variance.

None of the sample median distributions produced normal distributions ($p<0.0175$), and the population of medians without stratification by target brand or

brightness also produced a non-normal distribution ($p<2.2x10^{-16}$). This is likely a reflection of the non-uniform sampling of the ranges of inclinations and orientations (herein referred to as the target surface normal directions: zenith and azimuth respectively), which produce positively and negatively skewed distributions for dark and bright samples respectively (Fig. 4). The collection strategy had a biased sampling of geometries near nadir and decreasing sampling density with increasing zenith values (Fig. 5). The geometry-space sampling strategy over-represents nadir geometries (n=12) and under-samples illumination azimuths with larger illumination zenith angles. Polar coordinates of illumination geometry were translated to Cartesian coordinates where distance from the 0,0 position represent increasing zenith angles and radial positions represent azimuth angles or the direction of the target surface normal. (*i.e.* the y=0 profile represents a target with a constant azimuth that is inclined towards the illumination source (x=-45) and is level (x=0) then inclined away from the illumination source (x=45). The sampling strategy produces distributions that are not normally distributed and restricts statistical approaches to non-parametric hypothesis testing.

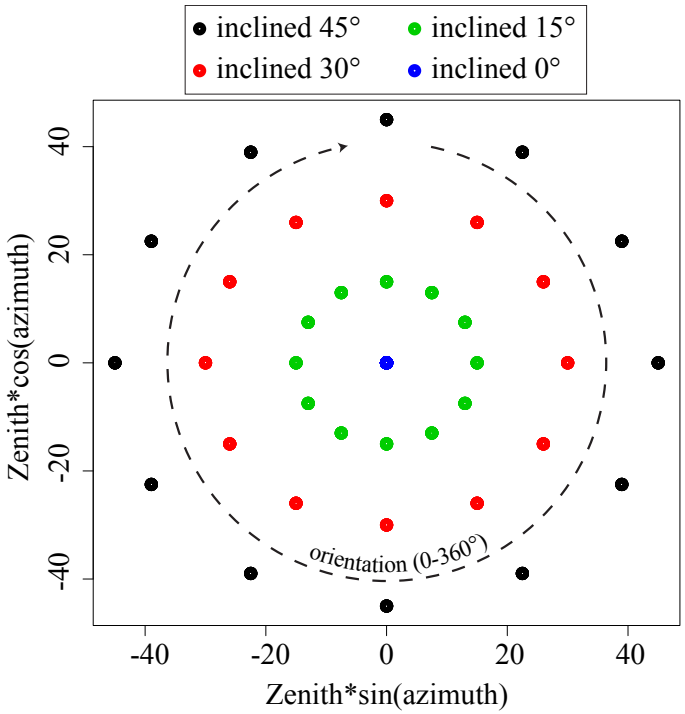


Figure 5 Geometry space sampling. For each sample, 48 geometries were measured. Observation azimuth is constant, while varying the target about two orthogonal axes of rotation modifies the illumination zenith, azimuth and observation zenith angles.

As both an assumption of the ANOVA analysis and an indication of the geometry dependence of the sample responses, an equality of variance test was performed. Provided that, the S-W tests were significant the non-parametric Fligner-Killeen (F-K) (linear rank test) and the more conservative B-F (modified Levene's version of F-stat) equality of variance test were conducted. These two tests have demonstrated resilience when applied to non-parametric distributions, and compared favourably to other variance equality tests [256]. It was expected that the variance of spectral medians would be different according to bright and dark samples because of the wide range of geometries sampled. The responses from extreme zenith angles with surface azimuths opposite to the source would approach zero in both bright and dark samples. However, the near-hotspot sampling would be much greater for bright than for dark targets. As expected, the scale

dependence of variation produced significant differences in variance for both tests (*p*: $<2.2x10^{-16}$) when considering all six sample median populations. To refine the analysis so that the brightest and the darkest target could be quantitatively identified the targets were stratified by brightness.

Under this approach the F-K test suggested that at least one of the black samples had a variance that was different, while the white samples did not produce significant variations. The significance value for the F-K test of the black samples was 0.0136, while that for the white samples was 0.852. The Brown-Forsyth test did not produce significant tests for either of the two brightness groupings (*p*: 0.731, 0.929 for black and white respectively). These tests did not provide evidence to suggest that there were differences in the spectral uniformity of the targets. To address the differences in median reflectance between the targets an ANOVA variant that is robust to violations of normality and variance homogeneity was used. The K-W rank sum test suggested that at least one of the samples was different (*p:* $<2.2e^{-16}$). When the targets were

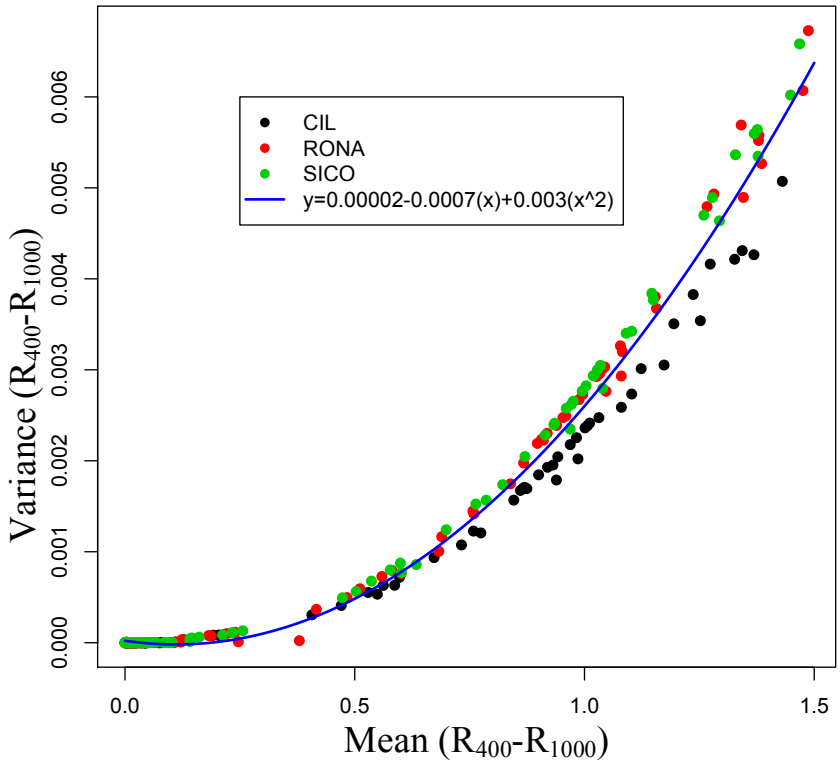


Figure 6 Spectral variability is associated with magnitude. Both bright and dark targets are plotted by each factor (paint brand). To investigate spectral uniformity a scale independent measure of variance is used.

stratified by target brightness the K-W test suggested that there may not be a difference in the median reflectance of the white targets, however the test applied to the dark targets demonstrated that at least one of the targets produced a different median value ($p=0.002$). The non-parametric post-hoc test (pairwise comparison using Wilcoxon rank sum test with adjusted p values by Holms and Bonferroni) suggested that the median reflectance of the Rona sample was significantly darker than CIL ($p=0.003$) and Sico ($p<0.014$). Therefore, it was concluded that the central tendency of the dark RONA spectra, (given variations in geometry) is darker than the other two brands of paint (Fig. 7 & 8). Having statistically demonstrated that one target was superior from the others in terms of their median spectral values the analysis was refocused on the variability within the spectra

and whether this variation is dependent on geometry. See figure 8 for geometry surfaces of median reflectance.

In a similar approach the spectral variability of measurements were investigated with reference to variations in collection geometry. Variance is assumed to be an indicatory of spectral uniformity and was thus sought as an indicator for targets that are least affected by geometry. The approach was initiated by building the distributions of a dispersion metric (R400-R1000nm) for each target. With the twelve azimuth orientations and four inclined zenith angles 48 values were used to build target distributions of spectral invariance.

The relationship between mean reflectance and the variation of reflectance, as represented by each sample and each geometry condition, was best described by a second order polynomial trend (Fig. 6). The strong curvilinear association (R^2: 0.99) was significant (coefficients p: $<2e^{-16}$, F-statistic: 11660 p: $< 2.2x10^{-16}$). The variations in geometry produced a wide range of intensities. Considering the observations made within the principal plane, extreme surface zenith values and a surface normal azimuth opposite to the illumination azimuth will produce low responses and conversely sample zeniths at half the illumination zenith relative to vertical (as opposed to the inclined target surface) and a surface azimuth equal to the illumination azimuth will sample the specular hotspot (law of reflection). The sampling strategy captures a wide range of mean and variance values. The relation between variance and mean is the product of absorption features that are superimposed on a scattering background. Brighter samples have a larger scattering baseline on which absorption features extend, the greater the scattering the deeper the feature and therefore the spectral variability. Because spectral variability is so intimately

associated with reflectance magnitude, to truly capture the spectral invariance without the effect of magnitude, a measure of scale independent variance was applied. Previous analysis also exposed the non-Gaussian nature of the data, thus a nonparametric scale invariant measure of variance was calculated. A non-parametric analogue of the coefficient of variation was adopted and was calculated as the ratio of the median absolute deviation from the median relative to the median (MAD/median, hereafter the NP-CV). Qualitative assessment of the distributions of the NP-CV revealed severely skewed distributions that were most evident in dark samples. The severe data points were attributed to three geometries that approached illumination zeniths >90° (surface ϕ: 45°, θ: 240-300°). From these geometries, the median deviation was greater than the median, which produced NP-CV >1.0 & <10.0, while all other geometries produced values less than 0.1. Because the three nap-cv values >1.0 were produced from geometries without direct illumination by the source they were omitted from analysis and visualizations. The filtered data were submitted to the statistical methods.

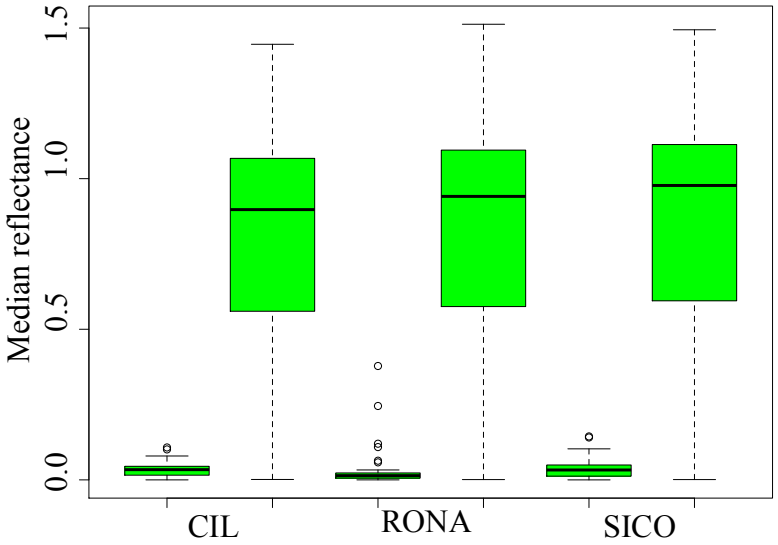


Figure 7 Boxplot of median reflectance from painted samples given varying geometry. Bright samples were not different from each other. The dark RONA sample was darker and potentially more variable than the other dark samples.

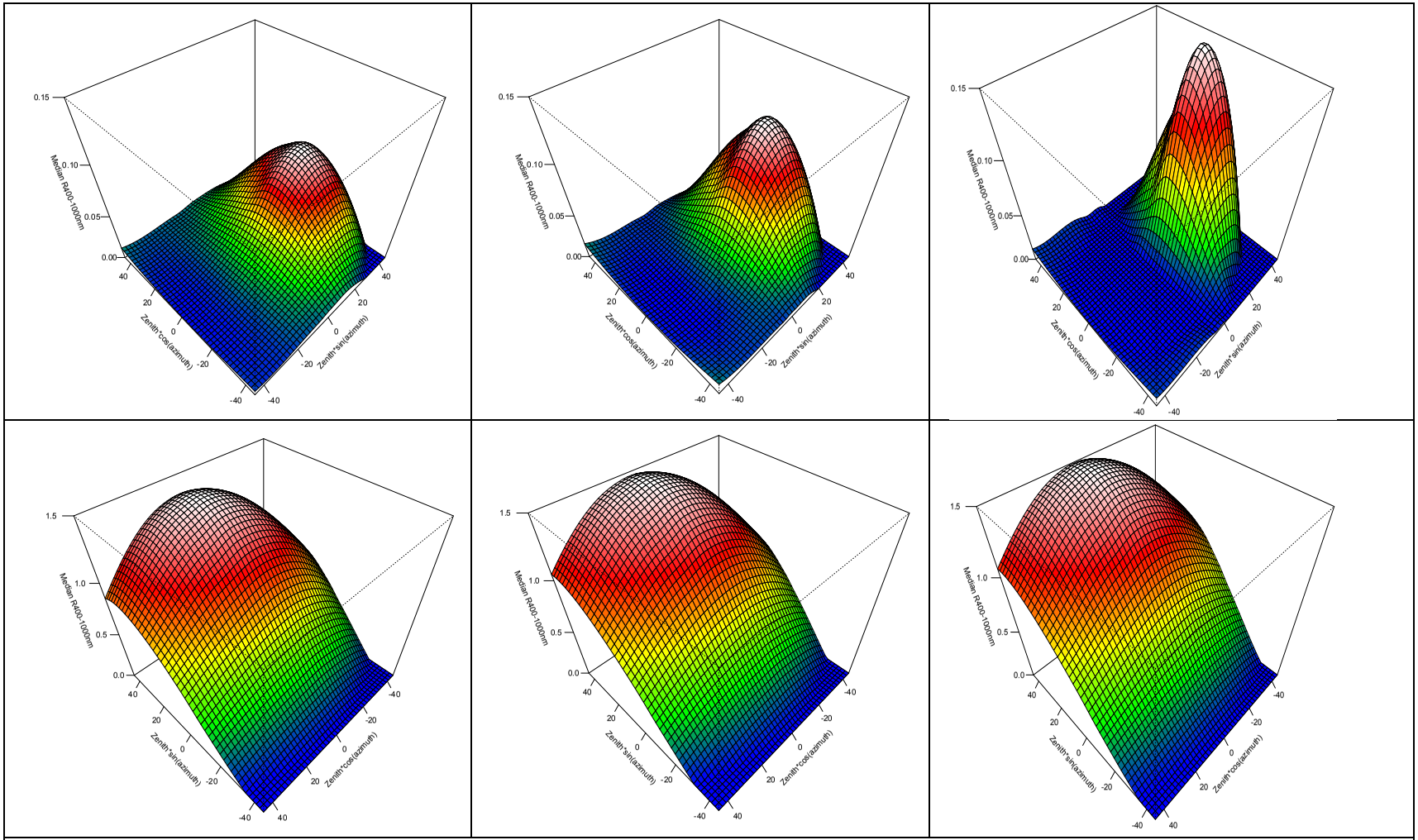


Figure 8 BRDF surfaces for bright and dark targets. Spectral medians (400-1000nm) are plotted to Cartesian coordinates from the surface polar coordinates (surface rotation and inclination). Dark and bright samples are illustrated on the first and second row respectively. Surfaces for brands CIL, SICO and RONA are in columns 1-3. Analysis and observations suggest that the RONA dark is the darkest and most uniform with variations in geometry. Qualitatively the RONA bright sample may be the brightest but there is little statistical evidence to support this claim. Note the scale difference between dark and bright samples

Relative to the bright samples, the dark targets produced spectra that were more variable, and this variability was less consistent with changing geometry (Fig. 10). The distribution data were to be submitted to a one-way analysis of variance test, and again must be evaluated in terms of the statistical assumptions. Regardless of the stratification approach (total population, bright and dark, individual target distributions), the distributions of the NP-CV data are significantly different from normal (p <1.52e^{-13}). The data could therefore not be addressed confidently by way of the traditional parametric ANOVA. Equality of variance was evaluated by the F-K and the B-F tests. The F-K test suggested that the variance of the NP-CV of the dark targets were significantly greater than that of the white targets (p =3.36e^{-15}). Stratified by target, the F-K test suggested that at least one dark target had a variance that was different from the other two black targets (p =4.22e^{-6}), while there was little evidence that the variance between the white targets were different (p =0.96). On the other hand the B-F test did not produce significant tests regardless of how the NP-CV data were stratified (p >0.14). Applying the non-parametric ANOVA by ranks suggested that the scale independent variance of the dark targets were greater than the bright targets (p =7.61e^{-4}). When stratified by target brightness there was little evidence that the white targets were different in NP-CV (p =0.76), and that at least one of the dark targets had a variance that was different from the other dark targets (p =1.04e^{-8}). Finally, the pairwise Wilcoxon ranks sum test with the significance adjustment by the holms method suggested that the NP-CV of the CIL target was lower than both the Rona (p =9.0e^{-5}) and the Sico (p =1.6e^{-10}) dark target samples. The post-hoc did not provide sufficient evidence to suggest the NP-CV of the Rona dark target was different from that of the Sico target (p =0.19). These same results were reproduced with the

Bonferroni method of significance adjustment for multiple comparisons. See figure 8 for geometry surfaces of median reflectance.

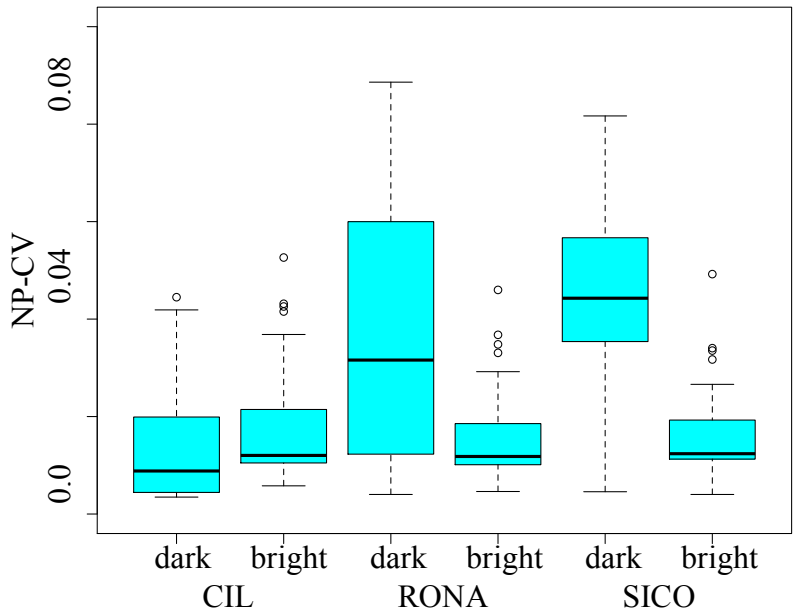


Figure 9 Boxplot of non-parametric coefficient of variation from painted samples given varying geometry. Bright sample spectra were less variable (central tendency of nap-cv) and more stable with geometry (less variable nap-cv). The dark Rona sample may have a greater geometry dependent spectral variability. The dark CIL sample is less spectrally variable.

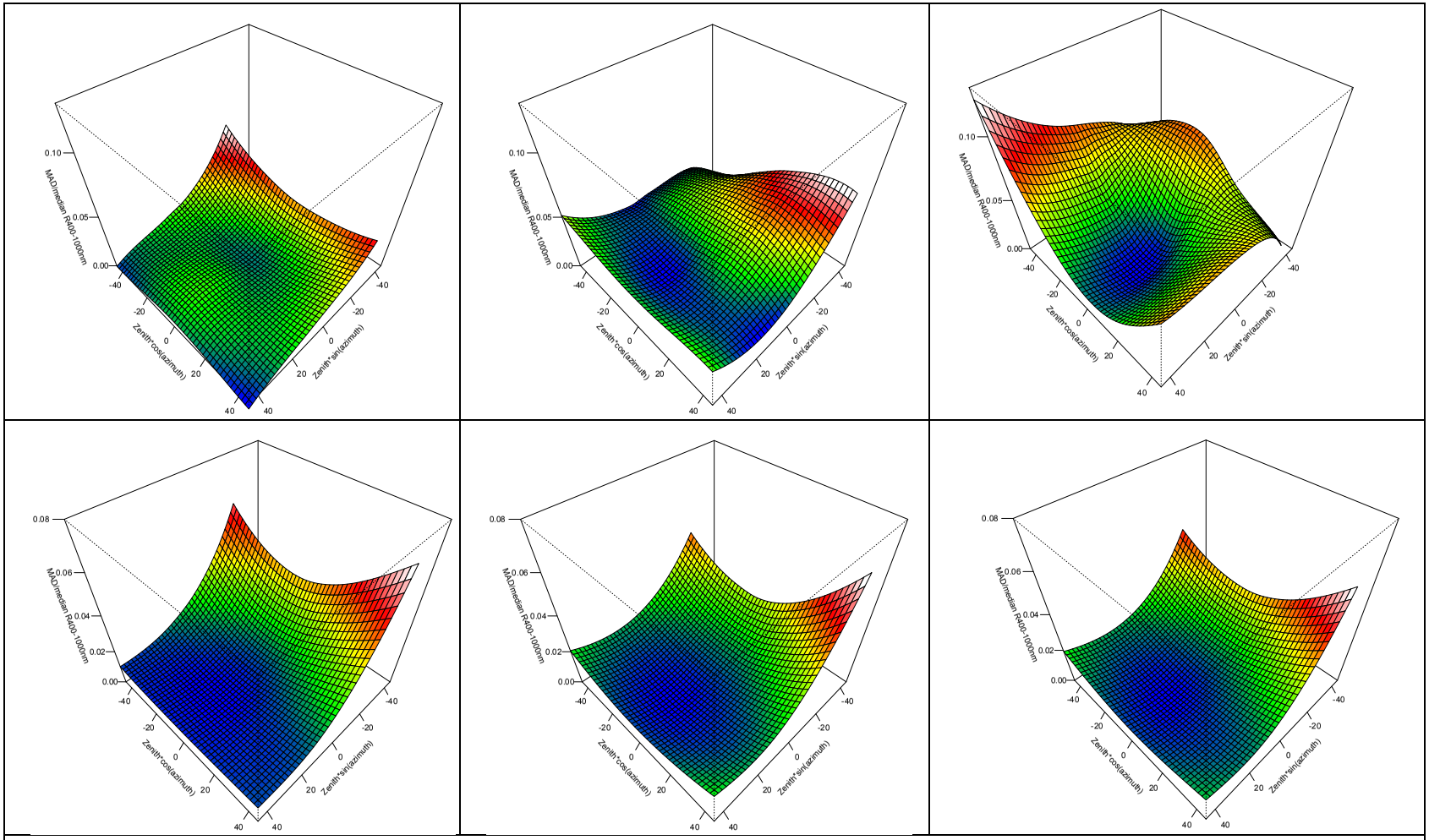


Figure 10 BRDF surfaces for bright and dark targets. Spectral uniformity as represented by non-parametric coefficient of variation (median absolute deviation from the median/median) was plotted to Cartesian coordinates from the surface polar coordinates (surface rotation and inclination). Dark and bright samples are illustrated on the first and second row respectively. Surfaces for brands CIL, SICO and RONA are in columns 1-3. Analysis and observations suggest that, of the dark samples, the CIL sample was most spectrally uniform and less variable with geometry. The white targets may not be different in either respect. Note scale difference between the dark and bright samples

1.2 *Target Deployment and Field Spectroscopy*

With the information derived from the lab based analysis full size targets were constructed. Hardboard sheets were painted with the Rona exterior flat finish formulations. The size of the calibration target is vitally important. Given a measured response from the airborne sensor is the product of all the material within the instantaneous field of view of the detector elements; it must be ensured that the entire sampling area is completely filled by the calibration surface. The spatial resolution, or the area sampled per pixel is variable on account of small variations in platform altitude, three dimensional orientation, integration time and forward velocity. To ensure that we achieve a 100% fill factor it is vital that the calibration target be roughly three times the nominal resolution in both dimensions. The airborne campaign was designed such that the spatial resolution of the spectrometer data would be nominally a 1.3m pixel size. Six hardboard sheets were used to construct each of the two calibration targets. Each hardboard sheet was 4x8 feet (~1.22 x 2.44m), thus the calibration targets were built from three by two hardboard sheets that produced an extent of 4.88 x 3.66m. Depending on the orientation of the target relative to the flight path, the altitude and platform attitude, a target of these dimensions should realistically produce between two to six pixels with 100% target fill factor, which are surrounded by target and background mixed pixels. If the flight path is at a 45° angle with the target orientation, there may be as many as four unmixed target pixels. It must be noted that this conceptualization of pixel dimensions and ground sampling is a coarse approximation and represents the pushbroom acquisition as analogous to a frame camera, which is not the case.

The twelve hardboard sheets were painted with three coats of the Rona brand paints. On September 13th 2012 the calibration targets were transported to the vicinity of the Shawnigan Lake Project forest. An abandoned dry sorting lot designated as district lot 17 was used as the calibration site. It was selected because of its wide exposure (~120x150m without vegetation), a flat (slope: 0.86° via lidar DSM) and fairly homogeneous paved surface and because it was only a little over a kilometer from the forest treatment plots (Fig. 11). Two collections were conducted one on the 13th (day 257) and one on the 19th (day 263), on the latter the targets were deployed at an aggregate quarry within the Greater Victoria Water Supply Area. The quarry had a slope of 1.17° (lidar DSM) in the flat area surrounding the target locations. The quarry had an exposed area of ~49x62m to the 20m tall quarry walls, which was considerably less than that at the SLP site (Fig. 12).

Concurrent with the airborne collection, spectral measurements were made of the deployed targets. An ASD VNIR handheld spectrometer was used to measure Spectralon white references and the two target surfaces in both radiance and reflectance scales. Transects of the targets were recorded in a geometry that avoided operator influence but still preserved a near nadir collection. As an additional check, the background, asphalt in the case of SLP and gravel within GVWSA, was also recorded. See figure 13 and 14 for field collected calibration spectra.

The ASD, Inc. handheld Vis/NIR spectrometer covers the spectral range of 325-1075nm with a FWHM of 3.5nm (at 700nm) and a sampling interval of 0.6nm. The angular field of view is 25° producing a footprint of approximately 40cm at a distance of 1m. The ASD was configured to save sample spectra as the average of 10 measurements

and to record 30 spectra that, barring quality checks, would be summarized as median spectra. Therefore each transect spectrum was generated from a total of 300 spectral measurements. The white references were also computed as an average of 10 measurements, while the dark current was averaged over 25 measurements. Figure 13 illustrates the radiance spectra collected during the ground campaigns.

Radiance data collected at GVWSA were contaminated by non-target materials and have been replaced by reflectance data transformed to radiance by the assumption that the Spectralon has a constant radiance response, which is not a valid assumption but is acceptable for a qualitative comparison. By forcing the Spectralon curves to be equivalent the other target curves are scaled accordingly and because the GVWSA bright target radiance is below that of the SLP, the plot suggests that either the scale is incorrect and that the GVWSA radiance data were brighter than the SLP collection or that there is a discrepancy between the distances from the fibre optic to the target (Spectralon or target) causing a difference between the relative reflectance of the two days. When the field data are compared in terms of their reflectance values, for which there was valid data for both dates, the two dates agree quite well (Fig. 14, 16-18). The discrepancy between the closest white targets for the two days has a maximum in the SWIR range, where the GVWD curve is ~2% brighter than that of the SLP collection. In addition the GVWD spectra were on average 2.92 times more variable than those measurements collected at SLP (evaluated as the average 5-95th percentile range). The suspected cause of the variability difference is the fact that the GVWSA spectra are computed from 10 spectra less than the SLP collection. Thus strictly by the sampling protocol the GVWSA would be 1.22 times ($\frac{1}{\sqrt{200}}/\frac{1}{\sqrt{300}}$) more variable than the SLP spectra. Superimposed on

this variability would be that caused by other confounding conditions including slight variations in geometry, observation height and irradiance stability. The consistency of the underlying surface may have also played a role, where the dry sorting lot paved surface was much more flat than the gravel aggregate surface of the quarry. The slight differences in slopes and aspects of the panels at GVWSA may have imposed variations caused by the BRDF, such variations in the panel orientations were less apparent at the SLP site.

Relative to the lab spectra collected in the darkroom, the field data agree quite well with only a slight magnitude bias and shape deviations (Fig. 16-18). The field spectra were on average 11.1% and 10.6% different from the static lab measured bright target (RMSE) for the SLP and GVWSA field spectra respectively.

There was an obvious dissimilarity between the two lab spectra of the bright target in both magnitude and variation. In the static collection two lamps were used in collection and for each of two target orientations (brush stroke striations parallel and perpendicular with illumination azimuth) 30 spectra were saved. No apparent orientation affect was observed so a total of 60 spectra (600 measurements) were used to represent the static target spectra. In the case of the BRDF collection (lab spectrum), these were generated from the data collected during the BRDF assessment with one illumination source and each spectra were generated from 10 saved spectra but 12 collections were conducted varying the target azimuth and preserving a level zenith angle. Thus the lab spectra were generated from 1200 measurements relative to the static conditions 600 measurements. In addition, for the static collection the distance to the sample was 4.5cm producing a footprint of 1.9cm in diameter, while the BRDF collection was conducted at

a distance of 6.7cm producing a footprint of 3.0cm. Thus the sampled area of the first collection is 60% smaller than the second. The different footprints sampled would suggest that the first collection with a smaller footprint would have greater variation than the second collection; however, the rotation of the surface azimuth in the second collection could not precisely maintain the very same footprint location and therefore samples different spatial locations on the target, where the static collection maintained the same location. The observed variation represented by the percentile range in figures 16-18, therefore does not represent the contribution of noise but rather the uncontrolled slight deviations from a level surface and potentially small departures from spatial uniformity within the target. This interpretation was supported through the observation that the individual azimuth spectra (n=100) were radiometrically discrete and lacked high frequency variations typical of noise. The magnitude difference between the two lab spectra might be explained by a slight difference in the white reference footprint relative to the target samples, where, in the BRDF experiment a platform apparatus was used for the samples but was removed during white references, which may have produced a slightly shorter distance to the reference and a smaller footprint thus inflating the sample spectra. These observations indicate that such lab based analysis must be conducted with upmost care to be repeatable to better than ~7.5%. It is suggested that these lab based analyses be conducted applying a dedicated sample stage that is flexible enough to accommodate different targets and capable of producing repeatable distances to the observation fore optics.

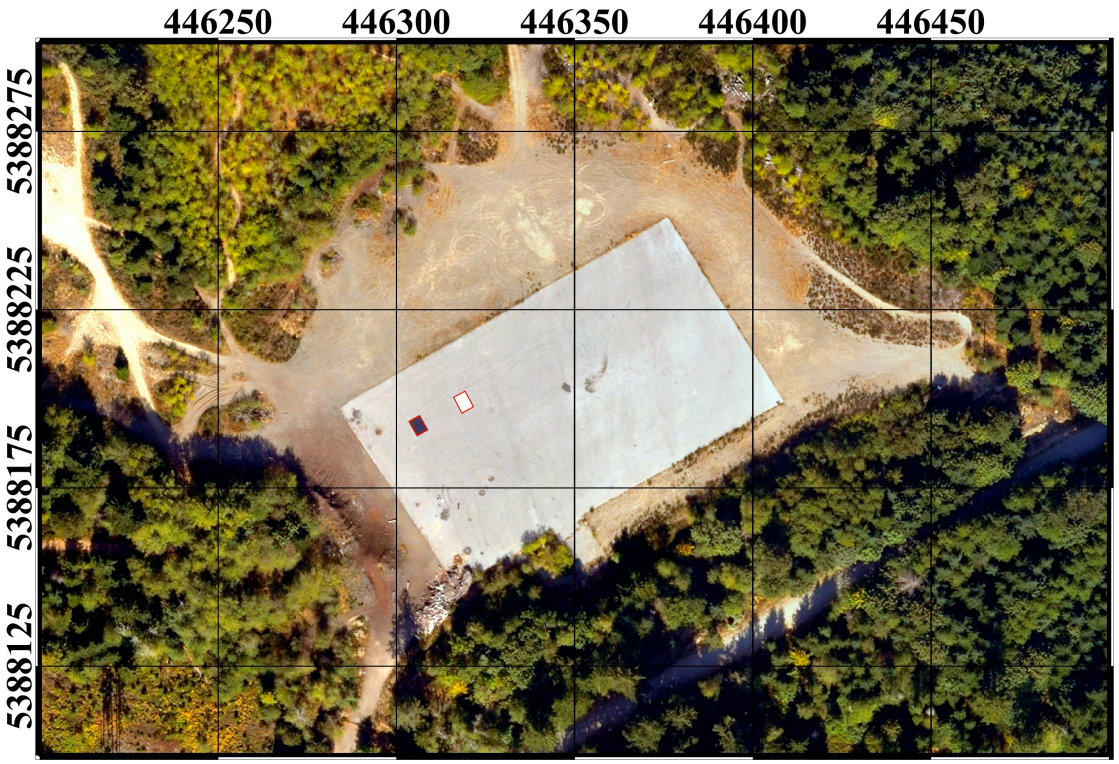


Figure 11 Calibration targets deployed at the dry sorting lot for the SLP project on September 13. The two 5x4m targets were positioned on a flat asphalt area

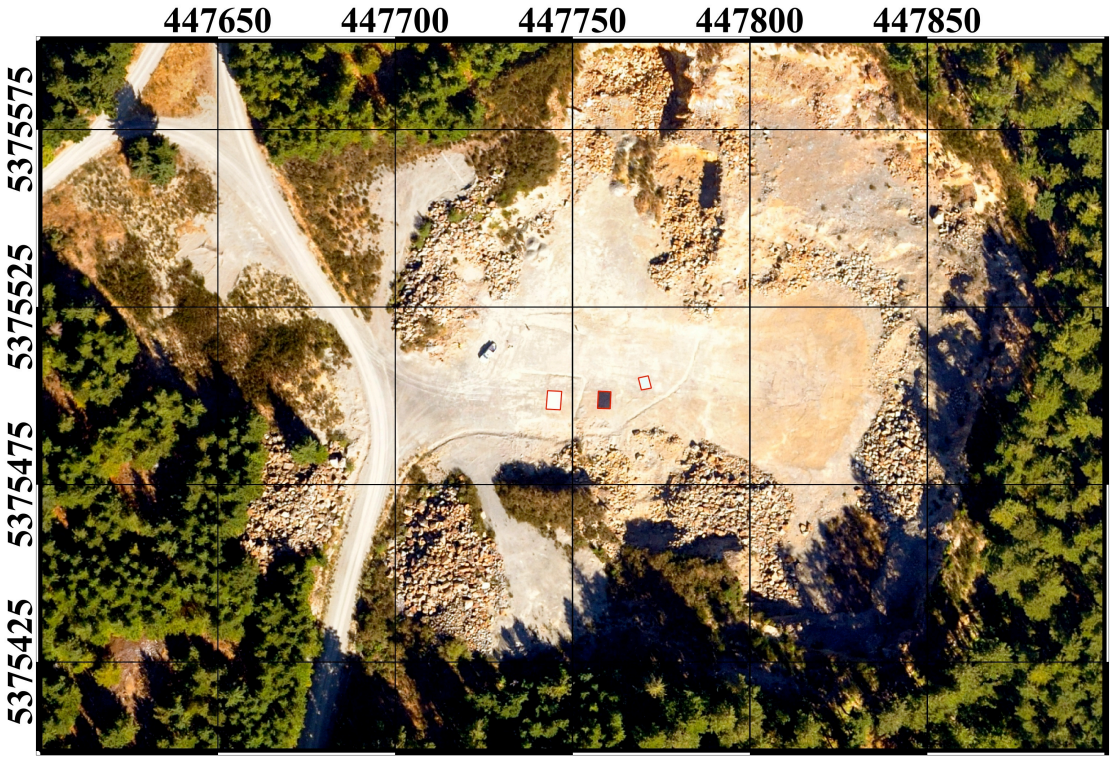


Figure 12 Calibration targets deployed at the saddle dam quarry within the GVWD for the airborne campaign on September 19th.

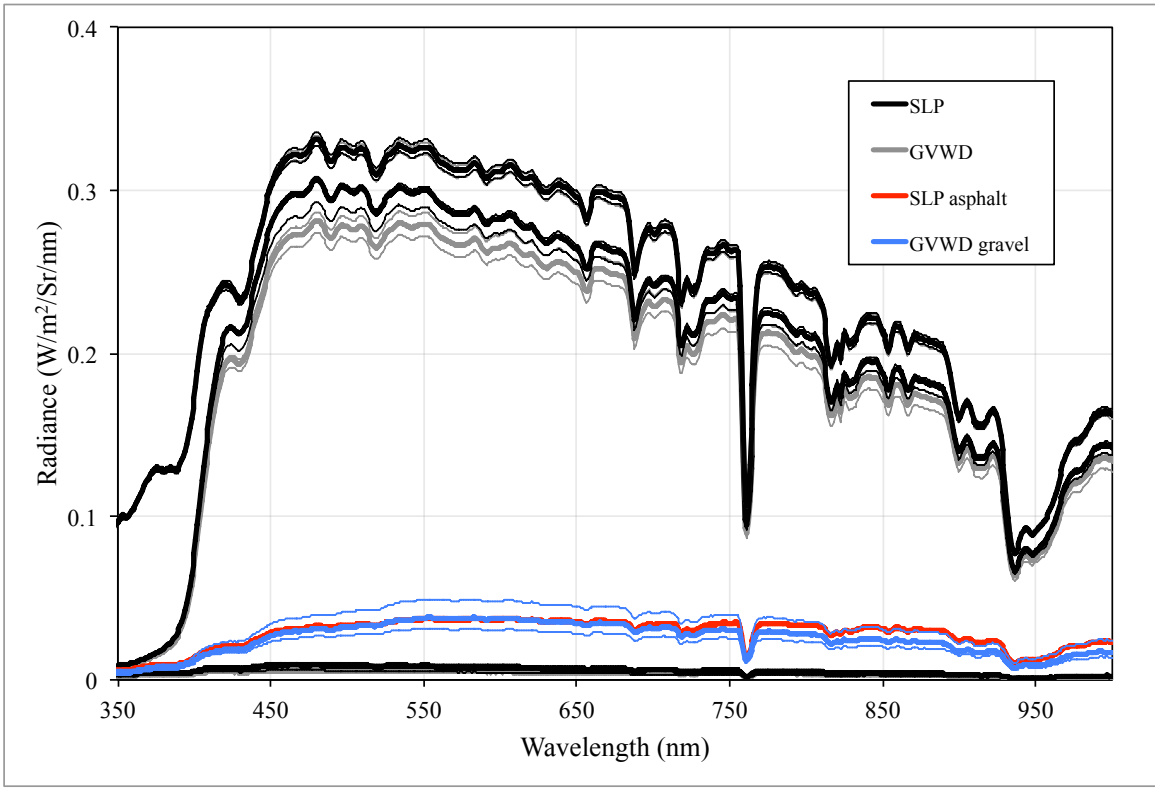


Figure 13 Field collected radiance of Spectralon white reference, targets and background at both the SLP and GVWD sites. The fine line width represent the 5-95% range, thick line width represents the median spectra. Note that radiance data for GVWD were computed from field reflectance data and the Spectralon median radiance collected at SLP. Spectralon and dark targets from SLP and GVWD are overlaid; GVWD curves are obscured by the SLP spectra.

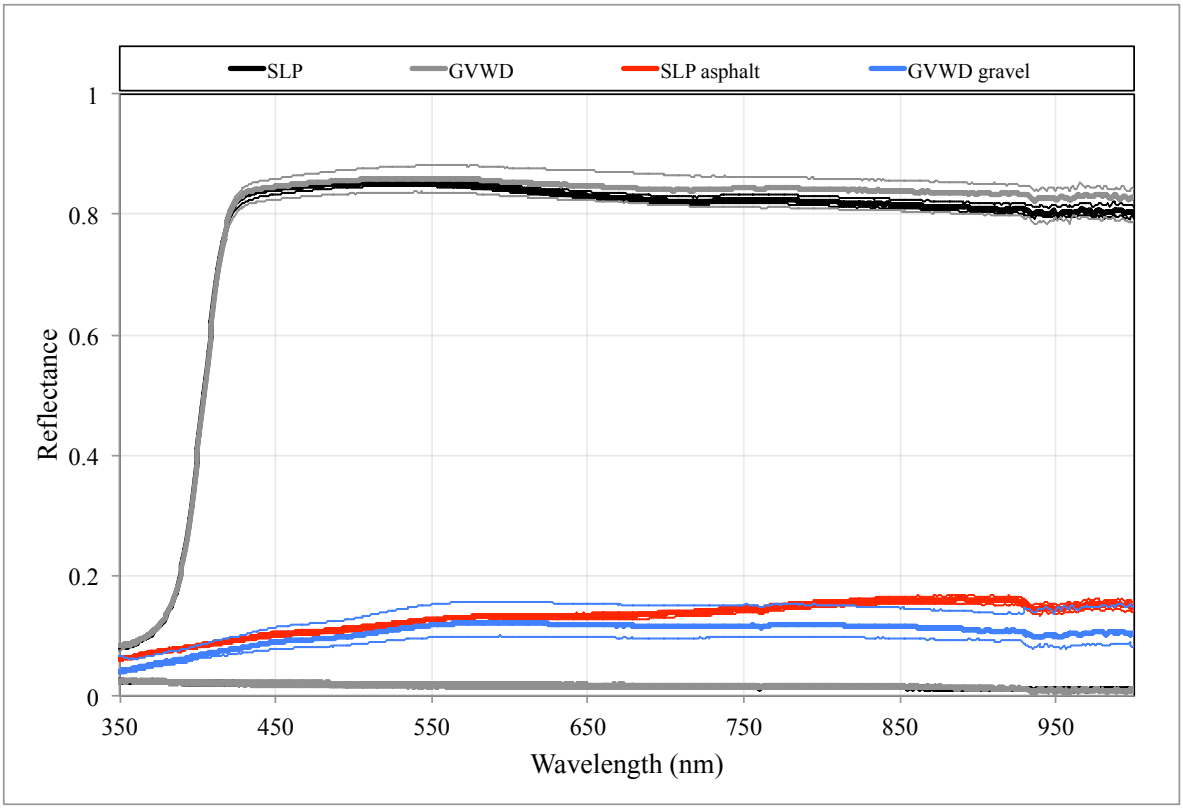


Figure 14 Field collected reflectance from calibration targets as well as background validation spectra (asphalt and gravel). The fine line width represent the 5-95% range, thick line width represents the median spectra. Note that the Shawnigan (SLP) dark target is overlaid and obscured by the Greater Victoria Watershed District (GVWD) dark target spectra

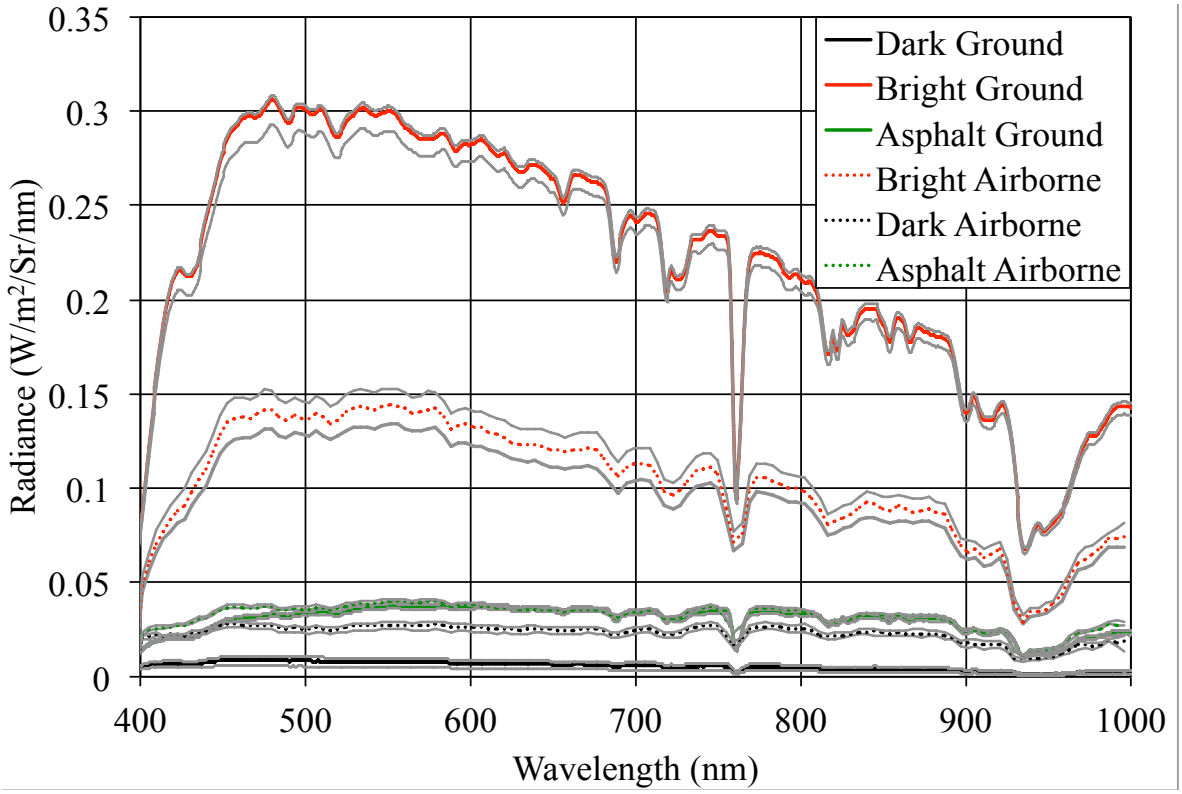


Figure 15 Comparison of field collected and airborne collected radiance responses of bright and dark calibration targets and the background asphalt at the SLP calibration site

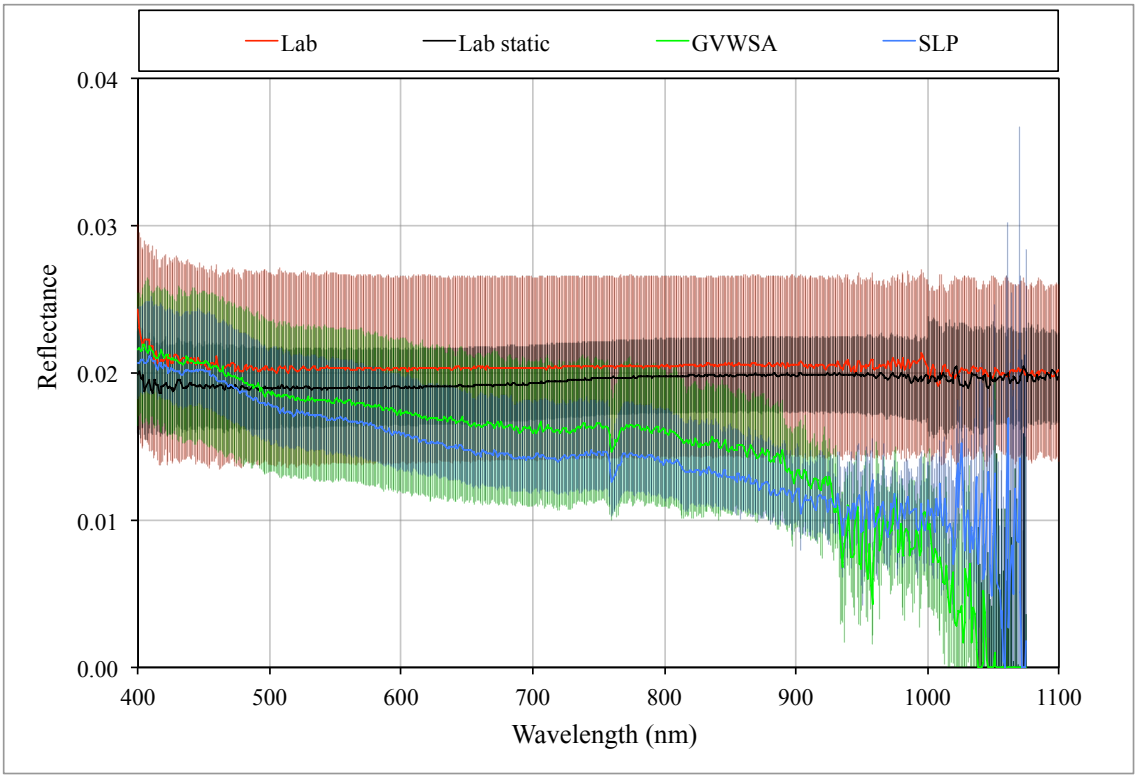


Figure 16 Comparison of lab collected reflectance of the dark calibration target samples and the deployed dark reference targets.

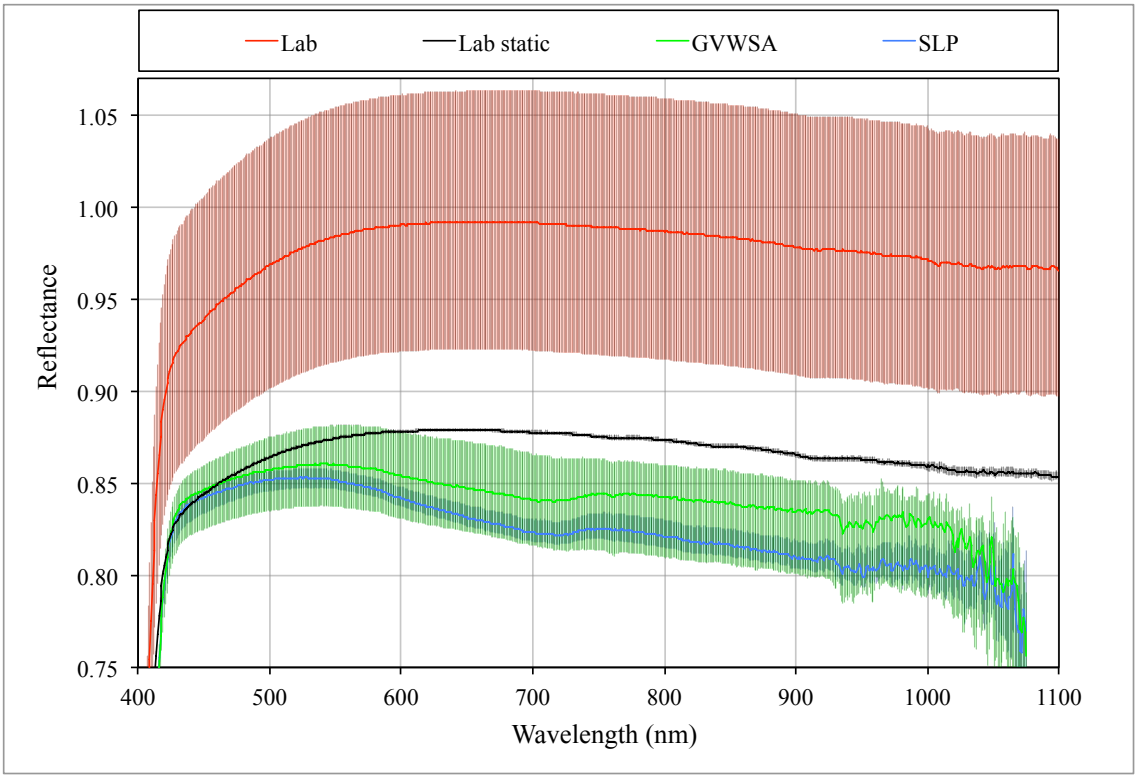


Figure 17 The dependence of reflectance on azimuth explains the large variation observed in the lab bright (with varied azimuth). As the initial collection used two light sources which eliminated any reflectance dependence on any particular illumination angle while also inflating the signal level See fig below where the range of variation attributed to azimuth is in the range of 10% leaving only ~1% of discrepancy between the two median spectra

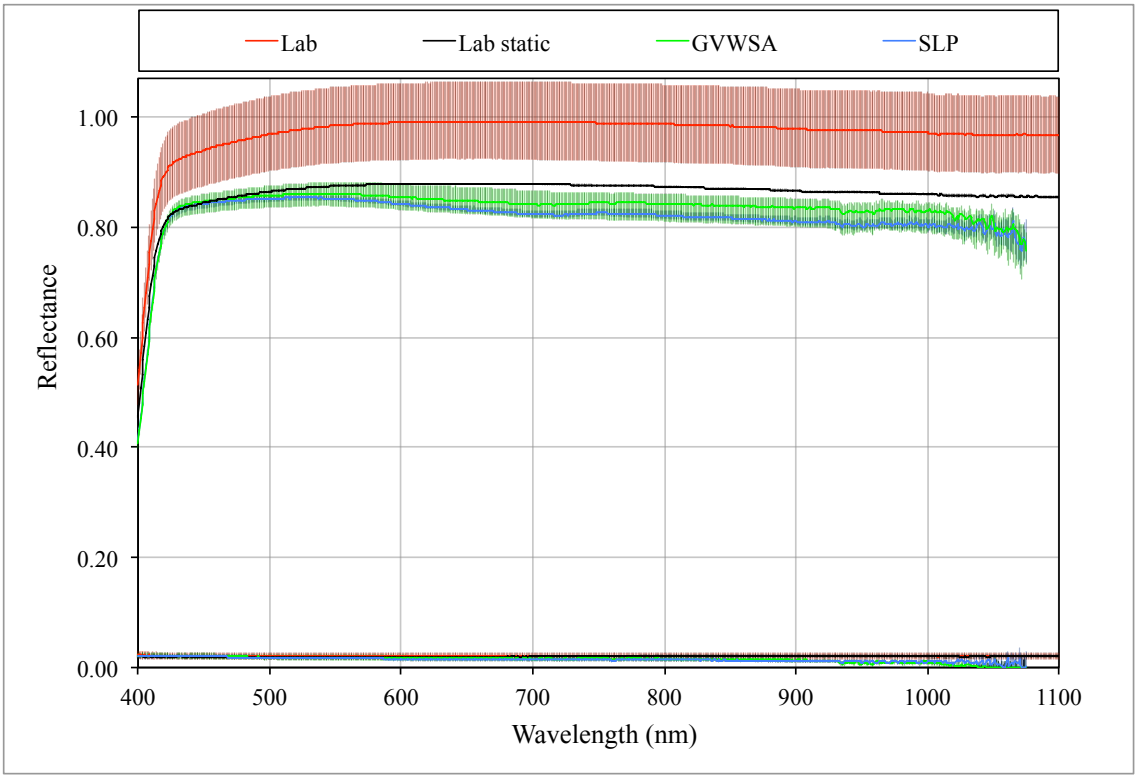


Figure 18 Reference target spectra for both bright and dark targets from both Shawnigan and GVWSA

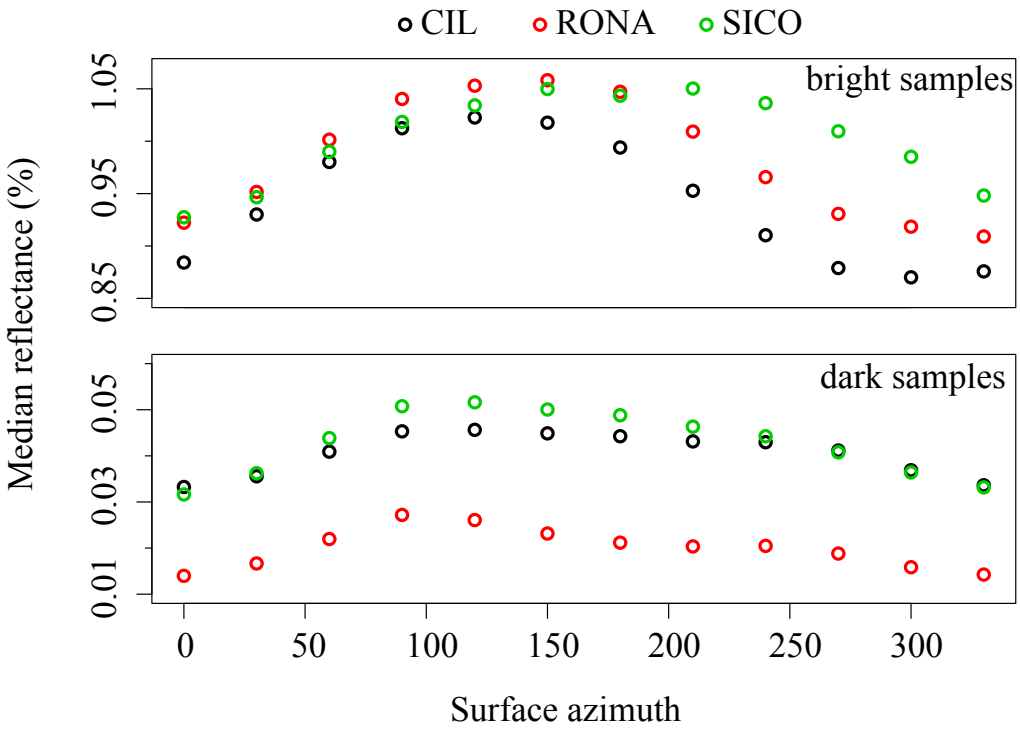


Figure 19 Median reflectance response to variations in surface geometry illustrates hot spot locations, which are slightly displaced due to the study design.

1.3 *AISA Eagle Radiometric Processing*

The AISA Eagle spectrometer data were received as raw unrectified digital number (DN). For the intended application these data need to be rectified or geometrically corrected and geo-located. Additionally, the data need to be spectrally transformed to represent energy interactions at the earth surface rather than detector sensitivity and atmospheric energy interactions. Specifically for this study the radiometric correction is vital to make any comparison with auxiliary radiometric data. Beginning with the radiance transformation, the multiplicative calibration coefficients were applied to the data. In the calibration files there is a coefficient for each sensor element in the detector array that converts the voltage DN representation of photon counts to the physical units of radiance ($W/m^2/Sr/nm$). These gain factors are provided by the manufacturer's sensor calibration.

In this case the radiometric calibration was provided for the unbinned configuration of the sensor, 1024 bands. The four times spectral binning option was applied for this collection, CaliGeo is able to convolve the calibration file to be compatible with the binned dataset (132 bands). Because the detector array is larger than the usable area of projected spectral light (assumed to be confounded by higher order spectral refractions) not all the binned bands are retained; only the center 132 channels are used. In this case the binning configuration used was a 4X hardware binning, where the detector electronics sum adjacent band DNs to effectively broaden the wavelength ranges, facilitating a faster integration time without a concurrent decrease in signal. Within the radiometric calibration process there is also a subtractive coefficient that is extracted from the dark current images collected before each flight line. These measurements characterize the baseline noise level on a detector element basis. The subtractive term is determined as a frame average (n=30) of the dark current values for each sensor element (spatial and spectral dimensions) while a shutter is closed and no light is projected onto the detector. These processes were performed through Specim's CaliGeo software version 4.9.7. Because the AISA Eagle is a frame transfer CCD sensor, the CaliGeo software is required to apply a frame transfer smear correction. The frame transfer smear correction removes the radiometric noise caused by the transfer of the area array detector to the masked readout portion of the sensor. The detector is still active for the duration of the frame transfer and therefore there is an effective smearing of detector frames that have a greater number of transfers, this affect is most apparent in columns that transfer bright DN values [110]. The radiance data are then calculated within CaliGeo as:

$$L_{k,i} = \frac{a_{k,i} * \left(\left(DN_{k,i} - b_{k,i} \right) - FTS_{k,i} \right)}{T} \qquad \text{[Equation 1]}$$

Where: $L_{k,i}$ is radiance in (μ m/cm^2*Sr*nm) in band k and spatial pixel *i*, a is the calibration gain factor (units: μ W/((Sr*cm^2*nm)(DN*ms)), DN is the image raw digital number, b is the average dark image digital number, FTS is the frame transfer digital number (see following equation) and T is the integration time in milliseconds.

$$FTS_{k,i} = (dt/T) * \sum_{j=0}^{k-1} s_{j,i} \qquad \text{[Equation 2]}$$

where: $FTS_{k,j}$ is the frame transfer smear at band k and spatial pixel *i*, dt is the time duration for the frame transfer in ms, T is the integration time in ms, $s_{j,i}$ is the dark subtracted DN at band j and spatial pixel *i*.

It should be noted that the smear retrieval method is slightly different when spectral hardware binning is applied, one option is to scale the above equation by the binning factor [111]. From the FTS equation it is seen that the smear for a given band and pixel is dependent on the measurements made at that spatial pixel in the bands before band k in the direction of the readout portion of the detector. Given the duration of frame transfer and the measurements made during the image capture period as an estimate of what would be captured during frame transfer the DN contribution of each frame transfer can be accounted for and removed before calibration factors are applied. The dependence of smear on the measured signal explains why this noise is not accounted for in dark current measurements. After the radiometric conversion to radiance was performed target spectra were extracted from the unrectified flight lines (Fig. 20). The unrectified images were selected because through the orthorectification process pixels can be omitted based on the projected pixel position and frame sequence. In the case of one flight line the purest bright target pixel was omitting from the rectified imagery, validating the approach to using the unrectified flight lines for target spectra extraction.

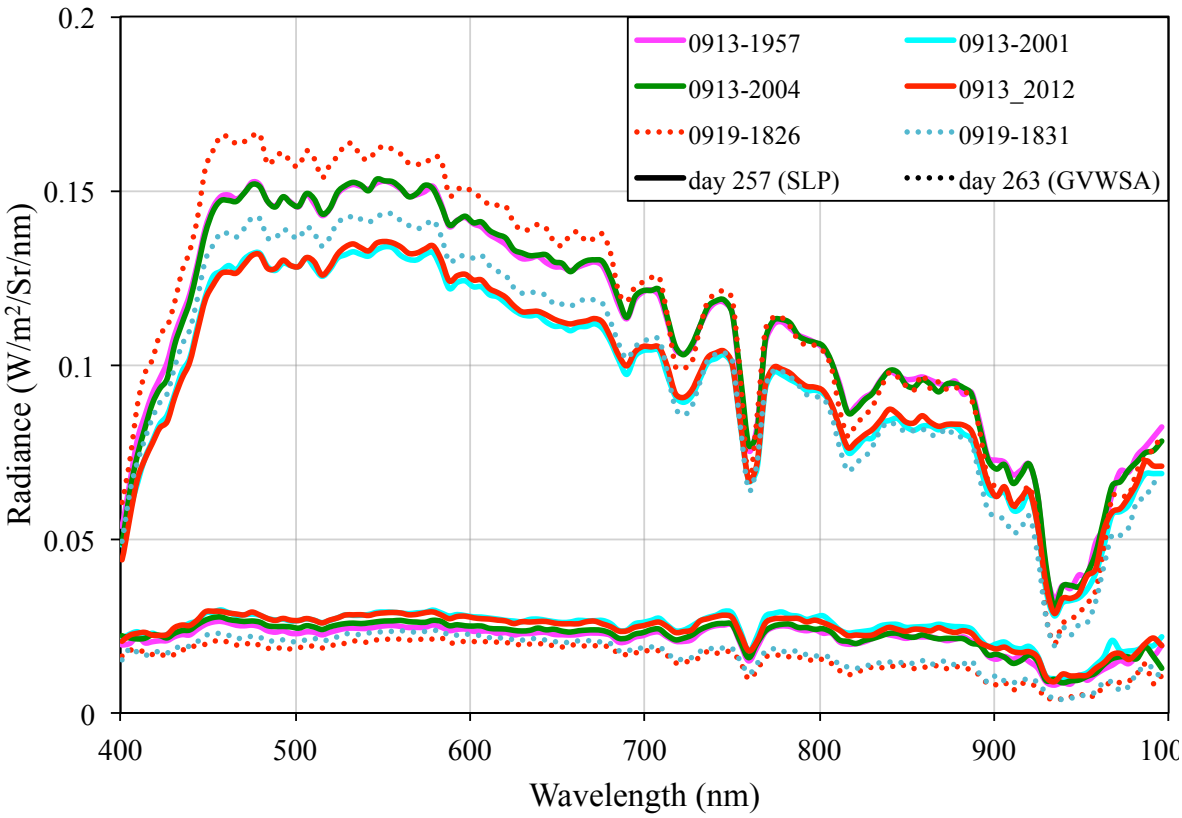


Figure 20 AISA Eagle radiance spectra of the deployed calibration targets

1.3.1 *Deriving Geometry From INS Measurements*

The underlying assumption of direct georeferencing is that there is precise data synchronization between the imaging system and the INS. The navigation data measured by the INS includes platform position, and instantaneous roll, pitch and heading values (Fig. 22). Although the orthorectified data was not necessary for this study the INS data provided information on the geometry of the sensing platform and therefore offered the opportunity to investigate the observed variation in target responses attributed to changing observation geometries. In order to extract the appropriate platform position and attitude data from the navigation data the time synchronization discrepancy had to be

resolved. In order to resolve timing synchronization issues the integer second signal that is generated by the Applanix POS/AV INS system is used to drive a timing signal that is directly read into the image. The AISA imaging system is designed such that the first 28 spatial pixels are reserved for metadata acquisition and FODIS (fibre optic down welling irradiance sensor), within this region of the detector array a light emitting diode is projected and operated by the integer second signal from the INS. The systems integrated hardware assigns a GPS time string with the integer second signal, the time of the first integer second of each flight line is read into the header file of each collected flight line. More precise timing synchronization is achieved by way of the constant frame rate. By counting the number of frames collected before the first pulse per second (PPS) signal transition and multiplying by the time duration for each frame, the timing synchronization is improved to less than 23.25ms. Occasionally the GPS integer time written into the header file actually references the integer second occurring before, not after, the first recorded data frame. In such cases the timing offset is adjusted to represent the time between the integer second and the time the first frame was collected (i.e. 1sec – (#frames*0.02325sec). See figure 21 for a graphical representation of the timing synchronization.

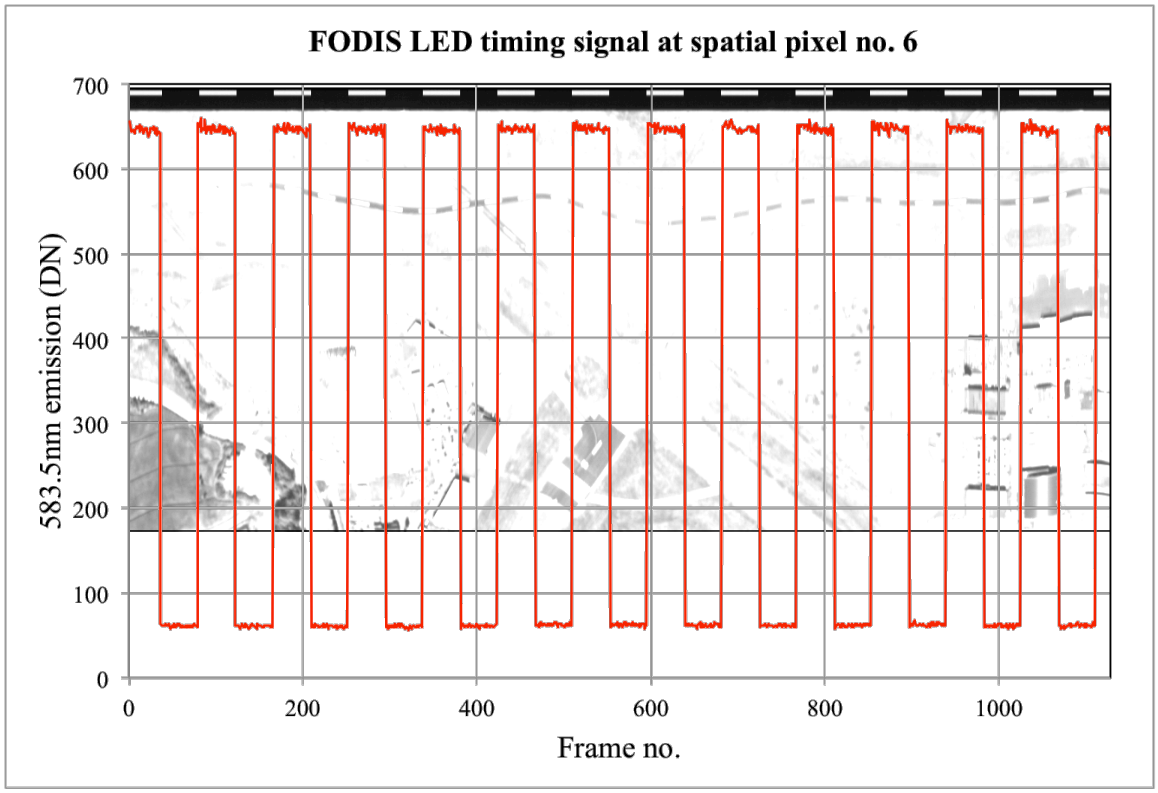


Figure 21 AISA Eagle time synchronization. An example of the LED PPS timing signal. Each transition from on to off and off to on mark the frame location of the integer second, the frame rate is 43f/s. Note the underlying grey scale image of band 583nm with FODIS PPS timing at top.

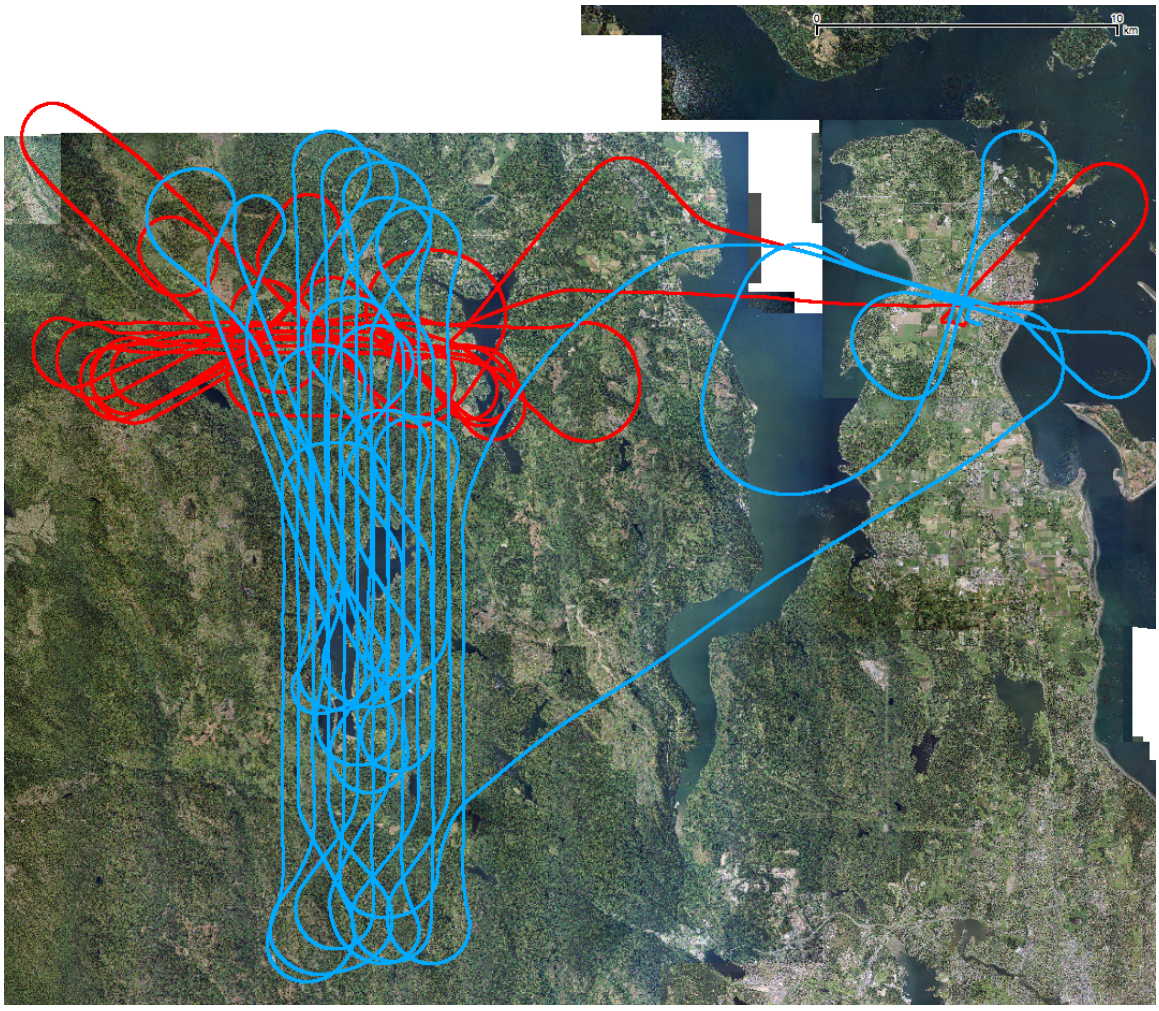


Figure 22 Flight path of airborne data acquisition overlaid the CRD orthophotos. Sept. 13th flight illustrated as a red polyline coverage including radiometric calibration flights at the dry sorting lot and the SLP collection. Sept 19th flight illustrated as a blue polyline coverage included the GVWSA and SLP, radiometric calibration site at the saddle dam quarry as well as the geometry calibration site at the Victoria International Airport.

With the timing synchronization resolved the precise time of collection for a particular frame could be determined. With the start of line time, the frame rate and the frame number that measured a deployed target, the time the measurements took place was determined. Platform latitude, longitude, altitude, roll, pitch and heading data that temporally corresponded with the frames that captured the calibration targets were extracted from the navigation data. Through the use of a lidar derived 50cm digital

surface model (ground and default) the platform altitude was translated to height above the surface (altitude-DSM). The platform attitude data was corrected for bore sight misalignment, caused by slight angular differences in the INS and spectrometer coordinate reference frames. The boresight calibration was performed using oppositely flown data over long linear ground features, the Victoria International Airport, in this case. Observation geometry (referenced to vertical) was then calculated using platform height, bore sight corrected roll and pitch, and the across-track pixel number (Eq. 3-6). Computing the observation zenith and azimuth angles from roll and pitch would be valid for only the principal pixel, therefore to correctly determine the observation geometry the roll used in the calculation must incorporate the angle between the spatial pixel that captured the target and the principal pixel. The AISA Eagle has an asymmetric field of view caused by the FODIS region, which occupies the first 28 detector elements. The optical axis is incident on the detector at element number 256.5, with a known focal length and the detector element dimensions the across track angle from the principal pixel can be calculated and incorporated into the roll parameter (Eq. 4).

$$y = (alt - dsm) * \tan(\varphi_p) \qquad \text{[Equation 3]}$$

where: y is the along track horizontal distance from the aircraft to the observed pixel position, alt is the altitude of the platform at the time the frame was captured, DSM is the ground elevation at the target pixel, $\varphi_p$is the pitch angle of the platform at the time the frame was captured.

$$x = (alt - dsm) * \tan\left[\varphi_r \pm \left[(p - s) * \tan^{-1}\left(\frac{d * bin}{f}\right)\right]\right] \qquad \text{[Equation 4]}$$

where: x is the across track horizontal distance from the aircraft to the observed pixel position, φ_r is the roll angle of the platform at the time the frame was captured, p is the principal pixel detector element number, s is the sample number that captured the target, d is the detector element size, bin is the spatial binning factor and *f* is the focal length. Note; where s>p roll was adjusted by summation, while s<p roll was adjusted by subtraction.

$$Azi_{obs} = \left(\varphi_h + \tan^{-1}\left(\frac{x}{y}\right)\right) \pm 180° \quad \text{[Equation 5]}$$

$$Zen_{obs} = 90° - \tan^{-1}\left[\frac{alt - dsm}{\sqrt{y^2 + x^2}}\right] \quad \text{[Equation 6]}$$

Where: Azi_{obs} is the observation azimuth from the ground surface perspective and relative to north, Zen_{obs} is the observation zenith from the ground surface perspective and relative to vertical and φ_h is the platform heading at the time the frame was captured,

The referencing of geometry to vertical is arbitrary and does not have a meaningful relation to the incident and reflected light. For this reason, the geometry should be related to the surface normal vector (Eq. 7-10). In addition, the azimuth angles relative to north is also an arbitrary convention, to investigate the impacts of varying geometries these angles should be reduced to relative azimuths, that is the angle between the observation and illumination azimuths (Eq. 11).

$$Sen_x = \sqrt{x^2 + y^2} * \sin(Azi_{obs} - 180°) \quad \text{[Equation 7]}$$

$$Sen_y = \sqrt{x^2 + y^2} * \cos(Azi_{obs} - 180°) \quad \text{[Equation 8]}$$

$$Sen_z = alt - dsm \quad \text{[Equation 9]}$$

where: $Sen_{x,y,z}$ is the three dimensional point representation of the observation vector with an origin located at the target pixel, these parameters were determined for the platform, the source and the ground surface normal vectors. Note that the azimuth constant term is based on the third quadrant (platform is south west of target pixel), but is different for each.

$$Obs_Tar_{norm} = \left[\cos^{-1}\left(\frac{\sum(Sen_i * Tar_i)}{\sqrt{\sum(Sen_i^2)} * \sqrt{\sum(Tar_i^2)}}\right)\right] * \frac{180}{\pi} \quad \text{[Equation 10]}$$

$$Azi_{rel} = \sqrt{(Azi_{obs} - Azi_{sol})^2} \quad \text{[Equation 11]}$$

Where: Zen_{obs} is the observation zenith angle from the ground surface perspective and relative to the ground surface normal, Sen_i is the x,y and z parameters for the point representation of the observation or sensor vector, Tar_i is the x,y and z parameters for the point representation of the surface or target normal vector. The solar zenith was computed in the same manner by substituting Sen_i with Sol_i, Azi_{rel} is the relative azimuth representing the angle between the solar azimuth and the observation azimuth.

While the observation geometry was captured in the INS data, the surface geometry was derived from a topographic analysis of the 50cm lidar digital surface model. Slope and aspect was computed by ITT's ENVI topographic modeling, where the estimates are determined by the partial first order differential equations of the general quadratic equation (*i.e.* z=ax2+by2+cxy+dx+ey+f) fitted to a 3x3 kernel. The partial derivatives are combined and the origin shifted to the kernel center to produce the slope equation: $slope\ (°) = \tan^{-1}\left(\sqrt{d^2 + e^2}\right)$, the aspect equation is also derived from the partial derivatives: $aspect\ (°) = \tan^{-1}(e/d)$ [112]. Lastly, the solar position was found through the NOAA Earth System Research Laboratory, Global Monitoring Division's Solar Calculator (URL: http://www.esrl.noaa.gov/gmd/grad/solcalc/). See table 1 & 2 for radiometric flight line ancillary data. The geometry data suggest that the footprints projected to the ground surface are slightly different between the two data collections, where the SLP have footprints that are roughly 10cm larger than those produced in the GVWSA collection (across track dimension). The geometry data also illustrate that there is very little variation (<7°) in the solar zenith angles between flight lines in the SLP

collection but the GVWSA solar zenith angles are approximately 6° smaller than those from the SLP collection. In terms of the observation zenith geometry flight line 0919-1826 is a significant departure from the other samples, with an angle roughly three times that observed for the other flight lines. The large observation zenith value for flight 1826 is produced by the collection geometry where the targets are captured at the edge of the swath width.

Table 1 BRDF geometry parameters for Eagle measurements of the bright calibration target						
Flight ID	0913-1957	0913-2001	0913-2004	0913-2012	0919-1826	0919-1831
Easting	446255.3	446396.9	446301.9	446289.1	448116.5	447632.3
Northing	5388151.5	5388154.9	5388323.4	5388284.0	5375384.3	5375642.7
Height a.g.l.	1236.3	1238.9	1232.7	1246.3	1161.4	1175.2
Roll	-0.110	1.053	3.921	-1.893	17.341	5.972
Pitch	3.599	3.876	4.082	3.337	4.6705	3.377
Heading	50.422	330.686	259.968	103.221	73.851	241.436
Across track IFOV	1.608	1.612	1.609	1.620	1.513	1.528
Along track IFOV	0.806	0.808	0.804	0.812	0.759	0.765
Along track sampling	1.231	1.282	1.252	1.234	1.187	1.222
Azi_{obs}	230.422	150.686	79.968	283.221	253.851	61.436
Zen_{obs}	3.601	4.016	5.651	3.834	17.888	6.849
Azi_{sol}	175.59	176.96	177.86	180.87	137.80	140.15
Zen_{sol}	45.31	45.27	45.25	45.24	39.39	38.65
Azi_{tar}	184.49	184.49	184.49	184.49	184.98	184.98
Zen_{tar}	3.19	3.19	3.19	3.19	5.27	5.27
$Sol\text{-}tar_{norm}$	44.98	44.94	44.92	44.91	38.92	38.18
$Obs\text{-}tar_{norm}$	3.38	3.72	5.58	3.75	17.68	6.55
Azi_{rel}	54.83	26.27	97.89	102.35	116.05	78.71
*Target perspective, Roll in 1826 is large because the spatial pixel number is 482 far from the principal pixel, Attitude values are corrected for bore sight misalignment and spatial pixel, All values pertain to only the specific sample and frame that collected the deployed target						

Table 2 BRDF geometry parameters for Eagle measurements of the dark calibration target						
Flight ID	0913-1957	0913-2001	0913-2004	0913-2012	0919-1826	0919-1831
Easting	446245.1	446393.5	446294.1	446285.8	448116.5	447632.3
Northing	5388141.7	5388158.1	5388314.2	5388287.3	5375384.3	5375642.7
Height a.g.l.	1236.3	1238.9	1232.6	1246.2	1161.3	1175.2
Roll	0.081	1.657	3.724	-2.480	16.672	6.567
Pitch	3.592	3.876	4.080	3.338	4.671	3.377
Heading	54.046	338.692	258.704	96.009	73.254	243.723
Across track IFOV	1.608	1.612	1.609	1.620	1.512	1.528
Along track IFOV	0.806	0.808	0.804	0.812	0.759	0.765
Along track sampling	1.231	1.282	1.252	1.234	1.187	1.222
Azi_{obs}	234.046	158.692	78.704	276.009	253.254	63.723
Zen_{obs}	3.593	4.213	5.515	4.155	17.246	7.371
Azi_{sol}	175.59	176.96	177.86	180.87	137.80	140.15
Zen_{sol}	45.31	45.27	45.25	45.24	39.39	38.65
Azi_{tar}	172.24	172.24	172.24	172.24	188.93	188.93
Zen_{tar}	6.58	6.58	6.58	6.58	11.75	11.75
Sol-tar_{norm}	44.63	44.59	44.56	44.57	38.29	37.54
Obs-tar_{norm}	3.16	3.55	5.33	4.05	16.71	6.71
Azi_{rel}	58.46	18.27	99.16	95.14	115.45	76.43
*Target perspective, Note: there is little difference in geometry between the flight lines, with the exception of 1826 which relative to others is closer to the principal plane and closer to the specular hotspot.						

1.3.2 *Characterization of Target BRDF*

As the motivation of this study it was considered important that ground based and airborne radiometric measurements of the calibration targets be as predictable as feasibly possible. From this perspective the variation in observed responses attributed to changing geometry had to be quantified. With the geometry of the airborne collection determined, an effort was made to coarsely reproduce the airborne geometry in the lab to empirically determine the variation in target response attributed to these geometries. From these measurements reflectance was empirically modeled from the sampled geometry. This approach applied a multiple linear approximation to fit geometry and reflectance values. The multiple linear regression approach is recognized as a coarse approximation to the true response, which is known to be cyclical response varying observation azimuth with constant observation zeniths and a constant illumination vector. The response is cyclical as the observation angle passes through the two hotspots, a backscattered and a specular bright response position.

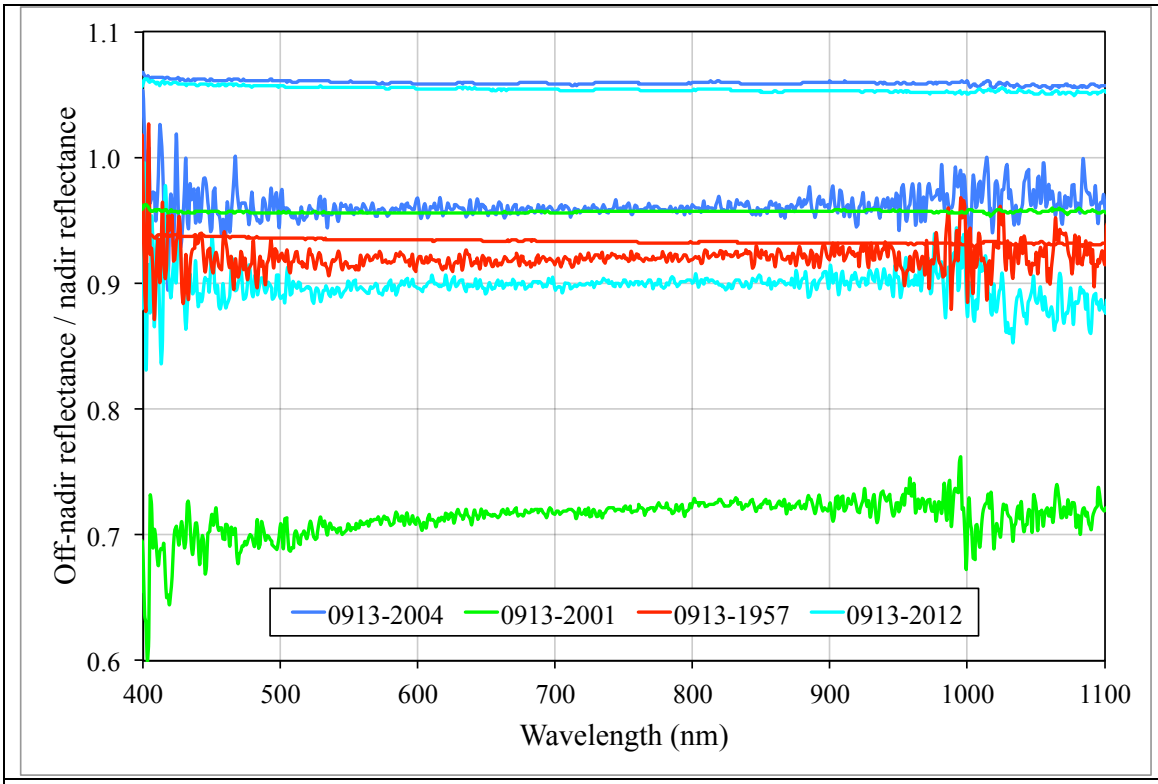


Figure 23 Off nadir measurements demonstrates spectral invariance with changes in observation geometry

For each airborne target spectrum from day 0913 the geometry was coarsely reproduced in the lab. The illumination geometry was considered constant at a 45° zenith while the relative azimuth and observation zenith angles were rounded to the nearest degree. Reflectance spectra were computed from nadir white references. Geometry correction factors were computed by normalizing the off-nadir measurements by the nadir equivalent. It was observed that these correction factor spectra were uniform with wavelength and only varied for the dark targets, which is largely the effect of lower signal to noise ratio (Fig. 23 & 24).

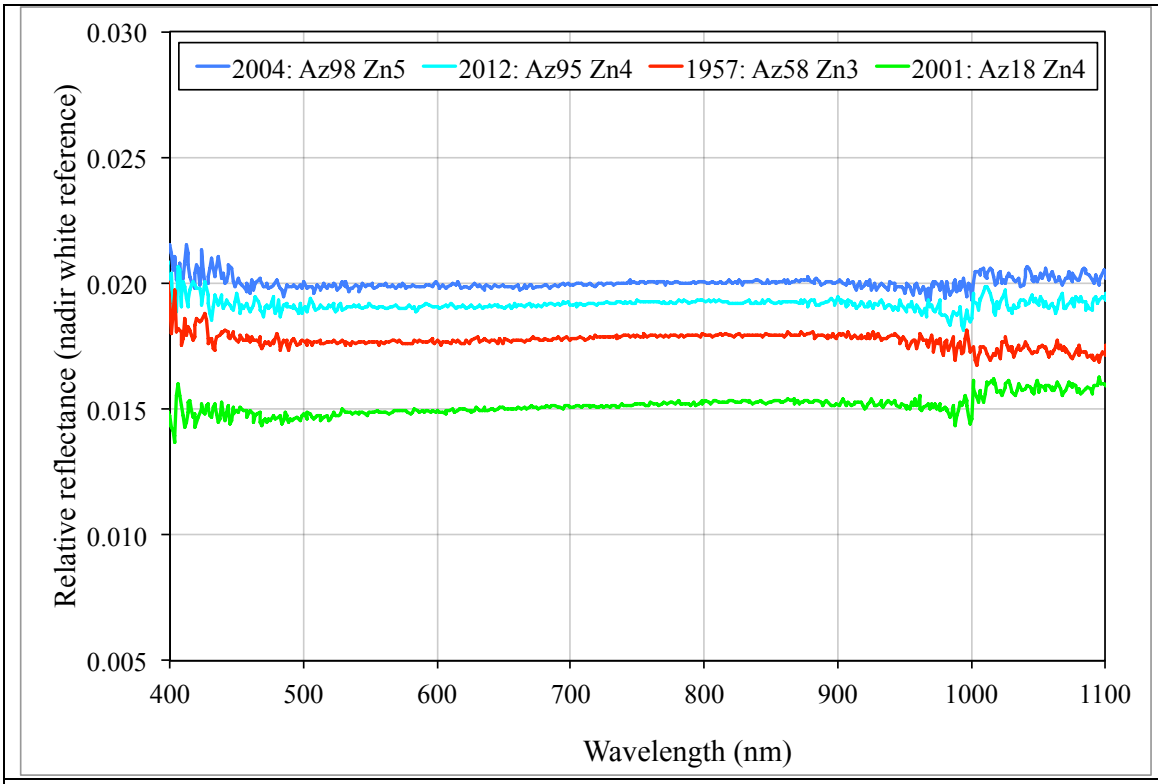


Figure 24 Airborne geometries during dark target collections reproduced in the lab setting

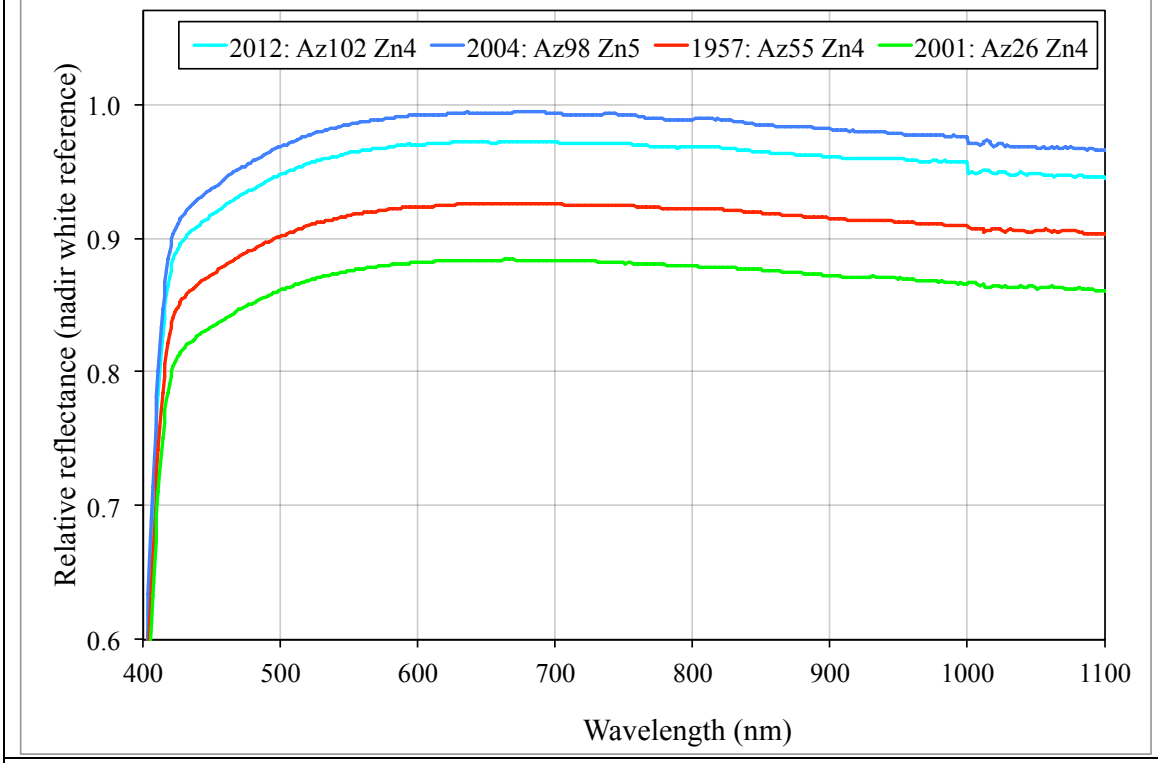


Figure 25 Airborne geometries during bright target collections reproduced in the lab setting

1.3.3 *Evaluation of Spectral Mixing in Airborne Spectra*

Since the patterns of BRDF from the airborne data did not correspond well with that found in the lab analysis the efforts to explain the variation in the target response was refocused on to the likelihood of spectral mixtures. A strategy to identify a mixed target was built based on the expectation that the ratio of a two spectra of a common target collected from two flight lines will be constant. For each unrectified flight line an average spectrum was computed for the dry sorting lot asphalt surface omitting the targets (n=160-165). For each combination of flight lines, a ratio spectrum of the average asphalt spectra was computed. These curves represented the general radiometric scale differences between the two flight lines largely determined by the acquisition geometry. The asphalt ratio is interpreted as ratio spectrum of no change between the two flight lines, in other

words the very same materials. Because a larger area was used to compute the spectra there was less potential for inaccurate spatial positions to impact the analysis. For each of the deployed targets and each of the flight lines the ratio spectra were computed. This spectrum with reference to the asphalt ratio would suggest significant departures from unmixed responses. If one of the two spectra used in the target ratio was mixed (or the proportions of the mixture were vastly different) then this ratio spectra would deviate significantly from the location of the asphalt ratio. For example, the average asphalt spectrum produced from flight line 2004 is divided by that of 1957 (where it can be confidently stated that the outliers that are not representative of the asphalt are few, and the spectra on average represent the same material). This curve is straight throughout the spectral range and any departure from a value of one represents the differences attributed to the acquisition geometry. The ratio of the bright target spectrum from flight line 2004 to that of 1957 is computed and compared to the ratio spectrum produced from the asphalt spectra; the same is done for the dark target. The closer the target ratio spectrum is to the asphalt ratio spectrum the less likely the two target spectra are mixed with background material (or perhaps the more equal the mixing proportions). In practice however, the target spectrum will rarely (should not) be the same as the asphalt ratio, because unlike the asphalt ratio, which is collected over a longer duration, the target spectra are single pixels and therefore have a greater likelihood of more significant geometry variations between the two individual pixels (platform attitude variations are not averaged out). One caveat in this analysis is that it assumes that there are flight lines with mixed target responses and flightiness with unmixed target responses. This approach suggested that flightiness 2004 and 1957 had the least amount of mixing for the target

responses. The bright target ratio was clearly more similar to the asphalt ratio than any other comparison. This conclusion is supported by the fact that the radiance of the bright targets within these lines were brighter than the others and the dark target were darker than the other flight lines. If these responses were mixed with the intermediate reflecting asphalt the bright target would appear darker and the dark target would appear brighter. The bright target ratio for flight line 1826 and 1831 also seemed to have little mixing relative to the other ratio comparisons. The dark target ratio for the 1826 and 1831 comparison was quite far from the asphalt ratio (in this case gravel ratio), suggesting that the two dark target spectra were not similar. From this investigation it was determined that for the SLP acquisition the most appropriate target response for the deployed targets were those collected in flight lines 2004 and 1957. These two flight lines were flown in a configuration that produced a slightly (10 & 20cm) smaller across track footprint relative to the others, which may have provided for a greater likelihood of capturing an unmixed target response (Table 1 & 2). Also supporting this perspective is the fact that the 1957 and 2004 flight lines were collected such that larger dimension of the targets were aligned in the across track direction, given the actual footprint dimensions are slightly wider than they are long by ~40cm, this also provides a greater likelihood of capturing an unmixed target compared to flight lines 2001 and 2012, which were flown perpendicular (not observation angles).

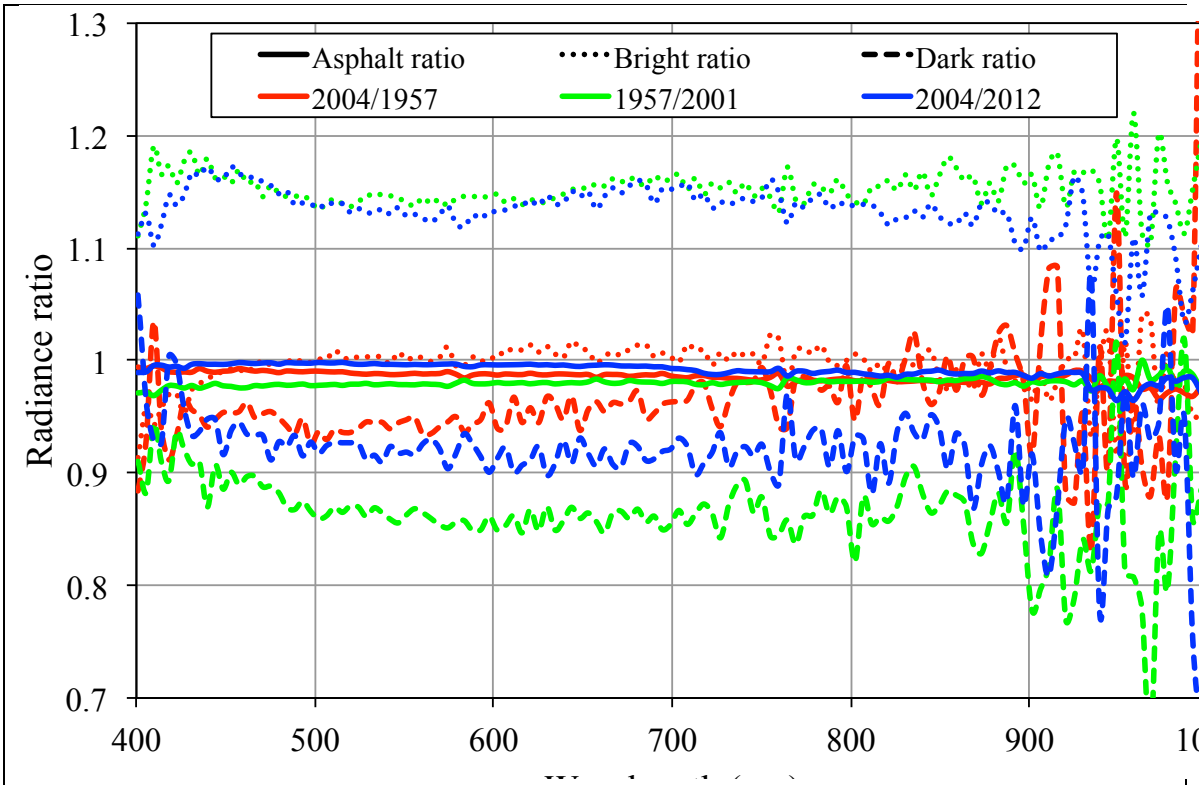


Figure 26 spectrum ratios used to evaluate degree of spectral mixing. Asphalt ratios indicate flight line to flight line geometry differences but do not contain mixing. If either measured target is mixed with background the ratio will be further displaced from the asphalt ratio spectrum. For clarity the dark ratio for the 2004 and 1957 is actually 1957/2004, all other spectra are as the label suggests.

1.4 *Radiometric Correction Discussion*

A study conducted by the crop physiology lab at Utah state university investigated the potential of mixing barium sulphate with untinted white latex paint [108]. Barium sulphate has been used as a low cost alternative to manufactured reflectance standards (Spectralon's sintered polytetrafluorethylene), which tend to be quite expensive. $BaSO_4$ however, does not produce a durable calibration surface and is therefore not temporally stable. Mixing the compound with paint effectively increased durability but had the detrimental effect of reducing reflectance (~5% >430nm) particularly in the shortwave spectral region less than

430nm. Still others determine that Italian ceramic tiles maybe a more appropriate target for estimating irradiance [261]. However, these assessments firstly have been focused on the full solar range (350-2500nm) and secondly have not considered the practicality of building a target for airborne campaigns. Ceramic tile is neither a cost effective nor a lightweight material and is therefore not ideal for the proposed application. Given the targeted collection is restricted to a spectral range no longer than 1000nm, the authors conclusions can be revisited to determine, that in fact the paint spectrum is the most appropriate target given cost, availability, spectral non-selectivity, reflectance magnitude and durability.

It is recognized that this experiment does not assess BRDF in the sense that four geometry variables are required to estimate the function *i.e.* $R=f(Az_i, Zn_i, Az_o, Zn_o)$. This analysis coarsely varied illumination zenith and azimuth and observation zenith angles by altering surface inclination and orientation. As such, the surface orientation should be translated into the traditional BRDF factors so that ultimately an appropriate, geometry explicit calibration spectrum can be applied in the radiometric correction process. Additionally, the BRDF sampling strategy produced biased distribution, similar studies should consider a strategy that uniformly samples the geometry space including one that is capable of capturing the backscattered hotspot.

1.5 *Radiometric Correction Conclusions*

Initial static geometry acquisitions suggested which targets were well separated and featureless. The second collection strategy sampled the bidirectional reflectance characteristic of each sample and treated these 48 observations as

distributions, which were, assessed qualitatively through reflectance surfaces and boxplots and statistically through hypothesis testing applying non-parametric analysis of variance and post hoc pairwise comparisons.

Of the initial materials assessed, several of the textiles were derived from plant-based materials. These samples produced a consistent feature in their reflectance responses that reduced their utility as a reference target. The red edge feature is characterized as a relatively sharp increase in reflectance ~680-770nm and is caused by the transition between optical properties of the materials. Spectral features within the ultraviolet and visible range are dominated by the effect of electron energy state transitions where photos at these wavelengths are absorbed by atoms whose electrons migrate to higher energy orbitals, this energy is then dissipated into heat energy (and photosynthesis in live plants). In contrast spectral features within the infrared region are dominated by vibration state transitions, where specific wavelengths are used to drive very specific molecular motions and deformations. Omitting the non-lambertian (specular) reflectance signal, these fore mentioned features are superimposed on the scattering continuum of a given material. The baseline scattering, which is specific to the material, is a function of the angular transmissivity or the refractive index of the components that make up the material and the size and distribution of the particles that make up the medium. The effect of greater frequencies of different angular transmissions (refractive index discontinuities) is an increase in scattering and the measured reflectance. It appears as though the fibrous structure of these plant-based fabrics have retained some of the NIR scattering properties that they

invariably demonstrate while actively growing. The absence of features in short wavelength ranges in the painted fabrics suggested that there was potential for paints to be used for the calibration material. However, there must be a surface to paint, and painting a fabric is not practical, as the paint would ultimately crack producing a heterogeneous target, which is unacceptable. Ultimately, it was determined that with the exception of two, all the plant based and synthetic textiles had apparent features within the spectral range covered by the airborne sensor. The brighter of the two had a reflectance factor of only ~40%. These two targets would be insufficient to capture the full range of radiometric values for the correction of airborne spectrometer datasets. The painted hardboard samples proved to be far superior to all other target material assessed. Qualitatively, the spectra of the painted spectra were much more uniform and extreme. The painted samples were, with the exception of <430nm (attributed to absorption by TiO_2), spectrally flat. The white painted samples where 20% brighter than the brightest textile assessed, while the black painted surfaces were ~1% darker than the darkest textile, considering the visible portion of the spectrum.

The spectroscopy of the painted surfaces analyzed the distributions of location and scale estimates. The analysis of location statistics stratified by sample brightness (dark and bright) was used to indicate the brightest and darkest painted sample and therefore the best material for deriving correction coefficients for airborne datasets. The analysis of the scale statistic was used to establish a hierarchy of targets according to their spectral uniformity and could be used to indicate the best targets for producing more consistent (from channel to channel)

correction residuals. Given the observations are made from different geometries, the variability of the location and scale statistics provided an indication of how isotropic these traits are, under the assumption that each target can have a unique bidirectional reflectance distribution function.

The statistical analysis of the location (spectral median) distributions determined that there was little evidence that the samples had different responses to geometry, evaluated by F-K and B-F tests once stratified by brightness. Analysis of variance (K-W test) stratified by brightness did not produce a significant test for bright targets but did for dark samples. The Wilcoxon post hoc test demonstrated that the Rona dark sample was significantly the darkest sample. Qualitatively, the Rona sample has a drastically more pronounced specular hotspot than the other targets, as seen in figure 7 & 8. This is supported by a significant result for the less conservative F-K variance homogeneity test applied to the dark samples. The hotspot observation suggests that the Rona sample has a more dominant specular reflectance component than the other relatively more lambertian dark samples. Because the hotspot is a narrow feature and the rest of the median geometry surface is uniformly low this sample is still considered the optimal choice of those assessed. There were few observations that would suggest that a white sample was superior to the others, however it is conceded that the Rona bright sample may be preferable as it produced the brightest median value figure 7 & 8 and is the most affordable. From a radiometric separation perspective the two Rona samples are best for calibration.

The statistical analysis of the scale (spectral np-cv) distributions, in parallel with the median analysis, provided little indication that there was a geometry dependent effect on spectral uniformity. Although the F-K test again suggested at least one dark sample had a different variability based on geometry, in opposition to the more conservative B-F test. The analysis of variance (K-W test) demonstrated that the dark samples exhibited greater variance (NP-CV) than the bright samples did. The greater variability exhibited by the dark targets was explained as the signal level approaching the noise baseline and thus the radiometric values having a greater portion of noise. This could also be seen in the measurements of bright samples collected from geometries without direct illumination, where high frequency spectral variations were present at reflectance magnitudes ~0.5%. Given the objective is to determine the best bright and best dark sample for calibration, the samples were stratified by brightness. The analysis of variance (K-W test) provided little evidence that there was a difference in variability (NP-CV) between the bright samples, but did suggest a difference was present between dark samples. The post hoc comparison demonstrated that, of the dark samples, the CIL sample was the least variable. The results of the statistical hypothesis testing of the coefficient of variation data was supported by np-cv surfaces in geometry space, where it is apparent that the surface of the CIL dark sample exhibits less relief than its dark counterparts (Fig. 9 & 10). The similarity of the bright sample surfaces also supports statistical testing. Thus the bright Rona sample is preferable due to its lower cost. If differences were present, the bright nap-cv surfaces might suggest that the CIL sample produces (very

subtly) more uniform spectra given variations in geometry, where there appears to be a greater proportion of low values in the surface. However, the extents of the surface appear to produce greater np-cv values (Fig. 9 & 10). It is concluded that there is little difference in spectral uniformity between the bright targets, while the CIL dark sample is the most spectrally flat of the dark samples. From a spectral uniformity perspective the bright Rona sample and the dark CIL sample is best for radiometric calibration. The pattern observed in the nap-cv surfaces of bright samples closely tracked the pattern of inverse reflectance magnitude. This observation leads us to conclude that the bright samples do not produce shape changes based on changing geometry and that the changes observed are a function of sensor signal to noise ratio. Some of the dark samples on the other hand did exhibit differences attributed to geometry. This observation suggested that the dark targets had different non-lambertian components of their reflectance even though all paint samples were flat finish formulations. The spectral uniformity of the dark samples, although more subtle, also tracked variations in signal to noise, but became less coherent at the surface extremes (large surface zenith angles).

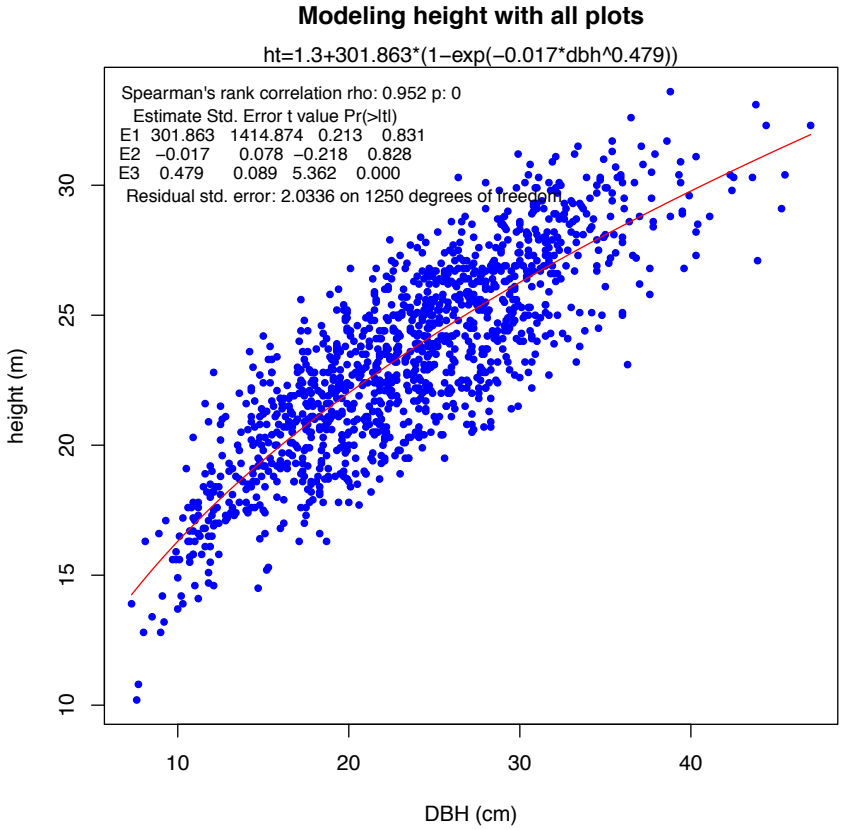
Ideally, targets will be featureless and well separated spectrally [107]. Results suggest that plant-based textiles are not spectrally invariant. Of the materials assessed and in general agreement with [108], optically thick surfaces of latex paints produced the best results. These samples were spectrally invariant in the specified range. However, some samples were more isotropic in terms of reflectance and spectral uniformity depending on the brand and brightness. Targets were constructed and deployed in the summer of 2012 (Fig. 27).

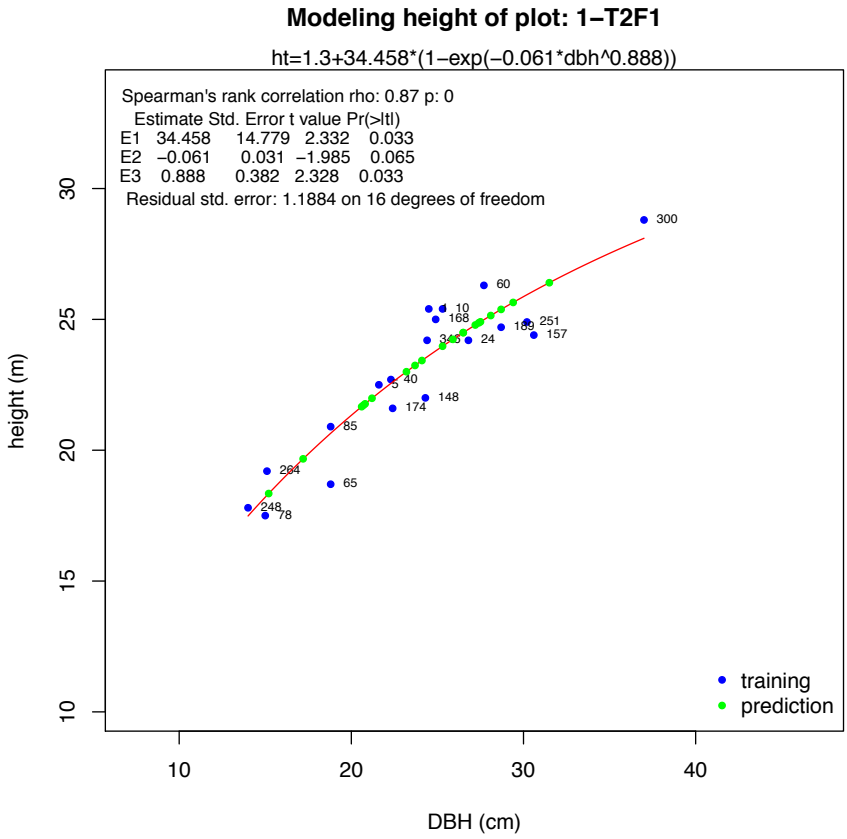


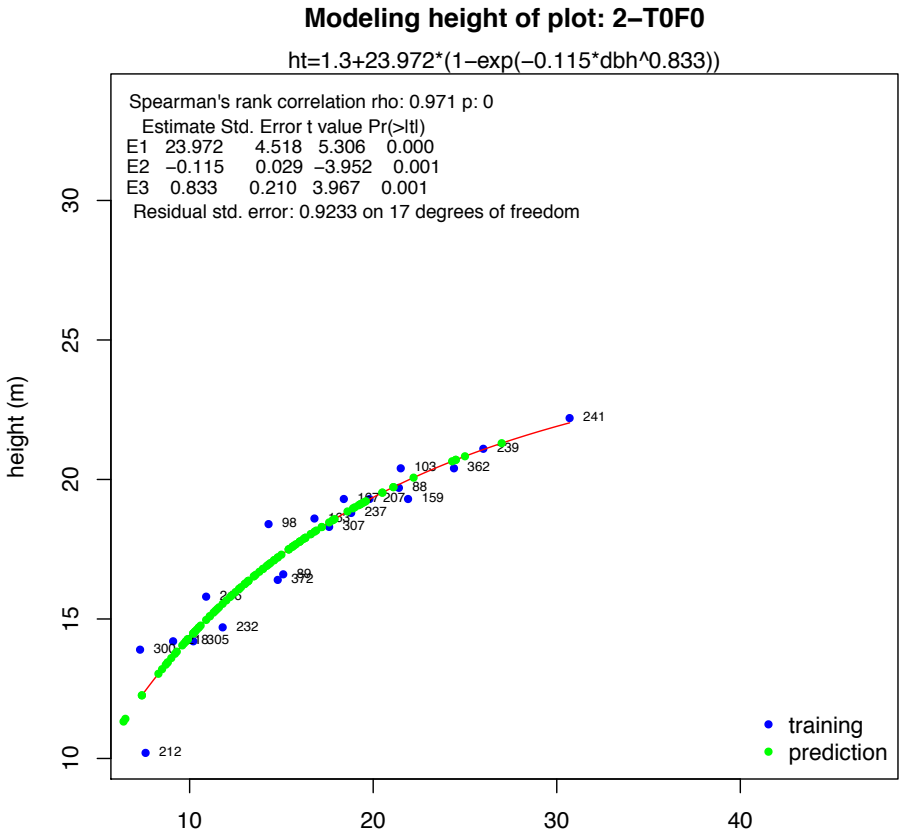
Figure 27 Calibration targets deployed in the field for the airborne campaign on September 19th 2012 for forestry applications, note the vehicle for scale

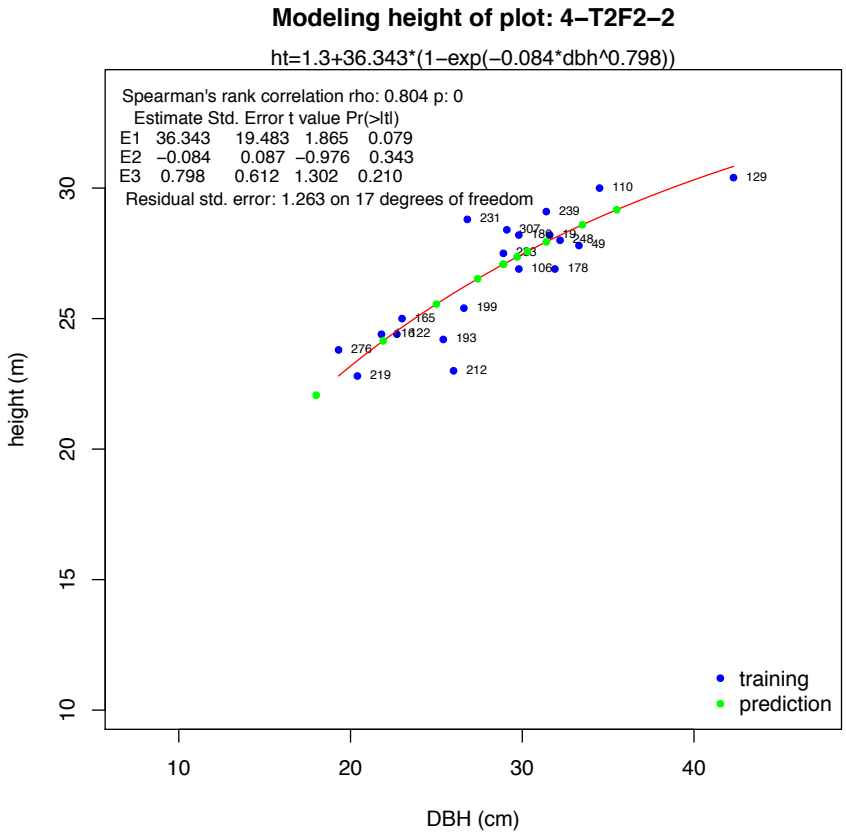
APPENDIX 3: Modelling Tree Height from DBH

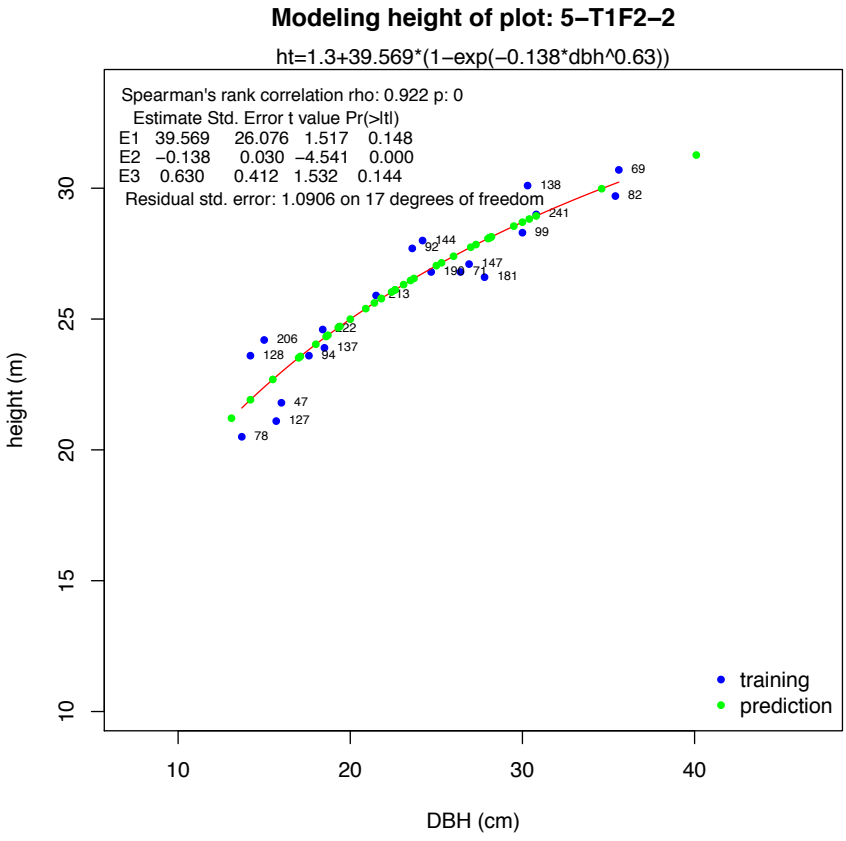
1.1 *Height-DBH Regression Fitting for Sampling Year 2002*

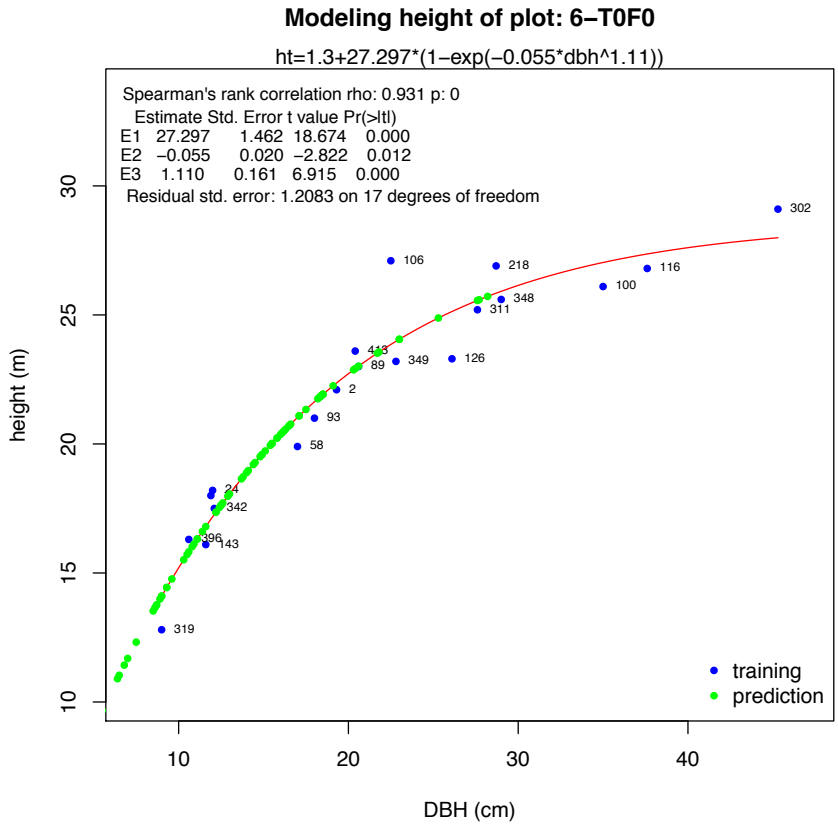


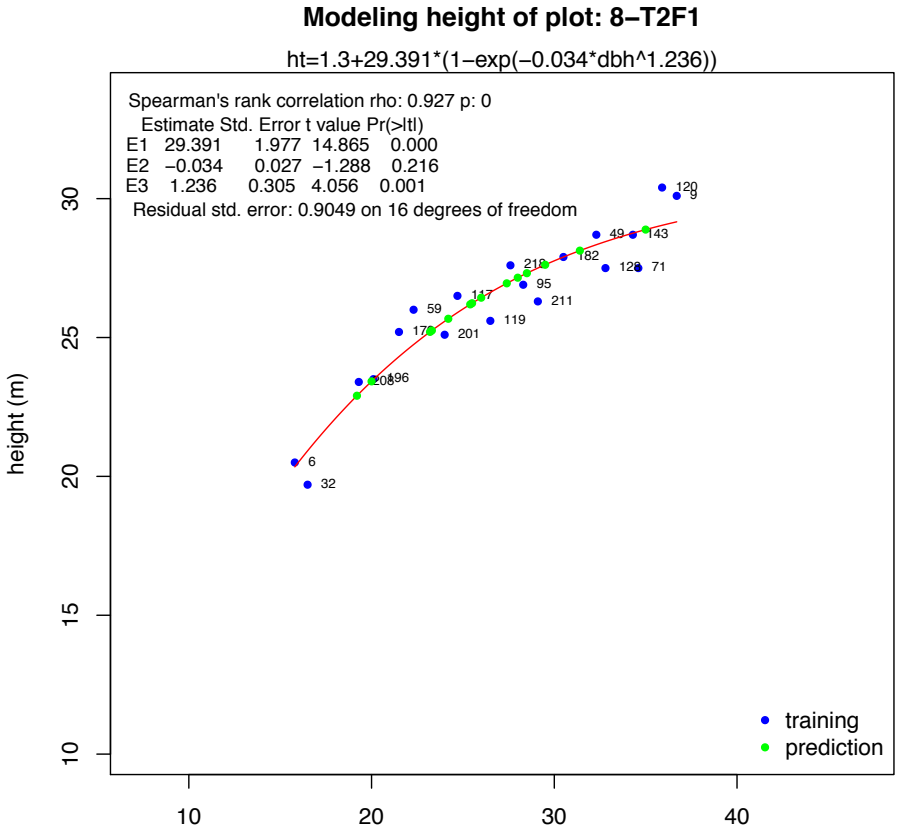

Modeling height of plot: 1–T2F1
ht=1.3+34.458*(1–exp(–0.061*dbh^0.888))
Spearman's rank correlation rho: 0.87 p: 0
Estimate Std. Error t value Pr(>|t|)
E1 34.458 14.779 2.332 0.033
E2 –0.061 0.031 –1.985 0.065
E3 0.888 0.382 2.328 0.033
Residual std. error: 1.1884 on 16 degrees of freedom
height (m)
DBH (cm)
training
prediction

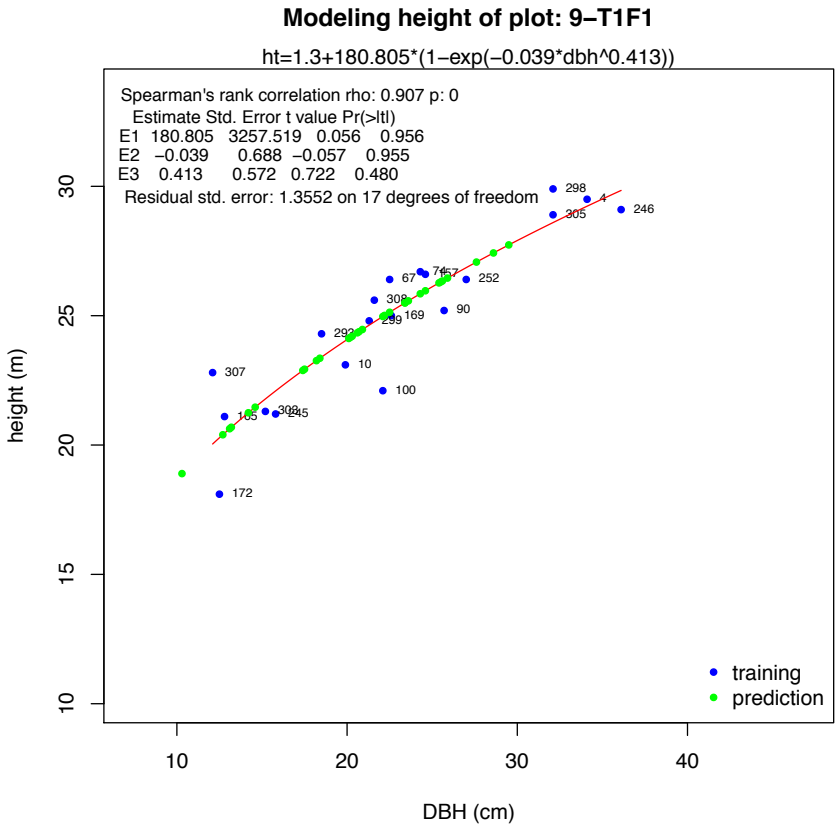

Modeling height of plot: 2–T0F0
ht=1.3+23.972*(1–exp(–0.115*dbh^0.833))
Spearman's rank correlation rho: 0.971 p: 0
Estimate Std. Error t value Pr(>|t|)
E1 23.972 4.518 5.306 0.000
E2 –0.115 0.029 –3.952 0.001
E3 0.833 0.210 3.967 0.001
Residual std. error: 0.9233 on 17 degrees of freedom
height (m)
training
prediction

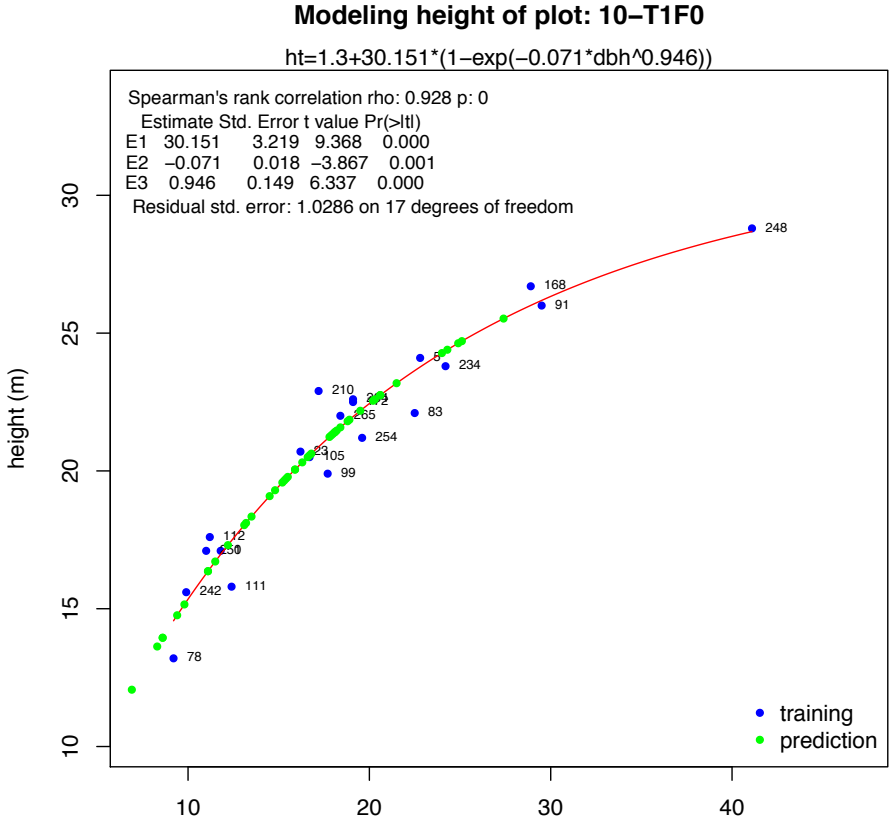

Modeling height of plot: 4–T2F2–2
ht=1.3+36.343*(1–exp(–0.084*dbh^0.798))
Spearman's rank correlation rho: 0.804 p: 0
Estimate Std. Error t value Pr(>|t|)
E1 36.343 19.483 1.865 0.079
E2 –0.084 0.087 –0.976 0.343
E3 0.798 0.612 1.302 0.210
Residual std. error: 1.263 on 17 degrees of freedom
height (m)
DBH (cm)
training
prediction

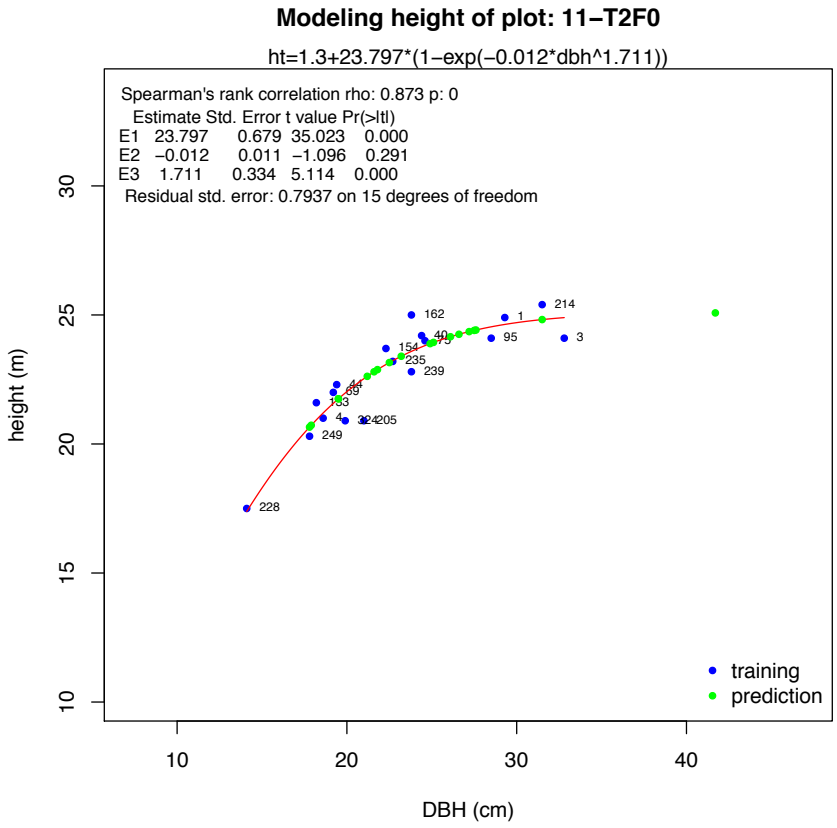

Modeling height of plot: 5–T1F2–2
ht=1.3+39.569*(1–exp(–0.138*dbh^0.63))
Spearman's rank correlation rho: 0.922 p: 0
Estimate Std. Error t value Pr(>|t|)
E1 39.569 26.076 1.517 0.148
E2 –0.138 0.030 –4.541 0.000
E3 0.630 0.412 1.532 0.144
Residual std. error: 1.0906 on 17 degrees of freedom
height (m)
DBH (cm)
training
prediction

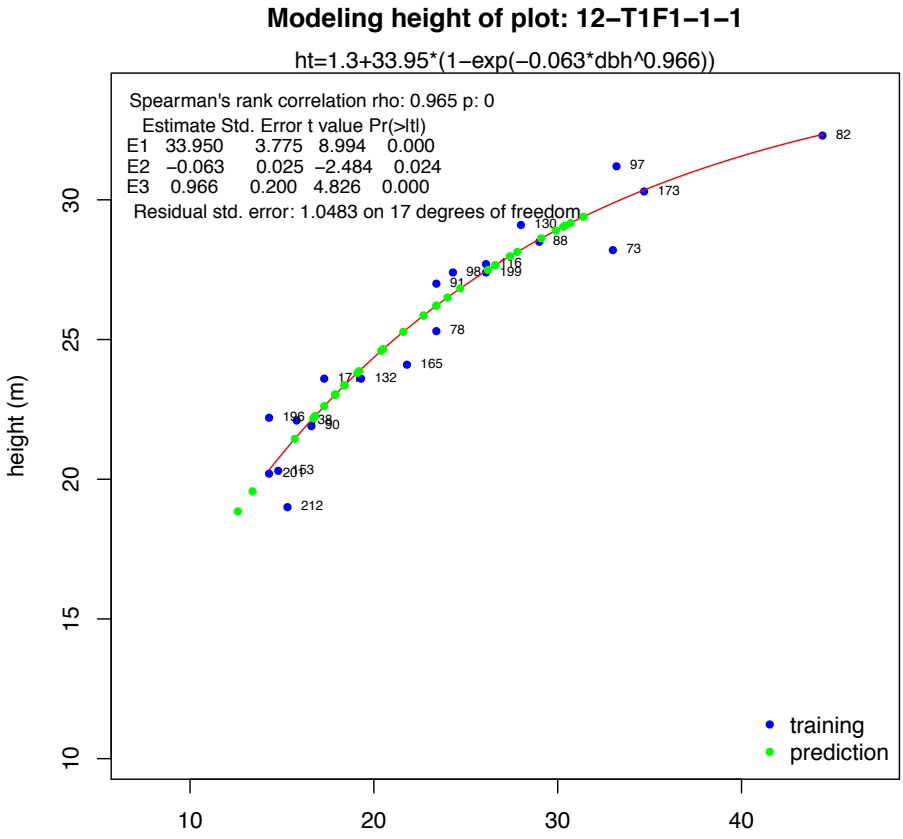

Modeling height of plot: 6–T0F0
ht=1.3+27.297*(1−exp(−0.055*dbh^1.11))
Spearman's rank correlation rho: 0.931 p: 0
Estimate Std. Error t value Pr(>|t|)
E1 27.297 1.462 18.674 0.000
E2 −0.055 0.020 −2.822 0.012
E3 1.110 0.161 6.915 0.000
Residual std. error: 1.2083 on 17 degrees of freedom
height (m)
DBH (cm)
training
prediction

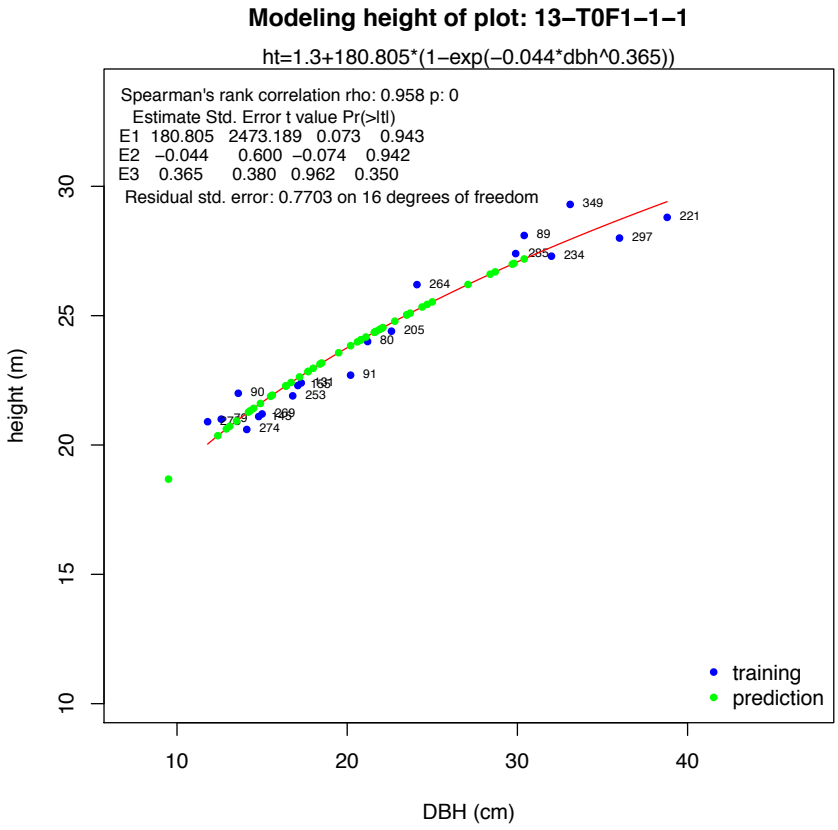

Modeling height of plot: 8–T2F1
ht=1.3+29.391*(1−exp(−0.034*dbh^1.236))
Spearman's rank correlation rho: 0.927 p: 0
Estimate Std. Error t value Pr(>|t|)
E1 29.391 1.977 14.865 0.000
E2 −0.034 0.027 −1.288 0.216
E3 1.236 0.305 4.056 0.001
Residual std. error: 0.9049 on 16 degrees of freedom
height (m)
training
prediction

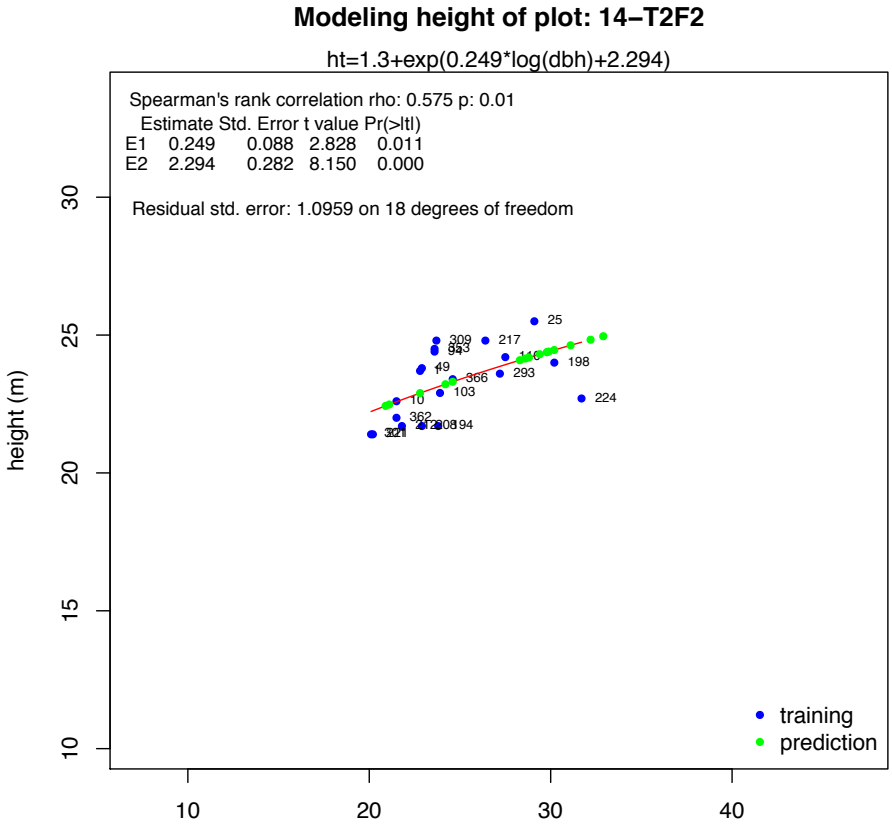

Modeling height of plot: 9–T1F1
ht=1.3+180.805*(1−exp(−0.039*dbh^0.413))
Spearman's rank correlation rho: 0.907 p: 0
Estimate Std. Error t value Pr(>|t|)
E1 180.805 3257.519 0.056 0.956
E2 −0.039 0.688 −0.057 0.955
E3 0.413 0.572 0.722 0.480
Residual std. error: 1.3552 on 17 degrees of freedom
height (m)
DBH (cm)
training
prediction

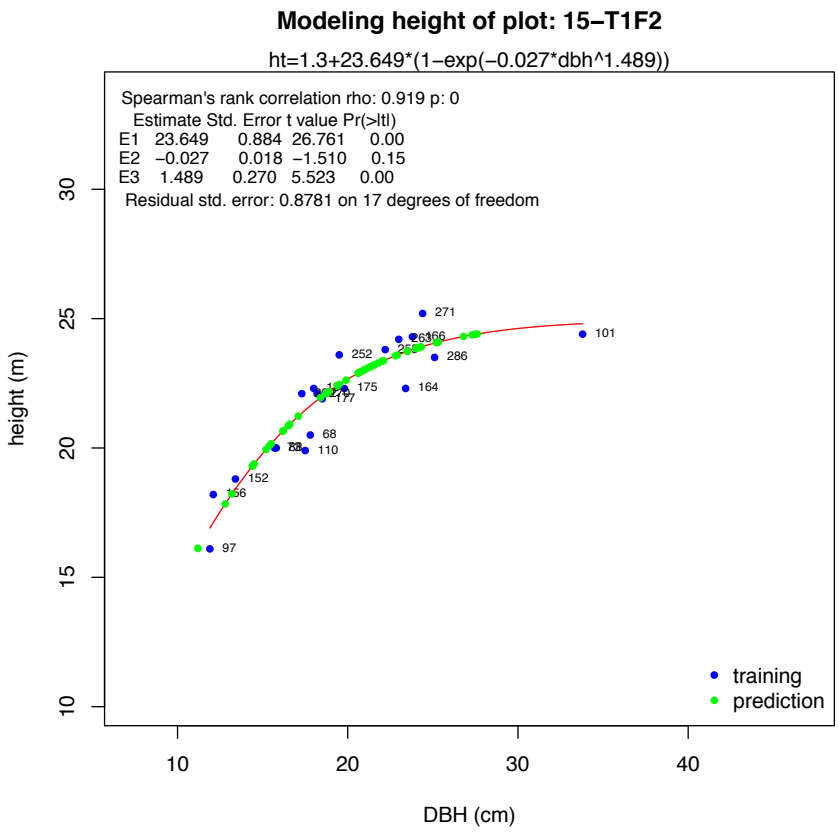

Modeling height of plot: 10–T1F0
ht=1.3+30.151*(1−exp(−0.071*dbh^0.946))
Spearman's rank correlation rho: 0.928 p: 0
Estimate Std. Error t value Pr(>|t|)
E1 30.151 3.219 9.368 0.000
E2 −0.071 0.018 −3.867 0.001
E3 0.946 0.149 6.337 0.000
Residual std. error: 1.0286 on 17 degrees of freedom
height (m)
training
prediction

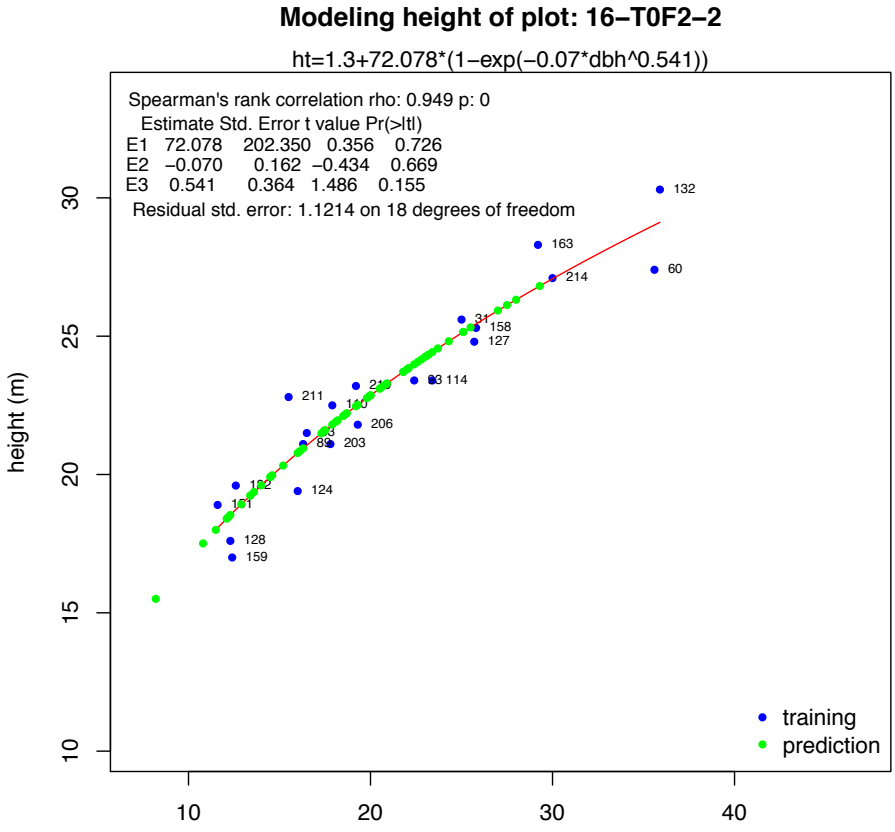

Modeling height of plot: 11−T2F0
ht=1.3+23.797*(1−exp(−0.012*dbh^1.711))
Spearman's rank correlation rho: 0.873 p: 0
Estimate Std. Error t value Pr(>|t|)
E1 23.797 0.679 35.023 0.000
E2 −0.012 0.011 −1.096 0.291
E3 1.711 0.334 5.114 0.000
Residual std. error: 0.7937 on 15 degrees of freedom
height (m)
DBH (cm)
training
prediction

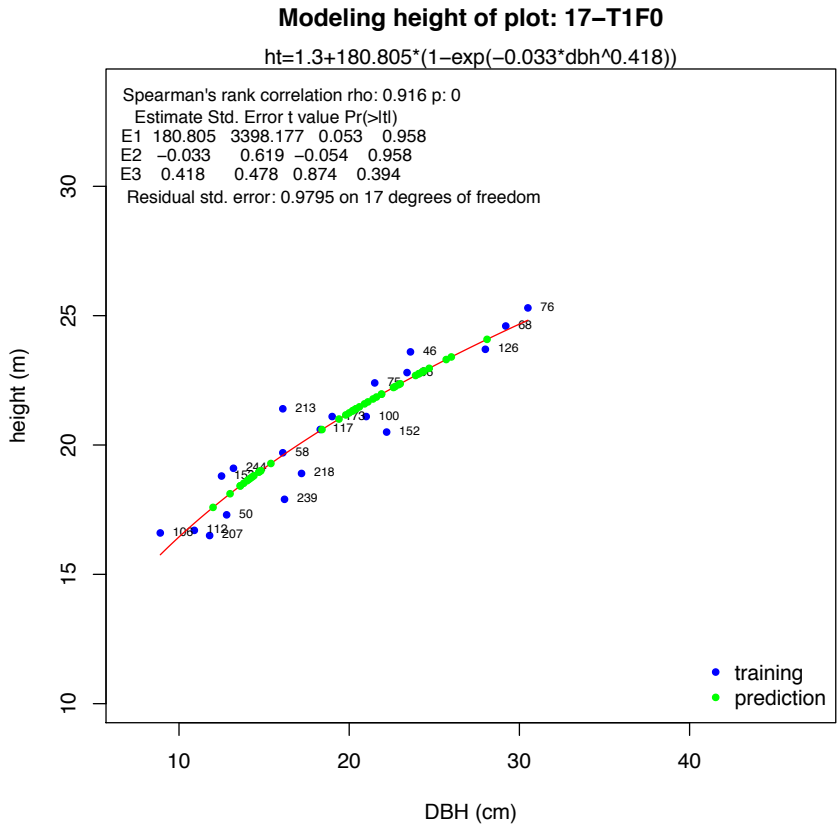

Modeling height of plot: 12−T1F1−1−1
ht=1.3+33.95*(1−exp(−0.063*dbh^0.966))
Spearman's rank correlation rho: 0.965 p: 0
Estimate Std. Error t value Pr(>|t|)
E1 33.950 3.775 8.994 0.000
E2 −0.063 0.025 −2.484 0.024
E3 0.966 0.200 4.826 0.000
Residual std. error: 1.0483 on 17 degrees of freedom
height (m)
training
prediction

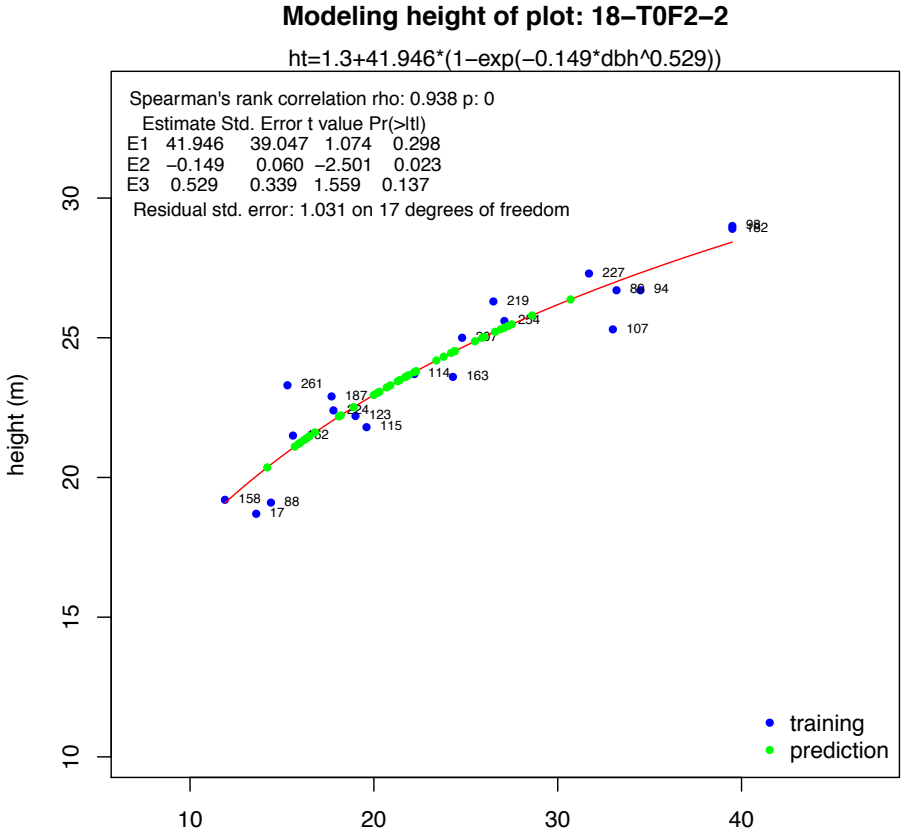

Modeling height of plot: 13−T0F1−1−1
ht=1.3+180.805*(1−exp(−0.044*dbh^0.365))
Spearman's rank correlation rho: 0.958 p: 0
Estimate Std. Error t value Pr(>|t|)
E1 180.805 2473.189 0.073 0.943
E2 −0.044 0.600 −0.074 0.942
E3 0.365 0.380 0.962 0.350
Residual std. error: 0.7703 on 16 degrees of freedom
height (m)
DBH (cm)
training
prediction

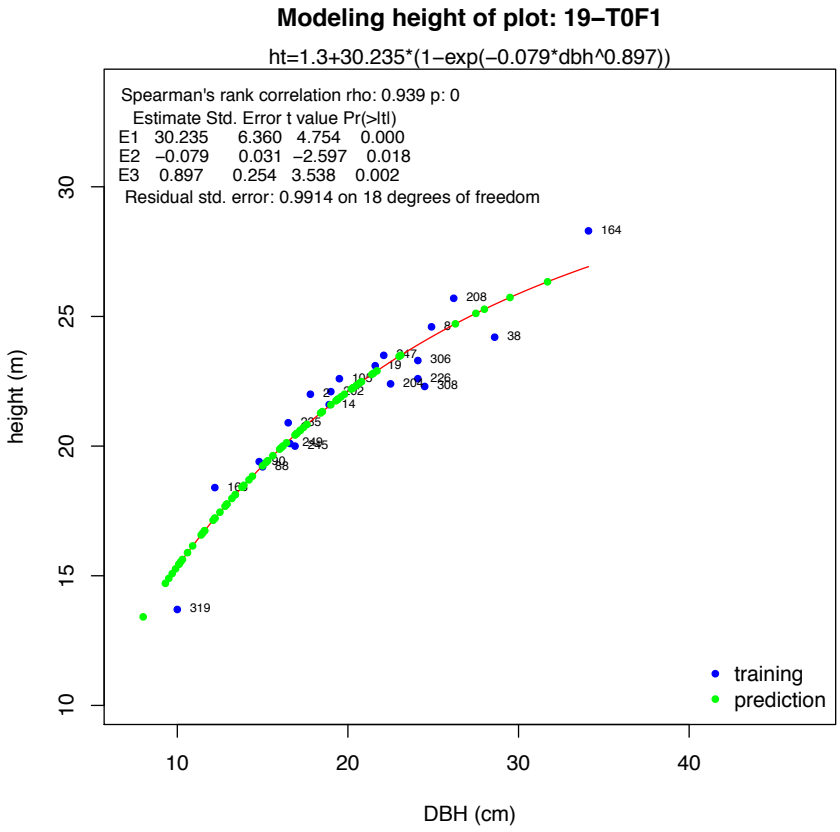

Modeling height of plot: 14−T2F2
ht=1.3+exp(0.249*log(dbh)+2.294)
Spearman's rank correlation rho: 0.575 p: 0.01
Estimate Std. Error t value Pr(>|t|)
E1 0.249 0.088 2.828 0.011
E2 2.294 0.282 8.150 0.000
Residual std. error: 1.0959 on 18 degrees of freedom
height (m)
training
prediction

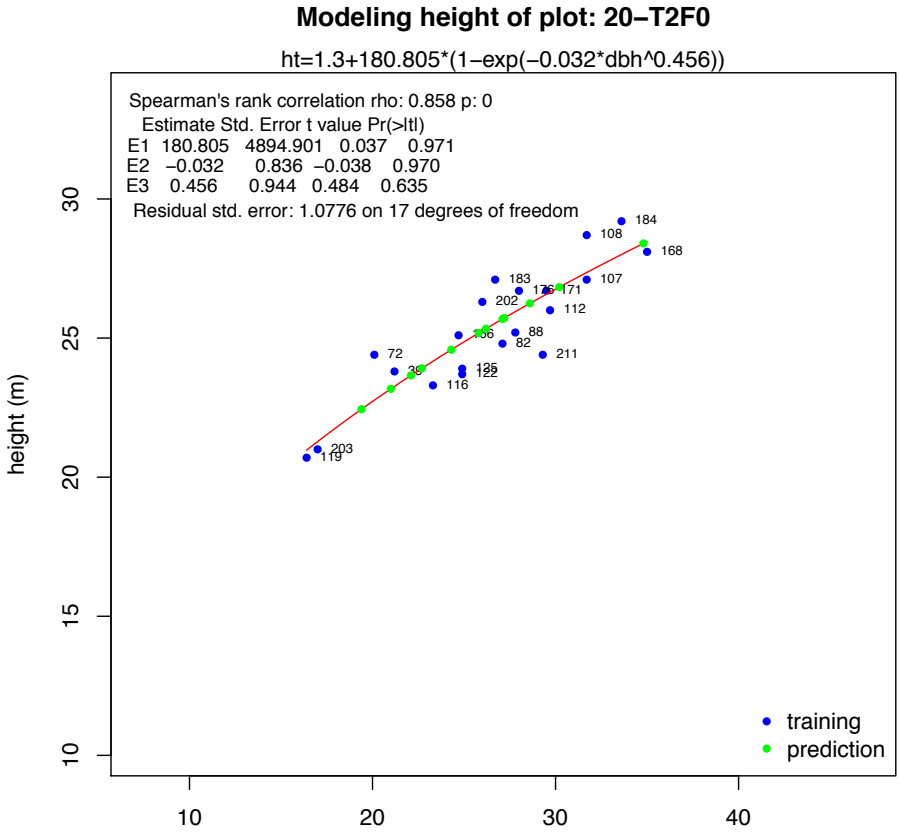

Modeling height of plot: 15–T1F2
ht=1.3+23.649*(1−exp(−0.027*dbh^1.489))
Spearman's rank correlation rho: 0.919 p: 0
Estimate Std. Error t value Pr(>|t|)
E1 23.649 0.884 26.761 0.00
E2 −0.027 0.018 −1.510 0.15
E3 1.489 0.270 5.523 0.00
Residual std. error: 0.8781 on 17 degrees of freedom
height (m)
DBH (cm)
training
prediction

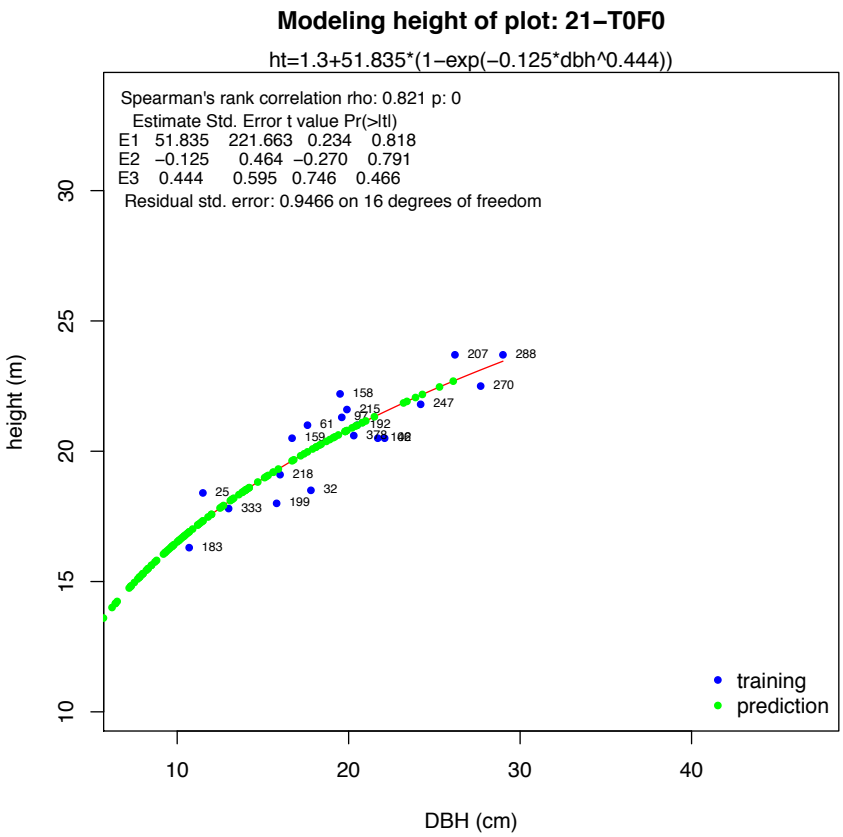

Modeling height of plot: 16–T0F2–2
ht=1.3+72.078*(1−exp(−0.07*dbh^0.541))
Spearman's rank correlation rho: 0.949 p: 0
Estimate Std. Error t value Pr(>|t|)
E1 72.078 202.350 0.356 0.726
E2 −0.070 0.162 −0.434 0.669
E3 0.541 0.364 1.486 0.155
Residual std. error: 1.1214 on 18 degrees of freedom
height (m)
training
prediction

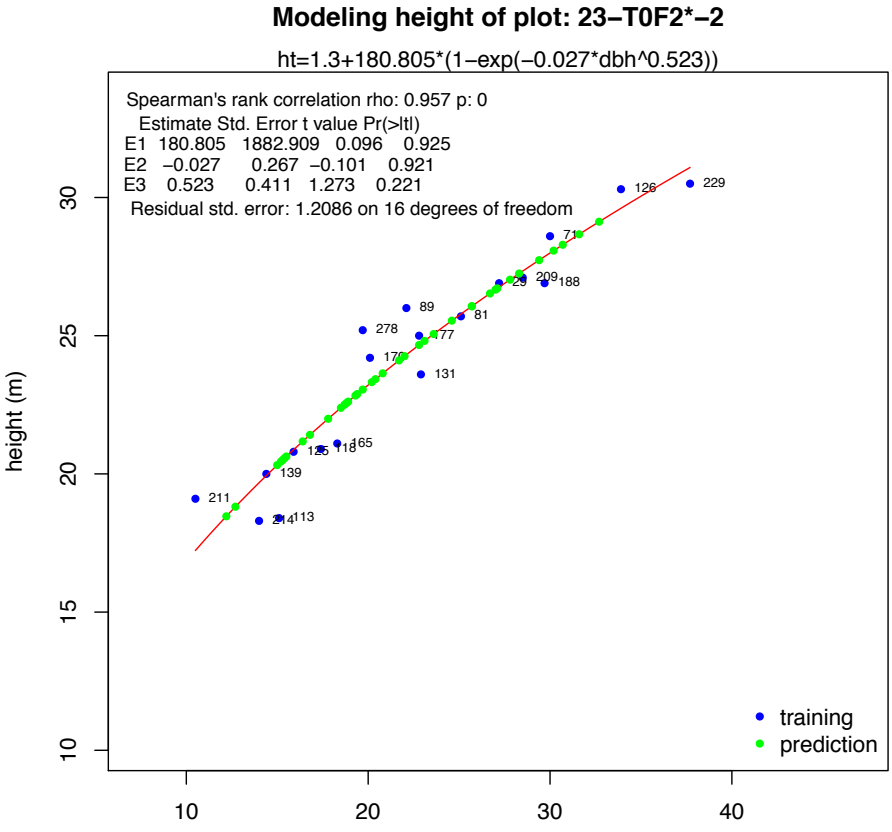

Modeling height of plot: 17−T1F0
ht=1.3+180.805*(1−exp(−0.033*dbh^0.418))
Spearman's rank correlation rho: 0.916 p: 0
Estimate Std. Error t value Pr(>|t|)
E1 180.805 3398.177 0.053 0.958
E2 −0.033 0.619 −0.054 0.958
E3 0.418 0.478 0.874 0.394
Residual std. error: 0.9795 on 17 degrees of freedom
height (m)
DBH (cm)
training
prediction

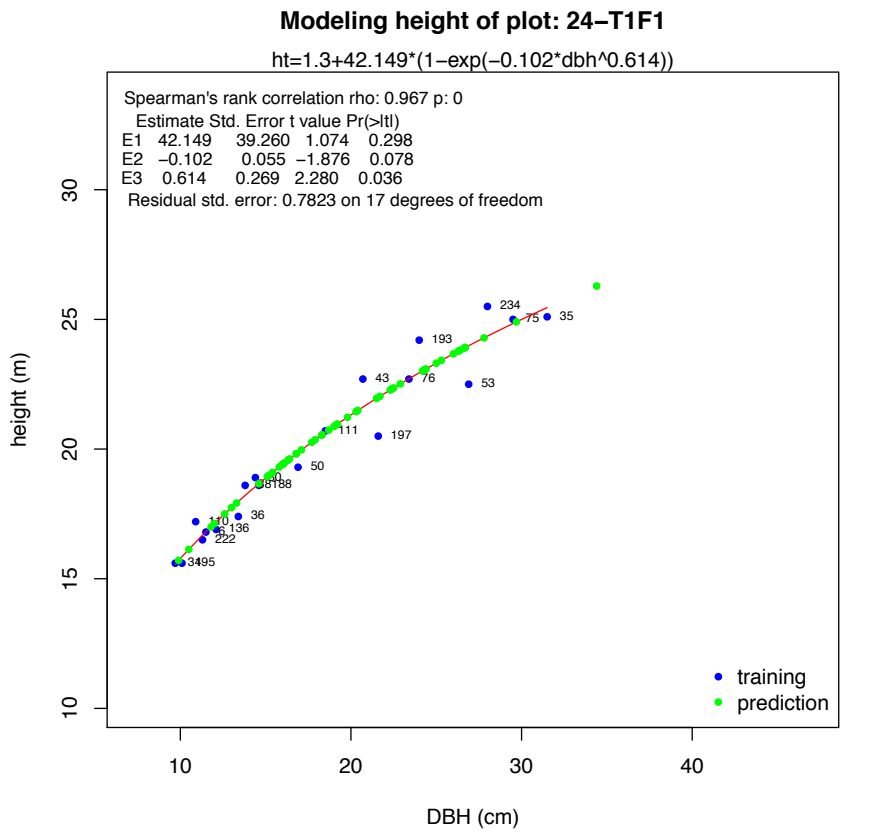

Modeling height of plot: 18−T0F2−2
ht=1.3+41.946*(1−exp(−0.149*dbh^0.529))
Spearman's rank correlation rho: 0.938 p: 0
Estimate Std. Error t value Pr(>|t|)
E1 41.946 39.047 1.074 0.298
E2 −0.149 0.060 −2.501 0.023
E3 0.529 0.339 1.559 0.137
Residual std. error: 1.031 on 17 degrees of freedom
height (m)
training
prediction

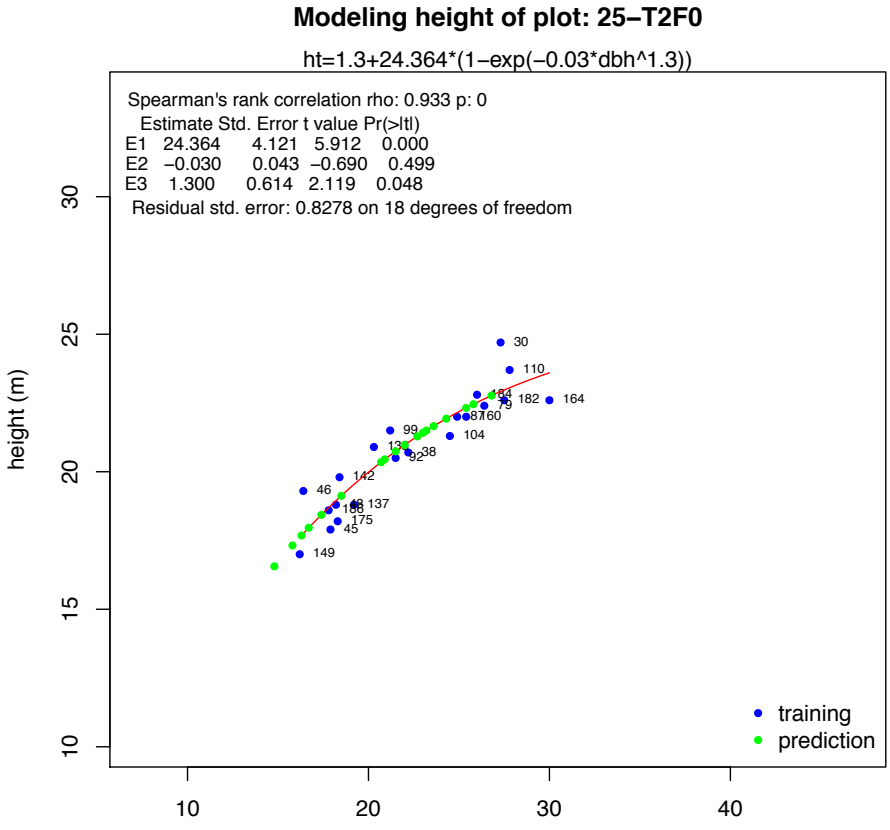

Modeling height of plot: 19–T0F1
ht=1.3+30.235*(1−exp(−0.079*dbh^0.897))
Spearman's rank correlation rho: 0.939 p: 0
Estimate Std. Error t value Pr(>|t|)
E1 30.235 6.360 4.754 0.000
E2 −0.079 0.031 −2.597 0.018
E3 0.897 0.254 3.538 0.002
Residual std. error: 0.9914 on 18 degrees of freedom
height (m)
DBH (cm)
training
prediction

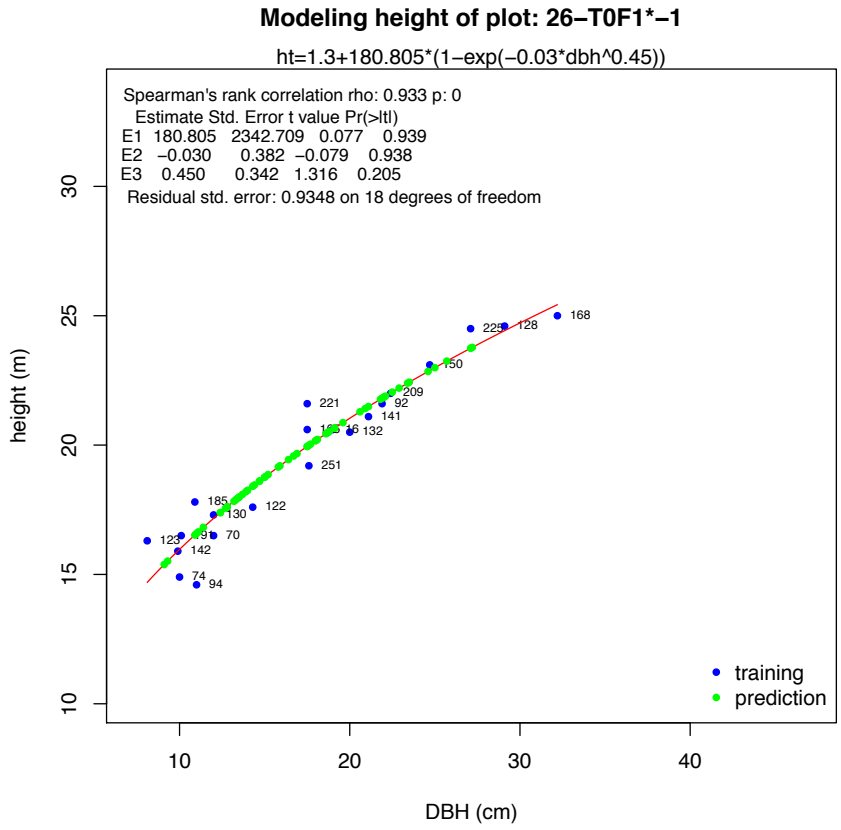

Modeling height of plot: 20–T2F0
ht=1.3+180.805*(1−exp(−0.032*dbh^0.456))
Spearman's rank correlation rho: 0.858 p: 0
Estimate Std. Error t value Pr(>|t|)
E1 180.805 4894.901 0.037 0.971
E2 −0.032 0.836 −0.038 0.970
E3 0.456 0.944 0.484 0.635
Residual std. error: 1.0776 on 17 degrees of freedom
height (m)
training
prediction

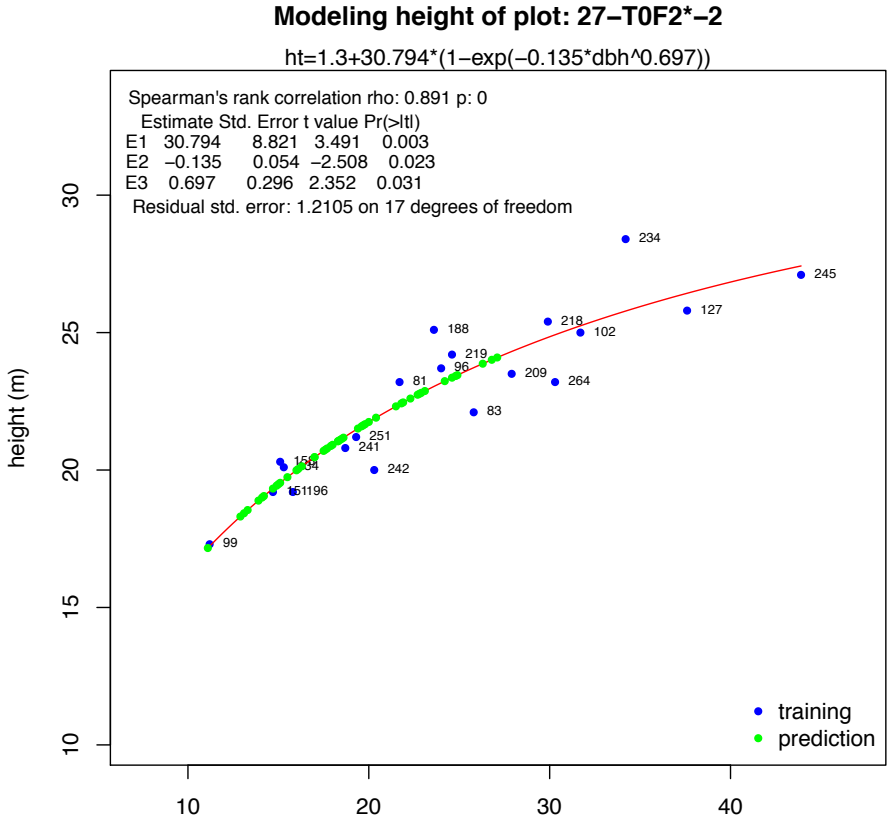

Modeling height of plot: 21–T0F0
ht=1.3+51.835*(1−exp(−0.125*dbh^0.444))
Spearman's rank correlation rho: 0.821 p: 0
Estimate Std. Error t value Pr(>|t|)
E1 51.835 221.663 0.234 0.818
E2 −0.125 0.464 −0.270 0.791
E3 0.444 0.595 0.746 0.466
Residual std. error: 0.9466 on 16 degrees of freedom
height (m)
DBH (cm)
training
prediction

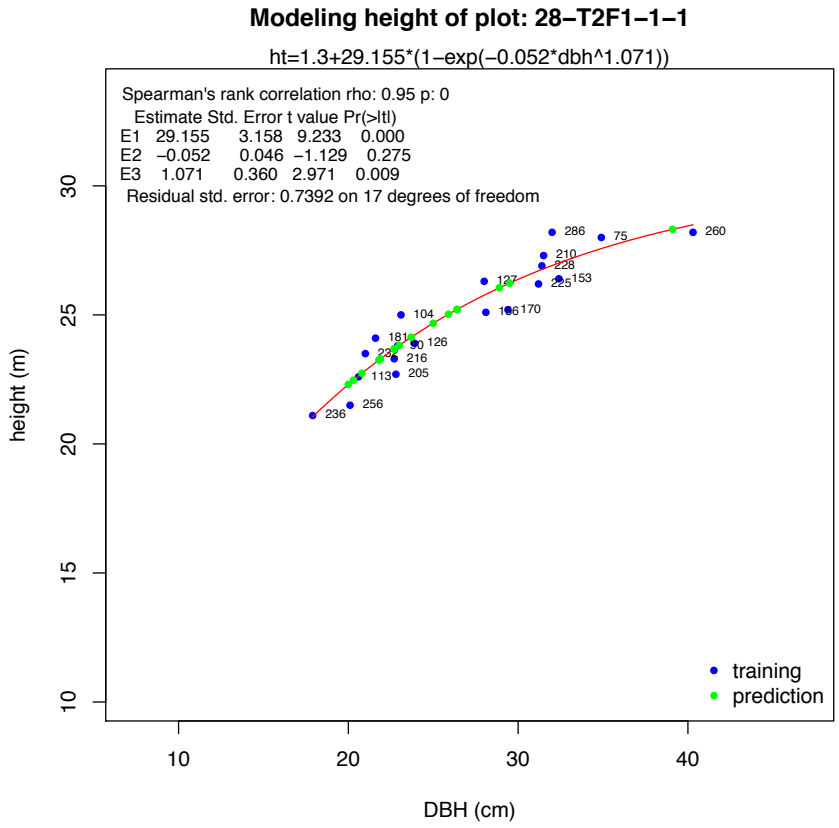

Modeling height of plot: 23–T0F2*–2
ht=1.3+180.805*(1−exp(−0.027*dbh^0.523))
Spearman's rank correlation rho: 0.957 p: 0
Estimate Std. Error t value Pr(>|t|)
E1 180.805 1882.909 0.096 0.925
E2 −0.027 0.267 −0.101 0.921
E3 0.523 0.411 1.273 0.221
Residual std. error: 1.2086 on 16 degrees of freedom
height (m)
training
prediction

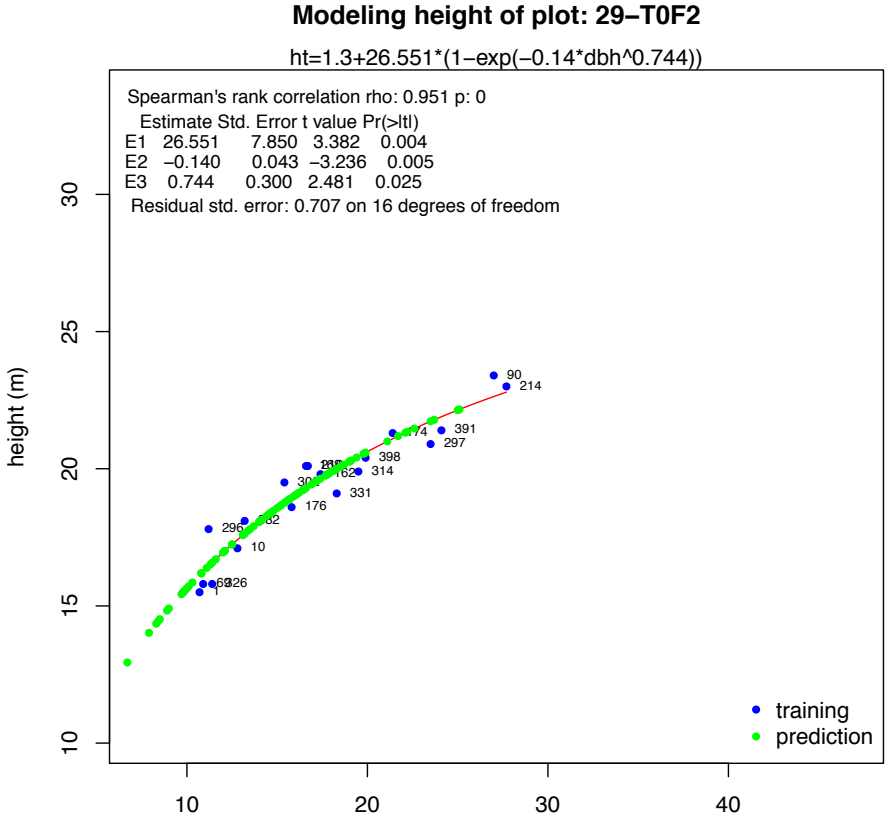

Modeling height of plot: 24−T1F1
ht=1.3+42.149*(1−exp(−0.102*dbh^0.614))
Spearman's rank correlation rho: 0.967 p: 0
Estimate Std. Error t value Pr(>|t|)
E1 42.149 39.260 1.074 0.298
E2 −0.102 0.055 −1.876 0.078
E3 0.614 0.269 2.280 0.036
Residual std. error: 0.7823 on 17 degrees of freedom
height (m)
DBH (cm)
training
prediction

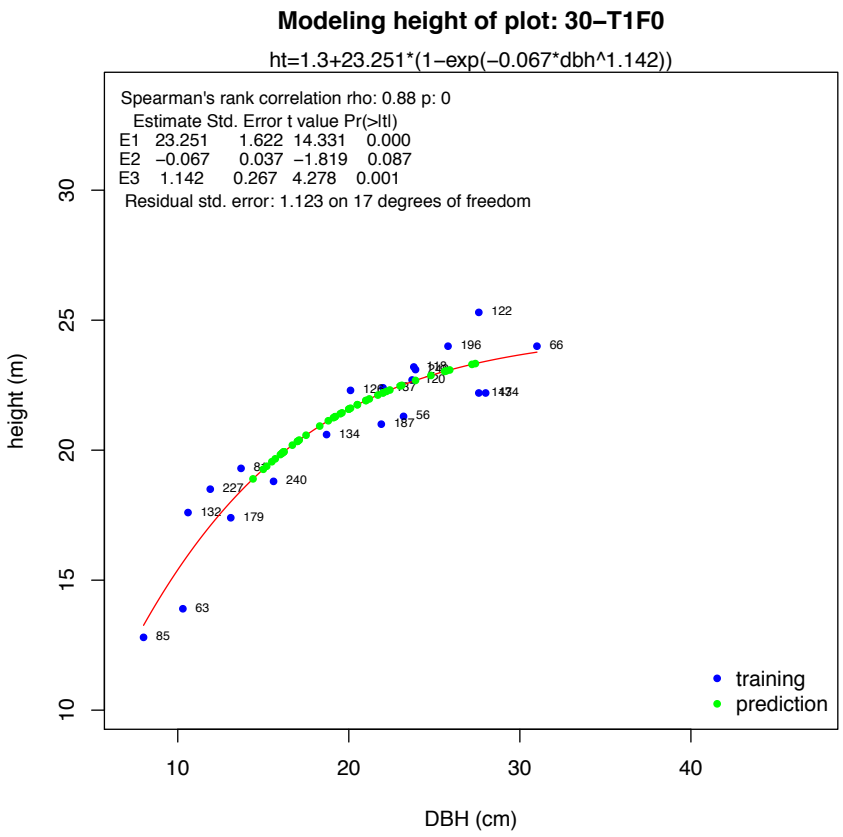

Modeling height of plot: 25−T2F0
ht=1.3+24.364*(1−exp(−0.03*dbh^1.3))
Spearman's rank correlation rho: 0.933 p: 0
Estimate Std. Error t value Pr(>|t|)
E1 24.364 4.121 5.912 0.000
E2 −0.030 0.043 −0.690 0.499
E3 1.300 0.614 2.119 0.048
Residual std. error: 0.8278 on 18 degrees of freedom
height (m)
training
prediction

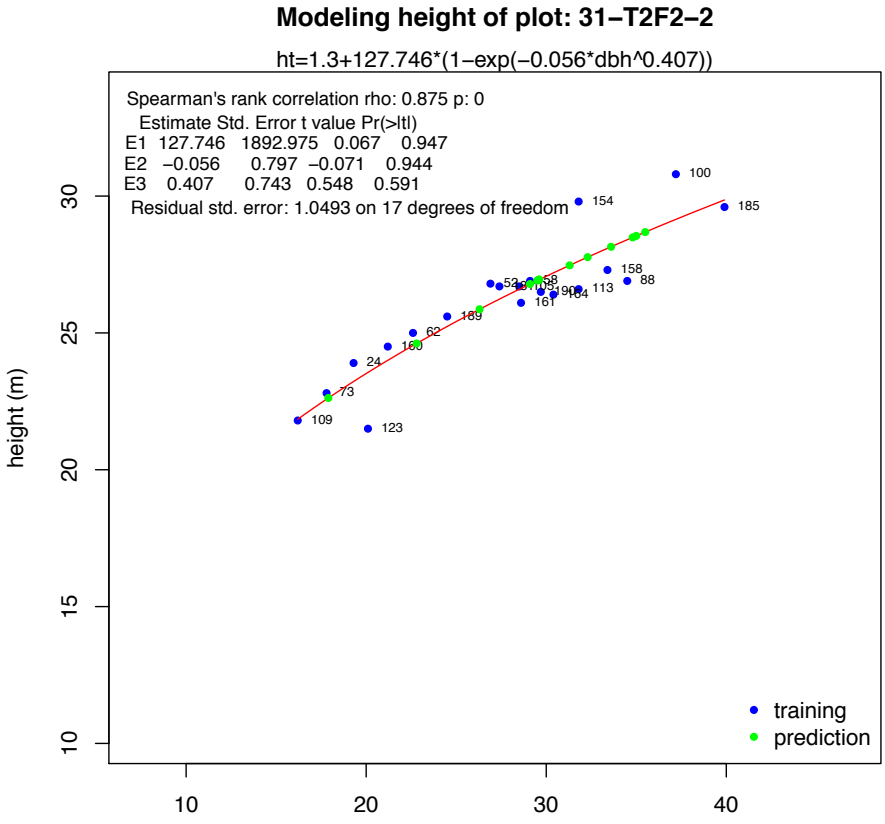

Modeling height of plot: 26−T0F1*−1
ht=1.3+180.805*(1−exp(−0.03*dbh^0.45))
Spearman's rank correlation rho: 0.933 p: 0
Estimate Std. Error t value Pr(>|t|)
E1 180.805 2342.709 0.077 0.939
E2 −0.030 0.382 −0.079 0.938
E3 0.450 0.342 1.316 0.205
Residual std. error: 0.9348 on 18 degrees of freedom
height (m)
DBH (cm)
training
prediction

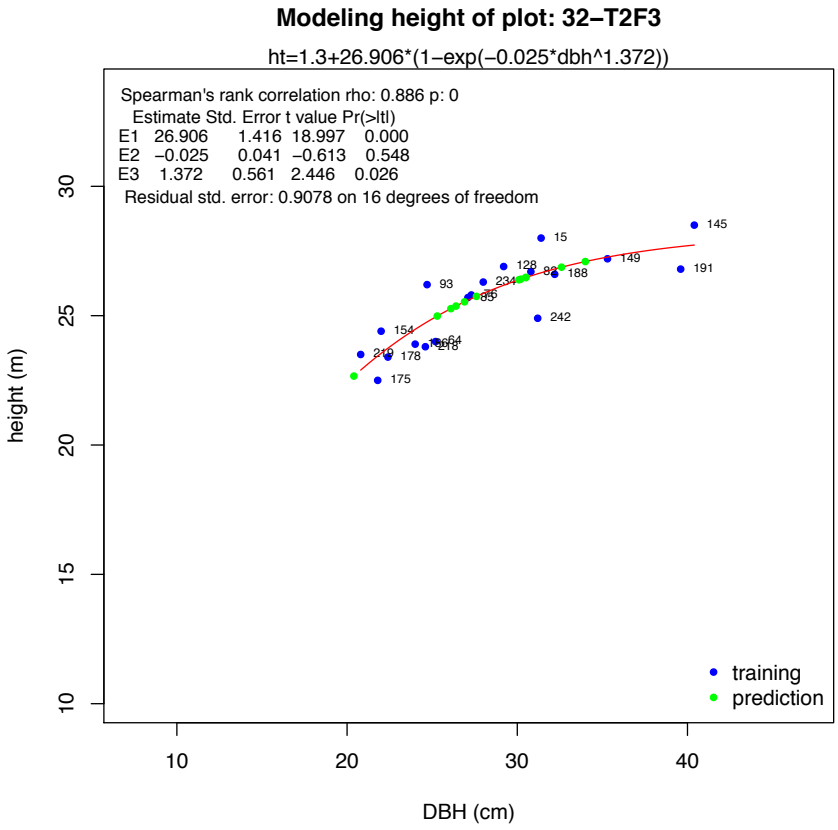

Modeling height of plot: 27−T0F2*−2
ht=1.3+30.794*(1−exp(−0.135*dbh^0.697))
Spearman's rank correlation rho: 0.891 p: 0
Estimate Std. Error t value Pr(>|t|)
E1 30.794 8.821 3.491 0.003
E2 −0.135 0.054 −2.508 0.023
E3 0.697 0.296 2.352 0.031
Residual std. error: 1.2105 on 17 degrees of freedom
height (m)
training
prediction

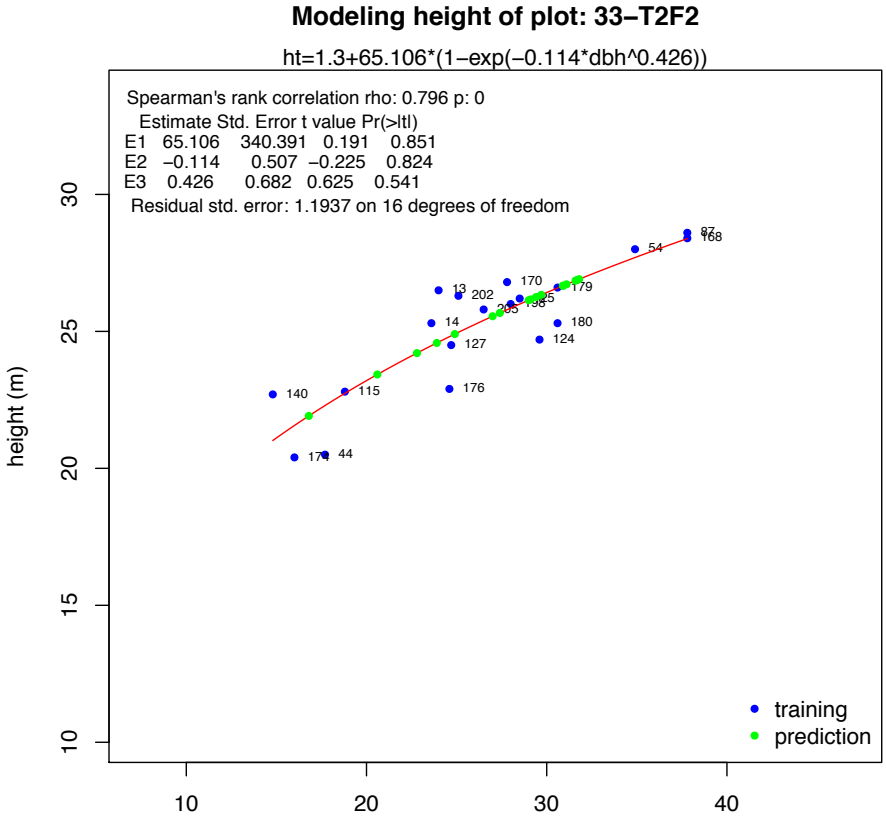

Modeling height of plot: 28−T2F1−1−1
ht=1.3+29.155*(1−exp(−0.052*dbh^1.071))
Spearman's rank correlation rho: 0.95 p: 0
Estimate Std. Error t value Pr(>|t|)
E1 29.155 3.158 9.233 0.000
E2 −0.052 0.046 −1.129 0.275
E3 1.071 0.360 2.971 0.009
Residual std. error: 0.7392 on 17 degrees of freedom
height (m)
DBH (cm)
training
prediction

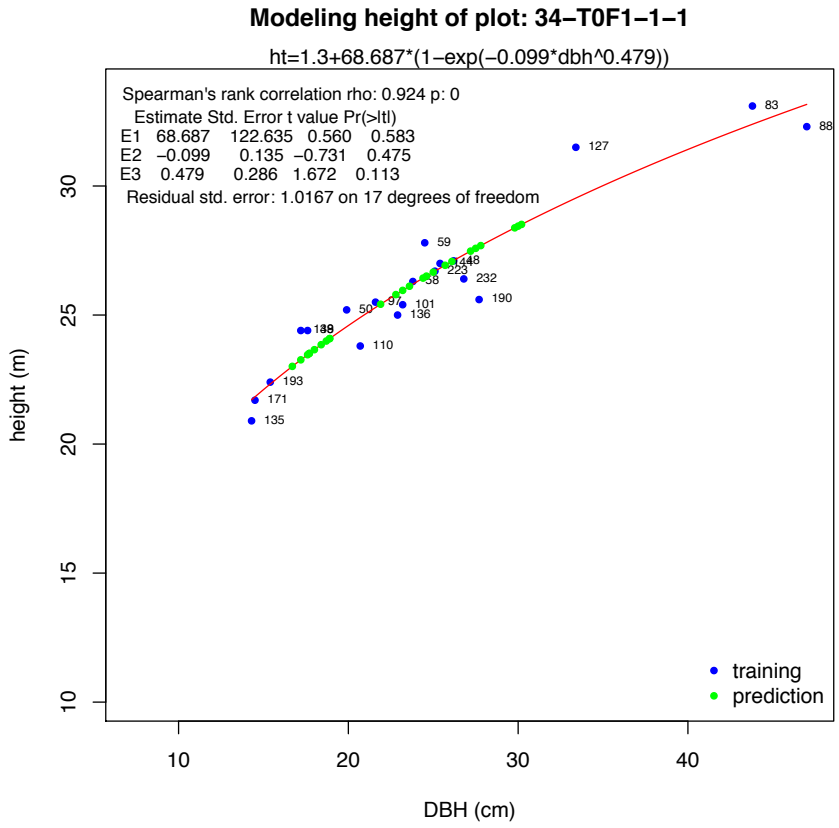

Modeling height of plot: 29−T0F2
ht=1.3+26.551*(1−exp(−0.14*dbh^0.744))
Spearman's rank correlation rho: 0.951 p: 0
Estimate Std. Error t value Pr(>|t|)
E1 26.551 7.850 3.382 0.004
E2 −0.140 0.043 −3.236 0.005
E3 0.744 0.300 2.481 0.025
Residual std. error: 0.707 on 16 degrees of freedom
height (m)
training
prediction

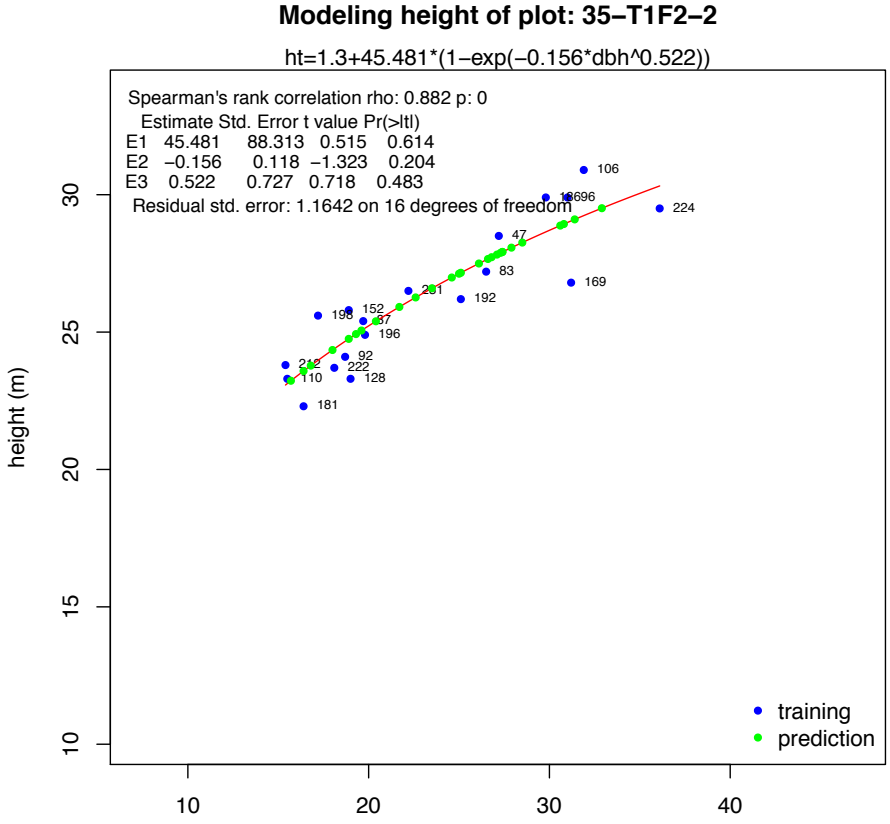

Modeling height of plot: 30–T1F0
ht=1.3+23.251*(1–exp(–0.067*dbh^1.142))
Spearman's rank correlation rho: 0.88 p: 0
Estimate Std. Error t value Pr(>|t|)
E1 23.251 1.622 14.331 0.000
E2 –0.067 0.037 –1.819 0.087
E3 1.142 0.267 4.278 0.001
Residual std. error: 1.123 on 17 degrees of freedom
height (m)
DBH (cm)
training
prediction

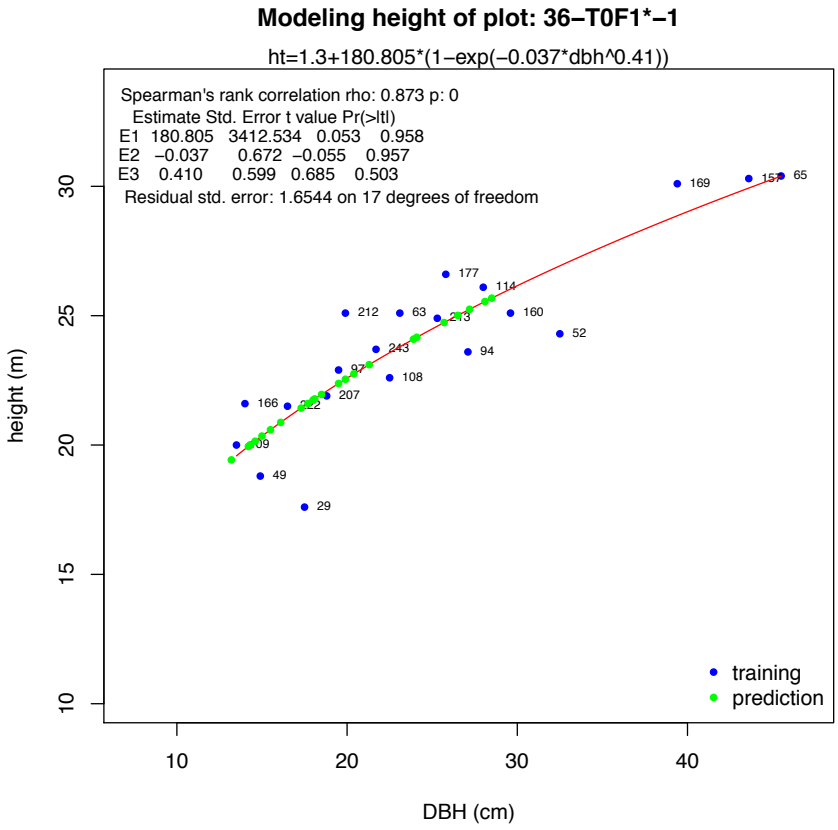

Modeling height of plot: 31–T2F2–2
ht=1.3+127.746*(1–exp(–0.056*dbh^0.407))
Spearman's rank correlation rho: 0.875 p: 0
Estimate Std. Error t value Pr(>|t|)
E1 127.746 1892.975 0.067 0.947
E2 –0.056 0.797 –0.071 0.944
E3 0.407 0.743 0.548 0.591
Residual std. error: 1.0493 on 17 degrees of freedom
height (m)
training
prediction

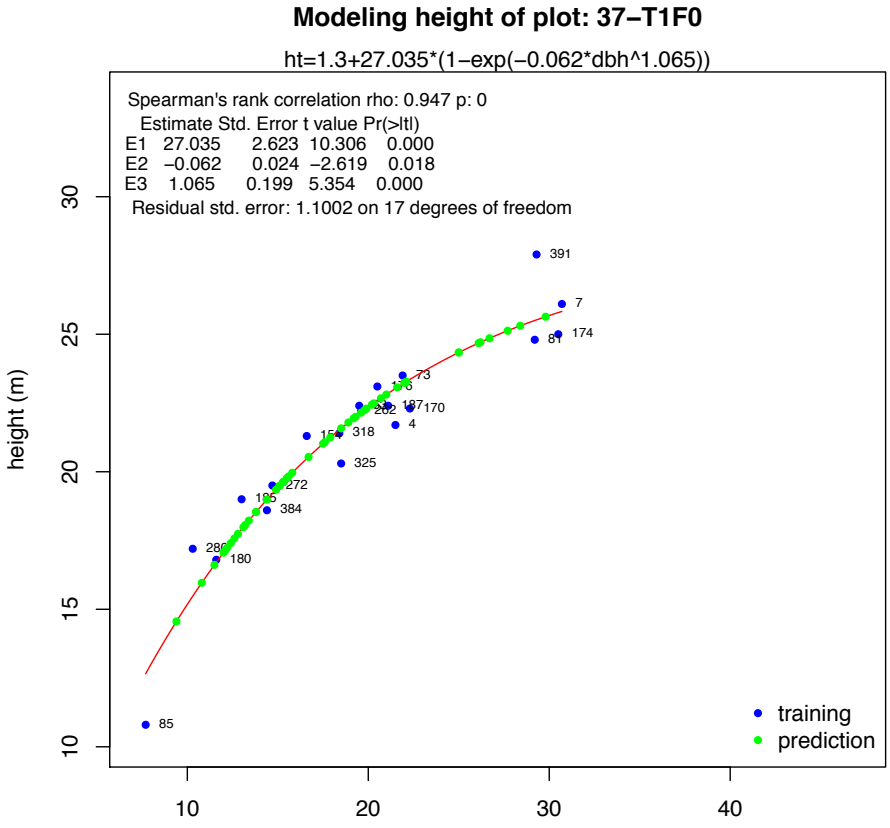

Modeling height of plot: 32−T2F3
ht=1.3+26.906*(1−exp(−0.025*dbh^1.372))
Spearman's rank correlation rho: 0.886 p: 0
Estimate Std. Error t value Pr(>|t|)
E1 26.906 1.416 18.997 0.000
E2 −0.025 0.041 −0.613 0.548
E3 1.372 0.561 2.446 0.026
Residual std. error: 0.9078 on 16 degrees of freedom
height (m)
DBH (cm)
training
prediction

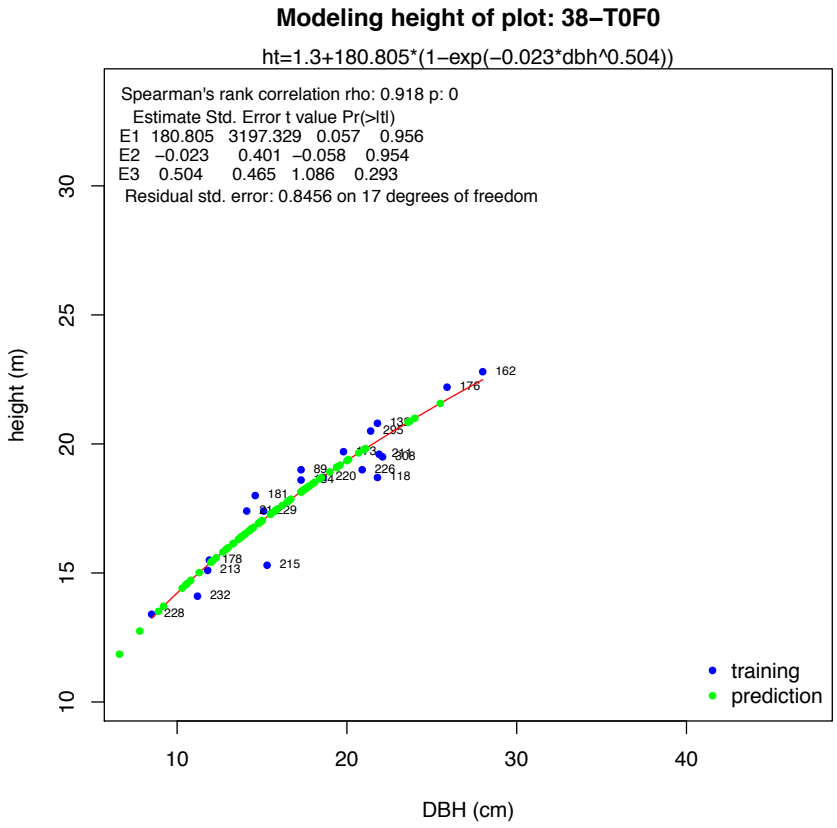

Modeling height of plot: 33−T2F2
ht=1.3+65.106*(1−exp(−0.114*dbh^0.426))
Spearman's rank correlation rho: 0.796 p: 0
Estimate Std. Error t value Pr(>|t|)
E1 65.106 340.391 0.191 0.851
E2 −0.114 0.507 −0.225 0.824
E3 0.426 0.682 0.625 0.541
Residual std. error: 1.1937 on 16 degrees of freedom
height (m)
training
prediction

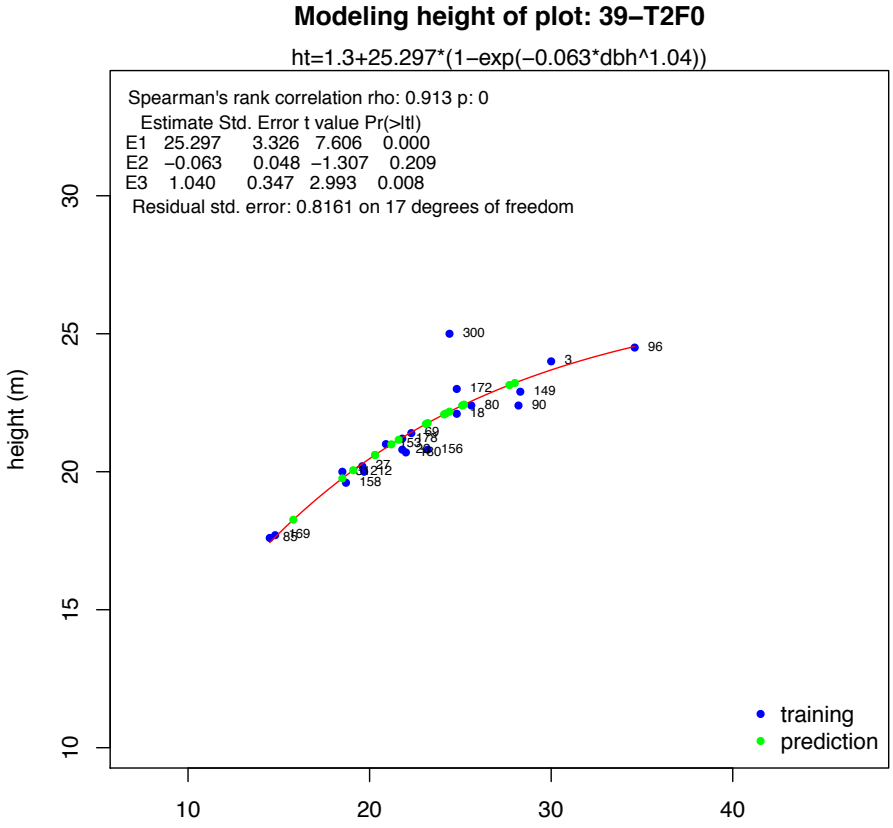

Modeling height of plot: 34–T0F1–1–1
ht=1.3+68.687*(1–exp(–0.099*dbh^0.479))
Spearman's rank correlation rho: 0.924 p: 0
Estimate Std. Error t value Pr(>|t|)
E1 68.687 122.635 0.560 0.583
E2 –0.099 0.135 –0.731 0.475
E3 0.479 0.286 1.672 0.113
Residual std. error: 1.0167 on 17 degrees of freedom
height (m)
DBH (cm)
training
prediction

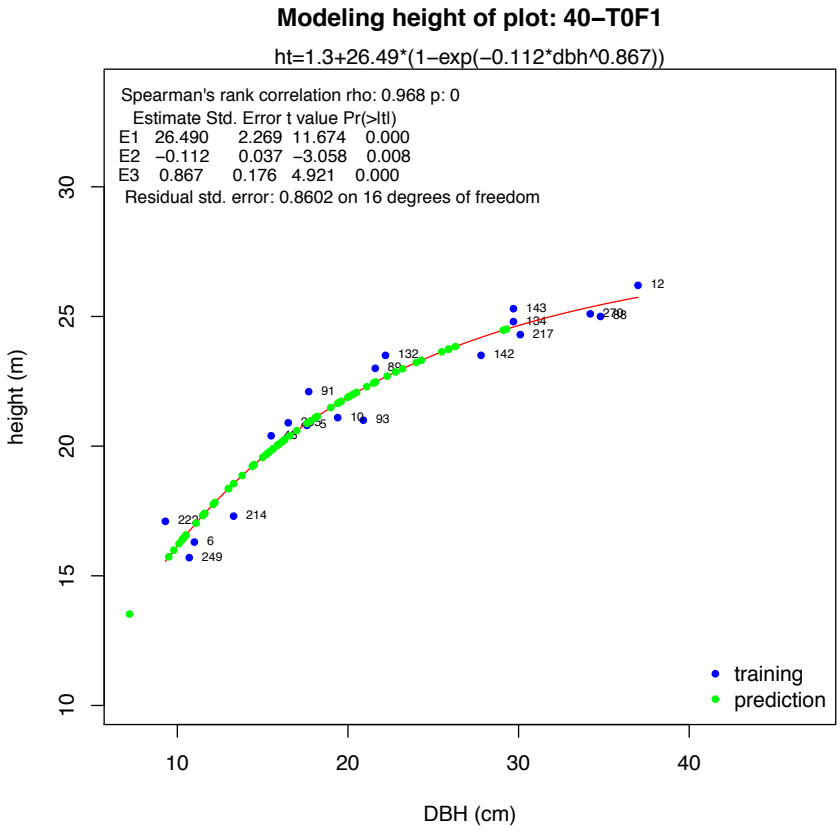

Modeling height of plot: 35–T1F2–2
ht=1.3+45.481*(1–exp(–0.156*dbh^0.522))
Spearman's rank correlation rho: 0.882 p: 0
Estimate Std. Error t value Pr(>|t|)
E1 45.481 88.313 0.515 0.614
E2 –0.156 0.118 –1.323 0.204
E3 0.522 0.727 0.718 0.483
Residual std. error: 1.1642 on 16 degrees of freedom
height (m)
training
prediction

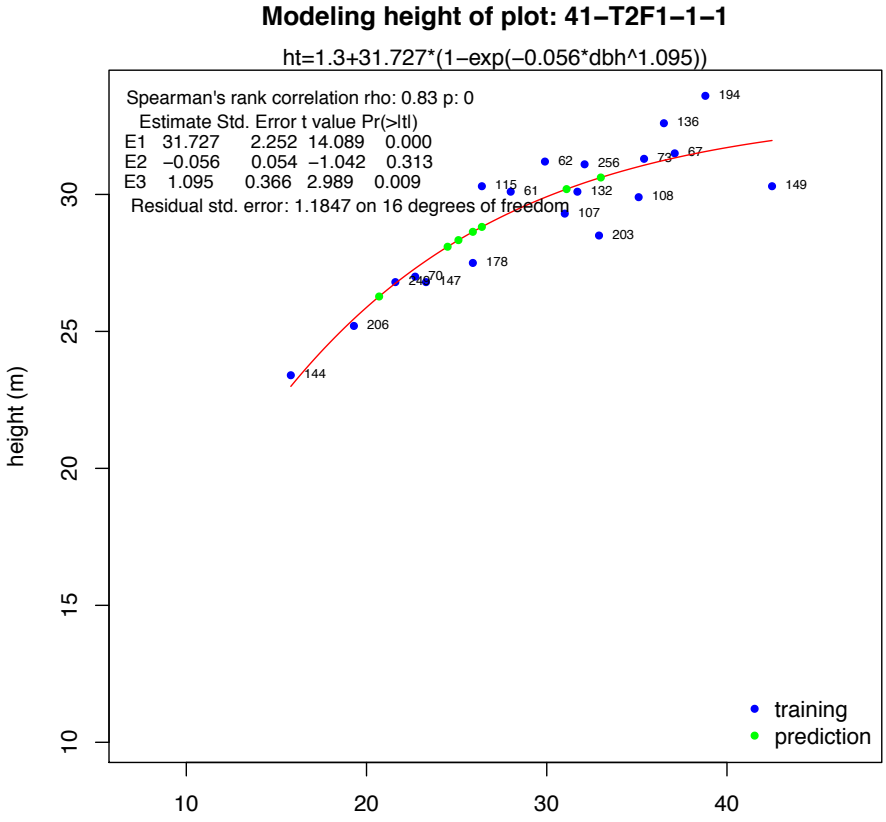

Modeling height of plot: 36−T0F1*−1
ht=1.3+180.805*(1−exp(−0.037*dbh^0.41))
Spearman's rank correlation rho: 0.873 p: 0
Estimate Std. Error t value Pr(>|t|)
E1 180.805 3412.534 0.053 0.958
E2 −0.037 0.672 −0.055 0.957
E3 0.410 0.599 0.685 0.503
Residual std. error: 1.6544 on 17 degrees of freedom
height (m)
DBH (cm)
training
prediction

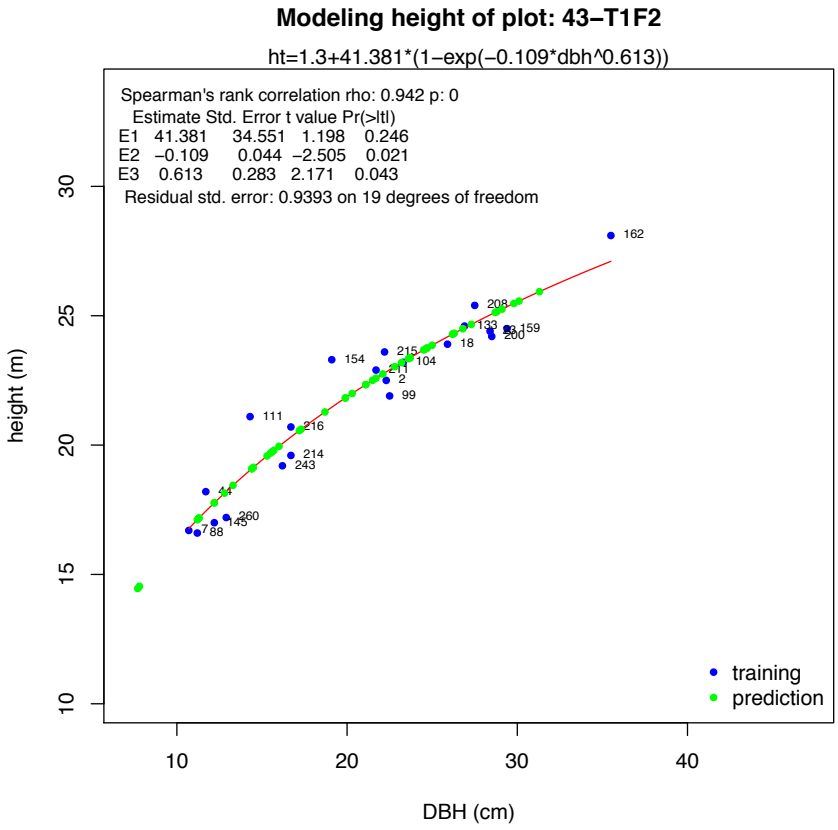

Modeling height of plot: 37−T1F0
ht=1.3+27.035*(1−exp(−0.062*dbh^1.065))
Spearman's rank correlation rho: 0.947 p: 0
Estimate Std. Error t value Pr(>|t|)
E1 27.035 2.623 10.306 0.000
E2 −0.062 0.024 −2.619 0.018
E3 1.065 0.199 5.354 0.000
Residual std. error: 1.1002 on 17 degrees of freedom
height (m)
training
prediction

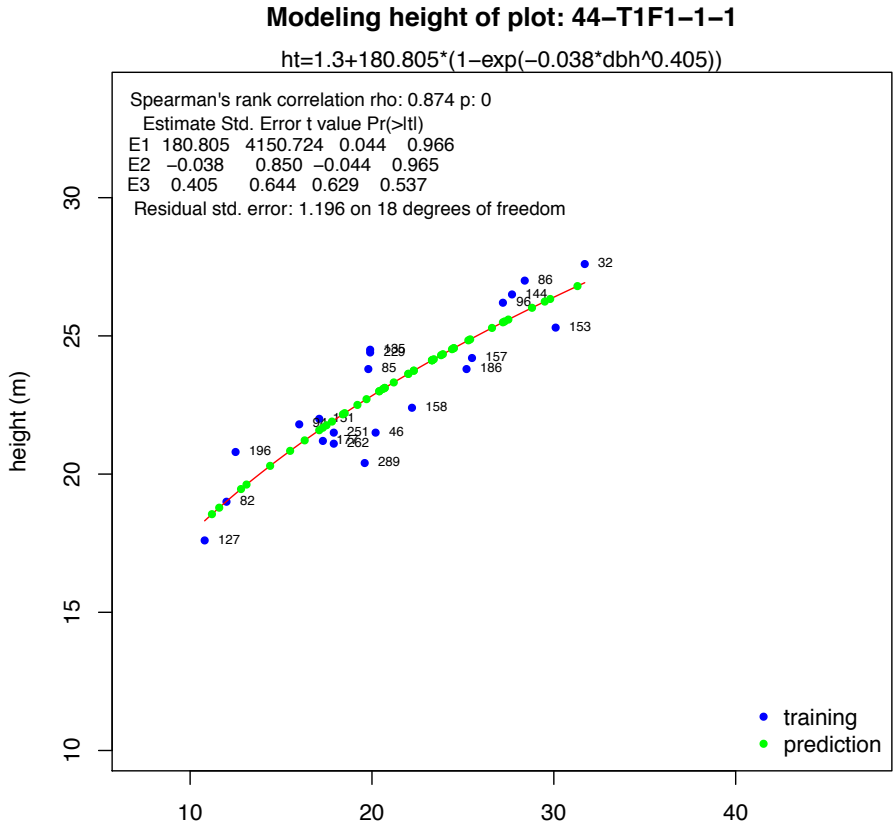

Modeling height of plot: 38−T0F0
ht=1.3+180.805*(1−exp(−0.023*dbh^0.504))
Spearman's rank correlation rho: 0.918 p: 0
Estimate Std. Error t value Pr(>|t|)
E1 180.805 3197.329 0.057 0.956
E2 −0.023 0.401 −0.058 0.954
E3 0.504 0.465 1.086 0.293
Residual std. error: 0.8456 on 17 degrees of freedom
height (m)
DBH (cm)
training
prediction

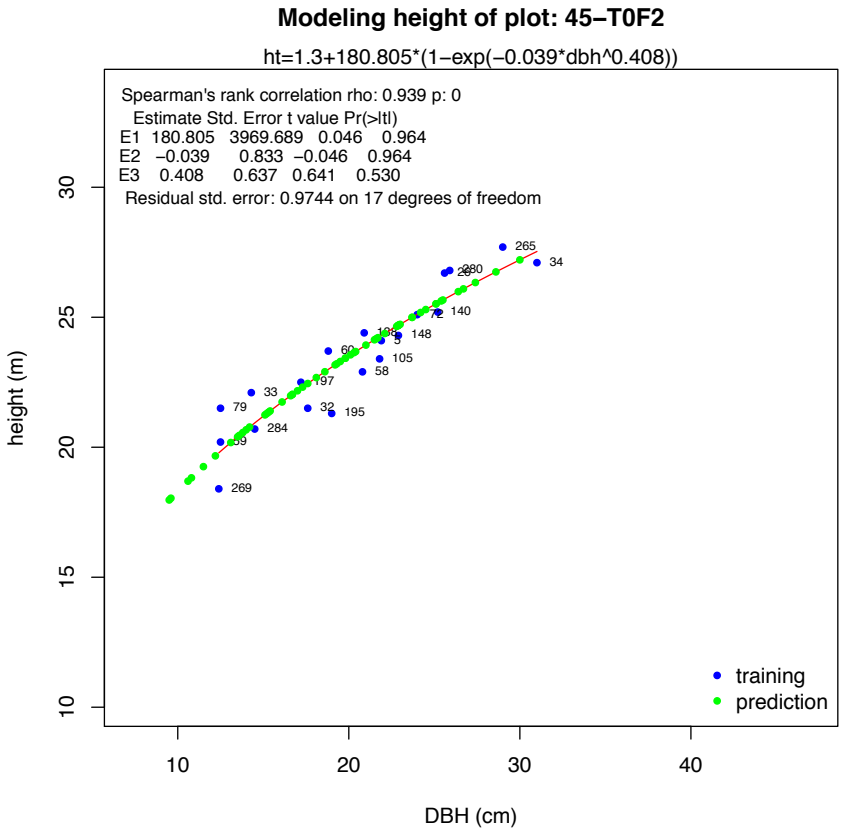

Modeling height of plot: 39−T2F0
ht=1.3+25.297*(1−exp(−0.063*dbh^1.04))
Spearman's rank correlation rho: 0.913 p: 0
Estimate Std. Error t value Pr(>|t|)
E1 25.297 3.326 7.606 0.000
E2 −0.063 0.048 −1.307 0.209
E3 1.040 0.347 2.993 0.008
Residual std. error: 0.8161 on 17 degrees of freedom
height (m)
training
prediction

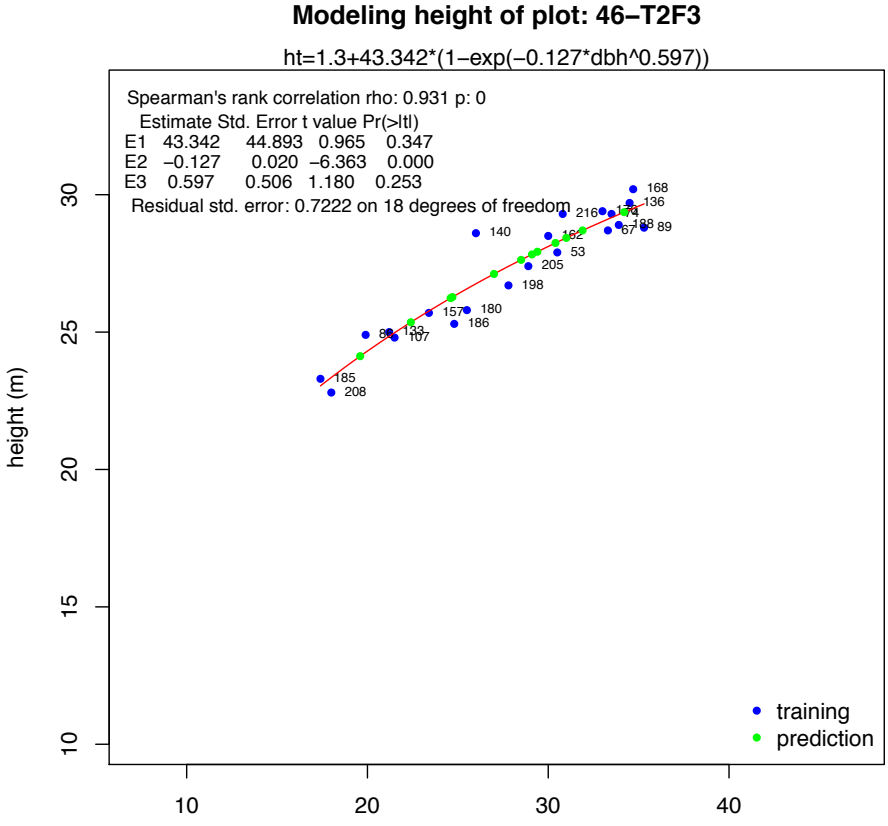

Modeling height of plot: 40−T0F1
ht=1.3+26.49*(1−exp(−0.112*dbh^0.867))
Spearman's rank correlation rho: 0.968 p: 0
Estimate Std. Error t value Pr(>|t|)
E1 26.490 2.269 11.674 0.000
E2 −0.112 0.037 −3.058 0.008
E3 0.867 0.176 4.921 0.000
Residual std. error: 0.8602 on 16 degrees of freedom
height (m)
DBH (cm)
training
prediction

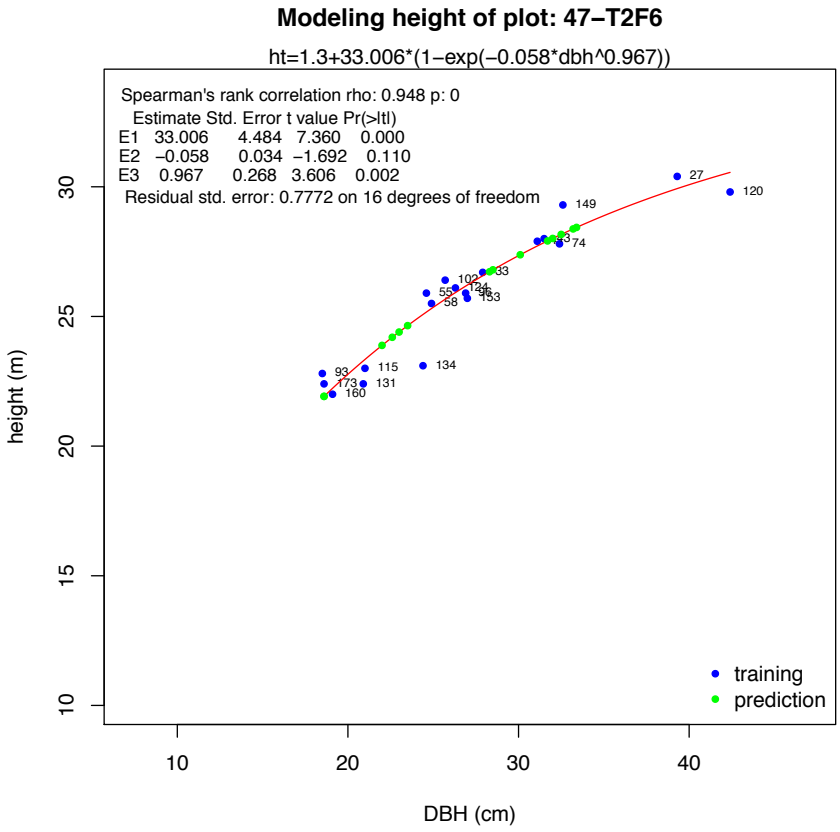

Modeling height of plot: 41−T2F1−1−1
ht=1.3+31.727*(1−exp(−0.056*dbh^1.095))
Spearman's rank correlation rho: 0.83 p: 0
Estimate Std. Error t value Pr(>|t|)
E1 31.727 2.252 14.089 0.000
E2 −0.056 0.054 −1.042 0.313
E3 1.095 0.366 2.989 0.009
Residual std. error: 1.1847 on 16 degrees of freedom
height (m)
training
prediction

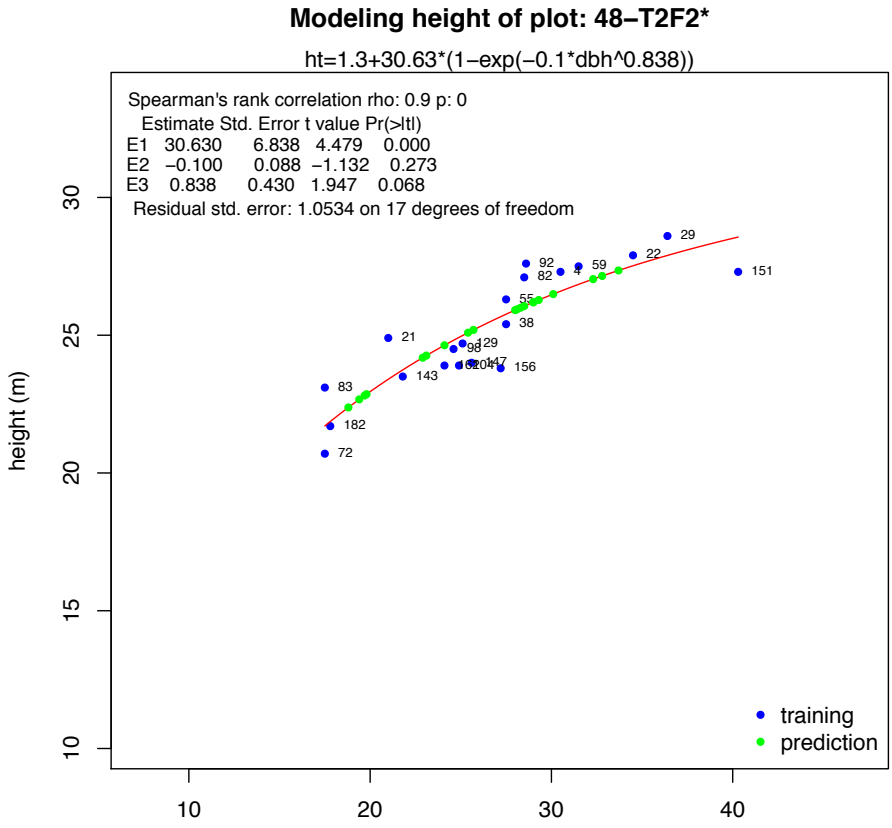

Modeling height of plot: 43–T1F2
ht=1.3+41.381*(1−exp(−0.109*dbh^0.613))
Spearman's rank correlation rho: 0.942 p: 0
Estimate Std. Error t value Pr(>|t|)
E1 41.381 34.551 1.198 0.246
E2 −0.109 0.044 −2.505 0.021
E3 0.613 0.283 2.171 0.043
Residual std. error: 0.9393 on 19 degrees of freedom
height (m)
DBH (cm)
training
prediction

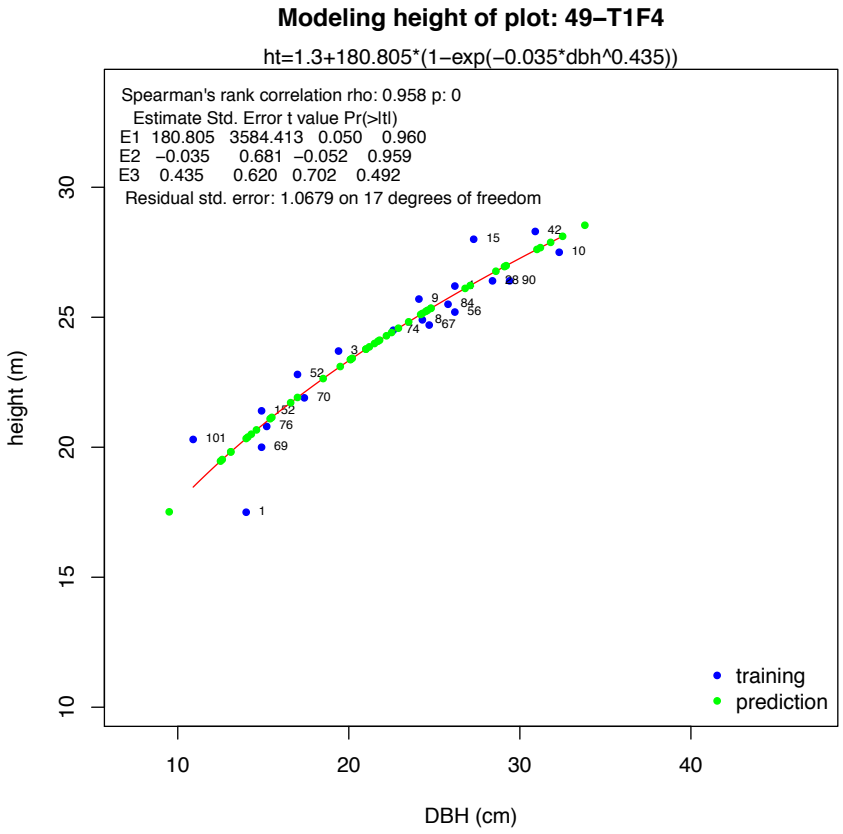

Modeling height of plot: 44–T1F1–1–1
ht=1.3+180.805*(1−exp(−0.038*dbh^0.405))
Spearman's rank correlation rho: 0.874 p: 0
Estimate Std. Error t value Pr(>|t|)
E1 180.805 4150.724 0.044 0.966
E2 −0.038 0.850 −0.044 0.965
E3 0.405 0.644 0.629 0.537
Residual std. error: 1.196 on 18 degrees of freedom
height (m)
training
prediction

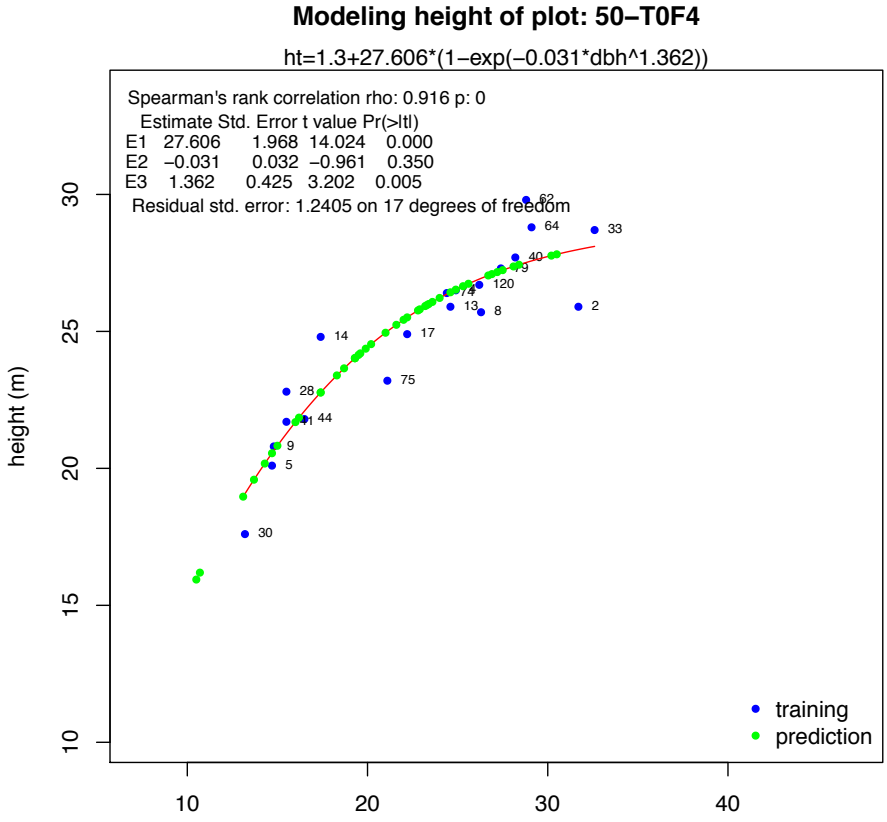

Modeling height of plot: 45–T0F2
ht=1.3+180.805*(1−exp(−0.039*dbh^0.408))
Spearman's rank correlation rho: 0.939 p: 0
Estimate Std. Error t value Pr(>|t|)
E1 180.805 3969.689 0.046 0.964
E2 −0.039 0.833 −0.046 0.964
E3 0.408 0.637 0.641 0.530
Residual std. error: 0.9744 on 17 degrees of freedom
height (m)
DBH (cm)
training
prediction

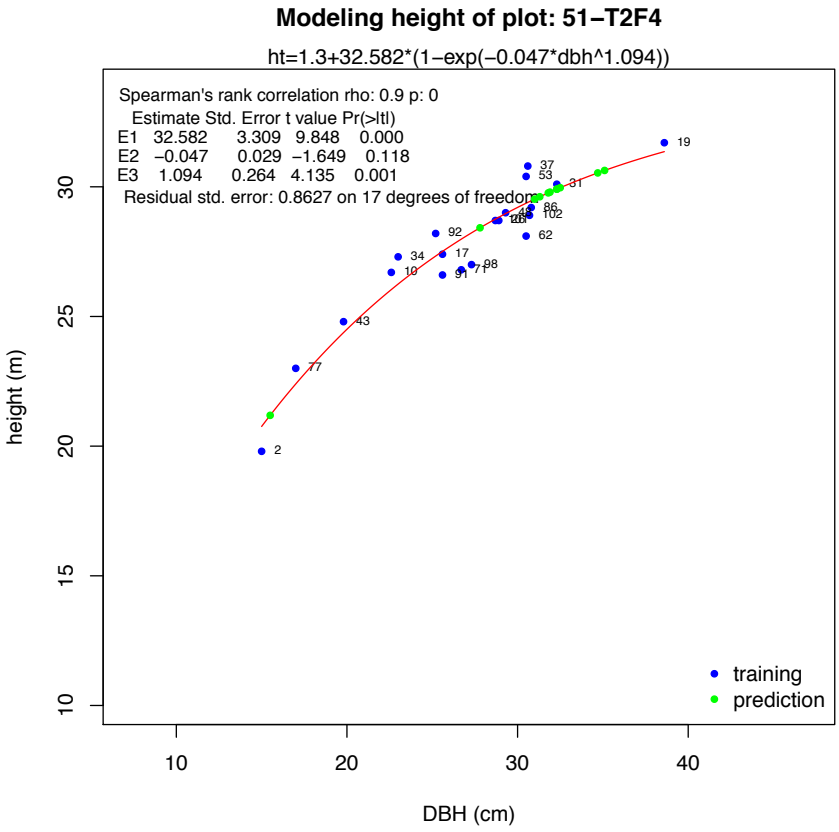

Modeling height of plot: 46–T2F3
ht=1.3+43.342*(1−exp(−0.127*dbh^0.597))
Spearman's rank correlation rho: 0.931 p: 0
Estimate Std. Error t value Pr(>|t|)
E1 43.342 44.893 0.965 0.347
E2 −0.127 0.020 −6.363 0.000
E3 0.597 0.506 1.180 0.253
Residual std. error: 0.7222 on 18 degrees of freedom
height (m)
training
prediction

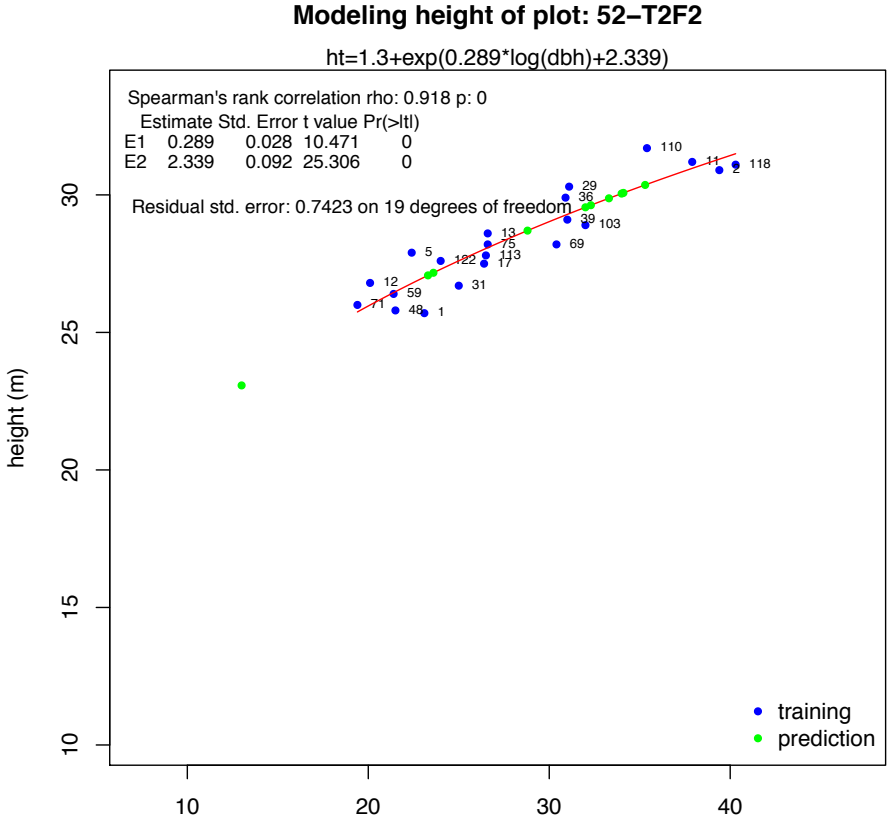

Modeling height of plot: 47–T2F6
ht=1.3+33.006*(1−exp(−0.058*dbh^0.967))
Spearman's rank correlation rho: 0.948 p: 0
Estimate Std. Error t value Pr(>|t|)
E1 33.006 4.484 7.360 0.000
E2 −0.058 0.034 −1.692 0.110
E3 0.967 0.268 3.606 0.002
Residual std. error: 0.7772 on 16 degrees of freedom
height (m)
DBH (cm)
training
prediction

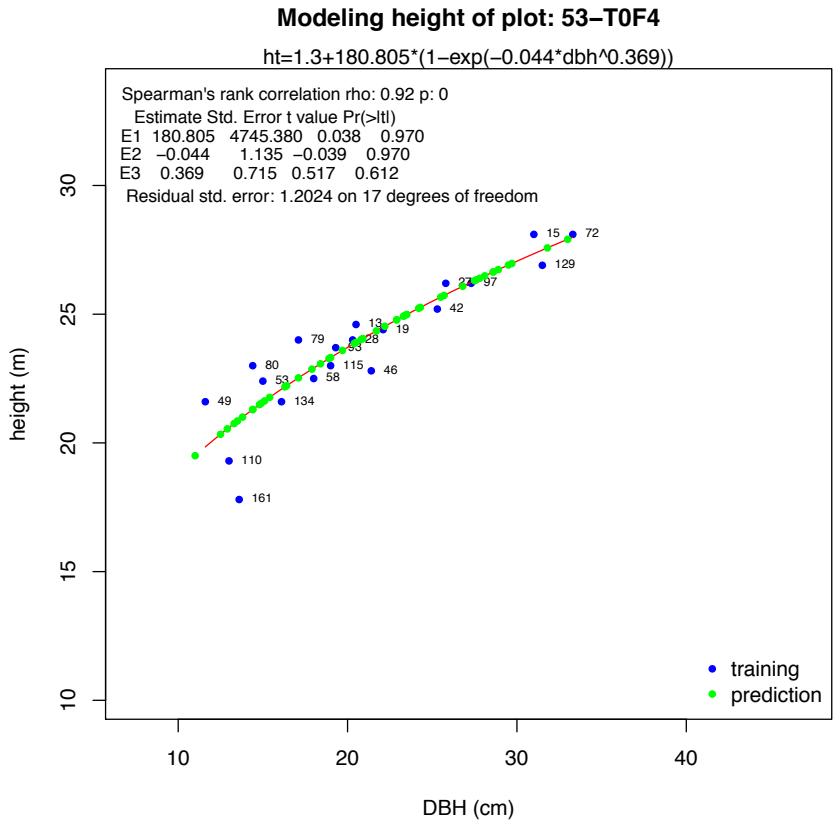

Modeling height of plot: 48–T2F2*
ht=1.3+30.63*(1−exp(−0.1*dbh^0.838))
Spearman's rank correlation rho: 0.9 p: 0
Estimate Std. Error t value Pr(>|t|)
E1 30.630 6.838 4.479 0.000
E2 −0.100 0.088 −1.132 0.273
E3 0.838 0.430 1.947 0.068
Residual std. error: 1.0534 on 17 degrees of freedom
height (m)
training
prediction

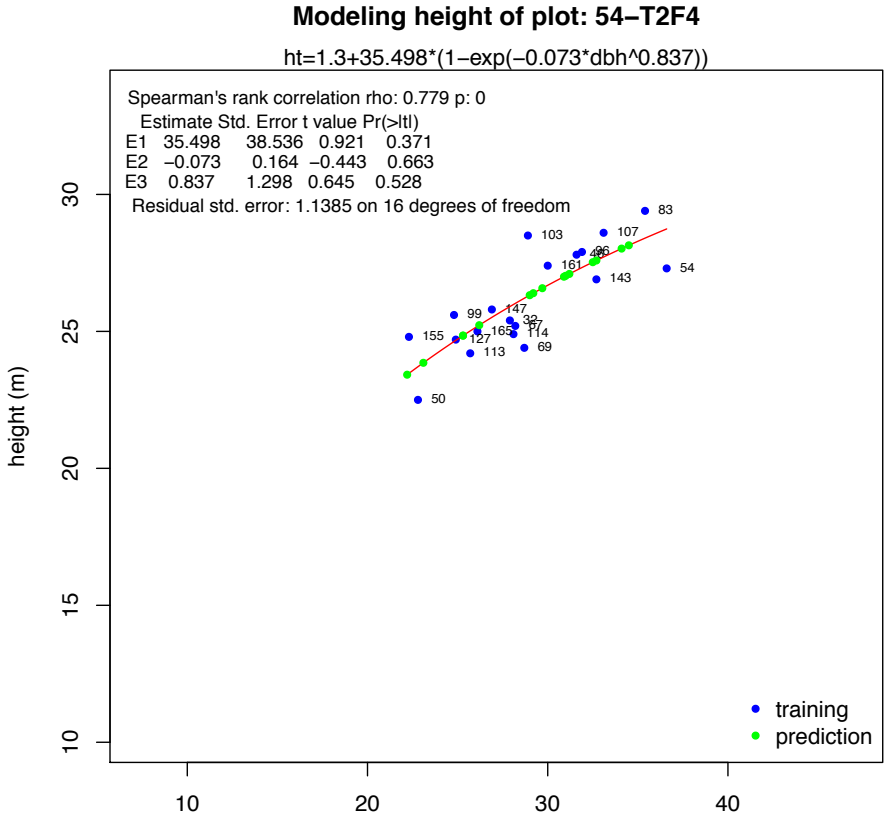

Modeling height of plot: 49–T1F4
ht=1.3+180.805*(1−exp(−0.035*dbh^0.435))
Spearman's rank correlation rho: 0.958 p: 0
Estimate Std. Error t value Pr(>|t|)
E1 180.805 3584.413 0.050 0.960
E2 −0.035 0.681 −0.052 0.959
E3 0.435 0.620 0.702 0.492
Residual std. error: 1.0679 on 17 degrees of freedom
height (m)
DBH (cm)
training
prediction

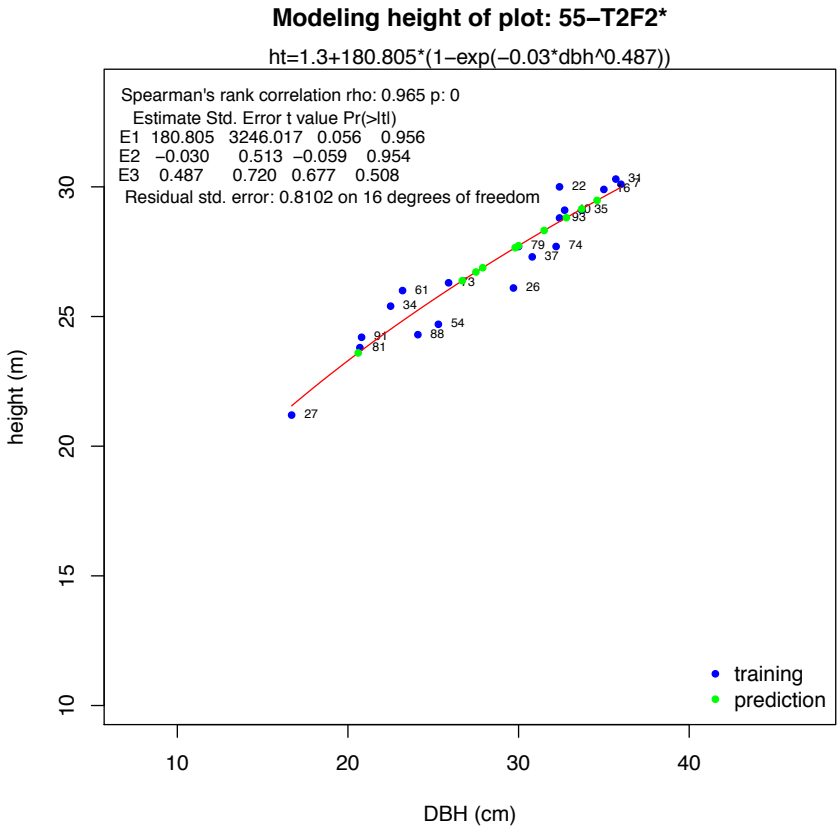

Modeling height of plot: 50–T0F4
ht=1.3+27.606*(1−exp(−0.031*dbh^1.362))
Spearman's rank correlation rho: 0.916 p: 0
Estimate Std. Error t value Pr(>|t|)
E1 27.606 1.968 14.024 0.000
E2 −0.031 0.032 −0.961 0.350
E3 1.362 0.425 3.202 0.005
Residual std. error: 1.2405 on 17 degrees of freedom
height (m)
training
prediction

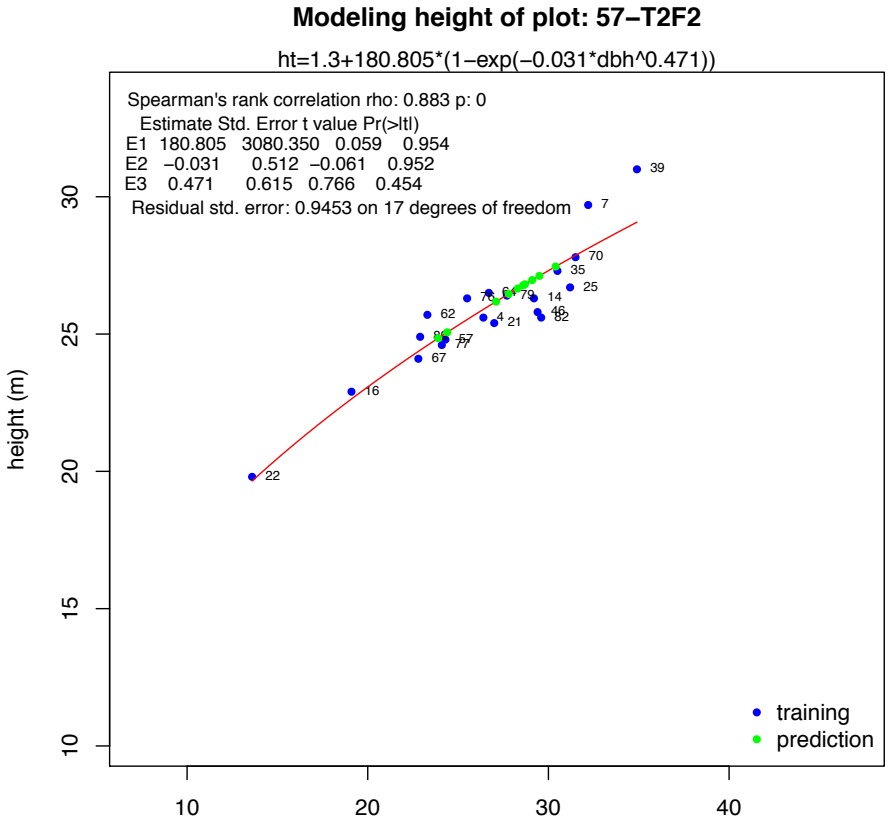

Modeling height of plot: 51−T2F4
ht=1.3+32.582*(1−exp(−0.047*dbh^1.094))
Spearman's rank correlation rho: 0.9 p: 0
Estimate Std. Error t value Pr(>|t|)
E1 32.582 3.309 9.848 0.000
E2 −0.047 0.029 −1.649 0.118
E3 1.094 0.264 4.135 0.001
Residual std. error: 0.8627 on 17 degrees of freedom
height (m)
DBH (cm)
training
prediction


Modeling height of plot: 52−T2F2
ht=1.3+exp(0.289*log(dbh)+2.339)
Spearman's rank correlation rho: 0.918 p: 0
Estimate Std. Error t value Pr(>|t|)
E1 0.289 0.028 10.471 0
E2 2.339 0.092 25.306 0
Residual std. error: 0.7423 on 19 degrees of freedom
height (m)
training
prediction

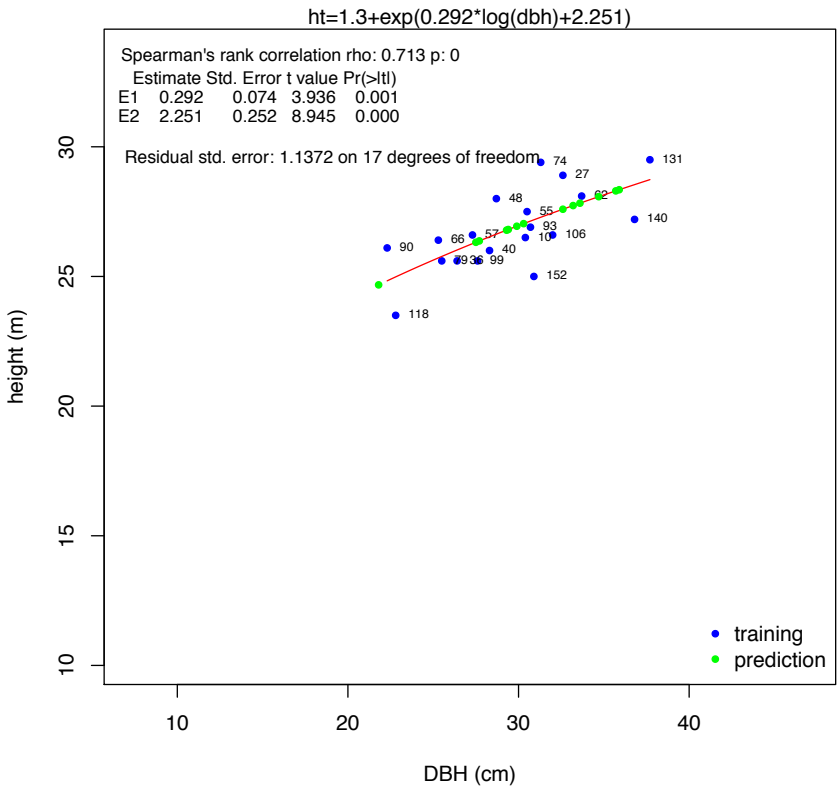

Modeling height of plot: 53–T0F4
ht=1.3+180.805*(1−exp(−0.044*dbh^0.369))
Spearman's rank correlation rho: 0.92 p: 0
Estimate Std. Error t value Pr(>|t|)
E1 180.805 4745.380 0.038 0.970
E2 −0.044 1.135 −0.039 0.970
E3 0.369 0.715 0.517 0.612
Residual std. error: 1.2024 on 17 degrees of freedom
height (m)
DBH (cm)
training
prediction


Modeling height of plot: 54–T2F4
ht=1.3+35.498*(1−exp(−0.073*dbh^0.837))
Spearman's rank correlation rho: 0.779 p: 0
Estimate Std. Error t value Pr(>|t|)
E1 35.498 38.536 0.921 0.371
E2 −0.073 0.164 −0.443 0.663
E3 0.837 1.298 0.645 0.528
Residual std. error: 1.1385 on 16 degrees of freedom
height (m)
training
prediction

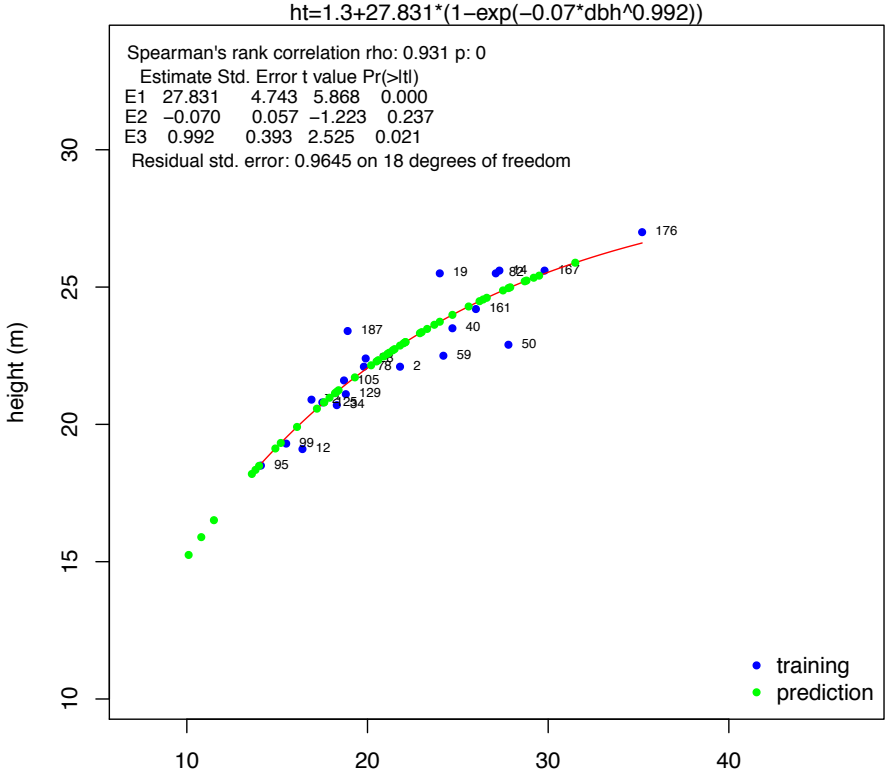

Modeling height of plot: 55–T2F2*
ht=1.3+180.805*(1−exp(−0.03*dbh^0.487))
Spearman's rank correlation rho: 0.965 p: 0
Estimate Std. Error t value Pr(>|t|)
E1 180.805 3246.017 0.056 0.956
E2 −0.030 0.513 −0.059 0.954
E3 0.487 0.720 0.677 0.508
Residual std. error: 0.8102 on 16 degrees of freedom
height (m)
DBH (cm)
training
prediction

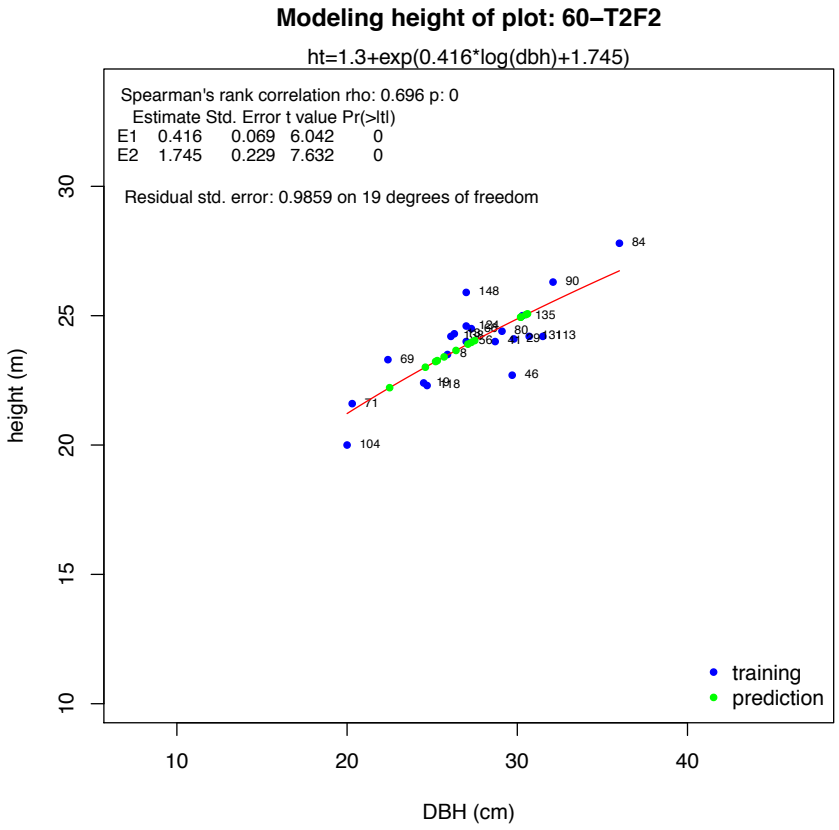

Modeling height of plot: 57–T2F2
ht=1.3+180.805*(1−exp(−0.031*dbh^0.471))
Spearman's rank correlation rho: 0.883 p: 0
Estimate Std. Error t value Pr(>|t|)
E1 180.805 3080.350 0.059 0.954
E2 −0.031 0.512 −0.061 0.952
E3 0.471 0.615 0.766 0.454
Residual std. error: 0.9453 on 17 degrees of freedom
height (m)
training
prediction

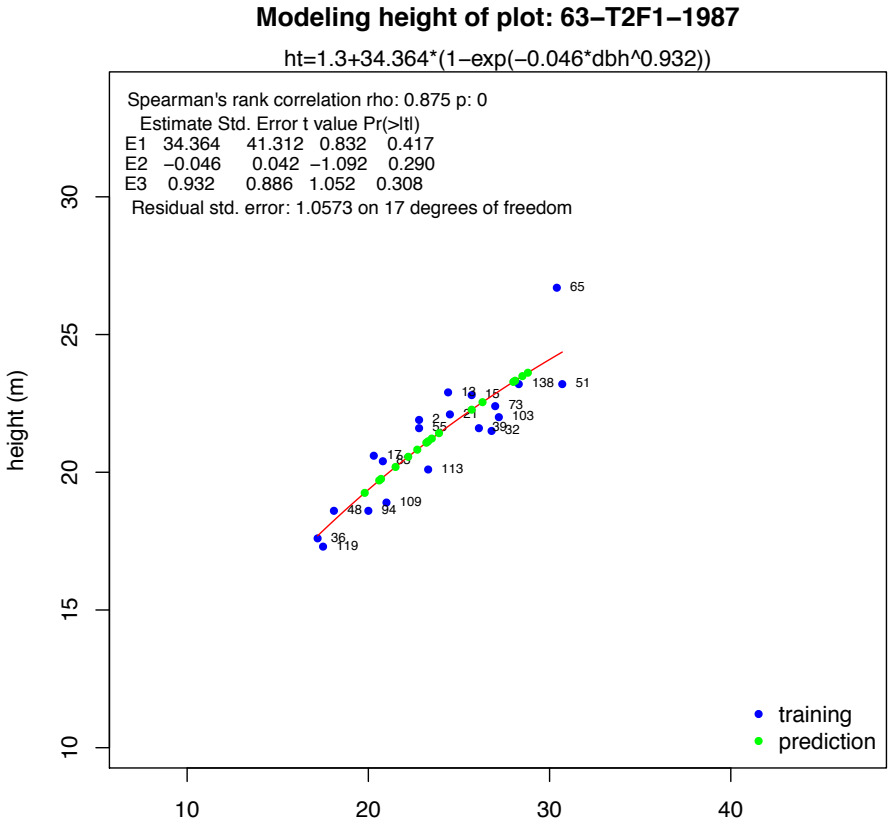
Modeling height of plot: 58–T2F6

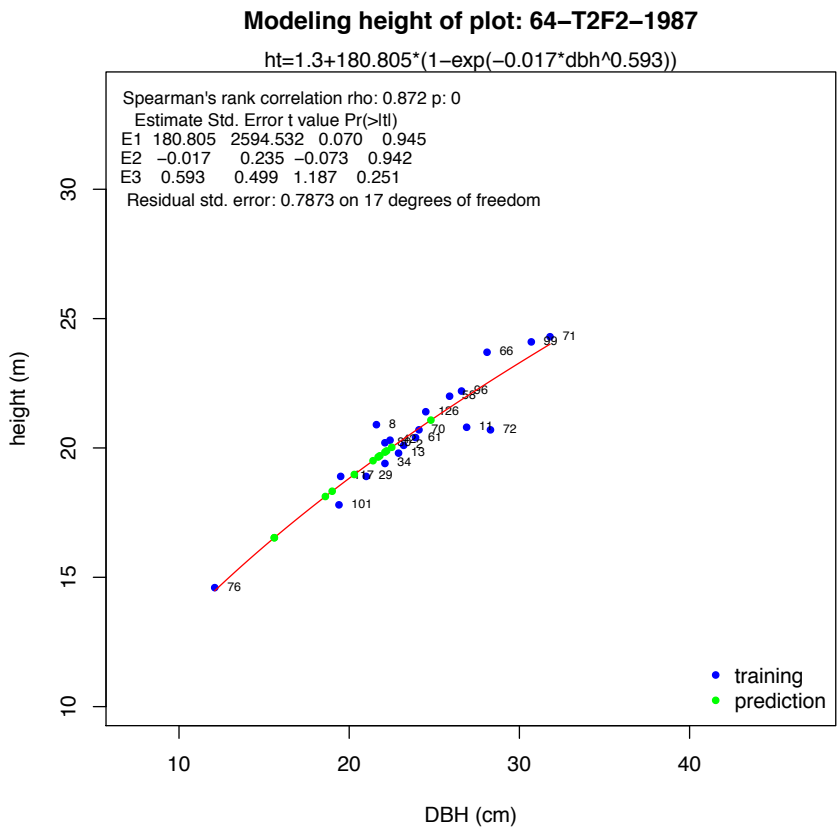


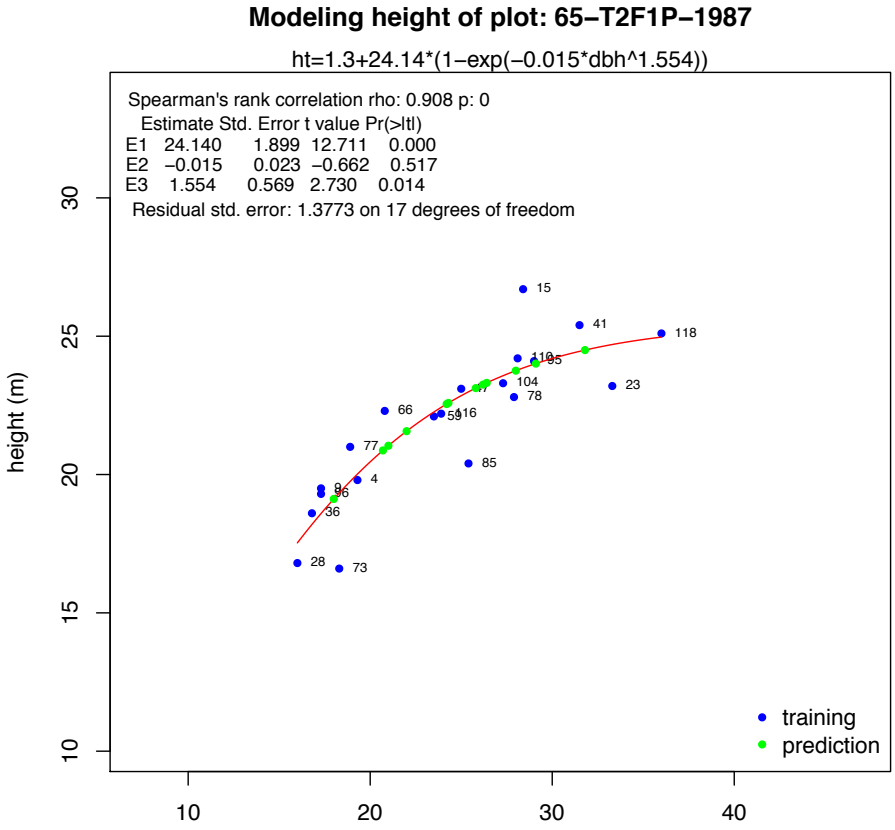
Modeling height of plot: 59–T1F4

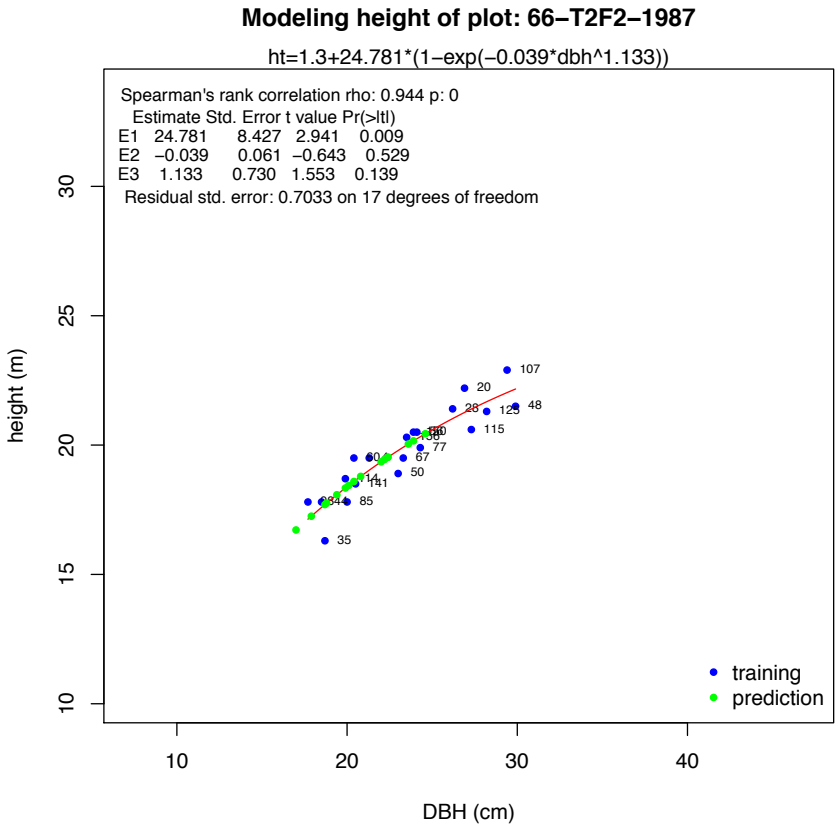


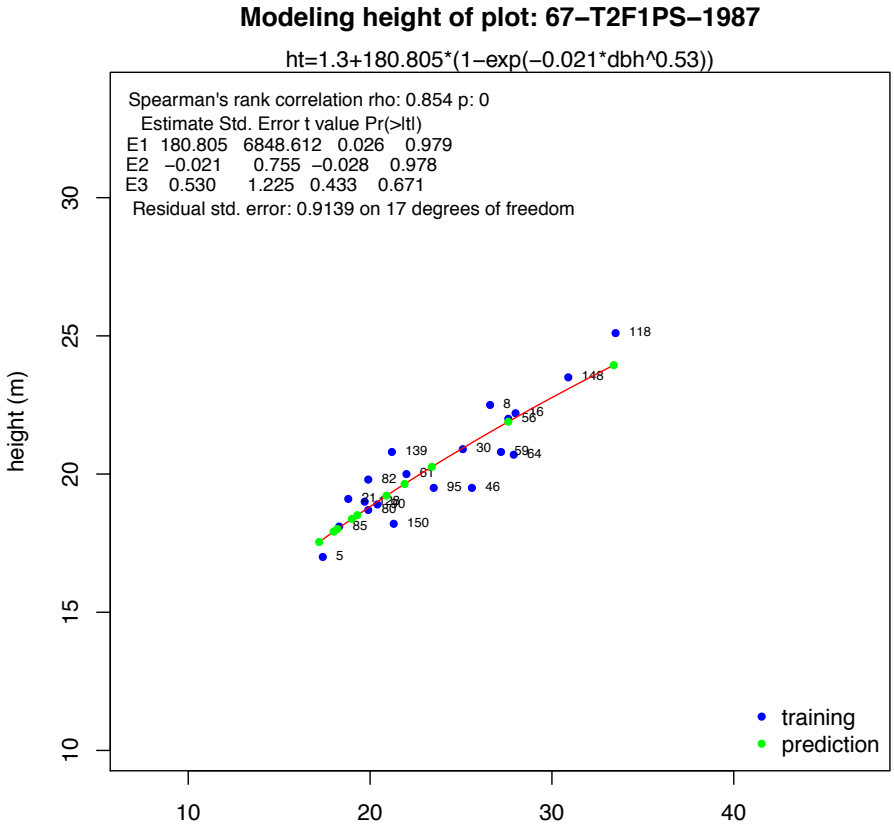

Modeling height of plot: 60–T2F2
ht=1.3+exp(0.416*log(dbh)+1.745)
Spearman's rank correlation rho: 0.696 p: 0
Estimate Std. Error t value Pr(>|t|)
E1 0.416 0.069 6.042 0
E2 1.745 0.229 7.632 0
Residual std. error: 0.9859 on 19 degrees of freedom
height (m)
DBH (cm)
training
prediction

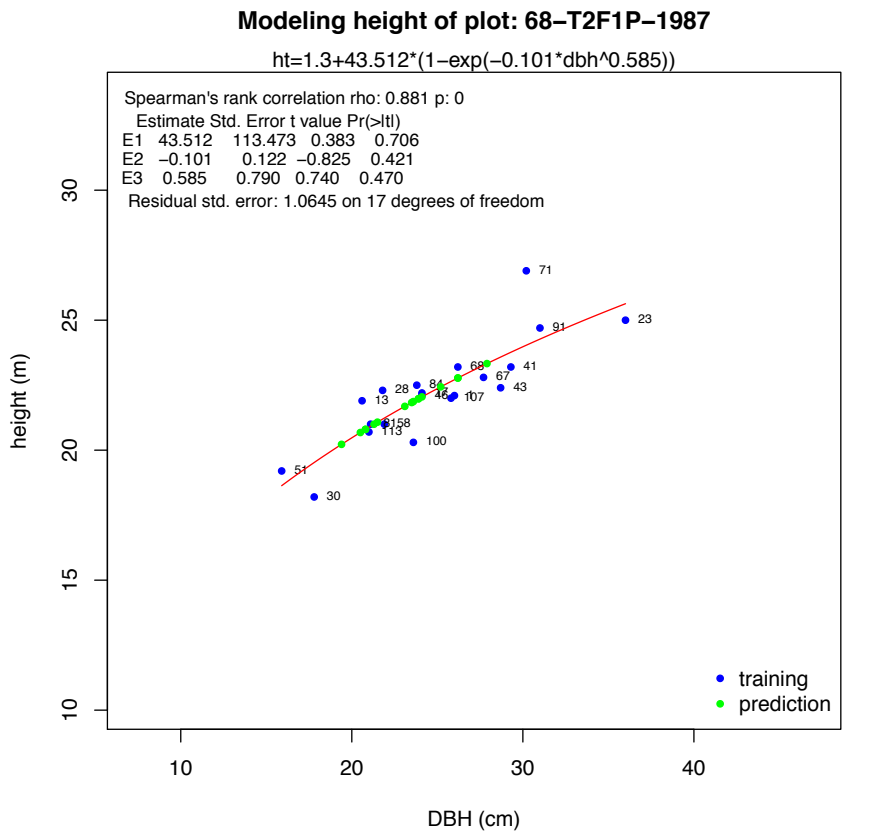

Modeling height of plot: 63–T2F1–1987
ht=1.3+34.364*(1–exp(–0.046*dbh^0.932))
Spearman's rank correlation rho: 0.875 p: 0
Estimate Std. Error t value Pr(>|t|)
E1 34.364 41.312 0.832 0.417
E2 –0.046 0.042 –1.092 0.290
E3 0.932 0.886 1.052 0.308
Residual std. error: 1.0573 on 17 degrees of freedom
height (m)
training
prediction

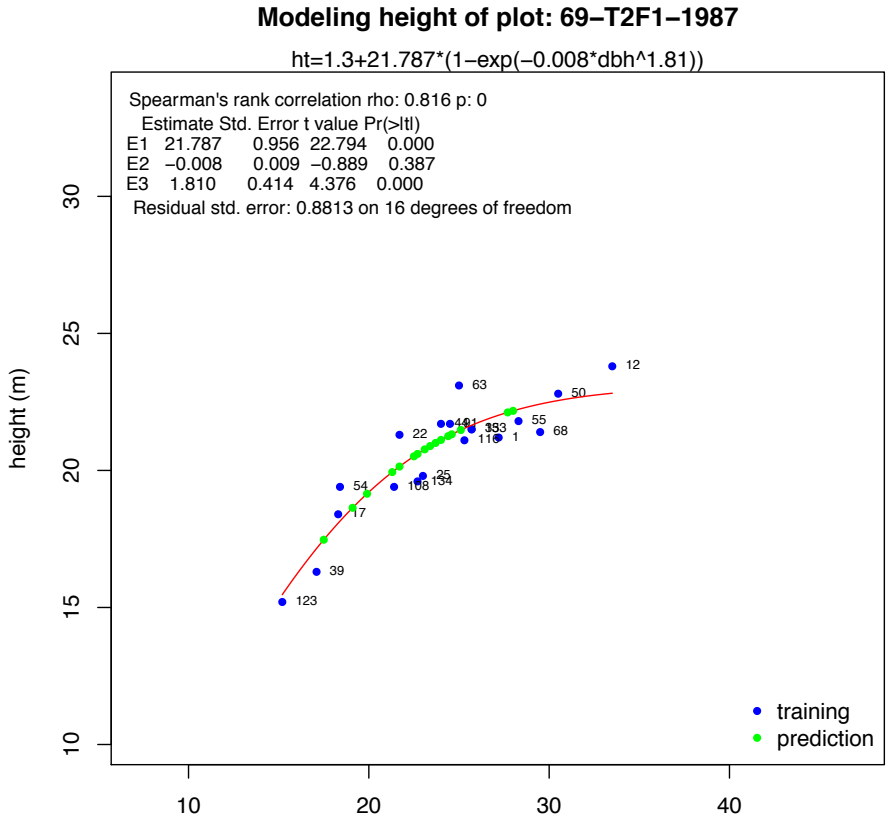

Modeling height of plot: 64–T2F2–1987
ht=1.3+180.805*(1−exp(−0.017*dbh^0.593))
Spearman's rank correlation rho: 0.872 p: 0
Estimate Std. Error t value Pr(>|t|)
E1 180.805 2594.532 0.070 0.945
E2 −0.017 0.235 −0.073 0.942
E3 0.593 0.499 1.187 0.251
Residual std. error: 0.7873 on 17 degrees of freedom
height (m)
DBH (cm)
training
prediction

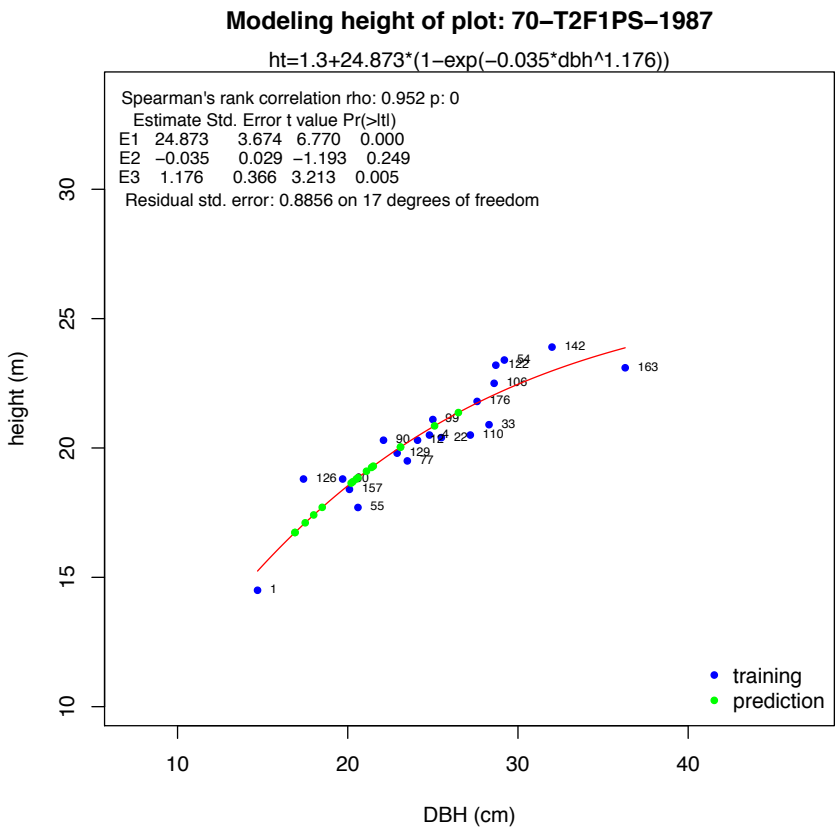

Modeling height of plot: 65–T2F1P–1987
ht=1.3+24.14*(1−exp(−0.015*dbh^1.554))
Spearman's rank correlation rho: 0.908 p: 0
Estimate Std. Error t value Pr(>|t|)
E1 24.140 1.899 12.711 0.000
E2 −0.015 0.023 −0.662 0.517
E3 1.554 0.569 2.730 0.014
Residual std. error: 1.3773 on 17 degrees of freedom
height (m)
training
prediction


Modeling height of plot: 66–T2F2–1987
ht=1.3+24.781*(1−exp(−0.039*dbh^1.133))
Spearman's rank correlation rho: 0.944 p: 0
Estimate Std. Error t value Pr(>|t|)
E1 24.781 8.427 2.941 0.009
E2 −0.039 0.061 −0.643 0.529
E3 1.133 0.730 1.553 0.139
Residual std. error: 0.7033 on 17 degrees of freedom
height (m)
DBH (cm)
training
prediction

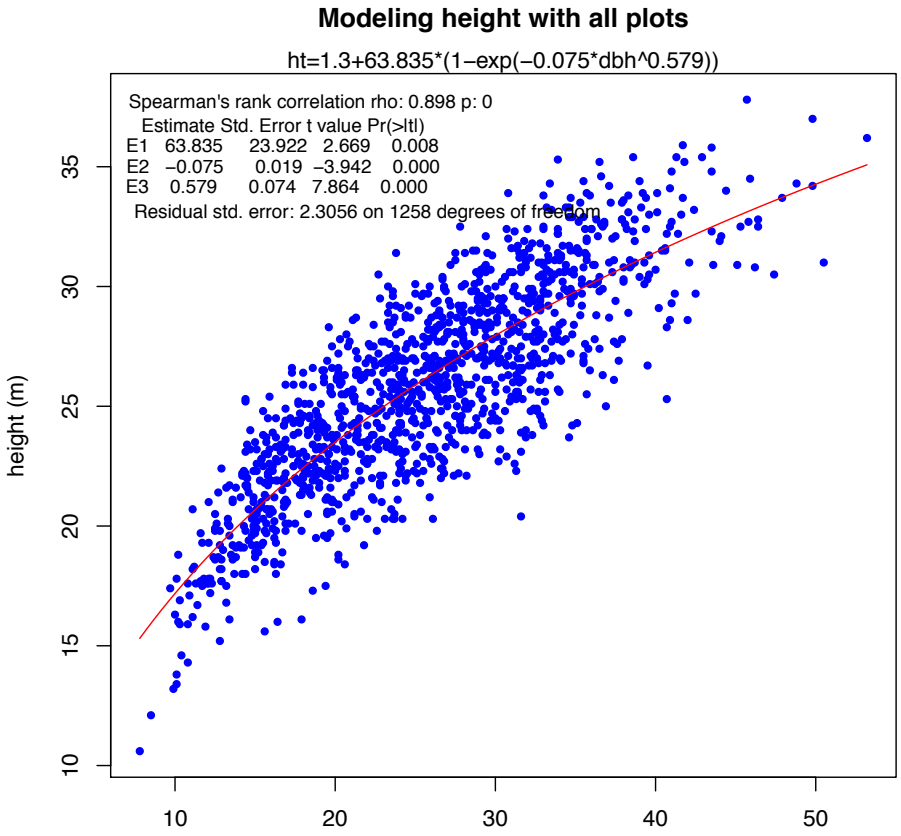

Modeling height of plot: 67–T2F1PS–1987
ht=1.3+180.805*(1−exp(−0.021*dbh^0.53))
Spearman's rank correlation rho: 0.854 p: 0
Estimate Std. Error t value Pr(>|t|)
E1 180.805 6848.612 0.026 0.979
E2 −0.021 0.755 −0.028 0.978
E3 0.530 1.225 0.433 0.671
Residual std. error: 0.9139 on 17 degrees of freedom
height (m)
training
prediction

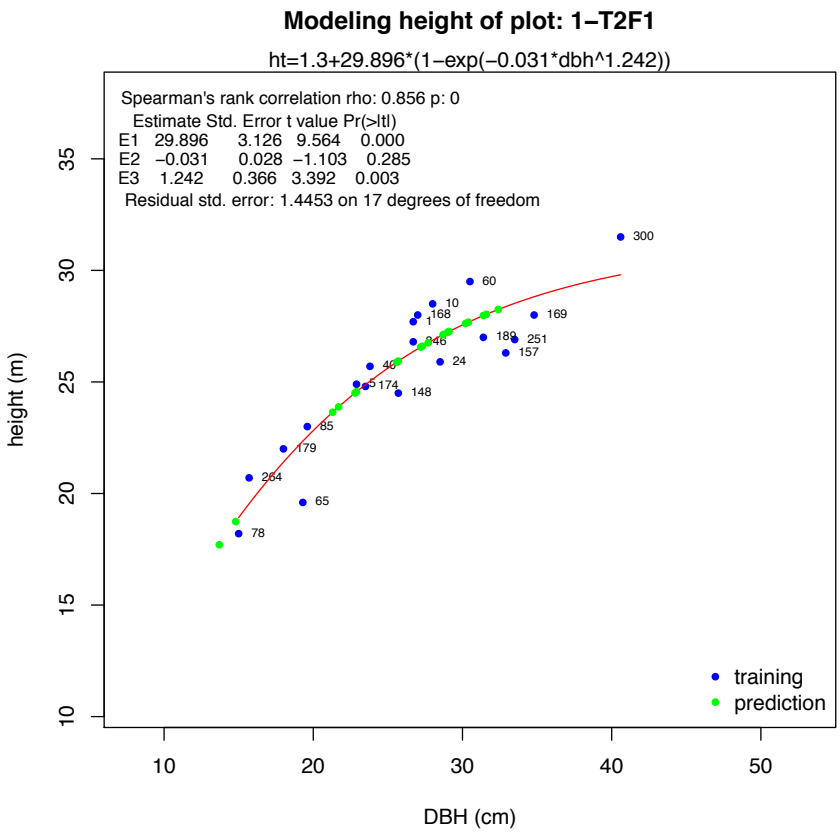

Modeling height of plot: 68–T2F1P–1987
ht=1.3+43.512*(1–exp(–0.101*dbh^0.585))
Spearman's rank correlation rho: 0.881 p: 0
Estimate Std. Error t value Pr(>|t|)
E1 43.512 113.473 0.383 0.706
E2 –0.101 0.122 –0.825 0.421
E3 0.585 0.790 0.740 0.470
Residual std. error: 1.0645 on 17 degrees of freedom
height (m)
DBH (cm)
training
prediction

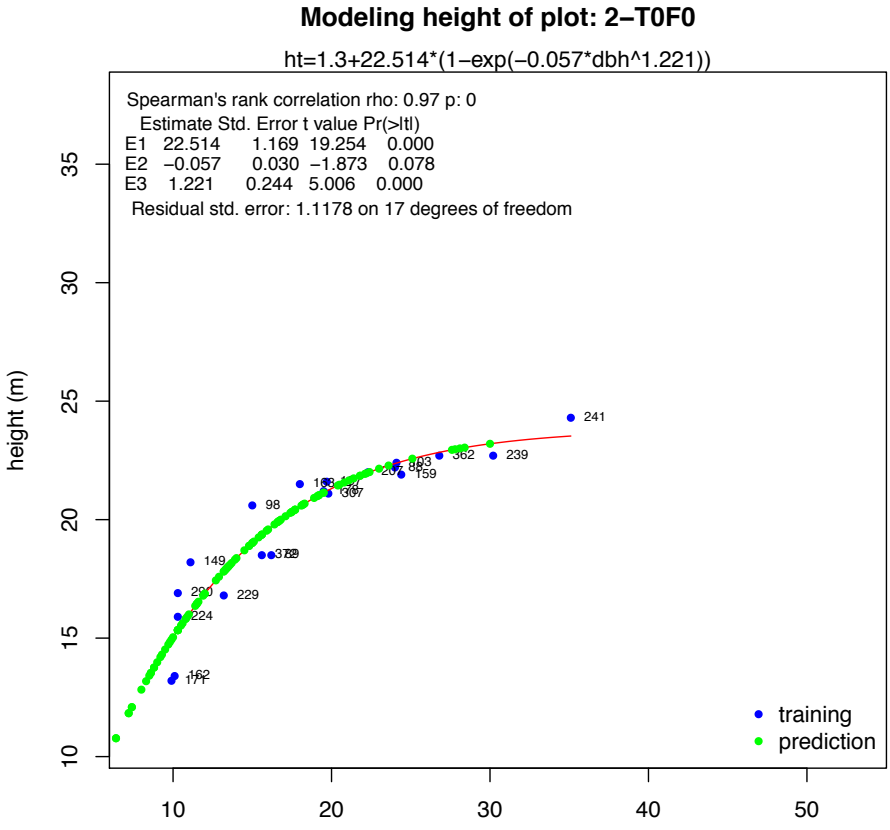

Modeling height of plot: 69–T2F1–1987
ht=1.3+21.787*(1–exp(–0.008*dbh^1.81))
Spearman's rank correlation rho: 0.816 p: 0
Estimate Std. Error t value Pr(>|t|)
E1 21.787 0.956 22.794 0.000
E2 –0.008 0.009 –0.889 0.387
E3 1.810 0.414 4.376 0.000
Residual std. error: 0.8813 on 16 degrees of freedom
height (m)
training
prediction

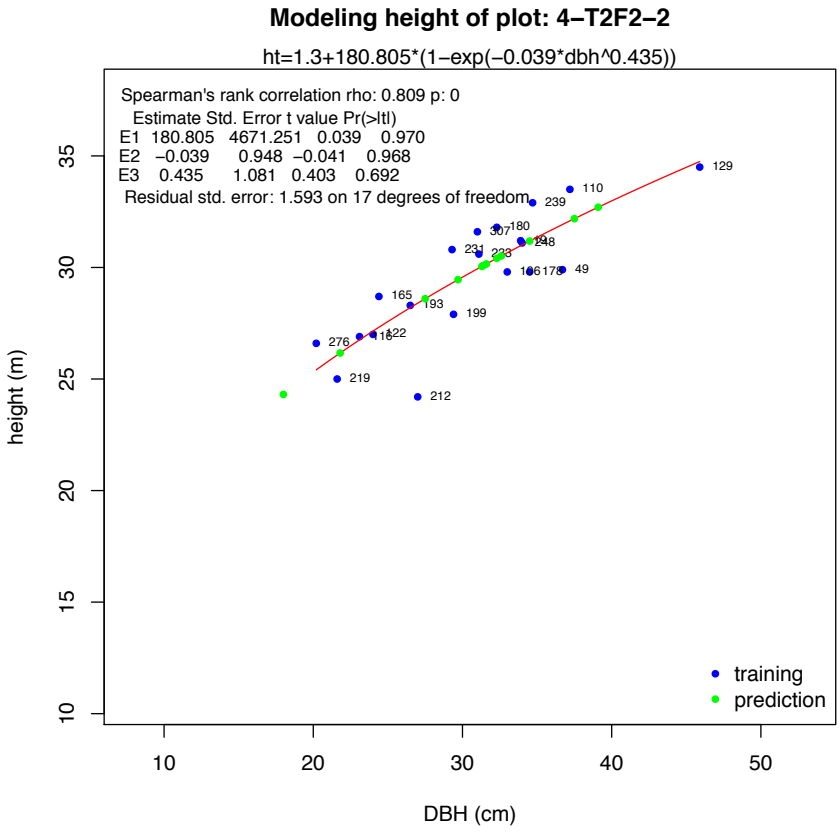

Modeling height of plot: 70−T2F1PS−1987
ht=1.3+24.873*(1−exp(−0.035*dbh^1.176))
Spearman's rank correlation rho: 0.952 p: 0
Estimate Std. Error t value Pr(>|t|)
E1 24.873 3.674 6.770 0.000
E2 −0.035 0.029 −1.193 0.249
E3 1.176 0.366 3.213 0.005
Residual std. error: 0.8856 on 17 degrees of freedom
height (m)
DBH (cm)
training
prediction

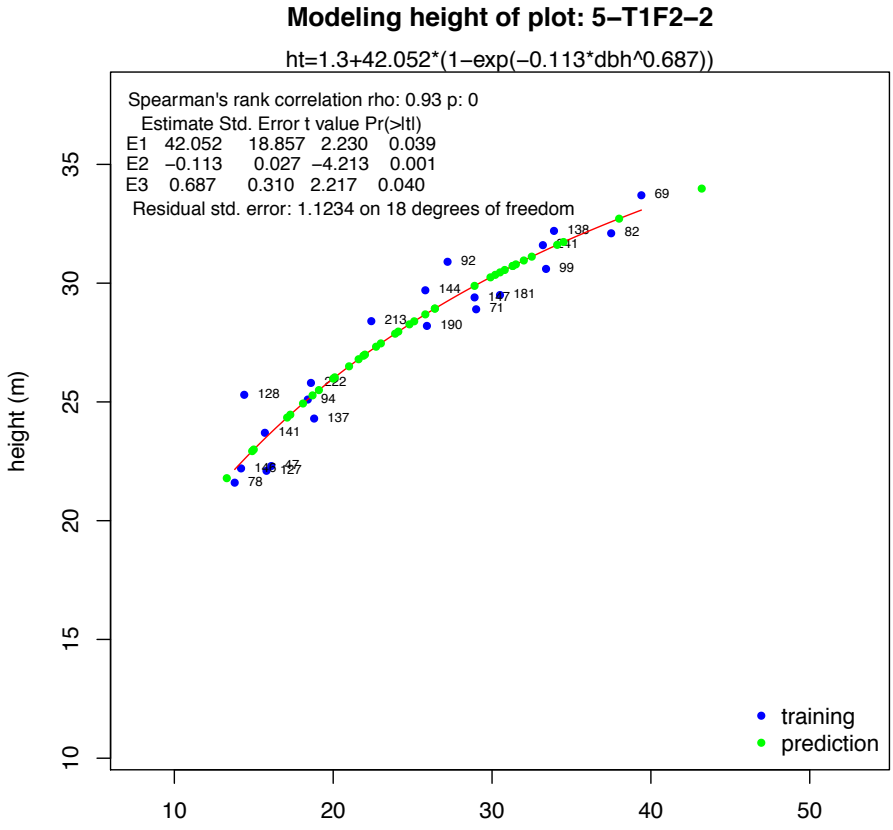
1.2 *Height-DBH Regression Fitting for Sampling Year 2012*

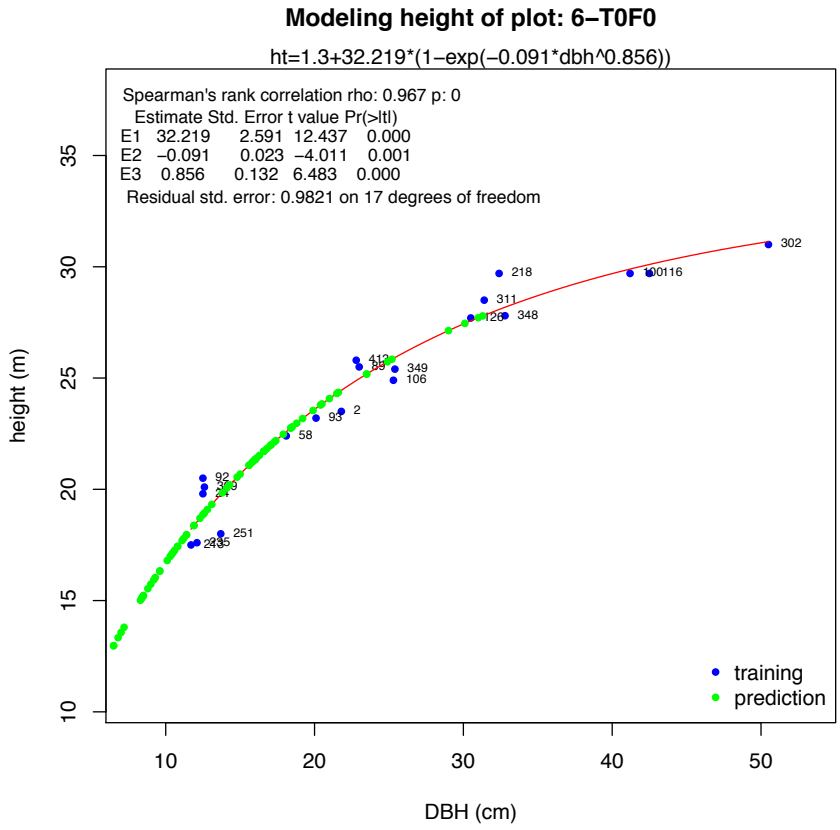


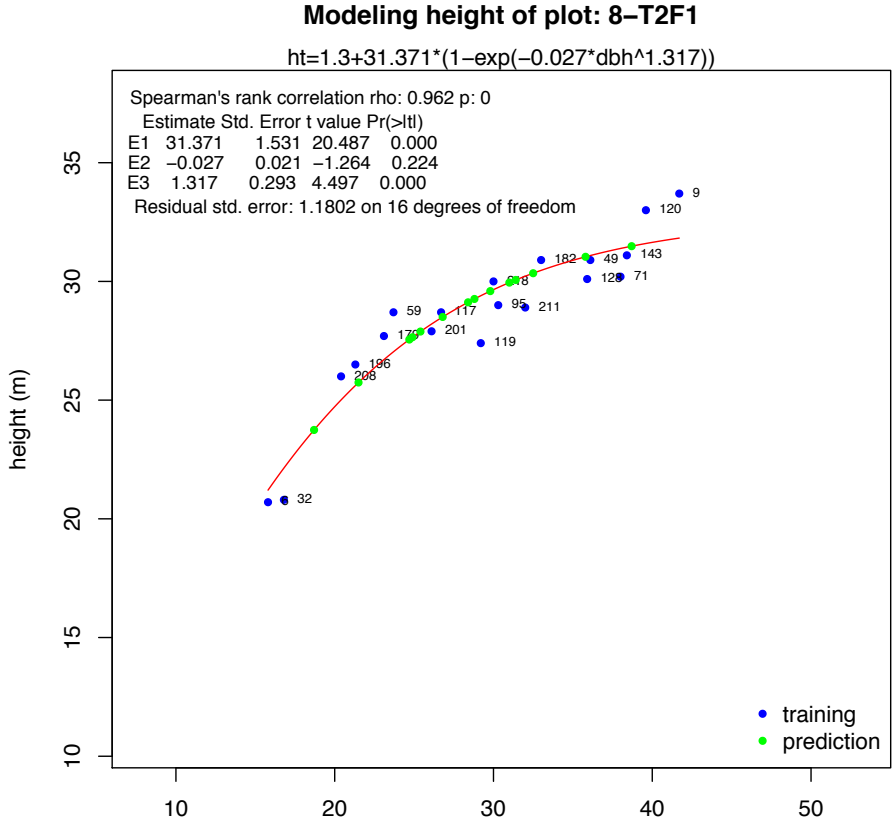

Modeling height of plot: 1−T2F1
ht=1.3+29.896*(1−exp(−0.031*dbh^1.242))
Spearman's rank correlation rho: 0.856 p: 0
Estimate Std. Error t value Pr(>|t|)
E1 29.896 3.126 9.564 0.000
E2 −0.031 0.028 −1.103 0.285
E3 1.242 0.366 3.392 0.003
Residual std. error: 1.4453 on 17 degrees of freedom
height (m)
DBH (cm)
training
prediction

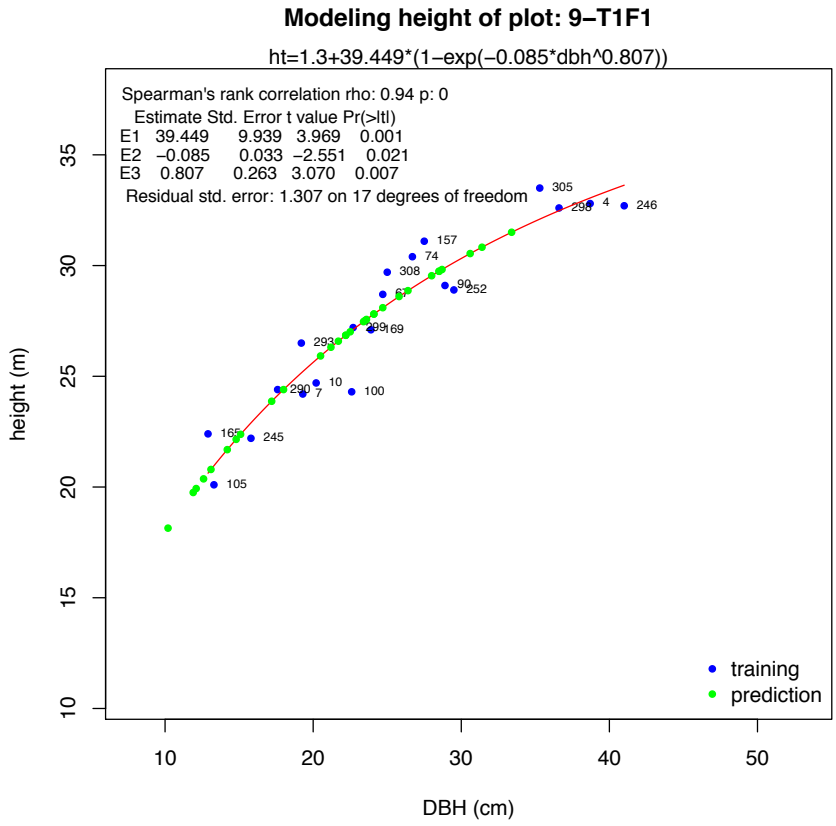

Modeling height of plot: 2−T0F0
ht=1.3+22.514*(1−exp(−0.057*dbh^1.221))
Spearman's rank correlation rho: 0.97 p: 0
Estimate Std. Error t value Pr(>|t|)
E1 22.514 1.169 19.254 0.000
E2 −0.057 0.030 −1.873 0.078
E3 1.221 0.244 5.006 0.000
Residual std. error: 1.1178 on 17 degrees of freedom
height (m)
training
prediction

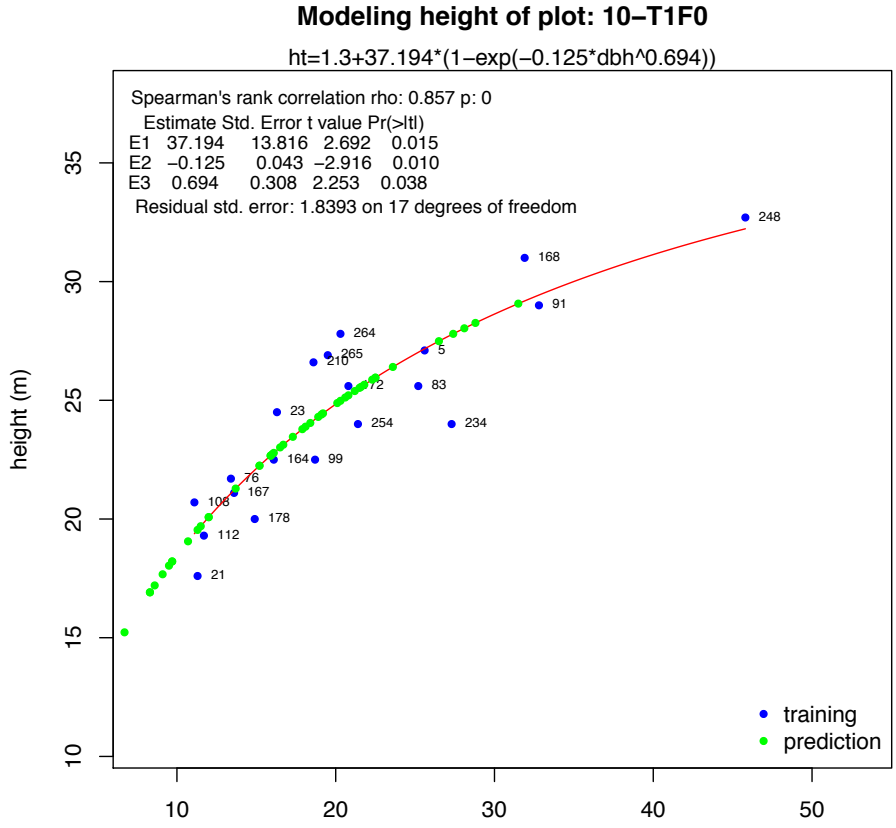

Modeling height of plot: 4–T2F2–2
ht=1.3+180.805*(1−exp(−0.039*dbh^0.435))
Spearman's rank correlation rho: 0.809 p: 0
Estimate Std. Error t value Pr(>|t|)
E1 180.805 4671.251 0.039 0.970
E2 −0.039 0.948 −0.041 0.968
E3 0.435 1.081 0.403 0.692
Residual std. error: 1.593 on 17 degrees of freedom
height (m)
DBH (cm)
training
prediction

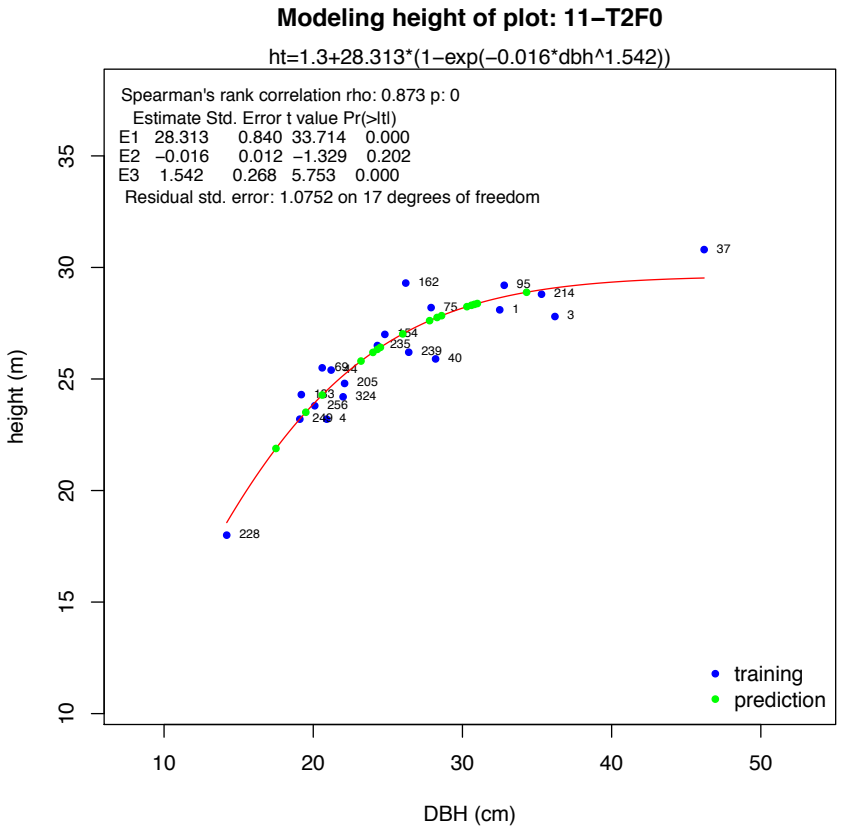

Modeling height of plot: 5–T1F2–2
ht=1.3+42.052*(1−exp(−0.113*dbh^0.687))
Spearman's rank correlation rho: 0.93 p: 0
Estimate Std. Error t value Pr(>|t|)
E1 42.052 18.857 2.230 0.039
E2 −0.113 0.027 −4.213 0.001
E3 0.687 0.310 2.217 0.040
Residual std. error: 1.1234 on 18 degrees of freedom
height (m)
training
prediction

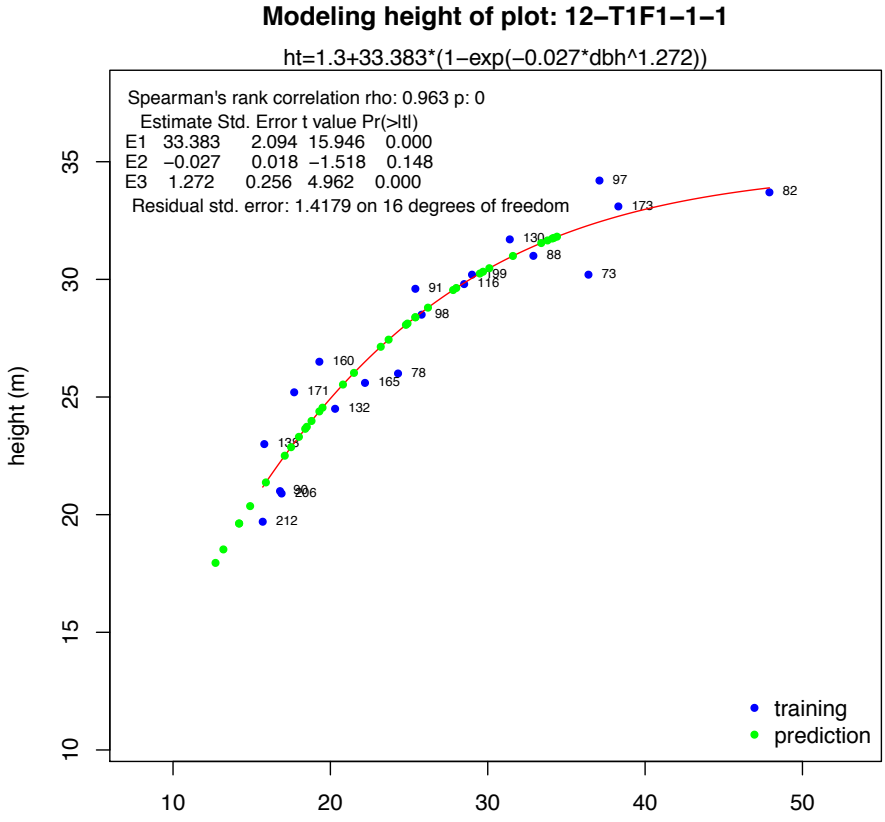

Modeling height of plot: 6–T0F0
ht=1.3+32.219*(1−exp(−0.091*dbh^0.856))
Spearman's rank correlation rho: 0.967 p: 0
Estimate Std. Error t value Pr(>|t|)
E1 32.219 2.591 12.437 0.000
E2 −0.091 0.023 −4.011 0.001
E3 0.856 0.132 6.483 0.000
Residual std. error: 0.9821 on 17 degrees of freedom
height (m)
DBH (cm)
training
prediction

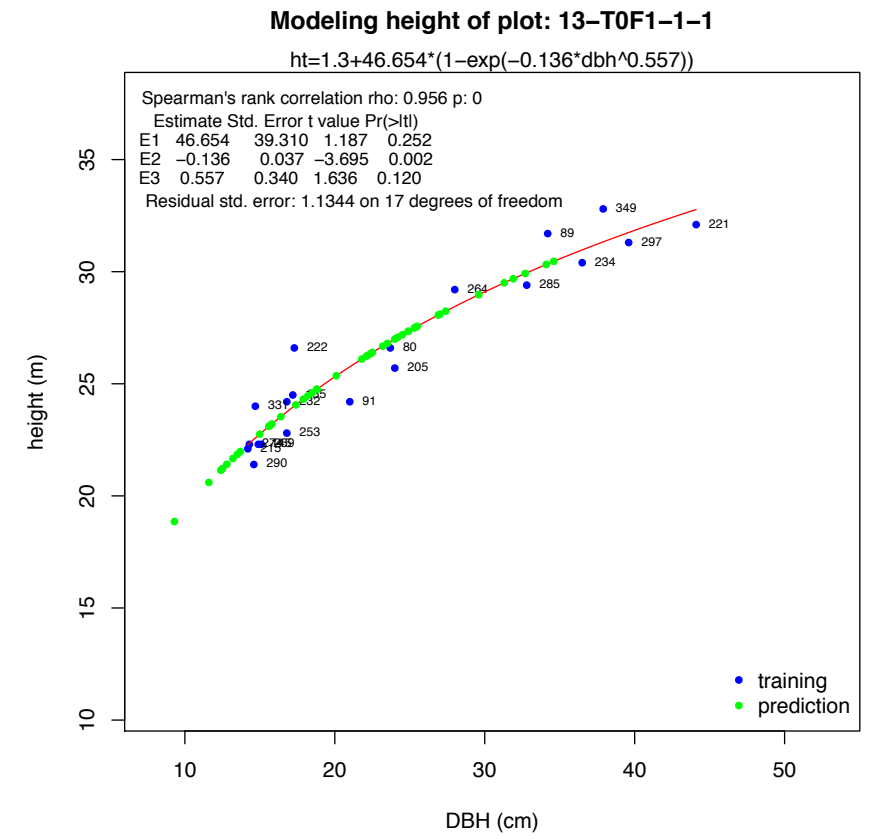

Modeling height of plot: 8–T2F1
ht=1.3+31.371*(1−exp(−0.027*dbh^1.317))
Spearman's rank correlation rho: 0.962 p: 0
Estimate Std. Error t value Pr(>|t|)
E1 31.371 1.531 20.487 0.000
E2 −0.027 0.021 −1.264 0.224
E3 1.317 0.293 4.497 0.000
Residual std. error: 1.1802 on 16 degrees of freedom
height (m)
training
prediction

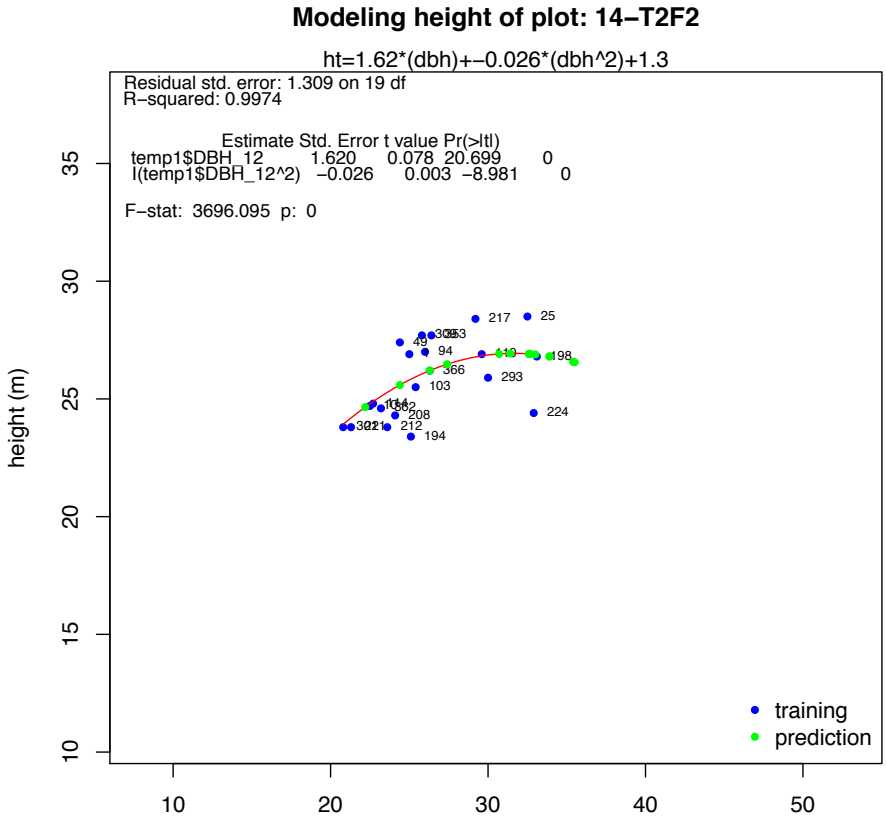

Modeling height of plot: 9–T1F1
ht=1.3+39.449*(1–exp(–0.085*dbh^0.807))
Spearman's rank correlation rho: 0.94 p: 0
Estimate Std. Error t value Pr(>|t|)
E1 39.449 9.939 3.969 0.001
E2 –0.085 0.033 –2.551 0.021
E3 0.807 0.263 3.070 0.007
Residual std. error: 1.307 on 17 degrees of freedom
height (m)
DBH (cm)
training
prediction

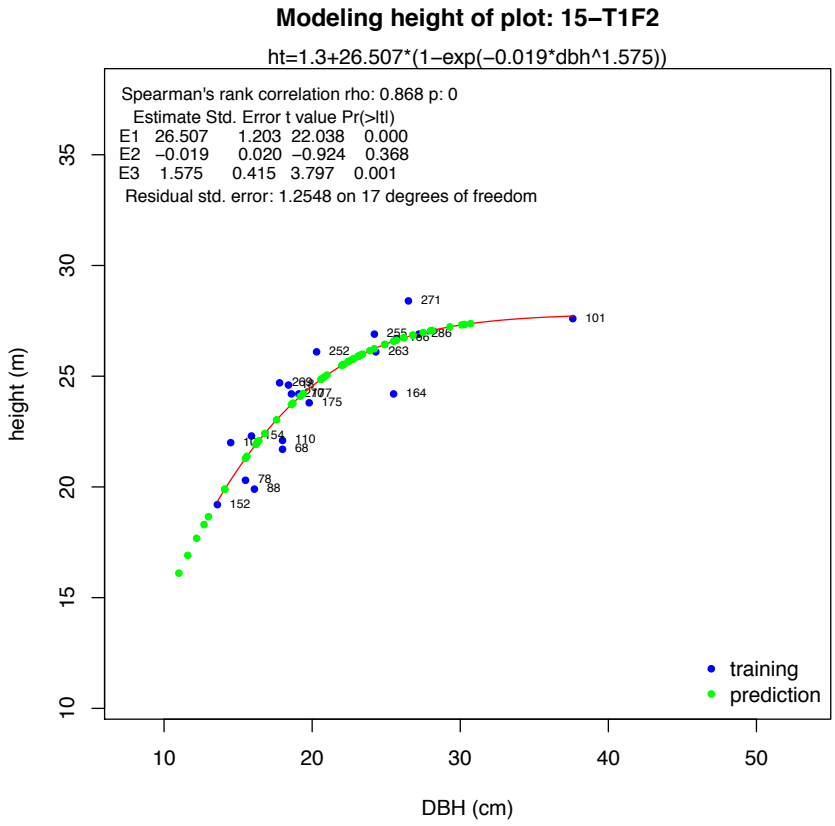

Modeling height of plot: 10–T1F0
ht=1.3+37.194*(1–exp(–0.125*dbh^0.694))
Spearman's rank correlation rho: 0.857 p: 0
Estimate Std. Error t value Pr(>|t|)
E1 37.194 13.816 2.692 0.015
E2 –0.125 0.043 –2.916 0.010
E3 0.694 0.308 2.253 0.038
Residual std. error: 1.8393 on 17 degrees of freedom
height (m)
training
prediction

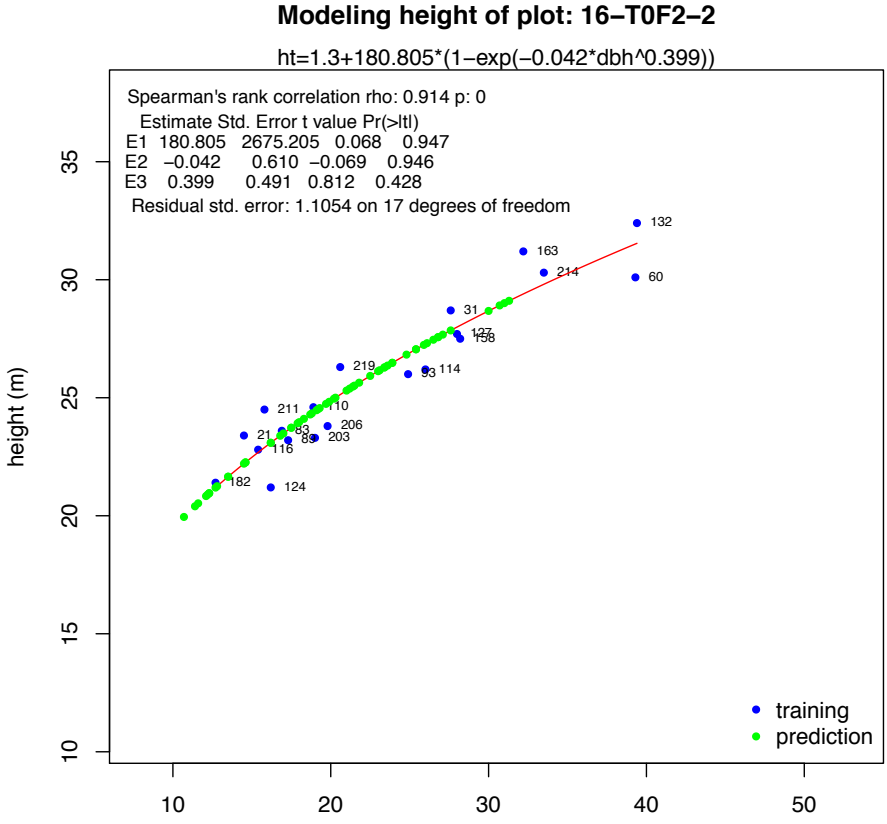

Modeling height of plot: 11−T2F0
ht=1.3+28.313*(1−exp(−0.016*dbh^1.542))
Spearman's rank correlation rho: 0.873 p: 0
Estimate Std. Error t value Pr(>|t|)
E1 28.313 0.840 33.714 0.000
E2 −0.016 0.012 −1.329 0.202
E3 1.542 0.268 5.753 0.000
Residual std. error: 1.0752 on 17 degrees of freedom
height (m)
DBH (cm)
training
prediction

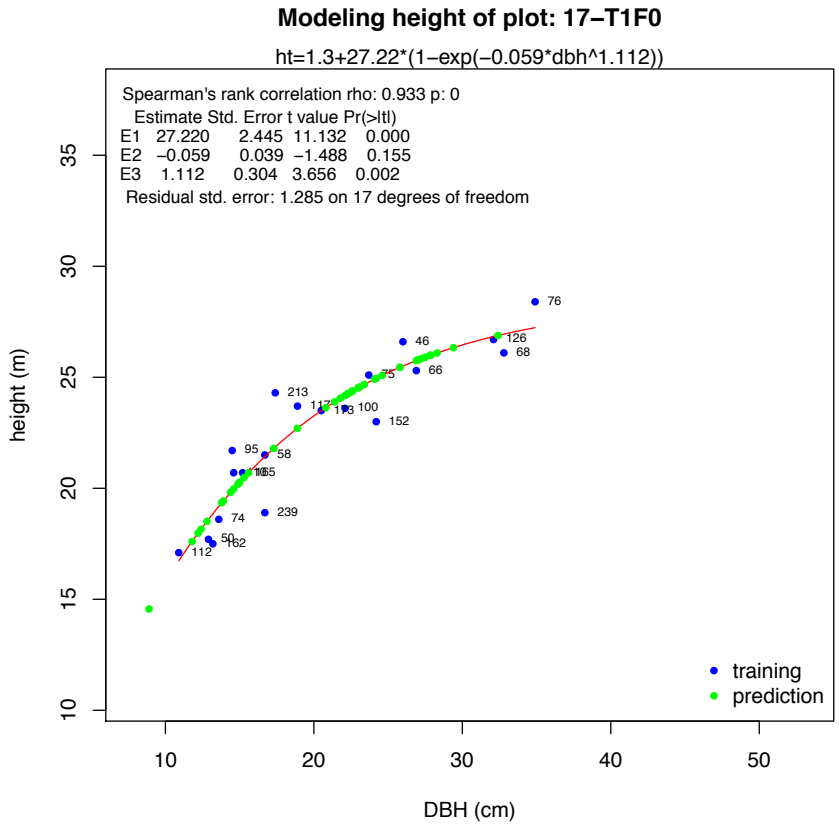

Modeling height of plot: 12−T1F1−1−1
ht=1.3+33.383*(1−exp(−0.027*dbh^1.272))
Spearman's rank correlation rho: 0.963 p: 0
Estimate Std. Error t value Pr(>|t|)
E1 33.383 2.094 15.946 0.000
E2 −0.027 0.018 −1.518 0.148
E3 1.272 0.256 4.962 0.000
Residual std. error: 1.4179 on 16 degrees of freedom
height (m)
training
prediction

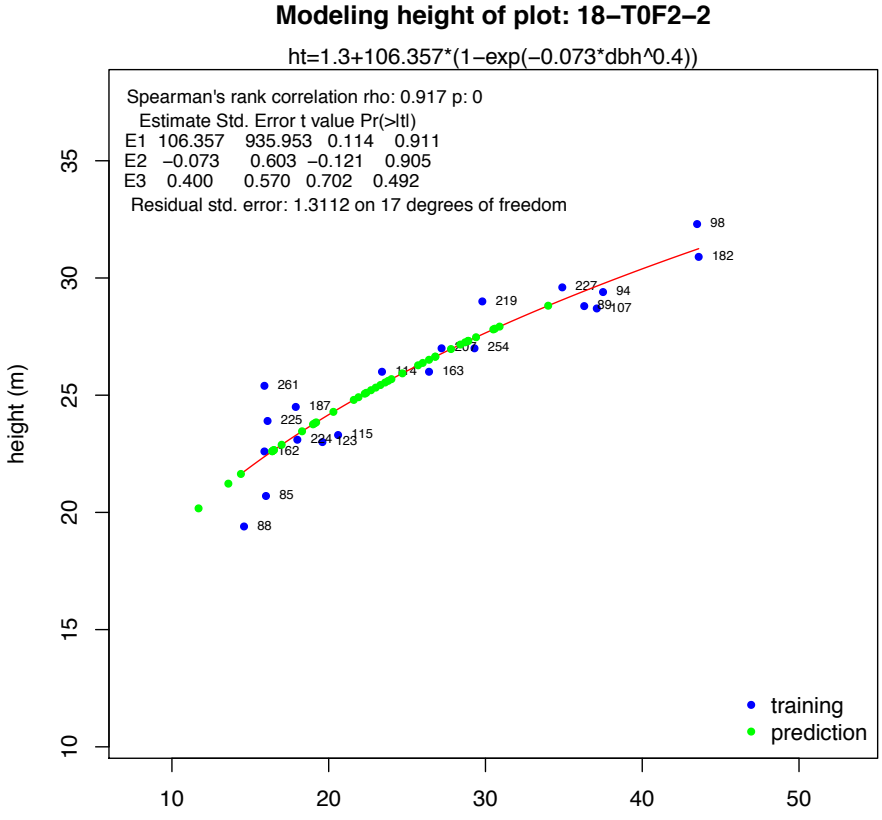

Modeling height of plot: 13−T0F1−1−1
ht=1.3+46.654*(1−exp(−0.136*dbh^0.557))
Spearman's rank correlation rho: 0.956 p: 0
Estimate Std. Error t value Pr(>|t|)
E1 46.654 39.310 1.187 0.252
E2 −0.136 0.037 −3.695 0.002
E3 0.557 0.340 1.636 0.120
Residual std. error: 1.1344 on 17 degrees of freedom
height (m)
DBH (cm)
training
prediction

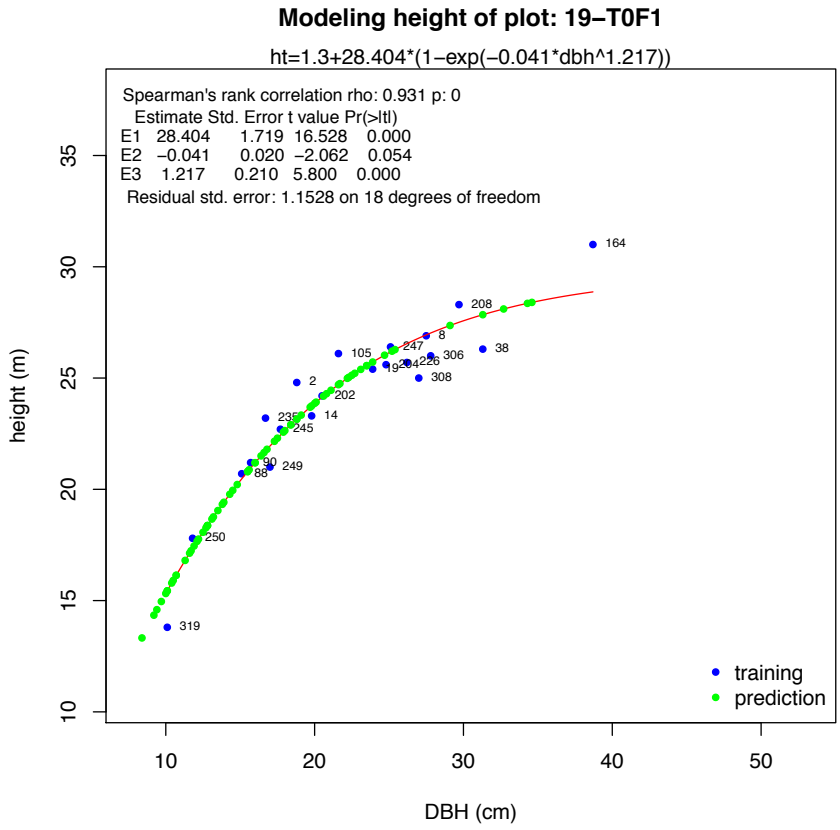

Modeling height of plot: 14−T2F2
ht=1.62*(dbh)+−0.026*(dbh^2)+1.3
Residual std. error: 1.309 on 19 df
R−squared: 0.9974
Estimate Std. Error t value Pr(>|t|)
temp1$DBH_12 1.620 0.078 20.699 0
I(temp1$DBH_12^2) −0.026 0.003 −8.981 0
F−stat: 3696.095 p: 0
height (m)
training
prediction

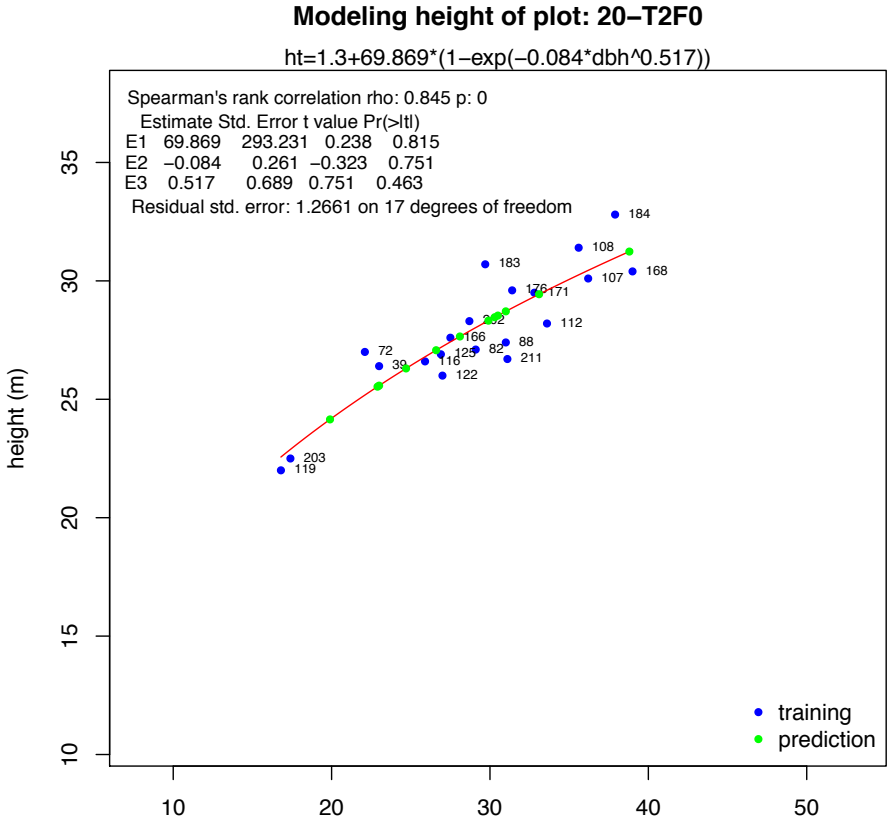

Modeling height of plot: 15−T1F2
ht=1.3+26.507*(1−exp(−0.019*dbh^1.575))
Spearman's rank correlation rho: 0.868 p: 0
Estimate Std. Error t value Pr(>|t|)
E1 26.507 1.203 22.038 0.000
E2 −0.019 0.020 −0.924 0.368
E3 1.575 0.415 3.797 0.001
Residual std. error: 1.2548 on 17 degrees of freedom
height (m)
DBH (cm)
training
prediction

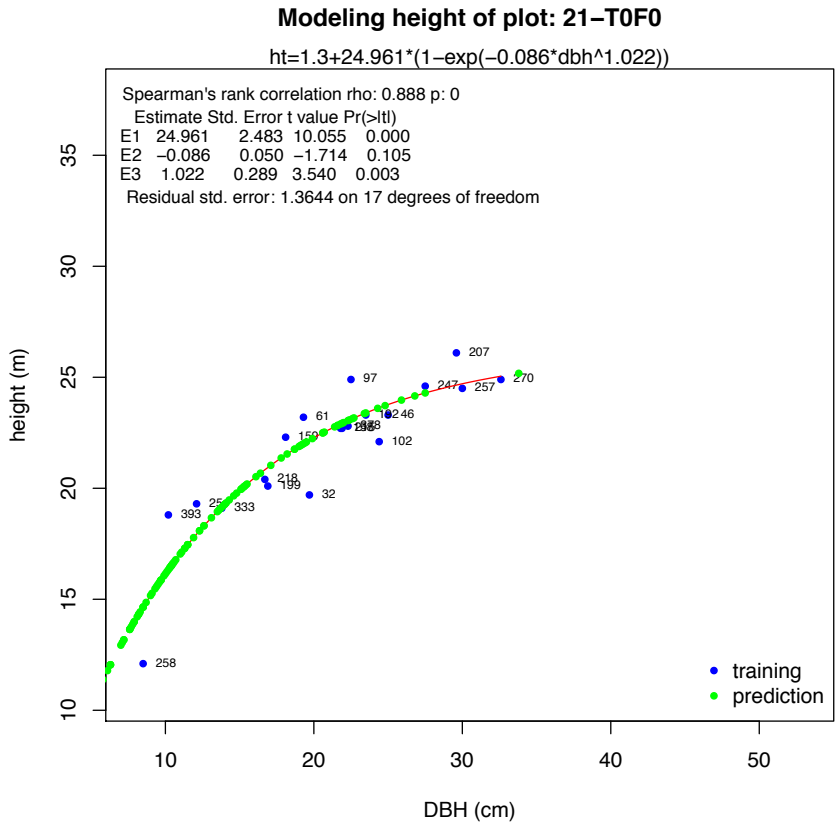

Modeling height of plot: 16−T0F2−2
ht=1.3+180.805*(1−exp(−0.042*dbh^0.399))
Spearman's rank correlation rho: 0.914 p: 0
Estimate Std. Error t value Pr(>|t|)
E1 180.805 2675.205 0.068 0.947
E2 −0.042 0.610 −0.069 0.946
E3 0.399 0.491 0.812 0.428
Residual std. error: 1.1054 on 17 degrees of freedom
height (m)
training
prediction

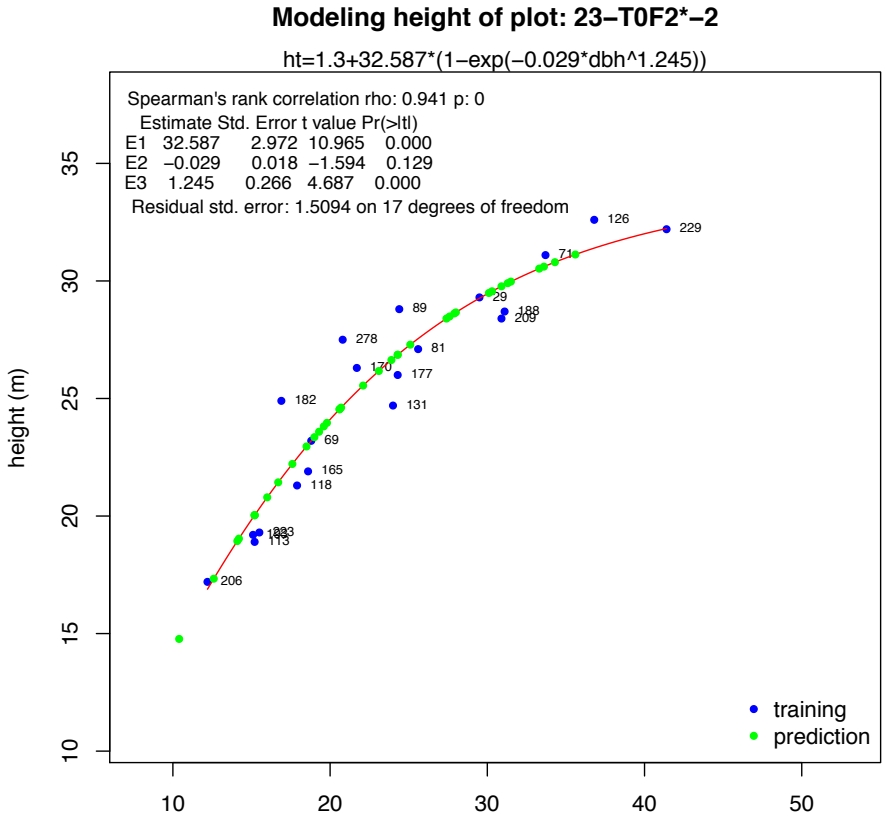

Modeling height of plot: 17–T1F0
ht=1.3+27.22*(1–exp(–0.059*dbh^1.112))
Spearman's rank correlation rho: 0.933 p: 0
Estimate Std. Error t value Pr(>|t|)
E1 27.220 2.445 11.132 0.000
E2 –0.059 0.039 –1.488 0.155
E3 1.112 0.304 3.656 0.002
Residual std. error: 1.285 on 17 degrees of freedom
height (m)
DBH (cm)
training
prediction

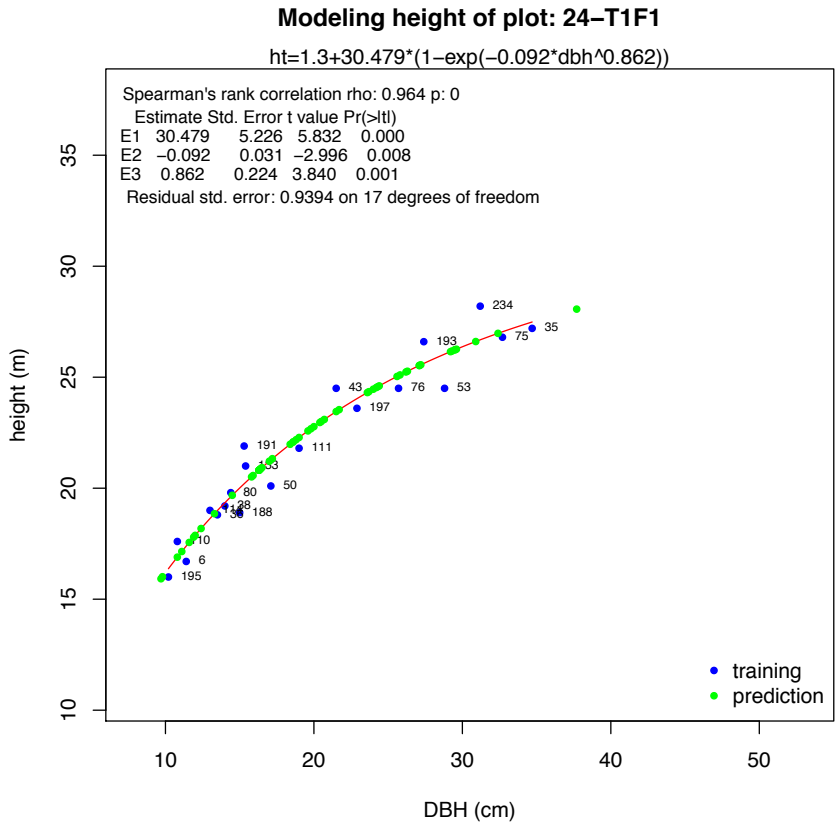

Modeling height of plot: 18–T0F2–2
ht=1.3+106.357*(1–exp(–0.073*dbh^0.4))
Spearman's rank correlation rho: 0.917 p: 0
Estimate Std. Error t value Pr(>|t|)
E1 106.357 935.953 0.114 0.911
E2 –0.073 0.603 –0.121 0.905
E3 0.400 0.570 0.702 0.492
Residual std. error: 1.3112 on 17 degrees of freedom
height (m)
training
prediction

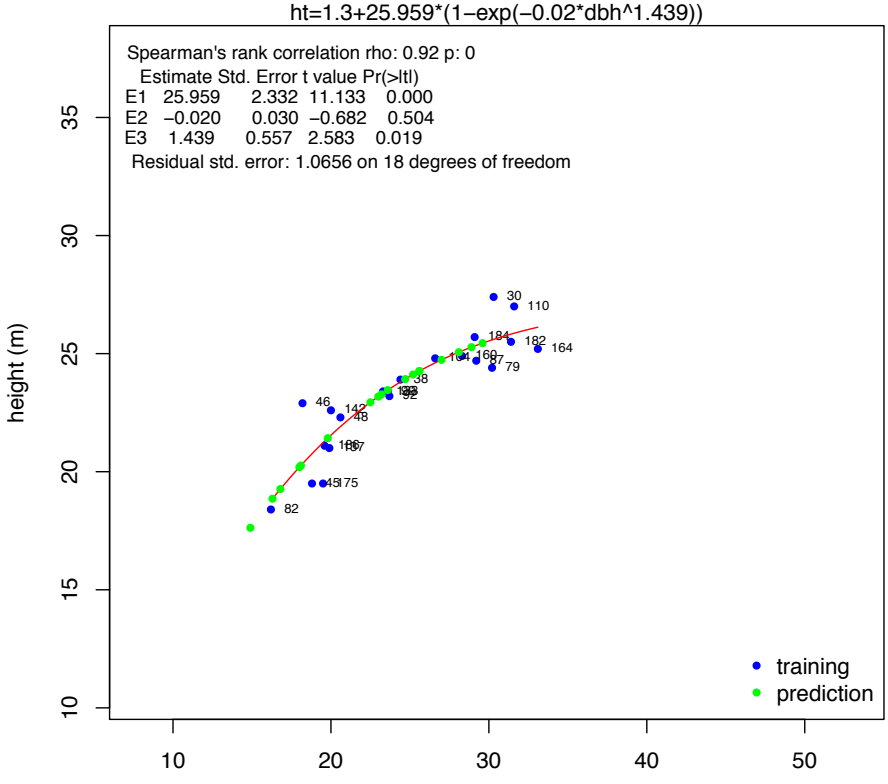

Modeling height of plot: 19–T0F1
ht=1.3+28.404*(1–exp(–0.041*dbh^1.217))
Spearman's rank correlation rho: 0.931 p: 0
Estimate Std. Error t value Pr(>|t|)
E1 28.404 1.719 16.528 0.000
E2 –0.041 0.020 –2.062 0.054
E3 1.217 0.210 5.800 0.000
Residual std. error: 1.1528 on 18 degrees of freedom
height (m)
DBH (cm)
training
prediction

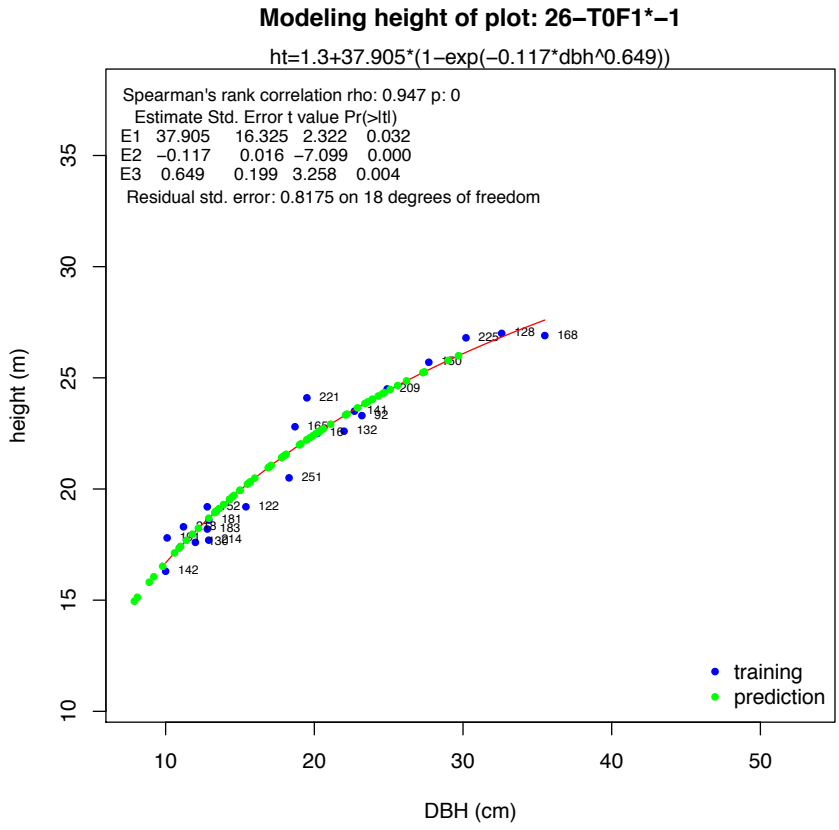

Modeling height of plot: 20–T2F0
ht=1.3+69.869*(1–exp(–0.084*dbh^0.517))
Spearman's rank correlation rho: 0.845 p: 0
Estimate Std. Error t value Pr(>|t|)
E1 69.869 293.231 0.238 0.815
E2 –0.084 0.261 –0.323 0.751
E3 0.517 0.689 0.751 0.463
Residual std. error: 1.2661 on 17 degrees of freedom
height (m)
training
prediction

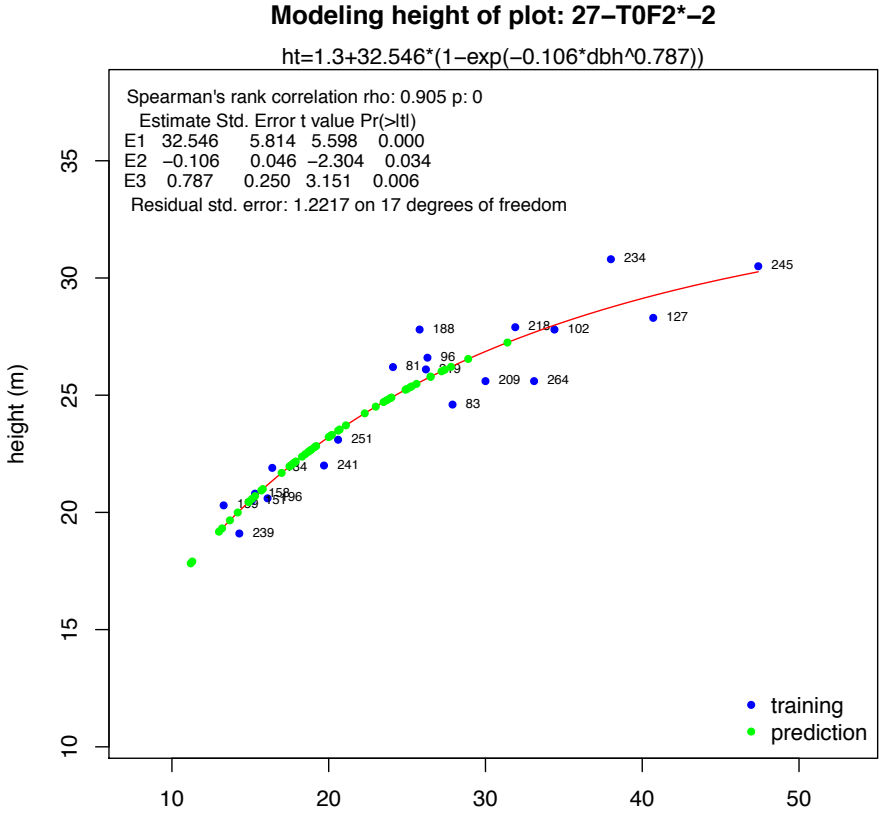

Modeling height of plot: 21–T0F0
ht=1.3+24.961*(1–exp(–0.086*dbh^1.022))
Spearman's rank correlation rho: 0.888 p: 0
Estimate Std. Error t value Pr(>|t|)
E1 24.961 2.483 10.055 0.000
E2 –0.086 0.050 –1.714 0.105
E3 1.022 0.289 3.540 0.003
Residual std. error: 1.3644 on 17 degrees of freedom
height (m)
DBH (cm)
training
prediction

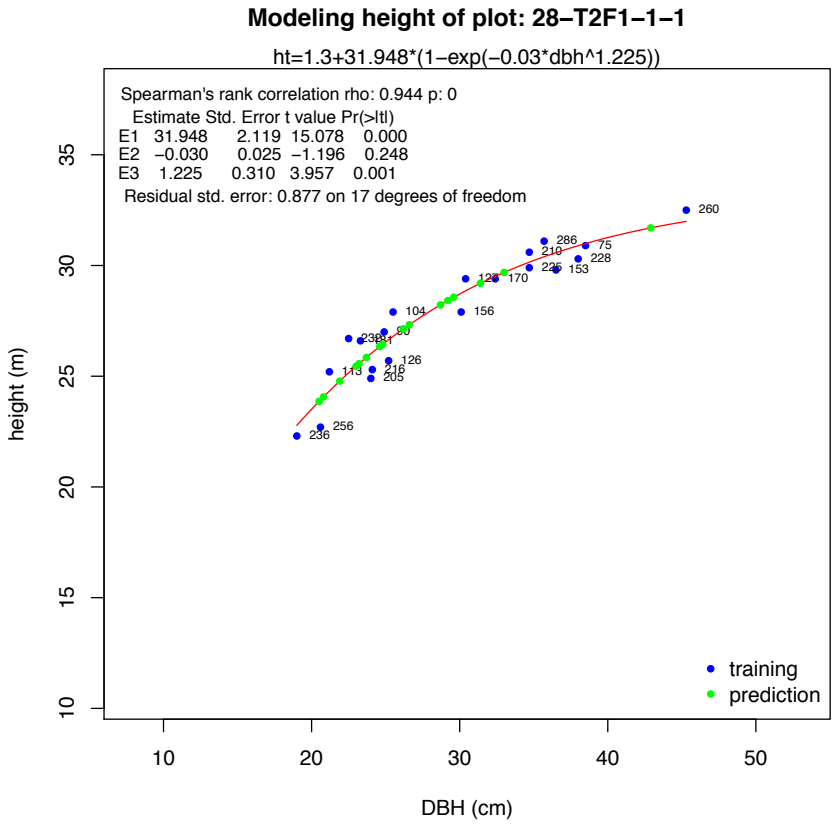

Modeling height of plot: 23–T0F2*–2
ht=1.3+32.587*(1–exp(–0.029*dbh^1.245))
Spearman's rank correlation rho: 0.941 p: 0
Estimate Std. Error t value Pr(>|t|)
E1 32.587 2.972 10.965 0.000
E2 –0.029 0.018 –1.594 0.129
E3 1.245 0.266 4.687 0.000
Residual std. error: 1.5094 on 17 degrees of freedom
height (m)
training
prediction

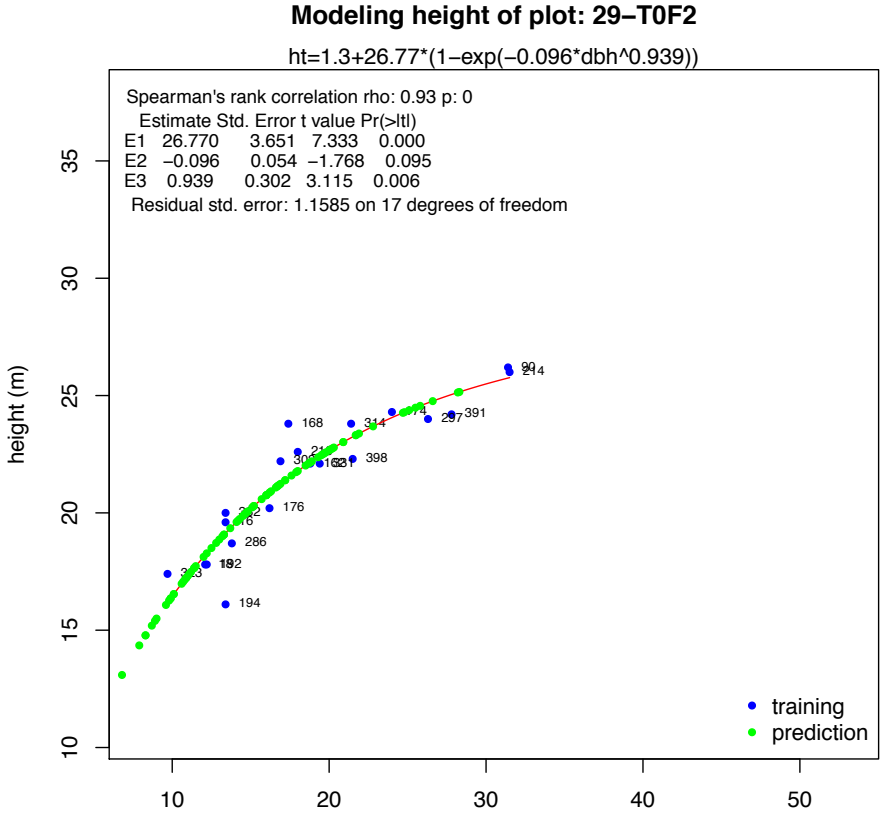

Modeling height of plot: 24–T1F1
ht=1.3+30.479*(1−exp(−0.092*dbh^0.862))
Spearman's rank correlation rho: 0.964 p: 0
Estimate Std. Error t value Pr(>|t|)
E1 30.479 5.226 5.832 0.000
E2 −0.092 0.031 −2.996 0.008
E3 0.862 0.224 3.840 0.001
Residual std. error: 0.9394 on 17 degrees of freedom
height (m)
DBH (cm)
training
prediction

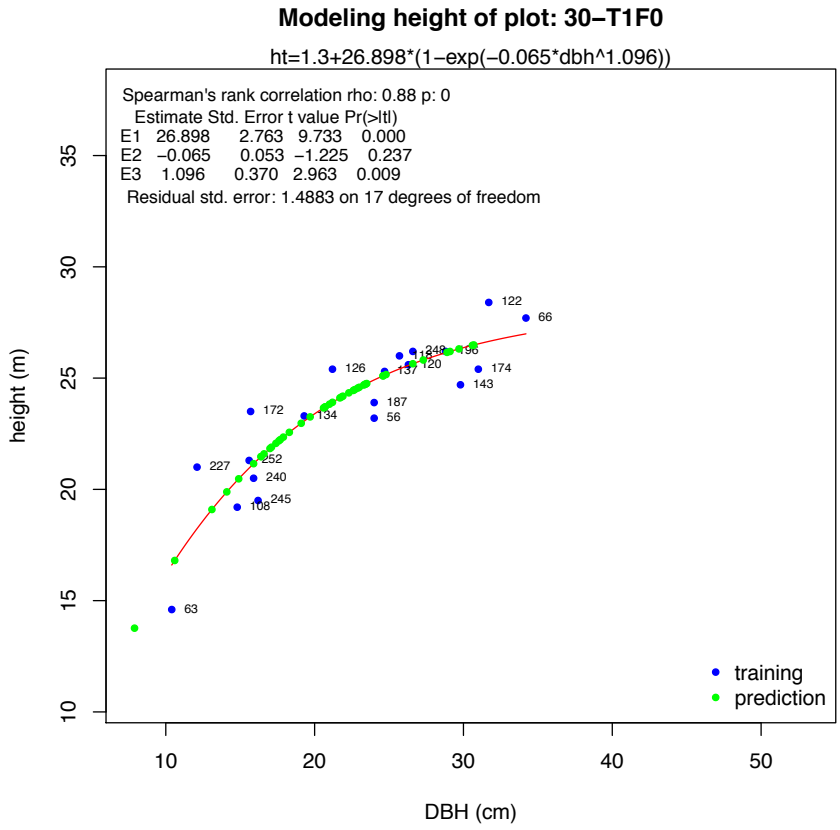

Modeling height of plot: 25–T2F0
ht=1.3+25.959*(1−exp(−0.02*dbh^1.439))
Spearman's rank correlation rho: 0.92 p: 0
Estimate Std. Error t value Pr(>|t|)
E1 25.959 2.332 11.133 0.000
E2 −0.020 0.030 −0.682 0.504
E3 1.439 0.557 2.583 0.019
Residual std. error: 1.0656 on 18 degrees of freedom
height (m)
training
prediction

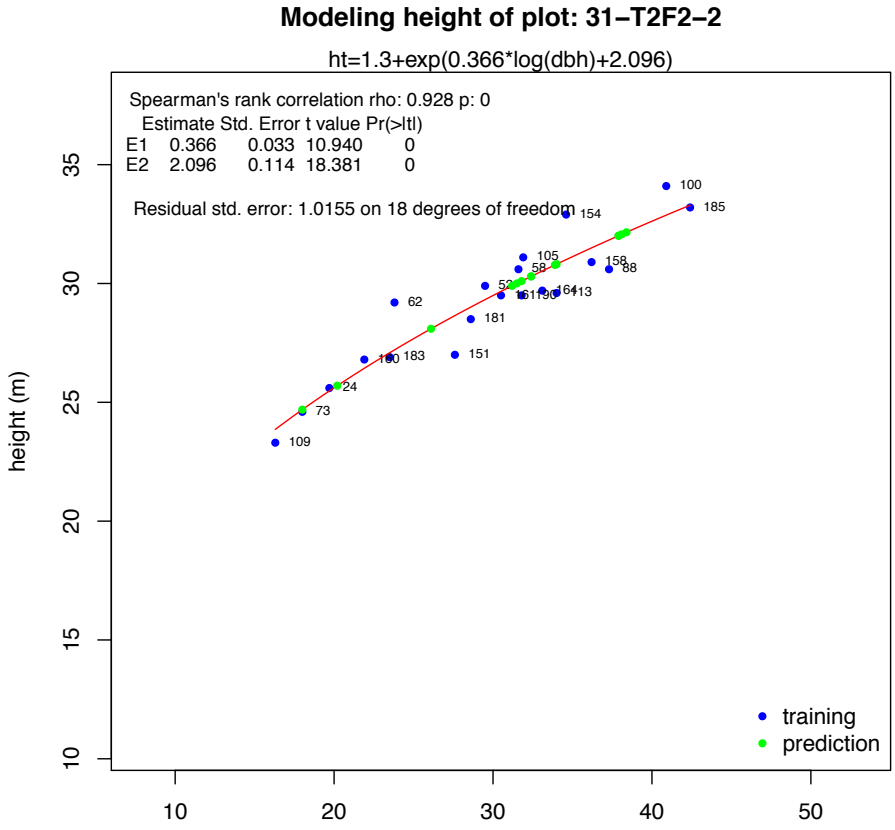

Modeling height of plot: 26–T0F1*–1
ht=1.3+37.905*(1–exp(–0.117*dbh^0.649))
Spearman's rank correlation rho: 0.947 p: 0
Estimate Std. Error t value Pr(>|t|)
E1 37.905 16.325 2.322 0.032
E2 –0.117 0.016 –7.099 0.000
E3 0.649 0.199 3.258 0.004
Residual std. error: 0.8175 on 18 degrees of freedom
height (m)
DBH (cm)
training
prediction

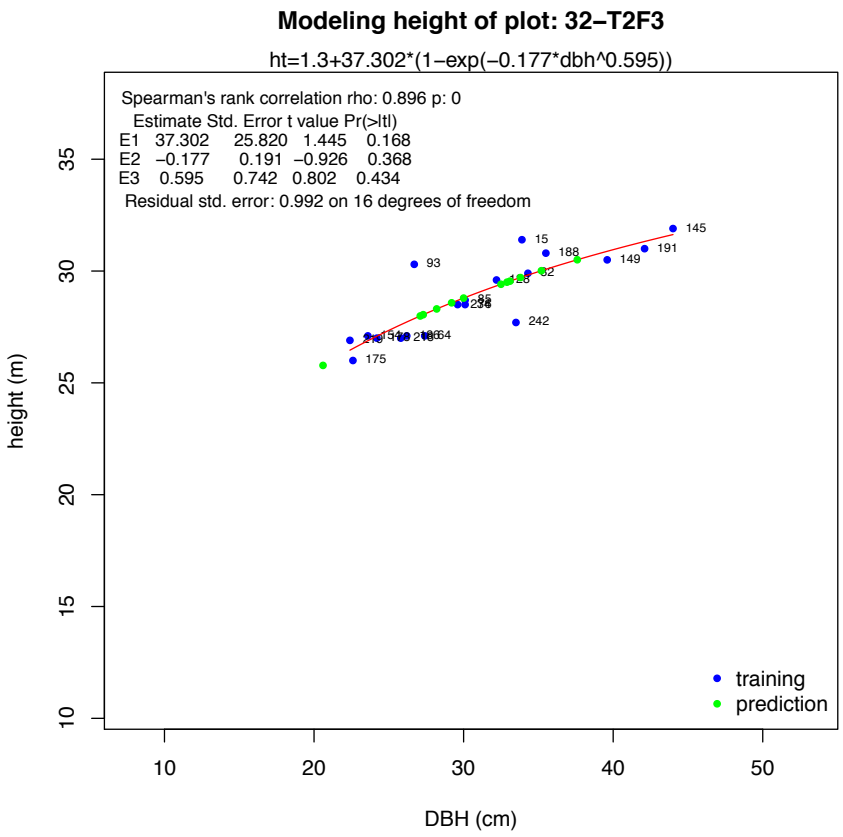

Modeling height of plot: 27–T0F2*–2
ht=1.3+32.546*(1–exp(–0.106*dbh^0.787))
Spearman's rank correlation rho: 0.905 p: 0
Estimate Std. Error t value Pr(>|t|)
E1 32.546 5.814 5.598 0.000
E2 –0.106 0.046 –2.304 0.034
E3 0.787 0.250 3.151 0.006
Residual std. error: 1.2217 on 17 degrees of freedom
height (m)
training
prediction

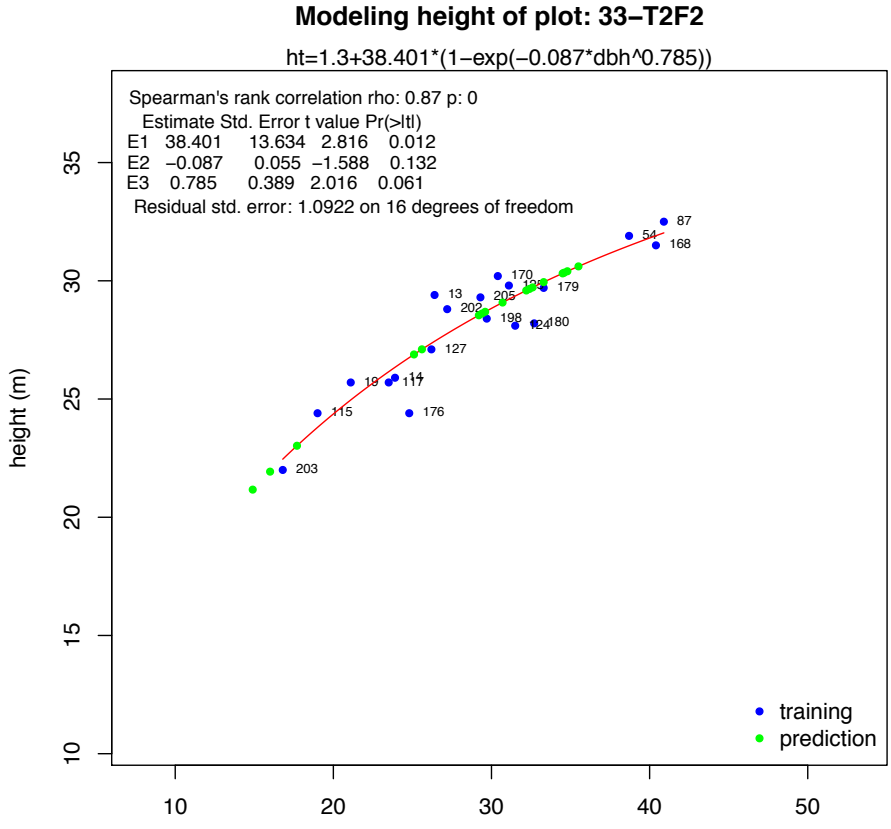

Modeling height of plot: 28−T2F1−1−1
ht=1.3+31.948*(1−exp(−0.03*dbh^1.225))
Spearman's rank correlation rho: 0.944 p: 0
Estimate Std. Error t value Pr(>|t|)
E1 31.948 2.119 15.078 0.000
E2 −0.030 0.025 −1.196 0.248
E3 1.225 0.310 3.957 0.001
Residual std. error: 0.877 on 17 degrees of freedom
height (m)
DBH (cm)
training
prediction

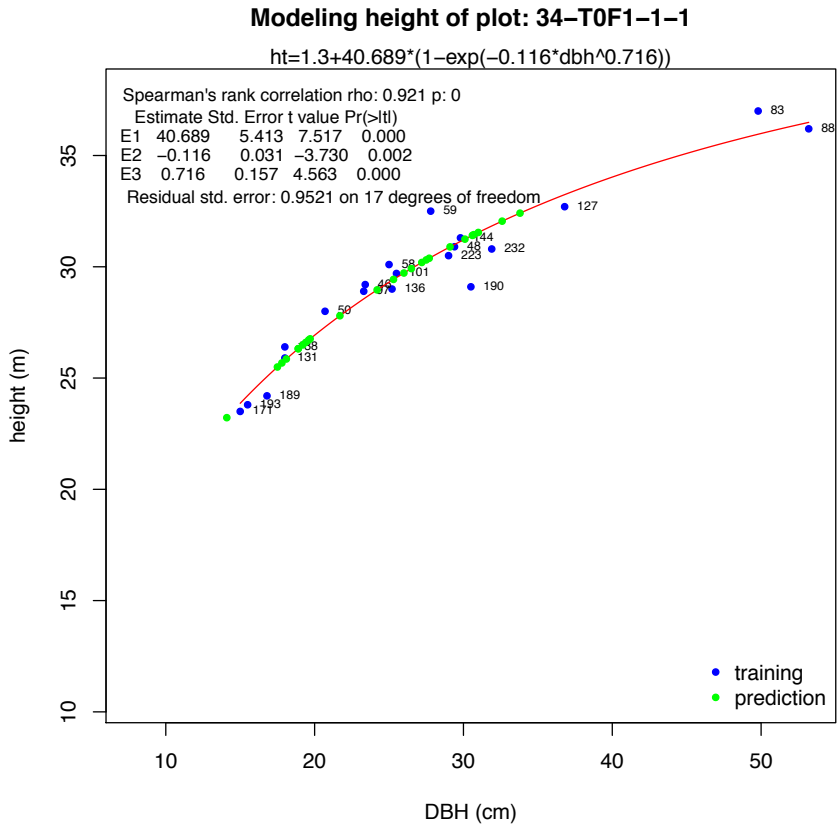

Modeling height of plot: 29−T0F2
ht=1.3+26.77*(1−exp(−0.096*dbh^0.939))
Spearman's rank correlation rho: 0.93 p: 0
Estimate Std. Error t value Pr(>|t|)
E1 26.770 3.651 7.333 0.000
E2 −0.096 0.054 −1.768 0.095
E3 0.939 0.302 3.115 0.006
Residual std. error: 1.1585 on 17 degrees of freedom
height (m)
training
prediction

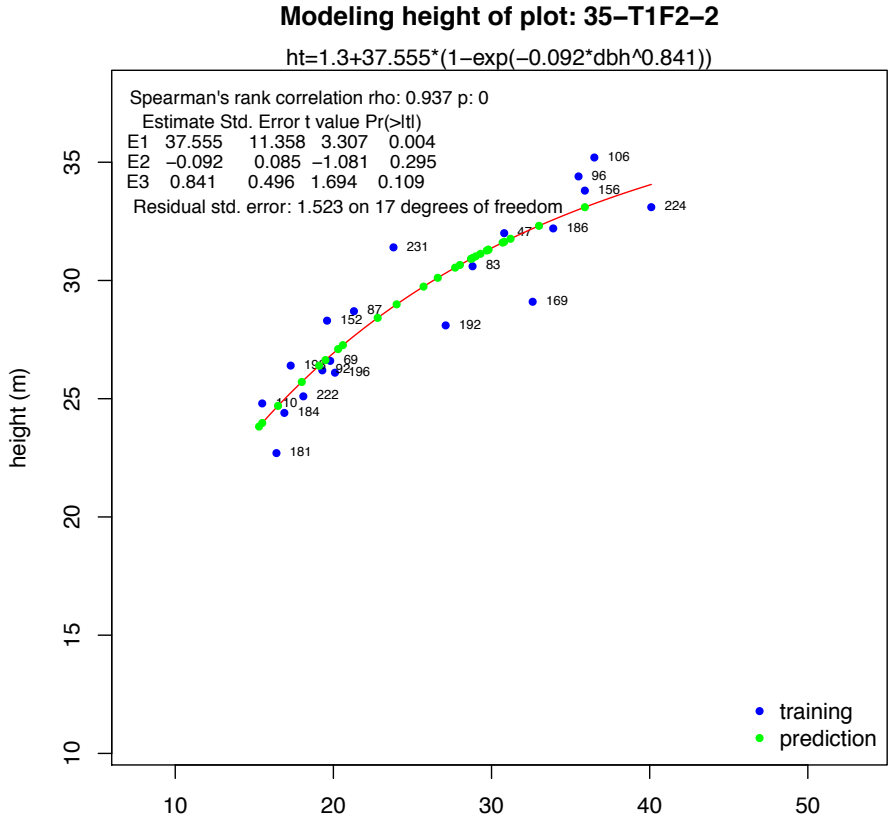

Modeling height of plot: 30−T1F0
ht=1.3+26.898*(1−exp(−0.065*dbh^1.096))
Spearman's rank correlation rho: 0.88 p: 0
Estimate Std. Error t value Pr(>|t|)
E1 26.898 2.763 9.733 0.000
E2 −0.065 0.053 −1.225 0.237
E3 1.096 0.370 2.963 0.009
Residual std. error: 1.4883 on 17 degrees of freedom
height (m)
DBH (cm)
training
prediction

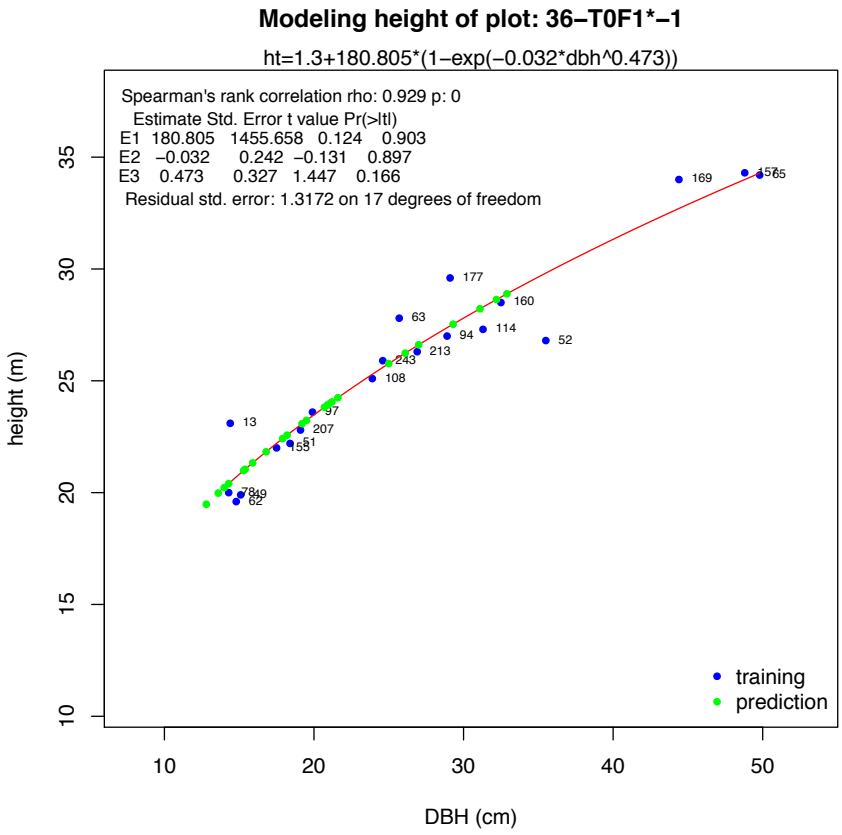

Modeling height of plot: 31−T2F2−2
ht=1.3+exp(0.366*log(dbh)+2.096)
Spearman's rank correlation rho: 0.928 p: 0
Estimate Std. Error t value Pr(>|t|)
E1 0.366 0.033 10.940 0
E2 2.096 0.114 18.381 0
Residual std. error: 1.0155 on 18 degrees of freedom
height (m)
training
prediction

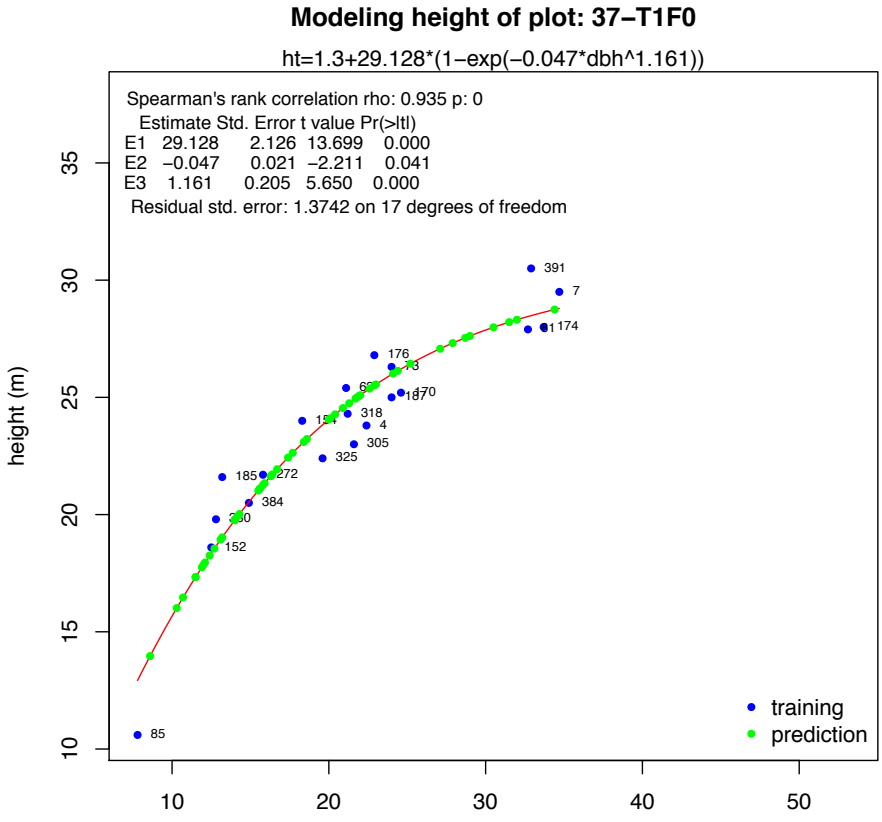

Modeling height of plot: 32–T2F3
ht=1.3+37.302*(1−exp(−0.177*dbh^0.595))
Spearman's rank correlation rho: 0.896 p: 0
Estimate Std. Error t value Pr(>|t|)
E1 37.302 25.820 1.445 0.168
E2 −0.177 0.191 −0.926 0.368
E3 0.595 0.742 0.802 0.434
Residual std. error: 0.992 on 16 degrees of freedom
height (m)
DBH (cm)
training
prediction

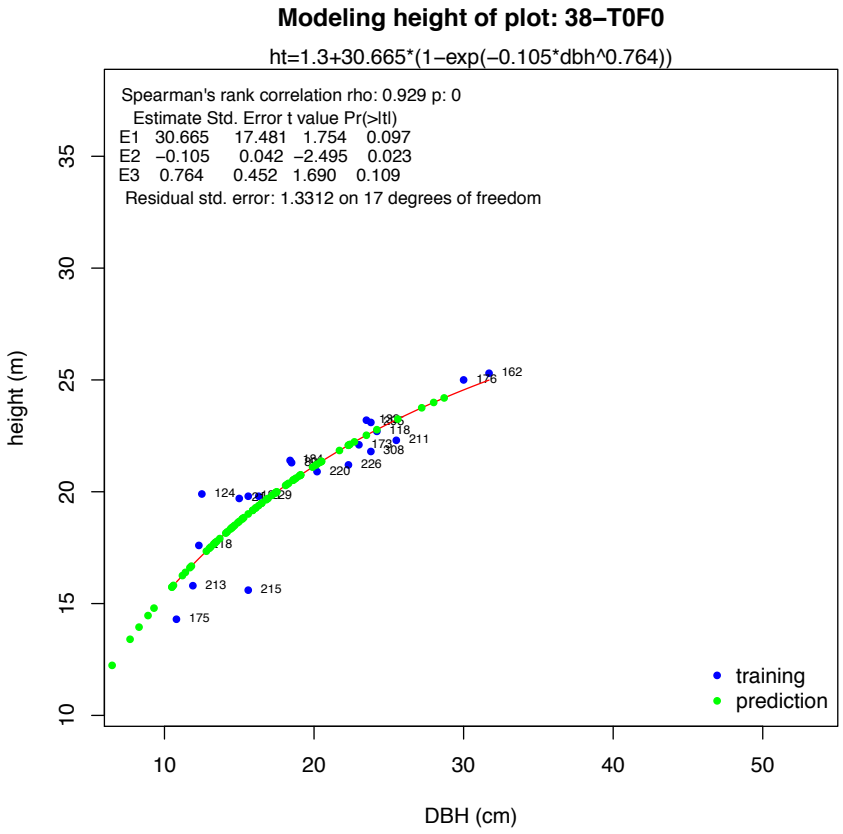

Modeling height of plot: 33–T2F2
ht=1.3+38.401*(1−exp(−0.087*dbh^0.785))
Spearman's rank correlation rho: 0.87 p: 0
Estimate Std. Error t value Pr(>|t|)
E1 38.401 13.634 2.816 0.012
E2 −0.087 0.055 −1.588 0.132
E3 0.785 0.389 2.016 0.061
Residual std. error: 1.0922 on 16 degrees of freedom
height (m)
training
prediction

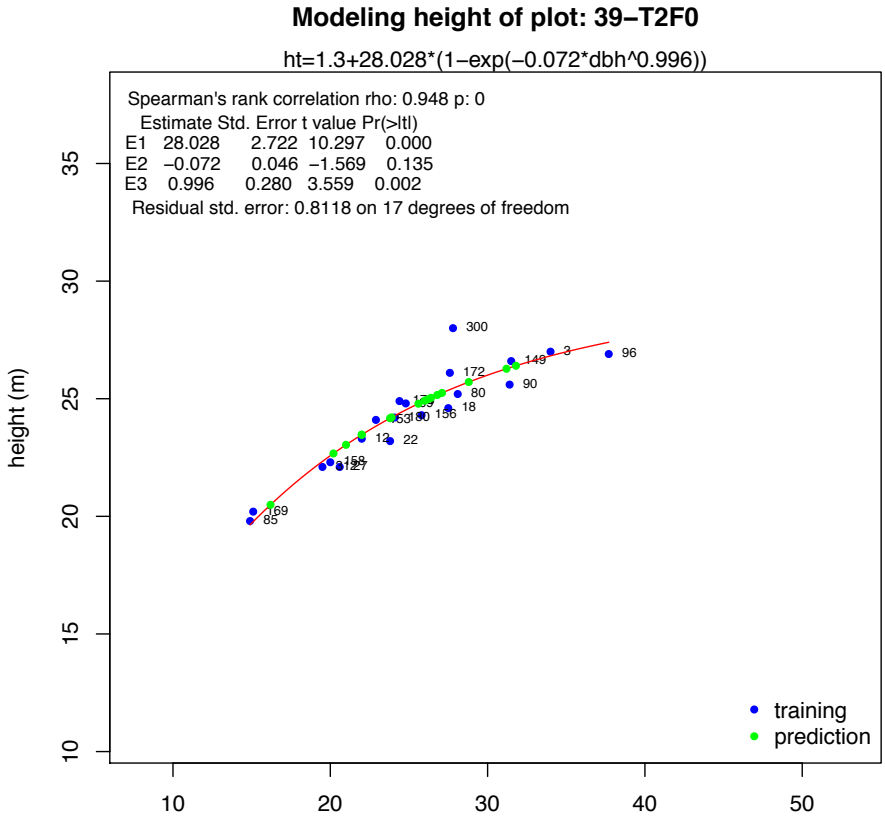

Modeling height of plot: 34–T0F1–1–1
ht=1.3+40.689*(1–exp(–0.116*dbh^0.716))
Spearman's rank correlation rho: 0.921 p: 0
Estimate Std. Error t value Pr(>|t|)
E1 40.689 5.413 7.517 0.000
E2 –0.116 0.031 –3.730 0.002
E3 0.716 0.157 4.563 0.000
Residual std. error: 0.9521 on 17 degrees of freedom
height (m)
DBH (cm)
training
prediction

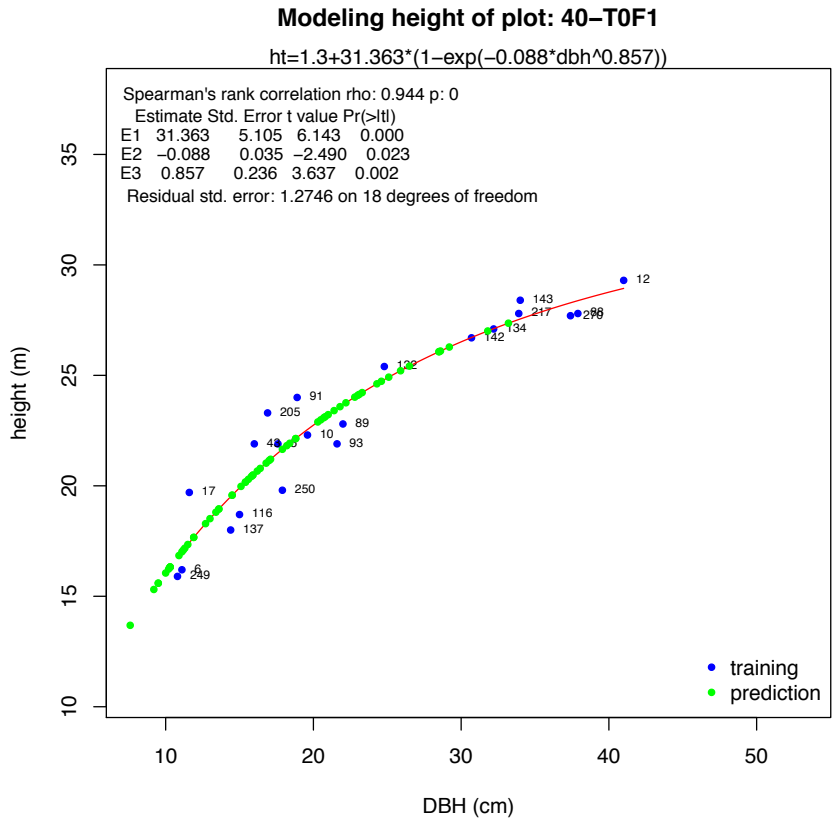

Modeling height of plot: 35–T1F2–2
ht=1.3+37.555*(1–exp(–0.092*dbh^0.841))
Spearman's rank correlation rho: 0.937 p: 0
Estimate Std. Error t value Pr(>|t|)
E1 37.555 11.358 3.307 0.004
E2 –0.092 0.085 –1.081 0.295
E3 0.841 0.496 1.694 0.109
Residual std. error: 1.523 on 17 degrees of freedom
height (m)
training
prediction

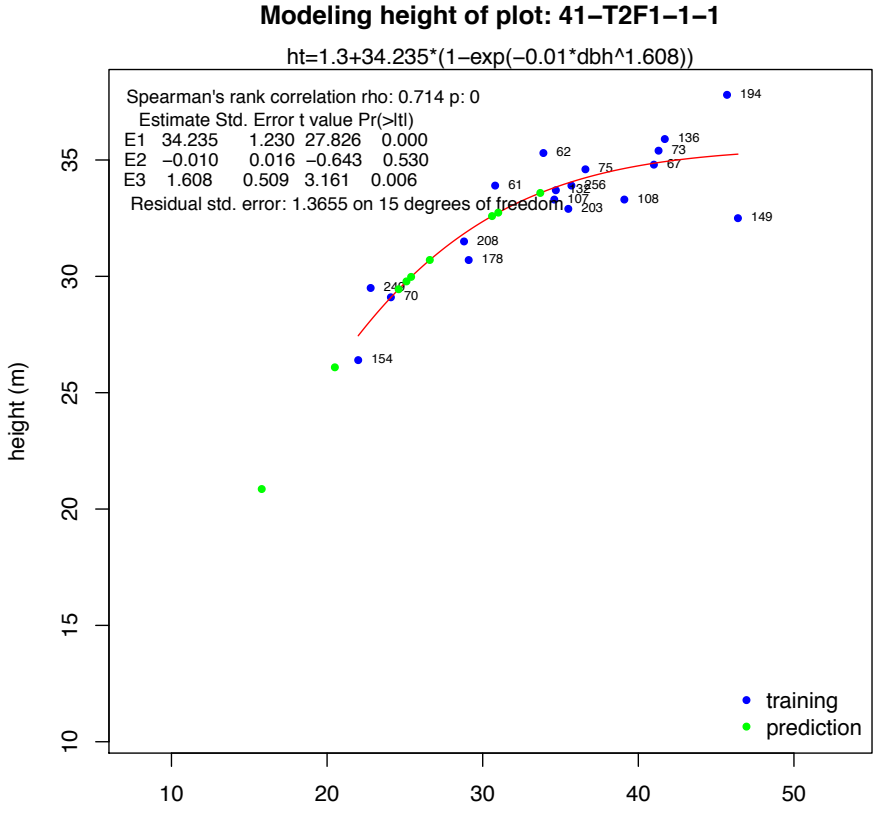

Modeling height of plot: 36–T0F1*–1
ht=1.3+180.805*(1−exp(−0.032*dbh^0.473))
Spearman's rank correlation rho: 0.929 p: 0
Estimate Std. Error t value Pr(>|t|)
E1 180.805 1455.658 0.124 0.903
E2 −0.032 0.242 −0.131 0.897
E3 0.473 0.327 1.447 0.166
Residual std. error: 1.3172 on 17 degrees of freedom
height (m)
DBH (cm)
training
prediction

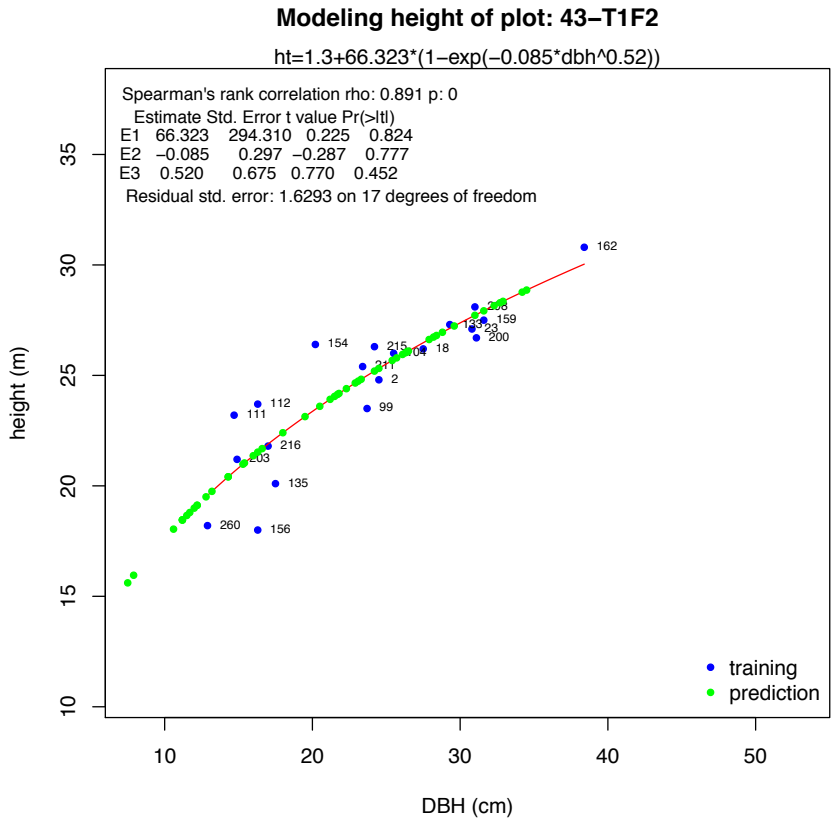

Modeling height of plot: 37–T1F0
ht=1.3+29.128*(1−exp(−0.047*dbh^1.161))
Spearman's rank correlation rho: 0.935 p: 0
Estimate Std. Error t value Pr(>|t|)
E1 29.128 2.126 13.699 0.000
E2 −0.047 0.021 −2.211 0.041
E3 1.161 0.205 5.650 0.000
Residual std. error: 1.3742 on 17 degrees of freedom
height (m)
training
prediction

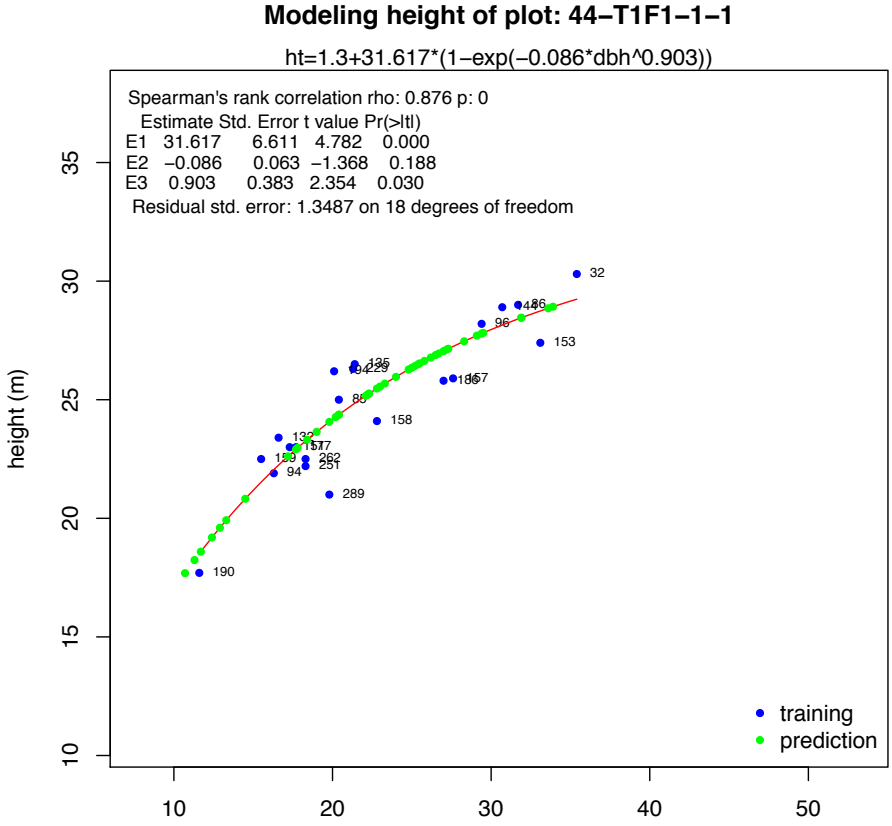

Modeling height of plot: 38–T0F0
ht=1.3+30.665*(1−exp(−0.105*dbh^0.764))
Spearman's rank correlation rho: 0.929 p: 0
Estimate Std. Error t value Pr(>|t|)
E1 30.665 17.481 1.754 0.097
E2 −0.105 0.042 −2.495 0.023
E3 0.764 0.452 1.690 0.109
Residual std. error: 1.3312 on 17 degrees of freedom
height (m)
DBH (cm)
training
prediction

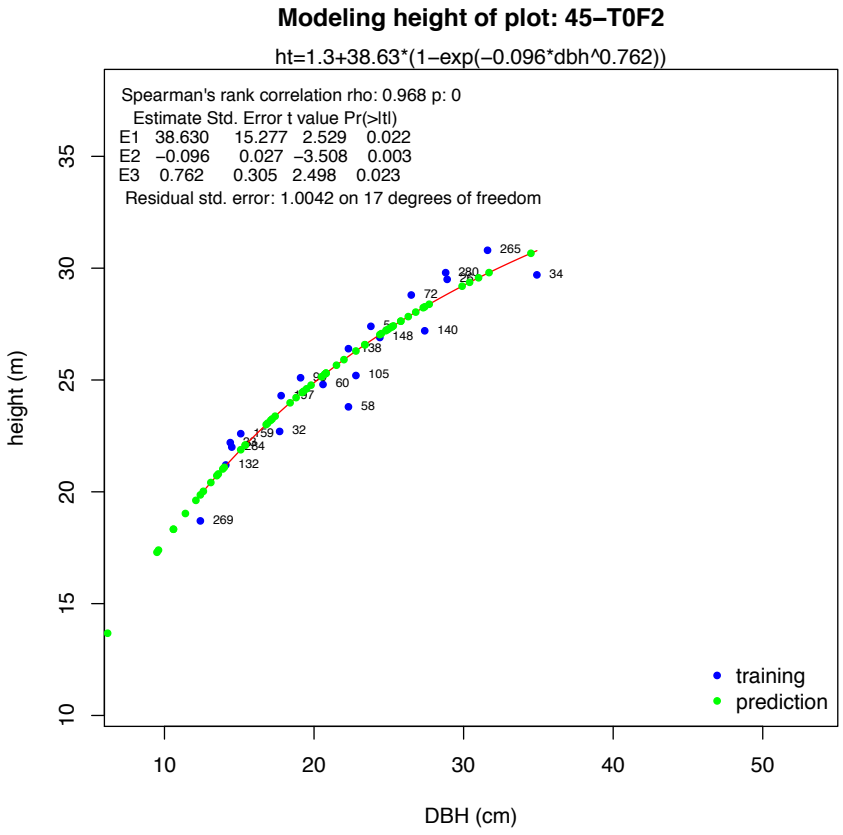

Modeling height of plot: 39–T2F0
ht=1.3+28.028*(1−exp(−0.072*dbh^0.996))
Spearman's rank correlation rho: 0.948 p: 0
Estimate Std. Error t value Pr(>|t|)
E1 28.028 2.722 10.297 0.000
E2 −0.072 0.046 −1.569 0.135
E3 0.996 0.280 3.559 0.002
Residual std. error: 0.8118 on 17 degrees of freedom
height (m)
training
prediction

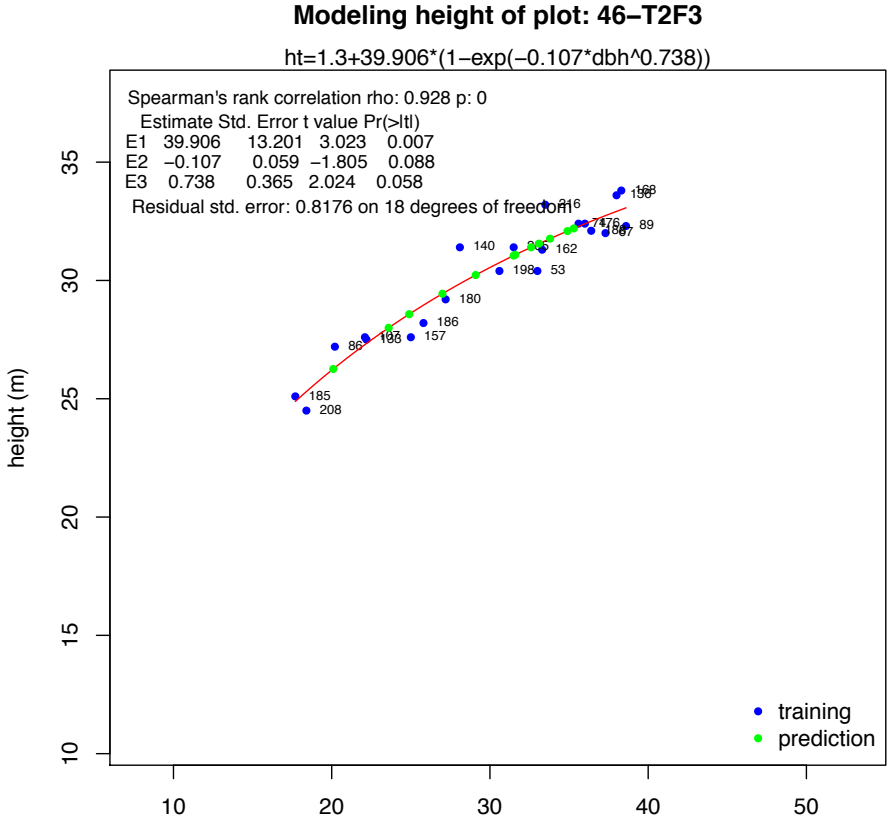

Modeling height of plot: 40−T0F1
ht=1.3+31.363*(1−exp(−0.088*dbh^0.857))
Spearman's rank correlation rho: 0.944 p: 0
Estimate Std. Error t value Pr(>|t|)
E1 31.363 5.105 6.143 0.000
E2 −0.088 0.035 −2.490 0.023
E3 0.857 0.236 3.637 0.002
Residual std. error: 1.2746 on 18 degrees of freedom
height (m)
DBH (cm)
training
prediction

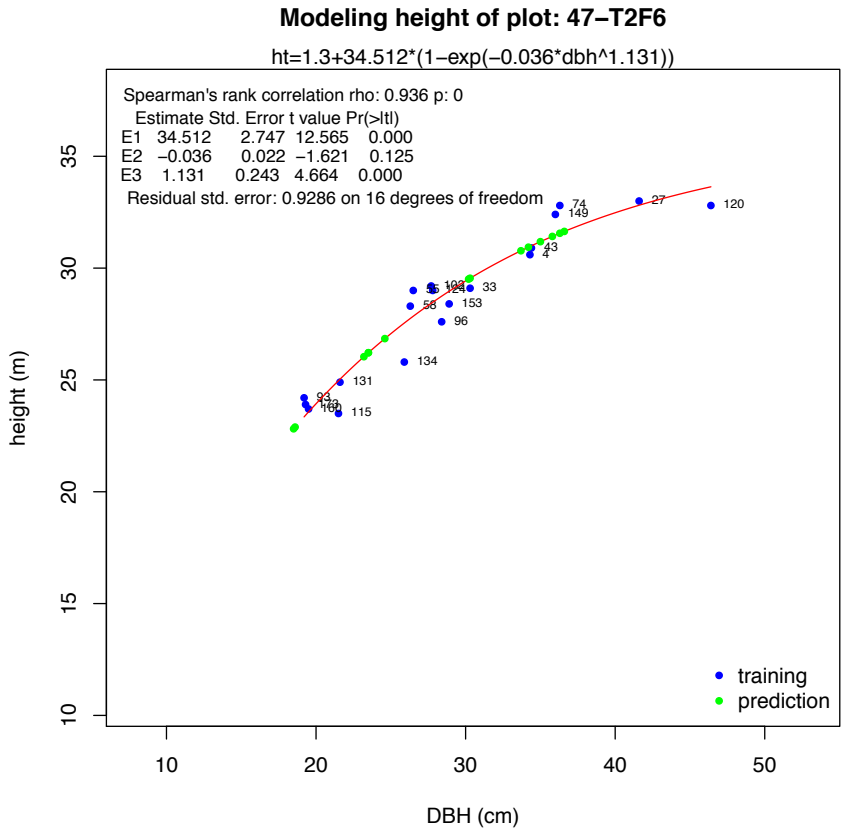

Modeling height of plot: 41−T2F1−1−1
ht=1.3+34.235*(1−exp(−0.01*dbh^1.608))
Spearman's rank correlation rho: 0.714 p: 0
Estimate Std. Error t value Pr(>|t|)
E1 34.235 1.230 27.826 0.000
E2 −0.010 0.016 −0.643 0.530
E3 1.608 0.509 3.161 0.006
Residual std. error: 1.3655 on 15 degrees of freedom
height (m)
training
prediction

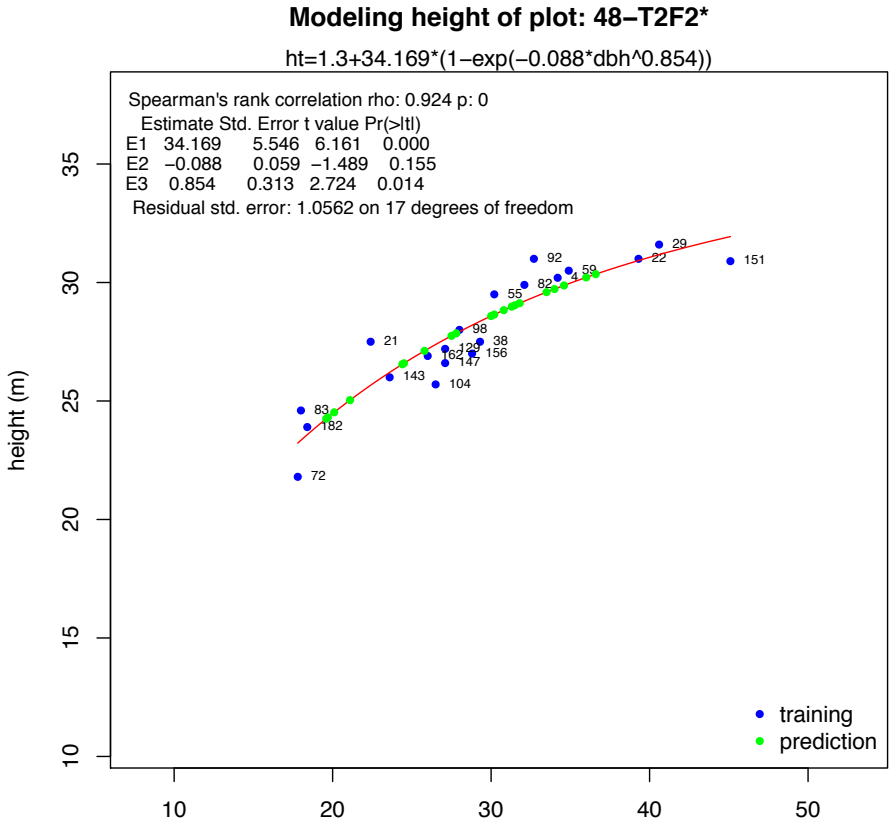

Modeling height of plot: 43–T1F2
ht=1.3+66.323*(1–exp(–0.085*dbh^0.52))
Spearman's rank correlation rho: 0.891 p: 0
Estimate Std. Error t value Pr(>|t|)
E1 66.323 294.310 0.225 0.824
E2 –0.085 0.297 –0.287 0.777
E3 0.520 0.675 0.770 0.452
Residual std. error: 1.6293 on 17 degrees of freedom
height (m)
DBH (cm)
training
prediction

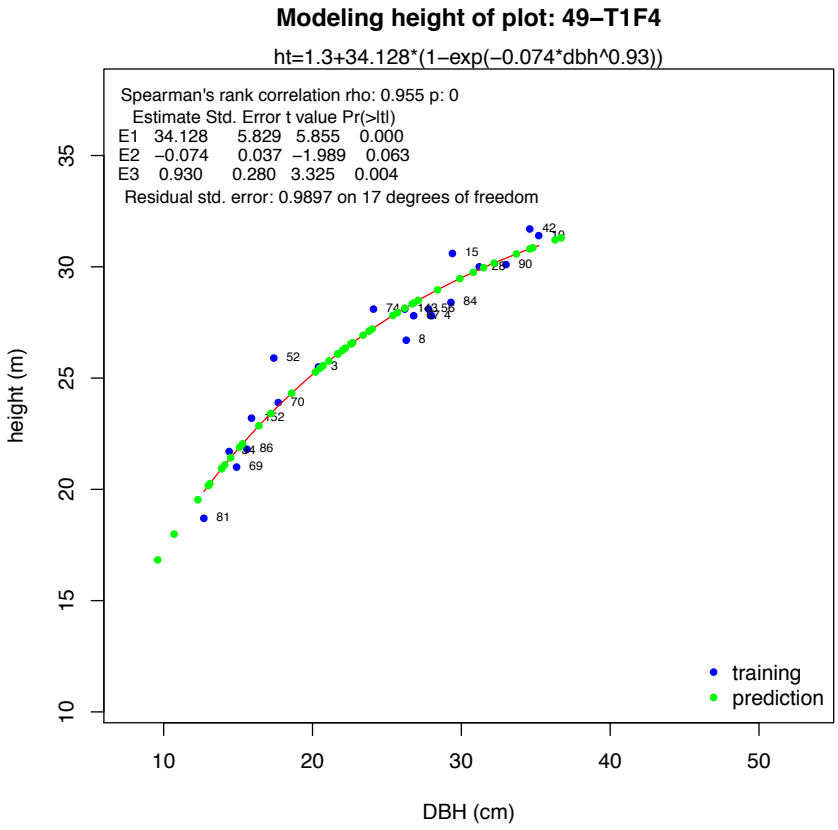

Modeling height of plot: 44–T1F1–1–1
ht=1.3+31.617*(1–exp(–0.086*dbh^0.903))
Spearman's rank correlation rho: 0.876 p: 0
Estimate Std. Error t value Pr(>|t|)
E1 31.617 6.611 4.782 0.000
E2 –0.086 0.063 –1.368 0.188
E3 0.903 0.383 2.354 0.030
Residual std. error: 1.3487 on 18 degrees of freedom
height (m)
training
prediction

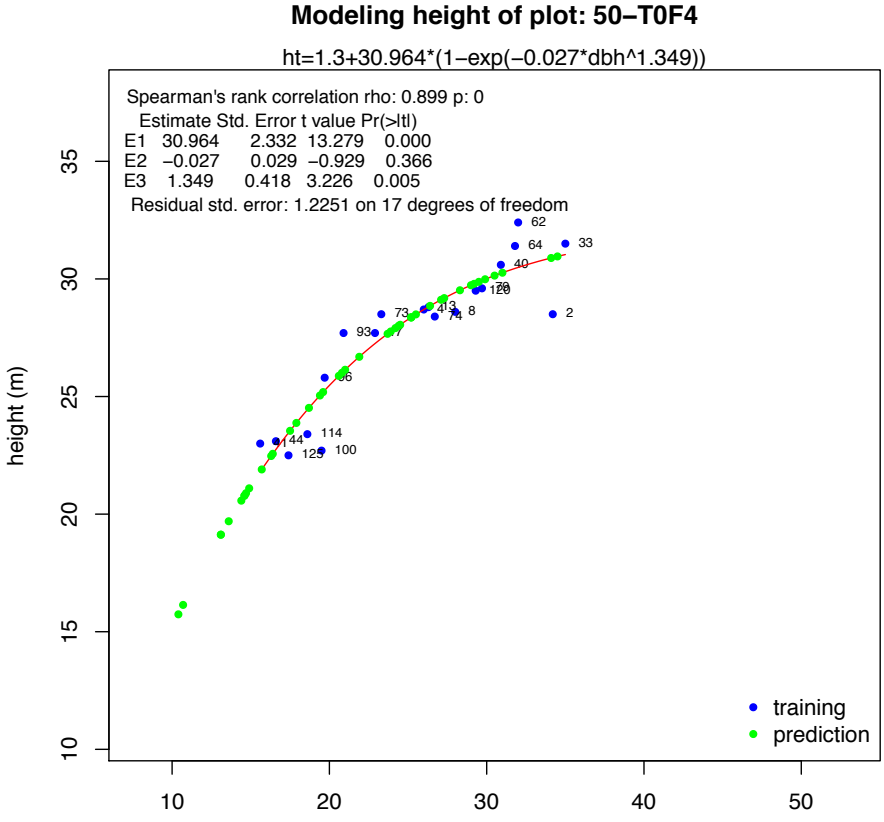

Modeling height of plot: 45–T0F2
ht=1.3+38.63*(1−exp(−0.096*dbh^0.762))
Spearman's rank correlation rho: 0.968 p: 0
Estimate Std. Error t value Pr(>|t|)
E1 38.630 15.277 2.529 0.022
E2 −0.096 0.027 −3.508 0.003
E3 0.762 0.305 2.498 0.023
Residual std. error: 1.0042 on 17 degrees of freedom
height (m)
DBH (cm)
training
prediction

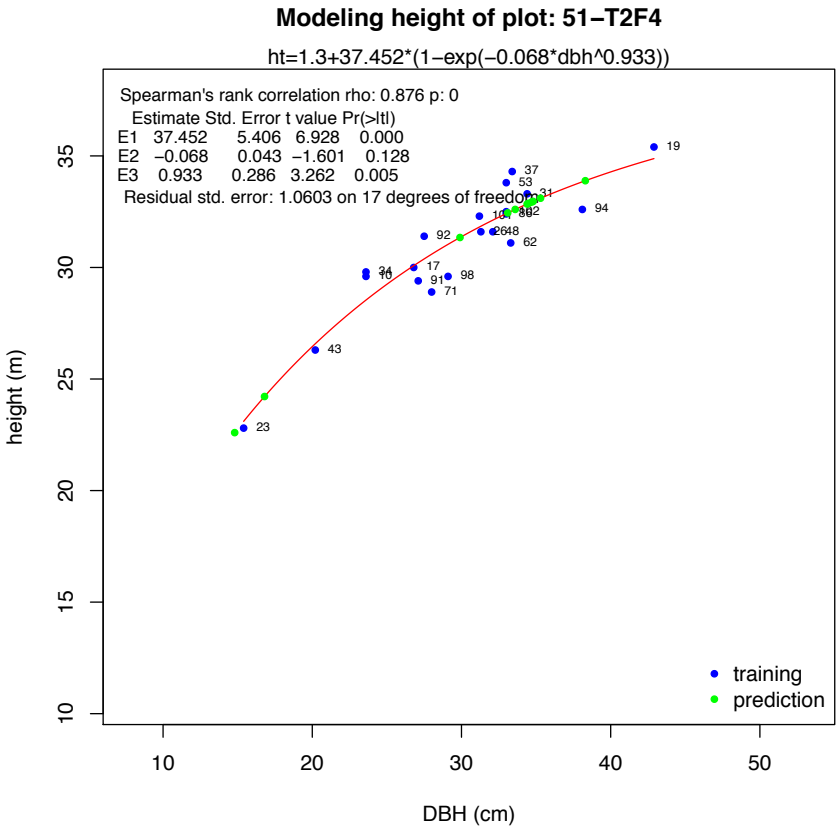

Modeling height of plot: 46–T2F3
ht=1.3+39.906*(1−exp(−0.107*dbh^0.738))
Spearman's rank correlation rho: 0.928 p: 0
Estimate Std. Error t value Pr(>|t|)
E1 39.906 13.201 3.023 0.007
E2 −0.107 0.059 −1.805 0.088
E3 0.738 0.365 2.024 0.058
Residual std. error: 0.8176 on 18 degrees of freedom
height (m)
training
prediction

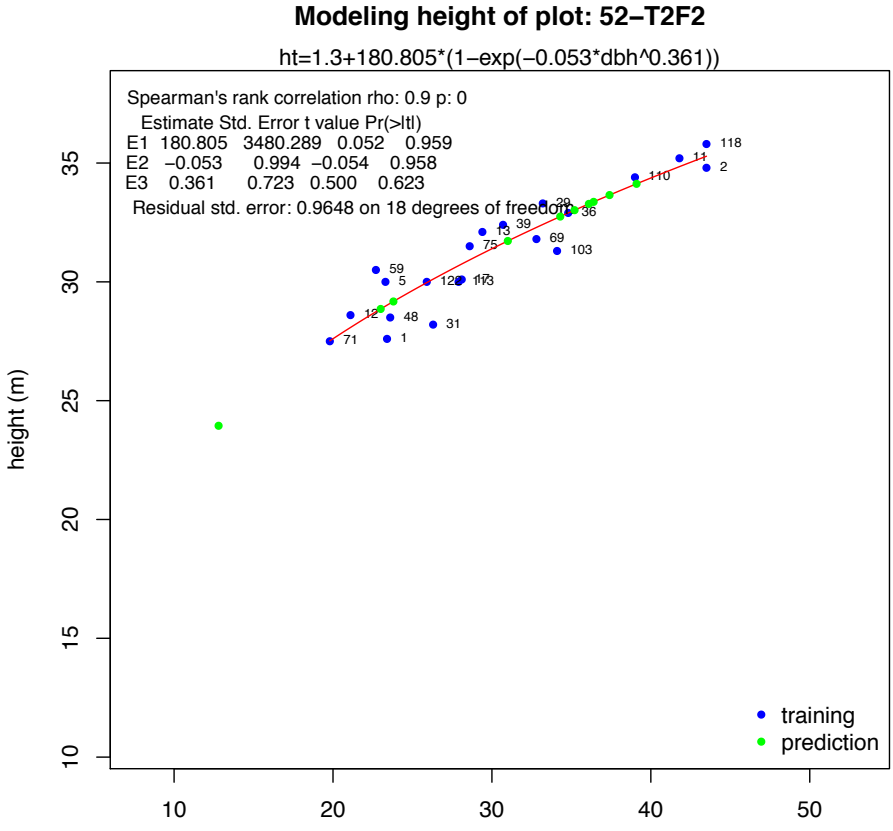

Modeling height of plot: 47–T2F6
ht=1.3+34.512*(1−exp(−0.036*dbh^1.131))
Spearman's rank correlation rho: 0.936 p: 0
Estimate Std. Error t value Pr(>|t|)
E1 34.512 2.747 12.565 0.000
E2 −0.036 0.022 −1.621 0.125
E3 1.131 0.243 4.664 0.000
Residual std. error: 0.9286 on 16 degrees of freedom
height (m)
DBH (cm)
training
prediction

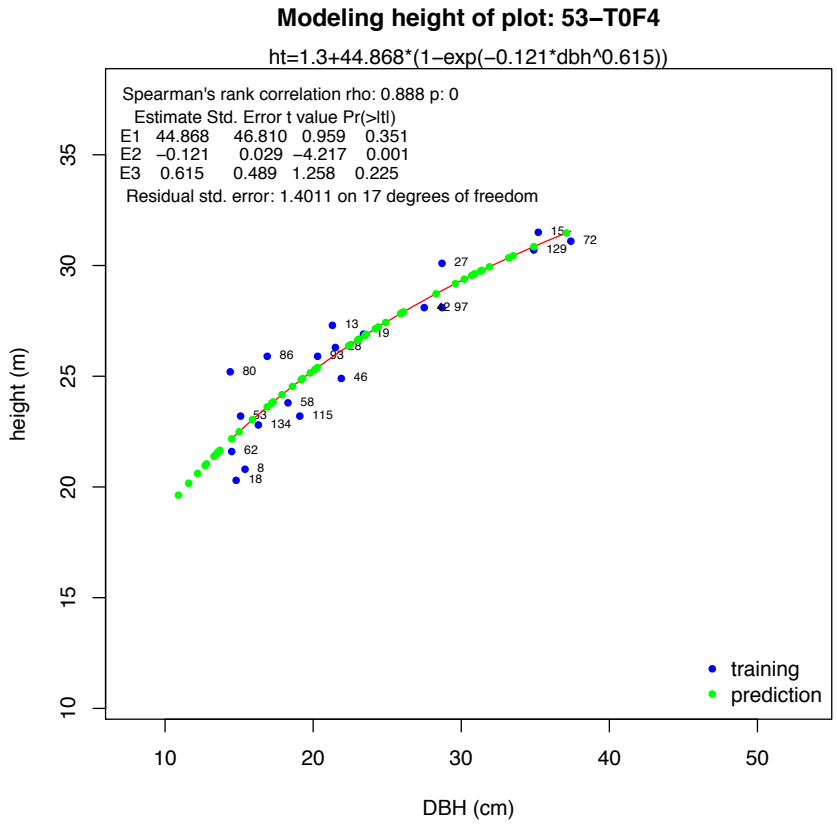

Modeling height of plot: 48–T2F2*
ht=1.3+34.169*(1−exp(−0.088*dbh^0.854))
Spearman's rank correlation rho: 0.924 p: 0
Estimate Std. Error t value Pr(>|t|)
E1 34.169 5.546 6.161 0.000
E2 −0.088 0.059 −1.489 0.155
E3 0.854 0.313 2.724 0.014
Residual std. error: 1.0562 on 17 degrees of freedom
height (m)
training
prediction

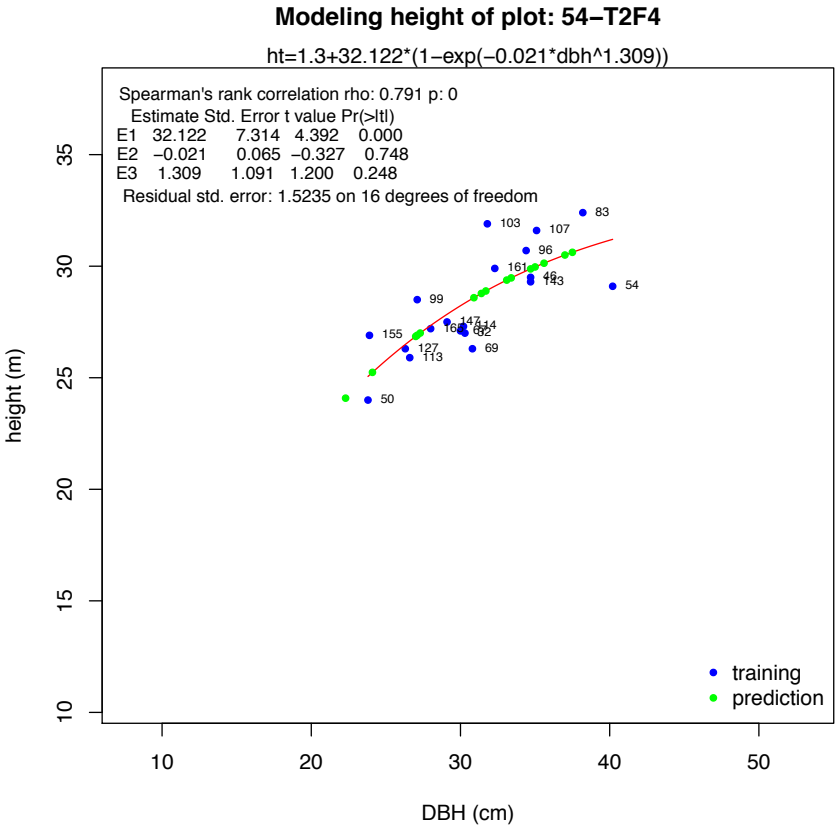

Modeling height of plot: 49–T1F4
ht=1.3+34.128*(1−exp(−0.074*dbh^0.93))
Spearman's rank correlation rho: 0.955 p: 0
Estimate Std. Error t value Pr(>|t|)
E1 34.128 5.829 5.855 0.000
E2 −0.074 0.037 −1.989 0.063
E3 0.930 0.280 3.325 0.004
Residual std. error: 0.9897 on 17 degrees of freedom
height (m)
DBH (cm)
training
prediction

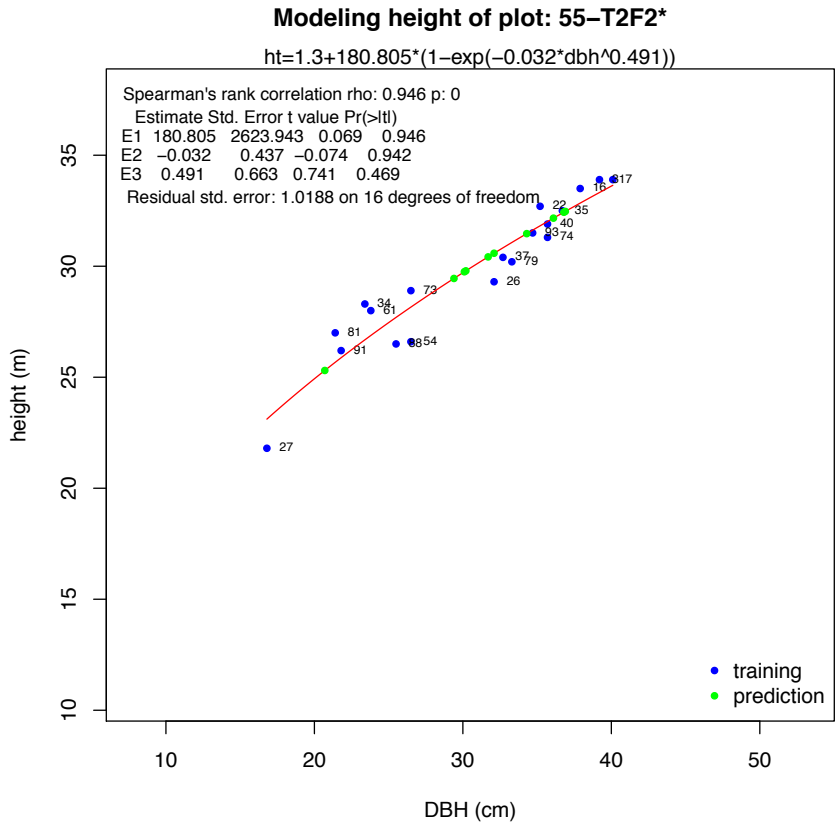

Modeling height of plot: 50–T0F4
ht=1.3+30.964*(1−exp(−0.027*dbh^1.349))
Spearman's rank correlation rho: 0.899 p: 0
Estimate Std. Error t value Pr(>|t|)
E1 30.964 2.332 13.279 0.000
E2 −0.027 0.029 −0.929 0.366
E3 1.349 0.418 3.226 0.005
Residual std. error: 1.2251 on 17 degrees of freedom
height (m)
training
prediction

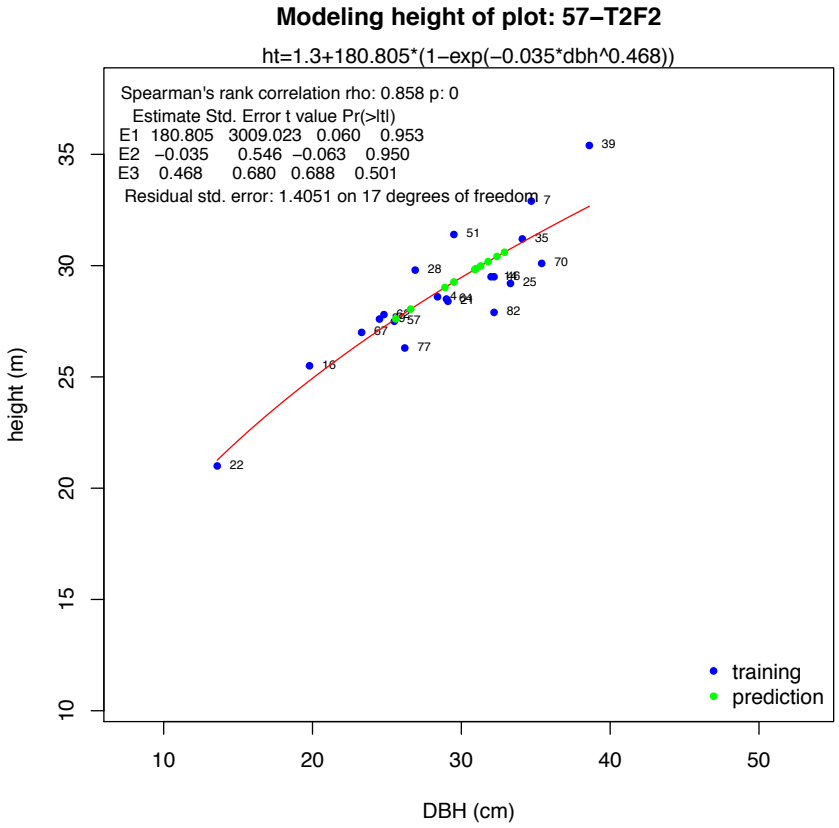

Modeling height of plot: 51−T2F4
ht=1.3+37.452*(1−exp(−0.068*dbh^0.933))
Spearman's rank correlation rho: 0.876 p: 0
Estimate Std. Error t value Pr(>|t|)
E1 37.452 5.406 6.928 0.000
E2 −0.068 0.043 −1.601 0.128
E3 0.933 0.286 3.262 0.005
Residual std. error: 1.0603 on 17 degrees of freedom
training
prediction
height (m)
DBH (cm)

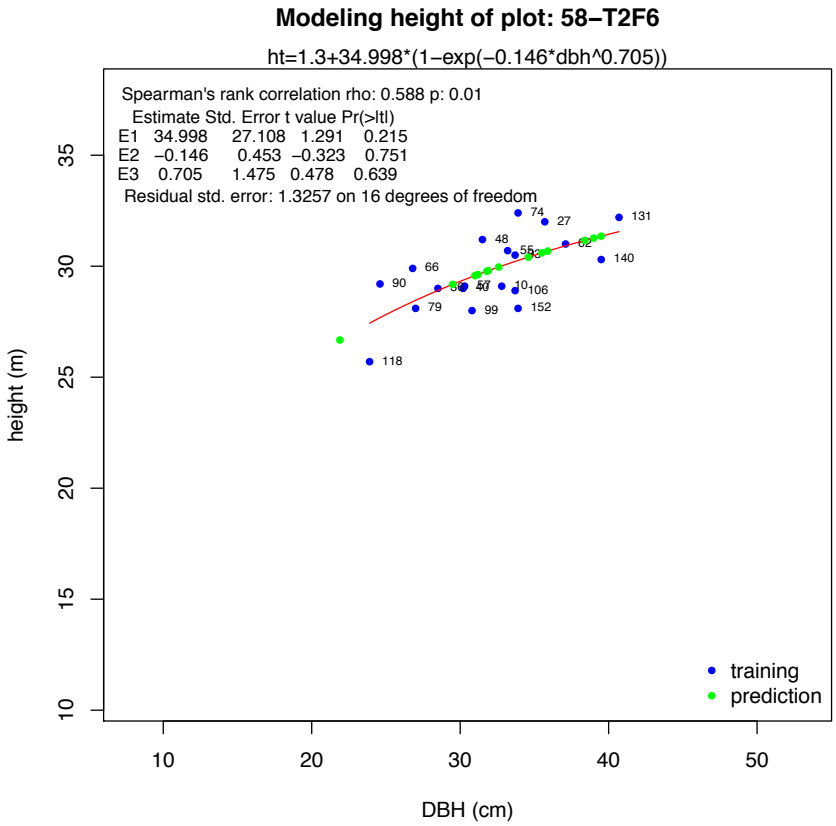

Modeling height of plot: 52−T2F2
ht=1.3+180.805*(1−exp(−0.053*dbh^0.361))
Spearman's rank correlation rho: 0.9 p: 0
Estimate Std. Error t value Pr(>|t|)
E1 180.805 3480.289 0.052 0.959
E2 −0.053 0.994 −0.054 0.958
E3 0.361 0.723 0.500 0.623
Residual std. error: 0.9648 on 18 degrees of freedom
training
prediction
height (m)

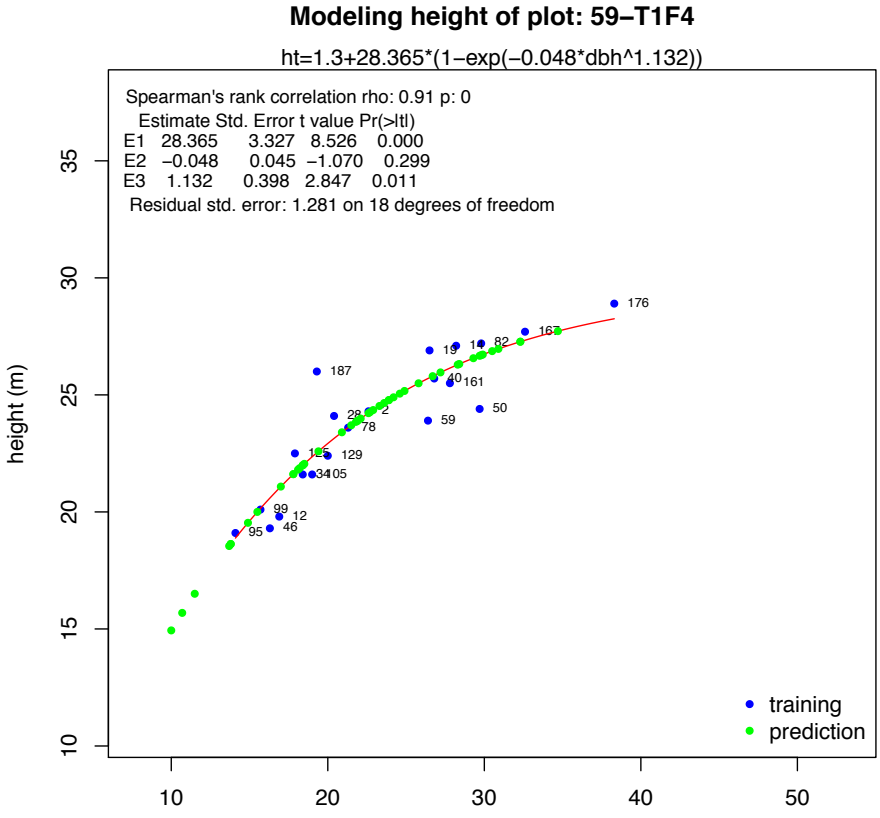

Modeling height of plot: 53–T0F4
ht=1.3+44.868*(1−exp(−0.121*dbh^0.615))
Spearman's rank correlation rho: 0.888 p: 0
Estimate Std. Error t value Pr(>|t|)
E1 44.868 46.810 0.959 0.351
E2 −0.121 0.029 −4.217 0.001
E3 0.615 0.489 1.258 0.225
Residual std. error: 1.4011 on 17 degrees of freedom
height (m)
DBH (cm)
training
prediction

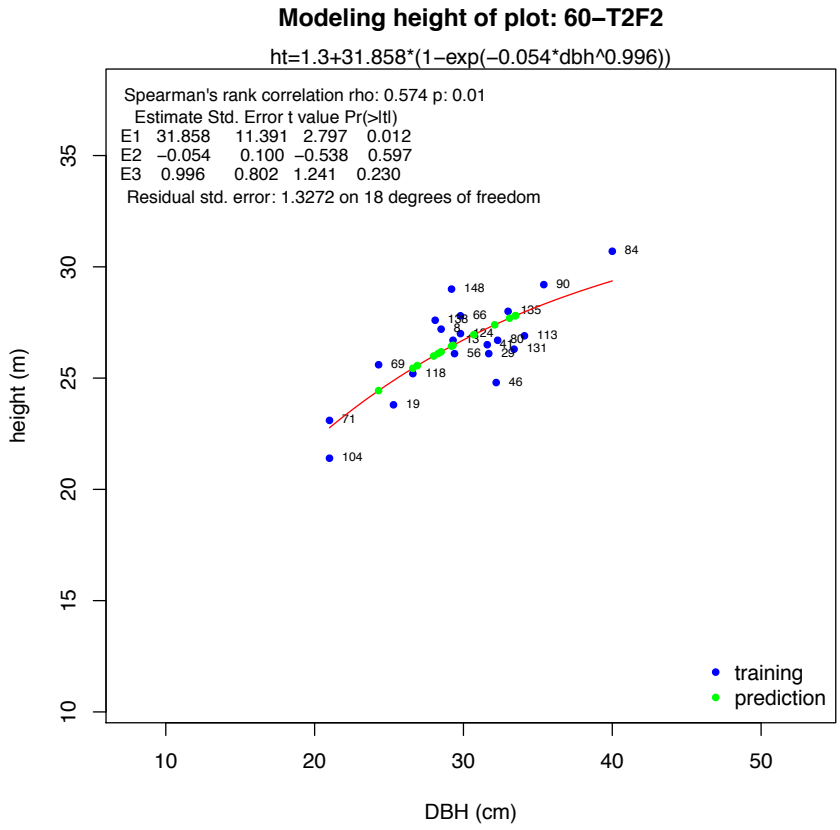

Modeling height of plot: 54–T2F4
ht=1.3+32.122*(1−exp(−0.021*dbh^1.309))
Spearman's rank correlation rho: 0.791 p: 0
Estimate Std. Error t value Pr(>|t|)
E1 32.122 7.314 4.392 0.000
E2 −0.021 0.065 −0.327 0.748
E3 1.309 1.091 1.200 0.248
Residual std. error: 1.5235 on 16 degrees of freedom
height (m)
DBH (cm)
training
prediction

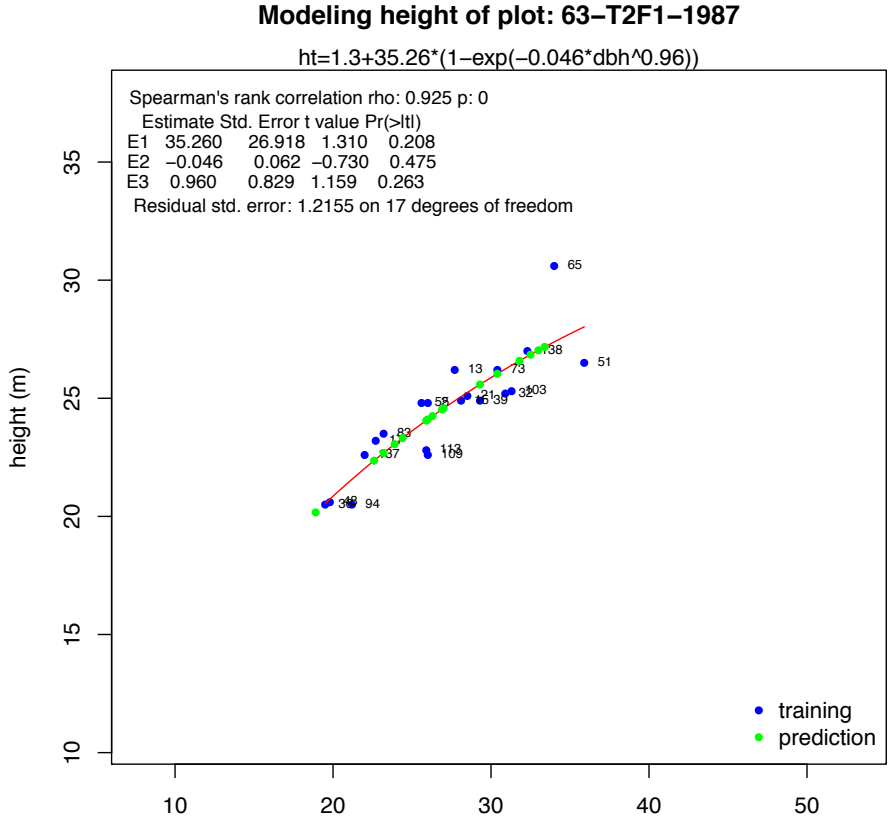

Modeling height of plot: 55–T2F2*
ht=1.3+180.805*(1−exp(−0.032*dbh^0.491))
Spearman's rank correlation rho: 0.946 p: 0
Estimate Std. Error t value Pr(>|t|)
E1 180.805 2623.943 0.069 0.946
E2 −0.032 0.437 −0.074 0.942
E3 0.491 0.663 0.741 0.469
Residual std. error: 1.0188 on 16 degrees of freedom
height (m)
DBH (cm)
training
prediction

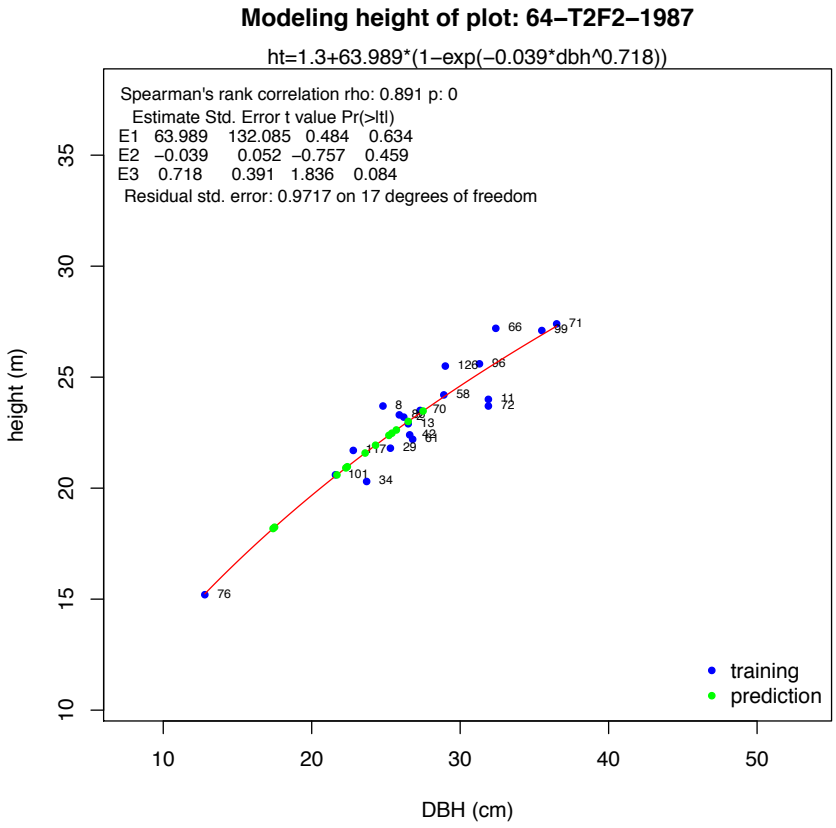

Modeling height of plot: 57–T2F2
ht=1.3+180.805*(1−exp(−0.035*dbh^0.468))
Spearman's rank correlation rho: 0.858 p: 0
Estimate Std. Error t value Pr(>|t|)
E1 180.805 3009.023 0.060 0.953
E2 −0.035 0.546 −0.063 0.950
E3 0.468 0.680 0.688 0.501
Residual std. error: 1.4051 on 17 degrees of freedom
height (m)
DBH (cm)
training
prediction

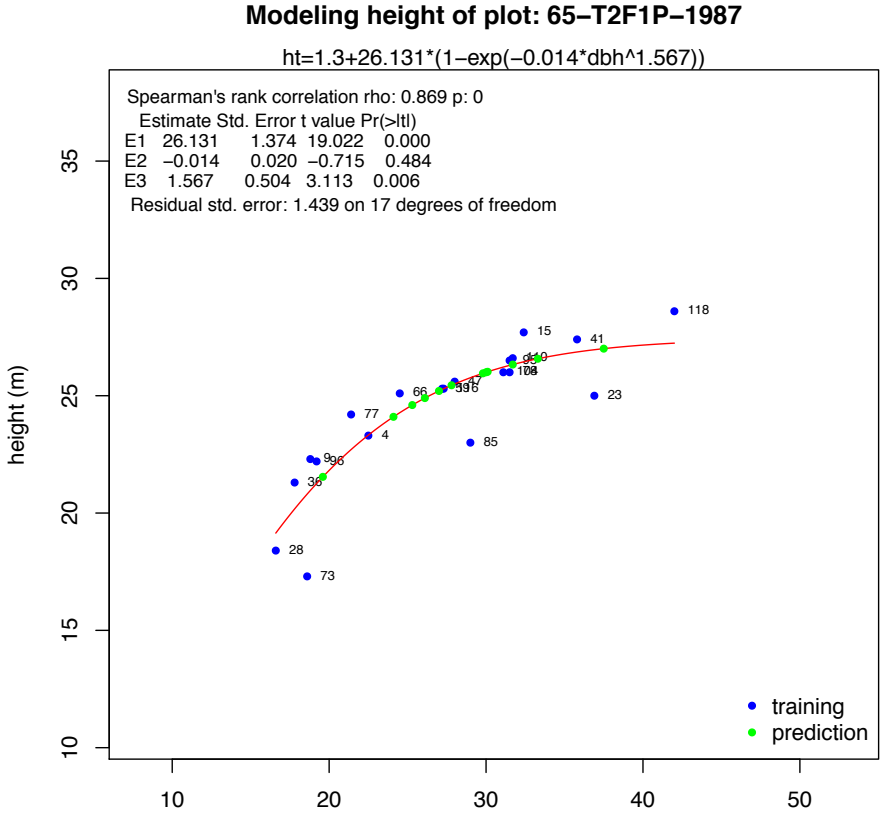

Modeling height of plot: 58–T2F6
ht=1.3+34.998*(1−exp(−0.146*dbh^0.705))
Spearman's rank correlation rho: 0.588 p: 0.01
Estimate Std. Error t value Pr(>|t|)
E1 34.998 27.108 1.291 0.215
E2 −0.146 0.453 −0.323 0.751
E3 0.705 1.475 0.478 0.639
Residual std. error: 1.3257 on 16 degrees of freedom
height (m)
DBH (cm)
training
prediction


Modeling height of plot: 59–T1F4
ht=1.3+28.365*(1−exp(−0.048*dbh^1.132))
Spearman's rank correlation rho: 0.91 p: 0
Estimate Std. Error t value Pr(>|t|)
E1 28.365 3.327 8.526 0.000
E2 −0.048 0.045 −1.070 0.299
E3 1.132 0.398 2.847 0.011
Residual std. error: 1.281 on 18 degrees of freedom
height (m)
training
prediction


Modeling height of plot: 60–T2F2
ht=1.3+31.858*(1−exp(−0.054*dbh^0.996))
Spearman's rank correlation rho: 0.574 p: 0.01
Estimate Std. Error t value Pr(>|t|)
E1 31.858 11.391 2.797 0.012
E2 −0.054 0.100 −0.538 0.597
E3 0.996 0.802 1.241 0.230
Residual std. error: 1.3272 on 18 degrees of freedom
height (m)
DBH (cm)
training
prediction

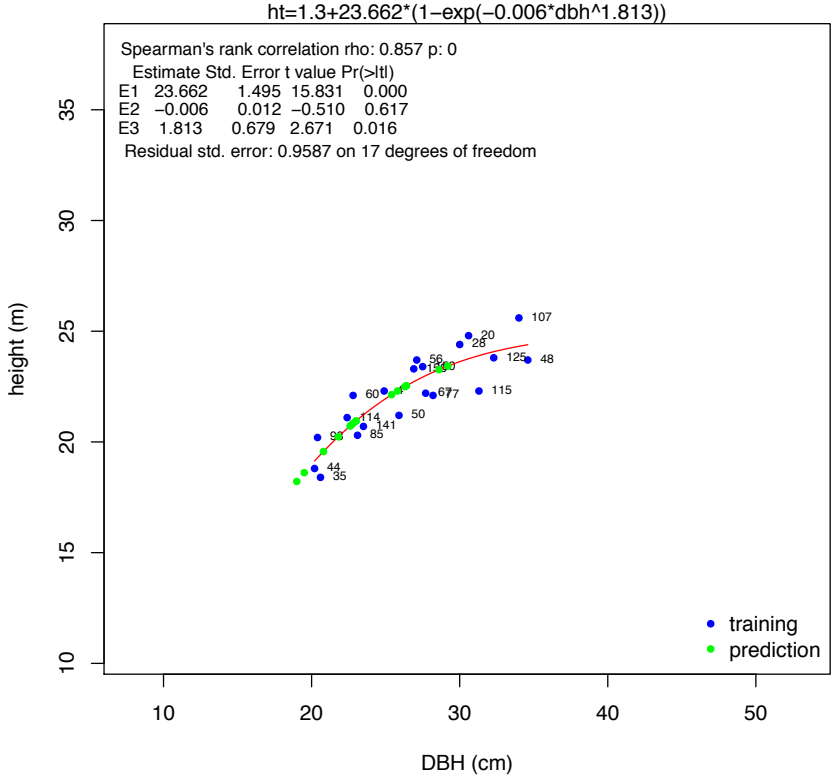

Modeling height of plot: 63–T2F1–1987
ht=1.3+35.26*(1−exp(−0.046*dbh^0.96))
Spearman's rank correlation rho: 0.925 p: 0
Estimate Std. Error t value Pr(>|t|)
E1 35.260 26.918 1.310 0.208
E2 −0.046 0.062 −0.730 0.475
E3 0.960 0.829 1.159 0.263
Residual std. error: 1.2155 on 17 degrees of freedom
height (m)
training
prediction


Modeling height of plot: 64–T2F2–1987
ht=1.3+63.989*(1−exp(−0.039*dbh^0.718))
Spearman's rank correlation rho: 0.891 p: 0
Estimate Std. Error t value Pr(>|t|)
E1 63.989 132.085 0.484 0.634
E2 −0.039 0.052 −0.757 0.459
E3 0.718 0.391 1.836 0.084
Residual std. error: 0.9717 on 17 degrees of freedom
height (m)
DBH (cm)
training
prediction


Modeling height of plot: 65–T2F1P–1987
ht=1.3+26.131*(1−exp(−0.014*dbh^1.567))
Spearman's rank correlation rho: 0.869 p: 0
Estimate Std. Error t value Pr(>|t|)
E1 26.131 1.374 19.022 0.000
E2 −0.014 0.020 −0.715 0.484
E3 1.567 0.504 3.113 0.006
Residual std. error: 1.439 on 17 degrees of freedom
height (m)
training
prediction

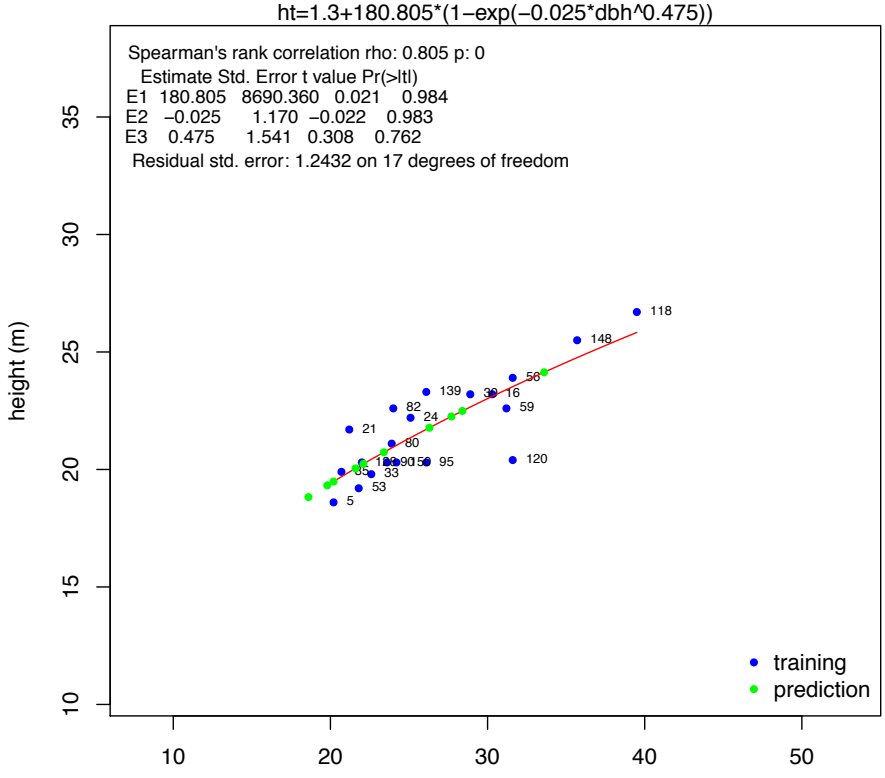
Modeling height of plot: 66–T2F2–1987

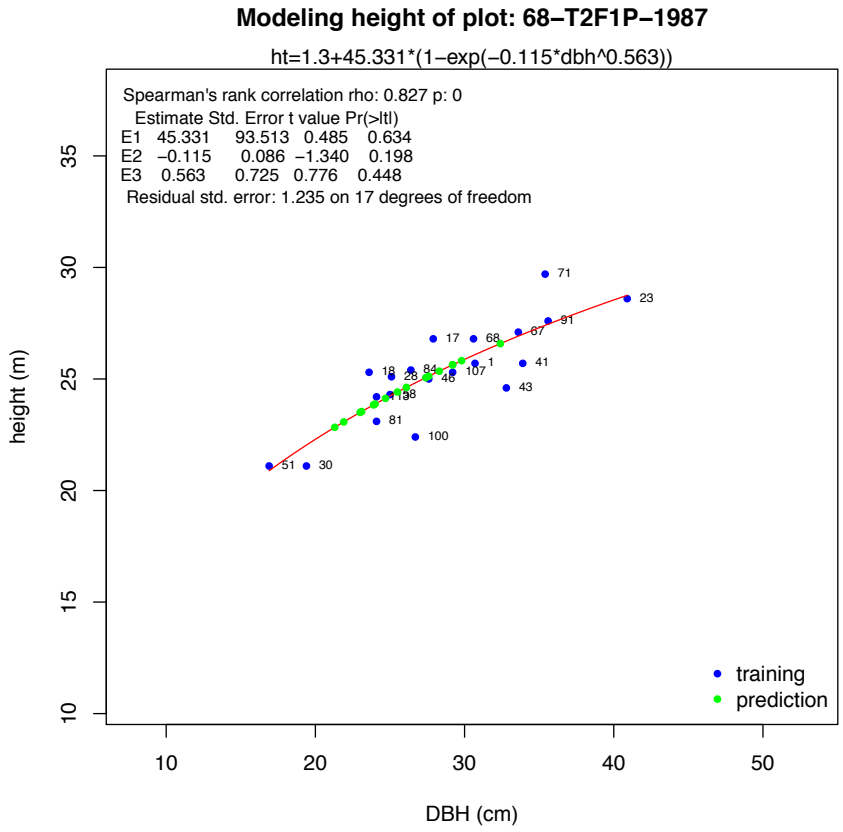
ht=1.3+23.662*(1−exp(−0.006*dbh^1.813))

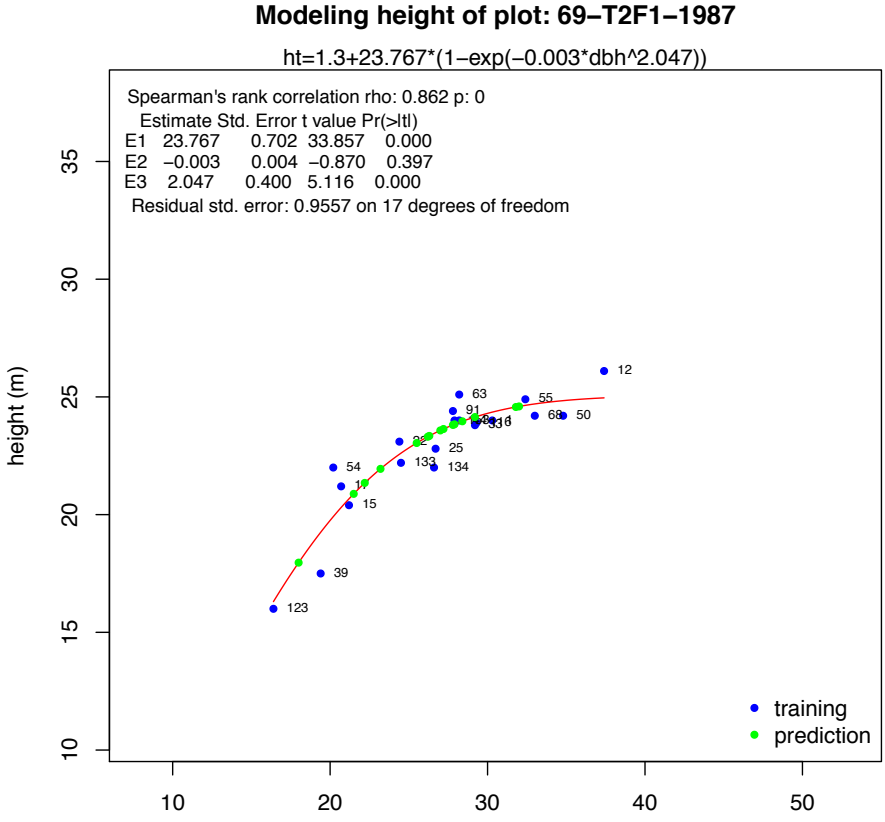


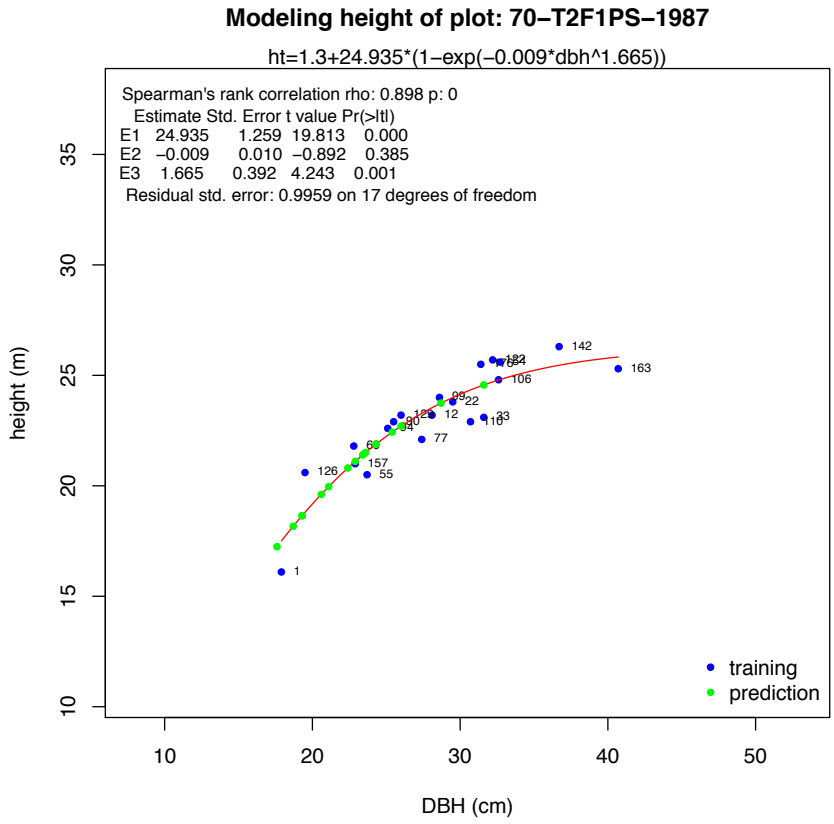
Modeling height of plot: 67–T2F1PS–1987

ht=1.3+180.805*(1−exp(−0.025*dbh^0.475))




Modeling height of plot: 68–T2F1P–1987
ht=1.3+45.331*(1–exp(–0.115*dbh^0.563))
Spearman's rank correlation rho: 0.827 p: 0
Estimate Std. Error t value Pr(>|t|)
E1 45.331 93.513 0.485 0.634
E2 –0.115 0.086 –1.340 0.198
E3 0.563 0.725 0.776 0.448
Residual std. error: 1.235 on 17 degrees of freedom
height (m)
DBH (cm)
training
prediction


Modeling height of plot: 69–T2F1–1987
ht=1.3+23.767*(1–exp(–0.003*dbh^2.047))
Spearman's rank correlation rho: 0.862 p: 0
Estimate Std. Error t value Pr(>|t|)
E1 23.767 0.702 33.857 0.000
E2 –0.003 0.004 –0.870 0.397
E3 2.047 0.400 5.116 0.000
Residual std. error: 0.9557 on 17 degrees of freedom
height (m)
training
prediction


Modeling height of plot: 70–T2F1PS–1987
ht=1.3+24.935*(1–exp(–0.009*dbh^1.665))
Spearman's rank correlation rho: 0.898 p: 0
Estimate Std. Error t value Pr(>|t|)
E1 24.935 1.259 19.813 0.000
E2 –0.009 0.010 –0.892 0.385
E3 1.665 0.392 4.243 0.001
Residual std. error: 0.9959 on 17 degrees of freedom
height (m)
DBH (cm)
training
prediction

1.3 *Plot Based Volume Increment Boxplots*

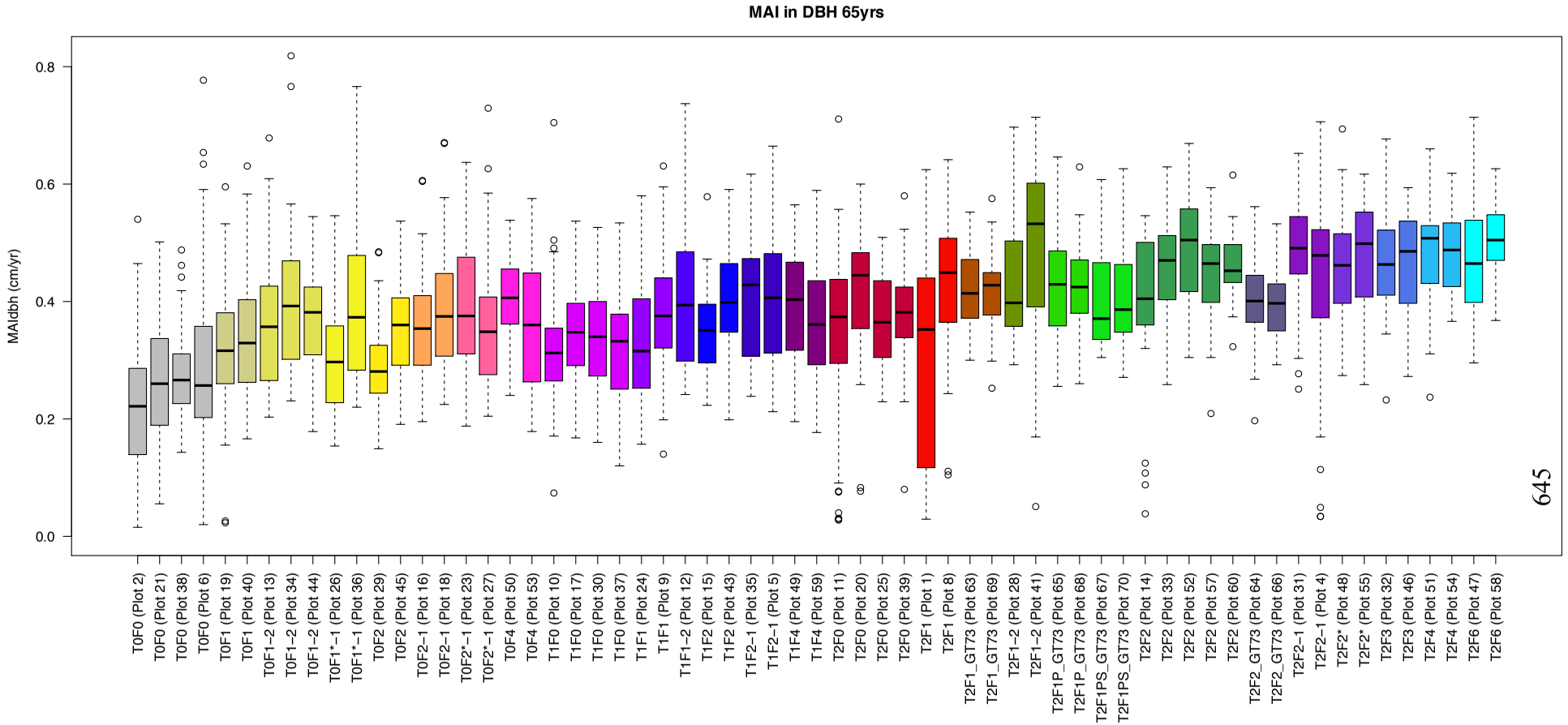


Figure 239. Boxplots of plot MAI of DBH distributions illustrating differences in central tendency and spread. The data are graphed by quartiles, the largest and smallest point no greater than 1.5*(IQR) from the median and all points greater than those limits. Although the treatments are indicated in the data labels they are also color coded to ease the use of such a large number of distributions.

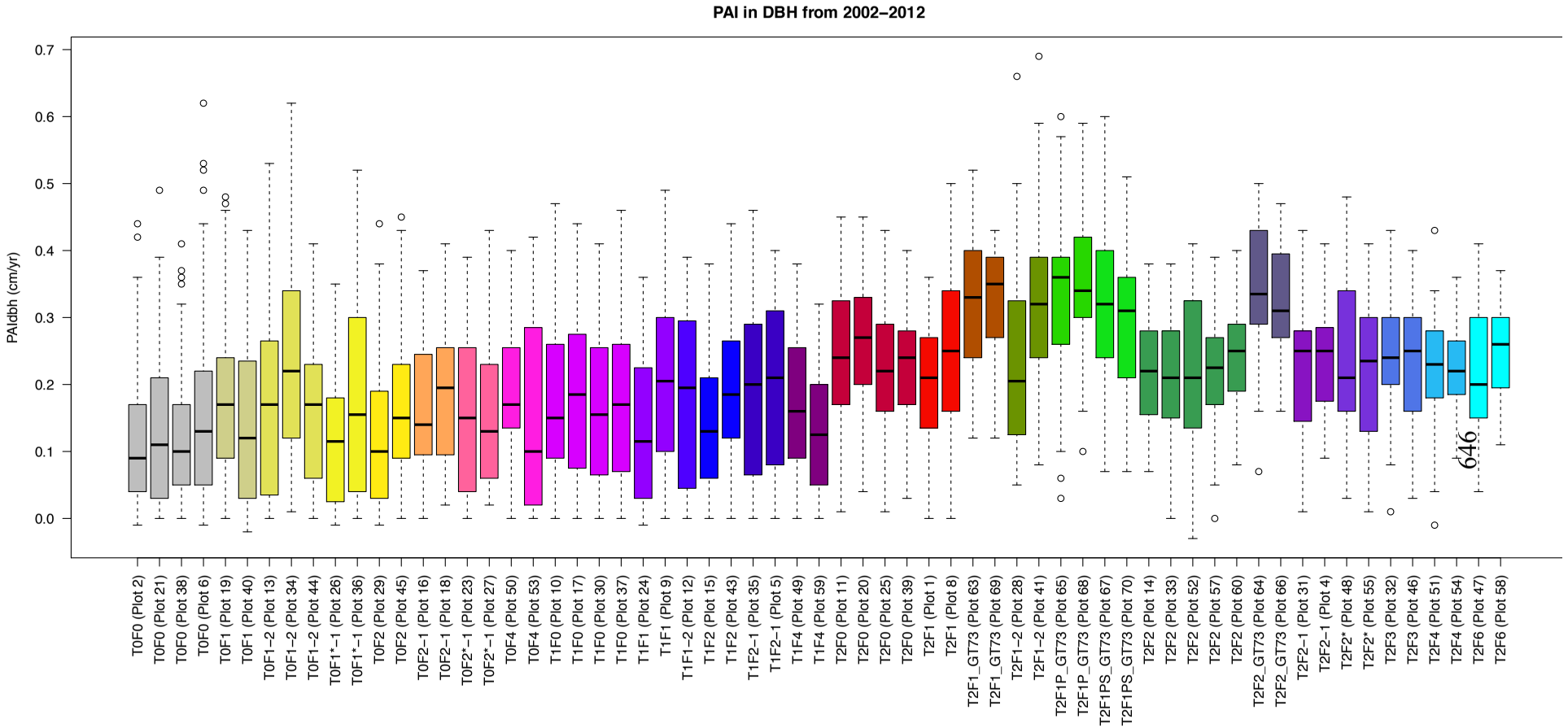


Figure 240. Boxplots of plot PAI of DBH distributions illustrating differences in central tendency and spread. The data are graphed by quartiles, the largest and smallest point no greater than 1.5*(IQR) from the median and all points greater than those limits. Although the treatments are indicated in the data labels they are also color coded to ease the use of such a large number of distributions.

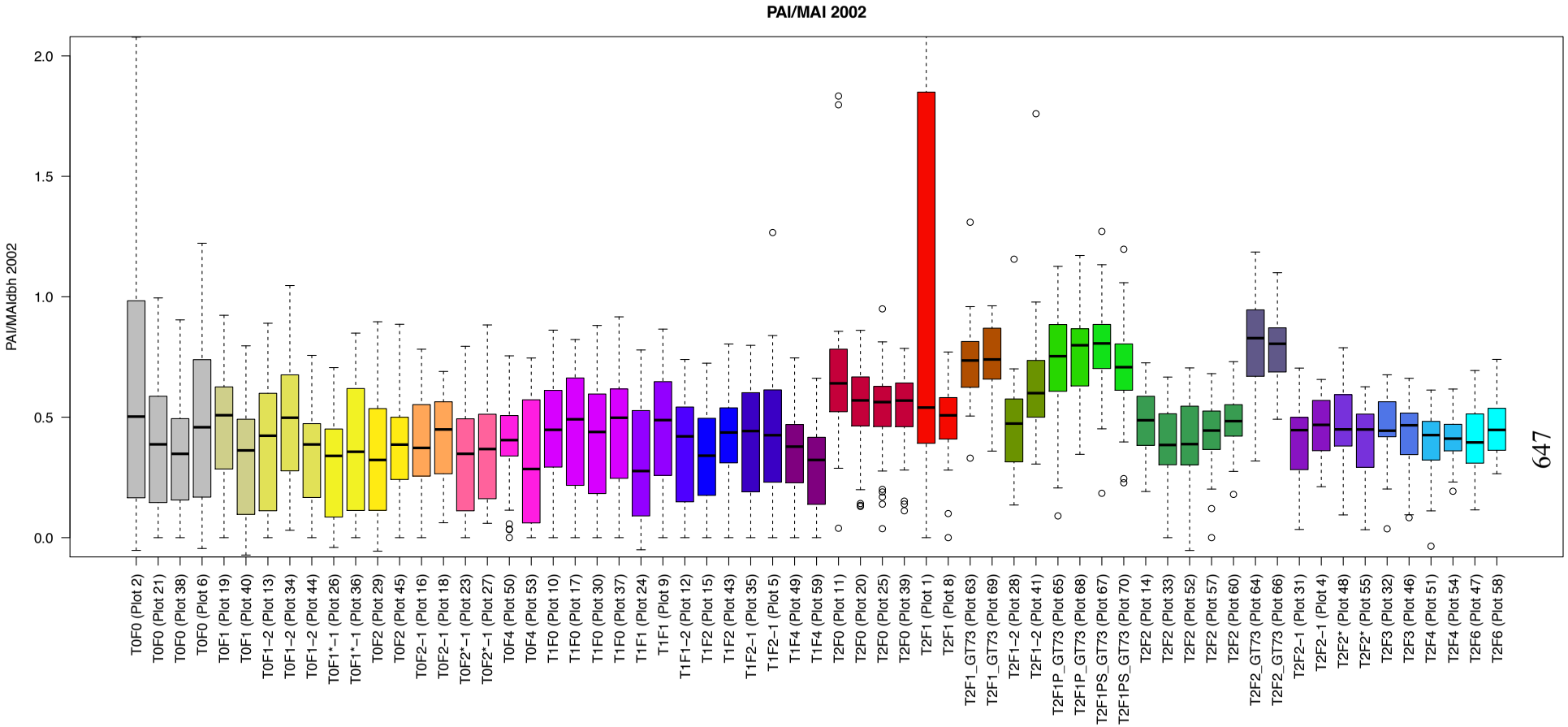


Figure 241. Boxplots of plot PAI/MAI of DBH distributions illustrating differences in central tendency and spread. The data are graphed by quartiles, the largest and smallest point no greater than 1.5*(IQR) from the median and all points greater than those limits. Although the treatments are indicated in the data labels they are also color coded to ease the use of such a large number of distributions.

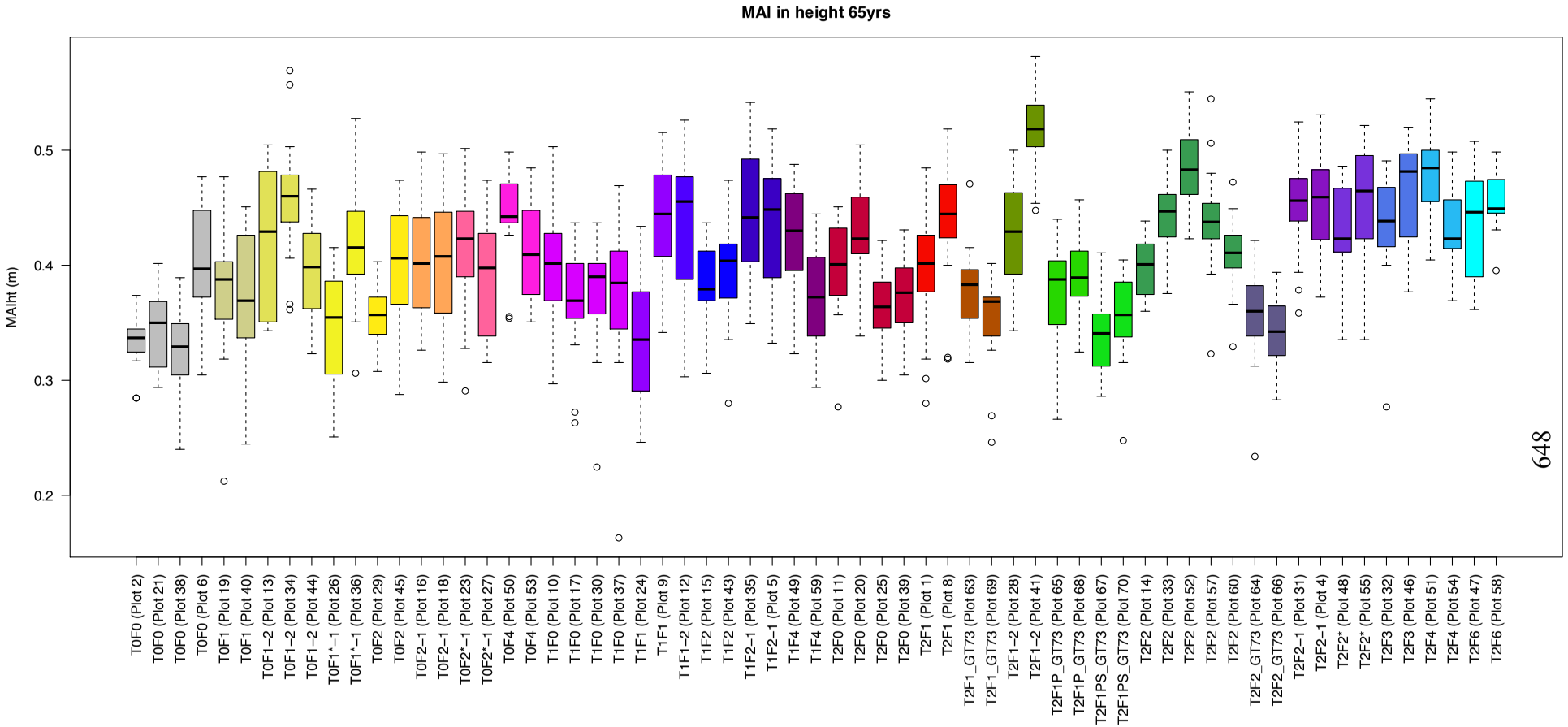


Figure 242. Boxplots of plot MAI of measured height distributions illustrating differences in central tendency and spread. The data are graphed by quartiles, the largest and smallest point no greater than 1.5*(IQR) from the median and all points greater than those limits. Although the treatments are indicated in the data labels they are also color coded to ease the use of such a large number of distributions.

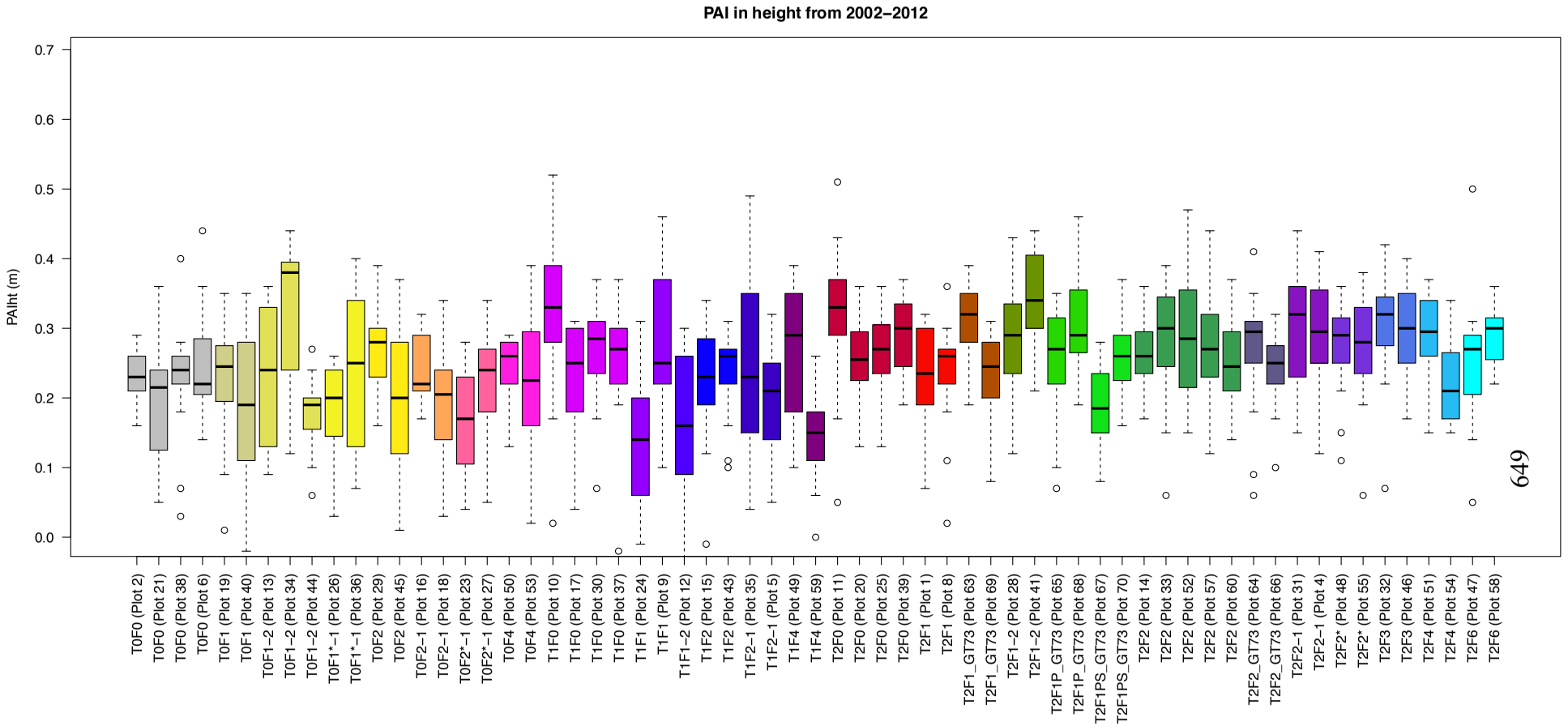


Figure 243. Boxplots of plot PAI of measured height distributions illustrating differences in central tendency and spread. The data are graphed by quartiles, the largest and smallest point no greater than 1.5*(IQR) from the median and all points greater than those limits. Although the treatments are indicated in the data labels they are also color coded to ease the use of such a large number of distributions.

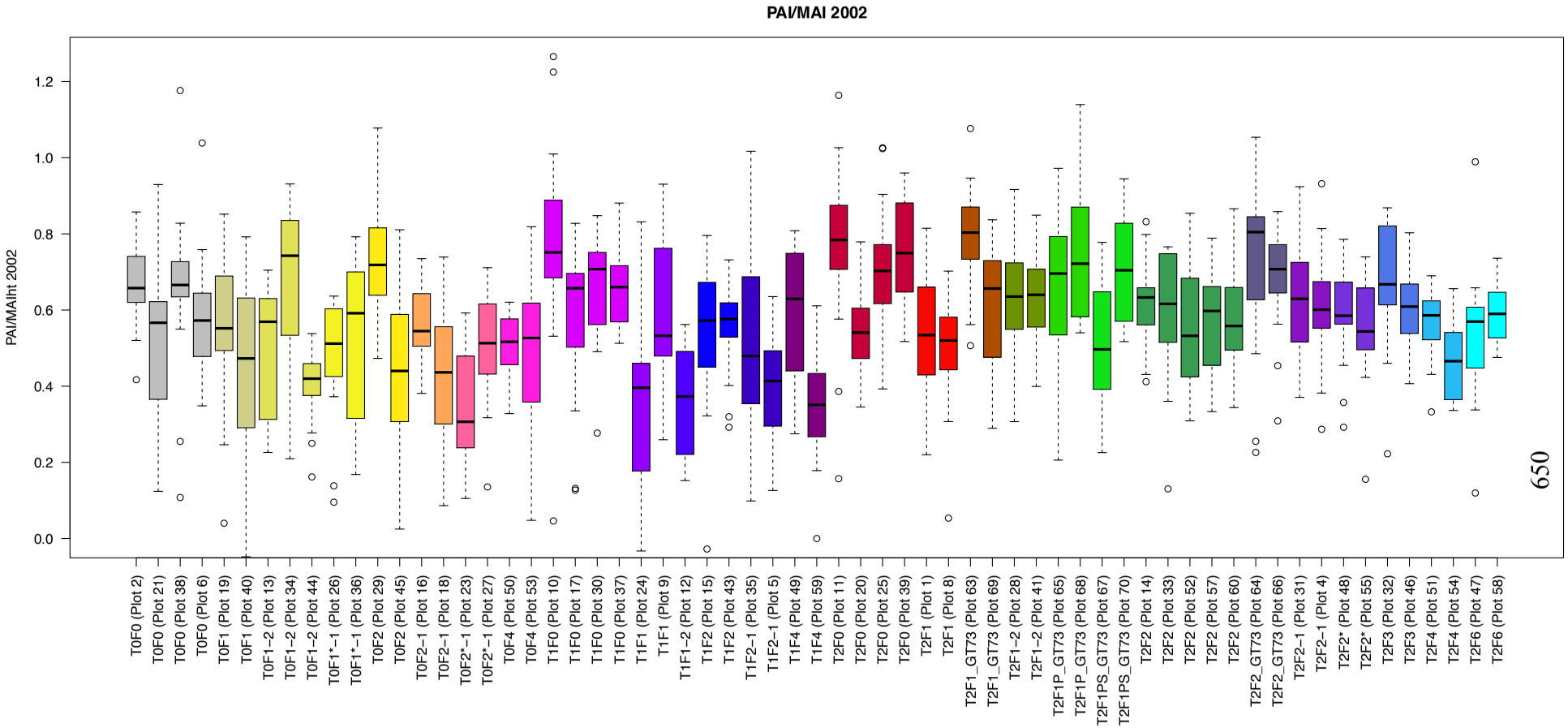


Figure 244. Boxplots of plot PAI/MAI of measured height distributions illustrating differences in central tendency and spread. The data are graphed by quartiles, the largest and smallest point no greater than 1.5*(IQR) from the median and all points greater than those limits. Although the treatments are indicated in the data labels they are also color coded to ease the use of such a large number of distributions.

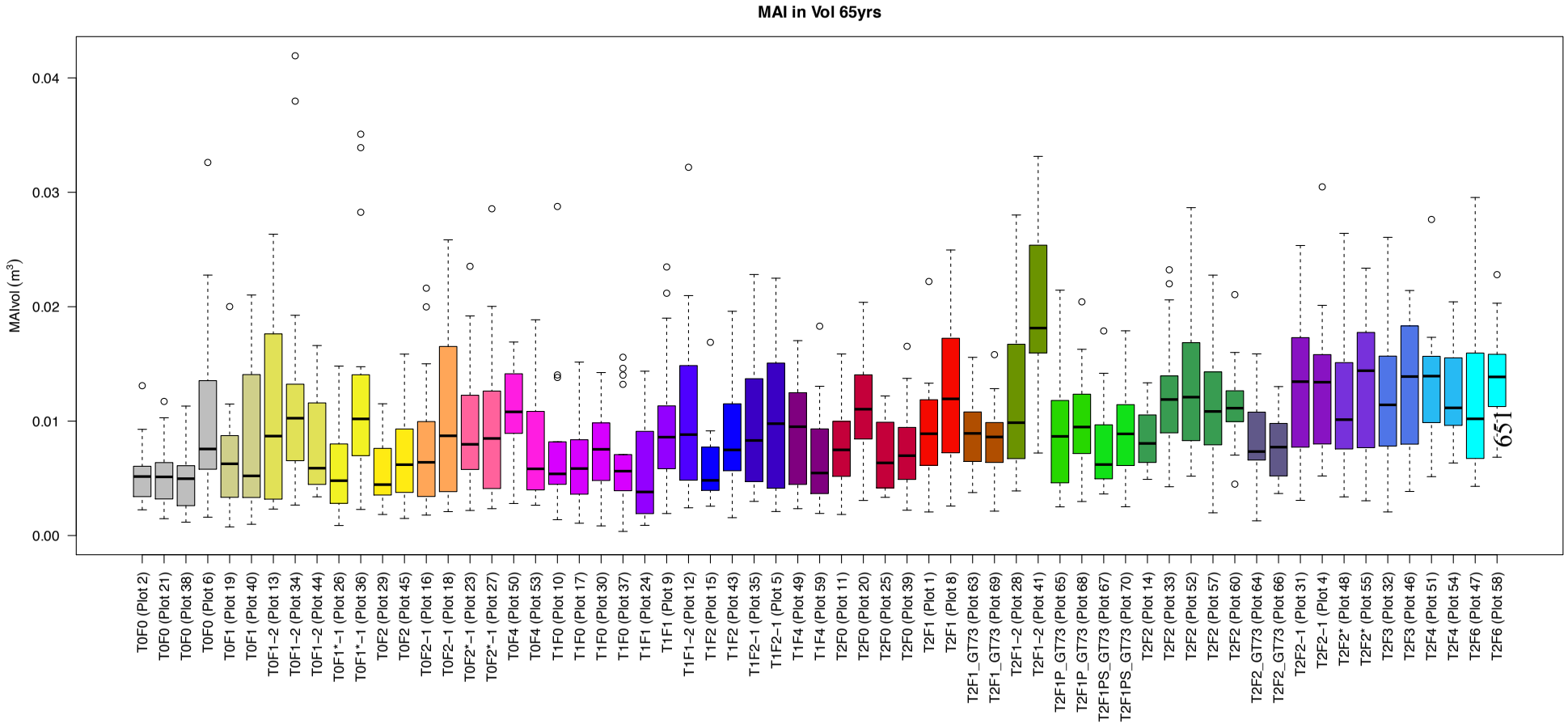


Figure 245. Boxplots of plot MAI of volume with measured height distributions illustrating differences in central tendency and spread. The data are graphed by quartiles, the largest and smallest point no greater than 1.5*(IQR) from the median and all points greater than those limits. Although the treatments are indicated in the data labels they are also color coded to ease the use of such a large number of distributions.

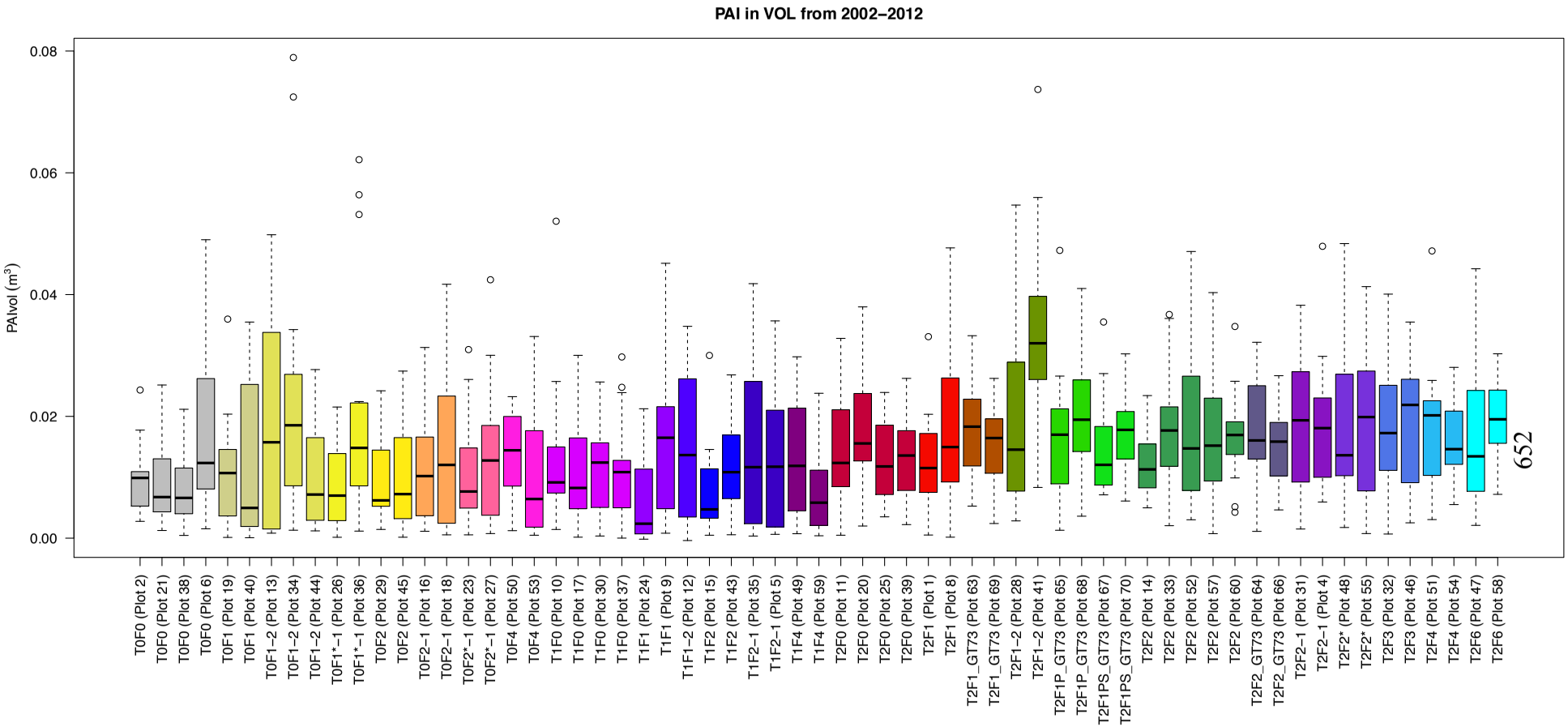


Figure 246. Boxplots of plot PAI of volume with measured height distributions illustrating differences in central tendency and spread. The data are graphed by quartiles, the largest and smallest point no greater than 1.5*(IQR) from the median and all points greater than those limits. Although the treatments are indicated in the data labels they are also color coded to ease the use of such a large number of distributions.

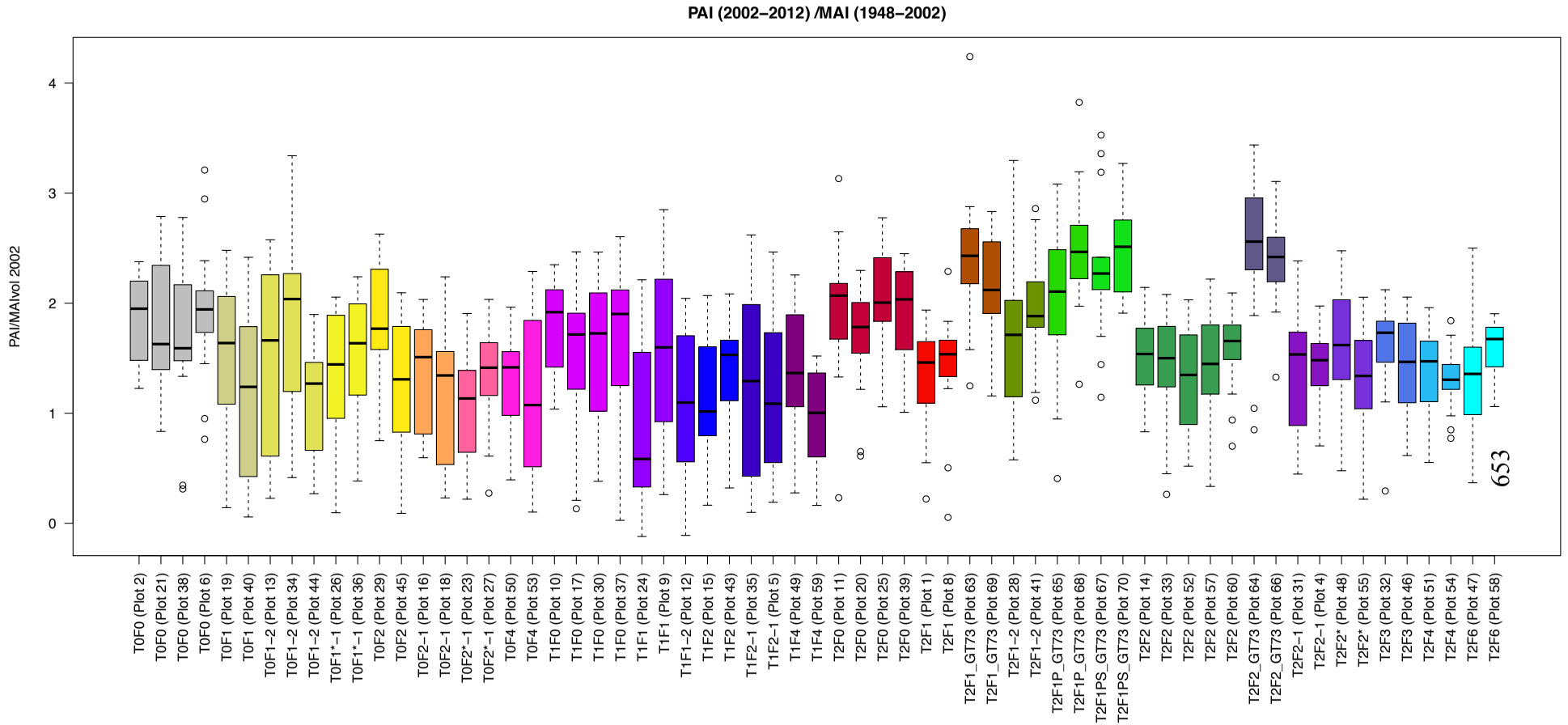


Figure 247. Boxplots of plot PAI/MAI of volume with measured height distributions illustrating differences in central tendency and spread. The data are graphed by quartiles, the largest and smallest point no greater than 1.5*(IQR) from the median and all points greater than those limits. Although the treatments are indicated in the data labels they are also color coded to ease the use of such a large number of distributions.

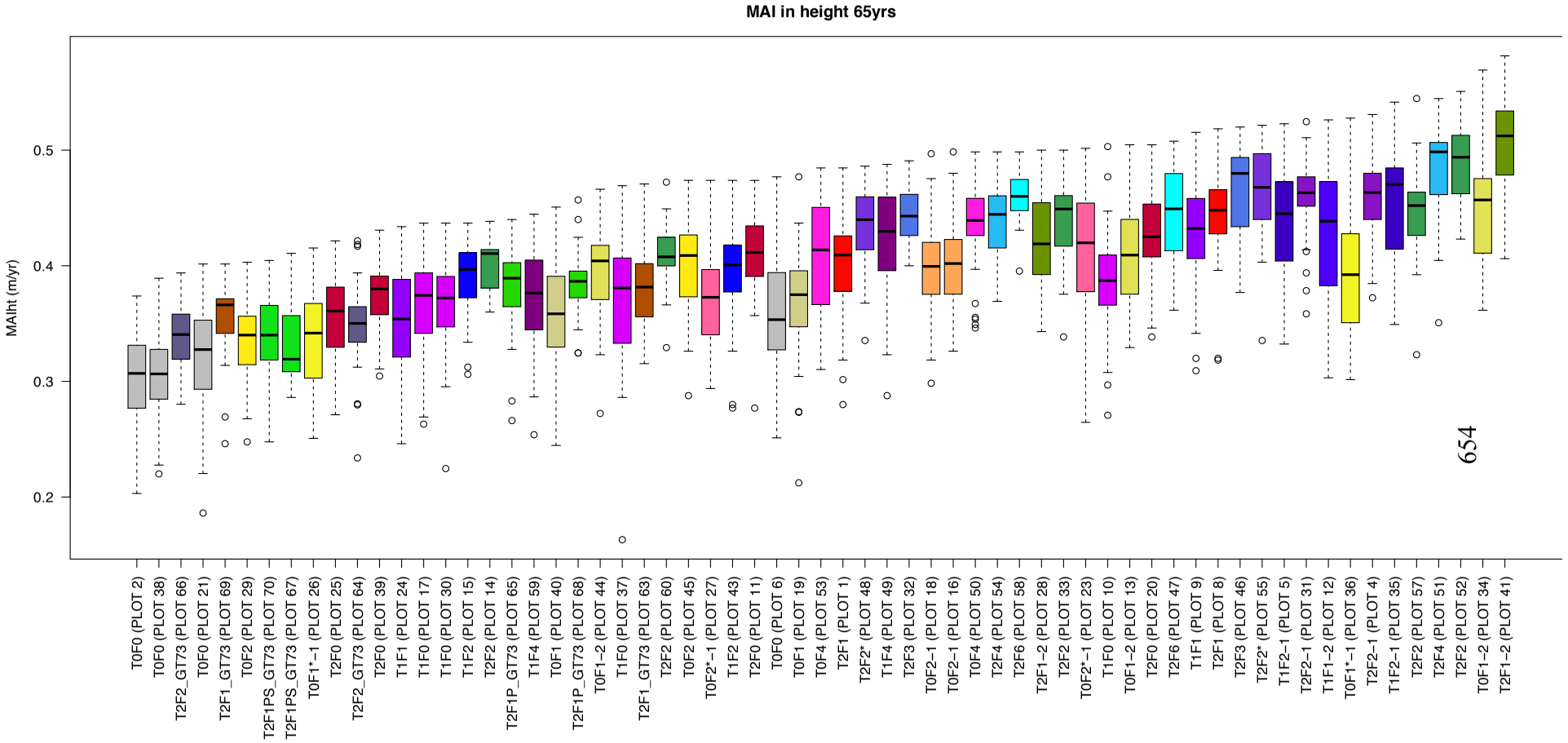


Figure 248. Boxplots of MAI of height with measured and modeled height illustrating differences in central tendency and spread. The data are graphed by quartiles, the largest and smallest point no greater than 1.5*(IQR) from the median and all points greater than those limits. Although the treatments are indicated in the data labels they are also color coded to ease the use of such a large number of distributions.

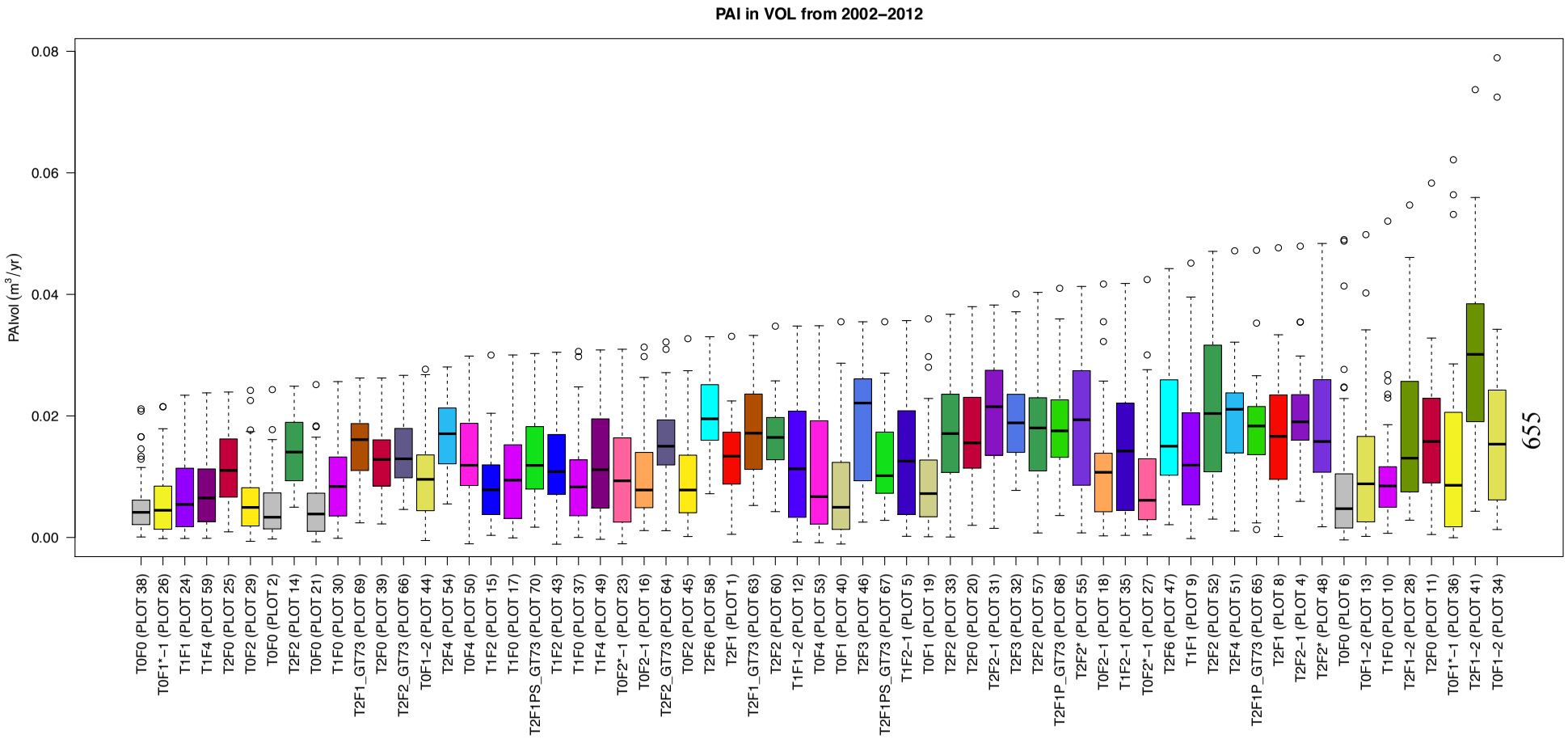


Figure 249. Boxplots of plot PAI of volume with measured and modeled height distributions illustrating differences in central tendency and spread. The data are graphed by quartiles, the largest and smallest point no greater than 1.5*(IQR) from the median and all points greater than those limits. Although the treatments are indicated in the data labels they are also color coded to ease the use of such a large number of distributions.